frontiers | Research Topics

(Paleo-) Pacific plate subduction tectonics and related magmatism and mineralization

Edited by
Fan Yang, Fei Xue, Gilby Jepson and Liang Zhang

Published in
Frontiers in Earth Science



FRONTIERS EBOOK COPYRIGHT STATEMENT

The copyright in the text of individual articles in this ebook is the property of their respective authors or their respective institutions or funders. The copyright in graphics and images within each article may be subject to copyright of other parties. In both cases this is subject to a license granted to Frontiers.

The compilation of articles constituting this ebook is the property of Frontiers.

Each article within this ebook, and the ebook itself, are published under the most recent version of the Creative Commons CC-BY licence. The version current at the date of publication of this ebook is CC-BY 4.0. If the CC-BY licence is updated, the licence granted by Frontiers is automatically updated to the new version.

When exercising any right under the CC-BY licence, Frontiers must be attributed as the original publisher of the article or ebook, as applicable.

Authors have the responsibility of ensuring that any graphics or other materials which are the property of others may be included in the CC-BY licence, but this should be checked before relying on the CC-BY licence to reproduce those materials. Any copyright notices relating to those materials must be complied with.

Copyright and source acknowledgement notices may not be removed and must be displayed in any copy, derivative work or partial copy which includes the elements in question.

All copyright, and all rights therein, are protected by national and international copyright laws. The above represents a summary only. For further information please read Frontiers' Conditions for Website Use and Copyright Statement, and the applicable CC-BY licence.

ISSN 1664-8714
ISBN 978-2-8325-3044-3
DOI 10.3389/978-2-8325-3044-3

About Frontiers

Frontiers is more than just an open access publisher of scholarly articles: it is a pioneering approach to the world of academia, radically improving the way scholarly research is managed. The grand vision of Frontiers is a world where all people have an equal opportunity to seek, share and generate knowledge. Frontiers provides immediate and permanent online open access to all its publications, but this alone is not enough to realize our grand goals.

Frontiers journal series

The Frontiers journal series is a multi-tier and interdisciplinary set of open-access, online journals, promising a paradigm shift from the current review, selection and dissemination processes in academic publishing. All Frontiers journals are driven by researchers for researchers; therefore, they constitute a service to the scholarly community. At the same time, the *Frontiers journal series* operates on a revolutionary invention, the tiered publishing system, initially addressing specific communities of scholars, and gradually climbing up to broader public understanding, thus serving the interests of the lay society, too.

Dedication to quality

Each Frontiers article is a landmark of the highest quality, thanks to genuinely collaborative interactions between authors and review editors, who include some of the world's best academicians. Research must be certified by peers before entering a stream of knowledge that may eventually reach the public - and shape society; therefore, Frontiers only applies the most rigorous and unbiased reviews. Frontiers revolutionizes research publishing by freely delivering the most outstanding research, evaluated with no bias from both the academic and social point of view. By applying the most advanced information technologies, Frontiers is catapulting scholarly publishing into a new generation.

What are Frontiers Research Topics?

Frontiers Research Topics are very popular trademarks of the *Frontiers journals series*: they are collections of at least ten articles, all centered on a particular subject. With their unique mix of varied contributions from Original Research to Review Articles, Frontiers Research Topics unify the most influential researchers, the latest key findings and historical advances in a hot research area.

Find out more on how to host your own Frontiers Research Topic or contribute to one as an author by contacting the Frontiers editorial office: frontiersin.org/about/contact

(Paleo-) Pacific plate subduction tectonics and related magmatism and mineralization

Topic editors

Fan Yang — Lanzhou University, China
Fei Xue — Hohai University, China
Gilby Jepson — University of Oklahoma, United States
Liang Zhang — China University of Geosciences, China

Citation

Yang, F., Xue, F., Jepson, G., Zhang, L., eds. (2023). *(Paleo-) Pacific plate subduction tectonics and related magmatism and mineralization*. Lausanne: Frontiers Media SA. doi: 10.3389/978-2-8325-3044-3

Table of contents

06 Editorial: (Paleo-) Pacific plate subduction tectonics and related magmatism and mineralization
Fan Yang, Fei Xue, Gilby Jepson and Liang Zhang

11 Batholith recorded mesozoic multistage tectonic evolution of the South china block: A case study of the guandimiao intrusions
Jin-Hua Qin, Fan Huang and Deng-Hong Wang

43 Deep exploration of Jiaodong type gold deposit, taking Shanhou gold deposit, southern part of Zhaoping fault as an example
Zhi-He Xu, Zheng-Jiang Ding, Guan-Wen Gu, Ji-Yi Jiang, Li Wang and Xing-Guo Niu

54 Identifying the source of gold geochemical anomalies in Jiaodong, eastern China: Tracking the occurrence of gold nanoparticles in a metallogenic system
Ruihong Li, Xueqiu Wang, Bimin Zhang, Qingqing Liu, Qinghua Chi, Yinsheng Meng and Yuxin Xiong

66 Metallogenic mechanism of the Houge'zhuang gold deposit, Jiaodong, China: Evidence from fluid inclusion, *in situ* trace element, and sulfur isotope compositions
Naijie Chi, Zuozhen Han, Chuan'e Liu, Wei Zhang, Yanhui Zhang, Wei Shan, Zengsheng Li, Min Li, Xiufeng Wang and Yuqin Sun

87 Intra-oceanic subduction in the southeastern Paleo-Asian ocean: Evidence from early Permian gabbro of the Diyanmiao ophiolite in central Inner Mongolia, North China
Xiawei Zhang, Yingjie Li, Genhou Wang, Shuai Wang, Xingrui Kong, Xiaodong Wang and Zhibin Liu

102 Early cretaceous ridge subduction in the Shandong Peninsula, Eastern China, indicated by Laoshan A-type granite
Jie Li, He Li, Congying Li, Mingchun Song, Mengyao Jiang, Shuai Yuan and Lipeng Zhang

123 Petrogenesis and relationship with REE mineralization of the quartz syenite from Chishan and Longbaoshan alkaline complex, southeastern North China Craton: Insights from zircon U–Pb geochronology, element, and Sr–Nd–Pb–Hf isotope geochemistry
Pengfei Wei, Dapeng Li, Zhigang Song, Qiang Liu, Ke Geng, Yan Zhang, Chengwu Ding, Na Cai, Zengsheng Li, Chao Zhang and Wei Xie

144 Cassiterite U-Pb dating and micro-XRF analysis constraint on the formation of Xinlu Sn-Zn deposit, South China
Chang-Hao Xiao, Ping-Ping Yu, Xiao-Hu Liu, Xiang-Chong Liu, Yan-Wen Tang, Wen-Lei Wang and Yu Zhang

161 Metallogeny of the Yi'nan Tongjing Au–Cu skarn deposit, Luxi district, North China Craton: Perspective from in-suit trace elements, sulfur and lead isotopes of sulfides
Wen-Yan Cai, Zhao-Lu Zhang, Xiao Liu, Ji-Lei Gao, Ming Ma, Yadong Li, Ying-Xin Song and Zeng-Sheng Li

183 Genesis of the Shibaogou Mo–Pb–Zn deposit in the Luanchuan ore district, China: Constraints from geochronology, fluid inclusion, and H–O–S–Pb isotopes
Yunchou Xu, Gongwen Wang, Meng Gao, Wangdong Yang, Shuren Yang, Hui Yun, Peijian Wu, Nana Guo and Yantao Feng

206 Imaging the subducting slab and mantle upwelling under the Japan islands revealed by double-difference tomography
Zhengshuai Zhang, Jianchang Zheng, Shuhao Wang, Cuiqin Li and Fangbin Liu

223 Geochemistry and zircon U–Pb ages of early Ordovician syenites from the Inexpressible Island, Antarctica and tectonic implications
Peng Gao, Limei Tang and Ling Chen

243 The present-day stress field along the Northwest Pacific Wadati-Benioff zone constrained by focal mechanisms of moderate earthquakes
Chengyu Liu, Fangbin Liu, Yin Cai, Ran Ni, Xiujie Xu, Guoyi Li, Weiduo Hao and Zhaoyang Tian

258 Polyphase deformation of the Youjiang fold-and-thrust belt during the Mesozoic: Implications for the tectonic transition of the South China block
Jia-Xiu Hu, Chang-Hao Xiao, Chang-Shan Wei, Yu-Ke Shen, Zheng-Le Chen, Yu Zhang and Da Zhang

272 Mineralization age and genesis of the makeng-style iron deposits in the Paleo-Pacific tectonic domain of South China: *In situ* LA-ICPMS garnet U-Pb chronological and geochemical constraints
Sen Wang, Ke Cao, Da Zhang, Jin-Jun Yi, Bo-Jie Hu, Jing Yang, Meng-Ying Cai, Yao-Yao Zhang, Yuan Yuan and Tian-Wang Pan

294 Genesis of the Yangjiakuang gold deposit, Jiaodong peninsula, China: Constraints from S-He-Ar-Pb isotopes, and Sm-Nd and U-Pb geochronology
Jun-Jian Li, Zhi-Cai Dang, Chao Fu, Peng-Peng Zhang, Jie-Peng Tian and Jiang-Tao He

309 Generation of the Early Cretaceous granitoid in the Dazeshan region, Jiaodong Peninsula: Implications for the crustal reworking in the North China Craton
Leilei Dong, Zhiming Yang, Xin Bai and Chen Deng

335 Melt- and fluid-inclusions studies in the Wunugetushan porphyry Cu–Mo deposit, NE China: Constraints on the separation of Cu and Mo
Wei Lu, Yuecheng Zhang, Jingguo Du and Zhiwei Song

348 Identification of Baihesi aluminous A-type granite: Magmatic response to the onset of Cretaceous extension in eastern Jiangnan Massif, South China
Bojie Hu, Da Zhang, Xinming Zhang, Zhihui Zhang, Sen Wang and Jiaxiu Hu

369 Enhanced arc magmatic productivity of the Western Pacific island arcs deduced from gravity-derived arc crustal growth rates
N. E. Parcutela, R. S. Austria, C. B. Dimalanta, G. T. V. Valera, J. A. S. Gabo-Ratio, B. D. Payot, L. T. Armada, K. J. F. Sangalang and G. P. Yumul Jr.

379 Spatial-temporal distribution, metallogenic mechanisms and genetic types of nephrite jade deposits in China
Cun Zhang, Fan Yang, Xiaoyan Yu, Jinhai Liu, Emmanuel John M. Carranza, Jie Chi and Peng Zhang

400 Petrogenesis and tectonic implications of the Late Jurassic A-type granite in central Inner Mongolia, North China
Shuai Wang, Yingjie Li, Song Jin, Peipei Dong, Xiawei Zhang, Dongfang Zhao, Xingrui Kong and Pengyu Liu

416 Preliminary investigation of the eruption time of kimberlite in the Late Devonian in Mengyin, Shandong
Ruicong Tian, Haiqin Wang, Jingxiang Tian, Wei Shan, Xiufeng Wang, Naijie Chi, Xiaodong Ma, Zhiyuan Chu, Shenghu Li and Qing Lv

frontiers | Frontiers in Earth Science

TYPE Editorial
PUBLISHED 06 July 2023
DOI 10.3389/feart.2023.1248758

Check for updates

OPEN ACCESS

EDITED AND REVIEWED BY
Derek Keir,
University of Southampton,
United Kingdom

*CORRESPONDENCE
Fan Yang,
fanyang@lzu.edu.cn

RECEIVED 27 June 2023
ACCEPTED 03 July 2023
PUBLISHED 06 July 2023

CITATION
Yang F, Xue F, Jepson G and Zhang L (2023), Editorial: (Paleo-) Pacific plate subduction tectonics and related magmatism and mineralization. *Front. Earth Sci.* 11:1248758. doi: 10.3389/feart.2023.1248758

COPYRIGHT
© 2023 Yang, Xue, Jepson and Zhang. This is an open-access article distributed under the terms of the Creative Commons Attribution License (CC BY). The use, distribution or reproduction in other forums is permitted, provided the original author(s) and the copyright owner(s) are credited and that the original publication in this journal is cited, in accordance with accepted academic practice. No use, distribution or reproduction is permitted which does not comply with these terms.

Editorial: (Paleo-) Pacific plate subduction tectonics and related magmatism and mineralization

Fan Yang[1]*, Fei Xue[2], Gilby Jepson[3] and Liang Zhang[4]

[1]Key Laboratory of Mineral Resources in Western China (Gansu Province), School of Earth Sciences, Lanzhou University, Lanzhou, China, [2]School of Earth Sciences and Engineering, Hohai University, Nanjing, China, [3]School of Geosciences, University of Oklahoma, Norman, OK, United States, [4]State Key Laboratory of Geological Processes and Mineral Resources, China University of Geosciences, Beijing, China

KEYWORDS

(Paleo-) Pacific Plate, subduction tectonics, magmatism and mineralization, cratonic destruction, circle-pacific zones

Editorial on the Research Topic
(Paleo-) Pacific plate subduction tectonics and related magmatism and mineralization

1 Introduction

The Pacific oceanic plate started forming in the Early Jurassic and is currently the largest oceanic plate on the Earth since Mesozoic (Boschman and Van Hinsbergen, 2016). The Pacific plate initially formed as the cores of the Izanagi, Farallon, and Phoenix plates as a result of the expansion of triangular three-ridge system (Li et al., 2019). During the Early Jurassic, the subduction of the Paleo-Pacific Plate along the eastern margin of Eurasia and related circum-Pacific terranes resulted in the formation of magmatic rocks, rejuvenation of pre-existing structures, and polymetallic mineralization (Yang et al., 2020a; Ma and Xu, 2021; Zeng et al., 2023). In the Cenozoic, the subducting Pacific Plate transitioned to steep subduction, which facilitated deformation and uplift of the overriding plate (Miller et al., 2006; Yang et al., 2020b; Ju et al., 2021). The complex subduction processes are correlated with widespread mineralization and weakening of stable terranes (e.g., North China Craton), propogating seismicity and volcanism into previously stable areas (Mao et al., 2018; Zhu and Xu, 2019; Zhao, 2021). As a result, the prolonged history of Mesozoic to Cenozoic subduction defines many geological and environmental conditions observed today. Thus, we propose the Research Topic of "(Paleo-) Pacific Plate Subduction Tectonics and Related Magmatism and Mineralization" in *Frontiers in Earth Science*. This Research Topic includes twenty-three papers (Figure 1) that have a link with the (Paleo-) Pacific plate subduction tectonics. In this special edition, nine papers focus on petrogenesis and tectonic implications of magmatic rocks, ten papers are concentrated on polymetallic mineralization, and four papers are related to the geodynamic implications of plate subduction. Below we sumarize a brief introduction to these papers in this Research Topic.

2 Summary of papers

2.1 Magmatism

Dong et al. this Research Topic conducted whole-rock major and trace element and zircon U-Pb and Lu-Hf isotope analyses on the granitic intrusions from the Dazeshan region, Jiaodong Peninsula, North China Craton. Zircon U-Pb dating constrain the emplacement ages of these granitic intrusions at ca. 120 Ma. Geochemical and isotopic data show that these magmatic rocks underwent variable crustal melting and differentiation processes. This study suggests that these intrusions were produced by the underplating of water-rich mafic magma. The mafic magma provided fluid and heat that sourced from the dehydration of the subducting Paleo-Pacific plate.

Gao et al. this Research Topic performed zircon U-Pb dating, and whole-rock major and trace element and Sr-Nd-Hf isotope analyses on the syenite from Inexpressible Island in the Antarctica's Ross Orogenic Belt within the framework of the convergence of Paleo-Pacific oceanic plate and Gondwana continental margin. Zircon U-Pb dating document the emplacement ages of these syenites at ca. 477–471 Ma. Zircon Lu-Hf and whole-rock Sr-Nd isotopes suggest partial melting of lithospheric mantle enriched with subduction slab fluids and subcontinental lithosphere for the formation of these syenites. Whole-rock geochemical data show that these syenties have island arc geochemical affinities. This study finally suggests that the Inexpressible Island magmatism was related to localized melting zone of an older previously enriched layer of subcontinental lithospheric mantle, which was metasomatized by a more recent subduction components.

Hu et al. this Research Topic present zircon U-Pb and Lu-Hf isotopes and whole-rock major and trace element analyses for the Baihesi aluminous A-type granite in the eastern Jiangnan Massif, South China. Zircon U-Pb dating document the onset of the Cretaceous extension in the eastern Jiangnan Massif at ca. 145–140 Ma. Zircon Lu-Hf isotopes suggest that the Baihesi granite was derived from partial melting of reworked juvenile crust associated with Neoproterozoic arc-related magmatism. This work also suggests that the formation of Baihesi granite was associated with the Paleo-Pacific plate subduction along the South

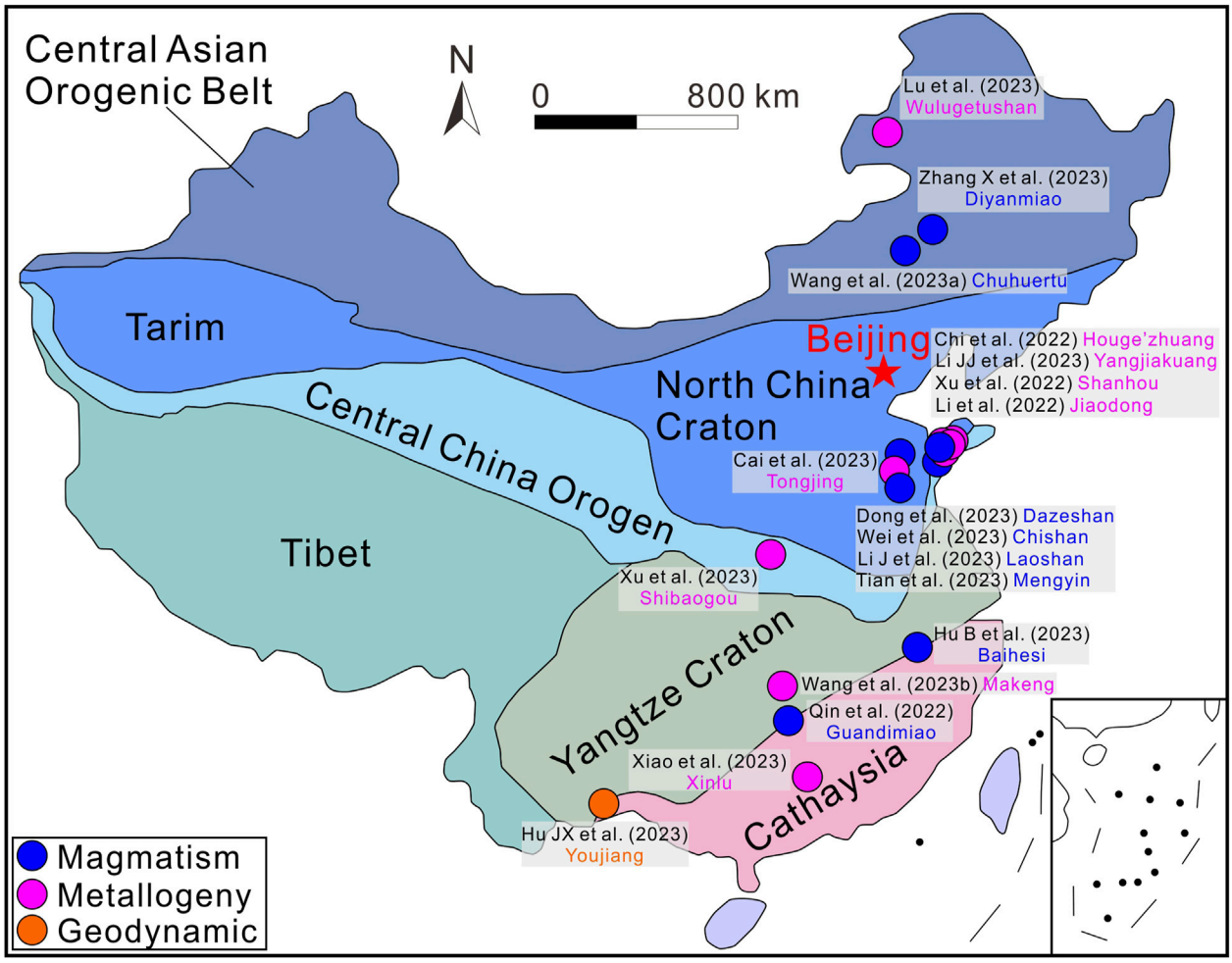


FIGURE 1
Simplified geological map of China (modified after Yang et al., 2022) showing the distribution of study areas of most papers in this Research Topic, but not including Liu et al. (Northwest Pacific Wadati-Benioff zone), Parcutela et al. (Western Pacific oceanic island arcs), Zhang et al. (nephrite jade deposits in China), and Zhang et al. (Japan Islands).

China active continental margin in the Late Jurassic to Early Cretaceous.

Li et al. this Research Topic present whole-rock geochemistry, zircon U-Pb isotope, and zircon and apatite trace element analyses for the Laoshan A-type granite in the Shandong Peninsula, eastern North China Craton. Zircon U-Pb dating constrain the emplacement ages of these granites at ca. 120–117 Ma, and associated geochemical data suggest that the Laoshan grainte is an A_1-type and crystallized under moderate and low oxygen fugacity conditions. This study suggests that the flat subduction of the spreading ridge between the Pacific and Izanagi plates was responsible for the formation of Laoshan A-type granite and the decratonization of North China Craton.

Qin et al. this Research Topic present zircon U-Pb isotopes, whole-rock major and trace element and Sr-Nd-Pb isotope analyses on the Guandimiao batholith in the South China Block. Four stages of magmatism at ~239 Ma, ~230–203 Ma, ~211–190 Ma and ~121 Ma were identified in the Guandimiao batholith. This study proposes that the Guandimiao batholith recorded the closure of the Paleo-Tethys Ocean in the Triassic, the regional extension during post-collision, the transition of tectonic and dynamic regimes in the Jurassic to Cretaceous (Yanshanian), and the rollback and steep subduction of Paleo-Pacific Ocean in the Jurassic to Cretaceous.

Tian et al. this Research Topic report carbonate U-Pb dating and fluid inclusions for the Mengyin kimberlite matrix and xenolithic marble in the Luxi terrane, Shandong Peninsula, North China Craton. Carbonate U-Pb dating yield the eruption age of kimberlite at ca. 383 Ma and the timing of marbleization at ca. 359 Ma. Fluid inclusions in xenolithic marble suggest formation temperature of 243°C–370°C, salinity of 2.57%–14.77% (NaCl), and pressure of 3.22–20.70 MPa. This study estimates that the overall denudation depth of the west Shandong area in the west Pacific domain is at about 900–1000 m and the overall crustal rise rate is at ca. 3 m/Ma since the Late Devonian.

Wang et al. this Research Topic preform zircon U-Pb isotopes and whole-rock major and trace element analysis on the Chuhuertu granite from the central Inner Mongolia, North China. Zircon U-Pb dating constrain the emplacement ages of the granite in the Late Jurassic (ca. 156 Ma). Whole-rock geochemical data suggest that the Chuhuertu granite is highly differentiated A-type granite which formed via partial melting of intermediate-mafic crust and differentiation crystallization. The study also suggests that the Chuhuertu granite was the product of extension of the closure of the Mongo-Okhotsk Ocean in the Late Jurassic, which was also superimposed the coeval tectonic effects of the Paleo-Pacific plate rollback.

Wei et al. this Research Topic present zircon U-Pb and Lu-Hf isotopes, and whole-rock Sr-Nd-Pb and major and trace element analyses from the quartz syenite from Chishan and Longbaoshan alkaline complex, North China Craton. Zircon U-Pb dating document that the quartz syenite was emplaced at ca. 126–123 Ma. Whole-rock geochemical data show arc- and extension-related geochemical affinities in response to the rollback and retreat of the subducting Paleo-Pacific plate. The Sr-Nd-Pb-Hf isotopic data indicate an EM-2 type lithospheric mantle source. This study also highlights homologous source characterisitics for quartz syenite and REE mineralization related to magmatic hydrothermal evolution.

Zhang et al. this Research Topic present zircon U-Pb isotopes and whole-rock major and trace element and Sr-Nd isotope analysis on a newly discovered gabbro in the Diyanmiao ophiolite zone, Inner Mongolia, North China. Zircon U-Pb dating yield an emplacement age of 294 Ma for gabbro. The whole-rock geochemical and Sr-Nd isotopes suggest N-MORB and subduction-related geochemical affinities. The gabbro formed at the initial stage of intra-oceanic subduction of the Paleo-Asian Ocean. The study also emphasizes the tectonic transition from the Paleo-Asian Ocean to Paleo-Pacific subduction during the Triassic to Jurassic in North China.

2.2 Metallogeny

Cai et al. this Research Topic perform systematic scanning electron microscope-backscattered electron imaging, electron probe microanalysis, and *in-situ* trace element, sulfur and lead isotope analyses on the Yi'nan Tongjing Au-Cu deposit, Luxi terrane, North China Craton. This study identifies five hydrothermal stages of early skarn, late skarn, oxide, sulfide and late quartz-calcite, with gold mostly as silver-bearing native grains. The trace element data of sulfides and oxides suggest that the ore-forming fluid is of medium-high temperature magmatic-hydrothermal origin. The S-Pb isotopes reveal that the ore-forming materials are derived mainly from the Early Cretaceous diorite porphyry and partly from the host rocks (carbonate rocks). These findings suggest that the Tongjing Au-Cu deposit occurs as an important metallogenic response to the decratonization of North China Craton induced by the Paleo-Pacific Plate rollback during the Early Cretaceous.

Chi et al. this Research Topic present fluid inclusions and *in-situ* trace element and sulfur isotope analyses for the Houge'zhuang gold deposit, Jiaodong Peninsula, North China Craton. Three different type pyrites and fluid inclusions document the role of arsenic and sulfur isotopes in gold precipitation and the association of gold with specific pyrite types. The study also proposes that the As-bearing pyrites have close spatiotemporal links with gold, and these pyrites play an important role in the formation and exploration of high-grade gold deposits in Jiaodong reigon of the west Pacific subduction zone.

Li et al. this Research Topic conducted calcite Sm-Nd and zircon U-Pb dating and S-Pb-He-Ar isotope analyses on the Yangjiakuang gold deposit from the Jiaodong Peninsula, North China Craton. Calcite Sm-Nd and zircon U-Pb dating document the Yangjiakuang deposit that formed in the Early Cretaceous (ca. 123 Ma). Pyrite S-Pb-He-Ar isotopes suggest that the ore-forming materials and fluids contain a mixture of crustal and mantle components. The formation of the Yangjiakuang deposit is correlated with crustal extension caused by the rollback of the subducting Izanagi Plate during the early Cretaceous.

Li et al. this Research Topic present results of gold nanoparticles in ore and build the fundamental linkage to geochemical anomaly distribution maps of gold in drainage sediments, wall rocks, and ore within Jiaodong gold province, North China Craton. This study suggests that the gold particles in Jiaodong Peninsula have a close relationship with the evolution of Mesozoic structural-controlled gold mineralization related to the Paleo-Pacific plate subduction and

could be used to interpret diverse geochemical anomalies for exploration. In addition, a migration pathway of gold nanoparticles was built to illustrate the processes of massive gold accumulation and prospecting in Jiaodong Peninsula.

Lu et al. this Research Topic present geochemical analysis of melt inclusions in porphyry intrusions and fluid inclusions in quartz veins from the Wunugetushan large porphyry Cu-Mo deposit in NE China (west Pacific domain). Melt inclusion data yield rhyolitic compositions of 71.7–85.3 wt% SiO_2, 1.9–31.3 ppm Cu and 1.7–2. 6 ppm Mo. Fluid inclusions suggest that the hydrothermal fluids evolved through three main stages of the early Mo mineralization, late Mo mineralization and Cu mineralization. This study also highlights that the separation of Cu and Mo was promoted by multiple factors, including the increased Cu/Mo ratios in residual melt and the changing redox state and acidity of ore-forming fluids.

Wang et al. this Research Topic carried out garnet U-Pb isotopes and rare Earth element analysis on the Makeng-style iron polymetallic deposits from SE China within the Paleo-Pacific tectonic domain. Garnet U-Pb dating suggest that these deposits formed at ca. 137–130 Ma. Garnet rare Earth element data have geochemical affinities of skarn deposits, and these Makeng-style deposits underwent distinct ore-forming processes and mineralizing fluids. This study provides valuable insight into mineralization age and genesis, in addition to the novel application of U-Pb dating in skarn-type deposits.

Xiao et al. this Research Topic report results of rock slab and thin section reflection mapping, element mapping by Micro-XRF (μ-XRF), and *in-situ* LA-ICP-MS cassiterite U-Pb dating for the Xinlu Sn-Zn deposit, Nanling Sn-W belt, South China. The μ-XRF analytical results reveal four mineralization episodes of prograde skarn, retrograde skarn-sulfide, quartz sulfide vein and barren calcite stages in the Baimianshan segment of Xinlu deposit. Cassiterite U-Pb dating determine the timing of retrograde skarn-sulfide mineralization at ca. 169 Ma, which indicate a Sn mineralization associated with the ca. 160–169 Ma magmatism in the Guposhan-Huashan district. The study suggests that there are links between the subduction of the Paleo-Pacific plate and the formation of the Xinlu Sn-Zn mineralization and the Middle-Late Jurassic Sn-W mineralization in the Nanling belt, South China.

Xu et al. this Research Topic present molybdenite Re-Os dating, fluid inclusions and H-O-S-Pb isotopes on the Shibaogou skarn-type Mo (Pb-Zn) deposit, East Qinling, China. This study documents that the Shibaogou deposit formed in the Late Jurassic (ca. 147 Ma). The ore-forming fluids are suggested to be from magmatic and atmospheric water, whereas the ore-forming material is derived from Shibaogou intrusion. The formation of the Shibaogou deposit is correlated with the subduction of Paleo-Pacific plate during the Late Mesozoic.

Xu et al. this Research Topic present results of high-precision geophysical surveys including gravity and controlled source audio frequency magnetotellurics for the Shanhou gold deposit in Jiaodong gold provice, eastern North China Craton. The spatial distribution of stratum, structure and magmatite of the Shanhou gold deposit were identified. The study revealed a gold orebody at depths greater than 1,015 m, which supports the presence of gold mineralization in the brittle deformation of the Zhaoping fracture zone, correlated with the subduction of Paleo-Pacific plate.

Zhang et al. this Research Topic review the nephrite jade deposits from different tectonic units in China, through integrating published geochronology, major and trace elements and H-O isotopes. This study divides the nephrite jade deposits in China into green jade-type (GJ-type) and white jade-type (WJ-type). The GJ-type nephrite deposits mainly formed through the late auto-metamorphic metasomatism of serpentine or the spontaneous crystallization/precipitation along suture/shear zones. The WJ-type nephrite jade, the main nephrite jade type in China, is generated via metamorphism-metasomatism during post continent-continent collisions. This study also suggests that the formation of the nephrite jade deposits is associated with multiple tectonic episodes (e.g., Pacific plate subduction) and the interaction between hydrothermal fluids and metamorphism under subduction accretion- and collision orogenesis-related settings. Further, this study provides insights into the genetic discrimination, mineral exploration, and quality assessment of nephrite jade deposits in China.

2.3 Geodynamic

Hu et al. this Research Topic present structural analysis at the middle of the Youjiang fold-and-thrust belt and discuss the Mesozoic tectonic transition of the South China Block. This study reveals four phases of deformation, including the Permian-Middle Triassic NE-SW shortening deformation, the Late Triassic nearly N-S extension, the Jurassic NW-SE shortening, and the Cretaceous nearly E-W extension. These structural episodes are correlated with the collision and post-collision during the Indosinian orogeny as well as the Paleo-Pacific plate subduction and subsequent slab-rollback during the Jurassic to Cretaceous. This findings also highlights the tectonic transition of South China Block in response to the subduction of Paleo-Pacific plate that likely occurred in the Early Jurassic.

Liu et al. this Research Topic document the present-day stress field along the Northwest Pacific Wadati-Benioff Zone (WBZ) through using earthquake focal mechanism. This study reveals pure compression in shallow WBZ segment and is correlated with negative buoyancy of plate and convergence between plates. A stress regime of pure compression was identified in the deep segment of northern Izu-Bonin trench WBZ, which is possibly triggered by the resistance offered by mantle to penetration of slab. The stress states at intermediate depths along the junction of the trench WBZ were inferred to have been influenced by lateral deformation due to increasing slab's dip.

Parcutela et al. this Research Topic carried out a comparison of gravity-derived magmatic growth rates of Western Pacific oceanic island arcs, using statistical correlation between the Bouguer anomalies and the seismic-derived crustal thicknesses to estimate the magmatic growth rates of the western Pacific island arcs and the Philippine island arc system. The results show that the magmatic growth rate of the Western Pacific island arcs is significantly higher (28–60 km^3/km/m.y), which is correlated with the Pacific Plate subduction. The growth rate of the Pacific island arcs is higher than other oceanic island arcs (12–25 km^3/km/m.y) and are derived from the subduction of other oceanic lithospheres (e.g., Philippine Plate).

Zhang et al. this Research Topic applied double-difference tomography to determine 3-D velocity structure of P- and S-waves from Japan Trench to back arc under Japan Islands. The results reveal the morphological and high-velocity characteristics of the subduction of Pacific plate and low-V anomalies in the surrounding mantle. The fluids released by the dehydration of the subducting plate and transported upward by mantle upwelling are indicated to have played crucial roles in the formation of arc magmatism and plate melting in the mantle wedge behind the Japan Trench.

Author contributions

All authors listed have made a substantial, direct, and intellectual contribution to the work and approved it for publication.

Funding

This Research Topic was jointly supported by the National Natural Science Foundation of China (42202077), the Natural Science Foundation of Gansu Province (22JR5RA440), the Fundamental Research Funds for the Central Universities (LZUJBKY-2022-42), the Professional Committee of Tectonophysicochemistry, Chinese Geophysical Society, and the Guiding Special Funds of "Double First-Class (First-Class University and First-Class Disciplines)" (561119201) of Lanzhou University, China.

Acknowledgments

The Editor-in-Chief Valerio Acocella is appreciated for his guidance and valuable support to this Research Topic. Also, we thank all the authors who contributed their papers and the referees who devoted their valuable time and efforts to insightful reviews.

Conflict of interest

The authors declare that the research was conducted in the absence of any commercial or financial relationships that could be construed as a potential conflict of interest.

Publisher's note

All claims expressed in this article are solely those of the authors and do not necessarily represent those of their affiliated organizations, or those of the publisher, the editors and the reviewers. Any product that may be evaluated in this article, or claim that may be made by its manufacturer, is not guaranteed or endorsed by the publisher.

References

Boschman, L. M., and Van Hinsbergen, D. J. (2016). On the enigmatic birth of the Pacific plate within the panthalassa ocean. *Sci. Adv.* 2, e1600022. doi:10.1126/sciadv.1600022

Ju, Y., Yu, K., Wang, G., Li, W., Zhang, K., Li, S., et al. (2021). Coupling response of the Meso–Cenozoic differential evolution of the North China Craton to lithospheric structural transformation. *Earth-Science Rev.* 223, 103859. doi:10.1016/j.earscirev.2021.103859

Li, S. Z., Cao, X. Z., Wang, G. Z., Liu, B., Li, X. Y., Suo, Y. H., et al. (2019). Meso-Cenozoic tectonic evolution and plate reconstruction of the Pacific Plate. *J. Geomechanics* 25, 642–677. doi:10.12090/j.issn.1006-6616.2019.25.05.060

Ma, Q., and Xu, Y. G. (2021). Magmatic perspective on subduction of Paleo-Pacific plate and initiation of big mantle wedge in East Asia. *Earth-Science Rev.* 213, 103473. doi:10.1016/j.earscirev.2020.103473

Mao, J. W., Xie, G. Q., Yuan, S. D., Liu, P., Meng, X. Y., Zhou, Z. H., et al. (2018). Current research progress and future trends of porphyry-skarn copper and granite-related tin polymetallic deposits in the Circum Pacific metallogenic belts. *Acta Petrol. Sin.* 34, 2501–2517.

Miller, M. S., Kennett, B. L. N., and Toy, V. G. (2006). Spatial and temporal evolution of the subducting Pacific plate structure along the Western Pacific margin. *J. Geophys. Res. Solid Earth* 111. doi:10.1029/2005JB003705

Yang, F., Mao, J., Ren, W., Qian, Z., Li, C., and Jepson, G. (2022). Temporal evolution and origin of the Yumugou Mo-W deposit, East Qinling, China: Evidence from molybdenite Re-Os age and U-Pb dating and geochemistry of titanite. *Ore Geol. Rev.* 150, 105172. doi:10.1016/j.oregeorev.2022.105172

Yang, F., Santosh, M., Glorie, S., Jepson, G., Xue, F., and Kim, S. W. (2020b). Meso-cenozoic multiple exhumation in the Shandong peninsula, eastern NorthNorth China Craton: Implications for lithospheric destruction. *Lithos* 370-371, 105597. doi:10.1016/j.lithos.2020.105597

Yang, F., Santosh, M., Kim, S. W., Zhou, H., and Jeong, Y. J. (2020a). Late mesozoic intraplate rhyolitic volcanism in the North China Craton: Far-field effect of the westward subduction of the Paleo-Pacific plate. *GSA Bull.* 132, 291–309. doi:10.1130/B35123.1

Zeng, Y., Wang, Q., Groves, D. I., Santosh, M., Wang, Y., Wang, T., et al. (2023). Prolonged Mesozoic intracontinental gold mineralization in the South China Block controlled by lithosphere architecture and evolving Paleo-Pacific Plate subduction. *Earth-Science Rev.* 240, 104387. doi:10.1016/j.earscirev.2023.104387

Zhao, D. (2021). Seismic imaging of Northwest Pacific and East asia: New insight into volcanism, seismogenesis and geodynamics. *Earth-Science Rev.* 214, 103507. doi:10.1016/j.earscirev.2021.103507

Zhu, R., and Xu, Y. (2019). The subduction of the west Pacific plate and the destruction of the North China Craton. *Sci. China Earth Sci.* 62, 1340–1350. doi:10.1007/s11430-018-9356-y

frontiers | Frontiers in Earth Science

TYPE Original Research
PUBLISHED 09 August 2022
DOI 10.3389/feart.2022.948723

Check for updates

OPEN ACCESS

EDITED BY
Fan Yang,
Lanzhou University, China

REVIEWED BY
Juquan Zhang,
Hebei GEO University, China
Abulimiti Aibai,
Xinjiang Institute of Ecology and Geography (CAS), China
Hua-Wen Cao,
China Geological Survey, China

*CORRESPONDENCE
Fan Huang,
hfhymn@163.com

SPECIALTY SECTION
This article was submitted to Petrology, a section of the journal Frontiers in Earth Science

RECEIVED 20 May 2022
ACCEPTED 30 June 2022
PUBLISHED 09 August 2022

CITATION
Qin J-H, Huang F and Wang D-H (2022), Batholith recorded mesozoic multistage tectonic evolution of the South china block: A case study of the guandimiao intrusions.
Front. Earth Sci. 10:948723.
doi: 10.3389/feart.2022.948723

COPYRIGHT
© 2022 Qin, Huang and Wang. This is an open-access article distributed under the terms of the Creative Commons Attribution License (CC BY). The use, distribution or reproduction in other forums is permitted, provided the original author(s) and the copyright owner(s) are credited and that the original publication in this journal is cited, in accordance with accepted academic practice. No use, distribution or reproduction is permitted which does not comply with these terms.

Batholith recorded mesozoic multistage tectonic evolution of the South china block: A case study of the guandimiao intrusions

Jin-Hua Qin, Fan Huang* and Deng-Hong Wang

MNR Key Laboratory of Metallogeny and Mineral Assessment, Institute of Mineral Resources, CAGS, Beijing, China

South China is a well-known grand felsic igneous rocks province. However, it is still controversial and not well understood whether the Mesozoic tectono-magmatic pattern is dominated by the subduction of the paleo-Pacific oceanic plate. In this study, we address this question by concentrating on the long-term evolutionary Guandimiao batholith, which has complex lithofacies with different formation ages and can be a superb record of the Mesozoic tectonic evolution in South China. Geochronologically, four stages of magmatism can be identified combined with previous reports: granodiorite (G1, 239 Ma), biotite monzogranite (G2-1) and two-mica monzogranite (G2-2) (230–203 Ma), granite porphyry (G3, 211–190 Ma), and lamprophyre (L4, 121 Ma). G1 and G2-1 have an affinity with I-type granite and were derived from metabasaltic to metatonalitic sources, whereas G2 and G3 show S-type granite characteristics and were derived from the para-metamorphic basement of the Cathaysia block. The L4 was derived from partial melting of garnet and spinel lherzolite and underwent mixing between Mesoproterozoic pelagic and/or terrigenous sediments and the subcontinental lithosphere mantle (SCLM) of South China. The granitoids of the Guandimiao batholith underwent intensely fractional crystallization of feldspar, Ti-bearing minerals, allanite and monazite. The zircon U–Pb dating of L4 in the Guandimiao batholith completely records the six stages of pre-Mesozoic tectonic events in the SCB. During the Mesozoic, the main body of the Guandimiao batholith (G1, G2-1 and G2-2) recorded the closure of the paleo-Tethys Ocean in the Triassic and the subsequent regional extension of the postcollision. G-3 and L4 of the Guandimiao batholith documented the transition of tectonic and dynamic regimes in the early Yanshanian and the rollback and steep subduction of the paleo-Pacific Ocean in the late Yanshanian.

KEYWORDS

Guandimiao batholith, granitoids, Lamprophyre, petrogenesis, tectonic evolution

1 Introduction

South China is a felsic large igneous rock province that developed large intrusions and volcanics with a total outcrop area of nearly 218,090 km^2. In particular, the outcrop area of granitoids occupies more than 90% of the total area of igneous rock (Zhou et al., 2006). Multiple stages of magmatic activity have been determined using accurate geochronological data (Zhou et al., 2006; Wang et al., 2010; Mao et al., 2011; Mao et al., 2014). Zhou et al. (2006) proposed four main stages of granitic magmatism: 251–234, 234–205, 180–142, and 142–67 Ma. Moreover, the mafic rocks contain three main clusters: the 190–160 Ma group (Zhao et al., 1998; Meng et al., 2012), the 160–110 Ma group (Wang et al., 2003; Wang et al., 2008; Ma et al., 2013) and the 110–80 Ma group (Chen et al., 2008a; Meng et al., 2012; Qin et al., 2020). Numerous models have been proposed for the systematic understanding of the evolutionary history of the regional geology. However, to date, the tectonic regime is not consistently well understood. Li and Li (2007) and Jiang et al. (2015) interpreted extensive igneous rocks in the early Mesozoic as a continual constraint of the plate subduction model of the Paleo-Pacific oceanic plate of the SCB. Wang et al. (2003), Mao et al. (2014), and Li et al. (2014) confirmed that the SCB suffered from the convergence of multiple plates in Indosinia. Subsequently, the postcollisional and postorogenic regimes occurred 234–203 Ma and 190–170 Ma, respectively (Zhou et al., 2006; Mao et al., 2014; Shu et al., 2019). Two supportable mechanisms have been presented with the controversy of whether the subduction of the Pacific Ocean dominated the tectono-magmatic pattern of the SCB in the middle to late Mesozoic (Li, 1990; Gilder et al., 1996; Chen et al., 2014; Li et al., 2014; Qin et al., 2020; Yang et al., 2020).

Batholith generally has complex lithofacies assemblage and long time span. It recorded the imprint of multiple stages of magmatism and thus can be considered an extremely advantageous object for studying the history of regional tectono-magmatic evolution (Hervé et al., 2007; Whalen et al., 2010; Zhao et al., 2012; Deng et al., 2017). Typical batholiths, such as South Patagonian batholiths, recorded magmatic activity over 100 Ma, which is essential for understanding the development of subduction from 157 to 40 Ma (Hervé et al., 2007). The Cumberland batholith (CB) in Canada provides evidence for Paleoproterozoic crustal and orogenic processes of the Trans-Hudson Orogen (Whalen et al., 2010), and the Lincang batholith in West China reveals the suture process of the Changning-Menglian belt (Deng et al., 2017). Thus, further research on Mesozoic batholiths of South China might be the key point for addressing the controversial geodynamic issues in the Mesozoic (Barbarin, 2005; Zhao et al., 2012).

The Guandimiao batholith is located in the middle Qing-Hang paleostylolitic zone in the SCB. Conspicuously, it is a sizeable Mesozoic batholith with a total area of approximately 300 km^2 that, with formation ages throughout the Mesozoic, could be considered a complete record of Mesozoic tectonic and magmatic events (Wang et al., 2003; Dai et al., 2008; Zhao et al., 2017). Spatially, mafic rocks (MME, lamprophyre) and felsic rocks (granitoids) are concomitant in the Guandimiao batholith. Geochemically, the Guandimiao batholith contains two distinct granitic end-members, I-type granite from the Jingtou area and S-type granite from the Shizhuqiao area (Zhao et al., 2017). Thus, it could also effectively reveal deep crust–mantle interactions and generally trace complicated regional tectonic evolution. Wang et al. (2003), Bai et al. (2014), and Zhao et al. (2017) proposed that the Guandimiao batholith was formed at the 239–220 Ma, which is associated with the post-orogeny regime. Miao (2014) obtained the zircon U-Pb age of 203 ± 1.4 Ma from bitotite granite in Zhoujialing area, which is nearly 20 Ma younger than the previous studies. Dai et al. (2008) reported the occurance of the granite porphyry and lamprophyre and claimed that the dikes are formed at 153 Ma. However, due to lack of systematic geochronological and geochemical investigations, the petrogenesis, geological framework and geodynamic backgrounds for various types of magmatic rocks in the Guandimiao batholith still remain quite unclear.

To confirm the exact chronological sequence, geochemical characteristics, and further discussion of the relationship between intrusions and multiple stages of tectonic setting, we report new LA-ICP–MS zircon U-Pb data and geochemical and Sr-Nd-Pb isotope data for the Guandimiao batholith.

2 Regional geology

The Guandimiao batholith is situated in the northern part of the middle SCB. The SCB consists of the Yangtze Block (YZB) to the west and the Cathaysia Block (CAB) to the east (Figure 1A). The area experienced closure of the YZB and subsequently, the South China folded orogenic multistage intraplate cleavage occurred in the late Neoproterozoic (Li et al., 1999; Li et al., 2001; Li et al., 2002; Greentree et al., 2006; Meng et al., 2012). The Jiuling batholith recorded magmatism in the Neoproterozoic with ages ranging from 848 to 794 Ma (Li et al., 2003; Zhong et al., 2005). During the Phanerozoic, the SCB was in a stable intraplate tectonic environment in South China, dominated by early Paleozoic tectonic stress and early Mesozoic closure of the ancient Tethys Ocean in East Asia (Liu, 1994; Rowley, 1997; Wang et al., 2005a; Mao et al., 2005; Shu, 2012). Subsequently, in the late Mesozoic, the tectonic environment was characterized by multiple periods of compressional and extensional orogeny and the development of widespread depression red basins and depression belts (Xia, 1991; Cheng, 1994; Gilder et al., 1995; Gilder and Courtillot, 1997; Wang et al., 2005b; Yang et al., 2019; Yang et al., 2020). Correspondingly, the famous Zhuguangshan batholith formed 500–90 Ma with a large, exposed area of more than 1,000 km^2 (Li, 1990; Deng et al., 2012; Zhang et al., 2020).

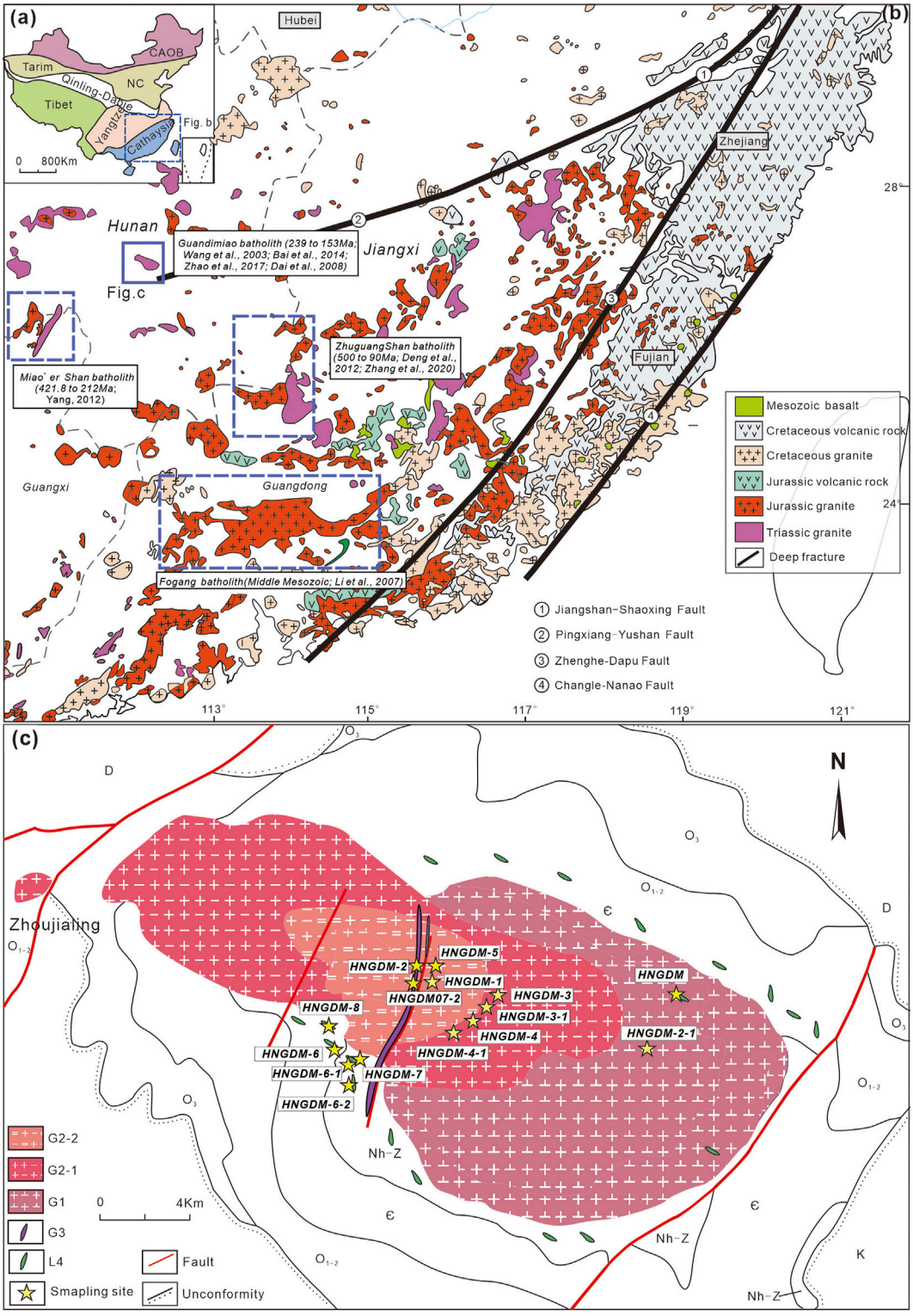


FIGURE 1
(A), Tectonic map of China (after Shu and Zhou, 2002); **(B)**, Regional tectonic map of south China (after Sun, 2006; Wang et al., 2013); **(C)**, Geological map of Guandimiao batholith (after Bai et al., 2014).

Miao'shan-Yuechengling batholith is exposed in the western part of the SCB with emplacement ages from 421.8 to 212 Ma (Yang, 2012). The Fogang batholith had a large volume with a single temporal distribution in the middle Mesozoic (Li et al., 2007). The Guandimiao batholith developed from 239 to 153 Ma (Wang et al., 2003; Dai et al., 2008; Bai et al., 2014; Zhao et al., 2017) (Figure 1B).

Multiple tectonic events and magmatic processes led to the unique geological features around the Guandimiao batholith. Numerous large abyssal faults, including basement faults and surface-cutting faults, are oriented in NE, NW, and E-W directions. "Checkerboard structure pattern" and "circular structures" are typical structural patterns (Zhang, 1984; Liang and Guo, 2002). NE- to NNE-directed subfaults and fractures closely connect with the abyssal faults and serve as necessary conduits for deep fluids. Precambrian to Cenozoic strata crop out. The Guandimiao batholith is located in a typical uplifted dome. In the center of the uplifted region, Precambrian strata are exposed as epi-metamorphic rocks in the Jiangkou Formation (Z_aj) and carbonate in the Dengying Formation (Zd). The Phanerozoic strata are Permian to Ordovician in age and include sandstone of the Tiaomajian Formation (D_2t), limestone and marble of the Qiziqiao Formation (D_2q) and Xikuangshan Formation (D_3x), and limestone of the Hutian Formation ($C_{2+3}h$). The exposed rock assemblages range from acidic to basic and are dominated by five lithofacies: granodiorite (*G1*), biotite monzogranite (*G2-1*), two-mica monzogranite (*G2-2*), dikes [granite porphyry (*G3*) and lamprophyre (*L4*)] (Figure 1C).

3 Petrography

Granodiorite (G1) is the marginal facies and is distributed along the eastern edge of the Guandimiao batholith. It has a medium-coarse granular texture with a mineral assemblage of quartz (~30%) + plagioclase (andesine, An≈40, 40%) + K-feldspar (~20%) + amphibole (~5%) + biotite (~5%) and minor apatite, zircon and magnetite/ilmenite (Figure 2K). Biotite monzogranite (G2-1) was exposed in the center of the Guandimiao batholith and intruded into Lower Ordovician and Upper Cambrian strata (Figure 2B). The mineral assemblage is dominantly plagioclase (~40%), perthitic K-feldspar (~30%), quartz (~20%), and biotite (~10%) with accessory zircon, garnet, magnetite or ilmenite (Figures 2G,I). MMEs, generally 2 × 3 cm in size, are exposed in the interior of the biotite monzogranite in Shuanghekou village (Figure 1C). Two-mica monzogranite (G2-2) occurs locally in Maohedian town (approximately 3 km in length, 1.5 km in width), which is the central facies of the batholith. The central lithological facies is structurally massive with the occurrence of muscovite grains. The mineral assemblage of two-mica granites consists of perthitic K-feldspar (~30%), plagioclase (~35%), quartz (~20%), biotite (~5%), muscovite (~5%) and magnetite/ilmenite (~2%) with accessory zircon and monazite (Figure 2J). Granite porphyry (G3) occurs in the interior and surroundings of the Guandimiao batholith. The granite porphyry vein is oriented NNE with a width of 5–10 m and intruded into biotite monzogranite (Figures 2A,H). Granite porphyry presents a typical porphyritic structure, and the phenocryst minerals are quartz (20%), K-feldspar (~15%), plagioclase (~10%), and biotite (<5%). Lamprophyre (L4) is exposed in the interior and around the granitic batholith and is 0.5–2 m in width and vertical in occurrence (Figures 2E,F). They are gray–green in color and intruded into Paleozoic silty slate and granitic batholith. Lamprophyre presents lamprophyric texture. The phenocrysts are mainly biotite and plagioclase, occupying 50% vol. Of the whole rocks. Biotite occurs as brown-light brown sheets 0.2–0.4 mm in size (30% vol). Plagioclase occurs as subhedral crystals that are 0.1–0.2 mm in size (approximately 30% vol). The matrix is mafic with extensive epidotization, chloritization, and carbonation (Figure.2L).

4 Sampling and method

15 samples, no obvious weathering or alteration, were collected from the Guandimiao batholith. The granodiorite sample (HNGDM-2-1) and biotite monzogranite samples (HNGDM-4, HNGDM-4-1, HNGDM-3 and HNGDM-3-1) were collected at Lingguandian town. The two-mica monzogranite samples (HNGDM-1 and HNGDM-5) were collected from the outside of Shiqiaopu lead-zinc ore deposit. The granite porphyry samples (HNGDM-2 and HNGDM07-2) were from Shuangjiangkou village. The lamprophyre samples (HNGDM, HNGDM-6, HNGDM-6-1, HNGDM-6-2, HNGDM-7, and HNGDM-8) were collected from the north of Qidong county. 8 out of 15 samples were chosen for accurately geochronological dating, 12 samples were chosen for geochemical analysis and 8 samples for Sr-Nd-Pb isotopic analysis.

4.1 LA–ICP–MS

Zircon U-Pb dating was performed the Institute of Mineral Resources, CAGS, Beijing, using a Finnigan, Neptune inductively coupled plasma mass spectrometer (MC LA-ICP-MS) with a new wave UP213 laser-ablation system. Helium was used as the carrier gas, and the beam diameter was 30 μm with 10-Hz repetition rate and a laser power of 2.5 J/cm^2. Eight ion counters were used to receive the ^{238}U, ^{235}U, ^{232}Th, ^{208}Pb, ^{207}Pb, ^{206}Pb, ^{204}Pb, and ^{202}Hg signals simultaneously, whereas data for ^{208}Pb, ^{232}Th, ^{235}U, and ^{238}U were collected on a Faraday cup. Zircon GJ-1 was used as standard, and Plešovice zircon was used to optimize the mass spectrometer. U, Th, and Pb concentrations were calibrated

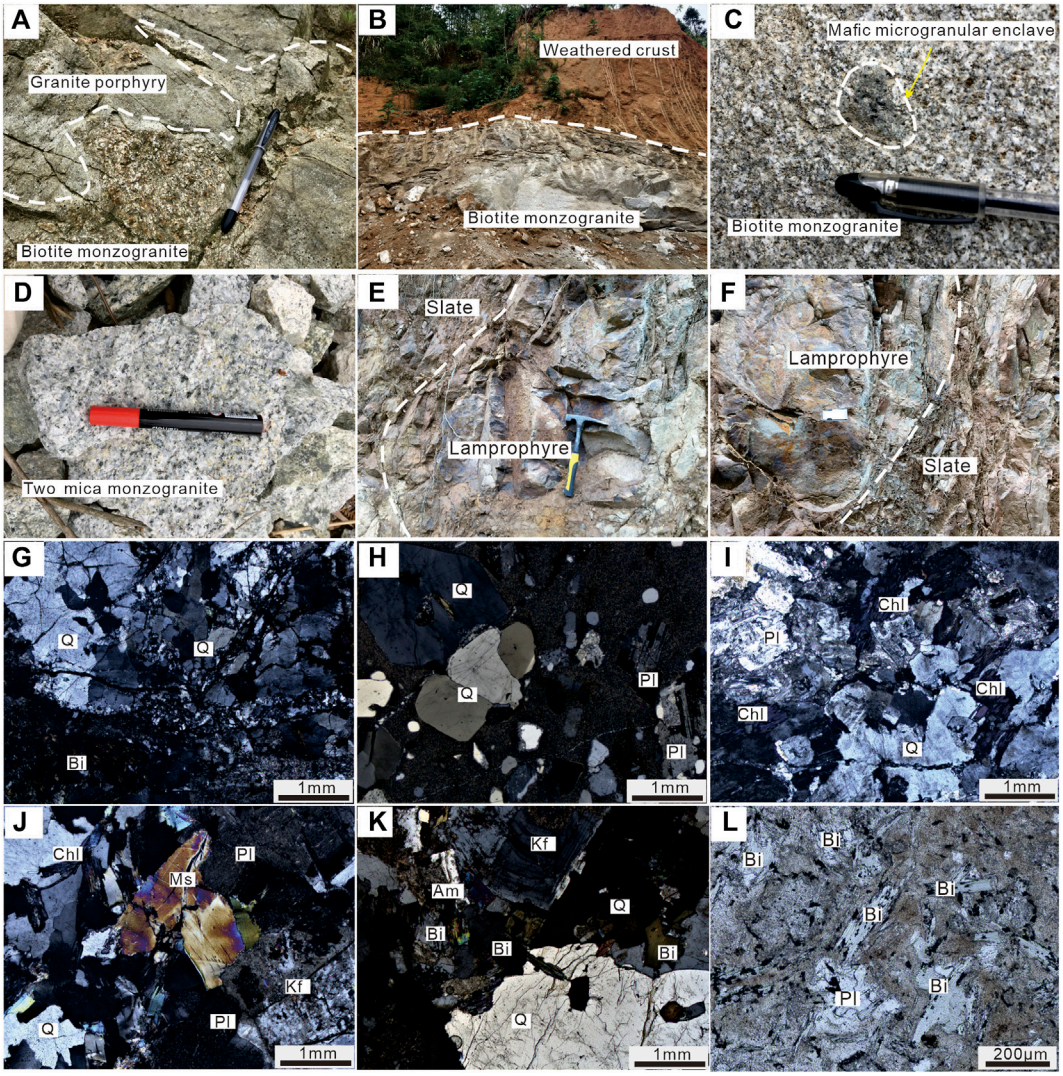


FIGURE 2
Petrographic photograph of Guandimiao batholith; **(A)**, Granite porphyry intruded into biotite monzogranite; **(B)**, Biotite monzogranite profile; **(C)**, MME (mafic microgranular enclave) in biotite monzogranite; **(D)**, Weathered two-mica monzogranite; **(E,F,L)**, Lamprophyre; **(G,I)** Biotite monzogranite; **(H)**, Granite prophyry; **(J)**, Two-mica monzogranite; **(K)**, Granodiorite. Abbreviation: Q-Quarz; Bi-Biotite; Pl-Plagioclase; Chl-Chlorite; Ms-Muscovite; Kf- Potassium feldspar; Am- Amphibole.

using 29 Si as internal standard and zircon M127 U: 923 ppm; Th: 439 ppm; Th/U: 0.475 (Nasdala et al., 2008) as external standard. $^{207}Pb/^{206}Pb$ and $^{206}Pb/^{238}U$ were calculated using the ICP-MS DataCal 4.3 program. Common Pb was not corrected because of the high $^{206}Pb/^{204}Pb$. Abnormally high ^{204}Pb data were deleted. The Plešovice zircon was dated as unknown and yielded a weighted mean $^{206}Pb/^{238}U$ age of 337 ± 2 Ma (2SD, n = 12), which is in good agreement with the recommended $^{206}Pb/^{238}U$ age of 337.13 ± 0.37 Ma (2SD) (Sláma et al., 2008). Age calculations were performed, and concordia diagrams were generated using the Isoplot/Ex 3.0 software (Ludwig, 2003).

4.2 Geochemstry

Whole-rock major, trace and rare earth element concentrations were analyzed at the National Geological Experiment Test Center, Beijing. Whole-rock major elements were analyzed using a plasma spectrometer (PE8300). All results were normalized against the Chinese rock reference standard JY/T015-1996; among them, H_2O^+ is analyzed on the basis of GB/T 14,506.2-2010, FeO contents are normalized to GB/T 14,506.14-2010, LOI contents are normalized to LY/T 1253–1999 and CO_2 contents are normalized to GB 9835–1988. The analytical uncertainties are less than ±2%.

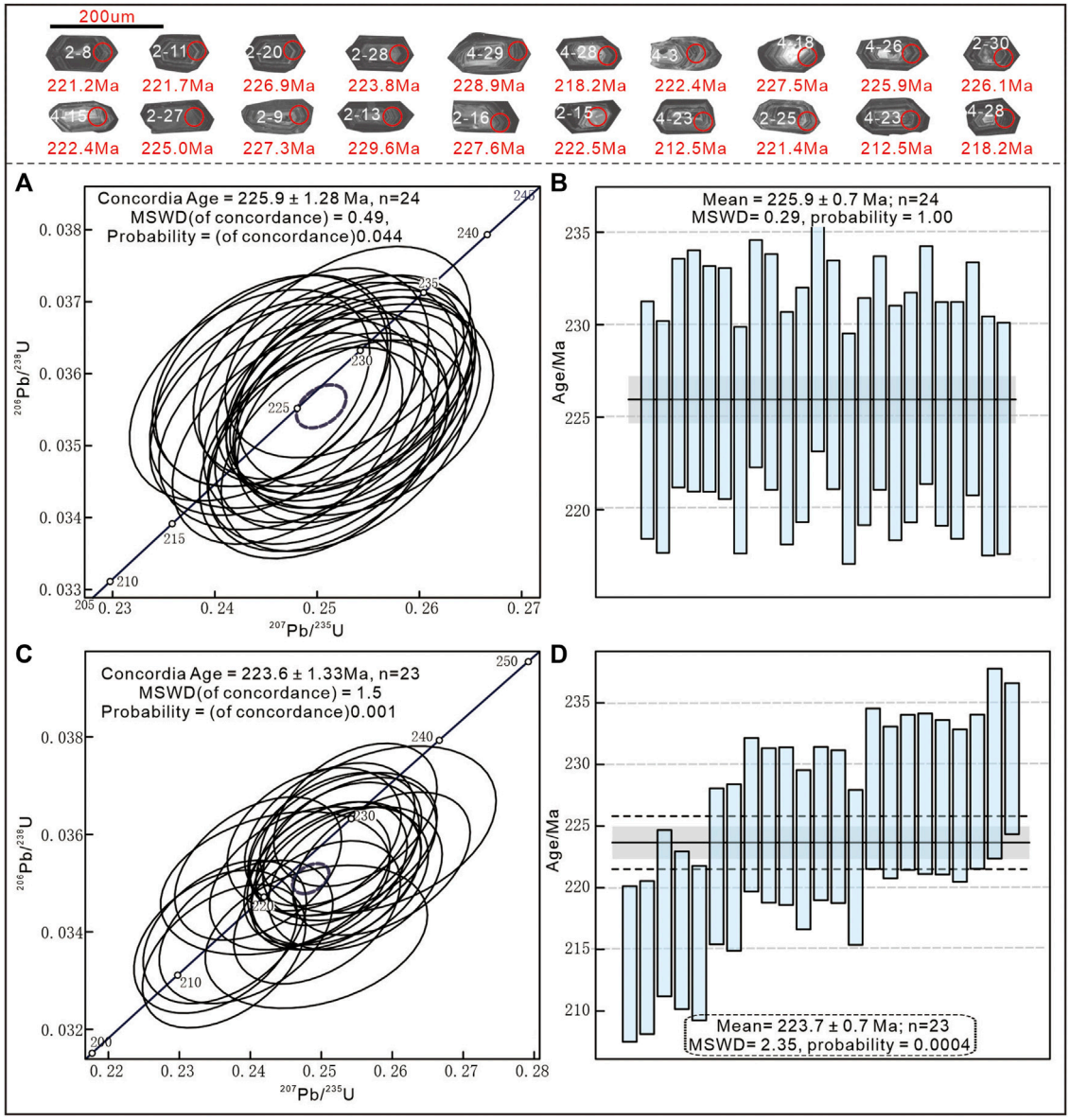


FIGURE 3
Zircon U–Pb concordia diagrams of Guandimiao biotite monzogranite. **(A,C)**, Concordia age diagrams; **(B,D)**, Mean age diagrams.

4.3 Sr-Nd-Pb isotope

Fresh samples were ground with an agate mill, and powders were spiked with mixed isotope tracers, dissolved in Teflon capsules with HF + HNO_3 acid, and separated by conventional cation exchange techniques. The isotopic measurements were performed on a VG-354 mass spectrometer at the Institute of Geology and Geophysics, Chinese Academy of Sciences. The mass fractionation corrections for Sr and Nd isotope ratios were based on $^{86}Sr/^{88}Sr = 0.1194$ and $^{146}Nd/^{144}Nd = 0.7219$. Repeat analyses yielded an $^{87}Sr/^{86}Sr$ ratio of 0.71023 ± 0.00006 for the NBS-987 Sr standard and a$^{143}Nd/^{144}Nd$ ratio of 0.511845 ± 0.000012 for the La Jolla standard. For Pb isotope determinations, 200 mg of powder was weighed into a Teflon vial, spiked and dissolved in concentrated HF at 80°C for 72 h. Pb was separated and purified by conventional cation exchange techniques (AG1 × 8,200–400 resin) with diluted HBr as an eluant. Isotopic ratios were measured with a VG-354 mass spectrometer at the Institute of Geology and Geophysics. Repeat analyses of NBS981 yielded $^{204}Pb/^{206}Pb = 0.05897 \pm 15$, $^{207}Pb/^{206}Pb = 0.91445 \pm 80$, and $^{208}Pb/^{206}Pb = 2.16170 \pm 180$. Detailed descriptions of the analytical

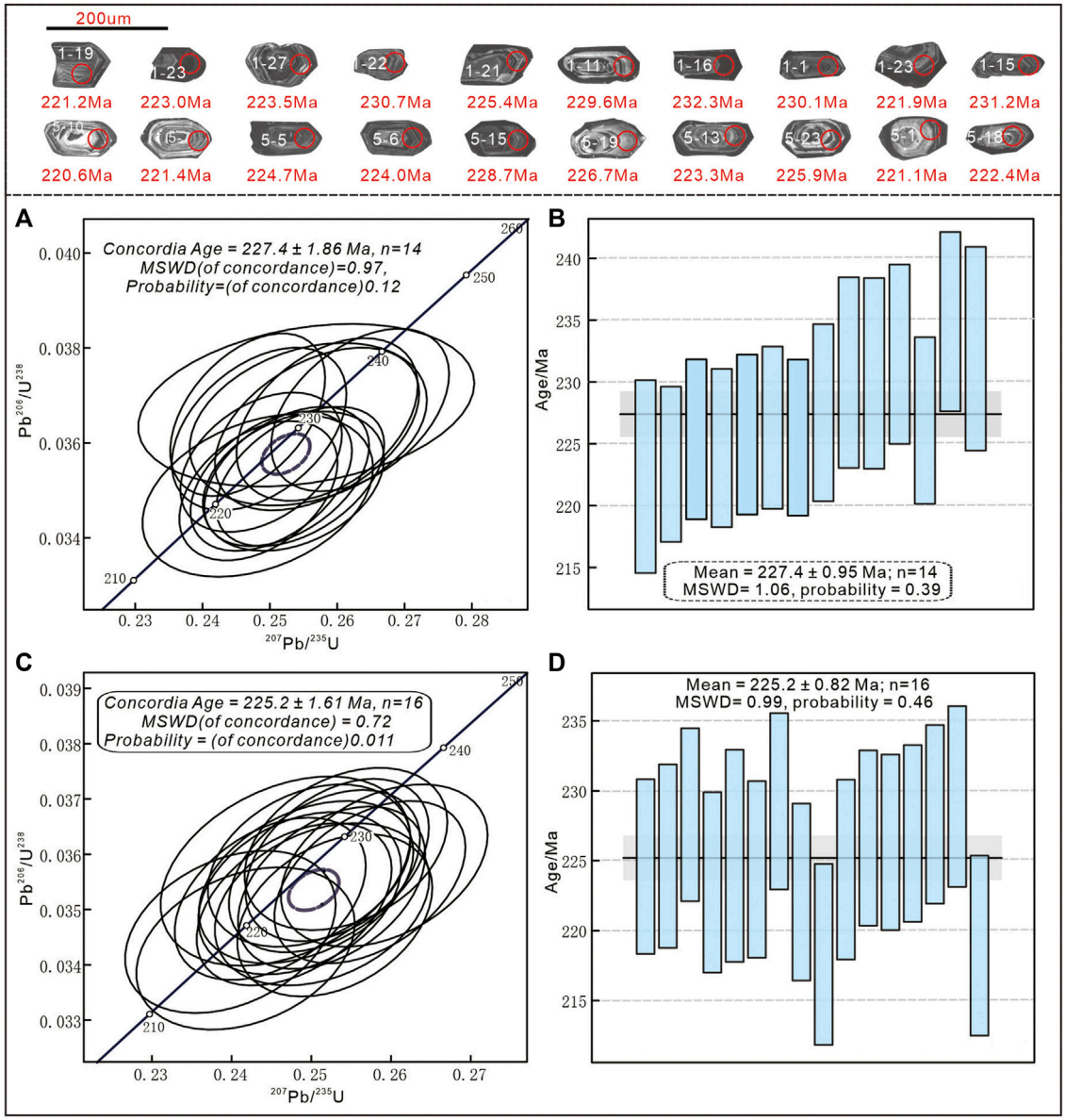


FIGURE 4
Zircon U–Pb concordia diagrams of Guandimiao two-mica monzogranite. **(A,C)**, Concordia age diagrams; **(B,D)**, Mean age diagrams.

techniques are given elsewhere (Zhang et al., 2002, and references therein).

5 Results

5.1 U-Pb chronology

5.1.1 G2-1

Zircons are long and columnar with length-to-width ratios close to 2:1. The sizes of zircons are between 100 and 150 μm. The edges of the zircons were obviously corroded. The U contents range from 446.6 to 1,515.8 ppm. Th contents range from 340.1 to 3,675.8 ppm. Th/U ratios varied from 0.4 to 1.7 (Table 1). The $^{206}Pb/^{238}U$ ages of sample HNGDM-2 are between 212.0 and 229.6 Ma, and yield the concordia age and mean age (n = 24) are 225.9 ± 1.28 Ma (MSWD = 0.49) and 225.9 ± 0.7 Ma (MSWD = 0.29), respectively (Figures 3A,B). The $^{206}Pb/^{238}U$ ages of Sample HNGDM-4 range from 236.1 to 207.6 Ma, and the concordia age and mean age (n = 19) of the zircon grains are 223.6 ± 1.3 Ma (MSWD = 1.5) and 223.7 ± 1.3 Ma (MSWD = 2.35), respectively (Figures 3C,D).

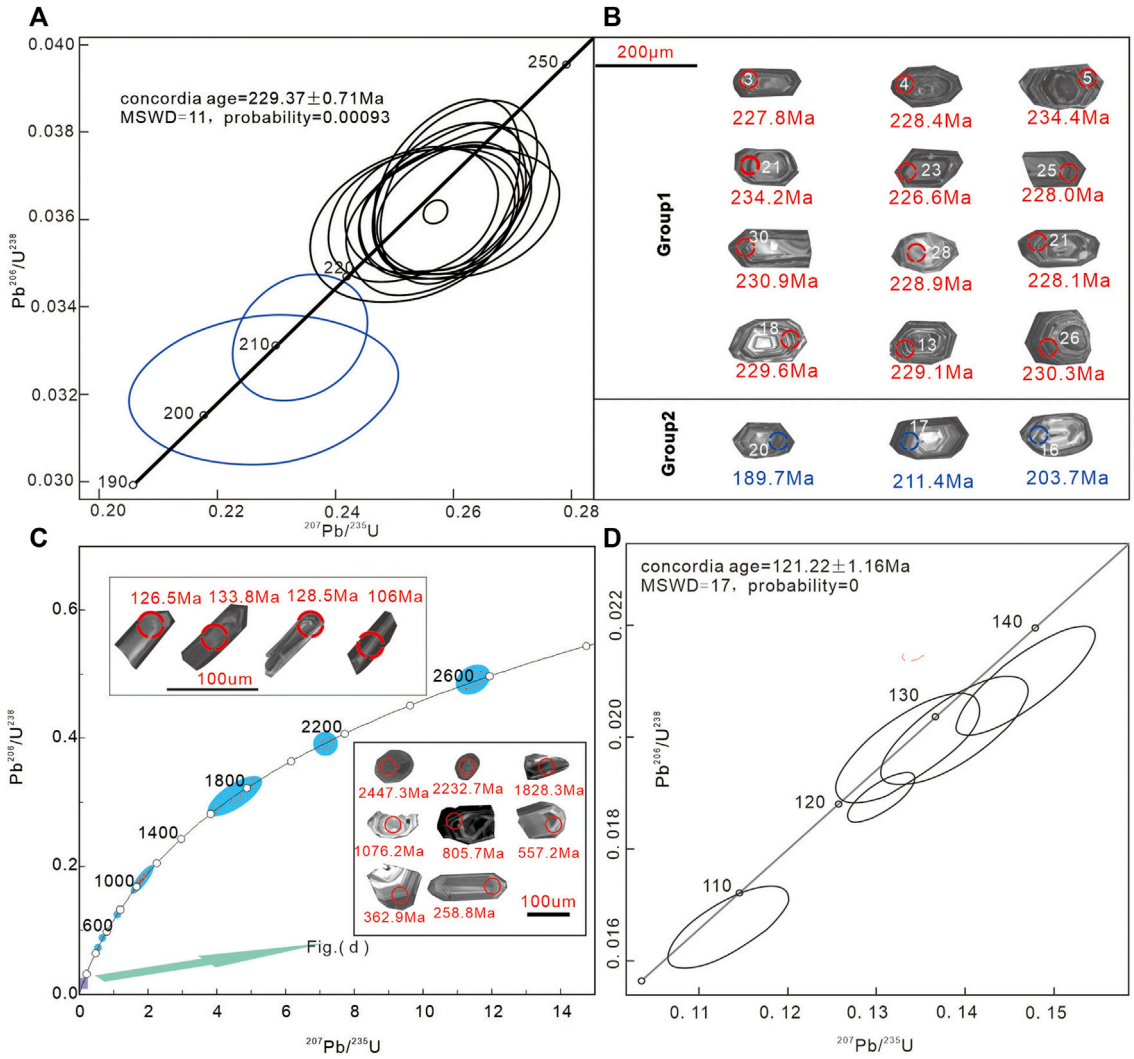


FIGURE 5
Zircon U–Pb concordia diagrams **(A)** and typical CL images **(B)** of Guandimiao granite porphyry; Zircon U–Pb concordia diagrams of Guandimiao lamprophyre **(C,D)**. The black circles in a and b represent $^{206}Pb/^{238}U$ ages of group1 zircons, the blue circles represent $^{206}Pb/^{238}U$ ages of group 2 zircons.

5.1.2 G2-2

Zircons exhibit length-to-width ratios between 1:1 and 2:1 and sizes of 100–200 μm. Most zircon grains developed obvious oscillatory zoning (Figure 4). The U contents range from 53.3 to 4,703.3 ppm (except for one spot value up to 9,301.8 ppm), Th contents range from 54.3 to 4,333.7 ppm (except for one spot value up to 6,293.6.8 ppm), and the Th/U ratios range from 0.5 to 1.9, suggesting an igneous origin (Rubatto, 2002; Wu and Zhen, 2004). Out of 30 spots in sample HNGDM-1, 14 analyses yield $^{206}Pb/^{238}U$ ages of 221.2–233.2 Ma, with a concordia U-Pb age of 227.4 ± 1.86 Ma (MSWD = 0.97) and a mean age of 227.41 ± 0.95 Ma (MSWD = 1.06) (Figures 4A,B). The $^{206}Pb/^{238}U$ ages of Sample HNGDM5-1 range from 217.3 to 228.7 Ma, with a concordia U-Pb age of 225.19 ± 1.61 Ma (MSWD = 0.72) and a mean age of 225.20 ± 0.82 Ma (MSWD = 0.99, n = 16) (Figures 4C,D).

5.1.3 G3

Zircons developed obvious oscillatory zoning. They exhibit length-to-width ratios from 1:1 to 2:1 with sizes from 100 to 200 μm (Figure 5B). U contents range from 516 to 3,309.6 ppm, Th contents range from 127.1 to 6,116.0 ppm, and Th/U ratios range from 0.1 to 2.2. Thirty spot analyses yield $^{206}Pb/^{238}U$ ages of 189.7–234.4 Ma. Two groups of $^{206}Pb/^{238}U$ ages can be identified. The first group is from 219.5 to 234.4 Ma with a concordia U-Pb age of 229.37 ± 0.71 Ma (MSWD = 2.6) (Figure 5A). The $^{206}Pb/$

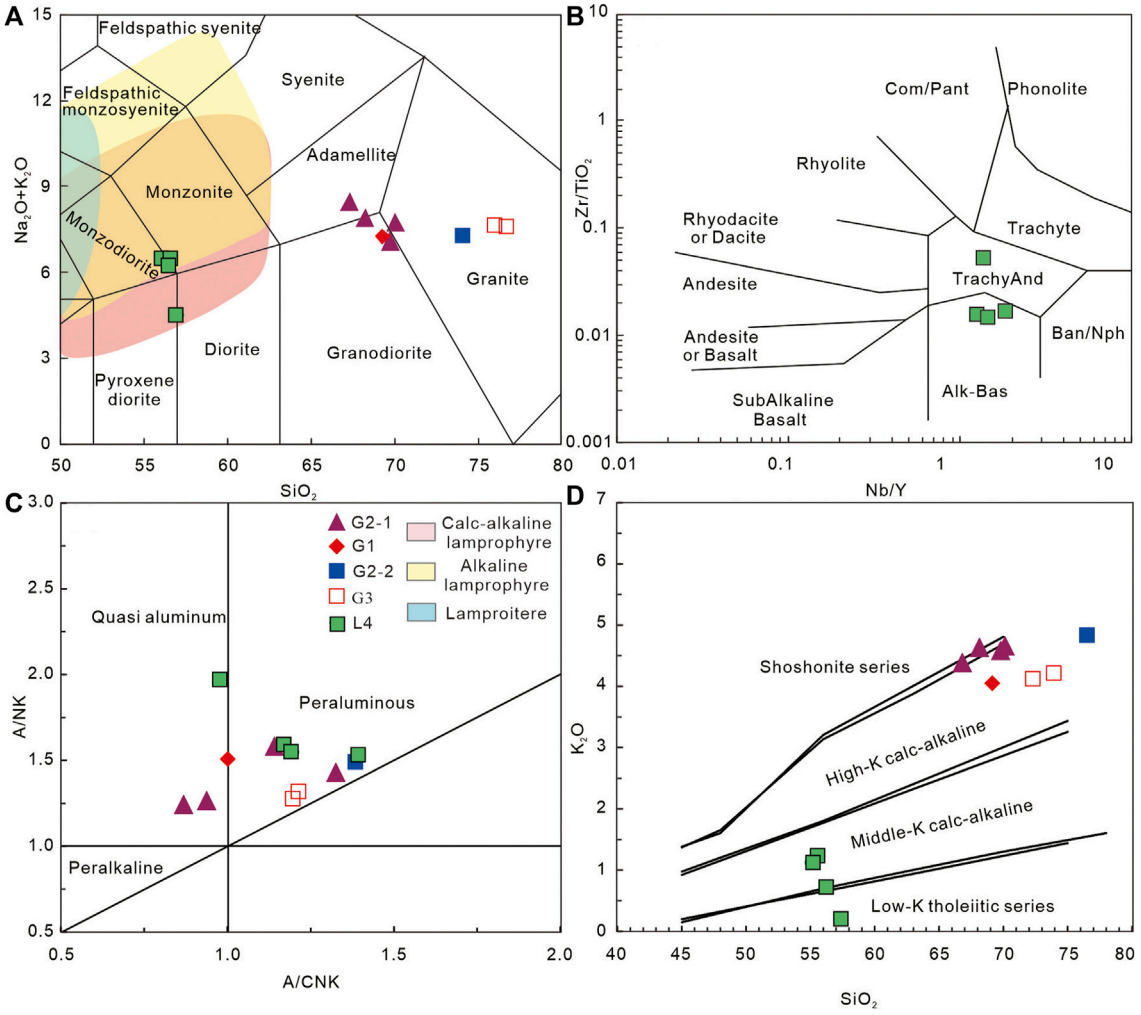


FIGURE 6
(A), TAS classification diagram of Guandimiao batholith; **(B)**, SiO_2 versus K_2O diagram; **(C)**, A/NK versus A/CNK diagram; **(D)**, K_2O versus SiO_2 diagram.

^{238}U ages of the second group range from 189.7 to 211.4 Ma (Figure 5A).

5.1.4 L4

Two distinct groups of zircons were identified. The first group of zircon grains are complex and exhibits length-to-width ratios from 1:1 to 2:1 and sizes from 50 to 200 μm, Most of them developed obvious oscillatory zoning and are generally incomplete in shape, wheras a small amount is smaller in size (50–100 μm) and round in shape. The second group exhibits length-to-width ratios from 3:1 to 4:1 and sizes of approximately 100–150 μm with U contents from 249.8 to 1,195.2 ppm, Th contents from 324.4 to 1,348.3 ppm, and Th/U ratios from 1.0 to 1.3. Out of 61 spot analyses of *L4*, 4 analysis points yield $^{206}Pb/^{238}U$ ages of 106.0–133.8 Ma, with a concordia U-Pb age of 121.22 ± 1.16 Ma (MSWD = 7) (Figures 5C,D). The first group of zircons exhibits a long-term span and contains at least nine stages of magmatism 1) 217.7–227.8 Ma; 2) 240.6–268.0 Ma; 3) 295.9–379.6 Ma; 4) 405.3–466.8 Ma; 5) 539.1–615.4 Ma; 6) 769.7–842.8 Ma; 7) 972.4–1,135.0 Ma; 8) 1,625.9–1931.6 Ma, and 9) 2,114.4–2,573.1 Ma, which could reveal the long chronological evolutionary history of South China.

5.2 Geochemistry

The obtained geochemical result of samples from Guandimiao Batholith are listed in Table 2.

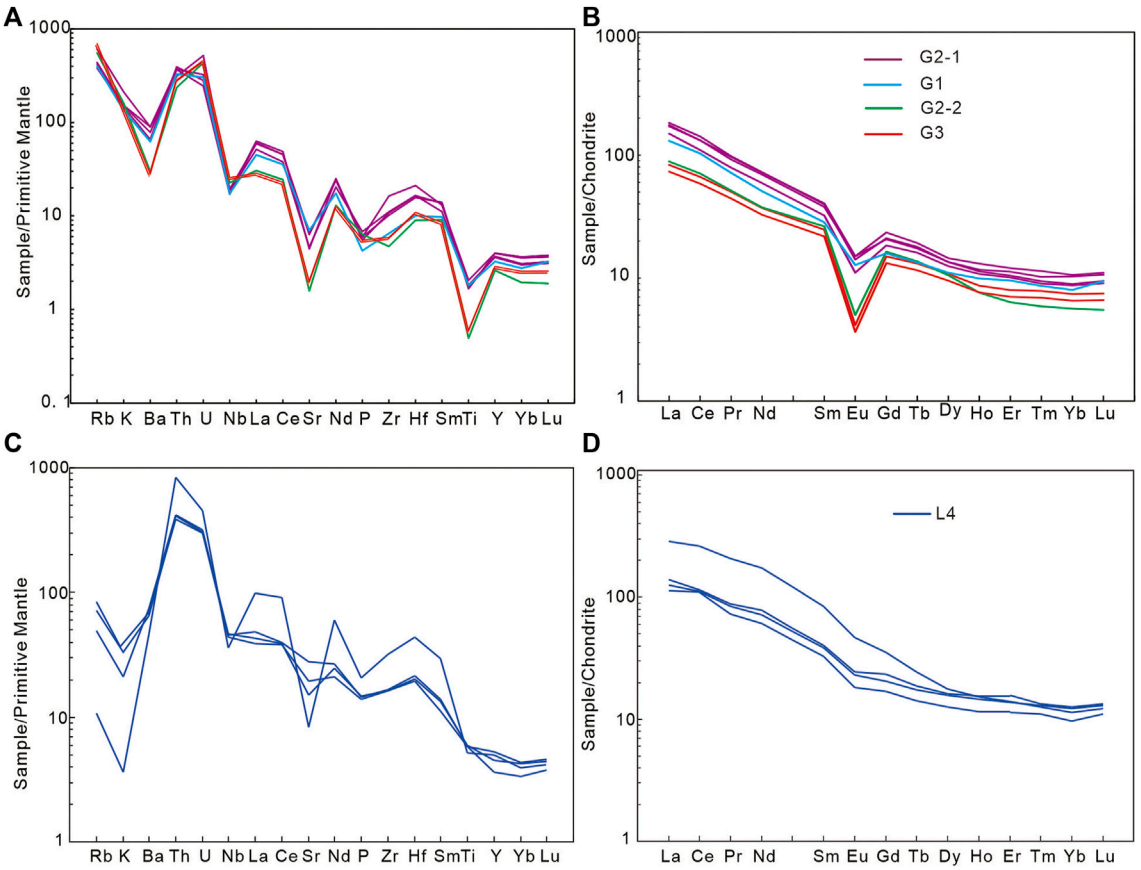


FIGURE 7
Rare earth element pattern and spidergrams of Guandimiao batholith (Standardized values according to Sun and McDonough, 1989); **(A,B)**, Standardization diagram of chondrite meteorites of REE; **(C,D)**, normalization diagram of the primitive mantle of trace elements.

G1 has low SiO_2 (69.29 wt%) and total alkalis (ALK = Na_2O + K_2O) (7.27 wt%) and higher Al_2O_3 (14.6 wt%), MgO (1.58 wt%), and CaO (2.7 wt%). The A/CNK and A/NK values are 1.00 and 1.51, respectively. G2-1 has high Al_2O_3 (14.36–14.71 wt%), ALK (7.76–8.53 wt%) and moderate SiO_2 (67.9–70.1 wt%) and FeO^T (2.96–3.39 wt%) contents and K/Na ratios (0.69–1.82). The ratios of A/CNK are 0.89–1.32, and those of A/NK are 1.24–1.58. The G2-2 have high contents of SiO_2 (74.09–75.2 wt%), ALK (6.43–7.30) and K/Na ratios (1.37–1.67) but low MgO (0.39–0.44 wt%), CaO (0.26–0.41 wt%), and FeO^T (1.22–1.47 wt%) contents.The G-3 is similar to the G2-2 but have higher content of SiO_2 (76.7 wt%), K_2O (4.84 wt%), ALK (7.63 wt%). L4 is characterized by low contents of SiO_2 (55.43–57.14 wt%), K_2O (0.11–1.01 wt%), ALK (4.12–6.70 wt%) and high contents of Al_2O_3 (12.83–17.02 wt%), FeO^T (6.66–7.31 wt%) and MgO (0.86–7.19 wt%). The SiO_2 versus (Na_2O + K_2O) and Zr/TiO_2 versus Nb/Y diagrams suggest monzonite-diorite affinity for G1 and G2-1, granite affinity for G2-2 and G3, and calc-alkaline lamprophyre for L4 (Figures 6A,B). On the A/CNK versus A/NK diagram and SiO_2 versus K_2O diagram, all samples plot in the metaluminous-peraluminous field, whereas G1, G2-1, G2-2, and G3 hold middle-high K calc-alkaline (CA) characteristics, and L4 has middle to low K calc-tholeiitic series affinity (Figures 6C,D).

The chondrite-normalized REE patterns of G2-2 and G3 show strongly negative Eu anomalies (δEu = 0.21–0.23) and have obviously lower differentiation of LREEs and HREEs [$(La/Yb)_N$ = 10.54–11.29, LREEs/HREEs = 8.84–9.81] than G1 and G2-1. The REE pattern of L4 has negative slopes with no obvious negative Eu anomalies (Eu/Eu^* = 0.73–0.78). Except for HNGDM-7, L4 shows the lowest fractionation of REEs (($La/Yb)_N$ = 9.66–10.98, LREEs/HREEs = 9.80–11.35). Spider diagrams normalized by a primitive mantle show enticed Rb, Th, U, La, Ce, Nd, Zr, and Hf and depleted Ba, Nb, Ce, P, and Ti for G1 and G2-1 (Figure 7A). G2-2 and G-3 are enriched in Rb, K, Th, U, La, Ce, Hf, and Y and depleted in Ba, Nb, Sr, Zr, and Ti (Figure 7B). L4 is enriched in Rb, Th, U, Nd, and Hf but depleted in K, Nb, Sr, and P. Sample HNGDM-7 of L4 obviously deviates from the main trend and presents stronger K, Nb, and Sr

TABLE 1 LA–ICP–MS U–Pb analysis results of the Guandimiao batholith.

Spot	WB/10^{-6}			Isotope ratio (± 1σ)						Isotope age (Ma) (± 1σ)					
	Th	U	Th/U	$^{207}Pb/^{206}Pb$		$^{207}Pb/^{235}U$		$^{206}Pb/^{238}U$		$^{207}Pb/^{206}Pb$		$^{207}Pb/^{235}U$		$^{206}Pb/^{238}U$	
				Ratio	Erro	Ratio	Erro	Ratio	Erro	Age	Erro	Age	Erro	Age	Erro
							G2-2								
HNGDM-1-18	1907.2	2079.4	0.9	0.0516	0.0012	0.2484	0.0055	0.0336	0.0006	267.9	50.2	225.3	4.5	213.2	3.8
HNGDM-1-28	1,552.9	1,219.3	1.3	0.0514	0.0012	0.246	0.006	0.0337	0.0006	257.2	54.5	223.3	4.9	213.3	3.8
HNGDM-1-26	957.1	3,665.1	0.3	0.0636	0.0013	0.3169	0.0064	0.0344	0.0006	728.9	42.7	279.5	4.9	218.2	3.8
HNGDM-1-19	1,341.1	1,186.1	1.1	0.0491	0.0014	0.2482	0.007	0.0349	0.0007	152.7	63.4	225.1	5.7	221.2	4.0
HNGDM-1-23	905.6	992.9	0.9	0.0501	0.001	0.2483	0.0048	0.035	0.0006	201.4	44.8	225.2	3.9	221.9	3.9
HNGDM-1-3	222.6	472.7	0.5	0.0528	0.0012	0.2535	0.0055	0.0352	0.0006	321.0	48.8	229.4	4.5	223.0	3.9
HNGDM-1-14	648.3	846.5	0.8	0.0511	0.001	0.2502	0.0049	0.0352	0.0006	247.1	45.2	226.8	4.0	223.0	3.9
HNGDM-1-12	1,645	2,378.6	0.7	0.0687	0.0014	0.3649	0.0075	0.0352	0.0006	888.5	42.0	315.9	5.6	223.2	3.9
HNGDM-1-27	287.5	528.5	0.5	0.051	0.001	0.2525	0.005	0.0353	0.0006	241.1	46.1	228.6	4.1	223.5	3.9
HNGDM-1-10	297	636.9	0.5	0.0514	0.001	0.2545	0.0051	0.0353	0.0006	259.0	45.8	230.2	4.1	223.7	3.9
HNGDM-1-20	3,090.9	1913.4	1.6	0.1226	0.0024	0.6158	0.0116	0.0355	0.0006	1993.8	33.9	487.2	7.3	224.9	3.9
HNGDM-1-21	780.8	810.5	1.0	0.0495	0.001	0.2487	0.0049	0.0356	0.0006	171.4	46.1	225.5	4.0	225.4	3.9
HNGDM-1-11	1961.5	1744.1	1.1	0.0528	0.001	0.2768	0.0053	0.0363	0.0006	319.5	43.6	248.1	4.2	229.6	4.0
HNGDM-1-29	754.6	557.7	1.4	0.0504	0.0011	0.2484	0.0053	0.0363	0.0007	211.3	48.9	225.3	4.3	229.6	4.0
HNGDM-1-1	1,170.5	894.1	1.3	0.0471	0.0011	0.257	0.0062	0.0363	0.0007	55.2	56.6	232.2	5.0	230.1	4.1
HNGDM-1-22	1,040.5	762.8	1.4	0.0482	0.0014	0.2557	0.0072	0.0364	0.0007	109.6	65.0	231.2	5.8	230.7	4.1
HNGDM-1-15	1,294.5	1,178.7	1.1	0.0501	0.0011	0.2585	0.0055	0.0365	0.0007	198.8	48.6	233.4	4.4	231.2	4.1
HNGDM-1-5	2,513.1	1,596.6	1.6	0.0581	0.0011	0.3011	0.0056	0.0365	0.0007	533.8	42.0	267.2	4.4	231.3	4.0
HNGDM-1-8	4,404.5	2,353.8	1.9	0.05	0.001	0.2467	0.0047	0.0366	0.0007	196.6	44.6	223.9	3.8	231.5	4.0
HNGDM-1-16	1,072	2,240.7	0.5	0.0525	0.0011	0.2634	0.0054	0.0367	0.0007	307.3	46.3	237.4	4.3	232.3	4.1
HNGDM-1-7	1,006.1	762	1.3	0.0483	0.0019	0.2554	0.0102	0.0368	0.0007	115.3	88.8	230.9	8.2	233.2	4.4
HNGDM-1-13	2,472.4	2,243.4	1.1	0.067	0.0013	0.3565	0.0067	0.0374	0.0007	837.4	39.4	309.6	5.0	236.4	4.1
HNGDM-1-6	1905.4	2,195.6	0.9	0.0518	0.0011	0.2696	0.0054	0.0383	0.0007	274.5	45.6	242.4	4.3	242.3	4.2
HNGDM-1-17	2,197.4	2,829.6	0.8	0.1495	0.0029	0.7968	0.0148	0.0385	0.0007	2,340.7	32.2	595.0	8.4	243.4	4.2
HNGDM-1-25	1,297.4	1,399.1	0.9	0.1493	0.0029	0.8237	0.0158	0.0391	0.0007	2,337.4	32.9	610.1	8.8	247.5	4.3
HNGDM-1-24	860.9	696.3	1.2	0.0501	0.0011	0.2736	0.0062	0.0395	0.0007	200.5	51.5	245.5	4.9	249.5	4.4
HNGDM-1-2	1,001.1	4,703.1	0.2	0.196	0.0037	1.0946	0.02	0.0408	0.0007	2,792.9	30.4	750.7	9.7	257.8	4.5
HNGDM-1-30	6,293.6	1,341.7	4.7	0.3095	0.0059	1.9078	0.0351	0.0425	0.0008	3,518.5	28.9	1,083.8	12.3	268.4	4.7
HNGDM-1-4	988	4,462	0.2	0.1513	0.0029	0.8726	0.0161	0.0427	0.0008	2,361.0	31.9	637.0	8.7	269.2	4.7
HNGDM-1-9	4,333.7	9,301.8	0.5	0.4406	0.0083	2.9242	0.0533	0.0491	0.0009	4,053.6	27.7	1,388.2	13.8	308.7	5.3
HNGDM-5-1_1	779.5	1,270.9	0.6	0.0515	0.0011	0.2530	0.0050	0.0349	0.0006	263.8	46.3	229.0	4.0	221.1	3.8
HNGDM-5-1_2	350.3	338.5	1.0	0.0668	0.0015	0.3612	0.0078	0.0396	0.0007	831.6	44.9	313.1	5.8	250.0	4.4
HNGDM-5-1_3	562.6	819.9	0.7	0.0466	0.0012	0.2555	0.0064	0.0343	0.0006	27.5	57.7	231.0	5.1	217.5	3.8
HNGDM-5-1_4	1,491.3	1,649.7	0.9	0.0562	0.0011	0.2903	0.0055	0.0355	0.0006	458.8	43.6	258.8	4.3	224.9	3.9
HNGDM-5-1_5	339.8	440.7	0.8	0.0496	0.0011	0.2494	0.0055	0.0355	0.0006	178.3	51.2	226.1	4.4	224.7	3.9
HNGDM-5-1_6	1963.6	3,203.5	0.6	0.0597	0.0012	0.3079	0.0058	0.0354	0.0006	592.8	41.4	272.6	4.5	224.0	3.9
HNGDM-5-1_7	910.9	1,453.6	0.6	0.0525	0.0011	0.2570	0.0049	0.0349	0.0006	305.6	44.9	232.2	4.0	221.4	3.8
HNGDM-5-1_8	821.5	1,158.8	0.7	0.0515	0.0010	0.2533	0.0047	0.0359	0.0006	260.9	43.9	229.2	3.8	227.6	3.9
HNGDM-5-1_9	1,322.1	1,478.9	0.9	0.0609	0.0012	0.3011	0.0058	0.0368	0.0007	634.6	42.4	267.2	4.5	232.9	4.0
HNGDM-5-1_10	603.6	983.2	0.6	0.0501	0.0011	0.2582	0.0056	0.0348	0.0006	199.6	50.5	233.2	4.5	220.6	3.9
HNGDM-5-1_11	54.3	53.3	1.0	0.0499	0.0010	0.2479	0.0050	0.0351	0.0006	189.9	47.9	224.9	4.1	222.5	3.9
HNGDM-5-1_12	284.2	331.1	0.9	0.0493	0.0013	0.2468	0.0064	0.0357	0.0007	161.1	59.2	224.0	5.2	226.1	4.1
HNGDM-5-1_13	510.0	646.3	0.8	0.0495	0.0011	0.2486	0.0052	0.0353	0.0006	170.0	49.8	225.4	4.3	223.3	3.9
HNGDM-5-1_14	537.8	671.1	0.8	0.0524	0.0014	0.2324	0.0060	0.0335	0.0006	303.4	57.9	212.1	4.9	212.3	3.8
HNGDM-5-1_15	337.8	473.6	0.7	0.0508	0.0011	0.2544	0.0052	0.0361	0.0006	233.8	47.6	230.1	4.2	228.7	4.0
HNGDM-5-1_16	969.0	1,158.8	0.8	0.0491	0.0010	0.2449	0.0049	0.0352	0.0006	154.5	47.4	222.5	4.0	223.3	3.9
HNGDM-5-1_17	133.7	192.2	0.7	0.0493	0.0012	0.2418	0.0056	0.0343	0.0006	161.6	54.5	219.9	4.6	217.3	3.8

(Continued on following page)

TABLE 1 (*Continued*) LA–ICP–MS U–Pb analysis results of the Guandimiao batholith.

Spot	WB/10^{-6}			Isotope ratio (± 1σ)						Isotope age (Ma) (± 1σ)					
	Th	U	Th/U	$^{207}Pb/^{206}Pb$		$^{207}Pb/^{235}U$		$^{206}Pb/^{238}U$		$^{207}Pb/^{206}Pb$		$^{207}Pb/^{235}U$		$^{206}Pb/^{238}U$	
				Ratio	Erro	Ratio	Erro	Ratio	Erro	Age	Erro	Age	Erro	Age	Erro
HNGDM-5-1_18	436.8	601.3	0.7	0.0519	0.0012	0.2514	0.0055	0.0351	0.0006	279.5	50.3	227.7	4.5	222.4	3.9
HNGDM-5-1_19	386.7	479.6	0.8	0.0494	0.0011	0.2498	0.0052	0.0358	0.0006	168.7	48.9	226.4	4.2	226.7	3.9
HNGDM-5-1_20	1,446.4	2051.6	0.7	0.0510	0.0010	0.2526	0.0048	0.0354	0.0006	241.9	45.1	228.6	3.9	224.0	3.9
HNGDM-5-1_21	575.9	843.2	0.7	0.0502	0.0010	0.2517	0.0049	0.0357	0.0006	203.9	46.6	228.0	4.0	226.0	3.9
HNGDM-5-1_22	636.0	860.3	0.7	0.0519	0.0010	0.2574	0.0049	0.0355	0.0006	280.4	45.0	232.6	4.0	224.7	3.9
HNGDM-5-1_23	934.8	1,201.2	0.8	0.0528	0.0011	0.2643	0.0053	0.0357	0.0006	319.8	46.6	238.1	4.3	225.9	3.9
HNGDM-5-1_24	2,139.8	2,761.3	0.8	0.0523	0.0011	0.2592	0.0053	0.0358	0.0006	298.3	47.2	234.0	4.3	226.6	3.9
HNGDM-5-1_25	386.2	595.3	0.6	0.0470	0.0011	0.2399	0.0054	0.0346	0.0006	48.6	53.8	218.4	4.4	219.5	3.8
G2-1															
HNGDM-4-24	343.7	419.1	0.8	0.0552	0.0015	0.2505	0.0068	0.0327	0.0006	420.6	58.7	227.0	5.5	207.6	3.8
HNGDM-4-23	859.3	976.9	0.9	0.0494	0.001	0.2363	0.0047	0.0335	0.0006	167.6	47.2	215.4	3.8	212.5	3.7
HNGDM-4-20	1,069.9	2071.1	0.5	0.0525	0.0011	0.2351	0.0047	0.0338	0.0006	308.3	46.3	214.4	3.9	214.0	3.7
HNGDM-4-25	274.5	426.6	0.6	0.053	0.0014	0.2493	0.0064	0.0339	0.0006	329.1	57.6	226.0	5.2	214.8	3.9
HNGDM-4-19	445.3	425.5	1.0	0.0515	0.0011	0.2394	0.005	0.034	0.0006	262.8	48.6	217.9	4.1	215.5	3.8
HNGDM-4-13	658.4	1,271.7	0.5	0.0491	0.001	0.2364	0.0047	0.034	0.0006	154.1	47.4	215.5	3.8	215.6	3.7
HNGDM-4-11	1,465	1,466.9	1.0	0.054	0.0011	0.258	0.0048	0.0343	0.0006	369.8	43.7	233.1	3.9	217.6	3.7
HNGDM-4-28	1,041.9	1,023.3	1.0	0.0505	0.001	0.2494	0.0048	0.0344	0.0006	219.5	46.1	226.1	3.9	218.2	3.8
HNGDM-4-9	1,236.3	1737.5	0.7	0.0472	0.0013	0.2435	0.0066	0.035	0.0006	57.2	63.6	221.3	5.4	221.8	3.9
HNGDM-4-3	1,019.8	940.8	1.1	0.0517	0.0011	0.2548	0.005	0.0351	0.0006	270.1	45.7	230.5	4.0	222.4	3.8
HNGDM-4-15	660	763.8	0.9	0.0505	0.0011	0.2526	0.0051	0.0351	0.0006	216.2	47.8	228.6	4.2	222.4	3.9
HNGDM-4-4	1,140.6	1,320	0.9	0.0532	0.0011	0.267	0.0055	0.0351	0.0006	336.1	47.3	240.3	4.4	222.5	3.9
HNGDM-4-7	1,157.7	1,358.3	0.9	0.051	0.001	0.2521	0.0049	0.0351	0.0006	241.3	46.1	228.3	4.0	222.5	3.8
HNGDM-4-1	473.8	648.3	0.7	0.0515	0.0011	0.247	0.0052	0.0351	0.0006	260.9	48.9	224.1	4.2	222.6	3.9
HNGDM-4-14	561.3	868.7	0.6	0.0512	0.0011	0.2518	0.005	0.0352	0.0006	250.0	46.6	228.0	4.0	222.9	3.9
HNGDM-4-12	660.2	1,247.2	0.5	0.0508	0.001	0.2506	0.0047	0.0352	0.0006	233.7	44.8	227.0	3.8	223.2	3.8
HNGDM-4-22	386.3	558.4	0.7	0.0495	0.001	0.2411	0.0048	0.0353	0.0006	171.5	47.3	219.3	3.9	223.6	3.9
HNGDM-4-2	1,090.5	1,271	0.9	0.0509	0.001	0.2585	0.0051	0.0354	0.0006	237.1	46.3	233.5	4.1	224.1	3.9
HNGDM-4-6	720.8	987.5	0.7	0.0516	0.0012	0.2638	0.0058	0.0354	0.0006	268.4	50.7	237.7	4.7	224.5	3.9
HNGDM-4-17	983.8	1,615.5	0.6	0.0585	0.0012	0.2952	0.0056	0.0355	0.0006	547.5	42.5	262.7	4.4	225.0	3.9
HNGDM-4-5	2013.5	1880.7	1.1	0.0506	0.001	0.2523	0.0047	0.0356	0.0006	222.6	44.4	228.4	3.8	225.4	3.9
HNGDM-4-26	721.1	1861.7	0.4	0.0484	0.001	0.254	0.005	0.0357	0.0006	120.5	47.2	229.8	4.0	225.9	3.9
HNGDM-4-21	506.3	653.9	0.8	0.0508	0.0011	0.2531	0.0054	0.0358	0.0006	232.2	49.7	229.1	4.4	226.4	3.9
HNGDM-4-27	598.2	579.3	1.0	0.0525	0.0011	0.2519	0.005	0.0358	0.0006	306.6	45.8	228.1	4.0	227.0	3.9
HNGDM-4-18	709	856	0.8	0.0508	0.0011	0.249	0.005	0.0359	0.0006	233.0	47.3	225.7	4.1	227.5	3.9
HNGDM-4-16	1,000.4	1,398.4	0.7	0.052	0.001	0.2642	0.005	0.0359	0.0006	287.2	44.7	238.1	4.0	227.6	3.9
HNGDM-4-10	3,675.8	1989.1	1.8	0.0491	0.001	0.2512	0.0049	0.036	0.0006	153.9	46.9	227.6	4.0	227.9	3.9
HNGDM-4-29	1,426.7	783.5	1.8	0.0484	0.0013	0.258	0.0068	0.0361	0.0007	118.2	61.0	233.0	5.5	228.9	4.1
HNGDM-4-8	1749.1	3,724.7	0.5	0.0511	0.001	0.2548	0.0047	0.0364	0.0006	244.9	44.0	230.5	3.8	230.5	4.0
HNGDM-4-30	265.2	317.9	0.8	0.049	0.0011	0.2452	0.0053	0.0373	0.0007	149.2	50.9	222.6	4.3	236.1	4.1
HNGDM-2_1	310.0	446.6	0.7	0.0497	0.0011	0.2466	0.0053	0.0356	0.0006	181.0	50.4	223.8	4.3	225.2	3.9
HNGDM-2_2	416.1	594.6	0.7	0.0499	0.0010	0.2454	0.0048	0.0355	0.0006	192.3	46.6	222.8	3.9	225.1	3.9
HNGDM-2_3	537.5	792.9	0.7	0.0495	0.0010	0.2519	0.0048	0.0358	0.0006	171.5	45.9	228.1	3.9	226.5	3.9
HNGDM-2_4	545.5	772.1	0.7	0.0515	0.0010	0.2704	0.0052	0.0390	0.0007	263.9	45.3	243.0	4.1	246.5	4.2
HNGDM-2_5	872.6	1,561.3	0.6	0.0524	0.0011	0.2514	0.0053	0.0359	0.0006	302.0	48.7	227.7	4.3	227.5	3.9
HNGDM-2_6	515.9	810.9	0.6	0.0497	0.0010	0.2494	0.0047	0.0360	0.0006	179.4	45.4	226.0	3.8	227.9	3.9
HNGDM-2_7	1,064.8	1,468.5	0.7	0.0523	0.0010	0.2537	0.0047	0.0354	0.0006	300.3	44.0	229.6	3.8	224.4	3.8
HNGDM-2_8	751.0	1,107.6	0.7	0.0491	0.0010	0.2500	0.0047	0.0349	0.0006	152.4	45.2	226.5	3.8	221.2	3.8
HNGDM-2_9	658.9	953.0	0.7	0.0509	0.0010	0.2537	0.0047	0.0359	0.0006	237.6	44.1	229.5	3.8	227.3	3.9

(Continued on following page)

TABLE 1 (*Continued*) LA–ICP–MS U–Pb analysis results of the Guandimiao batholith.

Spot	WB/10^{-6}			Isotope ratio (± 1σ)						Isotope age (Ma) (± 1σ)					
	Th	U	Th/U	$^{207}Pb/^{206}Pb$		$^{207}Pb/^{235}U$		$^{206}Pb/^{238}U$		$^{207}Pb/^{206}Pb$		$^{207}Pb/^{235}U$		$^{206}Pb/^{238}U$	
				Ratio	Erro	Ratio	Erro	Ratio	Erro	Age	Erro	Age	Erro	Age	Erro
HNGDM-2_10	381.6	556.1	0.7	0.0513	0.0010	0.2531	0.0049	0.0357	0.0006	256.0	45.7	229.1	4.0	225.9	3.9
HNGDM-2_11	490.5	788.6	0.6	0.0505	0.0010	0.2511	0.0048	0.0350	0.0006	216.9	45.9	227.5	3.9	221.7	3.8
HNGDM-2_12	567.9	841.1	0.7	0.0502	0.0010	0.2520	0.0049	0.0353	0.0006	203.0	46.5	228.2	4.0	223.3	3.8
HNGDM-2_13	588.5	851.8	0.7	0.0509	0.0010	0.2530	0.0049	0.0363	0.0006	234.1	45.8	229.0	4.0	229.6	3.9
HNGDM-2_14	272.9	437.4	0.6	0.0512	0.0011	0.2537	0.0050	0.0356	0.0006	249.1	46.6	229.6	4.1	225.4	3.9
HNGDM-2_15	720.9	918.6	0.8	0.0528	0.0010	0.2471	0.0046	0.0351	0.0006	319.7	43.5	224.2	3.7	222.5	3.8
HNGDM-2_16	666.3	969.3	0.7	0.0498	0.0010	0.2457	0.0047	0.0359	0.0006	185.6	45.7	223.0	3.8	227.6	3.9
HNGDM-2_17	564.8	847.6	0.7	0.0520	0.0010	0.2537	0.0048	0.0356	0.0006	283.0	45.0	229.6	3.9	225.5	3.9
HNGDM-2_18	813.5	1,077.1	0.8	0.0698	0.0014	0.3426	0.0065	0.0351	0.0006	923.2	40.0	299.1	4.9	222.1	3.8
HNGDM-2_19	508.7	760.4	0.7	0.0517	0.0010	0.2510	0.0048	0.0351	0.0006	274.0	44.8	227.4	3.9	222.3	3.8
HNGDM-2_20	746.3	1,074.5	0.7	0.0512	0.0010	0.2504	0.0047	0.0354	0.0006	249.4	44.8	226.9	3.8	224.3	3.9
HNGDM-2_21	445.1	709.9	0.6	0.0508	0.0010	0.2533	0.0050	0.0358	0.0006	229.7	46.7	229.3	4.1	226.9	3.9
HNGDM-2_22	1,072.0	1,642.6	0.7	0.0505	0.0011	0.2460	0.0049	0.0334	0.0006	218.2	47.3	223.3	4.0	212.0	3.7
HNGDM-2_23	565.7	832.6	0.7	0.0482	0.0010	0.2454	0.0047	0.0359	0.0006	107.6	46.5	222.8	3.8	227.2	3.9
HNGDM-2_24	415.7	612.5	0.7	0.0558	0.0011	0.2750	0.0053	0.0352	0.0006	442.1	43.7	246.7	4.2	223.1	3.8
HNGDM-2_25	585.9	1,009.9	0.6	0.0512	0.0010	0.2526	0.0049	0.0350	0.0006	248.1	45.5	228.7	3.9	221.4	3.8
HNGDM-2_26	837.9	1,075.1	0.8	0.0686	0.0014	0.3450	0.0067	0.0361	0.0006	885.8	40.9	301.0	5.0	228.8	3.9
HNGDM-2_27	806.2	1,037.7	0.8	0.0502	0.0011	0.2545	0.0052	0.0355	0.0006	202.5	48.5	230.2	4.2	225.0	3.9
HNGDM-2_28	858.1	1,515.8	0.6	0.0504	0.0011	0.2475	0.0053	0.0353	0.0006	212.3	49.8	224.5	4.3	223.8	3.9
HNGDM-2_29	580.5	835.9	0.7	0.0641	0.0014	0.3372	0.0071	0.0372	0.0007	745.3	44.9	295.1	5.4	235.4	4.1
HNGDM-2_30	340.1	545.4	0.6	0.0497	0.0010	0.2434	0.0048	0.0357	0.0006	180.5	47.3	221.2	3.9	226.1	3.9
L4															
HNGDM-6_1	993.7	489.9	2.0	0.0722	0.0015	0.5501	0.0117	0.0547	0.0010	992.5	41.8	445.1	7.6	343.0	6.0
HNGDM-6_2	497.2	365.1	1.4	0.1614	0.0030	10.1749	0.1946	0.4618	0.0082	2,470.1	31.2	2,450.8	17.7	2,447.3	36.1
HNGDM-6_3	2,593.4	857.9	3.0	0.0526	0.0011	0.2543	0.0055	0.0353	0.0006	309.5	48.3	230.1	4.4	223.7	4.0
HNGDM-6_4	836.0	574.9	1.5	0.0491	0.0010	0.2441	0.0050	0.0356	0.0006	150.2	47.3	221.8	4.0	225.2	4.0
HNGDM-6_5	130.7	88.2	1.5	0.1109	0.0021	4.9884	0.1042	0.3248	0.0058	1813.5	34.4	1817.4	17.7	1813.0	28.2
HNGDM-6_6	1,536.0	889.9	1.7	0.0655	0.0013	0.3494	0.0067	0.0380	0.0007	790.0	40.0	304.3	5.0	240.6	4.2
HNGDM-6_7	1,024.9	1,110.3	0.9	0.0495	0.0011	0.2523	0.0054	0.0360	0.0007	172.0	49.3	228.4	4.4	227.8	4.0
HNGDM-6_8	717.5	555.0	1.3	0.0505	0.0012	0.1388	0.0034	0.0201	0.0004	215.9	56.0	132.0	3.0	128.5	2.3
HNGDM-6_9	61.5	471.4	0.1	0.0717	0.0014	1.6530	0.0333	0.1671	0.0030	976.6	39.0	990.7	12.7	996.0	16.5
HNGDM-6_10	307.4	364.8	0.8	0.0503	0.0012	0.2453	0.0061	0.0352	0.0007	210.9	56.1	222.8	5.0	222.7	4.0
HNGDM-6_11	1,348.3	1,195.2	1.1	0.0521	0.0011	0.1468	0.0032	0.0210	0.0004	288.3	49.3	139.1	2.8	133.8	2.4
HNGDM-6_12	87.9	51.0	1.7	0.0568	0.0019	0.5433	0.0198	0.0699	0.0014	483.5	73.1	440.6	13.0	435.7	8.3
HNGDM-6_13	114.9	142.7	0.8	0.1087	0.0021	4.4792	0.0901	0.3034	0.0054	1777.6	34.3	1727.1	16.7	1708.1	26.8
HNGDM-6_14	44.2	96.6	0.5	0.1455	0.0028	8.0333	0.1736	0.4139	0.0074	2,293.6	32.4	2,234.8	19.5	2,232.7	33.9
HNGDM-6_15	38.0	22.3	1.7	0.0582	0.0027	0.5428	0.0273	0.0690	0.0015	535.8	97.6	440.3	18.0	430.3	9.3
HNGDM-6_16	171.8	997.2	0.2	0.1320	0.0025	6.6136	0.1232	0.3494	0.0062	2,124.3	32.3	2061.2	16.4	1931.6	29.7
HNGDM-6_17	530.3	512.1	1.0	0.0473	0.0012	0.1133	0.0028	0.0166	0.0003	61.6	58.7	108.9	2.6	106.0	1.9
HNGDM-6_18	35.1	28.6	1.2	0.0558	0.0022	0.5013	0.0215	0.0649	0.0014	442.3	85.7	412.6	14.5	405.3	8.2
HNGDM-6_19	90.8	434.7	0.2	0.1159	0.0022	5.3244	0.1019	0.3310	0.0059	1893.7	33.3	1872.8	16.4	1843.0	28.6
HNGDM-6_20	569.7	354.3	1.6	0.0665	0.0013	0.6790	0.0138	0.0736	0.0013	822.5	41.0	526.1	8.4	457.7	8.0
HNGDM-8_25	324.4	249.8	1.3	0.0491	0.0012	0.1335	0.0033	0.0198	0.0004	153.0	56.5	127.2	2.9	126.5	2.3
HNGDM-8_14	724.9	948.0	0.8	0.0500	0.0011	0.2348	0.0052	0.0339	0.0006	194.2	50.1	214.1	4.2	214.7	3.8
HNGDM-8_16	1,064.2	1,426.6	0.7	0.0471	0.0010	0.2501	0.0050	0.0348	0.0006	55.1	47.8	226.7	4.1	220.7	3.9
HNGDM-8_4	999.2	860.3	1.2	0.0503	0.0011	0.2480	0.0055	0.0349	0.0006	210.2	50.2	224.9	4.5	221.1	3.9
HNGDM-8_6	282.6	395.6	0.7	0.0513	0.0011	0.2514	0.0054	0.0355	0.0006	254.9	48.8	227.7	4.4	225.1	4.0
HNGDM-8_5	171.6	109.7	1.6	0.0551	0.0014	0.5145	0.0135	0.0658	0.0012	415.9	53.8	421.5	9.1	411.0	7.4
HNGDM-8_1	316.5	262.4	1.2	0.0531	0.0011	0.5303	0.0117	0.0697	0.0013	331.7	47.5	432.0	7.8	434.3	7.6

(Continued on following page)

TABLE 1 (*Continued*) LA–ICP–MS U–Pb analysis results of the Guandimiao batholith.

Spot	WB/10^{-6}			Isotope ratio (± 1σ)						Isotope age (Ma) (± 1σ)					
	Th	U	Th/U	$^{207}Pb/^{206}Pb$		$^{207}Pb/^{235}U$		$^{206}Pb/^{238}U$		$^{207}Pb/^{206}Pb$		$^{207}Pb/^{235}U$		$^{206}Pb/^{238}U$	
				Ratio	Erro	Ratio	Erro	Ratio	Erro	Age	Erro	Age	Erro	Age	Erro
HNGDM-8_18	593.6	595.3	1.0	0.0574	0.0011	0.5653	0.0113	0.0730	0.0013	505.0	43.4	455.0	7.3	454.5	7.8
HNGDM-8_21	83.3	107.8	0.8	0.0731	0.0016	0.7755	0.0183	0.0751	0.0014	1,015.3	43.9	582.9	10.5	466.8	8.2
HNGDM-8_9	15.6	423.7	0.0	0.0580	0.0012	0.6880	0.0155	0.0872	0.0016	530.3	46.6	531.6	9.3	539.1	9.4
HNGDM-8_13	594.1	328.2	1.8	0.1926	0.0036	2.6082	0.0498	0.1002	0.0018	2,764.5	30.6	1,303.0	14.0	615.4	10.5
HNGDM-8_27	224.0	84.9	2.6	0.0639	0.0013	1.1044	0.0242	0.1268	0.0023	739.7	42.9	755.5	11.7	769.7	13.1
HNGDM-8_19	100.0	76.7	1.3	0.0652	0.0014	1.1749	0.0275	0.1300	0.0024	779.2	44.4	788.9	12.9	787.6	13.4
HNGDM-8_20	98.3	56.1	1.8	0.0655	0.0015	1.1685	0.0308	0.1302	0.0024	791.8	48.0	785.9	14.4	789.0	13.7
HNGDM-8_3	315.1	240.0	1.3	0.0671	0.0013	1.2193	0.0245	0.1331	0.0024	841.4	40.0	809.4	11.2	805.7	13.5
HNGDM-8_24	170.0	181.2	0.9	0.0718	0.0014	1.6238	0.0327	0.1628	0.0029	979.0	38.9	979.4	12.7	972.4	16.1
HNGDM-8_28	204.7	214.6	1.0	0.0716	0.0014	1.6213	0.0316	0.1648	0.0029	973.7	38.4	978.5	12.2	983.3	16.2
HNGDM-8_23	120.7	104.2	1.2	0.0732	0.0015	1.7371	0.0416	0.1728	0.0031	1,020.7	41.9	1,022.4	15.4	1,027.8	17.2
HNGDM-8_8	45.8	104.5	0.4	0.0734	0.0015	1.7924	0.0384	0.1763	0.0032	1,023.8	39.6	1,042.7	14.0	1,046.8	17.3
HNGDM-8_2	44.7	644.4	0.1	0.0707	0.0013	1.7358	0.0324	0.1781	0.0032	949.9	37.8	1,021.9	12.0	1,056.5	17.3
HNGDM-8_12	147.2	121.0	1.2	0.0752	0.0015	1.8512	0.0383	0.1812	0.0032	1,073.4	38.6	1,063.8	13.6	1,073.4	17.7
HNGDM-8_22	366.3	358.4	1.0	0.0752	0.0014	1.8625	0.0355	0.1817	0.0032	1,074.1	37.4	1,067.9	12.6	1,076.2	17.6
HNGDM-8_26	49.5	85.6	0.6	0.0762	0.0015	1.9287	0.0401	0.1855	0.0033	1,099.6	38.6	1,091.1	13.9	1,096.9	18.0
HNGDM-8_11	116.2	222.4	0.5	0.0787	0.0015	2.0323	0.0399	0.1925	0.0034	1,164.2	37.2	1,126.4	13.4	1,135.0	18.5
HNGDM-8_29	17.2	715.5	0.0	0.0989	0.0018	3.9441	0.0723	0.2869	0.0051	1,602.6	34.2	1,622.8	14.8	1,625.9	25.4
HNGDM-8_30	128.3	303.0	0.4	0.1071	0.0020	4.5705	0.0859	0.3060	0.0054	1751.0	33.7	1743.9	15.7	1720.8	26.8
HNGDM-8_10	102.8	247.7	0.4	0.1114	0.0021	4.9857	0.0956	0.3279	0.0058	1822.7	33.4	1816.9	16.2	1828.3	28.2
HNGDM-8_7	177.6	262.2	0.7	0.1373	0.0026	7.1652	0.1440	0.3898	0.0069	2,193.4	32.2	2,132.2	17.9	2,121.7	32.1
HNGDM-8_15	75.4	77.4	1.0	0.1732	0.0033	11.4801	0.2406	0.4906	0.0087	2,588.6	30.9	2,563.0	19.6	2,573.1	37.8
HNGDM_1	193.06	334.74	0.6	0.06303	0.00238	0.09244	0.00144	0.7656	0.03605	709.1	78.2	569.9	8.5	577.2	20.7
HNGDM_2	559.10	1,297.83	0.4	0.052	0.0008	0.04191	0.0004	0.302	0.00483	285.4	34.9	264.7	2.5	268.0	3.8
HNGDM_3	99.28	149.70	0.7	0.12814	0.00147	0.38748	0.00361	7.02383	0.13113	2072.6	20.1	2,111.1	16.8	2,114.4	16.6
HNGDM_4	559.64	633.11	0.9	0.05435	0.00099	0.04637	0.00046	0.33833	0.00654	385.6	40.4	292.2	2.9	295.9	5.0
HNGDM_5	130.33	569.94	0.2	0.05512	0.00127	0.05993	0.00066	0.45338	0.0117	417.1	50.1	375.2	4.0	379.6	8.2
HNGDM_6	530.01	1,487.06	0.4	0.05334	0.00118	0.04098	0.00044	0.29027	0.00684	343.2	49.5	258.9	2.7	258.8	5.4
HNGDM_7	141.99	315.41	0.5	0.1715	0.00177	0.4839	0.00434	11.36067	0.17068	2,572.3	17.1	2,544.2	18.9	2,553.2	14.0
HNGDM_8	1,286.32	2071.90	0.6	0.1525	0.00163	0.06103	0.00055	1.29337	0.01432	2,374.1	18.1	381.9	3.3	842.8	6.3
HNGDM_9	742.85	1,479.61	0.5	0.06991	0.00133	0.04399	0.00046	0.42958	0.00886	925.8	38.5	277.5	2.9	362.9	6.3
HNGDM_10	1,678.17	822.21	2.0	0.05867	0.00246	0.03881	0.00063	0.27666	0.0124	554.9	89.0	245.5	3.9	248.0	9.9
HNGDM_11	731.74	1,115.60	0.7	0.05709	0.00072	0.07161	0.00065	0.55765	0.00742	494.4	27.9	445.9	3.9	450.0	4.8
HNGDM_12	480.04	854.75	0.6	0.05424	0.00161	0.04701	0.00059	0.35031	0.01142	380.9	65.4	296.2	3.7	305.0	8.6
G3															
HNGDM07-2_1	287.1	651.9	0.44	0.0523	0.0012	0.2625	0.0052	0.0364	0.0006	298.6	50.1	236.7	4.2	230.5	4.0
HNGDM07-2_2	144.9	2,333.5	0.06	0.0518	0.0011	0.2585	0.0049	0.0362	0.0006	277.4	48.4	233.5	3.9	229.1	4.0
HNGDM07-2_3	127.1	1,165.1	0.11	0.0506	0.0011	0.2507	0.0048	0.0360	0.0006	220.6	49.5	227.1	3.9	227.8	3.9
HNGDM07-2_4	686.2	3,309.6	0.21	0.0528	0.0011	0.2627	0.0050	0.0361	0.0006	322.1	47.9	236.9	4.0	228.4	3.9
HNGDM07-2_5	610.5	1,058.9	0.58	0.0509	0.0011	0.2597	0.0050	0.0370	0.0007	234.3	49.9	234.4	4.1	234.4	4.1
HNGDM07-2_6	800.5	519.1	1.54	0.0524	0.0012	0.2629	0.0056	0.0364	0.0007	301.7	52.8	237.0	4.5	230.6	4.0
HNGDM07-2_7	1,372.0	988.9	1.39	0.0866	0.0019	0.4325	0.0083	0.0362	0.0006	1,350.7	41.4	364.9	5.9	229.5	4.0
HNGDM07-2_8	876.2	1,099.3	0.80	0.0955	0.0021	0.4936	0.0095	0.0375	0.0007	1,537.4	40.6	407.4	6.5	237.3	4.1
HNGDM07-2_9	2,596.6	2,199.6	1.18	0.0663	0.0014	0.3267	0.0062	0.0357	0.0006	815.9	44.7	287.0	4.8	226.3	3.9
HNGDM07-2_10	2,112.1	2029.5	1.04	0.0691	0.0015	0.3422	0.0065	0.0359	0.0006	902.6	44.0	298.8	4.9	227.4	3.9
HNGDM07-2_11	486.7	599.4	0.81	0.0531	0.0012	0.2647	0.0054	0.0362	0.0006	331.5	51.3	238.5	4.4	229.1	4.0
HNGDM07-2_12	1997.0	2,219.6	0.90	0.0924	0.0020	0.4624	0.0089	0.0363	0.0006	1,474.5	40.8	385.9	6.1	229.9	4.0
HNGDM07-2_13	455.2	743.9	0.61	0.0518	0.0012	0.2585	0.0051	0.0362	0.0006	277.0	50.4	233.4	4.1	229.1	4.0
HNGDM07-2_14	2,147.5	998.5	2.15	0.0517	0.0012	0.2542	0.0050	0.0357	0.0006	271.2	50.2	230.0	4.1	226.0	3.9

(Continued on following page)

TABLE 1 (*Continued*) LA–ICP–MS U–Pb analysis results of the Guandimiao batholith.

Spot	WB/10^{-6}			Isotope ratio (± 1σ)						Isotope age (Ma) (± 1σ)					
	Th	U	Th/U	$^{207}Pb/^{206}Pb$		$^{207}Pb/^{235}U$		$^{206}Pb/^{238}U$		$^{207}Pb/^{206}Pb$		$^{207}Pb/^{235}U$		$^{206}Pb/^{238}U$	
				Ratio	Erro	Ratio	Erro	Ratio	Erro	Age	Erro	Age	Erro	Age	Erro
HNGDM07-2_15	6,116.0	2,551.7	2.40	0.0623	0.0014	0.2975	0.0057	0.0346	0.0006	684.1	45.9	264.4	4.5	219.5	3.8
HNGDM07-2_16	219.4	1,309.9	0.17	0.0515	0.0022	0.2278	0.0092	0.0321	0.0007	261.6	95.2	208.4	7.6	203.7	4.2
HNGDM07-2_17	470.9	1,055.5	0.45	0.0509	0.0012	0.2340	0.0047	0.0333	0.0006	236.8	51.3	213.5	3.9	211.4	3.7
HNGDM07-2_18	168.2	516.0	0.33	0.0520	0.0012	0.2600	0.0055	0.0363	0.0007	285.8	53.3	234.7	4.4	229.6	4.0
HNGDM07-2_19	441.6	1,458.4	0.30	0.0521	0.0012	0.2603	0.0051	0.0363	0.0006	288.8	49.6	234.9	4.1	229.5	4.0
HNGDM07-2_20	4,728.7	3,022.5	1.56	0.0908	0.0020	0.3737	0.0072	0.0299	0.0005	1,441.4	41.1	322.4	5.3	189.7	3.3
HNGDM07-2_21	828.7	1,473.1	0.56	0.0513	0.0011	0.2616	0.0052	0.0370	0.0007	253.4	50.5	235.9	4.2	234.2	4.1
HNGDM07-2_22	786.1	1,018.4	0.77	0.1583	0.0035	0.7949	0.0156	0.0364	0.0007	2,437.4	37.2	593.9	8.8	230.6	4.0
HNGDM07-2_23	1771.3	1,541.0	1.15	0.0512	0.0015	0.2525	0.0069	0.0358	0.0007	249.3	67.2	228.6	5.6	226.6	4.2
HNGDM07-2_24	307.6	706.0	0.44	0.0675	0.0016	0.3354	0.0072	0.0360	0.0007	854.4	49.0	293.7	5.5	228.1	4.0
HNGDM07-2_25	682.8	1,490.8	0.46	0.0518	0.0012	0.2573	0.0054	0.0360	0.0006	278.1	52.4	232.5	4.3	228.0	4.0
HNGDM07-2_26	388.6	747.8	0.52	0.0517	0.0012	0.2593	0.0053	0.0364	0.0007	272.8	51.7	234.1	4.3	230.3	4.0
HNGDM07-2_27	602.2	1787.8	0.34	0.0516	0.0012	0.2570	0.0052	0.0361	0.0006	268.4	51.3	232.2	4.2	228.7	4.0
HNGDM07-2_28	564.6	698.6	0.81	0.0511	0.0012	0.2547	0.0053	0.0362	0.0006	245.4	53.0	230.4	4.3	228.9	4.0
HNGDM07-2_29	1,082.0	772.8	1.40	0.0522	0.0012	0.2605	0.0054	0.0362	0.0006	294.3	52.1	235.0	4.4	229.1	4.0
HNGDM07-2_30	394.9	765.6	0.52	0.0517	0.0012	0.2597	0.0055	0.0365	0.0007	270.0	53.1	234.4	4.4	230.9	4.0

depletion and Th, U, La, Ce, Nd, and Hf enrichment (Figure 7C). The chondrite-normalized REE patterns of G1 and G2-1 are similar (Figure 7D), exhibiting negative slopes with strong light-heavy rare earth element fractionation [$(La/Yb)_N$ = 14.75–19.21; LREE/HREE = 12.00–14.08] and negative Eu anomalies (Eu/Eu* = 0.44–0.51). G1 and G2-1 have low Rb/Sr ratios (1.71–2.80) and high K/Rb ratios (136–155). However, G2-2 and G-3 have relatively higher Rb/Sr ratios (10.5–14.19) and lower K/Rb ratios (71.09–117). All granitic samples have Zr + Nb + Ce + Y values from 124.3 to 295.7 ppm, and the 10000 × Ga/Al ranges from 2.09 to 3.02, which is lower than the boundary value of 2.6 for A-type granite (Whalen et al., 1987),.

5.3 Sr–Nd–Pb isotopes

The $\varepsilon_{Nd}(t)$ values were calculated at 226–224 Ma for G2-1, 227–225 Ma for G2-2, 239 Ma for G1, 190 Ma for the granite porphyry and 121 Ma for L4 on the basis of zircon U-Pb dating. The Sr-Nd-Pb isotope compositions of the rocks from the Guandimiao batholith are shown in Table 3. The $^{87}Rb/^{86}Sr$ ratios of the Guandimiao batholith range from 7.95 to 8.74, and the calculated ISr values range from 7.1229 to 7.1796 (G2-2 and *G3* have high $^{87}Rb/^{86}Sr$ ratios, indicating that the calculated results cannot represent the actual isotopic compositions). The $^{87}Rb/^{86}Sr$ ratios of L4 range from 0.11 to 0.38, and the calculated ISr values range from 0.71449 to 0.71748. The calculated $\varepsilon_{Nd}(t)$ values are −9.37 to −10.54 for G2-1, −6.95 for G1 and −12.14 for G2-2. The $^{143}Nd/^{144}Nd$ ratios and calculated $\varepsilon_{Nd}(t)$ values are 0.512558 and −8.96 for G3 and 0.512042–0.512071 and −10.18 to −9.62 for L4, respectively. Since the $f_{Sm/Nd}$ of the samples deviates from the mean value for continental crust, a two-stage model is used. Thus, we obtain two stages of depleted mantle model ages (T_{DM2}) based on the model reported by Depaolo (1981). The calculated two-stage model ages are 1859–1764 Ma for G2-1, 1,568 Ma for G1, 1730 Ma for G2-1, 1928 Ma for *G3* and 1,577–1,435 Ma for L4.

The $^{206}Pb/^{204}Pb$, $^{207}Pb/^{204}Pb$, and $^{208}Pb/^{204}Pb$ ratios of G2-1 vary from 18.821 to 18.611, 15.707–15.712, and 38.977–39.056, respectively. For G1, the $^{206}Pb/^{204}Pb$ ratio is 18.707, the $^{207}Pb/^{204}Pb$ ratio is 15.71, and the $^{208}Pb/^{204}Pb$ ratio is 39.109. For G2-2, the $^{206}Pb/^{204}Pb$ ratio is 18.701, the $^{207}Pb/^{204}Pb$ ratio is 15.701, and the $^{208}Pb/^{204}Pb$ ratio is 38.887. For G3, the $^{206}Pb/^{204}Pb$ ratio is 19.21, the $^{207}Pb/^{204}Pb$ ratio is 15.738, and the $^{208}Pb/^{204}Pb$ ratio is 39.081. For L4, the $^{206}Pb/^{204}Pb$ ratio is 18.95–19.96, the $^{207}Pb/^{204}Pb$ ratio is 15.71–15.78, and the $^{208}Pb/^{204}Pb$ ratio is 39.87–43.090. These data reflect relatively uniform Pb isotope ratios. The initial Pb isotope ratios of the samples were calculated using the formulas of Hart (1984). The calculated results for $(^{206}Pb/^{204}Pb)_i$, $(^{207}Pb/^{204}Pb)_i$, and $(^{208}Pb/^{204}Pb)_i$ range from 17.875 to 18.113, 15.664–15.682, and 37.75–37.787, respectively, for G2-1. For G1, the $(^{206}Pb/^{204}Pb)_i$ ratio is 18.36, the $(^{207}Pb/^{204}Pb)_i$ ratio is 15.692, and the $(^{208}Pb/^{204}Pb)_i$ ratio is 38.613. For G2-2, the $(^{206}Pb/^{204}Pb)_i$ ratio is 17.662, the $(^{207}Pb/^{204}Pb)_i$ ratio is 15.648, and the $(^{208}Pb/^{204}Pb)_i$ ratio is 36.992. For *G3*, the $(^{206}Pb/^{204}Pb)_i$ ratio is 18.588, the $(^{207}Pb/^{204}Pb)_i$ ratio is 15.707, and the $(^{208}Pb/^{204}Pb)_i$ ratio is 38.57. For L4, the $(^{206}Pb/^{204}Pb)_i$ ratios range from 18.31 to 19.72, the $(^{207}Pb/^{204}Pb)_i$ ratios range from

TABLE 2 Whole-rock geochemical results of igneous rocks in Guandimiao batholith.

Sample	HNGDM2-1	HNGDM-3	HNGDM-3-1	HNGDM-4	HNGDM-4-1	HNGDM-5-1	HNGDM-2	HNGDM07-2	HNGDM-6	HNGDM-6-1	HNGDM-6-2	HNGDM-7
	G1	G2-1		G2-2			G3			L4		
SiO2	69.3	70.1	69.8	67.9	67.3	76.7	74.1	75.2	55.9	55.4	56.3	57.1
TiO2	0.39	0.41	0.39	0.42	0.43	0.12	0.15	0.15	1.22	1.21	1.23	1.07
Al2O3	14.6	14.6	14.4	14.7	14.6	12.6	14.4	14.4	16.6	16.4	17.0	12.8
Fe2O3	0.94	2.43	1.79	0.56	0.81	0.21	0.93	1.63	3.18	2.82	4.96	1.34
FeO	1.89	0.70	1.15	2.62	2.68	1.01	0.56	0.69	4.35	4.53	2.85	5.45
MnO	0.07	0.07	0.07	0.10	0.11	0.06	0.05	0.06	0.20	0.19	0.21	0.21
MgO	1.58	1.09	1.19	1.44	1.47	0.31	0.44	0.39	5.00	5.08	4.99	7.19
CaO	2.70	0.44	1.93	2.58	2.23	0.37	0.41	0.26	2.01	2.25	0.80	3.62
Na2O	3.22	3.19	2.51	4.95	4.12	2.79	3.08	2.41	5.37	5.40	6.07	4.01
K2O	4.05	4.57	4.57	3.39	4.41	4.84	4.22	4.02	1.01	0.92	0.63	0.11
P2O5	0.10	0.16	0.14	0.14	0.13	0.15	0.13	0.12	0.33	0.35	0.34	0.49
CO2	0.30	0.18	0.22	1.85	1.16	0.35	0.55	0.3	1.53	1.89	0.31	2.40
H2O+	1.08	2.24	1.86	1.00	1.26	0.80	1.26	1.54	3.18	3.84	4.58	4.54
LOI	0.63	2.07	1.67	2.93	1.96	0.73	1.33	1.82	4.55	5.13	4.25	5.91
SUM	99.5	99.8	99.6	102	100	99.9	99.8	101	99.9	100	100	100
Na2O + K2O	7.27	7.76	7.08	8.34	8.53	7.63	7.30	6.43	6.38	6.32	6.70	4.12
K2O/Na2O	1.26	1.43	1.82	0.69	1.07	1.73	1.37	1.67	0.19	0.17	0.10	0.03
A/CNK	1.00	1.32	1.14	0.89	0.94	1.19	1.38	1.61	1.10	1.05	1.34	0.80
A/NK	1.51	1.43	1.58	1.24	1.26	1.28	1.49	1.73	1.67	1.66	1.60	1.91
Fe/Mg	1.73	2.65	2.32	2.17	2.32	3.87	3.17	5.53	1.44	1.39	1.47	0.93
Li	73.9	47.7	63.8	75.90	80.70	63.60	34.80	32.0	64.2	72.5	72.1	72.4
Be	4.87	6.36	5.80	5.24	3.57	3.67	7.51	5.88	3.36	3.64	3.02	3.20
Co	9.01	7.61	7.41	8.87	9.60	1.63	1.69	1.86	33.2	30.2	30.8	38.4
Ni	24.90	19.40	18.40	21.60	21.60	2.07	2.96	3.72	131	85.7	135	274
Cu	20.40	32.80	36.20	7.73	16.50	2.94	20.10	24.8	47.8	33.3	42.4	12.6
Zn	44.30	116.00	68.30	56.60	63.60	67.70	40.40	58.1	108	94.6	96.6	111
Ga	18.60	18.90	15.90	19.10	18.80	17.90	23.00	24.0	17.5	17.4	17.9	19.3
Rb	253.00	268.00	278.00	386.00	242.00	352.00	441.00	427	53.6	45.7	31.6	6.81
Sr	148.00	97.90	134.00	138.00	93.90	33.40	41.60	30.1	408	318	583	177
Mo	0.31	0.43	0.25	13.80	1.13	1.89	0.24	0.67	0.46	0.30	0.32	0.38
Cd	0.06	0.40	0.21	0.08	<0.05	0.12	0.06	0.08	0.12	0.12	0.06	<0.05
In	<0.05	<0.05	<0.05	0.05	<0.05	0.05	<0.05	<0.05	0.06	0.05	0.06	0.06

(Continued on following page)

10.3389/feart.2022.948723

TABLE 2 (*Continued*) Whole-rock geochemical results of igneous rocks in Guandimiao batholith.

Sample	HNGDM2-1	HNGDM-3	HNGDM-3-1	HNGDM-4	HNGDM-4-1	HNGDM-5-1	HNGDM-2	HNGDM07-2	HNGDM-6	HNGDM-6-1	HNGDM-6-2	HNGDM-7
	G1	G2-1		G2-2			G3			L4		
Cs	22.00	19.10	18.00	17.50	10.80	35.90	60.70	47.9	6.70	6.47	2.50	0.63
Ba	435.00	628.00	546.00	626.00	459.00	208.00	196.00	189	487	455	522	326
Tl	1.38	1.62	1.65	2.40	1.50	1.98	2.25	2.01	0.29	0.25	0.20	<0.05
Pb	44.70	46.20	37.30	50.10	46.30	50.80	24.30	25.3	16.4	13.7	10.2	12.7
Bi	1.19	0.96	0.98	1.79	0.82	5.94	0.99	2.31	0.17	0.13	0.13	0.14
Th	28.00	26.50	31.20	31.40	33.30	20.10	24.20	22.4	32.70	34.80	35.80	71.00
U	6.37	10.90	5.15	6.83	5.90	9.12	9.66	7.57	6.29	6.35	6.68	9.52
Nb	12.4	13.1	12.2	13.8	12.6	16.2	18.3	18.1	31.6	33.5	32.8	25.8
Ta	1.72	1.70	1.46	1.89	1.65	3.81	3.43	3.35	2.23	2.37	2.43	1.65
Zr	72.8	124	114	183	121	52.9	66.0	81.8	181	183	186	359
Hf	3.11	5.11	4.86	6.52	5.08	2.78	3.38	2.92	6.03	6.28	6.65	13.5
W	6.33	11.4	45.7	2.91	1.42	4.08	5.16	8.76	3.74	3.84	4.03	5.69
V	51.5	43.2	39.8	50.0	43.6	7.44	15.6	10.5	188.0	188	186	171.0
La	30.9	35.4	41.5	40.6	43.3	21.0	19.7	22.6	26.7	29.8	33.0	67.6
Ce	63.0	67.2	80.5	80.8	86.7	43.3	40.6	48.6	67.4	68.7	70.8	161
Pr	6.80	7.50	9.16	8.73	9.29	4.88	4.77	5.48	6.96	8.06	8.37	19.8
Nd	23.7	27.6	33.6	32.4	33.8	17.5	17.3	19.4	28.4	33.7	36.4	81.6
Sm	4.34	4.93	6.19	5.79	6.08	4.02	3.78	4.34	5.01	5.92	6.18	13.0
Eu	0.74	0.64	0.87	0.87	0.82	0.29	0.24	0.23	1.05	1.33	1.42	2.73
Gd	3.26	3.78	4.82	4.24	4.32	3.36	3.08	3.35	3.50	4.24	4.81	7.30
Tb	0.50	0.60	0.72	0.65	0.67	0.51	0.49	0.57	0.53	0.65	0.70	0.91
Dy	2.80	3.17	3.68	3.43	3.42	2.67	2.74	3.06	3.18	4.02	4.13	4.46
Ho	0.56	0.61	0.74	0.66	0.64	0.43	0.49	0.53	0.65	0.83	0.88	0.87
Er	1.58	1.67	1.99	1.86	1.73	1.05	1.32	1.46	1.88	2.29	2.60	2.31
Tm	0.22	0.23	0.29	0.26	0.24	0.15	0.20	0.23	0.28	0.33	0.34	0.32
Yb	1.36	1.48	1.80	1.75	1.52	0.96	1.26	1.35	1.64	2.08	2.14	1.94
Lu	0.24	0.23	0.28	0.27	0.24	0.14	0.19	0.18	0.28	0.33	0.34	0.31
Y	14.8	16.4	18.2	18.1	16.8	11.9	13.1	15.6	16.4	20.7	24.1	22.6
Zr + Nb + Ce + Y	163	221	225	296	237	124	138	164				
10000×Ga/Al	2.41	2.45	2.09	2.32	2.43	2.69	3.02	3.14				
Rb/Sr	1.71	2.74	2.07	2.80	2.58	10.50	10.60	14.2				

(Continued on following page)

10.3389/feart.2022.948723

TABLE 2 (*Continued*) Whole-rock geochemical results of igneous rocks in Guandimiao batholith.

Sample	HNGDM2-1	HNGDM-3	HNGDM-3-1	HNGDM-4	HNGDM-4-1	HNGDM-5-1	HNGDM-2	HNGDM07-2	HNGDM-6	HNGDM-6-1	HNGDM-6-2	HNGDM-7
	G1	G2-1		G2-2			G3			L4		
K/Rb	136	145	139	140	155	117	81.1	78.1				
ΣREE	140	155	186	182	193	100	96.2	127	164	183	196	387
LREE	129	143	172	169	180	91.0	86.4	100	136	148	156	346
HREE	10.5	11.8	14.3	13.1	12.80	9.30	9.77	26.3	28.3	35.5	40.0	41.0
LREE/HREE	12.3	12.2	12.0	12.9	14.1	9.8	8.84	3.82	4.78	4.16	3.90	8.43
LaN/YbN	16.3	17.2	16.5	16.6	20.4	15.7	11.2	28.7	27.9	24.5	26.4	59.7
δEu	0.58	0.44	0.47	0.51	0.47	0.23	0.21	0.18	0.73	0.77	0.77	0.78
δCe	1.02	0.96	0.97	1.00	1.01	1.01	1.00	1.02	1.17	1.05	1.00	1.05
TZr(°C)	714	785	764	771	743	713	739					

15.68 to 15.77, and the $(^{208}Pb/^{204}Pb)_i$ ratios range from 39.79 to 42.94. All analyzed Pb isotope compositions are shown in Table 4.

6 Discussion

6.1 Magmatism stages of the guandimiao batholith

Previous research on the biotite granodiorite of the Guandimiao batholith found that it formed 239 Ma (Wang et al., 2005a). The biotite monzogranite and two-mica monzogranite have a wide range of formation ages (230–220 Ma; Huang and Depaolo, 1989; Zhao et al., 2015). The Zhoujialing biotite granite exposed west of the Guandimiao batholith are formed at 208–203 Ma (Miao, 2014). Dai et al. (2008) determined that the formation age of lamprophyre was 153 Ma (Table 5).

In this study, high-precision LA-ICP-MS zircon U-Pb data were obtained for the Guandimiao batholith. The U-Pb data for G2-1 range from 225.9 ± 0.72 to 223.64 ± 1.33 Ma and for G2-2 from 227.5 ± 1.0 to 225.5 ± 2.2 Ma. These ages indicate that the main part of the batholith was formed in the Late Triassic. Due to the high emplacement and fast cooling of G3 and L4, the time was insufficient for the crystallization of sufficient zircon crystals. In addition, mafic magma is generally unsaturated silicon, and it is very hard to crystallize sufficient and well-formed zircon grains. In G3, two age groups were identified. The first group of ages yields a concordia U–Pb age of 229.37 ± 0.71 Ma, much closer to the main ages of the batholith within the allowed error range. These results suggest that the U-Pb ages of zircons were captured from G2-1 and G2-2. The second group of ages of zircons ranges from 189.7 to 211.4 Ma, which is significantly lower than those of G2-1 and G2-2. This more likely represents the crystallization age of G3. Four zircon grains in group one collected from lamprophyre formed 106.0 to 133.8 Ma and yield a concordia U-Pb age of 121.22 ± 1.16 Ma. However, the U-Pb ages of zircons from group two range from 217.7 to 2,573.1 Ma. Due to the same characteristics as those from felsic granite (G1, G2-1, G2-2, and G3) and the long-term temporal span, there is no doubt that it was from the succession of the source area or the capture crystals from the surrounding rocks.

Thus, four main stages of magmatism can be determined in the Guandimiao batholith: Stage 1 (G1; 239 Ma)→Stage 2 (G2-1, G2-2; 230–203 Ma)→Stage 3 (G3; 211–190 Ma)→Stage 4 (L4; 121 Ma) (Figure 8). Zhou et al. (2006) proposed that the formation ages of igneous rocks in the SCB contain two principal periods and five main stages. The Indosinian magmatism was between 251 and 205 Ma and can be divided into two stages (251–234 Ma and 234–205 Ma). The first stage formed 251–234 Ma and is defined as S-type granite with high aluminum contents. The 234–205 Ma stage was dominated by postcollisional granitoids without contemporaneous volcanic

TABLE 3 Sr-Nd isotopic compositions of igneous rocks in Guandimiao batholith.

Lithology	Rb	Sr	^{87}Rb	^{87}Sr	ISr	Sm	Nd	^{147}Sm	^{143}Nd	TDM	T2DM	εNd(t)	References
	(ppm)	(ppm)	^{86}Sr	^{86}Sr		(ppm)	(ppm)	^{144}Nd	^{144}Nd				
G1	253.00	148.00	4.95	0.73	0.71	4.34	23.70	0.11	0.51	1,427.00	1,518.00	−6.17	This paper
G3	441.00	41.60	30.95	0.80	0.73	3.78	17.30	0.13	0.51	2,234.00	1928.00	−12.14	
G2-1	268.00	97.90	7.95	0.74	0.72	4.93	27.60	0.11	0.51	1704.00	1859.00	−10.54	
	386.00	138.00	8.12	0.74	0.72	5.79	32.40	0.11	0.51	1,619.00	1764.00	−9.37	
G2-2	352.00	33.40	30.76	0.80	0.70	4.02	17.50	0.14	0.51	2,150.00	1730.00	−8.96	
L4	53.60	408.00	0.38	0.72	0.72	5.01	28.40	0.11	0.51	1,577.00	1749.00	−10.18	
	6.81	177.00	0.11	0.72	0.72	13.00	81.60	0.10	0.51	1,435.00	1732.00	−9.95	
	53.60	408.00	0.38	0.72	0.71	5.01	28.40	0.11	0.51	1,536.00	1704.00	−9.62	
Biotite granite	268.00	128.00	6.09	0.73	0.71	3.96	21.99	0.11	0.51	1,650.00	1790.00	−9.75	Zhao et al. (2015)
Biotite granite	261.00	149.00	5.09	0.73	0.71	4.36	26.09	0.10	0.51	1,540.00	1780.00	−9.59	
Biotite granite	229.00	144.00	4.60	0.73	0.71	4.38	25.51	0.10	0.51	1,590.00	1790.00	−9.75	
Biotite granite	266.00	133.00	5.81	0.73	0.71	4.73	27.99	0.10	0.51	1,580.00	1810.00	−9.95	
Biotite granite	272.00	138.00	5.70	0.73	0.72	3.80	20.63	0.11	0.51		1750.00	−9.10	Bai et al. (2014)
Biotite granite	269.00	91.50	8.53	0.74	0.71	4.20	24.67	0.10	0.51		1720.00	−8.74	
Biotite granite	271.00	123.00	6.37	0.74	0.72	5.07	28.72	0.11	0.51		1820.00	−9.95	

activity. The contemporaneous G1, G2-1, and G2-2 developed in the main body of the Guandimiao batholith. Lower Yanshanian igneous rocks (180–147 Ma) of the SCB, containing high K calc-alkaline I-type granitoids, are widespread and distributed as parallel belts. Upper Yanshanian igneous rocks contain early-stage granitic-volcanic rocks and late-stage mafic rocks in south-southeastern China. Correspondingly, the Yanshanian felsic and mafic dikes (G3 and L4) were emplaced at the center and margin of the Guandimiao batholith. Igneous rocks of the Guandimiao batholith contain a complete record of multiple stages of magmatism and tectonic events since the Indosinian.

6.2 Petrogenesis

6.2.1 Genesis type of granitic rocks

The S- and I-type scheme was initially proposed by Chappell and White (1974); Chappell and White (1992), and this letter scheme classification has been widely developed in later studies (Loiselle and Wones, 1979; Whalen et al., 1987; Eby, 1990; Eby, 1992; King et al., 1997; Bonin, 2007; etc.). The mineral assemblage, with the absence of typical alkaline mafic minerals, indicates I- and S-type granitic characteristics for Guandimiao granitoids. In addition, G1 and G2-1 of the Guandimiao batholith have low SiO2 and high FeOT contents and K/Na and FeO^T/MgO ratios; G2-2 and G3 are enriched in SiO_2 contents, Al_2O_3 contents, and K/Na ratios but depleted in MgO and CaO contents. The values of (Zr + Nb + Ce + Y) for the Guandimiao granitoids range from 138 to 295.7 ppm. The ΣREEs are 96.2–193 ppm, and 10,000 × Ga/Al ratios are 2.09–3.02. These values are significantly lower than the lowest values observed in A-type granite (Whalen et al., 1987). Whole-rock Zr saturation temperatures suggest that crystallization temperatures (714–785°C) are consistent with crystallization temperatures < 800°C of I- and S-type granite rather than crystallization temperatures (>8 00°C, even possibly > 1,000°C) of A-type granite (Clemens et al., 1986). All samples plot in the S- and I-type granite fields on the FeO^T/MgO versus Zr + Nb + Ce + Y (Figure 9A).

On the ACF classification diagram, G2-2 and G3 plot in the S-type granite field, whereas G1 and G2-1 plot within the I-type granite field (Figure 9B).

6.2.2 Origin of the guandimiao batholith

The Pb isotope compositions of the Guandimiao granitoids present higher radiogenic Pb isotope compositions than syntectic granite and plot in the remelting granite of the South China field on the $(^{207}Pb/^{204}Pb)_i$ versus $(^{208}Pb/^{204}Pb)_i$ diagram and $^{207}Pb/^{204}Pb$ versus $^{206}Pb/^{204}Pb$ diagram. It is also above the mantle evolution line proposed by Hart (1984) (Figures 10A,B). This suggests that the Pb was mainly derived from the upper crust.

However, the existence of different genetic types (I- and S-type) and lithological compositions of intrusive rocks indicates diverse sources for the Guandimiao batholith (Chappell and White, 1974; Chappell et al., 1988). Zhou (2003) noted that the Indosinian granitoids are scattered across South China. Because of the uneven thickness of the Earth's crust, the granitoids are characterized by multiple sources and are dominated by thickened continental crust. G1 and G2-1 of the Guandimiao batholith enclosed mafic microgranular enclave,

TABLE 4 Pb isotopic compositions of igneous rocks in Guandimiao batholith.

Samples	U/ ppm	Th/ ppm	Pb/ ppm	$^{206}Pb/^{204}Pb$	$^{207}Pb/^{204}Pb$	$^{208}Pb/^{204}Pb$	$^{206}Pb/^{207}Pb$	μ	ω	Th/U	V1	Reference
HNGDM-2-1	6.37	28.00	44.70	239.00	18.71	15.71	39.11	9.65	38.64	3.88	91.25	This paper
HNGDM-2	9.66	24.30	24.20	153.00	19.21	15.74	39.08	9.66	36.16	3.62	97.02	
HNGDM-3	10.90	46.20	26.50	226.00	18.82	15.71	39.06	9.64	37.83	3.80	91.92	
HNGDM-4	6.83	50.10	31.40	226.00	18.61	15.71	38.98	9.65	38.62	3.87	84.59	
HNGDM-5-1	9.12	50.80	20.10	226.00	18.70	15.70	38.88	9.63	37.66	3.78	84.50	
HNGDM-6	6.29	16.40	32.70	18.95	15.71	39.87	1.21	9.63	40.30	4.05	107.46	
HNGDM-7	9.52	12.70	71.00	19.96	15.78	43.00	1.26	9.70	46.59	4.65	208.59	
HNGDM-8	6.35	13.70	34.80	19.48	15.77	40.91	1.24	9.70	41.80	4.17	146.06	
GDM11-4	6.34	26.10	38.39	223.00	18.63	15.76	39.29	9.75	40.24	3.99	92.41	Zhao et al. (2015)
GDM11-6	6.14	25.00	35.76	223.00	18.63	15.75	39.28	9.74	40.22	4.00	92.06	
GDM11-9	7.18	26.03	38.58	223.00	18.65	15.71	39.18	9.66	39.27	3.93	90.21	
Samples	V2	△α	△β	△γ	TSK/Ma	μ2	ω2	$(Th/U)^2$	$(^{206}Pb/^{204}Pb)_i$	$(^{207}Pb/^{204}Pb)_i$	$(^{208}Pb/^{204}Pb)_i$	Reference
HNGDM-2-1	67.68	96.51	25.55	54.27	168.00	10.09	40.93	3.93	18.36	15.69	38.61	This paper
HNGDM-2	88.98	118.96	26.98	49.68	−142.00	10.11	37.76	3.61	18.59	15.71	38.57	
HNGDM-3	73.28	102.14	25.62	52.26	89.00	10.07	39.83	3.83	17.88	15.66	37.75	
HNGDM-4	63.69	89.85	25.29	50.13	232.00	10.10	40.92	3.92	18.11	15.68	37.79	
HNGDM-5-1	69.10	95.12	24.90	47.44	154.00	10.05	39.58	3.81	17.66	15.65	36.99	
HNGDM-6	65.74	101.91	25.24	69.68	−7.00	10.05	42.94	4.14	18.31	15.68	39.79	
HNGDM-7	81.98	160.51	29.81	153.58	−604.00	10.19	51.09	4.85	19.72	15.77	42.94	
HNGDM-8	81.35	132.66	28.83	97.59	−279.00	10.19	45.12	4.29	18.97	15.74	40.83	
GDM11-4	62.18	90.81	28.41	58.37	312.00	10.31	43.48	4.08	18.20	15.73	38.72	Zhao et al. (2015)
GDM11-6	61.92	90.46	28.28	58.15	313.00	10.30	43.44	4.08	18.18	15.73	38.70	
GDM11-9	63.09	91.69	25.47	55.48	213.00	10.10	41.78	4.00	18.16	15.69	38.62	

TABLE 5 Formation ages of the ig rocks from Guandimiao batholith.

Sampling location	Lithology	Age/Ma	Method	Reference
Guandimiao	Two mica monzogranite	227.5 ± 1.0	LA	This paper
Guandimiao	Two mica monzogranite	225.5 ± 2.2	LA	
Guandimiao	Biotite monzogranite	226.2 ± 0.82	LA	
Guandimiao	Biotite monzogranite	225.9 ± 0.72	LA	
Guandimiao	Lamprophyre	121.22 ± 1.16	LA	
Guandimiao	Granite porphyry	189–211		
Guandimiao	Biotite granite	223.4 ± 1.7	LA	Zhao et al. (2015)
Guandimiao	Biotite granodiorite	239 ± 3	SHRIMP	Wang et al. (2005)
Guandimiao	Shizhuqiao two-mica alkali feldspar granite	226 ± 3	LA	Zhao et al. (2017)
Guandimiao	Jingtou hornblende-bearing biotite monzogranite	223 ± 2	LA	Zhao et al. (2017)
Guandimiao	Microgranular enclaves	220 ± 3	LA	Zhao et al. (2017)
Guandimiao	Granite	203–208		
Guandimiao	Granite	220 ± 3	LA	Miao B. F. (Unpublished),
Guandimiao	Monzonitic granite	230	K-Ar	Huang and Depaolo, (1989)
Zhoujialing	Biotite granite	203 ± 1.4	LA	Miao, (2014)

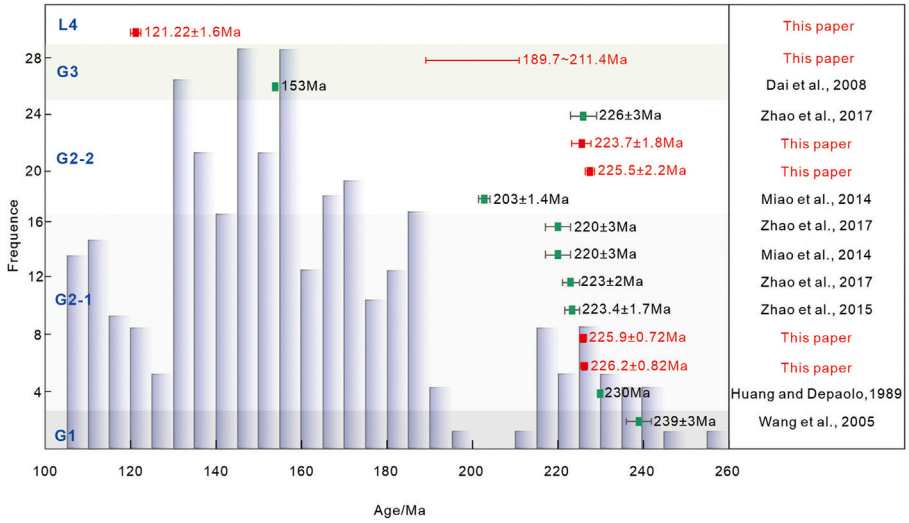


FIGURE 8
Histogram of formation ages of South China and distribution diagram of formation ages of Guandimiao batholith. The data of south China are from Zhou et al., 2006.

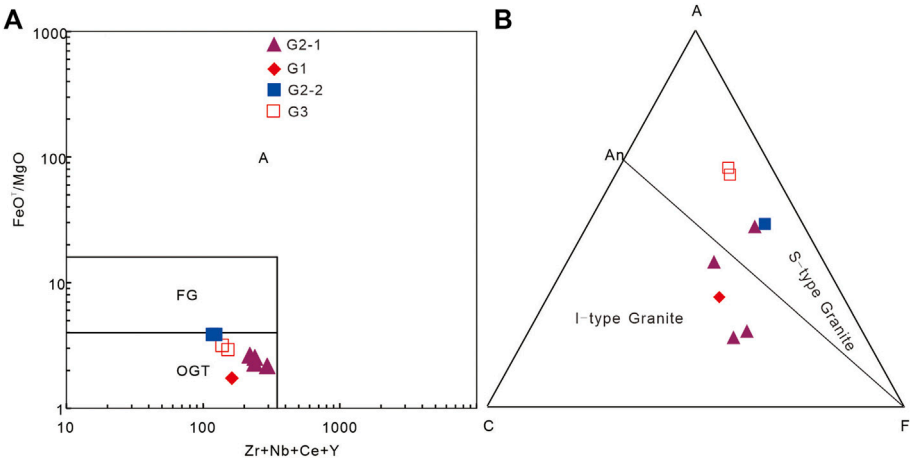


FIGURE 9
Discriminant diagram of type A granite (after Whalen et al., 1987); **(A)**, FeO^T/ MgO versus Zr + Nb + Ce + Y diagram; **(B)**, ACF diagram of Guandimiao batholith (after Hine et al., 1978).

which might have been formed by the rapid crystallization of mafic minerals upon chilling and reduction in viscosity instead of by the mixing of mantle-derived components (Vernon, 1984; Sparks and Marshall, 1986; Zhao et al., 2017).

In addition, G1 and G2-1 have obvious I-type granite affinities and are characterized by relatively high $\varepsilon N_d(t)$ values (−6.17 to −10.54), low initial $^{87}Sr/^{86}Sr$ ratios (0.712005–0.71758) and T_{DM2} values (1.52 Ga for G1 and 1.85 to 1.76 Ga for G2-1). G2-2 and G3 show S-type granite affinities and have high initial $^{87}Sr/^{86}Sr$ ratios (0.7344) and T_{DM2} values (1.73 Ga for G2-2 and 1.93 Ga for G3) but lower $\varepsilon_{Nd}(t)$ values (−8.96 to −12.14). All samples show characteristics of crustal sources on the T versus $\varepsilon_{Nd}(t)$ diagram (Figure 11A). The AMF [molar $Al_2O_3/(FeO^T + MgO)$] values of G1 and G2-1 range from 1.36 to 1.65, much lower than the values of G2-2 and G3 (3.59–4.63). The CMF [molar $CaO/(FeO^T + MgO)$] values of G1 and G2-1 are between 0.47 and 0.62, whereas the G2-2

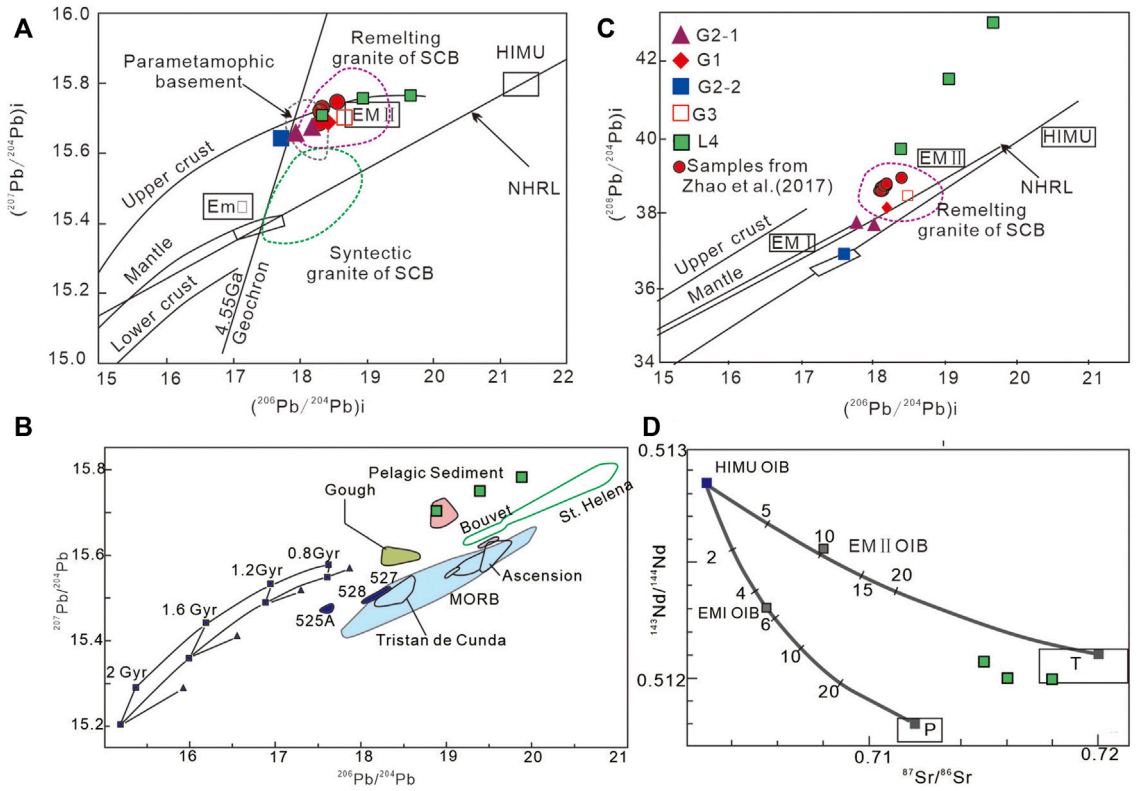


FIGURE 10
(A), $(^{207}Pb/^{204}Pb)_i$ versus $(^{208}Pb/^{204}Pb)_i$ diagram of Guandimiao batholith; **(B)**, The $^{207}Pb/^{204}Pb$ versus $^{206}Pb/^{204}Pb$ diagram of Guandimiao batholith (lines are after Zartman and Doe, 1981); **(C)**, $^{207}Pb/^{204}Pb$ versus $^{206}Pb/^{204}Pb$ diagram of lamprophyre; **(D)**, $^{143}Nd/^{144}Nd$ versus $^{87}Sr/^{86}Sr$ diagram of lamprophyre (after Weaver, 1991). Lines are after Zartman and Doe, 1981; data sources: EM (Zindler and Hart, 1986; Hofmann, 2003), NHRL (Hart, 1984), the Cathaysia Block parametamorphic basement (Hu, 1998), remelting and syntectic granites in the SCB (Shen et al., 1992). The datas of Hawaii, MORB, Gough, Kerguelen, Iceland, Easter Island are from Sun (1980). The Hawaii-OIB, HIMU, EMI, and EMII datas are modified from Hanan et al. (2008). NHRL-northern hemisphere reference line, HIMU-high U/Pb Mantle, EM-enriched mantle, OIB-ocean ridge basalt, P-pelagic sediments, T-terrigenous sediments.

and G3 values range from 0.24 to 0.27. On the diagram of AFM versus CFM, G1 and G2-1 are derived from metabasaltic to metatonalitic source fields, which is consistent with the Jingtou granite, which was derived from a high-K calc-alkaline amphibolite source with metabasaltic to metatonalitic compositions (Figure 11B; Altherr et al., 2000; Zhao et al., 2017). In contrast, G2-2 and G3 plot near the Shizhuqiao granite field, indicating a source similar to the para-metamorphic basement of the Cathaysia Block (Shen et al., 1993; Altherr et al., 2000; Zhao et al., 2015; Zhao et al., 2017).

Moreover, the variation features of two stages of Sm-Nd isotope model ages show an inhomogeneous source. The T_{DM2} of G1 is much younger than those of metamorphosed basement in the Cathaysia block (1.8–2.2 Ga) and might be derived from the remelting of meta-juvenile crust in the Mesoproterozoic. The T_{DM2} values of G2-1, G2-2 and *G3* range from 1.74 to 1.93 Ga, which is consistent with the Paleoproterozoic metamorphosed basement of the Cathaysia block. These results amply justify their geological affiliation. L4 of the Guandimiao batholith has low $\varepsilon_{Nd}(t)$ values (−10.18 to −9.62) but high I_{sr} (0.71449–0.71784) and T_{DM2} values (1.75–1.70 Ga), which represents significant deviation from the Mesozoic EM II-type OIB in the SCB (6.8–10.8; Meng et al., 2012; Qin et al., 2020). The $^{207}Pb/^{204}Pb$ versus $^{207}Pb/^{204}Pb$ and $^{143}Nd/^{144}Nd$ versus $^{87}Sr/^{86}Sr$ diagrams show that L4 was derived from a Mesoproterozoic pelagic and/or terrigenous sediment source (Figures 10C,D).

Garnet and spinel were mainly La-, Sm-, and Yb-bearing minerals in the magma source. They are significantly insensitive and can be used as an indicator to trace the melt source and the degree of partial melting (Aldanmaz et al., 2000; Zhao and Zhou, 2008). As the partial melting of a garnet lherzolite occurred in the source, the Sm/Yb ratio decreased sharply, while the La/Sm ratio decreased gradually. The partial melting of garnet lherzolite produces higher Sm/Yb ratios than spinel lherzolite melting (Johnson, 1994; Aldanmaz et al., 2000). The La/Sm versus Sm/Yb and Sm/Yb versus Yb diagrams show that the lamprophyre samples plot near the garnet lherzolite melting curves. These results suggest that the lamprophyre was mainly formed by partial melting of garnet lherzolite. However, a wide

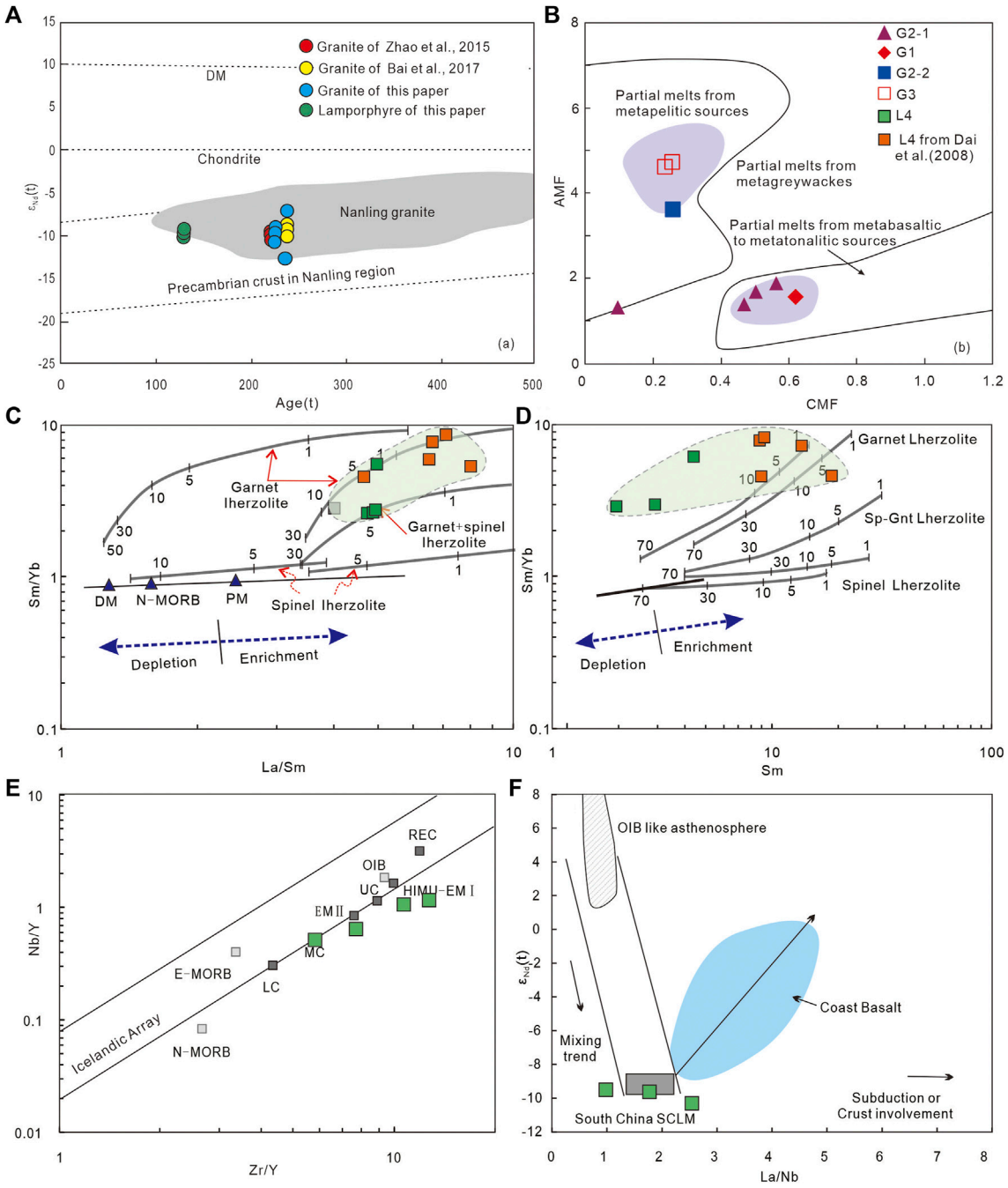


FIGURE 11
(A), ε_{Nd} (t) versus Age diagram; **(B)**, AMF versus CMF diagram; **(C,D)**, Sm/Yb versus La/Yb diagram and Sm/Yb versus Sm of lamprophyre; **(E)**, Nb/Y versus Zr/Y diagram; **(F)**, ε_{Nd} (t) versus La/Nb diagrams. Data source: Nanling granite (Yuan and Zhang, 1992), Precambrian crust in Nanling region (Shen et al., 1993). The gray field data from Zhao et al., 2015; Zhao et al., 2017; Orange samples from Dai et al., 2008; Coast Basalt field from Meng et al. (2012); South China SCLM from Chen et al. (2008b). Panels **(C,D)** are modified after Aldanmaz et al. (2000); DM from Mckenzie and Keith, 1995, N-MORB and PM from Sun and McDonough (1989). Melting curves of Spinel lherzolite (Ol53 + Opx 27 + Cpx 17 + Sp 11) and Garnet lherzolite (Ol 60 + Opx 20 + Cpx 10 + Gt 10) are from Aldanmaz et al. (2000).

degree of partial melting is also presented in Figures 11C,D, which indicates extensive crustal contamination. The same conclusion can also be drawn from the Nb/Y versus Zr/Y and ε_{Nd}(t) versus La/Nb diagrams. The lamprophyre samples deviate from the Iceland array and plot in the field of mixing trends between the OIB-like asthenosphere and South China SCLM. It

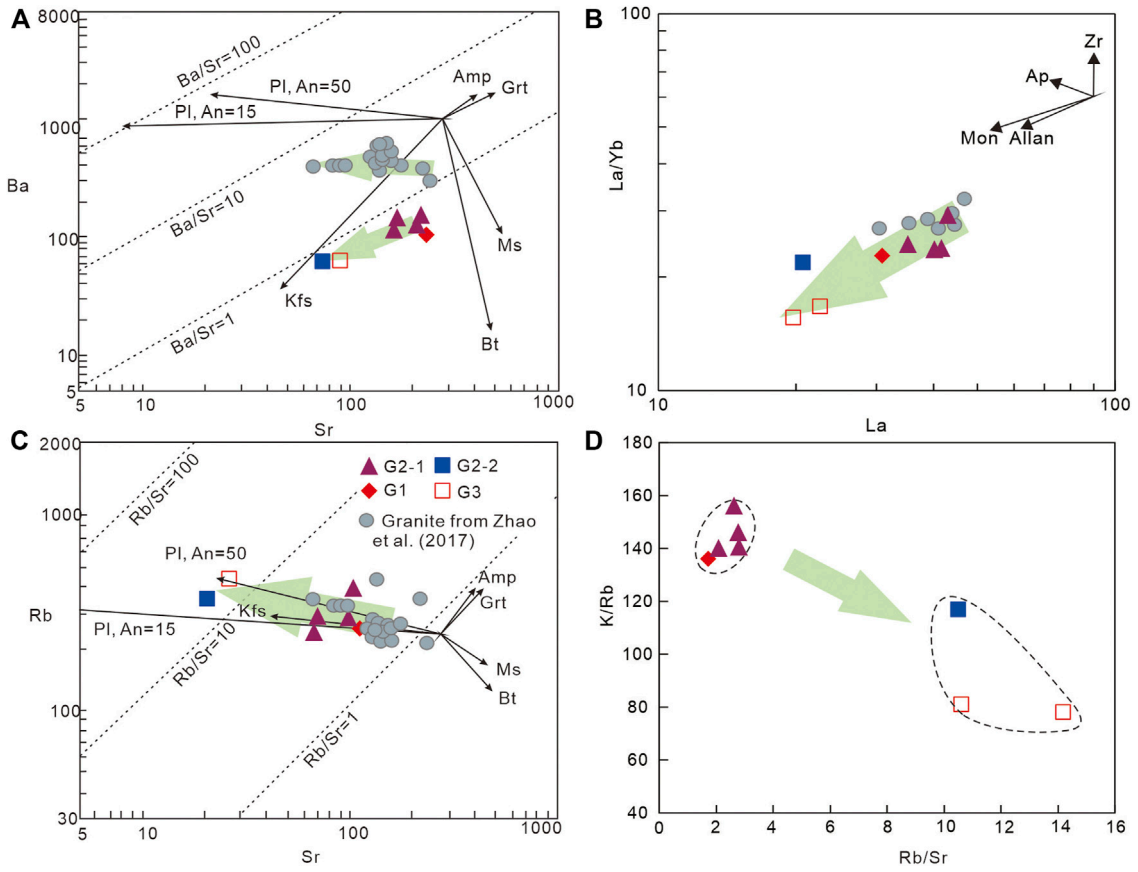


FIGURE 12
(A,B), Ba versus Sr diagram and Rb versus Sr diagram of granitoids from Guandimiao batholith; **(C)**, La/Yb versus La diagram; **(D)**, K/Rb versus Rb/Sr diagram.

shows strong crustal information (Condie, 2005; Meng et al., 2012; Figures 15E,F).

6.2.3 Magmatism

During granitic magmatism, the main Ti-bearing minerals (ilmenite, rutile, titanite, anatase, etc.) could lead to a significant depletion of Ti, Nb, Ta, etc. The fractional crystallization of apatite could significantly decrease the P concentration in the residual melt. Eu, Sr, and Ba could be depleted during fractional crystallization of feldspar, as they usually substitute K^+ and Ca^{2+} sites into K-feldspar and/or plagioclase. In the Guandimiao batholith, there is significant depletion in Ba, Nb, Sr, and Ti for G2-2 and G3 but less depletion in Ba, Nb, Sr, P, and Ti for G1 and G2-1. This may suggest that the Guandimiao granitoids experienced obvious fractional crystallization of feldspar, Ti-bearing minerals and apatite at the early stages of magmatism. In addition, the negative correlations between Ba and Sr and between Rb and Sr suggest that the magmatic system underwent intense fractional crystallization of K-feldspar and plagioclase (Figures 12A,B). For the rare earth elements (La and Yb), carrier minerals include zircon, apatite, allanite, monazite, etc. The negative relationship between La and La/Yb suggests that the fractional crystallization of allanite and monazite also played an important role in the evolution of magmatism (Figure 12C). It is worth mentioning that G1 and G2-1 have higher K/Rb ratios and lower Rb/Sr ratios than G2-2 and G3. More proof is required that the late stage of magmatism was higher in the degree of fractionation than the early stage (Figure 12D). The granitoids of the Guandimiao batholith were the result of multistage differentiation of an identical long-term magma chamber.

6.3 Implications for tectonic evolution

6.3.1 Complete record of the pre-mesozoic tectonic event of the SCB

Nine stages of lamprophyre (*L4*) fully reveal the episodic growth of the South China plate (Figure 13B). Similar evidence has been reported by Shu (2012) and Shu et al. (2020). Five time

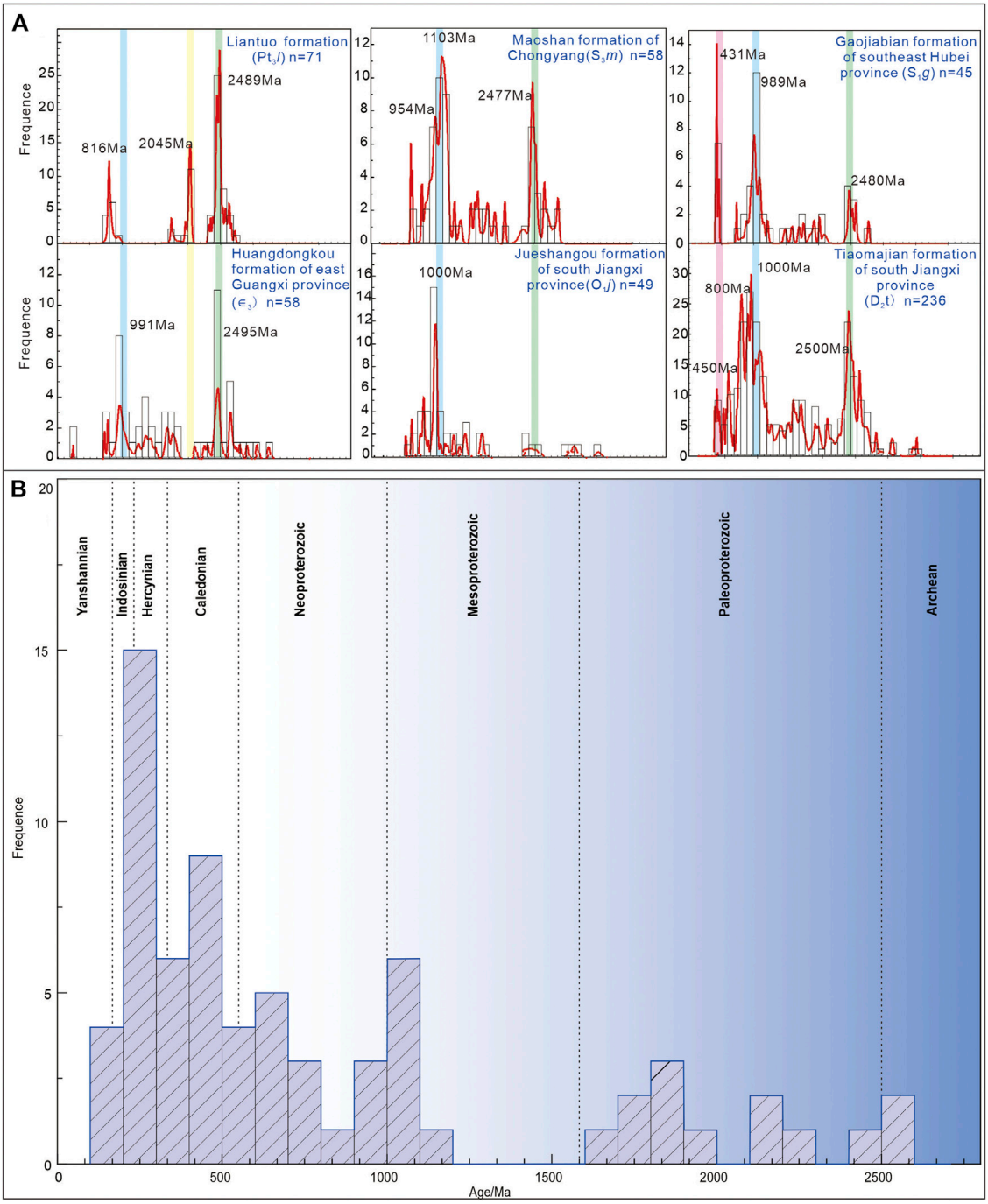


FIGURE 13
(A), Histogram of model ages of detrital zircons of South China, **(B)**, histogram of zircon U-Pb ages of lamprophyre from Guandimiao batholith.

intervals of detrital zircons dating from the Jinggangshan–Nanling region (2.56–2.38 Ga; 1.93–1.52 Ga; 1.3–0.9 Ga; 0.85–0.73 Ga; and 0.68–0.55 Ga) have been identified. The 5 time intervals could also be identified by detrital zircons from Hubei Province (Gaojiabei Formation), Jiangxi (Huangdongkou Formation, Jueshangou Formation and Tiaomajian Formation), Guangdong Province (gneiss), Sichuan Province (Pingyipu Formation), and Guizhou Province (Dazhuyuan Formation; Shu, 2012; Zhao et al., 2013; Wang D. H. et al., 2014; Wang X. L. et al., 2014) (Figure 13A).

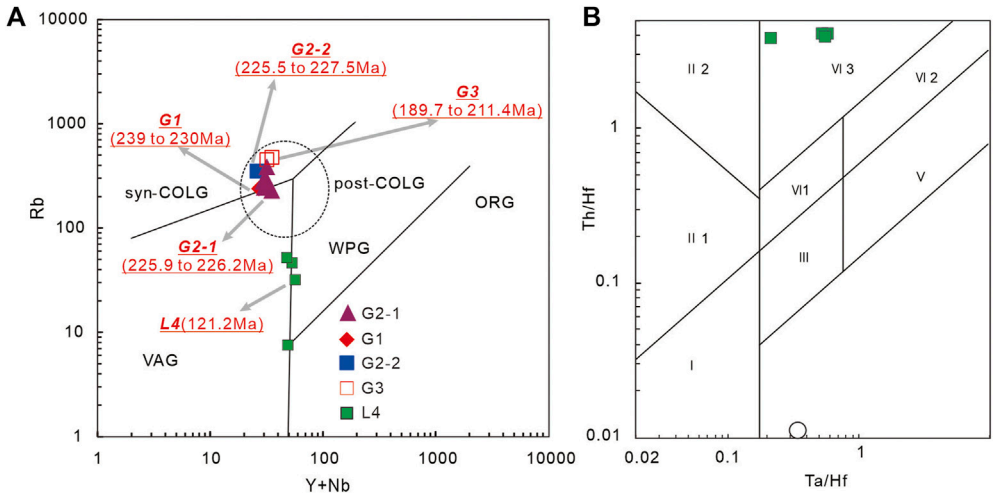


FIGURE 14
Rb versus Y + Nb diagram **(A)** and Th/Hf versus Ta/Hf diagrams **(B)** of Guandianmiao batholith. Syn-COLG, syncollisional granite, VAG, volcanic arc granite, WPG, within plate granite;ORG, ocean ridge granite. I, Extensional plate margin N-MORB; II1, Oceanic island arc basalt; II2, Continental margin island arc basalt; III, Oceanic intraplate basalt, seamount basalt and T-MORB, E-MORB; IV1, Intracontinental and continental marginal rift tholeiite basalt; IV2, Intracontinental rift alkaline basalt; IV3, Continental extensional basalt; V, Mantle plumes related basalt.

The Neoarchean to Paleoproterozoic ages (2,573.1–2,447.3 Ma) were extensively derived from xenolith crystals in mafic dikes and clastic zircons in Paleozoic strata (Zheng et al., 2008). They are obviously younger than the Kongling Group in the Yangtze block (3.3 Ga, Ma et al., 1997). They represent global continental nucleus growth events and mixing processes between Neoarchean mafic magma and more ancient crustal components.

The middle to late Paleoproterozoic data (2,232.7–2,114.4 Ma and 1931.6–1,625.9 Ma) is linked to the response of the convergence and breakup effect of the Columbia supercontinent. The convergence of the Columbia supercontinent began 2.1 Ga, which is represented by the formation of the Kora-Kareline conjunctive craton and West Australian craton and the outgrowth of the western Amazon ancient continental plate margin in South America (Hoffman, 1988). Correspondingly, significant tectonic magmatic events were also recorded in the North China craton (NCC) and Yangtze craton (Zhang et al., 2006; Yin et al., 2013). Subsequently, the tectonic regime transformed to breakup on a global scale 1.7–1.5 Ga. A large number of A-type granitoids and mafic dikes developed in the Yangtze craton, indicating the existence of intracontinental rifting (Rogers and Santosh, 2002; Zhao et al., 2002; Evans and Mitchell, 2011; Gibson et al., 2012; Geng et al., 2019).

During the early Neoproterozoic (1,135.0–769.7 Ma), the region experienced the suture of the Paleo-Huanan Ocean along the Jiangnan–Shaoxing large fault zone, and the collision between the Yangtze block and Cathaysia block created the initial appearance of the ancient SCB. This was completely documented by abundant ophiolites and associated pyroclastic rocks developed along the Dexin–Dongxiang and Zhuji–Lishui–Wuyi–Meixi belts in the southeastern Cathaysia block from 1.0–0.9 Ga. The I-type granite and mafic rocks of the southern Jiangnan orogenic belt, which formed 0.9–0.8 Ga, indicates the subduction of pristine oceanic crust (Ye et al., 2007; Shu et al., 2012; Zhou et al., 2018). The subsequent break-up of the supercontinent and extension events occurred along the paleo-suture and formed the Nanhua continental rift basin and three main tectonic domains (Nanling, Wuyi, and Yunkai) 825–760 Ma (Wang et al., 2017; Yang et al., 2018). The eventual Phanerozoic collage of the SCB (early Paleozoic, 466.8–405.3 Ma) and multistage intracontinental orogenic events (late Paleozoic, 268.0–258.8 Ma; 379.6–295.9 Ma) constituted the basic tectonic appearance in the Paleozoic (Liu et al., 1990; Shu et al., 2006; Shu et al., 2012).

6.3.2 Mesozoic tectonic evolution of the SCB

The Guandimiao batholith is the central part of the SCB. The G1, G2-1 and G2-2 phases were emplaced 239–203 Ma and were dominant in the period from 230 to 220 Ma. The structural discriminant diagram shows that these rocks formed in a postcollisional environment (Figure 14A; post-COLG field; Pearce, 1996). The lamprophyre plots near the WPG field and VI_3 field on the Rb versus Y + Nb diagram (intraplate basalt) (Figure 14B), which indicates an intracontinental extensional setting.

During the early Indosinian (250–240 Ma), the forceful collision and extensive metamorphism between the Indo-China block and the Sibumas-Qingtang block occurred in the Early-Middle Triassic and exerted a profound impact on the

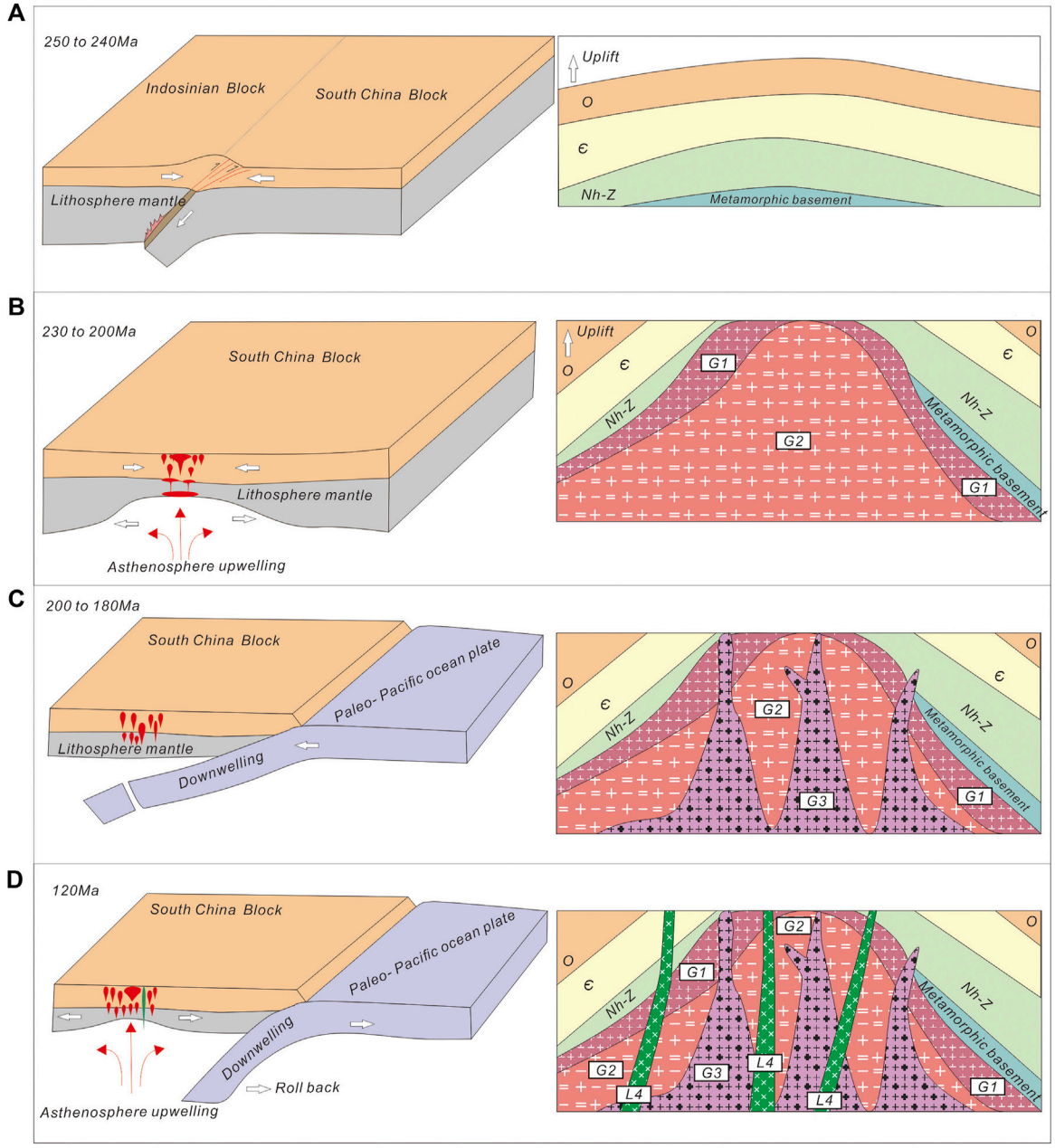


FIGURE 15
The brief model diagram of the tectonic evolution of south China at Mesozoic and the emplacement model of Guandimiao batholith. **(A)** the early Indosinian period (250–240 Ma); **(B)** the late Indosinian period (230–220 Ma); **(C)** the early Yanshanian period (200–180 Ma); **(D)** the late Yanshanian period (120 Ma).

southeastern Eurasian continent (Chen et al., 2002; Li et al., 2006). Meanwhile, the closure of the Paleo-Tethys Ocean caused southeastward subduction and collision between the NCC and the SCB. The SCB underwent multidirectional compression and massive shortening, accompanied by an approximately 50 km thickening of the continental lithosphere (Tapponnier et al., 1982; Gilder et al., 1995; Carter et al., 2001; Wang et al., 2002; Li et al., 2017) (Figure 15A). The collisional orogenic events immensely shortened the crust and resulted in a series of thrust faults and uplift structures. There was an approximately 10 Myr. Interval before granitoids melted following the end of crustal thickening (Patio Dounce et al., 1990), and Sylvester (1998) proposed a possible relaxation and thinning of the thickened crust with a time interval of 10–20 Myr. The Guandimiao dome developed at the center of the SCB. The main part of the Guandimiao batholith was formed in a postcollision setting

after the Indosinian crustal thickening events in the SCB. The thermal stress from crustal extension caused decompression and melting of thickened crust, along with continuous emplacement of mantle-derived magma (Pape et al., 2012). It induced extensive melting of Paleoproterozoic metamorphic basement in the SCB (Zhou et al., 2006; Guo et al., 2012; Qin et al., 2022) (Figure 15B).

Approximately 200–180 Ma, the transformation of the tectonic regime occurred from NE-directed paleo-Tethys ocean dominance to NE-directed paleo-Pacific ocean dominance. The continued subduction of the paleo-Pacific plate beneath the Eurasian plate affected more than 1,000 kilometers. Due to the stable structure and the shortage of transcrustal faults, there was a significant deficiency in magmatic rocks, and the volume and scale of magmatism were far less than those developed either in the early Insinian or late Mesozoic and have been confirmed as the break-in period (200–180 Ma) of igneous rocks in South China (Mao et al., 2004; Zhang et al., 2009) (Figure 15C). Scattershot intrusions occurred as stocks and dikes exposed in the interior batholith with limited scope.

In the Middle Jurassic, subduction of the paleo-Pacific oceanic plate converted to rollback steep subduction and caused large-scale extensional events in the back-arc basin. The uplift of asthenospheric mantle melted the ancient metamorphic basement and formed a large granitic melt 135–118 Ma (Zhou et al., 2006; Jiang et al., 2015; Yang, 2018; Li et al., 2019). Moreover, mafic magma rapidly intruded along the deeply penetrating faults and extensively contaminated the upper crustal materials. This made it possible for the formation of lamprophyre with intense crustal information (*L4*) (Figure 15D).

7 Conclusion

1 The Guandimiao batholith was dominated by four stages of magmatism. The granodiorite formed at 239 Ma (Stage 1). The biotite monzogranite (G2-1) and two-mica monzogranite (G2-2) formed at 230–203 Ma (Stage 2). The granite porphyry formed from 211 to 190 Ma (Stage 3). The lamprophyre (L4) formed 121 Ma (Stage 4).

2 G1 and G2-1 have I-type granite affinity, while G2-2 and G3 show S-type granite characteristics. G1 was derived from the remelting of meta-juvenile crust in the Mesoproterozoic. G2-1, G-2, and G3 were derived from the Paleoproterozoic metamorphosed basement of the Cathaysia block. The source of L4 was garnet and spinel lherzolite, which underwent mixing between the Mesoproterozoic pelagic and/or terrigenous sediment and SCLM of South China. The granitoids of the Guandimiao batholith underwent intensely fractional crystallization of feldspar, Ti-bearing minerals, allanite and monazite.

3 The zircon U-Pb dating of L4 in the Guandimiao batholith completely records the six stages of pre-Mesozoic tectonic events in the SCB. During the Mesozoic, the main body of the Guandimiao batholith (G1, G2-1, and G2-2) recorded the closure of the paleo-Tethys Ocean in the Triassic and the subsequent regional extension of the postcollision. The dikes of the Guandimiao batholith documented the transition of tectonic and dynamic regimes in the early Yanshanian and the rollback and steep subduction of the paleo-Pacific Ocean in the late Yanshanian.

Data availability statement

The original contributions presented in the study are included in the article/Supplementary Material, further inquiries can be directed to the corresponding author.

Author contributions

Conceptualization, J-HQ and FH; methodology, J-HQ; software, J-HQ; validation, FH and D-HW; formal analysis, J-HQ; investigation, J-HQ and FH; resources, J-HQ; data curation, D-HW; writing—original draft preparation, J-HQ; writing—review and editing, J-HQ and FH; visualization, J-HQ; supervision, D-HW; project administration, D-HW; funding acquisition, D-HW. All authors have read and agreed to the published version of the manuscript.

Funding

This study was financially supported by National Natural Science Foundation of China (42172097), China Geological Survey (DD20221695;DD20190379; DD20160346). We are grateful to Mr. Qin Jin-nin, Prof. Liu Shan-bao, Prof. Wang Cheng-hui and other geologists for their help during the field investigations and samples analysis.

Conflict of interest

The authors declare that the research was conducted in the absence of any commercial or financial relationships that could be construed as a potential conflict of interest.

Publisher's note

All claims expressed in this article are solely those of the authors and do not necessarily represent those of their affiliated organizations, or those of the publisher, the editors and the reviewers. Any product that may be evaluated in this article, or claim that may be made by its manufacturer, is not guaranteed or endorsed by the publisher.

References

Aldanmaz, E., Pearce, J. A., Thirlwall, M. F., and Mitchell, J. G. (2000). Petrogenetic evolution of late cenozoic, post-collision volcanism in Western anatolia, Turkey. *J. Volcanol. Geotherm. Res.* 102 (1-2), 67–95. doi:10.1016/S0377-0273(00)00182-7

Altherr, R., Holl, A., Hegner, E., Langer, C., and Kreuzer, H. (2000). High-potassium, calc-alkaline I-type plutonism in the European Variscides, northern Vosges (France) and northern Schwarzwald (Germany). *Lithos* 50 (1), 51–73. doi:10.1016/s0024-4937(99)00052-3

Bai, D. Y., Zhong, X., Jia, P. Y., Xiong, X., and Huang, W. Y. (2014). Geochemistry and petrogenesis of the Indosinian Guandimiao granitic pluton in central Hunan. *Sediment. Geol. Tethyan Geol.* 34 (4), 93–105. (in Chinese with English abstract).

Barbarin, B. (2005). Mafic magmatic enclaves and mafic rocks associated with some granitoids of the central sierra Nevada batholith, California: Nature, origin, and relations with the hosts. *Lithos* 80 (1-4), 155–177. doi:10.1016/j.lithos.2004.05.010

Bonin, B. (2007). A-Type granites and related rocks: Evolution of a concept, problems and prospects. *Lithos* 97, 1–29. doi:10.1016/j.lithos.2006.12.007

Carter, A., Roques, D., Bristow, C., and Kinny, P. (2001). Understanding mesozoic accretion in southeast Asia, significance of triassic thermotectonism. *Geology* 29 (29), 211–214. doi:10.1130/0091-7613(2001)029<0211:UMAISA>2.0.CO;2

Chappell, B. W., White, A. J. R., and Hine, R. (1988). Granite provinces and basement terranes in the lachlan fold belt, southeastern Australia. *Aust. J. Earth Sci.* 35 (4), 505–521. doi:10.1080/08120098808729466

Chappell, B. W., and White, A. J. R. (1992). I- and s-type granites in the lachlan fold belt. *Earth Environ. Sci. Trans. R. Soc. Edinb.* 83 (1-2), 1–26. doi:10.1017/S0263593300007720

Chappell, B. W., and White, A. J. R. (1974). Two contrasting granite types, Pacific. *Geology* 8, 173–174. doi:10.1046/j.1440-0952.2001.00882.x

Chen, C. H., Lee, C. Y., Lu, H. Y., and Hsieh, P. S. (2008b). Generation of Late Cretaceous silicic rocks in SE China, age, major element and numerical simulation constraints. *J. Asian Earth Sci.* 31, 479–498. doi:10.1016/j.jseaes.2007.08.002

Chen, C. H., Lee, C. Y., and Shinjo, R. (2008a). Was there jurassic paleo-pacificsubduction in south China? Constraints from $^{40}Ar/^{39}Ar$ dating, elemental and Sr–Nd–Pb isotopic geochemistry of the mesozoic basalt. *Lithos* 106, 83–92. doi:10.1016/j.lithos.2008.06.009

Chen, P., Hua, R., Zhang, B., Lu, J., and Fan, C. (2002). Early Yanshanian post-orogenic granitoids in the Nanling region. *Sci. China Ser. D-Earth. Sci.* 45 (8), 755–768. doi:10.1007/bf02878432

Chen, Y. C., Wang, D. H., Xu, Z. G., and Huang, F. (2014). Outline of regional metallogeny of ore deposits associated with the Mesozoic magmatism in South China. *Geotect. Metallogenia* 38 (2), 219–229. (in Chinese with English abstract). doi:10.3969/j.issn.1001-1552.2014.02.002

Cheng, Y. Q. (1994). *Concise regional geology of China*. Beijing: Geological Publishing House, 1–539. (in Chinese).

Clemens, J. D., Holloway, J. R., and White, A. J. R. (1986). Origin of A type granites: Experimental constraints. *Am. Mineral.* 71, 317–324. (in Chinese with English abstract).

Condie, K. C. (2005). High field strength element ratios in Archean basalt, a window to evolving sources of mantle plumes? *Lithos* 79 (3-4), 491–504. doi:10.1016/j.lithos.2004.09.014

Dai, F. Y., Chen, B. H., and Liu, F. G. (2008). Characteristics and geological significance of vein rocks in guandimiao area, hunan province. *Land Resour. Her.* 5 (1), 33–36. (in Chinese with English abstract). doi:10.3969/j.issn.1672-5603.2008.01.013

Deng, J., Wang, C. M., Zi, J. W., Xia, R., and Li, Q. (2017). Constraining subduction-collision processes of the paleo-tethys along the changning-menglian suture: New zircon U-Pb ages and Sr-Nd-Pb-Hf-O isotopes of the Lincang batholith. *Gondwana Res.* 62, 75–92. doi:10.1016/j.gr.2017.10.008

Deng, P., Ren, J. S., Ling, H. F., Sun, L. Q., Zhu, B., and Tan, Z. Z. (2012). SHRIMP zircon U-Pb ages and tectonic implications for Indosinian granitoids of southern Zhuguangshan granitic composite, South China. *Chin. Sci. Bull.* 57 (14), 1542–1552. doi:10.1007/s11434-011-4951-8

Depaolo, D. J. (1981). Trace element and isotopic effects of combined wallrock assimilation and fractional crystallization. *Earth Planet. Sci. Lett.* 53 (2), 189–202. doi:10.1016/0012-821x(81)90153-9

Eby, G. N. (1992). Chemical subdivision of the A-type granitoids, Petrogenetic and tectonic implications. *Geol.* 20, 641. doi:10.1130/0091-7613(1992)020<0641:csotat>2.3.co;2

Eby, G. N. (1990). The A-type granitoids: A review of their occurrence and chemical characteristics and speculations on their petrogenesis. *Lithos* 26, 115–134. doi:10.1016/0024-4937(90)90043-z

Evans, D. A. D., and Mitchell, R. N. (2011). Assembly and breakup of the core of Paleoproterozoic-mesoproterozoic supercontinent Nuna. *Geology* 39 (5), 443–446. doi:10.1130/G31654.1

Geng, Y. S., Kuang, H. W., Du, L. L., Liu, Y. Q., and Zhao, T. P. (2019). On the Paleo-Mesoproterozoic boundary from the breakup event of the Columbia supercontinent. *Acta Petrol. Sin.* 35 (8), 2299–2324. (in Chinese with English abstract). doi:10.18654/1000-0569/2019.08.0210.18654/1000-0569/2019.08.02

Gibson, G. M., Henson, P. A., Neumann, N. L., Southgate, P. N., and Hutton, L. J. (2012). Paleoproterozoic-earliest Mesoproterozoic basin evolution in the Mount Isa region, northern Australia and implications for reconstructions of the Nuna and Rodinia supercontinents. *Episodes* 35 (1), 131–141. doi:10.18814/epiiugs/2012/v35i1/012

Gilder, S. A., Coe, R. S., Wu, H., Kuang, G., Zhao, X., Qi, W., et al. (1995). Triassic paleomagnetic data from south China and their bearing on the tectonic evolution of the Western circum-pacific region. *Earth Planet. Sci. Lett.* 131 (3), 269–287. doi:10.1016/0012-821x(95)00030-g

Gilder, S. A., and Courtillot, V. (1997). Timing of the north-south China collision from new middle to late mesozoic paleomagnetic data from the north China block. *J. Geophys. Res.* 102 (B8), 17713–17727. doi:10.1029/97JB01201

Gilder, S. A., Gill, J., Coe, R. S., Zhao, X. X., Liu, Z. W., and Wang, G. X. (1996). Isotopic and paleomagnetic constraints on the Mesozoic tectonic evolution of south China. *J. Geophys. Res.* 101 (B7), 16137–16154. doi:10.1029/96JB00662

Greentree, M. R., Li, Z. X., Li, X. H., and Wu, H. (2006). Late mesoproterozoic to earliest neoproterozoic basin record of the sibao orogenesis in Western south China and relationship to the assembly of rodinia. *Precambrian Res.* 151 (1), 79–100. doi:10.1016/j.precamres.2006.08.002

Guo, C. L., Zheng, J. H., Lou, F. S., and Zeng, Z. L. (2012). Petrography, genetic, types and geological dynamical setting of the Indosinian granitoids in South China. *Geol. Metallogenia* 36 (3), 457–472. (In Chinese with English abstract). doi:10.1007/s11783-011-0280-z

Hanan, B. B., Shervais, W. J., and Vetter, S. (2008). Yellowstone plume-continental lithosphere interaction beneath the snake river plain. *Geol.* 36 (1), 51–54. doi:10.1130/G23935A.1

Hart, S. R. (1984). A large-scale isotope anomaly in the southern hemisphere mantle. *Nature* 309 (5971), 753–757. doi:10.1038/309753a0

Hervé, F., Pankhurst, R. J., and Yaxley, G. (2007). the South patagonian batholith: 150 my of granite magmatism on a plate margin. *Lithos* 97 (3-4), 373–394. doi:10.1016/j.lithos.2007.01.007

Hine, R., Williams, I. S., Chappell, B. W., and White, A. J. R. (1978). Contrasts between I- and S-type granitoids of the kosciusko batholith. *J. Geol. Soc. Aust.* 25 (3-4), 219–234. doi:10.1080/00167617808729029

Hofmann, A.W. (2003). Sampling mantle heterogeneity through oceanic basalts: Isotopes and trace elements. *Treatise on Geochem.* 2, 1–44. doi:10.1016/B0-08-043751-6/02123-X

Hoffman, P. F. (2003). Continental transform tectonics: Great Slave Lake shear zone (ca. 1.9 Ga), northwest Canada. *Geology* 15, 7852–7889. doi:10.1130/0091-7613

Hu, G. R. (1998). *Study on Geological Geochemistry, Isotopic chronogy and metamorphic P-T-t path of metamorphic rock belt in ccentral Jiangxi*. China: Nanjing University. (in Chinese with English abstract).

Huang, X., and Depaolo, D. J. (1989). Study of sources of paleozoic granitoids and the basement of south China by mean of Nd-Sr isotope. *Acta Petrol. Sin.* 5 (1), 28–36. (in Chinese with English abstract).

Jiang, Y. H., Wang, G. C., Zheng, L., Ni, C. Y., Qing, L., Zhang, Q., et al. (2015). Repeated slab advance-retreat of the Palaeo-Pacific plate underneath SE China. *Int. Geol. Rev.* 57 (4), 472–491. doi:10.1080/00206814.2015.1017775

Johnson, K. T. M. (1994). Experimental cpx/ and garnet/ melt partitioning of REE and other trace elements at high pressures; petrogenetic implications. *Mineral. Mag.* 58, 454–455. doi:10.1180/minmag.1994.58A.1.236

King, P. L., White, A. J. R., Chappell, B. W., and Allen, C. M. (1997). Characterization and origin of aluminous A-type granites from the Lachlan Fold Belt, southeastern Australia. *J. Petrology* 38, 371–391. doi:10.1093/petroj/38.3.371

Li, S. Z., Jahn, B. M., Zhao, S. J., Da, L. M., Li, X. Y., Suo, Y. H., et al. (2017). Triassic southeastward subduction of north China block to south China block:

Insights from new geological, geophysical and geochemical data. *Earth-Science Rev.* 166, 270–285. doi:10.1016/j.earscirev.2017.01.009

Li, X. H., Li, Z. X., Ge, W., Zhou, H., and Wingate, M. T. D. (2003). Neoproterozoic granitoids in South China: Crustal melting above a mantle plume at ca. 825 Ma? *Precambrian Res.* 122 (1), 45–83. doi:10.1016/s0301-9268(02)00207-3

Li, X. H., Li, Z. X., and Li, W. X. (2014). Detrital zircon U-Pb age and Hf isotope constrains on the generation and reworking of precambrian continental crust in the Cathaysia block, south China: A synthesis. *Gondwana Res.* 25 (3), 1202–1215. doi:10.1016/j.gr.2014.01.003

Li, X. H., Li, Z. X., Li, W. X., and Wang, Y. J. (2006). Initiation of the indosinian orogeny in south China: Evidence for a permian magmatic arc on hainan island. *J. Geol.* 114, 341–353. doi:10.1086/501222

Li, X. H., Li, Z. X., Li, W. X., Ying, L., Yuan, C., and Wei, G. (2007). U-Pb zircon, geochemical and Sr-Nd-Hf isotopic constraints on age and origin of jurassic I- and A-type granites from central guangdong, SE China: A major igneous event in response to foundering of a subducted flat-slab? *Lithos* 96 (1-2), 186–204. doi:10.1016/j.lithos.2006.09.018

Li, X. H., Li, Z. X., Zhou, H. W., Liu, Y., and Kinny, P. D. (2002). U-Pb zircon geochronology, geochemistry and Nd isotopic study of Neoproterozoic bimodal volcanic rocks in the Kangdian rift of South China, implications for the initial rifting of Rodinia. *Precambrian Res.* 113 (1), 135–154. doi:10.1016/s0301-9268(01)00207-8

Li, X. H. (1990). Magmatic age and crustal movement of the wanyangshan-Zhuguangshan granite complex batholith. *Sci. China* 7, 747–755. (In Chinese).

Li, X. H., Zhou, H. W., and Liu, Y. (2001). Mesozoic shoshonitic intrusives in the Yangchun basin, Western guangdong, and their tectonic significance, ii. trace elements and Sr-Nd isotopes. *Geochimica* 30, 57–65. (in Chinese with English abstract). doi:10.3321/j.issn:0379-1726.2001.01.007

Li, Z. X., and Li, X. H. (2007). formation of the 1300 km-wide intra-continental orogen and postorogenic magmatic province in mesozoic south China: A flat-slab subduction model. *Geol.* 35, 179. doi:10.1130/G23193A.1

Li, Z. X., Li, X. H., Kinny, P. D., and Wang, J. (1999). The breakup of Rodinia; did it start with a mantle plume beneath south China? *Earth Planet. Sci. Lett.* 173 (3), 171–181. doi:10.1016/S0012-821X(99)00240-X

Liang, X. Q., and Guo, D. L. (2002). Deep tectonic activation and its shellow response in Hunan province. *Chin. J. Geol.* 3, 332–342. (in Chinese with English abstract). doi:10.3321/j.issn:0379-1726.2001.01.007

Liu, B. J. (1994). *Lithofacies paleogeographic atlas of south China*. Beijing: Science Press, 1–239. (in Chinese with English abstract).

Liu, B. J., Zhou, M. K., and Wang, R. Z. (1990). Early palaeozoic palaeogeography and tectonic evolution of south China. *Acta Geosci. Sin.* 1, 97–98. (In Chinese with English abstract).

Loiselle, M. C., and Wones, D. R. (1979). Characteristics and origin of anorogenic granites. *Geol. Soc. Am. Prog. Abstr.* 12 (7), 468.

Ludwig, K. R. (2003). *Isoplot/ex, a geochronological toolkit for microsoft excel, version 3.00*. United States: Berkeley Geochronology Center.

Ma, D. H., Li, Z. C., and Xiao, Z. F. (1997). A Study on the boundary age between Jurassic and Cretaceous. *Acta Geoscientia Sinica* 3, 233–241. (in Chinese with English abstract).

Ma, X. X., Dong, C. W., Tang, L. M., Lv, Q., and Gu, H. Y. (2013). Petrological evidence of mesozoic tectonic extension in the coastal area of SE China, the spatial-temporal distribution and geochemical constraints on the mafic rocks from Hainan, Guangdong, Fujian and Zhejiang Provinces, South China. *J. Zhejiang Univ. Sci. Ed.* 40 (6), 683–692. doi:10.3785/j.issn.1008-9497.2013.06.015

Mao, J. R., Li, Z. L., and Ye, H. M. (2014). Mesozoic tectono-magmatic activities in South China: Retrospect and prospect. *Sci. China Earth Sci.* 44 (12), 2853–2877. doi:10.1007/s11430-014-5006-1

Mao, J. W., Chen, C. H., Yuan, S. D., and Guo, C. L. (2011). Characteristics and spatial-temporal regularity of mineral deposits in qinhang (or shihang) metallogenic belt, south China. *Acta Geol. Sin.* 85 (5), 636–658. (in Chinese with English abstract).

Mao, J. W., Xie, G. Q., Li, X. F., Zhang, C. Q., and Mei, Y. X. (2004). Meosozoic large scale mineralization and multiple lithospheric extension in South China. *Earth Sci. Front.* 11 (1), 45–55. China University of Geosciences, Beijing (in Chinese with English abstract). doi:10.3321/j.issn:1005-2321.2004.01.003

Mao, J. W., Xie, G. Q., Li, X. F., Zhang, Z. H., Wang, Y. T., and Wang, Z. L. (2005). Geodynamic process and metallogeny, history and present research trend, with a special discussion on continental accretion and related metallogeny throughout geological history in South China. *Mineral. Deposits* 24 (3), 193–205. (in Chinese with English abstract). doi:10.3969/j.issn.0258-7106.2005.03.001

Mckenzie, D., and Keith, O. R. (1995). The Source Regions of Ocean Island Basalts. *J. Petrol.* 1, 133–159. doi:10.1093/petrology/36.1.133

Meng, L. F., Li, Z. X., Chen, H., Li, X. H., and Wang, X. C. (2012). Geochronological and geochemical results from mesozoic basalts in southern south China block support the flat-slab subduction model. *Lithos* 132 (132-133), 127–140. doi:10.1016/j.lithos.2011.11.022

Miao, B. H. (2014). *Geologic characteristic and genesis mechanism of the qingshuitang Pb-Zn deposit in Qidong county, hunan province*. China: Nanjing University, 1–80. (in Chinese with English abstract).

Nasdala, L., Hofmeister, W., Norberg, N., Martinson, J. M., Corfu, F., Dörr, W., et al. (2008). Zircon M257–A homogeneous natural reference material for the ion microprobe U-Pb analysis of Zircon. *Geostand. Geoanal. Res.* 32 (3), 247–265. doi:10.1111/j.1751-908X.2008.00914.x

Pape, F. L., Jones, A. G., Vozar, J., and Wei, W. (2012). Penetration of crustal melt beyond the kunlun fault into northern tibet. *Nat. Geosci.* 5 (5), 330–335. doi:10.1038/NGEO1449

Patio Dounce, A. E., Humphreys, E. D., and Johnston, A. D. (1990). Anatexis and metamorphism in tectonically thickened continental crust exemplified by the Sevier hinterland, Western North America. *Earth Planet. Sci. Lett.* 97, 290–315. doi:10.1016/0012-821X(90)90048-3

Pearce, J. (1996). Sources and settings of granitic rocks. *Episodes* 19 (4), 120–125. doi:10.1002/(SICI)1096-9837(199612)21:12<1163::AID-ESP666>3.3.CO

Qin, J. H., Wang, D. H., and Chen, Y. C. (2022). Geochemical and geochronological constraints on a granitoid containing the largest indosinian tungsten (W) deposit in south China (SC): Petrogenesis and implications. *Minerals* 12 (1), 80. doi:10.3390/min12010080

Qin, J. H., Wang, D. H., and Chen, Y. C. (2020). Geochemical and Sr-Nd-Pb isotopic characteristics of basalt from eastern Hunan Province: New insight for the Late Cretaceous tectonic dynamic mechanism in South China. *Geol. J.* 55 (12), 8141–8168. doi:10.1002/gj.3914

Rogers, J. J. W., and Santosh, M. (2002). Configuration of Columbia, a mesoproterozoic super-continent. *Gondwana Res.* 5 (1), 5–22. doi:10.1016/S1342-937X(05)70883-2

Rowley, D. B., Jiayu, R., Jin, Z., Yuan-Dong, Z., and Ren-Bing, Z. (1997). Late precambrian through early paleozoic stratigraphic and tectonic evolution of the nanling region, Hunan Province, south China. *Int. Geol. Rev.* 39 (5), 469–478. doi:10.1080/00206819709465285

Rubatto, D. (2002). Zircon trace element geochemistry, Partitioning with garnet and the link between U-Pb ages and metamorphism. *Chem. Geol.* 84, 123–138. doi:10.1016/S0009-2541(01)00355-2

Shen, W. Z., Chen, F. R., Liu, C. S., and Wang, D. Z. (1992). Isotopic-geochemical characteristics and source material for two types of volcanic-intrusive complexes in Jiangxi Province. *Acta Petrol. Sin.* 8 (2), 177–184. (in Chinese with English abstract).

Shen, W. Z., Zhu, J. C., Liu, C. S., Xu, S. J., and Ling, H. F. (1993). Sm-Nd isotopic study of basement metamorphic rocks in south China and its constraint on material sources of granitoids. *Acta Petrol. Sin.* 9, 115–124. (in Chinese with English abstract).

Shu, L. S. (2012). An analysis of principal features of tectonic evolution in South China Block. *Geol. Bull. China* 31 (7), 1035–1053. (in Chinese with English abstract). doi:10.1111/j.1755-6724.2008.tb00581.x

Shu, L. S., Chen, X. Y., and Lou, F. S. (2019). Pre-jurassic tectonics of the south China. *Acta Geol. Sin.* 94 (2), 333–360. doi:10.1111/j.1755-6724.2008.tb00581.x

Shu, L. S., Zhou, X. M., Deng, P., and Yu, X. Q. (2006). Principal geological features of nanling tectonic belt, south China. *Geol. Rev.* 52 (2), 251–265. (in Chinese with English abstract). doi:10.3969/j.issn.1671-2552.2006.03.002

Shu, L. S., and Zhou, X. M. (2002). Late mesozoic tectonism of southeast China. *Geol. Rev.* 48 (3), 249–260. (in Chinese with English abstract). doi:10.3321/j.issn:0371-5736.2002.03.004

Shu, L. S. (2012). An analysis of pricipal features of tectonic evolution in South China Block. *Geol. Bullet. China* 31 (7), 1035–1053. (in Chinese with English abstract). doi:10.3969/j.issn.1671-2552.2012.07.003

Shu, L. S., Chen, X. Y., and Lou, F. S. (2020). Pre-Jurassic tectonics of the SouthChian. *Acta Geologica Sinica* 94 (2), 333–360.

Sláma, J., Košler, J., Condon, D. J., Crowley, J. L., Gerdes, A., Hanchar, J. M., et al. (2008). Plešovice zircon-a new natural reference material for U-Pb and Hf isotopic microanalysis. *Chem. Geol.* 249, 1–35. doi:10.1016/j.chemgeo.2007.11.005

Sparks, R. S. J., and Marshall, L. A. (1986). Thermal and mechanical constraints on mixing between mafic and silicic magmas. *J. Volcanol. Geotherm. Res.* 29 (1), 99–124. doi:10.1016/0377-0273(86)90041-7

Sun, S. S. (1980). Lead isotopic study of young volcanic rocks from midocean ridges, ocean islands and island arcs, Philos. *Trans. R. Soc. Lond.* 297, 409–445. doi:10.1098/rsta.1980.0224

Sun, S. S., and McDonough, W. F. (1989). *Chemical and systematics of oceanic basalts, Implication for mantle 682 composition and processes*, 42. London: Geological Society of London. Special Publication, 313–345. doi:10.1144/GSL.SP.1989.042.01.19

Sun, T. (2006). A new map showing the distribution of granites in South China and its egplauatory notes. *Geol. Bull. China* 25 (3), 332–337. (in Chinese with English abstract). doi:10.3969/j.issn.1671-2552.2006.03.002

Sylvester, P. J. (1998). Post-collisional strongly peraluminous granites. *Lithos* 45, 29–44. doi:10.1016/S0024-4937(98)00024-3

Tapponnier, P., Peltzer, G., Le Dain, A. Y., Armijo, R., and Cobbold, P. (1982). Propagating extrusion tectonics in Asia, new insights from simple experiments with plasticine. *Geol.* 10 (12), 611. doi:10.1130/0091-7613(1982)10<611:petian>2.0.co;2;2

Vernon, R. H. (1984). Microgranitoid enclaves in granites-globules of hybrid magma quenched in a plutonic environment. *Nature* 309 (5967), 438–439. doi:10.1038/309438a0

Wang, Y. J., Fan, W. M., Liang, X. Q., Peng, T. P., and Shi, Y. R. (2005). Zircon SHRIMP U-Pb age and genetic revelation of Indosinian granites in Hunan. *Chinese Science Bulletin* 50 (12), 1259–1266. (in Chinese with English abstract). doi:10.3321/j.issn:0023-074X.2005.12.018

Wang, D. H., Chen, Z. H., Chen, Y. C., Tang, J. X., Li, J. K., Ying, L. J., et al. (2010). New data of the rock forming and ore-forming chronology for China's important mineral resources areas. *Acta Geol. Sin.* 84 (7), 1030–1040. (in Chinese with English abstract).

Wang, D. H., Chen, Z. Y., Huang, F., Wang, C. H., Zhao, Z., Chen, Z. H., et al. (2014). Discussion on metallogenic specialization of the magmatic rocks and related issues in the Nanling Region. *Geotect. Metallogenia* 38 (2), 230–238. (in Chinese with English abstract).

Wang, X. L., Zhou, J. C., GriIIin, W. I., Zhao, G. C., Yu, J. H., Qiu, J. S., et al. (2014). Geochemical zonation across a Neoproterozoic orogenic belt isotopic evidence from granitoids and metasedimentary rocks of the Jiangnan orogen, China. *Precambrian Res.* 242, 154–171. doi:10.1016/j.precamres.2013.12.023

Wang, D. H., Li, P. G., Qu, W. J., Lei, Z. Y, Liao, Y. C., et al. (2013). Discovery and preliminary study of the high tungsten and lithium contents in the Dazhuyuan bauxite deposit, Guizhou, China. *Sci. China Earth Sci.* 56, 145–152. doi:10.1007/s11430-012-4504-2

Wang, X. L., Zhou, J. C., C'hen, X., Zhang, F. F., and Sun, Z. M. (2017). Formation and evolution of the jiangnan orogen. *Bull. Mineralogy, Petrology Geochem.* 360, 714–735. (in Chinese with English abstract). doi:10.3969/j.issn.1007-2802.2017.05.003

Wang, Y., Guan, T. Y., Liu, P. H., Yu, D. J., and Wu, J. H. (2002). Nd and Sr isopotic geochemical characteristics for Early Cretaceous volcanic rocks in Northeast Jiangxi Province. *J. Mineralogy Petrology* 22 (1), 36–40. (in Chinese with English abstract). doi:10.1080/12265080208422884

Wang, Y. J., Fan, W. M., Cawood, P. A., and Li, S. Z. (2008). Sr–Nd–Pb isotopic constraints on multiple mantle domains for Mesozoic mafic rocks beneath the South China Block hinterland. *Lithos* 106, 297–308. doi:10.1016/j.lithos.2008.07.019

Wang, Y. J., Fan, W. M., Guo, F., Peng, T. P., and Li, C. W. (2003). Geochemistry of Mesozoic mafic rocks adjacent to the Chenzhou-Linwu Fault, South China, implications for the lithospheric boundary between the Yangtze and Cathaysia blocks. *Int. Geol. Rev.* 45, 263–286. doi:10.2747/0020-6814.45.3.263

Wang, Y. J., Fan, W. M., Liang, X. Q., Peng, T. P., and Shi, Y. R. (2005a). Zircon SHRIMP U-Pb age and genetic revelation of Indosinian granites in Hunan. *Chin. Sci. Bull.* 50 (12), 1259–1266. (in Chinese with English abstract). doi:10.3321/j.issn:0023-074X.2005.12.018

Wang, Y. J., Fan, W. M., Peng, T. P., and Guo, F. (2005b). Elemental and Sr-Nd isotopic systematics of the early mesozoic volcanic sequence in southern jiangxi province, south China, petrogenesis and tectonic implications. *Int. J. Earth Sci.* 94 (1), 53–65. doi:10.1007/s00531-004-0441-4

Weaver, B. L. (1991). The origin of ocean Island basalt end-member compositions, trace element and isotopic constraints. *Earth Planet. Sci. Lett.* 104 (2-4), 381–397. doi:10.1016/0012-821X(91)90217-6

Whalen, J. B., Kenneth, L. C., and Bruce W, C. (1987). A-type granites, geochemical characteristics, discrimination and petrogenesis. *Contrib. Mineral. Pet.*. 95, 407–419. doi:10.1007/bf00402202

Whalen, J. B., Wodicka, N., Taylor, B. E., and Jackson, G. D. (2010). Cumberland batholith, trans-hudson orogen, Canada: Petrogenesis and implications for paleoproterozoic crustal and orogenic processes. *Lithos* 117 (1-4), 99–118. doi:10.1016/j.lithos.2010.02.008

Wu, Y. B., and Zhen, Y. F. (2004). Study on zirconium gallstone by mineralogy and its restriction on U-Pb age explanation. *Chin. Sci. Bull.* 49, 1589–1604. (in Chinese with English abstract).

Xia, W. C. (1991). Genetic stratigraphic framwork and its genetic relationship to oil and gas in Mesozoic and Cenozoic fault-controlled basin of Eastern China. *Geol. Sci. Technol. Inf.* 10 (1), 43–50. (in Chinese with English abstract).

Yang, F., Santosh, M., and Kim, S. W. (2018). Mesozoic magmatism in the eastern North China Craton: Insights on tectonic cycles associated with progressive craton destruction. *Gondwana Res.* 60, 153–178. doi:10.1016/j.gr.2018.04.003

Yang, F., Santosh, M., Kim, S. W., Zhou, H., and Jeong, Y. J. (2020). Late mesozoic intraplate rhyolitic volcanism in the north China craton: Far-field effect of the westward subduction of the paleo-Pacific plate. *GSA Bull.* 132 (1-2), 291–309. doi:10.1130/B35123.1

Yang, F., Xue, F., Santosh, M., Wang, G., Kim, S. W., Shen, Z., et al. (2019). Late mesozoic magmatism in the east qinling orogen, China and its tectonic implications. *Geosci. Front.* 10 (5), 1803–1821. doi:10.1016/j.gsf.2019.03.003

Yang, Z. (2012). *Pre-yanshanian magmatism and its mineralization in the miaoershan-yuechengling area, northern guangxi province*. China: Nanjing University, 1–64. (in Chinese with English abstract).

Yang, F., Santosh, M., and Kim, S. W. (2018). Mesozoic magmatism in the eastern North China Craton: Insights on tectonic cycles associated with progressive craton destruction. *Gondwana Research* 60, 153–178. doi:10.1016/j.gr.2018.04.003

Ye, M. F., Li, X. H., Li, W. X., Liu, Y., and Li, Z. X. (2007). SHRIMP zircon U-Pb geochronological and whole-rock geochemical evidence for an early Neoproterozoic Sibaoan magmatic arc along the southeastern margin of the Yangtze Block. *Gondwana Res.* 12 (1–2), 144–156. doi:10.1016/j.gr.2006.09.001

Yin, C. Q., Lin, S. F., Davis, D. W., Zhao, G. C., Xiao, W. J., Li, L. M., et al. (2013). 2.1–1.85Ga tectonic events in the Yangtze Block, South China: Petrological and geochronological evidence from the Kongling Complex and implications for the reconstruction of supercontinent Columbia. *Lithos* 183, 200–210. doi:10.1016/j.lithos.2013.10.012

Yuan, Z. X., and Zhang, Z. Q. (1992). Sm-Nd isotopic of granitoids in the nanling region and their petro-genetic analysis. *Geol. Rev.* 38 (1), 1–15. doi:10.16509/j.georeview.1992.01.001

Zartman, R. Z., and Doe, B. R. (1981). Plumbotectonics-themodel. *Tectonophysics* 75, 135–162. doi:10.1016/0040-1951(81)90213-4

Zhang, H. F., Sun, M., Zhou, X. H., Fan, W. M., Zhai, M. G., Yin, J. F., et al. (2002). Mesozoic lithosphere destruction beneath the north China craton, evidence from major-trace-element and Sr-Nd-Pb isotope studies of fangcheng basalts. *Contrib. Mineral. Pet.*. 144 (2), 241–254. doi:10.1007/s00410-002-0395-0

Zhang, L., Chen, Z. Y., Wang, F. Y., and Zhou, T. F. (2020). Apatite geochemistry as an indicator of petrogenesis and uranium fertility of granites: A case study from the zhuguangshan batholith, south China. *Ore Geol. Rev.* 128, 103886. doi:10.1016/j.oregeorev.2020.103886

Zhang, Y. X. (1984). Ring structiure and their genetic mechanism in the South China region. *Geol. Rev.* 30 (5), 437–445. (in Chinese with English abstract).

Zhang, S. B., Zheng, Y. F., Wu, Y. B., Zhao, Z. F., Gao, S., and Wu, F. Y. (2006). Zircon isotope evidence for ≥3.5Ga continental crust in the Yangtze craton of China. *Precambrian Research* 146 (1–2), 16–34. doi:10.1016/j.precamres.2006.01.002

Zhang, S. H., Zheng, Y. F., He, Z. F., and Wu, H. (2009). The 1.35Ga diabase sills from the northern North China Craton: Implications for breakup of the Columbia (Nuna) supercontinent. *Earth and Planetary Science Letters* 288 (3-4), 588–600. doi:10.1016/j.epsl.2009.10.023

Zhao, J. H., and Zhou, M. F. (2008). Neoproterozoic adakitic plutons in the northern margin of the Yangtze block, China, partial melting of a thickened lower crust and implications for secular crustal evolution. *Lithos* 104 (1-4), 231–248. doi:10.1016/j.lithos.2007.12.009

Zhao, K. D., Jiang, S. Y., Yang, S. Y., Dai, B. Z., and Lu, J. J. (2012). Mineral chemistry, trace elements and Sr–Nd–Hf isotope geochemistry and petrogenesis of Cailing and Furong granites and mafic enclaves from the Qitianling batholith in the Shi-Hang zone, South China. *Gondwana Res.* 22 (1), 310–324. doi:10.1016/j.gr.2011.09.010

Zhao, T. P., Zhou, M, F., Zhai, M. G., and Xia, B. (2002). Paleoproterozoic rift-related volcanism of the xiong'er group, north China craton: Implications for the breakup of Columbia. *Int. Geol. Rev.* 44 (4), 336–351. doi:10.2747/0020-6814.44.4.336

Zhao, Z. H., Bao, Z. H., and Zhang, B. Y. (1998). Geochemistry of the mesozoic basaltic rocks in southern Hunan province. *Sci. China Ser. D-Earth. Sci.* 41 (1), 102–112. doi:10.1007/BF02875640

Zhao, Z., Miao, B., Xu, Z., Lu, J., Lei, L., Zuo, C., et al. (2017). Petrogenesis of two types of late triassic granite from the guandimiao complex, southern hunan province, China. *Lithos* 282-283, 403–419. doi:10.1016/j.lithos.2017.02.021

Zhao, Z., Wang, D. H., Li, P. G., and Lei, Z. Y. (2013). Detrital zircon U-Pb geochronology of the Dazhuyuan formation in Northern Uuizhou; implications for bauxite mineralization. *Rock Mineral analysis* 32 (1), 166–173. (in Chinese with English abstract). doi:10.3969/j.issn.0254-5357.2013.01.027

Zhao, Z. X., Xu, Z. W., Miao, B. H., Zuo, C. H., Lu, J. J., Lu, R., et al. (2015). Diagenetic age and material source of the guandimiao granitic batholith, hengyang city, hunan province. *Acta Geol. Sin.* 89 (7), 1219–1230. (in Chinese with English abstract). doi:10.3969/j.issn.0001-5717.2015.07.006

Zheng, J. P., Griffin, W. L., Tang, H. Y., Zhang, Z. H., Su, Y. P., and Liu, G. P. (2008). Archean basement similar to the north China and Yangtze continents may Be existed beneath the western Cathaysia. *Geol. J. China Univ.* 4, 549–557. (in Chinese with English abstract). doi:10.3969/j.issn.1006-7493.2008.04.008

Zhong, Y. F., Ma, C. Q., Yu, Z. B., Lin, G. C., Xu, H. J., Wang, R. J., et al. (2005). SHRIMP U-Pb zircon geochronology of the jiuling granitic complex batholith in jiangxi province. *Earth Science-Journal China Univ. Geosciences* 30 (6), 685–681. (in Chinese with English abstract). doi:10.3321/j.issn:1000-2383.2005.06.005

Zhou, J. L., Li, X. H., Tang, U. Q., Uao, B. Y., Bao, Z. A., Ling, X. X., et al. (2018). Ca. 890 Ma magmatism in the northwest Yangtze block, south China: SIMS U-Pb dating, *in-situ* Hf-O isotopes, and tectonic implications. *J. Asian Earth Sci.* 151, 101–111. doi:10.1016/j.jseaes.2017.10.029

Zhou, X. M. (2003). My thinking about granite genesis of south China. *Geol. J. China Univ.* 9 (4), 556–565. (in Chinese with English abstract). doi:10.3321/j.issn:1000-2383.2005.06.005

Zhou, X. M., Sun, T., Shen, W. Z., Shu, L. S., and Niu, Y. L. (2006). Petrogenesis of Mesozoic granitoids and volcanic rocks in South China, a response to tectonic evolution. *Episodes* 29, 26–33. doi:10.18814/epiiugs/2006/v29i1/004

Zindler, A., and Hart, S. (1986). Chemical geodynamics. *Annu. Rev. Earth Planet. Sci.* 14, 493–571. doi:10.1146/annurev.ea.14.050186.002425

frontiers | Frontiers in Earth Science

TYPE Original Research
PUBLISHED 19 September 2022
DOI 10.3389/feart.2022.939375

Check for updates

OPEN ACCESS

EDITED BY
Liang Zhang,
China University of Geosciences, China

REVIEWED BY
Ahmed M. Eldosouky,
Suez University, Egypt
Sirui Wang,
China University of Geosciences, China

*CORRESPONDENCE
Zheng-Jiang Ding,
110357960@qq.com
Guan-Wen Gu,
sun_ggw@163.com

SPECIALTY SECTION
This article was submitted to Economic Geology, a section of the journal Frontiers in Earth Science

RECEIVED 09 May 2022
ACCEPTED 25 July 2022
PUBLISHED 19 September 2022

CITATION
Xu Z-H, Ding Z-J, Gu G-W, Jiang J-Y, Wang L and Niu X-G (2022), Deep exploration of Jiaodong type gold deposit, taking Shanhou gold deposit, southern part of Zhaoping fault as an example.
Front. Earth Sci. 10:939375.
doi: 10.3389/feart.2022.939375

COPYRIGHT
© 2022 Xu, Ding, Gu, Jiang, Wang and Niu. This is an open-access article distributed under the terms of the Creative Commons Attribution License (CC BY). The use, distribution or reproduction in other forums is permitted, provided the original author(s) and the copyright owner(s) are credited and that the original publication in this journal is cited, in accordance with accepted academic practice. No use, distribution or reproduction is permitted which does not comply with these terms.

Deep exploration of Jiaodong type gold deposit, taking Shanhou gold deposit, southern part of Zhaoping fault as an example

Zhi-He Xu[1,2,3,4], Zheng-Jiang Ding[2]*, Guan-Wen Gu[1,3]*, Ji-Yi Jiang[1,3], Li Wang[5] and Xing-Guo Niu[6]

[1]Institute of Disaster Prevention, Sanhe, China, [2]Shandong Provincial Engineering Laboratory of Application and Development of Big Data for Deep Gold Exploration, Weihai, China, [3]Hebei Key Laboratory of Earthquake Dynamics, Sanhe, China, [4]Engineering Research Center of Geothermal Resources Development Technology and Engineering, Ministry of Education, Jilin University, Changchun, China, [5]College of Earth Sciences, Jilin University, Changchun, China, [6]Inner Mongolia Non-ferrous Geological Mining Industry, Huhehaote, China

Crustal response induced by the subduction of Paleo-Pacific Plate, is crucial to study the metallogenic law and prediction of Jiaodong type gold deposit. Gold deposits are preferentially hosted in the lithospheric-scale second-order faults, which provide migration channels, mineralization corridors, and the physicochemical conditions. Super-large gold deposits in northwestern Jiaobei Terrane are generally controlled by regional linear faults, such as Sansandao, Jiaojia, Zhaoping and Qixia faults. However, Zhaoping fault is exposed sporadically (in Xiadian and Jiangjiayao gold deposits) beneath a thick cover of Quaternary basalts, which indicating that limited information can be obtained by traditional geological survey. In this study, high-precision geophysical surveys such as gravity and controlled source audio frequency magnetotellurics (CSAMT) are conducted in the Shanhou gold deposit, which hosted in southern part of Zhaoping fault. Three integrated geophysical profiles results further identified the spatial distribution of second-order oblique-slip faults of Zhaoping fault and established the relationships between brittle deformation and mineralization. The spatial variability of stratum (high density 2.82 g/cm^3 and intermediate to high specific resistivity 4000 Ω m), brittle-slip faults (intermediate density 2.73 g/cm^3 and low specific resistivity 200 Ω m) and magmatite (low density 2.57 g/cm^3 high specific resistivity 8000 Ω m) are identified by two inversion techniques, including the man-machine interactive inversion technology and nonlinear conjugate gradient technology. In addition, the geophysical inversion pseudo sections delicately portray a smooth-out waveform low specific resistivity anomaly, which strongly couples with the spatial ore-hosted locations and enrichment places. The gold mineralized alteration zones generally dips to southeast and the angle changing from 45° to 30°, which are strong coupling with the large-scale acid magmatic

intrusion and extensional tectonics occurred in the late Mesozoic. Finally, according to the deep prospecting prediction, a gold ore body with 10 m in thickness was revealed by drilling below the depth of 1,015 m, which is hosting in the brittle deformation of Zhaoping fracture zone.

KEYWORDS

deep exploration, decratonic gold deposit, subduction of Paleo-Pacific Plate, Jiaodong gold province, geophysical method, cratonic destruction

Introduction

Jiaodong type gold deposit, which is the primary type of gold endowment in the North China Craton (NCC), generally formed after prolonged stabilization of the craton (Zhu et al., 2011, 2015). This type deposit occurs under transpressinal condition from a transpressional to transtensional tectonic setting, which induced by Late Mesozoic breakoff of the subduction slab and rollback of the Paleo-Pacific Plate (Deng et al., 2015; Liang et al., 2019). The metallogenic law has an evidently relationship with the NNE-NE-trending oblique-slip faults (Li et al., 2012; Deng et al., 2020; Li et al., 2022). Generally, the formation of cratons remained stable in the early Precambrian and hardly triggered large-scale tectono-magmatic activities and gold mineralization (Groves and Bierlein, 2007). However, multi-disciplinary observations indicate that the lithosphere of NCC has experienced unsteady flow. Two important gold metallogenic belts (the East gold belt and the West gold belt, Figure 1) formed during the metasomatic transformation of mantle-derived fluids and magmatic activities (Li et al., 2012; Cai et al., 2018) (Figure 1).

The Jiaodong gold province, with more than 5000 t of proven gold resources, is considered as the only global district that preserved giant gold resources in the East gold belt (Zhu et al., 2011; Deng et al., 2020). The aim of early prospecting

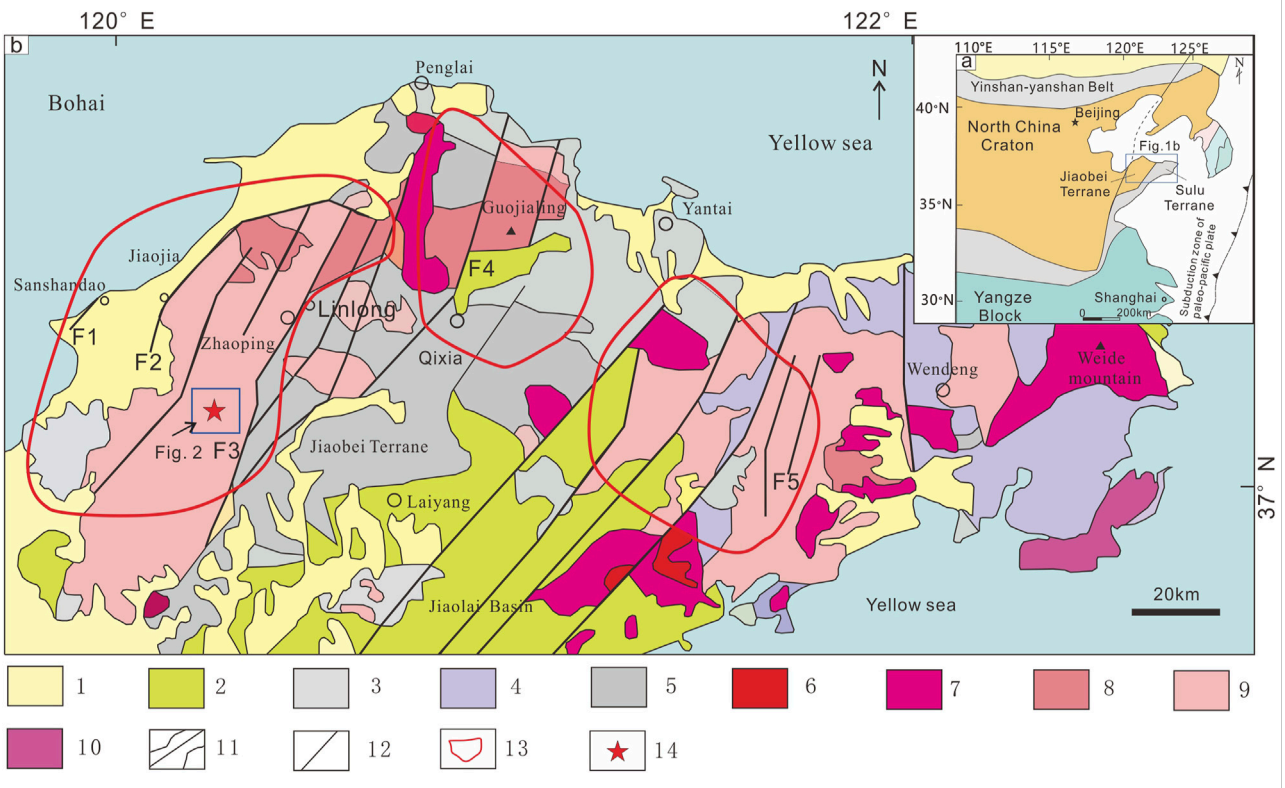


FIGURE 1
Simplified regional geological map, modified after Wu et al. (2022). **(A)** Simplified regional geological map of NCC; **(B)** Regional geological map of Jiaodong gold province. 1- Quaternary; 2- Mesozoic; 3- Proterozoic; 4- Neoproterozoic gneiss; 5- Archean greenstone belt; 6- Cretaceous Laoshan granite; 7- Cretaceous Weide mountain granite; 8- Cretaceous Guojialing granite; 9- Jurassic Linglong granite; 10- Triassic granite; 11- Geological boundary; 12- Fault; 13- Gold deposit accumulation region; 14- Laixi gold desposit; F1-Sanshandao fault; F2- Jiaojia fault; F3- Zhaoping fault; F4-Xilin-douya fault; F5-Jinniushan fault.

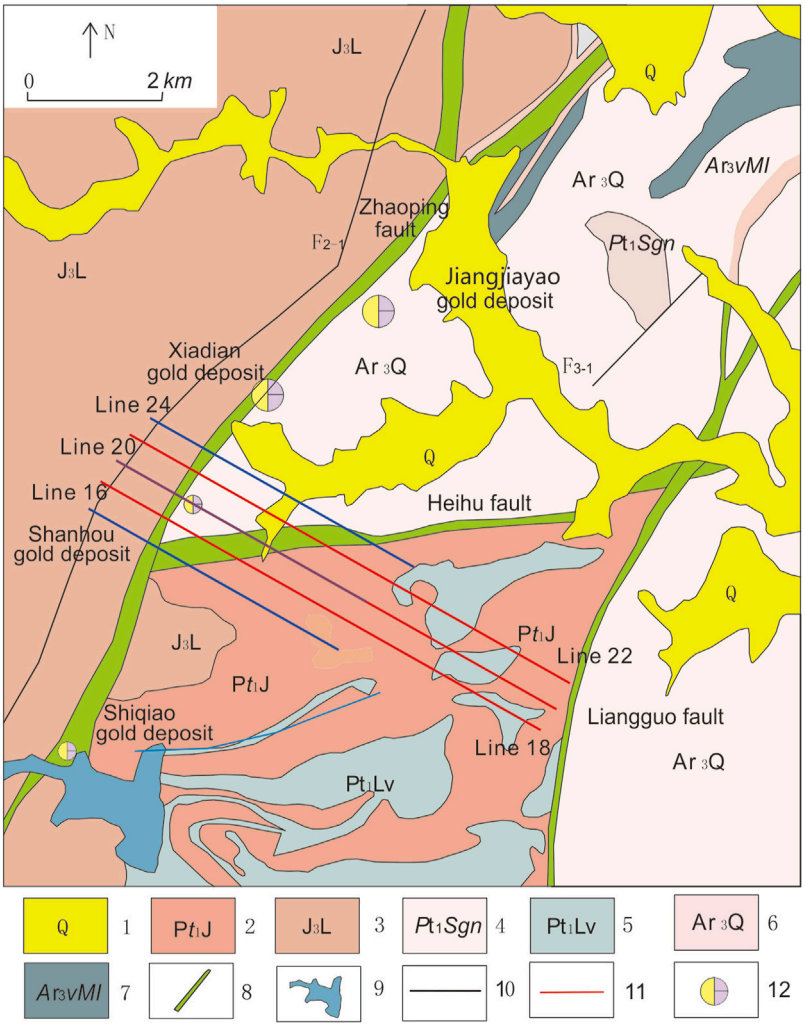


FIGURE 2
Simplified regional geological map of Shanhou gold deposit. 1- Quaternary; 2- Paleoproterozoic Jinshan Group; 3- Late Jurassic Linglong granite; 4- Paleoproterozoic Shuangdingshan gneiss; 5- Paleoproterozoic Penglai metabasite; 6- Archean Qixia gneiss; 7-Archean Luanjiazhai metabasite; 8- Deep-seated fault; 9-Reservoir; 10- Secondary fracture; 11- Geophysical profile; 12- Gold deposit.

direction is predominately the quartz vein type gold deposit and superficial prospecting. The proved gold reserves are only 340 t in the early stage of prospecting. As a result of the discovery of Jiaojia type gold deposit, geologists recognized that the regional faults not only created channels for transmitting ore, but also favored the occurrence space for mineralization (Groves et al., 2005, 2020; Zhang et al., 2020). Therefore, based on above metallogenic theory and geological practice, a host of large gold deposits (such as Sanshandao, Hexi, Fayunkuang) were successively discovered in the deep-seated structures (Li et al., 2013; Guo et al., 2017). The newly proven gold reserves have exceeded 2700 t, and the "stepped metallogenic model" is proposed (Goldfarb et al., 2001; Yang et al., 2003). However, the ore-controlling structure (Zhaoping fault and its secondary

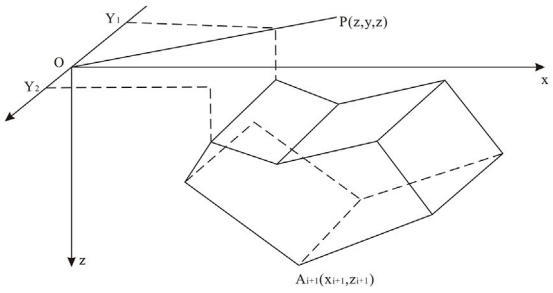


FIGURE 3
Schematic diagram of the two point five dimension level prism, modified after Fan et al., 2014.

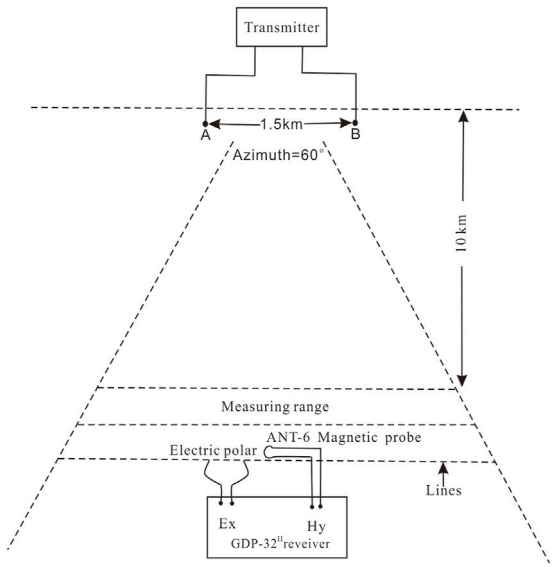


FIGURE 4
The CSAMT field observation system.

fault) of gold deposits is exposed sporadically (in Xiadian, Jiangjiayao gold deposits) beneath a thick cover of Quaternary basalts, which mean that only limited information can be obtained by traditional geological survey.

Here we present high-precision gravity and CSAMT methods to provide insights into spatial distribution of stratum, structure and magmatite for the Shanhou gold deposit hosting in southern part of Zhaoping fault. Moreover, relatively advanced data processing and inversion techniques help us to elucidate the coupling relationship between gold mineralized alteration zones and smooth-out waveform faults.

Geological setting

Regional geology

The Jiaodong gold province extends between the eastern NCC and northern SuLu metamorphic belt (Figure 1A) (Wei et al., 2001; Yang et al., 2016). It consists of Archean Jiaodong Group gneiss and Paleoproterozoic metamorphic sedimentary basement overlain by Proterozoic–Cenozoic carbonate rocks, volcano-sedimentary rocks, and loose sediment. The Late Jurassic Linglong granite, which are widespread in Jiaodong Peninsula and host large number of gold deposits. Geochronological results indicate that the formation age of granite was 166 ± 5.0 Ma (Figure 1B) (Yang et al., 2018; Deng et al., 2020). The middle Early Cretaceous Guojialing granite, which hosted several gold deposits, was emplaced between 133 and 126 Ma. The regional structures mainly consist of E-W- and NNE-NE-trending faults (Figure 1B) (Wang et al., 2014; Deng et al., 2020). The E-W-trending faults are mainly

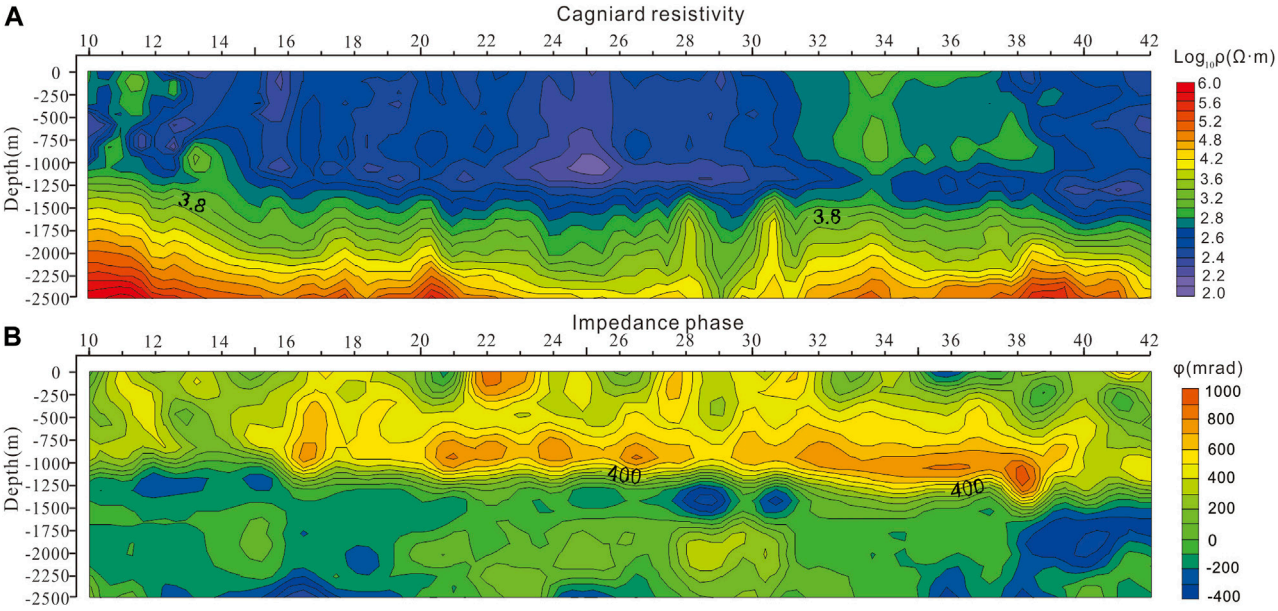


FIGURE 5
The pseudosection of the CSAMT profile; **(A)** Cagniard resistivity; **(B)** Impedance phase. The X-axis shows the survey point and the Y-axis shows the apparent depth.

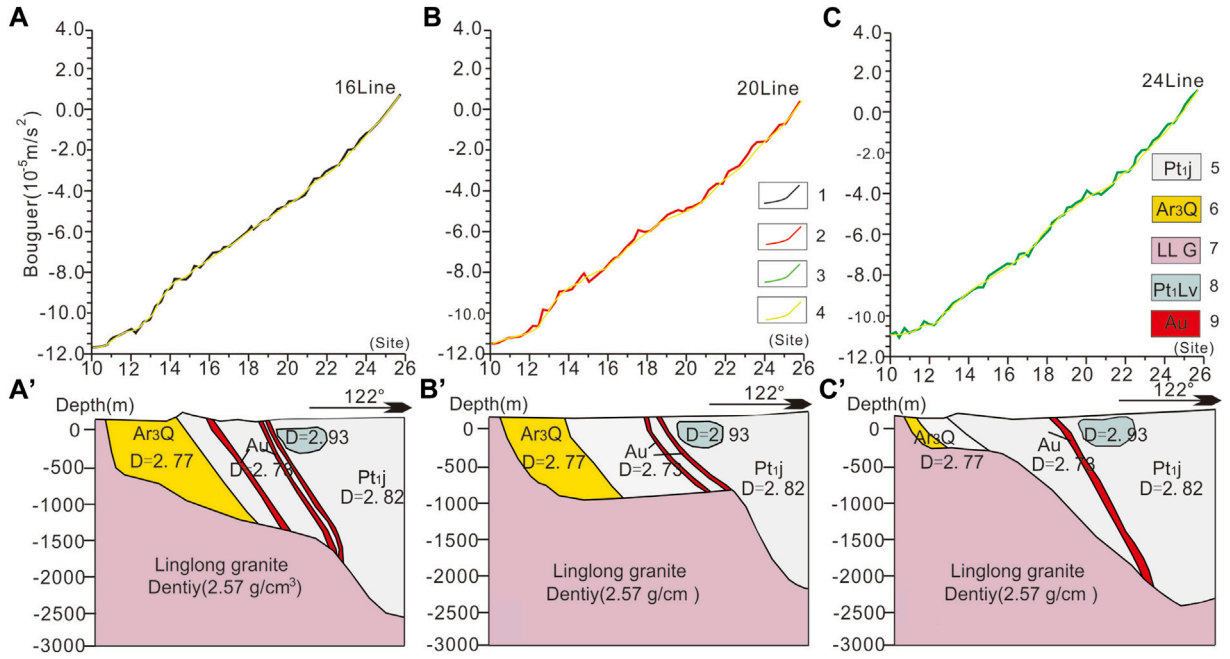


FIGURE 6
Man machine interactive inversion of three gravity profiles. **(A–C)** Observation curves and fitting curves; **(A′–C′)** Geologic interpretation. 1- Observation curve 16 line; 2- Observation curve 20 line; Observation curve 24 line; 4- Fitting curve; 5- Paleoproterozoic Jinshan Group; 6- Archean Qixia gneiss; 7-Late Jurassic Linglong granite; 8- Paleoproterozoic Lianzhou metabasite; 9- gold ore bodies.

metamorphic crystalline basement folds. The NNE-NE-trending ore-controlling faults are considered to be subparallel faults of the Tan-Lu fault. These ore-controlling faults are named Sanshandao, Jiaojia, Zhaoping, Xilin-douya, Jinniushan faults from west to east, respectively. The Zhaoping fault, for instance, with more than 1400 t of proven gold resources, directly controls the distribution of 17 large-scale gold deposits and 10 small-scale gold deposits (Yang et al., 2014).

Shanhou gold deposit is located in the southern part of the Zhaoping fault and is dominated by middle Early Cretaceous Guojialing granite, Archean Jiaodong Group gneiss, and Paleoproterozoic metamorphic rocks of the Jinshan Group (Figure 2). Three gold deposits (Xiadian, Beipo and Shanhou) are hosted in the granitic cataclastic rock and sericitized granitic cataclastic rock (Figure 2). Gold ore-bodies are typically controlled by brittle deformation structures, and show ductile-brittle deformation with sheared ores, altered rocks or pyrite aggregates, such as the elongated pyrite aggregates (Figure 2) (Yang et al., 2018).

TABLE 1 Density and specific resistivity data for the samples from the ore-bearing rocks and wall rocks in the Shanhou gold deposit.

Lithology	Number	Density	Specific resistivity
		Common value g/cm^3	Common value (Ω•m)
Paleoproterozoic Jinshan Group	23	2.82	4000
Linglong granite	30	2.57	8000
Archean Qixia gneiss	21	2.77	3000
Paleoproterozoic Lianzhou metabasite	6	2.93	7000
Ore-bearing rock	5	2.73	200

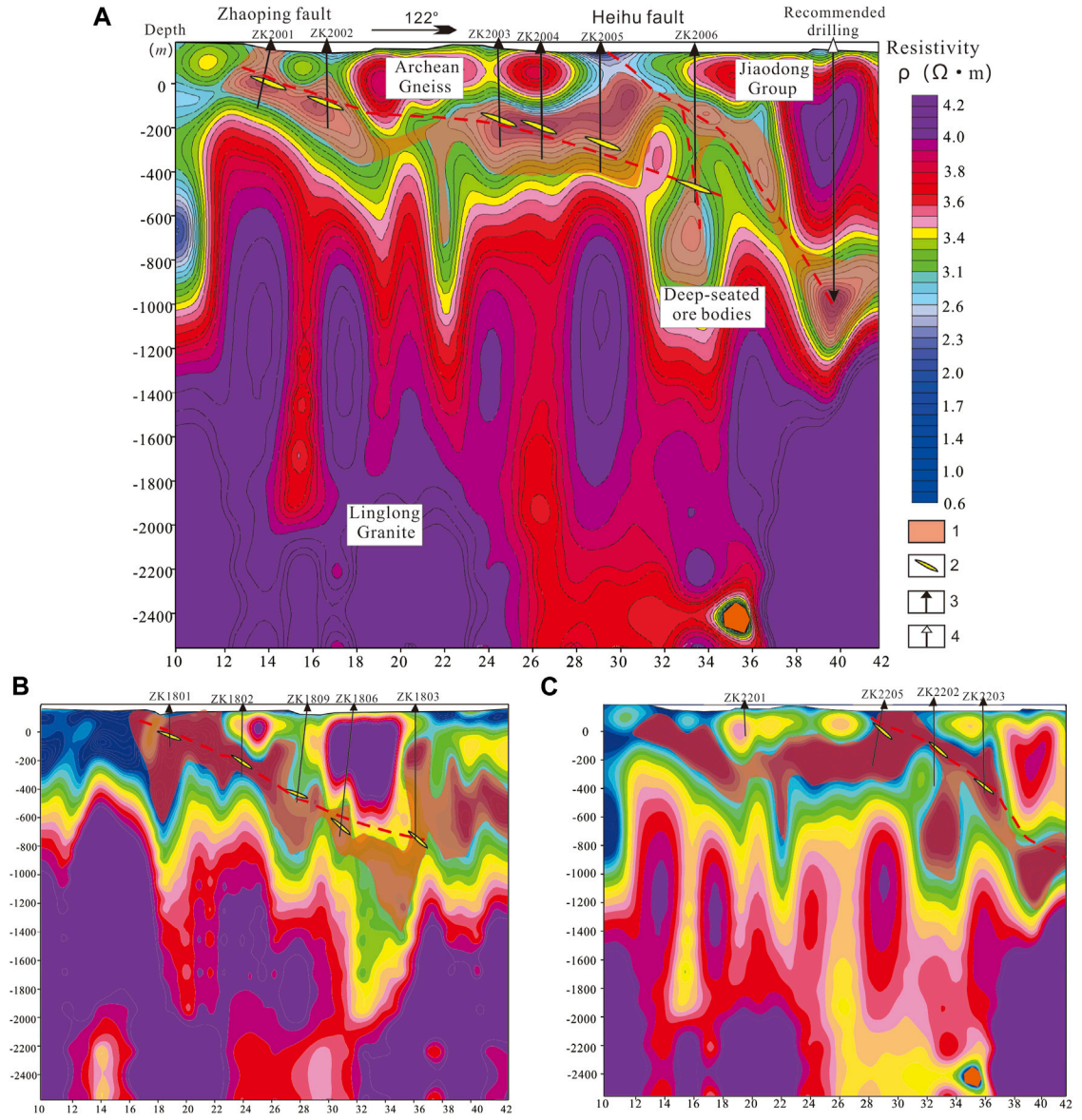


FIGURE 7
Inversion resistivity model of CSAMT by NLCG. **(A)** Line 20; **(B)** Line 18; **(C)** Line 22; 1- Ore-controlling brittle fracture; 2- The proven superficial gold bodies; 3- Drilled hole; 4- Recommended drilling.

Geophysical analytical techniques

Petrophysical parameters

Significant petrophysical parameters differences are the prerequisite of surveying geophysical research. Table 1 lists the petrophysical parameters in density and specific resistivity. The collected samples include the ore-bearing rocks and wall rocks in the Shanhou gold deposit. Samples from the Paleoproterozoic Jinshan Group yielded the relatively high density (2.82 g/cm^3) and high specific resistivity (4000 Ω m). The Linglong granite was characterized by low density (2.57 g/cm^3) and high specific resistivity (8000 Ω m), and the ore-bearing rocks by intermediate density (2.73 g/cm^3) and lowest specific resistivity (200 Ω m) (Table 1). This results are generally consistent with region petrophysical parameters statistics in Zhaoping fault (Xu et al., 2019).

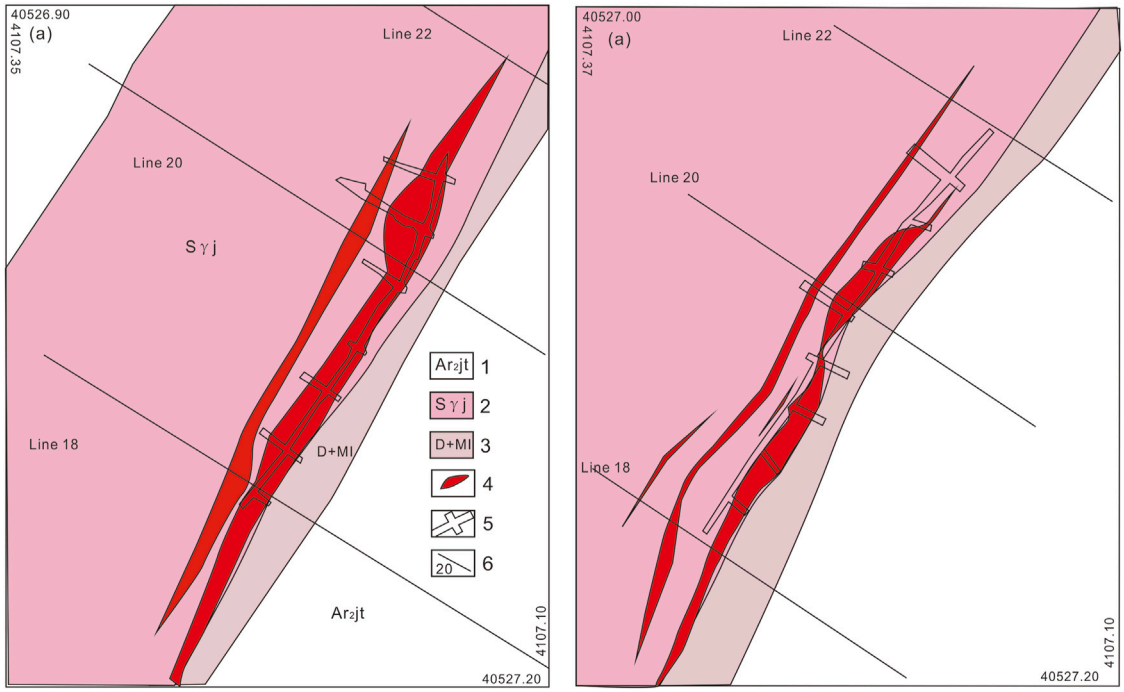


FIGURE 8
Geological map of tunnel samplings. **(A)** At the depth of –50 m; **(A)** At the depth of –100 m; 1- Archean plagioclase gneiss; 2- Sericitization granite; 3- Fault gouge and mylonite; 4- gold ore bodies; 5- tunnel; 6- geological profile.

High-precision gravity

Three high-precision gravimetric observation curves (Lines 16, 20 and 24) were collected along a section of 4.80 km long. These gravity profiles passes through the northeast–southwest–trending Zhaoping fault with the trend of NW. Each section included 33 continental gravity survey points at intervals of 50 m. It was collected by CG-5 type Gravimeter (Scintrex Corporation, Canada), which has the resolution less than 1 μGal, repeatability less than 5 μGal, and the static drift less than 0.02 mGal per day.

The two point five dimension man machine interactive inversion technology was applied to probe the deep-seated gold deposit (Figure 3). Firstly, the initial models are build according to the exiting gold metallogenic model. Then, the gravity forward modeling curves are subsequently calculated according to the initial models (Sui et al., 2004). The initial models were adjusted until the gravity forward modeling curves matching the field observation data (Yao et al., 1998). The gravity anomalies for any point, P (x, y, z), can be calculated using Eqs 1–5 (Yin et al., 2018) (Figure 3).

$$\Delta g(P) = G\sigma \sum_{i=1}^{N} \cos\varphi_i \left[I_i(Y_2) - I_i(Y_1) \right] \tag{1}$$

$$I_i(y) = y \ln \frac{u_{i+1} + R_{i+1}}{u_i + R_i} + u_{i+1} \ln(R_{i+1} + y) - u_i \ln(R_i + y) - w_i \left(\arctan \frac{u_{i+1} y}{w_i + R_{i+1}} - \arctan \frac{u_i y}{w_i R_i} \right) \tag{2}$$

$$u_i = x_i \cos\varphi_i + z_i \sin\varphi_i, u_{i+1} = x_{i+1} \cos\varphi_i + z_{i+1} \sin\varphi_i \tag{3}$$

$$R_i = \left(x_i^2 + y^2 + z_i^2 \right)^{1/2}, R_{i+1} = \left(x_{i+1}^2 + y^2 + z_{i+1}^2 \right)^{1/2} \tag{4}$$

$$\varphi_i = -x_i \sin\varphi_i + z_{i+1} \cos\varphi_i \tag{5}$$

where G, σ, and i are the gravitational constant, prism density, and prism corner number, respectively. The mean square error is about 7.20%.

Controlled source audio frequency magnetotellurics

CSAMT profile data were collected along a northwest–southeast-trending section of 3.10 km long (Figure 4). This section included 63 CSAMT survey points at intervals of 50 m. It was surveyed with broadband, multi-channel digital electromagnetic exploration system named GDP-32^{II} (Zonge Corporation, the United States of America). The GDP-32^{II} receiver is an 16-bit±1/2 low power consumption, high-accuracy data collected system, with one 250 mv/nT pass-band

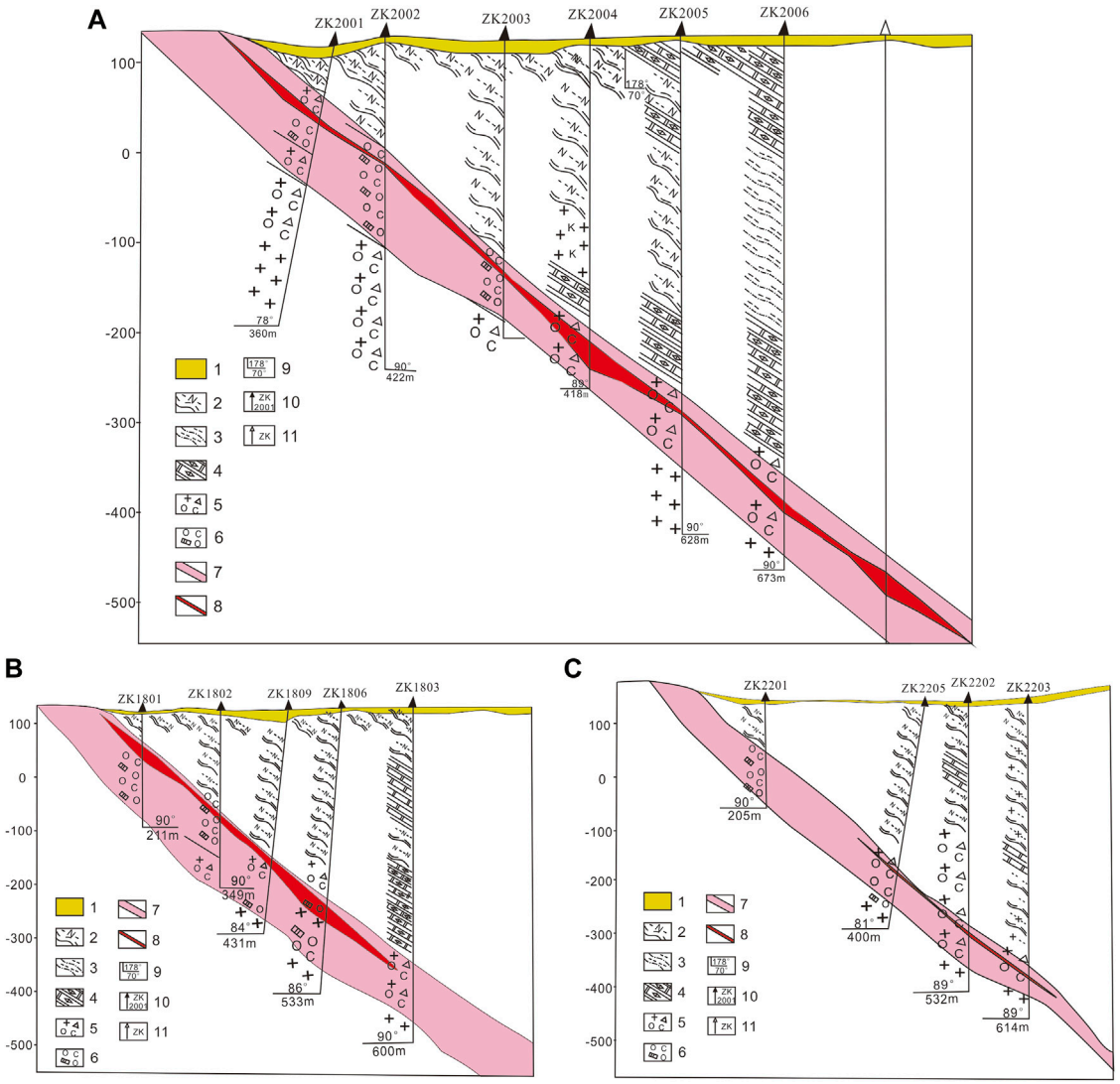


FIGURE 9
Geological profile of exploration in Shanhou gold deposit. **(A)** Line 20; **(B)** Line 18; **(C)** Line 22; 1- Quaternary; 2- Archean plagioclase gneiss; 3- Archean biotite granulite; 4- Paleoproterozoic dolomitic marble; 5- Sericitized cataclastic granite; 6- Pyrite sericite quartz; 7- Alteration zone; 8- gold bodies; 9- Occurrence $\frac{\text{inclination}}{\text{dip}}$; 10- Completed drilling; 11- Recommended drilling.

sensitivity ANT-6 senor, and 16 solid non-polarized poles for collecting electromagnetic signal instruments. The horizontal electric dipole transmitter was setting at E 120°18′12.02″, N 37°05′36.32″, and the emission current was about 30 A.

The results of smooth Cagniard resistivity and impedance phase indicate that the field survey data is true and effective (Figure 5). The commercial software gather the observed data and build a new model section, including line annotation, survey configuration, and inversion control. After multiple iterations, the initial inversion resistivity is obtain. Then the software automatically updates the model section and obtains the further inversion resistivity. Finally, the inversion errors (about 3.47%) satisfy the requirements (less than 7%).

Results

High-precision gravity

The amplitudes of high-precision gravity data are determined by two factors: lithology and fault. The overall trend of three gravity profiles are rising and degrading in some regional survey points. The black, red and green lines represent the field surveyed gravity curves. The yellow lines are the theoretical gravity curves which are calculated by two point five dimensional man-machine interactive inversion technology (Figures 6A–C). The assumed geological bodies were adjusted until the theoretical gravity curve is consistent with the measured gravity data (Yao et al., 1998).

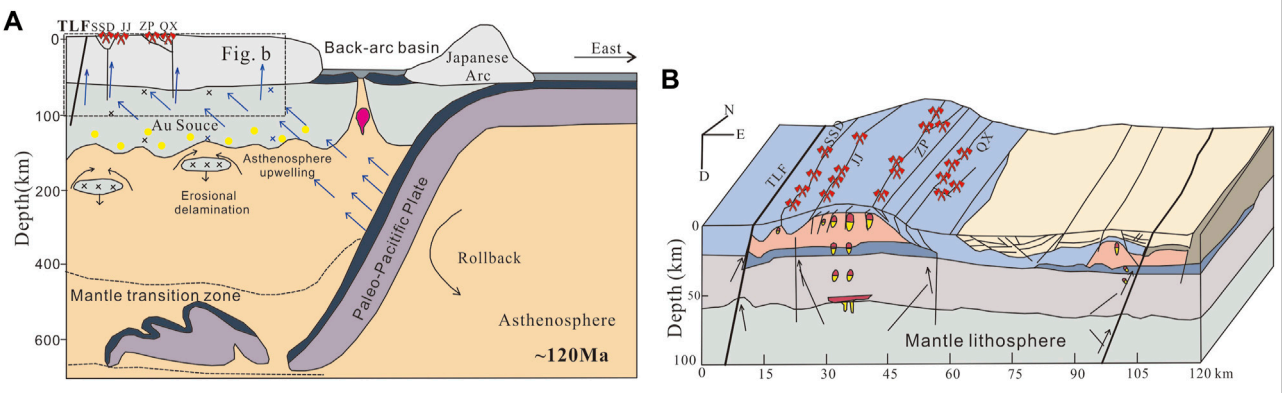


FIGURE 10
Cartoon showing the geodynamics of Jiaodong type gold deposit in Jiaodong gold province. **(A)** Metallogenic model of Jiaodong gold province; **(B)** Lithospheric and crustal architecture for the effective deposition of auriferous magma, modified from Deng et al. (2020).

According to the lithology exposed on the surface and regional petrophysical parameters, we conclude that the deeper subsurface geological body with the low value density (~2.57 g/cm^3) is consisted by the Late Jurassic Linglong granite. At shallow depth (top 1,000 m), between survey points 10 and 14, gravity profiles with an high density (~2.77 g/cm^3) should be corresponding to Archean Qixia gneiss. The intermediate to high gravity anomaly (~2.73 g/cm^3) likely corresponds to Zhaoping fault, which controls the distribution of Shanhou gold ore-bodies at survey points 16 and 18. The highest gravity anomaly (~2.82 g/cm^3), known as Paleoproterozoic Jinshan Group, lies in the southwestern part of Shanhou gold deposit, on one side of Zhaoping fault (Figures 6A'–C').

Controlled source audio frequency magnetotellurics profile

The CSAMT profile vertically passes through the trend of different geological bodies, producing a high resolution geoelectric structure (Figure 7). Laterally, two dimensional NLCG inversion results can be divided into three segments. The first one (sites 10–13) with intermediate to high apparent resistivity (~$10^{3.6}$ Ω m) should be corresponding to Late Jurassic Linglong granite. The second one (sites 15–28) with intermediate apparent resistivity (~$10^{3.2}$ Ω m) is the Archean gneisses. At survey point 14, an abrupt change in the apparent resistivity (10^4 to $10^{2.2}$ Ω m) is interpreted as a regional brittle fracture (named Zhaoping fault), which separates Linglong Granite from the Archean Qixia gneiss (Figure 7A). The third segment (sites 29–42) with highest apparent resistivity (~$10^{4.2}$ Ω m) is the Paleoproterozoic Jinshan Group. At survey point 28, Heihu fault with the low apparent resistivity (~$10^{2.2}$ Ω m) separates Archean Jiaodong Group from Paleoproterozoic Jinshan Group (Figure 7A).

Vertically, the inversion results can be segmented into three layers. The first layer (depths of 500 m) represents intermediate to high apparent resistivity ($10^{3.5}$–$10^{4.2}$ Ω m) geological bodies, including Late Jurassic Linglong granite, Archean Qixia gneiss and Paleoproterozoic Jinshan Group. The second layer (depths of 500–1000 m) with the lowest apparent resistivity (~$10^{2.0}$ Ω m) should be corresponding to deep-seated Zhaoping fault. This undulating fault no only controls the superficial Shanhou gold deposit, but also controls the deep-seated blind gold ore-bodies. According to the location of surface exposure and the apparent resistivity high value, the deeper layer should be consisted by Late Jurassic Linglong granite (Figure 7–9).

Discussion

Spatial correlation between gold mineralization and fault

The majority of Jiaodong type gold deposit, are characterized by massive gold ore bodies in deep-seated faults, such as Jiaodong Sanshandao gold deposit occurring in Sansandao fault, Liaodong Wulong gold deposit occurring in Jixingou fault, and Jilin Jiapigou gold deposit occurring in Jiapigou fault (Zhang et al., 2019; Zhang et al., 2020; Han et al., 2021).

The regional NNE-NE-trending faults in the Jiaodong gold province are regarded as the subsidiary fault of Tan-Lu fault. They are initially determined as the main gold ore-guided structures instead of the ore-controlling structures, such as Sanshandao, Jiaojia, Zhaoping, Qixia from west to east, respectively (Cox, 2010; Deng et al., 2019). Studies on the ore-forming fluid in above large gold belts indicated that the ore-forming fluid is basically consistent with the depths from deep to shallow domain (0 to −2,000 m) (Wu et al., 2022). Mineralization predictions in Jiaojia fault indicated that the occurring of gold

deposits in depth (−1700 to −1800 m) has great mineralization and a promising prospecting. However, Zhaoping fault is quite distinct from the other regional faults above with sporadically exposure. Therefore, the deep mineral prospecting has still faced a downturn.

Geodynamics of Jiaodong type gold deposit in Jiaodong gold province

Tectonic altered rock type or dissemination type gold deposits are commonly coupling with NNE-NE trending brittle faults, which are sub-parallel to the Tan-Lu fault to the west (Deng et al., 2015). Geological and geophysical results reveal that the Shanhou gold deposits are generally hosting in the footwall of the faults within Linglong Granite. The clustered gold deposits distributed in the smooth-out waveform faults indicated that Zhaoping fault has experienced transpression and extension (Deng et al., 2015, Deng et al., 2019). The development of strike-slip motion was triggered by the transition from transpression to transtension and then the gold ore-bodies with industrial grade deposited in the gentler-dipping parts of these NNE-NE trending faults. Thus, the lithospheric-scale Tan-Lu fault is the first-order architectural control on the Jiaodong Peninsula. This lithospheric-scale fault plays a role of connection between lithosphere and crust for its secondary parallel faults.

At plate tectonic scale, the Paleo-Pacific Plate had a slow northwesterly subduction earlier than ~135 Ma and then gradually deflected in a clockwise direction during 135–125 Ma. At the period of 125–100 Ma, the abrupt breakoff and roll-back of the subduction slab triggered the destruction of NCC, resulted in extension and thinning of lithosphere (Deng et al., 2015; Zhu et al., 2015; Liang et al., 2019; Wu et al., 2022). Within the Jiaodong gold province, the far-field stresses of subduction produced the development of lithosphere-scale Tan-Lu fault and its second-order faults (Figure 10A) (Deng et al., 2020).

The far-field stresses of subduction of Paleo-Pacific Plate triggered the temporal evolution of igneous activity and the structural geometries of gold deposits (Zhu and Sun, 2021). Thus, the Zhaoping fault can rapidly migrate the sub-crustal auriferous fluid without forming extensive melts and control the distribution of gold deposits, such as Jiangjiayao, Xiadian, Shanhou, and Shiqiao gold deposits (Figure 10B). The mineralization of Jiaodong type gold deposits was commonly related to subduction of Paleo-Pacific Plate (Deng et al., 2015).

Conclusion

1) Based on the results of the high-precision gravity and CSAMT profiles, smooth-out waveform geophysical anomaly regarded as ore-bearing zone was identified.
2) The smooth-out waveform fault is essential to the effective deposition of auriferous magma.
3) The mineralization of Jiaodong type gold deposits was commonly related to subduction of Paleo-Pacific Plate.

Data availability statement

The original contributions presented in the study are included in the article/Supplementary Material, further inquiries can be directed to the corresponding authors.

Author contributions

Z-HX designed the surveys and carried them out. G-WG performed the geophysical data processing. Z-JD and G-WG performed the geophysical data processing. J-YJ, LW, and X-GN prepared the manuscript with contributions from all co-authors. Z-JD prepared the manuscript with contributions from all co-authors.

Funding

This research benefited from the support of Fundamental Research Funds for the Central Universities (ZY2299211143), Shandong Provincial Engineering Laboratory of Application and Development of Big Data for Deep Gold Exploration Funds (SDK202221), and Science and Technology Research Project in Higher Learning Institutions of Hebei Province (ZC2022106), and Engineering Research Center of Geothermal Resources Development Technology and Engineering (22006).

Acknowledgments

We thank Frontiers in Earth Science Topic Editors for their critical reviews of an earlier version of this paper, which helped us to improve the quality. We thank Jilin University Fengyue Sun, LW and Jilin Exploration Geophysics Institute Chief Engineer Fuwen Li for their helpful suggestions during manuscript preparation, This research has been funded by the Engineering Research Center of Geothermal Resources DevelopmentTechnology and Engineering, Ministry of Education, Jilin University.

Conflict of interest

Author X-GN was employed by Inner Mongolia Non-ferrous Geological Mining Industry.

The remaining authors declare that the research was conducted in the absence of any commercial or financial relationships that could be construed as a potential conflict of interest.

Publisher's note

All claims expressed in this article are solely those of the authors and do not necessarily represent those of their affiliated organizations, or those of the publisher, the editors and the reviewers. Any product that may be evaluated in this article, or claim that may be made by its manufacturer, is not guaranteed or endorsed by the publisher.

References

Cai, Y. C., Fan, H. R., Santosh, M., Hu, F. F., Yang, K. F., and Li, X. H. (2018). Decratonic gold mineralization: Evidence from the Shangzhuang gold deposit, eastern North China Craton. *Gondwana Res.* 54, 1–22. doi:10.1016/j.gr.2017.09.009

Cox, S. F. (2010). The application of failure mode diagrams for exploring the roles of fluid pressure and stress states in controlling styles of fracture-controlled permeability enhancement in faults and shear zones. *Geofluids* 10, 217–233. doi:10.1111/j.1468-8123.2010.00281.x

Deng, J., Wang, C. M., Bagas, L., Carranza, E. J. M., and Lu, Y. (2015). Cretaceous–cenozoic tectonic history of the Jiaojia fault and gold mineralization in the Jiaodong Peninsula, China: Constraints from zircon U–Pb, illite K–Ar, and apatite fission track thermochronometry. *Min. Depos.* 50, 987–1006. doi:10.1007/s00126-015-0584-1

Deng, J., Yang, L. Q., Groves, D. I., Zhang, L., Qiu, K. F., and Wang, Q. F. (2020). An integrated mineral system model for the gold deposits of the giant Jiaodong province, eastern China. *Earth-Science Rev.* 208 (2), 103274. doi:10.1016/j.earscirev.2020.103274

Deng, J., Yang, L. Q., Li, R. H., Groves, D. I., Santosh, M., Wang, Z. L., et al. (2019). Regional structural control on the distribution of world class gold deposits: An overview from the giant Jiaodong gold province, China. *Geol. J.* 54, 378–391. doi:10.1002/gj.3186

Fan, Z. G., Huang, X. Z., Tan, L., Yang, X., Zhang, H., Zhou, D., et al. (2014). A study of iron deposits in the Anshan area, China based on interactive inversion technique of gravity and magnetic anomalies. *Ore Geol. Rev.* 57, 618–627. doi:10.1016/j.oregeorev.2013.09.017

Goldfarb, R., Groves, D. I., and Gardoll, S. (2001). Orogenic gold and geologic time: A global synthesis. *Ore Geol. Rev.* 18, 1–75. doi:10.1016/s0169-1368(01)00016-6

Groves, D. I., and Bierlein, F. P. (2007). Geodynamic settings of mineral deposit systems. *J. Geol. Soc. Lond.* 164, 19–30. doi:10.1144/0016-76492006-065

Groves, D. I., Santosh, M., and Zhang, L. (2020). A scale-integrated exploration model for orogenic gold deposits based on a mineral system approach. *Geosci. Front.* 11 (3), 719–738. doi:10.1016/j.gsf.2019.12.007

Groves, D. I., Vielreicher, R. M., Goldfarb, R. J., and Condie, K. C. (2005). Controls on the heterogeneous distribution of mineral deposits through time. *Geol. Soc. Lond. Spec. Publ.* 248 (1), 71–101. doi:10.1144/gsl.sp.2005.248.01.04

Guo, L. N., Goldfarb, R. J., Wang, Z. L., Li, R. H., Chen, B. H., and Li, J. L. (2017). A comparison of jiaojia-and linglong-type gold deposit ore-forming fluids: Do they differ? *Ore Geol. Rev.* 88, 511–533. doi:10.1016/j.oregeorev.2016.12.003

Han, J. L., Deng, J., Zhang, Y., Sun, J., Wang, Q., Zhang, Y., et al. (2021). Au mineralization-related magmatism in the giant Jiapigou mining district of Northeast China. *Ore Geol. Rev.* 141, 104638. doi:10.1016/j.oregeorev.2021.104638

Li, C., Li, L., Li, C. R., Santosh, M., and Shen, J. F. (2022). Geochemistry of hydrothermal zircon as a proxy to fingerprint ore fluids in late Mesozoic decratonic gold deposits. *Ore Geol. Rev.* 143, 104703. doi:10.1016/j.oregeorev.2022.104703

Li, J., W., Bi, S. J., Selby, D., Chen, L., Vasconcelos, P., Thiede, D., et al. (2012). Giant Mesozoic gold provinces related to the destruction of the North China craton. *Earth Planet. Sci. Lett.* 349-350, 26–37. doi:10.1016/j.epsl.2012.06.058

Li, X. C., Fan, H. R., Santosh, M., Hu, F. F., Yang, K. F., and Lan, T. G. (2013). Hydrothermal alteration associated with Mesozoic granite-hosted gold mineralization at the Sanshandao deposit, Jiaodong Gold Province, China. *Ore Geol. Rev.* 53, 403–421. doi:10.1016/j.oregeorev.2013.01.020

Liang, Y. Y., Deng, J., Liu, X., Wang, Q., Ma, Y., Gao, T., et al. (2019). Water contents of early cretaceous mafic dikes in the Jiaodong Peninsula, eastern north China craton: Insights into an enriched lithospheric mantle source metasomatized by paleo–Pacific plate subduction–related fluids. *J. Geol.* 127 (3), 343–362. doi:10.1086/702648

Sui, S. W., Yu, C. C., and Yao, C. L. (2004). The semi-intelligent processing and interpretation software for gravity and magnetic anomalies along the profile of rolling topography and its application. *Geophys. Geochem. Explor.* 28 (1), 65–68. doi:10.3969/j.issn.1000-8918.2004.01.017

Wang, Z. L., Yang, L. Q., Deng, J., Santosh, M., Zhang, H. F., Liu, Y., et al. (2014). Gold-hosting high Ba-Sr granitoids in the Xincheng gold deposit, Jiaodong Peninsula, East China: Petrogenesis and tectonic setting. *J. Asian Earth Sci.* 95, 274–299. doi:10.1016/j.jseaes.2014.03.001

Wei, W. S., Mu, T., and Zhang, H. H. (2001). *Geological map of Jiaodong gold Province showing the metallogenic belts, ore deposit types and distribution of the gold deposits*. Lang Fang, Hebei: Gold Geology Research Institute of China Armed Police Force.

Wu, J. J., Zeng, Q. D., Santosh, M., Fan, H., Bai, R., Li, X., et al. (2022). Deep ore-forming fluid characteristics of the Jiaodong gold province: Evidence from the Qianchen gold deposit in the Jiaojia gold belt. *Ore Geol. Rev.* 145, 104911. doi:10.1016/j.oregeorev.2022.104911

Xu, Z. H., Sun, F., Xin, W., Sun, N., Li, F., Niu, J., et al. (2019). formation and evolution of paleoproterozoic orogenic belt in southern Jilin, jiao–liao–ji belt, north China craton: Constraints from Geophysics. *Precambrian Res.* 333, 105433. doi:10.1016/j.precamres.2019.105433

Yang, J. H., Wu, F. Y., and Wilde, S. A. (2003). A review of the geodynamic setting of large-scale Late Mesozoic gold mineralization in the North China Craton: An association with lithospheric thinning. *Ore Geol. Rev.* 23, 125–152. doi:10.1016/s0169-1368(03)00033-7

Yang, L. Q., Deng, J., Wang, Z. L., Guo, L. N., Li, R. H., Groves, D. I., et al. (2016). Relationships between gold and pyrite at the xincheng gold deposit, Jiaodong Peninsula, China: Implications for gold source and deposition in a brittle epizonal environment. *Econ. Geol.* 111, 105–126. doi:10.2113/econgeo.111.1.105

Yang, L. Q., Dilek, Y., Wan, Z. L., Weinberg, R. F., and Liu, Y. (2018). Late jurassic, high Ba–Sr Linglong granites in the Jiaodong Peninsula, east China: Lower crustal melting products in the eastern north China craton. *Geol. Mag.* 155, 1040–1062. doi:10.1017/s0016756816001230

Yao, C. L., Li, Y. S., and Guan, Z. N. (1998). Improvement of real-time and visualized forward and inversion of gravity andmagnetic anomalies. *Geoscience* 12 (1), 115–122.

Yin, J. N., Lindsay, M., and Teng, S. R. (2018). Mineral prospectivity analysis for BIF iron deposits: A case study in the Anshan-Benxi area, Liaoning province, North-East China. *Ore Geol. Rev.* 120, 102746. doi:10.1016/j.oregeorev.2018.11.019

Zhang, L., Groves, D. I., Yang, L. Q., Wang, G. W., Liu, X. D., Li, D. P., et al. (2020). Relative roles of formation and preservation on gold endowment along the Sanshandao gold belt in the Jiaodong gold province, China: Importance for province- to district-scale gold exploration. *Min. Depos.* 55 (2), 325–344. doi:10.1007/s00126-019-00908-1

Zhang, Z., Wang, G., Carranza, E., Zhang, J., Tao, G., Zeng, Q., et al. (2019). Metallogenic model of the Wulong gold district, China, and associated assessment of exploration criteria based on multi-scale geoscience datasets. *Ore Geol. Rev.* 114, 103138. doi:10.1016/j.oregeorev.2019.103138

Zhu, R., and Sun, W. (2021). The big mantle wedge and decratonic gold deposits. *Sci. China Earth Sci.* 64 (9), 1451–1462. doi:10.1007/s11430-020-9733-1

Zhu, R. X., Chen, L., Wu, F. Y., and Liu, J. (2011). Timing, scale and mechanism of the destruction of the North China Craton. *Sci. China Earth Sci.* 547, 789–797. doi:10.1007/s11430-011-4203-4

Zhu, R. X., Fan, H. R., Li, J. W., Meng, Q., Li, S., and Zeng, Q. (2015). Decratonic gold deposits. *Sci. China Earth Sci.* 58, 1523–1537. doi:10.1007/s11430-015-5139-x

frontiers | Frontiers in Earth Science

TYPE Original Research
PUBLISHED 27 September 2022
DOI 10.3389/feart.2022.1008133

Check for updates

OPEN ACCESS

EDITED BY
Fan Yang,
Lanzhou University, China

REVIEWED BY
Qingjie Gong,
China University of Geosciences, China
Fuchuan Chen,
Kunming University of Science and Technology, China
Cun Zhang,
Qilu University of Technology, China

*CORRESPONDENCE
Xueqiu Wang,
wxueqiu@mail.cgs.gov.cn
Yinsheng Meng,
mengyinsheng@mail.cgs.gov.cn

†These authors have contributed equally to this work and share first authorship

SPECIALTY SECTION
This article was submitted to Geochemistry, a section of the journal Frontiers in Earth Science

RECEIVED 31 July 2022
ACCEPTED 12 September 2022
PUBLISHED 27 September 2022

CITATION
Li R, Wang X, Zhang B, Liu Q, Chi Q, Meng Y and Xiong Y (2022), Identifying the source of gold geochemical anomalies in Jiaodong, eastern China: Tracking the occurrence of gold nanoparticles in a metallogenic system. *Front. Earth Sci.* 10:1008133. doi: 10.3389/feart.2022.1008133

COPYRIGHT
© 2022 Li, Wang, Zhang, Liu, Chi, Meng and Xiong. This is an open-access article distributed under the terms of the Creative Commons Attribution License (CC BY). The use, distribution or reproduction in other forums is permitted, provided the original author(s) and the copyright owner(s) are credited and that the original publication in this journal is cited, in accordance with accepted academic practice. No use, distribution or reproduction is permitted which does not comply with these terms.

Identifying the source of gold geochemical anomalies in Jiaodong, eastern China: Tracking the occurrence of gold nanoparticles in a metallogenic system

Ruihong Li[1,2], Xueqiu Wang[1]*, Bimin Zhang[1], Qingqing Liu[1], Qinghua Chi[1], Yinsheng Meng[1*†] and Yuxin Xiong[3]

[1]Key Laboratory of Geochemical Exploration, Institute of Geophysical and Geochemical Exploration, Chinese Academy of Geological Sciences, Langfang, China, [2]Langfang Natural Resources Comprehensive Survey Center, China Geological Survey, Langfang, China, [3]Shandong Institute of Geological Sciences, Jinan, China

The gold particles induced geochemical anomaly shows good potential for the prospecting of gold deposits all around world. Most of the discovered gold resources are located at geochemical related anomaly area in Jiaodong, which are associated with Micro-to nanoscale particle matter. However, it has been known little about the relationship between the occurrence of gold nanoparticles and their geochemical anomaly in multimedia accommodating to the detailed process of gold mineralization system and geochemical exploration. Micro-to nanoscale gold as nanoparticles are related to the hydrothermal fluid flows and precipitation among elemental migration. This paper presents gold nanoparticles in ore, constructed the fundamental link to geochemical anomaly distribution maps of gold in drainage sediments, wall rocks, and ore, aimed to identify the source of primary and secondary geochemical anomalies according to careful observation at nanoscale gold and revealed the genesis of gold mineralization and their potential in Jiaodong. A potential model of migration pathway of gold nanoparticle was built to understand the process of massive gold accumulation and the further prospecting in the Jiaodong Peninsula.

KEYWORDS

geochemical anomalies, gold nanoparticles, multimedia, gold deposit, Jiaodong

Introduction

Nanoparticles in the ore-forming fluids control the gold mineralization of fault zones and form enormous portions of the geochemical anomalies (Cohen et al., 2010; Hough et al., 2011; Wang et al., 2020; Hastie et al., 2021), ranging from regional reconnaissance to *in-situ* mineral mapping. Thus, geochemical anomalies are considered to be major

contributors to gold exploration. Regional mineralization of hydrothermal deposits involves the formation of large-scale geochemical anomalies (Wang et al., 2007), which can be divided into primary geochemical anomalies and secondary geochemical anomalies according to their genesis. Recognizing primary geochemical anomalies, so-called hydrothermal alteration primary halos (Mackenzie et al., 2007; Qiu et al., 2021), could increase targeted mineralized zones and the potential volume associated with regional fault zones. Primary halos of hydrothermal mineralization are produced during the geochemical process of mineralization (Carranza and Sadeghi, 2012), which is strictly controlled by structural deformation, fluid flow, and fluid-rock interactions (Li et al., 2016). Accordingly, large-scale hydrothermal alteration halos depend on the development and maintenance of an efficient porosity-permeability system during fluid-rock interactions, emphasizing the importance of the mineral-assemblage replacement reactions during ore formation accompanied by elemental gains and losses (Jonas et al., 2014). Primary halos are the usual indicators of shallow ore bodies, which can be used to detect deep ore bodies, especially for products from the same hydrothermal mineralization system (de Palomera et al., 2012). Field evidence based on numerous experimental observations have indicated that more than 80% of the discovered gold resources are in geochemical anomalies in the Jiaodong Peninsula (Li et al., 2019a), emphasizing the importance of tracking the sources and influencing factors of geochemical anomalies for gold exploration.

Geochemical anomalies pattern are dominantly associated with mineral particles assemblage and structural control of orebodies, which are obscured by overburden ranging in thickness from decameters to hectometers in the Jiaodong Peninsula. Low-density, regional-scale geochemical prospecting has shown that the anomalies have obviously led to vast elementary migration, including geochemical blocks and geochemical provinces (Wang et al., 2007; Wang et al., 2015). However, it has been difficult to establish the relationships between regional geochemical anomalies and potential mineral deposits using traditional analytical methods and data processing. Thus, method for enhancing and detecting the composition of geochemical anomalies haves been debated over the years (Wang et al., 2021). In terms of concealed ore deposits, the development of analytical methods has led to the selective geochemical extractions (Zhang et al., 2019; Lu et al., 2022), and the implementation of large-scale geochemical surveys that in terms of concealed ore deposits have been conducted all around the world, such as Betze-Post-Screamer, Svetlinskoe, Tykotlov, Vaigul (Palenik et al., 2004; Osovetsky, 2016). The Mobile Metal ions (MMI) in Australia (Mann et al., 1998) and leaching of mobile forms of metals in overburden (MOMEO) in China (Wang, 1998). The gold nanoparticles of ore rock have been reported in the Xincheng gold deposit in the Jiaodong Peninsula (Yang et al., 2016). Meanwhile, the detailed relationship between regional geochemical anomalies and metal nanoparticles of host rocks, especially Precambrian metamorphic rock, and Mesozoic magmatic rock in the Jiaodong Peninsula gold deposits, have rarely been described. Therefore, careful examination of the relationships between the metal nanoparticles and geochemical anomalies (Wang et al., 2017), it has become a promising method to reveal the nature of orebodies.

In this paper, we present the gold distribution characteristic of drainage sediment, geological rock, and gold-bearing pyrite by comparing the occurrence of gold nanoparticles in multimedia and their genetic relationships, which could be helpful for the further deep mining exploration.

Regional geological background

The Jiaodong Peninsula is currently recognized as one of the largest gold provinces in the far-field of Pacific plate subduction zone (Li et al., 2015; Deng and Wang, 2016; Groves and Santosh, 2016; Deng et al., 2020a; Yang et al., 2020), where the majority of gold resources were formed at 120 Ma among Mesozoic granitoids (Deng et al., 2020b), which are prominently controlled by regional-scale NE-to NNE-trending fault zones (Figure 1). These gold deposits have been traditionally classified as disseminated-/stockwork-type (Jiaojia-type) and auriferous quartz-vein-type (Linglong-type) deposits, which are both enveloped with significant alteration halos from centimeters to decameters in width (Li et al., 2015). Chinese geologists have classified all these gold deposits are assigned to a special deposit type, namely, the “Jiaodong type” (Yang et al., 2014a; Goldfarb and Santosh, 2014; Deng et al., 2015; Groves et al., 2020; Qiu et al., 2020; Goldfarb et al., 2021).

Within these highly gold-mineralized terrane, the Precambrian metamorphic basement is dominated by Neoarchean to Neoproterozoic gneiss (Jahn et al., 2008), which occupys approximately half of the area. Neoarchean Jiaodong group metamorphic rocks and mafic granulites underwent regional deformation, with intrusion by Proterozoic mafic - ultramafic rocks and A-type granites (Wan et al., 2012). The Neoarchean Jiaodong group is mainly composed of biotite plagiogneiss, biotite granulite, amphibolite, and biotite-hornblende-plagioclase gneiss, etc. The subsequent Neoproterozoic Fenzishan group, Jinshan group, and Penglai group consist of a sequence of calc-silicate rocks, garnet-biotite schist, dolomitic marble, biotite-amphibole schist, and minor amphibolite.

The Paleozoic strata is absent from the region. Meanwhile, the Mesozoic Laiyang group, Qingshan group, and Wangshi group are mainly distributed in the Jiaolai basin (Figure 1). The Early Cretaceous Laiyang group consists of conglomerate, siltstone, gritstone and litharenite, which are unconformity contact relationships with the Neo-proterozoic Jinshan group

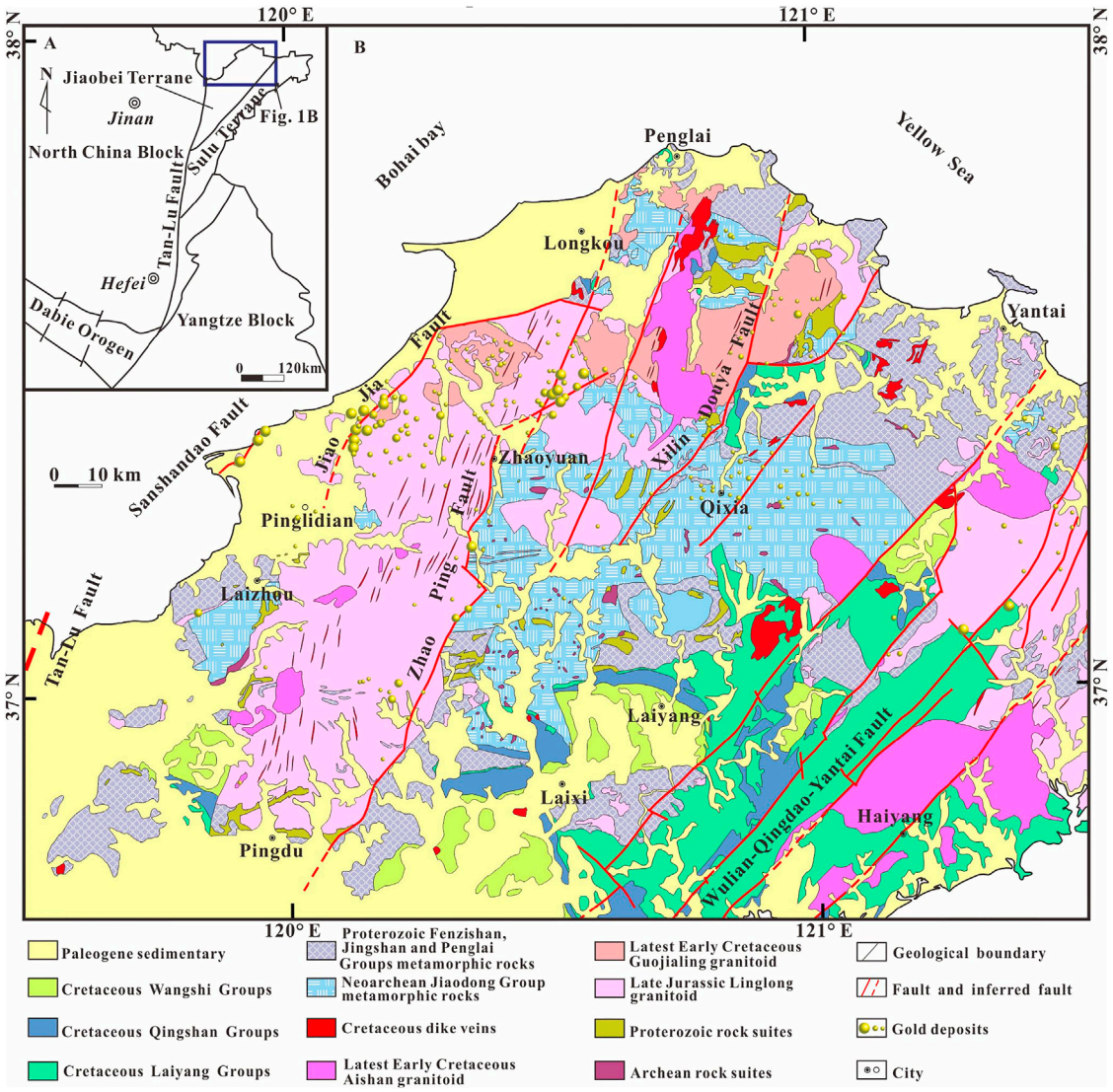


FIGURE 1
Sketch map of the Jiaodong Peninsula **(A)** and a regional geological map of the Jiaodong gold province showing the gold deposit locations **(B)** (modified from Yang et al., 2019; Li et al., 2020; Song et al., 2020).

(Yang et al., 2014a). The Qingshan group is a suite of volcanic rocks, consisting of rhyolite, tuff, basaltic andesite, dacite, etc (Zhang et al., 2008). The Wangshi group is dominated by glutenite with marlstone. The Cenozoic sediments are widely distributed, including sandy clay, silty clay, clay, sand and gravel.

There were three periods of large-scale Mesozoic magmatic activities from the late Jurassic to middle early Cretaceous (Yang et al., 2020), and these intrusions have been associated with gold mineralization in close spatial and temporal relationships (Figures 2, 3), which are widely exposed in the Jiaodong Pensinsula (Santosh and Pirajno, 2015; Deng et al., 2018; Song et al., 2020). The Late Jurassic Linglong granitoids mainly consist of biotite granite, monzogranite, quartz-diorite, and granodiorite. The Early Cretaceous Guojialing granitoids consist of porphyritic quartz monzonite, granodiorite, and monzogranite potassic feldspar. The Aishan granitoids mainly consist of monzonite and a small amount of granodiorite.

Geochemical anomalies of gold

The characteristics of geochemical anomalies reveal the complex geological processes during the Earth's evolution (Cohen et al., 2010). The spatial distribution of Au throughout the study area is shown on the contoured

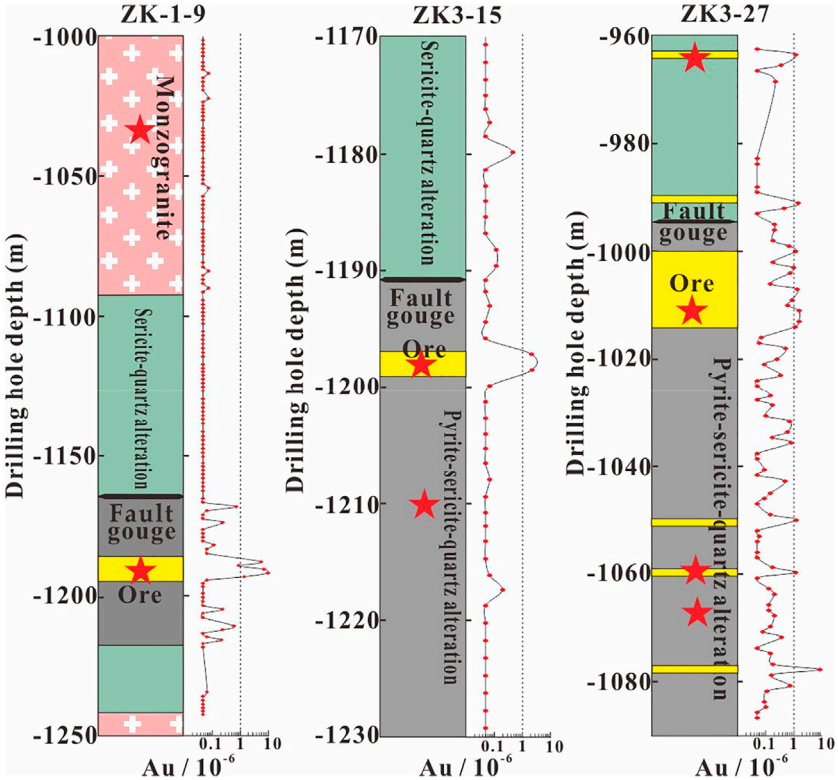


FIGURE 2
Comparison of Au distribution from three typical drilling hole (zk-1-9, zk3-15, and zk3-27) in Jiaodong area (Data from Shandong gold company).

geochemical maps. It can be observed that there are four different geochemical anomaly areas based on the statistical summaries for Au concentrations of China's Geochemical Baselines (CGB, sampling rock), the 1: 200,000 regional geochemistry national reconnaissance (RGNR, sampling stream sediments), and leaching of mobile forms of metals in overburden (MOMEO, sampling soil), which in general, have identified many gold deposits in the Jiaodong Peninsula (Li et al., 2019a; Wang et al., 2020). Most of the discovered gold resources have been in geochemical anomaly areas the Jiaodong Peninsula, which are dominantly controlled by the NE-to NNE-striking structures in greenfield. Chi and Yan (2007) calculated the median value (1.32 ppb) and the arithmetic mean value (2.03 ppb) of gold in the national drainage sediments based on 44,422 geochemical data of RGNR in China. It is quite clear that the median and arithmetic mean values of the Jiaodong gold province are higher than those of national drainage sediments (Table 1).

The most noticeable Au distribution pattern shown on the maps of MOMEO and CGB samples are closely associated with the density of regional faults to some degree (Figures 4, 5). The trend of increasing Au concentrations coincides with the primary halos within the hydrothermal alteration zones in this regional gold metallogenic system. Thus, Au anomalous centers are exactly correlated with gold mineralization and the regional fault zones in the Jiaodong gold province (Figure 5).

These distribution patterns are also related to geological bodies, including the Precambrian metamorphic basement, Late Jurassic Linglong granitoid, Latest Early Cretaceous Guojialing, and Aishan granitoid and Mesozoic strata, especially in the Archean Jiaodong Group metamorphic rocks (Yang et al., 2014b). However, the gold content of these CGB rocks is not strictly consistent with the geochemical anomaly patterns. Meanwhile, Low Au concentrations of drainage sediments are distributed in the Jiaolai basin, where the majority of geologic rocks belong to the comprised of Laiyang group (0.22–0.38 ppb) and the Qingshan group (0.13–0.88 ppb) containing comparatively low contents of Au. The Mesozoic intrusions especially for Late Jurassic Linglong granitoids (0.16–3.97 ppb) occur as the derived source of gold in the hydrothermal alteration zones in gold deposits, which are controlled by the lithospheric faults and regional EW-trending structure of metamorphic basement. The Jiaodong group has also been considered to be the original source of the Jiaodong gold

TABLE 1 Statistical parameters of gold content of multimedium in Jiaodong.

Sample type	Sample quantities	AM	SD	Min	Median	Max	CV
RGNR (ppb)	164	6.64	16.10	0.65	3.10	167	0.61
CGB Rock (ppb)	110	0.83	1.13	0.13	0.47	8.89	0.71
CGB soil (top) (ppb)	16	7.17	16.90	1.18	10.30	70.20	-
CGB soil (deep) (ppb)	16	4.23	7.78	0.58	5.63	33.20	-
Pyrite (ppm)	54	70	511	0.01	0.11	3,760	1.14
Ore rock (ppm)	10	0.83	1.40	0.03	1.08	418	-

AM, arithmetic mean; SD, standard deviation; CV, coefficient of variation.

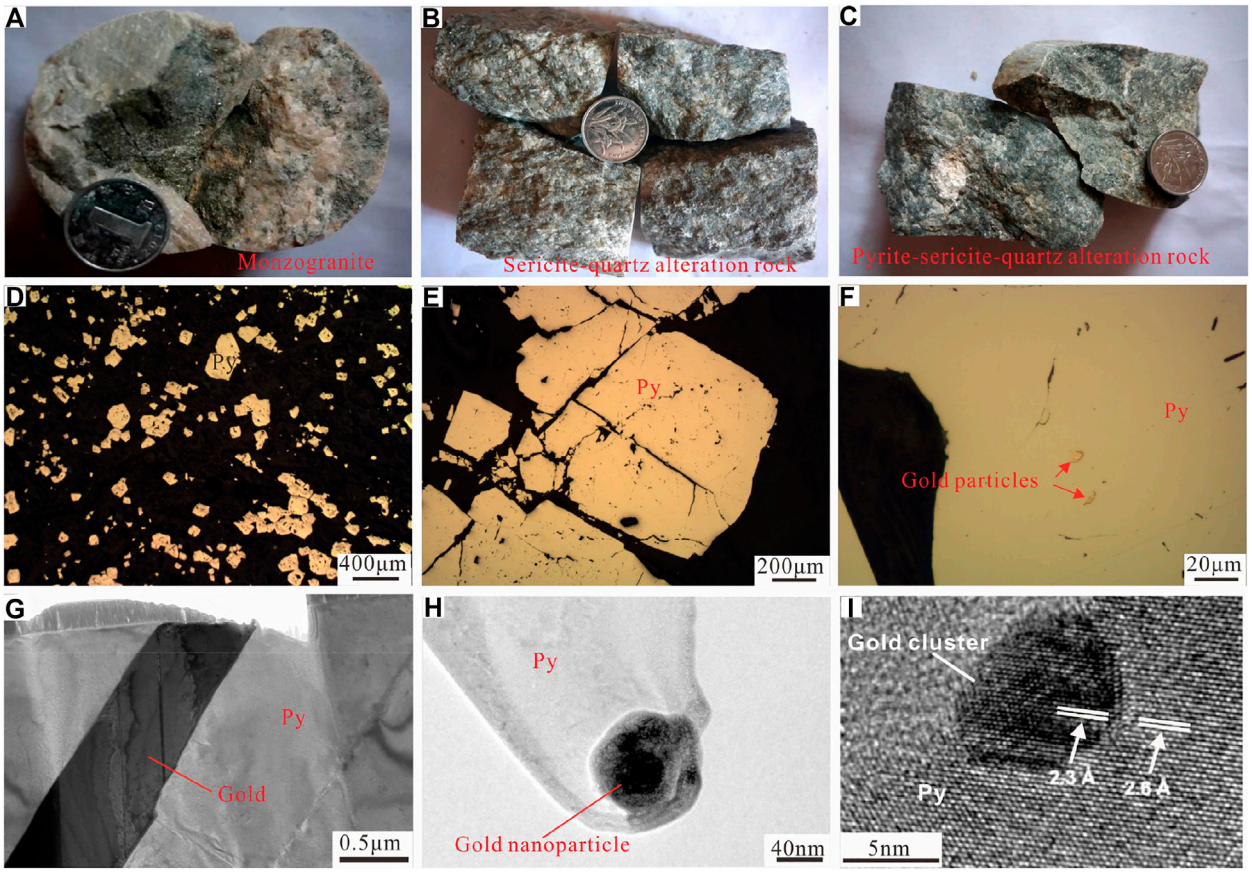


FIGURE 3
The handspecies of typical ore **(A–C)**; Gold bearing pyrite **(D–G)**; Nanogold particulate **(H)** (Yang et al., 2016) and gold cluster **(I)** (Palenik et al., 2004).

deposit, which played an important role in the reconcentration of the Jiaodong Peninsula (Yang et al., 2016).

Sampling and methods

Eight ore samples were collected from three drilling holes in the study area (Figure 2), including two samples from ZK-1-9 (−596 m ~ −1,193 m level), two samples from ZK3-15 (−639 ~ −1,212 m level) and four samples from ZK3-27 (−964 ~ −1,071 m level). An optical microscope and scanning electron microscope were used to count the number of gold particles in gold-bearing pyrite (Figure 3). The transmission electron microscopy was conducted at the Institute of Geology and Geophysics, Chinese Academy of Sciences (IGGCAS), for counting gold nanoparticles in multimedia.

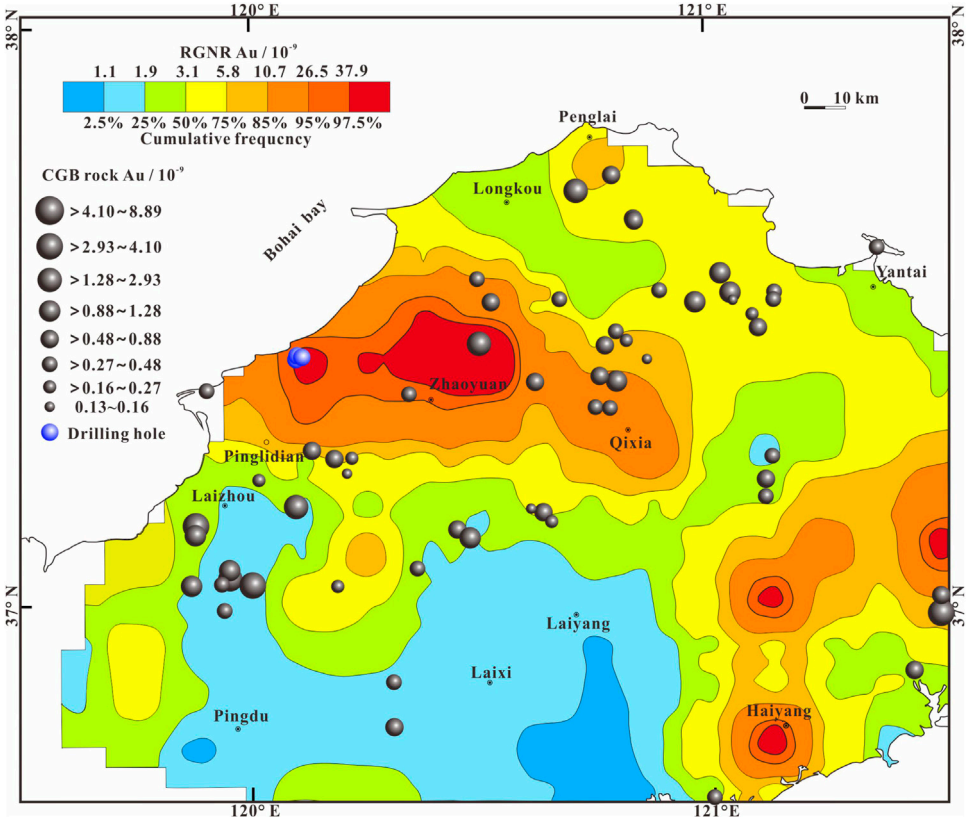


FIGURE 4
Geochemical map of gold of RGNR and CGB rock in Jiaodong gold province.

The regional geochemical data of gold in rocks were collected and provided by the China Geochemical Baselines (CGB) project. The sampling methods of the CGB project are described in detail in Wang et al. (2013, 2015), and 110 samples of CGB rock were analyzed using the MapGIS 6.7 and Geochemical Studio 3.0 software (Figure 4).

Results

The gold enrichment can be divided into two types, one is the gold complex enrichment in ore rock (30%–90%) during the process of ore-forming fluid migration and the other is ultra-scale enrichment of nanogold or ultrafine particle accumulation in soil (56%–85%), sediments (79%–90%) and wall rock (27%–86%) (Table 2; Figure 3) (Wang et al., 2013). The geochemical mapping of gold shows that it has been distributed in a 164.3 km^2 geochemical anomaly area that, controls over 60% of the gold deposit in the Jiaodong Peninsula. The arithmetic mean values of RGNR, CGB rock, and soil (top and deep) are 6.64, 0.83, 7.17, and 4.23 ppb, (Table 1; Figure 4), respectively. As compared with the Clark value of Au (1.0 ppb), the geochemical anomalies of RGNR and CGB topsoil are similar; their enrichment coefficients are both close to 7. These areas are the main secondary concentration center, and the primary gold mineralization center of the Jiaodong Peninsula. There is no clear geochemical relationship between RGNR and CGB rocks. During gold mineralization of the Jiaodong gold deposit, visible gold clusters experienced an enrichment process from nano/micron-to macro-scale mineral concentrator, including geochemical variation from primary anomalies of gold complex in ore forming fluid to invisible gold enrichment in wall rock and surface sediments. The 3D model for nonpoint source of geochemical anomalies has been used to explain the enrichment process of macro- and nanoscale gold in the local environment by nanogold and gold nanoparticle through multimedia the Jiaodong Peninsula (Wang et al., 2020).

A comparison of the content changes of Au among regional CGB rocks, gold bearing pyrite and ore rock in the Jiaodong Peninsula shows that the geochemical anomaly patterns result from gold particles. The Au content (proportion of gold particles) in different types of media is a significant reference for tracking massive gold deposits in deep prospecting targets accumulated by regional tectonic events.

TABLE 2 Proportion of gold particle and ultrafine gold in Jiaodong gold deposit.

Sample	Type	Total of Au (ppb)	Particle (>5 μm)		Ultrafine Particle (<5 μm)		Data Source
			Au (ppb)	Proportion (%)	Au (ppb)	Proportion (%)	
zk6-s	Soil	2.6	0.4	15	2.2	85	Wang et al. (2013)
zk7-s	Soil	2.5	1.1	44	1.4	56	Wang et al. (2013)
zk8-s	Soil	2.2	0.4	18	1.8	82	Wang et al. (2013)
SD-D1	Sediments	155.8	15	10	140.8	90	Wang et al. (2013)
SD-D2	Sediments	25	5.3	21	19.7	79	Wang et al. (2013)
SD-D3	Sediments	5.2	0.9	17	4.3	83	Wang et al. (2013)
zk6-1	Wall rock	7.9	1.1	14	6.8	86	Wang et al. (2013)
zk6-2	Wall rock	20.8	3.1	17	17.7	83	Wang et al. (2013)
zk7-1	Wall rock	4.8	1.4	29	3.4	71	Wang et al. (2013)
zk8-1	Wall rock	5.2	3.8	73	1.4	27	Wang et al. (2013)
zk7-2	Ore	913	110	12	813	88	Wang et al. (2013)
zk7-3	Ore	4,200	2,470	59	1730	41	Wang et al. (2013)
zk8-2	Ore	726.7	480	66	246	34	Wang et al. (2013)
zk8-3	Ore	3,200	1,540	48	1,660	52	Wang et al. (2013)
zk-1-9	Ore	150	≤15	≤10	>135	>90	This paper
zk-1-13	Ore	336	≤33.6	≤10	>302.4	>90	This paper
zk3-11	Ore	211	≤21.1	≤10	>189.9	>90	This paper
zk3-15	Ore	2,138	≤213.8	≤10	>1924.2	>90	This paper
zk3-27	Ore	510	≤510	≤10	>459	>90	This paper
zk10-18	Ore	56.8	39.8	70	17	30	This paper

Discussion

The occurrence of gold in a metallogenic system

Systematic gold geochemical anomaly patterns of the Jiaodong Peninsula are related to substances recycled by various geological agents within the metallogenic system of the Jiaodong gold province (Carranza and Sadeghi, 2012). These patterns are induced by multimedia including gold bearing-pyrite of ore bodies, high background value of different geological rock and secondary dispersion of drainage sediments. Micro- and nanoscale particles of gold have been widely reported in several sampling media in a metallogenic system (Osovetsky, 2016; Yang et al., 2016; Wang et al., 2020). Wang et al. (2013) proved that the proportion of gold (<5 um) in the Dayingezhuang gold deposit was as high as 88% in ore, 86% in wall rock, 85% in soil, and 90% in sediments (Table 2). These occurrences of gold all play an important role in the ore-forming process and geochemical exploration.

According to three drilling holes (ZK-1-9, ZK3-15, and ZK3-27) from wall rock (monzogranite) to orebodies (pyrite-sericite-quartz alteration rock) in the deep (below 1,000 m), the Au content is as low as 0.08 ppm in the wall rock (Figure 2), which is quite close to the detection limit (0.01 ppm), and the wall rock mainly consists particles gold (<5 um) similar to the Dayingezhuang gold deposit (Table 2) (Wang et al., 2013). The ore bodies, as shown in Figure 2, prove that the Au content is high, especially in the footwall of the ore-controlling fault. However, the majority of visible gold occurs in the microfracture or healed fractures of pyrite in hydrothermal alteration rocks (pyrite-sericite-quartz alteration rock and sericite-quartz alteration rock) in the Jiaodong Peninsula (Figures 3A–E). Irregular native particle gold usually occurs as inclusions (Figure 3F), suggesting the mobilization or precipitation of gold nanoparticles within pyrite grains during the hydrothermal process in the gold metallogenic system. Additionally, pyrite is the main source of invisible gold in the multimedia (Figure 3G). The distribution of gold content in pyrite is extremely inhomogeneous. The minimum value of gold is 10 ppb in pyrite, which is close to the abnormal threshold of 10.7 ppb in drainage sediments. The gold background value (median) in pyrite is 33.9 times that of RGNR drainage sediments and 223 times that of CGB rocks (Table 1).

Micro-to nanoscale gold particle clusters in ore are not new to science (Figures 3H,I), and neither are the resultant nanoparticles in soil or sediment samples that form from the weathering of original ore bodies. With the development of nanotechnology (Hochella et al., 2019), *in-situ* testing techniques such as focused ion beam-scanning electron microscope (FIB-SEM), high resolution transmission electron microscopy (HTEM), and atom probe microscope (APT)

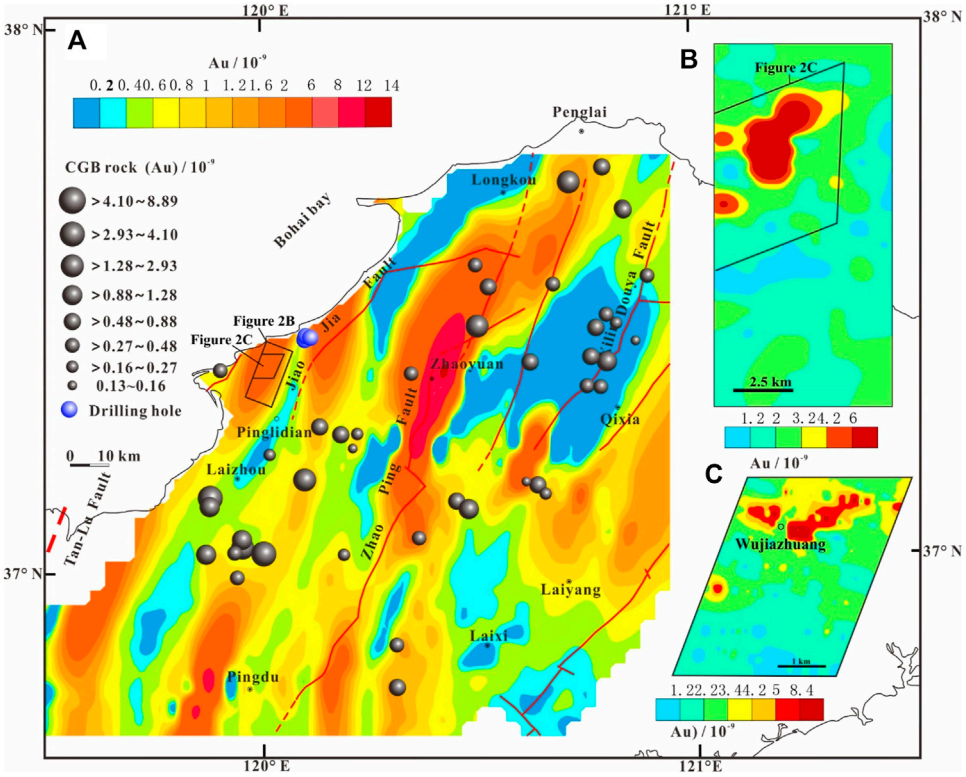


FIGURE 5
Geochemical map of gold by MOMEO and CGB in the Jiaodong gold province (modified from Wang et al., 2020).

(Fougerouse et al., 2016; Dubosq et al., 2018) have made it possible to determine the size, shape, and intrastructure of nanoparticles cluster in rocks, soils, and sediments over gold deposits (Figures 4, 5, 6A–C). The most obvious intra characteristics among nanoparticles observed in the samples of multimedia showed good uniformity with the different stages during the ore-forming process in the deposits. In addition, the elemental composition of nanoparticles is also an important indicator for different types of gold deposits.

The formation model of geochemical anomalies

The formation model of regional gold geochemical anomalies in the Jiaodong Peninsula has been built with comprehensive natural factors, superposing all the information related to large-scale gold mineralization, high value of Au content of different geological rocks, and secondary dispersion of drainage sediments (Li et al., 2019a). High background values of CGB rock are the initial source of ore-forming material source (Table 1; Figure 5).

The formation of large-scale regional Au geochemical anomalies in multimedium is a complicated process involving Au mobilization and migration from the different phases of the parent materials (Figures 6D–G). The different occurrences from micro-to nanoscale gold could be used for identifying the genesis of a geochemical anomaly (Palenik et al., 2004; Figure 6F). The gold enrichment of the Jiaodong Peninsula can be divided into two types: one type is the $Au(HS)^{2-}$ complex enrichment in the process of ore-forming fluid migration and the other type is ultrastructural deformation enrichment of nanogold and gold-bearing nanoparticles in the solid phase (Figures 3H,I; Figure 6E) (Li et al., 2019b). The gold particles or aggregations experienced an enrichment process from nano-to macroscale mineral concentrator, including chemical-structural variation from a gold complex in ore-forming fluid to micro- and ultrastructure of gold nanoparticles in pyrite and ore rock (Wang et al., 1995; Wang et al., 1999; Fougerouse et al., 2016). Triangles and hexagons of gold particles direct indicators of a natural reduction in the precipitation mechanisms. It has been proposed that the mobile phase is the transport of nanogold through the pathway within a fault (Deng et al., 2018). Gold nanoparticles have been absorbed to clay minerals in the laboratory (Wang et al., 2013), which is preferred for

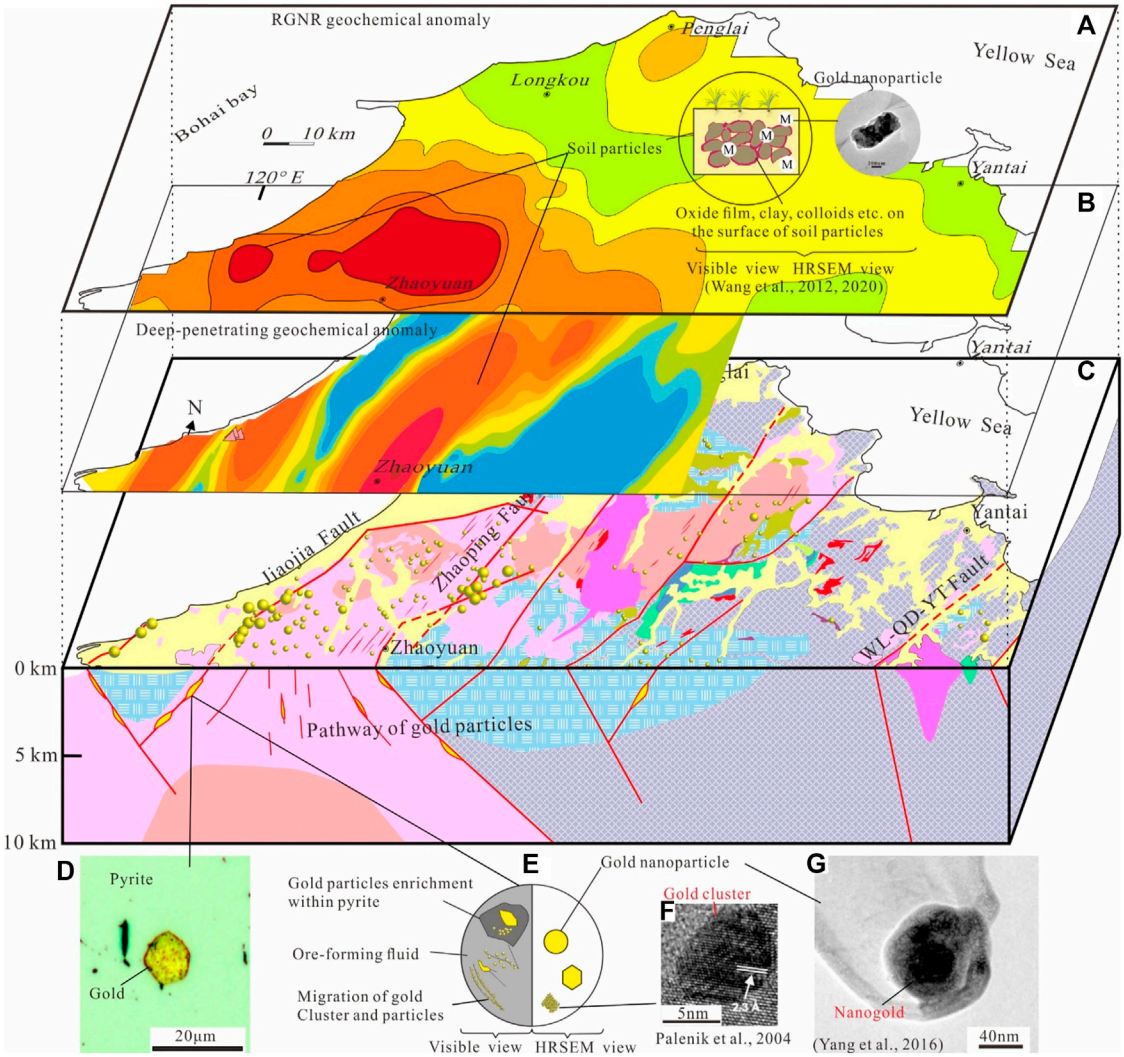


FIGURE 6
The occurrence of gold nanoparticle in the Jiaodong gold province related to the Deep-penetrating geochemical anomaly and the RGNR geochemical anomaly.

transport within the fault zones in a natural environment. The nanoscale Au–Cu alloy has also been observed for vertical transport from the concealed ore body in the depth to surface soil from the Jinwozi gold deposit in the Xinjiang provinces (Wang and Ye, 2011). Transport of gold among fault zones includes various of mechanisms in the form of a solution or mobilized as nanoparticles with subhedral to anhedral crystal shapes (Figures 5, 6D–G). The utilization of clay and bacteria instead of gold nanoparticles in the soil could also be useful for gold exploration in other areas of the world (Hough et al., 2008; Noble et al., 2009; Osovetsky, 2016).

Therefore, micro-to nanoscale particle clusters are critical for geochemical exploration in samples of multimedia sample, as mentioned above, which could effectively define a target area for potential deep mining of metal resources.

Conclusion

Ultrafine gold particles as micro-to nanoscale clusters have been increasingly reported in different types of gold deposits all around world. Ultrafine gold particles have been widely observed in ores in the Jiaodong gold deposits. More than 80% of the discovered gold resources have been discovered in the geochemical anomaly area in the Jiaodong Peninsula.

1 As an open metallogenic system in the Jiaodong Peninsula, the occurrence of micro-to nanoscale gold particles are the most important indicators for geochemical anomaly patterns among a metallogenic system. The characteristics of micro-to nanoscale gold are strongly associated with nanogeochemisty, which is related to the elemental migration as nanoparticles beyond traditional methods, using chemical hydrothermal fluid flows, and then precipitation. Thus, the gold particles also have a close relationship with the evolution of Mesozoic structural-controlled gold mineralization related to the subduction of Paleo-Pacific plate. Therefore, these could be used to interpret the geochemical anomaly of multimedia showing good potential for the prospecting of gold deposits in the Jiaodong Peninsula, Eastern China.

2 The occurrence of gold could be recognized as gene expression or a fingerprint of the detailed processes of gold mineralization and weathering. Thus, multiscale gold particles could be effectively used to interpret diverse geochemical anomaly patterns and for mineral exploration with the goal of refining and prioritizing known gold deposits and identifying new targets.

3 A potential model of migration pathway was built to construct the fundamental link between gold particles and geochemical anomalies according to careful observations at the nanoscale. The large-scale regional Au geochemical anomalies revealed the genesis of widely gold nanoparticles and their potential occurrence location of in the Jiaodong Peninsula. It is a complicated process that involves mobilizing the Au-bearing fluid, and transporting from chemical compound to nanoscale gold particle clusters in the fault zone.

Data availability statement

The raw data supporting the conclusion of this article will be made available by the authors, without undue reservation.

Author contributions

Conceptualization, XW; methodology, RL and YM; software, QL and QC; review and editing, BZ and YX.

Funding

This research was funded by the National Natural Science Foundation of China (Grant No. 42002108), the National Key R&D Program (Grant No. 2016YFC0600600), China Geological Survey Project (Grant No. ZD20220109), National Nonprofit Institute Research Grant of IGGE (Grant No. AS 2017J12).

Acknowledgments

Sincerely thanks to the help with professor Liqiang Yang from China university of geoscience (Beijing) and Deping Yang from Shandong Academy of Geosciences. Many thanks to the geochemists for their fieldwork at the RGNR and CGB program.

Conflict of interest

The authors declare that the research was conducted in the absence of any commercial or financial relationships that could be construed as a potential conflict of interest.

Publisher's note

All claims expressed in this article are solely those of the authors and do not necessarily represent those of their affiliated organizations, or those of the publisher, the editors and the reviewers. Any product that may be evaluated in this article, or claim that may be made by its manufacturer, is not guaranteed or endorsed by the publisher.

References

Carranza, E. J. M., and Sadeghi, M. (2012). Primary geochemical characteristics of mineral deposits — implications for exploration. *Ore Geol. Rev.* 45, 1–4. doi:10.1016/j.oregeorev.2012.02.002

Chi, Q. H., and Yan, M. C. (2007). *Handbook of elemental abundance for applied geochemistry.*. Beijing: Geological Publishing House, 1–148 [in Chinese].

Cohen, D. R., Kelley, D. L., Anand, R., and Coker, W. B. (2010). Major advances in exploration geochemistry, 1998–2007. *Geochem. Explor. Environ. Anal.* 10 (1), 3–16. doi:10.1144/1467-7873/09-215

de Palomera, P. A., van Ruitenbeek, F. J. A., van der Meer, F. D., and Fernández, R. (2012). Geochemical indicators of gold-rich zones in the La Josefina epithermal deposit, Deseado Massif, Argentina. *Ore Geol. Rev.* 45 (6), 61–80, doi:10.1016/j.oregeorev.2012.01.001

Deng, J., Qiu, K. F., Wang, Q. F., Goldfarb, R. J., Yang, L. Q., Zi, J. W., et al. (2020b). *In situ* dating of hydrothermal monazite and implications for the geodynamic controls on ore formation in the Jiaodong gold province, eastern China. *Econ. Geol.* 115 (3), 671–685. doi:10.5382/econgeo.4711

Deng, J., Wang, C. M., Bagas, L., Carranza, E. J. M., and Lu, Y. J. (2015). Cretaceous–cenozoic tectonic history of the jiaojia fault and gold mineralization in the Jiaodong peninsula, China: Constraints from zircon U–Pb, illite K–Ar, and apatite fission track thermochronometry. *Min. Depos.* 50 (8), 987–1006. doi:10.1007/s00126-015-0584-1

Deng, J., and Wang, Q. F. (2016). Gold mineralization in china: Metallogenic provinces, deposit types and tectonic framework. *Gondwana Res.* 36, 219–274. doi:10.1016/j.gr.2015.10.003

Deng, J., Yang, L. Q., Groves, D. I., Zhang, L., Qiu, K. F., and Wang, Q. F. (2020a). An integrated mineral system model for the gold deposits of the giant Jiaodong

province, eastern China. *Earth. Sci. Rev.* 208, 103274. doi:10.1016/j.earscirev.2020.103274

Deng, J., Yang, L. Q., Li, R. H., Groves, D. I., Santosh, M., Wang, Z. L., et al. (2018). Regional structural control on the distribution of world-class gold deposits: An overview from the Giant Jiaodong Gold Province, China. *Geol. J.* 54 (1), 378–391. doi:10.1002/gj.3186

Dubosq, R., Lawley, C. J. M., Rogowitz, A., Schneider, D. A., and Jackson, S. (2018). Pyrite deformation and connections to gold mobility: Insight from microstructural analysis and trace element mapping. *Lithos* 310–311, 86–104. doi:10.1016/j.lithos.2018.03.024

Fougerouse, D., Reddy, S. M., Saxey, D. W., Rickard, W. D. A., van Riessen, A., and Micklethwaite, S. (2016). Nanoscale gold clusters in arsenopyrite controlled by growth rate not concentration: Evidence from atom probe microscopy. *Am. Mineralogist* 101 (8), 1916–1919. doi:10.2138/am-2016-5781ccbyncnd

Goldfarb, R. J., Mao, J. W., Qiu, K. F., and Goryachev, N. (2021). The great Yanshanian metallogenic event of eastern Asia: Consequences from one hundred million years of plate margin geodynamics. *Gondwana Res.* 100, 223–250. doi:10.1016/j.gr.2021.02.020

Goldfarb, R. J., and Santosh, M. (2014). The dilemma of the Jiaodong gold deposits: Are they unique? *Geosci. Front.* 5, 139–153. doi:10.1016/j.gsf.2013.11.001

Groves, D. I., Santosh, M., Deng, J., Wang, Q. F., Yang, L. Q., and Zhang, L. (2020). A holistic model for the origin of orogenic gold deposits and its implications for exploration. *Min. Depos.* 55 (2), 275–292. doi:10.1007/s00126-019-00877-5

Groves, D. I., and Santosh, M. (2016). The giant Jiaodong gold province: The key to a unified model for orogenic gold deposits? *Geosci. Front.* 7 (3), 409–417. doi:10.1016/j.gsf.2015.08.002

Hastie, E. C. G., Schindler, M., Kontak, D. J., and Lafrance, B. (2021). Transport and coarsening of gold nanoparticles in an orogenic deposit by dissolution–reprecipitation and Ostwald ripening. *Commun. Earth Environ.* 2 (1), 57. doi:10.1038/s43247-021-00126-6

Hochella, M. F., Mogk, D. W., Ranville, J., Allen, I. C., Luther, G. W., Marr, L. C., et al. (2019). Natural, incidental, and engineered nanomaterials and their impacts on the Earth system. *Science* 363 (6434), eaau8299. doi:10.1126/science.aau8299

Hough, R. M., Noble, R., Hitchen, G. J., Hart, R., Reddy, S. M., Saunders, M., et al. (2008). Naturally occurring gold nanoparticles and nanoplates. *Geol.* 36 (7), 571–574. doi:10.1130/g24749a.1

Hough, R. M., Noble, R. R. P., and Reich, M. (2011). Natural gold nanoparticles. *Ore Geol. Rev.* 42 (1), 55–61. doi:10.1016/j.oregeorev.2011.07.003

Jahn, B. M., Liu, D. H., Wan, Y. S., Song, B., and Wu, J. J. (2008). Archean crustal evolution of the Jiaodong Peninsula, China, as revealed by zircon SHRIMP geochronology, elemental and Nd-isotope geochemistry. *Am. J. Sci.* 308 (3), 232–269. doi:10.2475/03.2008.03

Jonas, L., John, T., King, H. E., Geisler, T., and Putnis, A. (2014). The role of grain boundaries and transient porosity in rocks as fluid pathways for reaction front propagation. *Earth Planet. Sci. Lett.* 386 (1), 64–74. doi:10.1016/j.epsl.2013.10.050

Li, L., Santosh, M., and Li, S. R. (2015). The 'Jiaodong type' gold deposits: Characteristics, origin and prospecting. *Ore Geol. Rev.* 65, 589–611. doi:10.1016/j.oregeorev.2014.06.021

Li, R. H., Albert, N., Yun, M. H., Meng, Y. S., and Du, H. (2019b). Geological and geochemical characteristics of the Archean basement-hosted gold deposit in Pinglidian, Jiaodong peninsula, eastern China: Constraints on auriferous quartz-vein exploration. *Minerals* 9 (1), 62. doi:10.3390/min9010062

Li, R. H., Wang, X. Q., Chi, Q. H., Zhang, B. M., Liu, Q. Q., and Liu, H. H. (2019a). Distribution of geochemical anomaly of gold in drainage sediment in the Jiaodong Peninsula, China and its significance. *Earth Sci. Front.* 26 (4), 221–230. doi:10.13745/j.esf.sf.2019.5.15

Li, R. H., Wang, X. Q., Yang, L. Q., Zhang, B. M., Liu, Q. Q., and Liu, D. S. (2020). The characteristic of microstructural defor-mation of gold bearing pyrite in Jiaodong: The links between nanoscale gold enrichment and crystal distortion. *Ore Geol. Rev.* 122, 103495. doi:10.1016/j.oregeorev.2020.103495

Li, Y. Q., Zhang, D. H., Li, D., Wan, G. L., and Hou, B. J. (2016). Characteristics of structurally superimposed geochemical haloes at the polymetallic Xiasai silver-lead-zinc ore deposit in Sichuan Province, SW China. *J. Geochem. Explor.* 169, 100–122. doi:10.1016/j.gexplo.2016.07.007

Lu, Y. X., Zhang, B. M., Wang, X. Q., Liu, H. L., Yan, T. T., Wang, Q., et al. (2022). Application of the fine-grained soil prospecting method in a loess-covered area of central China. *Appl. Geochem.* 143, 105377. doi:10.1016/j.apgeochem.2022.105377

Mackenzie, D. J., Craw, D., and Begbie, M. (2007). Mineralogy, geochemistry, and structural controls of a disseminated gold-bearing alteration halo around the schist-hosted Bullendale orogenic gold deposit, New Zealand. *J. Geochem. Explor.* 93 (3), 160–176. doi:10.1016/j.gexplo.2007.04.001

Mann, A. W., Birrell, R. D., Mann, A. T., Humphreys, D. B., and Perdrix, J. L. (1998). Application of the mobile metal ion technique to routine geochemical exploration. *J. Geochem. Explor.* 61 (1–3), 87–102. doi:10.1016/s0375-6742(97)00037-x

Noble, R. P., Hough, R. M., and Grenik, E. M. (2009). Natural and experimental clues to understand the transport and deposition of supergene gold in Western Australia. *Explore Newsl. Assoc. Appl. Geochem.* 142, 1.

Osovetsky, B. M. (2016). Aggregation of nanogold particles in the environment. *Nat. Resour. Res.* 25 (2), 241–253. doi:10.1007/s11053-015-9277-9

Palenik, C. S., Utsunomiya, S., Reich, M., Kesler, S. E., Wang, L., and Ewing, R. C. (2004). Invisible" gold revealed: Direct imaging of gold nanoparticles in a carlin-type deposit. *Am. Mineralogist* 89 (10), 1359–1366. doi:10.2138/am-2004-1002

Qiu, K. F., Goldfarb, R. J., Deng, J., Yu, H. C., Gou, Z. Y., Ding, Z. J., et al. (2020). Gold deposits of the Jiaodong peninsula, eastern China. *Seg. Spec. Publ.* 23, 753–773, doi:10.5382/SP.23.35

Qiu, K. F., Yu, H. C., Hetherington, C., Huang, Y. Q., Yang, T., and Deng, J. (2021). Tourmaline composition and boron isotope signature as a tracer of magmatic-hydrothermal processes. *Am. Mineralogist* 106, 1033–1044. doi:10.2138/am-2021-7495

Santosh, M., and Pirajno, F. (2015). The Jiaodong-type gold deposits: Introduction. *Ore Geol. Rev.* 65, 565–567. doi:10.1016/j.oregeorev.2014.09.018

Song, M. C., Lin, S. Y., Yang, L. Q., Song, Y. X., Ding, Z. J., Li, J., et al. (2020). Metallogenic model of Jiaodong Peninsula gold deposits. *Mineral. Deposits* 39 (2), 215. doi:10.16111/j.0258-7106.2020.02.002

Wan, Y. S., Dong, C. Y., Xie, H. Q., Wang, S. J., Song, M. C., Xu, Z. Y., et al. (2012). Formation ages of early precambrian BIFs in the north China craton: SHRIMP zircon U-Pb dating. *Acta Geol. Sin.* 86 (9), 1447–1478 [in Chinese].

Wang, Q., Wang, X. Q., Liu, H. L., Tian, M., Zhang, B. Y., Li, R. H., et al. (2021). Targeting deep-seated gold deposits: A study from the qujia gold deposit, Shandong province, China. *Appl. Geochem.* 130, 104982. doi:10.1016/j.apgeochem.2021.104982

Wang, X. Q. (1998). Leaching of mobile forms of metals in overburden: Development and application. *J. Geochem. Explor.* 61 (1), 39–55. doi:10.1016/s0375-6742(97)00039-3

Wang, X. Q., Liu, X. M., Han, Z. X., Zhou, J., Xu, S. F., Zhang, Q., et al. (2015). Concentration and distribution of mercury in drainage catchment sediment and alluvial soil of China. *J. Geochem. Explor.* 154, 32–48. doi:10.1016/j.gexplo.2015.01.008

Wang, X. Q., Shen, W. J., Zhang, B. M., Nie, L. S., Chi, Q. H., and Xu, S. F. (2007). Relationship of geochemical blocks and ore districts: Examples from the eastern Tianshan metallogenic belt, Xinjiang, China. *Earth Sci. Front.* 14 (5), 116–120. doi:10.1016/s1872-5791(07)60040-2

Wang, X. Q., Xie, X. J., Cheng, Z. Z., and Liu, D. W. (1999). Delineation of regional geochemical anomalies penetrating through thick cover in concealed terrains — A case history from the olympic dam deposit, Australia. *J. Geochem. Explor.* 66 (1), 85–97. doi:10.1016/s0375-6742(99)00036-9

Wang, X. Q., Xie, X. J., and Ye, S. Y. (1995). Concepts for geochemical gold exploration based on the abundance and distribution of ultrafine gold. *J. Geochem. Explor.* 55 (1), 93–101. doi:10.1016/0375-6742(95)00026-7

Wang, X. Q., Xu, S. F., Chi, Q. H., and Liu, X. M. (2013). Gold geochemical provinces formation mechanism micro-and nanoparticles. *Acta Geol. Sin.* 87 (01), 1–8 [in Chinese].

Wang, X. Q., and Ye, R. (2011). Findings of nanoscale metal particles: Evidence for deep-penetrating geochemistry. *Acta Geosci. Sin.* 32 (01), 7–12. doi:10.3975/cagsb.2011.01.02

Wang, X. Q., Zhang, B. M., and Ye, R. (2017). Nanoparticles observed by TEM from gold, copper-nickel and silver deposits and implications for mineral exploration in covered terrains. *J. Nanosci. Nanotechnol.* 17 (9), 6014–6025. doi:10.1166/jnn.2017.14496

Wang, X. Q., Zhang, B. M., Yu, X. F., Yang, D. P., Xia, Y., Tan, Q. P., et al. (2020). Three-dimension geochemical patterns of gold deposits: Implications for the discovery of deep-seated orebodies, China. *Acta Geosci. Sin.* 41 (6), 869–885. doi:10.3975/cagsb.2020.102901

Yang, F., Santosh, M., Glorie, S., Jepson, G., Xue, F., and Kim, S. W. (2020). Mesozoic-cenozoic multiple exhumation in the Shandong peninsula, eastern north China craton: Implications for lithospheric destruction. *Lithos* 370-371, 105597. doi:10.1016/j.lithos.2020.105597

Yang, L. Q., Deng, J., Goldfarb, R. J., Zhang, J., Gao, B. F., and Wang, Z. L. (2014b). $^{40}Ar/^{39}Ar$ geochronological constraints on the formation of the dayingezhuang gold deposit: New implications for timing and duration of hydrothermal activity in the Jiaodong gold province, China. *Gondwana Res.* 25 (4), 1469–1483. doi:10.1016/j.gr.2013.07.001

Yang, L. Q., Deng, J., Song, M. C., Yu, X. F., Wang, Z. L., Li, R. H., et al. (2019). Transition of tectonic regime reactivation of basement structures detachment fault metamorphic core complex Jiaodong gold deposit. *Geotect. Metallogenia* 43 (03), 431–446. doi:10.16539/j.ddgzyckx.2019.03.005

Yang, L. Q., Deng, J., Wang, Z. L., Guo, L. N., Li, R. H., Groves, D. I., et al. (2016). Relationships between gold and pyrite at the Xincheng gold deposit, Jiaodong peninsula, China: Implications for gold source and deposition in a brittle epizonal environment. *Econ. Geol.* 111 (1), 105–126. doi:10.2113/econgeo.111.1.105

Yang, L. Q., Deng, J., Wang, Z. L., Zhang, L., Guo, L. N., Song, M. C., et al. (2014a). Mesozoic gold metallogenic system of the Jiaodong gold province, eastern China. *Acta Petrol. Sin.* 30 (09), 2447–2467 [in Chinese].

Zhang, B. M., Wang, X. Q., Han, Z. X., Liu, H. L., Liu, D. S., Lu, Y. X., et al. (2019). Evidence of metal migration over concealed gold deposit in loess terrain and its prospecting significance. *Appl. Geochem.* 145, 105422. doi:10.1016/j.apgeochem.2022.105422

Zhang, Y. Q., Li, J. L., Zhang, T., Dong, S. W., and Yuan, J. Y. (2008). Cretaceous to Paleocene tectono-sedimentary evolution of the Jiaolai basin and the contiguous areas of the Shandong peninsula (North China) and its geodynamic implications. *Acta Geol. Sin.* 82 (9), 1229–1257 [in Chinese].

frontiers | Frontiers in Earth Science

TYPE Original Research
PUBLISHED 10 November 2022
DOI 10.3389/feart.2022.1009715

Check for updates

OPEN ACCESS

EDITED BY
Liang Zhang,
China University of Geosciences, China

REVIEWED BY
Linnan Guo,
Chengdu Geological Survey Center, China
Peng Chai,
Chinese Academy of Geological Sciences (CAGS), China
Ruihong Li,
Chinese Academy of Geological Sciences (CAGS), China

*CORRESPONDENCE
Naijie Chi,
chinaijie@163.com
Zuozhen Han,
Hanzz@163.com

SPECIALTY SECTION
This article was submitted to Geochemistry, a section of the journal *Frontiers in Earth Science*

RECEIVED 02 August 2022
ACCEPTED 20 October 2022
PUBLISHED 10 November 2022

CITATION
Chi N, Han Z, Liu C, Zhang W, Zhang Y, Shan W, Li Z, Li M, Wang X and Sun Y (2022), Metallogenic mechanism of the Houge'zhuang gold deposit, Jiaodong, China: Evidence from fluid inclusion, *in situ* trace element, and sulfur isotope compositions.
Front. Earth Sci. 10:1009715.
doi: 10.3389/feart.2022.1009715

COPYRIGHT
© 2022 Chi, Han, Liu, Zhang, Zhang, Shan, Li, Li, Wang and Sun. This is an open-access article distributed under the terms of the Creative Commons Attribution License (CC BY). The use, distribution or reproduction in other forums is permitted, provided the original author(s) and the copyright owner(s) are credited and that the original publication in this journal is cited, in accordance with accepted academic practice. No use, distribution or reproduction is permitted which does not comply with these terms.

Metallogenic mechanism of the Houge'zhuang gold deposit, Jiaodong, China: Evidence from fluid inclusion, *in situ* trace element, and sulfur isotope compositions

Naijie Chi[1,2]*, Zuozhen Han[1]*, Chuan'e Liu[3], Wei Zhang[2], Yanhui Zhang[4], Wei Shan[2], Zengsheng Li[2], Min Li[2], Xiufeng Wang[2] and Yuqin Sun[2]

[1]College of Earth Science and Engineering, Shandong University of Science and Technology, Qingdao, China, [2]Key Laboratory of Gold Mineralization Processes and Resource Utilization, MNR Shandong Provincial Key Laboratory of Metallogenic Geological Process and Resource Utilization, Shandong Institute of Geological Sciences, Jinan, China, [3]Shandong Provincial Geo-mineral Engineering Exploration Institute, Jinan, China, [4]Shandong Institute of Geophysical and Geochemical Exploration, Jinan, China

The Houge'zhuang gold deposit, located in the Penglai–Qixia gold belt of the Jiaodong peninsula, is a representative auriferous quartz vein-style deposit. Pyrite is the most common and main gold-bearing mineral and shows complex textures in the Houge'zhuang gold deposit. Study of ore-related pyrite is of great significance for understanding the metallogenesis of this deposit, especially the gold precipitation mechanism. The present study applied systematic microscopic observation, fluid inclusion analysis, electron microprobes, *in situ* LA-ICP-MS trace-element analysis, and *in situ* sulfur isotope analyses. Three types of fluid inclusions were identified, among which the ore-forming fluids exhibited medium–low salinity and temperature, with the fluid inclusions mainly comprising H_2O and CO_2. Three types of pyrites were identified: 1) Py0, characterized by low concentrations of As and Au and low $\delta^{34}S$ values (5.51–6.86‰). 2) Py1, found in the gold-quartz-pyrite veins and homogeneous in chemical composition with no obvious zonal growth but with notably more gold and chalcopyrite inclusions. Py1 contained medium and uniform concentrations of As and was Au-rich, with $\delta^{34}S$ values ranging from 7.13 to 7.89‰ (mean 7.44‰). 3) Py2 contained arsenic-bearing pyrite and was found in quartz-polymetallic sulfide veins, with distinct As enrichment and As-rich rims of pyrite and growth zoning. Consequently, the primary ore-forming fluids passed through some arsenic and $\delta^{34}S$-rich sedimentary rocks, such as the Jingshan, Fenzishan, and Penglai groups. With the occurrence of stable water-rock interaction, the extracted fluids were enriched for As and $\delta^{34}S$. Furthermore, Au was closely associated with As, visible gold grains tended to occur in association with Py1 at stage II, and invisible gold was related to the Au-As-rich Py2 of stage III. The As-

bearing pyrites shared a close spatiotemporal relationship with gold, playing an important role in the formation and exploration of high-grade gold deposits.

KEYWORDS

Houge'zhuang gold deposit, ore-related pyrite, *in situ* trace element, lattice gold, *in situ* sulfur isotope

Introduction

The Jiaodong Peninsula is the largest and most productive gold province in China, with more than 5000 t of gold reserves. Although the Jiaodong area accounts for only 0.2% of the total area of the country, it holds about 25% of China's total gold reserves (Deng et al., 2006; Liu et al., 2014; Yang et al., 2016a; Fan et al., 2016; Yang et al., 2018; Chai et al., 2020a; Deng et al., 2020a; Deng et al., 2020b; Deng et al., 2020c; Zhang et al., 2020; Wang et al., 2021). In this region, pyrite is the most common and important metal sulfide mineral widely distributed within the gold orebodies and country rocks. The content of pyrite in gold ores directly affects the gold grade. Statistics of the main gold deposit types in the Jiaodong area indicate that pyrite accounts for more than 90% of the total metal minerals. More than 85% of the gold is distributed in the pyrite interstice and fissures, and within pyrite crystals (Li et al., 2007), with the remainder being invisible gold, primarily nanogold and lattice gold (Li J. et al., 2020). The nanogold is adsorbed by pyrite (Möller and Kersten, 1994; Simon et al., 1999a; Simon et al., 1999b; Li R. H. et al., 2020), while lattice Au is likely present as Au^{+} or Au^{3+} in the lattice of arsenic-bearing pyrite (Arehart et al., 1993; Chouinard et al., 2005; Reich et al., 2005; Deditius et al., 2014; Meng et al., 2022). Au is closely associated with As, such as As^{1-} + Au^{1+} sitting at the atom sites of S^{2-} + Fe^{2-} or As^{3+}+Au^{1+} replacing Fe^{2+}. The element changes in pyrite can appear in the micro-texture of pyrite. Consequently, the micro-composition and trace elements of pyrite can record the transportation and deposition of gold; thus, detailed studies on gold-bearing pyrite are crucial to elucidate the genesis and prospecting of gold deposits in this area (Barker et al., 2009; Large et al., 2009; Cook et al., 2009; Cook et al., 2013; Tanner et al., 2016; Yang et al., 2016a; Chai et al., 2019a,b,Chai et al., 2019c).

Previous studies on the gold deposits in the Jiaodong area have primarily focused on the petrology, geochronology, elemental and isotopic geochemistry, and structure, among others; however, the factors controlling the high-grade gold mineralization and the origin and relevant implication for transportation and deposition of gold remain controversial (Hou et al., 2006; Hou et al., 2007a; Goldfarb and Santosh, 2014; Yan et al., 2014; Li et al., 2015; Song et al., 2015; Zhu et al., 2015; Deng et al., 2017; Deng et al., 2018).

The Penglai–Qixia belt is an important gold belt in the Jiaodong Peninsula, which contains several medium-sized gold deposits. These deposits are notable for the local presence of native gold shoots, which are rarely seen in the other regions of the Jiaodong Peninsula. Several high-grade gold ores in many orogenic Au deposits are also present (Ma et al., 2015; Feng, et al., 2018; Feng, et al., 2020). They are commonly associated with As-rich pyrite and/or arsenopyrite. However, pyrites from the Jiaodong gold deposits generally contain negligible As, while arsenopyrite is rare, which restricts research on the relationship between Au and As in Jiaodong. However, arsenic-bearing pyrite (As up to 2.5wt%) and abundant visible gold grains have recently been reported in the Houge'zhuang gold deposit in the Penglai–Qixia belt, indicating a close spatial association with visible Au. This finding provides an opportunity to study the behaviors of Au and As during gold mineralization and to better understand the origin of high-grade ores in this deposit.

Advances in microanalytical techniques such as EMPA and LA-ICP-MS have allowed the observation of detailed elemental and isotopic information from individual pyrites with complex internal micro-textures. These details can help in unraveling the growth histories and deducing the sources, nature, and evolution of relevant ore-forming fluids.

Based on previous research, the present study systematically assessed gold-bearing pyrites from the Houge'zhuang deposit by conducting detailed field geological investigation, sampling, microscope observation, major and trace element mapping, and *in situ* trace element and sulfur isotopic analyses. These data may facilitate the better elucidation of the behaviors of As and Au during the gold mineralization process and provide a thorough understanding of the mechanism of gold mineralization and precipitation in the Houge'zhuang deposit.

Regional geology

The Jiaodong peninsula is an important gold-enriched area in China. Tectonically, this area is located in the Jiaobei uplift of the Jiaoliao uplift on the eastern margin of the North China Plate (Figure 1) (Zhai and Santosh, 2011; Yang et al., 2016a; Yang et al., 2016b; Deng and Wang, 2016). The basement rocks in the Jiaodong Peninsula include the Jiaodong Group of the Archean TTG rock series, the Jingshan and the Fenzishan Groups of lower Proterozoic metamorphic rocks, and the Penglai Group of upper Proterozoic metamorphic rocks (Wang et al., 2011). In upward sequence order, the clastic and carbonate rocks of the Penglai Group overlie the lower Proterozoic Jingshan and Fenzishan groups. The Linyi Formation of quaternary loose sediments is distributed along the seashore and riverside on the north of the study area.

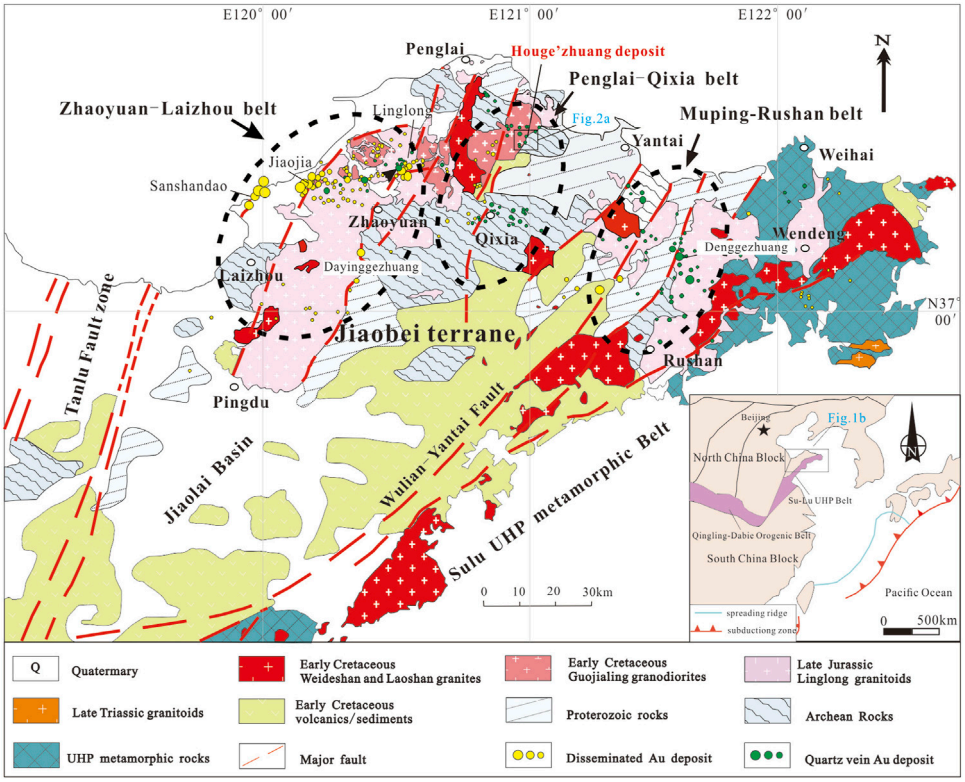


FIGURE 1
Geological map of the Jiaodong gold province showing the major gold deposits and lithological units. Modified after Wen et al. (2015).

Mesozoic granitoid, which covers more than two-thirds of the bedrock outcrops in this area, consists primarily of Linglong granite, aged 160–150 Ma(Yang et al., 2014; Deng et al., 2015a; Deng et al., 2015b; Yang et al., 2018a; Yang et al., 2018b; Yang et al., 2020), and Guojialing porphyritic granodiorite, aged 132–126 Ma, which contains most of the gold deposits in the area. Dyke rocks such as lamprophyre, diorite porphyrite, and diabase are also present in the study area.

The Jiaodong gold belt is divided into the Zhaoyuan–Laizhou, Penglai–Qixia, and Muping–Rushan belts. The Houge'zhuang deposit, the study area, is located in the Penglai–Qixia belt, which is characterized by many medium to large-sized quartz vein-style gold deposits controlled by the NE and NNE-trending Qixia, Xiaogu'jia faults (Feng et al., 2018; Feng et al., 2020).

Deposit geology

Geology of the Houge'zhuang deposit

The Houge'zhuang gold deposit is a medium-sized and representative auriferous quartz vein-style deposit controlled by the Daliu'hang fault, with a strike generally in the NNE direction (15°–30°) and dip to the SE, with steep dipping angles (60–65°) and lengths ranging from hundreds to thousands of meters but widths of only a few meters (Figure 2A).

In the gold field, the widely distributed magmatic rocks are Early Cretaceous Guojialing granodiorite, which is the main host for the Au-bearing quartz veins (Hou et al., 2004; Yan et al., 2014). The gold deposit is surrounded by basic-intermediate to felsic dikes, such as lamprophyre, diorite porphyrite, and granite porphyry, among others. The terrane is composed of the Proterozoic Jinshan Group, Early Cretaceous Qingshan Group, and Quaternary formation. Precambrian metamorphic basement and Cretaceous sedimentary are present in the southern part of this deposit.

The Houge'zhuang gold deposit is mainly composed of three gold veins, which occur mainly in the form of veinlets, reticulate veins, and agglomerates that strike generally in the NNE direction (5–20°) and dip to the NW, with steep dipping angles (60–75°), showing the characteristics of pinch-out and recurrence (Figures 2B, 3A). The gold grade varies from 0.3 to 52.4 g/t, with an average of 7.95 g/t. The ore is dominated by a massive and disseminated structure.

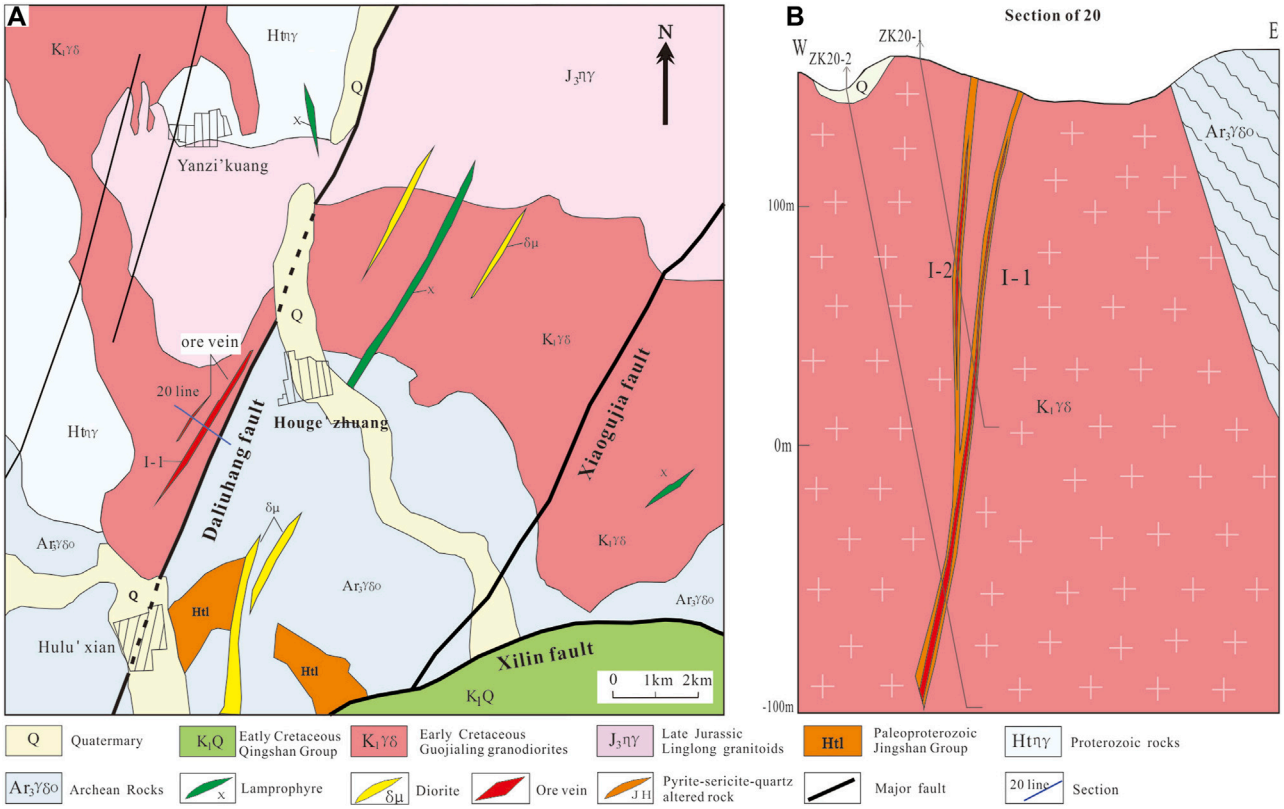


FIGURE 2
Geological map of the Houge'zhuang gold mining area **(A)** and the geological section of Line 20 **(B)**.

Mineral assemblage and paragenetic sequence

The ore minerals of the Houge'zhuang deposit include pyrite, sphalerite, galena, and other sulfides. The subordinate minerals are K-feldspar, carbonates, chlorite, kaolinite, chalcopyrite, and electrum. Tellurobismuthite occurs locally, with trace amounts of arsenopyrite, pyrrhotite, enargite, hessite, and tetrahedrite (Figure 4). Pyrite, sphalerite, galena, and other sulfides account for 10–60% of the total minerals; among them, pyrite is the most closely related to gold mineralization and is the most important gold-bearing mineral (Figure 5). The alteration halos are typically 0.2–1 m wide, are weakly developed, and include potassic alteration, silicification, sericitization, and sericite-quartz-pyrite alterations.

Based on the detailed microscopic observations and their cross-cutting relationships, four principal stages similar to the other Jiaodong gold deposits can be distinguished, namely, the pyrite-quartz (I), gold-quartz-pyrite (II), gold polymetallic sulfides (III), and quartz-carbonate (IV) stages, wherein stages II and III are the main gold mineralization stages. Stage I, which is the early stage of mineralization, mainly comprises milk-barren quartz, with minor sericite and fine pyrite as inclusions (Figure 4A). Very little or no gold mineralization occurs at this stage (Figure 3A). Stage II is defined by quartz-pyrite veins, which commonly cut stage I quartz veins (Figures 3B–D). In this stage, the predominant mineral is pyrite, with small amounts of quartz and chalcopyrite. Gold mainly occurs in the form of inclusion, interstitial, and fissure gold, which are commonly present in pyrite and quartz grains, as well as occasionally along the boundaries between pyrite grains. Stage III is characterized by gold-quartz-polymetallic sulfide veins dominated by pyrite, arsenopyrite, chalcopyrite, galena, sphalerite, and arsenic. The gold is primarily invisible gold, with the presence of nano-gold and crystal-gold. Stage IV is characterized by barren quartz–calcite veins, with almost no gold mineralization.

Sampling and analytical methods

Sampling and sample preparation

Representative samples were collected from the underground workings of the Houge'zhuang deposit. The samples were cut and

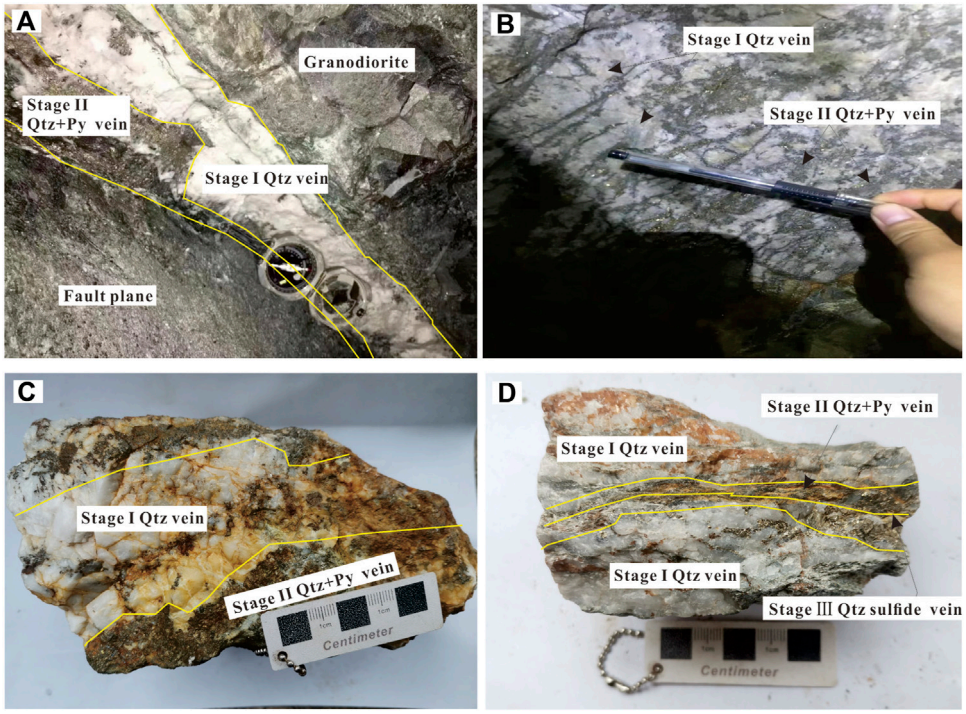


FIGURE 3
Photographs of various mineral assemblages and mineralization stages in the Houge'zhuang gold deposit.

polished to produce thin sections for microscopic observation, back-scattered electron (BSE) scanning microscopy, and *in situ* trace element and sulfur isotope analyses. The pyrite from stage IV was not analyzed in detail.

Fluid inclusion analysis

The fluid inclusion microthermometric experiments were conducted on a Linkam THMS600 heating/cooling stage mounted on a microscope at the Shandong Institute of Geological Sciences (SIGS), Jinan. Liquid nitrogen was used as a coolant and the stage was routinely calibrated at 0 and 374.1°C based on the ice-melting and homogenization temperatures of a pure water synthetic fluid inclusion with the critical density, and at −56.6°C based on the CO_2 melting temperature of a pure CO_2 fluid inclusion, respectively. The estimated uncertainties were ±0.2°C below room temperature and 5°C in the temperature range higher than 200°C, respectively (Bodnar, 1994; Shen et al., 2018; Shu et al., 2020).

The Raman spectroscopic analyses were conducted using a Renishaw inVia Raman microspectrometer at SIGS, with wavelengths of 532 nm and 785 nm. The spectra were recorded at a counting time of ~1 ectrum, with spectra ranging from 0 to 4500cm^{-1} for one accumulation. The salinity and compositions of the fluid inclusions were calculated using the HokieKlincs spreadsheet and algorithms described by Steele MacInnis et al. (2011 and 2016) for H_2O-NaCl and H_2O-CO_2-NaCl systems, respectively.

Electron microprobe analysis

Electron microprobe and element mapping analysis of gold-bearing pyrite was performed at the Jinan Mineral Resources Supervision and Inspection Center at the Ministry of Natural Resources, using a JEOL JXA8230 instrument. The instrument parameters were set with a quantitative acceleration voltage of 15 kV, a beam spot current of 2×10^{-8}A, a beam spot diameter of 0.5 μm, and a data collection time of 20~60s. The ZAF method was used to revise the data and ensure an analysis accuracy of better than 1%. The detection limits were 200 ppm (Fe), 175 ppm (Co), 196 ppm (Ni), 248 ppm (Cu), 281 ppm (Zn), 92 ppm (S), 478 ppm (Pb), 127 ppm (Ti), 235 ppm (Au), 114 ppm (Ag), 328 ppm (Bi), 354 ppm (Se), 144 ppm (Te), 140 ppm (Sb), and 233 ppm (As).

In situ trace element analysis

The *in situ* trace element analyses of gold-bearing pyrite in thin sections were conducted by LA-ICP-MS at the testing center of the Shandong Bureau of China Metallurgical geology bureau.

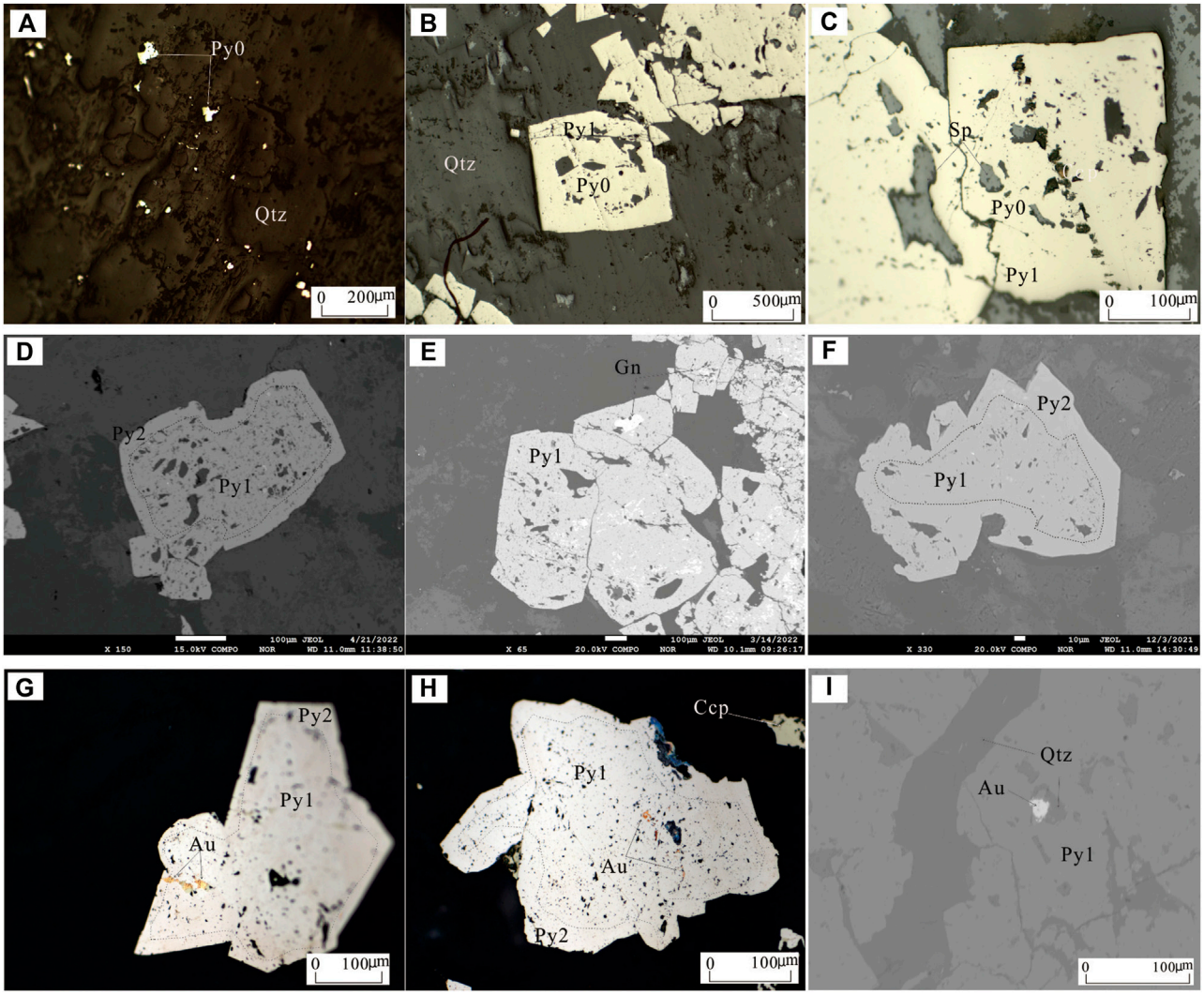


FIGURE 4
Representative reflected-photomicrographs **(A–C)** and backscattered electron (BSE) images. **(D–I)** Occurrences of visible gold and textural features of pyrite.

The GeoLasPro 193 nm ArF excimer system produced by Coherent (USA) was combined with a Thermo Fisher ICAP Q quadrupole ICP-MS for the experiments. The 193-nm ArF excimer laser, homogenized by a set of beam delivery systems, was focused on the mineral surface with a fluence of 10–12 J/cm^2. Each acquisition incorporated a 20 s background (gas blank), followed by a spot diameter of 30 um at a 5 Hz repetition rate for 60 s. Helium (750 ml/min) was applied as a carrier gas to efficiently transport aerosol out of the ablation cell and was mixed with argon *via* T-connector before entering the ICP torch.

The external calibration standards included American National Bureau of Standards and Technology synthetic standard glass, NIST610, and United States Geological Survey basaltic glasses, including GSD-1G and BCR-2G. Raw data were reduced offline by *ICPMSDataCal* software using a normalization strategy without applying an internal standard (Liu et al., 2008). Chinese Geological Standard Glasses MASS-1 were used for quality control.

In situ sulfur isotope analysis

The LA-MC-ICP-MS *in situ* sulfur isotope analysis was performed by the Jinan Mineral Resources Supervision and Inspection Center of the Ministry of Natural Resources on a Neptune Plus multi-receiver plasma mass spectrometer (Thermo Scientific) coupled with a GeoLasPro 193 nm laser ablation

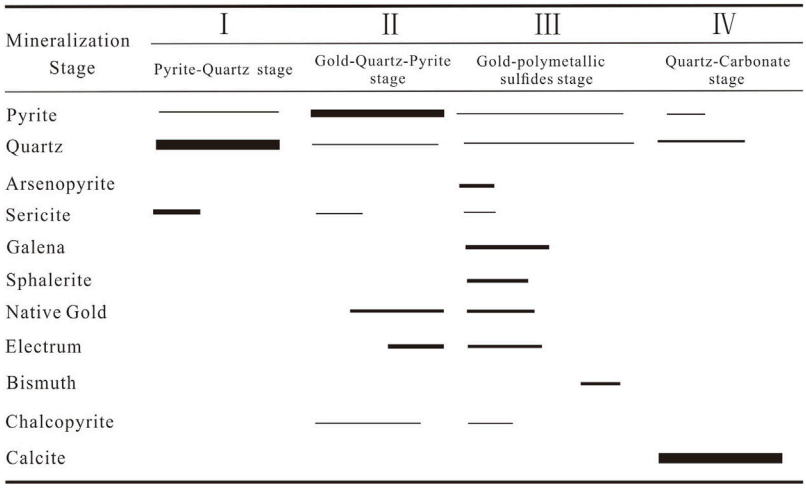


FIGURE 5
Paragenetic sequence of the Houge'zhuang gold deposit. Thick lines: high abundance. Thin lines: low abundance.

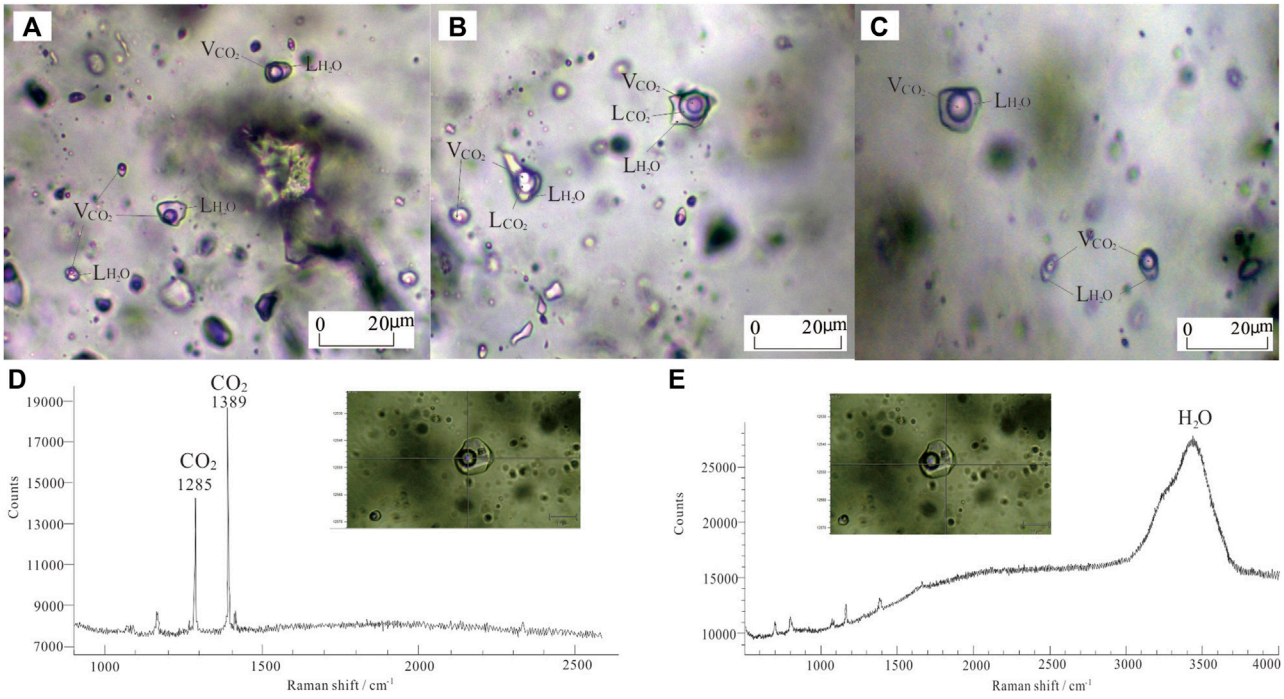


FIGURE 6
Photomicrographs **(A–C)** and laser Raman **(D,E)** spectrogram of fluid inclusions in the Houge'zhuang gold deposit.

system. The appropriate area was selected according to a scanned photo of the sample, and the laser ablation system was used to ablate the sulfide (point ablation). The diameter of the laser beam was 44 μm, with an energy density of 6J/cm^2, a frequency of 6Hz, and high-purity helium as the carrier gas. The sulfide standard samples HN, JX, and ZX were used to debug the instrument parameters. In the analytical process, sulfide similar to the sample matrix was used to replace the standard sample, and the standard-sample-standard crossover method was used for quality discrimination correction.

TABLE 1 Microthermometric measurements of fluid inclusions of different mineralization stages in the Houge'zhuang gold deposit.

Stage of mineralization	Rock type	Fl type	$TmCO_2$/°C	Ti/°C	TCl/°C	Tht/°C	Salinity (wt.%NaCl eq0	Data source
Stage I	Pyrite quartz vein	I	−56.2~−56.3	—	5.3~7.2	309.2~319.8	5.33~8.51	This article
		II	-	−1.6~−4.9	-	146.9~304.6	2.74~7.73	
		III	-	−1.4~−2.1	-	251.7~342.6	2.41~3.55	
Stage II	Gold pyrite vein	I	-	-	7.2~8.1	141.1~227.4	5.33~3.71	
		II	-	−5.7~−2.8		172.7~273.2	4.65~8.81	
		III	−56.1~−56.3	-	7.2~8.3	285.4~332.1	5.33~3.33	
Stage III	Gold-sulfide vein	I, II	-	-	-	211~252	3.58~4.51	Wang et al. (2018)

Tht/°C, homogenization temperature; Ti/°C, last melting temperature of ice; TCl/°C, last melting temperature of hydrohalite; TmCO2/°C, last melting temperature of CO_2.

Results

Fluid inclusion analysis

The fluid inclusions in the Houge'zhuang gold deposit are relatively developed and mainly distributed in transparent quartz grains with growth zoning. The present study primarily selected quartz inclusions from stages I and II of mineralization for testing. Based on the observed phases at room temperature, three types of fluid inclusions were observed from the ores: single-phase (type I), two-phase aqueous (type II) (Figures 6A,C), and CO_2-rich three-phase (type III) (Figure 6B) inclusions. Type I is the predominant type in the Houge'zhuang gold deposit, contributing approximately 40–50% of the total fluid inclusions, which is composed of the pure CO_2 (liquid or vapor) and pure H_2O (liquid or vapor) phases. Most of the type II inclusions are ellipse in shape, with those measuring <6 μm on the long axis accounting for ~20–30% of the total fluid inclusions, with vapor/liquid ratios <30–40%, predominant round and ellipse shapes, and measuring approximately 5–10 μm. The main components of the vapor and liquid in type I are CO_2 and H_2O, respectively. Type III is composed of CO_2 vapor and liquid phases and H_2O liquid phases, with round, ellipse, and irregular shapes ranging in size from 4 to 7 μm. All three types of fluid inclusions were found in stages I, II, and III of mineralization.

The microthermometric results showed that the homogenization temperatures of the fluid inclusions in stage I ranged between 146.9°C and 342.6°C, whereas those for stages II and III were 141.1–332.1°C and ~211 and 252°C, respectively (Table 1). As the CO_2–H_2O inclusions with variable phase ratios were trapped from the immiscible CO_2–H_2O fluids, the lower temperature (~ 141–211°C) was their formation temperature. The salinities in stages I, II, and III were similar, with NaCleq of ~2.74–8.51%, ~ 3.71–8.81%, and ~3.58–4.51%, respectively. These findings suggest that the ore-forming fluids were of medium-low salinity and temperatures.

Furthermore, the results of laser Raman spectroscopy showed that the fluid inclusions were mainly composed of H_2O and CO_2 (Figure 6), while the vapor phases were mainly CO_2, with less CH_4, N_2, H_2S, organic matter, etc.

Pyrite texture and chemical composition

Micro-texture and type of pyrite

The microstructure of pyrite is controlled by multiple factors including the distribution of elements and crystallization conditions (Reich et al., 2005; Large et al., 2009; Cook et al., 2009; Deditius et al., 2014; Peterson and Mavrogenes, 2014; Román et al., 2019; Hu et al., 2020). Increasing contents of trace elements such as As, Co, Ni, and Cu in pyrite can result in different bands in BSE images. Different crystallization conditions can also result in varied microstructures.

Based on microscope observation, BSE images, and element mapping, the pyrites in the Houge'zhuang gold deposit can be divided into three types, Py0, Py1, and Py2, which showed good correspondence with the mineralization stages Figures 7A–C.

Py0: This type is mainly present in pyrite-quartz veins (stage I), and is medium-fine-grained (~10–50 μm) with euhedral to subhedral shapes (Figure 4A). The symbiotic minerals are mainly quartz, with small amounts of sericite. Py0 mainly has two output forms in the gold ore, one of which occurs as single-grain disseminated in quartz veins (Figure 4A); the other form occurs as a core to form new pyrites with later-formed pyrites (Figures 7E,F). Py0 accounted for 10–20% of all pyrites in the gold ore.

Py1: This type occurs in gold-quartz-pyrite veins (stage II), and is coarse-medium-grained (~100–2000 μm) with euhedral to subhedral shapes. Py1 always occurs as aggregates or veins and is spatially associated with visible gold. This type is mainly porous

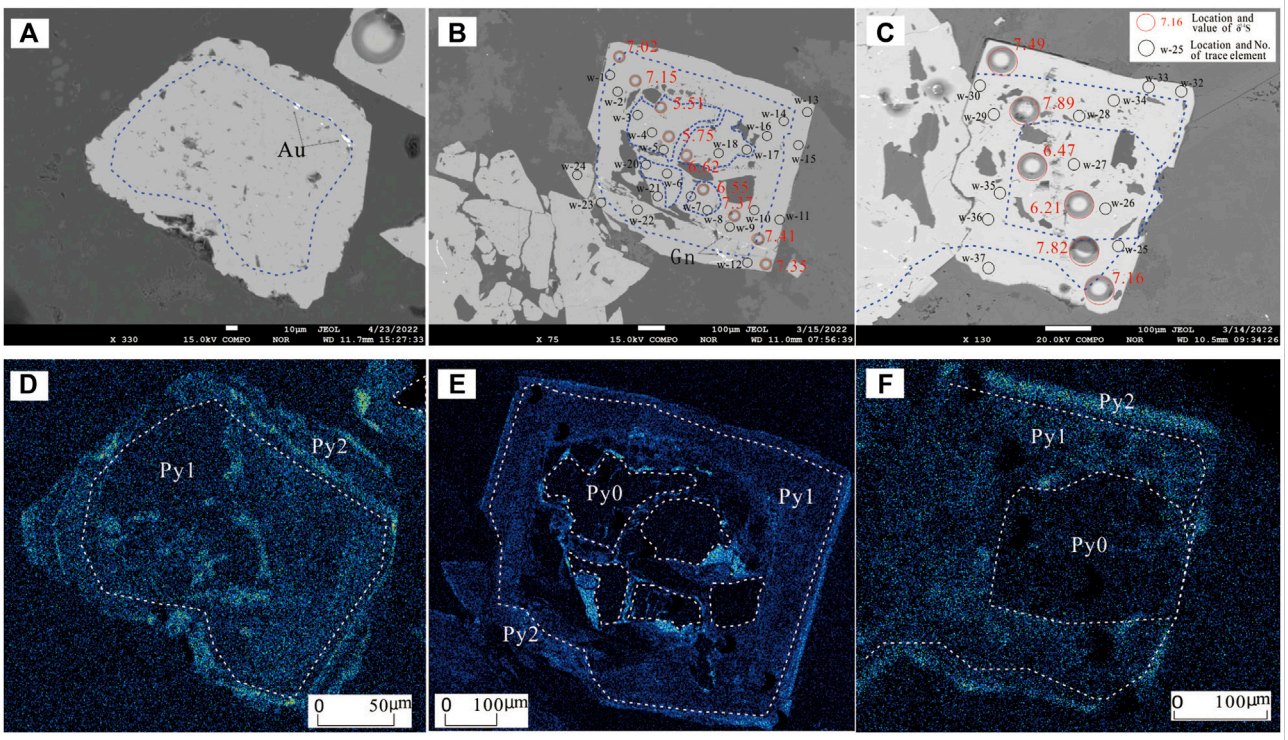


FIGURE 7
Backscattered electron (BSE) images **(A–C)** and element mapping images **(D–F)** of pyrites in the Houge'zhuang gold deposit.

and has a honeycomb structure and metasomatic-relict texture, and displays cataclastic textures due to later stress (Figures 4C–F), with micro-fractures locally filled with visible gold grains (Figures 4G–I). The symbiotic minerals are mainly quartz, chalcopyrite, and visible gold. The element mapping images showed a higher As content in Py1 than that in Py0, but less than that in arsenic-bearing pyrite (Py2) (Figures 7D–F). Py1 accounted for 70–80% of pyrites in the gold ore.

Py2: This type is arsenic-bearing and occurs in quartz-polymetallic sulfide veins (stage III) (Figures 7D,F). Py2 is produced in two forms. The first is characterized by distinctive core-rim textures, showing oscillatory or patchy zoning of arsenic. The core components of Py2 are mainly Py0 or Py1, which were formed early. The other form is independent arsenic-bearing pyrite, with fine-grained (~10–20 μm) distribution. Py2 is usually inter-grown with coarse-grained chalcopyrite, galena, sphalerite, tellurobismuthite, and magnetite, which occur adjacent to the boundary. Different from the gold in Py0 and Py1, the gold in Py2 is invisible, especially nanogold and lattice gold. Py2 accounted for 5–10% of pyrites in the gold ore.

In situ trace elements

Most of the trace elements in the pyrite crystals were classified as siderophile and sulfophile elements and are found in the periodic table between Fe and S. Some elements can readily enter the pyrite crystal lattice in the form of isomorphic substitution. For example, Co and Ni can replace Fe, while As, Se, Te, etc. can replace S in the pyrite crystal lattice. Another possibility is that trace elements such as Au, Ag, Cu, Pb, Zn, etc. occur in pyrite as mechanical mixtures (Bi et al., 2004; Zhang et al., 2014; Guo et al., 2019; Li J. et al., 2020; Chen et al., 2020c).

The results of the LA-ICP-MS trace element analysis of three different pyrite types from different mineralization stages of the Houge'zhuang gold ores are shown in Table 2. A total of 37 points were analyzed, including eight points for Py0, 19 points for Py1, and 10 points for Py2. All representative trace element contents, such as Co, Ni, Cu, Pb, Zn, As, Ag, Sb, Hg, Bi, and Se, showed regular variation in concentration in Py0, Py1, and Py2. Among them, As was the most abundant, with averages of 498 ppm in Py0, 5419 ppm in Py1, and 8113 ppm in Py2, with a gradual increase in concentration from Py0 to Py2. The change in Au concentration was similar to the change in As concentration, with averages of 1.14 ppm in Py0, 2.82 ppm in Py1, and 4.07 ppm in Py2. The calculated Co/Ni ratios were ~0.11–1.46 (average 0.54) in Py0, ~0.03–46.98 (average 7.16) in Py1, and ~0.28–8.79 (average 2.62) in Py2. In addition, all three pyrite types comprised Cu (~81.44–2414 ppm in Py0, ~0.56–726 ppm in Py1, and ~1.51–173 ppm in Py1), Zn

TABLE 2 Representative trace element concentrations (in ppm) of three pyrite types from the Houge'zhuang gold deposit analyzed by LA-ICP-MS.

Sample No.	Type	Co	Ni	Cu	Zn	As	Ag	Sb	Au	Hg	Bi	Pb	Se	Co/Ni
w-3	Py0	0.96	2.40	81.44	8.31	87.88	5.58	4.06	0.18	0.00	0.00	113.54	0.24	0.40
w-4		13.36	18.79	958.34	83.90	24.57	65.53	9.71	0.14	0.00	1.65	5791.07	0.00	0.71
w-18		3.28	15.11	664.22	21.98	14.93	22.55	1.81	0.09	0.01	0.00	26.33	0.00	0.22
w-19		18.48	29.28	2414.91	37.80	148.86	51.61	9.44	0.43	0.04	0.08	165.96	3.18	0.63
w-20		11.51	21.59	587.31	104.75	1598.79	39.33	11.51	5.66	0.26	0.22	1533.98	0.53	0.53
w-26		65.39	44.87	0.00	24.70	586.91	57.73	23.37	0.62	0.00	3.92	3914.61	3.07	1.46
w-27		95.38	351.18	2599.15	87.79	1466.84	70.31	59.08	1.78	0.05	1.11	2437.10	0.24	0.27
w-28		36.00	319.36	1730.80	36.44	36.88	64.15	9.08	0.26	0.00	0.01	192.29	0.00	0.11
w-1	Py1	465.44	200.01	1.03	0.06	5867.05	0.19	1.18	0.97	0.05	0.04	15.52	3.17	2.33
w-2		287.48	6.12	0.56	0.52	9290.97	0.08	0.21	0.18	0.06	0.02	2.49	0.00	46.98
w-5		5.47	8.73	227.26	17.70	4656.00	12.96	41.46	7.21	0.00	0.22	592.42	1.08	0.63
w-6		27.60	49.95	691.26	59.01	8066.78	30.43	34.45	8.34	0.01	0.07	2572.65	0.38	0.55
w-7		375.95	209.71	726.38	44.48	8370.30	30.96	14.62	9.09	0.01	0.28	532.86	0.00	1.79
w-8		171.75	150.78	190.21	8.03	5586.06	86.35	24.05	3.95	0.00	2.10	2938.74	0.00	1.14
w-9		1378.88	86.63	69.46	22.73	5847.85	20.19	5.25	1.98	0.00	0.82	1111.68	0.00	15.92
w-10		1524.58	164.84	2.23	12.24	7690.34	0.31	0.40	0.58	0.14	0.00	4.17	1.30	9.25
w-14		4.77	157.42	1.13	11.94	4387.27	0.57	3.21	0.30	0.16	0.05	17.66	3.42	0.03
w-16		1044.19	37.21	3.77	2.63	8674.15	1.64	6.14	3.25	0.08	0.03	42.60	2.58	28.06
w-17		52.68	55.63	16.16	2.61	5609.36	4.07	6.76	0.94	0.29	0.13	55.51	2.28	0.95
w-22		27.77	32.72	1.43	0.41	4248.24	1.14	2.10	0.56	0.24	0.05	13.56	0.00	0.85
w-24		0.00	408.17	5.48	9.63	1640.20	9.28	2.80	0.43	0.00	0.11	150.75	1.28	0.00
w-25		643.82	244.53	177.23	1.07	5847.32	2.67	6.99	3.22	0.09	0.60	311.31	0.00	2.63
w-29		193.66	176.89	731.99	83.48	2430.24	79.07	20.07	3.53	0.00	6.77	10639.46	0.00	1.09
w-30		427.09	41.94	0.54	0.76	3320.79	0.30	0.61	0.05	0.17	0.00	11.22	1.17	10.18
w-34		25.89	123.75	576.25	30.61	313.04	26.51	13.18	0.66	0.18	0.19	301.99	0.00	0.21
w-35		81.97	6.34	0.00	0.63	6499.52	3.52	8.03	8.01	0.00	0.13	181.75	0.00	12.93
w-36		12.03	27.18	2.99	5.48	4618.93	0.60	0.96	0.29	0.00	0.05	16.31	0.00	0.44
w-11	Py2	81.60	35.74	10.01	14.10	18199.02	1.09	9.09	10.82	0.23	0.12	30.25	0.00	2.28
w-12		391.23	181.09	3.41	8.96	13545.67	0.24	0.43	4.82	0.06	0.00	1.92	1.31	2.16
w-13		364.40	536.98	21.36	13.00	6688.88	0.09	0.22	5.08	0.04	0.04	1.69	0.00	0.68
w-15		491.76	370.84	0.00	10.39	3818.49	0.92	1.81	3.58	0.01	0.06	9.40	1.24	1.33
w-21		24.71	12.61	34.34	462.39	6994.45	9.17	6.03	5.25	0.00	0.18	802.69	0.00	1.96
w-23		91.93	15.10	1.51	1.45	4821.76	0.94	1.26	0.30	0.11	0.02	27.39	1.07	6.09
w-31		652.19	725.78	3.14	1.88	8823.44	0.00	0.09	5.08	0.00	0.00	3.06	0.00	0.90
w-32		315.98	1112.36	11.94	1.92	8396.25	6.41	3.42	1.97	0.14	0.28	565.26	1.51	0.28
w-33		1498.45	170.50	173.09	10.22	7473.56	11.16	11.93	3.45	0.00	0.15	311.02	0.00	8.79
w-37		173.95	98.52	21.92	4.90	2374.04	0.35	0.73	0.37	0.09	0.02	5.72	0.00	1.77

(~8.31–104.75 ppm in Py0, ~0.06–83.5 ppm in Py1, and ~1.45–462.4 ppm in Py1), Ag (~5.58–70.3 ppm in Py0, 0.08–86.4 ppm in Py1, and ~0.09–11.1 ppm in Py2), and Pb (~26.3–5791 ppm in Py0, 2.49–10639 ppm in Py1, and ~1.69–802.69 ppm in Py2).

The comparative trace element concentrations of the three pyrite types are illustrated in boxplots (Figure 8), showing the relative variations in trace elements in different types of pyrite grains. Co, Ni, and As were enriched in Py2, with an increasing trend from Py0 to Py2, similar to Au, indicating their close relationship to gold mineralization. The ore elements, such as Zn, Pb, Cu, Ag, Sb, and Bi, were enriched in Py0 and depleted in Py2 relative to Py1, with a downward concentration trend contrary to that in Au.

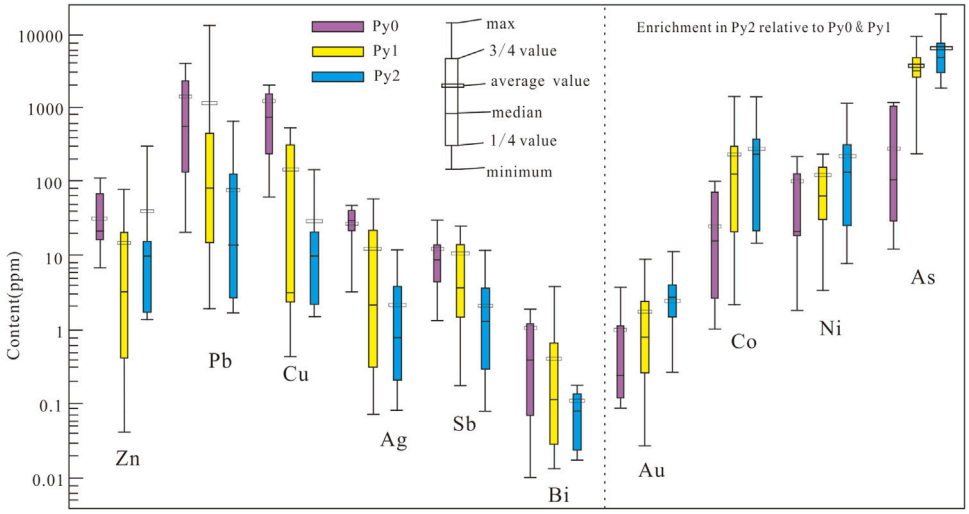


FIGURE 8
Comparative box plot of trace element concentrations in the three pyrite types.

Elemental mapping of pyrite

Electron microprobe mapping plays an important role in the study of element distributions. Element microprobe mapping analysis can intuitively reveal the combinations and spatial distributions of major, minor, and trace elements in pyrites at different stages. Thus, pyrites formed at different stages can be identified and used to study the evolution of ore-forming fluids (Chi et al., 2020).

The pyrite of stage III was selected for EMPA element mapping to reveal the distribution and correlation of the major and trace elements (Figures 7D–F). The As content in the core of the pyrite crystals was relatively low, with clear boundaries (Figures 7B,C), and was distributed irregularly in the intermediate part of the Py0 pyrite. In contrast, the As content at the edge of the pyrite crystal was significantly higher than that at the core of the pyrite and showed irregular oscillatory zoning (Py1). At the extreme edge of the pyrite, the As content increased significantly and was distributed in intermittent bands, forming arsenic-bearing pyrite (Py2). Therefore, according to the As concentration, the pyrite related to gold mineralization in the Houge'zhuang gold deposit can be divided into Py0, Py1, and Py2. Py0 with low As concentration and without obvious zoning occurred mainly in the core of pyrite crystals and was formed in stage I. Py1, with a higher As concentration than that in Py0, showed oscillating zoning and was formed in stage II. In contrast, Py2 occurred mainly at the crystal edge, with the highest As concentration, and was formed in stage III.

Gold distribution

The microscopic observations, BSE images, and EPMA mapping findings showed that the gold in the Houge'zhuang deposit was distributed in the pyrite interstice, fissures, and within pyrite crystals, while the rest was invisible gold (particularly nanogold and lattice gold).

Gold mainly occurred in stages II and III, but in different ways. Stage II showed a high amount of readily visible gold along with pyrite fissures (Figures 4G,H) distributed throughout the interstice and quartz inclusions (Figure 4I). The most common form was native gold, with bright golden yellow color, granular texture, and mainly fine particles (~5–30 μm). The other type was electrum, which had an irregular fine-grained and granular texture and a low amount of natural gold in comparison. In contrast to stage II, the gold in stage III was mainly invisible gold, such as nanogold and lattice gold, and was closely associated with arsenic-bearing pyrite (Py2) and arsenopyrite. Nanogold or fine-grained gold (~1–5 μm) was scattered in Py2. The lattice gold was most likely to be present in the lattice of the arsenic-bearing pyrite.

Sulfur isotopic compositions of pyrite

Sulfur isotopes are sensitive indicators of the source and migration process of ore-forming fluids and the genesis of ore deposits. These isotopes are often used to depict the physical and chemical conditions of petrogenesis and mineralization and the source of sulfur.

TABLE 3 Results of the *in situ* analysis of sulfur isotopes of pyrite in the Houge'zhuang gold deposit.

Sample No.	Type	$\delta^{34}S_{v\text{-}CDT}$	Average value	Sample No.	Type	$\delta^{34}S_{v\text{-}CDT}$	Average value
HGZ-1-04	Py0	6.55	6.28	HGZ-1-02	Py1	7.41	7.44
HGZ-1-05		6.62		HGZ-1-03		7.37	
HGZ-1-06		5.75		HGZ-1-08		7.15	
HGZ-1-07		5.51		HGZ-2-02		7.89	
HGZ-2-03		6.47		HGZ-2-05		7.82	
HGZ-2-04		6.21		HGZ-2-1_02		7.52	
HGZ-2-2_01		6.86		HGZ-2-1_03		7.62	
HGZ-1-01	Py2	7.35	7.45	HGZ-2-1_04		7.46	
HGZ-1-09		7.02		HGZ-2-1_05		7.38	
HGZ-2-01		7.49		HGZ-2-1_06		7.13	
HGZ-2-06		7.16		HGZ-2-1_09		7.30	
HGZ-2-1_01		7.58		HGZ-2-2_03-1		7.30	
HGZ-2-1_07		7.84		HGZ-2-2_03-2		7.33	
HGZ-2-1_08		7.46		HGZ-2-2_04		7.63	
HGZ-2-2_02		7.23		HGZ-2-2_04'		7.26	
HGZ-2-2_03		7.95					

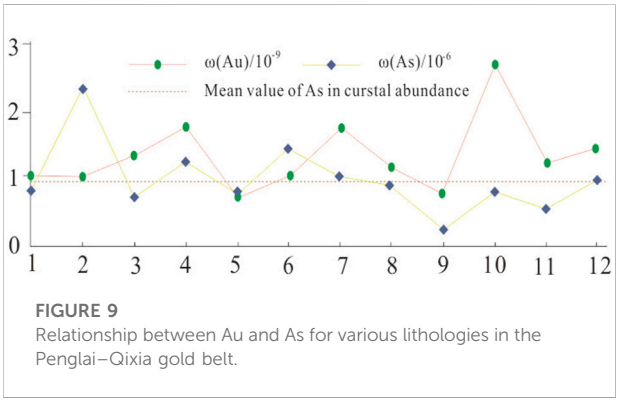


FIGURE 9
Relationship between Au and As for various lithologies in the Penglai–Qixia gold belt.

The results of *in situ* sulfur isotope analysis on the cores and different zones of gold-bearing pyrite crystals in this study are shown in Table 3. *In situ* analyses were performed on Py0 (N = 7), Py1(N = 15), and As-rich rim in Py2 (N = 9).

The $\delta^{34}S$ values of Py0 formed in stage I ranged from 5.51 to 6.86‰ (mean 6.28‰), those of Py1 formed in stage II ranged from 7.13 to 7.89‰ (mean 7.44‰), and those of Py2 formed in stage III ranged from 7.02 to 7.95‰ (mean 7.45‰), similar to that of Py1. Grain-scale variations in $\delta^{34}S$ in the pyrite grains were observed (Figures 7B,C). As shown in Figure 7B, the core (Py0) had $\delta^{34}S$ values of ~5.51–6.62‰, which increased to ~7.15–7.49‰ on the rim (Py1 and Py2). The $\delta^{34}S$ values of Py2 were slightly higher than those in Py1. These findings are in good agreement with the results obtained by LA-MC-ICP-MS on another pyrite grain (Figure 7C). The range of $\delta^{34}S$ values at the Houge'zhuang gold deposit was similar to those of other gold deposits in Jiaodong.

The grain-scale variations in sulfur isotopic compositions were small but regular, noticeably in pyrite from stages I and III. A rough, positive correlation was observed between the As content and $\delta^{34}S$ value.

Discussion

Characteristics of the ore-forming fluid

Immiscibility during fluid evolution is an important factor for the mineralization of certain metals. For example, immiscible fluid inclusions are frequently observed in contemporaneous quartz formed during the precipitation stage of large amounts of gold. Furthermore, physical and chemical experimental studies have confirmed that fluid immiscibility is beneficial for gold precipitation. The fluid inclusion types, quantities, homogenization temperature, and densities have similarities and differences, reflecting the evolution of ore-forming fluids (Ramboz et al., 1982; Roedder, 1984; Shepherd and Chenery, 1995; Lu et al., 2004).

The results of fluid inclusion studies and laser Raman spectroscopy suggest that the ore-forming fluid in different stages of the Houge'zhuang gold deposit exhibited chemical and physical properties similar to those in the other Jiaodong gold deposits (Hou et al., 2007b; Ma et al., 2015). The homogenization temperatures of the fluid inclusions gradually

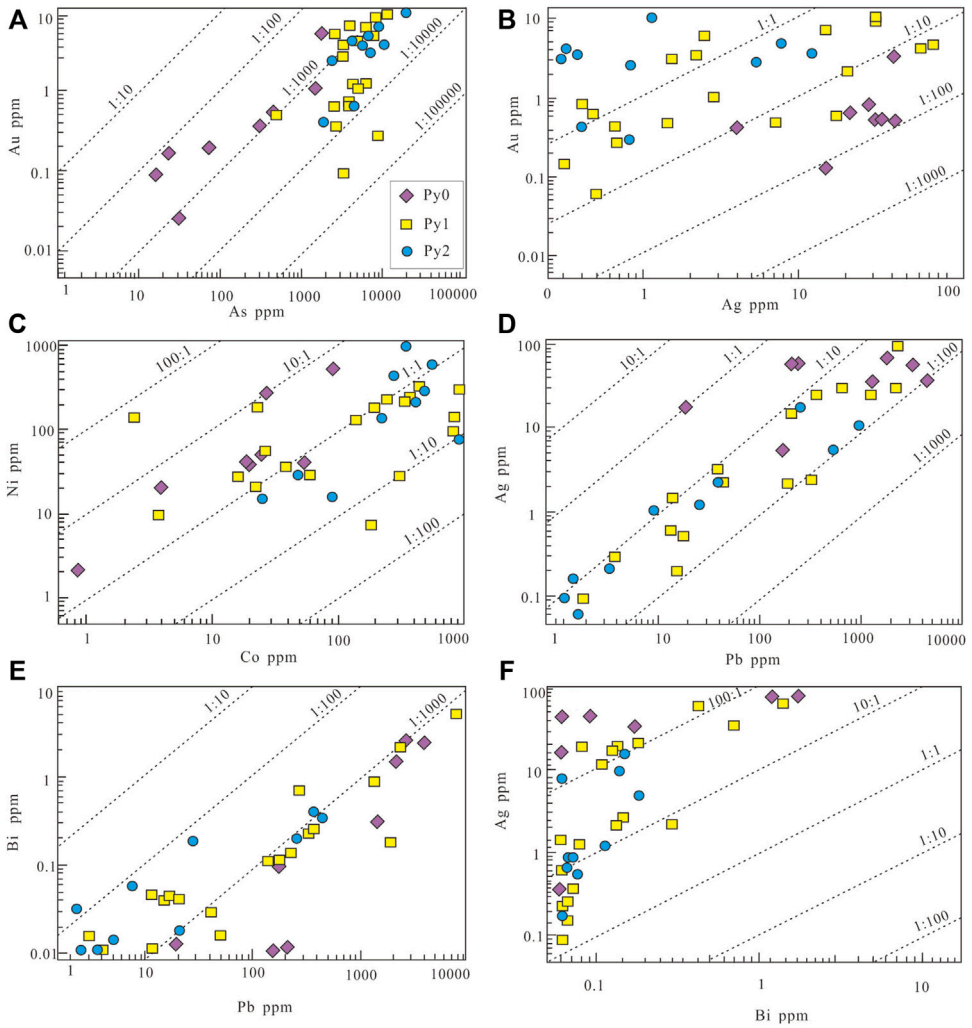


FIGURE 10
Binary plots of **(A)** Au *vs.* As, **(B)** Au *vs.* Ag, **(C)** Bi *vs.* Co, **(D)** Ag *vs.* Pb, **(E)** Bi *vs.* Pb, and **(F)** Ag *vs.* Bi in Py0, Py1, and Py2 from the Houge'zhuang gold deposit.

decreased from stages I to III and the type combinations of the fluid inclusions also changed. Combined with the results of the salinity analysis, the fluid inclusions in stage I were the fluid from the later stage of magmatic evolution, with high temperature—especially Type III fluid inclusions. In stages II and III, type III fluid inclusions decreased—especially type II fluid inclusions. The homogenization temperature was lower than that in stage I, indicating the evolution of the fluid post-phase separation and immiscibility. The evolution process plays an important role in gold precipitation.

The ore-forming fluids of the Houge'zhuang gold deposit were of medium-low salinity and temperatures, with H_2O and CO_2 being the predominant fluid inclusion components, and CO_2 being the predominant vapor phase component.

As enrichment mechanism

Sources of As fluid

The *in situ* trace element analysis revealed that the content of As, the most abundant trace element, gradually increased from Py0 to Py2 (498 ppm, 5419 ppm, and 8113 ppm, respectively) (Table 2). A clear paragenetic succession for various types of pyrite was observed in the elemental mapping (Figures 7D–F).

Py0 was characterized by low concentrations of As and Au, indicating that the initial hydrothermal fluids may not contain high concentrations of As and Au, which are not the main ore-forming fluids. In Py1, the concentration of As increased significantly, with a relatively uniform distribution and no obvious zonal growth, but notably more fine gold and chalcopyrite inclusions, indicating that fluids with high As and Au were the main ore-forming fluids.

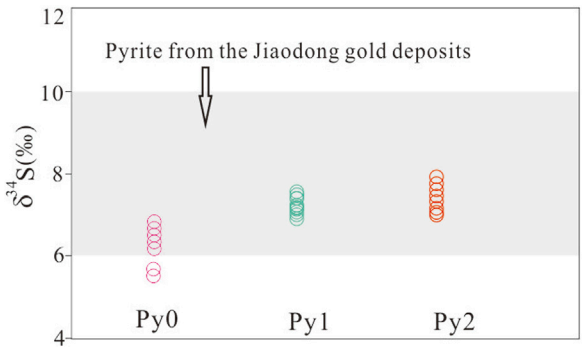


FIGURE 11
Variations in sulfur isotope compositions of various generations of pyrite in the Houge'zhuang gold deposit.

Relative to Py1, Py2 exhibited distinct As enrichment, with As-rich rims of pyrite and growth zoning but a smaller proportion of Py2. This phenomenon implied a lower content of the ore-forming fluid and is indicative of the direct precipitation of Py2 from As-Au-rich solutions.

Regarding the mechanism and source of As enrichment, two main theories have been proposed. First, they could directly precipitate from extremely As-rich auriferous fluids (Barker et al., 2009; Muntean et al., 2011; Peterson and Mavrogenes, 2014). Second, during the fluid migration process, the ore-forming fluid may react with As-rich sedimentary or metamorphic rocks to extract As, becoming more enriched, especially in Carlin-type gold deposits (Ilchik and Barton et al., 1997; Feng et al., 2018; Feng et al., 2020; Large et al., 2014).

The ore-forming fluids of the gold deposits in Jiaodong are mainly As-poor fluids, which are rare. Compared to the other gold belts in Jiaodong, the Penglai–Qixia gold belt developed many Proterozoic Jingshan, Fenzishan, and Penglai groups. Our analysis of the As content in the formation revealed As concentrations in the Fenzishan and Jingshan groups of 11.72 ppm and 2.27 ppm, respectively (Tian et al., 2022), both of which were higher than the average value (0.97 ppm) of the Jiaodong crust (Figure 9). Further considering the discovery of As-rich (~0.4–2.5%) pyrite in the surrounding Heilan'gou and Daliu'hang gold deposits, the primary ore-forming fluids may pass through some As-rich sedimentary rocks such as the Jingshan, Fenzishan, and Penglai groups, resulting in stable water-rock interaction, extraction, and enrichment of As.

Implications for gold mineralization

In hydrothermal gold deposits, pyrite is the main gold-bearing mineral, as the coupling relationship between Au and As has been widely recognized. Most scholars believe that this is the result of As controlling Au enrichment and that the same relationship exists in the Jiaodong gold deposits. The binary plots

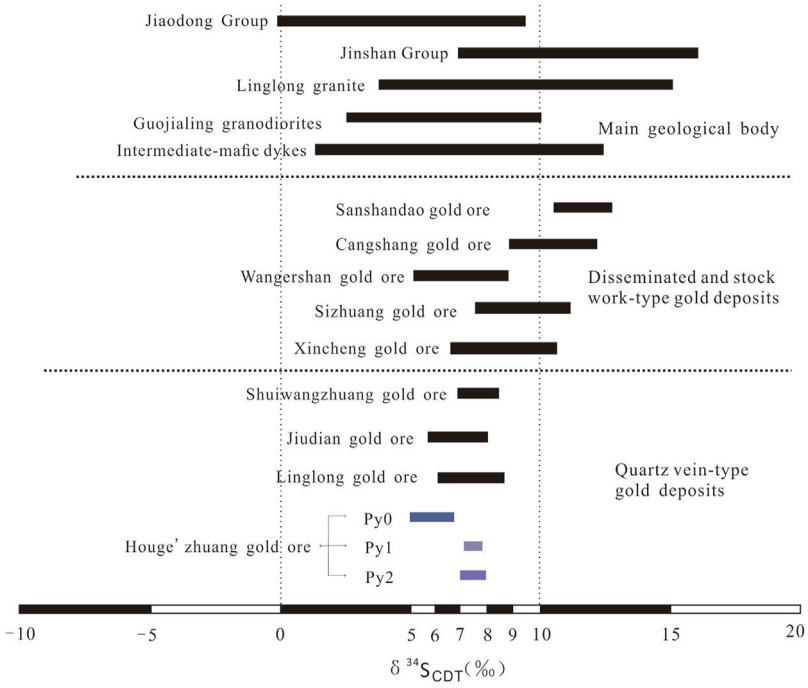


FIGURE 12
Sulfur isotope composition of Jiaodong group metamorphic rocks, granites, dykes, and ores of gold deposits in the northwestern Jiaodong area.

TABLE 4 Sulfur isotopes of typical gold deposits in North Jiaodong.

Area	Deposit name	Deposit type	Object	δ34S Value ‰)	δ34S average value (‰)	Number	Source
Jiao Xibei	Sanshandao	Disseminated-style	Py	11.0~12.6	12.2	7	Wang et al. (2002)
	Cangshang		Py	9.6~12.0	10.8	4	Huang (1994)
	Wangershan		Py	4.8~8.9	6.3	30	Guo et al. (2019)
	Sizhuang		Py	7.1-11.5	9.5	16	Yang et al. (2014)
	Xincheng		Py	7.9~10.7	9.8	18	Li et al. (2020b)
				6.63~9.65	7.61	12	Songet al., 2015
	Jiaojia		Py	7.5~11.46	9.61	15	Songet al., 2015
				7.71~12.58	10.32	12	Jiang (2020)
	Shuiwangzhuang	Quartz vein-style	Py	7.0~8.5	7.7	7	Zhang et al. (2018a)
	Linglong		Py	6.4~8.6	7.6	16	Hou et al. (2006)
	Jiudian		Py	5.7~8.1	7.4	14	Wang et al. (2002)
Penglai–Qixia	Heilan'gou	Quartz vein-style	Py	6.6~8.8	7.2	68	Feng et al. (2018)
				5.5~7.8	6.7		Yan et al. (2014)
				6.3~9.5	7.5	8	Hou et al. (2007a)
	Daliuhang		Py	3.7~8.3	7.1	62	Feng et al. (2020)
	Majiayao		Py	5.5~8.6	6.37		Tian et al. (2020)
	Hexi		Py	5.4~8.8	6.95	17	Hou et al. (2004)

of Au *vs.* As showed a good linear relationship (Figure 10A) and good correlations in different lithologies in Jiaodong (Figure 9).

The ore-forming fluids of the Houge'zhuang gold deposit showed medium-low salinity and temperatures, suggesting that Au may migrate mainly as $Au(HS)^{-2}$ complex (Benningand Seward, 1996; Stefánsson and Seward, 2004; Williams-Jones et al., 2009; Yang et al., 2016b; Chai et al., 2017).

The porous and honeycomb structures and the metasomatic relict texture of the Py1 indicated that fluid boiling occurred due to pressure/temperature changes and a continuous water-rock interaction, consistent with an altered rock-type mineralization mechanism. The water-rock interaction changes the physicochemical conditions, causing the $Au(HS)^{-2}$ complex to destabilize and precipitate Au. The visible gold is the paragenesis gold in Py1.

The difference between Py2 (arsenic-bearing pyrite) and Py1 suggests two distinct ore-forming fluids Figures 10B–F. The gold in Py2 was invisible gold, especially nanogold and lattice gold. Au atoms sit at the Fe atom sites in the As-bearing pyrite structure; moreover, Au and As in As-bearing pyrite are the most abundant chemically bound Au^{+} and As^{-}, respectively. Au^{+} and $As^{-}$are both structurally bound and sit at the Fe and S atom sites of pyrite, respectively; wherein As^{1-} changes the crystal structure of pyrite, rendering it easy for Au^{1+} to replace Fe^{2+}(Palenik et al., 2004; Kusebauch et al., 2019; Xing et al., 2019; Meng et al., 2022), resulting in the formation of lattice gold. The enrichment of As in pyrite may lead to high partition coefficients for Au between fluid and pyrite, which can effectively adsorb Au-HS complexes from the fluid onto the As-bearing pyrite growth interface through chemical adsorption, resulting in nanogold formation.

The analysis revealed that Au was closely associated with As. Fine and coarse visible gold grains tended to occur in association with the Py1 of stage II, while invisible gold was related to the Au-As-rich Py2 of stage III. These As-bearing pyrites showed a close spatiotemporal relationship to gold, thus playing an important role in the formation and exploration of high-grade gold deposits.

Sources of sulfur and ore metals

The sulfur isotope ratios of the sulfides that co-precipitated with gold have been used as a reliable measure to determine the source of gold, as gold commonly complexes with sulfide as $Au(HS)^{2-}$ in hydrothermal fluids (Hayashi and Ohmoto 1991; Benning and Seward, 1996; Stefansson and Seward, 2004; Williams-Jones et al., 2009).

The *in situ* sulfur isotope values of pyrite measured in the present study were relatively stable, with a narrow variation ($\delta^{34}S_{CDT}$ = ~ 5.51–7.95‰), showing a tower effect and a positive deviation from meteorite sulfur, similar to the other deposits in Jiaodong (Hou et al., 2007a; Yan et al., 2014; Wang et al., 2015; Wen et al., 2016; Feng et al., 2018; Yang et al., 2018; Chai et al., 2020b).

Grain-scale variations were observed in $\delta^{34}S$ in pyrite grains. The core (Py0) had $\delta^{34}S$ values of ~5.51–6.62‰, increasing to

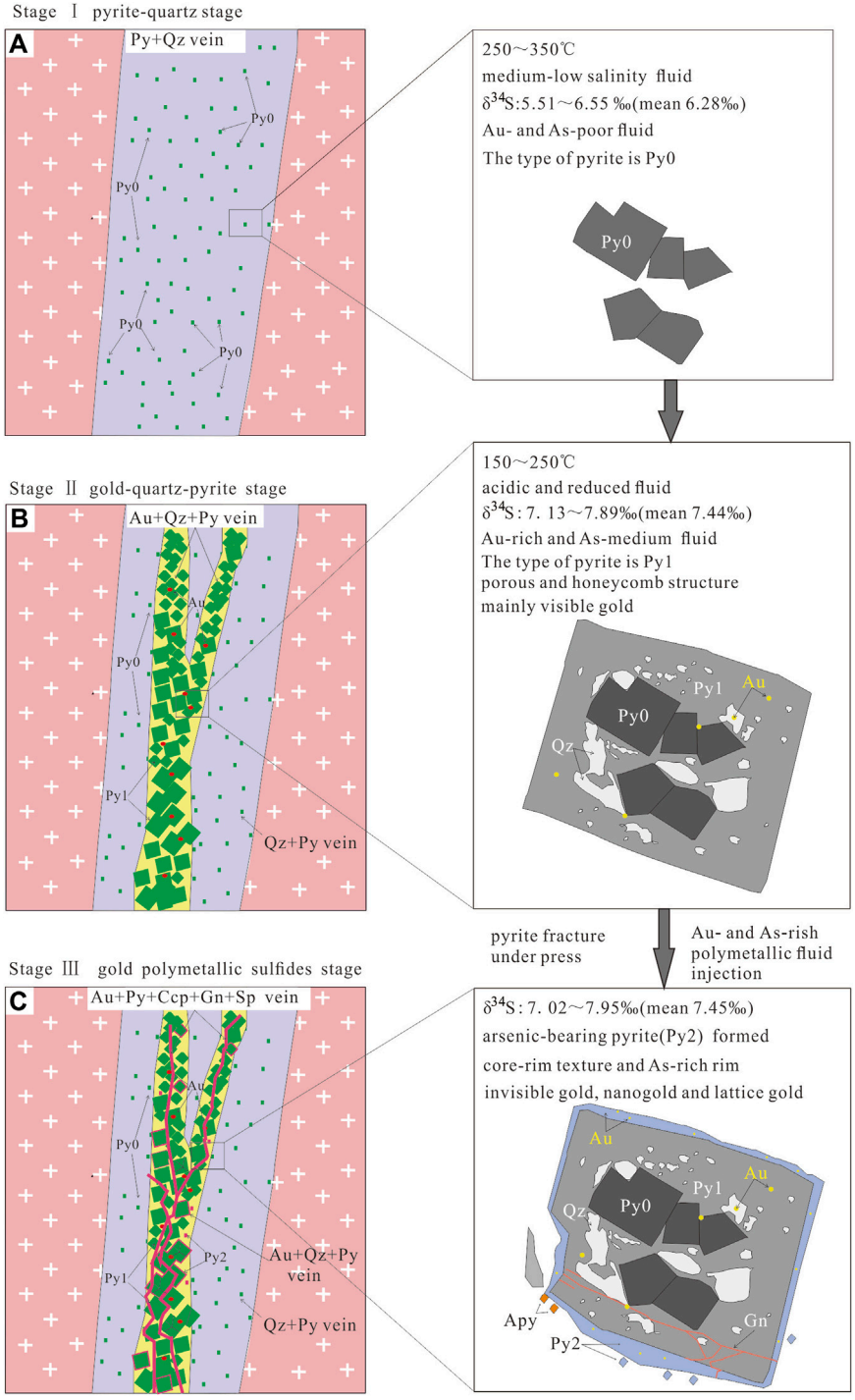


FIGURE 13
Gold metallogenic process of Houge'zhuang gold deposit for different mineralization stages.

~7.15–7.49‰ on the rim (Py1 and Py2). The $\delta^{34}S$ values of Py2 were slightly higher than those in Py1. The results indicated that the sulfur isotopes in Py1 and Py2 were highly homogenized and shared the same sources, while the sources of Py0 differed (Figure 11).

These $\delta^{34}S$ values were comparable to those from the Jiaodong and Jingshan groups, Linglong granite, Guojialing granodiorite, and certain basic dykes (Figure 12; Table 4). However, these $\delta^{34}S$ values were closer to those from the granite country rocks and the Precambrian metamorphites,

indicating that the sulfur in the gold deposits was inherited from these country rocks. Basic dykes showed a close spatiotemporal relationship to the gold deposits; however, due to their small scale, the basic dykes were insufficient to provide such a large amount of sulfur.

The Py0 in stage I had relatively low $\delta^{34}S$ values, ranging from 5.51 to 6.62‰ (mean of 6.28‰), which were like those of pyrite from the potassic zone ($\delta^{34}S$, mean of 7.1‰) and Guojialing granodiorite ($\delta^{34}S$, mean of 6.7‰; Wang et al., 2002). These similar sulfur isotopic compositions may indicate one major source of early fluids.

Compared to Py0, Py1 and Py2 showed higher $\delta^{34}S$ values (mean 7.45‰ and 7.44‰, respectively). Mass fractionation during the precipitation of pyrite cannot account for these elevated $\delta^{34}S$ values; rather, an external ^{34}S-rich fluid injection is likely. The $\delta^{34}S$ values of Py1 and Py2 were similar to those of the Jingshan group (8.2–12.0‰, average 9.7‰; Zhang, 1999), which is located around the Houge'zhuang gold deposit, indicating that some sulfur from the Jingshan group leached into the ore-forming fluid. This conclusion is also supported by elevated As and Au concentrations in ore-related pyrite (Feng et al., 2018; Feng et al., 2020), in which the ore-forming fluids passed through some $\delta^{34}S$-rich sedimentary rocks, leading to $\delta^{34}S$-enriched fluid.

Comprehensive analysis suggested that the sulfur in the Houge'zhuang gold deposit originated from mixed sulfur sources, especially the Jiaodong metamorphic basement and Mesozoic granite wall rocks, with precipitation of magmatic sulfur from the mantle and surface.

Au mineralization process in the Houge'Zhuang gold deposit

Pyrite is the most important ore and gold-bearing mineral in the Jiaodong gold deposits. Its precipitation process extends from the early gold mineralization stage to the late stage; thus, exploring the structural element and isotope changes of pyrite at the microscopic scale aids in understanding its complex growth history, accurately determining the source of ore materials, and providing an in-depth understanding of the mineralization process (Ogryzlo, 1935; Helgeson and Garrels, 1968; Henley, 1973; Renders and Seward, 1989; Wood, 1989; Hayashi and Ohmoto, 1991; Seward, 1991; Gammons and Williams Jones, 1995; Zotov et al., 1996; Archibald et al., 2002; Reich et al., 2005; Large et al., 2009; Wu et al., 2019a; Kusebauch et al., 2019).

The results of previous comprehensive studies on the fluid inclusions, *in situ* S isotope analysis, *in situ* LA-ICP-MS trace element analysis, and electron microprobe mapping analysis of the gold-bearing pyrite have shown that the Houge'zhuang gold deposit was formed during the evolution of multi-stage ore-forming fluids.

In stage I, the fluid was acidic and weakly reducing under medium-high temperature conditions (~250–350°C), while the Au and As content in the fluid was relatively low and only a small amount of gold was precipitated. The Py0 formed at this stage was medium-fine-grained. The $\delta^{34}S$ values of Py0 ranged from 5.51 to 6.86‰ (mean value 6.28‰) (Figure 13A).

In stage II, the main stage of gold mineralization, the ore-forming fluids flowed through some $\delta^{34}S$ and As-rich sedimentary rocks and were supersaturated with high sulfur fugacity at ~150–250°C. Fluid inclusion data showed that Au was dissolved and transported as gold bisulfide [$Au(HS)^0$, $Au(HS)^{2-}$)] (Shu et al., 2020). As the pressure of the ore-forming fluid decreased, it boiled, changing the physicochemical conditions and destabilizing the $Au(HS)^{2-}$ complex, resulting in the precipitation of visible gold and simultaneous Py1 formation (Figure 13B).

During the gold polymetallic sulfide stage (III), new ore-forming fluids formed in the deep, with a lower content than stage II but rich in polymetals. The ore-forming fluids passed through some As-rich sedimentary rock, resulting in fluid enriched with As. During this stage, with the precipitation of As-rich fluid and deep-circulating meteoric water, the physicochemical property of the ore-fluid changed from weakly acidic oxidation to weakly acidic reduction. During fluid migration, with changes in temperature and pressure, As^{1-} sat at the atom sites of S^{2+}, which changed the crystal structure of pyrite, rendering it easy for Au^{1+} to replace Fe^{2+}. Moreover, As enrichment in pyrite can lead to high partition coefficients for Au between fluid and pyrite, which can effectively adsorb Au-HS complexes from the fluid into the As-bearing pyrite growth interface through a chemical adsorption mechanism, resulting in the formation of nanogold and lattice gold. Meanwhile, H_2S and metal ions such as Fe^{2+}, Zn^{2+}, Pb^{2+}, and Cu^{2+} in the ore-forming hydrothermal fluid are consumed, forming metal sulfides such as sphalerite, galena, chalcopyrite, and arsenopyrite. Py2 (arsenic-bearing pyrite) is also formed during this period (Figure 13C).

In stage IV, the temperature of the injected fluid and oxygen and sulfur fugacity were low, while the gold content in the fluid was insufficient for mineralization.

Conclusion

1) Three types of fluid inclusions were identified from the ores: single-phase inclusions (type I), two-phase aqueous inclusions (type II), and CO_2-rich three-phase inclusions (type III). The ore-forming fluids of the Houge'zhuang gold deposit exhibited medium-low salinity and temperatures. The fluid inclusions were composed mainly of H_2O and CO_2, while the vapor phases were mainly CO_2.
2) The pyrite in the Houge'zhuang gold deposit can be divided into three types: Py0, Py1, and Py2, which showed good correlations with the mineralization stages. Py0 was

characterized by low concentrations of As and Au and low $\delta^{34}S$ values (5.51–6.86‰). Py1, hosted in the gold-quartz-pyrite veins, was chemically homogeneous with no obvious zonal growth but with significantly more gold and chalcopyrite inclusions. Py1 contained medium and uniform concentrations of As and Au and had $\delta^{34}S$ values ranging from 7.13 to 7.89‰ (mean 7.44‰). Py2, the arsenic-bearing pyrite, was hosted in quartz-polymetallic sulfide veins and showed distinct As enrichment with As-rich rims of pyrite and growth zoning.

3) The primary ore-forming fluids may pass through some As-rich sedimentary rocks, extracting and enriching As. Au was closely associated with As. Fine and coarse visible gold grains tended to occur in association with the Py1 of stage II, while invisible gold was related to the Au-As-rich Py2 of stage III.
4) The results of comprehensive analyses suggest that the sulfur in the Houge'zhuang gold deposit originated from mixed sulfur sources, especially from the Jiaodong metamorphic basement and Mesozoic granite wall rocks, with the participation of magmatic sulfur from the mantle and surface.
5) The gold metallogenic process of the Houge'zhuang gold deposit indicates that the deposit was formed during the evolution of multi-stage ore-forming fluids.

Data availability statement

The original contributions presented in the study are included in the article/Supplementary material. Further inquiries can be directed to the corresponding author.

Author contributions

NC, ZH, and CL wrote the manuscript. WZ, WS, YZ, and ZL revised the manuscript, conceived the experiments, and contributed to the data interpretation. The fieldwork and preliminary study of samples were carried out by ML and XW. YS conducted the geochemical analyses and reviewed both the science and English language. All authors have read and agreed to the published version of the manuscript.

Funding

The study was supported by the Natural Science Foundation Project of Shandong Province (grant numbers ZR2019PD019, ZR2020QD029, and ZR2020MD039).

Acknowledgments

The authors thank Shen Kun, who is 83 years old this year and still working in geology. His ideas and insights were very helpful. They acknowledge the efforts of the reviewers, which significantly improved the manuscript. They also thank the Natural Science Foundation of China for supporting our research (grant numbers 42172094, 42203034, and 42272122).

Conflict of interest

The authors declare that the research was conducted in the absence of any commercial or financial relationships that could be construed as a potential conflict of interest.

Publisher's note

All claims expressed in this article are solely those of the authors and do not necessarily represent those of their affiliated organizations, or those of the publisher, the editors, and the reviewers. Any product that may be evaluated in this article, or claim that may be made by its manufacturer, is not guaranteed or endorsed by the publisher.

References

ArchibaldMigdisov, S. A. A., and Williams-Jones, A. E. (2002). An experimental study of the stability of copper chloride complexes in water vapor at elevated temperatures and pressures. *Geochimica Cosmochimica Acta* 66 (9), 1611–1619. doi:10.1016/s0016-7037(01)00867-5

Arehart, G. B., Chryssoulis, S. L., and Kesler, S. E. (1993). Gold and arsenic in iron sulfides from sediment-hosted disseminated gold deposits-implications for depositional processes. *Econ. Geol.* 88, 171–185. doi:10.2113/gsecongeo.88.1.171

Barker, S. L., Hickey, K. A., Cline, J. S., Dipple, G. M., Kilburn, M. R., Vaughan, J. R., et al. (2009). Uncloaking invisible gold: Use of nanoSIMS to evaluate gold, trace elements, and sulfur isotopes in pyrite from carlin-type gold deposits. *Econ. Geol.* 104, 897–904. doi:10.2113/gsecongeo.104.7.897

Benning, L. G., and Seward, T. M. (1996). Hydrosulphide complexing of Au (I) in hydrothermal solutions from 150–400 °C and 500–1500 bar. *Geochim. Cosmochim. Acta* 60, 1849–1871. doi:10.1016/0016-7037(96)00061-0

Bi, X. W., Hu, R. Z., and Peng, J. T. (2004). REE and HFSE geochemical characteristics of pyrites in yao'an gold deposit: Tracing ore forming fluid signatures. *Bull. Mineralogy' Petrology Geochem.* 23 (1), 1–4.

Bodnar, R. J. (1994). Synthetic fluid inclusions: XII. The system H_2O-NaCl. Experimental determination of the halite liquidus and isochores for a 40 wt.% NaCl solution. *Geochimica Cosmochimica Acta* 58 (3), 1053–1063. doi:10.1016/0016-7037(94)90571-1

Chai, P., Hou, Z. Q., Zhang, H. R., and Dong, L. L. (2019b). Geology, fluid inclusion, and H–O–S–Pb isotope constraints on the mineralization of the xiejiagou gold deposit in the jiaodong peninsula. *Geofluids* 2019, 3726465. doi:10.1155/2019/3726465

Chai, P., Hou, Z. Q., and Zhang, Z. Y. (2017). Geology, fluid inclusion and stable isotope constraints on the fluid evolution and resource potential of the xiadian gold deposit, jiaodong peninsula. *Resour. Geol.* 67, 341–359. doi:10.1111/rge.12134

Chai, P., Zhang, H. R., Dong, L. L., and Zhang, Z. Y. (2019c). Geology and ore-forming fluids of the dayingezhuang gold deposit, jiaodong peninsula, eastern China: Implications for mineral exploration. *J. Geochem. Explor.* 204, 224–239. doi:10.1016/j.gexplo.2019.06.001

Chai, P., Zhang, H. R., Hou, Z. Q., and Zhang, Z. Y. (2020a). Geochronological framework of the Damoqujia gold deposit, Jiaodong Peninsula, China: Implications for the timing and geologic setting of gold mineralization. *Geol. J.* 55, 596–613. doi:10.1002/gj.3428

Chai, P., Zhang, H. R., Hou, Z. Q., Zhang, Z. Y., and Dong, L. L. (2020b). Ore geology, fluid inclusion, and stable isotope constraints on the origin of the Damoqujia gold deposit, Jiaodong Peninsula, China. *Can. J. Earth Sci.* 57, 1428–1446. doi:10.1139/cjes-2018-0247

Chai, P., Zhang, Z. Y., and Hou, Z. Q. (2019a). Geological and fluid inclusion constraints on gold deposition processes of the dayingezhuang gold deposit, jiaodong peninsula, China. *Acta Geol. sinica-. Engl. Ed.* 93 (4), 955–971. doi:10.1111/1755-6724.13849

Chen, F. C., Deng, J., Wang, Q. F., Jan, F. C., Deng, J., Wang, Q. F., et al. (2020c). LA-ICP-MS trace element analysis of magnetite and pyrite from the Hetaoping Fe-Zn-Pb skarn deposit in Baoshan block, SW China: Implications for ore-forming processes. *Ore Geol. Rev.* 117, 103309–103317. doi:10.1016/j.oregeorev.2020.103309

Chi, N. J., Han, Z. Z., and Shan, W. (2020). Typomorphic characteristics of gold-bearing pyrite in jiaojia fault deep zone of northwest jiaodong peninsula and its geological significance. *Acta Geosci. Sin.* 41 (6), 949–962. doi:10.3975/cagsb.2020.070101

Chouinard, A., Paquette, J., and Williams-Jones, A. E. (2005). Crystallographic controls on trace-element incorporation in auriferous pyrite from the Pascua epithermal high-sulfidation deposit, Chile-Argentina. *Can. Mineralogist* 43, 951–963. doi:10.2113/gscanmin.43.3.951

Cook, N. J., Ciobanu, C. L., and Mao, J. W. (2009). Textural control on gold distribution in as-free pyrite from the dongping, huangtuliang and hougou gold deposits, north China craton (hebei province, China). *Chem. Geol.* 264, 101–121. doi:10.1016/j.chemgeo.2009.02.020

Cook, N. J., Ciobanu, C. L., Meria, D., Silcock, D., and Wade, B. (2013). Arsenopyrite-pyrite association in an orogenic gold ore: Tracing mineralization history from textures and trace elements. *Econ. Geol.* 108, 1273–1283. doi:10.2113/econgeo.108.6.1273

Deditius, A. P., Reich, M., Kesler, S. E., Utsunomiya, S., Chryssoulis, S. L., Walshe, J., et al. (2014). The coupled geochemistry of Au and as in pyrite from hydrothermal ore deposits. *Geochim. Cosmochim. Acta* 140, 644–670. doi:10.1016/j.gca.2014.05.045

Deng, J., Qiu, K. F., Wang, Q. F., Goldfarb, R., Yang, L. Q., Zi, J. W., et al. (2020a). *In situ* dating of hydrothermal monazite and implications on the geodynamic controls of ore formation in the Jiaodong gold province, eastern China. *Econ. Geol.* 115, 671–685. doi:10.5382/econgeo.4711

Deng, J., Liu, X. F., Wang, Q. F., and Pan, R. G. (2015a). Origin of the Jiaodong-type Xinli gold deposit, Jiaodong Peninsula, China: Constraints from fluid inclusion and C-D–O–S–Sr isotope compositions. *Ore Geol. Rev.* 65, 674–686. doi:10.1016/j.oregeorev.2014.04.018

Deng, J., Liu, X., Wang, Q., Dilek, Y., and Liang, Y. (2017). Isotopic characterization and petrogenetic modeling of early cretaceous mafic diking—lithospheric extension in the north China craton, eastern Asia. *GSA Bull.* 129, 1379–1407. doi:10.1130/b31609.1

Deng, J., Wang, C. M., Bagas, L., Carranza, E. J. M., and Lu, Y. (2015b). Cretaceous -Cenozoic tectonic history of the Jiaojia Fault and gold mineralization in the Jiaodong Peninsula, China: Constraints from zircon U-Pb: Illite K-Ar and apatite fission track thermochronometry. *Min. Depos.* 50 (8), 987–1006. doi:10.1007/s00126-015-0584-1

Deng, J., Wang, C. M., Bagas, L., Santosh, M., and Yao, E. Y. (2018). Crustal architecture and metallogenesis in the south-eastern North China Craton. *Earth. Sci. Rev.* 182, 251–272. doi:10.1016/j.earscirev.2018.05.001

Deng, J., and Wang, Q. F. (2016). Gold mineralization in China: Metallogenic provinces, deposit types and tectonic framework. *Gondwana Res.* 36, 219–274. doi:10.1016/j.gr.2015.10.003

Deng, J., Wang, Q., Santosh, M., Liu, X., and Yang, L. (2020c). Remobilization of metasomatized mantle lithosphere: A new model for the jiaodong gold province, eastern China. *Min. Depos.* 55, 257–274. doi:10.1007/s00126-019-00925-0

Deng, J., Yang, L. Q., Groves, D. I., Zhang, L., and Wang, Q. F. (2020b). An integrated mineral system model for the gold deposits of the giant Jiaodong province, eastern China. *Earth-Science Rev.* 208, 103274. doi:10.1016/j.earscirev.2020.103274

Deng, J., Yang, L. Q., and Wang, Q. F. (2006). Introduction to the composition and evolution of the gold metallogenic system in the Jiaodong ore concentration area. *Mineral. Deposits* 25 (S1), 67–70.

Fan, H. R., Feng, K., and Li, X. H. (2016). Jiaodong-korea peninsula mesozoic gold mineralization. *Acta Petrol. Sin.* 32 (10), 3225–3238.

Feng, K., Fan, H. R., Groves., David I., Yang, K. F., Liu, X., Cai, Y. C., et al. (2020). Geochronological and sulfur isotopic evidence for the Genesis of the post-magmatic, deeply sourced, and anomalously gold-rich Daliuhang orogenic deposit, Jiaodong, China. *Min. Depos.* 55, 293–308. doi:10.1007/s00126-019-00882-8

Feng, K., Fan, H. R., Hu, F. F., Yang, K. F., Liu, X., Shangguan, Y. N., et al. (2018). Involvement of anomalously As-Au-rich fluids in the mineralization of the Heilan'gou gold deposit, Jiaodong, China: Evidence from trace element mapping and *in-situ* sulfur isotope composition. *J. Asian Earth Sci.* 160, 304–321. doi:10.1016/j.jseaes.2017.12.023

Gammons, C. H., and Williams Jones, A. E. (1995). The solubility of Au-Ag alloy + AgCl in HCl/NaCl solutions at 300˚C: New data on the stability of Au (1) chloride complexes in hydrothermal fluids. *Geochimica Cosmochimica Acta* 59 (17), 3453–3468. doi:10.1016/0016-7037(95)00234-q;

Goldfarb, R. J. M., and Santosh, M. (2014). The dilemma of the Jiaodong gold deposits: Are they unique? *Geosci. Front.* 5, 139–153. doi:10.1016/j.gsf.2013.11.001

Guo, L. N., Huang, C. M., and Zhang, L. (2019). Source of ore-forming fluids in the luoshan gold deposit, jiaodong: Constrains from REE and trace element features of auriferous pyrite in the altered-rock type and auriferous quartz vein type ores. *Geoscience* 33 (1), 121–136. doi:10.19657/j.geoscience.1000-8527.2019.01.12

Hayashi, K. I., and Ohmoto, H. (1991). Solubility of gold in NaCl- and H_2S-bearing aqueous solutions at 250–350 ˚C. *Geochim. Cosmochim. Acta* 55, 2111–2126. doi:10.1016/0016-7037(91)90091-i

Helgeson, H. C., and Garrels, R. M. (1968). Hydrothermal transport and deposition of gold. *Econ. Geol.* 63 (6), 622–635. doi:10.2113/gsecongeo.63.6.622

Henley, R. W. (1973). Solubility of gold in hydrothermal chloride solutions. *Solubility gold hydrothermal chloride solutionsChemical Geol.* 11 (2), 73–87. doi:10.1016/0009-2541(73)90044-2

Hou, M. L., Ding, X., and Jiang, S. Y. (2004). Lead and sulfur isotope geochemistry of the hexi gold deposit in Penglai, eastern Shandong. *Acta Geosci. Sin.* 25 (2), 145–150.

Hou, M. L., Jiang, S. Y., and Ling, H. F. (2006). S-Pb isotope geochemistry and Rb-Sr geochronology of the Penglai gold field in the eastern Shandong Province. *Acta Petrol. Sin.* 22 (10), 2525–2533.

Hou, M. L., Jiang, S. Y., Shen, K., Lian, G. J., Liu, Q. C., and Xiao, F. L. (2007a). Fluid inclusion and H-O isotope study of gold mineralization in the Penglai gold field, Eastern Shangdong. Acta Petrol. *Sin* 23, 2241–2256.

Hou, M. L., Jiang, Y. H., Jiang, S. Y., Ling, H. F., and Zhao, K. D. (2007b). Contrasting origins of late mesozoic adakitic granitoids from the northwestern jiaodong peninsula, east China: Implications for crustal thickening to delamination. *Geol. Mag.* 144, 619–631. doi:10.1017/s0016756807003494

Hu, H. L., Fan, H. R., Santosh, M., Liu, X., Cai, Y. C., and Yang, K. F. (2020). Ore-forming processes in the Wang'ershan gold deposit (Jiaodong, China): Insight from microtexture, mineral chemistry and sulfur isotope compositions. *Ore Geol. Rev.* 123, 103600. doi:10.1016/j.oregeorev.2020.103600

Huang, D. Y. (1994). Sulfur isotope studies of the metallogenic series of gold deposits in Jiaodong (East Shandong) area. *Mineral Deposits* 13, 75–87.

Ilchik, R. P., and Barton, M. D. (1997). An amagmatic origin of Carlin-type gold deposits. *Econ. Geol.* 92, 269–288.

Jiang, M. Y. (2019). Metallogeneses and Tectonic Setting Analysis of Shaling Gold Deposit in Jiaodong. *Diss. Subm. Hebei Geo Univ.*. Master Degree of Structural Geology, 1–60.

Kusebauch, C., Gleeson, S. A., and Oelze, M. (2019). Coupled partitioning of Au and as into pyrite controls formation of giant Au deposits. *Sci. Adv.* 5, eaav5891–8. doi:10.1126/sciadv.aav5891

Large, R. R., Danyushevsky, L., Hollit, C., Maslennikov, V., Meffre, S., Gilbert, S., et al. (2009). Gold and trace element zonation in Pyrite using a laser imaging technique: Implications for the timing of gold in orogenic and Carlin-Style sediment-hosted deposits. *Econ. Geol.* 104, 635–668. doi:10.2113/gsecongeo.104.5.635

Large, R. R., Halpin, J. A., Danyushevsky, L. V., Maslennikov, V. V., Bull, S. W., Long, J. A., et al. (2014). Trace element content of sedimentary pyrite as a new proxy for deep-time ocean–atmosphere evolution. *Earth Planet. Sci. Lett.* 389, 209–220. doi:10.1016/j.epsl.2013.12.020

Li, J., Song, M. C., Liang, J. L., MengYao, J., ShiYong, L., Zheng, D., et al. (2020a). Source of ore-forming fluids of the Jiaojia deeply-seated gold deposit: Evidences from trace elements and sulfur-helium-argon isotopes of pyrite. *Acta Petrol. Sin.* 36 (1), 297–313. doi:10.18654/1000-0569/2020.01.23

Li, L., Santosh, M., and Li, S. R. (2015). The 'jiaodong type' gold deposits: Characteristics, origin and prospecting. *Ore Geol. Rev.* 65, 589–611. doi:10.1016/j.oregeorev.2014.06.021

Li, R. H., Wang, X. Q., Yang, L. Q., Zhang, B. M., Liu, Q. Q., and Liu, D. S. (2020b). The characteristic of microstructural deformation of gold bearing pyrite in Jiaodong: The links between nanoscale gold enrichment and crystal distortion. *Ore Geol. Rev.* 122 495–504. doi:10.1016/j.oregeorev.2020.103495

Li, S. X., Liu, C. C., and An, Y. H. (2007). *Jiaodong gold mine geology*. Beijing: Geological Publishing House.

Liu, Y., Deng, J., and Wang, Z. L. (2014). Zircon U-Pb age, Lu-Hf isotopes and petrogeochemistry of the monzogranites from Xincheng gold deposit, northwestern Jiaodong Peninsula, China. *Acta Petrol. Sin.* 30 (9), 2559–2573.

Liu, Y. S., Hu, Z. C., Gao, S., Detlef, G., Xu, J., Gao, C. G., et al. (2008). *In situ* analysis of major and trace elements of anhydrous minerals by LA-ICP-MS without applying an internal standard. *Chem. Geol.* 257, 34–43. doi:10.1016/j.chemgeo.2008.08.004

Lu, H. Z., Fan, H. R., and Ni, P. (2004). *Fluid inclusions*. Beijing: Science Publishing House, 1–485.

Ma, W. D., Zhang, D. R., Wang, Z. L., Lu, A. H., Cui, Y., and Zuo, H. Y. (2015). A comparison study on mineralization characteristics in Dayingezhuang and Xiadian gold deposits, Eastern Shangdong Province. *Bull. Miner. Petrol* 34, 191–200.

Meng, L., Zhu, S. Y., Li, X. C., Chen, W. T., Xian, H. Y., Gao, X. Y., et al. (2022). Incorporation mechanism of structurally bound gold in pyrite: Insights from an integrated chemical and atomic-scale microstructural study. *Am. Mineralogist* 107, 603–613. doi:10.2138/am-2021-7812

Möller, P., and Kersten, G. (1994). Electrochemical accumulation of visible gold on pyrite and arsenopyrite surfaces. *Min. Depos.* 29, 404–413. doi:10.1007/bf01886958

Muntean, J. L., Cline, J. S., Simon, A. C., and Longo, A. A. (2011). Magmatic-hydrothermal origin of Nevada's Carlin-type gold deposits. *Nat. Geosci.* 4, 122–127. doi:10.1038/ngeo1064

Ogryzlo, S. P. (1935). Hydrothermal experiments with gold. *Econ. Geol.* 30 (4), 400–424. doi:10.2113/gsecongeo.30.4.400

Palenik, C. S., Utsunomiya, S., Reich, M., Kesler, S. E., Wang, L., and Ewing, R. C. (2004). Invisible" gold revealed: Direct imaging of gold nanoparticles in a Carlin-type deposit. *Am. Mineralogist* 89, 1359–1366. doi:10.2138/am-2004-1002

Peterson, E. C., and Mavrogenes, J. A. (2014). Linking high-grade gold mineralization to earthquake-induced fault-valve processes in the Porgera gold deposit, Papua New Guinea. *Geology* 42, 383–386. doi:10.1130/g35286.1

Ramboz, C., Pichavant, M., and Weisbrod, A. (1982). Fluid immiscibility in natural processes: Use and misuse of fluid inclusion data. *Chem. Geol.* 37 (1/2), 29–48. doi:10.1016/0009-2541(82)90065-1

Reich, M., Kesler, S. E., Utsunomiya, S., Palenik, C. S., Chryssoulis, S. L., and Ewing, R. (2005). Solubility ofgold in arsenianpyrite. *Geochim. Cosmochim. Acta* 69, 2781–2796. doi:10.1016/j.gca.2005.01.011

Renders, P. J., and Seward, T. M. (1989). The stability of hydrosulphido- and sulphido-complexes of Au(I) and Ag(I) at 25°C. *Geochim. Cosmochim. Acta* 53 (2), 245–253. doi:10.1016/0016-7037(89)90377-3

Roedder, E. (1984). "Fluid inclusions," in *Mineralogical society of America* (Chantilly: Mineralogical Society of America), 646.

Román, C. C., Yagüe, C., Arrillaga, J. A., Lothon, M., Pardyjak, E. R., Lohou, F., et al. (2019). Comparing mountain breezes and their impacts on CO_2 mixing ratios at three contrasting areas. *Atmos. Res.* 221, 111–126. doi:10.1016/j.atmosres.2019.01.019

Seward, T. M. (1991). The hydrothermal geochemistry of gold. *Gold Metallogeny Explor.* 42, 37–62. doi:10.1007/978-1-4613-0497-5_2

Shen, K., Shu, L., and Liu, P. R. (2018). Origin and significance of mica-bearing fluid inclusions in the altered wall rocks of wangjiazhuang copper-molybdenum deposit, zouping country, Shandong province. *Acta Petrol. Sin.* 34 (12), 3509–3524.

Shepherd, T. J., and Chenery, S. R. (1995). Laser ablation ICP-ms elemental analysis of individual fluid inclusions:an evaluation study. *Geochimica Cosmochimica Acta* 59 (19), 3997–4007. doi:10.1016/0016-7037(95)00294-a

Shu, L., Shen, K., Yang, R. C., Song, Y., Sun, Y., Shan, W., et al. (2020). SEM-CL study of quartz containing fluid inclusions in wangjiazhuang porphyry copper (-Molybdenum) deposit, western Shandong, China. *J. Earth Sci.* 31 (2), 330–341. doi:10.1007/s12583-019-1025-3

Simon, G., Huang, H., Penner-Hahn, J. E., Kesler, S. E., and Kao, L. S. (1999a). Oxidation state of gold and arsenic in gold-bearing arsenian pyrite. *Am. Mineralogist* 84, 1071–1079. doi:10.2138/am-1999-7-809

Simon, G., Kesler, S. E., and Chryssoulis, S. (1999b). Geochemistry and textures of gold-bearing arsenian pyrite, Twin Creeks, Nevada: Implications for deposition of gold in Carlin-type deposit. *Econ. Geol.* 94, 405–421. doi:10.2113/gsecongeo.94.3.405

Song, M. C., Li, S. Z., Santosh, M., Zhao, S., Yu, S., Yi, P. H., et al. (2015). Types, characteristics and metallogenesis of gold deposits in the jiaodong peninsula, eastern north China craton. *Ore Geol. Rev.* 65, 612–625. doi:10.1016/j.oregeorev.2014.06.019

Steele-MacInnis, M., Ridley, J., Lecumberri-Sanchez, P., Schlegel, T. U., and Heinrich, C. A. (2016). Application of low-temperature microthermometric data for interpreting multicomponent fluid inclusion compositions. *Earth-Science Rev.* 159, 14–35. doi:10.1016/j.earscirev.2016.04.011

Steele-MacInnis, M., Bodna, R. J., and Naden, J. (2011). Numerical model to determine the composition H_2O-NaCl-$CaCl_2$ fluid inclusions based on microthermometric and microanalytical data. *Geochimica Cosmochimica Acta* 75 (1), 21–40. doi:10.1016/j.gca.2010.10.002

Stefánsson, A., and Seward, T. M. (2004). Gold (I) complexing in aqueous sulphide solutions to 500°C at 500 bar. *Geochim. Cosmochim. Acta* 68, 4121–4143. doi:10.1016/j.gca.2004.04.006

Tanner, D., Henley, R. W., Mavrogenes, J. A., and Holden, P. (2016). Sulfur isotope and trace element systematics of zoned pyrite crystals from the El Indio Au-Cu-Ag deposit, Chile. *Contrib. Mineral. Pet.* 171, 33–17. doi:10.1007/s00410-016-1248-6

Tian, R. C., Li, D. P., Zhang, W., Tian, J. X., Yu, X. W., Geng, K. K., et al. (2022). The mixingof Mesozoic crust-mantle magma is the key to the source of large amounts of gold deposits in the Jiaobei uplift, China. *Acta Petrol. Sinica.* 38, 23–40. doi:10.18654/1000-0569/2022.01.03

Wang, Q. F., Lin, Q. W., Zhao, H. S., Groves, D. I., Weng, W. J., Xue, S. C., et al. (2021). Towards a universal model for orogenic gold systems: A perspective based on Chinese examples with geodynamic, temporal, and deposit-scale structural and geochemical diversity. *Earth-Science Rev.* 224, 103861. doi:10.1016/j.earscirev.2021.103861

Wang, Y. J., Shen, L. J., and Zhu, Y. Z. (2018). Characteristics of fluid inclusion of Houge'Zhuang gold deposit in Penglai area in Shandong province. *Shandong Land Resour.* 34 (3), 15–20.

Wang, Y. W., Zhu, F. S., and Gong, R. T. (2002). Tectonic isotope geochemistry further study on sulphur isotope of Jiaodong Gold Concentration Area. *Gold* 23, 1–16.

Wang, Z. L., Gong, Q. J., and Yang, L. Q. (2011). Timing of structural-thermal events in the Wang'ershan gold deposit, Eastern Shandong: Evidences from field investigations. *Geol. Explor.* 47 (6), 1067–1076.

Wang, Z. L., Yang, L. Q., Guo, L. N., Marsh, E., Liu, Y., Zhang, C., et al. (2015). Fluid immiscibility and gold deposition in the xincheng deposit, jiaodong peninsula, China: A fluid inclusion study. *Ore Geol. Rev.* 65, 701–717. doi:10.1016/j.oregeorev.2014.06.006

Wen, B. J., Fan, H. R., Hu, F. F., Liu, X., Yang, K. F., Sun, Z. F., et al. (2016). Fluid evolution and ore Genesis of the giant sanshandao gold deposit, jiaodong gold province, China: Constrains from geology, fluid inclusions and H-O-S-He-Ar isotopic compositions. *J. Geochem. Explor.* 171, 96–112. doi:10.1016/j.gexplo.2016.01.007

Wen, B. J., Fan, H. R., Santosh, M., Hu, F. F., Pirajno, F., and Yang, K. F. (2015). Genesis of two different types of gold mineralization in the Linglong gold field, China: Constrains from geology, fluid inclusions and stable isotope. *Ore Geol. Rev.* 65, 643–658. doi:10.1016/j.oregeorev.2014.03.018

Williams-Jones, A. E., Bowell, R. J., and Migdisov, A. A. (2009). Gold in solution. *Elements* 5, 281–287. doi:10.2113/gselements.5.5.281

Wood, S. A. (1989). Raman spectroscopic determination of the speciation of ore metals in hydrothermal solutions: I. Speciation of antimony in alkaline sulfide solutions at 25°C. *Geochimica Cosmochimica Acta* 53, 237–244. doi:10.1016/0016-7037(89)90376-1

Wu, Y. F., Evans, K., Li, J. W., Fougerouse, D., Large, R. R., and Guagliardo, P. (2019a). Metal remobilization and ore-fluid perturbation during episodic replacement of auriferous pyrite from an epizonal orogenic gold deposit. *Geochim. Cosmochim. Acta* 245, 98–117. doi:10.1016/j.gca.2018.10.031

Xing, Y. L., Brugger, J., Tomkins, A., and Shvarov, Y. R. (2019). Arsenic evolution as a tool for understanding formation of pyritic gold ores. *Geology* 47, 335–338. doi:10.1130/g45708.1

Yan, Y. T., Zhang, N., Li, S. R., and Li, Y. S. (2014). Mineral chemistry and isotope geochemistry of pyrite from the Heilangou gold deposit, Jiaodong Peninsula, Eastern China. *Geosci. Front.* 5, 205–213. doi:10.1016/j.gsf.2013.05.003

Yang, F., Santosh, M., Glorie, S., Jepson, G., Xue, F., and Kim, S. W. (2020). Meso-cenozoic multiple exhumation in the Shandong peninsula, eastern north China craton: Implications for lithospheric destruction. *Lithos* 370, 105597. doi:10.1016/j.lithos.2020.105597

Yang, F., Santosh, M., and Kim, S. W. (2018a). Mesozoic magmatism in the eastern North China Craton: Insights on tectonic cycles associated with progressive craton destruction. *Gondwana Res.* 60, 153–178. doi:10.1016/j.gr.2018.04.003

Yang, F., Santosh, M., and Tang, L. (2018b). Extensive crustal melting during craton destruction: Evidence from the mesozoic magmatic suite of junan, eastern north China craton. *J. Asian Earth Sci.* 157, 119–140. doi:10.1016/j.jseaes.2017.07.010

Yang, K. F., Jiang, P., Fan, H. R., Zuo, Y. B., and Yang, Y. H. (2018). Tectonic transition from a compressional to extensional metallogenic environment at ~120 Ma revealed in the Hushan gold deposit, Jiaodong, North China Craton. *J. Asian Earth Sci.* 160, 408–425. doi:10.1016/j.jseaes.2017.08.014

Yang, L. Q., Deng, J., Guo, R. P., Guo, L., Wang, Z., Chen, B., et al. (2016a). World-class Xincheng gold deposit: An example from the giant Jiaodong gold province. *Geosci. Front.* 7 (3), 419–430. doi:10.1016/j.gsf.2015.08.006

Yang, L. Q., Deng, J., Wang, Z. L., Guo, L. N., Li, R. H., Groves, D. I., et al. (2016b). Relationships between gold and pyrite at the Xincheng gold deposit, Jiaodong Peninsula, China: Implications for gold source and deposition in a brittle epizonal environment. *Econ. Geol.* 111, 105–126. doi:10.2113/econgeo.111.1.105

Yang, L. Q., Deng, J., Wang, Z. L., Zhang, L., Guo, L. N., Song, M. C., et al. (2014). Mesozoic gold metallogenic system of the Jiaodong gold province, eastern China. *Acta Petrol. Sin.* 30 (9), 2447–2467.

Zhai, M. G., and Santosh, M. (2011). The early precambrian odyssey of the north China craton: A synoptic overview. *Gondwana Res.* 20 (1), 6–25. doi:10.1016/j.gr.2011.02.005

Zhang, J., Deng, J., Chen, H. Y., Yang, L. Q., Cooke, D., Danyushevsky, L., et al. (2014). LA-ICP-MS trace element analysis of pyrite from the Chang'an gold deposit, Sanjiang region, China: Implication for ore-forming process. *Gondwana Res.* 26, 557–575. doi:10.1016/j.gr.2013.11.003

Zhang, L., Weinberg, R. F., Yang, L. Q., Groves, D. I., Deng, J., Matchan, E., et al. (2020). Mesozoic orogenic gold mineralization in the jiaodong peninsula, China: A focused event at 120±2 Ma during cooling of pregold granite intrusions:. *Econ. Geol.* 115, 415–441. doi:10.5382/econgeo.4716

Zhang, Z., Mandal, A. K., Wang, N., Keck, C. L., Zimonjic, D. B., Popescu, N. C., et al. (1999). Palmitoyl-protein thioesterase gene expression in the developing mouse brain and retina: Implications for early loss of vision in infantile neuronal ceroid lipofuscinosis.Super large gold deposit exploration perspective in jiaolai basin of jiaodong gold metallogenetic domain. *Gene* 28, 203–211. doi:10.1016/s0378-1119(99)00050-5

Zhu, R. X., Fan, H. R., Li, J. W., Meng, Q. R., Li, S. R., and Zeng, Q. D. (2015). Decratonic gold deposits. *Sci. China Earth Sci.* 58, 1523–1537. doi:10.1007/s11430-015-5139-x

Zotov, A. V., Baranova, N. N., and Bannykh, L. N. (1996). Solubility of the gold sulfides Au 2S and AuAgS in solutions containing hydrogen sulfide at 25 ~ 80°C and pressures of 1 and 500 bar. *Geochem. Int.* 34 (3), 216–221.

frontiers | Frontiers in Earth Science

TYPE Original Research
PUBLISHED 04 January 2023
DOI 10.3389/feart.2022.1031842

Check for updates

OPEN ACCESS

EDITED BY
Fan Yang,
Lanzhou University, China

REVIEWED BY
Yinhang Cheng,
China Geological Survey, China
Leilei Dong,
University of Science and Technology Beijing, China

*CORRESPONDENCE
Yingjie Li,
liyingjie820@126.com

SPECIALTY SECTION
This article was submitted to Structural Geology and Tectonics, a section of the journal Frontiers in Earth Science

RECEIVED 30 August 2022
ACCEPTED 12 December 2022
PUBLISHED 04 January 2023

CITATION
Zhang X, Li Y, Wang G, Wang S, Kong X, Wang X and Liu Z (2023), Intra-oceanic subduction in the southeastern Paleo-Asian ocean: Evidence from early Permian gabbro of the Diyanmiao ophiolite in central Inner Mongolia, North China.
Front. Earth Sci. 10:1031842.
doi: 10.3389/feart.2022.1031842

COPYRIGHT
© 2023 Zhang, Li, Wang, Wang, Kong, Wang and Liu. This is an open-access article distributed under the terms of the Creative Commons Attribution License (CC BY). The use, distribution or reproduction in other forums is permitted, provided the original author(s) and the copyright owner(s) are credited and that the original publication in this journal is cited, in accordance with accepted academic practice. No use, distribution or reproduction is permitted which does not comply with these terms.

Intra-oceanic subduction in the southeastern Paleo-Asian ocean: Evidence from early Permian gabbro of the Diyanmiao ophiolite in central Inner Mongolia, North China

Xiawei Zhang[1,2], Yingjie Li[2,3]*, Genhou Wang[1], Shuai Wang[1,2], Xingrui Kong[3], Xiaodong Wang[3] and Zhibin Liu[3]

[1]School of the Earth Sciences and Resources, China University of Geosciences, Beijing, China, [2]Hebei Key Laboratory of Strategic Critical Mineral Resources, Heibei GEO University, Shijiazhuang, China, [3]College of Earth Sciences, Hebei GEO University, Shijiazhuang, China, [4]Hebei Province Collaborative Innovation Center for Strategic Critical Mineral Research, Hebei GEO University, Shijiazhuang, China

Investigation of intra-oceanic subduction can improve our understanding of plate tectonic processes and the history of continental growth. Evidence for intra-oceanic subduction in the Paleo-Asian Ocean has recently become an important focus of research, including the Diyanmiao ophiolite in central Inner Mongolia, North China. Here, we report a newly discovered occurrence of early Permian gabbro in the Diyanmiao ophiolite zone. The gabbro yields a weighted mean zircon U–Pb age of 294.4 ± 2.2 Ma. The gabbro samples are characterized by moderate SiO_2 (47.32–50.51 wt%), low TiO_2 (0.26–0.54 wt %) and K_2O (0.04–0.75 wt%), and high Na_2O (1.84–4.52 wt%) contents, high Na_2O/K_2O ratios (2.92–58.29), and depleted chondrite-normalized light rare Earth element patterns that are similar to N-MORB. The gabbros show slightly lower contents of high-field-strength elements (e.g., Nb, Ta, and Ti) and slightly higher contents of large-ion lithophile elements (e.g., K, Rb, Ba, and U) relative to N-MORB. In addition, the gabbros show high ε_{Nd} (t) values (8.0–9.8) that are similar to those of forearc basalt in the Diyanmiao ophiolite and N-MORB. Integrating these new data with available results for ophiolite and arc-magmatic rocks of central Inner Mongolia, we propose that the studied gabbro was formed during the initial stage of intra-oceanic subduction and that the Paleo-Asian Ocean was still in a subduction setting during the early Permian.

KEYWORDS

geochronology, gabbro, early permian, intra-oceanic subduction, Paleo-Asian Ocean

1 Introduction

Ophiolites represent fragments of ancient oceanic lithosphere in continental orogenic belts and record the magmatic evolution, metamorphic history, and structural processes of oceanic lithosphere, and also provide important information on the development and extinction of ancient oceanic basins (Nicolas, 1989). Ophiolites form in a variety of plate tectonic settings (e.g., Nicolas, 1989; Dilek and Robinson, 2003; Dilek and Furnes, 2009, 2011, 2014; Kusky, 2011; Santosh et al., 2016) and are eventually obducted onto continental margins or incorporated into accretionary prisms and orogens, thereby serving as marker zones of accretion and suturing between crustal blocks that were originally separated by oceanic basins (Dilek and Furnes, 2011). Consequently, the geology, geochemistry, and geochronology of ophiolites and spatially associated lithological units provide important insights into the evolution of major orogenic belts (Shervais et al., 2004).

The Central Asian Orogenic Belt (CAOB) was formed during a prolonged process involving subduction, accretion, and collision of the Paleo-Asian oceanic plate (Dobretsov et al., 1995). This belt was subsequently superimposed and transformed by the Mesozoic Mongolia–Okhotsk and Pacific tectonic regimes. The CAOB is considered the world's largest Phanerozoic accretionary orogen and is located between the Siberian Craton to the north and the Tarim and North China cratons to the south (Figure 1A). The belt contains intra-oceanic forearc materials, oceanic islands and seamounts, and ancient oceanic crust fragments as a result of the subduction of the Paleo-Asian oceanic plate (Badarch et al., 2002; Windley et al., 2007; Xiao et al., 2009, 2014; Kröner et al., 2017; Safonova, 2017; Yang et al., 2017, 2021; Cheng et al., 2019; Ma et al., 2021).

The southeastern part of the CAOB is a key area for exploring the Paleozoic tectonic evolution of this orogenic belt, as it contains numerous ophiolite belts, including the Erenhot–Hegenshan ophiolite belt (EHOB), Linxi belt, and Xar Moron River belt (XMRB), which are thought to mark the location of final closure of the Paleo-Asian Ocean (PAO) (Wang and Liu, 1986; Tang, 1990; BGMRIMAR, 1996; Xiao et al., 2003; Song et al., 2015; Yuri et al., 2020) (Figures 1B, C). Although the EHOB is traditionally considered to have formed in a mid-ocean ridge basalts (MORB) (Nozaka and Liu, 2002), the formation of most Inner Mongolia ophiolites is ascribed to a supra-subduction zone (SSZ) environment on the basis of the geochemistry of their magmatic rocks (e.g., Shervais, 2001). Such ophiolites include the Neo-Tethyan ophiolite in SW Turkey (Aldanmaz et al., 2009) and the Troodos ophiolite in Cyprus (Osozawa et al., 2012).

Two models have been proposed for the late Paleozoic evolution of the PAO. Some studies have suggested that continuous subduction of the Paleo-Asian oceanic plate induced multiple accretion events on the Uliastai continental margin (UCM) and the northern margin of the Sino-Korean paleoplate during the Paleozoic. The collision of two paleoplates along the Solonker–Linxi or Xar Moron River belts led to the final formation of the CAOB during the late Permian or Early Triassic (Windley, 1993; Xiao et al., 2003; Cheng et al., 2014, 2015). Other studies have argued that the PAO closed during the early or middle Paleozoic along the EHB or the Xilin Hot–Heihe suture zone and that the Carboniferous and Permian ophiolites in the area formed in a rift setting (Xu et al., 2013; Zhao et al., 2015). The main difference between the two models is whether the southeastern PAO was in a subduction or extensional tectonic setting during the late Paleozoic.

During recent work, we identified early Permian gabbro fragments in the Diyanmiao ophiolitic mélange of southeastern Inner Mongolia. These fragments represent northward subduction of the Paleo-Asian oceanic plate beneath the southern margin of the Siberian plate and formed after the early Carboniferous–early Permian (Li et al., 2018) (Figure 2). In this paper, we combine new data on the petrology, geochronology, and geochemistry of gabbro from the Diyanmiao ophiolite with results of previous studies in this area to establish the evolution of the PAO during the late Carboniferous and early Permian.

2 Geological setting

Five NEE–SWW-trending tectonic zones have been identified in southeastern Inner Mongolia: the Southern orogenic belt, the Solonker suture zone, the Northern orogenic belt (NOB), the EHOB, and the UCM from south to north (Figure 1B) (Xiao et al., 2003; Jian et al., 2012).

The UCM contains post-collisional basalts, andesites, and pyroclastic deposits of late Carboniferous–Permian age. These volcanic–sedimentary sequences overlie Cambrian to Devonian shallow-marine and continental fine clastic rocks (Zhang et al., 2011; Li et al., 2014; Anas et al., 2020). The EHOB lies to the south of the UCM and is characterized by numerous ophiolite slices, including the Hegenshan, Baiyinbulage, and Diyanmiao ophiolites from west to east (Li et al., 2015), which are enclosed in Carboniferous–Permian flysch (Wang and Liu, 1986; Liang, 1991). The EHOB extends from Erenhot, close to the China–Mongolia border, in the southwest to Hegenshan in the northeast. The EHOB is separated from the NOB to the south by the Solonker suture zone (Figure 1B). The NOB comprises the Xilin Gol and Baolidao Arc complexes (Xiao et al., 2003). The Xilin Gol complex, which is thought to represent Precambrian basement (e.g., Ge et al., 2011; Sun et al., 2013), consists mainly of biotite and muscovite schists, quartz–feldspar gneisses, and plagioclase amphibolites (Xiao et al., 2003; Chen et al., 2009). This complex is unconformably overlain by a cover of late Carboniferous

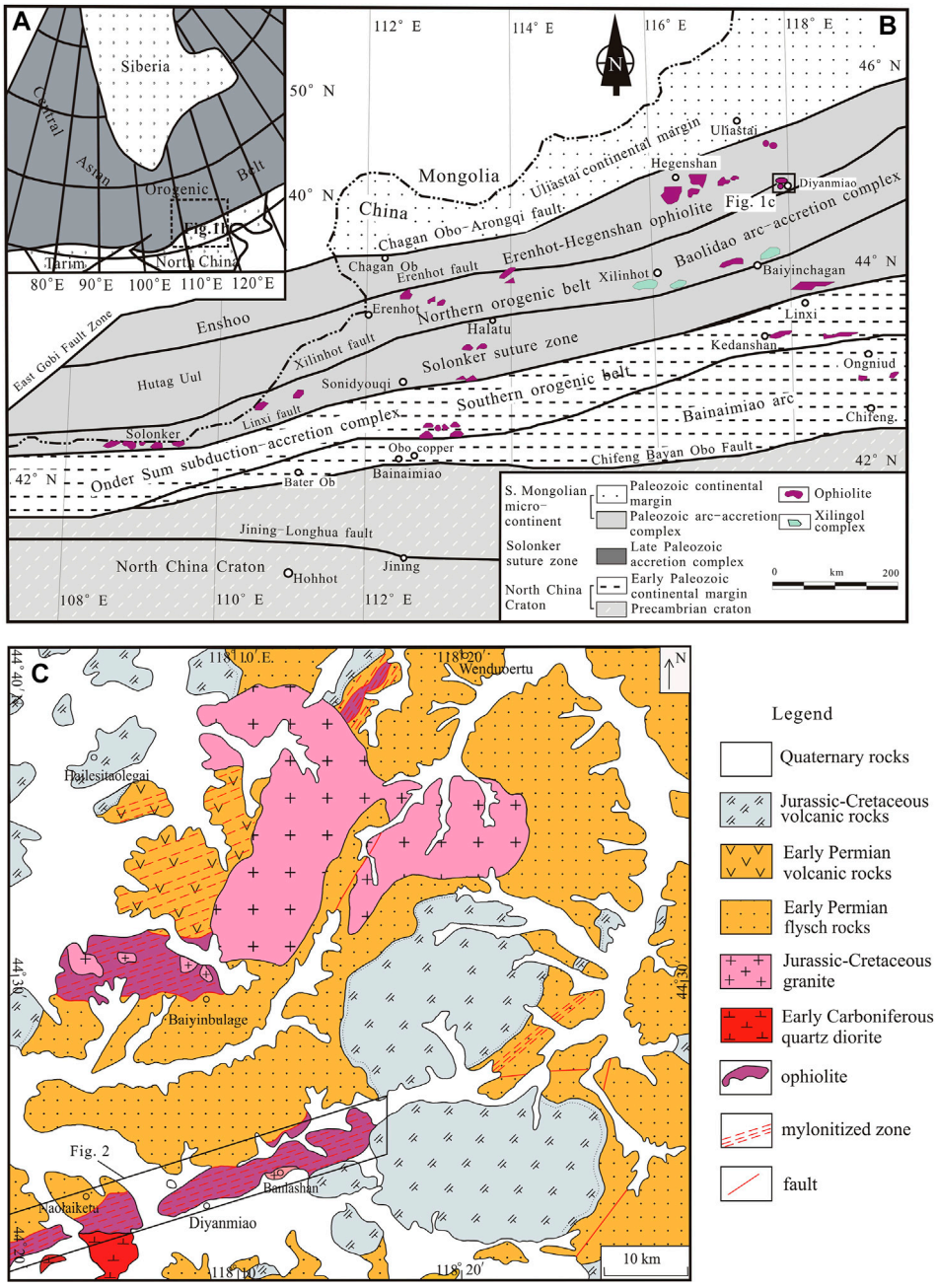


FIGURE 1
(A) Schematic tectonic division of north China-Mongolia segment (modified from Jahn, 2004). **(B)** Sketch geological map of the late Paleozoic crust of southeastern Inner Mongolia (modified from Xiao et al., 2003). **(C)** Simplified geological map of the Diyanmiao area (modified after Li et al., 2020a).

and Permian marine strata (Li et al., 2018). The Baolidao Arc complex, which extends from Bayanbaolidao to Xilinhot, is composed of cumulate gabbros, gabbro diorites, quartz diorites, tonalites, and granites, and represents a magmatic arc formed by northward seafloor subduction (Xiao et al., 2003, 2009; Jian et al., 2008).

3 Field and petrographic features

The Diyanmiao ophiolite is located in West Ujimqin, eastern Inner Mongolia (Figure 1B), and is divided into the Naolaiketu ophiolite to the south and the Baiyinbulage ophiolite to the north (Li et al., 2018; 2020a). The

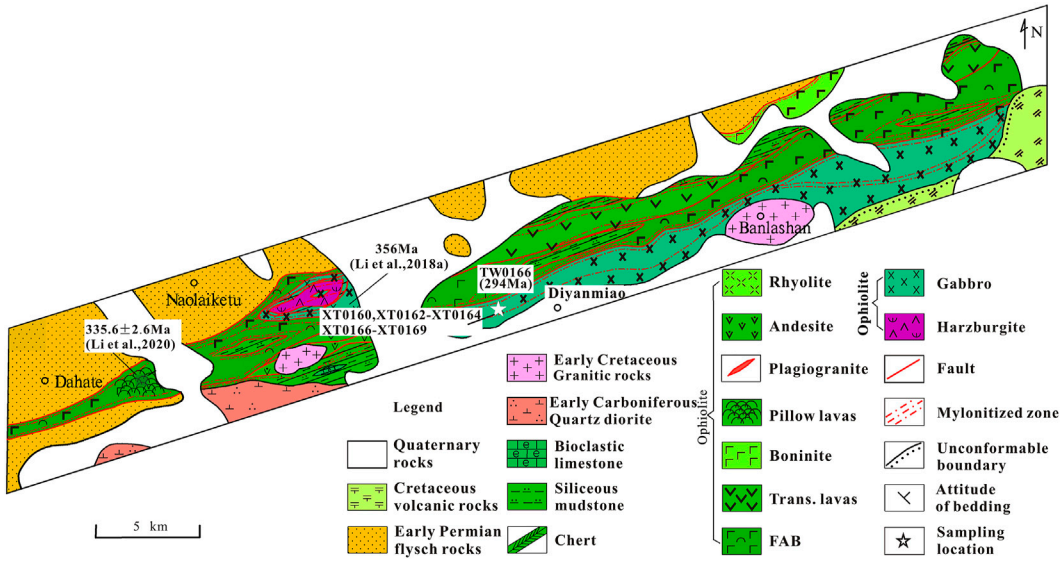


FIGURE 2
Simplified geological map of the Naolaiketu ophiolite in Diyanmiao (modified after Li et al., 2020a).

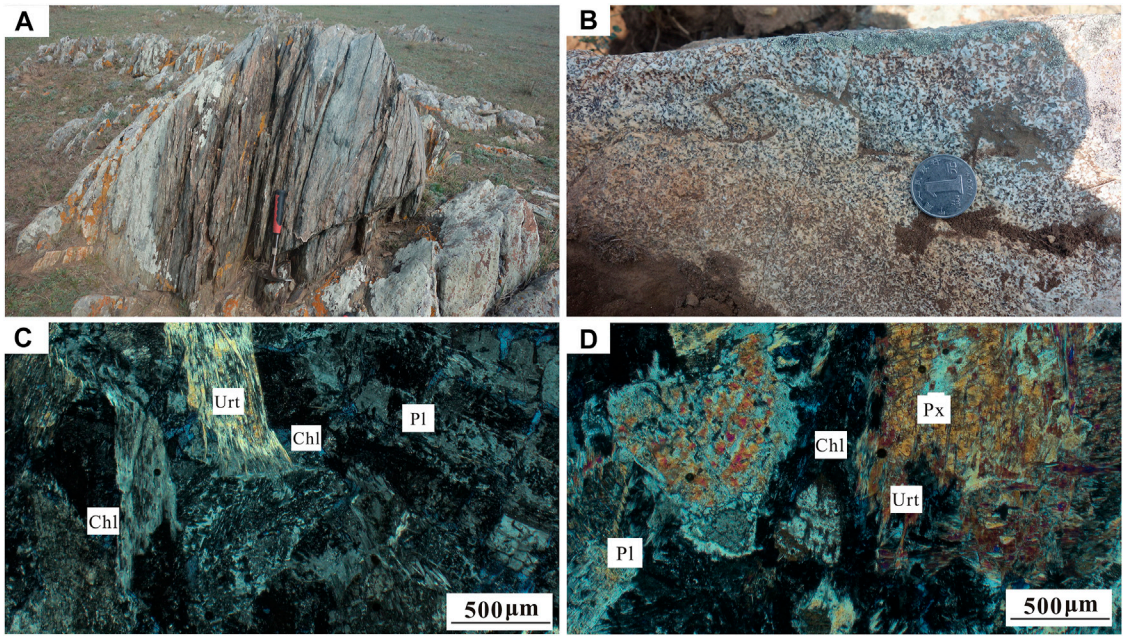


FIGURE 3
Macrofeatures and photomicrographs of the gabbro in Diyanmiao ophiolite. **(A)**-outcrop of gabbro; **(B)**-hand specimen of gabbro; **(C,D)**-photomicrographs of gabbro; Pl, plagioclase; Px, pyroxene; Chl, chlorite; Urt, uralite.

Naolaiketu ophiolite is exposed in the Naolaiketu–Diyanmiao area as an ENE–WSW-trending belt with a width of ~3 km and length of ~28 km. In the ophiolite belt, well-developed ductile deformation is shown by the development of folds, ENE–WSW-trending stretching lineations, and mylonitic microstructures, as well as domains with strongly developed rhombic-meshed structure and weakly deformed domains. The lithological units comprise serpentinized

harzburgite, layered gabbro, fine-grained isotropic gabbro, spilite, basalt, and quartz keratophyres, from bottom to top, and are overlain by chert. Of these, spillite and fine-grained isotropic gabbro are the most widely exposed. At the site of fault contact of the ophiolite and early Permian strata (Shoushangou and Dashizhai formations), well-developed brittle deformation structures are observed, including cleavages and cataclasite bands. Compressed and fragmented belts of ophiolite range in width from several meters to hundreds of meters.

For this study, samples of fine-grained isotropic gabbro (Figure 2) were obtained for geochemical and geochronological analyses (Figures 3A, B). The gabbro mainly consists of fine-grained, tabular plagioclase (40–45 vol%) and granular pyroxene (35–40 vol%), with minor magnetite and ilmenite (~5 vol%). The rock shows hypidiomorphic and granular textures under the microscope (Figures 3C, D). The rocks have been strongly altered, including replacement of plagioclase by zoisite and pyroxene by uralite.

4 Analytical techniques

4.1 *In situ* zircon U–Pb dating

One sample of gabbro (TW0166) was selected for *in situ* zircon U–Pb dating. Zircon grains were separated by crushing, sieving, and standard heavy-liquid techniques, followed by hand-picking under a binocular microscope at the Laboratory of Regional Geology and Mineral Resources Research Institute of Hebei Province, Langfang, China. The separated zircons were mounted in epoxy resin discs and polished to expose the grain interiors for analyses. Transmitted- and reflected-light photomicrographs, as well as cathodoluminescence (CL) images, were obtained to reveal zircon internal structure. CL images were acquired using a scanning electron microscope (JSM6510) equipped with a GATAN CL instrument at Beijing Gaonianlinghang Geo Analysis, Beijing, China.

Zircon U–Pb dating was performed using laser-ablation–multi-collector–inductively coupled plasma–mass spectrometry (LA–MC–ICP–MS) at the Tianjin Institute of Geology and Mineral Resources, China. The instrumental conditions and analytical processes were similar to those described by Liu et al. (2008). Operating conditions included a laser spot diameter of 32 μm and a laser frequency of 7 Hz. Contents of U and Pb were calibrated by using the standard zircon TEMORA (417 Ma), while zircon GJ-1 (597 Ma) was used as the external standard. The Excel-based software ICPMSDataCal program (Liu et al., 2008) was used to calculate U and Th contents and U–Pb dating results, including calibrations, and the ISOPLOT 4.15 program (Ludwig, 2003) was used to plot results.

4.2 Whole-rock major and trace element analyses

We selected eight representative samples of the gabbro for bulk-rock major- and trace-element analyses at the Tianjin Geological Survey Center of China Geological Survey, China. Major elements were analyzed using X-ray fluorescence (XRF) spectrometry (Rigaku 3270E) with high-dispersion Echelle optics. Analyses of Chinese national standard rock samples GSR-1, GSR-2, and GSR-3 revealed that the analytical precision is generally better than ±2% for most major elements.

Bulk-rock trace-element analyses were performed using ICP–MS at the Tianjin Geological Survey Center of China Geological Survey following the analytical procedure of Liu et al. (2008). The analytical precision for most trace elements is better than 5%, as monitored by analyses of Chinese national standard samples GSR-1 and GSR-3. The analytical precision was better than ±5% for trace elements.

4.3 Sr and Nd isotopes

Sr and Nd isotope ratios were measured for 12 samples using a Thermo-Finnigan VG Sector 54 thermal ionization mass spectrometer at the Tianjin Geological Survey Center of China Geological Survey following the analytical procedures described by Miao et al. (2008). Ratios of $^{87}Rb/^{86}Sr$ and $^{147}Sm/^{144}Nd$ were calculated using the Rb, Sr, Sm, and Nd contents determined by ICP–MS. The mass fractionation corrections for isotopic ratios were measured using a value of 0.1194 for $^{86}Sr/^{88}Sr$ and 0.7219 for $^{146}Nd/^{144}Nd$. The USGS rock standard BCR-2 was used to evaluate the separation and purification process of Rb, Sr, Sm, and Nd, yielding $^{87}Sr/^{86}Sr = 0.704963 \pm 0.000003$ and $^{143}Nd/^{144}Nd = 0.512354 \pm 0.000004$.

5 Analytical results

5.1 Zircon U–Pb geochronology

Zircon CL images from the fine-grained isotropic gabbro sample TW0166 are shown in Figure 4, and zircon U–Pb isotope data are given in Table 1. Most of the zircons are clear, euhedral, and short or granular prismatic crystals with lengths of 50–100 μm and aspect ratios of 1:1 to 2:1. The grains show well-developed straight and wide oscillatory zoning in CL images, consistent with mafic volcanic or gabbroic rocks (Song et al., 2015).

Fifteen spots were analyzed on 15 zircon grains from sample TW0166. Contents of Th and U and Th/U ratios of the zircons are 14–354 ppm, 40–399 ppm, and 0.73–4.67, respectively. All ages show concordance on a $^{206}Pb/^{238}U$–$^{207}Pb/^{235}U$ concordia diagram (Figure 4). The analytical result yield a weighted

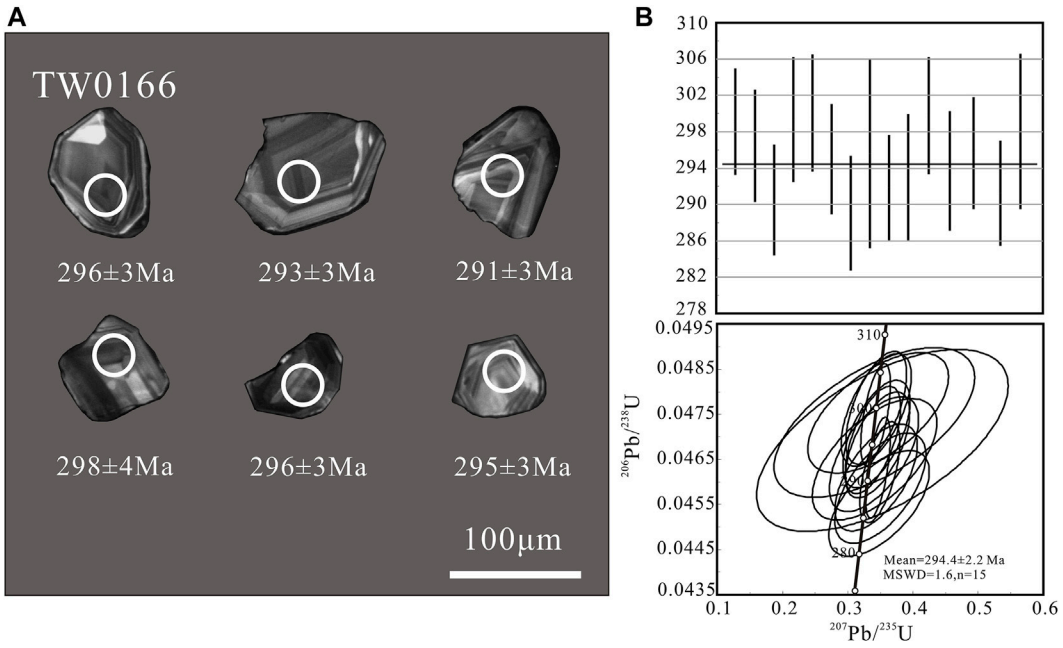


FIGURE 4
(A) Representative cathodoluminescence (CL) images of zircons from gabbro sample TW0166 **(B)** Zircon U-Pb concordia diagrams and weighed mean age for the gabbro sample TW0166.

mean $^{206}Pb/^{238}U$ age of 294.4 ± 2.2 Ma (MSWD = 1.6, 2σ), which is interpreted as the crystallization age of the gabbro.

5.2 Major and trace element compositions

The Diyanmiao gabbro samples have SiO_2 = 46.94–50.51 wt% (mean = 48.62 wt%) and MgO = 7.56–10.02 wt% (mean = 8.88 wt%), with $Mg^{\#}$ values of 65.0–75.6 (mean = 70.3). The samples are characterized by high contents of Al_2O_3 (14.26–17.53 wt%) and CaO (9.92–14.61 wt%), but low contents of $Fe_2O_3^T$ (as FeO + Fe_2O_3, 5.53–8.31 wt%), TiO_2 (0.26–0.54 wt%), MnO (0.12–0.17 wt%), and P_2O_5 (0.01–0.04 wt%). The gabbro samples also have low contents of total rare Earth elements (REEs) (∑REEs) (10.76–20.68 ppm, mean = 15.98 ppm) and low ratios of light REEs to heavy REEs (LREE/HREE) (0.97–1.31), $(La/Yb)_N$ (0.47–0.89), $(Gd/Yb)_N$ (0.91–1.07), $(La/Sm)_N$ (0.56–0.99), and $(Sm/Nd)_N$ (1.12–1.28). But positive Eu anomalies (Eu/Eu* = 1.12–1.53), similar to the characteristics of N-MORB, including flat REE patterns (Table 2; Figure 5A). In a primitive-mantle-normalized spider diagram (Figure 5B), the gabbros show positive Rb, K, and Sr anomalies and negative Th, Ta, Zr, and Nb anomalies. Depletion in Nb relative to La and Th indicates the involvement of continental crust or arc materials during magmatic evolution (e.g., Santosh et al., 2017).

5.3 Sr and Nd isotopic compositions

The Diyanmiao gabbros show high ε_{Nd} (t = 294.4 Ma) values (+8.0 to +9.8). The ε_{Nd} (t) values are similar to FABs of the Diyanmiao ophiolite (Table 3; Figure 6). In contrast, the gabbros have lower $^{87}Sr/^{86}Sr$ values (0.702934–0.703131) compared with the FABs (0.70466–0.70517) (Figure 6; Table 3), which might be due to alteration, given the high mobility Figure 7 of Rb and Sr.

6 Discussion

6.1 Geochronology of the gabbro in Diyanmiao ophiolite

Previous zircon U–Pb analyses of gabbro from the Diyanmiao ophiolite have yielded ages of 346 ± 2, 357 ± 4, and 340 ± 14 Ma (Song et al., 2015; Li et al., 2018), and Diyanmiao FAB has LA-ICP-MS zircon U-Pb age of 335.6 ± 2.6 Ma (Li et al., 2020a). Previous studies have reported SHRIMP U–Pb ages of 354 ± 7 Ma and 333 ± 4 Ma for microgabbro and plagiogranite from the Hegenshan ophiolite, respectively (Jian et al., 2012), 354 ± 5 Ma and 353 ± 4 Ma for gabbro and 345 ± 6 Ma for plagiogranite from the Eastern Erenhot ophiolite (Zhang et al., 2015), and 343 ± 7 Ma for plagiogranite from the Jiaoqier ophiolite (Miao et al., 2007).

TABLE 1 LA-MC-ICP-MS zircon U-Pb isotopic analysis of the gabbro in Diyanmiao ophiolite.

Spots no.	Element (ppm)		Th/U	Isotopic ratios						Apparent age (Ma)					
	Th	U		$^{206}Pb/^{238}U$	1σ	$^{207}Pb/^{235}U$	1σ	$^{207}Pb/^{206}Pb$	1σ	$^{206}Pb/^{238}U$	1σ	$^{207}Pb/^{235}U$	1σ	$^{207}Pb/^{206}Pb$	1σ
TW0166 Gabbro															
01	354	340	1.04	0.0475	0.0005	0.3425	0.0093	0.0523	0.0014	299	3	299	8	299	61
02	98	122	0.80	0.0471	0.0005	0.3439	0.0210	0.0530	0.0032	296	3	300	18	328	139
03	131	102	1.28	0.0461	0.0005	0.3434	0.0258	0.0540	0.0041	291	3	300	22	372	171
04	16	74	0.22	0.0475	0.0005	0.3465	0.0442	0.0529	0.0069	299	3	302	38	323	294
05	65	138	0.47	0.0476	0.0005	0.3435	0.0190	0.0523	0.0029	300	3	300	17	298	125
06	83	159	0.52	0.0468	0.0005	0.3455	0.0201	0.0535	0.0031	295	3	301	18	351	129
07	308	135	2.28	0.0459	0.0005	0.3500	0.0285	0.0553	0.0045	289	3	305	25	426	183
08	156	399	0.39	0.0463	0.0005	0.3461	0.0077	0.0542	0.0012	292	3	302	7	379	49
09	22	78	0.28	0.0465	0.0006	0.3411	0.0391	0.0532	0.0062	293	3	298	34	337	262
10	50	125	0.40	0.0476	0.0005	0.3435	0.0220	0.0523	0.0033	300	3	300	19	300	145
11	36	87	0.41	0.0466	0.0005	0.3400	0.0279	0.0529	0.0044	294	3	297	24	324	188
12	14	178	0.08	0.0469	0.0005	0.3385	0.0174	0.0523	0.0027	296	3	296	15	299	116
13	215	239	0.90	0.0455	0.0005	0.3479	0.0314	0.0554	0.0049	287	3	303	27	429	198
14	281	335	0.84	0.0462	0.0005	0.3490	0.0125	0.0548	0.0019	291	3	304	11	403	80
15	21	40	0.52	0.0473	0.0007	0.3407	0.0629	0.0522	0.0097	298	4	298	55	295	422

10.3389/feart.2022.1031842

TABLE 2 Major (wt%), trace element (×I0^{-6}) analyzing results of the gabbro in Diyanmiao ophiolite and N-MORB.

Rock type	Gabbro								N-MORB
Sample NO.	XT0160	XT0162	XT0163	XT0164	XT0166	XT0167	XT0168	XT0169	
SiO_2	47.75	48.38	49.10	50.51	46.94	48.92	50.07	47.32	49.30
Al_2O_3	16.68	16.56	16.94	17.53	16.88	15.26	14.26	15.11	17.04
$Fe_2O_3^T$	8.74	8.00	8.04	7.27	5.86	6.99	6.67	7.23	6.82
CaO	12.11	11.03	10.14	9.92	15.70	13.47	14.50	14.61	11.70
MgO	8.24	8.04	8.23	7.56	9.19	10.02	9.92	9.86	7.19
K_2O	0.75	0.26	0.25	0.27	0.04	0.05	0.04	0.09	0.16
Na_2O	2.19	4.52	3.78	3.65	2.39	1.84	1.84	2.59	2.73
TiO_2	0.54	0.48	0.51	0.51	0.26	0.44	0.35	0.47	1.49
P_2O_5	0.04	0.03	0.03	0.03	0.02	0.02	0.01	0.03	0.16
MnO	0.15	0.13	0.14	0.12	0.12	0.16	0.17	0.17	0.17
LOI	2.75	2.44	2.78	2.57	2.58	2.57	2.12	2.49	
Na_2O/K_2O	2.92	17.38	15.12	13.52	58.29	40.00	48.42	30.47	17.06
$Mg^{\#}$	65.00	66.48	66.84	67.2	75.56	73.84	74.53	72.88	65.27
Rb	10	8	8	8	5	5	5	5	0.56
Cr	352	296	348	318	581	769	646	612	
Co	37	32.1	36.3	33	32.1	38.2	35.8	31.3	
Ni	115	125	148	136	107	96.7	103	99.9	
Sc	34.8	28	36	28.1	37	68	43.6	41.4	
V	193	138	157	143	154	238	214	208	
Zr	20.1	15.6	14.8	15.4	4.23	11.8	7.48	13.7	74
Hf	0.75	0.6	0.58	0.6	0.21	0.54	0.3	0.55	2.05
Rock type	Gabbro								N-MORB
Sample NO.	XT0160	XT0162	XT0163	XT0164	XT0166	XT0167	XT0168	XT0169	
Ta	0.04	0.04	0.04	0.04	0.03	0.03	0.03	0.03	0.13
Sr	122	138	143	152	141	117	112	127	90
Ba	45.1	68.2	74.3	94.9	41.8	58.4	43.6	43.7	6.3
Nb	1.06	0.82	0.79	0.96	0.84	1.06	1.02	0.86	2.33
Cs	0.78	0.7	0.77	0.78	0.45	0.54	0.42	0.72	0.01
Ga	15.2	13.1	14.4	14	10.9	14.2	10.2	12.4	
Pb	3.07	3.07	2.9	2.77	5.54	3.29	3.17	3.31	0.3
Th	0.05	0.04	0.04	0.03	0.03	0.10	0.14	0.06	0.12
U	0.05	0.04	0.05	0.04	0.05	0.03	0.03	0.04	0.05
Y	14.3	10.6	11.1	10.6	7.62	13.1	10.3	10.9	28
La	1.47	1.32	1.35	1.27	0.96	1.08	1.57	1.30	2.50
Ce	3.18	2.55	2.62	2.41	1.52	2.23	1.63	2.47	7.50

(Continued on following page)

TABLE 2 (*Continued*) Major (wt%), trace element (×10^{-6}) analyzing results of the gabbro in Diyanmiao ophiolite and N-MORB.

Rock type	Gabbro								N-MORB
Sample NO.	XT0160	XT0162	XT0163	XT0164	XT0166	XT0167	XT0168	XT0169	
Pr	0.67	0.55	0.57	0.52	0.33	0.48	0.5	0.47	1.32
Nd	3.80	3.07	3.15	2.91	1.82	2.89	2.58	2.73	7.30
Sm	1.46	1.15	1.15	1.07	0.73	1.21	0.99	1.07	2.63
Eu	0.75	0.54	0.6	0.57	0.43	0.56	0.49	0.49	1.02
Gd	2.05	1.54	1.7	1.6	1.01	1.89	1.44	1.54	3.68
Tb	0.38	0.3	0.31	0.3	0.2	0.36	0.29	0.3	0.67
Dy	2.53	1.96	2.08	1.93	1.39	2.42	1.98	2.03	4.55
Ho	0.56	0.42	0.46	0.43	0.31	0.53	0.42	0.44	1.01
Er	1.62	1.2	1.31	1.18	0.90	1.50	1.20	1.27	2.97
Tm	0.25	0.18	0.20	0.18	0.14	0.22	0.18	0.19	0.46
Yb	1.69	1.22	1.30	1.20	0.89	1.52	1.18	1.23	3.05
Lu	0.27	0.18	0.20	0.18	0.13	0.24	0.18	0.19	0.46
∑REE	20.68	16.18	17	15.75	10.76	17.13	14.63	15.72	39.11
LREE	11.33	9.18	9.44	8.75	5.79	8.45	7.76	8.53	22.27
HREE	9.35	7.00	7.56	7.00	4.97	8.68	6.87	7.19	16.84
LREE/HREE	1.21	1.31	1.25	1.25	1.16	0.97	1.13	1.19	1.32
$(La/Yb)_N$	0.59	0.73	0.70	0.71	0.73	0.48	0.90	0.71	0.59
δEu	1.33	1.24	1.31	1.33	1.53	1.13	1.25	1.17	1.00

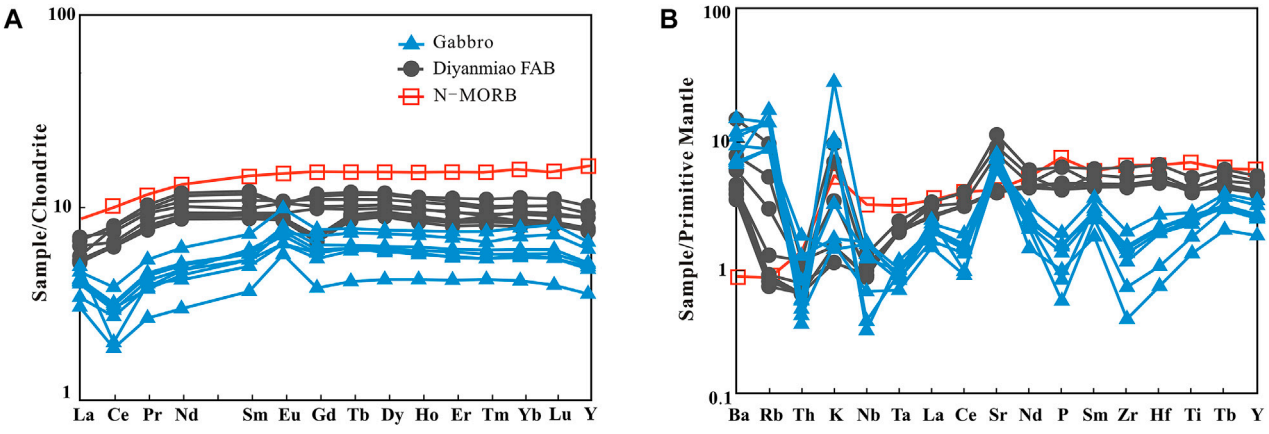


FIGURE 5
(A) Chondrite-normalized REE (Boynton, 1984)and **(B)** trace element patterns (Sun and McDonough, 1989) for the gabbro and fore-arc basalt (FAB) in the Diyanmiao ophiolite. Data of Diyanmiao FAB is after (Li et al., 2020a). N-MORB values are after Sun and McDonough, 1989.

The EHOB is considered to be a giant ophiolitic complex that developed during the Carboniferous (Wang and Liu, 1986; Tang, 1990; Song et al., 2015). Li et al. (2018) suggested that the Erenhot–Hegenshan paleo-ocean underwent intra-oceanic subduction, resulting in the formation of incipient arc crust during the early Carboniferous. The structural location

TABLE 3 Sr–Nd isotopic compositions of the gabbro in Diyanmiao ophiolite.

Sample	Age	$^{87}Rb/^{86}Sr$	$^{87}Sr/^{86}Sr$	2δ*	$(^{87}Sr/86Sr)i$	$^{147}Sm/^{144}Nd$	$^{143}Nd/^{144}Nd$	2δ	ε_{Nd} (*t*)
Gabbro									
XT0166	294	0.1026	0.703131	0.000007	0.7028	0.2425	0.513092	0.000001	8.0
XT0167	293	0.1236	0.703052	0.000009	0.7027	0.2532	0.513206	0.000001	9.8
XT0168	295	0.1291	0.702934	0.000007	0.7025	0.2320	0.513128	0.000001	9.1
XT0169	295	0.1139	0.702975	0.000008	0.7026	0.2370	0.513174	0.000001	9.8

[87]Note: (1) $(^{87}Sr/^{86}Sr)_i = Sr/^{86}Sr - ^{87}Rb/^{86}Sr \times (e^{\lambda T}-1)$, where $\lambda_{Rb} = 1.42 \times 10^{-11} year^{-1}$. (2) $\varepsilon_{Nd}(t) = \{[^{143}Nd/^{144}Nd - ^{147}Sm/^{144}Nd \times (e^{\lambda T}-1)]/[^{143}Nd/^{144}Nd]_{CHUR(0)} - (^{147}Sm/^{144}Nd)_{CHUR(0)} \times (e^{\lambda T}-1) - 1\} \times 10{,}000$, where $\lambda_{Sm} = 6.54 \times 10^{-12} year^{-1}$; $(^{143}Nd/^{144}Nd)_{CHUR(0)} = 0.512638$; $(^{147}Sm/^{144}Nd)_{CHUR(0)} = 0.1967$.

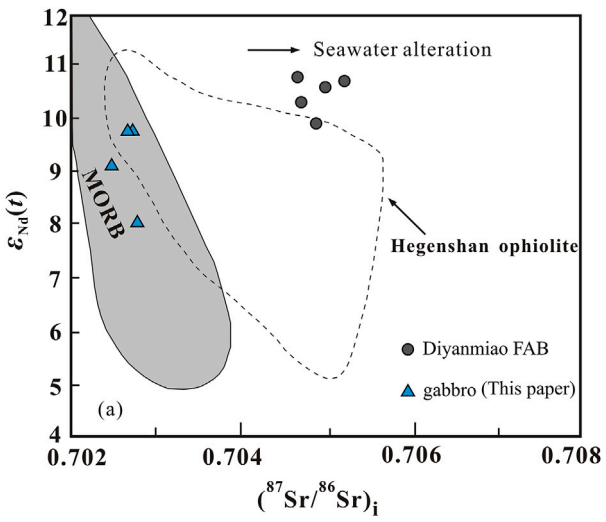


FIGURE 6
Isotopic plot of whole-rock ε_{Nd} (*t*) vs. $(^{87}Sr/^{86}Sr)_i$ for the gabbro in the Diyanmiao ophiolite; Data sources: Miao et al. (2008) for the field of Hegenshan ophiolite; Li et al. (2020a) for Diyanmiao FAB.

between the early Permian Shoushangou and Dashizhai formations indicates that the tectonic emplacement of the Diyanmiao ophiolite occurred after the early Permian.

The new LA–MC–ICP–MS zircon U–Pb age of 294.4 ± 2.2 Ma obtained from the Diyanmiao gabbro in this study gives an early Permian age for the Diyanmiao ophiolite. The age distribution of magmatic rocks of the Diyanmiao ophiolitic mélange indicates that the mélange includes rocks corresponding to at least two magmatic events, which provides important evidence regarding the timing of closure of the PAO.

6.2 Petrogenesis of the gabbro in Diyanmiao ophiolite

The studied gabbro samples show high LOI values (2.12–2.78 wt%), indicating variable alteration (Li et al., 2018), and some of the major elements (e.g., Si, Ca, K, and Ba) and trace elements (Cs and Rb) may have been mobilized to variable extents during post-magmatic hydrothermal alteration or metamorphism (Gillis and Banerjee, 2000). In contrast, some transition elements (e.g., Cr, Ti, Ni, and V), Th, high-field-strength elements (HFSEs), and REEs (Pearce, 1983) are considered to be relatively immobile during hydrothermal seafloor alteration and low-grade metamorphism (Pearce, 2008). Consequently, the following discussion of petrogenesis is based mainly on the transition elements, HFSEs, and REEs.

Although there are differences in the major element contents between the Diyanmiao gabbros and FABs, the compositional signatures of REEs, HFSEs, and large-ion lithophile elements (LILEs) are similar (Figure 5; Li et al., 2020a), suggesting a similar origin. The major-element compositions of the gabbros are similar to those of N-MORB, while the gabbros show a depleted REE pattern, indicating that their source more depleted than N-MORB source region. In comparison with N-MORB, the gabbros have variable enrichment in Rb, Ba, and K, and depletion in Nb, Ta, Zr, and Ti (Figure 5B), consistent with the characteristics of island-arc tholeiite in a subduction zone, suggesting the involvement of subduction fluids.

In a Th–Hf–Ta diagram, five gabbro samples plot in the N-MORB field, and two plots on or near the boundary between N-MORB and tholeiitic basalt (Figure 7A). In an Nb/Yb vs Th/Yb discrimination diagram, three gabbro samples plot within the weak subduction field, and four plots in the N-MORB field (Figure 7B). These results reveal a subduction-related signature for the gabbros. The gabbros also display a depletion trend relative to the estimated bulk mantle composition, as well as a Th enrichment trend in the volcanic arc field (Figure 7A), which is consistent with rock genetic models for the initial stages of the evolution of ensimatic marginal basins (Pearce et al., 1984). The Nb/La values of gabbro is 0.58–0.98 (mean=0.73), which is higher than the mean value of continental crust (Nb/La mean=0.7), but the crystallization differentiation does not lead to a decrease in Nb/La (Zhao et al., 1997). Therefore, the original magma of the Diyanmiao gabbro likely evolved by fluid metasomatism in an island-arc setting during oceanic subduction, rather than by crystallization and differentiation processes.

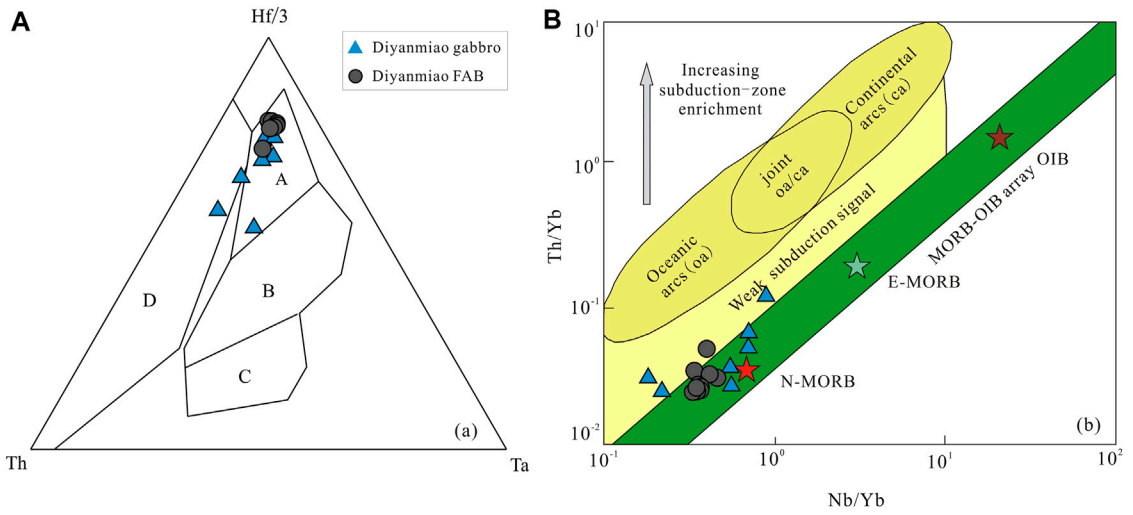


FIGURE 7
(A) Th-Hf-Ta diagram and **(B)** Th/Yb-Nb/Yb diagram for the gabbro and FAB in the Diyanmiao ophiolite. Data for FAB from Li et al., 2020a.

6.3 Tectonic implications of the gabbro: Constraints of intra-oceanic subduction in the southern Paleo-Asian ocean

The tectonic evolution of the CAOB is not yet fully resolved. This orogenic belt is thought to have formed by continuous accretion *via* multistage trench retreat or the simultaneous operation of multiple subduction zones (e.g., Xiao et al., 2009; Kröner et al., 2017). However, other studies have argued that the belt was formed by a series of orogenic processes involving collision, prolonged post-collisional stratification, and extension, with the PAO closing during the late Carboniferous–early Permian (e.g., Jahn et al., 2009; Han et al., 2011).

Uncertainty remains concerning the tectonic evolution of the EHOB, including the formation of the Hegenshan ophiolite, despite the efforts of many studies (e.g., Tang and Yan, 1993; Robinson et al., 1999; Xiao et al., 2003, 2009; Jian et al., 2008, 2010; Miao et al., 2008; Zhang et al., 2011; Eizenhöfer et al., 2014, 2015; Song et al., 2015). Some studies have proposed that the Hegenshan ophiolite formed in a mid-ocean-ridge environment (e.g., Nozaka and Liu, 2002; Song et al., 2015). Other studies have considered that the Hegenshan ophiolite formed in an SSZ environment, such as a back-arc tectonic environment (Miao et al., 2008; Wang et al., 2008; Eizenhöfer et al., 2014, 2015; Zhang et al., 2015) or an island arc–marginal basin system (Robinson et al., 1999).

The zircon U–Pb age of 294.4 ± 2.2 Ma obtained in this study for the Diyanmiao gabbro coincides with the formation age of late Carboniferous island-arc magmatic rocks in central Inner Mongolia that are found together with early Carboniferous Diyanmiao ophiolite (~340 Ma) (Li et al., 2018), forearc basalt (335.6 Ma), and boninite (~328 Ma) (Li et al., 2020a), and late Carboniferous adakite (315 Ma) (Wang et al., 2021). These results support the interpretation that the southern PAO had not closed by the early Permian but was undergoing intra-oceanic subduction. In other words, the late Carboniferous and early Permian ages record the initial stages of subduction of the Diyanmiao intra-oceanic arc within the southern PAO, with subsequent subduction of oceanic crust. On the basis of our field observations, geochemical data for the Diyanmiao ophiolite, and a comparison with the Izu–Bonin–Mariana initial subduction system (Ishizuka et al., 2014), we infer a model of subduction initiation in the Diyanmiao intra-oceanic arc during the early Carboniferous to early Permian. The initiation of early Carboniferous intra-oceanic subduction in the southeastern PAO began along a transform fault or fault zone (Li et al., 2020b) (Figure 8A). After the initial sinking of the slab, asthenospheric upwelling and decompression melting (Reagan et al., 2017) led to forearc spreading and the formation of the Diyanmiao FABs (335.6 Ma; Figure 8B; Li et al., 2020a; 2020b). As the subduction initiation process continued, leading to further decompression melting, boninites (328 Ma) were generated at this stage (Figure 8C). The newly discovered gabbro (294 Ma) may represent the magma event of the subducted plate at a greater depth (Figure 8D). The above information revealed that the initial subduction of intra-oceanic may have occurred in the eastern part of the Paleo-Asian Ocean from the early Carboniferous to the early Permian.

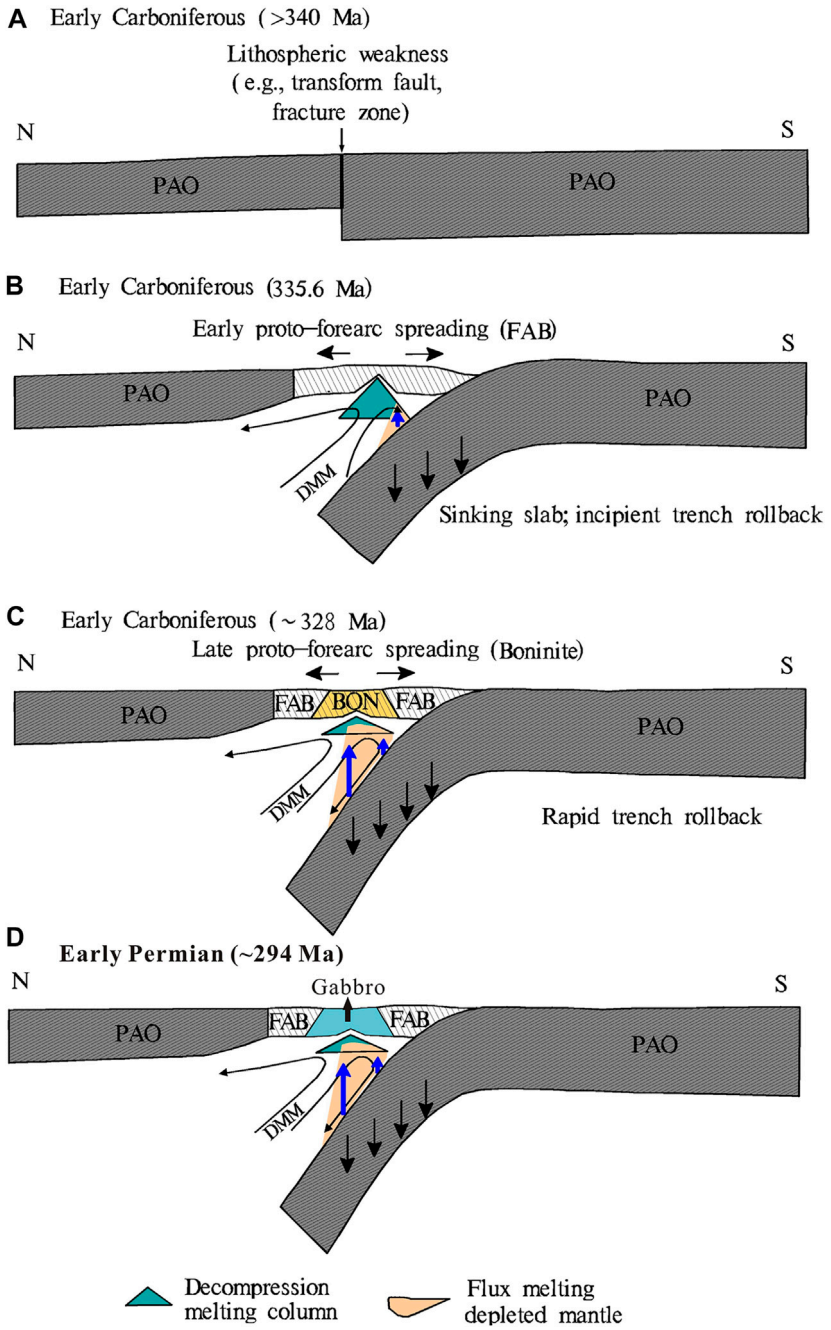


FIGURE 8
Evolution of the Early Carboniferous Diyanmiao intra-oceanic forearc system in the central Inner Mongolia, N China, as a typical example of subduction initiation of the southeastern PAO, based on the subduction infancy model (Whattam and Stern, 2011; Reagan et al., 2017). **(A)** Oceanic crust boundary preceding subduction initiation. **(B)** Early Carboniferous subduction initiation, leading to forearc spreading and formation of FABs. **(C)** As the subduction initiation process continued, boninites and transitional lavas were formed. **(D)** As the subduction process continued, the gabbro were formed. DMM is depleted MORB mantle.

The timing of the transformation of the PAO tectonic domain to the Paleo-Pacific tectonic domain has become an important Research Topic. Most studies have argued that the PAO tectonic system ended during the late Permian or Middle Triassic and continued locally through to the early Late Triassic (Xiao et al., 2003; Li, 2006; Wilde, 2015; Guo et al., 2016). Mao et al. (2020) proposed that late Permian to late Triassic igneous rocks on both sides of the Mongol–Okhotsk suture belt record an

active-continental-margin environment associated with bidirectional subduction of Mongol–Okhotsk oceanic lithosphere. Liang et al. (2021) argued that subduction of the Paleo-Pacific Plate began in the early Permian. Continued subduction triggered back-arc basin spreading during the early Permian–late Triassic (280–232 Ma). Closure of the basin resulted in the emplacement of accretionary materials in the Yuejinshan area during the late Triassic–early Jurassic (232–180 Ma), which also corresponds to the time of formation of high-pressure metamorphic belts on the southern margin of the Khanka Massif (230–220 Ma) and western margin of the Jiamusi Massif (210–180 Ma) (Zhou et al., 2014; Sun et al., 2015; Guo, 2016; Bi et al., 2017).

7 Conclusion

The geochemical characteristics of the Diyanmiao gabbro are similar to those of the Diyanmiao FABs. The gabbro is characterized by depletion in Nb, Ta, and Ti, similar to N-MORB, suggesting that the gabbro formed in a subduction setting in the Paleo-Asian Ocean. LA–MC–ICP–MS U–Pb dating of zircon grains from the Diyanmiao gabbro yielded an age of 294.4 ± 2.2 Ma, indicating that the gabbro from the Diyanmiao ophiolite formed during the early Permian. The initial subduction of intra-oceanic may have occurred in the eastern part of the Paleo-Asian Ocean from the early Carboniferous to the early Permian. Karimov et al., 2020, Shcherbakov et al., 2020, Xiao and Santosh, 2014.

Data availability statement

The original contributions presented in the study are included in the article/supplementary material, further inquiries can be directed to the corresponding author.

Author contributions

XZ: Investigation, Formal analysis, Visualization, Conceptualization, Supervision, Project administration, Funding acquisition, Writing—original draft, Writing—review & editing. YL: Supervision, Project administration, Funding acquisition. GW : Supervision, Project administration. SW: Project administration, Funding acquisition. XK: Project administration, Funding acquisition. XW: Project administration. ZL: Formal analysis, Funding acquisition.

Funding

This research was funded by the National Natural Science Foundation of China, Grant/Award Numbers: 41972061, China Geological Survey, Grant/Award Numbers: 1212011120711 and the Science and technology innovation team program of Hebei GEO University (KJCXTD-2021-07).

Conflict of interest

The authors declare that the research was conducted in the absence of any commercial or financial relationships that could be construed as a potential conflict of interest.

Publisher's note

All claims expressed in this article are solely those of the authors and do not necessarily represent those of their affiliated organizations, or those of the publisher, the editors and the reviewers. Any product that may be evaluated in this article, or claim that may be made by its manufacturer, is not guaranteed or endorsed by the publisher.

References

Aldanmaz, E., Schmidt, M. W., Gourgaud, A., and Meisel, T. (2009). Mid-ocean ridge and supra-subduction geochemical signatures in spinel-peridotites from the neotethyan ophiolites in sw Turkey: Implications for upper mantle melting processes. *Lithos* 113 (3-4), 691–708. doi:10.1016/j.lithos.2009.03.010

Badarch, G., Gunningham, W. D., and Windley, B. F. (2002). A new terrane subdivision for Mongolia: Implications for the phanerozoic crustal growth of central asia. *J. Asian Earth Sci.* 21, 87–110. doi:10.1016/s1367-9120(02)00017-2

Bgmrimar (1996). Lithostratigraphy of the inner mongolia autonomous region. *Bureau of geology and mineral Resources of inner Mongolia autonomous region*, Wuhan: China University of Geosciences Press, 1–344. (in Chinese with English abstract).

Bi, J. H., Ge, W. C., Yang, H., Wang, Z. H., Tian, D. X., Liu, X. W., et al. (2017). Geochemistry of MORB and OIB in the yuejinshan complex, NE China: Implications for petrogenesis and tectonic setting. *J. Asian Earth Sci.* 145, 475–493. doi:10.1016/j.jseaes.2017.06.025

Boynton, W. V. (1984). "Cosmochemistry of the rare earth elements: Meteorite studies," in *Rare earth element geochemistry. Developments in geochemistry*. Editor P. E. Henderson (Amsterdam: Elsevier), 63–114.

Chen, B., Jahn, B. M., and Tian, W. (2009). Evolution of the solonker suture zone: Constraints from zircon U-Pb ages, Hf isotopic ratios and whole-rock Nd-Sr isotope compositions of subduction-and collision-related magmas and forearc sediments. *J. Asian Earth Sci.* 34, 245–257. doi:10.1016/j.jseaes.2008.05.007

Cheng, Y. H., Duan, L. F., Wang, S. Y., Li, Y., Teng, X. J., and Zhang, T. F. (2019). Termination of the hegenshan orogen in the xing'an-Mongolian orogenic belt, north China: Geochemical and zircon U-Pb geochronological constraints from early permian mafic dykes. *Geol. J.* 55 (1), 845–861. doi:10.1002/gj.3463

Cheng, Y. H., Li, M., Zhang, T. F., Li, Y. F., Li, Y., Niu, W. C., et al. (2015). Late Paleozoic crustal extensional regime on the Southeastern Siberian Plate:new evidences from geochronology and geochemistry of the bojite in the Dong Ujimqi. *Acta Geol. Sin.* 89 (2), 262–271. (in Chinese with English abstract).

Cheng, Y. H., Teng, X. J., Li, Y. F., Li, M., and Zhang, T. F. (2014). Early permian east-ujimqin mafic–ultramafic and granitic rocks from the xing'an–Mongolian orogenic belt, north China: Origin, chronology, and tectonic implications. *JAES* 96, 361–373. doi:10.1016/j.jseaes.2014.09.027

Dilek, Y., and Furnes, H. (2011). Ophiolite Genesis and global tectonics: Geochemical and tectonic fingerprinting of ancient oceanic lithosphere. *Geol. Soc. Am. Bull.* 123, 387–411. doi:10.1130/b30446.1

Dilek, Y., and Furnes, H. (2014). Ophiolites and their origins. *Elements* 10, 93–100. doi:10.2113/gselements.10.2.93

Dilek, Y., and Furnes, H. (2009). Structure and geochemistry of Tethyan ophiolites and their petrogenesis in subduction rollback systems. *Lithos* 113, 1–20. doi:10.1016/j.lithos.2009.04.022

Dilek, Y., and Robinson, P. T. (2003). Ophiolites in Earth history: Introduction. *Geol. Soc. Lond. Special Publ.* 218 (1), 1–8. doi:10.1144/gsl.sp.2003.218.01.01

Dobretsov, N. L., Berzin, N. A., and Buslov, M. M. (1995). Opening and tectonic evolution of the paleo-Asian ocean. *Int. Geol. Rev.* 37, 335–360. doi:10.1080/00206819509465407

Eizenhöfer, P. R., Zhao, G., Sun, M., Zhang, J., Han, Y. G., and Hou, W. (2015). Geochronological and Hf isotopic variability of detrital zircons in Paleozoic strata across the accretionary collision zone between the North China craton and Mongolian arcs and tectonic implications. *Geol. Soc. Am. Bull.* 127, 1422–1436. doi:10.1130/b31175.1

Eizenhöfer, P. R., Zhao, G., Zhang, J., and Sun, M. (2014). Final closure of the paleo-Asian ocean along the solonker suture zone: Constraints from geochronological and geochemical data of permian volcanic and sedimentary rocks. *Tectonics* 33, 441–463. doi:10.1002/2013tc003357

Ge, M. C., Zhou, W. X., Yu, Y., Sun, J. J., Bao, J. Q., and Wang, S. H. (2011). Dissolution and supracrustal rocks dating of Xilin Gol complex, Inner Mongolia, China. *Earth Sci. Front.* 18 (5), 182–195.

Gillis, K. M., and Banerjee, N. R. (2000). "Hydrothermal alteration patterns in supra-subduction zone ophiolites," in *Special Paper of the Geological Society of America*. 349, Editors Y. Dilek and E. M. Moores, 283–297.

Guo, Y. (2016). *The nature of yuejinshan complex in the eastern part of heilongjiang Province and its evolution PhD thesis*. Jilin University. Changchun, China, (in Chinese with English abstract).

Han, B. F., He, G. Q., Wang, X. C., and Guo, Z. J. (2011). Late carboniferous collision between the Tarim and Kazakhstan-yili terranes in the Western segment of the south tian Shan orogen, central asia, and implications for the northern xinjiang, Western China. *Earth Sci. Rev.* 109, 74–93. doi:10.1016/j.earscirev.2011.09.001

Ishizuka, O., Tani, K., and Reagan, M. K. (2014). Izu-Bonin-Mariana forearc crust as a modern ophiolite analogue. *Elements* 10, 115–120. doi:10.2113/gselements.10.2.115

Jahn, B. M. (2004). The Central Asian Orogenic Belt and growth of the continental crust in the Phanerozoic. *Geological Society of London, Special Publication*, 226, 73–100, doi:10.1144/GSL.SP.2004.226.01.05

Jahn, B. M., Litvinovsky, B. A., Zanvilevich, A. N., and Reichow, M. (2009). Peralkaline granitoid magmatism in the Mongolian–Transbaikalian Belt: Evolution, petrogenesis and tectonic significance. *Lithos* 113, 521–539. doi:10.1016/j.lithos.2009.06.015

Jian, P., KrÖner, A., Windley, B. F., Shi, Y. R., Zhang, W., Zhang, L. Q., et al. (2012). Carboniferous and cretaceous mafic–ultramafic massifs in inner Mongolia (China): A SHRIMP zircon and geochemical study of the previously presumed integral "hegenshan ophiolite". *Lithos* 142 (143), 48–66. doi:10.1016/j.lithos.2012.03.007

Jian, P., Liu, D., KrÖner, A., Windley, B. F., Shi, Y., Zhang, F., et al. (2008). Time scale of an early to mid-paleozoic orogenic cycle of the long-lived central asian orogenic belt, inner Mongolia of China: Implications for continental growth. *Lithos* 101, 233–259. doi:10.1016/j.lithos.2007.07.005

Jian, P., Liu, D., Kroner, A., Windley, B. F., Shi, Y., Zhang, W., et al. (2010). Evolution of a permian intraoceanic arc-trench system in the solonker suture zone, central asian orogenic belt, China and Mongolia. *Lithos* 118, 169–190. doi:10.1016/j.lithos.2010.04.014

Karimov, A. A., Gornova, M. A., Belyaev, V. A., Ya Medvedev, A., V Bryanskiy, N., and V. Bryanskiy, N. (2020). Genesis of pyroxenite veins in supra-subduction zone peridotites: Evidence from petrography and mineral composition of Egiingol massif (Northern Mongolia). *China Geol.* 3, 299–313. doi:10.31035/cg2020035

Kröner, A., Kovach, V., Aledeiev, D., Wang, K. L., Wong, J., Degtyarev, K., et al. (2017). No excessive crustal growth in the central asian orogenic belt: Further evidence from field relationships and isotopic data. *Gondwana Res.* 50, 135–166. doi:10.1016/j.gr.2017.04.006

Kusky, T. M. (2011). Geophysical and geological tests of tectonic models of the North China Craton. *Gondwana Res.* 20 (1), 26–35. doi:10.1016/j.gr.2011.01.004

Li, J. Y. (2006). Permian geodynamic setting of northeast China and adjacent regions: Closure of the paleo-Asian ocean and subduction of the Paleo-Pacific Plate. *J. Asian Earth Sci.* 26, 207–224. doi:10.1016/j.jseaes.2005.09.001

Li, K., Zhang, Z. C., Feng, Z. S., Li, J. F., Tang, W. H., and Luo, Z. W. (2014). Zircon SHRIMP U-Pb dating and its geological significance of the Late-Carboniferous to Early-Permian volcanic rocks in Bayanwula area, the central of Inner Mongolia. *Acta Petrol. Sin.* 30 (7). (in press)(in Chinese with English abstract).

Li, Y. J., Wang, G. H., Santosh, M., Wang, J. F., Dong, P. P., and Li, H. Y. (2020a). Subduction initiation of the SE paleo-Asian ocean: Evidence from a well preserved intra-oceanic forearc ophiolite fragment in central inner Mongolia, north China. *Earth Planet. Sci. Lett.* 535 (1), 116087doi:10.1016/j.epsl.2020.116087

Li, Y. J., Wang, G. H., Santosh, M., Wang, J. F., Dong, P. P., and Li, H. Y. (2018). Supra-subduction zone ophiolites from inner Mongolia, north China: Implications for the tectonic history of the southeastern central asian orogenic belt. *Gondwana Res.* 59, 126–143. doi:10.1016/j.gr.2018.02.018

Li, Y. J., Wang, J. F., Li, H. Y., and Dong, P. P. (2015). Recognition of meilaotewula ophiolite in xi Ujimqin banner, inner Mongolia. *Acta Petrol. Sin.* 31 (5), 1461–1470. (in Chinese with English abstract).

Li, Y. J., Wang, J. F., Xin, H. T., and Dong, P. P. (2020b). Subduction initiation in the southeastern Palaeo-Asian Ocean: Constraints from early Permian adakites in suprasubduction zone ophiolites, central Inner Mongolia, North China. *Geol. J.* 55, 2044–2061. doi:10.1002/gj.3696

Liang, R. (1991). "The characteristics of the ophiolite sequences and its rock associations in central and eastern Inner Mongolia," in *Pre-jurassic geology of inner Mongolia, China*. Editors K. Ishii, X. Liu, K. Ichikawa, and B. Huang (Osaka: China-Japan Cooperative Research Group), 65–84.

Liang, Y., Zheng, H., Li, H., Algeo, T., and Sun, X. M. (2021). Late paleozoic–mesozoic subduction and accretion of the Paleo-Pacific Plate: Insights from ophiolitic rocks in the wandashan accretionary complex, NE China. *Geosci. Front.* 12 (6), 101242doi:10.1016/j.gsf.2021.101242

Liu, Y. S., Hu, Z. C., Gao, S., Detlef, G., Xu, J., Gao, C. G., et al. (2008). *In situ* analysis of major and trace elements of anhydrous minerals by LA–ICP–MS without applying an internal standard. *Chem. Geol.* 257 (1–2), 34–43. doi:10.1016/j.chemgeo.2008.08.004

Ludwig, K. R. (2003). *User's manual for isoplot 3.00: A geochronological toolkit for microsoft excel*, 4. Berkeley: Special Publication Geochronology Center, 1–70.

Ma, Y. F., Liu, Y. J., Peskov, A., Wang, Y., Song, W. M., Zhang, Y. J., et al. (2021). Paleozoic tectonic evolution of the eastern central asian orogenic belt in NE China, *China geology*, 5.

Mao, A. Q., Sun, D. Y., Gou, J., Yang, D. G., and Zheng, H. (2020). Late palaeozoic–early mesozoic southward subduction of the mongol–okhotsk oceanic slab: Geochronological, geochemical, and Hf isotopic evidence from intrusive rocks in the erguna massif (NE China). *Int. Geol. Rev.* 63 (10), 1262–1287. doi:10.1080/00206814.2020.1758968

Miao, L. C., Zhang, F. Q., Fan, W. M., and Liu, D. Y. (2007). Phanerozoic evolution of the Inner Mongolia-Daxinganling orogenic belt in North China: constraints from geochronology of ophiolites and associated formations, *Geological Society of London, Special Publication*, 280, 223–237.

Miao, L. C., Fan, W. M., Liu, D. Y., Zhang, F. Q., Shi, Y. R., and Guo, F. (2008). Geochronology and geochemistry of the hegenshan ophiolitic complex: Implications for late-stage tectonic evolution of the inner Mongolia-daxinganling orogenic belt, China. *J. Asian Earth Sci.* 32 (5–6), 348–370. doi:10.1016/j.jseaes.2007.11.005

Nicolas, A. (1989). *Structures of ophiolites and dynamics of oceanic lithosphere*. Kluwer Academic Publishers, New York, MA, UK, 367.

Nozaka, T., and Liu, Y. (2002). Petrology of the Hegenshan ophiolite and its implication for the tectonic evolution of northern China. *Earth Planet. Sci. Lett.* 202, 89–104. doi:10.1016/s0012-821x(02)00774-4

Osozawa, S., Shinjo, R., Lo, C. H., Jahn, B. M., Hoang, N., Sasaki, M., et al. (2012). Geochemistry and geochronology of the Troodos ophiolite: An SSZ ophiolite generated by subduction initiation and an extended episode of ridge subduction? *Lithosphere* 4, 497–510. doi:10.1130/l205.1

Pearce, J. A. (1983). "The role of sub-continental lithosphere in magma Genesis at destructive plate margins. et al," in *Continental basalts and mantle xenoliths*. Editor Hawkesworth Cheshire, England, (Nantwich Shiva), 230–249.

Pearce, J. A. (2008). Geochemical fingerprinting of oceanic basalts with applications to ophiolite classification and the search for Archean oceanic crust. *Lithos* 100, 14–48. doi:10.1016/j.lithos.2007.06.016

Pearce, J. A., Lippard, S. J., and Roberts, S. (1984). Characteristics and tectonic significance of supra-subduction zone ophiolites. *Geol. Soc. Lond. Spec. Publ.* 16, 77–94. doi:10.1144/gsl.sp.1984.016.01.06

Reagan, M. K., Pearce, J. A., Petronotis, K., Almeev, R., Avery, A. J., Carvallo, C., et al. (2017). Subduction initiation and ophiolite crust: New insights from IODP drilling. *Int. Geol. Rev.* 59, 1439–1450. doi:10.1080/00206814.2016.1276482

Robinson, P. T., Zhou, M. F., Hu, X. F., Reynolds, P., Bai, W. J., and Yang, J. (1999). Geochemical constraints on the origin of the Hegenshan ophiolite, Inner Mongolia, China. *J. Asian Earth Sci.* 17, 423–442. doi:10.1016/s1367-9120(99)00016-4

Safonova, I. (2017). Juvenile versus recycled crust in the central asian orogenic belt: Implications from ocean plate stratigraphy, blueschist belts and intra-oceanic arcs. *Gondwana Res.* 47, 6–27. doi:10.1016/j.gr.2016.09.003

Santosh, M., Hu, C. N., He, X. F., Li, S. S., Tsunogae, T., Shaji, E., et al. (2017). Neoproterozoic arc magmatism in the southern madurai block, India: Subduction, relamination, continental outbuilding, and the growth of gondwana. *Gondwana Res.* 45, 1–42. doi:10.1016/j.gr.2016.12.009

Santosh, M., Teng, X. M., He, X. F., Tang, L., and Yang, Q. Y. (2016). Discovery of neoarchean suprasubduction zone ophiolite suite from yishui complex in the north China craton. *Gondwana Res.* 38, 1–27. doi:10.1016/j.gr.2015.10.017

Shcherbakov, Y. D., Perepelov, A. B., and Svetlana Tsypukova, S. (2020). Report on Late Paleozoic bimodal volcanic associations discovered in Northern Mongolian Rift zone. *China Geol.* 3, 496–500.

Shervais, J. W., Kimbrough, D. L., Renne, P., Murchey, B., Snow, C. A., Schaman, R. M. Z., et al. (2004). Multi-stage origin of the coast range ophiolite, California: Implications for the life cycle of supra-subduction zone ophiolites. *Int. Geol. Rev.* 46, 289–315. doi:10.2747/0020-6814.46.4.289

Shervais, J. W. (2001). Birth, death, and resurrection: The life cycle of suprasubduction zone ophiolites. *Geochem. Geophys. Geosystems* 2. doi:10.1029/2000gc000080

Song, S. G., Wang, M. M., Xu, X., Wang, C., Niu, Y., Allen, M. B., et al. (2015). Ophiolites in the xing'an-inner Mongolia accretionary belt of the CAOB: Implications for two cycles of seafloor spreading and accretionary orogenic events. *Tectonics* 34, 2221–2248. doi:10.1002/2015tc003948

Sun, L. X., Ren, B. F., Zhao, F. Q., Gu, Y. C., Li, Y. C., and Liu, H. (2013). Zircon U–Pb dating and Hf isotopic compositions of the Mesoporterozoic granitic gneiss in Xilinhot Block, Inner Mongolia. *Geol. Bull. China* 32, 327–340. (in Chinese with English abstract).

Sun, M. D., Xu, Y. G., Wilde, S. A., Chen, H. L., and Yang, S. F. (2015). The permian dongfanghong island-arc gabbro of the wandashan orogen, NE China: Implications for paleo-pacific subduction. *Tectonophys* 659, 122–136. doi:10.1016/j.tecto.2015.07.034

Sun, S. S., and McDonough, W. F. (1989). *Chemical and isotopic systematics of oceanic basalts: implications for mantle composition and processes,. Geological Society of London, Special Publication*, 42, 313–340.

Tang, K. D. (1990). Tectonic development of Paleozoic foldbelts at the north margin of the Sino-Korean Craton. *Tectonics* 9, 249–260. doi:10.1029/tc009i002p00249

Tang, K., and Yan, Z. (1993). Regional metamorphism and tectonic evolution of the Inner, *J. Metamorph. Geol.*, 11, 511–522.

Wang, Q., and Liu, X. Y. (1986). Paleoplate tectonics between cathaysia and angaral and in inner Mongolia of China. *Tectonics* 5, 1073–1088. doi:10.1029/tc005i007p01073

Wang, S., Li, Y. J., Wang, J. F., Dong, P. P., Li, H. Y., Guo, L. L., et al. (2021). Discovery of late carboniferous adakite in manita, inner Mongolia, and its constrains on intra-oceanic subduction in eastern paleo-Asian ocean. *Geol. Bull. China* 40, 82–94. (In Chinese with English Abstract).

Wang, S. Q., Xu, J. F., Liu, X. J., and Hou, Q. Y. (2008). Geochemistry of the chaokeshan ophiolite: Product of intra-oceanic back-arc basin? *Acta Petrol. Sin.* 24, 2869–2879. (in Chinese with English abstract).

Whattam, S. A., and Stern, R. J. (2011). The'subduction initiation rule': A key for linking ophiolites, intra-oceanic forearcs, and subduction initiation. *Contrib. Mineral. Pet.* 162, 1031–1045. doi:10.1007/s00410-011-0638-z

Wilde, S. A. (2015). Final amalgamation of the central asian orogenic belt in ne China: Paleo-Asian ocean closure versus Paleo-Pacific Plate subduction — a review of the evidence. *Tectonophysics* 662, 345–362. doi:10.1016/j.tecto.2015.05.006

Windley, B. F., Alexeiev, D., Xiao, W. L., KrÖner, A., and Badarch, G. (2007)., 164. London, 31–47. doi:10.1144/0016-76492006-022Tectonic models for accretion of the central asian orogenic belt*J. Geol. Soc.*

Windley, B. F., and Allen, M. B. (1993). Mongolian plateau: Evidence for a late cenozoic mantle plume under central Asia. *Geology* 21 (4), 295–298. doi:10.1130/0091-7613(1993)021<0295:mpefal>2.3.co;2

Xiao, W. J., and Santosh, M. (2014). The Western central asian orogenic belt: A window to accretionary orogenesis and continental growth. *Gondwana Res.* 25, 1429–1444. doi:10.1016/j.gr.2014.01.008

Xiao, W. J., Windley, B. F., Hao, J., and Zhai, M. G. (2003). Accretion leading to collision and the permian solonker suture, inner Mongolia, China: Termination of the central asian orogenic belt. *Tectonics* 22 (1069). doi:10.1029/2002tc001484

Xiao, W. J., Windley, B. F., Yuan, C., Sun, M., Han, C. M., Lin, S. F., et al. (2009). Paleozoic multiple subduction-accretion processes of the southern Altaids. *Am. J. Sci.* 309, 221–270. doi:10.2475/03.2009.02

Xu, B., Charvet, J., Chen, Y., Zhao, P., and Shi, G. (2013). Middle Paleozoic convergent orogenic belts in Western Inner Mongolia (China): Framework, kinematics, geochronology and implications for tectonic evolution of the Central Asian Orogenic Belt. *Gondwana Res.* 23 (4), 1342–1364. doi:10.1016/j.gr.2012.05.015

Yang, F., Kim, S. W., Tsunogae, T., and Zhou, H. (2021). Multiple enrichment of subcontinental lithospheric mantle with Archean to Mesozoic components: Evidence from the Chicheng ultramafic complex, North China Craton. *Gondwana Res.* 94, 201–221.

Yang, F., Santosh, M., Tsunogae, T., Tang, L., and Teng, X. (2017). Multiple magmatism in an evolving suprasubduction zone mantle wedge: the case of the composite mafic-ultramafic complex of Gaositai, North China Craton. *Lithos* 284, 525–544.

Zhang, X. H., Wilde, S. A., Zhang, H. F., and Zhai, M. G. (2011). Early permian high-K calc-alkaline volcanic rocks from NW inner Mongolia, north China: Geochemistry, origin and tectonic implications. *J. Geol.Soc* 168, 525–543. doi:10.1144/0016-76492010-094

Zhang, Z. C., Li, K., Li, J. F., Tang, W. H., Chen, Y., and Luo, Z. W. (2015). Geochronology and geochemistry of the eastern Erenhot ophiolitic complex: Implications for the tectonic evolution of the inner Mongolia–daxinganling orogenic belt. *J. Asian Earth Sci.* 97, 279–293. doi:10.1016/j.jseaes.2014.06.008

Zhao, P., Faure, M., Chen, Y., Shi, G. Z., and Xu, B. (2015). A new Triassic shortening-extrusion tectonic model for Central-Eastern Asia: Structural, geochronological and paleomagnetic investigations in the Xilamulun Fault (North China). *Earth Planet. Sci. Lett.* 426, 46–57. doi:10.1016/j.epsl.2015.06.011

Zhao, Z. H., and Zhou, L. D. (1997). REE geochemistry of some alkali-rich intrusive rocks in China. *Sci. China Ser. D* 40 (2), 145–158. doi:10.1007/bf02878373

Zhou, J. B., Cao, J. L., Wilde, S. A., Zhao, G. C., Zhang, J. J., and Wang, B. (2014). Paleo-Pacific subduction-accretion: Evidence from Geochemical and U-Pb zircon dating of the Nadanhada accretionary complex, NE China. *Tectonics* 33 (12), 2444–2466. doi:10.1002/2014tc003637

frontiers | Frontiers in Earth Science

TYPE Original Research
PUBLISHED 06 January 2023
DOI 10.3389/feart.2022.1000603

Check for updates

OPEN ACCESS

EDITED BY
Fan Yang,
Lanzhou University, China

REVIEWED BY
Zesheng Qian,
Lanzhou University, China
Peng-Peng Yu,
Sun Yat-sen University, China
Liang Liu,
Institute of Geochemistry, Chinese Academy of Sciences (CAS), China

*CORRESPONDENCE
He Li,
lihe@qdio.ac.cn

SPECIALTY SECTION
This article was submitted to Geochemistry, a section of the journal Frontiers in Earth Science

RECEIVED 22 July 2022
ACCEPTED 20 September 2022
PUBLISHED 06 January 2023

CITATION
Li J, Li H, Li C, Song M, Jiang M, Yuan S and Zhang L (2023), Early cretaceous ridge subduction in the Shandong Peninsula, Eastern China, indicated by Laoshan A-type granite.
Front. Earth Sci. 10:1000603.
doi: 10.3389/feart.2022.1000603

COPYRIGHT
© 2023 Li, Li, Li, Song, Jiang, Yuan and Zhang. This is an open-access article distributed under the terms of the Creative Commons Attribution License (CC BY). The use, distribution or reproduction in other forums is permitted, provided the original author(s) and the copyright owner(s) are credited and that the original publication in this journal is cited, in accordance with accepted academic practice. No use, distribution or reproduction is permitted which does not comply with these terms.

Early cretaceous ridge subduction in the Shandong Peninsula, Eastern China, indicated by Laoshan A-type granite

Jie Li[1,2], He Li[2,3]*, Congying Li[2,3], Mingchun Song[1,4], Mengyao Jiang[1], Shuai Yuan[2,3] and Lipeng Zhang[2,3]

[1]Hebei Key Laboratory of Strategic Critical Mineral Resources, Hebei GEO University, Shijiazhuang, China, [2]Institute of Oceanology, Chinese Academy of Sciences, Qingdao, China, [3]Laoshan Laboratory, Qingdao, China, [4]Shandong Provincial No 6 Exploration Institute of Geology and Mineral Resources, Weihai, China

Early Cretaceous A-type granites are widespread in the Shandong Peninsula, which can be used to elucidate the tectonic evolution of the eastern China and the destruction of the North China Craton. However, their genesis is still controversial. Several competing models, ranging from slab break-off, postorogenic extension, foundering of the lower crust and ridge subduction, were proposed. Here, we report zircon U–Pb ages, whole-rock and apatite geochemical compositions of the Laoshan granite and discuss its tectonic implications. The Laoshan granite has typical characteristics of A-type granite with high $FeO^T/(FeO^T + MgO)$ ratios (0.90–0.97) and 10000*Ga/Al ratios (2.70–3.36) and high total alkali ($Na_2O + K_2O$: 7.95–8.70 wt%) contents and Zr+Nb+Ce+Y (most >350 ppm) concentrations. The Laoshan granite is further classified as A_1-type based on the Yb/Ta-Y/Nb and Ce/Nb-Y/Nb diagrams and the Nb-Y-3Ga and Nb-Y-Ce triangular discriminant diagrams. Zircon U–Pb dating of two Laoshan granite samples yielded emplacement ages of 117.8 ± 1.0 Ma and 120.1 ± 1.3 Ma, respectively. The oxygen fugacity of the Laoshan granite magma is low, as indicated by zircon Ce^{4+}/Ce^{3+} ratios (most <300). The crystallization temperature of zircon varies significantly, ranging from 652 to 830°C. The apatite compositions show that the Laoshan granite has high F (2.09–2.72 wt%) and low Cl (0.01–0.09 wt%) contents, consistent with influence by fluid released from the decomposition of phengite. Apatite rare earth elements show that mantle sources are also involved in Laoshan A-type granite. Combined previous studies of A-type granitic plutons in the Shandong Province and the Lower Yangtze River belt with the drifting history of the Pacific plate, we propose that the flat subduction of the spreading ridge between the Pacific and the Izanagi plates was responsible for the formation of Laoshan A-type granite.

KEYWORDS

ridge subduction, apatite, zircon U-Pb age, Laoshan A-type granite, Shandong peninsula

Introduction

The North China Craton (NCC) is one of the oldest and most stable cratons in the world. In the Paleozoic, the lithospheric thickness of the NCC reached 200 km. However, after the Mesozoic, the lithospheric thickness in the eastern NCC decreased to about 80 km (Fan and Menzies, 1992; Xu, 2001), accompanied by a series of Yanshanian (Early Cretaceous) tectonic movements and magmatic activities (Wu et al., 2005), which produced a large amount of granitic magma, mainly concentrated ca. 160 ~ 110 Ma (Li et al., 2014; Song et al., 2015, 2017, 2019). The genesis and tectonic background of these granites have been controversial, mainly including slab break-off, slab rollback, postorogenic extension, foundering of the lower lithosphere (Yang et al., 2005, 2018a, 2020a; Liu et al., 2008, 2013; Xie et al., 2009; Goss et al., 2010) and flat ridge subduction (Li et al., 2012a, 2014; Ling et al., 2013), which limit the in-depth understanding of the regional tectonic background.

A-type granite is a special rock formed in an extensional environment, which refers to non-orogenic and water-poor alkaline granite (Loiselle and wones, 1979). According to the tectonic setting, it can be formed not only in the extensional environment within the plate but also in the extensional environment of the plate margin after the collision (Whalen et al., 1987; Eby, 1990, 1992; Bonin, 2007). Eby (1992) classified A-type granites into A1-type and A2-type granites according to their element ratios. A-type granites have unique geochemical characteristics and specific formation conditions and especially have important indicative significance for the tectonic environment. Therefore, the study of Mesozoic A-type granites has important geological significance for Yanshanian tectonic activity in eastern China.

There is an NEE-trending A-type granite belt developed along the Shandong Peninsula, mainly distributed in Wulian, Jiaonan, Laoshan, Haiyang and other places (Wang et al., 1995; Li et al., 2014; Yuan et al., 2022), which provides a good object for us to study the Mesozoic tectonic background and crustal evolution. In this study, we conduct whole-rock geochemistry, zircon U–Pb dating and trace element and apatite trace element composition studies of the Laoshan A-type granite and compare it with A-type granites in the Lower Yangtze River (LYR) belt and Haiyang A_1-A_2-type granite in the Shandong Peninsula, aiming at understanding the genesis of the Early Cretaceous A-type granite in the Shandong Peninsula and discussing the dynamic mechanism of the NCC.

Geological background

The Shandong Peninsula is located at the southeastern margin of the NCC and the eastern part of the Dabie-Sulu orogenic belt (Sun et al., 2002a). The eastern extension of the Qinling-Dabie-Sulu orogenic belt cuts across the southern Peninsula (Li et al., 1993; Goss et al., 2010). It is famous for a large number of gold deposits (Zhai et al., 2002; Deng et al., 2015, 2020; Song et al., 2015, 2021; Fan et al., 2016; Zhang et al., 2017a, 2020a, 2020b; Groves et al., 2020; Li et al., 2020, 2021) with a total controlled Au reserve of more than 5,000 tons (Song et al., 2021). The famous Tan-Lu fault zone separates the Shandong Peninsula into the Luxi and Jiaodong segments (Li et al., 1993; Goss et al., 2010; Tan et al., 2012).

The tectonic units of the Jiaodong segment include the Jiaobei uplift, the Jiaolai basin, and the Weihai uplift. Multistage Mesozoic plutons emplaced within the Precambrian geological units occur in the Jiaobei uplift and the Weihai uplift, including Jurassic granites (the Linglong-type granite, the Wendeng-type granite and the Duogushan-type granite) and Cretaceous granites (the Guojialing-type granodiorite, the Weideshan-type granite and the Laoshan-type granite) (Song et al., 2015, 2017, 2019).

There is an NEE-trending A-type granite belt of approximately 500 km in length across the whole Shandong Peninsula (Wang et al., 1995, 2009). The epochs of the Cretaceous A-type granites range between 110 Ma and 123 Ma (Zhao et al., 1997; Goss et al., 2010; Liu et al., 2013; Li et al., 2014; Yan and Shi, 2014; Gao et al., 2019; Yuan et al., 2022).

The Laoshan granite is located in eastern Qingdao city with a total outcrop area of ~600 km^2. It is a part of the Early Cretaceous A-type granite belt in the Shandong Peninsula (Wang et al., 1995, 2009), which intruded into the Proterozoic basement metamorphic rocks of the Jiaonan Group and the Cretaceous sandstone of the Laiyang Group (Figure 1B). The Laoshan granites contain monzogranite, syenogranite, alkali feldspar granite and quartz syenite. We collected monzogranite samples from the western parts of the Laoshan granitic pluton and were composed of medium-to coarse-grained monzogranite. The coordinates of sample LS-40 are 120°26.98′E, 36°14.71′N, and 120°35.03′, 36°8.10′ for LS-41 (Figure 2A). They are slightly fleshy red with massive structures and developed joints (Figures 2B,C). The main minerals include potassium feldspar, quartz, plagioclase, biotite and hornblende (Figures 2D,E). The accessory minerals include zircon and apatite.

Analytical methods

The whole-rock major element contents were analyzed using X-ray fluorescence spectrometry at the State Key Laboratory of Isotope Geochemistry, Guangzhou Institute of Geochemistry, Chinese Academy of Sciences (GIGCAS), and zircon U–Pb dating and trace elements, whole-rock trace elements and apatite trace elements were analyzed using LA-ICPMS at the Key Laboratory of Mineralogy and Metallogeny, GIGCAS. The major elements (including Cl and F) of apatite were analyzed using a JXA-8100 electron microprobe at the State Key

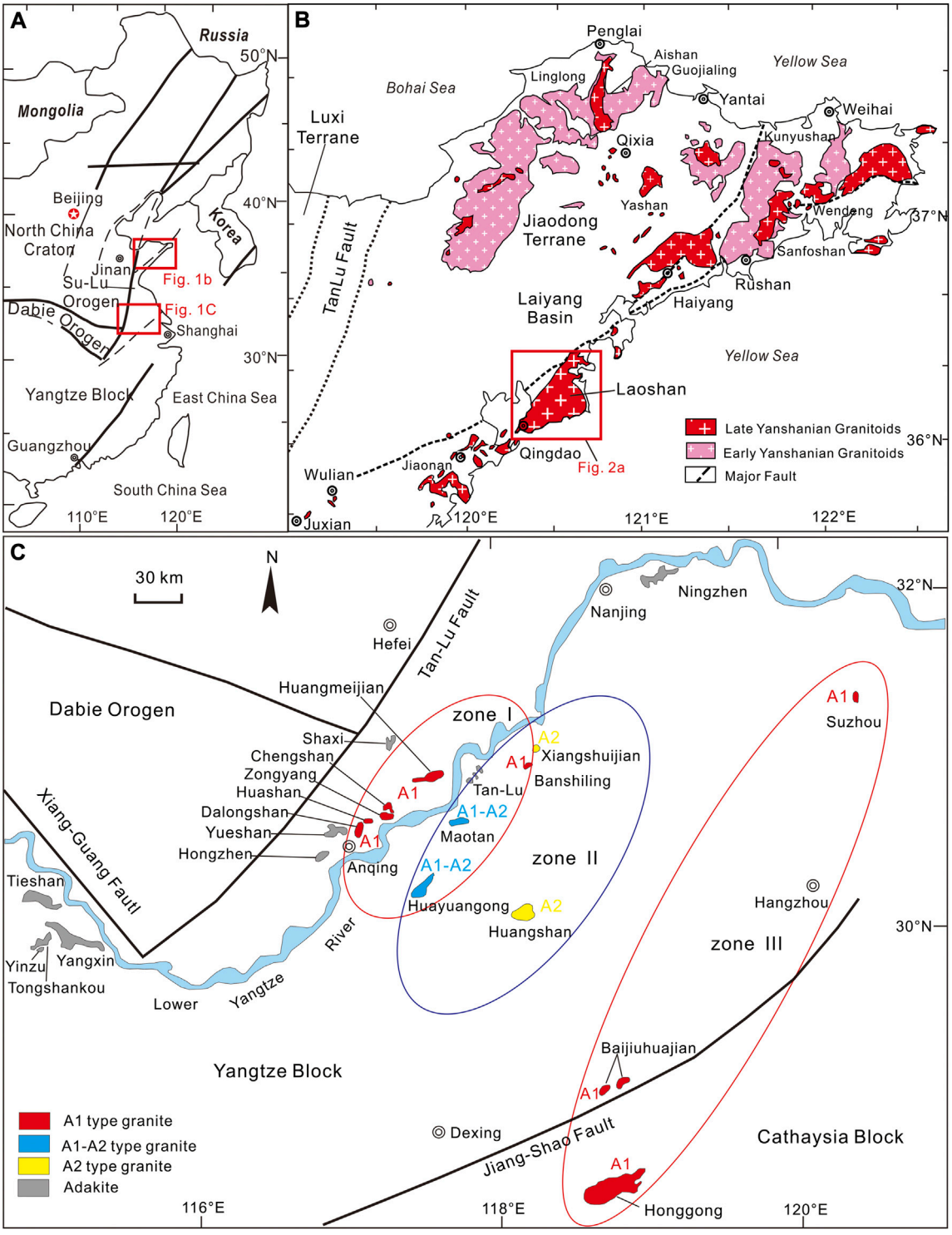


FIGURE 1
(A), Sketch map of the late Mesozoic A-type granites in eastern China. **(B)**, Geological map of the Shandong Peninsula, showing the distribution of Early Yanshanian and Late Yanshanian granitoids of the Jiaodong Terrane (modified after Li et al., 2014). **(C),** Geological map of the Lower Yangtze River (LYR) belt (modified after Li et al., 2012a and related references).

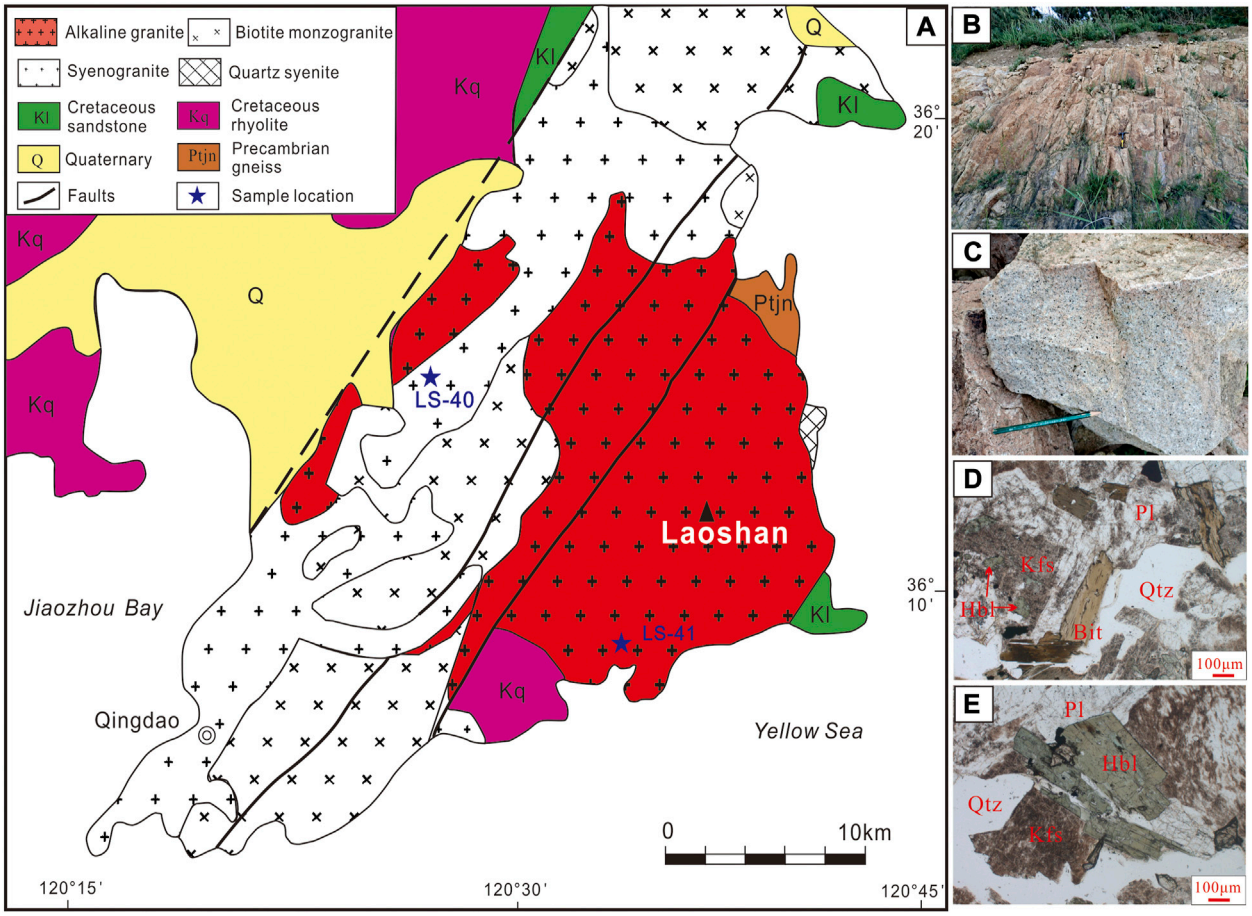


FIGURE 2
(A), Simplified geologic map of the Laoshan granitic complex (modified after Zhao et al., 1997). Field photographs showing **(B,C)** monzogranite of the Laoshan pluton and microphotographs showing **(D,E)** the coarse-grained K-feldspar (Kfs), quartz (Qtz), plagioclase (Pl), biotite (Bit) and hornblende (Hbl) of monzogranite.

Laboratory of Mineral Deposits Research, Nanjing University. The calculations of zircon isotope ratios, the apatite, zircon and whole-rock trace element concentrations were performed using ICPMSDataCal 7.0 (Liu et al., 2010; Lin et al., 2016).

Whole-rock major and trace element analyses

The whole-rock major and trace element contents were analyzed at the State Key Laboratory of Isotope Geochemistry, GIGCAS. The whole-rock major elements were analyzed using X-ray fluorescence spectrometry. The typical analytical precisions were better than 1% (Li et al., 2005). Whole-rock trace element analyses were carried out on fused glasses using LA-ICPMS. The analytical method has been described in more detail by previous authors (Liang et al., 2009; Tu et al., 2011; Li et al., 2012a, Li et al., 2012b). The whole-rock trace element data were calculated using ICPMSDataCal 7.0 (Liu et al., 2010; Lin et al., 2016).

Zircon U–Pb dating and trace element analyses

Zircon grains were obtained through conventional procedures. First, whole rock samples were crushed to about 60 mesh, desliming in water, followed by density separation, magnetic separation and handpicking. Zircon grains were then mounted in epoxy and polished down to nearly half sections to expose internal structures. Cathodoluminescent and optical microscopy images were taken to ensure that the least fractured, inclusion-free parts were analyzed. Zircon U–Pb dating and trace element analyses were carried out at the Key Laboratory of Mineralogy and Metallogeny, GIGCAS. LA-ICPMS was performed following the same technique as that

used for whole-rock analyses (Li et al., 2012a; Li et al., 2012b). The calculations of zircon isotope ratios and zircon trace element concentrations were performed using ICPMSDataCal 7.0 (Liu et al., 2010; Lin et al., 2016). Zircon Ce anomalies were calculated using software from the Research School of Earth Sciences, Australian National University (Ballard et al., 2002; Liang et al., 2006), and the zircon age was calculated using Isoplot (Version 3.23).

Apatite major and trace element analyses

Fluorine and chlorine compositions of apatite were determined using a JXA-8100 electron microprobe at the State Key Laboratory of Mineral Deposits Research, Nanjing University. The analysis conditions were 15 keV and 10 nA current, with a 10 μm diameter electron beam. A norbergite grain was used as a standard for F, $Ba_5(PO_4)_3Cl$ for Cl, and apatite for Ca and P standards. The detailed method was described previously (Li et al., 2012b). The apatite trace elements were analyzed using LA-ICPMS at the Key Laboratory of Mineralogy and Metallogeny, GIGCAS. The conditions were 80 mJ laser energy, with a repetition rate of 6 Hz, a spot size of 41 μm in diameter and a 40 s ablation time. NIST 612 was used as an external standard, NIST 610 was used as a monitoring standard, and ^{43}Ca was used as an internal standard (Liang et al., 2009; Tu et al., 2011; Li H. et al., 2012a, Li et al., 2012b). The calculations of the apatite trace element concentrations were performed using ICPMSDataCal 7.0 (Liu et al., 2008; Lin et al., 2016).

Results

Whole-rock major and trace elements

Major and trace element results of the Laoshan granite samples (*N*=23) are summarized in Table 1. These granite samples have high SiO_2 (76.0–78.2 wt%), K_2O (4.23–4.79 wt%), and Na_2O (3.38–4.09 wt%) contents and low Al_2O_3 (12.3–13.3 wt%), TiO_2 (0.09–0.19 wt%), MgO (0.03–0.10 wt%), $Fe_2O_3^T$ (0.73–1.21 wt%), CaO (0.04–0.33 wt%) and P_2O_5 (0–0.01 wt%) contents. In Harker diagrams, CaO, MgO, Al_2O_3, TiO_2, $Fe_2O_3^T$, and P_2O_5 contents of the Laoshan granite, together with syenogranite and alkali feldspar granite from previous studies (Zhao et al., 1997; Goss et al., 2010; Yan and Shi, 2014), are negatively correlated with SiO_2, whereas no obvious correlation exists between Na_2O, K_2O and SiO_2. The whole-rock Ti thermometer gave a formation temperature of approximately 652–830°C for the monzogranite (Schiller and Finger, 2019; Yu et al., 2022) (Figure 3). The K_2O/Na_2O ratios (1.08–1.39) and $FeO^T/(FeO^T + MgO)$ ratios (0.90–0.97) are lower than those of the Haiyang syenite (0.76–0.87, 1.28–1.58). They are peraluminous with A/CNK ratios from 1.06 to 1.20 and are alkaline rocks with total alkali contents ($K_2O + Na_2O$) ranging from 7.95 to 8.70 wt%.

The Laoshan granite is characterized by high field strength elements, such as Th, U, Zr, and Hf, and high concentrations of large iron lithophile elements, such as K, Rb, Ba, and Na (Table 1; Figure 4A). The samples are depleted in HREEs and enriched in LREEs with $(La/Yb)_N$ from 4.62 to 12.03 and with strong negative Eu anomalies (Figure 4B).

Zircon U–Pb ages

Zircon grains from monzogranite samples LS-40 and LS-41 are mostly prismatic, transparent, pale yellow in color, and approximately 200 μm in size. All zircon grains show clear zonation, as revealed in CL images, which is consistent with typical igneous zircons. Inherited cores are rare and, if there are any, surrounded by prismatic and transparent rims. The zircon U–Pb isotope compositions are shown in Table 2 and are also shown in the concordia diagram (Figure 5).

\Twenty-two available zircon data points for sample LS-4002 were obtained. The zircon Th and U concentrations range from 104 to 2,845 ppm and from 182 to 1,146 ppm, respectively (Table 2), corresponding to Th/U ratios from 0.43 to 2.48. Eighteen zircon grains from sample LS-4109 were analyzed. The zircon Th concentrations range from 295 to 3,678 ppm, and the U concentrations range from 182 to 1,298 ppm (Table 2), with Th/U ratios ranging from 1.37 to 3.63. These Th/U ratios are typical magmatic geneses (Hoskin and Black, 2000; Belousova et al., 2002; Sun et al. 2002b). Samples LS-4002 and LS-4109 yield a weighted mean $^{206}Pb/^{238}U$ age of 117.8 ± 1.0 Ma and 120.1 ± 1.3 Ma, respectively (Figure 5; Table 2), which represent crystallization ages of 117.8 ± 1.0 Ma to 120.1 ± 1.3 Ma for the monzogranite.

Zircon trace elements

The zircon trace element concentrations are shown in Table 3. The negative Eu and positive Ce anomalies are shown in the chondrite-normalized REE diagram. The zircon Ce^{4+}/Ce^{3+} ratios of sample LS-4002 range from 8 to 181, indicating relatively low oxygen fugacities. The zircon Ce^{4+}/Ce^{3+} ratios of sample LS-4109 have relatively higher variations (from 1 to 380, except one of 505) than those from LS-4002, but most of them have low oxygen fugacities (Ballard et al., 2002; Liang et al., 2006). The crystallization temperature of zircon ranges from 652 to 830°C according to zircon Ti concentrations (Schiller and Finger, 2019; Yu et al., 2022) (Table 2). These temperatures are comparable to the temperatures of A_2-type granites in the LYR Belt, which range from 650 to 800°C (Li et al., 2012a), and are marginally higher than those of the Haiyang syenite, which ranges from 620 to 780 °C (Li et al., 2014).

TABLE 1 Major and trace element compositions of Laoshan granite.

Sample	LS-4001	LS-4002	LS-4003	LS-4004	LS-4005	LS-4006	LS-4007	LS-4008	LS-4009	LS-4101	LS-4102	LS-4103	LS-4104	LS-4105	LS-4106	LS-4107	LS-4108	LS-4109	LS-4110	LS-4111	LS-4112	LS-4113	LS-4114
SiO_2	76.7	76.0	76.9	76.8	76.8	77.2	76.4	76.6	76.5	76.9	77.5	77.4	76.6	76.8	77.4	76.8	76.4	77.0	77.6	76.6	78.0	76.4	78.2
TiO_2	0.10	0.10	0.11	0.10	0.10	0.09	0.11	0.10	0.10	0.10	0.12	0.11	0.11	0.10	0.12	0.11	0.16	0.19	0.11	0.19	0.11	0.11	0.10
Al_2O_3	13.2	13.3	12.8	13.1	13.0	12.9	13.3	13.1	12.8	12.7	12.3	12.8	13.2	13.1	12.7	13.2	13.2	12.7	12.6	12.6	12.5	13.3	12.5
Fe_2O_3	0.99	1.12	1.10	1.04	1.08	0.90	1.02	1.02	0.91	0.76	0.75	0.85	0.92	0.94	1.07	0.96	1.21	1.18	0.89	0.92	0.81	0.96	0.73
MnO	0.02	0.11	0.04	0.03	0.03	0.03	0.02	0.02	0.05	0.01	0.01	0.01	0.00	0.00	0.01	0.02	0.01	0.01	0.01	0.01	0.01	0.02	0.01
MgO	0.08	0.08	0.08	0.10	0.08	0.06	0.06	0.07	0.06	0.06	0.03	0.04	0.03	0.03	0.04	0.03	0.04	0.03	0.03	0.05	0.03	0.05	0.04
CaO	0.30	0.33	0.33	0.22	0.25	0.25	0.25	0.28	0.32	0.27	0.19	0.13	0.19	0.19	0.10	0.18	0.21	0.2	0.13	0.22	0.16	0.07	0.04
Na_2O	3.48	3.77	3.41	3.37	3.38	3.41	3.56	3.61	3.75	3.45	3.95	3.96	4.01	3.97	3.87	3.91	4.03	3.89	3.85	3.97	3.86	4.09	3.75
K_2O	4.60	4.59	4.61	4.57	4.66	4.72	4.76	4.60	4.53	4.79	4.26	4.38	4.54	4.43	4.29	4.44	4.41	4.40	4.34	4.59	4.23	4.60	4.32
P_2O_5	0.01	0.01	0.01	0.01	0.01	0.01	0.01	0.01	0.00	0.00	0.00	0.01	0.01	0.01	0.01	0.01	0.01	0.01	0.01	0.00	0.01	0.01	0.01
L.O.I	0.50	0.51	0.51	0.61	0.54	0.34	0.44	0.47	0.43	0.37	0.24	0.20	0.24	0.35	0.29	0.26	0.30	0.30	0.30	0.30	0.23	0.25	0.26
Total	99.9	99.9	99.9	99.9	99.9	99.9	99.9	99.9	99.4	99.4	99.4	99.9	99.9	99.9	99.9	99.9	99.9	99.9	99.9	99.4	99.9	99.9	99.9
Sc	1.15	0.98	1.24	1.05	1.39	1.56	0.82	0.97	1.45	0.98	1.53	1.72	3.13	1.89	1.91	2.25	2.00	2.55	1.28	2.23	1.75	1.62	1.00
Ti	578	595	657	605	607	527	637	586	624	605	729	633	646	602	726	660	935	1,112	671	1,147	655	661	575
V	6.29	6.39	6.71	6.44	5.95	6.44	6.67	6.63	6.41	7.81	6.37	6.64	7.17	7.35	6.68	6.88	7.01	8.26	6.65	8.81	7.28	8.12	6.86
Cr	4.31	2.75	1.36	10.14	5.54	4.32	4.46	5.93	2.89	18.1	32.2	5.83	19.1	5.61	8.17	8.57	9.03	5.73	14.0	25.4	3.91	14.6	23.95
Mn	145	815	314	230	213	232	183	176	415	98.0	65.0	47.0	23.0	31.0	109	123	62.0	70.0	94.0	74.0	63.0	125	46.0
Co	0.93	1.22	1.15	2.12	1.71	1.91	1.53	1.17	0.91	0.49	0.72	0.78	0.98	0.81	0.71	1.02	0.49	0.79	0.82	0.88	0.87	0.84	1.30
Ni	4.47	5.94	6.95	2.56	5.47	2.78	4.11	2.56	3.98	18.0	11.2	9.05	20.2	16.2	8.61	7.38	22.7	6.03	22.4	10.6	16.4	8.89	10.5
Zn	49.3	58.3	53.9	48.3	54.3	59.3	38.9	53.0	66.5	83.7	43.5	39.6	50.5	53.9	60.6	67.0	72.7	50.8	58.2	58.9	58.5	58.2	51.0
Ga	19.5	20.3	18.9	18.7	20.3	20.6	19.6	19.6	19.2	20.8	18.9	19.6	20.3	22.3	22.6	23.3	20.8	20.6	21.4	21.9	22.6	19.7	20.3
Rb	196	210	185	147	117	169	155	216	196	182	183	147	163	179	180	171	173	167	176	170	185	137	176
Sr	14.7	15.7	16.4	16.2	16.7	15.7	15.3	13.7	11.4	7.19	14.0	6.73	7.03	8.07	7.81	7.03	7.57	6.17	7.67	7.46	6.92	7.54	5.09
Y	25.7	28.8	28.1	27.1	30.5	30.7	29.1	25.6	31.3	26.6	18.4	20.3	17.0	21.5	20.8	20.9	27.8	35.1	24.7	37.5	24.1	23.2	13.8
Zr	155	156	144	162	192	176	131	154	190	207	117	187	226	239	223	335	240	300	248	281	314	180	141
Nb	54.7	58.2	56.3	48.8	57.5	55.5	44.2	53.2	56.7	36.0	48.4	27.9	30.2	34.5	32.0	38.0	36.5	34.2	35.1	43.9	49.0	27.9	27.0
Ba	64.1	49.6	76.1	65.6	65.5	77.7	65.8	58.5	39.9	28.3	54.6	30.6	28.5	31.1	32.2	35.8	29.7	28.7	29.4	32.2	34.3	26.1	27.5
La	44.0	39.5	49.1	43.6	47.7	43.1	34.9	44.6	46.1	33.6	38.8	26.5	25.7	36.1	33.8	33.6	28.6	45.4	34.7	46.6	40.1	26.2	21.6
Ce	67.9	72.8	86.9	55.8	72.8	82.6	61.6	72.1	75.6	50.1	52.3	43.9	38.7	48.3	45.2	46.0	38.7	62.2	44.7	63.2	56.3	41.2	32.9
Pr	7.76	7.36	8.49	7.89	8.48	7.89	6.48	8.09	8.40	5.04	6.58	3.89	3.72	4.57	4.23	4.41	4.26	7.12	4.71	7.13	5.07	4.30	3.32
Nd	26.9	26.1	32.5	27.8	30.6	28.6	23.3	29.0	30.2	15.2	24.8	12.8	11.5	14.1	14.1	14.8	14.3	25.4	16.8	24.4	16.1	12.9	10.7
Sm	5.04	5.30	6.65	5.56	6.58	5.74	4.73	5.16	6.16	2.55	4.92	1.95	1.89	2.63	2.45	2.58	2.48	4.99	2.74	4.47	2.64	2.03	1.70
Eu	0.15	0.17	0.14	0.19	0.07	0.12	0.15	0.17	0.15	0.09	0.04	0.13	0.14	0.16	0.16	0.21	0.30	0.22	0.25	0.37	0.18	0.16	0.13

(Continued on following page)

10.3389/feart.2022.1000603

TABLE 1 (*Continued*) Major and trace element compositions of Laoshan granite.

Sample	LS-4001	LS-4002	LS-4003	LS-4004	LS-4005	LS-4006	LS-4007	LS-4008	LS-4009	LS-4101	LS-4102	LS-4103	LS-4104	LS-4105	LS-4106	LS-4107	LS-4108	LS-4109	LS-4110	LS-4111	LS-4112	LS-4113	LS-4114
Gd	4.23	4.99	4.93	4.49	5.57	4.69	4.34	4.94	5.31	3.00	3.86	2.13	2.00	2.69	2.57	2.37	3.67	5.12	3.08	4.53	2.30	2.81	1.66
Tb	0.65	0.79	0.76	0.68	0.83	0.80	0.70	0.62	0.88	0.44	0.54	0.34	0.25	0.33	0.33	0.34	0.46	0.80	1.41	0.70	0.50	0.53	0.24
Dy	4.58	5.41	5.34	4.88	5.48	5.13	4.37	4.42	5.30	3.44	3.55	2.70	2.17	2.48	2.64	2.77	3.35	5.24	3.18	5.13	3.05	3.29	2.14
Ho	0.91	1.14	1.01	0.88	1.00	1.04	0.97	0.92	1.08	0.77	0.78	0.58	0.55	0.58	0.49	0.67	0.82	1.16	0.72	1.14	0.70	0.74	0.45
Er	2.43	3.09	2.99	2.86	3.04	3.24	3.11	2.72	3.05	2.50	1.83	1.93	2.01	2.09	1.89	2.26	2.84	3.72	2.66	4.07	2.60	2.15	1.56
Tm	0.46	0.49	0.44	0.38	0.52	0.47	0.46	0.42	0.50	0.47	0.28	0.40	0.31	0.40	0.37	0.43	0.46	0.57	0.50	0.78	0.50	0.41	0.32
Yb	3.17	3.62	3.67	3.23	3.54	4.09	3.19	3.42	4.02	3.54	2.31	3.61	2.52	3.16	2.89	3.51	4.04	4.36	3.55	5.06	4.72	4.07	1.95
Lu	0.55	0.53	0.50	0.44	0.48	0.57	0.40	0.50	0.56	0.47	0.38	0.40	0.41	0.49	0.51	0.59	0.63	0.65	0.51	0.69	0.64	0.40	0.42
Hf	6.58	6.70	6.31	7.12	8.36	7.68	5.68	7.03	8.76	6.98	5.12	7.06	8.41	9.88	8.66	13.3	10.8	9.48	8.61	12.4	14.0	7.16	5.61
Ta	4.68	4.21	3.46	3.85	4.25	3.95	4.17	3.63	4.66	1.93	4.20	2.01	1.79	2.16	2.15	2.18	2.42	2.26	2.41	2.71	3.35	1.66	1.75
Pb	19.2	20.8	26.4	16.6	18.4	29.1	21.4	19.2	22.3	13.1	17.6	6.78	9.94	8.60	7.43	13.1	26.5	18.9	13.7	16.2	16.2	12.0	9.32
Th	16.3	17.9	17.1	16.9	18.6	18.2	16.7	17.3	19.4	16.1	13.1	15.6	16.0	24.6	22.6	28.1	21.3	15.4	21.9	20.1	37.0	15.4	15.1
U	1.90	2.13	1.62	2.24	1.90	2.29	1.93	1.87	2.17	4.89	1.79	3.44	3.43	3.59	2.85	2.99	5.28	4.06	3.26	4.93	4.60	5.90	2.72
$(La/Yb)_N$	9.94	7.83	9.59	9.67	9.68	7.55	7.85	9.35	8.23	6.82	12.03	5.26	7.32	8.19	8.39	6.87	5.07	7.47	7.01	6.60	6.09	4.62	7.93
Eu/Eu*	0.10	0.10	0.07	0.12	0.04	0.07	0.10	0.10	0.08	0.10	0.03	0.19	0.22	0.18	0.20	0.26	0.31	0.13	0.26	0.25	0.22	0.20	0.23
10000*Ga/Al	2.80	2.88	2.79	2.70	2.95	3.03	2.80	2.82	2.84	2.80	3.10	2.90	2.90	2.90	3.21	3.36	3.33	2.98	3.07	3.21	3.29	3.42	2.79
Zr+Nb+Ce+Y	303	316	316	293	353	345	266	305	354	319	236	279	312	343	321	440	343	432	353	426	443	272	215
Y/Nb	0.47	0.49	0.50	0.56	0.53	0.55	0.66	0.48	0.55	0.74	0.38	0.73	0.56	0.62	0.65	0.55	0.76	1.03	0.70	0.85	0.49	0.83	0.51
Ce/Nb	1.24	1.25	1.54	1.14	1.27	1.49	1.39	1.36	1.33	1.39	1.08	1.57	1.28	1.40	1.41	1.21	1.06	1.82	1.27	1.44	1.15	1.48	1.22
Yb/Ta	0.68	0.86	1.06	0.84	0.83	1.04	0.76	0.94	0.86	1.83	0.55	1.80	1.41	1.46	1.34	1.61	1.67	1.93	1.47	1.87	1.41	2.45	1.11
La/Nb	0.80	0.68	0.87	0.89	0.83	0.78	0.79	0.84	0.81	0.93	0.80	0.95	0.85	1.05	1.05	0.89	0.78	1.33	0.99	1.06	0.82	0.94	0.80

Wt% for major element and ppm for trace element.

10.3389/feart.2022.1000603

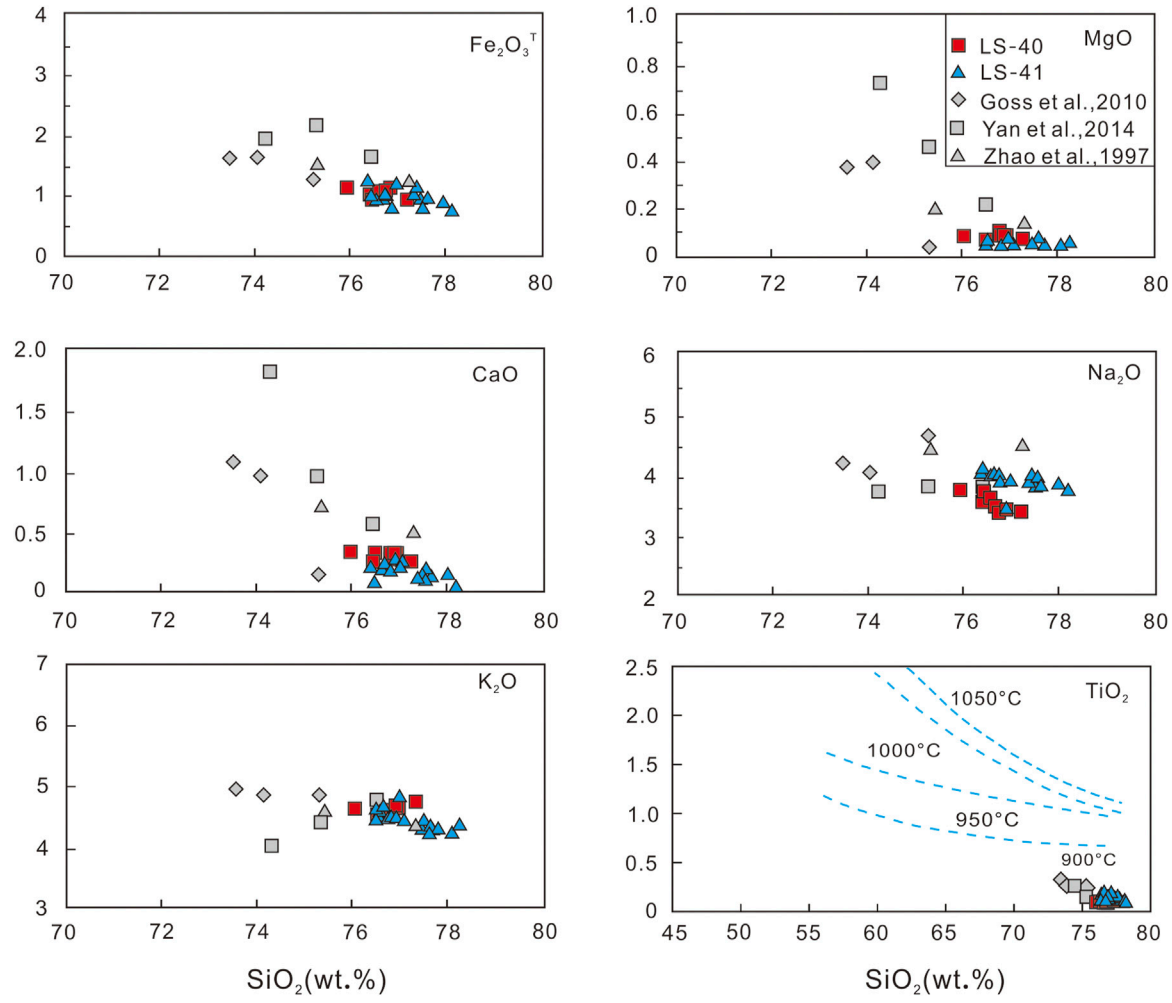


FIGURE 3
Harker diagrams for monzogranite, syenogranite, and alkali feldspar granite of the Laoshan granite complex. The monzogranite samples are from this article, and the data of Laoshan syenogranite and alkali feldspar granite are from references (Zhao et al., 1997; Goss et al., 2010; Yan and Shi, 2014).

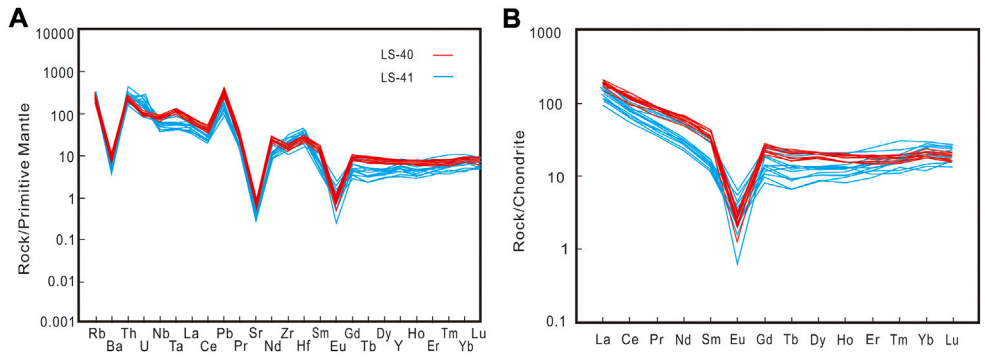


FIGURE 4
(A) Chondrite-normalized REE diagram. Chondritic values were from Sun and McDonough (1989). **(B)** Primitive mantle-normalized trace element diagram. Primitive mantle values are from Sun and McDonough (1989).

TABLE 2 LA-ICPMS zircon U–Pb data for Laoshan A-type granite (LS4002&LS4109).

Sample	$^{207}Pb/^{235}U$	$^{207}Pb/^{235}U$	$^{206}Pb/^{238}U$	$^{206}Pb/^{238}U$	$^{206}Pb/^{238}U$	$^{206}Pb/^{238}U$	Pb	Th	U	Ti	Th/U	Ce^{4+}/Ce^{3+}	T
	Ratio	2sigma	Ratio	2sigma	Age(Ma)	2sigma	ppm	ppm	ppm	ppm			°C
LS-4002-01	0.1163	0.0060	0.0178	0.0003	113.6	1.9	26.21	2042	973	4.69	2.10	76	740
LS-4002-02	0.1276	0.0078	0.0187	0.0004	119.3	2.7	10.40	757	339	8.73	2.23	54	801
LS-4002-03	0.1218	0.0059	0.0182	0.0003	116.5	1.9	20.42	1,199	814	6.52	1.47	40	771
LS-4002-04	0.1306	0.0075	0.0180	0.0004	115.2	2.5	7.68	329	344	4.24	0.96	46	730
LS-4002-05	0.1196	0.0083	0.0184	0.0005	117.7	2.9	7.67	381	315	5.10	1.21	67	748
LS-4002-06	0.1253	0.0054	0.0186	0.0003	118.8	2.0	14.90	448	684	1.90	0.66	33	662
LS-4002-07	0.1240	0.0074	0.0189	0.0004	120.5	2.3	12.14	406	562	3.68	0.72	43	718
LS-4002-08	0.1316	0.0078	0.0188	0.0004	120.0	2.5	13.08	684	491	3.97	1.39	102	725
LS-4002-09	0.1275	0.0102	0.0184	0.0006	117.3	3.7	6.60	300	267	5.38	1.13	98	753
LS-4002-10	0.1188	0.0098	0.0181	0.0004	115.9	2.8	9.88	762	325	11.44	2.34	32	830
LS-4002-11	0.1253	0.0062	0.0186	0.0003	119.0	1.8	22.47	644	1,037	2.22	0.62	79	675
LS-4002-12	0.1372	0.0075	0.0190	0.0004	121.1	2.8	23.22	1,059	943	6.04	1.12	14	764
LS-4002-13	0.1229	0.0092	0.0187	0.0005	119.3	3.0	15.17	821	596	7.55	1.38	49	786
LS-4002-14	0.1260	0.0106	0.0177	0.0005	113.3	3.0	4.04	161	182	6.75	0.89	181	775
LS-4002-15	0.1298	0.0099	0.0180	0.0004	114.9	2.6	9.27	607	344	6.62	1.76	113	773
LS-4002-16	0.1334	0.0070	0.0190	0.0004	121.2	2.4	37.87	2,845	1,146	9.06	2.48	45	805
LS-4002-17	0.1244	0.0119	0.0183	0.0006	116.6	3.6	3.88	104	186	2.43	0.56	75	682
LS-4002-18	0.1222	0.0066	0.0186	0.0004	118.5	2.4	12.10	365	565	3.27	0.65	112	707
LS-4002-19	0.1201	0.0059	0.0186	0.0003	118.6	2.2	16.21	595	725	5.44	0.82	123	754
LS-4002-20	0.1294	0.0075	0.0188	0.0004	120.4	2.6	11.60	289	536	3.48	0.54	8	713
LS-4002-21	0.1183	0.0056	0.0178	0.0004	113.5	2.2	18.71	403	931	2.72	0.43	130	691
LS-4002-22	0.1229	0.0075	0.0186	0.0004	118.6	2.4	27.94	1839	1,020	5.47	1.80	23	754
LS-4109-01	0.1211	0.0066	0.0186	0.0004	118.8	2.4	23.03	1,631	793	4.60	2.06	505	738
LS-4109-02	0.1208	0.0096	0.0184	0.0004	117.7	2.8	8.92	475	348	2.19	1.37	136	674
LS-4109-03	0.1252	0.0083	0.0189	0.0004	120.6	2.7	18.25	1,242	610	1.87	2.03	109	661
LS-4109-04	0.1264	0.0071	0.0191	0.0004	122.3	2.3	28.91	2,718	825	6.39	3.30	176	769
LS-4109-05	0.1201	0.0086	0.0183	0.0004	117.0	2.5	15.67	962	591	1.98	1.63	135	665
LS-4109-06	0.1207	0.0087	0.0180	0.0004	115.3	2.8	10.02	678	380	3.73	1.78	263	719
LS-4109-07	0.1219	0.0093	0.0187	0.0005	119.3	3.2	13.38	788	496	1.66	1.59	108	652
LS-4109-08	0.1302	0.0134	0.0187	0.0006	119.7	3.9	5.03	295	182	4.59	1.62	29	738
LS-4109-09	0.1336	0.0112	0.0189	0.0005	120.7	3.2	15.31	1,051	545	3.33	1.93	376	709
LS-4109-10	0.1273	0.0103	0.0187	0.0005	119.2	2.9	11.82	779	439	3.57	1.78	154	715

(Continued on following page)

10.3389/feart.2022.1000603

TABLE 2 (*Continued*) LA-ICPMS zircon U–Pb data for Laoshan A-type granite (LS4002&LS4109).

Sample	$^{207}Pb/^{235}U$		$^{207}Pb/^{235}U$	$^{206}Pb/^{238}U$		$^{206}Pb/^{238}U$		$^{206}Pb/^{238}U$	Pb	Th	U	Ti	Th/U	Ce^{4+}/Ce^{3+}	T
	Ratio		2sigma	Ratio		2sigma		Age(Ma)	2sigma	ppm	ppm	ppm			°C
LS-4109-11	0.1233		0.0082	0.0187		0.0004		119.7	2.7	19.64	1,158	700	5.00	1.66	76	746
LS-4109-12	0.1367		0.0086	0.0193		0.0004		122.9	2.7	43.09	3,678	1,298	6.58	2.83	359	772
LS-4109-13	0.1220		0.0108	0.0185		0.0005		118.0	3.3	10.67	707	382	2.54	1.85	48	686
LS-4109-14	0.1258		0.0107	0.0189		0.0005		120.8	3.2	21.62	1,474	717	2.54	2.05	379	686
LS-4109-15	0.1365		0.0145	0.0191		0.0006		121.7	3.8	10.58	1,013	279	7.21	3.63	41	781
LS-4109-16	0.1351		0.0094	0.0192		0.0004		122.9	2.7	22.74	1,578	785	2.25	2.01	1	676
LS-4109-17	0.1292		0.0098	0.0194		0.0005		123.8	3.1	11.61	633	414	4.28	1.53	258	731
LS-4109-18	0.1295		0.0108	0.0193		0.0005		123.4	3.1	12.40	716	449	3.11	1.60	128	703

log (Ti) = 5.711 ± 0.072 - 4,800(±86)/T(K) - log (aSiO2) + log (aTiO2) (Schiller and Finger, 2019; Yu et al., 2022).

Apatite major and trace elements

The apatites of the LS-40 sample have prismatic grains with smooth surface planes, indicating that they are magmatic apatite. The SiO_2 concentrations range from 0.21 wt% to 0.53 wt%, and the MnO concentrations range from 0.08 wt% to 0.30 wt%, which reflect the characteristics of the parent magma (Chen et al., 2017; Chen and Zhang, 2018; Sun et al., 2019; Yang et al., 2020c). The apatite major and trace elements show enriched fluorine (2.09–2.71 wt%) and low chlorine contents (0.01–0.09 wt%), with F/Cl ratios of 23.2–577 (Table 4). The apatites in these samples are enriched in LREEs ($(La/Yb)_N$ = 11.3 to 37.8; $(La/Gd)_N$ =3.07 to 8.31; $(Gd/Yb)_N$ =2.80–4.74) with a downwards sloping pattern toward HREEs (Figure 6). The apatite Ce/Pb ratios are 577–1,197, and Th/U ratios are 3.12–9.94.

Discussion

A-type granite affinity of the laoshan granite

A-type granite was originally used to describe the granite generated along rift zones and anorogenic environments (Loiselle and Wones, 1979). There is still debate about its petrogenesis and classification (Loiselle and Wones, 1979; Collins et al., 1982; Clemens et al., 1986; Whalen et al., 1987; Eby, 1990; Martin et al., 1994; Douce, 1997; King et al., 1997; Frost et al., 2001; Yang et al., 2006; Bonin, 2007; Huang et al., 2011). It is generally believed that A-type granite is derived from anhydrous and alkaline magma.

The geochemical compositions of A-type granite are characterized by enrichments in Na_2O + K_2O, REEs (except Eu), Nb, Ta, Zr and Ga, low MgO, CaO, Cr, Co, Ni, Sc, Sr, Ba, and Eu contents, and usually high $FeO^T/(FeO^T$ + MgO) ratios. Aluminous granites with depleted high field-strength elements may also plot in the VAG and WPG areas in the Rb–(Nb + Y) diagrams of Pearce and are classified as A-type granites (Pearce et al., 1984; Whalen et al., 1987; Bonin, 2007).

The major elements of the Laoshan granite display typical A-type granite characteristics, with high FeO^T/MgO ratios (11.6–33.6), K_2O/Na_2O ratios (1.08–1.39), K_2O + Na_2O (7.95–8.70 wt%), K_2O (4.23–4.79 wt%) and low P_2O_5 (0–0.01 wt%), CaO (0.04–0.33 wt%) contents (Figures 7A,B; Table 1; Frost et al., 2001).

The trace element compositions of the Laoshan granite also present A-type granite affinities. They are enriched in high field-strength elements (Zr, Y, Nb, Ta), with obvious depletions in Ba, Eu, Sr, and P. Low La/Nb ratios (mostly <1, except three samples 1.05–1.06) and high 10000*Ga/Al ratios (>2.6) are also consistent with typical A-type granite (Whalen et al., 1987).

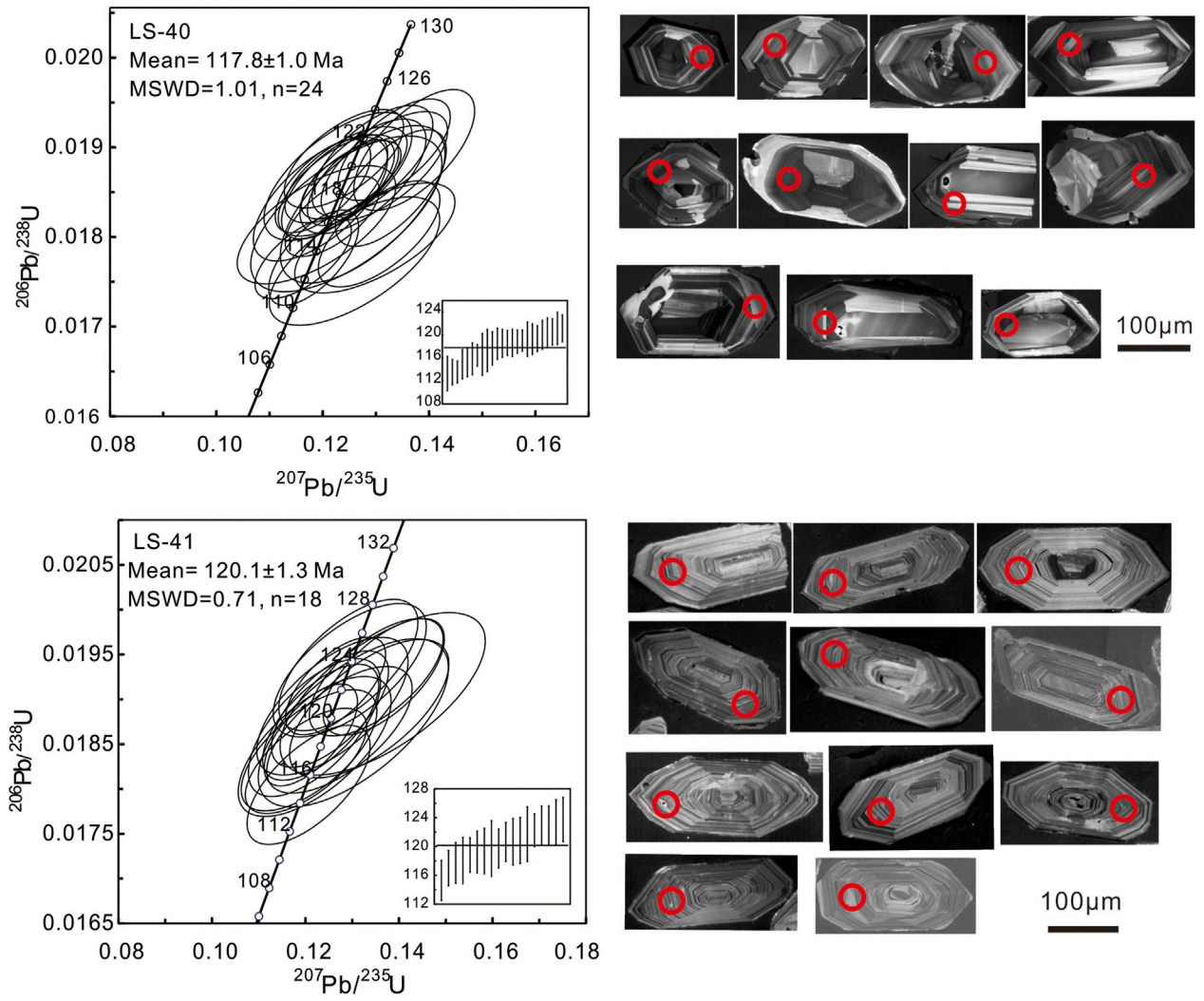


FIGURE 5
U–Pb concordia diagrams and cathodoluminescence (CL) image of zircons in monzogranites from the Laoshan granite. The average mean age of LS-41 is slightly older than that of LS-40.

A-type granite may contain low Zr, Nb, Ce, and Y because of extensive fractionation (Landenberger and Collins, 1996; Jiang et al., 2009), such that the effect of magmatic differentiation should be evaluated. Therefore, it is reliable to distinguish A-type granite by using these parameters. In addition, other discrimination diagrams based on key parameters also indicate that the Laoshan granite is an A-type granite (Figures 7C,D).

A-type granite has been further divided into A_1-type and A_2-type chemical subgroups (Eby, 1992). A_1-type granite has geochemical characteristics similar to those observed for oceanic island basalt (OIB) derived in an intraplate setting. In contrast, A_2-type granite has geochemical characteristics similar to those of rocks of island arc or continental crust origin located in a postcollisional setting (Eby, 1992). The arc signature of A_2-type granites has been considered to have been introduced through subduction-released fluids (Li et al., 2012a, 2014; Zhang et al., 2017b). The samples of Laoshan granite plot in the field of OIB (Figures 8A,B) and are classified as A_1-type granite based on high Nb and Ga relative to Ce and Y (Figures 8C,D). In addition, all the Y/Nb ratios of the Laoshan granite (0.38–1.03) are less than 1.2, supporting that it was derived from sources of oceanic island basalts (Eby, 1990). They plot in the field of within-plate type granite (WPG), and a few plot in the field of volcanic arc type granite (VAG) based on the diagram of Rb vs. (Y + Nb) (Figure 9).

Previous studies have shown that A_1-type and A_2-type granites form belts distributed parallel to each other in the LYR belt in eastern China (Figure 1C). This was explained by ridge subduction, which was also responsible for the genesis of

TABLE 3 Zircon trace element compositions for Laoshan A-type granite.

Sample	La (ppm)	Ce	Pr	Nd	Sm	Eu	Gd	Tb	Dy	Ho	Er	Tm	Yb	Lu	Hf	Ti
LS-4002-01	0.22	171	0.39	6.10	14.8	1.13	83.8	29.0	330	120	505	105	938	161	9,712	4.69
LS-4002-02	6.51	126	2.05	11.6	11.3	1.25	48.4	15.1	169	61.0	256	53.1	489	87.0	8,621	8.73
LS-4002-03	0.50	236	0.90	13.7	28.5	1.52	145	48.3	531	186	765	151	1,337	229	9,006	6.52
LS-4002-04	8.22	83.2	3.02	15.8	12.5	0.93	56.2	19.4	237	90.0	396	84.2	776	140	10,992	4.24
LS-4002-05	0.01	85.7	0.25	4.36	9.40	0.89	47.8	16.4	194	72.9	318	67.5	624	112	10,214	5.10
LS-4002-06	1.56	51.0	0.81	7.60	11.9	0.25	66.5	24.5	303	113	492	102	903	155	11,751	1.90
LS-4002-07	3.25	67.3	1.38	9.20	10.4	0.40	48.4	17.7	216	79.0	346	73.5	662	114	11,497	3.68
LS-4002-08	3.44	120	1.27	8.46	9.36	0.86	48.5	17.4	209	77.4	346	73.4	671	121	9,829	3.97
LS-4002-09	0.19	68.6	0.20	3.12	5.89	0.38	35.1	12.3	148	53.0	235	48.7	442	82.1	9,932	5.38
LS-4002-10	0.06	131	0.71	10.8	16.6	0.55	74.5	22.5	236	80.4	331	65.9	595	109	7,660	11.44
LS-4002-11	2.18	86.2	0.81	6.50	10.2	0.12	65.5	24.9	316	118	516	106	932	162	13,008	2.22
LS-4002-12	13.1	183	5.60	42.0	49.8	0.70	213	66.7	744	258	1,068	212	1859	330	9,494	6.04
LS-4002-13	0.60	138	0.49	7.09	15.9	0.73	81.1	27.3	311	111	471	93.6	826	149	10,563	7.55
LS-4002-14	0.01	73.2	0.14	2.56	5.43	0.66	29.6	11.3	144	59.3	279	62.3	603	117	9,584	6.75
LS-4002-15	0.04	102	0.21	3.54	7.38	0.94	42.7	14.7	172	62.9	276	57.7	530	99.3	9,280	6.62
LS-4002-16	0.25	421	1.18	20.4	41.4	3.07	192	61.8	687	240	1,003	199	1721	300	7,413	4.69
LS-4002-17	0.06	26.3	0.09	1.80	3.88	0.36	23.9	8.7	109	41.8	191	40.6	382	70.8	12,925	8.73
LS-4002-18	4.52	62.0	1.53	8.42	5.80	0.22	32.8	12.5	163	62.9	287	61.1	557	101	12,496	6.52
LS-4002-19	0.04	87.2	0.24	3.55	7.39	0.76	47.3	18.4	227	85.9	380	80.2	724	129	11,069	4.24
LS-4002-20	190	517	60.3	268	65.9	0.73	87.4	20.9	213	74.1	319	66.2	599	108	12,707	5.10
LS-4002-21	0.00	57.7	0.13	1.75	5.88	0.06	42.8	18.0	241	92.1	414	86.3	774	134	12,618	1.90
LS-4002-22	4.63	160	2.75	20.1	25.5	0.85	111	35.8	387	130	532	105	901	155	11,268	3.68
LS-4109-01	0.04	302	0.12	1.72	5.31	0.50	35.9	15.1	222	101	537	127	1,268	250	10,789	4.60
LS-4109-02	0.09	128	0.11	1.34	4.24	0.36	28.3	12.1	173	79.9	420	97.9	976	193	9,856	2.19
LS-4109-03	0.08	320	0.48	6.08	9.82	0.86	57.9	24.5	361	166	896	212	2090	413	10,831	1.87
LS-4109-04	0.00	335	0.19	3.81	11.6	1.69	79.6	29.3	360	141	629	128	1,119	201	9,315	6.39
LS-4109-05	0.00	219	0.11	1.42	3.33	0.40	25.0	12.5	193	96.1	531	131	1,319	264	9,606	1.98
LS-4109-06	0.00	183	0.24	3.30	5.80	0.45	34.6	15.2	225	108	595	144	1,427	284	11,593	3.73
LS-4109-07	0.08	203	0.16	3.01	6.81	0.60	40.0	17.4	249	114	585	133	1,293	251	9,762	1.66
LS-4109-08	0.04	117	0.18	3.73	7.40	1.01	46.2	17.5	218	88.3	410	87.0	793	146	10,032	4.59
LS-4109-09	2.46	225	0.71	4.51	7.52	0.72	47.3	18.9	252	105	503	111	1,041	197	10,175	3.33
LS-4109-10	0.00	239	0.28	4.34	8.31	0.90	53.8	23.2	320	143	739	169	1,660	323	10,691	3.57
LS-4109-11	0.01	298	0.10	1.89	4.59	0.65	37.8	17.1	247	115	609	142	1,397	276	9,482	5.00
LS-4109-12	0.03	613	0.20	3.01	7.91	0.77	52.3	22.8	344	161	873	206	2039	394	10,122	6.58
LS-4109-13	0.06	179	0.32	5.25	10.4	1.13	62.7	24.4	327	139	673	148	1,390	261	10,574	2.54
LS-4109-14	0.40	348	0.56	5.22	8.75	0.82	51.3	23.0	332	156	840	199	1972	389	9,584	2.54
LS-4109-15	0.37	624	3.20	54.3	108	11.34	457	136	1,377	432	1,588	276	2,142	352	6,778	7.21
LS-4109-16	0.43	348	0.29	2.29	5.36	0.57	38.4	17.0	257	122	659	157	1,563	303	9,037	2.25
LS-4109-17	0.00	159	0.13	1.69	4.79	0.64	33.0	13.7	195	85.4	438	100	966	190	9,812	4.28
LS-4109-18	0.03	166	0.10	1.46	3.70	0.43	27.2	12.3	185	87.5	466	112	1,104	219	9,341	3.11

adakites and copper-gold deposits there in the Early Cretaceous (Ling et al., 2009; Sun et al., 2010; Li et al., 2012a; Jiang et al., 2018). Geochemical studies on apatite from A_1-type and A_2-type granites in the LYR belt also showed systematic variations (Jiang et al., 2018). This ridge was moving northwards (Sun et al., 2007; Ling et al., 2013). The Early Cretaceous adakites and basalts in the Xuhuai and Shandong regions were explained as a result of ridge subduction in the Shandong Peninsula, which triggered the decratonization of the NCC (Ling et al., 2013; Wu et al., 2017). Many Early Cretaceous A-type granites crop out in this

TABLE 4 Major and trace element compositions of apatite from Laoshan granite samples.

Element	LS-4002-01	LS-4002-02	LS-4002-03	LS-4002-04	LS-4002-05	LS-4002-06	LS-4002-07	LS-4002-08	LS-4002-09	LS-4002-10	LS-4002-11	LS-4002-12	LS-4002-13
CaO	54.5	54.1	53.8	54.9	54.4	54.5	55.4	53.3	53.5	54.0	54.0	54.8	54.6
P_2O_5	42.5	42.4	41.3	42.3	42.6	42.6	41.9	42.3	41.2	43.0	43.0	43.1	41.8
SiO_2	0.38	0.26	0.56	0.22	0.27	0.37	0.44	0.28	0.53	0.21	0.21	0.26	0.38
FeO	0.05	0.04	0.05	0.15	0.07	0.09	0.12	0.47	0.11	0.16	0.06	0.05	0.06
MnO	0.23	0.25	0.20	0.20	0.14	0.30	0.10	0.23	0.27	0.25	0.20	0.08	0.23
MgO	0.01	0.00	0.01	0.02	0.00	0.01	0.02	0.01	0.02	0.00	0.01	0.01	0.01
SrO	0.00	0.00	0.02	0.00	0.02	0.00	0.03	0.01	0.01	0.00	0.02	0.03	0.00
F	2.72	2.58	2.71	2.52	2.59	2.68	2.09	2.35	2.61	2.31	2.66	2.27	2.42
Cl	0.01	0.04	0.02	0.03	0.04	0.03	0.09	0.04	0.03	0.00	0.01	0.04	0.02
Total	99.2	98.7	97.6	99.3	99.1	99.4	99.3	98.0	97.1	99.0	99.1	99.6	98.6
F/Cl	248	66.2	129	97.0	63.1	83.8	23.2	65.4	84.3	577	190	51.6	115
Rb	0.49	0.58	0.42	0.35	8.99	0.03	0.84	0.11	2.10	0.40	0.12	0.22	
Sr	36.7	168	39.7	41.3	60.6	43.5	1,572	337	174	42.3	34.3	1,341	
Y	3,568	1,383	2031	1994	1,453	2014	280	756	1,485	1,544	1930	476	
La	3,174	2,118	2,753	1779	2,404	2,191	499	2,386	1841	2,384	2,465	578	
Ce	8223	5,061	6,586	4,564	5,621	5,615	1,087	5,146	4,625	5,455	5,937	1,461	
Pr	1,079	617	811	591	668	715	134	588	590	653	730	174	
Nd	4,489	2,504	3,264	2,436	2,675	2,994	577	2,320	2,451	2,691	3,036	771	
Sm	1,047	493	660	568	519	621	107	359	511	515	607	150	
Eu	15.2	14.3	17.7	7.79	17.6	10.8	25.5	26.5	20.8	13.8	14.6	33.2	
Gd	896	389	530	477	379	480	83.1	249	388	394	482	124	
Tb	124	50.4	71.2	66.0	49.9	64.9	9.22	29.6	52.0	52.6	64.8	14.3	
Dy	716	280	409	385	285	381	47.7	163	288	287	367	80.1	
Ho	124	48.0	68.7	65.3	47.1	67.2	9.06	28.4	49.7	51.0	63.5	15.6	
Er	297	114	165	153	116	164	25.7	69.8	124	121	152	42.7	
Tm	35.0	13.5	19.8	18.4	13.2	19.5	3.38	8.49	15.4	14.2	18.2	5.74	
Yb	174	67.9	97.9	92.5	68.3	108	22.2	45.3	84.8	73.6	94.4	36.8	
Lu	19.9	8.31	11.5	11.7	7.94	13.6	3.31	5.81	10.8	8.47	11.05	5.39	

region. Similar to the A-type granites in the LYR belt, the A-type granites in the Shandong Peninsula have similar geochemical characteristics and distribution patterns.

Origin of the laoshan A-type granite

The Laoshan monzogranite is enriched in LILEs (such as Rb and Pb) and LREEs, pointing to LREE- and LILE-enriched sources. In the diagram of Ce/Pb vs. Nb/U, the LS-40 samples have systematically higher Nb/U ratios (21.8–34.7) than LS-41 (4.73–12.7, except for one sample of 27.0) with comparable Ce/Pb ratios (1.46–6.48) (Figure 10). The Nb/U and Ce/Pb ratios of LS-41 are lower than those of MORB and OIB (~25 and ~47, respectively) (Hofmann, 1997; Sun et al., 2008, 2013), but the Nb/U ratios of LS-41 are similar to those of the upper continental crust (~4.44), and the Ce/Pb ratios are equivalent to the average of the bulk continental crust (~3.91) (Rudnick and Gao, 2003). Nevertheless, the high temperatures of Laoshan A-type granites do not support direct continental crust origins. Given that Pb is more mobile than Ce, the lower Ce/Pb ratios indicate the influence of subduction-released fluids during plate subduction (McCulloch and Gamble, 1991; Pearce and Peate, 1995; Sun et al., 2008).

Apatite, containing volatiles and REEs, can provide information on metasomatic processes (Boyce and Hervig, 2008; Harlov, 2015) and petrogenetic processes that are usually obscure according to whole-rock geochemistry (Li et al., 2014; Miles et al., 2014; Bruand et al., 2017; Jiang et al., 2018). Apatite from the Laoshan granite contains low Cl and high F contents, indicating that the magmatic source of the Laoshan granite is characterized by low Cl and high F contents (Sun et al., 2019). During the evolution of granitic magma, most fluorine tends to enter crystallizing apatite, whereas there is a linear correlation between the Cl concentration of apatite and the concentration of Cl in the fluid (Webster et al., 2009).

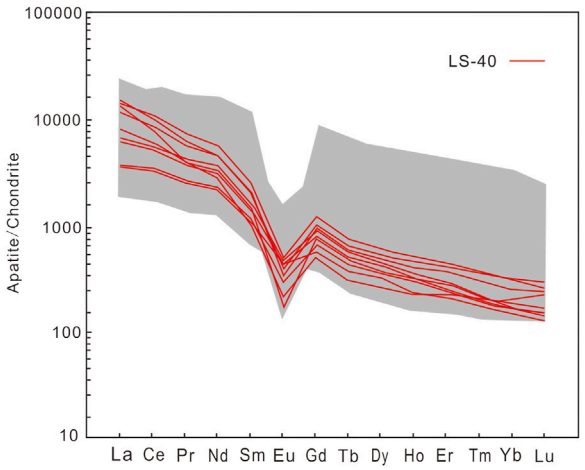


FIGURE 6
Apatite chondrite-normalized REE diagram for the Laoshan granite. Chondritic values were from Sun and McDonough (1989). All REEs have a decline to the right. Apatites of Laoshan granite have lower HREEs than Haiyang syenite and A-type granite in the LYR belt (gray area) (Li et al., 2014; Jiang et al., 2018).

During plate subduction, the majority of fluorine is retained in apatite and phengite (Sorensen et al., 1997), and it may be released during the rollback of a flatly subducting slab (Schmidt et al., 2004; Li et al., 2012a, 2014; Schmidt and Poli, 2014; Jiang et al., 2018). Cl is mainly hosted in amphibole, which tends to decompose at low pressure and release Cl into fluids at shallow depths (Volfinger et al., 1985; Zhang, 2012). The low Cl and high F contents may reflect that the source of the Laoshan granite involved fewer contributions from amphibole at shallow depths and more contributions from phengite (Figure 11).

Apatites from the Laoshan granite show mantle components in the source, as illustrated by the REE discrimination diagram (Figure 12) (Zhu et al., 2004), similar to those of the Haiyang syenite in the Shandong Peninsula and the A-type granite in the LYR belt (Li et al., 2014; Jiang et al., 2018).

Apatites in LS-40 samples are enriched in LREEs and depleted in HREEs with a right sloping pattern (Figure 6) with $(La/Yb)_N$ of 11.3–37.8, which is systematically lower than those from syenite and K-feldspar granite of Haiyang rock ($(La/Yb)_N$ = 22.5–64.0). The Ce/Pb ratios of apatites from Laoshan granite are similar to those of Huangmeijian (HMJ) A_1-type

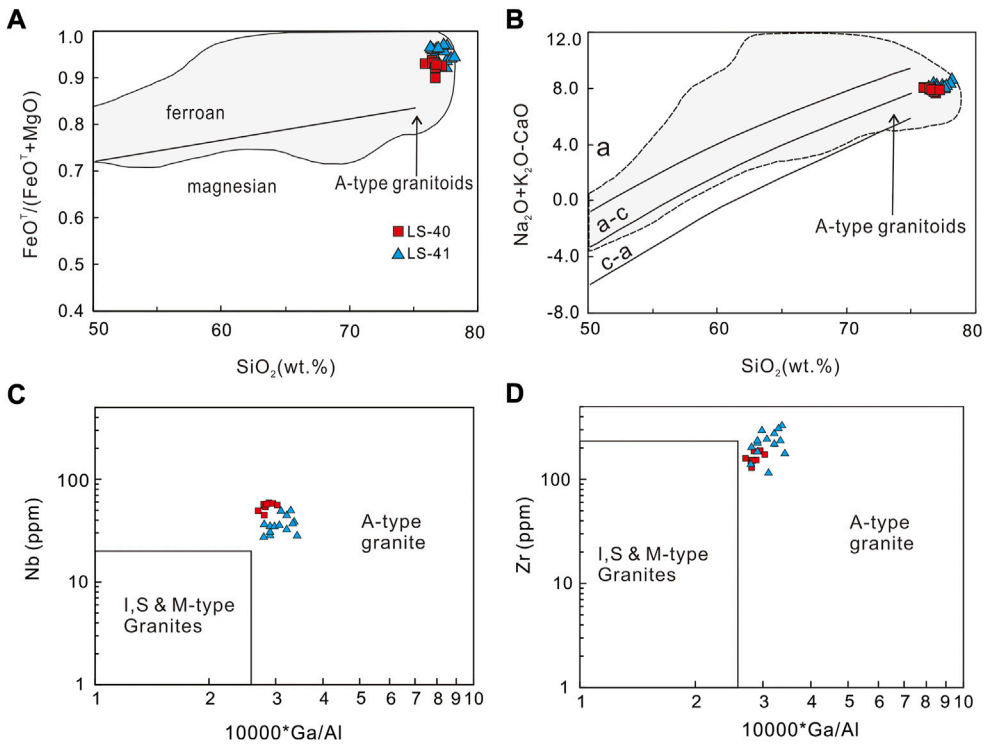


FIGURE 7
(A) FeOT/(FeOT + MgO) vs. SiO2 diagram, showing that all samples are ferroan granite A-type granites; **(B)**. K2O + Na2O−CaO vs. SiO2 discrimination diagram. Modified after Frost et al. (2001). **(C)** and **(D)** Various geochemical discrimination diagrams for A-type granite. Base maps are after Whalen et al. (1987) and Eby (1990).

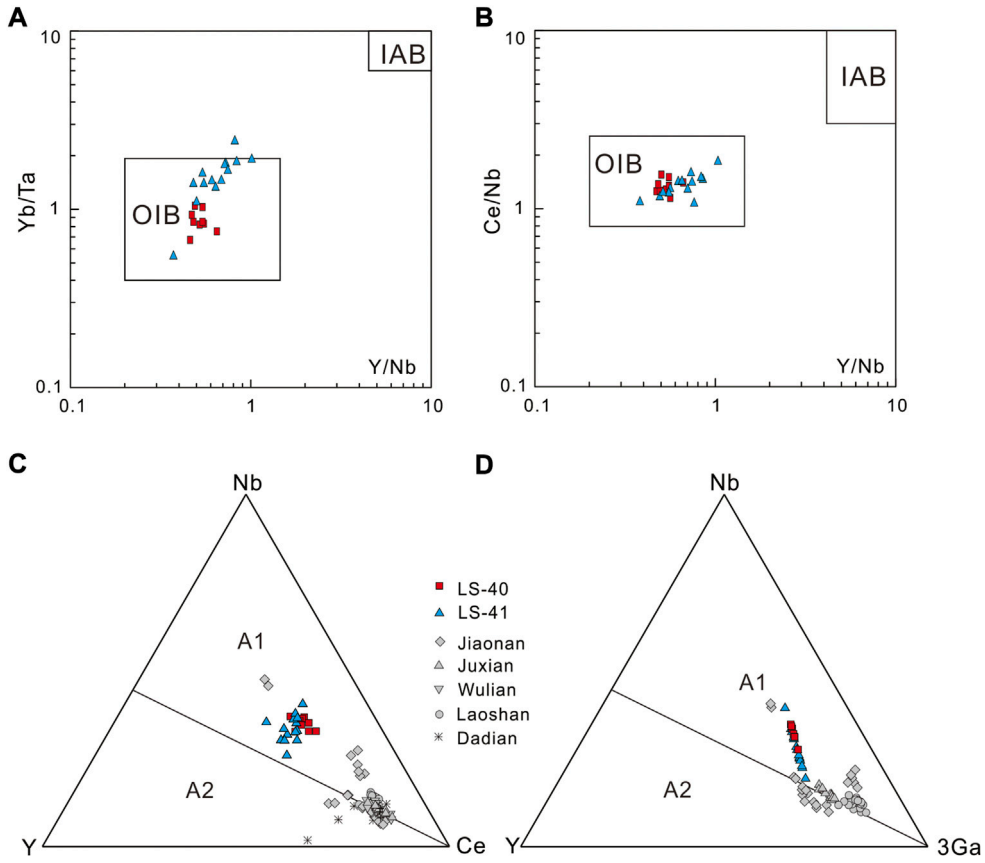


FIGURE 8
Representative geochemical diagrams for distinguishing between A1-type and A2-type granites. **(A)** Yb/Ta versus Y/Nb and **(B)** Ce/Nb versus Y/Nb diagrams for the Laoshan A-type granites. OIB = oceanic island basalt; IAB = island arc basalt. Base maps are after Eby (1992). In the **(C)** and **(D)** diagrams, the dashed line corresponds to Y/Nb ratios of 1.2 (Eby 1992). The data of the Laoshan pluton plot in the A1-type granite field; the data of the Haiyang, Juxian, Wulian and Jiaonan plutons plot near the line of demarcation of A1-type to A2-type granite (Zhao et al., 1997; Goss et al., 2010; Liu et al., 2013; Li et al., 2014; Yan and Shi 2014).

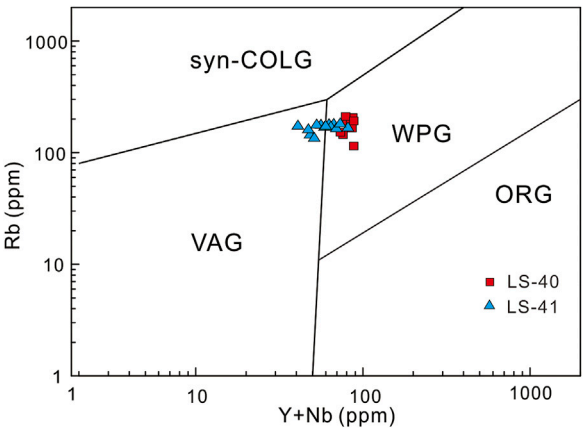


FIGURE 9
Tectonic setting discrimination diagram for granite (after Pearce et al., 1984). COLG = syncollisional granites; VAG = volcanic arc granites; ORG = ocean ridge granites; WPG =within-plate granites.

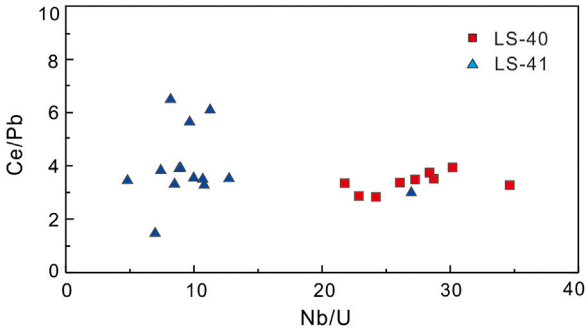


FIGURE 10
Ce/Pb vs. Nb/U ratio diagram, showing that LS-40 samples have higher Nb/U ratios than LS-41 but comparable Ce/Pb ratios.

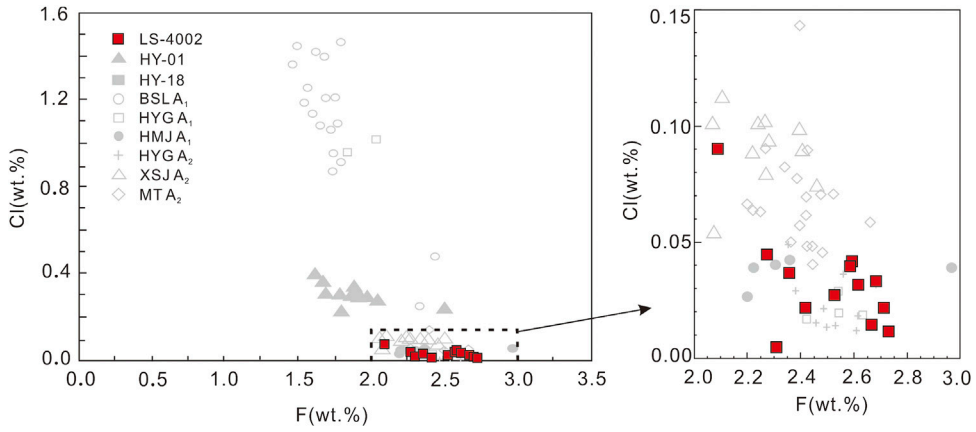


FIGURE 11
Cl vs. F diagram of the apatites, showing Laoshan granite with high F content and low Cl content. The apatite F-Cl composition of the Laoshan granite is similar to that of Huangmeijian (HMJ) A1-type granite in the LYR belt (Li et al., 2014; Jiang et al., 2018).

granite in the LYR belt. The Th/U ratios of samples from the Laoshan, Haiyang, and LYR belts are comparable. The Laoshan A_1-type granite is enriched in LREEs, similar to Huangmeijian (HMJ) A_1-type granite in the LYR belt (Debret et al., 2013; Jiang et al., 2018).

In the early stage of subduction, chrysotile transforms to antigorite and releases a large number of LREEs. As subduction continues, the antigorite transforms to secondary olivine, which contains much lower REEs. This results in higher LREE contents in the fluids released at the early stage (Debret et al., 2013) and may explain why apatites from the Laoshan A_1-type granite have higher $(Gd/Yb)_N$ and $(La/Yb)_N$ ratios but less variation in $(La/Gd)_N$ (Figure 13).

Cretaceous ridge subduction under the north China craton

The A-type granite belt in the Shandong Peninsula is NE-trending, including the Juxian, Wulian, Jiaonan, Laoshan, and Haiyang plutons, from southwest to northeast (Figure 1B). It can be further divided into A1-type and A1-A2 transitional-type granites (Figures 8C,D). The A1-type granite is mainly distributed in the Laoshan area, and the A1-A2 transitional type is distributed on both sides of the A1 granite, such as the Jiaonan, Juxian, Wulian and Haiyang areas (Figure 1B). All the A-type granites were formed at 110–123 Ma (Zhao et al., 1997; Goss et al., 2010; Liu et al., 2013; Li et al., 2014; Yan and Shi, 2014).

In the Early Cretaceous, the geodynamic setting in eastern China was mainly influenced by two subducting plates: the northwestward subducted Izanagi plate and the southwestward subducted Pacific plate (Maruyama et al., 2010). At ~125 Ma, the drifting direction of the Pacific plate changed to northwestward (Sun et al., 2007). Consequently, the ridge between these two plates moved northwards (Sun et al., 2007; Wu et al., 2017). This ridge moved westward and subducted to the Middle and Lower Yangtze River at approximately 140 Ma (Ling et al., 2009; Sun et al., 2010). Then, it moved to the Shandong Peninsula at ~120–130 Ma (Ling et al., 2009; Wu et al., 2017).

As subduction continued, the ridge gradually opened to form a slab window, and the asthenospheric material upwelled, forming A-type granite (Thorkelson and Breitsprecher, 2005; Li et al., 2011; Ling et al., 2011). Because the spreading oceanic ridge is hotter and drier than the normal oceanic crust, A1-type granite forms near the subducting ridge. The oceanic crust is increasingly wetter and colder with increasing distance from the oceanic ridge. Dehydration increases while partial melting decreases, forming A2-type granite during slab rollback (Ling et al., 2009, 2011; Li et al., 2011, 2014). Therefore, the distribution characteristics of A1-type and A2-type granites can be used to identify the locations of subduction ridges. This view has been well confirmed by the distribution of Mesozoic A-type granites in the LYR belt (Ling et al., 2009, 2013; Li et al., 2012a).

The mechanism of the destruction of the NCC has been debated for several decades. There are several competing models, including delamination (Wu et al., 2002; Gao et al., 2004), thermal erosion (Xu, 2007; Xu et al., 2014) and plate subduction (Niu, 2005; Sun et al., 2007; Zhu et al., 2011, 2012b, 2015). Previous studies have shown that ridge subduction at ~130 ± 5 Ma along the Xu-huai region and Shandong Peninsula was the key to the destruction of the NCC, and this subducting ridge migrated grandually northwards (Ling et al., 2013; Wu et al., 2017). Ridge subduction is usually flat with a strong power of physical erosion on the lithospheric mantle. Moreover, the duration of ridge subduction in Shandong Peninsula coincided with the peak of the destruction of the

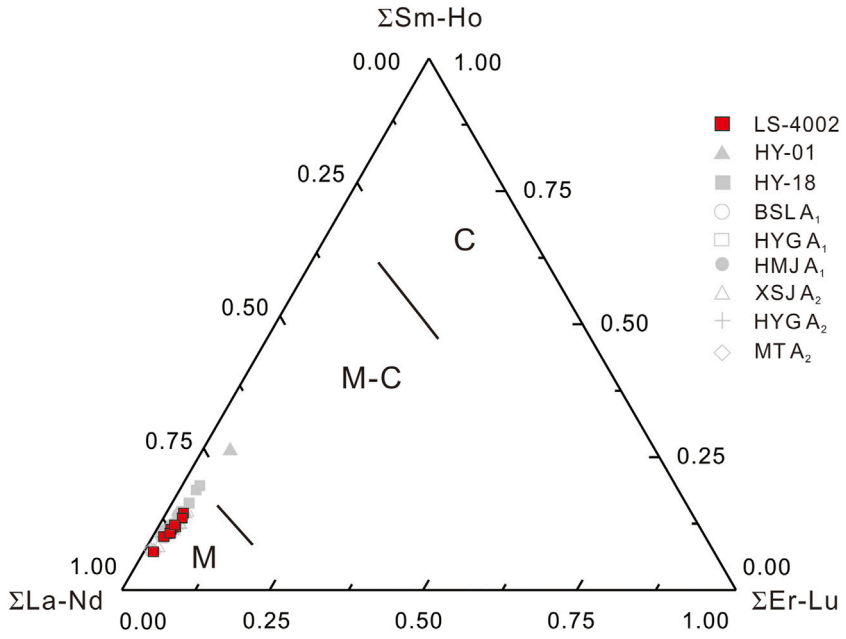


FIGURE 12
∑La~Nd−∑Sm~Ho−∑Er~Lu triangle diagram of the apatites, showing that the Laoshan granite has mantle components similar to those of the A-type granite in the LYR belt (Jiang et al., 2018). The Haiyang K-feldspar granite (HY-01) and syenite (HY-18) have major mantle contributions, with slight crustal addition (Li et al., 2014). M stands for mantle origin; M−C stands for mixing of mantle and crust origin; and C stands for crustal origin.

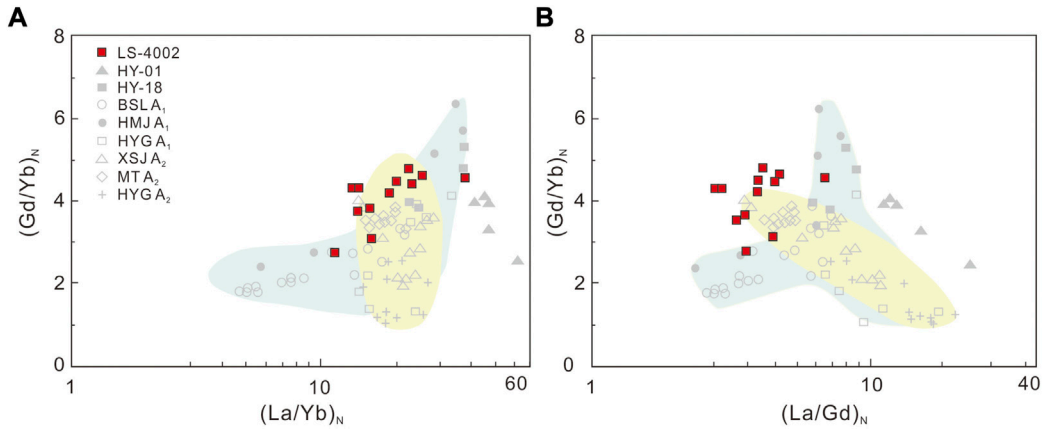


FIGURE 13
(A) (Gd/Yb)N versus (La/Yd)N, **(B)** (Gd/Yb)N versus (La/Gd)N diagrams of apatite from Laoshan A1-type granites. The gray figure represents A1- and A2-type granites in the LYR belt and the data after Jiang et al. (2018). The green field designates the A1-type granite, and yellow designates the A2-type granite.

NCC. This interpretation is supported by later studies that suggested that the advancing flat slab can scrape off the lowermost 20–50 km of continental mantle lithosphere (Axen et al., 2018). During the Early Cretaceous, the destruction of the NCC was followed by extensive granitic magmatic activity (Xu, 2001; Xu et al., 2004, 2012; Menzies et al., 2007; Yang et al., 2018b, 2020b). These intrusions, which record large-scale magmatic activity information, are important in revealing the geodynamic mechanism of eastern China. In particular, A-type granites, formed in extensional environments, can elucidate

regional tectonic settings (Loiselle and Wones, 1979; Whalen et al., 1987). Ridge subduction is usually flat, which is followed by slab rollback. Flat subduction and subsequent slab rollback can plausibly explain the destruction and subsequent large-scale magmatism in eastern China (Ling et al., 2013; Wu et al., 2017). Combined with the spatial distribution of the A-type granites in Shandong Peninsula and the drift history of the Izanagi plate in the Early Cretaceous, we propose that the Laoshan A-type granite and other A-type intrusions, i.e., the Haiyang A1-A2-type complex in Shandong Peninsula, were the result of ridge subduction.

Conclusion

The Laoshan granites formed at 117.8 ± 1.0 Ma to 120.1 ± 1.3 Ma. The geochemical characteristics indicate that the Laoshan plutons belong to A-type granites with high total alkali contents, high Ga/Al and FeO^T/MgO ratios, and LILE enrichments. It is further classified into the A_1 subgroup. It crystallized under moderate and low oxygen fugacity conditions, as indicated by zircon Ce^{IV}/Ce^{III} ratios. Apatites from Laoshan granites show high F and low Cl contents, with high $(Gd/Yb)_N$ and $(La/Yb)_N$ ratios, indicating influences from high F fluid in the source as the result of decomposition of the phengite in the subducted slab. The genesis of the A-type granite in the Shandong Peninsula can plausibly be interpreted with a ridge subduction model, which may have triggered the decratonization of the NCC.

Data availability statement

The raw data supporting the conclusions of this article will be made available by the authors, without undue reservation.

Author contributions

JL and HL conceived and designed the ideas. CL participated in field investigation. MS and LZ performed the data processing. MJ and reviewed and edited the draft, SY revised illustrations.

Funding

This study was supported by the National Natural Science Foundation of China (91958110) and the Strategic Priority Research Program of the Chinese Academy of Sciences (No. XDB42020203), the Hebei Natural Science Foundation (D2020403061), the Key Projects of Science and Technology Research in Universities of Hebei Province (ZD2021018), and the National Natural Science Foundation of China Shandong Joint Fund Project (U2006201).

Conflict of interest

The authors declare that the research was conducted in the absence of any commercial or financial relationships that could be construed as a potential conflict of interest.

Publisher's note

All claims expressed in this article are solely those of the authors and do not necessarily represent those of their affiliated organizations, or those of the publisher, the editors and the reviewers. Any product that may be evaluated in this article, or claim that may be made by its manufacturer, is not guaranteed or endorsed by the publisher.

References

Axen, G. J., Van Wijk, J. W., and Currie, C. A. (2018). Basal continental mantle lithosphere displaced by flat-slab subduction. *Nat. Geosci.* 11 (12), 961–964. doi:10.1038/s41561-018-0263-9

Ballard, J. R., Palin, J. M., and Campbell, I. H. (2002). Relative oxidation states of magmas inferred from Ce(IV)/Ce(III) in zircon: Application to porphyry copper deposits of northern Chile. *Contrib. Mineral. Pet.* 144, 347–364. doi:10.1007/s00410-002-0402-5

Belousova, E. A., Griffin, W. L., Suzanne, Y. O. R., and Fisher, N. I. (2002). Igneous zircon: Trace element composition as an indicator of source rock type. *Contrib. Mineral. Pet.* 143, 602–622. doi:10.1007/s00410-002-0364-7

Bonin, B. (2007). A-type granites and related rocks: Evolution of a concept, problems and prospects. *Lithos* 97, 1–29. doi:10.1016/j.lithos.2006.12.007

Boyce, J. W., and Hervig, R. L. (2008). Apatite as a monitor of late-stage magmatic processes at Volcán Irazú, Costa Rica. *Contrib. Mineral. Pet.* 157 (2), 135–145. doi:10.1007/s00410-008-0325-x

Bruand, E., Fowler, M., Storey, C., and Darling, J. (2017). Apatite trace element and isotope applications to petrogenesis and provenance. *Am. Mineralogist* 102, 75–84. doi:10.2138/am-2017-5744

Chen, L., Yan, Z., Wang, Z. Q., and Wang, K. M. (2017). Characteristics of apatite from 160-140 Ma Cu(Mo) and Mo(W) deposits in east qinling. *Acta Geol. Sin.* 91. 1925–19402.

Chen, L., and Zhang, Y. (2018). *In situ* major-trace-elements and Sr-Nd isotopic compositions of apatite from the luming porphyry Mo deposit, NE China: Constraints on the petrogenetic-metallogenic features. *Ore Geol. Rev.* 94, 93–103. doi:10.1016/j.oregeorev.2018.01.026

Clemens, J. D., Holloway, J. R., and White, A. J. R. (1986). Origin of an A-type granite; experimental constraints. *Am. Mineralogist* 7, 317–324.

Collins, W. J., Beams, S. D., White, A. J. R., and Chappell, B. W. (1982). Nature and origin of A-type granites with particular reference to southeastern Australia. *Contr. Mineral. Pet.* 80, 189–200. doi:10.1007/bf00374895

Debret, B., Nicollet, C., Andreani, M., Schwartz, S., and Godard, M. (2013). Three steps of serpentinization in an eclogitized oceanic serpentinization front (Lanzo Massif – western Alps). *J. Metamorph. Geol.* 31, 165–186. doi:10.1111/jmg.12008

Deng, J., Wang, C. M., Bagas, L., Carranza, E. M., and Lu, Y. J. (2015). Cretaceous-cenozoic tectonic history of the jiaojia fault and gold mineralization in the Jiaodong peninsula, China: Constraints from zircon U-Pb, illite K-Ar, and apatite fission track thermochronometry. *Min. Depos.* 50, 987–1006. doi:10.1007/s00126-015-0584-1

Deng, J., Wang, Q. F., Santosh, M., Liu, X. F., Liang, Y. Y., Yang, L. Q., et al. (2020). Remobilization of metasomatized mantle lithosphere: A new model for the Jiaodong gold province, eastern China. *Min. Depos.* 55 (3), 257–274. doi:10.1007/s00126-019-00925-0

Douce, A. E. P. (1997). Generation of metaluminous A-type granites by low-pressure melting of calc-alkaline granitoids. *Geol.* 25, 743–746. doi:10.1130/0091-7613(1997)025<0743:gomatg>2.3.co;2

Eby, G. N. (1992). Chemical subdivision of the A-type granitoids:Petrogenetic and tectonic implications. *Geol.* 20, 641–644. doi:10.1130/0091-7613(1992)020<0641:csotat>2.3.co;2

Eby, G. N. (1990). The A-type granitoids: A review of their occurrence and chemical characteristics and speculations on their petrogenesis. *Lithos* 26, 115–134. doi:10.1016/0024-4937(90)90043-z

Fan, H. R., Feng, K., Li, X. H., Hu, F. F., and Yang, K. F. (2016). Mesozoic gold mineralization in the Jiaodong and Korean peninsulas. *Acta Petrol. Sin.* 32, 3225–3238. (in Chinese with English abstract).

Fan, W. M., and Menzies, M. A. (1992). Destruction of aged lower lithosphere and accretion of asthenosphere mantle beneath eastern China. *Geotect. Metallogenia* 16, 171–180.

Frost, B. R., Barnes, C. G., Collins, W. J., Arculus, R. J., Ellis, D. J., and Frost, C. D. (2001). A geochemical classification for granitic rocks. *J. Petrology* 42, 2033–2048. doi:10.1093/petrology/42.11.2033

Gao, S., Rudnick, R. L., Yuan, H. L., Liu, X. M., Liu, Y. S., Xu, W. L., et al. (2004). Recycling lower continental crust in the North China craton. *Nature* 432, 892–897. doi:10.1038/nature03162

Gao, Y. J., Niu, Y. L., Duan, M., Xue, Q. Q., Sun, P., Chen, S., et al. (2019). The petrogenesis and tectonic significance of the Early Cretaceous intraplate granites in eastern China: The Laoshan granite as an example. *Lithos* 328–329, 200–211. doi:10.1016/j.lithos.2019.01.031

Goss, S. C., Wilde, S. A., Wu, F. Y., and Yang, J. H. (2010). The age, isotopic signature and significance of the youngest mesozoic granitoids in the Jiaodong Terrane, Shandong province, North China craton. *Lithos* 120, 309–326. doi:10.1016/j.lithos.2010.08.019

Groves, D. I., Zhang, L., and Santosh, M. (2020). Subduction, mantle metasomatism, and gold: A dynamic and genetic conjunction. *GSA Bull.* 132 (7-8), 1419–1426. doi:10.1130/b35379.1

Harlov, D. E. (2015). Apatite: A fingerprint for metasomatic processes. *Elements* 11, 171–176. doi:10.2113/gselements.11.3.171

Hofmann, A. W. (1997). Mantle geochemistry: The message from oceanic volcanism. *Nature* 385, 219–229. doi:10.1038/385219a0

Hoskin, P. W. O., and Black, L. P. (2000). Metamorphic zircon formation by solid-state recrystallization of protolith igneous zircon. *J. Metamorph. Geol.* 18, 423–439. doi:10.1046/j.1525-1314.2000.00266.x

Huang, H. Q., Li, X. H., Li, W. X., and Li, Z. X. (2011). Formation of high $\delta^{18}O$ fayalite-bearing A-type granite by high temperature melting of granulitic metasedimentary rocks, southern China. *Geology* 39, 903–906. doi:10.1130/g32080.1

Jiang, N., Zhang, S. Q., Zhou, W. G., and Liu, Y. S. (2009). Origin of a mesozoic granite with A-type characteristics from the north China craton: Highly fractionated from I-type magmas? *Contrib. Mineral. Pet.* 158, 113–130. doi:10.1007/s00410-008-0373-2

Jiang, X. Y., Li, H., Ding, X., Wu, K., Guo, J., Liu, J. Q., et al. (2018). formation of A-type granites in the lower Yangtze River belt: A perspective from apatite geochemistry. *Lithos* 304–307, 125–134. doi:10.1016/j.lithos.2018.02.005

King, P. L., White, A. J. R., Chappell, B. W., and Allen, C. M. (1997). Characterization and origin of aluminous A-type granites from the lachlan fold belt, southeastern Australia. *J. Petrology* 38, 371–391. doi:10.1093/petroj/38.3.371

Landenberger, B., and Collins, W. J. (1996). Derivation of A-type granites from a dehydrated charnockitic lower crust: Evidence from the chaelundi complex, eastern Australia. *J. Petrol.* 37, 145–170. doi:10.1093/petrology/37.1.145

Li, C. Y., Zhang, H., Wang, F. Y., Liu, J. Q., Sun, Y. L., Hao, X. L., et al. (2012b). The formation of the Dabaoshan porphyry molybdenum deposit induced by slab rollback. *Lithos* 150, 101–110. doi:10.1016/j.lithos.2012.04.001

Li, H., Ling, M. X., Ding, X., Zhang, H., Li, C. Y., Liu, D. Y., et al. (2014). The geochemical characteristics of Haiyang A-type granite complex in Shandong, eastern China. *Lithos* 200, 142–156. doi:10.1016/j.lithos.2014.04.014

Li, H., Ling, M. X., Li, C. Y., Zhang, H., Ding, X., Yang, X. Y., et al. (2012a). A-type granite belts of two chemical subgroups in central eastern China: Indication of ridge subduction. *Lithos* 150, 26–36. doi:10.1016/j.lithos.2011.09.021

Li, H., Zhang, H., Ling, M. X., Wang, F. Y., Ding, X., Zhou, J. B., et al. (2011). Geochemical and zircon U-Pb study of the huangmeijian A-type granite: Implications for geological evolution of the lower Yangtze River belt. *Int. Geol. Rev.* 53, 499–525. doi:10.1080/00206814.2010.496202

Li, J., Li, C. Y., Song, M. C., Liang, J. L., Zhang, L. P., and Song, Y. X. (2021). Mineralization of the shangjiazhuang Mo deposit in the Jiaodong peninsula, China: Constraints from S-H-O isotopes and fluid inclusions. *Solid Earth Sci.* 6 (4), 370–384. doi:10.1016/j.sesci.2021.08.001

Li, J., Song, M. C., Liang, J. L., Jiang, M. Y., Li, S. Y., Ding, Z. J., et al. (2020). Source of ore-forming fluids of the Jiaojia deeply-seated gold deposit: Evidences from trace elements and sulfur-helium-argon isotopes of pyrite. *Acta Petrol. Sin.* 36 (1), 297–313. (in Chinese with English abstract). doi:10.18654/1000-0569/2020.01.23

Li, S. G., Xiao, Y. L., Liou, D. L., Chen, Y. Z., Ge, N. J., Zhang, Z. Q., et al. (1993). Collision of the North China and Yangtse blocks and formation of coesite-bearing eclogites; timing and processes. *Chem. Geol.* 109, 89–111. doi:10.1016/0009-2541(93)90063-o

Li, X. H., Qi, C. S., Liu, Y., Liang, X. R., Tu, X. L., Xie, L. W., et al. (2005). Petrogenesis of the Neoproterozoic bimodal volcanic rocks along the Western margin of the Yangtze Block: New constraints from Hf isotopes and Fe/Mn ratios. *Chin. Sci. Bull.* 50, 2481–2486. doi:10.1360/982005-287

Liang, H. Y., Campbell, I. H., Allen, C., Sun, W. D., Liu, C. Q., Yu, H. X., et al. (2006). Zircon Ce^{4+}/Ce^{3+} ratios and ages for Yulong ore-bearing porphyries in eastern Tibet. *Min. Depos.* 41, 152–159. doi:10.1007/s00126-005-0047-1

Liang, J. L., Ding, X., Sun, X. M., Zhang, Z. M., Zhang, H., and Sun, W. D. (2009). Nb/Ta fractionation observed in eclogites from the Chinese continental scientific drilling Project. *Chem. Geol.* 268, 27–40. doi:10.1016/j.chemgeo.2009.07.006

Lin, J., Liu, Y. S., Yang, Y. H., and Hu, Z. C. (2016). Calibration and correction of LA-ICP-MS and LA-MC-ICP-MS analyses for element contents and isotopic ratios. *Solid Earth Sci.* 1, 5–27. doi:10.1016/j.sesci.2016.04.002

Ling, M. X., Li, Y., Ding, X., Teng, F. Z., Yang, X. Y., Fan, W. M., et al. (2013). Destruction of the north China craton induced by ridge subductions. *J. Geol.* 121, 197–213. doi:10.1086/669248

Ling, M. X., Wang, F. Y., Ding, X., Hu, Y. H., Zhou, J. B., Zartman, R. E., et al. (2009). Cretaceous ridge subduction along the lower Yangtze River Belt, eastern China. *Econ. Geol.* 104, 303–321. doi:10.2113/gsecongeo.104.2.303

Ling, M. X., Wang, F. Y., Ding, X., Zhou, J. B., and Sun, W. D. (2011). Different origins of adakites from the dabie mountains and the lower Yangtze River belt, eastern China: Geochemical constraints. *Int. Geol. Rev.* 53, 727–740. doi:10.1080/00206814.2010.482349

Liu, S., Feng, G. Y., Qi, Y. Q., Gao, S., Wang, T., et al. (2013). Zircon U-Pb age, geochemical, and Sr-Nd-Pb isotopic constraints on the;origin of alkaline intrusions in eastern Shandong Province, China. *Mineral. Pet.* 107, 591–608. doi:10.1007/s00710-013-0285-3

Liu, Y. S., Gao, S., Hu, Z. C., Gao, C. G., Zong, K. Q., and Wang, D. B. (2010). Continental and oceanic crust recycling-induced melt-peridotite interactions in the trans-north China orogen: U-Pb dating, Hf isotopes and trace elements in zircons from mantle xenoliths. *J. Petrology* 51, 537–571. doi:10.1093/petrology/egp082

Liu, Y. S., Hu, Z. C., Gao, S., Gunther, D., Xu, J., Gao, C. G., et al. (2008). *In situ* analysis of major and trace elements of anhydrous minerals by LA-ICP-MS without applying an internal standard. *Chem. Geol.* 257, 34–43. doi:10.1016/j.chemgeo.2008.08.004

Loiselle, M. C., and Wones, D. R. (1979). *Characteristics and origin of anorogenic granites*. New York: Geological society of America abstracts with programs, 468.

Martin, H., Bonin, B., Capdevila, R., Jahn, B. M., Lameyre, J., and Wang, Y. (1994). The kuiqi peralkaline granitic complex (SE China): Petrology and geochemistry. *J. Petrology* 35, 983–1015. doi:10.1093/petrology/35.4.983

Maruyama, S., Isozaki, Y., Kimura, G., and Terabayashi, M. (2010). Paleogeographic maps of the Japanese Islands: Plate tectonic synthesis from 750 Ma to the presen. *Isl. Arc* 6, 121–142.

McCulloch, M. T., and Gamble, J. A. (1991). Geochemical and geodynamical constraints on subduction zone magmatism. *Earth Planet. Sci. Lett.* 102, 358–374. doi:10.1016/0012-821x(91)90029-h

Menzies, M., Xu, Y. G., Zhang, H. F., and Fan, W. M. (2007). Integration of geology, geophysics and geochemistry: A key to understanding the north China craton. *Lithos* 96, 1–21. doi:10.1016/j.lithos.2006.09.008

Miles, A. J., Graham, C. M., Hawkesworth, C. J., Gillespie, M. R., Hinton, R. W., and Bromiley, G. D. (2014). Apatite: A new redox proxy for silicic magmas? *Geochimica Cosmochimica Acta* 132, 101–119. doi:10.1016/j.gca.2014.01.040

Niu, Y. L. (2005). Generation and evolution of basaltic magmas: Some basic concepts and a new view on the origin of mesozoic-cenozoic basaltic volcanism in eastern China. *Geol. J. China Univ.* 11, 9–46.

Pearce, J. A., Harris, N. B. W., and Tindle, A. G. (1984). Trace element discrimination diagrams for the tectonic interpretation of granitic rocks. *J. Petrology* 25, 956–983. doi:10.1093/petrology/25.4.956

Pearce, J. A., and Peate, D. W. (1995). Tectonic implications of the composition of volcanic arc magmas. *Annu. Rev. Earth Planet. Sci.* 23, 251–285. doi:10.1146/annurev.ea.23.050195.001343

Rudnick, R. L., and Gao, S. (2003). "Composition of the continental crust," in *Treatise on geochemistry*. Editor R. L. Rudnick (Elsevier), 1–64.

Schiller, D., and Finger, F. (2019). Application of Ti-in-zircon thermometry to granite studies: Problems and possible solutions. *Contrib. Mineral. Pet.* 174, 51. doi:10.1007/s00410-019-1585-3

Schmidt, M. W., and Poli, S. (2014). "Devolatilization during subduction," in *The crust*. *Treatise on geochemistry*. Editors R. L. Rudnick, H. D. Holland, and K. K. Turekian. Second edition (Oxford: Elsevier-Pergamon), 669–701.

Schmidt, M. W., Vielzeuf, D., and Auzanneau, E. (2004). Melting and dissolution of subducting crust at high pressures: The key role of white mica. *Earth Planet. Sci. Lett.* 228, 65–84. doi:10.1016/j.epsl.2004.09.020

Song, M. C., Li, J., Yu, X. F., Song, Y. X., Ding, Z. J., and Li, S. Y. (2021). Metallogenic characteristics and tectonic setting of the Jiaodong gold deposit, China. *Solid Earth Sci.* 6 (4), 385–405. doi:10.1016/j.sesci.2021.07.002

Song, M. C., Li, S. Z., Santosh, M., Zhao, S. J., Yu, S., Yi, P. H., et al. (2015). Types, characteristics and metallogenesis of gold deposits in the Jiaodong peninsula, eastern North China craton. *Ore Geol. Rev.* 65, 612–625. doi:10.1016/j.oregeorev.2014.06.019

Song, M. C., Wang, S. S., Yang, L. X., Li, J., Li, S. Y., and Ding, Z. J. (2017). Metallogenic epoch of nonferrous metallic and silver deposits in the Jiaodong peninsula, China and its geological significance. *Acta Geol. Sin. - Engl. Ed.* 91 (4), 1305–1325. doi:10.1111/1755-6724.13363

Song, M. C., Zhou, J. B., Song, Y. X., Wang, B., Li, S. Y., Li, J., et al. (2019). Mesozoic Weideshan granitoid suite and its relationship to large-scale gold mineralization in the Jiaodong Peninsula, China. *Geol. J.* 55 (8), 5703–5724. doi:10.1002/gj.3607

Sorensen, S. S., Grossman, J. N., and Perfit, M. R. (1997). Phengite-hosted LILE enrichment in eclogite and related rocks: Implications for fluid-mediated mass transfer in subduction zones and arc magma Genesis. *J. Petrology* 38, 3–34. doi:10.1093/petroj/38.1.3

Sun, S. J., Yang, X. Y., Wang, G. J., Sun, W. D., Zhang, H., Li, C. Y., et al. (2019). *In situ* elemental and Sr-O isotopic studies on apatite from the Xu-Huai intrusion at the southern margin of the North China Craton: Implications for petrogenesis and metallogeny. *Chem. Geol.* 510, 200–214. doi:10.1016/j.chemgeo.2019.02.010

Sun, S. S., and McDonough, W. F. (1989). "Chemical and isotopic systematics of oceanic basalts: Implications formantle composition andprocesses," in *Magmatism in the ocean basalts*. Editors A. D. Saunders and M. J. Norry (Geological Society, London: Special Publications), 313–345.

Sun, W. D., Ding, X., Hu, Y. H., and Li, X. H. (2007). The golden transformation of the Cretaceous plate subduction in the west Pacific. *Earth Planet. Sci. Lett.* 262, 533–542. doi:10.1016/j.epsl.2007.08.021

Sun, W. D., Hu, Y. H., Kamenetsky, V. S., Eggins, S. M., Chen, M., and Arculus, R. J. (2008). Constancy of Nb/U in the mantle revisited. *Geochimica Cosmochimica Acta* 72, 3542–3549. doi:10.1016/j.gca.2008.04.029

Sun, W. D., Li, S. G., Chen, Y. D., and Li, Y. J. (2002a). Timing of synorogenic granitoids in the south qinling, central China: Constraints on the evolution of the qinling-dabie orogenic belt. *J. Geol.* 110, 457–468. doi:10.1086/340632

Sun, W. D., Li, S., Yang, X. Y., Ling, M. X., Ding, X., Duan, L. A., et al. (2013). Large-scale gold mineralization in eastern China induced by an Early Cretaceous clockwise change in Pacific plate motions. *Int. Geol. Rev.* 55, 311–321. doi:10.1080/00206814.2012.698920

Sun, W. D., Ling, M. X., Yang, X. Y., Fan, W. M., Ding, X., and Liang, H. Y. (2010). Ridge subduction and porphyry copper-gold mineralization: An overview. *Sci. China Earth Sci.* 53, 475–484. doi:10.1007/s11430-010-0024-0

Sun, W. D., Williams, I. S., and Li, S. G. (2002b). Carboniferous and triassic eclogites in the Western dabie mountains, east-central China: Evidence for protracted convergence of the north and south China blocks. *J. Metamorph. Geol.* 20, 873–886. doi:10.1046/j.1525-1314.2002.00418.x

Tan, J., Wei, J. H., Audétat, A., and Pettke, T. (2012). Source of metals in the Guocheng gold deposit, Jiaodong Peninsula, North China Craton: Link to early Cretaceous mafic magmatism originating from Paleoproterozoic metasomatized lithospheric mantle. *Ore Geol. Rev.* 48, 70–87. doi:10.1016/j.oregeorev.2012.02.008

Thorkelson, D. J., and Breitsprecher, K. (2005). Partial melting of slab window margins: Genesis of adakitic and non-adakitic magmas. *Lithos* 79, 25–41. doi:10.1016/j.lithos.2004.04.049

Tu, X. L., Zhang, H. F., Deng, W. F., Liang, H. Y., and Sun, W. D. (2011). Application of RESOlution laser ablation ICPMS in trace element analyses. *Geochimica* 40, 83–98. (in Chinese with English abstract).

Volfinger, M., Robert, J. L., Vielzeuf, D., and Neiva, A. M. R. (1985). Structural control of the chlorine content of OH-bearing silicates (micas and amphiboles). *Geochimica Cosmochimica Acta* 49, 37–48. doi:10.1016/0016-7037(85)90189-9

Wang, D. Z., Zhao, G. T., and Qiu, J. S. (1995). The Tectonic constraint on the late mesozoic A-type granitoids in eastern China. *Geol. J. Univ.* 1, 13–21. (in Chinese with English abstract).

Wang, T., Liu, S., Hu, R. Z., Feng, C. X., Qi, Y. Q., Feng, G. Y., et al. (2009). Elemental geochemistry and petrogenesis of A-type granites in the sulu orogen. *J. Jilin Univ. Earth Sci. Ed.* 39, 676–688. (in Chinese with English abstract).

Webster, J. D., Tappen, C. M., and Mandeville, C. W. (2009). Partitioning behavior of chlorine and fluorine in the system apatite-melt-fluid. II: Felsic silicate systems at 200 MPa. *Geochimica Cosmochimica Acta* 73, 559–581. doi:10.1016/j.gca.2008.10.034

Whalen, J. B., Currie, K. L., and Chappell, B. W. (1987). A-type granites geochemical characteristics, discrimination and petrogenesis. *Contrib. Mineral. Pet.* 95, 407–419. doi:10.1007/bf00402202

Wu, F. Y., Lin, J. Q., Wilde, S. A., Zhang, X. O., and Yang, J. H. (2005). Nature and significance of the Early Cretaceous giant igneous event in eastern China. *Earth Planet. Sci. Lett.* 233, 103–119. doi:10.1016/j.epsl.2005.02.019

Wu, F. Y., Sun, D. Y., Li, H. M., Jahn, B. M., and Wilde, S. (2002). A-Type granites in northeastern China: Age and geochemical constraints on their petrogenesis. *Chem. Geol.* 187, 143–173. doi:10.1016/s0009-2541(02)00018-9

Wu, K., Ling, M. X., Sun, W. D., Guo, J., and Zhang, C. C. (2017). Major transition of continental basalts in the early cretaceous: Implications for the destruction of the north China craton. *Chem. Geol.* 470, 93–106. doi:10.1016/j.chemgeo.2017.08.025

Xie, J. C., Yang, X. Y., Sun, W. D., Du, J. G., Xu, W., Wu, L. B., et al. (2009). Geochronological and geochemical constraints on formation of the Tongling metal deposits, middle Yangtze metallogenic belt, east-central China. *Int. Geol. Rev.* 51, 388–421. doi:10.1080/00206810802712004

Xu, Y. G. (2007). Diachronous lithospheric thinning of the North China Craton and formation of the Daxin'anling–Taihangshan gravity lineament. *Lithos* 96, 281–298. doi:10.1016/j.lithos.2006.09.013

Xu, Y. G., Huang, X. L., Ma, J. L., Wang, Y. B., IizukaXu, Y. J. F., Wang, Q., et al. (2004). Crust-mantle interaction during the tectono-thermal reactivation of the north China craton: Constraints from SHRIMP zircon U-Pb chronology and geochemistry of mesozoic plutons from Western Shandong. *Contrib. Mineral. Pet.* 147, 750–767. doi:10.1007/s00410-004-0594-y

Xu, Y. G. (2001). Thermo-tectonic destruction of the archaean lithospheric keel beneath the Sino-Korean Craton in China: Evidence, timing and mechanism. *Phys. Chem. Earth Part A Solid Earth Geodesy* 26, 747–757. doi:10.1016/s1464-1895(01)00124-7

Xu, Y. G., Wei, X., Luo, Z. Y., Liu, H. Q., and Cao, J. (2014). The early permian tarim large igneous province: Main characteristics and a plume incubation model. *Lithos* 204, 20–35. doi:10.1016/j.lithos.2014.02.015

Xu, Y. G., Zhang, H. H., Qiu, H. N., Ge, W. C., and Wu, F. Y. (2012). Oceanic crust components in continental basalts from Shuangliao, Northeast China: Derived from the mantle transition zone. *Chem. Geol.* 328, 168–184. doi:10.1016/j.chemgeo.2012.01.027

Yan, Q. S., and Shi, X. F. (2014). Geochemistry and petrogenesis of the Cretaceous A-type granites in the Laoshan granitic complex, eastern China. *Isl. Arc* 23, 221–235. doi:10.1111/iar.12070

Yang, F., Santosh, M., Glorie, S., Jepson, G., Xue, F., and Kim, S. W. (2020a). Meso-cenozoic multiple exhumation in the Shandong peninsula, eastern North China craton: Implications for lithospheric destruction. *Lithos* 370-371, 105597. doi:10.1016/j.lithos.2020.105597

Yang, F., Santosh, M., Glorie, S., Xue, F., Zhang, S., and Zhang, X. (2020c). Apatite geochronology and chemistry of luanchuan granitoids in the east qinling orogen, China: Implications for petrogenesis, metallogenesis and exploration. *Lithos* 378, 105797. doi:10.1016/j.lithos.2020.105797

Yang, F., Santosh, M., and Kim, S. W. (2018a). Mesozoic magmatism in the eastern North China Craton: Insights on tectonic cycles associated with progressive craton destruction. *Gondwana Res.* 60, 153–178. doi:10.1016/j.gr.2018.04.003

Yang, F., Santosh, M., Kim, S. W., Zhou, H., and Jeong, Y. J. (2020b). Late mesozoic intraplate rhyolitic volcanism in the north China craton: Far-field effect of the westward subduction of the paleo-Pacific plate. *GSA Bull.* 132, 291–309. doi:10.1130/b35123.1

Yang, F., Santosh, M., and Tang, L. (2018b). Extensive crustal melting during craton destruction: Evidence from the Mesozoic magmatic suite of Junan, eastern North China Craton. *J. Asian Earth Sci.* 157, 119–140. doi:10.1016/j.jseaes.2017.07.010

Yang, J. H., Wu, F. Y., Chung, S. L., Wilde, S. A., and Chu, M. F. (2006). A hybrid origin for the qianshan A-type granite, northeast China: Geochemical and Sr–Nd–Hf isotopic evidence. *Lithos* 89, 89–106. doi:10.1016/j.lithos.2005.10.002

Yang, J. H., Wu, F. Y., Chung, S. L., Wilde, S. A., Chu, M. F., Lo, C. H., et al. (2005). Petrogenesis of Early Cretaceous intrusions in the Sulu ultrahigh-pressure orogenic

belt, east China and their relationship to lithospheric thinning. *Chem. Geol.* 222, 200–231. doi:10.1016/j.chemgeo.2005.07.006

Yu, P. P., Weinberg, R. F., Zheng, Y., and Finch, M. A. (2022). Multiple crustal melting pulses and Hf systematics in zircons. *Lithos* 410–411, 106583. doi:10.1016/j.lithos.2021.106583

Yuan, S., Li, H., Zhang, L. P., Li, C. Y., Liu, H. Y., Xue, Y. Y., et al. (2022). Geochemical and zircon Hf-O isotopic constraints on the origin of wulian A-type granite in Shandong peninsula, eastern China. *J. Earth Sci.* 33 (3), 609–622. doi:10.1007/s12583-021-1592-y

Zhai, M. G., Yang, J. H., Fan, H. R., Miao, L. C., and Li, Y. G. (2002). A large-scale cluster of gold deposits and metallogenesis in the eastern North China craton. *Int. Geol. Rev.* 44, 458–476. doi:10.2747/0020-6814.44.5.458

Zhang, H. F. (2012). Destruction of ancient lower crust through magma underplating beneath Jiaodong peninsula, North China craton: U–Pb and Hf isotopic evidence from granulite xenoliths. *Gondwana Res.* 21, 281–292. doi:10.1016/j.gr.2011.05.013

Zhang, L., Groves, D. I., Yang L QWang, G. W., Liu, X. D., Li, D. P., et al. (2020b). Relative roles of formation and preservation on gold endowment along the sanshandao gold belt in the Jiaodong gold province, China: Importance for province- to district-scale gold exploration. *Min. Depos.* 55, 325–344. doi:10.1007/s00126-019-00908-1

Zhang, L. P., Zhang, R. Q., Hu, Y. B., Liang, J. L., Ouyang, Z. X., He, J. J., et al. (2017b). the formation of the late cretaceous xishan Sn-W deposit, south China: Geochronological and geochemical perspectives. *Lithos* 290–291, 253–268. doi:10.1016/j.lithos.2017.08.013

Zhang, L., Weinberg, R. F., Yang, L. Q., Groves, D. I., Sai, S. X., Matchan, E., et al. (2020a). Mesozoic orogenic gold mineralization in the Jiaodong peninsula, China: A focused event at 120 ± 2 Ma during cooling of pregold granite intrusions. *Econ. Geol.* 115 (2), 415–441. doi:10.5382/econgeo.4716

Zhang, L., Yang, L. Q., Wang, Y., Weinberg R FAn Pand Chen B Y (2017a). Thermochronologic constrains on the processes of formation and exhumation of the Xinli orogenic gold deposit, Jiaodong Peninsula, eastern China. *Ore Geol. Rev.* 81, 140–153. doi:10.1016/j.oregeorev.2016.09.026

Zhao, G. T., Cao, Q. C., Wang, D. Z., and Li, H. M. (1997). Zircon U-Pb dating on the Laoshan granitoids and its significance. *J. Ocean Univ. Qingdao* 27, 382–388. (in Chinese with English abstract).

Zhu, R. X., Chen, L., Wu, F. Y., and Liu, J. L. (2011). Timing, scale and mechanism of the destruction of the North China Craton. *Sci. China Earth Sci.* 54, 789–797. doi:10.1007/s11430-011-4203-4

Zhu, R. X., Fan, H. R., Li, J. W., Meng, Q. R., Li, S. R., and Zeng, Q. D. (2015). Decratonic gold deposits. *Sci. China Earth Sci.* 58, 1523–1537. doi:10.1007/s11430-015-5139-x

Zhu, R. X., Yang, J. H., and Wu, F. Y. (2012b). Timing of destruction of the north China craton. *Lithos* 149, 51–60. doi:10.1016/j.lithos.2012.05.013

Zhu, X. Q., Wang, Z. G., Huang, Y., and Wang, H. L. (2004). REE content and distribution in apatite and its geological tracing significance. *Chin. Rare Earths* 25, 41. (in Chinese with English abstract).

frontiers | Frontiers in Earth Science

TYPE Original Research
PUBLISHED 09 January 2023
DOI 10.3389/feart.2022.1046071

Check for updates

OPEN ACCESS

EDITED BY
Liang Zhang,
China University of Geosciences, China

REVIEWED BY
Xiaowei Li,
China University of Geosciences, China
Xin shang Bao,
Chang'an University, China
Jinbao Yang,
Guilin University of Technology, China

*CORRESPONDENCE
Dapeng Li,
dpengli@126.com
Zhigang Song,
zgsong@sdust.edu.cn

SPECIALTY SECTION
This article was submitted to Geochemistry, a section of the journal Frontiers in Earth Science

RECEIVED 16 September 2022
ACCEPTED 01 November 2022
PUBLISHED 09 January 2023

CITATION
Wei P, Li D, Song Z, Liu Q, Geng K, Zhang Y, Ding C, Cai N, Li Z, Zhang C and Xie W (2023), Petrogenesis and relationship with REE mineralization of the quartz syenite from Chishan and Longbaoshan alkaline complex, southeastern North China Craton: Insights from zircon U–Pb geochronology, element, and Sr–Nd–Pb–Hf isotope geochemistry. *Front. Earth Sci.* 10:1046071. doi: 10.3389/feart.2022.1046071

COPYRIGHT
© 2023 Wei, Li, Song, Liu, Geng, Zhang, Ding, Cai, Li, Zhang and Xie. This is an open-access article distributed under the terms of the Creative Commons Attribution License (CC BY). The use, distribution or reproduction in other forums is permitted, provided the original author(s) and the copyright owner(s) are credited and that the original publication in this journal is cited, in accordance with accepted academic practice. No use, distribution or reproduction is permitted which does not comply with these terms.

Petrogenesis and relationship with REE mineralization of the quartz syenite from Chishan and Longbaoshan alkaline complex, southeastern North China Craton: Insights from zircon U–Pb geochronology, element, and Sr–Nd–Pb–Hf isotope geochemistry

Pengfei Wei[1], Dapeng Li[1]*, Zhigang Song[1,2]*, Qiang Liu[1], Ke Geng[1], Yan Zhang[1], Chengwu Ding[3], Na Cai[1], Zengsheng Li[1], Chao Zhang[1] and Wei Xie[1]

[1]Shandong Institute of Geological Sciences, Key Laboratory of Gold Mineralization Processes and Resources Utilization, Ministry of Natural Resources, Shandong Provincial Key Laboratory of Metallogenic Geological Processes and Resource Utilization in Metallic Minerals, Jinan, China, [2]College of Earth Science and Engineering, Key Laboratory of Depositional Mineralization and Sedimentary Mineral of Shandong Province, Shandong University of Science and Technology, Qingdao, China, [3]Shandong University of Technology, Zibo, China

Mesozoic alkaline complexes associated with the rare earth element (REE) mineralization are developed in southeastern North China Craton (NCC), and they recorded some important information about the lithospheric thinning and destruction of the NCC. Zircon U–Pb dating results reveal that syenitic rocks from the Chishan and Longbaoshan alkaline complexes were emplaced at *ca.* 126.2–123.7 Ma. These syenitic rocks have an arc-like affinity with enriched LREEs and LILEs (e.g., Ba and Th) and depleted HFSE (e.g., Nb and Ta). However, they plot within the extensional alkaline–calc-alkaline field in the lg ($CaO/(K_2O + Na_2O)$) versus SiO_2 discrimination diagram and plot within the fields of the divergent plate and within-plate settings in the Nb_N versus Th_N discrimination diagram, implying an extensional tectonic setting. Thus, we suggest that the syenitic rocks should form in an extensional tectonic settings related to rollback and retreat of the subducting Paleo-Pacific plate. These syenitic rocks have similar Sr–Nd–Pb–Hf isotope compositions ($(^{87}Sr/^{86}Sr)_i$ = 0.7062 to 0.7101, $\varepsilon_{Nd}(t)$ = –8.2 to –15.0, $\varepsilon_{Hf}(t)$ = –13.5 to –9.6), which are the same as the enriched subcontinental lithospheric mantle (SCLM) of the NCC. Taking into account not only our new data but also previously published data regarding the evolution of NCC in the Mesozoic, we conclude that the syenitic rocks from the Chishan and Longbaoshan complexes are derived from partial melting of the lithospheric mantle triggered by the Paleo-Pacific plate subduction. Moreover, the

geochemical and Sr–Nd–Pb isotopic similarity between the Chishan REE ores, Longbaoshan altered rocks, and the syenitic rocks implied that they are homologous products of Early Cretaceous and that the mineralization shows inheritance to the magmatic hydrothermal evolution.

KEYWORDS

zircon U–Pb dating, Sr–Nd–Pb isotope composition, alkaline complexes, enriched lithospheric mantle, REE mineralization

1 Introduction

The North China Craton (NCC) is the largest cratonic area at the easternmost point of Eurasia (Yang et al., 2020). It experienced extensive destruction and lithospheric thinning during the Mesozoic (Fan et al., 2000; Goss et al., 2010; Zhai and Santosh, 2011; Zhu et al., 2011; Li and Santosh, 2017; Yang et al., 2018a; Yang et al., 2018b; Yang and Santosh, 2020). This transformation and destruction disturbed the stability of the coupling between the crust and lithospheric mantle and caused activation of the crust, which led to eruption of large-scale magmatism and mineralization during the Mesozoic (Wu et al., 2005; Chen et al., 2007; Goldfarb and Santosh, 2014). Although controversies about the timing, tectonic setting, and mechanism of the lithospheric thinning remain hotly continued (Gao et al., 2002; Zhang H. F. et al., 2007; Wu et al., 2008; Santosh, 2010; Zhu et al., 2011; Zhang et al., 2013), it is generally accepted that the interaction between the crust and the mantle had an important impact during this process (Wilde, et al., 2003; Xu et al., 2004; Gao et al., 2008). Alkaline rocks, as a kind of mantle-derived intrusions, are generally developed in extensional settings (Tu et al., 1984; Qiu, 1993), for instance, post-collisional extension (Bonin et al., 1998) or along deep faults (Jung et al., 2007). They are considered one of the ideal options to study the crust–mantle interaction and continental crust evolution (Yang et al., 2007; Lan et al., 2011).

There are a large number of magmatic rocks related to NCC destruction during the Mesozoic, especially the widespread late Mesozoic alkaline rocks in the Luxi Block, southeastern NCC (Zhang et al., 2005; Lan et al., 2011). These magmatic rocks recorded some important information about lithospheric thinning and destruction of the NCC (Xu et al., 2004; Zhang et al., 2005; Lan et al., 2011; Yang D. B. et al., 2012; Zhang et al., 2014; Yang et al., 2018a), including the lithospheric architecture, crust–mantle interaction, tectonic reactivation, timing, mechanism, and geodynamic setting (Gao et al., 2002; Wu et al., 2008; Santosh, 2010; Zhu et al., 2011; Deng et al., 2018; Yang et al., 2020). Moreover, alkaline rocks in the Luxi Block have a close relationship with the gold and rare earth element (REE) mineralization. For instance, the Longbaoshan complex, which is relatively larger than other alkaline intrusions in the Luxi Block, is closely associated with the mineralization of gold and REE deposits. The Chishan alkaline complex is considered the ore-forming parent rock of the Chishan REE deposit, which holds the third-largest light REE deposit in China, after the Inner Mongolia Bayan Obo and Sichuan Maoniuping REE deposits. With regard to the Longbaoshan and Chishan complexes, the lithologic assemblage is dominated by syenitic rocks, which are the most closely related to REE mineralization. However, the petrogenesis of these syenitic rocks has not been systematically researched until now (Zhang et al., 2005; Lan et al., 2011). In this study, we carried out detailed fieldwork, petrological and mineralogical observations, and obtained element geochemical, zircon U–Pb–Hf isotopic, and Sr–Nd–Pb isotopic data of the quartz syenite from the Longbaoshan and Chishan complexes to identify the nature and petrogenesis of the syenitic rocks and to understand their significance to the crust–mantle interaction. The final goal, using the results from the Longbaoshan and Chishan complexes, is to further our understanding on how magmatic processes control REE enrichment in alkaline magmas in southeastern NCC.

2 Geological background and sampling

2.1 Geological background

The NCC is China's oldest and largest craton due to its 2.5–3.8 Ga Archean core (Liu et al., 1992). It is separated from the Yangtze Craton by the Qinling–Dabie–Sulu Orogenic Belt to the south and east and from the Central Asian Orogenic Belt by the Bayan Obo–Chifeng–Kaiyuan fault to the north (Figure 1A) (Li et al., 1993; Zhao et al., 2001). In many popular models, the NCC is divided into the Western Block (WB) and Eastern Block (EB), which were welded along the nearly north–south trending Trans-North China Orogen (TNCO) (Zhao et al., 2001; Zhao and Zhai, 2013). The basement rocks within the EB are primarily dominated by Archean to Paleoproterozoic tonalite–trondhjemite–granodiorite (TTG) (Zhao and Zhai, 2013). The WB was the outcome of amalgamation between the Ordos and Yinshan blocks along the Khondalie Belt at 1.95–1.92 Ga (Santosh, 2010; Yang et al., 2018a). The TNCO is a collision orogenic belt between the EB and WB in the Paleoproterozoic (1.85 Ga), with basement rocks of late Neoarchean–Paleoproterozoic TTG gneisses and granitoids (Zhao et al., 2005).

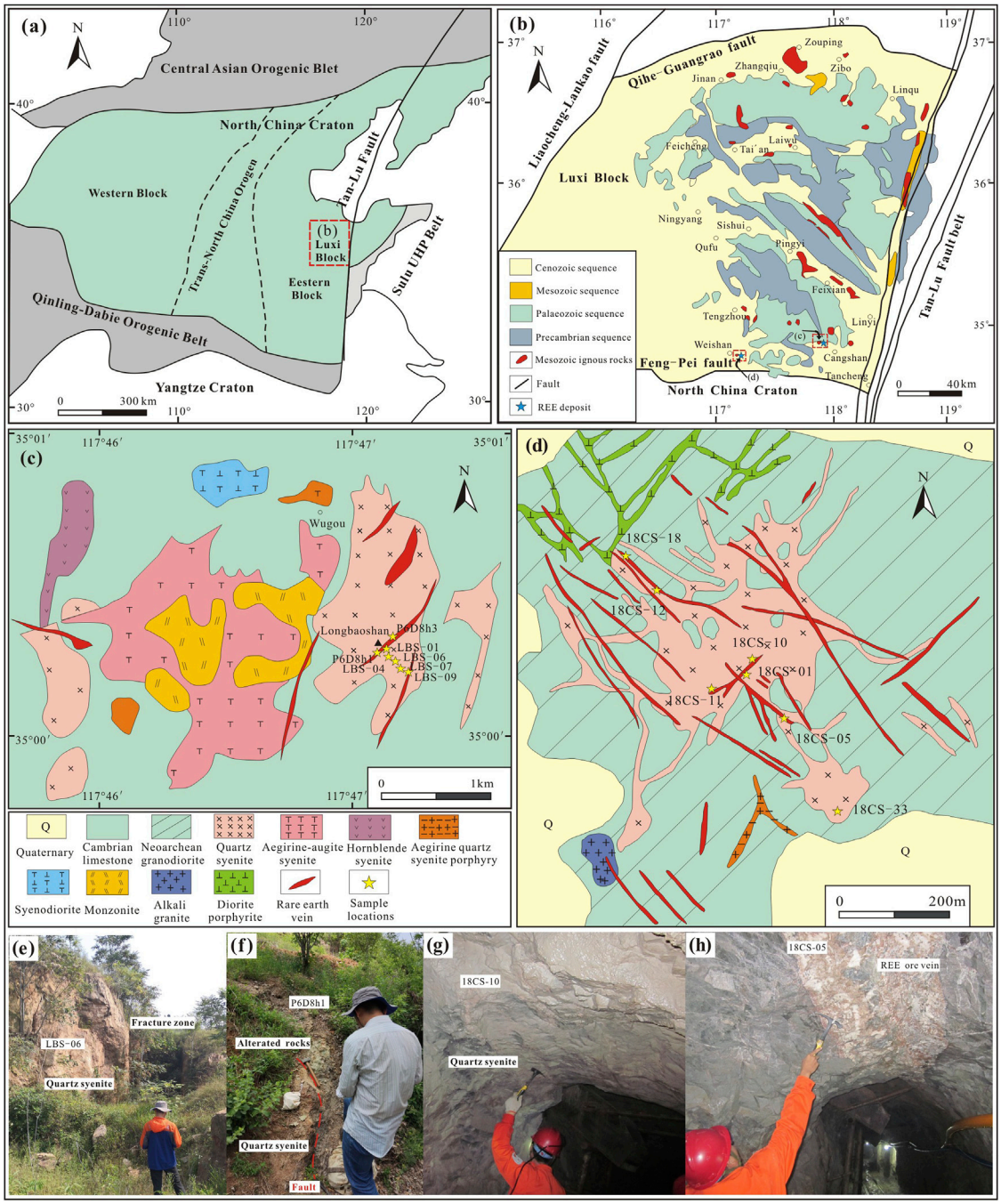


FIGURE 1
(A) Simplified geological map of the North China Craton and the location of the Luxi Block (after Zhao et al., 2001; Zhang et al., 2005). **(B)** Simplified geological map of the Luxi Block (after Zhang H. F. et al., 2007). **(C)** Simplified geological map of the Longbaoshan alkaline complex (after Lan et al., 2011). **(D)** Simplified geological map of the Chishan alkaline complex (Wei et al., 2019). **(E–H)** Photos of field outcrops where the four kinds of samples were collected in.

The Luxi Block is bordered by the Tan-Lu fault in the east, the Liaocheng–Lankao fault in the west, the Qihe–Guangrao fault in the north, and the Fengpei fault in the south (Figure 1B) (Zhang X. M. et al., 2007). The crystalline basement of the Luxi Block incorporates a suite of Neoarchean metamorphic rocks (e.g., gneiss, amphibolite, and deformed/metamorphosed TTG) and Paleoproterozoic granitoids. The sedimentary cover is mainly composed of Paleozoic carbonates and clastic rocks,

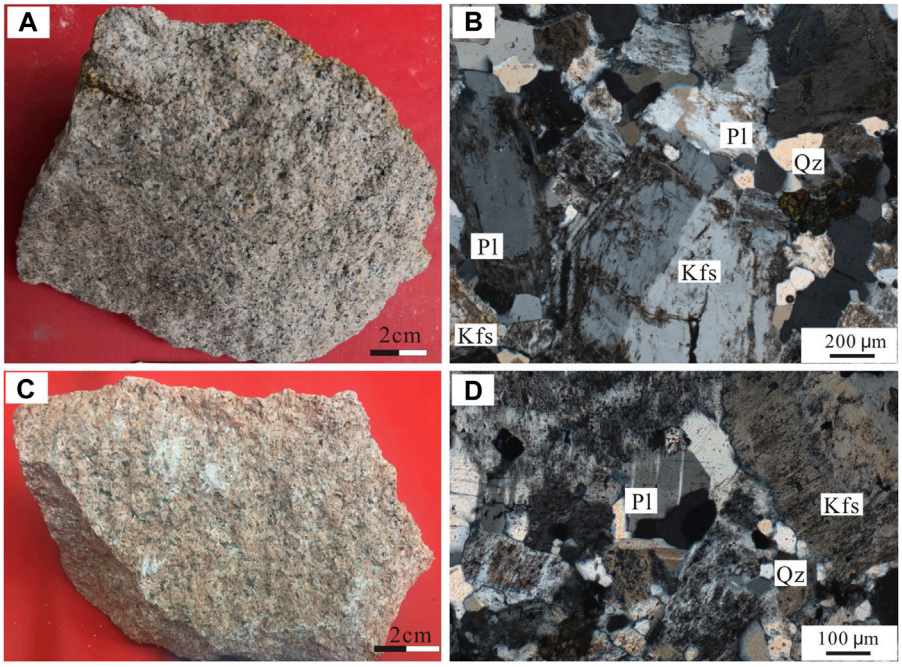


FIGURE 2
Photographs of the quartz syenite **(A,B)** from the Chishan complex and porphyritic quartz syenite **(C,D)** from the Longbaoshan complex. Abbreviations: Kfs = K-feldspar, Pl = plagioclase, and Qtz = quartz.

Mesozoic to Cenozoic terrigenous clastic rocks, and volcaniclastic rocks. In addition, some intermediate-basic rocks, mafic dikes, and alkaline rocks are also exposed (Figure 1B) (Xu et al., 2015; Wang et al., 2018; Yang et al., 2020). Especially in the Jurassic–Early Cretaceous period, a large number of alkaline rocks were developed as batholiths, stocks, or dykes (Wei et al., 2019). Their lithology was mainly syenite, syenite porphyrite, diorite porphyrite, diabase, and lamprophyre. The representative alkaline rocks are the Tongshi complex, Shagou complex, Chishan alkaline complex, and Longbaoshan alkaline complex. The Longbaoshan alkaline complex, with an area of 3.5 km^2, is exposed near the Wugou village of the Cangshan county. It is predominantly composed of quartz syenite, syenite, aegirine–augite syenite, and syenodiorite assemblages (Figure 1C). The NW-trending Longhui fault is the major structure in the study area, and its SN-, EW-, and NNE-trending secondary fracture and alteration zone are developed, controlling the distribution of the Longbaoshan complex and REE ore veins (Figures 1E,F). The Chishan alkaline complex covers an area of 0.5 km^2 and crops out in the Chishan village of the Weishan county. It mainly consists of quartz syenite, alkali granite, and aegirine quartz syenite (Figure 1D). The regional structure mainly comprises the NW-, NE-, SN-, and EW-trending faults. The Chishan complex extends in NE- and SW-trending controlled by the regional faults and contacts with gneiss in irregular branches. The REE ore veins occurred within the quartz and gneiss (Figures 1D,H).

2.2 Samples

In this study, five samples of quartz syenite (18CS-01, −10, −11, −12, and −33) and two samples of REE ore (18CS-05 and 18CS-18) were collected from the −160 m level of the Chishan REE deposit (Figures 1D,G,H). A total of five samples of porphyritic quartz syenite samples (LBS-01, -04, -06, -07, and -09) and two samples of alterated rock (P6D8h1 and P6D8h3) were collected from outcrops (Figures 1C,E,F) of the Longbaoshan alkaline complex. Petrographic observations, whole-rock geochemical, and Sr–Nd–Pb isotopic analyses were performed on all the samples. The zircon U-Pb dating and Hf isotopic analyses were conducted only on samples 18CS-01 and LBS-01.

The quartz syenite of the Chishan alkaline complex, with gray to light pink color, has generally porphyroid or porphyritic textures and a massive structure (Figure 2A). It consists mainly of K-feldspar (53 vol%), plagioclase (25 vol%), quartz (15 vol%), and hornblende (5 vol%). The K-feldspar grains have grain sizes of 1.0–1.5 mm and are subhedral columnar or granular, some of which show Carlsbad twinning (Figure 2B). The porphyritic quartz syenite of the Longbaoshan complex is generally gray

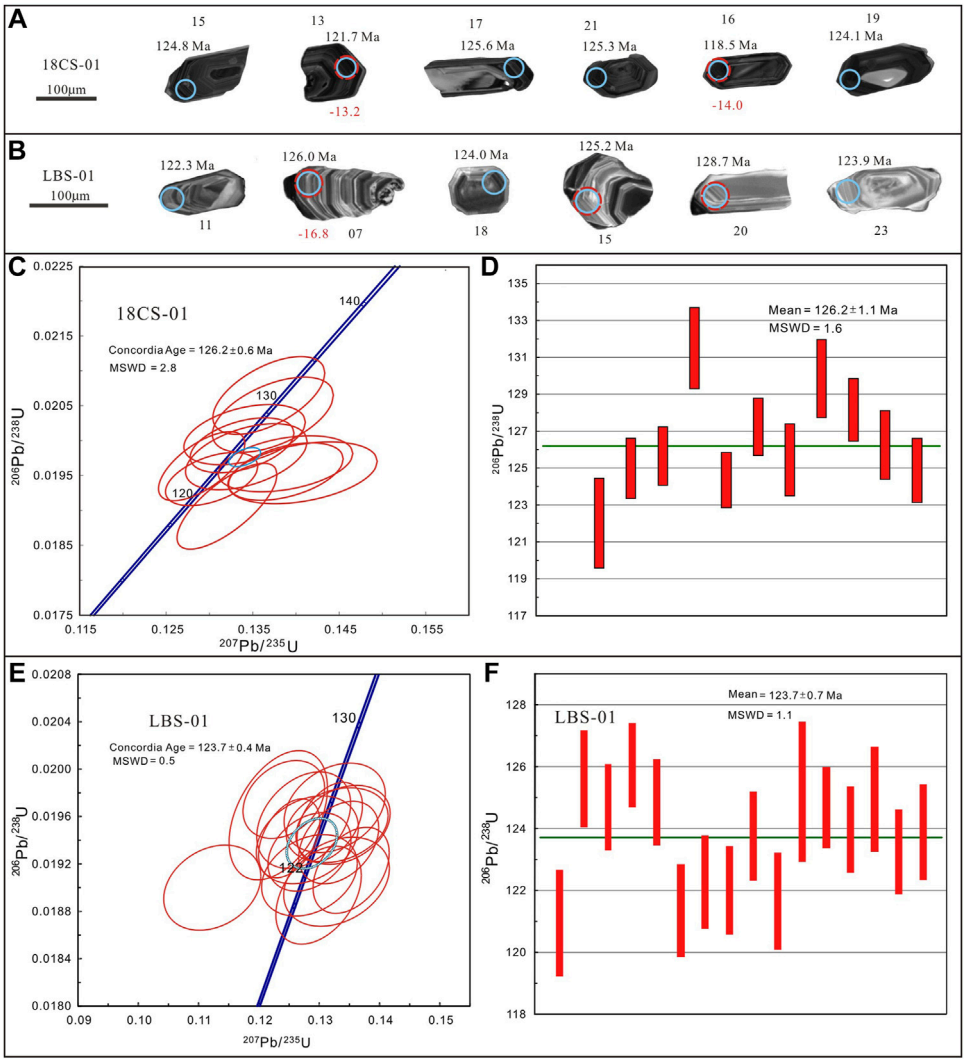


FIGURE 3
(A,B) Cathodoluminescence (CL) images of representative zircon grains in sample 18CS-01 and LBS-01, showing analytical positions, $^{206}Pb/^{238}U$ ages, and $\varepsilon_{Hf}(t)$ values. **(C–F)** U-Pb concordia diagram and weighted mean $^{206}Pb/^{238}U$ ages of zircons from Chishan and Longbaoshan complexes.

to light pink in color and shows a porphyritic texture (Figure 2C). K-feldspar (1.0–2.5 mm), plagioclase (0.3–1.0 mm), and quartz (0.1–0.3 mm) phenocrysts are distributed in the groundmass (Figure 2D), while the matrix is dominated by K-feldspar, plagioclase, and quartz with sizes of 0.01–0.05 mm.

3 Analytical methods

3.1 Zircon LA-ICP-MS U–Pb dating

Zircon separation was conducted using standard density and magnetic separation techniques followed by hand-picking at Langfang Fengzeyuan Rock and Mineral Testing Technology Co., Ltd. (Langfang, China). The zircons grains were selected under a stereo-microscope, sealed in an epoxy resin target, and polished until the mid-sections were exposed. Cathodoluminescence (CL) transmitted and reflected images were taken prior to U–Pb dating analysis to identify the internal textures of zircon grains and select target spots with no cracks, no inclusions, and good growth zones for U–Pb dating and Hf isotopic analysis.

Zircon U–Pb dating was conducted at Beijing Createch Testing Technology Co., Ltd. (Beijing, China) using a Neptune multi-collector inductively coupled plasma mass spectrometry (MC-ICP-MS) equipped with a New Wave 193-nm laser sampler. The diameter of the laser beam was 35 μm, and the carrier gas was He. Detailed analytical processes were

TABLE 1 LA-ICP-MS zircon U–Pb isotope analyses of the quartz syenite from Chishan and Longbaoshan complexes.

Spots	Content (ppm)			$^{232}Th/^{238}U$	Ratio/deviation						Age (Ma)/deviation						Concordance
	Th^{232}	U^{238}	Pb		$^{207}Pb/^{206}Pb$	1σ	$^{207}Pb/^{235}U$	1σ	$^{206}Pb/^{238}U$	1σ	$^{207}Pb/^{206}Pb$	1σ	$^{207}Pb/^{235}U$	1σ	$^{206}Pb/^{238}U$	1σ	
18CS-01 Quartz syenite[a]																	
18CS-01-13	788.5	1671.6	103.37	0.47	0.0505	0.0010	0.1320	0.0025	0.0191	0.0003	216.7	44.4	125.9	2.3	121.7	1.7	96%
18CS-01-15	586.9	1444.8	83.75	0.41	0.0516	0.0012	0.1388	0.0029	0.0196	0.0002	333.4	53.7	132.0	2.6	124.9	1.1	94%
18CS-01-16	1576.0	1557.1	167.32	1.01	0.0526	0.0011	0.1345	0.0030	0.0186	0.0002	322.3	52.8	128.2	2.7	118.5	1.3	92%
18CS-01-17	332.9	1256.5	57.45	0.26	0.0511	0.0012	0.1388	0.0034	0.0197	0.0002	255.6	53.7	132.0	3.1	125.6	1.1	95%
18CS-01-18	228.6	1247.1	48.29	0.18	0.0480	0.0009	0.1369	0.0028	0.0206	0.0002	101.9	42.6	130.2	2.5	131.7	1.5	98%
18CS-01-19	823.8	1948.8	108.82	0.42	0.0485	0.0008	0.1303	0.0023	0.0194	0.0002	124.2	37.0	124.3	2.1	124.2	1.1	99%
18CS-01-20	660.9	1571.5	90.21	0.42	0.0486	0.0009	0.1338	0.0026	0.0199	0.0002	131.6	42.6	127.5	2.4	127.2	1.1	99%
18CS-01-21	420.8	1472.0	65.17	0.29	0.0477	0.0007	0.1291	0.0022	0.0196	0.0002	83.4	32.4	123.3	2.0	125.3	1.4	98%
18CS-01-22	156.6	737.6	28.85	0.21	0.0490	0.0011	0.1373	0.0031	0.0204	0.0002	150.1	58.3	130.7	2.7	130.0	1.5	99%
18CS-01-23	278.2	755.6	39.66	0.37	0.0484	0.0011	0.1341	0.0031	0.0201	0.0002	120.5	47.2	127.7	2.8	128.2	1.2	99%
18CS-01-24	431.8	1025.0	53.69	0.42	0.0492	0.0010	0.1343	0.0031	0.0198	0.0002	166.8	48.1	127.9	2.8	126.2	1.3	98%
18CS-01-25	542.3	1066.9	70.03	0.51	0.0520	0.0012	0.1408	0.0038	0.0195	0.0002	287.1	54.6	133.7	3.4	124.7	1.2	93%
LBS-01 Porphyritic quartz syenite																	
LBS-01-01	358.3	274.8	39.69	1.30	0.0501	0.0019	0.1299	0.0047	0.0189	0.0003	211.2	95.4	124.0	4.2	120.9	1.7	97%
LBS-01-03	368.3	263.3	41.42	1.40	0.0491	0.0021	0.1326	0.0055	0.0197	0.0002	153.8	102.8	126.4	5.0	125.6	1.6	99%
LBS-01-05	432.9	275.1	46.46	1.57	0.0496	0.0017	0.1339	0.0052	0.0195	0.0002	172.3	76.8	127.6	4.6	124.7	1.4	97%
LBS-01-07	456.0	338.4	49.93	1.35	0.0458	0.0017	0.1241	0.0045	0.0197	0.0002	100.1	77.8	118.8	4.0	126.0	1.4	94%
LBS-01-09	640.9	441.4	69.31	1.45	0.0490	0.0014	0.1317	0.0036	0.0196	0.0002	150.1	66.7	125.7	3.2	124.8	1.4	99%
LBS-01-11	449.6	387.9	50.98	1.16	0.0515	0.0017	0.1353	0.0042	0.0191	0.0002	264.9	76.8	128.8	3.7	122.3	1.5	94%
LBS-01-12	227.9	211.1	28.56	1.08	0.0490	0.0021	0.1284	0.0052	0.0191	0.0002	150.1	93.5	122.6	4.7	122.0	1.4	99%
LBS-01-13	590.1	375.5	64.84	1.57	0.0498	0.0015	0.1332	0.0044	0.0194	0.0002	183.4	65.7	127.0	3.9	123.7	1.5	97%
LBS-01-14	224.1	193.9	24.67	1.16	0.0507	0.0022	0.1329	0.0058	0.0190	0.0002	227.8	98.1	126.7	5.2	121.6	1.6	95%
LBS-01-15	294.3	282.8	37.27	1.04	0.0460	0.0023	0.1232	0.0054	0.0196	0.0004	183.4	65.7	118.0	4.9	125.2	2.3	94%
LBS-01-17	250.7	239.2	30.02	1.05	0.0496	0.0020	0.1330	0.0056	0.0195	0.0002	176.0	128.7	126.8	5.0	124.7	1.3	98%
LBS-01-18	620.8	600.8	71.74	1.03	0.0468	0.0013	0.1250	0.0034	0.0194	0.0002	39.0	66.7	119.6	3.0	124.0	1.4	96%
LBS-01-19	338.8	241.8	37.38	1.40	0.0481	0.0022	0.1274	0.0051	0.0196	0.0003	101.9	103.7	121.8	4.6	124.9	1.7	97%
LBS-01-22	379.0	350.5	41.58	1.08	0.0485	0.0018	0.1284	0.0045	0.0193	0.0002	120.5	87.0	122.6	4.1	123.2	1.4	99%
LBS-01-23	295.5	206.9	31.16	1.43	0.0482	0.0021	0.1280	0.0056	0.0194	0.0002	105.6	−97.2	122.3	5.0	123.9	1.5	98%

[a]Note: The quartz syenite zircon U–Pb data are obtained from previously published work (Wei et al., 2019).

described by Yuan et al. (2004). The results were corrected with the measured ^{204}Pb for U–Th–Pb isotopic fractionation and the presence of common Pb (from the measured ^{204}Pb). The final data were processed with ICP-MS DataCal software (Liu et al., 2008). Zircon U-Pb concordia diagrams and mean ages were obtained with ISOPLOT 3.0 software (Ludwig, 2003).

3.2 Major and trace elements

The major and trace element concentrations were determined at Beijing Createch Testing Technology Co., Ltd. (Beijing, China). Fresh samples were crushed to less than 200 meshes. Major elements were analyzed by X-ray fluorescence spectrometry (XRF-1800), with an accuracy of better than 1%. Fused glass disks were prepared by mixing the samples with $Li_2B_4O_7$–$LiBO_2$ flux, with an automated fusion system. The trace elements were analyzed using the lithium borate melting method and determined by quantitative ICP-MS (Agilent 7500ce), with an accuracy of better than 5%.

3.3 Whole rock Sr–Nd–Pb isotopes

Whole rock Sr, Nd, and Pb isotopes were determined in Beijing Createch Testing Technology Co., Ltd. (Beijing, China) by using a Finnigan MAT 262 multi-channel thermal ionization mass spectrometer (TIMS). Samples were weighted into Teflon capsules along with ^{84}Sr, ^{87}Rb, ^{150}Nd, and ^{147}Sm isotopic spikes and then digested in $HClO_4$ and HF. The separation of lead was used as the conventional anionic resin-exchange technique with HCl. After ion exchange separation, the Sr–Nd isotope ratios were analyzed using a Finnigan MAT 262 thermal ionization mass spectrometer. The chemical analytical procedures were described by Pin et al. (2014).

The correction of Sr and Nd isotope ratios mass fractionation used were ^{87}Sr/^{88}Sr = 0.1194 and ^{146}Nd/^{144}Nd = 0.7219, respectively. The procedural blanks for Rb and Sr were <100 pg, and for Sm and Nd were <50 pg. The obtained standard results are as follows: NBS-987 ^{87}Sr/^{86}Sr = 0.710248 ± 13; GSB ^{143}Nd/^{144}Nd = 0.512185 ± 8. Repeated analyses of BCR-2 standard yielded the ratio of ^{206}Pb/^{204}Pb = 18.7477 ± 3, ^{207}Pb/^{204} Pb = 15.6111 ± 3, and ^{208}Pb/^{204}Pb = 38.6921 ± 7, respectively, and all of them are within the error range (Yang et al., 2010).

3.4 Zircon Lu–Hf isotopes

The zircon Lu–Hf isotope analysis was proceeded on or close to the U-Pb dating spots at Beijing Createch Testing Technology Co., Ltd. (Beijing, China) using a Neptune MC-ICP MS system. The laser and mass spectrometry conditions are the same with the zircon U–Pb dating. Analytical conditions, instrument settings, and procedures were described by Geng et al. (2011). In this study, the adopted ^{176}Lu decay constant was 1.867×10^{-11}year^{-1} (Söderlund et al., 2004), the ^{176}Hf/^{177}Hf ratio value of chondrite was 0.0332, and the ^{176}Lu/^{177}Hf ratio value was 0.282772 (Blichert-Toft and Albarède, 1997). Depleted mantle model ages (t_{DM1}) were calculated based on present-day depleted mantle ^{176}Lu/^{177}Hf and ^{176}Hf/^{177}Hf ratios (^{176}Lu/^{177}Hf = 0.0384, ^{176}Hf/^{177}Hf = 0.28325) (Griffin et al., 2000). The ^{176}Lu/^{177}Hf ratio of 0.015 (Griffin et al., 2002) was used to calculate the depletedmantlemodelage (t_{DM2}). The detailed analysis and calculation procedures were described by Wu et al. (2007).

4 Results

4.1 Zircon U–Pb dating

Zircon grains from sample 18CS-01 (quartz syenite) of the Chishan complex are dark in color and euhedral to short columnar in shape, with the sizes of 100–200 μm and aspect ratios from 1:2.5 to 1:1.25. The CL images show that most of the grains have smooth surfaces and oscillatory zoning, indicative of a magmatic origin (Figure 3A). Zircon grains from sample LBS-01 (porphyritic quartz syenite) of the Longbaoshan complex are light black to colorless. They are euhedral to subhedral and range in size from 50 to 150 μm, with aspect ratios of 1:1 to 1:2.5. In the CL images, most zircon grains also display obvious oscillatory zonation (Figure 3B).

A total of 50 spots from two samples were analyzed in this study. In order to ensure the accuracy and reliability of the results, age data having the concordance below 90% in the ^{207}Pb/^{235}U-^{206}Pb/^{238}U plot were deleted. The adjusted data are listed in Table 1.

Zircons from Chishan quartz syenite have ^{238}U contents of 738–1672 ppm, ^{232}Th concentrations of 157–1576 ppm, and ^{232}Th/^{238}U ratios of 0.18–1.01. The ^{206}Pb/^{238}U ages of all the analyzed zircons are concentrated and fall on the concordia line (Figure 3C) and yield a mean age of 126.2 ± 1.1 Ma (MSWD = 1.6) (Figure 3D), which is considered to be the crystallization age of the quartz syenite.

Zircons from Longbaoshan porphyritic quartz syenite have ^{238}U contents of 194–601 ppm, ^{232}Th concentrations of 224–641 ppm, and ^{232}Th/^{238}U ratios of 1.08–1.57. The ^{206}Pb/^{238}U ages of all the analyzed zircons fall on or near the concordia line (Figure 3E) and yield a mean age of 123.7 ± 0.7 Ma (MSWD = 1.1) (Figure 3F). It is suggested that the porphyritic quartz syenite was emplaced contemporaneous with the quartz syenite (18CS-01) in the Early Cretaceous.

4.2 Major and trace elements

Major and trace element contents and associated parameters of all samples from the Longbaoshan and Chishan complexes are

TABLE 2 Whole-rock major and trace element compositions of the quartz syenite, REE ore samples, and alterated rocks from Chishan and Longbaoshan REE deposits.

Sample number	18CS-01	18CS-10	18CS-11	18CS-12	18CS-33	18CS-05	18CS-18	LBS-01	LBS-04	LBS-06	LBS-07	LBS-09	P6D8h1	P6D8h3
Rock type	Quartz syenite[a]					REE ore		Porphyritic quartz syenite					Altered rocks	
SiO_2	70.20	71.35	71.72	69.02	69.42	—	—	67.53	68.82	69.01	68.42	62.87	—	—
Al_2O_3	15.25	13.74	13.51	16.12	15.41	—	—	17.03	16.77	16.85	16.96	17.64	—	—
MgO	0.49	0.16	0.19	0.15	0.48	—	—	0.27	0.07	0.07	0.08	0.74	—	—
Na_2O	5.53	6.25	6.12	7.13	7.11	—	—	6.80	6.84	6.75	6.89	6.61	—	—
K_2O	3.34	4.29	4.43	3.82	3.67	—	—	5.02	5.08	5.21	5.06	5.08	—	—
P_2O_5	0.07	0.03	0.04	0.10	0.11	—	—	0.06	0.04	0.04	0.04	0.27	—	—
TiO_2	0.17	0.08	0.06	0.11	0.11	—	—	0.19	0.16	0.16	0.16	0.24	—	—
CaO	1.59	0.73	0.74	0.38	1.15	—	—	0.41	0.19	0.19	0.16	1.49	—	—
TFe_2O_3	1.32	2.35	2.31	1.38	1.50	—	—	2.04	1.41	1.36	1.48	3.02	—	—
MnO	0.02	0.13	0.12	0.05	0.05	—	—	0.03	0.01	0.01	0.01	0.06	—	—
LOI	2.45	0.77	0.71	0.96	0.63	—	—	0.56	1.18	0.92	1.37	0.98	—	—
TOTAL	100.4	99.9	99.9	99.2	99.7	—	—	99.9	100.6	100.6	100.6	99.0	—	—
Na_2O+K_2O	8.87	10.53	10.56	10.94	10.78	—	—	11.82	11.91	11.95	11.95	11.69	—	—
A/NK	1.199	0.921	0.908	1.017	0.983	—	—	1.02	1.00	1.01	1.01	1.08	—	—
A/CNK	0.977	0.846	0.833	0.974	0.867	—	—	0.98	0.98	0.99	0.99	0.92	—	—
Rb	55	103	110	53	54	34	31	129	108	111	107	108	146	225
Sr	1236	340	338	831	1381	61432	73381	598	372	416	297	2742	491	1407
Ba	1695	1572	1866	3825	3976	55297	37466	1229	1697	1725	1345	3488	3988	5193
Th	5.80	342.33	362.58	23.00	34.86	41.55	27.25	33.94	32.46	28.56	32.50	26.49	107.08	80.47
U	1.77	23.87	26.92	2.99	6.55	2.60	1.46	7.41	6.30	6.03	5.84	4.53	7.19	8.75
Nb	7.09	148.94	187.67	44.96	53.76	12.20	7.95	59.21	55.71	55.71	55.11	36.95	54.05	12.06
Ta	0.23	2.30	2.75	1.16	1.29	0.35	0.61	2.52	2.30	2.31	2.33	1.51	3.41	1.15
Zr	106	1197	1413	176	256	0.66	1.36	381	290	298	271	390	352	396
Hf	2.35	16.56	19.43	3.16	4.67	0.66	0.43	7.76	6.07	6.52	6.02	7.02	11.55	11.15
Co	4.62	1.82	1.32	2.35	3.45	0.96	0.67	2.35	0.22	0.35	0.26	8.82	2.05	25.09
Ni	3.27	14.14	1.99	4.01	9.86	9.18	5.58	2.81	0.43	0.34	1.25	12.43	7.95	32.08
Cr	12.69	29.35	10.00	18.35	19.12	27.39	7.50	9.32	7.33	6.78	11.86	19.13	17.46	68.16
V	23.75	32.94	31.11	25.39	27.36	3.48	1.18	21.09	25.76	26.22	23.16	43.07	23.61	112.25
Sc	7.15	6.38	6.99	8.74	7.85	3.08	3.52	8.51	7.07	6.10	6.33	10.85	1.62	17.12
Cs	0.91	0.27	0.32	0.18	0.22	0.34	0.71	0.43	0.31	0.33	0.32	0.53	1.05	5.77
Ga	58.10	60.66	61.71	67.52	46.97	239.06	219.45	70.72	74.47	72.92	73.52	68.60	27.25	235.55
Cu	9.62	8.52	8.03	6.73	5.69	18.27	11.07	8.04	9.53	8.62	11.51	48.36	39.53	208.92
Pb	13.27	61.06	50.37	14.47	15.78	2374.56	121.32	30.43	34.73	42.65	46.68	31.32	47.46	26.92
Zn	36.49	99.67	104.08	37.83	73.80	856.10	40.44	118.26	53.12	33.90	56.07	85.28	85.33	360.15
Be	2.30	17.92	18.15	3.89	4.89	1.23	0.15	9.11	5.43	5.90	5.62	5.81	4.37	9.62
La	81.50	174.62	187.46	330.85	383.69	23164.39	18674.57	130.30	100.29	85.64	72.21	208.09	1446.48	7859.43
Ce	128.85	244.16	231.99	489.15	560.84	40390.16	36939.65	192.62	168.54	136.41	112.47	336.19	1687.38	9308.62
Pr	10.20	16.42	16.97	30.48	32.84	3016.81	2800.64	14.49	11.48	12.63	10.50	24.74	163.24	774.89
Nd	43.37	74.72	76.91	97.28	101.77	8811.86	7671.86	67.00	51.66	44.19	37.27	86.56	583.33	2473.67
Sm	4.78	8.64	8.78	13.91	13.26	838.34	544.55	8.73	6.91	5.24	4.92	13.85	69.01	206.97
Eu	1.38	2.23	2.29	4.15	3.94	136.96	109.51	2.02	1.67	1.38	1.32	4.29	16.98	35.69
Gd	3.58	7.52	7.73	13.43	13.04	733.01	570.27	6.98	5.44	4.17	4.18	12.46	44.15	104.89
Tb	0.26	0.70	0.73	1.03	1.00	62.38	45.65	0.71	0.56	0.45	0.49	1.13	5.42	13.48
Dy	0.83	3.08	3.21	3.36	3.25	137.42	86.28	3.14	2.47	2.17	2.48	4.34	22.22	18.03
Ho	0.14	0.64	0.70	0.58	0.84	18.60	12.29	0.64	0.50	0.44	0.51	0.78	4.11	5.11

(Continued on following page)

TABLE 2 (*Continued*) Whole-rock major and trace element compositions of the quartz syenite, REE ore samples, and alterated rocks from Chishan and Longbaoshan REE deposits.

Sample number	18CS-01	18CS-10	18CS-11	18CS-12	18CS-33	18CS-05	18CS-18	LBS-01	LBS-04	LBS-06	LBS-07	LBS-09	P6D8h1	P6D8h3
Er	0.39	1.89	1.99	1.51	1.67	75.85	59.68	1.70	1.31	1.20	1.30	1.93	11.69	16.25
Tm	0.04	0.33	0.36	0.18	0.28	4.46	3.25	0.29	0.21	0.20	0.22	0.26	1.60	1.58
Yb	0.30	2.61	2.77	1.08	1.19	26.05	18.18	2.03	1.51	1.47	1.46	1.76	10.38	9.34
Lu	0.04	0.40	0.42	0.15	0.15	3.06	2.24	0.30	0.21	0.20	0.21	0.24	1.49	1.28
Y	6.44	21.15	22.93	20.51	18.35	366.08	290.98	21.71	16.01	14.24	16.35	24.79	138.79	144.60
∑REE	275.7	538.0	542.3	987.2	1117.8	77419.3	67538.6	440.1	358.2	301.7	255.2	702.4	4067.5	20829.2
LREE/HREE	18.1	19.1	17.6	21.4	17.2	17.3	19.1	28.9	28.0	28.3	29.4	28.1	39.3	121.6
La_N/Yb_N	32.0	41.7	35.6	31.5	23.5	23.1	29.0	72.2	69.8	69.4	77.7	70.5	99.9	603.5
δEu	0.97	0.82	0.83	0.92	0.91	0.52	0.60	0.77	0.80	0.87	0.86	0.98	0.88	0.66

[a]Note: The whole-rock major and trace element data of quartz syenite are obtained from previously published work (Wei et al., 2019).

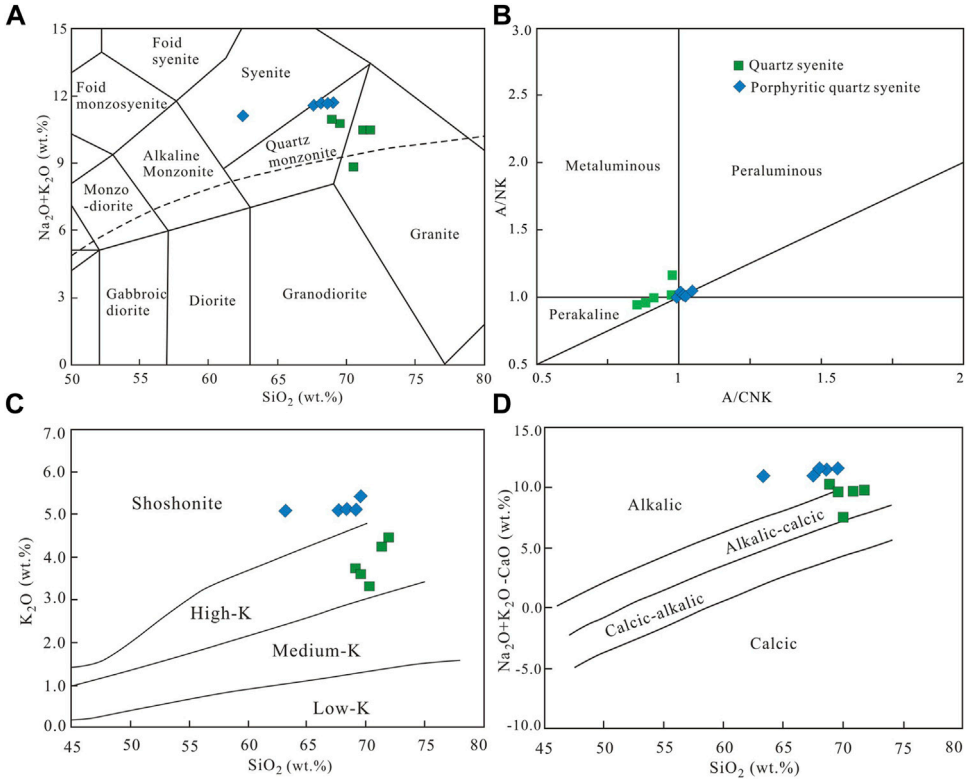


FIGURE 4
Geochemical diagrams for the (porphyritic) quartz syenite analyzed in this study. **(A)** SiO_2 versus K_2O (after Middlemost, 1994. The dotted line of alkaline and subalkaline series from Irvine and Baragar, 1971); **(B)** A/CNK [molar ratio $Al_2O_3/(K_2O + Na_2O + CaO)$] versus A/NK [molar ratio $Al_2O_3/(K_2O + Na_2O)$] (after Maniar and Piccoli, 1989); **(C)** SiO_2 versus K_2O (after Peccerillo and Taylor, 1976); **(D)** SiO_2 versus $K_2O + Na_2O-CaO$ (after Frost et al., 2001).

listed in Table 2. The Chishan quartz syenite samples have SiO_2 contents of 69.02–71.72 wt%, $A1_2O_3$ contents of 13.51–16.12 wt %, and Na_2O, K_2O, and CaO contents of 5.53–7.13 wt%, 3.34–4.43 wt%, and 0.38–1.59 wt%, respectively. These samples are relatively high in SiO_2, total alkali ($Na_2O + K_2O$) and $A1_2O_3$ and low in TiO_2 (0.06–0.17 wt%). These samples are mainly

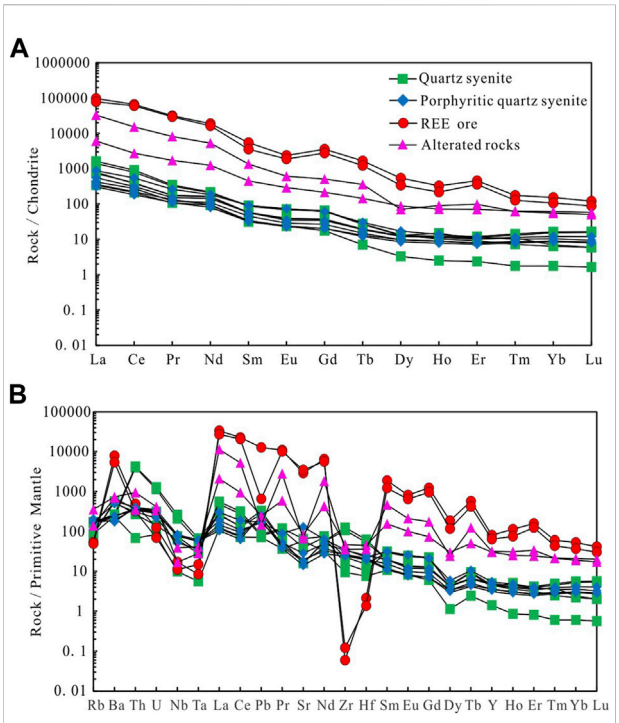


FIGURE 5
(A) Chondrite-normalized REE distribution pattern of the Chishan and Longbaoshan complexes (chondrite values after Sun and McDonough, 1989). **(B)** Primitive mantle-normalized spider diagram of the Chishan and Longbaoshan complexes (primitive mantle values after Sun and McDonough, 1989).

classified as belonging to the alkaline series (Figure 4A), with an aluminum saturation index (A/CNK) of 0.83–0.98, showing a metaluminous to peralkaline characteristic (Figure 4B). They plot within the high-K field on the SiO_2 versus K_2O diagram (Figure 4C), mainly in the alkali-calcic field in the SiO_2 versus $K_2O + Na_2O$—CaO diagram (Figure 4D).

The Longbaoshan porphyritic quartz syenite samples have SiO_2 = 62.87–69.01 wt%, $A1_2O_3$ = 16.77–17.64 wt%, Na_2O = 6.61–6.89 wt%, K_2O = 5.02–5.21 wt%, and CaO = 0.16–1.49 wt%. On the total alkali versus silica (TAS) diagram (Figure 4A), the majority of these sample plots fall within the quartz monzonite field. As shown in the A/CNK versus A/NK diagram, these samples show a peraluminous to metaluminous affinity (Figure 4B). All the samples plot within the shoshonite field on the SiO_2 versus K_2O diagram (Figure 4C), and within the alkalic field on the SiO_2 versus $K_2O + Na_2O$—CaO diagram (Figure 4D).

The chondrite normalized REE patterns (Figure 5A) show that both the Chishan quartz syenite samples and Longbaoshan porphyritic quartz syenite samples show obvious REE fractionation and have the features of enrichment in light REEs (LREEs) and depletion in heavy REEs (HREEs). Moreover, they have similar REE components with total REE concentrations (ΣREE) of 255.2–1117.8 ppm, LREE/HREE ratios of 17.2–29.4, $(La/Yb)_N$ values of 23.5–77.7, and Eu anomalies (δEu) of 0.77–0.98. On the primitive mantle-normalized trace element spider diagram (Figure 5B), they are characterized by enrichment in large-ion lithophile elements (LILEs, e.g., Rb, Ba, and Sr), depletion in high field strength elements (HFSEs, e.g., Nb and Ta), and positive Pb anomalies and negative Nd and Dy anomalies.

The Chishan REE ores and Longbaoshan altered rocks are highly enriched in REEs (ΣREE = 4067.5–77419.3 ppm), with LREE/HREE ratios of 17.3–121.6 and $(La/Yb)_N$ values of 23.1–603.5. In the chondrite-normalized REE patterns (Figure 5A), these samples exhibit distinct REE fractionation and features of enrichment in LREEs and depletion in HREEs with mild negative Eu (δEu = 0.52–0.88) anomalies. On the primitive mantle-normalized trace element spider diagram (Figure 5B), they are characterized by exceeding enrichment in LILEs (Rb and Ba), depletion in HFSEs (Nb, Ta, Zr, and Hf), and negative Pb and Dy anomalies.

4.3 Whole rock Sr–Nd–Pb isotopes

The Sr–Nd–Pb isotopic analysis results are listed in Table 3. The Chishan quartz syenite samples have uniform initial $(^{87}Sr/^{86}Sr)_i$ ratios (0.7062–0.7088) and negative $\varepsilon_{Nd}(t)$ values (−12.9 to −9.3), whereas the Longbaoshan porphyritic quartz syenite samples have high initial $(^{87}Sr/^{86}Sr)_i$ ratios (0.7083–0.7100) and lower $\varepsilon_{Nd}(t)$ values (−14.6 to −13.6). The Chishan REE ore samples have similar initial $(^{87}Sr/^{86}Sr)_i$ ratios (0.7073–0.7077) and $\varepsilon_{Nd}(t)$ values (−9.3 to −8.8) to the quartz syenite, and the Longbaoshan altered rocks also have similar initial $(^{87}Sr/^{86}Sr)_i$ ratios (0.7087–0.7089) and $\varepsilon_{Nd}(t)$ values (−13.3 to −13.1) to the porphyritic quartz syenite.

The Chishan quartz syenite samples and the Longbaoshan porphyritic quartz syenite samples have coincident Pb isotope compositions with the $(^{206}Pb/^{204}Pb)_t$, $(^{207}Pb/^{204}Pb)_t$, and $(^{208}Pb/^{204}Pb)_t$ ratios of 17.25–17.63, 15.41–15.51, and 36.25–37.84, respectively. The Chishan REE ore samples and Longbaoshan altered rocks also have similar Pb isotope compositions to the (porphyritic) quartz syenite samples ($(^{206}Pb/^{204}Pb)_t$ =17.19 to 17.52, $(^{207}Pb/^{204}Pb)_t$ = 15.44 to 15.53, and $(^{208}Pb/^{204}Pb)_t$ =36.99–37.81).

4.4 Zircon Hf isotopes

The *in situ* Hf isotopic analysis results of the (porphyritic) quartz syenite are listed in Table 4. The results show that they have analogical $\varepsilon_{Hf}(t)$ values. In total, five zircon grains from sample 18CS-01 yield $\varepsilon_{Hf}(t)$ values from −15.8 to −13.2 (mean = −14.4) and Hf model ages (T_{DM}^C) of 2.07–2.19 Ga

TABLE 3 Sr-Nd-Pb isotopic compositions of the quartz syenite, REE ore samples, and altered rocks from Chishan and Longbaoshan REE deposits.

Samples	18CS-01	18CS-10	18CS-11	18CS-12	18CS-33	18CS-05	18CS-18	LBS-01	LBS-04	LBS-06	LBS-07	LBS-09	P6D8h1	P6D8h3
Rb (ppm)	55	103	110	53	54	34	31	130	108	111	107	108	146	225
Sr (ppm)	1236	340	338	831	1381	61432	73381	598	372	416	297	2742	491	1407
$^{87}Rb/^{86}Sr$	0.044506	0.303209	0.325829	0.063802	0.039096	0.000553	0.000422	0.216465	0.290766	0.268058	0.360800	0.039409	0.297352	0.159915
$^{87}Sr/^{86}Sr$	0.708933	0.709161	0.709365	0.706476	0.706293	0.707704	0.707326	0.709185	0.710136	0.710079	0.710716	0.708466	0.709253	0.709229
2s	0.000007	0.000005	0.000007	0.000007	0.000007	0.000007	0.000007	0.000007	0.000005	0.000007	0.000006	0.000005	0.000007	0.000007
Sm (ppm)	4.78	8.64	8.78	13.91	13.26	838.34	544.55	8.73	6.91	5.24	4.92	13.85	69.01	206.97
Nd (ppm)	74.72	76.91	97.28	101.77	73.75	6397.63	19.19	8811.86	1539.23	1298.24	67.00	51.66	583.33	2473.67
$^{147}Sm/^{144}Nd$	0.110207	0.115629	0.114154	0.142984	0.130293	0.095138	0.07098	0.130289	0.133756	0.118573	0.132022	0.160013	0.118304	0.083669
$^{143}Nd/^{144}Nd$	0.511906	0.512078	0.512081	0.512094	0.512107	0.51208	0.512085	0.511871	0.511874	0.511879	0.511891	0.511862	0.511895	0.511874
2s	0.000004	0.000004	0.000005	0.000006	0.000006	0.000005	0.000005	0.000005	0.000005	0.000006	0.000006	0.000005	0.000004	0.000004
t (Ma)	126	126	126	126	126	126	126	124	124	124	124	124	124	124
$(^{87}Sr/^{86}Sr)_i$	0.708854	0.708622	0.708786	0.706363	0.706224	0.707703	0.707325	0.708804	0.709624	0.709607	0.710080	0.708397	0.708729	0.708947
$\varepsilon_{Nd}(t)$	−12.9	−9.6	−9.6	−9.8	−9.3	−9.3	−8.8	−13.9	−13.9	−13.6	−13.6	−14.6	−13.3	−13.1
t_{DM1} (Ma)	1830	1666	1636	2272	1904	1376	1139	2331	2426	2033	2344	3635	2002	1495
t_{DM2} (Ma)	1967	1702	1695	1712	1675	1672	1633	2048	2048	2020	2019	2101	1995	1983
$^{206}Pb/^{204}Pb$	16.2773	17.7739	18.1029	17.8867	18.0279	17.2471	17.2076	17.5402	17.6768	17.7527	17.427	17.633	17.5717	17.9221
$^{207}Pb/^{204}Pb$	15.1747	15.4568	15.4734	15.4361	15.4377	15.4486	15.4369	15.5013	15.5111	15.5169	15.4979	15.5219	15.5181	15.5523
$^{208}Pb/^{204}Pb$	36.2755	38.8985	39.3357	38.1085	38.1546	37.5938	37.899	37.8525	38.0413	38.1104	37.7826	37.9901	37.8748	38.9284
Pb (ppm)	13.27	61.06	50.37	14.47	15.78	2374.6	121.32	30.43	34.73	42.65	46.68	31.32	47.46	26.92
Th (ppm)	5.80	342.33	362.58	23.00	34.86	41.55	27.25	33.94	32.46	28.56	32.50	26.49	107.08	80.47
U (ppm)	1.77	23.87	26.92	2.99	6.55	2.60	1.46	7.41	6.30	6.03	5.84	4.53	7.19	8.75
$(^{206}Pb/^{204}Pb)_t$	17.3209	17.2863	17.4291	17.6314	17.5138	17.2458	17.1929	17.2464	17.4569	17.5809	17.2764	17.4579	17.3887	17.5217
$(^{207}Pb/^{204}Pb)_t$	15.4671	15.4331	15.4407	15.4237	15.4127	15.4485	15.4362	15.487	15.5004	15.5086	15.4906	15.5134	15.5092	15.5329
$(^{208}Pb/^{204}Pb)_t$	36.7078	36.6091	36.5848	37.4656	37.2588	37.5868	37.8093	37.4119	37.6703	37.8441	37.5083	37.6548	36.9826	37.7227

10.3389/feart.2022.1046071

TABLE 4 Zircon Hf isotopic compositions of the quartz syenite from Chishan and Longbaoshan complexes.

Rock type	Spots	$^{176}Yb/^{177}Hf$	2σ	$^{176}Lu/^{177}Hf$	2σ	$^{176}Hf/^{177}Hf$	2σ	t (Ma)	ε_{Hf} (0)	ε_{Hf} (t)	T_{DM}(Ma)	T_{DM}^{C}(Ma)	$f_{Lu/Hf}$
Quartz syenite*	18CS-01-01	0.013407	0.000144	0.000586	0.000006	0.282297	0.000018	126	−16.8	−14.1	1334	2078	−0.98
	18CS-01-03	0.015576	0.000126	0.000718	0.000005	0.282282	0.000029	126	−17.3	−14.6	1359	2112	−0.98
	18CS-01-08	0.013584	0.000105	0.000573	0.000005	0.282248	0.000025	126	−18.5	−15.8	1400	2186	−0.98
	18CS-01-13	0.011379	0.000058	0.000519	0.000003	0.282322	0.000019	126	−15.9	−13.2	1296	2020	−0.98
	18CS-01-16	0.022202	0.000914	0.000943	0.000037	0.282299	0.000021	126	−16.7	−14.0	1343	2074	−0.97
Porphyritic quartz syenite	LBS-01-02	0.031167	0.000339	0.001094	0.000011	0.282287	0.000031	124	−17.2	−14.5	1365	2102	−0.97
	LBS-01-07	0.017183	0.000082	0.000660	0.000004	0.282291	0.000027	124	−17.0	−14.3	1344	2090	−0.98
	LBS-01-15	0.025887	0.000169	0.001168	0.000008	0.282306	0.000030	124	−16.5	−13.8	1342	2060	−0.96
	LBS-01-20	0.023971	0.000295	0.000908	0.000010	0.282228	0.000028	124	−19.2	−16.5	1440	2231	−0.97
	LBS-01-24	0.025287	0.000207	0.000986	0.000007	0.282191	0.000029	124	−20.5	−17.9	1495	2315	−0.97

Note: constants used in calculation: $(^{176}Lu/^{177}Hf)_{CHUR}$, 0.0332, $(^{176}Hf/^{177}Hf)_{CHUR,\ 0}$=0.282772; $(^{176}Lu/^{177}Hf)_{DM}$, 0.0384, $(^{176}Hf/^{177}Hf)_{DM,\ 0}$=0.28325; constant λ=1.867×10^{-11}a^{-1}. * Note: The zircon Hf compositions of quartz syenite are obtained from previously published work (Wei et al., 2019).

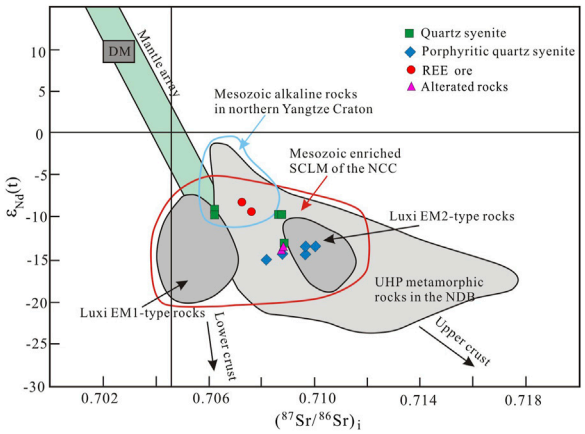


FIGURE 6
Initial $^{87}Sr/^{86}Sr$ versus ε_{Nd} (t) diagram of the Chishan and Longbaoshan complexes. Isotopic data for ultrahigh pressure metamorphic rocks in the North Dabie (NDB) zone (from Dai et al., 2016), Mesozoic-enriched SCLM of the NCC (from Dai et al., 2016), Paleo-Pacific oceanic crust (from Hauff et al., 2003), Mesozoic alkali-rich intrusive rocks near the TLFZ in northern Yangtze Craton (from Yan et al., 2008), and the EM1-type rocks and EM2-type rocks in the Luxi Block (from Zhang et al., 2004, Zhang et al., 2005; Lan et al., 2011).

(mean = 2.09 Ga). In total, five zircon grains from sample LBS-01 yield ε_{Hf}(t) values of −17.9 to −13.8 (mean = −15.4) and T_{DM}^{C} of 2.06–2.32 Ga (mean = 2.16 Ga).

5 Discussion

5.1 Timing of magmatism

The zircon grains from the (porphyritic) quartz syenite exhibit growing oscillatory zoning (Figures 3A,B), which coupled with relatively high Th/U ratios (>0.2 and 1.0) (Table 1), indicate a magmatic origin. Therefore, the weighted mean $^{206}Pb/^{238}U$ ages of 126.2 ± 1.1 Ma and 123.7 ± 0.7 Ma can represent the emplacement ages of the syenitic rocks from the Chishan and Longbaoshan complexes, respectively.

The emplacement age of the Chishan quartz syenite agreed with the previously reported ages (122–126 Ma) of the alkaline complex within the error range (Liang et al., 2017; Wei et al., 2019; Ding et al., 2022). However, the obtained diagenetic age (123.7 ± 0.7 Ma) of the porphyritic quartz syenite is slightly less than the precious reported poorly defined Rb–Sr isochron age (129.3 Ma, Zhang et al., 2005) and LA-ICP-MS zircon U–Pb ages (129.4–131.7 Ma, Lan et al., 2011) of the Longbaoshan complex. The slight difference between the ages of this study and those of predecessors indicates that the Longbaoshan complex was formed in a magmatic activity lasting relatively for a long duration.

Comparing the emplacement ages of the quartz syenite and porphyritic quartz syenite, it is found that they are both formed in the late Early Cretaceous. There is a broad consensus that the NCC has undergone large-scale lithospheric thinning or destruction since the late Paleozoic (Zhai et al., 2002; Deng

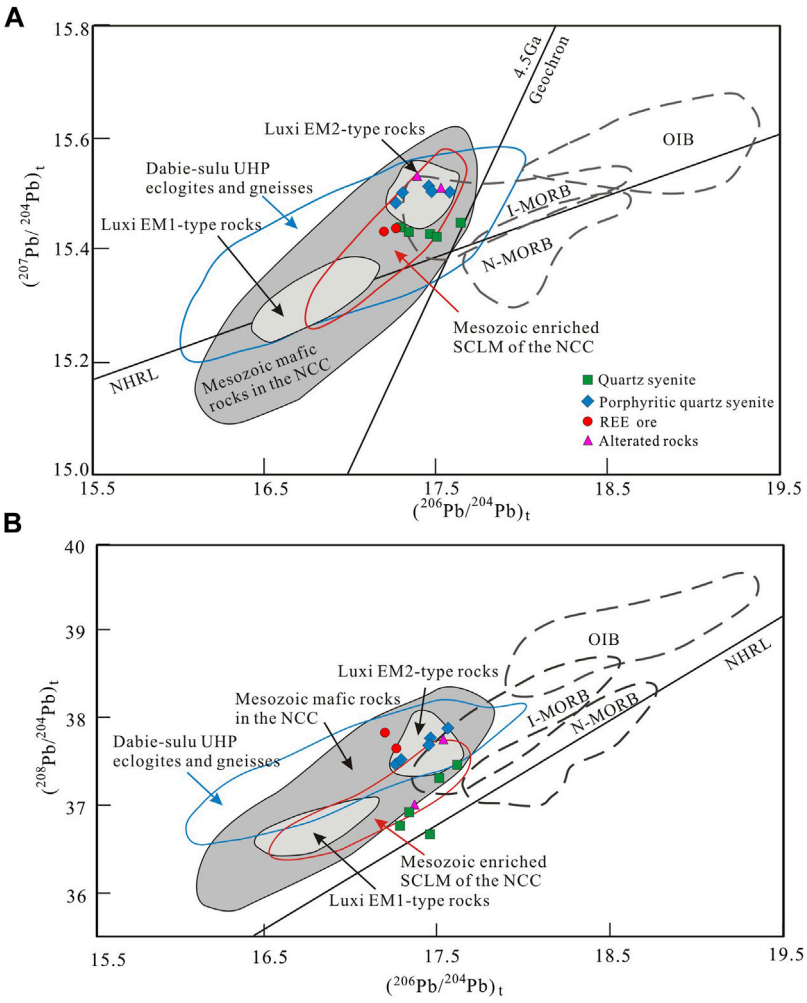


FIGURE 7
Diagrams of $^{207}Pb/^{204}Pb$ versus $^{206}Pb/^{204}$ Pb **(A)** and $^{208}Pb/^{204}Pb$ versus $^{206}Pb/^{204}Pb$ **(B)** for the Chishan and Longbaoshan complexes. Data are also plotted for Mesozoic-enriched SCLM of the NCC (from Dai et al., 2016), Dabie-Sulu UHP eclogites and gneisses (from Yang K. F. et al., 2012), Mesozoic mafic rocks in the NCC (from Li and Yang, 2003) and the EM1-type rocks and EM2-type rocks in the Luxi Block (from Zhang et al., 2005; Lan et al., 2011).

et al., 2003; Chen, 2010; Yang et al., 2018b), and the peak time of destruction and thinning was the Early Cretaceous (125–120 Ma) (Wu et al., 2005; Zhang et al., 2014; Zheng et al., 2018; Yang et al., 2020; Zhang et al., 2020; Zeng et al., 2022). Thus, the diagenesis time of the Chishan and Longbaoshan complexes is consistent with the peak period of the NCC destruction process.

5.2 Petrogenesis

5.2.1 Magma source

The spatial isolated Chishan quartz syenite and Longbaoshan porphyritic quartz syenite have the similar diagenetic ages, chemical characteristics, Sr–Nd–Pb isotopic and zircon Hf isotopic compositions, and normalized trace element and REE patterns, indicating that they may be of cogenetic origin.

The Chishan quartz syenite samples and Longbaoshan porphyritic quartz syenite samples have similar chemical characteristics of relatively high alkalis ($Na_2O + K_2O$ = 7.62–10.94 wt%), high potassium (Na_2O/K_2O = 0.28–0.89) and metaluminous (A/CNK = 0.75–1.00), and low TiO_2 content (0.06–0.17 wt%). In the SiO_2 versus K_2O diagram (Figure 4C), all the sample plots fall within the high-K and shoshonite fields. The rocks display peraluminous to peralkaline features in the A/CNK versus A/NK diagram (Figure 4B). In the SiO_2 versus $K_2O + Na_2O$—CaO diagram (Figure 4D), all the sample plots fall within the alkalic and alkali–calcic fields. Therefore, they have the obvious characteristics of alkaline and metaluminous rocks.

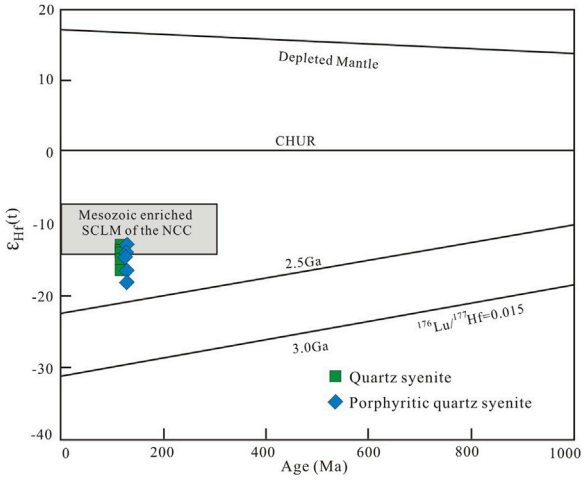


FIGURE 8
$\varepsilon_{Hf}(t)$ versus U-Pb age diagram of zircons from the quartz syenite at the Chishan and Longbaoshan complexes. (Data for the enriched NCC mantle are from Yang et al., 2006; Lan et al., 2013).

The syenitic rocks from the Chishan and Longbaoshan complexes show similar REE and trace element patterns (Figure 5 and Table 2) with the characteristics of enrichment in LREEs and LILEs (Rb, Ba, Pb, and K) and depletion in HFSEs (Ti, Nb, and Ta), along with a slight negative Eu anomaly (Figure 5B). The chondrite-normalized REE patterns also display strongly fractionated LREE/HREE patterns (Figure 5A). Those chemical characteristics are almost the same as the mantle-derived mafic intrusions and volcanics in southeastern NCC during the Early Cretaceous (Zhang et al., 2002; Zhang et al., 2005; Lan et al., 2011).

The Chishan quartz syenite samples and Longbaoshan porphyritic quartz syenite samples have high initial $^{87}Sr/^{86}Sr$ ratios and low $\varepsilon_{Nd}(t)$ values ($(^{87}Sr/^{86}Sr)_i$ = 0.7062 to 0.7100 and $\varepsilon_{Nd}(t)$ = −14.6 to −9.3), which are characteristics of the EM2-like character (Zhang et al., 2005; Lan et al., 2011). In the $\varepsilon_{Nd}(t)$–$(^{87}Sr/^{86}Sr)_i$ diagram (Figure 6), all the sample plots fall near the mantle array despite the variations and fall within the subcontinental lithospheric mantle (SCLM), also suggesting a mantle origin. The (porphyritic) quartz syenite samples have low $(^{206}Pb/^{204}Pb)_i$ (17.2–17.6), slightly high $(^{207}Pb/^{204}Pb)_i$ (Δ7/4=15.4–15.5), and very high $(^{208}Pb/^{204}Pb)_i$ (Δ8/4=36.5–37.8) (Table 3 and Figure 7), similar to the I-MORB and EM2-type rocks (Zhang et al., 2002, Zhang et al., 2005). In the Pb isotopic diagrams (Figure 7), majority of sample plots fall within the Mesozoic mafic rock field, suggesting that they have similar characteristics to the Mesozoic basalts and mafic intrusive rocks in the NCC (Zhang et al., 2002, Zhang et al., 2004). In addition, the (porphyritic) quartz syenite samples have similar $(^{176}Hf/^{177}Hf)_i$ and $\varepsilon_{Hf}(t)$ values (0.28219 to 0.28232 and −17.9 to −13.2, respectively) (Table 4), and in the Hf isotope diagram (Figure 8), all the sample plots fall above the 2.5 Ga continental crust evolutional line, as well as within the Mesozoic enriched SCLM field. Thus, it is reasonable to deduce that the (porphyritic) quartz syenites were derived predominantly from enriched lithospheric mantle (EM2-type).

Previous studies have revealed that the mafic intrusions and volcanic rocks that formed in the Early Cretaceous in southeastern NCC were originated from a mantle domain of arc-like and isotopically enriched (Wu et al., 2017; Dai et al., 2019; Ding et al., 2022). The (porphyritic) quartz syenite samples are characterized by low Nb/Th (0.52–1.95), Nb/La (0.09–0.85) ratios, relatively higher La/Nb (1.00–26.76), Th/Ta (12.39–148.65), Ba/Nb (9.90–239.12) ratios, and negative Nb–Ta anomalies, which are similar to the sub-continental mantle-derived magma contaminated with crustal material (Santosh et al., 2016; Yang et al., 2018b). Moreover, this is also well-demonstrated by the Nd and zircon Hf model ages (t_{DM2} of 1633–2048 Ma and T_{DM}^{C} from 2060 Ma to 2315 Ma, Tables 3, 4), which indicates variable proportions of the Paleoproterozoic crustal material. The crustal source is predominantly a reworked Paleoproterozoic crustal zone originating from the Yangtze Craton (Deng et al., 2018). In the La/Nb versus Ba/Nb diagram (Figure 9A), most of the syenitic sample plots fall within the arc volcanic field, indicative of the similar mantle source of the subducted mantle wedge (Lan et al., 2011). Furthermore, these samples have high $(Hf/Sm)_N$ and relative low $(Ta/La)_N$ ratios which are identical to the Jinan gabbros in the Luxi Block (Figure 9B), suggesting that this enriched mantle source may be related to subduction metasomatism (Lan et al., 2011). In addition, these isotopic compositions of the (porphyritic) quartz syenite are consistent with the Fangcheng basalts and mafic rocks in this region, which were considered to be originated from a lithospheric mantle highly reformed by subducted crust melts (Zhang et al., 2002; Xu et al., 2004; Yang K. F. et al., 2012). Thus, we propose that the (porphyritic) quartz syenites are also derived from lithospheric mantle, which is reformed by the SCLM melts.

5.2.2 Genetic model and process

Three models have been suggested for the generation of syenitic rocks: 1) partial melting of crustal rocks (Miyazaki et al., 2000; Martin, 2006) or an over-thickened crust (Tchameni et al., 2001); 2) partial melting of the enriched mantle or metasomatized mantle (Litvinovsky et al., 2002) or differential evolution of alkalic basaltic magma (Macdonald and Scaillet, 2006); 3) mixing of silica-undersaturated alkaline or mafic magmas derived from the mantle with granitic magmas derived from the lower crust (Zhao et al., 1995; Jung et al., 2007). Based on the aforementioned discussion, we consider that the origin of the (porphyritic) quartz syenite from the Chishan and Longbaoshan complexes should follow the second model. They derived from the lithospheric mantle converted by SCLM melts.

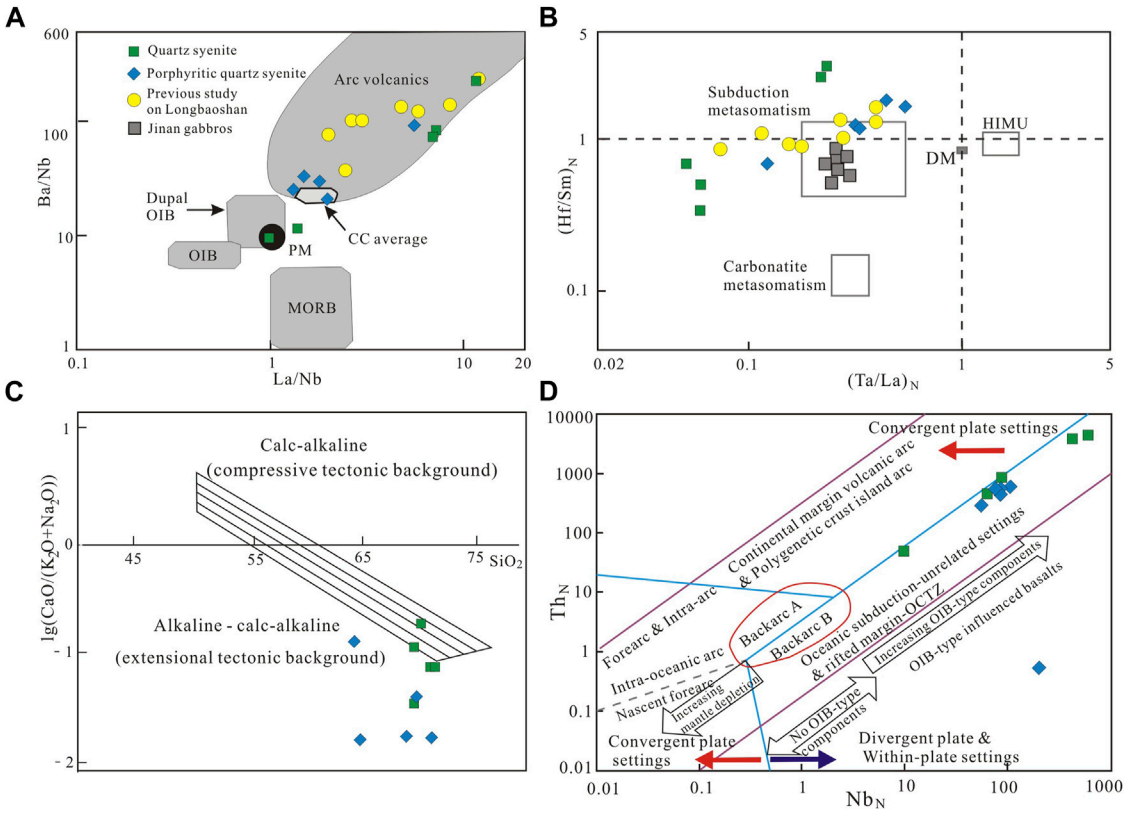


FIGURE 9
(A) La/Nb versus Ba/Nb diagram for the Chishan and Longbaoshan complexes. The fields of MORB, PM, OIB, Dupal OIB, continental crust (CC) average, and arc volcanics are referred to Jahn et al. (1999). **(B)** $(Ta/La)_N$ versus $(Hf/Sm)_N$ diagram for the Chishan and Longbaoshan complexes. The trends of the subduction- and carbonatite-related metasomatism are from La Flèche et al. (1998). **(C)** SiO_2 versus lg ($CaO/(K_2O + Na_2O)$) discrimination diagrams of the quartz syenite from the Chishan and Longbaoshan complexes (after Pearce, 1996). **(D)** Nb_N versus Th_N diagrams for the Chishan and Longbaoshan complex (after Saccani, 2015).

However, for the rocks formed by partial melting in the mantle source area, two main mechanisms have been proposed to reveal the reformation of lower crust materials: 1) the direct transformation of the magma source area by delaminated continental crust materials; 2) the assimilation or contamination of the crustal materials in the magma ascending process (Yang D. B. et al., 2012). In the $\varepsilon_{Nd}(t)$-SiO_2 and $(^{87}Sr/^{86}Sr)_i$-SiO_2 diagrams (Figure 10), the initial $^{87}Sr/^{86}Sr$ ratios and $\varepsilon_{Nd}(t)$ values have no significant changes with the increase of SiO_2 contents, which is consistent with the evolution trend of fractional crystallization, manifesting that the assimilation of continental crust materials may have occurred principally in the magma chamber (Zhang et al., 2005; Lan et al., 2011). Therefore, we conclude that the alkaline magma derived from the enriched lithospheric mantle was unevenly assimilated by melts derived from the continental crust in the magma chamber and then produced the parent magma of the (porphyritic) quartz syenites.

Through the aforementioned discussion, the formation process of the (porphyritic) quartz syenite can be summarized as follows: before 130 Ma, the lithospheric mantle under the southeastern part of the Luxi Block reformed by the SCLM melts and transformed from EM1-type into EM2-type in response to the subduction of the Yangtze continental crust (Figure 11A) (Zhang et al., 2002, Zhang et al., 2004; Lan et al., 2011). At ~130 Ma, due to subduction of the Paleo-Pacific plate, the converted EM2-type lithospheric mantle was partially melted and produced potassium-rich alkaline magma marked by enrichment of LREEs and LILEs and depletion of HFSEs (Figure 11B) (Zhang et al., 2002; Zhang et al., 2004, Zhang et al., 2005). This magma assimilated the crust-derived melts and were up-invaded with the lithospheric thinning and asthenosphere mantle upwelling, forming the Chishan and Longbaoshan alkaline complexes (Figure 11C).

5.3 Tectonic setting

All the studied syenitic rocks from the Chishan and Longbaoshan complexes have an arc-like affinity with enriched LREEs and LILEs (e.g., Ba and Th) and depleted HFSE (e.g., Nb and Ta). This can be further evidenced by the

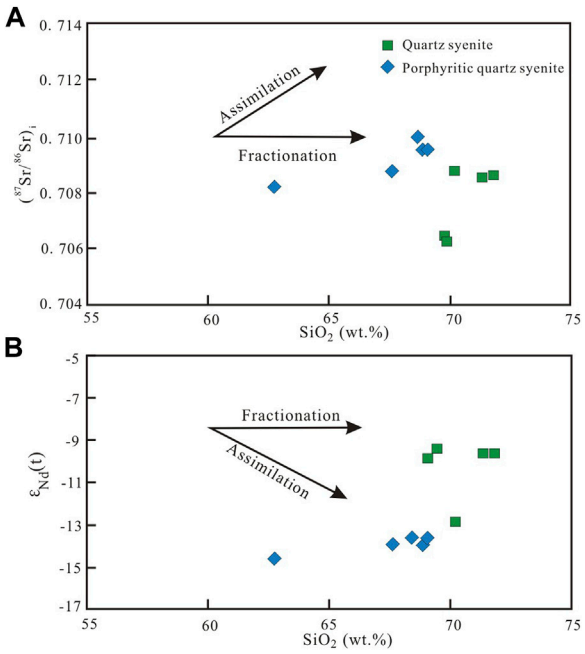


FIGURE 10
Diagrams of initial $^{87}Sr/^{86}Sr$ ratio versus SiO_2 **(A)** and $\varepsilon_{Nd}(t)$ value versus SiO_2 **(B)** for the Chishan and Longbaoshan complexes.

La/Nb versus Ba/Nb diagram (Figure 9A), in which most syenitic samples plot within the arc volcanic field. In addition, the high $(Hf/Sm)_N$ and low $(Ta/La)_N$ ratios (Figure 9B) of these samples suggest that the enriched mantle source may be associated with subduction metasomatism (La Flèche et al., 1998; Lan et al., 2011). Nevertheless, it is noteworthy that the syenitic samples plot within the extensional alkaline-calc-alkaline field in the lg $(CaO/(K_2O + Na_2O))$ versus SiO_2 discrimination diagram (Figure 9C) and plot within the fields of divergent plate and within-plate settings in the Nb_N versus Th_N discrimination diagram (Figure 9D), implying an extensional tectonic setting (Wei et al., 2019; Ding et al., 2022). Moreover, the paleostress regimes reconstructed results of the Jiaolai Basin based on the effective fault-slip data and fold hinge data inversion showed that it has experienced E–W extension (135–121 Ma) and NW–SE extension (120–93 Ma) since the Cretaceous (Zhang et al., 2020). The study on the structural geology, paleomagnetism, and gravity modeling of Fengjiayu–Xibailianyu and Gubeikou plutons revealed that the NCC was also in a NW–SE trending extensional tectonics during 130–110 Ma with severe extension after *ca.* 127 Ma (Zeng et al., 2022).

Numerous studies have shown that the NCC was in an extensional tectonic environment during the Mesozoic and underwent craton destruction and extensive lithospheric thinning indicated by intense magmatism (Zhai et al., 2002; Deng et al., 2003; Yang et al., 2007). It has already been confirmed that the Early Cretaceous was a peak period for NCC destruction and lithospheric thinning (Wu et al., 2005; Zheng, 2009; Goss et al., 2010) due to the rollback and retreat of subducting the Paleo-Pacific plate (Santosh, 2010; Zhu et al., 2012). In the early Mesozoic, the Paleo-Pacific plate subducted in a low angle along the continental margin of the eastern NCC and showed an important impact on the destruction and thinning of the latter continental lithosphere (Xu et al., 2012; Zheng et al., 2018; Zhu and Xu, 2019). It has been proposed that the angle of subduction gradually increased with the rollback and retreat of the subduction zone during the Early Cretaceous (Zhu and Xu, 2019). The transition of subduction angle may have occurred at *ca.* 140 Ma (Wu et al., 2005; Zhang et al., 2014; Zhao et al., 2017). In addition, partial melting of the SCLM as well as the destruction and extension of the lithosphere was also caused during this process (Zhu et al., 2012; Yang et al., 2021).

5.4 Relationship between quartz syenite and REE mineralization

It is widely accepted that REE mineralization is genetically relevant to mantle-derived carbonatite-alkaline magmatism (Goodenough et al., 2016; Smith et al., 2016; Liu et al., 2019; Fan et al., 2020; Xie et al., 2020). At Chishan and Longbaoshan, the REE mineralization generally occurred within quartz syenite and porphyritic quartz syenite, which were under the control of NW- and NE-trending faults and NNE- and NE-trending faults, respectively. Preciously published Rb–Sr isochron ages and ^{40}Ar-^{39}Ar and U–Th dating results have yielded ages of 110–124 Ma of the REE mineralization (Tian et al., 2002; Lan et al., 2011; Ding et al., 2022), which are generally consistent with diagenetic ages of the syenitic rocks in this study. Actually, this age difference is basically consistent with the age error for magmatic hydrothermal deposits (Li et al., 1992; Tan et al., 2006). This spatial and temporal distribution consistency of the syenitic rocks and REE indicates that the mineralization has a certain genetic relationship with these alkaline rocks (Tian et al., 2002; Yu et al., 2010, 2014; Lan et al., 2011; Wei et al., 2019).

The aforementioned conclusions are also demonstrated by the geochemical and Sr–Nd–Pb isotopic characteristics of the syenitic rocks, REE ores, and altered rocks. The Chishan REE ores and Longbaoshan altered rocks are characterized by enrichment of LREEs and LILEs and depletion of HFSEs, which is similar to those of the syenitic rocks. From the chondrite-normalized REE patterns (Figure 5A), it can be seen that the REE distribution curve shapes of the Chishan REE ores and Longbaoshan altered rocks are basically similar to those of syenitic rocks. They all show a right-inclined distribution pattern, indicating that they have the characteristics of evolutionary inheritance. Furthermore, the Chishan REE ores and Longbaoshan altered rocks have similar Sr–Nd–Pb isotopic compositions to the syenitic rocks (Table 3; Figures 6, 7), indicating that the Chishan REE ores and

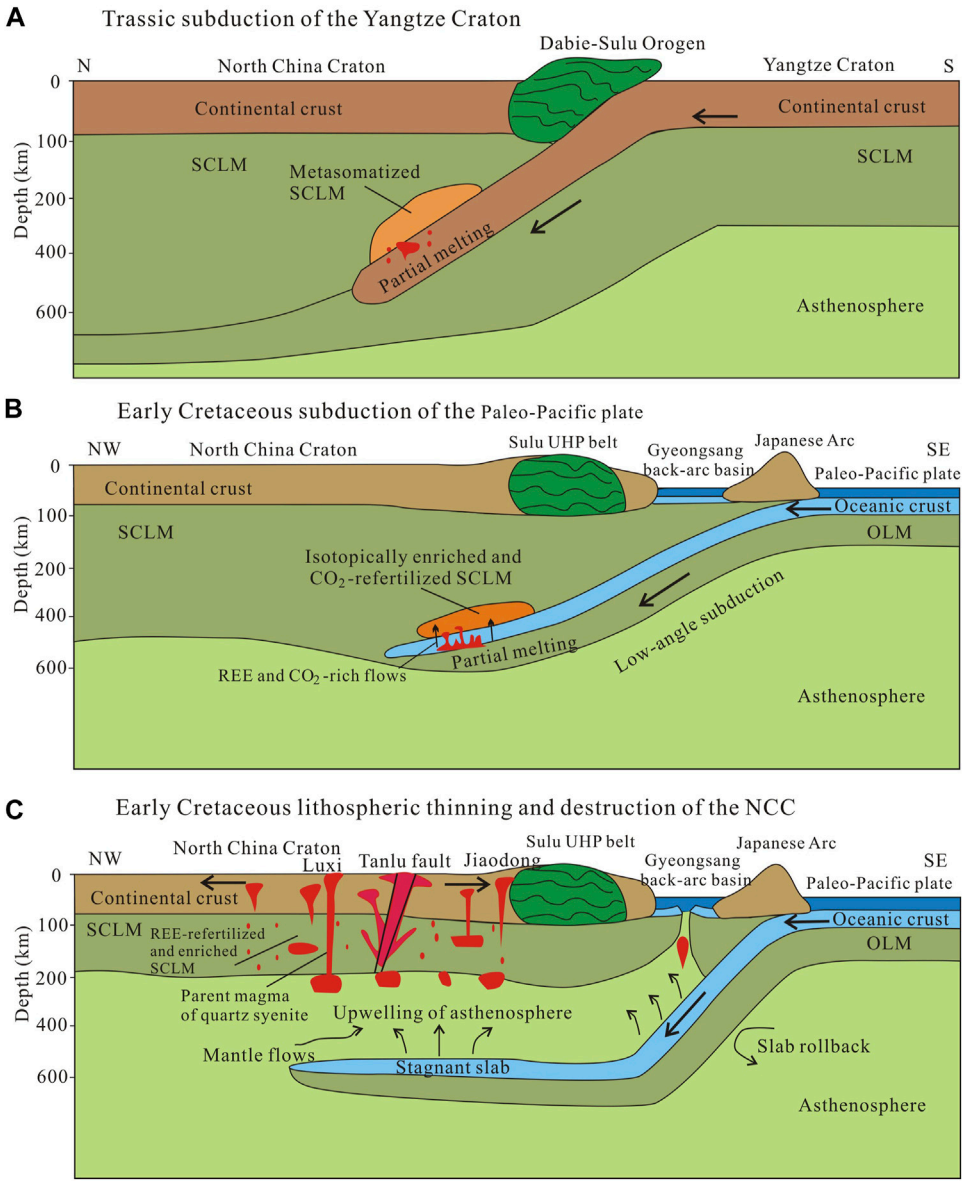


FIGURE 11
Simplified genetic model cross-sections of quartz syenite (modified after Zhu and Xu, 2019; Deng et al., 2020; Ding et al., 2022). **(A)** Trassic subduction of the Yangtze Craton. **(b)** Early Cretaceous subduction of the Paleo-Pacific plate. **(C)** Early Cretaceous lithospheric thinning and destruction of the NCC.

Longbaoshan altered rocks have identical material sources with the syenitic rocks which were originated from the enriched mantle. Moreover, the *in situ* Nd isotopic compositions from single minerals of bastnasite and monazite at the Chishan REE deposit also suggested that the REE was derived from the enriched lithospheric mantle (Lan et al., 2011), which is also identical to that of the syenitic rocks.

Some studies have shown that the sources of ore-forming materials of Bayan Obo and Maoniuping REE deposits are closely related to those of the enriched mantle (Hou et al., 2009; Xie et al., 2009; Yang et al., 2009), indicating that the enriched mantle should be the source area of REE deposits. It has been suggested that melt-enriched LREE were derived from an enriched mantle metasomatized by REE- and CO_2-rich fluids that were released from subducted marine sediments (Walter et al., 2008; Yang et al., 2011; Hou et al., 2015; Liu et al., 2015; Ding et al., 2022).

In summary, based on the similar diagenetic/metallogenic ages, Sr–Nd–Pb isotopic compositions, and direct coexistence in space, we propose that the REE minerals have a genetic relationship with the syenitic rocks and they are homologous

products, and the mineralization shows inheritance to the magmatic hydrothermal evolution.

6 Conclusion

1) LA-ICP-MS zircon U-Pb dating indicated that the diagenetic ages of the Chishan quartz syenite and Longbaoshan porphyritic quartz syenite were 126.2 ± 1.1 Ma and 123.7 ± 0.7 Ma, respectively, which belong to the Early Cretaceous and correspond to the peak period for NCC destruction and lithospheric thinning.
2) Geochemical and Sr–Nd–Pb–Hf isotopic characteristics suggest that the Chishan quartz syenite and Longbaoshan porphyritic quartz syenite have the identical material source of an EM-2 type lithospheric mantle that was modified by SCLM melts while the Yangtze block subducted.
3) The Chishan quartz syenite and Longbaoshan porphyritic quartz syenite show an arc affinity, implying in an extensional tectonic setting associated with rollback and retreat of the subducting Paleo-Pacific plate.
4) Based on the similar diagenetic/metallogenic ages, Sr–Nd–Pb isotopic compositions, and direct coexistence in space, we propose that the quartz syenite and the REE ore-forming material are homologous products. The REE mineralization shows inheritance to the magmatic hydrothermal evolution.

Data availability statement

The original contributions presented in the study are included in the article/Supplementary Material; further inquiries can be directed to the corresponding authors.

Author contributions

PW, DL, and ZS conceived this research. PW wrote the manuscript and prepared the figures. DL, ZS, and KG reviewed and edited the draft. QL, KG, YZ, and CD participated in field investigation. ZL, NC, WX, and CZ analyzed the data. All authors finally approved the manuscript and thus agreed to be accountable for this work.

Funding

This study was financially supported by the National Natural Science Foundation of China (Grant Nos. 42272104, 42172094, 41372086, 41672084, and 41772076), Natural Science Foundation of Shandong Province (Grant Nos. ZR2020QD028, ZR2020QD031, ZR2018QD002, and ZR2020MD032), Geological Exploration Project of Shandong Province (Grant Nos. LKZ (2020) 7, LKZ (2021) 7, LKZ (2022) 9), and a special fund for "Taishan scholars" project in the Shandong province.

Acknowledgments

We would like to express our thanks to the reviewers who offered constructive and valuable comments to improve the manuscript.

Conflict of interest

The authors declare that the research was conducted in the absence of any commercial or financial relationships that could be construed as a potential conflict of interest.

Publisher's note

All claims expressed in this article are solely those of the authors and do not necessarily represent those of their affiliated organizations, or those of the publisher, the editors, and the reviewers. Any product that may be evaluated in this article, or claim that may be made by its manufacturer, is not guaranteed or endorsed by the publisher.

References

Blichert-Toft, J., and Albarède, F. (1997). The Lu-Hf isotope geochemistry of chondrites and the evolution of the mantle-crust system. *Earth Planet. Sci. Lett.* 148 (1-2), 243–258. doi:10.1016/S0012-821X(97)00040-X

Bonin, B., Azzouni-Sekkal, A., Bussy, F., and Ferrag, S. (1998). Alkali-calcic and alkaline post-orogenic (PO) granite magmatism: Petrologic constraints and geodynamic settings. *Lithos* 45, 45–70. doi:10.1016/S0024-4937(98)00025-5

Chen, B., Zhai, M. G., and Tian, W. (2007). Origin of the mesozoic magmatism in the north China craton: Constraints from petrological and geochemical data. *Geol. Soc. Lond. Spec. Publ.* 280, 131–151. doi:10.1144/SP280.6

Chen, L. (2010). Concordant structural variations from the surface to the base of the upper mantle in the North China Craton and its tectonic implications. *Lithos* 120 (1-2), 96–115. doi:10.1016/j.lithos.2009.12.007

Dai, F. Q., Zhao, Z. F., Zheng, Y. F., and Dai, L. Q. (2016). Slab–Mantle interaction in the petrogenesis of andesitic magmas: Geochemical evidence from postcollisional intermediate volcanic rocks in the Dabie orogen, China. *J. Petrol.* 57, 1109–1134. doi:10.1093/petrology/egw034

Dai, F. Q., Zhao, Z. F., Zheng, Y. F., and Sun, G. C. (2019). The geochemical nature of mantle sources for two types of Cretaceous basaltic rocks from Luxi and Jiaodong in east-central China. *Lithos* 344-345, 409–424. doi:10.1016/j.lithos.2019.07.007

Deng, J., Wang, C. M., Bagas, L., Santosh, M., and Yao, E. Y. (2018). Crustal architecture and metallogenesis in the south-eastern North China Craton. *Earth. Sci. Rev.* 182, 251–272. doi:10.1016/j.earscirev.2018.05.001

Deng, J., Yang, L. Q., Groves, D. I., Zhang, L., Qiu, K. F., and Wang, Q. F. (2020). An integrated mineral system model for the gold deposits of the giant Jiaodong province, eastern China. *Earth. Sci. Rev.* 208, 103274. doi:10.1016/j.earscirev.2020.103274

Deng, J., Yang, L. Q., Sun, Z. S., Wang, J. P., Wang, Q. F., Xin, H. B., et al. (2003). A metallogenic model of gold deposits of the Jiaodong granite-greenstone belt. *Acta Geol. sin-engl.* 77 (4), 537–546. doi:10.1111/j.1755-6724.2003.tb00134.x

Ding, C. W., Zhao, B. C., Dai, P., Li, D. P., Zhang, Z. L., Sun, R. T., et al. (2022). Geochronology, geochemistry and Sr-Nd-Pb-Hf isotopes of the alkaline-carbonatite complex in the Weishan REE deposit, Luxi Block: Constraints on the Genesis and tectonic setting of the REE mineralization. *Ore Geol. Rev.* 147, 104996. doi:10.1016/j.oregeorev.2022.104996

Fan, H. R., Niu, H. C., Li, X. C., Yang, K. F., Yang, Z. F., and Wang, Q. W. (2020). The types, ore Genesis and resource perspective of endogenic REE deposits in China. *Chin. Sci. Bull.* 65, 3778–3793. (in Chinese with English abstract). doi:10.1360/TB-2020-0432

Fan, W. M., Zhang, H. F., Baker, J., Jarvis, K. E., Mason, P. R. D., and Menzies, M. A. (2000). On and off the north China craton: Where is the archaean keel? *J. Petrol.* 41, 933–950. doi:10.1093/petrology/41.7.933

Frost, B. R., Barnes, C. G., Collins, W. J., Arculus, R. J., Ellis, D. J., and Frost, C. D. (2001). A geochemical classification for granitic rocks. *J. Petrol.* 42 (11), 2033–2048. doi:10.1093/petrology/42.11.2033

Gao, S., Rudnick, R. L., Xu, W. L., Yuan, H. L., Liu, Y. S., Walker, R. J., et al. (2008). Recycling deep cratonic lithosphere and generation of intraplate magmatism in the North China Craton. *Earth Planet. Sci. Lett.* 270, 41–53. doi:10.1016/j.epsl.2008.03.008

Gao, S., Rundnick, R. L., Carlson, R. W., Mc Donough, W. F., and Liu, Y. S. (2002). Re-Os evidence for replacement of ancient mantle lithosphere beneath the North China Craton. *Earth Planet. Sci. Lett.* 198, 307–322. doi:10.1016/S0012-821X(02)00489-2

Geng, J. Z., Li, H. K., Zhang, J., Zhou, H. Y., and Li, H. M. (2011). Zircon Hf isotope analysis by means of LA-MC-ICP-MS. *Geol. Bull. China* 30 (10), 1508–1513. (in Chinese with English abstract).

Goldfarb, R. J., and Santosh, M. (2014). The dilemma of the jiaodong gold deposits: Are they unique? *Geosci. Front.* 5, 139–153. doi:10.1016/j.gsf.2013.11.001

Goodenough, K. M., Schilling, J., Jonsson, E., Kalvig, P., Charles, N., Tuduri, J., et al. (2016). Europe's rare Earth element resource potential: An overview of REE metallogenetic provinces and their geodynamic setting. *Ore Geol. Rev.* 72, 838–856. doi:10.1016/j.oregeorev.2015.09.019

Goss, S. C., Wilde, S. A., Wu, F., and Yang, J. (2010). The age, isotopic signature and significance of the youngest mesozoic granitoids in the jiaodong terrane, shandong province, north China craton. *Lithos* 120, 309–326. doi:10.1016/j.lithos.2010.08.019

Griffin, W. L., Pearson, N. J., Belousova, E., Jackson, S. E., Van Achterbergh, E., O'Reilly, S. Y., et al. (2000). The Hf isotope composition of cratonic mantle: LAM-MC-ICPMS analysis of zircon megacrysts in kimberlites. *Geochim. Cosmochim. Acta* 64 (1), 133–147. doi:10.1016/S0016-7037(99)00343-9

Griffin, W. L., Wang, X., Jackson, S. E., Pearson, N. J., O'reilly, S. Y., Xu, X. S., et al. (2002). Zircon chemistry and magma mixing, SE China: *In-situ* analysis of Hf isotopes, tonglu and pingtan igneous complexes. *Lithos* 61 (3-4), 237–269. doi:10.1016/S0024-4937(02)00082-8

Hauff, F., Hoernle, K., and Schmidt, A. (2003). Sr-Nd-Pb composition ofMesozoic Pacific oceanic crust (Site 1149 and 801, ODP Leg 185): Implications for alteration of ocean crust and the input into the Izu-Bonin-Mariana subduction system. *Geochem. Geophys. Geosyst.* 4, 8913. doi:10.1029/2002gc000421

Hou, Z. Q., Liu, Y., Tian, S. H., Yang, Z. M., and Xie, Y. L. (2015). Formation of carbonatite-related giant rare-Earth-element deposits by the recycling of marine sediments. *Sci. Rep.* 5 (1), 10231–10310. doi:10.1038/srep10231

Hou, Z. Q., Tian, S. H., Xie, Y. L., Yang, Z. S., Yuan, Z. X., Yin, S. P., et al. (2009). The Himalayan Mianning-Dechang REE belt associated with carbonatite-alkaline complexes, eastern Indo-Asian collision zone, SW China. *Ore Geol. Rev.* 36 (1-3), 65–89. doi:10.1016/j.oregeorev.2009.03.001

Irvine, T. N., and Baragar, W. R. A. (1971). A guide to the chemical classification of the common volcanic rocks. *Can. J. Earth Sci.* 8, 523–548. doi:10.1139/e71-055

Jahn, B. M., Wu, F. Y., Lo, C. H., and Tsai, C. H. (1999). Crust-mantle interaction induced by deep subduction of the continental crust: Geochemical and Sr-Nd isotopic evidence from post-collisional mafic-ultramafic intrusions of the northern Dabie complex, central China. *Chem. Geol.* 157, 119–146. doi:10.1016/S0009-2541(98)00197-1

Jung, S., Hoffer, E., and Hoernes, S. (2007). Neo-proterozoic rift-related syenites (northern damara belt, Namibia): Geochemical and Nd-Sr-Pb-O isotope constraints for mantle sources and petrogenesis. *Lithos* 96, 415–435. doi:10.1016/j.lithos.2006.11.005

La Flèche, M. R., Camire, G., and Jenner, G. A. (1998). Geochemistry of post-acadian, carboniferous continental intraplate basalts from the maritimes basin, magdalen islands, quebec, Canada. *Chem. Geol.* 148, 115–136. doi:10.1016/s0009-2541(98)00002-3

Lan, T. G., Fan, H. R., Hu, F. F., Tomkins, A. G., Yang, K. F., and Liu, Y. (2011). Multiple crust-mantle interactions for the destruction of the North China craton: Geochemical and Sr–Nd–Pb–Hf isotopic evidence from the longbaoshan alkaline complex. *Lithos* 122 (1-2), 87–106. doi:10.1016/j.lithos.2010.12.001

Lan, T. G., Fan, H. R., Santosh, M., Hu, F. F., Yang, K. F., Yang, Y. H., et al. (2013). Crust-mantle interaction beneath the Luxi block, eastern North China craton: Evidence from coexisting mantle-and crust-derived enclaves in a quartz monzonite pluton. *Lithos* 177, 1–16. doi:10.1016/j.lithos.2013.05.017

Li, C. J., Xu, B. T., Jiang, X. L., and Hu, Y. H. (1992). Time interval between the formation of host rock and the mineralization in some hydrothermal deposits of Southeast China with a discussion on some related problems. *Mineral. Deposits* 11 (2), 106–112+105. (in Chinese with English abstract).

Li, S. G., Xiao, Y. L., Liou, D. L., Chen, Y. Z., Ge, N. J., Zhang, Z. Q., et al. (1993). Collision of the north China and yangtse blocks and formation of coesite-bearing eclogites: Timing and processes. *Chem. Geol.* 109, 89–111. doi:10.1016/0009-2541(93)90063-o

Li, S. G., and Yang, W. (2003). Decoupling of surface and subsurface sutures in the Dabie orogen and a continent-collisional lithospheric-wedging model:Sr-Nd-Pb isotopic evidences of Mesozoic igneous rocks in eastern China. *Chin. Sci. Bull.* 48, 831–838. doi:10.1360/01wd0554

Li, S. R., and Santosh, M. (2017). Geodynamics of heterogeneous gold mineralization in the North China Craton and its relationship to lithospheric destruction. *Gondwana Res.* 50, 267–292. doi:10.1016/j.gr.2017.05.007

Liang, Y. W., Lai, Y., Hu, H., and Zhang, F. (2017). Zircon U-Pb ages and geochemical characteristics study of syenite from Weishan REE deposit, Western Shandong. *Acta Sci. Nat. Univ. Pekin.* 53 (4), 652–666. (in Chinese with English abstract). doi:10.13209/j.0479-8023.2017.010

Litvinovsky, B. A., Jahn, B. M., Zanvilevich, A. N., and Shadaev, M. G. (2002). Crystal fractionation in the petrogenesis of an alkali monzodiorite-syenite series: The oshurkovo plutonic sheeted complex, transbaikalia, Russia. *Lithos* 64, 97–130. doi:10.1016/S0024-4937(02)00179-2

Liu, D. Y., Nutman, A. P., Compston, W., Wu, J. S., and Shen, Q. H. (1992). Remnants of ≥3800 Ma crust in the Chinese part of the Sino-Korean craton. *Geol.* 20, 339–342. doi:10.1130/0091-7613(1992)020<0339:romcit>2.3.co;2

Liu, Y., Chakhmouradian, A. R., Hou, Z. Q., Song, W. L., and Kynicky, J. (2019). Development of REE mineralization in the giant Maoniuping deposit (Sichuan, China): Insights from mineralogy, fluid inclusions, and trace-element geochemistry. *Min. Depos.* 54, 701–718. doi:10.1007/s00126-018-0836-y

Liu, Y., Chen, Z. Y., Yang, Z. S., Sun, X., Zhu, Z. M., Zhang, Q. C., et al. (2015). Geochemical and mineralogical characteristics of weathered ore in the dalucao REE deposit, mianning–dechang REE belt, Western sichuan province, southwestern China. *Ore Geol. Rev.* 70, 437–456. doi:10.1016/j.oregeorev.2015.06.009

Liu, Y. S., Hu, Z. C., Gao, S., Günther, D., Xu, J., Gao, C. G., et al. (2008). *In situ* analysis of major and trace elements of anhydrous minerals by LA-ICP-MS without applying an internal standard. *Chem. Geol.* 257 (1-2), 34–43. doi:10.1016/j.chemgeo.2008.08.004

Ludwig, K. R. (2003). *Isoplot 3.00: A geochronological toolkit for microsoft excel*. Berkeley Geochronology Center Special Publication. No. 4.

Macdonald, R., and Scaillet, B. (2006). The central Kenya peralkaline province: Insights into the evolution of peralkaline salic magmas. *Lithos* 91, 59–73. doi:10.1016/j.lithos.2006.03.009

Maniar, P. D., and Piccoli, P. M. (1989). Tectonic discrimination of granitoids. *Geol. Soc. Am. Bull.* 101 (5), 635–643. doi:10.1130/0016-7606(1989)101<0635:tdog>2.3.co;2

Martin, R. F. (2006). A-type granites of crustal origin ultimately result from open-system fenitization-type reactions in an extensional environment. *Lithos* 91, 125–136. doi:10.1016/j.lithos.2006.03.012

Middlemost, E. A. K. (1994). Naming materials in the magma/igneous rock system. *Earth. Sci. Rev.* 37 (3-4), 215–224. doi:10.1016/0012-8252(94)90029-9

Miyazaki, T., Kagami, H., Shuto, K., Mohan, V. R., and Rajasekaran, K. C. (2000). Rb-Sr geochronology, Nd-Sr isotopes and whole rock geochemistry of Yelagiri and

Sevattur syenites, Tamil Nadu, South India. *Gondwana Res.* 3, 39–53. doi:10.1016/S1342-937X(05)70056-3

Pearce, J. A. (1996). Sources and settings of granitic rocks. *Episodes* 19 (4), 120–125. doi:10.18814/epiiugs/1996/v19i4/005

Peccerillo, A., and Taylor, S. R. (1976). Geochemistry of Eocene calc-alkaline volcanic rocks from the Kastamonu area, northern Turkey. *Contr. Mineral. Petrol.* 58 (1), 63–81. doi:10.1007/BF00384745

Pin, C., Gannoun, A., and Dupont, A. (2014). Rapid, simultaneous separation of Sr, Pb, and Nd by extraction chromatography prior to isotope ratios determination by TIMS and MC-ICP-MS. *J. Anal. At. Spectrom.* 29, 1858–1870. doi:10.1039/c4ja00169a

Qiu, J. X. (1993). *The alkaline rocks in Qin-Bashan area*. Beijing: Geological Publishing House, 1–137. (in Chinese).

Saccani, E. (2015). A new method of discriminating different types of post-Archean ophiolitic basalts and their tectonic significance using Th-Nb and Ce-Dy-Yb systematics. *Geosci. Front.* 6, 481–501. doi:10.1016/j.gsf.2014.03.006

Santosh, M. (2010). Assembling north China craton within the columbia supercontinent: The role of double-sided subduction. *Precambrian Res.* 178, 149–167. doi:10.1016/j.precamres.2010.02.003

Santosh, M., Teng, X. M., He, X. F., Tang, L., and Yang, Q. Y. (2016). Discovery of Neoarchean suprasubduction zone ophiolite suite from Yishui Complex in the North China Craton. *Gondwana Res.* 38, 1–27. doi:10.1016/j.gr.2015.10.017

Smith, M. P., Moore, K., Kavecs´anszki, D., Finch, A. A., Kynicky, J., and Wall, F. (2016). From mantle to critical zone: A review of large and giant sized deposits of the rare Earth elements. *Geosci. Front.* 7 (3), 315–334. doi:10.1016/j.gsf.2015.12.006

Söderlund, U., Patchett, P. J., Vervoort, J. D., and Isachsen, C. E. (2004). The ^{176}Lu decay constant determined by Lu-Hf and U-Pb isotope systematics of Precambrian mafic intrusions. *Earth Planet. Sci. Lett.* 219 (3-4), 311–324. doi:10.1016/S0012-821X(04)00012-3

Sun, S. S., and McDonough, W. F. (1989). "*Chemical and Isotopic Systematics of Oceanic Basalts: Implications for Mantle Composition and Processes*". Editors A. D. Saunder and M. J. Norry (London: Geological Society, London, Special Publications 42, 313–345. doi:10.1144/gsl.sp.1989.042.01.19

Tan, J., Wei, J. H., Tan, W. J., and Guo, D. Z. (2006). Statistic study of diagenesis-mineralization time gap for comagmatic gold deposits. *Geol. Rev.* 52 (01), 54–62. (in Chinese with English abstract). doi:10.16509/j.georeview.2006.01.010

Tchameni, R., Mezger, K., Nsifa, N. E., and Pouclet, A. (2001). Crustal origin of early proterozoic syenites in the Congo craton (ntem complex), south Cameroon. *Lithos* 57, 23–42. doi:10.1016/S0024-4937(00)00072-4

Tian, J. X., Zhang, R. T., Fan, Y. C., Li, X. Z., Xu, H. Y., and Wang, B. Y. (2002). Geological characteristics and relation with rare Earth elements of alkalic complex in Chishan of Shandong Province. *Shandong Geol.* 18 (1), 21–25. (in Chinese with English abstract).

Tu, G. Z., Zhang, Y. Q., and Zhao, Z. H. (1984). "The preliminary study on two alkali rich intrusive rocks zones," in *Granite geology and mineralization: International symposium on granites*. Editors K. Q. Xu and G. C. Tu (Nanjing: Science and Technology Publishing House of Jiangsu), 21–37. (in Chinese).

Walter, M. J., Bulanova, G. P., Armstrong, L. S., Keshav, S., Blundy, J. D., Gudfinnsson, G., et al. (2008). Primary carbonatite melt from deeply subducted oceanic crust. *Nature* 454, 622–625. doi:10.1038/nature07132

Wang, C. M., Bagas, L., Deng, J., and Dong, M. M. (2018). Crustal architecture and its controls on mineralisation in the North China Craton. *Ore Geol. Rev.* 98, 109–125. doi:10.1016/j.oregeorev.2018.05.016

Wei, P. F., Yu, X. F., Li, D. P., Liu, Q., Yu, L. D., Li, Z. S., et al. (2019). Geochemistry, zircon U-Pb geochronology, and Lu-Hf isotopes of the chishan alkaline complex, western shandong, China. *Minerals* 9 (5), 293. doi:10.3390/min9050293

Wilde, S. A., Zhou, X. H., Nemchin, A. A., and Sun, M. (2003). Mesozoic crust-mantle interaction beneath the north China craton: A consequence of the dispersal of gondwanaland and accretion of asia. *Geol.* 31, 817–820. doi:10.1130/G19489.1

Wu, F. Y., Li, X. H., Zheng, Y. F., and Gao, S. (2007). Lu-Hf isotopic systematics and their applications in petrology. *Acta Petrol. Sin.* 23 (2), 185–220. (in Chinese with English abstract).

Wu, F. Y., Lin, J. Q., Wilde, S. A., Zhang, X. O., and Yang, J. H. (2005). Nature and significance of the Early Cretaceous giant igneous event in eastern China. *Earth Planet. Sci. Lett.* 233, 103–119. doi:10.1016/j.epsl.2005.02.019

Wu, F. Y., Xu, Y. G., Gao, S., and Zheng, J. P. (2008). Lithosphere thinning and destruction of the north China craton. *Acta Petrol. Sin.* 24, 1145–1174. (in Chinese with English abstract).

Wu, K., Ling, M. X., Sun, W. D., Guo, J., and Zhang, C. C. (2017). Major transition of continental basalts in the early cretaceous: Implications for the destruction of the north China craton. *Chem. Geol.* 470, 93–106. doi:10.1016/j.chemgeo.2017.08.025

Xie, Y. L., Hou, Z. Q., Yin, S. P., Dominy, S. C., Xu, J. H., Tian, S. H., et al. (2009). Continuous carbonatitic melt-fluid evolution of a REE mineralization system: Evidence from inclusions in the Maoniuping REE Deposit, Western Sichuan, China. *Ore Geol. Rev.* 36 (1-3), 90–105. doi:10.1016/j.oregeorev.2008.10.006

Xie, Y. L., Xia, J. M., Cui, K., Qu, Y. W., Liang, P., and Zhong, R. C. (2020). Rare Earth elements deposits in China: Spatio-temporal distribution and ore-forming processes. *Chin. Sci. Bull.* 65, 3794–3808. (in Chinese with English abstract). doi:10.1360/TB-2020-0371

Xu, W. G., Fan, H. R., Hu, F. F., Santosh, M., Yang, K. F., Lan, T. G., et al. (2015). Geochronology of the guilaizhuang gold deposit, Luxi block, eastern North China craton: Constraints from zircon U-Pb and fluorite-calcite Sm-Nd dating. *Ore Geol. Rev.* 65, 390–399. doi:10.1016/j.oregeorev.2014.10.010

Xu, Y. G., Huang, X. L., Ma, J. L., Wang, Y. B., Iizuka, Y., Xu, J. F., et al. (2004). Crust–mantle interaction during the tectono-thermal reactivation of the north China craton: Constraints from SHRIMP zircon U-Pb chronology and geochemistry of mesozoic plutons from Western shandong. *Contrib. Mineral. Petrol.* 147, 750–767. doi:10.1007/s00410-004-0594-y

Xu, Z., Zhao, Z. F., and Zheng, Y. F. (2012). Slab-mantle interaction for thinning of cratonic lithospheric mantle in North China: Geochemical evidence from Cenozoic continental basalts in central Shandong. *Lithos* 146-147, 202–217. doi:10.1016/j.lithos.2012.05.019

Yan, G. H., Cai, J. H., Ren, K. X., Mu, B. L., Li, F. T., and Chu, Z. Y. (2008). Nd、Sr and Pb isotopic geochemistry of late-mesozoic alkaline-rich intrusions from the tanlu fault zone: Evidence of the magma source. *Acta Petrol. Sin.* 24 (6), 1223–1236. (in Chinese with English abstract).

Yang, C. X., and Santosh, M. (2020). Ancient deep roots for mesozoic world-class gold deposits in the north China craton: An integrated genetic perspective. *Geosci. Front.* 11, 203–214. doi:10.1016/j.gsf.2019.03.002

Yang, D. B., Xu, W. L., Pei, F. P., Yang, C. H., and Wang, Q. H. (2012a). Spatial extent of the influence of the deeply subducted South China Block on the southeastern North China Block: Constraints from Sr-Nd-Pb isotopes in Mesozoic mafic igneous rocks. *Lithos* 136-139, 246–260. doi:10.1016/j.lithos.2011.06.004

Yang, F., Santosh, M., Glorie, S., Jepson, G., Xue, F., and Kim, S. W. (2020). Meso-cenozoic multiple exhumation in the shandong peninsula, eastern North China craton: Implications for lithospheric destruction. *Lithos* 370, 105597. doi:10.1016/j.lithos.2020.105597

Yang, F., Santosh, M., and Kim, S. W. (2018b). Mesozoic magmatism in the eastern North China craton: Insights on tectonic cycles associated with progressive craton destruction. *Gondwana Res.* 60, 153–178. doi:10.1016/j.gr.2018.04.003

Yang, F., Santosh, M., and Tang, L. (2018a). Extensive crustal melting during craton destruction: Evidence from the mesozoic magmatic suite of junan, eastern North China craton. *J. Asian Earth Sci.* 157, 119–140. doi:10.1016/j.jseaes.2017.07.010

Yang, J. H., Wu, F. Y., Chung, S. L., Wilde, S. A., and Chu, M. F. (2006). A hybrid origin for the qianshan A-type granite, northeast China: Geochemical and Sr-Nd-Hf isotopic evidence. *Lithos* 89 (1-2), 89–106. doi:10.1016/j.lithos.2005.10.002

Yang, J. H., Wu, F. Y., Xie, L. W., and Liu, X. M. (2007). Petrogenesis and tectonic implications of kuangdonggou syenites in the liaodong peninsula, east north China craton: Constraints from *in-situ* zircon U-Pb ages and Hf isotopes. *Acta Petrol. Sin.* 23 (2), 263–276. (in Chinese).

Yang, J. H., Xu, L., Sun, J. F., Zeng, Q., Zhao, Y. N., Wang, H., et al. (2021). Geodynamics of decratonization and related magmatism and mineralization in the North China Craton. *Sci. China Earth Sci.* 64 (9), 1409–1427. doi:10.1007/s11430-020-9732-6

Yang, K. F., Fan, H. R., Santosh, M., Hu, F. F., and Wang, K. Y. (2011). Mesoproterozoic carbonatitic magmatism in the Bayan Obo deposit, Inner Mongolia, North China: Constraints for the mechanism of super accumulation of rare Earth elements. *Ore Geol. Rev.* 40 (1), 122–131. doi:10.1016/j.oregeorev.2011.05.008

Yang, K. F., Fan, H. R., Santosh, M., Hu, F. F., Wilde, S. A., Lan, T. G., et al. (2012b). Reactivation of the archean lowercrust: Implicationsfor zircon geochronology, elemental and Sr-Nd-Hf isotopic geochemistry of late mesozoic granitoids from northwestern jiaodong terrane, the north China craton. *Lithos* 146, 112–127. doi:10.1016/j.lithos.2012.04.035

Yang, X. Y., Sun, W. D., Zhang, Y. X., and Zheng, Y. F. (2009). Geochemical constraints on the Genesis of the bayan Obo Fe-Nb-REE deposit in inner Mongolia, China. *Geochim. Cosmochim. Acta* 73 (5), 1417–1435. doi:10.1016/j.gca.2008.12.003

Yang, Y. H., Zhang, H. F., Chu, Z. Y., Xie, L. W., and Wu, F. Y. (2010). Combined chemical separation of Lu, Hf, Rb, Sr, Sm and Nd from a single rock digest and precise and accurate isotope determinations of Lu-Hf, Rb-Sr and Sm-Nd isotope systems using Multi-Collector ICP-MS and TIMS. *Int. J. Mass Spectrom.* 290, 120–126. doi:10.1016/j.ijms.2009.12.011

Yu, X. F., Tang, H. S., and Li, D. P. (2014). Study on the mineralization of Chishan rare Earth element deposit related to alkaline rock, Shandong Province. *Acta Geol. Sin. - Engl. Ed.* 88 (2), 480–481. doi:10.1111/1755-6724.12373_31

Yu, X. F., Tang, H. S., Han, Z. Z., and Li, C. Y. (2010). Geological characteristics and origin of rare Earth elements deposits related with alkaline rock in the Chishan-Longbaoshan area, Shandong Province. *Acta Petrol. Sin.* 84 (3), 407–417. (in Chinese with English abstract).

Yuan, H. L., Gao, S., Liu, X. M., Li, H. M., Gunther, D., and Wu, F. Y. (2004). Accurate U-Pb age and trace element determinations of zircon by laser ablation-inductively coupled plasma-mass spectrometry. *Geostand. Geoanal. Res.* 28 (3), 353–370. doi:10.1111/j.1751-908X.2004.tb00755.x

Zeng, J. P., Lin, W., Qiu, H. B., Wei, W., Meng, L. T., Chu, Y., et al. (2022). When did the large-scale extensional tectonics begin in North China Craton? *Tectonophysics* 840, 229563. doi:10.1016/j.tecto.2022.229563

Zhai, M. G., and Santosh, M. (2011). The early precambrian odyssey of the north China craton: A synoptic overview. *Gondwana Res.* 20, 6–25. doi:10.1016/j.gr.2011.02.005

Zhai, M. G., Yang, J. H., Fan, H. R., Miao, L. C., and Li, Y. G. (2002). A large-scale cluster of gold deposits and metallogenesis in the eastern North China Craton. *Int. Geol. Rev.* 44 (5), 458–476. doi:10.2747/0020-6814.44.5.458

Zhang, B., Liu, S. F., Lin, C. F., Shen, W. J., and Li, X. Y. (2020). Reconstruction of the stress regime in the Jiaolai Basin, East Asian margin, as decoded from fault-slip analysis. *J. Struct. Geol.* 141 (2020), 104190–190. doi:10.1016/j.jsg.2020.104190

Zhang, H. F., Sun, M., Zhou, M. F., Fan, W. M., Zhou, X. H., and Zhai, M. G. (2004). Highly heterogeneous late mesozoic lithospheric mantle beneath the north China craton: Evidence from Sr-Nd-Pb isotopic systematics of mafic igneous rocks. *Geol. Mag.* 141 (1), 55–62. doi:10.1017/S0016756803008331

Zhang, H. F., Sun, M., Zhou, X. H., Fan, W. M., Zhai, M. G., and Yin, J. F. (2002). Mesozoic lithosphere destruction beneath the north China craton: Evidence from major-trace-element and Sr-Nd-Pb isotope studies of Fangcheng basalts. *Contrib. Mineral. Petrol.* 144, 241–254. doi:10.1007/s00410-002-0395-0

Zhang, H. F., Sun, M., Zhou, X. H., and Ying, J. F. (2005). Geochemical constraints on the origin of mesozoic alkaline intrusive complexes from the north China craton and tectonic implications. *Lithos* 81 (1-4), 297–317. doi:10.1016/j.lithos.2004.12.015

Zhang, H. F., Ying, J. F., Shimoda, G., Kita, N. T., Morishita, Y., Shao, J. A., et al. (2007a). Importance of melt circulation and crust-mantle interaction in the lithospheric evolution beneath the north China craton: Evidence from mesozoic basalt-borne clinopyroxene xenocrysts and pyroxenite xenoliths. *Lithos* 96, 67–89. doi:10.1016/j.lithos.2006.10.002

Zhang, H. F., Zhu, R. X., Santosh, M., Ying, J. F., Su, B. X., and Hu, Y. (2013). Episodic widespread magma underplating beneath the north China craton in the phanerozoic: Implications for craton destruction. *Gondwana Res.* 23, 95–107. doi:10.1016/j.gr.2011.12.006

Zhang, S. H., Zhao, Y., Davis, G. A., Ye, H., and Wu, F. (2014). Temporal and spatial variations of mesozoic magmatism and deformation in the north China craton: Implications for lithospheric thinning and decratonization. *Earth. Sci. Rev.* 131, 49–87. doi:10.1016/j.earscirev.2013.12.004

Zhang, X. M., Zhang, Y. Q., and Ji, W. (2007b). Fault distribution patterns of the Luxi Block, Shandong, and Mesozoic sedimentary-magmatic-structural evolution sequence. *J. Geomechanics* 13, 163–172. (in Chinese with English abstract).

Zhao, G. C., Sun, M., Wilde, S. A., and Li, S. Z. (2005). Late archean to paleoproterozoic evolution of the north China craton: Key issues revisited. *Precambrian Res.* 136, 177–202. doi:10.1016/j.precamres.2004.10.002

Zhao, G. C., Wilde, S. A., Cawood, P. A., and Sun, M. (2001). Archean blocks and their boundaries in the north China craton: Lithological, geochemical, structural and P-T path constraints and tectonic evolution. *Precambrian Res.* 107, 45–73. doi:10.1016/S0301-9268(00)00154-6

Zhao, G., and Zhai, M. (2013). Lithotectonic elements of precambrian basement in the north China craton: Review and tectonic implications. *Gondwana Res.* 23, 1207–1240. doi:10.1016/j.gr.2012.08.016

Zhao, J. X., Shiraishi, K., Ellis, D. J., and Sheraton, J. W. (1995). Geochemical and isotopic studies of syenites from the Yamato Mountains, East Antarctica: Implications for the origin of syenitic magmas. *Geochim. Cosmochim. Acta* 59, 1363–1382. doi:10.1016/0016-7037(95)00050-A

Zhao, Z. F., Liu, Z. B., and Chen, Q. (2017). Melting of subducted continental crust: Geochemical evidence from Mesozoic granitoids in the Dabie-Sulu orogenic belt, east-central China. *J. Asian Earth Sci.* 145, 260–277. doi:10.1016/j.jseaes.2017.03.038

Zheng, J. P. (2009). Comparison of mantle-derived matierals from different spatiotemporal settings: Implications for destructive and accretional processes of the north China craton. *Sci. Bull. (Beijing).* 54, 3397–3416. doi:10.1007/s11434-009-0308-y

Zheng, Y. F., Xu, Z., Zhao, Z. F., and Dai, L. Q. (2018). Mesozoic mafic magmatism in North China: Implications for thinning and destruction of cratonic lithosphere. *Sci. China Earth Sci.* 61, 353–385. doi:10.1007/s11430-017-9160-3

Zhu, R. X., Chen, L., Wu, F. Y., and Liu, J. L. (2011). Timing, scale and mechanism of the destruction of the North China Craton. *Sci. China Earth Sci.* 54, 789–797. doi:10.1007/s11430-011-4203-4

Zhu, R. X., and Xu, Y. G. (2019). The subduction of the west Pacific plate and the destruction of the North China Craton. *Sci. China Earth Sci.* 62, 1340–1350. doi:10.1007/s11430-018-9356-y

Zhu, R. X., Yang, J. H., and Wu, F. Y. (2012). Timing of destruction of the north China craton. *Lithos* 149, 51–60. doi:10.1016/j.lithos.2012.05.013

frontiers | Frontiers in Earth Science

TYPE Original Research
PUBLISHED 09 January 2023
DOI 10.3389/feart.2022.1031681

Check for updates

OPEN ACCESS

EDITED BY
Fan Yang,
Lanzhou University, China

REVIEWED BY
Hua-Wen Cao,
China Geological Survey, China
Xiaoqiang Zhu,
Anhui Normal University, China
Yi-Qu Xiong,
Central South University, China

*CORRESPONDENCE
Chang-Hao Xiao,
xiaochanghao1986@126.com

†These authors have contributed equally to this work and share first authorship

SPECIALTY SECTION
This article was submitted to Economic Geology,
a section of the journal
Frontiers in Earth Science

RECEIVED 30 August 2022
ACCEPTED 31 October 2022
PUBLISHED 09 January 2023

CITATION
Xiao C-H, Yu P-P, Liu X-H, Liu X-C, Tang Y-W, Wang W-L and Zhang Y (2023), Cassiterite U-Pb dating and micro-XRF analysis constraint on the formation of Xinlu Sn-Zn deposit, South China.
Front. Earth Sci. 10:1031681.
doi: 10.3389/feart.2022.1031681

COPYRIGHT
© 2023 Xiao, Yu, Liu, Liu, Tang, Wang and Zhang. This is an open-access article distributed under the terms of the Creative Commons Attribution License (CC BY). The use, distribution or reproduction in other forums is permitted, provided the original author(s) and the copyright owner(s) are credited and that the original publication in this journal is cited, in accordance with accepted academic practice. No use, distribution or reproduction is permitted which does not comply with these terms.

Cassiterite U-Pb dating and micro-XRF analysis constraint on the formation of Xinlu Sn-Zn deposit, South China

Chang-Hao Xiao [1,2*†], Ping-Ping Yu[1,2†], Xiao-Hu Liu[3], Xiang-Chong Liu[1,2], Yan-Wen Tang[4], Wen-Lei Wang[1,2] and Yu Zhang[5]

[1]Laboratory of Dynamic Diagenesis and Metallogenesis, Institute of Geomechanics, Chinese Academy of Geological Sciences, Beijing, China, [2]Key Laboratory of Paleomagnetism and Tectonic Reconstruction, Ministry of Natural Resources, Beijing, China, [3]College of Earth Sciences, Guilin University of Technology, Guilin, China, [4]Stake Key Laboratory of Ore Deposit Geochemistry, Institute of Geochemistry, Chinese Academy of Sciences, Guiyang, China, [5]School of Earth Sciences and Resources, China University of Geosciences, Beijing, China

This study presents rock slab and thin section reflection mapping, element mapping by Micro-XRF (μ-XRF) analysis, and *in situ* cassiterite U-Pb laser ablation-inductively coupled plasma mass spectrometer (LA-ICP-MS) ages of the Xinlu Sn-Zn deposit, Nanling Sn-W belt, South China. The new results provided constraints on the age and processes of Sn mineralization and thus further discussed the role of the Paleo-Pacific plate in the formation of Sn-W mineralization in the Nanling Sn-W belt. Based on mineralogy and μ-XRF analysis, four mineralization episodes are distinguished in the Baimianshan segment, Xinlu deposit, including 1) prograde skarn stage characterized by the mineral assemblages of garnet, pyroxene, marble, hornfels; 2) retrograde skarn-sulfide composed of massive pyrrhotite, sphalerite with parts of epidote, cassiterite; 3) quartz sulfide vein stage consisting of arsenopyrite, pyrite, quartz, and 4) barren calcite crosscutting the former episodes. The time of retrograde skarn-sulfide mineralization is dated by LA-ICP-MS cassiterite U-Pb at 168.7 ± 1.3 Ma. These U-Pb ages, combined with previous geochronological studies, support one Sn mineralization event associated with the 159.5–168.7 Ma magmatism in the Guposhan-Huashan district. The Xinlu Sn-Zn mineralization and the Middle-Late Jurassic Sn-W mineralization in the Nanling belt, South China is genetically related to asthenospheric upwelling and crust-mantle interaction caused by the subduction of the Paleo-Pacific plate. Our results demonstrate that thin section reflection and μ-XRF element mapping are powerful tools for determining paragenesis in ore deposits and are highly effective to guide the selection of analytical positions for cassiterite U-Pb dating. This method may also be applicable to *in-situ* geochronology of other minerals.

KEYWORDS

micro-XRF, Xinlu deposit, Nanling Sn-W belt, South China, Paleo-Pacific, cassiterite U-Pb geochronology

Introduction

The Nanling Sn-W belt is a world-class Sn and W province within the South China Block (SCB) (Figures 1A,B; Mao et al., 2021b). Most tungsten and tin deposits are related to the late Jurassic felsic rocks (Xiao et al., 2019; Mao et al., 2021a). The spatial distribution of these rocks displays a southeastward younging trend (Figure 1C), which was interpreted to be related to the flat-slab subduction of the Paleo-Pacific Ocean plate (Figure 1D; Li and Li, 2007; Yang et al., 2020). In contrast, the Sn-W mineralization in this region does not display a similar age pattern. The ore-forming ages of most of large-scale W and Sn deposits in the Nanling Sn-W belt concentrated in 160–150 Ma. Therefore, whether the Paleo-Pacific plate contributed to the formation of Sn-W mineralization is equivocal.

Cassiterite U-Pb dating has proved to be a robust method to precisely and directly date the tin mineralization of W-Sn deposits (Yuan et al., 2008; Zhang et al., 2015; Xiao et al., 2022). Most published cassiterite U-Pb dating required mineral separation and grain mounts. A major drawback of these two methods is that they may mix polygenetic populations of cassiterite. Hence, the rapid identification of cassiterite on the hand specimen or thin section before the cassiterite U-Pb dating is quite essential. Micro-XRF analyses are a powerful and non-destructive technique to determine the trace elements in the geological samples, and to identify the minerals and their contents (Flude et al., 2017; Wang et al., 2022).

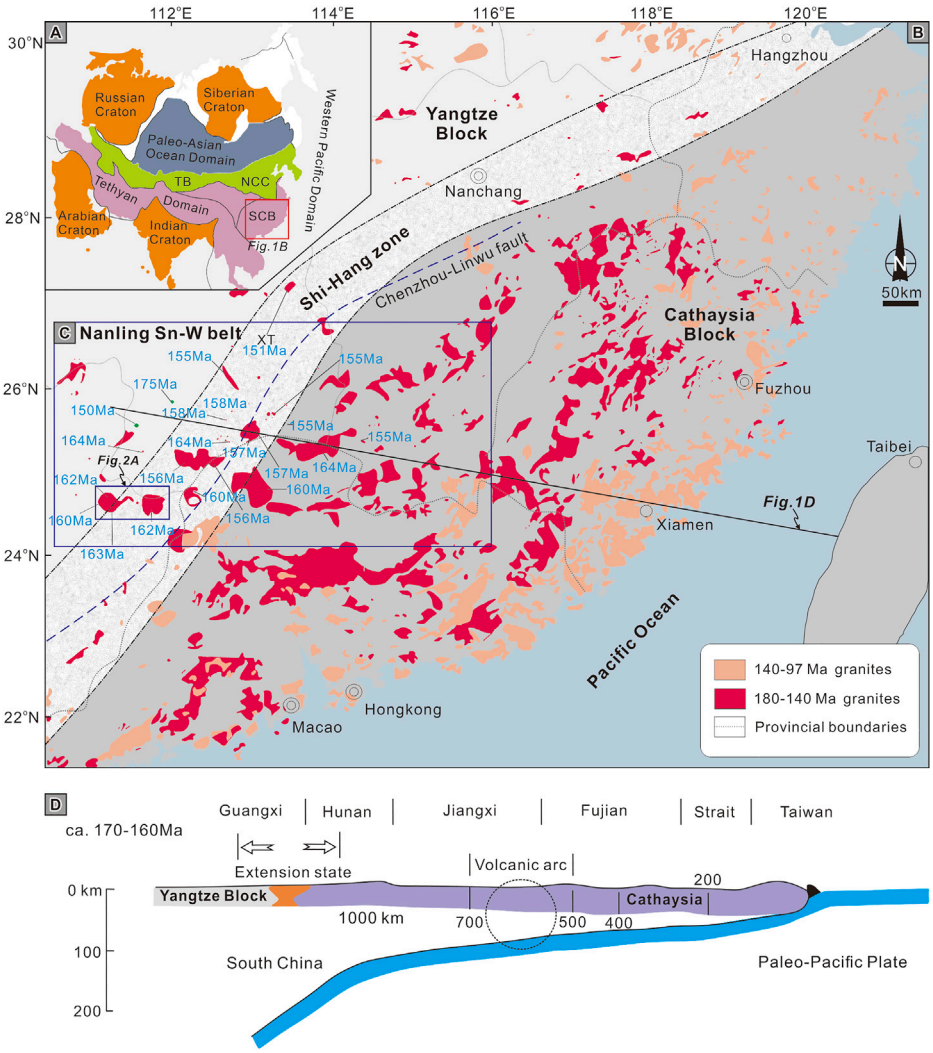


FIGURE 1
(A) Tectonic map of Asia showing continental blocks and bounding sutures (modified after Cawood et al., 2018). **(B)** Distribution of the Jurassic-Early Cretaceous intrusions in South China (modified after Xiao et al., 2019 and references therein). **(C)** Sketch map of the Nanling Sn-W belt (Mao et al., 2021a). **(D)** Simplified map showing the Middle-Late Jurassic Paleo-Pacific subduction in southeast China (Zhou and Li, 2000).

Above all, the μ-XRF analyses have great potential to guide the selection of analytical spots for cassiterite U-Pb dating.

The Guposhan-Huashan Sn-W district is one of the most important districts in the western of the Nanling Sn-W belt (Figure 1C). The Sn-W deposits in this district (e.g., Xinlu Sn-Zn deposit, Shuiyanba Sn deposit, Keda Sn deposit, Huashan Sn deposit, and Shanhu W-Sn deposit) are located at the contact zone of the Guposhan-Huashan granite pluton and its vicinity (Figures 1C, 2A; Feng et al., 2019; Gu et al., 2007a, b; Kang et al., 2012; Li et al., 2016; Xiao et al., 2011; Zhang et al., 2020; Zhao et al., 2010). Considerable uncertainty and controversy remains regarding the exact timing of W-Sn mineralization. For example, some studies revealed that no direct genetic link between Sn-W mineralization in the Xinlu deposit and the Guposhan pluton based on whole-rock K-Ar ages and fluid inclusion Rb-Sr ages of the ores (Dong, 1991; Zhu et al., 2006; Gu et al., 2007a). Many researchers have demonstrated that W-Sn mineralization was related to the Guposhan pluton based on zircon U-Pb, molybdenite Re-Os, and muscovite/biotite Ar-Ar dating results in the Xinlu deposit (Kang et al., 2012; Li et al., 2016; Feng et al., 2019). Besides, molybdenite, with Re-Os ages representing the ore-forming ages, is not a major mineral in the Xinlu deposit, and most other tested minerals could not be directly dated for ore-forming ages (Feng et al., 2019). Thirdly, the skarn Sn-Zn mineralization with great economic values lacks investigation compared to the abundant studies on the quartz vein type Sn-W mineralization. All these lead to the ambiguous timing of the tin mineralization in the Guposhan-Huashan Sn-W district.

In this contribution, we applied microscopic observation and μ-XRF analysis to determine the paragenetic sequence and cassiterite occurrence in the Xinlu deposit. We performed laser ablation-inductively coupled plasma-mass spectrometry (LA-ICP-MS) U-Pb dating of cassiterite to directly date tin mineralization. From our new cassiterite U-Pb age, and previously published cassiterite U-Pb ages, we refined the spatial and temporal distribution of Sn-W mineralization and discussed the role of the Paleo-Pacific plate in the formation of Sn-W mineralization in the Nanling Sn-W belt.

Geological setting

Regional geology

The South China Block is composed of the Yangtze Block in the northwest and the Cathaysia Block in the southeast (Figure 1B). These two blocks were welded along the "Shi-Hang zone" during the Early Neoproterozoic, which was a tectonic-granitoid belt (Figure 1B; Gilder et al., 1996). The SCB subsequently underwent the Early Paleozoic NS shortening intraplate tectono-magmatism (Shu et al., 2021), the Triassic intraplate orogeny (Li et al., 2022), and the Late Mesozoic tectonic transformation (Shu, 2012). Large-scale Sn-W mineralization events occurred during the Mesozoic in the eastern SCB. Numerous studies have demonstrated that the subduction of the Paleo-Pacific plate was responsible for producing large-scale magmatism and Sn-W mineralization (Li and Li, 2007; Mao et al., 2021a, b; Zhou and Li, 2000).

The Nanling Sn-W belt locates in the central south of the SCB. In this belt, there are intensive folded and deformed basement, magmatic rocks, and rifting basins (Zhang et al., 2015). The basement is composed of a metamorphosed Neoproterozoic-Ordovician flysch-volcanic series, covered by unmetamorphosed Late Devonian to Early Triassic sedimentary rocks. Five episodic magmatism events (Neoproterozoic, Silurian, Permian, Triassic, Jurassic, and Cretaceous) occurred in this belt (Zhang et al., 2015). Previous studies indicate that W and Sn mineralization occurred in the belt in the Neoproterozoic and Mesozoic (Figure 1C; Hu and Zhou, 2012), of which the latter is economically more important.

This study focuses on the Guposhan-Huashan W-Sn district in the western of the Nanling Sn-W belt, which is located in the eastern of the Guangxi Zhuang Autonomous Region (GZAR). The study area mainly consists of semipelagic flysch sedimentary rocks and subsequently underwent the Early Paleozoic intraplate orogeny. Scattered Mo-W, Pb-Zn, and Au mineralization associated with this orogeny are represented by the Baishiding, Zhanggongling, and Longshui deposits in the eastern of the district (Figure 2A; Li et al., 2016). From Early Devonian to Jurassic, carbonate platforms with sporadic clastic rocks formed in this area under a shore-shallow sea-slope setting (Shu, 2012). The Jurassic clastic rocks, formed in a graben basin, unconformably overly the Paleozoic rocks (Figure 2A). Large-scale magmatism and associated Sn-W mineralization occurred in response to the subduction of the Pacific plate in the Middle-Late Jurassic and Cretaceous (Figure 2A; Feng et al., 2019; Gu et al., 2007a; Gu et al., 2007b; Kang et al., 2012; Li et al., 2016; Xiao et al., 2011; Zhang et al., 2020; Zhao et al., 2010). The Quaternary system hosts alluvial tin, which is widely distributed in the south of the district. Folds and faults are widely developed in this district.

Ore deposit geology

The Xinlu Sn-Zn deposit is located at the south contact zone of the Guposhan granite pluton and its vicinity. It consists of the Shihuichong Sn-Fe, Xinlu Sn-Zn, Liuheao Sn, Muqiaomian Sn-Zn, Baimianshan Sn-Zn, and Shimen Sn-Zn segments from north to south (Figure 2B). The main sedimentary rocks in the deposit are composed of middle Devonian Xindu Formation (D_2x) and Yujiang Formation (D_2y) clastic rocks, Donggangling Formation (D_2d) carbonate rocks, upper Devonian Guilin (D_3g) and Rongxian (D_3r) formations, and

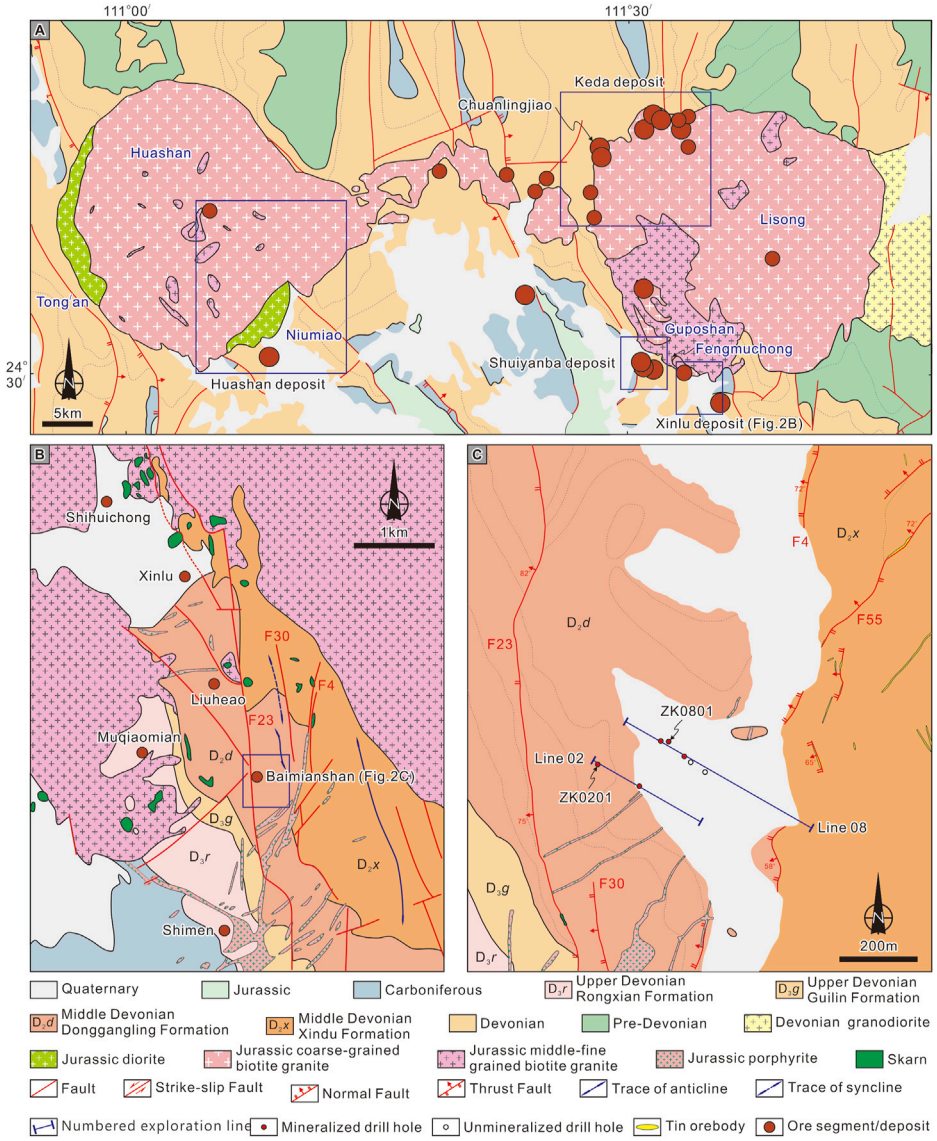


FIGURE 2
(A) Geological map of Guposhan-Huashan Sn-W district (modified after Geological Prospecting Institute of Guangxi (GPIG), 2021). **(B)** Geological map of Xinlu Sn-Zn deposit (modified after Feng et al., 2019). **(C)** Geological map of Baimianshan Zn-Sn segment (modified after GPIG, 2021).

Lower Carboniferous carbonate rocks. The NNW-, NW-, NE-, and EW-striking faults are widely developed in the deposit. The NNW-striking faults control the distribution of major ore segments in the deposit (Figure 2B). The dextral EW-striking faults crosscut the NNW-, and NW-striking faults. The NNW-striking faults plunge to the directions of 260°–290° at dip angles of 58°–85°. Most of the NE-striking faults plunge in the directions of 330°–340° at angles of 72°–85°. Fault-parallel folds are developed in the southeastern of the deposit. The Guposhan granite is distributed in the northern half of the deposit. Minor intermediate-felsic dykes are distributed along or crosscut the NE-, and NW-striking faults in the southern part of the deposit. Minor skarn and fault-controlled oxidized orebodies crop out on the surface in the deposit (Figure 2C).

The Baimianshan Sn-Zn segment is controlled by the NNW-striking normal faults (F_{23}) and is located in the middle of the Xinlu deposit (Figures 2B,C). The carbonate rocks of the Donggangling Formation and clastic rocks of the Xindu Formation are distributed on the east and west sides of the segments, respectively. The Devonian system developed in the west limb of the Kejiashan anticline and the stratum dipped SWW at 12°–30° (Hu et al., 1992). The Quaternary sediments

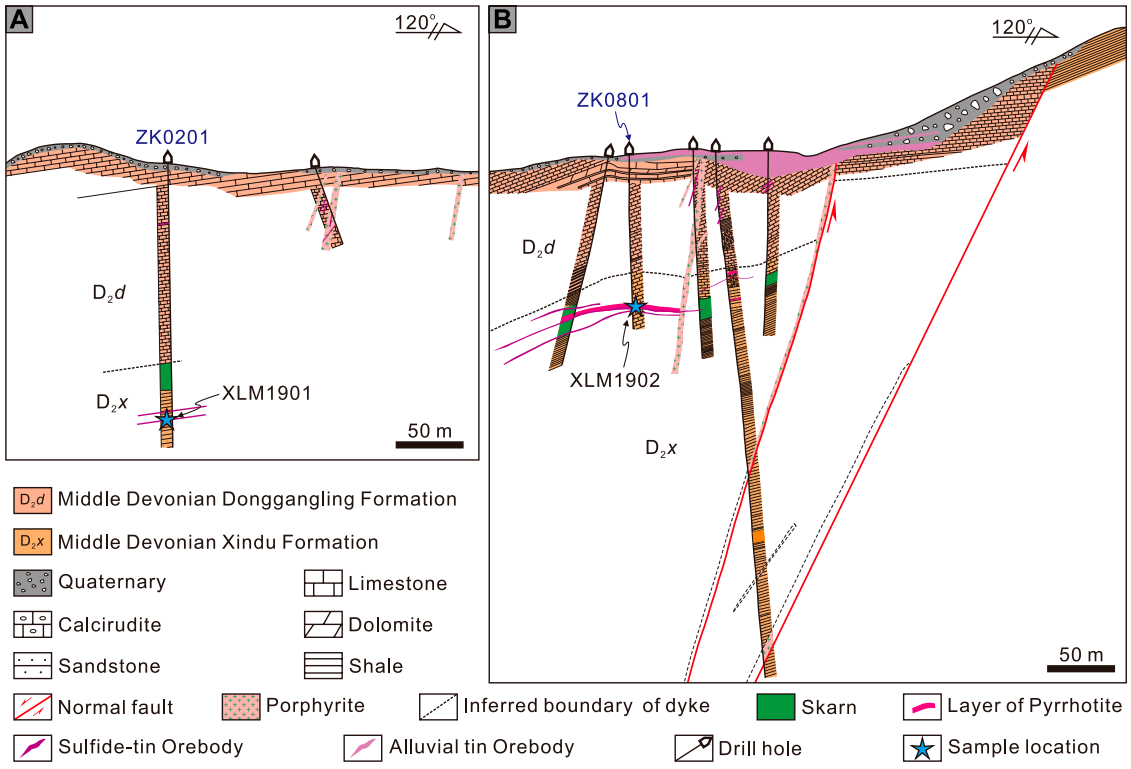


FIGURE 3
Geological cross-section along the No. 2 exploration line **(A)** and No. 8 exploration line **(B)** in the Baimianshan segment (modified after GPIG, 2021).

unconformably overly the Devonian in the middle of the segment. The NS-striking F_{23} and F_4 normal faults vertical cross throughout the segment. Previous studies revealed that these NS-striking faults underwent nearly E–W compression following an E–W extension (Ou, 1989). The main NE-trending concealed orebody was formed between these two faults. Parts of oxidized orebodies were formed along the NE-, and small NS-striking faults in the eastern of the segment. Most of the NE-striking faults are normal faults except for the F_{55} fault. A few of NS-, and NE-striking dykes spread in the south of the segment. The alteration is not developed on the surface, and it includes silicification, potassic alteration, and sericitization. Some small skarn is found in the F_{23} fault. The orebodies are mainly buried underground with insignificant oxidized ore exposed on the surface.

Sampling and analytical methods

The hand specimens in this study were collected from drill cores ZK0201 and ZK0801 from two of the new holes of the Baimianshan segment in 2019 (Figures 3, 4). The two drill cores have ferrous-sphalerite-cassiterite sulfide orebodies at the lithological contacts in the upper of the Xindu Formation (D_2x) with a small number of sulfide orebodies in the Donggangling Formation (D_2d) limestone. Two types of ores including XLM1901 and XLM1902 were sampled. Sample XLM1901 is massive ferrous sphalerite-cassiterite-arsenopyrite sulfide that was formed in the Donggangling Formation limestone at 49.64 m of drill hole ZK0201. The Sn and Zn ore grades of XLM1901 are 0.31% and 8.65%, respectively. Sample XLM1902 is a layer-parallel skarn cassiterite sulfide orebody that was formed in the upper part of the Xindu Formation at 133 m of drill hole ZK0801 with 2.46% Sn and 2.04% Zn. The ore was formed in the contacts between pellet marlstone and argillaceous siltstone. We carried out observation on 10 hand specimens, micro-observation, reflection mapping, and μ-XRF analysis on 2 representative polished slabs and 1 polished thin section, and cathodoluminescence (CL) imaging of targeted cassiterite grains, and LA-ICP-MS dating to obtain detailed paragenesis and cassiterite U-Pb ages of the Baimianshan segment, Xinlu deposit.



FIGURE 4
Photographs of representative ore and rocks within the Baimianshan Zn-Sn segment. **(A)** Core from drill hole ZK0801. **(B)** Massive garnet and marble were crosscut by steep-dipping calcite veins. **(C)** Steep-dipping branching veins or veinlets and layer-parallel massive ores overly on the layer-parallel marble and hornfels. **(D)** Steep-dipping pyrite-quartz-calcite veins crosscut the marble. **(E)** The arsenopyrite replaced the massive pyrrhotite-chalcopyrite-sphalerite and both were crosscut by the pyrite-quartz-calcite veins. **(F)** Massive pyrrhotite-chalcopyrite-sphalerite ore.

Thin section reflection mapping and element mapping by μ-XRF

Sample XLM1901 is a 6.5*6.5 cm^2 half drill core piece and XLM1902 is a cylindrical rock chip of 6.8 cm in diameter and 1.6 cm in height. The analytical areas included the whole surface of the polished slabs and thin sections for petrographic observations and element mapping. Polished sections and slabs were examined using transmitted and reflected optical microscopes (DM4500P, Leica, Germany). Reflection mapping of the whole polished slabs on the microscope was completed by manual splicing through Image Analysis System software (Figures 5A,B). The μ-XRF analyses on rock slabs and thin sections were performed on the benchtop M4 Tornado (Bruker, Germany) under vacuum conditions (20 mbar, 50 kV, 200 μA) with a diameter of 20 μm X-ray beam with 40 μm pixel size. Element mapping scanning and sample navigation on the benchtop M4 were run by a motorized stage that moves the sample beneath the static X-ray beam. Data were collected for Fe, Zn, W, Ga, Ge, As, Pb, Bi, Sn, Cu, W, Si, Al, Ca, and S (Figures 6–8). The analytical procedures of element mapping were described in detail by Flude et al. (2017) and Wang et al. (2022). These analyses were conducted at the Laboratory of Dynamic Diagenesis and Metallogenesis, Institute of Geomechanics, Chinese Academy of Geological Science (LDDM-IGM, CAGS). All data acquisition and processing were carried out using the proprietary Bruker software supplied with the instrument.

Cassiterite U-Pb dating and cathodoluminescence imaging

Based on the microscopic observation and μ-XRF analysis, we mixed the two samples to separate cassiterite grains at the LDDM-IGM, CAGS. And then, the cassiterite was mounted on epoxy resin discs. Cassiterite grains were observed under the microscope, and CL and BSE images were obtained to characterize the texture of cassiterite and avoid cracks and mineral/fluid inclusions before U–Pb dating. Selected cassiterite domains without any obvious mineral inclusion were analyzed for U-Pb ages using the Agilent 7900 LA-ICP-MS at the Stake Key Laboratory of Ore Deposit Geochemistry, Institute of Geochemistry, Chinese Academy of Sciences. Cassiterite grains have a core-rim microstructure, and

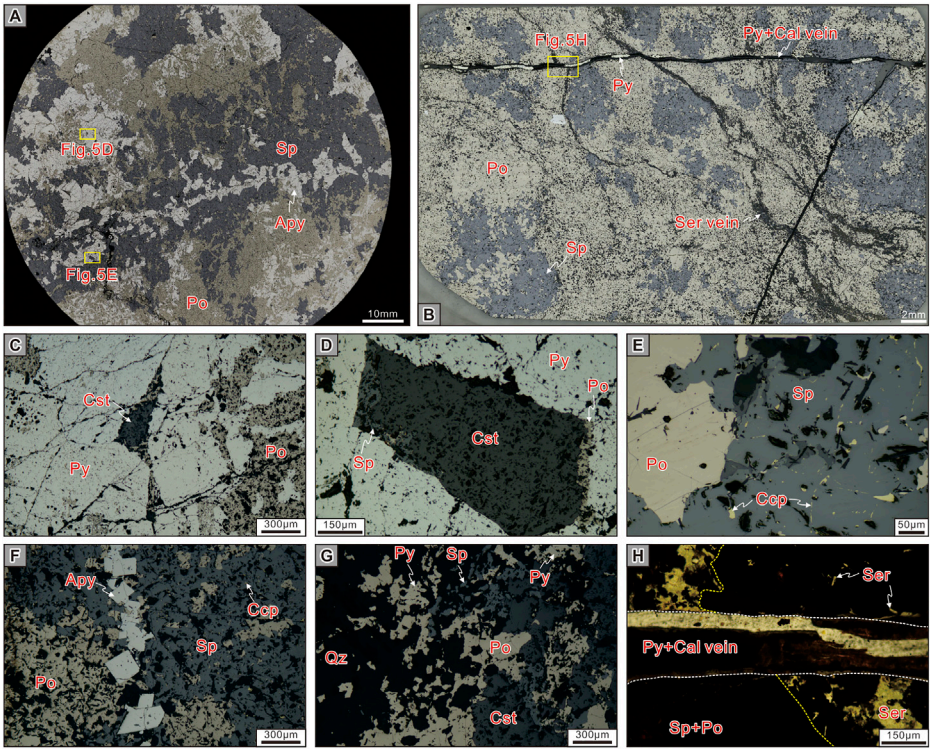


FIGURE 5
Representative textures and mineral assemblages within ores and wall rocks of Baimianshan Zn-Sn segment. **(A)** The reflected mapping of polished slab of XLM1902. **(B)** The reflected mapping of thin section XLM1901T showing the pyrite vein replaced the massive pyrrhotite-sphalerite. **(C–D)** Cassiterite coexisted with arsenian pyrite and replaced by the pyrrhotite, sphalerite. **(E)** The pyrrhotite laths and lamellae, chalcopyrite blebs intergrew with sphalerite and pyrrhotite. **(F)** The euhedral arsenopyrite quartz veinlet crosscut the pyrrhotite and sphalerite. **(G)** The pyrite quartz replaced the sphalerite and pyrrhotite. **(H)** The pyrite-calcite vein cut the massive pyrrhotite and sphalerite which were replaced sericite.

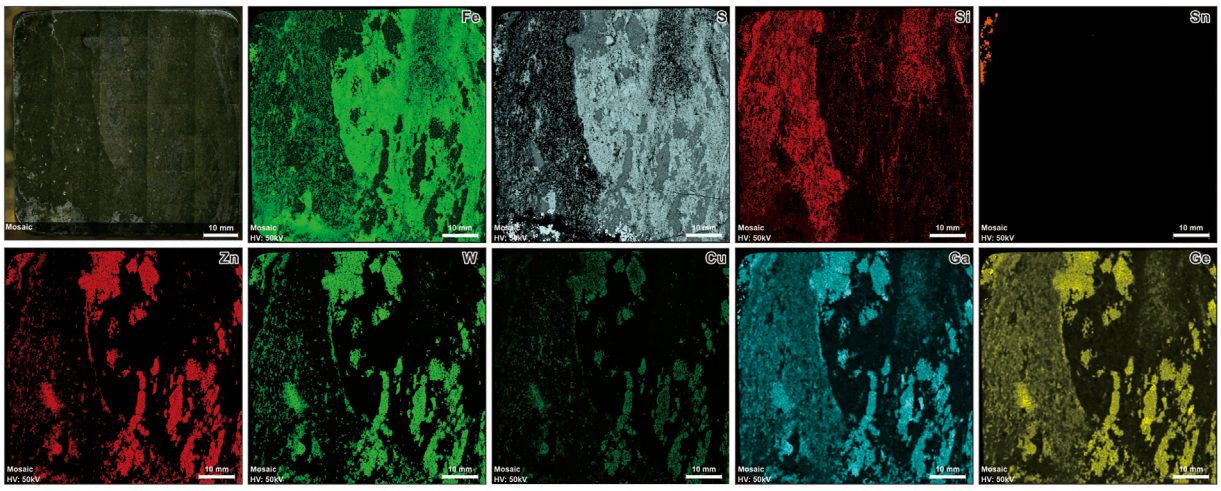


FIGURE 6
Photograph and corresponding μ-XRF single-element maps (Fe, S, Si, Sn, Zn, W, Cu, Ga, Ge) of rock slab XLM1901.

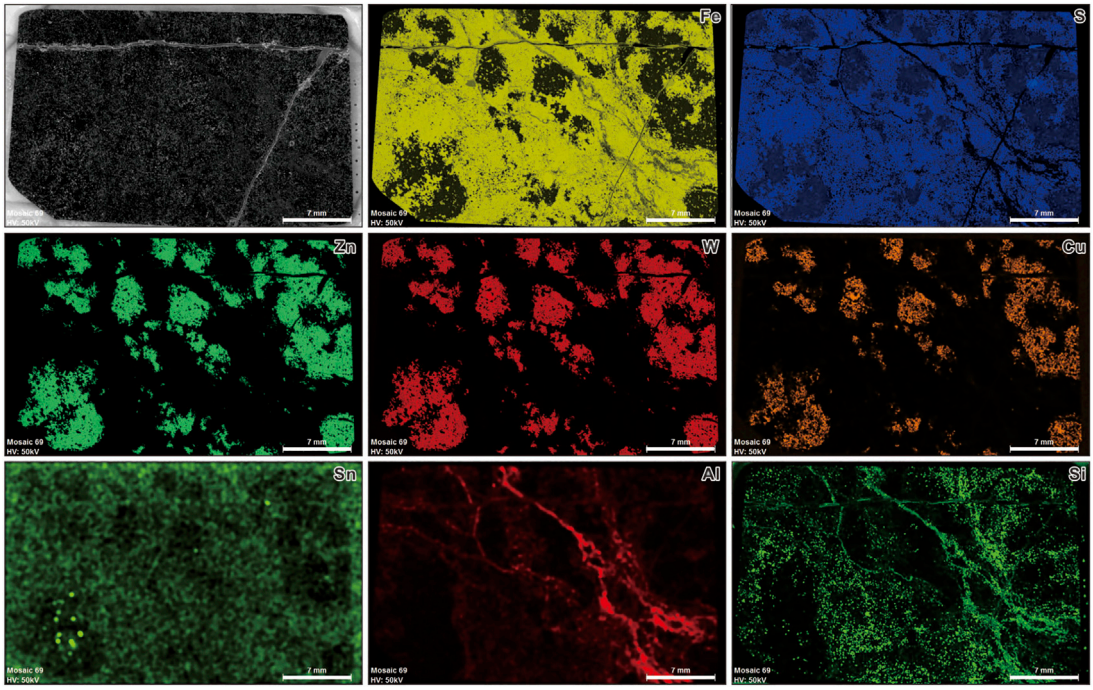


FIGURE 7
Photograph and single-element μ-XRF maps (Fe, S, Zn, W, Cu, Sn, Al, Si) of thin section XLM1901T.

thirty spots including 17 fully-dark cores and 13 gray oscillatory rims were analyzed. The reference materials used were AY-4 cassiterite for $^{206}Pb/^{238}U$ ratios (ID-TIMS U-Pb age of 158.2 ± 0.4 Ma; Yuan et al., 2008) and NIST SRM 612 for U, Th, and Pb concentrations of cassiterite.

Cassiterite grains were analyzed using LA-ICP-MS with a laser energy density of 5 J/cm^2, a spot size of 60 μm, and a repetition rate of 6 Hz. NIST SRM 612 was analyzed twice and AY-4 was analyzed three times for every ten analyses of the unknown cassiterite grains. Each spot analysis incorporated a background signal acquisition of approximately 20 s followed by 35 s of sample data acquisition. Other conditions were listed by Tang et al. (2022). The uncertainty of the single population, ratio uncertainty of the AY-4 reference material, and decay constant uncertainties were propagated to the final results during the process of offline raw data reduction by ICPMSDataCal (Liu et al., 2008). Data errors for isotopic ratios in the cassiterite samples are 1σ. Isoplot 3.0 was used to calculate the U–Pb ages and draw Concordia diagrams (Ludwig, 2003).

Results

Mineralogy and paragenesis

According to the field observation, the Baimianshan segment is similar to most Zn skarn deposits which occur distal from the causative pluton (Meinert et al., 2005). Most ores on drilling cores are present as massive with minor skarn minerals or hosted by veins and veinlets with skarn alteration halos (Figure 4). Based on microscopic observations, the mineralization process of the Baimianshan segment could be divided into prograde skarn (stage I), retrograde skarn-sulfide (stage II), quartz sulfide veins (stage III), and barren carbonate (stage IV) stages. The prograde stage is characterized by the mineral assemblages of garnet, pyroxene, marble, and hornfels (Figure 4B). The prograde stage is zoned, and the zoning pattern is thick hornfels with parts of pyroxene-bearing pale-brown garnet, banded skarn, marbleization-limestone from the deep to shallow (Figures 3, 4A). The retrograde skarn-sulfide stage is the main mineralization stage. This stage is associated with the formation of steep-dipping branching veins or veinlets and layer-parallel massive ores with dominated ore minerals such as massive pyrrhotite, sphalerite with parts of epidote, cassiterite, arsenian pyrite, and minor chalcopyrite. The euhedral coarse cassiterite (100–700 μm) is followed by pyrrhotite, and then sphalerite base metal sulfides in this stage (Figures 5C,D). The pyrrhotite laths and lamellae, and chalcopyrite blebs intergrew with sphalerite (Figure 5E). The quartz sulfide veins stage is associated with the formation of middle- and steep-dipping veins with the mineral assemblage of arsenopyrite, pyrite, quartz, sericite, and small amounts of chlorite. This stage could be divided into two sub-stages. Anhedral pyrite, euhedral coarse

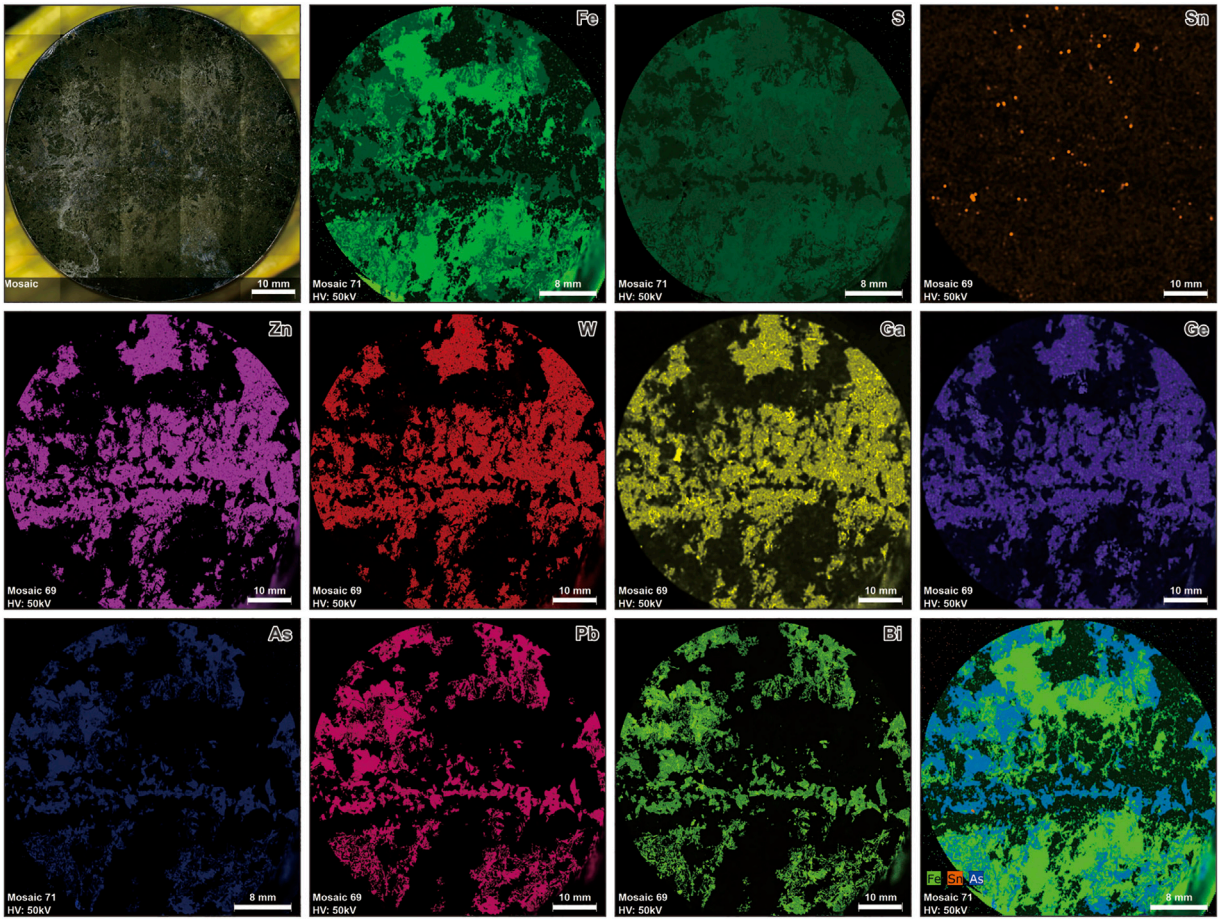


FIGURE 8
Photograph, single-element μ-XRF maps (Fe, S, Sn, Zn, W, Ga, Ge, As, Pb, Bi) and multi-element map of rock slab XLM1902.

arsenopyrite, and fine quartz, sericite of sub-stage I intensively replaced the cassiterite, pyrrhotite, and sphalerite of stage II (Figures 5G,H, 7). The euhedral arsenopyrite-quartz veinlets of sub-stage ii crosscut the veins of sub-stage I (Figure 5F). Steep-dipping barren pyrite-calcite veins (stage IV) crosscut the former veins (Figures 4B,D, 5A,H).

Element mapping

Two polished slabs (XLM1901 and XLM1902) and one thin section (XLM1901T) were measured and elemental distribution maps were obtained. Each map was compared to a reflected light image that came from a section close to the one data was collected from (Figures 6–8).

Figure 6 shows the Fe, S, Si, Sn, Zn, W, Cu, Ga, and Ge distributions compared to the hand specimen of XLM1901. Copper, W, Ga, and Ge show an intensive positive correlation with Zn. Copper could be proved by chalcopyrite blebs coexisting with sphalerite (Figure 5E). Tungsten mineral is not found in this study. Gallium and Ge are thought to be substituted with Zn in sphalerite. Tin distributed in the top-left corner corresponds to the position of cassiterite. The distribution of Fe with help of S could identify different iron-bearing minerals (pyrrhotite and pyrite) and could determine the paragenetic sequence that pyrite replaced pyrrhotite and sphalerite at the left-bottom of the sample.

Figure 7 shows the Fe, S, Zn, W, Cu, Sn, Al, and Si distributions compared to the hand specimen and reflected light image of XLM1901T. The observed depositional sequences are pyrrhotite + sphalerite + epidote followed by quartz + potassium feldspar + arsenopyrite and pyrite + quartz + calcite veinlet. Some disseminated Sn is distributed in the sphalerite aggregation. The distribution characteristics of other elements are similar to those of the XLM1901.

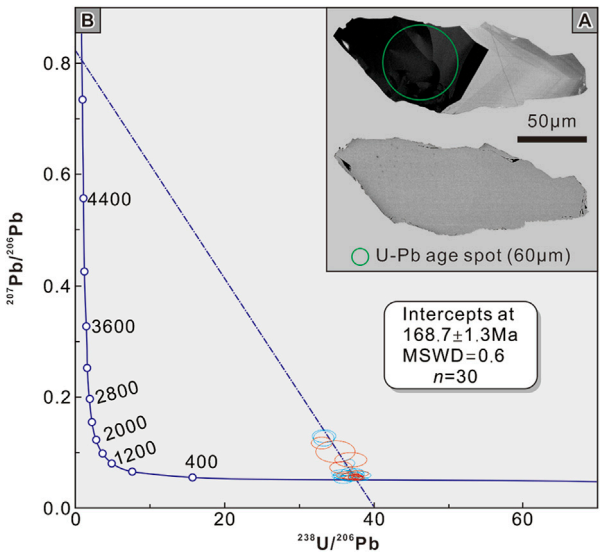


FIGURE 9
(A) Representative CL and BSE images of cassiterite crystals and **(B)** U–Pb Concordia plot for cassiterite from the Baimianshan segment, Xinlu Sn-Zn deposit. The red and blue plots are the data from the rim and core of cassiterite, respectively.

Figure 8 shows single-element distributions of 9 elements (Fe, S, Sn, Zn, W, Pb, Bi, Ga, and Ge), a multi-element map with Fe, Sn, and As, and phases based on multi-element Fe-Zn-As compared to the hand specimen and reflected light image of XLM1902. The distribution characteristics of most elements (Fe, S, Sn, Zn, W, Ga, and Ge) are similar to those of the XLM1901 and XLM1901T. This sample has obvious high counts of As, Pb, and Bi. The high content of As corresponds to the position of arsenopyrite on the reflected light image (Figure 5A), whereas no lead and bismuth minerals were found in this sample. Multi-element maps with Fe, Sn, and As, and phases based on multi-element Fe-Zn-As also clearly reveal the paragenetic sequences of stages II and III.

Cassiterite U-Pb ages

The cassiterite grains are dark brown to black, generally euhedral to subhedral with a size of 100–700 μm. Internal textures of cassiterite are solid dark cores with oscillatory rims. Some cassiterite grains have cracks and are porous with tiny metallic inclusions as revealed by the CL and BSE images (Figure 9A).

The analytical results of U–Pb isotopes of the cassiterite grains are listed in Table 1 and illustrated in Figure 9B. These grains have relatively low total Pb contents of <0.1 ppm, low Th contents of <0.01 ppm, and U contents varying from 0.31 to 2.85 ppm. The analyzed dark cores have higher U concentrations (1.01–2.85 ppm, 1.77 ppm average) than the oscillatory rims (0.31–1.63 ppm, 0.82 ppm average). The plots of 17 cores and 13 rims define a good Concordia line with a lower intercept at 168.7 ± 1.3 Ma (1σ; MSWD = 0.6; n = 30) (Figure 9B).

Discussion

Application of thin section reflection and element mapping

Our results demonstrate the reflection mapping and μ-XRF element mapping on thin section and hand specimens together with detailed petrographic paragenesis in ore deposits can guide the selection of analytical spots for cassiterite U-Pb dating, which would enhance the study of ore formation processes.

Reflection and element mapping of representative samples could provide compositional and mineralogical information across a range of scales. This work is summarized as follows. First, the element mapping could easily distinguish different iron-bearing or sulfur-bearing minerals [such as pyrrhotite (Fe: 63.53%, S: 36.47%), pyrite (Fe: 46.55%, S: 53.45%), arsenopyrite (Fe: 34.3%, S:19.69%), and sphalerite (Fe: <10%, S: 32.9%)] owing to the differences in theoretical composition. The color intensity of Fe-mineral gradually decreases from pyrrhotite, pyrite, arsenopyrite, and sphalerite (Figures 6–8). At the bottom of Figure 6, the light green parts overlap and crosscut the bright green parts, suggesting that the pyrite was formed later than pyrrhotite. In Figure 8, it is obvious that the light green areas overlap and crosscut the bright green and black areas. This is consistent with the microscopic observation that arsenopyrite replaced pyrrhotite and sphalerite. The color intensity of S gradually decreases from pyrite, pyrrhotite, sphalerite, and arsenopyrite (Figures 6–8). The distribution of Fe and S elements can accurately determine the sequence of mineral formation in the Xinlu deposit. Second, element mapping could provide some information on mineralization that cannot be observed under a microscope. The multi-elements distribution shows that W is positively related to Zn (Figure 8). However, no tungsten mineral (such as sanmartinite) was recognized, implying that the ore-forming fluid was rich in tungsten as supported by the quartz vein type tungsten mineralization after the skarn mineralization in the Xinlu deposit (Gu et al., 2007a; Li S. Z. et al., 2012). In the quartz sulfide veins stage, As, Pb, and Bi show a positive correlation and correspond to the position of arsenopyrite (Figures 6–8). Bismuth-lead sulfosalts may be a reasonable explanation. Bismuth-lead sulfosalt is common in the late stage of tin deposits and well documented in the Sn-sulfide-sulfosalts deposits of the Bolivia Sn province

TABLE 1 LA-ICP-MS U-Pb dating results of cassiterite from the Baimianshan segment, Xinlu Sn-Zn deposit, South China.

Analysis spots		U-Th-Pb contents			U–Pb isotopic ratios					
		^{238}U	^{232}Th	Common Pb	$^{207}Pb/^{206}Pb$	1σ	$^{207}Pb/^{235U}$	1σ	$^{206}Pb/^{238}U$	1σ
XLM from the Baimianshan segment, Xinlu Sn-Zn deposit, South China										
Core	XLM01	1.86	0.00	0.01	0.05703	0.00353	0.21094	0.01273	0.02713	0.00070
	XLM02	1.01	0.00	0.04	0.11751	0.00687	0.48280	0.02807	0.03032	0.00084
	XLM03	1.40	0.00	0.05	0.06371	0.00387	0.24246	0.01479	0.02792	0.00079
	XLM04	1.02	0.00	0.01	0.05935	0.00420	0.22082	0.01569	0.02742	0.00078
	XLM09	2.85	0.00	0.04	0.05236	0.00251	0.18823	0.00890	0.02640	0.00068
	XLM10	2.10	0.00	0.00	0.06203	0.00309	0.22339	0.01127	0.02639	0.00068
	XLM11	1.91	0.00	0.02	0.05784	0.00413	0.20748	0.01435	0.02692	0.00075
	XLM12	1.99	0.00	0.05	0.05423	0.00319	0.19918	0.01220	0.02711	0.00081
	XLM13	1.27	0.00	0.00	0.05670	0.00317	0.20845	0.01188	0.02762	0.00095
	XLM14	1.82	0.00	0.03	0.05473	0.00289	0.19620	0.00997	0.02676	0.00068
	XLM17	1.63	0.00	0.04	0.06507	0.00371	0.23344	0.01210	0.02664	0.00052
	XLM18	1.29	0.00	0.00	0.06184	0.00389	0.22389	0.01404	0.02648	0.00046
	XLM19	1.95	0.00	0.01	0.05530	0.00301	0.20043	0.01061	0.02666	0.00046
	XLM20	2.53	0.00	0.02	0.05379	0.00213	0.19805	0.00855	0.02651	0.00042
	XLM24	1.51	0.00	0.01	0.05982	0.00344	0.21782	0.01228	0.02663	0.00042
	XLM25	1.98	0.00	0.03	0.05588	0.00289	0.20491	0.01034	0.02687	0.00033
	XLM27	1.93	0.00	0.02	0.05662	0.00256	0.20861	0.00968	0.02669	0.00033
Rim	XLM05	0.44	0.00	0.01	0.10130	0.01294	0.44026	0.07709	0.02870	0.00143
	XLM06	0.47	0.00	0.03	0.07352	0.00702	0.26956	0.02122	0.02808	0.00080
	XLM07	0.31	0.00	0.02	0.08698	0.00885	0.30960	0.02723	0.02709	0.00103
	XLM08	0.73	0.00	0.00	0.12933	0.00790	0.53831	0.03588	0.03006	0.00095
	XLM15	0.55	0.00	0.05	0.05872	0.00509	0.21787	0.01968	0.02696	0.00122
	XLM16	0.55	0.00	0.02	0.12528	0.00910	0.49936	0.03468	0.03006	0.00084
	XLM21	1.63	0.00	0.02	0.05570	0.00330	0.20408	0.01195	0.02658	0.00047
	XLM22	0.51	0.00	0.00	0.05217	0.00494	0.19877	0.01906	0.02784	0.00070
	XLM23	0.69	0.00	0.00	0.05504	0.00477	0.20303	0.01608	0.02724	0.00062
	XLM26	1.93	0.00	0.04	0.05438	0.00248	0.19697	0.00927	0.02639	0.00039
	XLM28	0.58	0.00	0.02	0.06435	0.00521	0.23583	0.01727	0.02725	0.00054
	XLM29	1.01	0.00	0.02	0.08087	0.00476	0.30205	0.01766	0.02723	0.00037
	XLM30	1.23	0.00	0.05	0.05619	0.00305	0.20395	0.01132	0.02648	0.00035
Standard cassiterite AY-4										
	AY-4std	1.46	0.00	0.3	0.52392	0.01993	5.07543	0.37015	0.06793	0.00364
	AY-4std	6.09	0.03	0.8	0.43967	0.02259	3.86378	0.41684	0.05767	0.00423
	AY-4std	0.92	0.00	0.1	0.49297	0.04751	3.92224	0.38889	0.05402	0.00284
	AY-4std	345	0.00	41	0.31090	0.03718	3.34334	0.66889	0.05364	0.00670
	AY-4std	1.45	0.00	0.1	0.27295	0.01958	1.54498	0.15290	0.03628	0.00151
	AY-4std	147	0.00	4.3	0.21764	0.01115	0.98451	0.06717	0.03179	0.00074
	AY-4std	1.92	0.00	0.1	0.20174	0.01508	0.95790	0.09040	0.03142	0.00094
	AY-4std	3.21	0.00	0.2	0.19384	0.01778	0.89486	0.07745	0.03020	0.00120
	AY-4std	67	0.00	1.7	0.16370	0.01996	0.66193	0.07045	0.02790	0.00087
	AY-4std	8.65	0.00	0.4	0.14081	0.01539	0.62852	0.07514	0.02765	0.00096

(Continued on following page)

TABLE 1 (*Continued*) LA-ICP-MS U-Pb dating results of cassiterite from the Baimianshan segment, Xinlu Sn-Zn deposit, South China.

Analysis spots	U-Th-Pb contents			U–Pb isotopic ratios					
	^{238}U	^{232}Th	Common Pb	^{207}Pb/^{206}Pb	1σ	^{207}Pb/^{235}U	1σ	^{206}Pb/^{238}U	1σ
AY-4std	3.14	0.00	0.0	0.11874	0.01239	0.46164	0.04956	0.02719	0.00104
AY-4std	0.08	0.00	0.0	0.10436	0.02845	0.30422	0.07150	0.02689	0.00149
AY-4std	15	0.00	0.0	0.08293	0.00559	0.31168	0.02182	0.02677	0.00071
AY-4std	66	0.00	1.7	0.12044	0.01668	0.46544	0.05747	0.02637	0.00092
AY-4std	0.97	0.00	0.0	0.08996	0.00466	0.32390	0.01752	0.02615	0.00040
AY-4std	213	0.00	3.9	0.12359	0.01338	0.45961	0.04720	0.02611	0.00072
AY-4std	49	0.00	0.5	0.06693	0.00801	0.23368	0.02575	0.02497	0.00077
AY-4std	14	0.00	1.0	0.07360	0.01043	0.21904	0.02460	0.02300	0.00071
NIST reference glass SRM 612									
SRM 612	98	37		0.92112	0.12499	32.90046	3.71038	0.24484	0.00826
SRM 612	101	39		0.92721	0.11829	33.63997	3.56754	0.24918	0.00790
SRM 612	100	38		0.94022	0.07948	34.05289	2.52080	0.25511	0.00470
SRM 612	100	38		0.94842	0.08621	34.95647	2.77951	0.25968	0.00513
SRM 612	99	37		0.84393	0.04970	27.21569	1.65231	0.22700	0.00365
SRM 612	100	38		0.83753	0.04991	26.80127	1.64293	0.22487	0.00360
SRM 612	37	37		0.93942	0.07635	29.77904	2.28620	0.22463	0.00840
SRM 612	38	39		0.94003	0.07406	29.79229	2.22115	0.22455	0.00813
SRM 612	37	37		0.91044	0.02008	28.89959	0.72585	0.22739	0.00214
SRM 612	38	38		0.90875	0.02065	28.97643	0.74343	0.22848	0.00216
SRM 612	38	39		0.92143	0.01898	28.86141	0.71193	0.22596	0.00157
SRM 612	36	36		0.92808	0.01973	29.00782	0.72734	0.22568	0.00184

(Gemmrich et al., 2021; Routhier, 1980), the Dachang Sn-Zn district (Huang et al., 1986; Fan et al., 2004), and the Bawang Fe-Zn-Sn deposit of Wuxu Sb-Zn district, South China (Xiao et al., 2022). Based on the two above-mentioned works, the generated elemental maps can provide information on the mineralization process and more meaningful results than a single micro-observation.

Reflection and element mapping can also greatly improve the efficiency of positioning for cassiterite U-Pb dating when the sample contains minor cassiterite. Commonly, it is hard to identify the position of cassiterite in the coexistence of fine-grained cassiterite and sphalerite sulfide. In our study, the element mapping by μ-XRF all display the distribution of tin (Figures 6–8), which was then confirmed to be cassiterite by quick microscopic observation (Figures 5C,D). Therefore, we confirm that the cassiterite was only formed in the retrograde skarn-sulfide stage. Moreover, the element mapping also avoided potential mixed ages of cassiterite. This method is also a powerful tool for *in situ* geochronology of polyphase minerals and provides a more accurate process of mineralization.

Age relationship between Sn-Zn (-W) mineralization and magmatism of Guposhan-Huashan district during Jurassic

Published high-precision geochronological investigations, including zircon U-Pb and biotite ^{40}Ar-^{39}Ar dating on the causative intrusions and multiple dating methods (Sm-Nd, Re-Os, ^{40}Ar-^{39}Ar, Rb-Sr) on the skarn and hydrothermal minerals, have revealed the magma emplacement and mineralization in the Guposhan-Huashan district. However, the relationship between the Sn-Zn (-W) mineralization and magmatism remains confusing based on these studies. An overview of the timing of magmatic-hydrothermal ore formation in the Guposhan-Huashan district is described as follows.

The Huashan and Guposhan complex plutons are the main intrusions in this district. The Huashan complex pluton composes of Huashan biotite granite in the core, the Tong'an quartz monzonite in the west, and the Niumiao diorite in the southeast. Available zircon U-Pb ages show these three intrusions

were formed at 160–163 Ma (Zhao et al., 2010). The $\varepsilon_{Hf}(t)$ (−2.8 to +7.4), $\varepsilon_{Nd}(t)$ (−3.18 to +0.91), and initial ($^{87}Sr/^{86}Sr$) ratios (0.70472–0.70714) revealed these three intrusions were generated by mantle-crust interaction (Cai et al., 2018 and references therein; Zhao et al., 2010; Zhu et al., 2005, 2006). Zhu et al. (2006) reported the younger felsic dykes with an age of 148.0 ± 4.0 Ma intruded into the Huashan granite along the fractures. The Guposhan complex pluton includes Lisong hornblende biotite granite in the core, Guposhan coarse biotite granite, and Fengmuchong fine felsic dykes in the south (Figure 2A). Published zircon U-Pb ages show that the Lisong and Guposhan granites were formed at 161.0–163.0 Ma and 159.5–165.0 Ma, respectively (Zhu et al., 2006; Gu et al., 2007b; Zhao et al., 2010; Shu et al., 2011; Cai et al., 2020; Cao et al., 2020). Li et al. (2016) dated the causative Shimen quartz monzodiorite in the Xinlu deposit and Fengmuchong biotite granite in the Shuiyanba deposit by igneous biotites ^{40}Ar-^{39}Ar dating at 168.7 ± 1.9 Ma and 165.0 ± 1.1 Ma, respectively. The $\varepsilon_{Hf}(t)$ (−3.6 to −2.3), $\varepsilon_{Nd}(t)$ (−5.5 to +1.9), and initial ($^{87}Sr/^{86}Sr$) ratios (0.70473–0.70742) of the Lisong and Guposhan granites and dark mafic enclaves imply the Guposhan main pluton also resulted from mantle-crust interaction. The later felsic dykes were dated by zircon U-Pb at 146.8 ± 2.3 Ma to 154.2 ± 3.1 Ma (Zhu et al., 2006; Wang et al., 2014). Initial Sr isotopic data ($(^{87}Sr/^{86}Sr)_i$ = 0.7173) and $\varepsilon_{Nd}(t)$ (-5) of later felsic dykes are obvious different from those of the main pluton in this district (Gu et al., 2007b). The high initial Sr isotopic and low $\varepsilon_{Nd}(t)$ values suggest the later dykes were generated from crust components. Thus, based on geochronology, two episodes of magmatism (159.5–168.7 Ma and 146.8–154.2 Ma) occurred in the Guposhan-Huashan district during Jurassic, of which the former was predominant.

Our robust *in-situ* LA-ICP-MS cassiterite U-Pb data, integrated with previous geochronological studies, support one stage magmatic-hydrothermal mineralization associated with 159.5–168.7 Ma magmatism in this district. Our new age directly yielded from cassiterite in this study demonstrates that the Sn-Zn mineralization in the Baimianshan segment occurred at 168.7 ± 1.3 Ma, coinciding with the age of quartz monzodiorite in the Xinlu deposit. Cassiterite U-Pb age is a little older than muscovite ^{40}Ar-^{39}Ar age of skarn-type ores (160.0 ± 2.0 Ma) and molybdenite Re-Os age of quartz-vein type wolframite ores (154.4 ± 3.5 Ma) from the Liuheao segment (Feng et al., 2019). Due to the lack of detailed microscopic observation, the muscovite ^{40}Ar-^{39}Ar isotopic data are doubtful to represent the skarn stage. Li et al. (2016) obtained hydrothermal muscovite ^{40}Ar-^{39}Ar age of 160.6 ± 1.5 Ma for the Liuheao altered granite. Therefore, we could speculate the muscovite ^{40}Ar-^{39}Ar isotopic data obtained by Feng et al. (2019) may represent the age of the quartz-vein stage rather than the skarn stage. This conclusion could be supported by the euhedral sericite-quartz of stage III replacing the massive skarn-type pyrrhotite and sphalerite of stage II (Figures 5A,H). From a temporal perspective, the skarn Sn-Zn mineralization is associated with quartz monzodiorite. Spatially, the skarn Sn-Zn mineralization is related to the Guposhan coarse biotite granite.

In the following, we also compare the obtained cassiterite U-Pb age to published geochronological data of mineralization in the Guposhan-Huashan district to further constrain the Sn-Zn-W formation age. Previous work on the mineralization age of the Shuiyanba Sn deposit used muscovite ^{40}Ar-^{39}Ar dating (162.0 ± 1.9 Ma and 162.5 ± 1.2 Ma; Kang et al., 2012; Li et al., 2016) of quartz + muscovite + wolframite veins and Rb-Sr dating of quartz fluid inclusions (136.1 ± 2.0 Ma; Gu et al., 2007a) from the wolframite + scheelite + arsenopyrite + cassiterite quartz veins in the Lantoushan segment. It is difficult to confirm whether the Rb-Sr isotopes of different hand specimens were at isotopic equilibrium or the ore-forming fluids have homogeneous initial $^{87}Sr/^{86}Sr$ ratios. Furthermore, quartz from the W-Sn quartz veins has a different initial $^{87}Sr/^{86}Sr$ ratio (0.72015–0.72735) from the Guposhan-Huashan pluton (0.7056–0.7066) (Gu et al., 2007b). To sum up, the muscovite ^{40}Ar-^{39}Ar dating results are more reliable and the quartz vein type W-Sn mineralization of the Shuiyanba Sn deposit probably occurred at 162 Ma.

Published Sm-Nd isotopic data of skarn minerals (pyroxene, hornblende, garnet) from the skarn-type ores in the Chuanlingjiao segment of the Keda Sn deposit suggest the skarn minerals occurred at 160.4 ± 4.8 Ma (Cao et al., 2020). Li et al. (2016) obtained muscovite ^{40}Ar-^{39}Ar ages of 164.5 ± 2.6 Ma for W-Sn quartz veins hosted in the Devonian marble at Maohedong segment and 161.2 ± 1.3 Ma for wolframite bearing quartz veins hosted in the Devonian sandstone at Sanchachong segment. According to the above, both the skarn Sn and quartz vein W-Sn mineralization occurred during 160–164 Ma.

As aforementioned, we conclude the Sn-W mineralization in the Guposhan-Huashan district was related to the intermediate felsic intrusions rather than the later felsic dykes. The skarn mineral Sm-Nd isotopic data represent the formation age of the prograde skarn stage (Stage I). Our new cassiterite U-Pb age represents the formation age of retrograde massive skarn-sulfides (stage II). All the muscovite ^{40}Ar-^{39}Ar ages represent the formation ages of quartz sulfide veins (stage III). No geochronological data of barren carbonate stage (stage IV) have been obtained in the Guposhan-Huashan district to date.

Relationship between the subduction of Paleo-Pacific plate and Jurassic tin-tungsten mineralization in the Nanling belt of South China

To understand the timing of magmatic-hydrothermal ore formation on the scale of the Nanling belt and SCB, we incorporated our new geochronological data into the existing

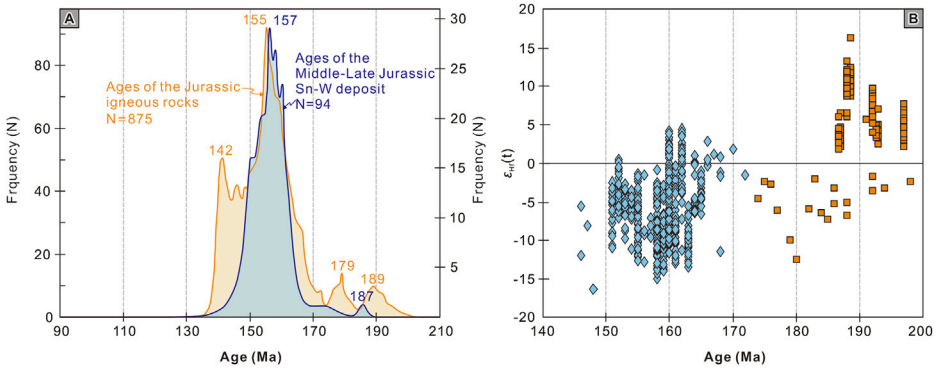


FIGURE 10
(A) Histogram of the Jurassic igneous rocks and Sn-W mineralization in South China. Data are from Cao et al., 2021; Feng et al., 2019; Mao et al., 2019; Xiao et al., 2019, and references therein. **(B)** $\varepsilon_{Hf}(t)$-age diagram for zircons from the Jurassic igneous rocks, South China. Data are from Li et al., 2018, Yang et al., 2021, and references therein. The orange square represents the Early Jurassic igneous rocks with ages of 174–198 Ma. The slightly blue rhombus represents the Middle-Late Jurassic igneous rocks with ages of 146–172 Ma.

geochronological framework of the Nanling Sn-W belt and South China W-Sn provinces during the Jurassic. On the probability density distribution plots of the Jurassic intrusions, two main peaks (~142 and 155 Ma) and two small peaks (~179 and 189 Ma) can be recognized (Figure 10A). The former two peaks with dominated negative $\varepsilon_{Hf}(t)$ values were associated with W-Sn mineralization, whereas the latter two peaks with dominated positive $\varepsilon_{Hf}(t)$ values were associated with Mo-Co mineralization (Figure 10B; Li et al., 2018; Yang et al., 2021). The four age clusters indicate multiphase tectonic events in the SCB. On the probability density distribution plots of the Jurassic W-Sn mineralization, a single peak (~157 Ma) is observed. The W-Sn formation ages overlapped with the second peak of intrusions (Figure 10A). The spatial distribution of W-Sn mineralization and associated intrusions display a slight southeastward younging trend in the Nanling Belt. However, in the entire South China, this trend is not obvious (Figure 1C). Recent research shows that W-Sn mineralization causative intrusions are A-type granites (Li et al., 2018; Xiao et al., 2019; Mao et al., 2021b). It is commonly accepted that the Jurassic mafic-ultramafic intrusions, A-type granites, and bimodal basalt-rhyolite volcanic rocks are formed in the extensional setting, but the geodynamic setting is still puzzling (Zhou and Li, 2000; Zhou et al., 2006; Li and Li, 2007; He et al., 2010; Mao et al., 2021b; Cao et al., 2021). The generally accepted dynamic domain includes the Paleo-Tethyan domain to the southwest and the Paleo-Pacific domain to the southeast. Therefore, two models have been proposed for the Jurassic evolution, including the Paleo-Tethyan post-collisional intra-continental extension model (He et al., 2010; Gan et al., 2017) and Izanagi or Paleo-Pacific plate subduction-related model (Zhou et al., 2006; Li and Li, 2007; Zaw et al., 2007; Mao et al., 2021b; Cao et al., 2021; Gan et al., 2021). Although the latter view is more popular, it is inconsistent with the fact that the orientation of the distribution of Middle-Late Jurassic rocks is opposite to the subduction of the Paleo-Pacific plate (Gan et al., 2017). The difference in geochemical signatures between the Early-Middle Jurassic mafic and shoshonitic rocks and Cretaceous arc-related rocks in the SCB also indicate that the Paleo-Pacific slab-derived components didn't modify the lithospheric mantle (Gan et al., 2021 and references therein). This conclusion is also confirmed by previous whole rock geochemistry and Sr-Nd-Hf isotope and zircon Hf-O isotope data from the early Jurassic gabbro-syenite-alkali-feldspar granite in South China (Yang et al., 2021). As described above, many facts are still in debate in the Paleo-Pacific subduction model, such as the variations of slab dip angles (Zhou et al., 2006; Li et al., 2018); flat-slab subduction and slab foundering (Li and Li, 2007); polyphase slab subduction and retreat (Li et al., 2020); slab window in the back-arc region (Mao et al., 2021b); and mantle upwelling model (Cao et al., 2021). According to the available data, the Paleo-Pacific subduction model is currently the most reasonable one. First, the geochemical signatures and higher zircon $\varepsilon Hf_{(t)}$-$\delta^{18}O$ values of the Middle-Late Jurassic igneous rocks all indicate an extensional setting corresponding to asthenospheric upwelling and crust-mantle interaction (Cao et al., 2021; Gan et al., 2021 and references therein). Previous studies have shown that tin granites generally occurred in an extensional environment corresponding to mantle upwelling (Romer and Kroner, 2016; Xiao et al., 2019; Guo et al., 2021). The upwelling of the basaltic intrusions might provide additional heat and trigger a partial melting of the lower crust to form W-Sn causative granite. Second, the Jurassic compressional deformation in the SCB is consistent with the

coeval advancing motion of the Izanagi trench (Li X. F. et al., 2012; Cao et al., 2021). The Jurassic arc-related granitoids have been also observed in the coastal regions and the South China Sea basin (Xu et al., 2017). Cao et al. (2021) also pointed out that Jurassic magmatism was accompanied by crustal deformation in the SCB. Last, numerical models suggest that flat-slab exists (Dai et al., 2020).

Conclusion

(1) Thin section reflection and μ-XRF element mapping represent a powerful tool for determining paragenesis in ore deposits and are highly effective to guide the selection of analytical points for cassiterite U-Pb dating. This method may also be applicable for *in-situ* dating of other minerals.
(2) Four mineralization episodes are identified in the Baimianshan segment, Xinlu deposit. They are prograde skarn (stage I), retrograde skarn-sulfide (stage II), quartz sulfide veins (stage III), and barren carbonate (stage IV) stages. The retrograde skarn-sulfide stage is the main mineralization stage and consists of massive pyrrhotite, and sphalerite with parts of epidote, cassiterite, and minor chalcopyrite and arsenian pyrite.
(3) The time of retrograde skarn-sulfide mineralization is dated by LA-ICP-MS cassiterite U-Pb at 168.7 ± 1.3 Ma. Our robust *in-situ* LA-ICP-MS cassiterite U-Pb data, coupled with previous geochronological studies, support one stage magmatic-hydrothermal mineralization associated with 159.5–168.7 Ma magmatism in the Guposhan-Huashan district.
(4) The Xinlu Sn-Zn mineralization and the Middle-Late Jurassic Sn-W mineralization in the Nanling belt, South China corresponded to asthenospheric upwelling and crust-mantle interaction caused by the subduction of the Paleo-Pacific plate.

Data availability statement

The original contributions presented in the study are included in the article/supplementary material, further inquiries can be directed to the corresponding author.

Author contributions

C-HX designed the study, collected the samples for analysis, and compiled the results and wrote the manuscript. P-PY and X-HL collected and processed previously published data. X-HL also finished the figures and table. C-HX and W-LW performed the μ-XRF analysis and process of the data. Y-WT performed cassiterite U-Pb dating and process of the data. X-CL, P-PY, YZ provided feedback to the manuscript.

Funding

This research was jointly supported by the National Natural Science Foundation of China (Grants: 41702095), the CGS Research Fund (Grants: DZLXJK202203) and the China Geological Survey (Grants: DD20190161, DD20221600-3).

Acknowledgments

We would like to thank Xing-Wen Le and Changshan Wei for his help in the field works. We also thank Guest Editor Fan Yang for his handling our paper, and Hua-Wen Cao and other three reviewers for their constructive comments that greatly improved our paper.

Conflict of interest

The authors declare that the research was conducted in the absence of any commercial or financial relationships that could be construed as a potential conflict of interest.

Publisher's note

All claims expressed in this article are solely those of the authors and do not necessarily represent those of their affiliated organizations, or those of the publisher, the editors and the reviewers. Any product that may be evaluated in this article, or claim that may be made by its manufacturer, is not guaranteed or endorsed by the publisher.

References

Cai, Y. F., Liu, F. L., Feng, Z. H., Zhou, Y., and Zeng, C. Y. (2020). Mineral compositional and chronological characteristics of Guposhan pluton in Guangxi and its petrogenetic and metallogenic significance. *J. Jilin Univ. Earth Sci. Ed.* 50 (03), 842–856. doi:10.13278/j.cnki.jjuese.20180316

Cai, Y. F., Ma, Y. C., Zhou, Y., Su, X. Q., Feng, Z. H., Ma, L. H., et al. (2018). Characteristics of mineralogy, geochronology and geochemistry of the granite in Huashan, Guangxi and its tectonic implication. *Geol. Explor.* 54 (05), 940–956. (in Chinese with English abstract). doi:10.13712/j.cnki.dzykt.2018.05.006

Cao, J. Y., Yang, X. Y., Lu, Y., Fu, J. M., and Yang, L. Z. (2020). Zircon U–Pb and Sm–Nd geochronology and geochemistry of the Sn–W deposits in the northern Guposhan ore field, Nanling Range, southern China. *Ore Geol. Rev.* 118, 103323. doi:10.1016/j.oregeorev.2020.103323

Cao, X. Z., Flament, N., Li, S. Z., and Müller, R. D. (2021). Spatio-temporal evolution and dynamic origin of Jurassic-Cretaceous magmatism in the South China Block. *Earth. Sci. Rev.* 217, 103605. doi:10.1016/j.earscirev.2021.103605

Cawood, P. A., Zhao, G. C., Yao, J. L., Wang, W., Xu, Y. J., and Wang, Y. J. (2018). Reconstructing south China in phanerozoic and precambrian supercontinents. *Earth. Sci. Rev.* 186, 173–194. doi:10.1016/j.earscirev.2017.06.001

Dai, L., Wang, L., Lou, D., Li, Z. H., Dong, H., Ma, F., et al. (2020). Slab rollback versus delamination: Contrasting fates of flat-slab subduction and implications for south China evolution in the mesozoic. *J. Geophys. Res. Solid Earth* 125 (4). doi:10.1029/2019JB019164

Dong, Z. C. (1991). The REE Geochemical characteristics in the Xinlu tin orefield, Guangxi. *J. Guilin Inst. Technol.* 011 (003), 277–286.

Fan, D., Zhang, T., Ye, J., Pašava, J., Kribek, B., Dobes, P., et al. (2004). Geochemistry and origin of tin–polymetallic sulfide deposits hosted by the Devonian black shale series near Dachang, Guangxi, China. *Ore Geol. Rev.* 24 (1-2), 103–120. doi:10.1016/j.oregeorev.2003.08.006

Feng, Y., Feng, Z. H., Fu, W., Kang, Z. Q., Jiang, J., Guo, A., et al. (2019). Magmatic-hydrothermal mineralization sequence in Xinlu ore field, Guangxi, south China: Constraints from zircon U-Pb, molybdenite Re-Os, and muscovite Ar-Ar dating. *Resour. Geol.* 69 (4), 430–447. doi:10.1111/rge.12212

Flude, S., Haschke, M., and Storey, M. (2017). Application of benchtop micro-XRF to geological materials. *Mineral. Mag.* 81 (4), 923–948. doi:10.1180/minmag.2016.080.150

Gan, C. S., Wang, Y. J., Zhang, Y. Z., and Zhang, J. (2017). The earliest Jurassic A-type granite in the Nanling Range of southeastern South China: Petrogenesis and geological implications. *Int. Geol. Rev.* 59 (3), 274–292. doi:10.1080/00206814.2016.1254574

Gan, C., Zhang, Y. Z., Wang, Y. J., Qian, X., and Wang, Y. (2021). Reappraisal of the mesozoic tectonic transition from the paleo-tethyan to paleo-pacific domains in south China. *GSA Bull.* 133 (11-12), 2582–2590. doi:10.1130/B35755.1

Gemmrich, L., Torró, L., Melgarejo, J. C., Laurent, O., Vallance, J., Chelle-Michou, C., et al. (2021). Trace element composition and U-Pb ages of cassiterite from the Bolivian tin belt. *Min. Deposita* 56, 1491–1520. doi:10.1007/s00126-020-01030-3

Gilder, S. A., Gill, J., Coe, R. S., Zhao, X., Liu, Z., Wang, G., et al. (1996). Isotopic and paleomagnetic constraints on the Mesozoic tectonic evolution of south China. *J. Geophys. Res.* 101 (B7), 16137–16154. doi:10.1029/96JB00662

Gu, S. Y., Hua, R. M., and Qi, H. W. (2007a). A genetic study of Xinlu-Shuiyanba W-Sn orefield, Northeast Guangxi. *Min. Depos.* 3, 265–276. (in Chinese with English abstract). doi:10.16111/j.0258-7106.2007.03.003

Gu, S. Y., Hua, R. M., and Qi, H. W. (2007b). Zircon LA-ICP-MS U-Pb dating and Sr-Nd isotope study of the Guposhan granite complex, Guangxi, China. *Chin. J. Geochem.* 26 (03), 290–300. doi:10.1007/s11631-007-0290-5

Guo, J., Wu, K., Seltmann, R., Zhang, R., Ling, M., Li, C., et al. (2021). Unraveling the link between mantle upwelling and formation of Sn-bearing granitic rocks in the world-class Dachang tin district, South China. *GSA Bull.* 134 (3-4), 1043–1064. doi:10.1130/B35492.1

He, Z. Y., Xu, X. S., and Niu, Y. (2010). Petrogenesis and tectonic significance of a Mesozoic granite-syenite-gabbro association from inland South China. *Lithos* 119 (3-4), 621–641. doi:10.1016/j.lithos.2010.08.016

Hu, H. Y., Qiu, L. B., Xie, G. Y., and You, J. S. (1992). Metallogenetic regularities and prediction of concealed deposits in the Xinlu tin orefield Guangxi, China. *Geotecton. Metallog.* 03, 221–238. (in Chinese with English abstract). doi:10.16539/j.ddgzyckx.1992.03.001

Hu, R. Z., and Zhou, M. F. (2012). Multiple Mesozoic mineralization events in South China- an introduction to the thematic issue. *Min. Depos.* 47, 579–588. doi:10.1007/s00126-012-0431-6

Huang, M. Z., Wu, G. B., Chen, Y. C., and Tang, S. H. (1986). Mineralogical study of the franckeite from the Dachang cassiterite-sulphide polymetallic ore filed, Guangxi. *Acta Geol. Sin.* 2, 164–175. (in Chinese with English abstract).

Kang, Z. Q., Feng, Z. H., Li, X. F., Liao, J. F., Yu, Y., and Pan, H. B. (2012). 40Ar-39Ar age of muscovite in the Shuiyanba tungtsen-tin ore field in Northeast Guangxi and its geological significance. Bull. Mineral. *Pet. Geochem.* 31 (6), 606–611. (in Chinese with English abstract). doi:10.3969/j.issn.1007-2802.2012.06.008

Li, H., Palinkaš, L. A., Watanabe, K., and Xi, X. S. (2018). Petrogenesis of Jurassic A-type granites associated with Cu-Mo and W-Sn deposits in the central Nanling region, South China: Relation to mantle upwelling and intra-continental extension. *Ore Geol. Rev.* 92, 449–462. doi:10.1016/j.oregeorev.2017.11.029

Li, J. H., Cawood, P. A., Ratschbacher, L., Zhang, Y. Q., Dong, S. W., Xin, Y. J., et al. (2020). Building Southeast China in the late Mesozoic: Insights from alternating episodes of shortening and extension along the Lianhuashan fault zone. *Earth. Sci. Rev.* 201, 103056. doi:10.1016/j.earscirev.2019.103056

Li, J. H., Zhang, Y. Q., Ratschbacher, L., Zhao, G. C., Dong, S. W., Xin, Y. J., et al. (2022). Polyphase deformation in the badu complex: Insights into triassic intraplate orogeny in south China. *J. Struct. Geol.* 154, 104475. doi:10.1016/j.jsg.2021.104475

Li, S. Z., Santosh, M., Zhao, G. C., Zhang, G. W., and Jin, C. (2012). Intracontinental deformation in a frontier of super-convergence: A perspective on the tectonic milieu of the south China block. *J. Asian Earth Sci.* 49, 313–329. doi:10.1016/j.jseaes.2011.07.026

Li, X. F., Feng, Z. H., Xiao, R., Song, C. A., Feng, Y., and Wang, C. Y. (2012). Spatial and temporal distributions and the geological setting of the W-Sn-Mo-Nb-Ta deposits at the northeast Guangxi, south China. *Acta Geol. Sin.* 86 (11), 1713–1725. (in Chinese with English abstract). doi:10.3969/j.issn.0001-5717.2012.11.001

Li, X. F., Xiao, R., Feng, Z. H., Wei, C. X., Tang, Y. W., Bai, Y. P., et al. (2016). Ar-Ar ages of hydrothermal muscovite and igneous biotite at the guposhan-huashan district, northeast Guangxi, south China: Implications for mesozoic W-Sn mineralization. *Resour. Geol.* 65 (2), 160–176. doi:10.1111/rge.12062

Li, Z. X., and Li, X. H. (2007). formation of the 1300-km-wide intracontinental orogen and postorogenic magmatic province in mesozoic south China: A fl at-slab subduction model. *Geol.* 35 (2), 179–182. doi:10.1130/G23193A.1

Liu, Y. S., Hu, Z. C., Gao, S., Günther, D., Xu, J., Gao, C. G., et al. (2008). *In situ* analysis of major and trace elements of anhydrous minerals by LA-ICP-MS without applying an internal standard. *Chem. Geol.* 257, 34–43. doi:10.1016/j.chemgeo.2008.08.004

Ludwig, K. R. (2003). *Isoplot v. 3.0: a geochronological toolkit for microsoft excel*, 4. USA: Berkeley Geochronology Center, 1–70. Special Publication.

Mao, J. W., Liu, P., Goldfarb, R. J., Goryachev, N. A., Pirajno, F., Zheng, W., et al. (2021a). Cretaceous large-scale metal accumulation triggered by post-subductional large-scale extension, East Asia. *Ore Geol. Rev.* 136, 104270. doi:10.1016/j.oregeorev.2021.104270

Mao, J. W., Zheng, W., Xie, G. Q., Lehmann, B., and Goldfarb, R. (2021b). Recognition of a Middle-Late Jurassic arc-related porphyry copper belt along the southeast China coast: Geological characteristics and metallogenic implications. *Geology* 49 (5), 592–596. doi:10.1130/G48615.1

Meinert, L. D., Dipple, G. M., Nicolescu, S., Hedenquist, J. W., Thompson, J. F. H., Goldfarb, R. J., et al. (2005). "World skarn deposits," in *One hundredth anniversary volume* (USA: Society of Economic Geologists). doi:10.5382/AV100.11

Ou, Z. Y. (1989). Analysis of structural control on mineralization and metallogenic prognosis in Xinlu tin orefield Guangxi. *J. Guilin Inst. Technol.* 04, 387–397. (in Chinese with English abstract).

Romer, R. L., and Kroner, U. (2016). Phanerozoic tin and tungsten mineralization-Tectonic controls on the distribution of enriched protoliths and heat sources for crustal melting. *Gondwana Res.* 31, 60–95. doi:10.1016/j.gr.2015.11.002

Shu, L. S. (2012). An analysis of principal features of tectonic evolution in South China Block. *Geol. Bull. China* 31 (07), 1035–1053. (in Chinese with English abstract). doi:10.3969/j.issn.1671-2552.2012.07.003

Shu, L. S., Yao, J. L., Wang, B., Faure, M., Charvet, J., and Chen, Y. (2021). Neoproterozoic plate tectonic process and Phanerozoic geodynamic evolution of the South China Block. *Earth. Sci. Rev.* 216, 103596. doi:10.1016/j.earscirev.2021.103596

Shu, X. J., Wang, X. L., Sun, T., Xu, X., and Dai, M. N. (2011). Trace elements, U–Pb ages and Hf isotopes of zircons from Mesozoic granites in the Western Nanling Range, South China: Implications for petrogenesis and W–Sn mineralization. *Lithos* 127 (3-4), 468–482. doi:10.1016/j.lithos.2011.09.019

Tang, Y. W., Han, J. J., Lan, T. G., Gao, J. F., Liu, L., Xiao, C. H., et al. (2022). Two reliable calibration methods for accurate *in-situ* U-Pb dating of scheelite. *J. Anal. At. Spectrom.* 37 (2), 358–368. doi:10.1039/D1JA00387A

Wang, H., Treble, P., Baker, A., Rich, A. M., Bhattacharyya, S., Oriani, F., et al. (2022). Sulphur variations in annually layered stalagmites using benchtop micro-XRF. *Spectrochim. Acta Part B At. Spectrosc.* 189, 106366. doi:10.1016/j.sab.2022.106366

Wang, Z. Q., Chen, B., and Ma, X. H. (2014). Petrogenesis of the late Mesozoic Guposhan composite plutons from the nanling range, South China: Implications for W-Sn mineralization. *Am. J. Sci.* 314 (1), 235–277. doi:10.2475/01.2014.07

Xiao, C. H., Chen, Z. L., Liu, X. C., Wei, C. S., Wu, Y., Tang, Y. W., et al. (2022). Structural analysis, mineralogy, and cassiterite U–Pb ages of the Wuxu Sb-Zn-polymetallic district, Danchi Fold-and-Thrust belt, South China. *Ore Geol. Rev.* 150, 105150. doi:10.1016/j.oregeorev.2022.105150

Xiao, C. H., Shen, Y. K., and Wei, C. S. (2019). Petrogenesis of low Sr and high Yb A-type granitoids in the xianghualing Sn polymetallic deposit, south China: Constrains from geochronology and Sr–Nd–Pb–Hf isotopes. *Minerals* 9 (3), 182. doi:10.3390/min9030182

Xiao, R., Li, X. F., Feng, Z. H., Yang, F., and Song, C. A. (2011). ^{40}Ar-^{39}Ar dating of muscovite from tungsten-quartz veins in Shanhu tungsten-tin deposit and its geological significance. *Min. Depos.* 30, 488–496. (in Chinese with English abstract). doi:10.16111/j.0258-7106.2011.03.010

Xu, C. H., Zhang, L., Shi, H. S., Brix, M., Huhma, H., Chen, L. H., et al. (2017). Tracing an early jurassic magmatic arc from south to east China seas. *Tectonics* 36 (3), 466–492. doi:10.1002/2016TC004446

Yang, F., Santosh, M., Kim, S. W., Zhou, H., and Jeong, Y. J. (2020). Late mesozoic intraplate rhyolitic volcanism in the north China craton: Far-field effect of the westward subduction of the Paleo-Pacific plate. *GSA Bull.* 132, 291–309. doi:10.1130/B35123.1

Yang, J. H., Zhang, J. H., Chen, J. Y., and Sun, J. F. (2021). Mesozoic continental crustal rejuvenation of South China: Insights from zircon Hf-O isotopes of early Jurassic gabbros, syenites and A-type granites. *Lithos* 402-403, 105678–106403. doi:10.1016/j.lithos.2020.105678

Yuan, S. D., Peng, J. T., Hu, R. Z., Bi, X. W., Qi, L., Li, Z. L., et al. (2008). Characteristics of rare-earth elements (REE), strontium and neodymium isotopes in hydrothermal fluorites from the Bailashui tin deposit in the Furong ore field, southern Hunan Province, China. *Chin. J. Geochem.* 27 (4), 342–350. doi:10.1007/s11631-008-0342-5

Zaw, K., Peters, S. G., Cromie, P., Burrett, C., and Hou, Z. (2007). Nature, diversity of deposit types and metallogenic relations of South China. *Ore Geol. Rev.* 31 (1-4), 3–47. doi:10.1016/j.oregeorev.2005.10.006

Zhang, D., Zhao, K. D., Wang, B. D., Cheng, K. D., Luo, X. L., Zhang, W., et al. (2020). Cretaceous granitic magmatism and mineralization in the Shanhu W-Sn ore deposit in the Nanling Range in South China. *Ore Geol. Rev.* 126, 103758. doi:10.1016/j.oregeorev.2020.103758

Zhang, R. Q., Lu, J. J., Wang, R. C., Yang, P., Zhu, J. C., Yao, Y., et al. (2015). Constraints of *in situ* zircon and cassiterite U-Pb, molybdenite Re-Os and muscovite 40Ar-39Ar ages on multiple generations of granitic magmatism and related W-Sn mineralization in the wangxianling area, nanling range, south China. *Ore Geol. Rev.* 65, 1021–1042. doi:10.1016/j.oregeorev.2014.09.021

Zhao, K. D., Jiang, S. Y., Zhu, J. C., Li, L., Dai, B. Z., Jiang, Y. H., et al. (2010). Hf isotopic composition of zircons from the Huashan-Guposhan intrusive complex and their mafic enclaves in northeastern Guangxi:Implication for petrogenesis. *Chin. Sci. Bull.* 55 (06), 509–519. doi:10.1007/s11434-009-0314-0

Zhou, X. M., and Li, W. X. (2000). Origin of Late Mesozoic igneous rocks in southeastern China: Implications for lithosphere subduction and underplating of mafic magmas. *Tectonophysics* 326 (3-4), 269–287. doi:10.1016/S0040–1951(00)00120–7

Zhou, X. M., Sun, T., Shen, W., Shu, L., and Niu, Y. (2006). Petrogenesis of mesozoic granitoids and volcanic rocks in south China: a response to tectonic evolution. *Episodes* 29 (1), 26–33. doi:10.18814/epiiugs/2006/v29i1/004

Zhu, J. C., Zhang, H., Xie, C. F., Zhang, P. H., and Yang, C. (2005). Zircon SHRIMP U-Pb geochronology, petrology and geochemistry of the Zhujianshui granite, Qitianling pluton, southern Hunan province. *Geol. J. China Univ.* 11, 335–342. Available at: https://geology.nju.edu.cn/EN/Y2005/V11/I3/335 (in Chinese with English abstract).

Zhu, J. C., Zhang, P. H., Xie, C. F., Zhang, H., and Yang, C. (2006). The huashan-guposhan A-type granitoid belt in the western part of the nanling mountains: petrology, geochemistry and genetic interpretations. *Acta Geol. Sin.* 04, 529–542. (in Chinese with English abstract).

frontiers | Frontiers in Earth Science

TYPE Original Research
PUBLISHED 10 January 2023
DOI 10.3389/feart.2022.1084212

Check for updates

OPEN ACCESS

EDITED BY
Fei Xue,
Hohai University, China

REVIEWED BY
Leilei Dong,
University of Science and Technology Beijing, China
Qihai Shu,
China University of Geosciences, China
Xiangguo Guo,
Inner Mongolia University of Technology, China

*CORRESPONDENCE
Zhao-Lu Zhang,
zhzhl@sdut.edu.cn

SPECIALTY SECTION
This article was submitted to Economic Geology, a section of the journal Frontiers in Earth Science

RECEIVED 30 October 2022
ACCEPTED 06 December 2022
PUBLISHED 10 January 2023

CITATION
Cai W-Y, Zhang Z-L, Liu X, Gao J-L, Ma M, Li Y, Song Y-X and Li Z-S (2023), Metallogeny of the Yi'nan Tongjing Au–Cu skarn deposit, Luxi district, North China Craton: Perspective from in-suit trace elements, sulfur and lead isotopes of sulfides.
Front. Earth Sci. 10:1084212.
doi: 10.3389/feart.2022.1084212

COPYRIGHT
© 2023 Cai, Zhang, Liu, Gao, Ma, Li, Song and Li. This is an open-access article distributed under the terms of the Creative Commons Attribution License (CC BY). The use, distribution or reproduction in other forums is permitted, provided the original author(s) and the copyright owner(s) are credited and that the original publication in this journal is cited, in accordance with accepted academic practice. No use, distribution or reproduction is permitted which does not comply with these terms.

Metallogeny of the Yi'nan Tongjing Au–Cu skarn deposit, Luxi district, North China Craton: Perspective from in-suit trace elements, sulfur and lead isotopes of sulfides

Wen-Yan Cai[1,2], Zhao-Lu Zhang[1]*, Xiao Liu[1], Ji-Lei Gao[3], Ming Ma[3], Yadong Li[3], Ying-Xin Song[4] and Zeng-Sheng Li[4]

[1]School of Resources and Environmental Engineering, Shandong University of Technology, Zibo, China, [2]MNR Key Laboratory for Exploration Theory and Technology of Critical Mineral Resources, China University of Geosciences, Beijing, China, [3]Shandong Provincial No. 1 Exploration Institute of Geology and Mineral Resources, Ji'nan, China, [4]Key Laboratory of Gold Mineralization Processes and Resource Utilization MNR, Ji'nan, China

Gold–Cu skarn deposits are characterized by a diverse mineral assemblage, whose *in-situ* major/trace elements and isotope compositions can provide key constraints to the migration and enrichment of Au during hydrothermal processes. The Yi'nan Tongjing Au–Cu deposit is located in the central part of the Luxi district, and both skarn and Au–Cu ore bodies occur at the contact between the Early Cretaceous diorite porphyry and the Neoproterozoic to Cambrian carbonate rocks. Five stages of mineralization were identified: 1) early skarn (garnet–diopside–wollastonite); 2) late skarn (magnetite–epidote–actinolite±tremolite); 3) oxide (specularite–hematite); 4) sulfide (pyrite–chalcopyrite–sphalerite–quartz–chlorite); and 5) late quartz–calcite. The mineralization process in the Tongjing Au-Cu deposit was revealed by detailed scanning electron microscope-backscattered electron imaging, electron probe microanalysis, *in-situ* trace element, sulfur and lead isotope analysis. Magnetite is enriched in chalcophile elements (Cu, Zn, Pb), Co and Ni, probably due to hydrothermal overprint. The substitution of As and other elements in the formation of pyrite is conducive to the entry of Au into pyrite. The increase of Se and As contents in pyrite from stage IVa to IVb indicates that the temperature, salinity and oxygen fugacity of the ore-forming fluid decrease while the pH rises, resulting in the unloading of Au. The temperature of Au mineralization based on the Se content in pyrite does not exceed 300°C. Furthermore, V positively correlated with Ti and Ni/Cr ratios ≥1 in magnetite and most Co/Ni ratios in pyrite >10 all confirm their hydrothermal origins. The restricted sulfur ($\delta^{34}S_{V\text{-}CDT}$ = −0.5–1.2‰; mean = 0.4‰) and lead ($^{206}Pb/^{204}Pb$ = 17.323–17.383; $^{207}Pb/^{204}Pb$ = 15.424–15.452; $^{208}Pb/^{204}Pb$ = 37.367–37.454) isotopic compositions suggest that the deep magma provided the primary mineralized material, accompanied by a relatively small amount of shallow crustal material. The Yi'nan Tongjing Au–Cu skarn deposit was formed in the Early Cretaceous, which is an important metallogenic response to the strong decratonization of the North China Craton induced by the paleo-Pacific Plate

roll-back. This study shows that there is a large potential of Early Cretaceous skarn mineralization in the Luxi district.

KEYWORDS

***in-situ* trace elements analyses, *in-situ* sulfur and lead isotopes, Au precipitation mechanism, Yi'nan Tongjing, skarn deposit, Luxi district**

1 Introduction

Skarn deposits are an important resource of Au, Ag, Pb, Zn, W, Sn, Fe, and Cu and other metals on a global scale (Einaudi et al., 1981; Hedenquist and Lowenstern, 1994; Meinert et al., 2005; Chen et al., 2007; Chang et al., 2019; Shu et al., 2021; Niu et al., 2022). Skarn deposits, also known as contact metasomatic deposits, form at the contact between intermediate-acid intrusions and carbonate strata (Meinert et al., 2005; Shu et al., 2017; Chang et al., 2019). It has experienced a complex mineralization process (magma/fluid-rock interaction), resulting in a diverse mineral assemblage (Meinert, 1992; Meinert et al., 2005). Minerals, especially mineralization-related (e.g., pyrite, chalcopyrite and magnetite; Cook et al., 2009; Deditius et al., 2014; Nadoll et al., 2014; George et al., 2018a), can be used to reveal the key mineralization information such as ore-forming temperature, elemental substitution and physicochemical conditions as they often are treated as a recorder of mineralization processes. Most types of Au deposits (e.g., orogenic-, epithermal-, intrusion-related, and carlin-type; Groves et al., 1998; Thompson et al., 1999; Hedenquist et al., 2005; Baker et al., 2006; Goldfarb and Groves, 2015) are relatively simple in mineral assemblages, mainly pyrite and chalcopyrite, where only gold-bearing pyrite can constrain the detailed mineralization process (Sung et al., 2009; Fougerouse et al., 2017; Hastie et al., 2020; Chinnasamy et al., 2021). On the other hand, skarn Au deposits have a wide range of mineral assemblages and the major and trace elements of these minerals record a wealth of mineralization information, which helps us to better understand the ore-forming mechanism.

The Luxi district is located in the eastern part of North China Craton (NCC) (Figure 1), and hosts a range of Fe and Au–Cu skarn deposits (Figure 2). These deposits are closely associated with Early Cretaceous intermediate magmatic rocks (diorite and/or diorite porphyry; Xu et al., 2007; Wang et al., 2011; Duan et al., 2020). The Yi'nan Tongjing is a representative Au–Cu deposit in the district. Previous studies mainly focused on fluid inclusions, bulk-ore C–H–O–S–Pb–He–Ar isotopes, zircon U-Pb and whole-rock geochemistry (Qiu et al., 1996; Dong, 2008; Gu et al., 2008; Li et al., 2009; Wang, 2010; Li et al., 2011; Tian et al., 2015; Zhu et al., 2018), revealing that fluid immiscibility led to the precipitation of mineralized material, but the physicochemical conditions for occurrence, migration and unloading of ore-forming elements are still unclear. The wide range of sulfur and lead isotopic compositions of metal minerals makes it difficult to determine the source of the ore-forming material, and lacks sufficient spatial resolution to reveal the possible multi-stage mineralization processes.

In this study, the possible substitution mechanism between elements, elemental behavior during mineralization and key controlling factors were investigated, and the source of ore-forming material was also constrained. Based on detailed field geological investigations and ore texture, electron probe microanalysis and *in-situ* laser ablation-inductively coupled plasma-mass spectrometry (LA-ICP-MS) trace element composition analyses were performed on metal minerals (magnetite, pyrite, sphalerite and chalcopyrite), and *in-situ* LA–ICP–MC–MS sulfur and lead isotope analyses were conducted on pyrite and chalcopyrite.

2 Geological setting

The NCC is adjacent to the Central Asian Orogenic Belt in the north, and the Qinling–Dabie Su–Lu Orogenic Belt in the south (Figure 1). The NCC is the oldest and largest craton in China (Zhai and Santosh, 2011; Zhao and Cawood, 2012) and eventually cratonized and stabilized at approximately 1.85 Ga (Zhao et al., 2001; Santosh, 2010; Zhai, 2011). During the Mesozoic, the nature and thickness of the subcontinental lithospheric mantle beneath the eastern NCC were changed (Menzies et al., 1993; Xu, 2001; Zhu et al., 2011; Yang et al., 2012), which triggered extensive tectonism, magmatism, and large-scale metal mineralization (e.g., Au, Fe and Cu) (Mao et al., 2003; Wu et al., 2005a; 2005b; Zhu et al., 2012; Zeng et al., 2013, 2020). The NCC holds approximately 50% Au production and proven reserves of China (Deng and Wang, 2016; Yang et al., 2021). These Au deposits are mainly distributed in the Xiaoqinling-Xiong'ershan, Liaodong, Chifeng-Chaoyang, Yanshan, Zhangjiakou, Bayan Obo-Baotou, Jiaodong and Luxi districts (Figure 1B).

The Luxi terrane is dominantly composed of Neoarchaean gneisses, amphibolites and TTGs and Paleoproterozoic granitoids (Song et al., 2001; Wan et al., 2011; Wu et al., 2013), which are overlain by Neoproterozoic Tumen Group (littoral clastic and carbonate rocks) and Paleozoic to Cenozoic sequences (Guo et al., 2014; Deng et al., 2018). The Paleozoic strata are widely exposed in Luxi, including carbonate,

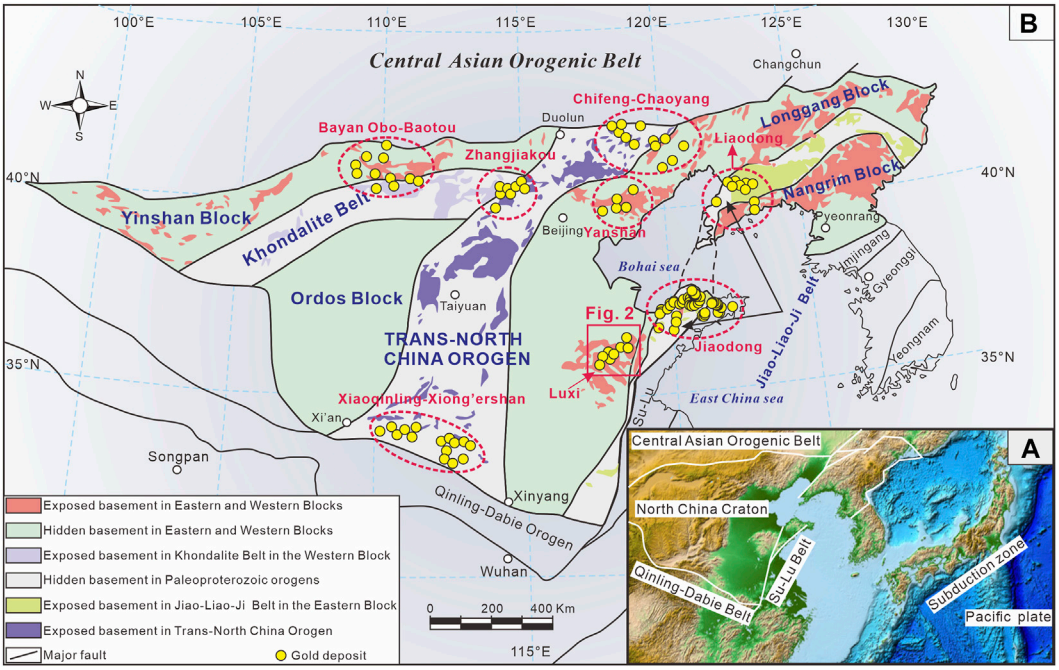


FIGURE 1
(A) Simplified geological and tectonic map of the NCC (modified after Yang et al., 2021); **(B)** Geological map with the distribution of gold deposits in the NCC (modified after Zhao et al., 2005; Deng and Wang, 2016; Li and Santosh, 2017; Li et al., 2020).

shale and clastic rocks (Dong, 2008), whilst the Mesozoic to Cenozoic strata mainly consist of terrestrial clastic and volcanic-sedimentary rocks (Niu et al., 2004; Hu et al., 2006).

Ninety-five percent of the exposed igneous rocks in Luxi are Precambrian units, and the rest are small-scale Mesozoic intrusive rocks, mainly formed in the Early Jurassic (ca. 185–180 Ma; Lan et al., 2012) and Early Cretaceous (ca. 135–125 Ma; Xu et al., 2004; Yang et al., 2006; 2008; Zhang et al., 2021). The Early Cretaceous magmatism is exemplified by the Laiwu kuangshan and Yi'nan Tongjing intrusive complex (Wang et al., 2011; Duan et al., 2020; Gao et al., 2022). They are mainly composed of diorite and gabbro, with a small amount of granite, which is closely related to the large-scale Fe and Au deposits in the area (Hu et al., 2010; Wang, 2010; Duan and Li, 2017).

3 Deposit geology

The Yi'nan Tongjing Au-Cu deposit is located 8 km north of Yi'nan County in western Shangdong Province, China, which is mainly composed of six ore segments: Shanzijian, Gongquan, Jinlong, Gongquandong, Duijinshan and Tonghanzhuang (Figure 3).

Cambrian sequences are widely exposed in the ore district (Figure 3), including Changqing Group (Zhushadong and Mantou formations) and Jiulong Group (Zhangxia and Gushan formations), which are the main ore-hosting rocks (Figure 4A; Liu et al., 2014). They consist of limestone, dolomite, sandstone and shale (Figure 4A; Dong, 2008), whilst these rocks extend along NW–SE (300°) and incline to the SW at angles of 10–30° (SDGG, 2008). The Archean Taishan Group (metabasic volcanic–sedimentary rocks; Guo et al., 2014) is overlain by the Proterozoic Tumen Group (Tongjiazhuang Formation) in unconformable contact (Figure 4A; Dong, 2008). The Tongjiazhuang Formation includes shale intercalated with thin limestone, in which skarnization occurred (Figure 4A; SDGM, 2015). Faults in Tongjing are affected by the Tan-lu fault, mainly including NNE-, NW-, and SN-trending faults (Figure 3). The NNE- and NW-trending faults are characterized by multi-stage activities, which are filled with mineralized quartz or carbonate veins (SDGG, 2008). Besides, the NNE-trending faults were cut by NW-trending faults. Magmatic intrusion (e.g., Tongjing intrusive complex) often occurred at the intersections of these two sets of faults (Dong, 2008). Tongjing complex comprises pyroxene/quartz diorite in the middle as xenoliths, a small volume of hornblende diorite porphyry in the west and quartz diorite porphyry distributed around them (Figure 3), which were formed in the Early Cretaceous (136–126 Ma; Xu et al., 2007; Wang, 2010; Wang et al.,

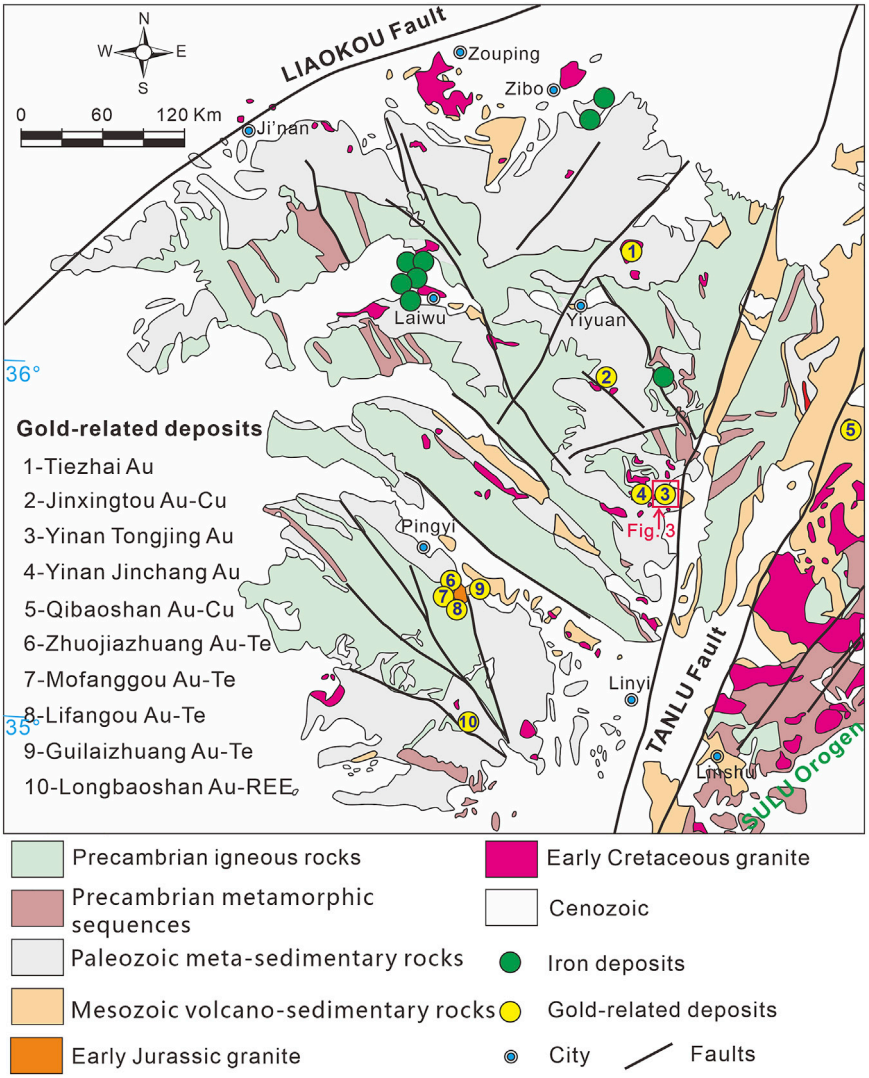


FIGURE 2
Simplified geological map of the Luxi district with major deposits marked (modified after Deng et al., 2018).

2011; Li et al., 2011; Duan et al., 2020). Diorite is intruded by the diorite porphyry or occurs as xenoliths in the latter, indicating its early emplacement (Duan et al., 2020). Skarnization and Au-Cu mineralization mainly occur in the contact zone between the Tongjing complex and Proterozoic to Cambrian carbonate sequences (Figure 4A) and in the structurally weak zone of the strata (Dong, 2008; SDGG, 2008).

More than ten major ore bodies have been identified in Tongjing, and they are mainly hosted in Neoproterozoic to Cambrian strata or the contact between these strata and diorite porphyry (Figure 4A; SDGM, 2015). The ore bodies occur around intrusive rocks in a circular belt (Dong, 2008), so the trends of the ore bodies vary greatly. The ore bodies are layered and lenticular (Figure 4B), with lengths of 15–240 m, widths of 0.5–25 m and depths of 200 m (SDGG, 2008). However, the scale of a single Au–Cu ore body is generally small (Figure 4B). For example, the No. 1 ore body is hosted in thin sandstone and shale of the Zhushadong Formation and occurs in layers. The ore body has a strike of 134° and dips at 10–15° to the SW. It is approximately 160 m long, 0.5–8.95 m thick, and extends to depths of 150 m. The average grades of Au, Cu and Fe in the ore body are 2.89 g/t, 0.19% and 0.63%, respectively (SDGG, 2008).

Based on field and petrographic observations, five paragenetic stages at Tongjing deposit are recognized: 1) early skarn; 2) late skarn; 3) oxide; 4) sulfide; and 5) late quartz–calcite (Figure 5, Figure 6, Figure 7). The mineral assemblage of the early

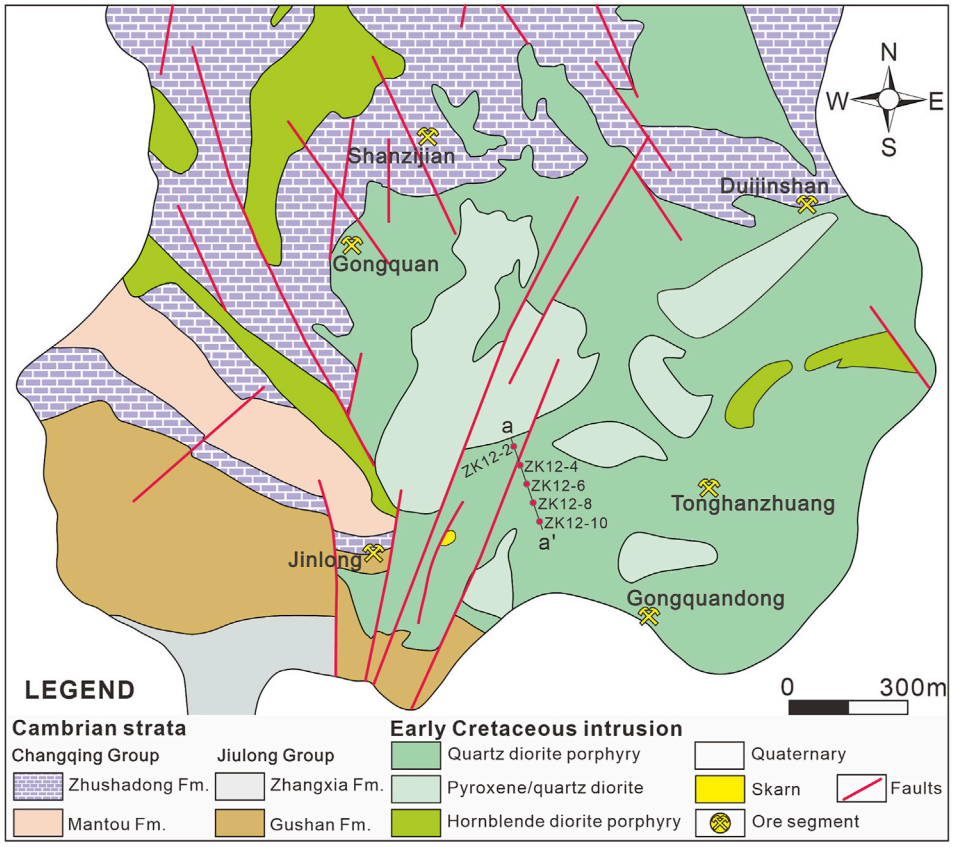


FIGURE 3
Geological map of the Yi'nan Tongjing Au–Cu deposit, modified after SDGM (2015) and Duan et al. (2020). The cross section of the exploration line (a-a') is shown in Figure 4B.

skarn stage consists mainly of anhydrous garnet, diopside and wollastonite. They are mainly present in striped, veinlet, and scarce relics in Au-Cu ores (Figures 5F,H). The coarse garnet is replaced by an epidote along the edge (Figure 6K). The wollastonite occurs as long-prismatic and platelike. As the main stage of Fe mineralization, the late skarn is characterized by the occurrence of epidote, tremolite, actinolite and magnetite (Figures 5B,E–G), which are widely developed in strips or blocks. Magnetite and epidote are filled by late pyrite, chalcopyrite and calcite along the gap between particles (Figures 6A,L). The oxide stage is marked by the pervasive occurrence of hematite, specularite and quartz, occurring in veinlets and lumpy, which is superimposed on the early skarn stage. Specularite is mostly acicular and cut by late sulfides or chlorite veins (Figures 5H, 6C), whilst hematite grew along the edge of magnetite. Pyrite and chalcopyrite as well as minor sphalerite and bornite occur in the sulfide stage (Figure 6B). These minerals often replace the skarn minerals (Figures 5B,E), occurring as interstitial fillings or cross-cut veins (Figures 5F,G, 6A). The gangue minerals in this stage include chlorite, quartz, sericite, fluorite and calcite. Chlorite is veined, striped or irregularly shaped and overprinted on the early reddish brown or dark green hornstone (Figure 5H). This is the main Au-Cu mineralization stage, and the formation of native gold is related to chalcopyrite and pyrite (Figures 6D–G). Gold is wrapped in pyrite and chalcopyrite in granular or irregular shape (Figures 6D,G; Supplementary Figure S1A,B), and occurs along the edge of euhedral pyrite (Figure 6E; Supplementary Figure S1D) or in quartz vein (Figure 6F; Supplementary Figure S1C,E). Stage IV is further divided into two sub-stages: Stage IV-a mainly includes pyrite and minor chalcopyrite, occurring in massive, disseminated or stripped, and quartz is rare in this sub-stage (Figure 5A); Chalcopyrite-pyrite-quartz veins occur in the stage IV-b, and these veins cut through the stage IV-a and earlier stages (Figures 5C,D,F–G). The quartz–calcite veins in stage V are poor in sulfides, and both they and fluorite veins cut early ores (Figure 5I, Figures 6K,L).

4 Samples and analytical methods

Twenty-two samples (21YNT01 to 21YNT22) in this investigation were selected from the Jinlong ore segment

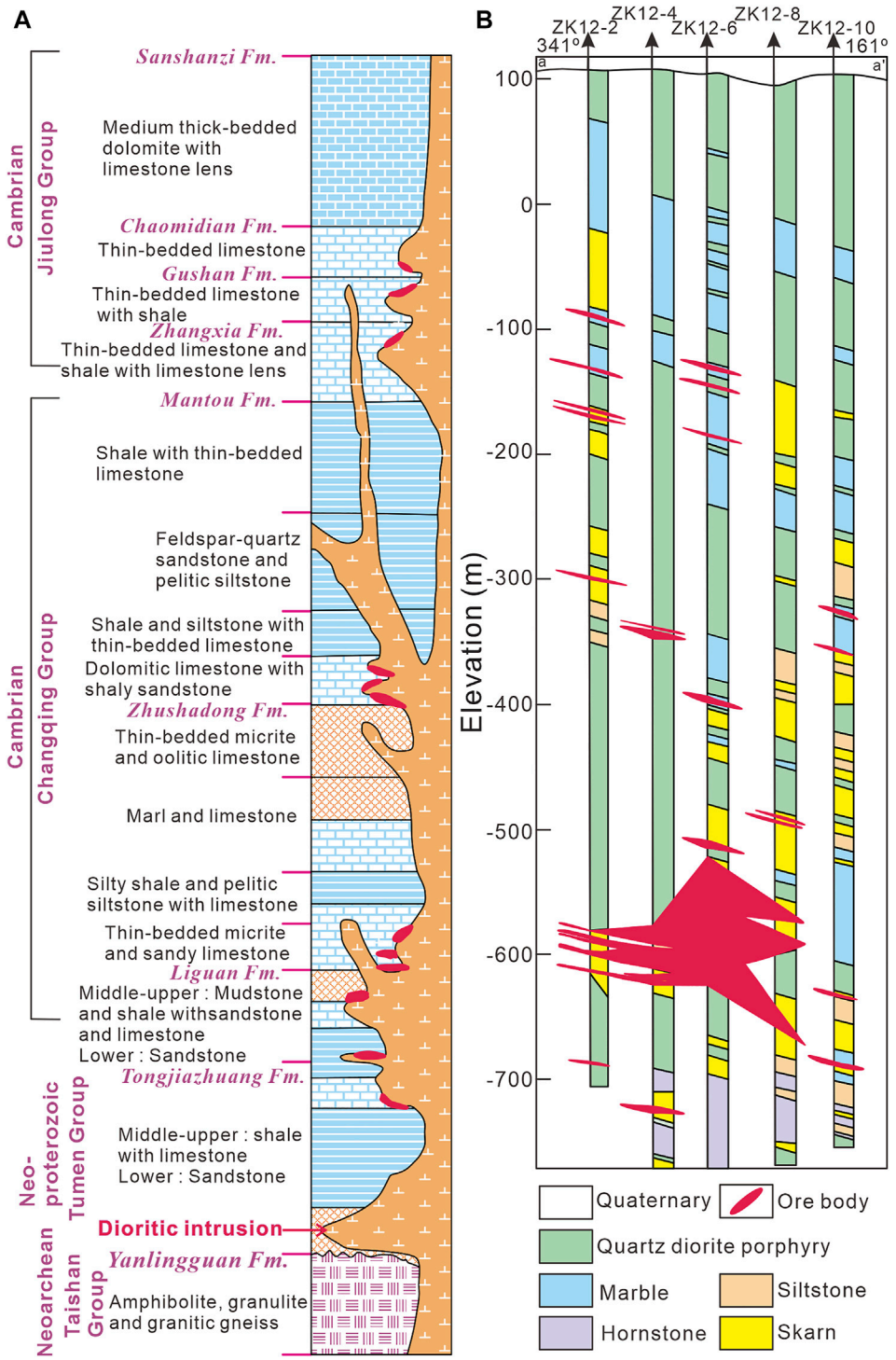


FIGURE 4
Sketch map showing the stratigraphy and the occurrence of ore bodies in the Yi'nan Au–Cu skarn deposit **(A)**, modified after Dong et al. (2008); Geological cross-section along exploration line 12 of Jinlong ore segment **(B)**, modified after SDGM (2015).

526 m level and the Gongquandong ore segment 180 m level. Forty-one polished thin sections with thicknesses of 30 and 50 μm for subsequent mineralogical and geochemical analyses. Pyrite, chalcopyrite, sphalerite and magnetite from Au-Cu ores were chosen for EPMA, LA–ICP–MS and *in-situ* S and Pb isotope analyses.

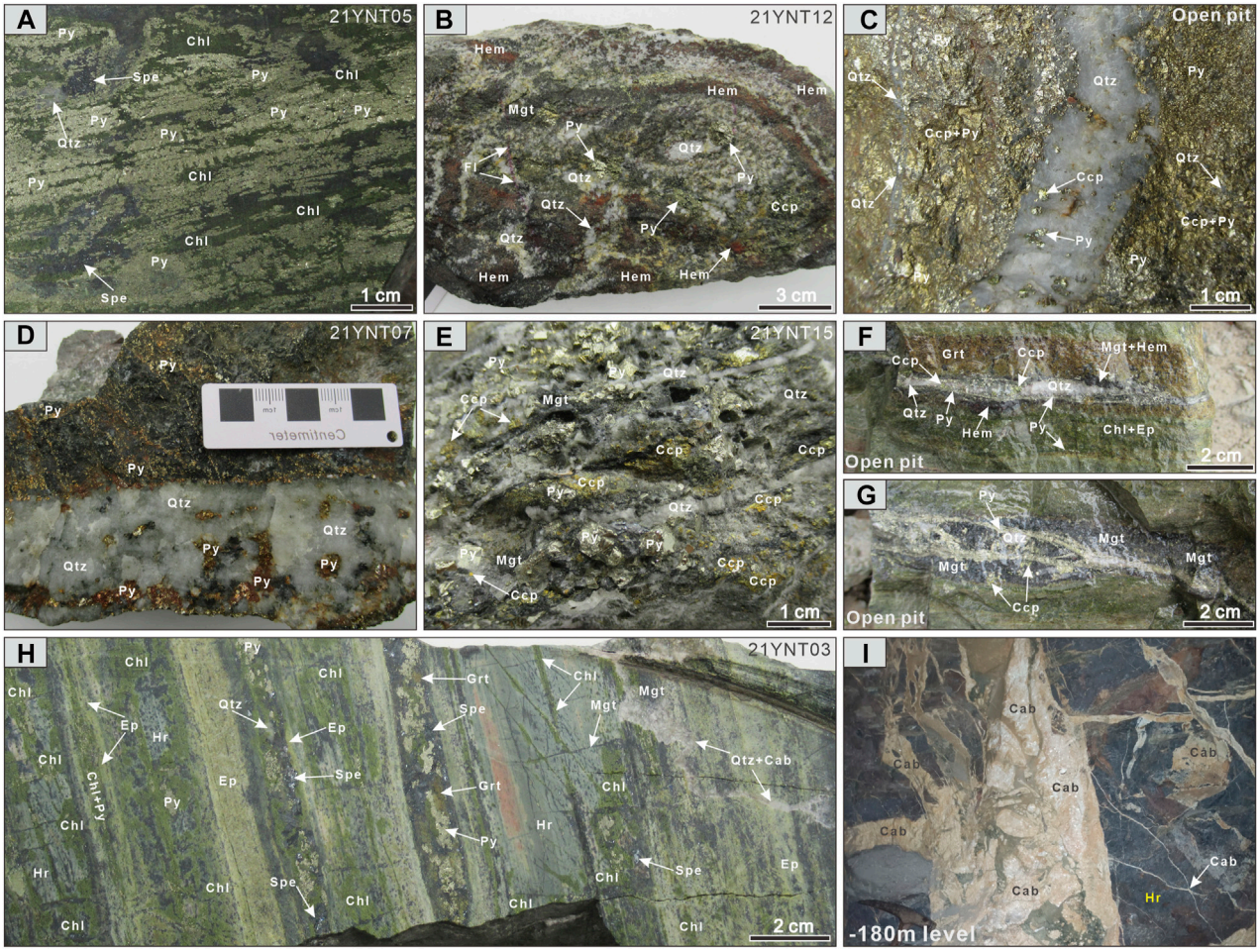


FIGURE 5
Photographs of hand specimens from the Tongjing Au–Cu deposit. **(A)** Striped Au ore with specularite precursor, accompanying chlorite and pyrite; **(B)** Au–Cu ore including chalcopyrite, pyrite and magnetite and hematite relic, cut by later quartz and fluorite veinlets; **(C)** Chalcopyrite–pyrite–quartz vein cutting the massive Au–Cu ore; **(D)** Pyrite–quartz vein cutting the disseminated Au ore; **(E)** Au–Cu ore with magnetite relics, crossed by later quartz veinlets; **(F,G)** Garnet or epidote skarn with magnetite and hematite, cut by chalcopyrite–pyrite–quartz vein; **(H)** Au–Cu ore showing striped sulfides and oxides, reddish and grey hornstone, epidote, chlorite and garnet relic. Most specularite and magnetite are replaced by pyrite *in situ*, the irregular (pyrite–) chlorite veins cutting hornstone or magnetite vein, with late carbonate–quartz vein cutting the ore; **(I)** Multistage carbonate veins cutting early dark grey hornstone. Abbreviations: Cab–carbonate; Ccp–chalcopyrite; Chl–chlorite; Ep–epidote; Fl–fluorite; Grt–garnet; Hem–hematite; Hr–hornstone; Mgt–magnetite; Py–pyrite; Qtz–quartz; Spe–specularite.

4.1 Electron probe microanalysis (EPMA)

Mineral compositions of gold, sulfides and oxides grains were analyzed by a Japan JEOL JXA-8320 electron probe with four wavelength-dispersive spectrometers at Shandong institute of geological sciences, Ji'nan, China. Gold and sulfides analyses were conducted using an accelerating voltage of 20 kV, a beam current of 20 nA and a beam size of 1 μm. Natural pyrite (S, Fe), chalcopyrite (Cu), sphalerite (Zn), galena (Pb), bismuth selenide (Bi, Se), antimony telluride (Te, Sb) and arsenopyrite (As) were used for standardization, while other elements (Co, Ni, Au, Ag) were standardized on metals. The operational voltage was 15 kV, with a beam current of 10 nA, and a diameter of 5 μm for oxides analyses. The standardized natural minerals and synthetic compounds were followed: magnetite (Fe), almandine (Al), jadeite (Si), diopside (Mg), rutile (Ti), rhodonite (Mn), celestite (Sr), nickel (Ni), vanadium (V), chromium trioxide (Cr), sphalerite (Zn). Raw data ZAF corrections were made with proprietary JEOL software. The minimum detection limit is usually <0.01 wt%.

4.2 LA-ICP-MS *in situ* trace element analysis

Element analysis of mineral in thin sections was conducted by LA–ICP–MS at Nanjing FocuMS Technology Co. Ltd.

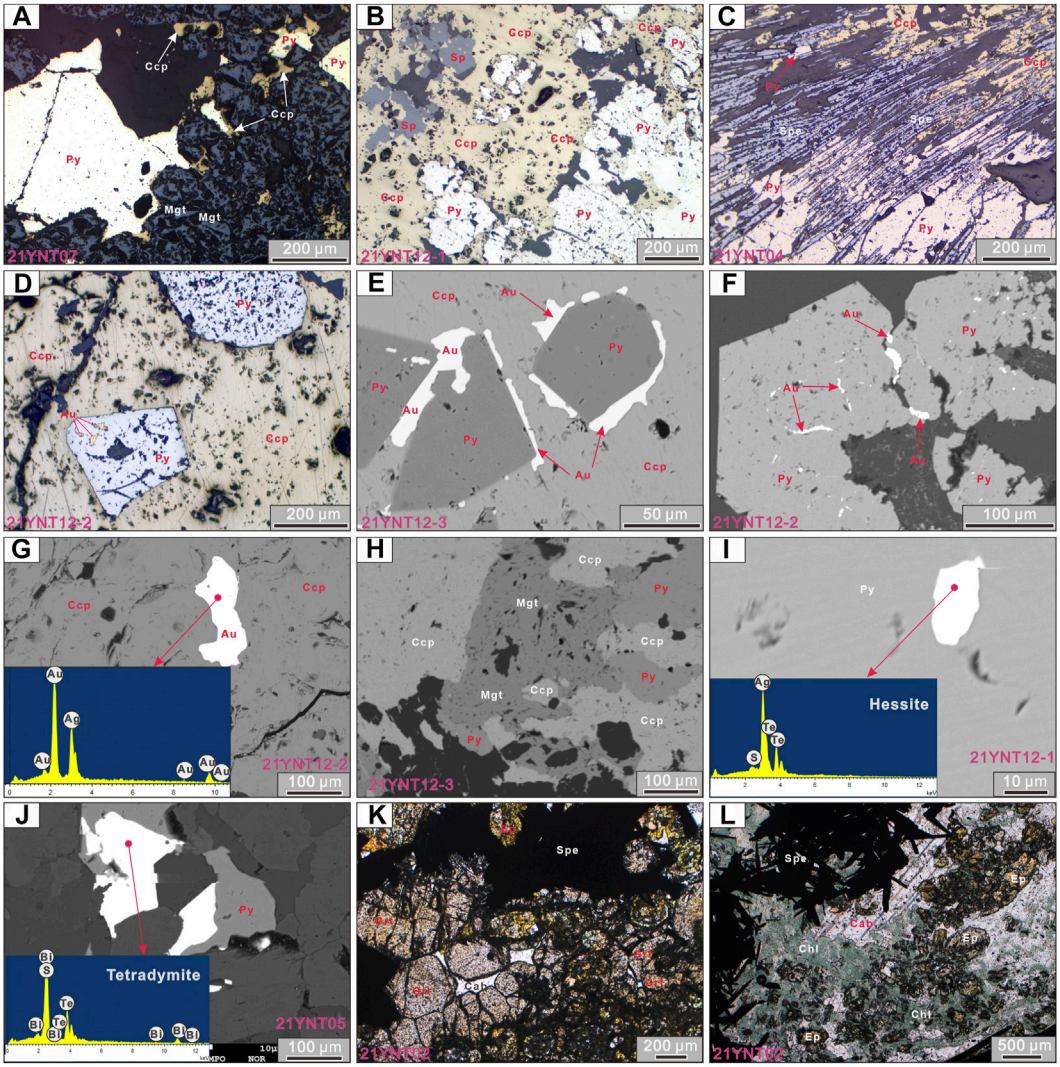


FIGURE 6
Photomicrographs of Au–Cu mineralization in Tongjing deposit. **(A)** Pyrite and chalcopyrite filled along the gap of subhedral magnetite; **(B)** Pyrite is replaced by chalcopyrite along the edges of pyrite, chalcopyrite overprinted by sphalerite; **(C)** Acicular specularite filled or replaced by pyrite and chalcopyrite; **(D)** Natural gold occurring in euhedral pyrite as irregular particles, they wrapped by chalcopyrite; **(E)** Irregular or granular natural gold grew along the outer edge of euhedral pyrite, they appearing in chalcopyrite in BSE images; **(F)** Irregular stripped native gold occurring in fissures inside the euhedral pyrite in BSE images; **(G)** Silver-bearing natural gold wrapped in chalcopyrite in BSE images; **(H)** Chalcopyrite, pyrite and early residual magnetite occurring in Au–Cu ores; **(I)** Pyrite containing spindle-shaped hessite; **(J)** Pyrite and tetradymite growing together; **(K)** Carbonate veins filled along the gap of euhedral garnet, epidote replacing garnet around the edge of garnet; **(L)** Epidote, chlorite and carbonate alterations with specularite. Sp–sphalerite; Au–native gold; other abbreviations as for Figure 5.

LA–ICP–MS analyses of metal oxides and sulfides were performed using a Teledyne Cetac Analyte Excite laser-ablation system coupled to an Agilent 7,700× quadrupole ICP–MS. The 193 nm ArF excimer laser was focused on the surface of oxides and sulfides, with a fluence of 6.0 J/cm^2 and 3.0 J/cm^2 respectively. Each acquisition incorporated 20 s background (gas blank), followed by a spot diameter of 40 um at 6 Hz (oxides) or 5 Hz (sulfides) repetition rate for 40 s. Helium (370 ml/min) was applied as a carrier gas to efficiently transport aerosol and was mixed with argon (~1.15 L/min) *via* T-connector before entering the ICP torch.

Forty-one isotope signals in sulfide were collected in this experiment, and the values were calculated by using MASS-1 and GSE-1G as an external standard and no internal standard. For oxide, United States Geological Survey basaltic glasses, including BIR-1G, BHVO-2G, BCR-2G and GSE-1G, were used as external calibration standards as these are of the similar matrix as anhydrous silicate. Raw data was performed offline by

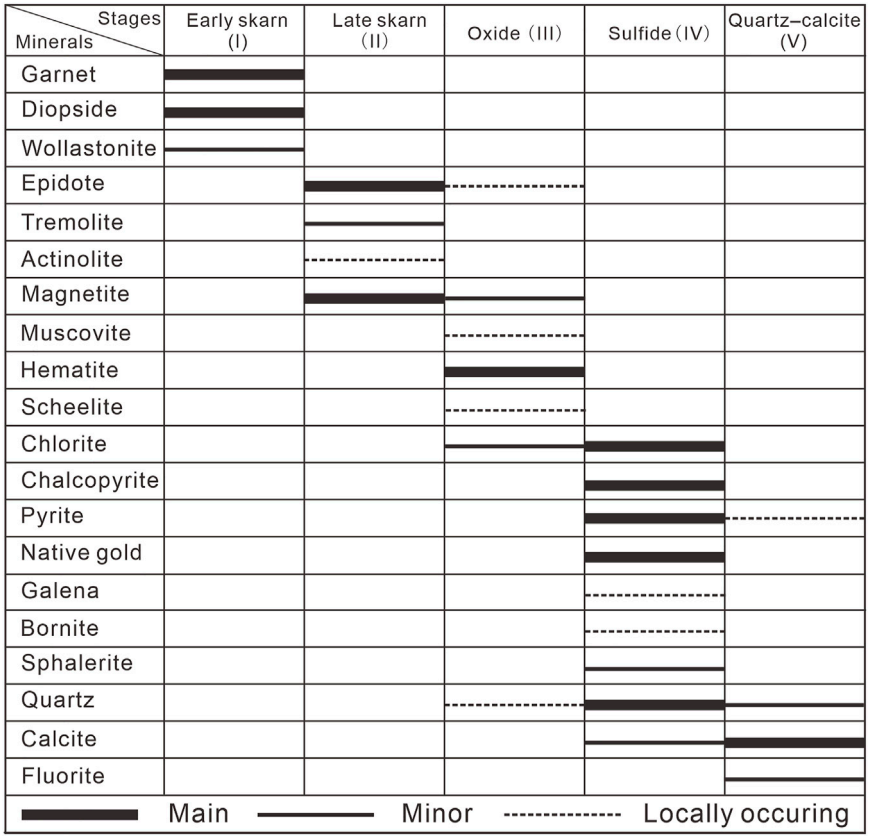


FIGURE 7
Mineral paragenesis for the Yi'nan Tongjing Au–Cu deposit.

ICPMSDataCal software (Liu et al., 2008). The precision of each analysis is better than 20% for the most elements.

4.3 *In-situ* S isotope analysis

In-situ sulfur isotope spot analysis of sulfides (pyrite and chalcopyrite) was carried out at Nanjing FocuMS Technology Co. Ltd., utilizing an Analyte Excite laser-ablation system (Bozeman, Montana, United States) and a Nu Plasma II MC–ICP–MS (Wrexham, Wales, United Kingdom). The 193 nm ArF excimer laser was focused on the surface with a spot of 50 μm pit size for chalcopyrite, 33 μm for pyrite and 40 μm for sphalerite, 5 Hz pulse frequency and 2.5 J/cm^2 fluences. The single spot was ablated for 30 s collection of background signal and 35 s data. The integration time of Nu Plasma II was set to 0.3 s (equating to 115 cycles during the 35 s). Natural pyrite Wenshan ($\delta^{34}S$ = +1.1‰) was used as an external bracketing standard every fourth analysis to ensure precision and account for instrument drift. Pressed powder pellets of pyrite GBW07267 and chalcopyrite GBW07268 ($\delta^{34}S$ = +3.6‰, −0.3‰ respectively, from the National Research Center for Geoanalysis, China) and fine-grained sphalerite SRM 123 ($\delta^{34}S$ = +17.5‰, from National Institute of Standards and Technology, U.S) were treated as quality control. All measurements are presented relative to CDT, and the long-term reproducibility of $\delta^{34}S$ is better than 0.6‰ (1 Standard Deviation).

4.4 *In-situ* Pb isotope analysis

The *in-situ* lead isotope analyses of pyrite were performed on a Neptune Plus MC–ICP–MS (Thermo Fisher Scientific, Bremen, Germany) equipped with a Geolas HD excimer ArF laser ablation system (Coherent, Göttingen, Germany) at the Wuhan Sample Solution Analytical Technology Co., Ltd., Hubei, China. The spot diameter ranged from 60 to 90 μm dependent on Pb signal intensity, with 8 Hz pulse frequency and 6.0 J/cm^2 fluence. A new signal-smoothing and mercury-removing device were used downstream from the sample cell to efficiently eliminate the short-term variation of the signal and remove the mercury from

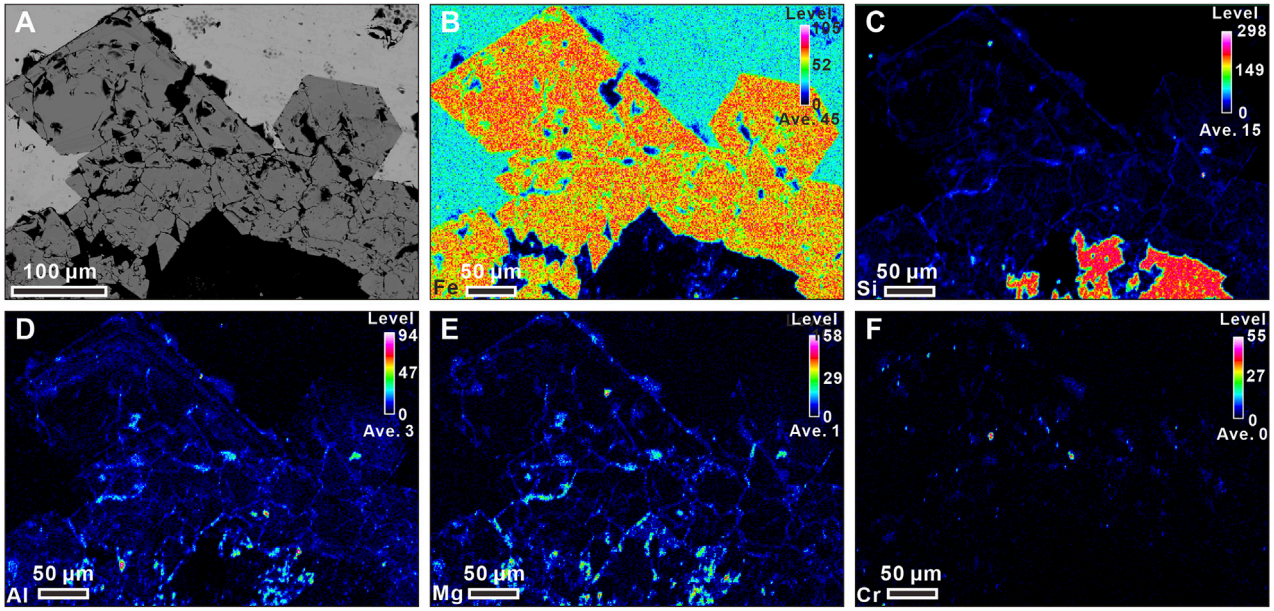


FIGURE 8
BSE image **(A)** and maps of Fe **(B)**, Si **(C)**, Al **(D)**, Mg **(E)** and Cr **(F)** in zoned magnetite from Tongjing Au-Cu deposit.

the background and sample aerosol particles (Hu et al., 2015). Sph-HYLM as an external standard was used to monitor the precision and accuracy of the measurements. The obtained accuracy is estimated to be equal to or better than ±0.2‰ for $^{208}Pb/^{204}Pb$, $^{207}Pb/^{204}Pb$, and $^{206}Pb/^{204}Pb$, with an external precision of 0.4‰ (2σ). More detail of the *in-situ* Pb isotopic ratios analysis was described. All data reduction for the MC–ICP–MS analysis of Pb isotope ratios was conducted using "Iso-Compass" software (Zhang et al., 2020).

5 Results

5.1 Major element compositions analyzed by EPMA

A total of 76 EPMA analyses spots were completed on single particles of metal oxides and sulfides, including 45 spots of pyrite, 12 spots of chalcopyrite, 4 spots of sphalerite from the stage IVa and IVb and 15 spots of magnetite as euhedral-subhedral octahedron in stage II or relics in stage IV. The above EPMA results are listed in Supplementary Table S1.

The Fe content of the magnetite ranged from 65.39 to 71.33 wt%, lower than the stoichiometric value of 72.40 wt%. In general, the trace element contents for the magnetite vary from below detection limits to ~2 wt% (Supplementary Table S1). Silicon, Mg and Al contents of magnetite are 0.17–1.70 wt% (avg. 1.24 wt%), 0–0.57 wt% (avg. 0.23 wt%) and 0–0.75 wt% (avg. 0.36 wt%). EPMA elements mappings of magnetite show the oscillatory variation of Si, Al and Mg (Figure 8), indicating a change in the composition of ore-forming fluid.

Iron and S contents of pyrite are 46.11–46.75 wt% (avg. 46.42 wt%) and 53.32–53.62 wt% (avg. 53.49 wt%) in stage IVa, 40.49–46.78 wt% (avg. 45.38wt%) and 51.72–53.29 wt% (avg. 53.35 wt%) in stage IVb. The contents of Fe, Cu, S and Zn in chalcopyrite from stage IVb are 28.55–30.12 wt% (avg. 29.64 wt%), 33.39–34.83 wt% (avg. 34.26 wt%), 33.52–35.11 wt% (avg. 34.44 wt%) and 0.01–1.51 wt% (avg. 0.21 wt%), respectively. Zinc and S contents of sphalerite are 51.36–59.13 wt% (avg. 55.73 wt%) and 32.38–32.83 wt% (avg. 32.62 wt%) in stage IVb, with a Fe content of 3.74–7.07 wt% (avg. 4.94 wt%) and a Cu content of 3.54–7.84 wt% (avg. 5.25 wt%).

The fineness [1,000·Au/(Au+Ag), by weight; Hough et al. (2009)] of Au grains has been calculated based on EPMA results (n = 11), with the detailed data in Supplementary Table S1. The two generations of visible gold have distinct characteristics in mineral assemblage and composition (Supplementary Table S1). Au-1 exhibits irregular droplets and is wrapped by chalcopyrite and euhedral pyrite (Figures 6D,G; Supplementary Figure S1A,B), and the Au content of Au-1 (85.94–97.02 wt%, avg. 91.16 wt%) is significantly higher than that of Au-2 (62.03–84.91 wt%, avg. 71.70 wt%). Au-2 mainly occurs at the edge of pyrite or in pyrite–quartz vein (Figures 6E,F; Supplementary Figure S1C,E), and the Au-2 has a higher Ag content (14.65–29.68 wt%, avg. 24.24 wt%) than the Au-1 (1.51–7.51 wt%, avg. 5.88 wt%). The average fineness of Au-1

and Au-2 is 939.17 (919.65–984.69, n = 5) and 745.68 (690.28–852.89, n = 6), respectively. According to the gold and silver series mineral classification (Zhang and Chen, 1995), the Au fineness indicates that Au-1 and Au-2 belong to the high-medium temperature Au–Ag series in the Yi'nan Tongjing Au–Cu deposit.

5.2 Trace element chemistry by LA–ICP–MS

The 98 individual LA–ICP–MS spots were analyzed for the pyrite, chalcopyrite, sphalerite and magnetite relics from Au-Cu ores. The analytical results are presented in Supplementary Table S2 and Figures 9, 11–13 and Supplementary Figure S1, S2. We selected chalcopyrite and pyrite with no inclusions for analysis to obtain precise results.

5.2.1 Magnetite

The lithophile elements in magnetite grains include Na (179–380 ppm, avg. 251 ppm), Mg (27.06–186 ppm, avg. 109 ppm), Al (146–4,427 ppm, avg. 2069 ppm), Si (7,316–116616 ppm, avg. 8,965 ppm), K (202–605 ppm, avg. 371 ppm), Ti (15.44–283 ppm, avg. 113 ppm), Sr (8.04–17.30 ppm, avg. 12.14 ppm) and Ba (5.20–20.60 ppm, avg. 10.15 ppm). Magnetite has a high content of chalcophile elements, including Cu (4.74–1,199 ppm, avg. 216 ppm), Zn (19.51–81.83 ppm, avg. 50.74 ppm), Ga (1.83–13.12 ppm, avg. 7.47 ppm), In (0.38–13.71 ppm, avg. 3.72 ppm) and Pb (9.12–66.76 ppm, avg. 27.82 ppm). The contents of As (319–1,456 ppm, avg. 703 ppm), Ni (39.39–369 ppm, avg. 182 ppm), Cr (12.35–1,416 ppm, avg. 236 ppm), W (5.39–176 ppm, avg. 86.34 ppm) and Mo (6.52–65.48 ppm, avg. 34.77 ppm) in magnetite are relatively high, and the Ca content is lower than the detection limit.

5.2.2 Pyrite

Pyrite in stage IVa has large compositional variations (Supplementary Table S2, Figure 9). The contents of Co (75.60–285 ppm, avg. 146 ppm), Ni (1.22–6.01 ppm, avg. 2.99 ppm), As (50.10–104 ppm, avg. 84.20 ppm), Se (1.99–3.36 ppm, avg. 2.64 ppm) and Te (7.55–56.53 ppm, avg. 21.01 ppm) are distinctly higher than other trace elements in pyrite, such as Cu (3.60 ppm), Zn (1.13 ppm) and Au (0.02–0.13 ppm, avg. 0.06 ppm). Compared with pyrite in stage IVa, pyrite in stage IVb contains relatively higher trace elements (Co (350–84521 ppm, avg. 39,259 ppm), Ni (25.06–13117 ppm, avg. 2,408 ppm), Cu (0.55–5,227 ppm, avg. 582 ppm), Se (16.49–215 ppm, avg. 43.26 ppm), Ag (0.24–3,921 ppm, avg. 443 ppm), Bi (0.45–3,641 ppm, avg. 201 ppm), Pb (0.06–7,021 ppm, avg. 271 ppm), Te (1.77–3,877 ppm, avg. 257 ppm), As (1.08–4,899 ppm, avg. 842 ppm), Zn (1.02–28.15 ppm, avg. 4.65 ppm; 309–674 ppm, avg. 455 ppm), Au (0.05–444 ppm, avg. 28.42 ppm), and Sb (0.07–2.01 ppm, avg. 0.48 ppm)).

5.2.3 Chalcopyrite

Trace element data of chalcopyrite from stage IVb are shown in Figure 9. The contents of Zn (3.80–2,799 ppm, avg. 979 ppm), Co (0.36–5,839 ppm, avg. 410 ppm), Ni (0.27–2,451 ppm, avg. 177 ppm), Ag (8.80–72.34 ppm, avg. 34.02 ppm), Pb (1.50–42.00 ppm, avg. 20.54 ppm), Bi (2.45–31.07 ppm, avg. 11.42 ppm) and Se (12.23–28.61 ppm, avg. 21.90 ppm) from chalcopyrite are distinctly higher than other trace elements (Figure 9). The contents of Ti, As, Cd, In, Sn, Sb, Te and Au from chalcopyrite are 0.87–2.34 ppm (avg. 1.45 ppm), 1.15–111 ppm (avg. 32.86 ppm), 0.30–12.05 ppm (avg.4.91 ppm), 2.00–3.74 ppm (avg. 3.11 ppm), 0.71–3.40 ppm (avg. 1.70 ppm), 0.23–1.91 ppm (avg.0.57 ppm), 1.22–28.62 ppm (avg. 8.26 ppm), and 0.03–1.09 ppm (avg. 0.22 ppm), respectively (Supplementary Table S2, Figure 9).

5.3 Sulfur and lead isotope compositions

Sulfur isotope compositions were determined in chalcopyrite and pyrite by LA–MC–ICP–MS, and the results are listed in Supplementary Table S3, Supplementary Figure S2 and plotted in Figure 10A,B. In general, the sulfur isotope compositions of different sulfides are consistent and fall within a narrow $\delta^{34}S$ range of -0.54 to +1.22‰ (avg. 0.44‰, n = 38). The $\delta^{34}S$ values of pyrite in stage IVa and stage IVb are -0.54 ~ +0.95‰ (avg. 0.24‰, n = 8) and 0.11 ~ +1.22‰ (avg. 0.65‰, n = 18), respectively; the $\delta^{34}S$ values of chalcopyrite in stage IVb range from -0.19 to +0.73‰ (avg. 0.26‰, n = 12). The *in-situ* Pb isotopic ratios of pyrite in stage IVb are presented in Supplementary Table S4, Supplementary Figure S2 and Figure 10C,D, and the $^{206}Pb/^{204}Pb$, $^{207}Pb/^{204}Pb$ and $^{208}Pb/^{204}Pb$ ratios are 17.323–17.383, 15.424–15.452 and 37.367–37.454, respectively (n = 12).

6 Discussion

6.1 Element behavior during the skarn formation process

6.1.1 Magnetite

There are weak positive correlations between Al (Mg, Na) and Si in magnetite (Supplementary Figure S1), which may indicate the absence of sub-micro-scale silicate inclusions in magnetite (Bowles et al., 2011; Xie et al., 2017), consistent with their flat depth profiles (Figure 13A). Considering magnetite with pervasive micro-porosities is wrapped in metal sulfide (Figure 6H), magnetite in Tongjing deposit was interpreted as a hydrothermal overprint that may have

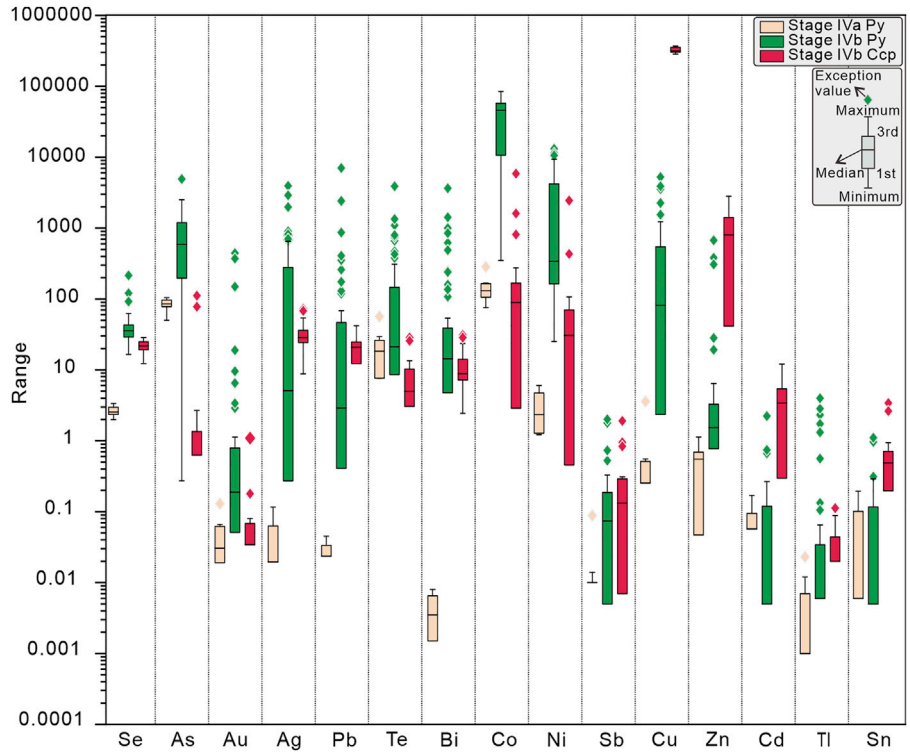


FIGURE 9
Trace element distribution diagram showing the variation in the Se, As, Au, Ag, Pb, Te, Bi, Co, Ni, Sb, Cu, Zn, Cd, Tl, and Sn concentrations (in ppm) for pyrite and chalcopyrite.

leached Mg, Si, Al and Ca during the dissolution–reprecipitation process (Hu et al., 2014). Positive correlations exist for Sn vs W, Pb vs W and Sn vs Pb (Figure 11A–C) showing that these elements behave similarly during the skarn formation process. A correlation between Al and Ga (Figure 11D) indicates similar geochemical behaviors (Huang et al., 2016). The contents of Co, Ni, Mo, Cu, Zn and Pb in magnetite would be affected by sulfides because these elements can partition into magnetite and sulfide phases in sulfide-bearing magmatic and hydrothermal systems (Huang et al., 2016). Pyrrhotite and pentlandite do not occur in the Tongjing deposit, so Ni tends to partitioned into magnetite (Dare et al., 2012), with a high content of Ni (39–369 ppm; avg. 182.2 ppm; n = 9) in magnetite. The low Co content of magnetite in the Tongjing and a positive correlation of Cu vs Co (Figure 11E) imply the increasing amounts of sulfides during the skarn formation (Huang et al., 2014; Zhao and Zhou, 2015), consistent with the fact that magnetite is wrapped by pyrite (Figure 6H).

6.1.2 Sulfide (pyrite and chalcopyrite)

Although the As content of pyrite in stage IVa is lower than in stage IVb, all points plot well below the solubility saturation line on the Au-As discrimination diagram (Figure 12) proposed by Reich et al. (2005), suggesting that Au^{+} is the dominant form of Au within the pyrite crystal lattice and that gold-bearing ore fluids deposited this sulfide were largely undersaturated (Reich et al., 2013). Arsenic is relatively rich in pyrite, generally greater than 20 ppm. A positive correlation exists between As and Au (Figure 12A) as described by numerous scholars (Mumin et al., 1994; Reich et al., 2005; Deditius et al., 2014), which is related to the preferential precipitation of Au in the As-rich sulfides (Voute et al., 2019). The above positive correlation indicates As could enter the pyrite lattice through coupled substitution with Au ($Au^{+} + As^{3+} \leftrightarrow 2Fe^{2+}$; Deditius et al., 2008), illustrated by the fact that As has a flat depth profile (Figures 13C,D) and the negative correlation between As and Fe (Figure 12B).

The Co and Ni contents of pyrite in stage IVb are higher than those in stage IVa and they have nearly flat depth profiles (Figures 13B–E). The atomic radius and ionic charge of Co and Ni are very close to Fe^{2+} (Vaughan and Rosso, 2006; George et al., 2018b), indicating that Co and Ni were lattice-bound or homogeneously distributed as nanoparticles in the pyrite crystals (e.g., Zhang et al., 2022). Almost all pyrite are below the Au solubility line

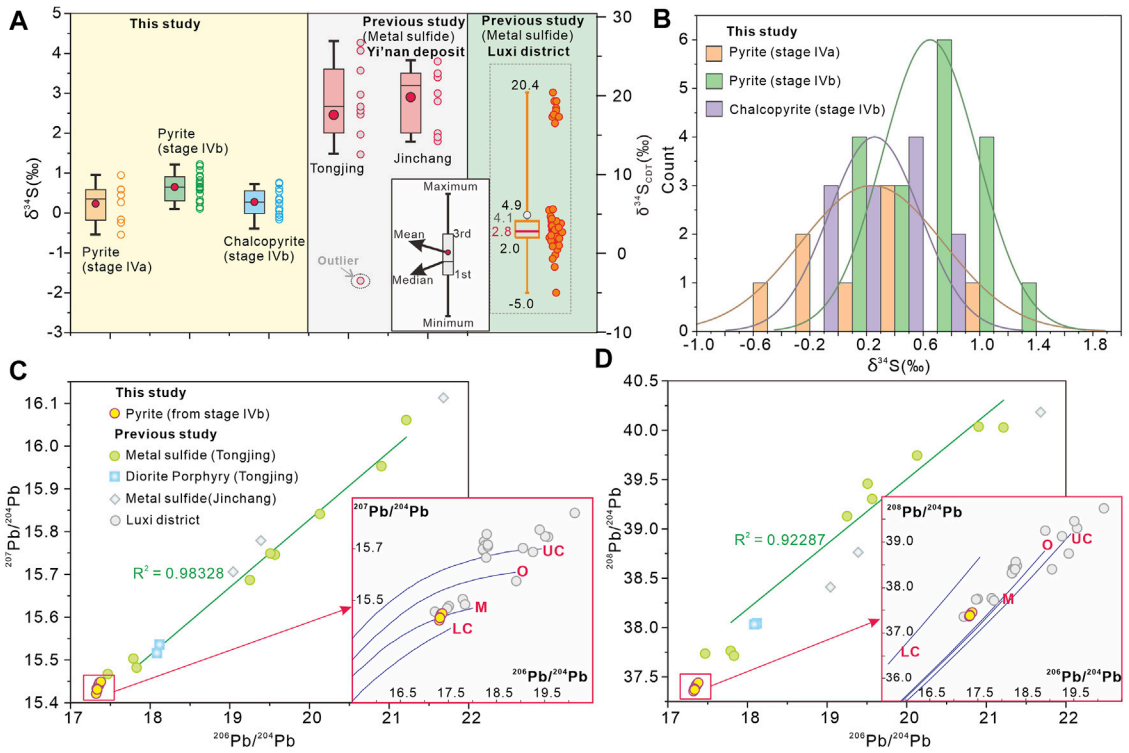


FIGURE 10
(A). Sulfur isotope compositions of various sulfide minerals in the Yi'nan Tongjing Au-Cu deposit; **(B)**. The histogram of sulfur isotope compositions; **(C)**. $^{206}Pb/^{204}Pb$ vs $^{207}Pb/^{204}Pb$ diagram; **(D)**. $^{206}Pb/^{204}Pb$ vs $^{208}Pb/^{204}Pb$ diagram (Zartman and Doe, 1981). The data from the previous study were obtained from Wan et al., 1992; Qiu et al., 1996; Lin et al., 1997; Hu et al., 2007; Li et al., 2009; Shi, 2014; Zhu, 2014; Tian et al., 2015; Abbreviations: LC = lower crust; UC = upper crust; O = orogen; M = mantle.

(Figure 12A) but above the Te solubility line (Figure 12C), despite the fact that the Te content of pyrite in stageIVb is higher than stage IVa. Hence, potential telluride inclusions may be characterized by high Te/Au ratios either due to high Te content or high abundances of other elements, such as Cu, Ag, Pb and Bi (e.g., high-sulfidation epithermal pyrite; Naden and Henney, 1995; Berger et al., 2014). Tellurium of pyrite in stage IV is positively correlated with Bi ($R^2 = 0.57$, Figure 12D) but also with Ag ($R^2 = 0.79$, Figure 12E), which may be related to the occurrence of Bi-Te or Ag-Te mineral inclusions. The identification of the hessite (Ag_2Te), cervelleite (Ag_4TeS) and tetradymite (Bi_2Te_2S) by microscopic observation (Figures 6I,J; Supplementary Figure S1F) and their similar peaks and irregular depth profiles (Figures 13B–D) prove the above conclusion. It is also worth noting that the concentrations of Ag, Bi and Pb are highly variable in pyrite and chalcopyrite (Supplementary Table S2), and they are significantly positively correlated (Figures 12F,G). The ionic radius of Ag, Pb and Bi are quite different from those of Cu and Fe (Wang et al., 2021), thus they cannot enter the lattice of chalcopyrite or pyrite in the form of a solid solution. Furthermore, they have similar peaks and irregular depth profiles (Figure 13E), probably due to the micron-scale inclusions of matildite ($AgBiS_2$), galenobismutite ($PbBi_2S_4$) and gustavite ($AgPbBi_3S_6$) or bismuth-bearing galena (Maslennikov et al., 2009). Almost all pyrite, chalcopyrite and sphalerite samples show elevated Bi content (>1 ppm) (Figure 12H), which probably reflects the contribution of sedimentation to the hydrothermal system (Koski et al., 1988; Zierenberg et al., 1993). This is consistent with the fact that Proterozoic to Cambrian carbonate sequences was involved during the formation of the Tongjing skarn deposit.

Given the high contents of Co (350–84521 ppm) and Ni (25–13117 ppm) in stage IVb pyrite, the high Co and Ni contents in stage IVb chalcopyrite may be due to the inheritance of the replaced pyrite in stage IVb (Figure 6H; e.g., the Yaman-Kasy volcanic-hosted massive sulfide deposit; Maslennikov et al., 2009). The contents of As, Co and Ni in chalcopyrite vary greatly (Supplementary Table S2) and generally show a similar peak on the depth profiles (Figures 13F,G), suggesting the existence of inclusions, for example siegenite ($CoNi_2S_4$). The high Zn content in chalcopyrite (mostly >100 ppm) may be attributed to the

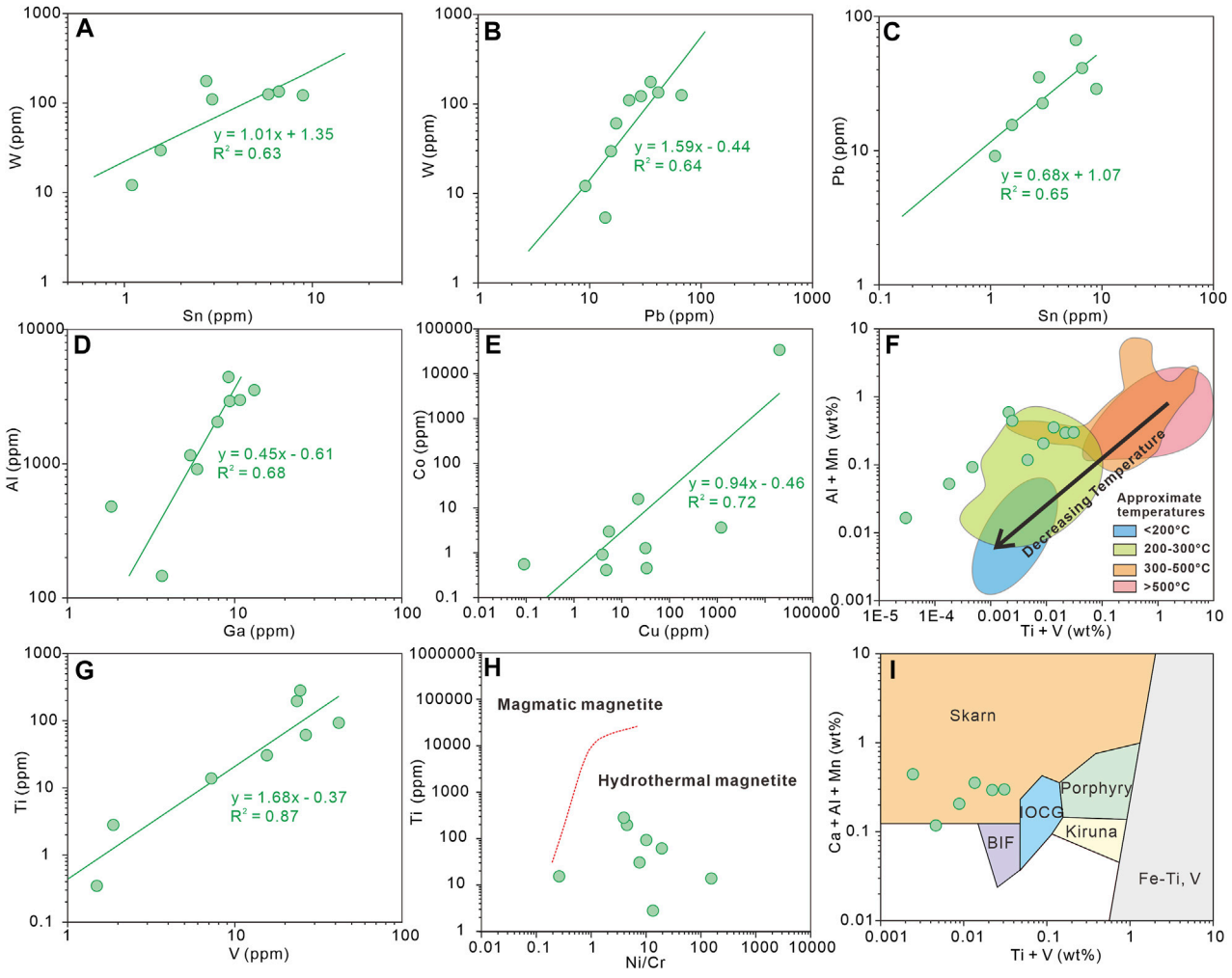


FIGURE 11
Correlation diagrams of various trace elements (in ppm) in the studied magnetite from the Yi'nan Tongjing Au–Cu deposit. **(A)** Sn vs W; **(B)** Pb vs W; **(C)** Sn vs Pb; **(D)** Ga vs Al; **(E)** Cu vs Co; **(F)** The Ti + V vs Al + Mn plots displays are clear decreasing temperature trend. Note that those temperatures are estimates based on published values (Ahmad and Rose, 1980; Beane and Titley, 1981; Leach et al., 1988; Hayes, 1990; Landis and Hofstra, 1991; Doughty and Chamberlain, 1996; Manske and Paul, 2002; Audetat and Pettke, 2006; Thorne et al., 2008; Sillitoe, 2010; Nadoll et al., 2012); **(G)** V vs Ti; **(H)** Ni/Cr vs Ti; **(I)** Ti + V vs Ca + Al + Mn (Dupuis and Beaudoin, 2011). Abbreviations: BIF–Banded iron formation, IOCG–Iron oxide-copper-gold deposits, PCDs–Porphyry Cu deposits, Kiruna–Kiruna apatite–magnetite deposits, Fe–Ti, V–Magmatic Fe–Ti–oxide deposits.

inclusion of sphalerite or zinc-bearing minerals (e.g., Song et al., 2019). Furthermore, the Zn vs Cd diagram (Figure 12I) shows a positive correlation between the two elements in chalcopyrite, and they share the same irregular depth profiles (Figure 13H). This also suggests that the Zn content reflects the proportion of sphalerite inclusions. In addition, the multi-peaked curve of Zn on the depth profiles (Figures 13F–H) implies the presence of zinc-bearing minerals inclusions in chalcopyrite. Chalcopyrite samples with high Ag/As ratios plotting outside of the triangular wedge-shaped zone (Figure 12J) may suggest the presence of silver-bearing inclusions, as supported by a positive correlation between Pb and Ag (Figure 12F).

6.2 Possible factors controlling the composition of magnetite and sulfides

It is well known that oxygen fugacity (f_{O2}) is a major factor that governs element behavior and possibly influenced Au speciation during the ore-forming process (e.g., Keith et al., 2014; Ma et al., 2022). The content of V in magnetite can be used to estimate the relative oxygen fugacity during the ore-forming process (Nadoll et al., 2014, 2015; Canil et al., 2016), and increasing oxygen fugacity would decrease the V content in magnetite by converting V^{3+} to V^{4+} or V^{5+}(Takeno, 2005; Papike et al., 2015). The low V content in magnetite varies from 1.50 ppm to 41.87 ppm (avg. 18.06 ppm), implying a

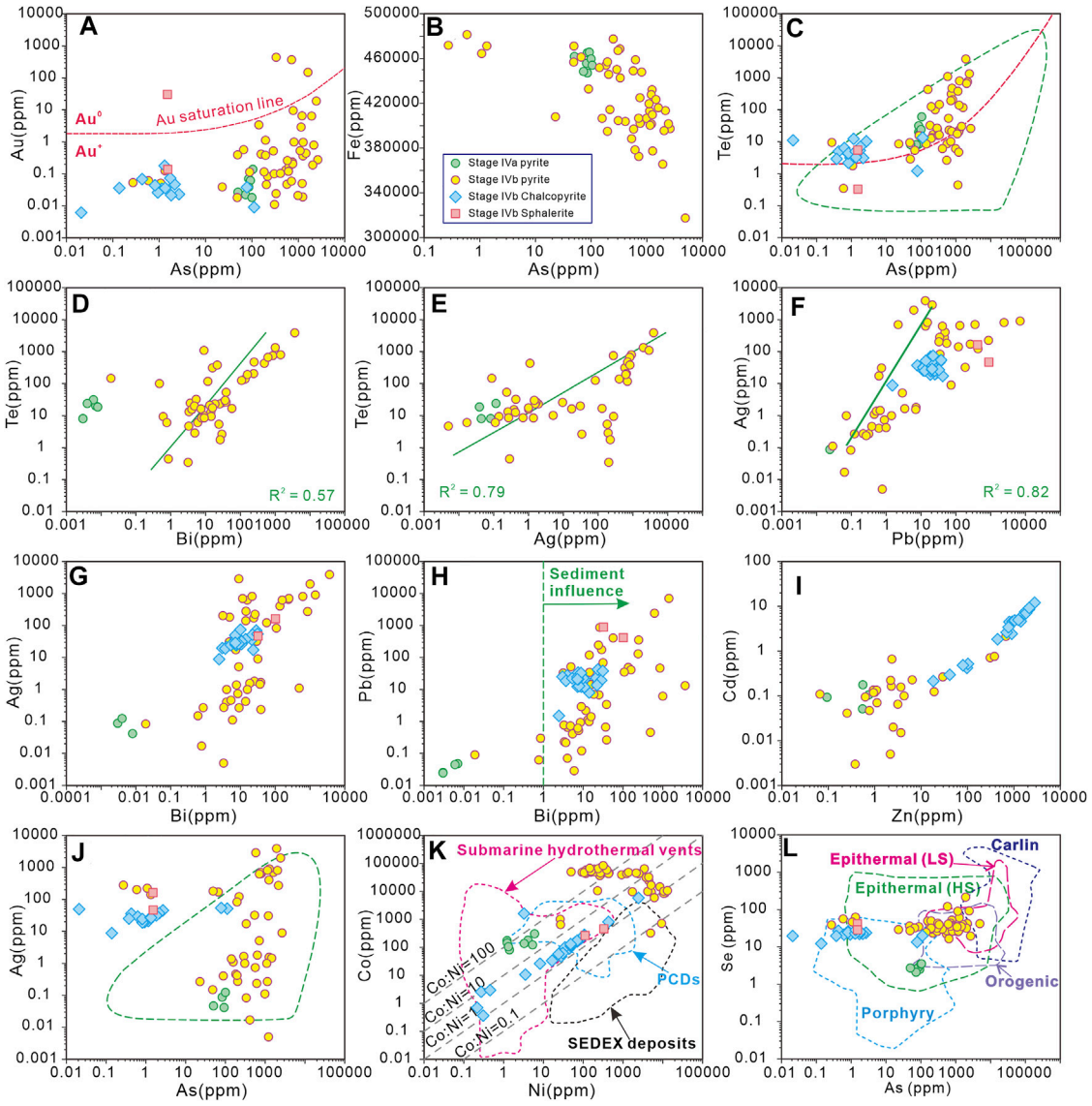


FIGURE 12
Plots of various trace elements in the studied pyrite from the Yi'nan Tongjing Au–Cu deposit. **(A)** Au vs As (Gold saturation line is from Reich et al., 2005); **(B)** As vs Fe; **(C)** As vs Te (The green dashed line defines the wedge-shaped zone indicating Te solid solution for pyrites. The red dashed line defines the solubility limit for Te solid solution in pyrite as a function of As, which is based on the equation presented by Reich et al. (2005) for the Au-As system.); **(D)** Bi vs Te; **(E)** Ag vs Te; **(F)** Pb vs Ag; **(G)** Bi vs Ag; **(H)** Bi vs Pb (after Keith et al., 2016); **(I)** Zn vs Cd; **(J)** As vs Ag (The green dashed line define the wedge-shaped zone indicating Ag solid solution for pyrites; Reich et al., 2005); **(K)** Ni vs Co (Deditius et al., 2013; Cioacă et al., 2014; Keith et al., 2016); (L) As vs Se (Gadd et al., 2016; Mukherjee and Large, 2017; Keith et al., 2018 and references therein).

high oxygen fugacity. Temperature is considered another major governing factor for the composition of hydrothermal magnetite, and Ti is a good temperature indicator (Nadoll et al., 2014). There is a visible temperature trend in the data. Figure 11F shows a Ti + V vs Al + Mn plot where data points have been attributed with approximate temperatures—from low temperature (Thorne et al., 2008), intermediate temperature to high temperature (e.g., Manske and Paul, 2002; Sillitoe, 2010). The magnetite grains mainly fall in the overlapping area of medium temperature (200–300°C) and high temperature (300–500°C), higher than the formation temperature of pyrite (see below).

Selenium in pyrite can be used as a proxy for relative temperature estimations in ore-forming fluids (Huston et al., 1995; Keith et al., 2018). Selenium can substitute for S in pyrite (Chouinard et al., 2005), and its concentration increases as fluid temperature decreases (Keith et al., 2018). Selenium is nearly completely removed from the fluid at temperatures above 300°C (Huston et al., 1995). Compared with the Se content

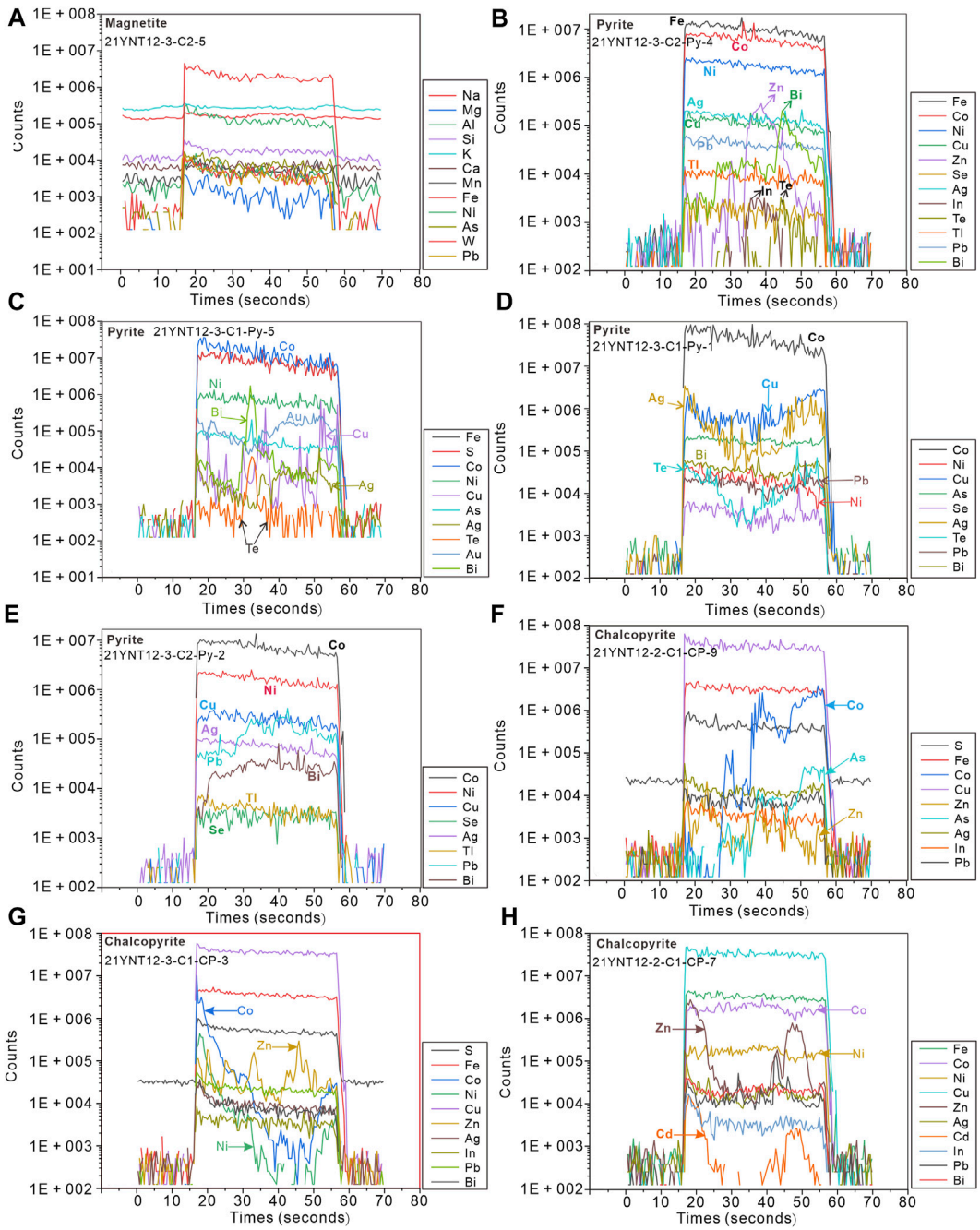


FIGURE 13
Representative time-resolved LA–ICP–MS depth profiles for magnetite **(A)**, pyrite **(B–E)** and chalcoprite **(F–H)**.

(16.49–214.74 ppm) of pyrite in stage IVb, the Se content of pyrite in stage IVa is low, distributed between 1.99 and 3.36 ppm. It indicates that the temperature of ore-forming fluids in the Tongjing deposit is not high (<300 °C), consistent with previous studies (190–250°C; Dong, 2008), but it cannot be excluded from the genetic relationship with magmatic activities. The Se content of pyrite may vary with the pH and redox conditions of the ore-forming fluid (Keith et al., 2018).

The low Se (<10 ppm) and (As < 100 ppm) contents of pyrite are consistent with the Se (avg. 2.64 ppm) and As (avg. 84.20 ppm) contents of pyrite from stage IVa, indicating that the ore-forming fluid is characterized by high temperatures, high f_{O2}, moderate to high salinity and acidic pH, for example porphyry deposit (Figure 12L; Goldfarb et al., 2005). The high Se (>10 ppm) and As (>100 ppm) contents of pyrite are consistent with the Se (avg.

43.26 ppm) and As (avg. 842 ppm) contents of pyrite from Stage IVb, suggesting that the ore-forming fluids were distinguished by low temperatures, low f_{O2}, low salinity and near-neutral pH, as in orogenic and epithermal (LS) deposits (Figure 12L; Goldfarb et al., 2005; Simmons et al., 2005). Thus, as ore-forming fluid evolves, the temperature, salinity and f_{O2} of the ore-forming fluid decrease and the pH rises, resulting in the unloading of Au. Furthermore, pyrite and telluride precipitation in the Tongjing deposit was caused by a decrease in f_{O2} but pH-independent (Cooke and McPhail, 2001; Grundler et al., 2013; Keith et al., 2018), which is similar to the Dongping Au deposit (Cook et al., 2009; Gao et al., 2017).

6.3 Source of ore-forming materials

The sulfur isotope composition of hydrothermal minerals depends on the total sulfur isotope composition, f_{O2}, pH and temperature of the fluid (Ohmoto, 1972). At Tongjing, pyrite has higher $\delta^{34}S$ values (avg. 0.52‰; Supplementary Table S3; Figures 10A,B) than chalcopyrite (avg. 0.26‰), indicating that the ore-forming system is in equilibrium for sulfur isotope fractionation (Chen et al., 2008). Thus, the total sulfur isotope value of hydrothermal fluids can be used to indicate the source of ore-forming material (Chen et al., 2008). The $\delta^{34}S_{Sulfide\text{-}H2S}$ of pyrite at 200°C and 250°C are 0.1‰ and -0.3‰ respectively (Kajiwara and Krouse, 1971). Previous microthermometric measurements of fluid inclusions (Dong, 2008) and this study of Se content in pyrite indicated that the ore-forming temperatures of stages IVa and IVb are approximately 200°C and 250°C, respectively. According to the formula ($\delta^{34}S_{\sum S}= \delta^{34}S_{Sulfide}\text{-}\delta^{34}S_{Sulfide\text{-}H2S}$; Ohmoto, 1972), the $\delta^{34}S_{\sum S}$ values were calculated to be 0.14‰ and 0.95‰ (Supplementary Table S3) for stages IVa and IVb, respectively. This narrow variation is comparable to magmatic origin ($\delta^{34}S = 0 \pm 3$‰; Ohmoto and Rye, 1979; Chaussidon and Lorand, 1990). Combined with previous bulk-sulfur isotope analyses (Figure 10A), high $\delta^{34}S$ values (up to 5‰) do not exclude a small contribution from wall rocks (sedimentary or metamorphic rocks). Such a sulfur isotopic composition, consistent with the sulfur isotope composition of the other gold deposits in the Luxi district (Figure 10A), is common in skarn-type deposits (e.g., Shu et al., 2013; Peng et al., 2016; Cai et al., 2021).

Lead isotope composition can be used to infer the source of Pb, and thus the ore-forming materials. The Pb isotope data in this study show a strong linear relationship with the previous data obtained by bulk analyses (sulfides and diorite porphyry) (Figures 10C,D), implying that diorite porphyry is a key source of ore-forming material for mineralization. The *in-situ* Pb isotope data are more concentrated ($^{206}Pb/^{204}Pb$ = 17.323–17.383; $^{207}Pb/^{204}Pb$ = 15.424–15.452; $^{208}Pb/^{204}Pb$ = 37.367–37.454), indicating a uniform source. In the $^{206}Pb/^{204}Pb$ vs $^{207}Pb/^{204}Pb$ diagram, the Pb isotope data of pyrite from the Tongjing deposit fall near the mantle evolution curve (Figure 10C); the data are close to the mantle/orogen and lower crust curves in the $^{206}Pb/^{204}Pb$ vs $^{208}Pb/^{204}Pb$ diagrams (Figure 10D). This implies that diorite porphyry (major) and marble/limestone are the source of the ore-forming materials, consistent with what is suggested by the sulfur isotope composition.

6.4 Ore genesis of Tongjing Au-Cu deposit

Magnetite shows a positive correlation between V and Ti (Figure 11G), and the behavior of Ni and Cr in magnetite is decoupled (Ni/Cr ratios ≥1; Figure 11H; Dare et al., 2014), indicating a hydrothermal magnetite origin (e.g., Huang et al., 2016). Magnetite is Ca-depleted (below detection limit) and has low REE contents (1.66–12.15ppm; avg. 4.87ppm), consistent with the characteristics of hydrothermal magnetite (Knipping et al., 2015). Furthermore, the plot of Ca + Al + Mn vs Ti + V (Figure 11I; Dupuis and Beaudoin, 2011) can distinguish magnetite from various origins. For the Tongjing deposit, the data of magnetite plot into the skarn field, though a small number of grains plot in the undefined field due to lower Ca + Al + Mn contents (Figure 11I).

Cobalt and Ni contents of pyrite can reflect the temperature and origin of pyrite (Bralia et al., 1979; Campbell and Ethier, 1984; Bajwah et al., 1987; Gregory et al., 2015). Cobalt prefers to enter pyrite at high temperatures, while Ni prefers to enter pyrite at low temperatures (Maslennikov et al., 2009; Zhang et al., 2020). The Co/Ni ratios of pyrite from Tongjing vary widely, ranging from 0.07 to 1,009 (Figure 12K). Most values are greater than 10, suggesting that pyrite was formed at a high temperature and originated from hydrothermal/magmatic (Bralia et al., 1979; Bajwah et al., 1987; Meng et al., 2018). Low Co/Ni ratios (generally <1; Figure 12K) are suggested to represent pyrite of syn-sedimentary origin (Koglin et al., 2010; Large et al., 2014). A few Co/Ni ratios are between 0.01 and 1, indicating the mixing of carbonate rocks during mineralization. The variable Co and Ni contents of the studied pyrite are mainly plotted in or outside the porphyry copper deposit area (away from the submarine hydrothermal vents and SEDEX deposits areas) (Figure 12K), also indicating the result of magmatic–hydrothermal processes. Chalcopyrite and pyrite have low U and V contents (Supplementary Table S2), indicating that they precipitated in the hydrothermal fluids.

Deditius et al. (2009) and Tardani et al. (2017) pointed out that processes such as fluid boiling can fractionate trace elements in hydrothermal fluids causing systematic compositional differences and chemical zonation in precipitated pyrite. Results of Loftus-Hill and Solomon (1967) and Schirmer et al. (2014) highlighted that oceanic sediments and carbonate-bearing rocks are enriched in Te compared to other rocks. As the ore-forming intrusion of the Tongjing Au-Cu deposit, the formation of the Tongjing pluton is related to the mantle metasomatism by the paleo-Pacific plate (Guo et al., 2014). The Cambrian sequences are the main wall rock of the Tongjing Au-Cu deposit, mainly including carbonate rocks such as limestone and dolomite (Figure 4A; Dong, 2008). We conclude that the Te of pyrite from the Tongjing deposit may be controlled by its concentration in the source rocks, which is also supported by the

occurrence of the nearby Mesozoic Guilaizhuang Au (-Te) deposit (Yu et al., 2019).

During the Late Mesozoic, the NCC underwent significant decratonization and massive thinning of the lithospheric mantle, accompanied by huge upwelling of the asthenosphere due to the roll-back of the paleo-Pacific plate (Zhu et al., 2011; Li et al., 2020; Yang et al., 2021). The response to this tectonic event in the eastern part of the NCC is mainly characterized by large-scale gold mineralization in the Jiaodong and Luxi districts. The highly concentrated sulfur and lead isotope values/ratios in this study indicate that deep magma (probable mantle) source of ore-forming materials. That is the Tongjing diorite porphyry enriched in ore-forming elements intruded into limestone and formed a large number of skarn and Cu–Au ore bodies.

Conclusion

1) Five hydrothermal stages are identified in the Yi'nan Tongjing Au-Cu deposit: 1) early skarn; 2) late skarn; 3) oxide; 4) sulfide; and 5) late quartz–calcite.
2) Gold occurs mainly as (silver-bearing) native grains. The trace element composition of the sulfides and oxides implies that the original ore-forming fluid is of medium-high temperature magmatic-hydrothermal origin. The decrease in temperature, salinity and f_{O2} of the ore-forming fluid, and the increased pH of the ore-forming fluid are critical to the precipitation of ore minerals.

3) *In-situ* LA–ICP–MS sulfur and lead isotope compositions indicate that the origin of ore-forming materials comes from the Early Cretaceous diorite porphyry and partly from the host rocks (carbonate rocks).
4) The present study provides new constraints for the mineralization process of skarn deposits in the Luxi district.

Data availability statement

The original contributions presented in the study are included in the article/Supplementary Material, further inquiries can be directed to the corresponding author.

Author contributions

Conceptualization, W-YC and Z-LZ; methodology, W-YC and XL; validation, J-LG, MM and Y-DL; formal analysis and data curation, Y-XS and Z-SL; project administration, W-YC and Z-LZ; writing—original draft, W-YC. All authors have read and agreed to the published version of the manuscript.

Funding

This study was financially supported by the Natural Science Foundation of Shandong Province (no. ZR2021QD056 and ZR2021QD106), Open Project Fund of Key Laboratory of Gold Mineralization Processes and Resource Utilization, MNR (no. Kfkt202108 and Kfkt202124) and Early Cretaceous Magmatism and Metallogenesis in TYD-ZS Fault (no. KC202005 and KC202102).

Acknowledgments

We are grateful to Xiangbiao-Sun and Bingbing-Liu from the Yi'nan Gold Mine of Shandong Gold Group and Associate Professors Yongming-Zhang and Liping-Liu of Shandong University of Technology for their help and support during the fieldwork.

Conflict of interest

The authors declare that the research was conducted in the absence of any commercial or financial relationships that could be construed as a potential conflict of interest.

The reviewer QS declared a shared affiliation with the author WC to the handling editor at time of review.

Publisher's note

All claims expressed in this article are solely those of the authors and do not necessarily represent those of their affiliated organizations, or those of the publisher, the editors and the reviewers. Any product that may be evaluated in this article, or claim that may be made by its manufacturer, is not guaranteed or endorsed by the publisher.

Supplementary material

The Supplementary Material for this article can be found online at: https://www.frontiersin.org/articles/10.3389/feart.2022.1084212/full#supplementary-material

SUPPLEMENTARY FIGURE S1
BSE and EDS images for native gold and sulfides **(A–F)**; scatter plot of trace elements in magnetite **(G–I)**.

SUPPLEMENTARY FIGURE S2
Photomicrograph of pyrite in stages IVa **(A)** and IVb **(B,C)**, including the spots of *in situ* trace element and sulfur-lead isotope analysis.

SUPPLEMENTARY TABLE S1
Major element composition of magnetite, native gold and sulfides determined by EPMA.

SUPPLEMENTARY TABLE S2

Trace element composition of magnetite and sulfides determined by LA-ICP-MS.

SUPPLEMENTARY TABLE S3

Sulfur isotope composition of sulfides from Tongjing Au-Cu deposit.

SUPPLEMENTARY TABLE S4

Lead isotope composition of sulfides from Tongjing Au-Cu deposit.

References

Ahmad, S. N., and adn Rose, A. W. (1980). Fluid inclusions in porphyry and skarn ore at Santa Rita. *New Mex. Econ. Geol.* 75, 229–250.

Audetat, A., and Pettke, T. (2006). Evolution of a porphyry-Cu mineralized magma system at Santa Rita, New Mexico (USA). *J. Petrology* 47, 2021–2046. doi:10.1093/petrology/egl035

Bajwah, Z. U., Seccombe, P. K., and Offler, R. (1987). Trace element distribution Co: Ni ratios and Genesis of the big cadia iron-copper deposit, new south Wales, Australia. *Mineral. Deposita* 22, 292–300. doi:10.1007/bf00204522

Baker, T., Ebert, S., Rombach, C., and Ryan, C, G. (2006). Chemical compositions of fluid inclusions in intrusion-related gold systems, Alaska and Yukon, using PIXE microanalysis. *Econ. Geol.* 101, 311–327. doi:10.2113/gsecongeo.101.2.311

Beane, R. E., and Titley, S. R. (1981). Porphyry copper deposits, part II. Hydrothermal alteration and mineralization. *Econ. Geol.*, 235–269. (75th Anniversary).

Berger, B. R., Henley, R. W., Lowers, H. A., and Pribil, M. J. (2014). The lepanto Cu–Au deposit, Philippines: A fossil hyperacidic volcanic lake complex. *J. Volcanol. Geotherm. Res.* 271, 70–82. doi:10.1016/j.jvolgeores.2013.11.019

Bowles, J. F. W., Howie, R. A., Vaughan, D. J., and Zussman, J. (2011). *Rock-forming minerals —non-silicates: Oxides, hydroxides and sulphides*. 2nd ed. London: Geological Society.

Bralia, A., Sabatini, G., and Troja, F. (1979). A revaluation of the Co/Ni ration in pyrite as geochemical tool in ore Genesis problems. *Min. Deposita* 14, 353–374.

Cai, W. Y., Wang, K. Y., Li, J., Fu, L. J., Li, S. D., Yang, H., et al. (2021). Genesis of the bagenheigeqier Pb–Zn skarn deposit in inner Mongolia, NE China: Constraints from fluid inclusions, isotope systematics and geochronology. *Geol. Mag.* 158, 271–294. doi:10.1017/s0016756820000473

Campbell, F. A., and Ethier, V. G. (1984). Nickel and cobalt in pyrrhotite and pyrite from the Faro and Sullivan orebodies. *Can. Mineral.* 22, 503–506.

Canil, D., Grondahl, C., Lacourse, T., and Pisiak, L. K. (2016). Trace elements in magnetite from porphyry Cu-Mo-Au deposits in British Columbia. Canada. *Ore Geol. Rev.* 72, 1116–1128. doi:10.1016/j.oregeorev.2015.10.007

Chang, Z., Shu, Q., and Meinert, L. D. (2019). *Skarn deposits of China*, 22. Littleton, Colorado: Society of Economic Geologists, Special Publication, 189–234.

Chaussidon, M., and Lorand, J. P. (1990). Sulphur isotope composition of orogenic spinel lherzolite massifs from Ariege (North-Eastern Pyrenees, France): An ion microprobe study. *Geochimica Cosmochimica Acta* 54, 2835–2846. doi:10.1016/0016-7037(90)90018-g

Chen, L., Tao, W., Zhao, L., and Zheng, T. (2008). Distinct lateral variation of lithospheric thickness in the Northeastern North China Craton. *Earth Planet. Sci. Lett.* 267, 56–68. doi:10.1016/j.epsl.2007.11.024

Chen, Y., J., Chen, H. Y., Zaw, K., Pirajno, F., and Zhang, Z. J. (2007). Geodynamic settings and tectonic model of skarn gold deposits in China: An overview. *Ore Geol. Rev.* 31, 139–169. doi:10.1016/j.oregeorev.2005.01.001

Chinnasamy, S. S., Hazarika, P., Pal, D., Sen, R., and Govindaraj, G. (2021). Pyrite textures and trace element compositions from the granodiorite-hosted gold deposit at jonnagiri, eastern dharwar craton, India: Implications for gold mineralization processes. *Econ. Geol.* 116, 559–579. doi:10.5382/econgeo.4787

Chouinard, A., Paquette, J., and Williams-Jones, A. E. (2005). Crystallographic controls on trace-element incorporation in auriferous pyrite from the Pascua epithermal high-sulfidation deposit, Chile-Argentina. *Can. Mineralogist* 43, 951–963. doi:10.2113/gscanmin.43.3.951

Cioacă, M. E., Munteanu, M., Qi, L., and Costin, G. (2014). Trace element concentrations in porphyry copper deposits from metaliferi mountains, Romania: A reconnaissance study. *Ore Geol. Rev.* 63, 22–39. doi:10.1016/j.oregeorev.2014.04.016

Cook, N. J., Ciobanu, C. L., and Mao, J. (2009). Textural control on gold distribution in as-free pyrite from the dongping, huangtuliang and hougou gold deposits, north China craton (hebei province, China). *Chem. Geol.* 264, 101–121. doi:10.1016/j.chemgeo.2009.02.020

Cooke, D. R., and McPhail, D. C. (2001). Epithermal Au-Ag-Te mineralization, Acupan, Baguio district, Philippines: Numerical simulations of mineral deposition. *Econ. Geol.* 96, 109–131. doi:10.2113/96.1.109

Dare, S. A., Barnes, S.-J., Beaudoin, G., Méric, J., Boutroy, E., and Potvin-Doucet, C. (2014). Trace elements in magnetite as petrogenetic indicators. *Min. Deposita* 49, 785–796. doi:10.1007/s00126-014-0529-0

Dare, S. A. S., Barnes, S. J., and Beaudoin, G. (2012). Variation in trace element content of magnetite crystallized from a fractionating sulfide liquid, Sudbury, Canada: Implications for provenance discrimination. *Geochimica Cosmochimica Acta* 88, 27–50. doi:10.1016/j.gca.2012.04.032

Deditius, A., Chryssoulis, S., Li, J. W., Ma, C. Q., Parada Reyes, M., Barra, F., et al. (2013). Pyrite as a record of hydrothermal fluid evolution in a porphyry copper system: A SIMS/EMPA trace element study. *Geochimica Cosmochimica Acta* 104, 42–62. doi:10.1016/j.gca.2012.11.006

Deditius, A. P., Reich, M., Kesler, S. E., Utsunomiya, S., Chryssoulis, S. L., Walshe, J., et al. (2014). The coupled geochemistry of Au and as in pyrite from hydrothermal ore deposits. *Geochimica Cosmochimica Acta* 140, 644–670. doi:10.1016/j.gca.2014.05.045

Deditius, A. P., Utsunomiya, S., Renock, D., Ewing, R. C., Ramana, C. V., Becker, U., et al. (2008). A proposed new type of arsenian pyrite: Composition, nanostructure and geological significance. *Geochimica Cosmochimica Acta* 72, 2919–2933. doi:10.1016/j.gca.2008.03.014

Deditius, A., Utsunomiya, S., Ewing, R. C., Chryssoulis, S., Venter, D., and Kesler, S. E. (2009). Decoupled geochemical behavior of as and Cu in hydrothermal systems. *Geology* 37, 707–710. doi:10.1130/g25781a.1

Deng, J., Wang, C., Bagas, L., Santosh, M., and Yao, E. (2018). Crustal architecture and mallogenesis in the south-eastern North China Craton. *Earth-Science Rev.* 182, 251–272. doi:10.1016/j.earscirev.2018.05.001

Deng, J., and Wang, Q. F. (2016). Gold mineralization in China: Metallogenic provinces, deposit types and tectonic framework. *Gondwana Res.* 36, 219–274. doi:10.1016/j.gr.2015.10.003

Dong, S. Y. (2008). Beijing: China University of Geosciencese, 60–68. Ph.d. thesis(in Chinese with English abstract). Metallogenesis, metallogenic laws and metallogenic prediction of the yinan gold deposit, shandong province

Doughty, P. T., and Chamberlain, K. R. (1996). Salmon River arch revisited: New evidence for 1370 Ma rifting near the end of deposition in the Middle Proterozoic belt basin. *Can. J. Earth Sci.* 33, 1037–1052. doi:10.1139/e96-079

Duan, Z., Gleeson, S. A., Gao, W. S., Wang, F. Y., and Li, J. W. (2020). Garnet U-Pb dating of the Yinan Au-Cu skarn deposit, Luxi District, North China Craton: Implications for district-wide coeval Au-Cu and Fe skarn mineralization. *Ore Geol. Rev.* 118, 103310. doi:10.1016/j.oregeorev.2020.103310

Duan, Z., and Li, J. W. (2017). Zircon and titanite U-Pb dating of the Zhangjiawa iron skarn deposit, Luxi district, North China Craton: Implications for a craton-wide iron skarn mineralization. *Ore Geol. Rev.* 89, 309–323. doi:10.1016/j.oregeorev.2017.06.022

Dupuis, C., and Beaudoin, G. (2011). Discriminant diagrams for iron oxide trace element fingerprinting of mineral deposit types. *Min. Deposita* 46, 319–335. doi:10.1007/s00126-011-0334-y

Einaudi, M. T., Meinert, L. D., and Newberry, R. J. (1981). "Skarn deposits," in *Economic Geology : Seventy-fifth anniversary volume*. Editor B. J. Skinner (Littleton, Colorado: Society of Economic Geologist), 317–391.

Fougerouse, D., Micklethwaite, S., Ulrich, S., Miller, J., Godel, B., Adams, D. T., et al. (2017). Evidence for two stages of mineralization in West Africa's largest gold deposit: Obuasi, Ghana. *Econ. Geol.* 112, 3–22. doi:10.2113/econgeo.112.1.3

Gadd, M. G., Layton-Matthews, D., Peter, J. M., and Paradis, S. J. (2016). The world-class howard's pass SEDEX Zn-Pb district, selwyn basin, yukon. Part I: Trace element compositions of pyrite record input of hydrothermal, diagenetic, and metamorphic fluids to mineralization. *Min. Deposita* 51, 319–342. doi:10.1007/s00126-015-0611-2

Gao, M. B., Gao, J. L., Zhang, Y. M., Zhang, Z. L., Liu, L. P., Zhang, Y. D., et al. (2022). Magma source and genesis of the kuangshan complex in Laiwu county of the western shandong: Constraints from geochronology, geochemistry, bulk rock Sr-Nd-Pb isotopes and zircon Hf isotopes. *Bull. Mineralogy, Petrology Geochem.*, 1–20. (in Chinese with English abstract).

Gao, S., Xu, H., Li, S. X., Santosh, M., Zhang, D., Yang, L., et al. (2017). Hydrothermal alteration and ore-forming fluids associated with gold-tellurium

mineralization in the Dongping gold deposit, China. *Ore Geol. Rev.* 80, 166–184. doi:10.1016/j.oregeorev.2016.06.023

George, L. L., Cook, N. J., Crowe, B. B. P., and Ciobanu, C. L. (2018a). Trace elements in hydrothermal chalcopyrite. *Mineral. Mag.* 82, 59–88. doi:10.1180/minmag.2017.081.021

George, L. L., Cristian, B., Massimo, D., and Cook, N. J. (2018b). Textural and trace element evolution of pyrite during greenschist facies metamorphic recrystallization in the southern apuan alps (tuscany, Italy): Influence on the formation of Tl-rich sulfosalt melt. *Ore Geol. Rev.* 102, 59–105. doi:10.1016/j.oregeorev.2018.08.032

Goldfarb, R. J., Baker, T., Dube, B., Groves, D. I., Hart, C. J., and Gosselin, P. (2005). Distribution, character, and Genesis of gold deposits in metamorphic terranes. *Econ. Geol.* 100, 407–450.

Goldfarb, R. J., and Groves, D. I. (2015). Orogenic gold: Common or evolving fluid and metal sources through time. *Lithos* 233, 2–26. doi:10.1016/j.lithos.2015.07.011

Gregory, D. D., Large, R. R., Halpin, J. A., Baturina, E. L., Lyons, T. W., Wu, S., et al. (2015). Trace element content of sedimentary pyrite in Black Shales. *Econ. Geol.* 110, 1389–1410. doi:10.2113/econgeo.110.6.1389

Groves, D. I., Goldfarb, R. J., Gebre-Mariam, M., and Robert, F. (1998). Orogenic gold deposits: A proposed classification in the context of their crustal distribution and relationship to other gold deposit types. *Ore Geol. Rev.* 13, 7–27. doi:10.1016/s0169-1368(97)00012-7

Grundler, P. V., Brugger, J., Etschmann, B. E., Helm, L., Liu, W. H., Spry, P. G., et al. (2013). Speciation of aqueous tellurium(IV) in hydrothermal solutions and vapors, and the role of oxidized tellurium species in Te transport and gold deposition. *Geochimica Cosmochimica Acta* 120, 298–325. doi:10.1016/j.gca.2013.06.009

Gu, X. X., Dong, S. Y., Wang, Y. X., Hu, G. Z., Du, S. H., and Jiao, P. (2008). A new example of unconformity-related endogenic metallization: The Yinan Au-Cu-Fe deposit in Shandong Province, China. *Geoscience* 22, 151–161. (in Chinese with English abstract).

Guo, P., Santosh, M., Li, S. R., and Li, Q. (2014). Crustal evolution in the central part of Eastern NCC: Zircon U-Pb ages from multiple magmatic pulses in the Luxi area and implications for gold mineralization. *Ore Geol. Rev.* 60, 126–145. doi:10.1016/j.oregeorev.2014.01.002

Hastie, E. C. G., Kontak, D. J., and Lafrance, B. (2020). Gold remobilization: Insights from gold deposits in the archean swayze greenstone belt, abitibi subprovince, Canada. *Econ. Geol.* 115, 241–277. doi:10.5382/econgeo.4709

Hayes, T. S. (1990). A preliminary study of thermometry and metal sources of the Spar Lake stratabound copper–silver deposit, Belt Supergroup, Montana. *U.S. Geol. Surv. Open-File Rep.* 90–48430.

Hedenquist, J. W., and Lowenstern, J. B. (1994). The role of magmas in the formation of hydrothermal ore deposits. *Nature* 370, 519–527. doi:10.1038/370519a0

J. W. Hedenquist, J. F. H. Thompson, R. J. Goldfarb, and J. P. Richards (Editors) (2005). *Economic Geology 100th anniversary* (Littleton, Colorado: Society of Economic Geologists, Inc.), 1133.

Hough, R. M., Butt, C. R., and Fischer-Bühner, J. (2009). The crystallography, metallography and composition of gold. *Elements* 5, 297–302. doi:10.2113/gselements.5.5.297

Hu, F. F., Wang, Y., Fan, H. R., Zheng, X. L., and Jiao, P. (2010). Geochronology and ore-forming fluids in the jinchang skarn goldcopper deposit, yinan county, Western shandong province. *Acta Petrol. Sin.* 26, 1503–1511. (in Chinese with English abstract).

Hu, H. B., Mao, J. W., Niu, S. Y., Li, Y. F., and Li, M. W. (2006). Geology and geochemistry of telluridebearing Au deposits in the Pingyi area, Western Shandong, China. *Mineralogy Petrology* 87, 209–240. doi:10.1007/s00710-006-0126-8

Hu, H. B., Sun, A. Q., Niu, S. Y., Wang, B. D., and Li, Y. P. (2007). Helium and argon isotopic compositions of theLongquanzhan gold deposit in the Yishu fault zone and their geological implications. *Chin. J. Geochem.* 26, 46–51. (in Chinese with English abstract). doi:10.1007/s11631-007-0046-2

Hu, H., Li, J. W., Lentz, D., Ren, Z., Zhao, X. F., Deng, X. D., et al. (2014). Dissolutionreprecipitation process of magnetite from the Chengchao iron deposit: Insights into ore Genesis and implication for *in-situ* chemical analysis of magnetite. *Ore Geol. Rev.* 57, 393–405. doi:10.1016/j.oregeorev.2013.07.008

Hu, Z. C., Zhang, W., Liu, Y. S., Gao, S., Li, M., Zong, K. Q., et al. (2015). Wave" signal-smoothing and mercury-removing device for laser ablation quadrupole and multiple collector ICPMS analysis: Application to lead isotope analysis. *Anal. Chem.* 87, 1152–1157. doi:10.1021/ac503749k

Huang, X., Gao, J., Qi, L., Meng, Y., Wang, Y., and Dai, Z. (2016). *In-situ* LA-ICP-MS trace elements analysis of magnetite: The Fenghuangshan Cu-Fe-Au deposit, Tongling. Eastern China. *Ore Geol. Rev.* 72, 746–759. doi:10.1016/j.oregeorev.2015.09.012

Huang, X., Qi, L., and Meng, Y. (2014). Trace element geochemistry of magnetite from the Fe(−Cu) deposits in the hami region, eastern tianshan orogenic belt, NW China. *Acta Geol. Sin. - Engl. Ed.* 88, 176–195. (English Edition). doi:10.1111/1755-6724.12190

Huston, D. L., Sie, S. H., Suter, G. F., Cooke, D. R., and Both, R. A. (1995). Trace elements in sulfide minerals from eastern Australian volcanic-hosted massive sulfide deposits: Part I. Proton microprobe analyses of pyrite, chalcopyrite and sphalerite, and Part II. Selenium levels in pyrite: Comparison with $\delta^{34}S$ values and implications for the source of sulfur in volcanogenic hydrothermal systems. *Econ. Geol.* 90, 1167–1196. doi:10.2113/gsecongeo.90.5.1167

Keith, M., Haase, K. M., Klemd, R., Krumm, S., and Strauss, H. (2016). Systematic variations of trace element and sulfur isotope compositions in pyrite with stratigraphic depth in the Skouriotissa volcanic-hosted massive sulfide deposit, Troodos ophiolite, Cyprus. *Chem. Geol.* 423, 7–18. doi:10.1016/j.chemgeo.2015.12.012

Keith, M., Haase, K. M., Schampera, U. S., Klemd, R., Petersen, S., and Bach, W. (2014). Effects of temperature, sulfur, and oxygen fugacity on the composition of sphalerite from submarine hydrothermal vents. *Geology* 42, 699–702. doi:10.1130/g35655.1

Keith, M., Smith, D. J., Jenkin, G. R. T., Holwell, D. A., and Dye, M. D. (2018). A review of Te and Se systematics in hydrothermal pyrite from precious metal deposits: Insights into oreforming processes. *Ore Geol. Rev.* 96, 269–282. doi:10.1016/j.oregeorev.2017.07.023

Knipping, J. L., Bilenker, L. D., Simon, A. C., Reich, M., Barra, F., Deditius, A. P., et al. (2015). Trace elements in magnetite from massive iron oxide-apatite deposits indicate a combined formation by igneous and magmatic-hydrothermal processes. *Geochimica Cosmochimica Acta* 171, 15–38. doi:10.1016/j.gca.2015.08.010

Koglin, N., Frimmel, H. E., Minter, W. L., and Brätz, H. (2010). Trace-element characteristics of different pyrite types in Mesoarchaean to Palaeoproterozoic placer deposits. *Min. Deposita* 45, 259–280. doi:10.1007/s00126-009-0272-0

Koski, R. A., Shanks, W. C., III, Bohrson, W. A., and Oscarson, R. L. (1988). The composition of massive sulfide deposits from the sediment-covered floor of escanaba trough, gorda ridge: Implications for depositional processes. *Can. Mineral.* 26, 655–673.

Lan, T. G., Fan, H. R., Santosh, M., Hu, F. F., Yang, K. F., Yang, Y. H., et al. (2012). Early jurassic high-K calc-alkaline and shoshonitic rocks from the tongshi intrusive complex, eastern north China craton: Implication for crust–mantle interaction and post-collisional magmatism. *Lithos* 140, 183–199. doi:10.1016/j.lithos.2012.01.015

Landis, G. P., and Hofstra, A. H. (1991). Fluid inclusion gas chemistry as a potential minerals exploration tool: Case studies from creede, CO, jerritt canyon, NV, coeur d'Alene district, ID and MT, southern Alaska mesothermal veins, and mid-continent MVT's. *J. Geochem. Explor.* 42, 25–59. doi:10.1016/0375-6742(91)90059-4

Large, R. R., Halpin, J. A., Danyushevsky, L. V., Maslennikov, V. V., Bull, S. W., Long, J. A., et al. (2014). Trace element content of sedimentary pyrite as a new proxy for deep-time ocean-atmosphere evolution. *Earth Planet. Sci. Lett.* 389, 209–220. doi:10.1016/j.epsl.2013.12.020

Leach, D. L., Landis, G. P., and Hofstra, A. H. (1988). Metamorphic origin of the Coeur d'Alene baseand precious-metal veins in the Belt Basin, Idaho and Montana. *Geol.* 16, 122–125. doi:10.1130/0091-7613(1988)016<0122:mootcd>2.3.co;2

Li, H. K., Geng, K., Li, Y. F., and Zhuo, C. Y. (2011). Zircon SHRIMP U-Pb age of Tongjing gold deposit in Yinan County, Shandong and its geological significance. *Mineral. deposits* 30, 497–503. (in Chinese with English abstract).

Li, J., Song, M. C., Yu, J. T., Bo, J. W., Zhang, Z. L., and Liu, X. (2022). Genesis of Jinqingding Gold Deposit in eastern Jiaodong peninsula, China: Constrain from trace elements of sulfide ore and wall-rock. *Geol. Bull. China* 41, 1010–1022. (in Chinese with English abstract).

Li, J., Wang, K. Y., Cai, W. Y., Sun, F. Y., Liu, H. L., Fu, L. J., et al. (2020). Triassic gold-silver metallogenesis in Qingchengzi orefield, North China Craton: Perspective from fluid inclusions, REE and H-O-S-Pb isotope systematics. *Ore Geol. Rev.* 121, 103567. doi:10.1016/j.oregeorev.2020.103567

Li, K., Gu, X. X., and Dong, S. Y. (2009). Isotopic geochemistry of yinan Au-Cu-Fe deposit in shandong province: Mineral deposits. v. 28, no. 1, p. 93–104 (in Chinese with English abstract).

Li, S. R., and Santosh, M. (2017). Geodynamics of heterogeneous gold mineralization in the North China Craton and its relationship to lithospheric destruction. *Gondwana Res.* 50, 267–292. doi:10.1016/j.gr.2017.05.007

Lin, J. Q., Tan, D. J., Yu, X. F., Li, B. R., Li, Y., and Xu, W. L. (1997). in *Genesis of the Guilaizhuang gold deposit in western Shandong* (Jinan: Shandong Science and Technology Press), 1–160. (in Chinese with English abstract).

Liu, Y., Santosh, M., Li, S. R., and Guo, P. (2014). Stable isotope geochemistry and Re–Os ages of the Yi'nan gold deposit, Shandong Province, northeastern China. *Int. Geol. Rev.* 6, 695–710. doi:10.1080/00206814.2014.886167

Liu, Y. S., Hu, Z. C., Gao, S., Günther, D., Xu, J., Gao, C. G., et al. (2008). *In situ* analysis of major and trace elements of anhydrous minerals by LA-ICP-MS without applying an internal standard. *Chem. Geol.* 257, 34–43. doi:10.1016/j.chemgeo.2008.08.004

Loftus-Hill, G., and Solomon, M. (1967). Cobalt, nickel and selenium in sulphides as indicators of ore Genesis. *Mineral. Deposita* 2, 228–242.

Ma, Y., Jiang, S. Y., Frimmel, H. E., and Zhu, L. Y. (2022). *In situ* chemical and isotopic analyses and element mapping of multiple-generation pyrite: Evidence of episodic gold mobilization and deposition for the Qiucun epithermal gold deposit in Southeast China. *Am. Mineralogist* 107, 1133–1148. doi:10.2138/am-2022-8030

Manske, S. L., and Paul, A. H. (2002). Geology of a major new porphyry copper center in the Superior (Pioneer) district, Arizona. *Econ. Geol.* 97, 197–220. doi:10.2113/gsecongeo.97.2.197

Mao, J. W., Wang, Y. T., Zhang, Z. H., Yu, J. J., and Niu, B. G. (2003). Geodynamic settings of mesozoic large-scale mineralization in north China and adjacent areas—implication from the highly precise and accurate ages of metal deposits. *Sci. China Ser. D.* 46, 838–851. doi:10.1360/03yd0202

Maslennikov, V. V., Maslennikova, S. P., Large, R. R., and Danyushevsky, L. V. (2009). Study of trace element zonationin vent chimneys from the Silurian Yaman-Kasy volcanic-hosted massive sulfide deposit (Southern Urals, Russia) using laser ablation-inductively coupled plasma mass spectrometry (LA-ICPMS). *Econ. Geol.* 104, 1111–1141. doi:10.2113/gsecongeo.104.8.1111

Meinert, L. D., Dippl, G. M., and Nicolescu, S. (2005). World skarn deposits. *Econ. Geol.* 100, 299–366.

Meinert, L. D. (1992). Skarns and skarn deposits. *Geosci. Can.* 19 (4), 145–162.

Meng, Y. M., Hu, R. Z., Huang, X. W., Gao, J. F., Qi, L., and Lyu, C. (2018). The relationship between stratabound Pb-Zn-Ag and porphyry-skarn Mo mineralization in the laochang deposit, southwestern China: Constraints from pyrite Re-Os isotope, sulfur isotope, and trace element data. *J. Geochem. Explor.* 194, 218–238. doi:10.1016/j.gexplo.2018.08.008

Menzies, M. A., Fan, W., and Zhang, M. (1993). Palaeozoic and Cenozoic lithoprobes and the loss of >120 km of Archaean lithosphere, Sino-Korean craton, China. *Geol. Soc. Lond Spec. Publ.* 76, 71–81. doi:10.1144/gsl.sp.1993.076.01.04

Mukherjee, I., and Large, R. (2017). Application of pyrite trace element chemistry to exploration for SEDEX style Zn-Pb deposits: McArthur basin, northern territory, Australia. *Ore Geol. Rev.* 81, 1249–1270. doi:10.1016/j.oregeorev.2016.08.004

Mumin, A. H., Fleet, M. E., and Chryssoulis, S. L. (1994). Gold mineralization in as-rich mesothermal gold ores of the BogosuPrestea mining district of the ashanti gold belt, Ghana: Remobilization of "invisible" gold. *Mineral. Deposita* 29, 445–460. doi:10.1007/bf00193506

Naden, J., and Henney, P. J. (1995). *Characterisation of gold from Fiji*. Keyworth, Nottinghamshire: British Geological Survey, 1–17. Technical report WC/95/41.

Nadoll, P., Angerer, T., Mauk, J. L., French, D., and Walshe, J. (2014). The chemistry of hydrothermal magnetite: A review. *Ore Geol. Rev.* 61, 1–32. doi:10.1016/j.oregeorev.2013.12.013

Nadoll, P., Mauk, J. L., Hayes, T. S., Koenig, A. E., and Box, S. E. (2012). Geochemistry of magnetite from hydrothermal ore deposits and host rocks of the Mesoproterozoic Belt Supergroup, United States. *Econ. Geol.* 107, 1275–1292. doi:10.2113/econgeo.107.6.1275

Nadoll, P., Mauk, J. L., Leveille, R. A., and Koenig, A. E. (2015). Geochemistry of magnetite from porphyry Cu and skarn deposits in the southwestern United States. *Min. Deposita* 50, 493–515. doi:10.1007/s00126-014-0539-y

Niu, S. Y., Hu, H. B., Mao, J. W., Sun, A. Q., Xu, C. S., and Hou, Q. L. (2004). Adapting English into Chinese. *Engl. Today* 31, 34–39. (in Chinese with English abstract). doi:10.1017/s0266078404002068

Niu, X., Shu, Q., Xing, K., Yuan, S., Wei, L., Zhang, Y., et al. (2022). Evaluating Sn mineralization potential at the Haobugao skarn Zn-Pb deposit (NE China) using whole-rock and zircon geochemistry. *J. Geochem. Explor.* 234, 106938. doi:10.1016/j.gexplo.2021.106938

Ohmoto, H., and Rye, R. O. (1979). "Isotopes of sulfur and carbon," in *Geochemistry of hydrothermal ore deposits*. Editor H. L. Barnes. second edition (New York: John Wiley), 509–567.

Papike, J. J., Burger, P. V., Bell, A. S., Shearer, C. K., Le, L., and Jones, J. (2015). Normal to inverse transition in martian spinel: Understanding the interplay between chromium, vanadium, and iron valence state partitioning through a crystal-chemical lens. *Am. Mineralogist* 100, 2018–2025. doi:10.2138/am-2015-5208

Peng, H. J., Mao, J. W., Hou, L., Shu, Q. H., Zhang, C. Q., Liu, H., et al. (2016). Stable isotope and fluid inclusion constraints on the source and evolution of ore fluids in the Hongniu-Hongshan Cu skarn deposit, Yunnan Province, China. *Econ. Geol.* 111, 1369–1396. doi:10.2113/econgeo.111.6.1369

Qiu, J. S., Wang, D. Z., and Ren, Q. J. (1996). Geological geochemical characteristics and Genesis of the Jinchang skarn type gold-copper deposit. *Yinan Cty. Shandong Prov. Mineral. Deposits* 15, 330–340. (in Chinese with English abstract).

Reich, M., Deditius, A., Chryssoulis, S., Li, J. W., Ma, C. Q., Parada, M. A., et al. (2013). Pyrite as a record of hydrothermal fluid evolution in a porphyry copper system: A SIMS/EMPA trace element study. *Geochimica Cosmochimica Acta* 104, 42–62. doi:10.1016/j.gca.2012.11.006

Reich, M., Kesler, S. E., Utsunomiya, S., Palenik, C. S., Chryssoulis, S. L., and Ewing, R. C. (2005). Solubility of gold in arsenian pyrite. *Geochimica Cosmochimica Acta* 69, 2781–2796. doi:10.1016/j.gca.2005.01.011

Santosh, M. (2010). Assembling North China craton within the columbia supercontinent: The role of double-sided subduction. *Precambrian Res.* 178, 149–167. doi:10.1016/j.precamres.2010.02.003

Schirmer, T., Koschinsky, A., and Bau, M. (2014). The ratio of tellurium and selenium in geological material as a possible paleo-redox proxy. *Chem. Geol.* 376, 44–51. doi:10.1016/j.chemgeo.2014.03.005

SDGG (Shandong Gold Group Co., Ltd.) (2008). *Detailed geological survey report on deep and peripheral Au-Cu mineralization in Tongjing*. Yi'nan County, Shandong Province. (in Chinese).

SDGM(Shandong Gold Geological Minerals Survey Co. Ltd) (2015). *Detailed geological survey report of the Tongjing and Jinchang Au-Cu deposits*. Yi'nan County, Shandong Province. (in Chinese).

Shi, W. J. (2014). *The late mesozoic tectonic-magematic EvolutionProcess in the yishu fault zone and adjacent regions, Shandong province: Implication for gold mineralization*. Wuhan: China University of Geosciences for the Doctor Degree, 1–142. (in Chinese with English abstract).

Shu, Q., Chang, Z., Hammerli, J., Lai, Y., and Huizenga, J-M. (2017). Composition and evolution of fluids forming the baiyinnuo'er Zn-Pb skarn deposit, northeastern China: Insights from laser ablation ICP-ms study of fluid inclusions. *Econ. Geol.* 112, 1441–1460. doi:10.5382/econgeo.2017.4516

Shu, Q., Chang, Z., and Mavrogenes, J. (2021). Fluid compositions reveal fluid nature, metal deposition mechanisms, and mineralization potential: An example at the Haobugao Zn-Pb skarn, China. *Geology* 49, 473–477. doi:10.1130/g48348.1

Shu, Q., Lai, Y., Sun, Y., Wang, C., and Meng, S. (2013). Ore Genesis and hydrothermal evolution of the baiyinnuo'er zinc-lead skarn deposit, northeast China: Evidence from isotopes (S, Pb) and fluid inclusions. *Econ. Geol.* 108, 835–860. doi:10.2113/econgeo.108.4.835

Sillitoe, R. H. (2010). Porphyry copper systems. *Econ. Geol.* 105, 3–41. doi:10.2113/gsecongeo.105.1.3

Simmons, S. F., White, N. C., and John, D. A. (2005). Geological characteristics of epithermal precious and base metal deposits. *Econ. Geol.* 100, 485–522.

Song, K. R., Tang, L., Zhang, S. T., Santosh, M., Spencer, C. J., Zhao, Y., et al. (2019). Genesis of the Bianjiadayuan Pb–Zn polymetallic deposit, Inner Mongolia, China: Constraints from *in-situ* sulfur isotope and trace element geochemistry of pyrite. *Geosci. Front.* 10, 1863–1877. doi:10.1016/j.gsf.2019.02.004

Song, M. C., and Li, H. K. (2001). Study on regional geological structural evolution in Shandong Province. *Shandong Geol.* 17, 12–21. (in Chinese with English abstract).

Sung, Y.-H., Brugger, J., Ciobanu, C., Pring, A., Skinner, W., and Nugus, M. (2009). Invisible gold in arsenian pyrite and arsenopyrite from a multi-stage Archaean gold deposit: Sunrise dam, Eastern Goldfields province, Western Australia. *Min. Deposita* 44, 765–791. doi:10.1007/s00126-009-0244-4

Takeno, N. (2005). Atlas of Eh-pH diagrams: Intercomparison of thermodynamic data bases. *Geol. Surv. Jpn. Open File Rep.* 419, 285.

Tardani, D., Reich, M., Deditius, A. P., Chryssoulis, S., Sanchez-Alfaro, P., Wrage, J., et al. (2017). Copper-arsenic decoupling in an active geothermal system: A link between pyrite and fluid composition. *Geochimica Cosmochimica Acta* 204, 179–204. doi:10.1016/j.gca.2017.01.044

Thompson, J. F. H., Sillitoe, R. H., Baker, T., Lang, J. R., and Mortensen, J. K. (1999). Intrusion-related gold deposits associated with tungsten-tin provinces. *Miner. Deposita* 34, 323–334. doi:10.1007/s001260050207

Thorne, W. S., Hagemann, S. G., Webb, A., and Clout, J. (2008). "Banded iron formation-related iron ore deposits of the Hamersley Province, Western Australia," in *Banded iron formation-related highgrade iron ore*. Editors S. G. Hagemann, C. A. Rosière, J. Gutzmer, and N. J. Beukes, 197–222.

Tian, J. X., Li, X. Z., Song, Z. Y., Liu, H. D., Huang, Y. B., and Zhu, D. C. (2015). Environment formation age and material sources of mesozoic golddeposits in Western shandong a synthesis. *Acta Geol. Sin.* 89, 1530–1537. (in Chinese with English abstract).

Vaughan, D. J., and Rosso, K. M. (2006). Chemical bonding in sulfide minerals. *Rev. Mineralogy Geochem.* 61, 231–264. doi:10.2138/rmg.2006.61.5

Voute, F., Hagemann, S. G., Evans, N. J., and Villanes, C. (2019). Sulfur isotopes, trace element, and textural analyses of pyrite, arsenopyrite and base metal sulfides associated with gold mineralization in the pataz-parcoy district, Peru: Implication

for paragenesis, fluid source, and gold deposition mechanisms. *Min. Deposita* 54, 1077–1100. doi:10.1007/s00126-018-0857-6

Wan, T. F. (1992). Tectonic evolution and stress field in shandong province. *Geol. Shandong* 8, 70–101. (in Chinese with English abstract).

Wan, Y. S., Liu, D. Y., Wang, S. J., Yang, E. X., Wang, W., Dong, C. Y., et al. (2011). ~2.7Ga juvenile crust formation in the North China Craton (Taishan-Xintai area, Western Shandong Province): Further evidence of an understated event from U–Pb dating and Hf isotopic composition of zircon. *Precambrian Res.* 186, 169–180. doi:10.1016/j.precamres.2011.01.015

Wang, Q. L., Zhang, J. Y., Yan, D. T., Min, H., Liu, S., and Li, C. (2021). Genesis of ore deposits indicated by trace elements of chalcopyrite. *Bull. Geol. Sci. Technol.*, 1–19. (in Chinese with English abstract).

Wang, Y., Fan, H. R., Hu, F. F., Lan, T. G., Jiao, P., and Wang, S. P. (2011). Zircon U-Pb ages and geoche mistry of ele ments and isotopes of the diorite from Tongjing 'Yinan 'Western Shandong Province. *Mineralogy Petrology* 30, 553–566. (in Chinese with English abstract).

Wang, Y. (2010). *Late Mesozoic magmatism and gold-coppermineraliztion in the southwestern part of Shandong province. Ph.D. thesis.* Beijing: Chinese Academy of Sciences, 1–199. (In Chinese).

Wu, F. Y., Lin, J. Q., Wilde, S. A., Zhang, X. O., and Yang, J. H. (2005a). Nature and significance of the Early Cretaceous giant igneous event in Eastern China. *Earth Planet. Sci. Lett.* 233, 103–119. doi:10.1016/j.epsl.2005.02.019

Wu, F. Y., Yang, J. H., Wilde, S. A., and Zhang, X. O. (2005b). Geochronology, petrogenesis and tectonic implications of Jurassic granites in the Liaodong Peninsula, NE China. *Chem. Geol.* 221, 127–156. doi:10.1016/j.chemgeo.2005.04.010

Wu, M. L., Zhao, G. C., Sun, M., Li, S. Z., He, Y. H., and Bao, Z. A. (2013). Zircon UPb geochronology and Hf isotopes of major lithologies from the yishui terrane: Implications for the crustal evolution of the eastern block, north China craton. *Lithos* 171, 164–178. doi:10.1016/j.lithos.2013.03.005

Xie, Q. H., Zhang, Z. C., Hou, T., Jin, Z. L., and Santosh, M. (2017). Geochemistry and oxygen isotope composition of magnetite from the Zhangmatun deposit, North China Craton: Implications for the magmatic-hydrothermal evolution of Cornwall-type iron mineralization. *Ore Geol. Rev.* 88, 57–70. doi:10.1016/j.oregeorev.2017.04.014

Xu, Y. G., Ma, J. L., Huang, X. L., Iizuka, Y., Chung, S. L., Wang, Y. B., et al. (2004). Early cretaceous gabbroic complex from yinan, shandong province: Petrogenesis and mantle domains beneath the North China craton. *Int. J. Earth Sci.* 93, 1025–1041. doi:10.1007/s00531-004-0430-7

Xu, Y. G. (2001). Thermo-tectonic destruction of the archaean lithospheric keel beneath the Sino-Korean craton in China: Evidence, timing and mechanism. *Phys. Chem. Earth Part A Solid Earth Geodesy* 26, 747–757. doi:10.1016/s1464-1895(01)00124-7

Xu, Y. G., Wu, X. Y., Luo, Z. Y., Ma, J. L., Huang, X. L., and Xie, L. W. (2007). Zircon Hf isotope compositions of middle jurassic-early cretaceous intrusions in shandong province and its implications. *Acta Petrol. Sin.* 23, 307–316. (in Chinese with English abstract).

Yang, C. H., Xu, W. L., Yang, D. B., Liu, C. C., Liu, X. M., and Hu, Z. C. (2006). Petrogenesis of the mesozoic high-Mg diorites in west shandong: Evidence from chronology and petro-geochemistry. *J. China Univ. Geosciences (Earth Sci.* 31, 81–92. (in Chinese with English abstract).

Yang, C. H., Xu, W. L., Yang, D. B., Wang, W., Wang, W. D., and Liu, J. M. (2008). Genesis of shangyu gabbro diorite in Western shandong: Evidence from geochronology and petrogeochemistry. *Sci. China Earth Sci.* 01, 44–55. (In Chinese).

Yang, J. H., Sun, J. F., Zhang, J. H., and Wilde, S. A. (2012). Petrogenesis of Late Triassic intrusive rocks in the northern Liaodong Peninsula related to decratonization of the North China Craton: Zircon U–Pb age and Hf–O isotope evidence. *Lithos* 153, 108–128. doi:10.1016/j.lithos.2012.06.023

Yang, J. H., Xu, L., Sun, J. F., Zeng, Q., Zhao, Y. N., Wang, H., et al. (2021). Geodynamics of decratonization and related magmatism and mineralization in the North China Craton. *Sci. China Earth Sci.* 64, 1409–1427. doi:10.1007/s11430-020-9732-6

Yu, X. F., Li, D. P., Li, Z. S., Wei, P. F., and Rana, N. S. S. (2019). Research on geochemical process of Te-Au elements in Guilaizhuang gold deposit of Western Shandong. *Mineral. Deposits* 38, 277–290.

Zartman, R. E., and Doe, B. R. (1981). Plumbotectonics–the model. *Tectonophysics* 75, 135–162. doi:10.1016/0040-1951(81)90213-4

Zeng, Q. D., Liu, J. M., Qin, K. Q., Fan, H. R., Chu, S. X., Wang, Y. B., et al. (2013). Types, characteristics, and time-space distribution of molybdenum deposits in China. *Int. Geol. Rev.* 55, 1311–1358. doi:10.1080/00206814.2013.774195

Zeng, Q. D., Wang, Y. B., Yang, J. H., Guo, Y. P., Yu, B., Zhou, L. L., et al. (2020). Spatial-temporal distribution and tectonic setting of gold deposits in the northern margin gold belt of the North China Craton. *Int. Geol. Rev.* 63, 941–972. doi:10.1080/00206814.2020.1737839

Zhai, M. G. (2011). Cratonization and the ancient north China continent: A summary and review. *Sci. China Earth Sci.* 54, 1110–1120. doi:10.1007/s11430-011-4250-x

Zhai, M. G., and Santosh, M. (2011). The early precambrian odyssey of the North China craton: A synoptic overview. *Gondwana Res.* 20, 6–25. doi:10.1016/j.gr.2011.02.005

Zhang, C., Cui, F. H., and Geng, R. (2021). The petrogenesis of early cretaceous quartz diorite in skarn iron deposits, jinling area, Luxi: Evidence of geochronology and geochemistry. *Mineralogy Petrology* 41, 80–92. (in Chinese with English abstract).

Zhang, W., Hu, Z. C., Gunther, D., Liu, Y. S., Ling, W. L., Zong, K. Q., et al. (2016). Direct lead isotope analysis in Hg-rich sulfides by LA-MC-ICP-MS with a gas exchange device and matrix-matched calibration. *Anal. Chim. Acta* 948, 9–18. doi:10.1016/j.aca.2016.10.040

Zhang, W., Hu, Z. C., and Liu, Y. S. (2020). Iso-compass: New freeware software for isotopic data reduction of LA-MC-ICP-MS. *J. Anal. At. Spectrom.* 35, 1087–1096. doi:10.1039/d0ja00084a

Zhang, Y. Y., Zhen, S. M., Wang, D. Z., Liu, J. J., Wang, J., Zha, Z. J., et al. (2022). *In situ* trace elements and sulfur isotopes of sulfides in the Dabaiyang Te-Au deposit, Hebei Province, China: Implications for Au remobilization from pyrite. *Ore Geol. Rev.* 140, 104626. doi:10.1016/j.oregeorev.2021.104626

Zhang, Z. R., and Chen, M. X. (1995). The application of the gold fineness research in geology. *Gold Sci. Technol.* 3, 21–24. (in Chinese).

Zhao, G. C., and Cawood, P. A. (2012). Precambrian geology of China. *Precambrian Res.* 222, 13–54. doi:10.1016/j.precamres.2012.09.017

Zhao, G. C., Sun, M., Wilde, S. A., and Li, S. Z. (2005). Late archean to paleoproterozoic evolution of the North China craton: Key issues revisited. *Precambrian Res.* 136, 177–202. doi:10.1016/j.precamres.2004.10.002

Zhao, G. C., Wilde, S. A., Cawood, P. A., and Sun, M. (2001). Archean blocks and their boundaries in the North China Craton: Lithological, geochemical, structural and P-T path constraints and tectonic evolution. *Precambrian Res.* 107, 45–73. doi:10.1016/s0301-9268(00)00154-6

Zhao, W. W., and Zhou, M. F. (2015). *In-situ* LA–ICP-MS trace elemental analyses of magnetite: The mesozoic tengtie skarn Fe deposit in the nanling range south China. *Ore Geol. Rev.* 65, 872–883. doi:10.1016/j.oregeorev.2014.09.019

Zhu, D. C., Tian, R. C., Tian, J. X., Yu, X. F., Yang, Z. Y., and Yang, S. P. (2018). He-Ar isotopic determination of skarn type copper gold deposits in western shandong and its geological significance-taking tongjing type copper gold deposits in yinan area as an example. *Shandong Land Resour.* 34, 1–5. (in Chinese with English abstract).

Zhu, G., Jiang, D. Z., Zhang, B. L., and Chen, Y. (2012). Destruction of the Eastern North China Craton in a backarc setting: Evidence from crustal deformation kinematics. *Gondwana Res.* 22, 86–103. doi:10.1016/j.gr.2011.08.005

Zhu, J. (2014). *Geochronology,Metallogenic model and ore prospecting of the Guilaizhuang gold deposit , west of Shandong province.* Beijing: China University of Geosciences for the master Degree, 1–78. (in Chinese with English abstract).

Zhu, R. X., Chen, L., Wu, F. Y., and Liu, J. L. (2011). Timing, scale and mechanism of the destruction of the North China Craton. *Sci. China Earth Sci.* 54, 789–797. doi:10.1007/s11430-011-4203-4

Zierenberg, R. A., Koski, R. A., Morton, J. L., Bouse, R. M., and Shanks, W. C., III (1993). Genesis of massive sulfide deposits on a sediment-covered spreading center, Escanaba Trough, Southern Gorda Ridge. *Econ. Geol.* 88, 2069–2098. doi:10.2113/gsecongeo.88.8.2069

frontiers | Frontiers in Earth Science

TYPE Original Research
PUBLISHED 10 January 2023
DOI 10.3389/feart.2022.1032183

Check for updates

OPEN ACCESS

EDITED BY
Fei Xue,
Hohai University, China

REVIEWED BY
Qi Li,
China University of Geosciences, China
Zhenjun Sun,
Institute of Disaster Prevention, China
Xiaochao Shu,
China University of Mining and Technology, China

*CORRESPONDENCE
Gongwen Wang,
gwwang@cugb.edu.cn

SPECIALTY SECTION
This article was submitted to Economic Geology, a section of the journal Frontiers in Earth Science

RECEIVED 30 August 2022
ACCEPTED 03 November 2022
PUBLISHED 10 January 2023

CITATION
Xu Y, Wang G, Gao M, Yang W, Yang S, Yun H, Wu P, Guo N and Feng Y (2023), Genesis of the Shibaogou Mo–Pb–Zn deposit in the Luanchuan ore district, China: Constraints from geochronology, fluid inclusion, and H–O–S–Pb isotopes.
Front. Earth Sci. 10:1032183.
doi: 10.3389/feart.2022.1032183

COPYRIGHT
© 2023 Xu, Wang, Gao, Yang, Yang, Yun, Wu, Guo and Feng. This is an open-access article distributed under the terms of the Creative Commons Attribution License (CC BY). The use, distribution or reproduction in other forums is permitted, provided the original author(s) and the copyright owner(s) are credited and that the original publication in this journal is cited, in accordance with accepted academic practice. No use, distribution or reproduction is permitted which does not comply with these terms.

Genesis of the Shibaogou Mo–Pb–Zn deposit in the Luanchuan ore district, China: Constraints from geochronology, fluid inclusion, and H–O–S–Pb isotopes

Yunchou Xu[1], Gongwen Wang[1,2,3]*, Meng Gao[1], Wangdong Yang[1], Shuren Yang[1], Hui Yun[4], Peijian Wu[5], Nana Guo[6] and Yantao Feng[7]

[1]School of Earth Science and Resources, China University of Geosciences, Beijing, China, [2]MNR Key Laboratory for Exploration Theory & Technology of Critical Mineral Resources, China University of Geosciences, Beijing, China, [3]Beijing Key Laboratory of Land and Resources Information Research and Development, Beijing, China, [4]Henan Institute of Geology, Zhengzhou, China, [5]Shandong Province Nuclear Industry Geological Group, Yantai, China, [6]Luoyang City Natural Resources Bureau, Luoyang, China, [7]Luanchuan Xinshu Weibo Mining Co., Ltd., Luoyang, China

The Shibaogou deposit is located in the Luanchuan ore district within the East Qinling orogenic belt (EQOB), central China, which is a newly discovered Mo–Pb–Zn skarn deposit. The skarn and Mo–Pb–Zn ore bodies are mostly hosted in the contact zones between the Shibaogou porphyritic granite and carbonaceous sedimentary rocks from the Luanchuan and Guandaokou sets. A study combined of geochronology, fluid inclusion (FI), and stable isotopes was performed to constrain the mineralization age, source of ore materials, and the origin and evolution of the ore-forming fluids and their relationship with the subduction of the Paleo-Pacific Plate. The mineralization process includes skarn and quartz–sulfide episodes, which has four stages: skarn (I), quartz–molybdenite (II), quartz–galena–sphalerite (III), and quartz–calcite (IV). Molybdenite Re-Os dating suggests that the deposit was formed in the Late Jurassic (147.4 ± 7.2 Ma). Reportedly, there are five primary types of fluid inclusions: L-type, V-type, H-type, S-type, and C-type. In the skarn stage, coexisting H-type (35.58 wt%–46.05 wt% NaCl equiv.) and low-salinity V-type (0.35 wt%–5.7 wt% NaCl equiv.) fluid inclusions show similar homogenization temperatures, which suggests that fluid boiling occurred at 513–550°C and 580–650 bar (2.19–2.45 km). In the quartz–molybdenite stage, the homogenization temperatures of L-type, V-type, minor H-type, and S-type fluid inclusions indicate continued fluid boiling at 324–387°C and 180–250 bar (0.49–0.94 km). In the quartz–galena–sphalerite stage, a fewer number of coexisting V-type and L-type fluid inclusions in quartz shows different salinities with similar homogenization temperatures, indicating that they are trapped at 303–347°C and <150 bar in the boiling process (<0.56 km hydrostatic depth). The minor primary L-type fluid inclusions that have lower salinities of 0.88 wt%–11.34 wt% NaCl equiv were observed in quartz and calcite in the

quartz–calcite stage; in addition, their homogenization temperatures are 103–247°C (typical post-ore conditions). This study found that the ore-forming fluids at the Shibaogou deposit were dominantly magmatic water at the early stage, with input of atmospheric water during fluid evolution, with $\delta^{18}O_{fluid}$ values from –1.168‰ to 8.997‰ and $\delta^{18}D_{fluid}$ values from –106.5‰ to –79.9‰, based on the O and H isotope data from garnet, quartz, and calcite. Furthermore, the S isotopic compositions were measured ranging from 0.8‰ to 14.7‰, and it demonstrated that the ore-forming fluid was mainly derived from magmatic sources. The relatively homogeneous Pb isotopic compositions are similar to those of Shibaogou granite porphyry, which demonstrated that the ore-forming materials were mainly derived from magmatic sources. Molybdenite was precipitated as a result of fluid–rock interactions and fluid boiling, and the galena and sphalerite were precipitated as a result of the decreasing temperature. The subduction of the Paleo-Pacific plate has a critical impact on the complex evolution of ore formation in the Shibaogou skarn deposit in EQOB.

KEYWORDS

molybdenite Re-Os age, fluid inclusion, H–O–S isotopes, Shibaogou Mo–Pb–Zn, Luanchuan ore district

1 Introduction

During the Mesozoic, the lithosphere in and around northeast China was thinned and extended on a large scale because of the subduction of the Paleo-Pacific plate into the Eurasian plate, resulting in not only strong magmatism but also extensive metallogenic events (Hua and Mao, 1999; Mao et al., 2005,2013; Ouyang et al., 2013; Xue F et al., 2021). The East Qinling molybdenum (Mo) belt (EQMB) hosting the largest Mo ore district on the earth (Mao et al., 2011; Zeng et al., 2013) provides excellent areas to study the genetic relationship between the Paleo-Pacific Plate subduction and the mineralization in eastern China (Mao et al., 2011; Zeng et al., 2013). Up to date, most studies are about the deposit type, mineralization ages, evolution of ore-forming fluids, and their geodynamic setting (Li et al., 2007, 2013; Mao et al., 2011; Zeng et al., 2013).

In recent mineral exploration events in the EQMB, some typical skarn-type Mo deposits have been found whose genesis is still debated. Skarn-type deposits are formed from the complex metasomatic processes between carbonate-rich rocks and hydrothermal fluids. They are essential sources for W, Cu, Fe, Zn, Pb, Ag, and Au but seldom for Mo (Newberry and Swanson, 1986; Hedenquist and Lowenstern, 1994; Meinert et al., 2005; Marcoux et al., 2019; Tang et al., 2021; Tang et al., 2022). Therefore, some controversies are remaining on the metallic and fluid sources of skarn-type Mo deposits, including igneous and sedimentary rocks (Yokoro et al., 2013), and other wall rocks (Gemmell et al., 1992).

The Shibaogou deposit is a typical skarn-type Mo (Pb–Zn) in the Luanchuan ore district (LOD) within the EQOB. The Shibaogou deposit contains 87,000 t Mo (avg. 0.11%),79,614 t Pb (avg. 4.2%), and 73,141 t Zn (avg. 3.86%). Xue et al. (2018) reported the petrogenesis and geochronology of the ore-related Shibaogou granitic intrusions; however, the source and evolution of the ore-forming fluids of the Shibaogou skarn-type Mo (Pb–Zn) deposit remain poorly elucidated. The present study showed the new data on molybdenite Re-Os ages, as well as fluid inclusions and H–O–S–Pb isotopes. We aim to determine the mineralization age and source of ore materials and to understand the characteristics of the ore-forming fluids and their evolution, eventually revealing the metallogenic genesis and providing evidence to explore the impact of the subduction of the Paleo-Pacific Plate on the mineralization within the East Qinling orogenic belt.

2 Local geology

The Luanchuan ore concentration area has played an important economic role in the production of Mo–W–Pb–Zn–Ag minerals (Figure 1). In the East Qinling area, Mo > 1.5 Mt, ~ 0.5 Mt WO_3, 7 Mt Pb and Zn, and 8000 t Ag ore belt were discovered (Mao et al., 2011; Wang et al., 2019). Shibaogou is located on the southern edge of the North China Craton. The Luanchuan fault zone, North China Craton to the north, and North Qinling fold system to the south define the tectonic units. The main strata in this area are the Mesoproterozoic Guandaokou Group, Kuanping Group, Neoproterozoic Luanchuan Group, and Paleozoic Taowan Group. The Mesoproterozoic sedimentary rocks are composed of sandstone, dolomite, greenschist, and a small amount of quartzite, which are partially interbedded with marble. The

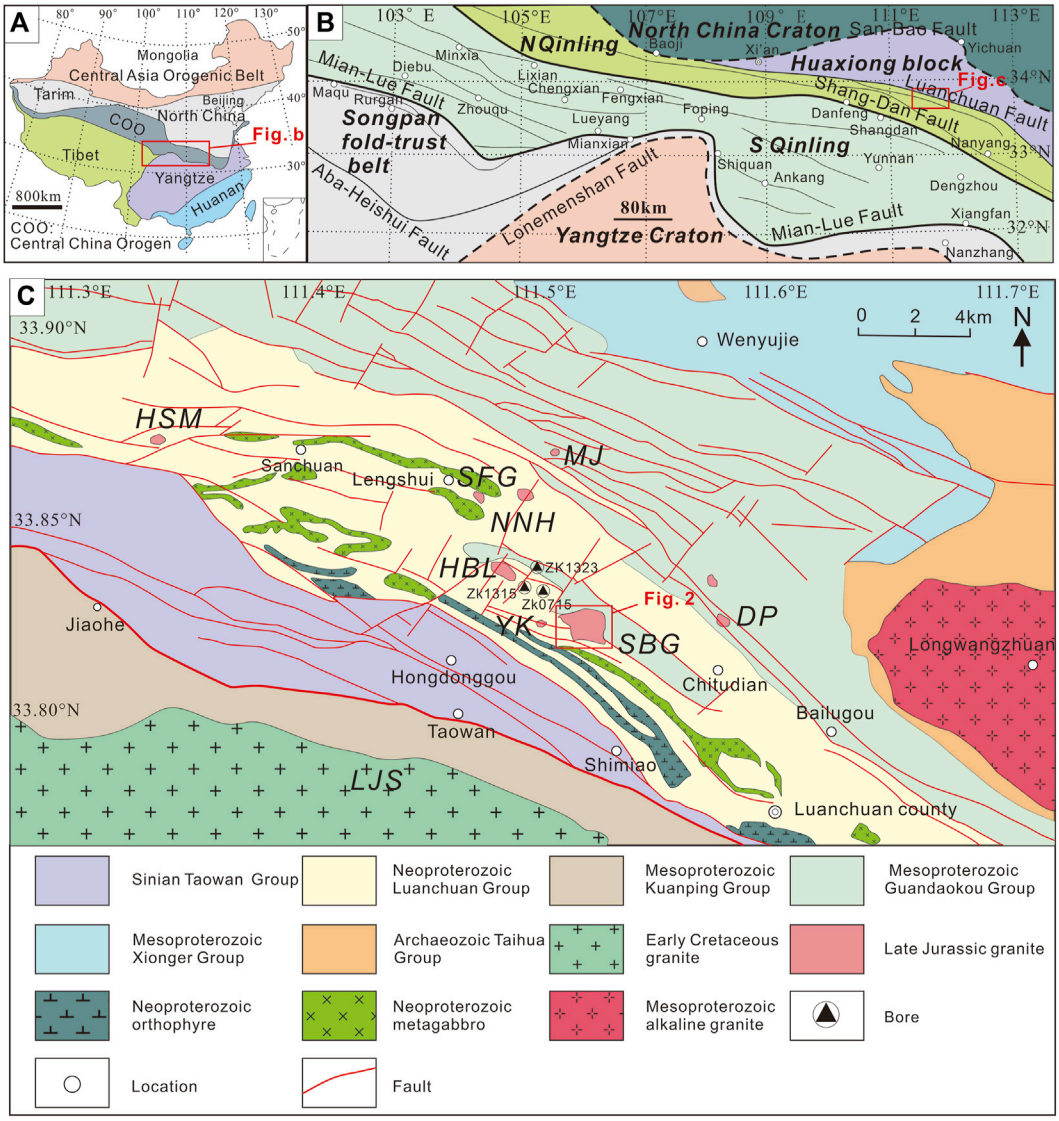


FIGURE 1
(A) Tectonic map of China showing the location of Central China belt and North China Craton; **(B)** tectonic subdivision of the Qinling Orogen showing the location of Luanchuan ore district; and **(C)** geological map of Luanchuan ore district displaying the geology and the distribution of granites, modified after Duan et al. (2010), Mao et al. (2011) and Yang et al. (2016). YK, Yuku; SBG, Shibaogou; HBL, Huangbeiling; NNH, Nannihu; SFG, Shangfanggou; MJ, Majuan; DP, Daping; HSM, Huoshenmiao; and LJS, Laojunshan.

Luanchuan Group is composed of dolomite and schist, and the Taowan Group is composed of limestone, schist, and conglomerate. The sedimentary unit of the Luanchuan mining area (Figure 1) is intruded by extensive Late Jurassic to Early Cretaceous porphyritic granites and a small amount of contemporaneous quartz diorites. The main structures of the Luanchuan mining area are the WNW-ESE-trending Luanchuan and Miaozi faults, and the NE-SW-trending Huangbeiling–Nannihui–Maquan and Shibaogou–Zhuangke faults. Mesozoic LOD magmatic activity was particularly intense and widespread, forming a broad range of generations of granites associated with molybdenum, tungsten, gold, silver, copper, galena, and sphalerite mineralization. Granite porphyry is the most common and important parent rock for molybdenum mineralization, with phenocrysts of quartz (20%–35%), potassium feldspar (40%–55%), plagioclase (10%), and, occasionally, black Mica. According to the zircon U–Pb dating results, the porphyritic granites were in place in a relatively short period of 158–141 Ma (Mao et al., 2005; Li et al., 2015; Xue et al., 2018).

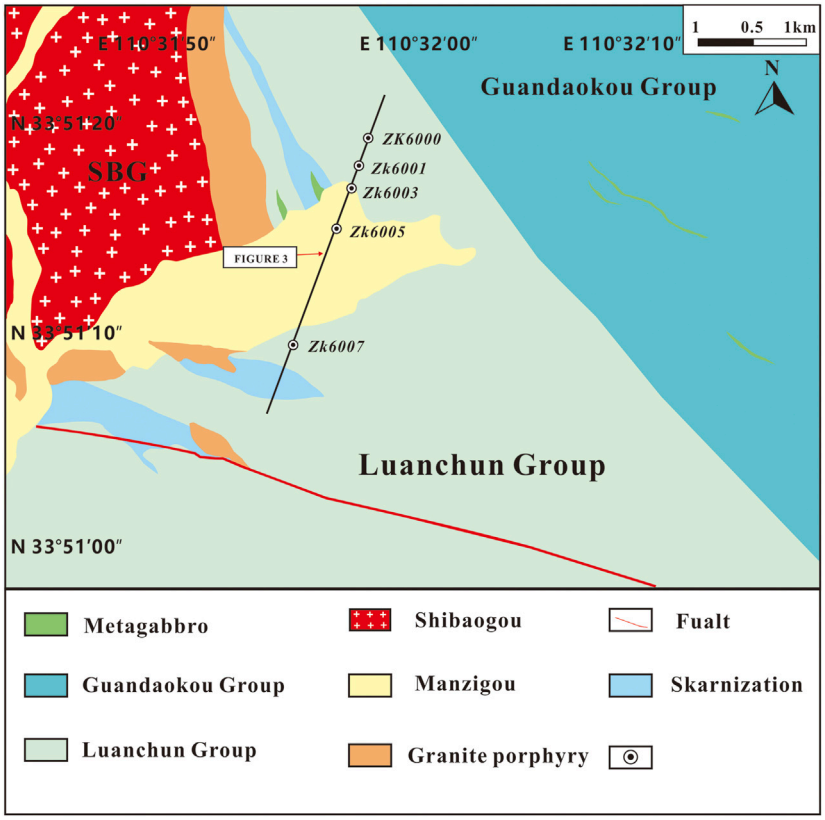


FIGURE 2
Geology of the Luanchuan ore district showing the Shibaogou Mo–Pb–Zn deposit (after Xue L. W et al., 2021).

3 Deposit geology

3.1 Geology

The Luanchuan Group has abundant mineral resources, including galena–sphalerite ore, iron ore, vanadium ore, stone coal, and other types of ore. The Xiaohonggounao–Xiaolaohugoukou Fault, Maquan–Daping Fault, and Huangbeiling–Shibaogou Fault have all developed, with the latter two faults compounded near Guodian. In total, two dense belts of the north (north) east-trending faults are the Huangbeiling–Nanihu–Maquan belt and Shibaogou–Qinghetang fault dense belt. The sedimentary rocks related to the Shibaogou deposit comprise the Guandaokou and Luanchuan groups (Figures 2, 3), which consist mainly of marble, metasandstone, schist, and quartzite. In the Shibaogou Mo–Pb–Zn deposit, the Guandaokou group is mainly the Baishugou Formation and the Luanchuan group is dominantly Sanchuan, Nannihu, and Meiyaogou formations. The Meiyaogou Formation is in fault contact with the Baishugou Formation and has a conformable contact with the Nannihu Formation. The Shibaogou granite porphyry intrudes into the Guandaokou group and Luanchuan group, and intrudes into the Guandaokou group more. The mineralization is also mostly in the place where the Shibaogou granite porphyry contacts with the Guandaokou group. A total of five economic Mo ore bodies (No. 1–5) have been found at the Shibaogou deposit, in which the number 1 ore body is of greatest worth. The Mo-1 ore body is the largest molybdenum ore body in the mining area. It is located between the Heng 72 exploration line and the 58 exploration line. The occurrence elevation is 534–1245 m, the minimum is 339 m, the true thickness of a single project is 16.19–59.57 m, the average true thickness is 38.89 m, and the thickness variation coefficient is 45.12%. A total of nine economic Pb–Zn ore bodies (No. 1–9) have been explored at the Shibaogou deposit, and the No. 1 ore body was found the greatest worth. It is 1400 m long and 0.41–1.85 m wide. The ore body has obvious rock-control characteristics as a whole, and it often occurs in the lower side of the strata of the upper Meiyaogou Formation and in siliceous stripe (zone) of dolomite marble within 20–30 m of the lower part of the carbonaceous slate, and the thickness is of a stable type alteration and mineralization.

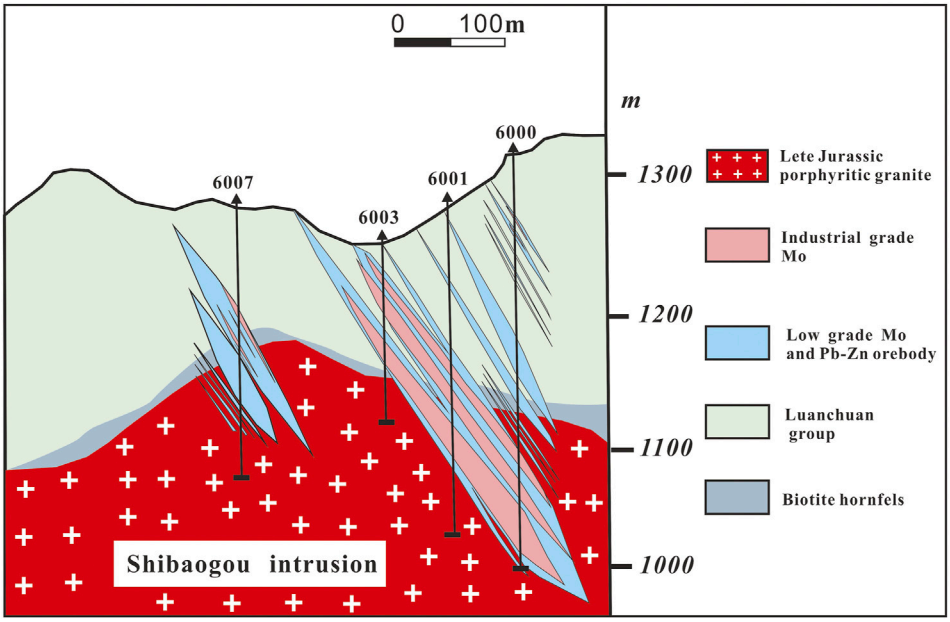


FIGURE 3
Geological map of the Shibaogou Mo–Pb–Zn deposit geologic cross section showing the spatial relationship among strata, intrusion, alteration, and ore bodies.

3.2 Alteration and mineralization

3.2.1 Skarn stage (stage I)

3.2.1.1 Prograde skarn stage

The Shibaogou skarn Mo deposit has a typical skarn prograde alteration assemblage. Based on field observation, the rock types vary from inner Shibaogou granite porphyry to outer garnet–pyroxene skarn, pyroxene–garnet skarn, and garnet–wollastonite skarn termed as a prograde alteration. The prograde skarn occurs as an initial alteration assemblage. This stage is dominated by anhydrous fine-to-coarse-grained (0.06–4 mm) and euhedral-to-subhedral crystal garnet minerals (Figures 4A,E,G), which were developed widely in the Shibaogou deposit. In addition, pyroxene minerals exhibit colors of light grayish to dark green and sizes of 0.06–2.5 mm (Figure 4F). Wollastonite minerals are sometimes associated with garnet minerals occurring near the marbles as subhedral radiating clusters (Figures 4G, 5A–C).

3.2.1.2 Retrograde skarn stage

Compared to other skarn deposits, the Shibaogou Mo deposit is characterized by weakly developed retrograde skarns, which are dominated by epidote minerals forming together with interstitial quartz (Figures 4H, 5E), or as replacements of garnet minerals. They are euhedral to subhedral with variable sizes from 0.03 up to 1 mm occurring as veins cutting the pyroxene–garnet skarn.

3.2.2 Quartz–molybdenite stage (stage II)

Quartz–molybdenite veins that have a length of 3–50 cm are the main economic product at the dominant mineralization stage in the shibaogou deposit. A large number of platy molybdenite minerals occur at the edges of quartz veins in contact with skarn minerals or in disseminated form in garnets (Figures 4B,F,J, 5D–F), while some fine-grained crystals assembled in flakes along the veinlet walls. In addition, a few clumps of quartz–molybdenite veins developed in banded garnet and pyroxene skarns. These veins crosscut pyroxene and altered garnet minerals, implying that they formed after garnet and pyroxene in the skarn stage (Figure 4K).

3.2.3 Quartz–galena–sphalerite stage (stage III)

The quartz–galena–sphalerite stage is another important metallogenic stage in the Shibaogou deposit generating various sulfides including pyrite, sphalerite, galena, and chalcopyrite. Among these sulfides, galena is the major ore mineral, which is commonly leaden-colored but varies from fine to coarse grained occurring with sphalerite as intergranular aggregates (Figures 5G–I). They also occur together with quartz grains, cutting across that quartz–molybdenite vein (Figures 4C,D).

3.2.4 Carbonate stage (stage IV)

During the post-mineralization stage, some low-temperature alteration minerals formed consisting of dominant calcites, which occur as veinlets crosscutting skarn and sulfides (Figure 4M).



FIGURE 4
(A) Calcite–quartz vein cross-cutting a quartz–molybdenum–vein molybdenum; **(B)** molybdenum mineralization in skarn; **(C)** galena mineralization in the quartz–galena–sphalerite stage; **(D)** galena mineralization coexisting with pyrite in the quartz–galena–sphalerite stage; **(E)** molybdenum mineralization in garnet skarn; **(F)** molybdenum–quartz vein cross-cutting pyroxene skarn; **(G)** wollastonite skarn (Wo>Grt>Pyx); **(H)** chlorite alteration overprinting skarn; **(I)** dikes intrude into ore bodies; **(J)** galena–sphalerite–quartz vein cross-cutting molybdenum–quartz vein; **(K)** quartz–sulfide vein cross-cutting molybdenum–quartz vein; **(L)** galena mineralization coexisting with sphalerite in the quartz–galena–sphalerite stage; and **(M)** calcite–quartz vein cross-cutting molybdenum–quartz vein and garnet skarn (Grt>Pyx). Chl = chlorite; Gn = galena; Grt = garnet; Mo = molybdenite; Py = pyrite; Pyx = pyroxene; Q = quartz; Sph = sphalerite; and Wo = wollastonite.

4 Sampling and analytical methods

4.1 Microthermometry and laser Raman spectroscopy

Quartz and calcite inclusions that are fluid-filled were studied throughout multiple hydrothermal phases. In Beijing, in Chinese College of Technology and Academic Research, the Linkam THMSG600 high-temperature chiller and the Zeiss microscope was employed to implement experimental fluid inclusions micromeasurement. The 195 to + 600°C fluid inclusions was frozen at 150°C degrees and gradually heated to complete uniformity. Near the phase transition, the heating/freezing rate is 15°C/min, and the low temperature is 1–0.1°C/min. The ultimate ice melting point was employed to establish the concentration of salt of the inclusion complex that incorporated water (NaCl H_2O). Accessing the approach developed by Sterner et al. (1988), the salinity of insertion coordination compounds limestone salts (high salt) was approximated (Collins, 1979). The salt concentration of aqueous (NaCl H_2O) or CO_2 actually contains elements served as a

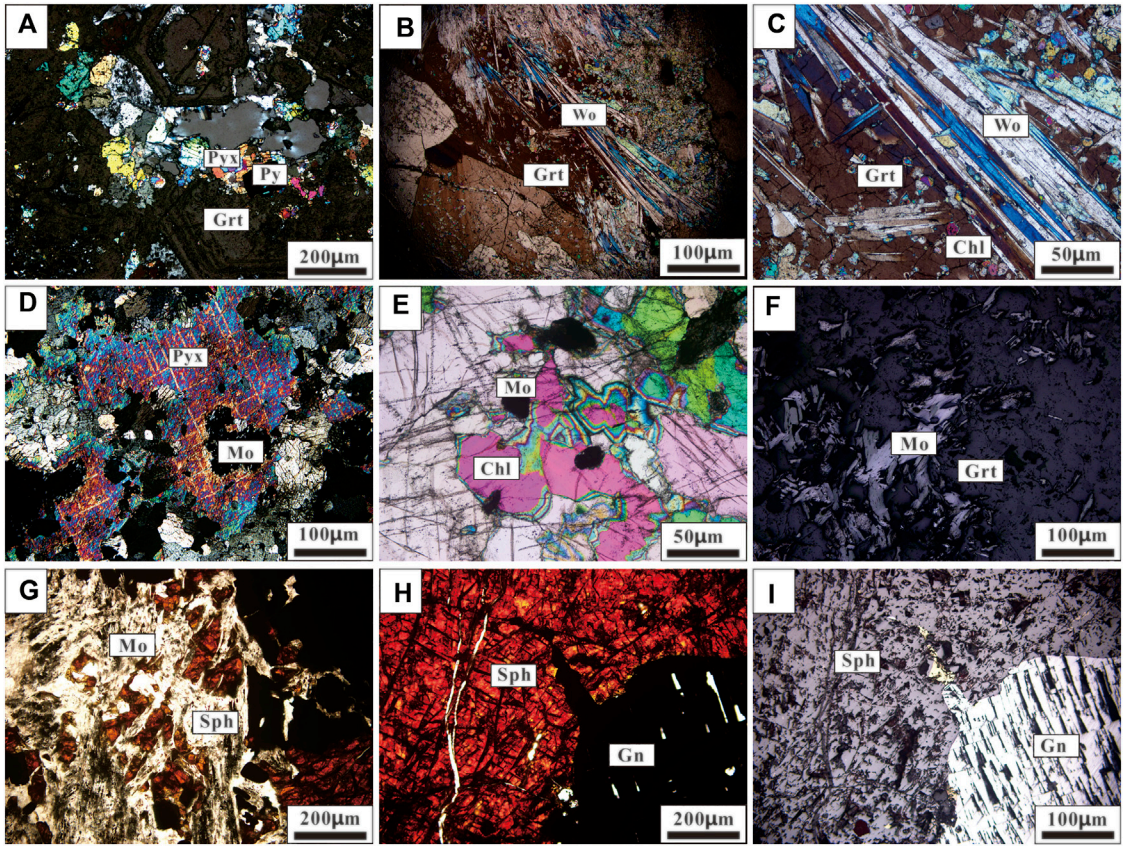


FIGURE 5
(A) Garnet skarn (Grt>Pyx); **(B)** wollastonite skarn (Wo>Grt>Pyx); **(C)** wollastonite skarn (Wo>Grt>Pyx). Chlorite alteration overprinting garnet skarn; **(D)** pyroxene with clear orthorhombic cleavage coexisting with molybdenum; **(E)** chlorite alteration; **(F)** molybdenum mineralization in the quartz–sulfide stage; **(G)** molybdenum coexisting with galena and sphalerite; and **(H–I)** galena coexisting with sphalerite in the quartz–galena–sphalerite stage. Chl = chlorite; Gn = galena; Grt = garnet; Mo = molybdenite; Py = pyrite; Pyx = pyroxene; Q = quartz; Sph = sphalerite; and Wo = wollastonite.

premise for estimation methods (daughter ore that is invisible or translucent).

For an optical analysis, upwards of 50 quintuple grinding discs have been manufactured, and 18 representative participants were taken for micro-temperature detection and Raman spectroscopic–independent inquiry. The Chinese Training Institute of Geographical Studies' Hydraulic Addition Center in Beijing, China, used RM-2000 optical Raman spectrometer to characterize the structure of water exclusions. The Ar^{+} laser really does have a spectral resolution of 1 cm^{-1}, a wavelength of 514.5 nm, a scanning speed of 40 mW, and a girder beam of 2 μm.

4.2 S isotopes

The S isotope ratios are provided as $\delta^{34}S$ relative to the Canyon Diablo troilite, and the analytical repeatability is ±0.2‰ (Mao et al., 2008). For the sulfur isotopic analysis, 12 sulfide samples from ores and veins with sulfides at various phases of mineralization were chosen. The Sulfur Isotope Center at the Department of Mineral Reserves, Chinese Ministry of Geosciences, Beijing, harnessed a Finnegan MAT-251EM atomic absorption spectrophotometer. Compared to Caón Diablo Troilite (CDT), the amount of sulfur isotopes is in per mil (‰) units. The accuracy of this method can within ±0.2‰. At the MLR Central Research Lab of Mineral deposits and Mineral Characterization, CAGS, measurements took place using the MAT251EM spectrometer. This analytical method is consistent with Duan et al. (2010). The analytical reproducibility was ±0.2‰, and the proportion of the S element to the black meteorites in the canyon was $\delta^{34}S$ (Mao et al., 2008).

4.3 Pb isotopes

For galena isotopic analyses, 16 samples including 12 sulfides and four granitoid rocks were selected. Thermoelectric ablation

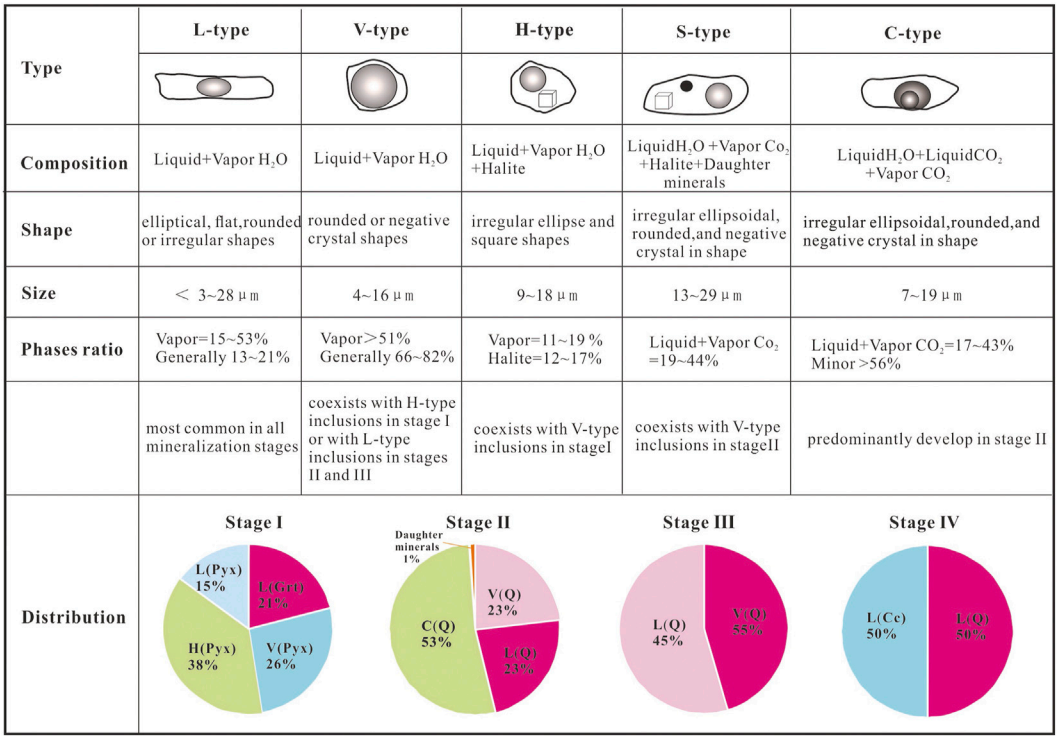


FIGURE 6
Characteristics and distributions of fluid inclusions in the Shibaogou Mo–Pb–Zn deposit.

absorption spectroscopy by ISOPROBE-T was used to revise the feldspars in the datasets. Galena isotope compositions are analyzed using a Phoenix thermo desorption Raman spectroscopy with a single band, M^{+}, and an adjustable multi-Faraday receiver. When the vacuum in the analysis chamber is less than 2.0E-8 mbar, take measurements. Sweep the peak to modify the focusing parameters and control the intensity of the highest abundant isotope ion current to achieve 1×10^{-11}. For measurement after heating to an appropriate temperature, NBS981s standard sample data is $^{208}Pb/^{206}Pb$ = 2.1673–2.1689, $^{207}Pb/^{206}Pb$ = 0.91431–0.91497, and $^{204}Pb/^{206}Pb$ = 0.059005–0.059079, with a background Pb of 100 pg during the entire process.

4.4 H–O isotopes

Shibaogou granite metamorphic rock and carbonate's contact area possessed skarn minerals which been probed. This article assessed the quartz in columns representing lamellar molybdenite. Moreover, two kinds of quartz, galena and sphalerite, were isolated in quartz veins in this test. In the later stages of quartz veins and calcite deposits, a total of two calcites are obtained. A CAGS Mineralogical composition Organization MAT253EM spectrometer was deployed to scan minerals. The monitoring and estimation approach devised by Zhang, (2014) was verified through inspection of H and O isotopes, and the determination accuracy of the O isotope is greater than ±0.1‰, while that of the H isotopic element is above ±0.1‰ (Mao et al., 2008). The Beijing Bureau of Mineral Resources' carbon isotope treatment center undertook modeling and simulation on the isotopic of both hydrogen and oxygen. Before water was extracted from the 40–80 mg rock isolation solution, the specimens were divided *via* magnetic tape extraction processes and hand diagnostic tests. Then, at a high temperature of 600°C, the liquid is separated from the liquid. Before performing the D/H test, measure the exhaust gas with a pressure gauge. In the $^{18}O/^{16}O$ analysis, 1 mg of oxygenates were treated with laser-heated chlorine trifluoride (Macaulay et al., 2000) and his men. Similar to Fallick et al. (1993), the oxygen isotope laser fluorination process was discussed, which described the hydrogen isotopes. For $\delta^{18}O$ and δD tests, the accuracy determined by repeated analysis was ±0.2‰. At the assumed crystallization temperature, the isotopic composition of the fluids studied in the study was determined using appropriate fractionation factors (Table 1). The compositions of oxygen and hydrogen isotopes are stated in ‰ terms of Vienna Standard Mean Ocean Water ($V_{\text{-SMOW}}$).

TABLE 1 Summary of microthermometric data fluid inclusions from the Shibaogou Mo–Pb–Zn deposit.

Stage	Type[a]	Host mineral	Tm, ice (°C)[b]	Tm, CO_2 (°C)[c]	Tm, cla (°C)[d]	Th, CO_2 (°C)[e]	Tm, halite (°C)[f]	Th, total (°C)[g]	Peak of Th	Salinity (wt%)
I	L	Grt	−10.9 ~ −6.2					453 ~ >550	500–550	9.47–14.94
		Pyx	−6.0 ~ −0.3					357–432		0.53–9.21
	V	Pyx	−3.5 ~ −0.2					513–550		0.35–5.7
	H	Pyx					264–387	413–562		35.58–46.05
II	L	Qtz	3–8.2					256–397	350–400	3.57–11.97
	V	Qtz	8.6–9.7					314–397		0.62–2.81
	C_1	Qtz	5.2–9.8		−59.4 ~ −57.1			324–387		0.41–8.77
III	L	Qtz	−5.8 ~ −0.5					163–347	200–250	0.87–8.94
	V	Qtz	−5.7 ~ −1					303–347		1.73–8.81
IV	L	Qtz	−14 ~ −0.8					103–247		0.88–11.34
		Cc	−3 ~ −0.2					151–231		2.07–8.41

[a]Fluid inclusion type: L = liquid-rich; V = vapor-rich; H = halite-bearing; C_1 = CO_2-bearing two-phase; C_2 = CO_2-bearing three phase.
[b]Tm, ice: final ice melting temperature.
[c]Tm, CO_2: final solid CO_2 melting temperature.
[d]Tm, cla: final CO_2 clathrate dissociation temperature.
[e]Th, CO_2: CO_2 phase homogenization temperature.
[f]Tm, halite: halite dissociation temperature.
[g]Th, total: total homogenization temperature.

TABLE 2 Molybdenite Re-Os dating results of the Shibaogou Mo–Pb–Zn deposit.

Sample	Weight (g)	Re (μg/g)		Os (ng/g)		^{187}Re (μg/g)		^{187}Os (ng/g)		Model age (Ma)	
		Value	2σ	Value	2σ	Value	2σ	Value	2σ	Value	2σ
710–10	0.02089	3.9163	0.0353	0.3938	0.0542	2.4614	0.0222	62.09	0.37	151.2	2.2
710–10	0.03049	2.5258	0.0233	2.9949	0.0279	1.5875	0.0146	39.67	0.29	149.8	2.3
710–15	0.01000	2.9130	0.0255	0.2141	0.0495	1.8309	0.0160	45.32	0.33	148.4	2.2
710–7	0.02034	1.7848	0.0132	0.0224	0.0405	1.1218	0.0083	27.76	0.17	148.4	2.0
Sbj710-1	0.03022	5.2229	0.0719	0.0204	0.0078	3.2827	0.0452	80.09	0.46	146.3	2.6
710–20	0.03128	4.4319	0.0558	0.2950	0.0083	2.7855	0.0350	69.24	0.40	149.0	2.5

4.5 Molybdenite Re-Os dating

A total of seven molybdenites with a weight >300 μg, a purity >93% and a particle size of less than 0.2 mm were determined from samples taken at 20-m intervals down the shibaogou mine. Our sampling can reduce the coupling consequence of Re and Os, resulting in higher accuracy (Stein et al., 2003). The TJA-X series ICP-MS apparatus, National Geographical Analysis and Research Center, Chinese Academies of Geosciences, was harnessed in accordance with the analytical procedure described by (Du et al., 2001) The molybdenite age was calculated to be model years (Smoliar et al., 1996). The model age of molybdenite was estimated.

5 Results

5.1 Molybdenite Re-Os dating

The Re-Os data of six molybdenite samples collected at intervals of 20 m from the Shibaogou mine are shown in Table 2. The content of ^{187}Re was 11.218–32.827 μg/g with an average value of 21.783 μg/g, and the content of ^{187}Os was in the range of 27.76–80.09 ng/g with an average value of 54.03 ng/g. Re-Os model ages ranged from 146.3 to 151.2 Ma, with a weighted mean age of 148.9 ± 1.7 Ma. The ^{187}Re-^{187}Os isochronous age is 147.4 ± 7.2 Ma. All age values were processed and obtained using ISOPLOT software (Ludwig, 2003) and are similar to model age.

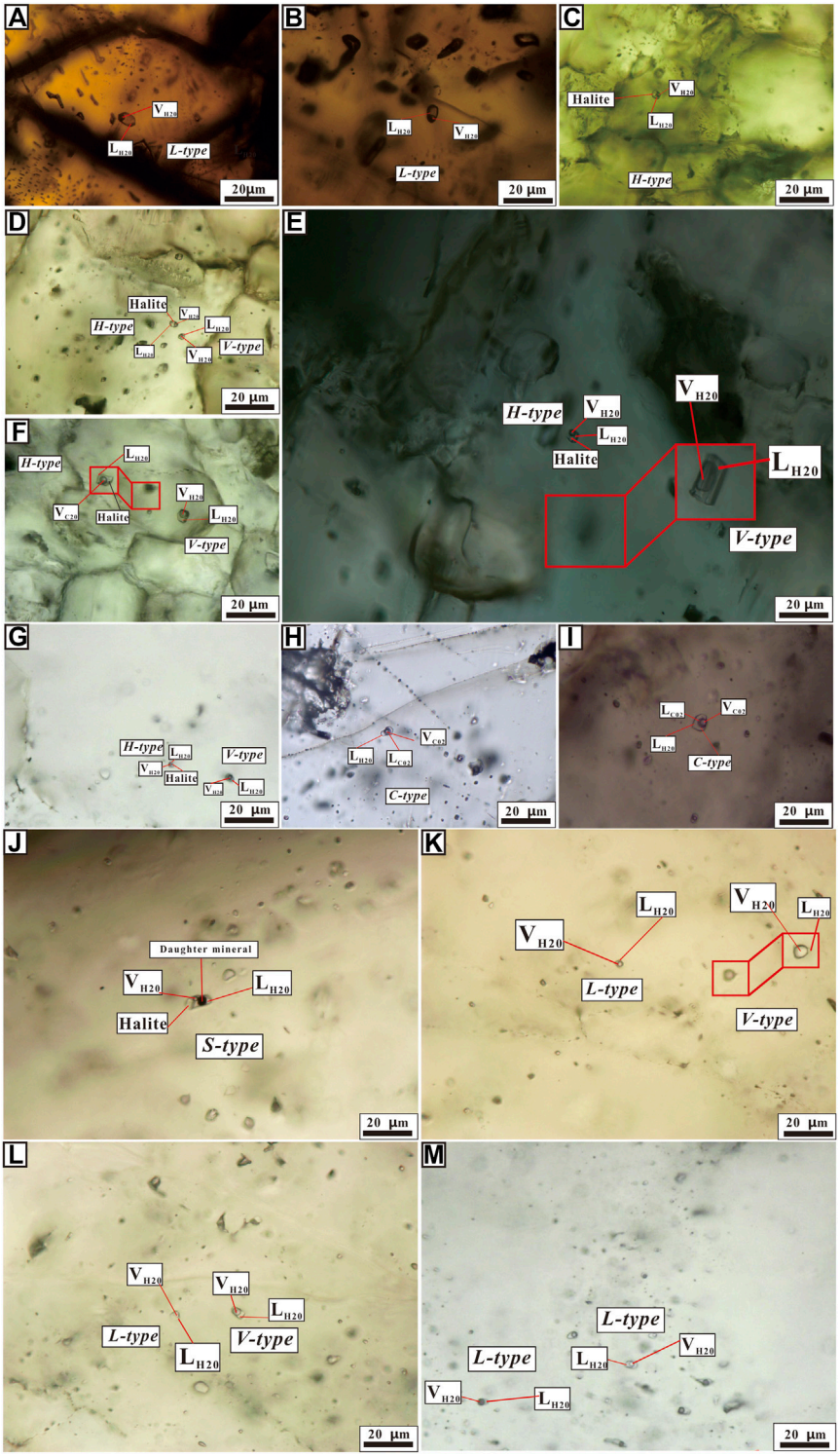


FIGURE 7
Photomicrographs of representative fluid inclusions (fluid influsions) of different types in the Shibaogou W (Mo) deposit. **(A)** Liquid-rich (L-type) fluid inclusions in garnet; **(B)** liquid-rich (L-type) fluid inclusions in garnet; **(C)** halite-bearing/hypersaline (H-type) fluid influsions in pyroxene; **(D)** halite-bearing/hypersaline (H-type) fluid influsions in pyroxene; **(E)** coexisting vapor-rich (V-type) inclusion and halite-bearing/hypersaline (H-type) inclusion in pyroxene; **(F)** coexisting V-type fluid inclusions and L-type fluid inclusions hosting a quartz crystal in stage I pyroxene; **(G)** coexisting vapor-rich (V-type) inclusion and halite-bearing hypersaline (H-type) inclusion in pyroxen; **(H)** CO_2-bearing three phase inclusions (C-type) in stage II quart; **(I)** CO_2-bearing three phase inclusions (C-type) in stage II quart; **(J)** S-type inclusion in stage II quart; **(K)** L-type and V-type fluid influsions in stage III quartz; **(L)** L-type fluid influsions in stage IV calcite; and **(M)** L-type fluid influsions in stage IV calcite.

5.2 Fluid inclusion

Based on the classification principles (Roedder 1984; Lu et al., 2004), primary fluid inclusions in garnet and pyroxene from the first stage, quartz from the second and third stages, and calcite from the fourth stage at room temperature are observed. The Shibaogou deposit has fluid inclusions of five distinct types (Figures 6, 7).

The L-type fluid inclusions consist of a 10–50 vol% vapor phase (V_{H2O}) and a liquid phase (L_{H2O}) at air conditions. From stage I through stage IV, L-type fluid influsions are most prevalent. L-type fluid inclusions frequently range in size from 2 to 30 μm. Oval, flat, or circular fluid inclusions help compensate the L-type (Figures 7A,B,M).

The V-type fluid inclusions can be found a larger vapor ratio. At ambient temperature, the additions' darkly colored bubbles represent more than half of the total volume (Figures 7C,D). The size of V-type fluid inclusions is about 5–15 μm, and the shapes are mostly oval, triangular, and irregular. Now at sedimentary deposits stage (Figures 7C,D), they mix with H-type fluid inclusions, and at the II and III phases in quartz, they cohabit with L-type fluid inclusions (Figures 7D–F).

The C-type fluid inclusions are characterized by coexisting three phases includingV_{CO2} phases, L_{CO2} phases and L_{H2O} phases (Figures 7H,I). The V_{CO2} and L_{CO2} phases occupy 35%–70% of the total inclusion volume. The fluid inclusions of the C-type variation are elliptic, round, and also have deformed crystalline structure. The C-type fluid inclusions spanned around 8–20 μm in size which have predominantly developed in stages II and very few in stage III.

The H-type fluid inclusions contain three phases including L_{H2O} phases, V_{H2O} phases and halite phases. The H-type fluid inclusions are negative crystal shapes with 9–18 μm in size (Figures 7D–F). In phases II, there are very few pyroxene and quartz crystals, but in the sedimentary deposits stage, these grains are valuable international with V-type fluid inclusions. The H-type fluid influsions are significantly neglected in the Shibaogou deposit in contrast to other types of fluid influsions. Furthermore, this species of fluid influsions is homogenized by burst departure following the slow breakdown of cubic halite (Figure 7G).

The S-type fluid inclusions contain three phases including L_{H2O} phases, V_{H2O} phases, halite phases and stages of daughter elements. The S-type fluid inclusions are mainly negative crystal shapes. The S-type fluid inclusions are 10–20 μm in size (Figures 7D,J). The S-type fluid inclusions are much less observed than other liquid inclusions types but are mainly found in quartz grains in stages II. The S-type liquid inclusions are homogenization by bubble disappearance after cubic halite gradually dissolution but daughter minerals are not homogenized.

5.2.1 Microthermometry

The microthermometric data were collected from isolated inclusions in transparent mineral from stage I to stage IV excluding those secondary inclusions which have necking or leaking features. The results of fluid inclusion salinity and homogenization temperature from different mineralization stages are summarized in (Table 1; Figure 7) and the following paragraphs.

1) In the skarn stage, the pyroxene minerals are characterized by predominant H-type, L-type, and V-type fluid inclusions, and garnet grains host numerous L-type and minor V-type fluid inclusions (Figures 7D–F). In garnet, the median temperature of L-type fluid influsions is between 453 and 550°C, between −10.9 and −6.2°C, and between 9.47 and 14.94 wt% NaCl equiv. (Table 1 and Figures 7A,B). In contrast, the augite minerals of L-type fluid influsions are between 357 and 432°C, −6.0~−0.3°C, and 0.53 wt%–9.21 wt% NaCl equiv. (Table 1 and Figures 8A,B). Nevertheless, H-type fluid influsions are still detectable in pyroxene, and even when the rock ice melts, the liquid water in these clathrates remains persistent. The H-type fluid influsions had salinity levels of 35.58 wt%–46.05 wt% NaCl equiv, a mean temperature of 413–562°C, and a soluble of rock salt of 264–387°C (Table 1 and Figures 7D–F). The results demonstrate that 513–550°C is the ultimate homogenized temperature of V-type fluid influsions in pyroxene.
2) In the quartz–molybdenite stage, homogeneity heats, and eventual glacial melt temperatures of the L-type fluid influsions in the quartz–molybdenite vein are 256–397°C, −3~ −8.2°C, 3.57 wt%–11.97 wt% (NaCl equiv.). Alternating V-type fluid inclusions and L-type fluid inclusions (Figure 7K), with salt concentrations that varied (0.62–2.81 and 3.57 wt%–11.97 wt% NaCl equiv., separately), and homogenized temperatures and is equivalent (314–397°C and 256–397°C, correspondingly; Table 1). C-type fluid inclusions were homogenized in 0.41 wt%–8.77 wt% NaCl equiv in the range of 324–387°C. In addition, there is an S-type inclusion that yielded a homogenization temperature of 381°C (Figure 9C).
3) In the quartz–galena–sphalerite stage, the predominant L-type fluid influsions in quartz grains possess homogenized temperatures between 163 and 347°C and final glacial melt temperatures between −5.8 and −0.5°C, with salinities ranging from 0.8 wt% to 7.94 wt% NaCl equivalent. The temperature measurement in the V-type fluid influsions in quartz ranges from 1.73 wt% to 8.81 wt % NaCl equiv., 173–347°C for homogeneity, and −5.7 to −1°C for terminal ice melting, respectively. (Table 1 and Figures 7L, 9E,F).
4) In the carbonate stage, considering homogenized temperatures of 151–231°C, eventual melting ice

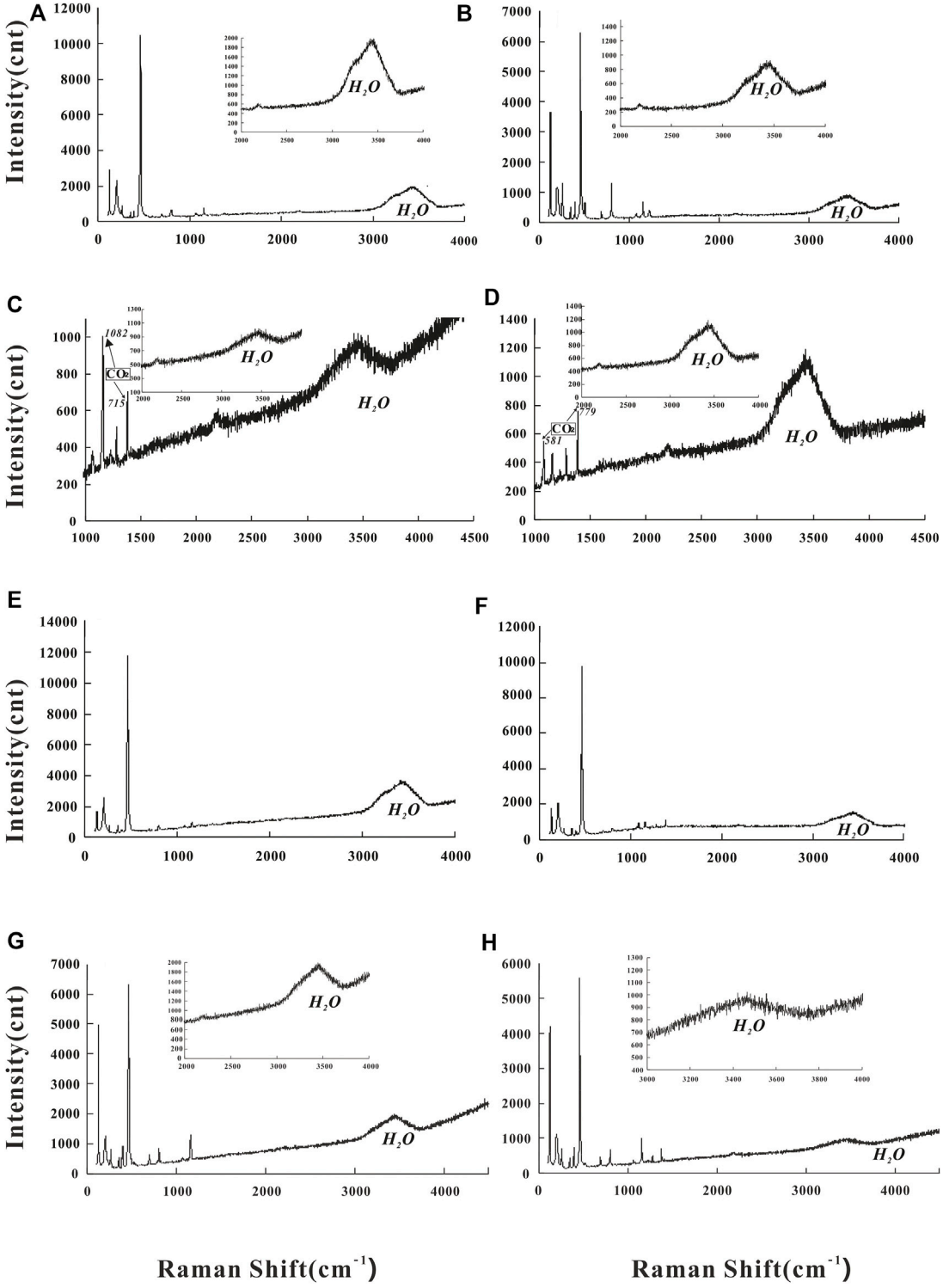


FIGURE 8
Representative laser Raman spectra for fluid inclusions from the Shibaogou Mo–Pb–Zn deposit. **(A)** H-type fluid inclusion in the anhydrous skarn stage I; **(B)** L-type fluid inclusion in the hydrous skarn stage I; **(C)** C-type fluid inclusion in the quartz–molybdenite stage II; **(D)** C-type and L-type fluid inclusion in the quartz–sulfide stage II; **(E,F)** L-type fluid inclusion in the quartz–galena–sphalerite stage III; **(F)** L-type fluid inclusion in the carbonate stage IV; and **(G,H)** L-type fluid inclusion in the carbonate stage IV.

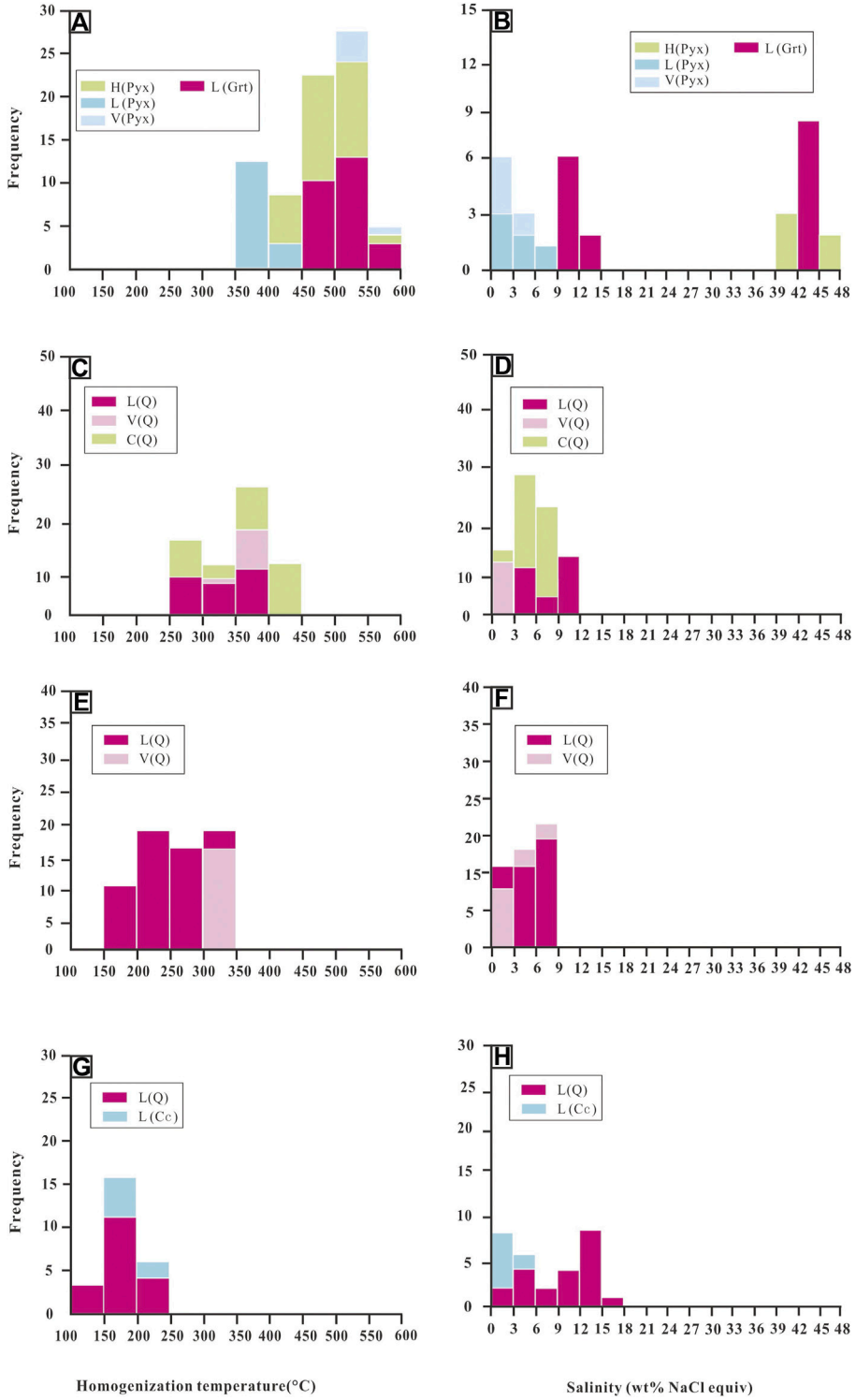


FIGURE 9
Histograms of homogenization temperatures and salinities for all inclusion types in the Shibaogou Mo–Pb–Zn deposit; **(A,B)** variations of homogenization temperatures and salinities in the anhydrous skarn stage; **(C,D)** variations of homogenization temperatures and salinities in the hydrous skarn stage; **(E,F)** variations of homogenization temperatures and salinities in the quartz–sulfide stage; and **(G,H)** variations of homogenization temperatures and salinities in the carbonate stage.

TABLE 3 H–O isotope data of garnet, scheelite, and quartz from the Shibaogou Mo–Pb–Zn deposit.

Stage	Sample	Mineral	$\delta^{18}O_{SMOW}$ (%)	$\delta^{18}O_{fluid}$ (%)	δD_{SMOW} (%)	δD_{SMOW} (%)
I	65–1	Garnet	5.9	4.163	−79.9	−79.9
	65–2	Garnet	6	4.288	−83.3	−83.3
II	710–1	Quartz	14.5	8.997	−98.2	−98.2
	710–10	Quartz	10.8	6.325	−91.8	−91.8
III	710–20	Quartz	10.3	1.809	−105.4	−105.4
	710–16	Quartz	11.5	3.009	−104.3	−104.3
IV	710–6	Quartz	12.2	−1.768	−102.7	−102.7
	710–19	Quartz	12.8	−1.168	−106.5	−106.5

Isotope fractionation equilibrium formulas used in the following mineral-water system (Kelvin for T), including (1) garnet–water (Taylor, 1974), (2) scheelite-water (Wesolowski and Ohmoto, 1986), and quartz–water (Clayton et al., 1972).

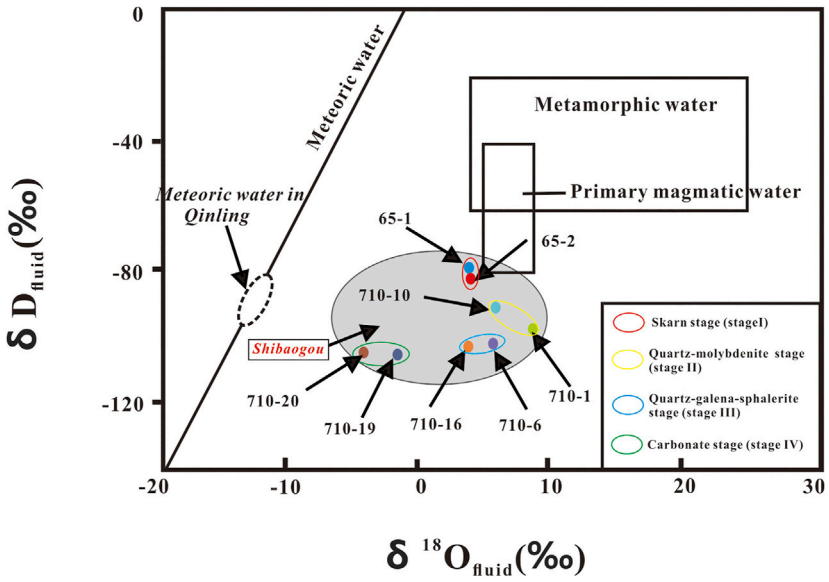


FIGURE 10
The $\delta^{18}O_{fluid}$ vs. δD_{fluid} diagram of the Shibaogou Mo–Pb–Zn deposit.

temperatures of −3 to −0.2°C, and salt concentrations ranging from 2.07 wt% to 8.41 wt% NaCl equiv, calcite minerals include a rich source of L-type fluid influsions (Table 1 and Figure 9H). The L-type fluid influsions also predominate in quartz, with homogenized temperatures ranging from 130 to 249°C, utmost ice melting temperatures of −14 to −0.8°C, and high salinity from 0.88 wt% to 11.34 wt% NaCl equiv (Figures 9G,H).

5.2.2 Laser Raman spectroscopy

In order to restrict the gas–liquid two-phase components in the liquid inclusions, Laser Raman spectroscopy was performed to identify the fluid inclusions from all stages. H_2O–NaCl appears to be the predominant constituent of the flow in the sedimentary deposits stage (I) since it is present in both the liquid and gas phases of the H-type inclusions in the pyroxene crystals (Figure 8A). The solvent phase and gasoline phase of the predominant C-type clathrate of quartz (quartz–molybdenite stage) are close to CO_2 (Figures 8C,D), indicating that the components of the quartz–molybdenite section are H_2O–NaCl–CO_2 (stage II).

The gas phase and liquid phase components of the L-shaped aggregates inside the quartz–galena–sphalerite stage and carbonate stage (stage IV) were confirmed only in H_2O, lacking CO_2, indicating the feature of the H_2O–NaCl system (Figures 8E–H).

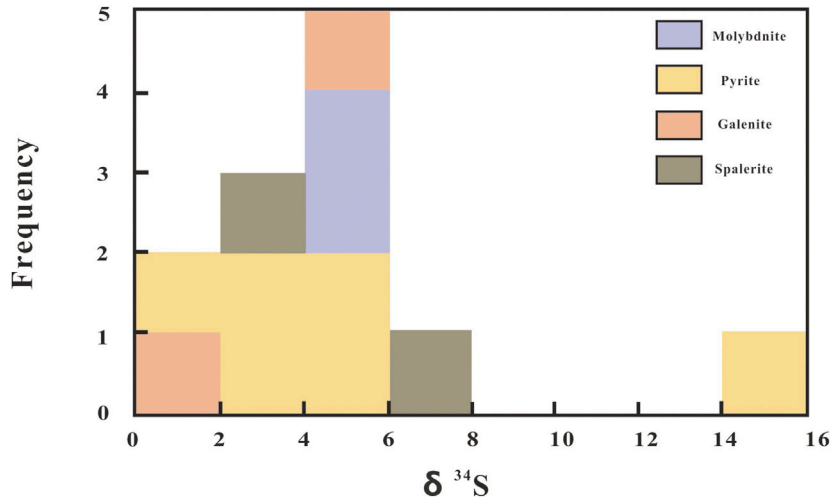


FIGURE 11
Histogram of sulfur isotope values of sulfide minerals in the Shibaogou Mo–Pb–Zn deposit.

TABLE 4 Pb isotope data and S isotope composition of sulfides from the Shibaogou deposit.

Sample	Mineral	$\delta^{34}S$ (‰)	$^{206}Pb/^{204}Pb$	$^{207}Pb/^{204}Pb$	$^{208}Pb/^{204}Pb$
710–1	Galenite	5.1	17.541	15.457	38.549
710–19		0.8	17.644	15.503	38.449
710–1	Sphalerite	6.3	17.571	15.497	38.675
710–19		2.4	17.678	15.534	38.575
710–1	Pyrite	5.7	17.557	15.505	38.69
710–6		4.1	17.383	15.508	38.432
710–10		3.4	17.383	15.499	38.366
710–19		2.3	17.67	15.538	38.575
710–7	Molybdenite	14.7	18.037	15.592	38.834
710–16		1.9	17.654	15.524	38.616
710–20		5.1	17.53	15.442	38.371
sbg858-2		5.9	17.589	15.458	38.365
716–1	Granite		17.696	15.468	38.553
716–2			18.064	15.473	38.631
868–1			18.741	15.510	38.592
858–4			17.826	15.463	38.742

5.3 H–O–S–Pb isotopes

Table 3 and Figure 10 including information on the hydrogen and oxygen isotopic in garnet, quartz, and calcite from stage I to stage IV of the Shibaogou Mo–Pb–Zn deposit. The solution absorption temperature is employed to quantify all hydrogen and oxygen isotopes. The hydrogen as well as oxygen isotopic proportions of two garnets from Skarn are $\delta^{18}O_{fluid}$ = 4.163‰–4.288‰ (averaging 4.25‰) and δD_{fluid} = −79.9‰ to −83.3‰ (averaging −81.6‰). In the quartz–molybdenite stage, the oxygen isotope ($\delta^{18}O_{fluid}$) values were obtained for two quartz samples (6.325‰–8.997‰, with a mean of 7.6‰). Hydrogen isotope in quartz samples was from −98.2% to −91.8‰ (averaging −95‰).

In the quartz–galena–sphalerite stage, the $\delta^{18}O_{fluid}$ and δD_{fluid} measurements from two quartz extracts were 1.8‰–3.4‰ (median 2.6‰), and −95.7‰ to −85.2‰ (averaging −90.45‰), correspondingly. The hydrogen and

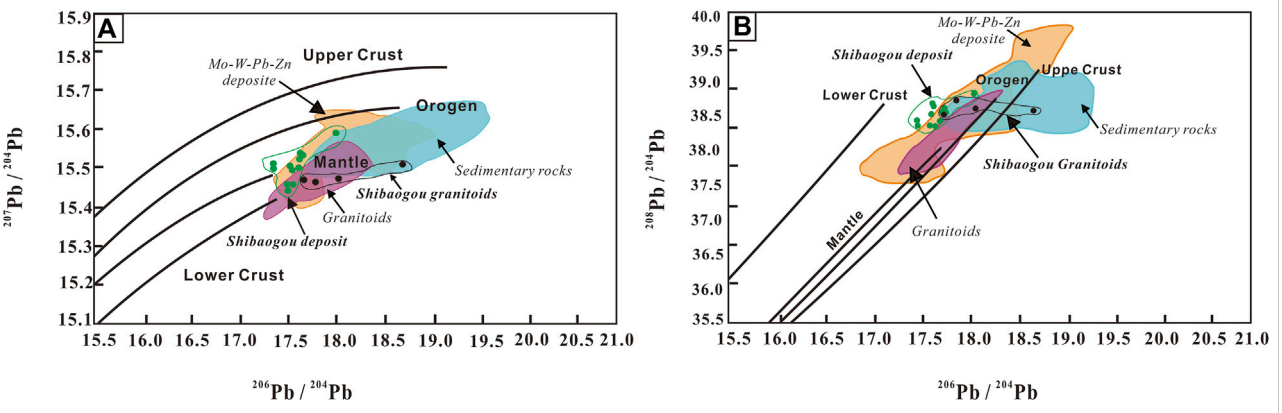


FIGURE 12
Plot of $^{207}pb/^{204}pb$ vs. $^{206}pb/^{204}pb$ **(A)** and $^{208}pb/^{204}pb$ vs. $^{206}pb/^{204}pb$ **(B)** for the Shibaogou sulfides, local granitoids, and host rocks. Pb isotope compositions of sulfides in the Shibaogou deposit. Pb isotope compositions in the Mo–W–Pb–Zn deposits of the Luanchuan ore district are after Huang et al., 1984; Luo et al., 1991; Yan, 2004; Qi, 2006; Yan et al., 2009; Duan et al., 2011; Cao et al., 2015; Yang et al., 2017. Pb isotope compositions causative granitoids are cited from Huang et al., 1984; Luo et al., 1991; Guo, 2018. Galena isotope values of sedimentary rocks are from Liu et al., 2007; Yan et al., 2009.

oxygen isotopes compositions of two calcite samples in the quartz–calcite stage are $\delta^{18}O_{fluid}$ = −1.769‰ to −1.168‰ (averaging −1.46‰) and δD_{fluid} = −106.5‰ to −102.7‰ (averaging −104.6‰).

Figure 11 as well as Table 4 both display the conclusions of the measurement of 12 sulfides' sulfur isotopes from the Shibaogou molybdenum deposit. The $\delta^{34}S$ values of three molybdenite samples are between 1.9‰ and 14.7‰, and four pyrite samples are 2.3‰–5.7‰, two sphalerite specimen range from 2.4‰ to 6.3‰, and two galena samples are 0.8‰–5.1‰.

Four molybdenite samples host Pb isotope $^{206}Pb/^{204}Pb$ = 17.53–18.037, $^{207}Pb/^{204}Pb$ = 15.442–15.592, and $^{208}Pb/^{204}Pb$ = 38.365–38.834. Four pyrite samples have $^{206}Pb/^{204}Pb$ ratios of 17.383–17.67, $^{207}Pb/^{204}Pb$ ratios of 15.499–15.538, and $^{208}Pb/^{204}Pb$ ratios of 38.366–38.69. Two sphalerite samples have $^{206}Pb/^{204}Pb$ ratios of 17.571–17.678, $^{207}Pb/^{204}Pb$ ratios of 15.497–15.534, and $^{208}Pb/^{204}Pb$ ratios of 38.575–38.675. Two galena samples have $^{206}Pb/^{204}Pb$ ratios of 17.541–17.644, $^{207}Pb/^{204}Pb$ ratios of 15.457–15.503, and 208Pb/^{204}Pb ratios of 38.449–38.549. Four granite samples have $^{206}Pb/^{204}Pb$ ratios of 17.696–18.741, $^{207}Pb/^{204}Pb$ ratios of 15.463–15.510, and $^{208}Pb/^{204}Pb$ ratios of 38.553–38.742 (Table 4; Figure 12).

6 Discussion

6.1 Age of skarn Mo mineralization

Because the Re-Os isotope system is relatively closed, the influence of later transformation is small, and the metallogenic age of the deposit can be directly and accurately determined (Suzuki et al., 1996; Stein et al., 2001). In this study, the Re-Os isochron age and the model age-weighted average age of molybdenite in contact zone are 147.4 ± 7.2 Ma and 148.9 ± 1.7 Ma, respectively, which represents the age of the mineralization in the Shibaogou Mo deposit. The metallogenic age is identical to the zircon U–Pb ages of the Shibaogou granitic intrusions (148 ± Ma, Xue et al., 2018), which indicates the mineralization of the Shibaogou Mo deposit is genetically relevant to the Shibaogou granites.

In the EQOB, there are multiple Mo mineralization events from Late Paleoproterozoic to Late Cretaceous including Late Paleoproterozoic to Early 1875–1686 Ma, ~429 Ma, 233–210 Ma, 156–132 Ma, and 128–107 Ma revealing the complicated tectonic evolution of the Qinling orogenic belt (Li et al., 2009, 2011; Wei et al., 2009; Deng et al., 2013). Our brand molybdenite Re-Os dating results demonstrate that the Shibaogou skarn Mo deposit also belongs to the Early Yanshanian episodes of Mo mineralization similar to some porphyry and skarn-porphyry Mo deposits in the LOD indicating the possible post-collisional extension between the NCC and Yangtze Craton and the subduction of the Paleo-Pacific Plate during the Early Cretaceous in the EQOB (Yang et al., 2019).

6.2 Source of the ore-forming fluids by H–O isotopes and materials by S–Pb isotopes

The Hydrogen and oxygen isotopes compositions of minerals from the deposit are widely used to trace the sources of mineralizing fluids and materials (Hedenquist and Lowenstern, 1994; Meinert et al., 2005; Peng et al., 2016). Garnet in the skarn stage shows relatively high and a narrow range of $\delta^{18}O_{fluid}$ values (5.9‰–6‰) which is similar to the other skarn deposits in the world (Meinert

et al., 2003; Kodõera et al., 2010; Peng et al., 2016; Lei et al., 2018; Li et al., 2020) and maybe indicate the magmatic origin (5.0‰–9.0‰; Hugh and Taylor, 1974; Hedenquist and Lowenstern, 1994). Furthermore, the $\delta^{18}O_{fluid}$ values of the quartz minerals from the quartz–molybdenite stage is a narrow range (6.3‰–8.9‰), which are similar to the values of magmatic water (Figure 10), it shows the characteristics of a magma. In the quartz–galena–sphalerite stage, the values of $\delta^{18}O_{fluid}$ (1.8‰–3.0‰) are lower than values in the quartz–molybdenite stage but still close to the magmatic water which may be caused by the meteoric water. But, the δD_{H2O} values in all stages (−106.5‰ to −79.9‰) are lower than the values of magmatic water (Figure 10), and it maybe the product of open-system degassing of parental magm (Hedenquist and Richards, 1998; Peng et al., 2016; Yang et al., 2020).

The values of $\delta^{18}O_{fluid}$ in the quartz–molybdenite and quartz–galena–sphalerite stages are higher than in the skarn stage which may be achieved *via* the mineral precipitation from a boiling solution (Lynch et al., 1990; Bowers, 1991), or a result of interactions between magmatic fluids and surrounding carbonate rocks (Hoefs, 2009; Catchpole et al., 2015). However, the boiling occurring in fluids of the syn-ore stage could not have been responsible for the >10‰ increase in the $\delta^{18}O_{fluid}$ value of the fluids (Peng et al., 2016). Thus, the elevated $\delta^{18}O_{fluid}$ values in syn-ore-stage minerals are mainly contributed by the fluid–rock interactions between the magmatic fluid and the surrounding carbonate rocks. At first, the $\delta^{18}O_{fluid}$ values of the calcites from the post-ore-stage vein are lower than in quartz–galena–sphalerite stage minerals, further suggesting the termination of the fluid–rock interactions between the magmatic fluid and the surrounding carbonate rocks. In addition, the values of $\delta^{18}O_{smow}$ in the Shibaogou Mo deposit are consistent with the $\delta^{18}O_{smow}$ values of the carbonate rocks from the Luanchuan group, indicating the fluid–rock interactions (Table 3).

The lack of sulfate minerals indicates that ore-forming fluids are mainly H_2S, as well as low $f(O_2)$ and pH (Duan et al., 2010). Besides, the variations of $\delta^{34}S$ values in the Shibaogou Mo deposit conform to the fractionation sequence molybdenite > pyrite > sphalerite > galena (Zheng, 1990), revealing that they were in equilibrium during ore deposition (Figure 11). In a word, the values of the $\delta^{34}S$ composition for the sulfides from Shibaogou Mo deposit can show the S isotopic composition of the ore-forming fluids. At the Shibaogou Mo deposit, the $\delta^{34}S$ values of sulfide minerals exhibit a narrow range of 1.9‰–6.3‰ (only one exceptional value of 14.3‰ from pyrite) indicating a homogeneous sulfur source. Similar to the H–O isotopes, the $\delta^{34}S$ values in the Shibaogou Mo deposit are similar to the values of typical skarn deposits throughout the world (Soloviev and Kryazhev, 2018a; 2018b; Lei et al., 2018; Xue et al., 2018; Soloviev et al., 2019; Wang et al., 2019), indicating the major magmatic source with some contributions from sedimentary rocks. The Pb isotopes were also used here to constrain the source ore materials. The similarities between the ores and the Shibaogou granites suggest the ore-forming materials originated from the magmas which formed the Shibaogou granites. As shown in (Figure 12), the sample points plot in the domain between the orogen and the mantle, the lower crust, and the mantle, respectively implying the mixing sources of crust and mantle in general. Previous studies have proven the assignable role of mantle materials in the generations of granites and deposits in the LOD (Richards, 2009; Richards, 2011; Wang et al., 2015; Yang et al., 2016; Xu et al., 2021).

In conclusion, the source of the ore-forming fluids were the fluid–rock interactions between the magmatic fluid and the surrounding carbonate rocks, and the ore-forming metal materials were camed from the magmas which generated the Luanchuan granites having a mixing source of crust and mantle.

6.3 Evolution of the ore-forming fluids

By studying the properties of primary fluids, we can further understand the evolution of fluids in the process of mineralization (Roedder, 1984). Modification of fluid inclusions after entrapment may confuse their interpretation (AudeAtat and Günther, 1999) through changes in bulk density and/or composition (Roedder, 1984; Bakker and Jansen, 1994; AudeAtat and Günther, 1999). In this study, features such as decrepitation halos, movement tracks, stretching or shrinkage, and extremely irregular inclusions were therefore avoided.

As shown by this study, the ore-forming fluids are moderate to high salinities (35.58 wt%–46.05 wt% NaCl equiv.) and high homogenization temperatures of 513–550°C, similar to those in typical skarn deposits (Bao et al., 2014; Cao et al., 2015; Xue et al., 2018). In pyroxene, H-type inclusions and V-type inclusions coexist (Figures 7D–F). They have similar temperature but different salinity (Figures 9A,B), indicating that fluid boiling occurs during the mineralization process (Roedder and Bodnar, 1980). Therefore, through the study of boiling inclusions, we can calculate the accurate trapping pressure and infer the mineralization depth. The Fls of the deposit could have been formed at 580–650 bar estimated by the isobar equations (Figure 13A), and the lithostatic depth of the region is between 2.19 and 2.45 km, which is similar with the emplacement depth of the Shibaogou granite porphyry (1.49–3.99 km; Xue et al., 2018). Moreover, the primary L-type fluid inclusions trapped in pyroxenes are homogenized by sudden vapor disappearance instead of gradual disappearance or expansion could represent the initial single-phase supercritical fluid derived from a magmatic–hydrothermal system (Veksler, 2004; Zajacz et al., 2008). Thus, the fluid with a salinity of 6 wt%–8 wt% NaCl equiv. is an initially supercritical exsolved from the Shibaogou intrusion (Hedenquist and Lowenstern, 1994; Shu et al., 2013). When the fluid continued to rise along the structural fissure to a depth of 2.19–2.45 km, the exsolved fluid intersected

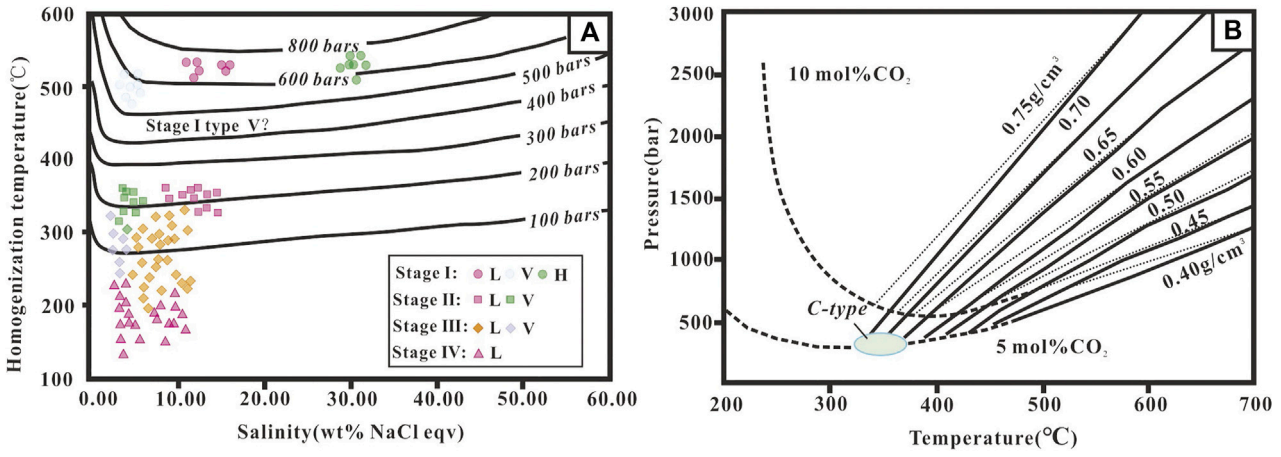


FIGURE 13
Pressure estimation for ore stage I to IV fluid inclusions. **(A)** Fluid inclusion assemblages from stages I to III were trapped under boiling conditions, and isobar was calculated from the equations of Driesner and Heinrich (2007). **(B)** Isochrones for fluid of 4 wt% NaCl, 5 mol% CO_2 and 10 mol% CO_2. The solid lines mark the solvi for fluids in the system H_2O (6 wt%)–NaCl–CO_2 (5–10 mol% CO_2; Gehrig et al., 1986). Data for the C-type fluid inclusions plot in the oval field, indicating trapping pressures of <500 bar.

the solution to form two fluids with different properties, high-salinity and low-salinity fluids (path 1 in Figure 14).

Comparatively, the mineralizing fluids have characteristics of moderate temperatures (256–397°C) and salinities (3.57 wt%–11.97 wt% NaCl equiv.) in stage (II). Some authors suggested that such changes in fluid properties can be caused by gradual mixing with atmospheric water, but the isotopic results have proven the insignificant role of the meteoric water and the dominance of magmatic water in this stage (Figure 10). As the magma cools and crystallizes, the upwelling fluid no longer intersects the two-phase surface due to the lack of power and heat from the magma (Shinohara and Hedenquist, 1997). However, we found a large number of dykes (Figure 4I) in the ore body, which provided heat to the upwelling fluids, which caused the ore-forming fluids to intersect again with the two-phase surface to form two fluids with different properties, medium-to-high-salinity and low-salinity fluids. Thus, the pressure of the phase separation may be happened at 180–250 bar in stage II (Figure 13A), and the lithostatic depth waa about between 2.19 and 2.45 km. Furthermore, the entrapment pressure would increase because of the addition of CO_2 (Bowers and Helgeson, 1983; Peng et al., 2016; Wang Y. H et al., 2018). Fluid would increase the pressure by approximately 100 bar at 600°C when the addition of 5 mol% CO_2 to a 4 wt% NaCl equiv. It is consistent with the calculated pressure (<500 bar) of C-type inclusions (Figure 13B).

In the quartz–galena–sphalerite stage, the mineralizing fluids show features of moderate temperatures (163–347°C) and low salinities (0.87 wt%–8.94 wt% NaCl equiv.). In contrast to the quartz–molybdenite stage, temperature decreases limitedly, whereas salinity increases sharply. The fluids show an apparent trend towards the input of the meteoric water (as discussed above; Figure 9). As the magma cools and crystallizes, the upwelling fluid no longer intersects the two-phase surface due to the lack of power and heat from the magma (Shinohara and Hedenquist, 1997). However, when the temperature dropped below 400°C, which is considered to be the transition temperature from lithostatic to hydrostatic conditions caused by the change from ductile to brittle behavior of the system (Fournier, 1999), the pressure of the fluid would fall rapidly and result in the supercritical fluid intersecting the two-phase surface again and boil to form two fluids with different properties, medium-to-high-salinity and low-salinity fluids (Shu et al., 2013; Zhu et al., 2015). The influence of CO_2 to pressure estimate can be ignored as the C-type inclusions occupy a very small fraction. In conclusion, the pressure of the fluid in this stage is ~150 bar (Figure 13A), corresponding to a depth of ~0.56 km in the hydrostatic condition. At last, in the quartz–calcite stage (IV), the low temperatures (151–231°C) and low salinities (0.88 wt%–11.34 wt% NaCl equiv) may be caused by mixing with meteoric water.

6.4 Mechanisms of ore precipitation

6.4.1 Mechanisms of molybdenite precipitation

There are four mechanisms that can lead to metal complex destabilization and ore precipitation, which are fluid boiling, fluid mixing, reduction in temperature, pressure and salinity, and fluid–rock interactions (Li et al., 2012; Wang S et al., 2018). First, cooling causes a significant reduction in the solubility of molybdenum in porphyry (Ulrich and Mavrogenes, 2008),

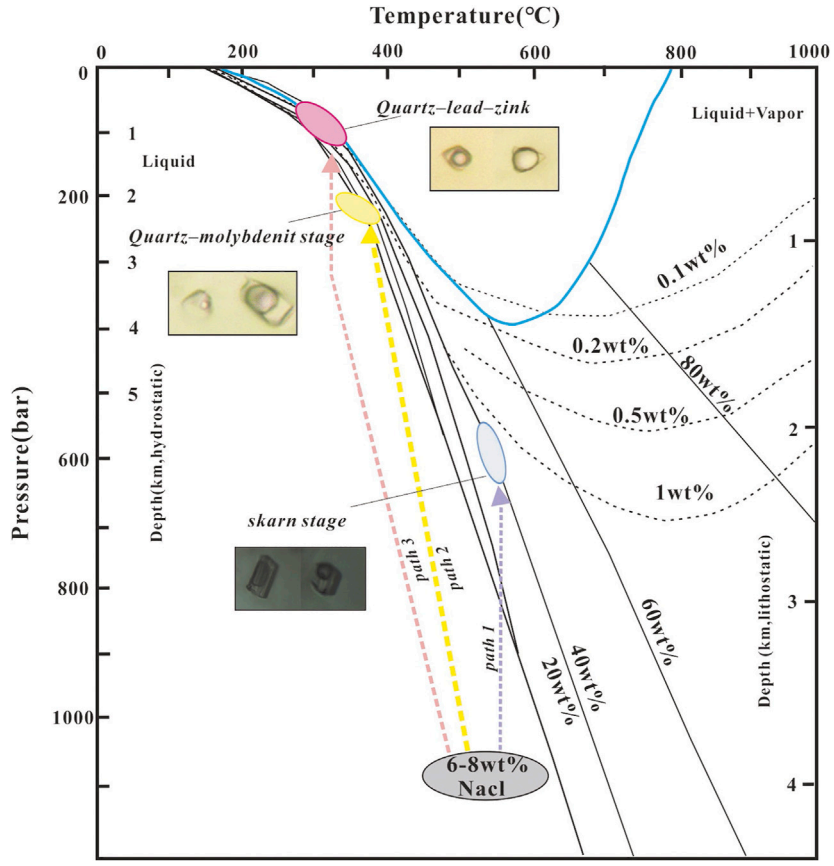


FIGURE 14
Fluid evolution paths of the Shibaogou Mo (Mo) deposit (after Meinert et al., 2003; Shu et al., 2013; Peng et al., 2016). The initial fluids exsolved from the deep magma chamber are assumed supercritical magmatic fluids with an initial salinity of 6–8 wt% NaCl equiv. (Hedenquist and Lowenstern, 1994). These fluids followed three different cooling paths: (1) path 1 shows the fluid trajectory forming skarn (513–550 °C, 580–650 bar, and 2.19–2.45 km under a lithostatic condition); (2) path 2 shows the trajectory forming Mo-dominated mineralization (324–387 °C, 180–250 bar, and 0.49–0.94 km under a hydrostatic depth); (3) path 3 shows the trajectory forming quartz–galena–sphalerite stage of mineralization (303–347 °C, <150bar, and <0.56 km under a hydrostatic depth). For details see text.

while in the Shibaogou Mo deposit, the temperature decreased less significantly from skarn stage to quartz–molybdenite stage with still high temperatures (>300°C) excluding the possibility of temperature-decreasing mechanism. Second, the intrusion of atmospheric fluids causes a reduction in both temperature and salinity, which reduces the solubility of molybdenum, this process is vital in during the precipitation of molybdenite (Shu and Lai, 2017). However, as showed in Figure 10, the ore-forming fluids in the quartz–molybdenite stage were dominated by magmatic fluids. Therefore, the mixing of ore-forming fluids with meteoric water may have little effect on the precipitation process of molybdenite in the Shibaogou deposit.

Third, as revealed by the close spatial relationship between the alteration mineral and mineralization, the ore-forming process was genetically related to the alteration process. In addition, the H–O isotopic data (Figure 10) indicate that fluid–rock interactions occurred in the quartz–molybdenite stage. Thus, we speculate that a more acidic fluid (e.g., pH = 3.9 in the Bismark skarn deposit; Bertelli et al., 2009) which was separated from the source magma (Sillitoe, 2010), reacts with pre-ore-stage skarn minerals (garnet, pyroxene, and wollastonite), which forcing the pH to rise and consequently leading to sulfide precipitation (Bertelli et al., 2009). This mechanism is also evidenced by the numerous C-type fluid inclusions, which is produced by the water-rock reaction of the intrusion of the shibaogou granite porphyry into the Guandaokou group in quartz formed in the stage II. Fourth, the intensity of the fluid boiling in obvious, which is evidenced by coexisting of less H-type, V-type and L-type inclusion.

As a result, the fluid boiling and fluid–rock interactions may be the important processes in controlling molybdenum mineralization in the Shibaogou molybdenum–lead–zinc deposit.

6.4.2 Mechanisms of galena and sphalerite precipitation

Chloride and hydrosulfide complexes are the main medium to transport sphalerite and galena in hydrothermal fluids (Tagirov and Seward, 2010; Zhong et al., 2015). Especially under high-temperature and moderate-salinity conditions, chloride complexes are more stable than sulfide species (Zhang et al., 2016). We infer that galena and sphalerite are transported through chloride complexes because the zinc-lead mineralization fluids of the Shibaogou deposit are characterized by medium to high temperatures, mainly 200–250°C. From the stage I to stage III, the intensity of the fluid boiling gradually descends. In stage III, the fluid boiling event has been not obvious which is evidenced by the declining number of coexisting V-type and L-type fluid inclusion assemblages. Therefore, fluid boiling is not the main reason for the precipitation of galena and sphalerite. The hydrothermal fluid temperatures and salinities of the Shibaogou deposit decreased strikingly from skarn Stage (500–550°C; 0.35 wt%–46.05 wt% NaCl equiv.) to quartz–galena–sphalerite stage (200–250°C; 0.87 wt%–8.94 wt% NaCl equiv.) (Figure 9). Galena and sphalerite are likely to have precipitated in the Shibaogou deposit as a result of the considerable reduction in temperature since chloride complexes of sphalerite and sphalerite are destabilized with a significant decrease in temperature (Reed and Palandri, 2006).

6.5 Tectonic implications

A large amount of geochronological data are analyzed and sorted out, and dividing the molybdenum mineralization in the East Qinling orogenic belt. The molybdenum mineralization in the East Qinling orogenic belt can be divided into three periods from the middle and late Triassic to the middle and late Cretaceous (Mao et al., 2008). Molybdenite Re-Os geochronology in the Shibaogou deposit yields ^{187}Re-^{187}Os isochron age of 146.3–151.2 Ma, indicating that it was the product of the subduction of the Paleo-Pacific plate under Eurasia (Mao et al., 2011). The Late Mesozoic tectonic regime led to the subduction event, which was characterized by a transition from post-collision compression to extension in eastern China, leading to an intense tectonic-magmatic events (Yang et al., 2018b; Li et al., 2018; Xue et al., 2018, 2019, 2020; Tang et al., 2019; Yang et al., 2019). During the period from the Late Jurassic to the Early Cretaceous, the lithosphere in eastern China experienced a strong thinning process (Yang et al., 2018a; Yang et al., 2018b; Yang et al., 2019), the asthenospheric upwelling and underplating triggered deep penetration of the lower crust and injection of mafic magma into the mantle (Mao et al., 2008). The felsic magma rises to the magma chamber of the upper crust with a small amount of mafic magma, and the interaction between felsic and mafic forms monzonitic granite and high-fractionated I-type granite porphyries formed by segregation crystallization rock (Mao et al., 2005, 2013; Li et al., 2018; Yang et al., 2019). More and more melts are rapidly released from the fractionated magma chambers, and the melts carrying rich mineral-forming materials gradually rise from the magma chambers to higher levels and into the crustal extent. The Shibaogou Mo–Pb–Zn deposit was created as a result of the release of ore-bearing fluids following the emplacement of the Shibaogou granitic intrusions.

7 Conclusion

1) Molybdenite Re-Os model ages of the Shibaogou deposit vary from 146.3 ± 2.6 to 151.2 ± 2.2 Ma, with a weighted mean age of 148.9 ± 1.7 Ma.
2) The H–O–S–Pb isotope indicates that the ore-forming fluid came from magmatic water in the early stage, and was gradually added by meteoric water in the later stage, and the ore-forming material mainly came from the Shibaogou granite porphyry intrusion.
3) The major factors controlling Mo precipitation are boiling and fluid–rock interaction during this stage. The decrease in temperature and salinity are the main factors controlling Pb–Zn precipitation at the Shibaogou deposit.
4) The complex evolution of the ore-forming fluids was related to the subduction of the Paleo-Pacific Plate, which induced the lithospheric thinning in the eastern China and the post-collisional extension triggered resulting from the Yangtze Craton and NCC collision.

Data availability statement

The original contributions presented in the study are included in the article/Supplementary Material; further inquiries can be directed to the corresponding author.

Author contributions

GW, MG, SY, and WY revised the manuscript, conceived the experiments, and contributed to the data interpretation. The fieldwork and preliminary study of samples were carried out by HY and PW. NG and YF conducted the geochemical analyses and reviewed both the science and English language. YX led data interpretations and manuscript preparation through discussion with all co-authors. All authors have read and agreed to the published version of the manuscript.

Funding

The research was supported by the China Ministry of Science and Technology, Ministry of Land and Resources Public Service

Sectors Fund (Grant No. 201111007-4) and Scientifific research Project of Geological and Mineral Exploration and Development Bureau of Henan Province (2021KC-8, 202202).

Acknowledgments

The authors would like to thank Liwei Xue, MG, YF, HY, Yi Cao, Yulin Chang, SY, and WY for their assistance with the experiments.

Conflict of interest

Author YF was employed by Luanchuan Xinshu Weibo Mining Co., Ltd.

The remaining authors declare that the research was conducted in the absence of any commercial or financial relationships that could be construed as a potential conflict of interest.

The reviewer AL declared a shared affiliation with the authors YX, GW, MG, WY, and SY to the handling editor at time of review.

Publisher's note

All claims expressed in this article are solely those of the authors and do not necessarily represent those of their affiliated organizations, or those of the publisher, the editors, and the reviewers. Any product that may be evaluated in this article, or claim that may be made by its manufacturer, is not guaranteed or endorsed by the publisher.

References

AudeÂtat, A., and Gunther, D. (1999). Mobility and H_2O loss from fluid inclusions in natural quartz crystals. *Contributions Mineralogy Petrology* 137, 1–14. doi:10.1007/s004100050578

Bakker, R. J., and Jansen, J. B. H. (1994). A mechanism for preferential H_2O leakage from fluid inclusions in quartz, based on TEM observations. *Contr. Mineral. Pet.* 116, 7–20. doi:10.1007/bf00310686

Bao, Z. W., Wang, C. Y., Zhao, T., Li, C., and Gao, X. (2014). Petrogenesis of the Mesozoic granites and Mo mineralization of the Luanchuan ore field in the East Qinling Mo mineralization belt, Central China. *Ore Geol. Rev.* 57, 132–153. doi:10.1016/j.oregeorev.2013.09.008

Bertelli, M., Baker, T., Cleverley, J. S., and Ulrich, T. (2009). Geochemical modelling of a Zn-Pb skarn: Constraints from LA-ICP-MS analysis of fluid inclusions. *J. Geochem. Explor.* 102, 13–26. doi:10.1016/j.gexplo.2008.11.015

Bowers, T. S., and Helgeson, H. C. (1983). Calculation of the thermodynamic and geochemical consequences of nonideal mixing in the system H_2O-CO_2-NaCl on phase relations in geologic systems: Equation of state for H_2O-CO_2-NaCl fluids at high pressures and temperatures. *Geochimica Cosmochimica Acta* 47, 1247–1275. doi:10.1016/0016-7037(83)90066-2

Bowers, T. S. (1991). The deposition of gold and other metals: Pressureinduced fluid immiscibility and associated stable isotope signatures. *Geochimica Cosmochimica Acta* 55, 2417–2434. doi:10.1016/0016-7037(91)90363-a

Cao, H. W., Zhang, S. T., Santosh, M., Zheng, L., Tang, L., Li, D., et al. (2015). The Luanchuan Mo-W-Pb-Zn-Ag magmatic-hydrothermal system in the East Qinling metallogenic belt, China: Constrains on metallogenesis from C-H-O-S-Pb isotope compositions and Rb-Sr isochron ages. *J. Asian Earth Sci.* 111, 751–780. doi:10.1016/j.jseaes.2015.06.005

Catchpole, H., Kouzmanov, K., Putlitz, B., Seo, J. H., and Fontbote, L. (2015). Zoned base metal mineralization in a porphyry system: Origin and evolution of mineralizing fluids in the Morococha district, Peru. *Econ. Geol.*, 110, 39–71, doi:10.2113/econgeo.110.1.39

Collins, P. L. F. (1979). Gas hydrates in CO_2-bearing fluid inclusions and the use of freezing data for estimation of salinity. *Econ. Geol.* 74, 1435–1444. doi:10.2113/gsecongeo.74.6.1435

Deng, X. H., Chen, Y. J., Santosh, M., and Yao, J. M. (2013). Genesis of the 1.76 Ga zhaiwa Mo–Cu and its link with the xiong'er volcanics in the North China craton: Implications for accretionary growth along the margin of the columbia supercontinent. *Precambrian Res.* 227, 337–348. doi:10.1016/j.precamres.2012.02.014

Driesner, T., and Heinrich, C. A. (2007). The system H_2O NaCl. Part I: Correlation formulae for phase relations in temperature pressure composition space from 0 to 1000 C, 0 to 5000 bar, and 0 to 1 X NaCl. *Geochimica Cosmochimica Acta* 71, 4880–4901. doi:10.1016/j.gca.2006.01.033

Du, A. D., Zhao, D. M., Wang, S. X., Sun, D. Z., and Liu, D. Y. (2001). Precise ReeOs dating for molybdenite by IDeNTIMS with carius tube sample preparation. *Rock Mineral Analysis* 20, 247 (in Chinese with English abstract). doi:10.15898/j.cnki.11-2131/td.2001.04.002

Duan, S., G., Xue, C. J., Chi, G. X., Liu, G. Y., Yan, C. H., Feng, Q. W., et al. (2011). Ore geology, fluid inclusion, and S- and Pb-isotopic constraints on the genesis of the chitudian Zn-Pb deposit, southern margin of the north China craton. *Resour. Geol.* 61, 224–240. doi:10.1111/j.1751-3928.2011.00160.x

Duan, S. G., Xue, C. J., Liu, G. Y., Yan, C. H., Feng, Q. W., Song, Y. W., et al. (2010). Geology and sulfur isotope geochemistry of lead-zinc depositsin Luanchuan district, Henan province, China. *Earth Sci. Front.* 17, 375(in Chinese with English abstract).

Fallick, A. E., Macaulay, C. I., and Haszeldine, R. S. (1993). Implications of linearly correlated oxygen and hydrogen isotopic compositions for kaolinite and illite in the magnus sandstone, north sea. *Clays Clay Min.* 41, 184–190. doi:10.1346/ccmn.1993.0410207

Fournier, R. O. (1999). Hydrothermal processes related to movement of fluid from plastic into brittle rock in the magmatic-epithermal environment. *Econ. Geol.* 94, 1193–1211. doi:10.2113/gsecongeo.94.8.1193

Gehrig, M., Lentz, H., and Franck, E. (1986). The system water-carbon dioxide-sodium chloride to 773 K and 300 MPa. *Berichte Bunsenges. fur Phys. Chem.* 90, 525–533. doi:10.1002/bbpc.19860900606

Gemmell, J. B., Zantop, H., and Meinert, L. D. (1992). Genesis of the Aguilar zinc-lead-silver deposit, Argentina; contact metasomatic vs. sedimentary exhalative. *Econ. Geol.* 87 (8), 2085–2112. doi:10.2113/gsecongeo.87.8.2085

Guo, B. (2018). *Geochemical and geological characteristics of the concealed granitic batholith and Yuku Mo-W deposit at the Luanchuan ore cluster*. BeijingBeijing): China University of Geosciences.

Hedenquist, J. W., and Lowenstern, J. B. (1994). The role of magmas in the formation of hydrothermal ore deposits. *Nature* 370, 519–527. doi:10.1038/370519a0

Hedenquist, J. W., and Richards, J. P. (1998). The influence of geochemical techniques on the development of genetic models for porphyry copper deposits. *Rev. Econ. Geol.* 10, 235

Hoefs, J. (2009). *Stable isotope geochemistry*. Berlin Heidelberg: Springer-Verlag.

Hua, R. M., and Mao, J. W. (1999). A preliminary discussion on the Mesozoic metallogenic explosion in East China. *Mineral. Deposits* 18, 300

Huang, D. H., Nie, F. J., Wang, Y. C., and Jiang, X. J. (1984). Lead isotopic compositions of molybdenum deposits in East Qinling as applied to the problem of ore sources. *Min. Deposita* 3, 20(in Chinese with English abstract).

Hugh, P., and Taylor, J. R. (1974). The application of oxygen and hydrogen isotope studies to problems of hydrothermal alteration and ore deposition. *Econ. Geol.* 60, 843–883. doi:10.2113/gsecongeo.69.6.843

Kodõera, P., Lexa, J., and Fallick, A. E. (2010). Formation of the Vysoká–Zlatno Cu–Au skarn–porphyry deposit, Slovakia. *Min. Depos.* 45, 817–843. doi:10.1007/s00126-010-0304-9

Lei, X. F., Duan, D. F., Jiang, S. Y., and Xiong, S. F. (2018). Ore-forming fluids and isotopic (H-O-C-S-Pb) characteristics of the fujiashan-longjiaoshan skarn W-Cu-

(Mo) deposit in the edong district of hubei province, China. *Ore Geol. Rev.* 102, 386–405. doi:10.1016/j.oregeorev.2018.09.019

Li, D., Han, J., Zhang, S., Yan, C., Cao, H., and Song, Y. (2015). Temporal evolution of granitic magmas in the Luanchuan metallogenic belt, east Qinling Orogen, central China: Implications for Mo metallogenesis. *J. Asian Earth Sci.* 111, 663–680. doi:10.1016/j.jseaes.2015.05.017

Li, H. M., Ye, H. S., Mao, J. W., Wang, D. H., Chen, Y. C., Qu, W. J., et al. (2007). Re-Os dating of molybdenites from Au (-Mo) deposits in Xiaoqinling gold are district and its geological significance. *Mineral. Deposits* 26, 417(in Chinese with English abstract).

Li, H. M., Ye, H. S., Wang, D. H., Chen, Y. C., Qu, W. J., and Du, A. D. (2009). Re-Os dating of molybdenites from Zhaiwa Mo deposit in Xiong'er Mountain, Western Henan Province, and its geological significance. *Mineral. Deposits* 28, 133(in Chinese with English abstract).

Li, N., Chen, Y.-J., Santosh, M., and Pirajno, F. (2018). Late mesozoic granitoids in the qinling orogen, central China, and tectonic significance. *Earth. Sci. Rev.* 182, 141–173. doi:10.1016/j.earscirev.2018.05.004

Li, N., Chen, Y.-J., Ulrich, T., and Lai, Y. (2011). Fluid inclusion study of the Wunugetu Cu-Mo deposit, Inner Mongolia, China. *Min. Depos.* 47, 467–482. doi:10.1007/s00126-011-0384-1

Li, N., Chen, Y. J., Pirajno, F., and Ni, Z. y. (2013). Timing of the Yuchiling giant porphyry Mo system, and implications for ore Genesis. *Min. Depos.* 48, 505–524. doi:10.1007/s00126-012-0441-4

Li, N., Ulrich, T., Chen, Y. J., Thomsen, T. B., Pease, V., and Pirajno, F. (2012). Fluid evolution of the yuchiling porphyry Mo deposit, East Qinling. China. *Ore Geol. Rev.* 48, 442–459. doi:10.1016/j.oregeorev.2012.06.002

Li, N., Yang, F. Q., and Zhang, Z. X. (2020). Fluid inclusions and isotope (C, H, O, S, He, and Ar) study of the Xiaobaishitou skarn W-(Mo) deposit, East Tianshan, NW China. *Ore Geol. Rev.* 122, 103520. doi:10.1016/j.oregeorev.2020.103520

Liu, G. Y., Yan, C. H., Song, Y. W., and Duan, S. G. (2007). Characteristics and Genesis of Chitudian lead-zinc deposits in Luanchuan county. *Geol. Surv. Res.* 30, 263

Lu, H. Z., Fan, H. R., Ni, P., Ou, G. X., Shen, K., Zhang, W. H., et al. (2004). *Fluid inclusion* (Beijing: Science Press), 1–487. (in Chinese with English abstract).

Ludwig, K. R. (2003). User's manual for isoplot 3.0" in *A Geochronological Toolkit Microsoft Excel*, 4. Berkeley Geochron Center Special publication, 1

Luo, M. J., Zhang, F. M., Dong, Q. Y., Xu, Y. R., Li, S. M., and Li, K. H. (1991). *Molybdenum deposits in China, zhengzhou*. Henan Science Technology Press.

Lynch, J. V. G., Longstaffe, F. J., and Nesbitt, B. E. (1990). Stable isotopic and fluid inclusion indications of large-scale hydrothermal paleoflow, boiling, and fluid mixing in the Keno Hill Ag-Pb-Zn district, Yukon Territory, Canada. *Geochimica Cosmochimica Acta* 54, 1045–1059. doi:10.1016/0016-7037(90)90438-q

Macaulay, C. I., Fallick, A. E., Haszeldine, R. S., and Graham, C. M. (2000). Methods of laser-based stable isotope measurement applied to diagenetic cements and hydrocarbon reservoir quality *Clay Min.*, 35, 313–322, doi:10.1180/000985500546684

Mao, J., Wang, Y., Li, H., Pirajno, F., Zhang, C., and Wang, R. (2008). The relationship of mantle-derived fluids to gold metallogenesis in the Jiaodong Peninsula: Evidence from D-O-C-S isotope systematics. *Ore Geol. Rev.*, 33, 361–381, doi:10.1016/j.oregeorev.2007.01.003

Mao, J. W., Pirajno, F., Xiang, J. F., Gao, J. J., Ye, H. S., Li, Y. F., et al. (2011). Mesozoic molybdenum deposits in the east Qinling-Dabie orogenic belt: Characteristics and tectonic settings. *Ore Geol. Rev.* 43, 264–293. doi:10.1016/j.oregeorev.2011.07.009

Mao, J. W., Xie, G. Q., Zhang, Z. H., Li, X. F., Wang, Y. T., Zhang, C. Q., et al. (2005). Mesozoic large-scale metallogenic pulses in North China and corresponding geodynamic setting. *Acta Petrol. Sin.* 21, 169(in Chinese with English abstract).

Mao, W., Li, X., and Yang, F. (2013). Zircon LA-ICP-MS U-Pb ages of granites at Dabaoshan polymetallic deposit and its geological significance, Guangdong, South China. *Acta Petrol. Sin.* 29, 4104(in Chinese with English abstract).

Marcoux, É., Breillat, N., Guerrot, C., Négrel, P., Hmima, S. B., and Selby, D. (2019). Multi-isotopic tracing (Mo, S, Pb, Re, Os) and Genesis of the Mo W Azegour skarn deposit (High-Atlas, Morocco). *J. Afr. Earth Sci.*, 155, 109–117, doi:10.1016/j.jafrearsci.2019.04.007

Meinert, L. D., Dipple, G. M., and Nicolescu, S. (2005). World skarn deposits. *Econ. Geol. 100th Anniv.* Volume, 299

Meinert, L. D., Hedenquist, J. W., Satoh, H., and Matsuhisa, Y. (2003). Formation of anhydrous and hydrous skarn in Cu-Au ore deposits by magmatic fluids. *Econ. Geol.* 98, 147–156. doi:10.2113/gsecongeo.98.1.147

Newberry, R. J., and Swanson, S. E. (1986). Scheelite skarn granitoids: An evaluation of the roles of magmatic source and process. *Ore Geol. Rev.* 1 (1), 57–81. doi:10.1016/0169-1368(86)90005-3

Ouyang, H. G., Mao, J. W., Santosh, M., Zhou, J., Zhou, Z. H., Wu, Y., et al. (2013). Geodynamic setting of Mesozoic magmatism in NE China and surrounding regions: Perspectives from spatio-temporal distribution patterns of ore deposits. *J. Asian Earth Sci.* 78, 222–236. doi:10.1016/j.jseaes.2013.07.011

Peng, H. J., Mao, J. W., Hou, L., Shu, Q. H., Zhang, C. Q., Liu, H., et al. (2016). Stable isotope and fluid inclusion constraints on the source and evolution of ore fluids in the Hongniu-Hongshan Cu skarn deposit, Yunnan Province. China. *Econ. Geol.* 111, 1369–1396. doi:10.2113/econgeo.111.6.1369

Qi, J. P. (2006). *Geology, geochemistry and genesis of vein type lead-zinc-silver deposits in Luanchuan*. HenanBeijing: Peking University, 1–114. (in Chinese with English abstract).

Reed, M., and Palandri, J. (2006). *A database of equilibrium constants for minerals and aqueous species*. Eugene, OregonH06: University of OregonSOLTHERM.

Richards, J. P. (2011). Magmatic to hydrothermal metal fluxes in convergent andcollided margins. *Ore Geol. Rev.* 40, 1–26. doi:10.1016/j.oregeorev.2011.05.006

Richards, J. P. (2009). Postsubduction porphyry Cu-Au and epithermal Au deposits: Products of remelting of subduction-modified lithosphere. *Geology* 37, 247–250. doi:10.1130/g25451a.1

Roedder, E., and Bodnar, R. J. (1980). Geologic pressure determinations fromfluid inclusion studies. *Annu. Rev. Earth Planet. Sci.* 8, 263–301. doi:10.1146/annurev.ea.08.050180.001403

Roedder, E. (1984). *Fluid inclusions, review in mineralogy*, 12. Mineralogical Society of America, 644

Shinohara, H., and Hedenquist, J. W. (1997). Constraints on magma degassing beneath the Far Southeast porphyry Cu-Au deposit, Philippines. *J. Petrology* 38, 1741–1752. doi:10.1093/petroj/38.12.1741

Shu, Q. H., and Lai, Y. (2017). *Fluid inclusion and oxygen isotope constraints on the origin and hydrothermal evolution of the Haisugou Porphyry Mo deposit in the Northern Xilamulun District, NE China*. Geofluids. 1

Shu, Q. H., Lai, Y., Sun, Y., Wang, C., and Meng, S. (2013). Ore Genesis and hydrothermal evolution of the Baiyinnuoer zinc-lead Skarn deposit, Northeast China evidence from isotopes (S, Pb) and fluid inclusions. *Econ. Geol.* 108, 835–860. doi:10.2113/econgeo.108.4.835

Sillitoe, R. H. (2010). Porphyry copper systems. *Econ. Geol.* 105, 3–41. doi:10.2113/gsecongeo.105.1.3

Smoliar, M. I., Walker, R. J., and Morgan, J. W. (1996). Re-Os ages of group IIA, IIIA, IVA and IVB iron meteorites. *Science* 271, 1099–1102. doi:10.1126/science.271.5252.1099

Soloviev, S. G., Kryazhev, S. G., and Dvurechenskaya, S. S. (2019). Geology, mineralization, and fluid inclusion characteristics of the Meliksu reduced tungsten skarn deposit, Alai Tien Shan, Kyrgyzstan: Insights into conditions of formation and regional links to gold mineralization. *Ore Geol. Rev.* 111, 103003. doi:10.1016/j.oregeorev.2019.103003

Soloviev, S. G., and Kryazhev, S. G. (2018a). Magmatic-hydrothermal evolution at the Lyangar redox-intermediate tungsten-molybdenum skarn deposit, Western Uzbekistan, Tien Shan: Insights from igneous petrology, hydrothermal alteration, and fluid inclusion study. *Lithos* 316-317, 154–177. doi:10.1016/j.lithos.2018.07.015

Soloviev, S. G., and Kryazhev, S. G. (2018b). Tungsten mineralization in the Tien Shan Gold Belt: Geology, petrology, fluid inclusion, and stable isotope study of the Ingichke reduced tungsten skarn deposit, Western Uzbekistan. *Ore Geol. Rev.* 101, 700–724. doi:10.1016/j.oregeorev.2018.08.020

Stein, H. J., Markey, R. J., Morgan, J. W., Hannah, J. L., and Scherstén, A. (2001). The remarkable Re-Os chronometer in molybdenite: How and why it works. *Terra nova*. 13, 479–486. doi:10.1046/j.1365-3121.2001.00395.x

Stein, H., Scherstén, A., Hannah, J., and Markey, R. (2003). Subgrain-scale decoupling of Re and ^{187}Os and assessment of laser ablation ICP-MS spot dating in molybdenite. *Geochimica Cosmochimica Acta* 67, 3673–3686. doi:10.1016/s0016-7037(03)00269-2

Sterner, S. M., Hall, D. L., and Bodnar, R. J. (1988). Synthetics fluid inclusions: V. Solubility relations in the system NaCl-KCl-H_2O under vapor-saturated conditions. *Geochimica Cosmochimica Acta* 52, 989–1005. doi:10.1016/0016-7037(88)90254-2

Suzuki, K., Shimizu, H., and Masuda, A. (1996). ReOs dating of molybdenites from ore deposits in Japan: Implication for the closure temperature of the ReOs system for molybdenite and the cooling history of molybdenum ore deposits. *Geochimica Cosmochimica Acta* 60, 3151–3159. doi:10.1016/0016-7037(96)00164-0

Tagirov, B. R., and Seward, T. M. (2010). Hydrosulfide sulfide complexes of zinc to 250 °C and the thermodynamic properties of sphalerite. *Chem. Geol.* 269, 301–311. doi:10.1016/j.chemgeo.2009.10.005

Tang, L., Hu, X. K., Santosh, M., Zhang, S. T., Spencer, C. J., Jeon, H., et al. (2019). Multistage processes linked to tectonic transition in the Genesis of orogenic gold deposit: A case study from the shanggong lode deposit, East Qinling, China. *Ore Geol. Rev.* 111, 102998. doi:10.1016/j.oregeorev.2019.102998

Tang, L., Wagner, T., Fusswinkel, T., Zhang, S., Hu, X., and Schlegel, T. (2022). Fluid inclusion evidence for the magmatic-hydrothermal evolution of closely linked porphyry Au, porphyry Mo, and barren systems, East Qinling, China. *GSA Bull.* 134, 1529–1548. doi:10.1130/b36170.1

Tang, L., Zhao, Y., Zhang, S., Sun, L., Hu, X., Sheng, Y., et al. (2021). Origin and evolution of a porphyry-breccia system: Evidence from zircon U-Pb, molybdenite Re-Os geochronology, *in situ* sulfur isotope and trace elements of the qiyugou deposit, China. *Gondwana Res.* 89, 88–104. doi:10.1016/j.gr.2020.08.013

Ulrich, T., and Mavrogenes, J. (2008). An experimental study of the solubility of molybdenum in H_2O and KCl-H_2O solutions from 500°C to 800°C, and 150 to 300MPa. *Geochimica Cosmochimica Acta* 72, 2316–2330. doi:10.1016/j.gca.2008.02.014

Veksler, I. V. (2004). Liquid immiscibility and its role at the magmatic-hydrothermal transition: A summary of experimental studies. *Chem. Geol.* 210, 7–31. doi:10.1016/j.chemgeo.2004.06.002

Wang, G. W., Li, R. X., Carranza, E. J. M., Zhang, S. T., Yan, C. H., Zhu, Y. Y., et al. (2015). 3D geological modeling for prediction of subsurface Mo targets in the Luanchuan district, China. *Ore Geol. Rev.* 71, 592–610. doi:10.1016/j.oregeorev.2015.03.002

Wang, S., Li, B., Zhang, X., Wang, P., Chao, W., Ye, H., et al. (2019). Genesis of the Huoshenmiao Mo deposit in the Luanchuan ore district, China: Constraints from geochronology, fluid inclusion, and H-O-S isotopes. *Geosci. Front.* 10, 331–349. doi:10.1016/j.gsf.2017.12.020

Wang, S, S., Zhang, Y., Zhang, H., Zhu, A. M., Wang, H. M., Shi, X. F., et al. (2018). Petrogenesis and tectonic setting of the mesozoic Huoshenmiao intrusion in the luanchuan ore district, henan province, north China. *J. Asian Earth Sci.* 160, 239–257. doi:10.1016/j.jseaes.2018.02.019

Wang, Y. H, Y. H., Zhang, F. F., Liu, J. J., Xue, C. J., Li, B. C., and Xian, X. C. (2018). Ore Genesis and hydrothermal evolution of the Donggebi porphyry Mo deposit, Xinjiang, Northwest China: Evidence from isotopes (C, H, O, S, Pb), fluid inclusions, and molybdenite Re-Os dating. *Econ. Geol.* 113, 463–488. doi:10.5382/econgeo.2018.4558

Wei, Q. G., Yao, J. M., Zhao, T. P., Sun, Y. L., Yuan, Z. L., and Qiao, B. (2009). Discovery of a 1.9 Ga Mo deposit in the eastern qinling orogen: Molybdenite Re-Os ages of the longmendian Mo deposit in henan province. *Acta Petrol. Sin.* 25, 2747–2751. (in Chinese with English abstract).

Xu, B., Hou, Z., Griffin, W. L., Zheng, Y., Wang, T., Guo, Z., et al. (2021). Cenozoic lithospheric architecture and metallogenesis in southeastern Tibet. *Earth. Sci. Rev.* 214, 103472. doi:10.1016/j.earscirev.2020.103472

Xue, F., Santosh, M., Tsunogae, T., and Yang, F. (2019). Geochemical and isotopic imprints of early cretaceous mafic and felsic dyke suites track lithosphere-asthenosphere interaction and craton destruction in the North China Craton. *Lithos*, 326-327, 174–199, doi:10.1016/j.lithos.2018.12.013

Xue, F., Santosh, M., Tsunogae, T., Yang, F., and Zhou, H. (2020). The Genesis of high Ba-Sr adakitic rocks: Insights from an Early Cretaceous volcanic suite in the central North China Craton. *Geol. J.* 55, 5398–5416. doi:10.1002/gj.3720

Xue, F., Wang, G. W., Santosh, M., Yang, F., Shen, Z. W., Kong, L., et al. (2018). Geochemistry and geochronology of ore-bearing and barren intrusions in the Luanchuan ore fields of East Qinling metallogenic belt, China: Diverse tectonic evolution and implications for mineral exploration. *J. Asian Earth Sci.* 157, 57–77. doi:10.1016/j.jseaes.2017.04.027

Xue, F, F., Santosh, M., Kim, S. W., Tsunogae, T., and Yang, F. (2021). Thermo-mechanical destruction of archean cratonic roots: Insights from the mesozoic laiyuan granitoid complex, north China craton. *Lithos* 400-401, 106394–106401. doi:10.1016/j.lithos.2021.106394

Xue, L. W, L. W., Wang, G. W., Tang, L., Cao, Y., Du, J. G., Du, Y. S., et al. (2021). Genesis and hydrothermal evolution of the Zhazigou skarn W (Mo) deposit, East Qinling, China: Constraints from fluid inclusions and H-O-S-Pb isotopes. *Ore Geol. Rev.* 138, 104374. doi:10.1016/j.oregeorev.2021.104374

Yan, C. H., Liu, G. Y., Peng, Y., Song, Y. W., Wang, J. Z., Zhao, R. J., et al. (2009). *The metallogenetical characteristics of the lead–zinc–silver deposits in southwest Henan*. Beijing: Geological Press, 1–365. (in Chinese).

Yan, C. H. (2004). *Study on inner structure of lead–zinc–silver mineralization system in Eastern Qinling*. Beijing: Geological Press, 1–144. (in Chinese with English abstract).

Yang, F., Santosh, M., and Kim, S. W. (2018b). Mesozoic magmatism in the eastern North China Craton: Insights on tectonic cycles associated with progressive craton destruction. *Gondwana Res.* 60, 153–178. doi:10.1016/j.gr.2018.04.003

Yang, F., Santosh, M., and Tang, L. (2018a). Extensive crustal melting during craton destruction: Evidence from the Mesozoic magmatic suite of Junan, eastern North China Craton. *J. Asian Earth Sci.* 157, 119–140. doi:10.1016/j.jseaes.2017.07.010

Yang, F., Xue, F., Santosh, M., Wang, G., Kim, S. W., Shen, Z., et al. (2019). Late mesozoic magmatism in the east qinling orogen, China and its tectonic implications. *Geosci. Front.* 10, 1803–1821. doi:10.1016/j.gsf.2019.03.003

Yang, Y., Liu, Z. J., and Deng, X. H. (2017). Mineralization mechanisms in the Shangfanggou giant porphyry-skarn Mo–Fe deposit of the east Qinling, China: Constraints from HO–C–S–Pb isotopes. *Ore Geol. Rev.* 81, 535–547. doi:10.1016/j.oregeorev.2016.06.026

Yang, Y. L., Ni, P., Pan, J. Y., Zhe, C., Ding, J. Y., and Wang, Q. (2020). Episodic fluid evolution in the formation of the largescale Luoyang Fe deposit, Fujian, eastern China. *Ore Geol. Rev.*, 120, 103412, doi:10.1016/j.oregeorev.2020.103412

Yang, Z. M., Hou, Z. Q., Chang, Z. S., Li, Q. Y., Liu, Y. F., Qu, H. C., et al. (2016). Cospatial Eocene and Miocene granitoids from the Jiru Cu deposit in Tibet: Petrogenesis and implications for the formation of collisional and postcollisional porphyry Cu systems in continental collision zones. *Lithos* 245, 243–257. doi:10.1016/j.lithos.2015.04.002

Yokoro, Y., Hanamuro, T., and Nakashima, K. (2013). Unique origin of skarn at the ohori base metal deposit, yamagata prefecture, NE Japan: C, O and S isotopic study. *Resour. Geol.*, 63, 384–393, doi:10.1111/rge.12017

Zajacz, Z., Halter, W. E., Pettke, T., and Guillong, M. (2008). Determination of fluid melt partition coefficients by LA-ICPMS analysis of co-existing fluid and silicate melt inclusions: Controls on element partitioning. *Geochimica Cosmochimica Acta* 72, 2169–2197. doi:10.1016/j.gca.2008.01.034

Zeng, Q., Sun, Y., Duan, X., and Liu, J. (2013). U-Pb and Re-Os geochronology of the Haolibao porphyry Mo-Cu deposit, NE China: Implications for a Late Permian tectonic setting. *Geological Magazine* 150 (6), 975–985. doi:10.1017/S0016756813000186

Zhang, F. F., Wang, Y. H., and Liu, J. J. (2016). Fluid inclusions and H–O–S–Pb isotope systematics of the Baishan porphyry Mo deposit in Eastern Tianshan, China. *Ore Geol. Rev.* 78, 409–423. doi:10.1016/j.oregeorev.2016.04.015

Zhang, Y. H. (2014). *Late-mesozoic tectonic-magama evolution and its relationship with mineralization in luanchuan county*. Master's thesis. Beijing: China University of Geosciences.

Zheng, Y. F. (1990). Sulfur isotope fractionation in magmatic systems: Models of Rayleigh distillation and selective flux. *Chin. J. Geochem.* 9, 27–45. doi:10.1007/bf02837946

Zhong, R. C., Brugger, J., Chen, Y. J., and Li, W. B. (2015). Contrasting regimes of Cu, Zn and Pb transport in ore-forming hydrothermal fluids. *Chem. Geol.* 395, 154–164. doi:10.1016/j.chemgeo.2014.12.008

Zhu, J. J., Hu, R., Richards, J. P., Bi, X., and Zhong, H. (2015). Genesis and magmatic-hydrothermal evolution of the yangla skarn Cu deposit, southwest China. *Econ. Geol.* 110, 631–652. doi:10.2113/econgeo.110.3.631

frontiers | Frontiers in Earth Science

TYPE Original Research
PUBLISHED 12 January 2023
DOI 10.3389/feart.2022.1019408

Check for updates

OPEN ACCESS

EDITED BY
Fei Xue,
Hohai University, China

REVIEWED BY
Hu Yaping,
East China University of Technology, China
Hailiang Xin,
Geophysical Exploration Center, China Earthquake Administration, China

*CORRESPONDENCE
Jianchang Zheng,
zjcmail@yeah.net
Fangbin Liu,
liufangbin8908@163.com

SPECIALTY SECTION
This article was submitted to Structural Geology and Tectonics, a section of the journal Frontiers in Earth Science

RECEIVED 15 August 2022
ACCEPTED 31 October 2022
PUBLISHED 12 January 2023

CITATION
Zhang Z, Zheng J, Wang S, Li C and Liu F (2023), Imaging the subducting slab and mantle upwelling under the Japan islands revealed by double-difference tomography.
Front. Earth Sci. 10:1019408.
doi: 10.3389/feart.2022.1019408

COPYRIGHT
© 2023 Zhang, Zheng, Wang, Li and Liu. This is an open-access article distributed under the terms of the Creative Commons Attribution License (CC BY). The use, distribution or reproduction in other forums is permitted, provided the original author(s) and the copyright owner(s) are credited and that the original publication in this journal is cited, in accordance with accepted academic practice. No use, distribution or reproduction is permitted which does not comply with these terms.

Imaging the subducting slab and mantle upwelling under the Japan islands revealed by double-difference tomography

Zhengshuai Zhang[1,2], Jianchang Zheng[1]*, Shuhao Wang[3], Cuiqin Li[1] and Fangbin Liu[4]*

[1]Shandong Earthquake Agency, Jinan, China, [2]Hebei Key Laboratory of Earthquake Dynamics, Sanhe, China, [3]School of Earth Sciences and Resources, China University of Geosciences, Beijing, China, [4]Key Laboratory of Western China's Environmental Systems, Ministry of Education, College of Earth and Environmental Sciences, Lanzhou University, Lanzhou, China

In this paper, we collected the seismic phase arrival data of 14,033 local natural earthquakes above magnitude 3.0 recorded by 435 seismograph stations in the study area provided by the International Seismological Centre (ISC), covering the period from January 2011 to April 2020. We selected the first arrival P- and S-wave arrival time data and obtained 281,859 P- and 112,926 S-wave absolute arrival times and 528,250 P-differential and 207,968 S-differential arrival times. Then we determined 3-D P and S wave velocity structures from the Japan Trench to the back arc area under the Japan Islands by using double-difference tomography method. The results show strong lateral heterogeneities under the forearc region. The subducting Pacific slab is imaged clearly as a high-velocity (high-V) faster than the surrounding mantle. Low-velocity (low-V) zones are imaged in the mantle wedge with significant along arc variations under the volcanic front. The vertical section shows that the low velocity zone extends to a depth of approximately 70–150 km below the arc. The crust and mantle wedges beneath the front and back arcs of the volcanoes reveal a low-V anomaly, the likely main source of which is the partial melting of plate and mantle wedge material. Referring to the previous results of plate dehydration, mineral composition and thermal state, it is found that fluids play a crucial role in the arc magmatism and plate melting of mantle wedge behind Japan Trench. The fluids brought down by the Pacific subducting plate are released into the mantle wedge by dehydration and subsequently transported upward by the upwelling flow in the mantle wedge. The present results obtained using new and advanced imaging methods enrich the understanding of the velocity structure beneath Japan Islands, which may improve the understanding of the dynamic processes of subduction zones and mantle upwelling.

KEYWORDS

double-difference tomography, Pacific plate, subduction zone, mantle wedge, arc magmatism

1 Introduction

The Northwest Pacific subduction zone is located at the eastern edge of the Eurasian continent, and is a product of the mutual subduction and collision between the Eurasian plate, the Pacific plate, the Philippine Sea (PHS) plate and the Okhotsk plate (Bird, 2003; DeMets et al., 2010), as shown in Figure 1. Strong interactions of the four lithospheric plates control the geological structure and tectonic evolution of this region, which are characterized by active subduction of oceanic plates (i.e., the Pacific and PHS plates). The Pacific plate is subducting under the Okhotsk and Philippine Sea plates at a rate of 8~9 cm yr^{-1} from the Japan Trench (DeMets et al., 1994). From the southeast the Philippine Sea plate is descending beneath SW Japan at a rate of 4–5 cm yr^{-1} (Heki and Miyazaki, 2001; Miyazaki and Heki, 2001; Huang et al., 2011). Intensive seismicity, arc mechanisms, and volcanic activity are caused by the subduction process. In the upper mantle, the temperature varies laterally from several hundred to over 1,400°C due to the subduction processes and related magmatic and volcanic activities (Honda, 1985; Wada et al., 2015; Wang and Zhao, 2019). Abundant fluids released from the subducting Pacific and PHS slabs participate in mantle convection, making the dynamic processes beneath the Japan Islands even more

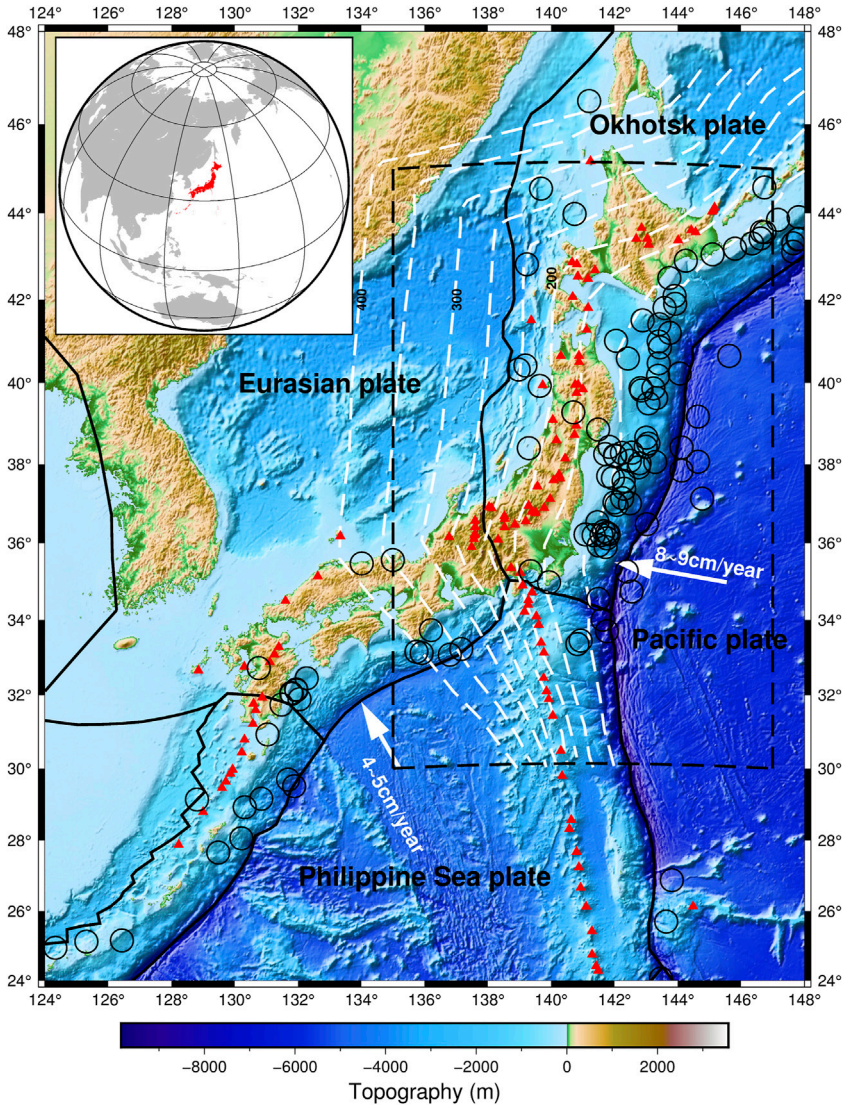


FIGURE 1
Seismicity in the study region (black pane) and surrounding regions. Major tectonic units are labeled, including the Pacific Plate, Philippine Sea Plate, Eurasian Plate, Okhotsk Plate. The solid white arrow represents the subduction direction of plate. The red triangles denote the active arc volcanoes. Plate boundary data are from Bird (2003). The white dotted line represents the depth of the subducting Pacific plate (Zhao et al., 2012). The top left sub-map represents the location of the island of Japan in the world.

vigorous and complicated (Zhao, 2017; Niu et al., 2018). These features make the Japan Islands an ideal place to understand subduction dynamics. Subduction zones are an important link in understanding material circulation and energy exchange in the Earth, continental lithosphere evolution, seismic and volcanic activities, and distribution of mineral resources. Subduction zones have become a research hotspot in the field of Earth sciences (Zhang et al., 2019; Wang et al., 2020; Yang et al., 2021). The high-resolution seismic tomography can provide an effective technical way to understand and explore these scientific issues. Since the end of the last century, with the continuous advancement of Earth science theories, methods and computing power, Earth scientists can not only observe the current surface geological processes of the Pacific Northwest subduction zone, but also explore its deep structural features and understand its evolution process. Among them, seismic tomography methods provide great constraints for identifying subducting plate morphology, discussing the physicochemical properties of the mantle wedge, and understanding the origin of island arc volcanoes and related geodynamic processes (Zhao et al., 1992; Zhao et al., 1994; Huang and Zhao, 2006; Wang and Zhao, 2008; Wang and Zhao, 2009; Wang and Zhao, 2010; Wang and Zhao, 2012; Wei et al., 2012; Zhao et al., 2012; Zhao et al., 2013; Zhao et al., 2015; Tao et al., 2018; Wang and Zhao, 2019; Zhao, 2021; Wang et al., 2022). It is of great importance to investigate the detailed 3-D crustal and mantle structure of this typical subduction zone so as to better understand the seismotectonics, volcanism and subduction dynamics.

In the last decades, many researchers have used seismic tomography to investigate the 3-D seismic velocity structure beneath Japan (Zhao et al., 2002; van Keken, 2003; Hasegawa et al., 2005; Zhao et al., 2007; Zhao et al., 2009; Huang et al., 2011). These tomographic studies have greatly improved the understanding of arc magmatism, seismogenesis and plate subductions in this region. Tomography was first proposed by Aki et al. (1977). Following, natural seismic tomography methods have been gradually developed and perfected, and new technologies such as travel-time tomography, finite frequency tomography, seismic wave attenuation tomography, and background noise layer imaging have emerged. Zhang and Thurber developed a double-difference tomography method (*tomoDD*) (Zhang, 2003; Zhang and Thurber, 2006), using both absolute and differential arrival times in a joint solution for event locations and velocity structure. Differential arrival times is mainly used to determine the fine structure of the source area, and arrival times are mainly used to determine the velocity structure of the area outside the source area. With standard absolute travel-time tomography, seismic event locations are somewhat scattered due to errors such as inaccurate pickup of the seismic phase, but in *tomoDD*, the use of the differential arrival times removes most of these errors, which will in turn remove some fuzziness from the velocity model. In addition, Since the double-difference tomography method takes into account the spatial variation of the velocity structure of the medium, it overcomes the assumption that the path between the station and the event pair is a constant velocity for the double-difference positioning pair, the earthquake event location results obtained are more accurate. The velocity model obtained with double difference tomography should also be superior to that from standard absolute travel-time tomography. The *tomoDD* method can reveal the detailed seismic velocity structure than standard absolute travel-time tomography methods. The *tomoDD* has been widely used to study the fine structure of basins, volcanoes and active fault areas (Zhang et al., 2004; Statz-Boyer et al., 2009; Panayotopoulos et al., 2014; Wang et al., 2018; Xin et al., 2019; Zhang et al., 2021).

In this work, we collected a large number of high-quality the seismic phase data that covers the Japan Islands densely and uniformly. we applied advanced double-difference tomography method to the Japan subduction zone dataset to obtain a more detailed model of the 3-D P- and S-wave velocity structure of the subduction zone around and within the subducting slab. Combined with previous analyses of mineralogical composition, thermal structure and attenuation imaging, the results of this paper provide further insight into the structure and dynamics of the Japanese subduction zone.

2 Data and method

In this paper, we collected the seismic phase data of natural earthquakes above 3.0 in the research region (130°-146°E,30°-45°N) and covered the period from January 2011 to April 2020 provided by International Seismological Centre (ISC). The distribution of earthquakes is shown in Figure 2A. In order to improve the resolution of the lithospheric structure, seismic phase data including *Pg*, *Sg*, *Pn*, *Sn*, *P*, and *S* were collected. Firstly, since the raw data format is different from the standard format followed by *tomoDD*, we wrote a program script to convert it to the standard input format. Then, we extract the first arrival seismic phases of different stations. Secondly, in order to ensure the data quality, we preferentially selected the travel time data according to the following principles: 1) the original data with travel time residuals kept within ±5 s are selected; 2) all selected events need to be recorded by at least 10 stations. After this selection, there are a total of 14,033 earthquake events, and then we used the *ph2dt* executable program in the *hypoDD* software to construct differential travel-times for event pairs that will be used for double-difference tomography (Waldhauser, 2002). It is required that the number of event pair links should be within the range of 10–600 and the maximum hypocentral separation should be no more than 10 km. Figures 3A,B show the distribution of seismic rays in the longitudinal and latitudinal planes for P- and S-waves, respectively. Seismic rays basically

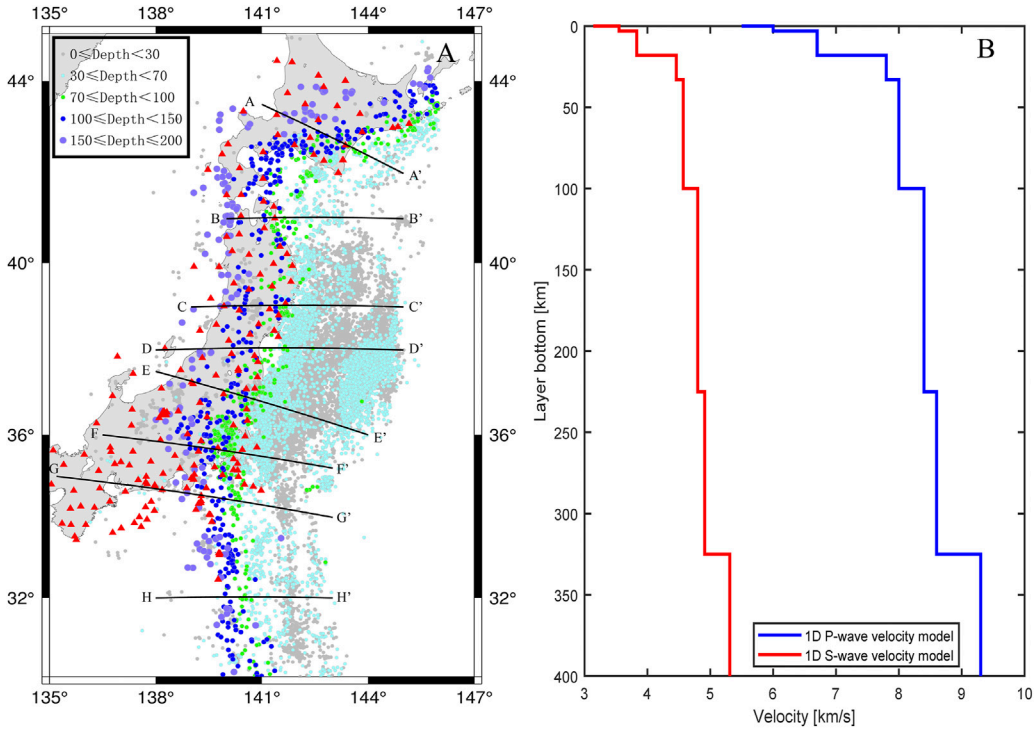


FIGURE 2
(A) Spatial distribution of the data set and 8 profiles location shown on the inset map. **(B)** The One-dimensional initial velocity model.

cover the Japan Islands from the Japan Trench to the back arc area. Figures 3C,D show the distribution of rays in the depth range for P- and S-wave, respectively. Due to the lack of the data recorded by ocean bottom seismometers in the Sea of Japan, there is a clear lack of ray coverage west of longitude 138° from Figures 3C,D. Finally, we obtained a total of 281,859 absolute P- and 112,926 absolute S-wave arrivals and 528,250 P- and 207,968 S-differential arrival times from 14,033 local earthquakes were recorded by 435 seismograph stations. Figure 3E shows the P- and S-wave travel-time distance curves for all selected earthquakes.

The double-difference tomography is an efficient method for charactering the local and regional velocity structures and earthquake hypocenters. The double-difference tomography algorithm uses the differential arrival times from event pairs observed on common stations to simultaneously determine seismic event locations and velocity structure. The theoretical principle of *tomoDD* is that it is assumed that two seismic events are similar in spatial distance, recorded by the same seismic station and their seismic ray paths to the same station are similar. For a pair of events i and j recorded by stations k, the misfit between the observed and predicted arrival times is linearly related to the desired perturbations to the hypocenter location, origin time and velocity structure parameters, along with a station correction term, as follows (Zhang and Thurber, 2006):

$$r_k^i = \sum_{m=1}^{3} \frac{\partial T_k^i}{\partial x_m^i} \Delta x_m^i + \Delta\tau^i + \int_i^k \delta \boldsymbol{u} dl \tag{1}$$

$$r_k^j = \sum_{m=1}^{3} \frac{\partial T_k^j}{\partial x_m^j} \Delta x_m^j + \Delta\tau^j + \int_j^k \delta \boldsymbol{u} dl \tag{2}$$

where r_k^i and r_k^j are arrival time residuals from events i and j recorded by stations k, T_k^i is the observed time of arrival of the body wave from the earthquake source i to the seismic observation station k. By subtracting Eq. 2 from Eq. 1, we obtain:

$$r_k^i - r_k^j = \sum_{m=1}^{3} \frac{\partial T_k^i}{\partial x_m^i} \Delta x_m^i + \Delta\tau^i + \int_i^k \delta \boldsymbol{u} dl - \sum_{m=1}^{3} \frac{\partial T_k^j}{\partial x_m^j} \Delta x_m^j - \Delta\tau^j - \int_j^k \delta \boldsymbol{u} dl \tag{3}$$

Assuming that two seismic events are near each other so that the paths from the events to a common station are almost identical and the velocity structure is known, then Equation 3 can be simplified as

$$dr_k^{ij} = r_k^i - r_k^j = \sum_{m=1}^{3} \frac{\partial T_k^i}{\partial x_m^i} \Delta x_m^i + \Delta\tau^i - \sum_{m=1}^{3} \frac{\partial T_k^j}{\partial x_m^j} \Delta x_m^j - \Delta\tau^j \tag{4}$$

where dr_k^{ij} is called the double difference. In the double-difference tomography method, the absolute travel-time is

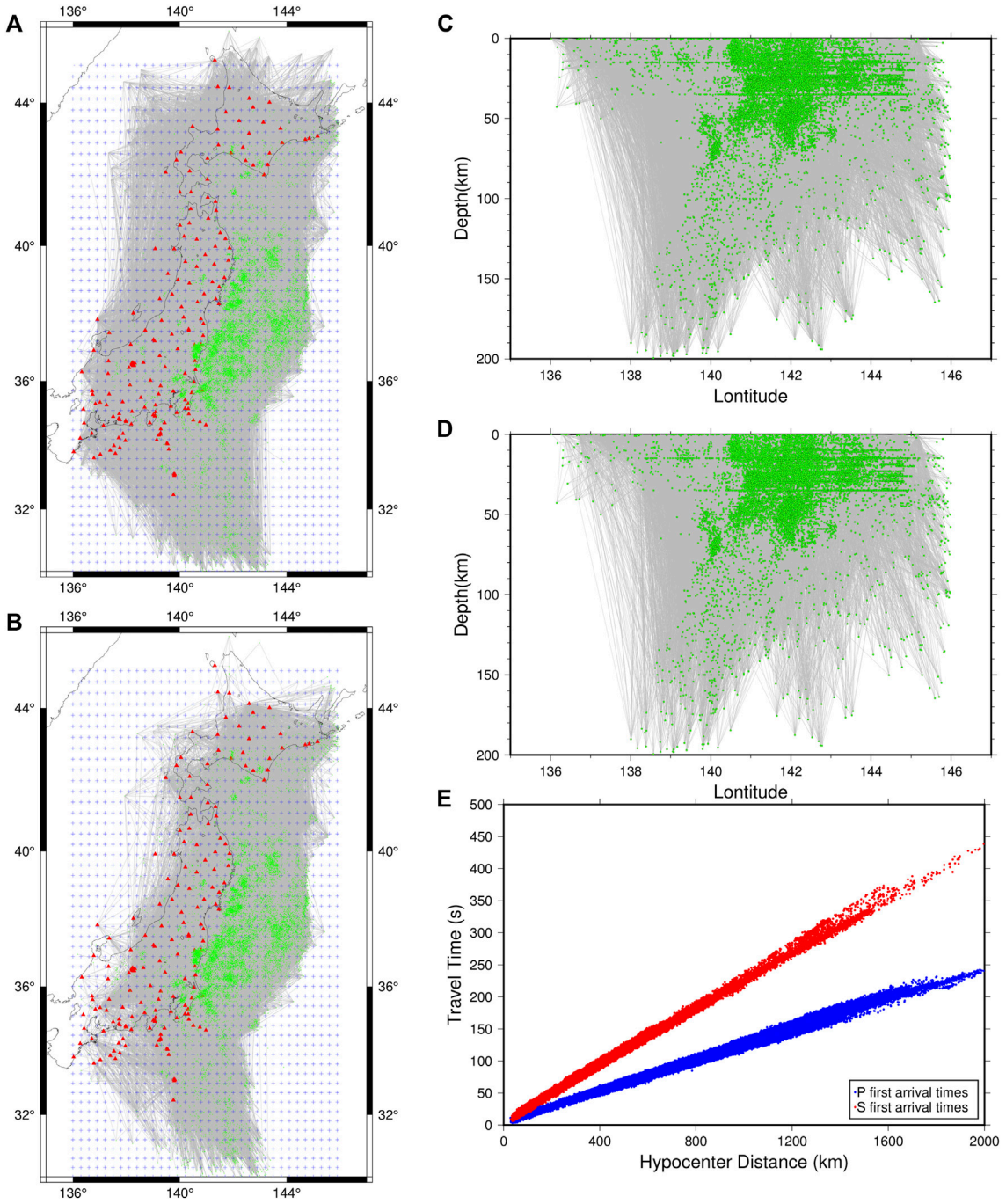


FIGURE 3
Seismic ray paths of P-wave **(A)** and S-wave **(B)** in the studied. Red triangles indicate seismic stations, green solid dots indicate earthquake locations, and blue crosses indicate inversion grid points. Seismic ray paths of P-wave **(C)** and S-wave **(D)** vertical projection; **(E)** Travel time distance curves of P and S wave.

introduced to overcome the assumption that the velocity is constant between the station and the seismic event. The *tomoDD* avoiding the dispersion phenomenon in conventional seismic positioning, therefore the earthquake relocation is more accurate and imaging resolution is close to several hundred meters. The *tomoDD* inverts iteratively for hypocenter locations and velocity structure using LSQR (Least Square QR factorization). It takes the second-order norm of the travel-time

residual as the objective function, and iterates many times until a stable solution is obtained. The double-difference tomography algorithm alternates between joint inversions for both hypocentral parameters and velocity. Because in the joint inversion, the convergence rate of the velocity structure is faster than hypocenters, so we need to add a separate positioning inversion after each joint inversion.

3 Inversion details and regularization parameter

Double-difference tomography algorithm is essentially based on linear inversion, so a reliable initial velocity model is necessary (Comte et al., 2016). Here, we used an initial One-dimensional velocity model considering both shallow and deep parts (Kubo et al., 2002), and translated it to a three-dimensional velocity grid model. The initial P and S velocity model is shown in Figure 2B. The nodes of the velocity model grid are shown in Figure 3A, and node spacing is 0.3°in the latitude and the longitude direction (as shown in Figures 3A,B in the blue cross grid), and inversion nodes in the vertical direction are located at 10, 30, 50, 80,120,150,200 and 250 km depth. In the current version of *tomoDD*, we use the pseudo-bending ray-tracing algorithm (Um and Thurber, 1987) to find the rays and calculate the travel-times between events and stations. The model is represented as a regular set of 3-D nodes, and the velocity values are interpolated by using the trilinear interpolation method. In the process of inversion, the velocity values on grid nodes are updated, and the velocity values between grid nodes are obtained by linear interpolation (Zhang, 2003). Two types of data, the absolute arrival times, the catalog differential arrival times are used in the inversion. To combine these two types of data into one system, we apply a hierarchical weighting scheme during the inversion, similar to the double-difference hypocenter locations (*hypoDD*). We first give more weight to the absolute data to obtain the large-scale velocity structure, and then gradually reduce the weight of the absolute data while increase the weight of the differential data. In this way, fine-scale velocity structures in the source region can be obtained. A total of 10 iterations are carried out in the whole inversion process, with two simultaneous seismic relocation and velocity tomography and one seismic relocation only performing alternately.

The complete system of linear Eqs 2, 3, along with the smoothing constraint equations, is solved by means of the LSQR algorithm (Paige and Saunders, 1982) for the damped least-squares problem. The trade-off of damping and smoothing weight parameters has a greater impact on the stability of the inversion results (Eberhart-Philips, 1986; Eberhart-Phillips and Michael, 1993; Lin et al., 2010). Therefore, in order to make the inversion more stable, we tested the damping factor (from 10 to 1,500) and the smoothing weight factor (from 0.001 to 10,000), and the equilibrium curve of the data variance and the model variance is drawn (Figure 4). Since the optimal regularization parameter corresponds to the point with the maximum curvature of the L-curve, and the point is called the L-corner, so the use of L-curve method to choose the optimal regularization parameter is actually to find the L-corner. After trade-off analysis, we choose the best smoothing factor 20 and damping factor 300 as the control parameters in the inversion process.

4 Analysis and results

Double-difference tomography can simultaneously invert the seismic position and 3-D P- and S-wave velocity structure. Figure 5 shows the P- and S-wave travel-time residuals histogram before and after earthquake relocation. Figure 5A shows that the initial P-wave travel time residuals were mainly distributed in the range of −4 to 4 s, and the average travel time residuals were 0.87 s, while the P-wave travel time residuals were mainly distributed in the range of 0.4 s after relocation, and the average residuals were reduced to 0.26 s. Figure 5B shows that the residuals of the initial S-wave travel time were also significantly reduced from 1.19 s to 0.37 s. Figure 5C shows that the residuals of the overall seismic travel time after relocation are mainly distributed in the range of −2 to 2 s, over 75% of the data have misfits within ±0.4 s after the inversion. The average residual error decreased from 0.89 s before relocation to 0.29 s after relocation, and the accuracy of seismic location was significantly improved.

Conditions such as earthquake distribution, station distribution, seismic ray density, and ray intersection will affect the resolution of the inversion results. In order to assess the ability of the inversions to recover known structure throughout the model, we conducted the checkerboard resolution tests (CRTs) to evaluate the resolutions of the 3-D tomographic structures before seismic tomography (Humphreys and Clayton, 1988). We created synthetic data with a checkerboard model (a pattern of alternate high and low attenuation elementary) by assigning ±5% positive and negative velocity anomalies to the grid nodes adjacent to P and S velocities. Secondly, use this theoretical checkerboard model to obtain the theoretical travel-time through forward calculation. Finally, according to the theoretical travel-time and the initial velocity model, each grid point velocity is inverted. It should be noted that the control parameters used in the checkboard test are consistent with the real data inversion. We made detailed resolution analyses using our dataset. Figures 6, 7 show the results of the resolution tests for P- and S-wave tomography with a grid spacing of 0.3° × 0.3°. Both the checkerboard pattern and amplitude of velocity anomalies are well reconstructed at different depth, except for the very edges of the model. Because of the use of more abundant P-wave arrival time dataset, the P-wave checkerboard resolution tests can still be

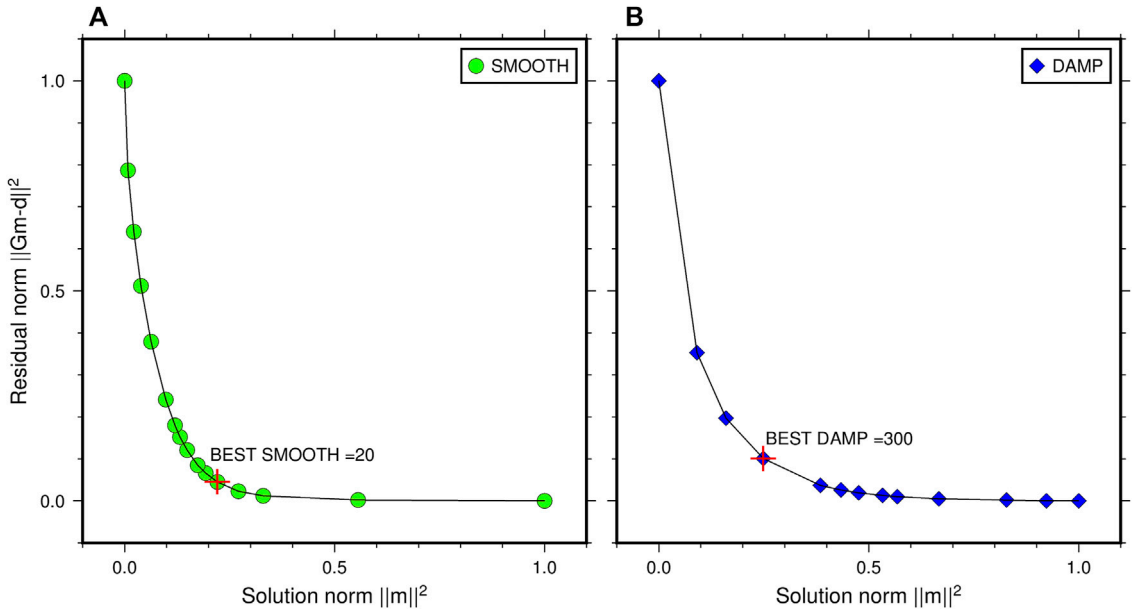


FIGURE 4
Trade-off curves of smoothing **(A)** and damping **(B)** weight parameters. The horizontal axis represents the normalized norm of slowness variation, the vertical axis represents the normalized norm of overall travel-time residual.

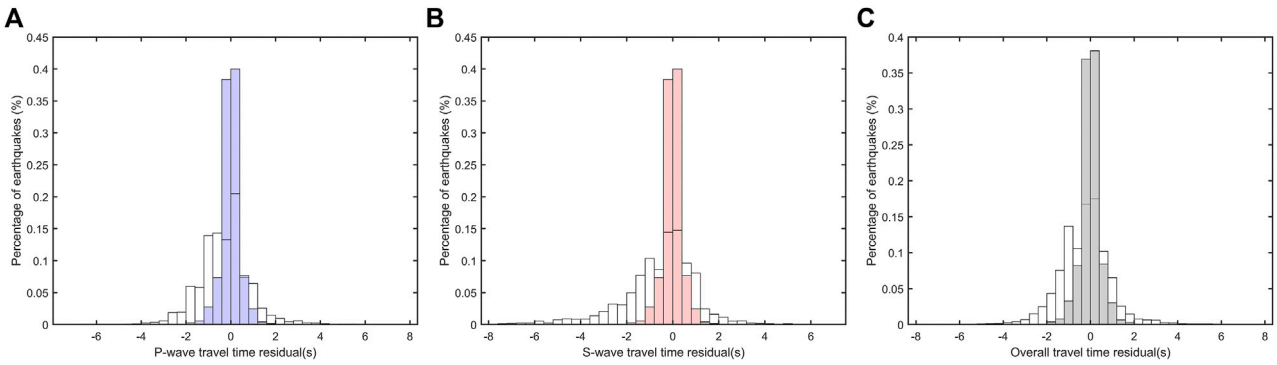


FIGURE 5
The colored filled histograms (blue filled, red filled, gray filled) represent the P-wave **(A)**, S-wave **(B)** and Overall travel time **(C)** residuals after relocate, respectively; The unfilled histograms represent the initial travel time residuals.

reconstructed at a depth of 200 km. Compared to P-wave CRTs, S-wave CRTs shows good resolution mainly at depths <120 km, since the S-wave arrival data is about one-third the size of the P-wave. In terms of overall CRTs, main features of our tomographic results are reliable. In the actual analysis, Because the inversion uses natural seismic data, the distribution of earthquakes and stations is uneven. It is necessary to select a high-resolution region to analysis imaging results.

Figures 8, 9 show map views of high-resolution 3-D tomographic P and S wave velocity model of the crust and mantle under the Japan subduction zone determined by this study; also shown in the maps are background seismicity distribution with in a layer of ≤30 km. Combined with the checkerboard resolution tests, this paper mainly analyzes the results of 3-D velocity structure imaging with the RES (resolution) higher than 0.7 (the highest resolution is 1). From the overall analysis, the crustal and mantle velocity structure in

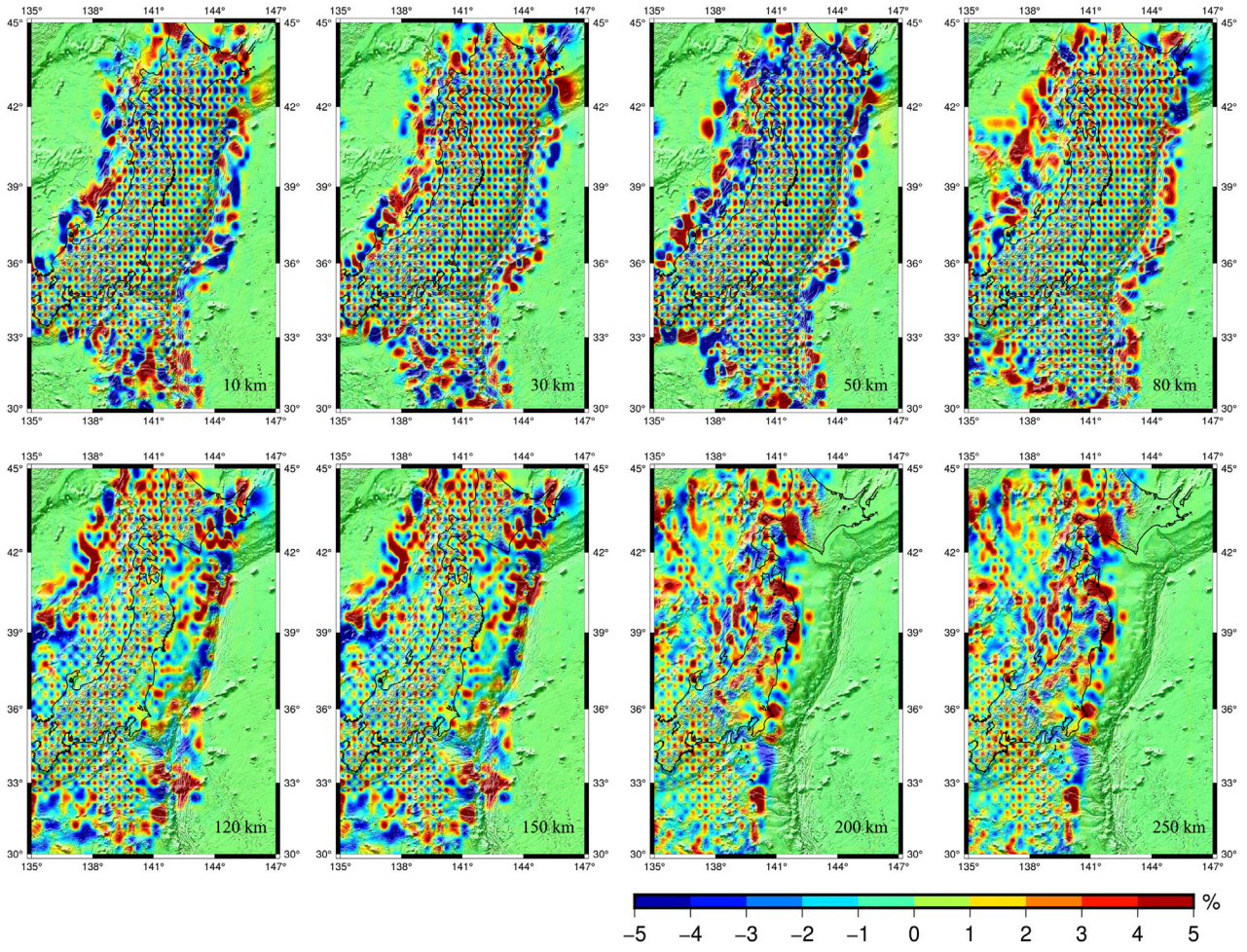


FIGURE 6
Results of a checkerboard resolution test for P-wave tomography. The velocity perturbation (in percent) scale is shown at the bottom. The amplitude of velocity perturbations is 5 percent in the input model. The layer depth is shown at the lower-right corner of each map.

the study area shows obvious unevenness in the vertical and horizontal directions. This unevenness is not only manifested in different blocks, but also in the interior of the block. The most outstanding feature of *Vp*, *Vs* horizontal slice images is that two belts of negative and positive anomalies are disclosed along the volcanic front and the forearc region, respectively. As the subduction zone continues to subduct westward, the positive anomaly also expands westward. Figures 10, 11 show that the subducting Pacific slab is revealed as a high-V zone down to the mantle transition zone and Low-V exist in the mantle wedge. These features are generally consistent with the previous tomographic results in this region (Zhao et al., 1992; Nakajima et al., 2001; Huang and Zhao, 2006; Abdelwahed and Zhao, 2007; Hasegawa et al., 2009; Zhao et al., 2009; Wang and Zhao, 2010). Because seismic stations are located only on the land area, the results of this paper are also in the range of the Japan Islands and the eastern trench, so it is difficult to see the shape of the Pacific slab continuing to subduct westward. Recent regional and global tomographic models suggest that the Pacific plate has subducted to a depth of about ~600 km below the eastern margin of the Asian continent, and then the plate stalled in the mantle transition zone in eastern China (Zhao, 2004; Huang and Zhao, 2006). The vertical cross-sections indicate significant low-V anomalies basically subparallel with the subducting slab are visible in the crust and uppermost mantle beneath the active arc volcanoes and in the middle of the mantle wedge under the back-arc side. Zhao (2004) proposed that a big mantle wedge (BMW) has formed above the stagnant slab, and the BMW exhibits low velocities under the Japan Sea and East China, which is consistent with the existence of active intraplate volcanoes (such as Changbai Mountain and Wudalianchi) and a thin lithosphere under Eastern China (Menzies et al., 2007).

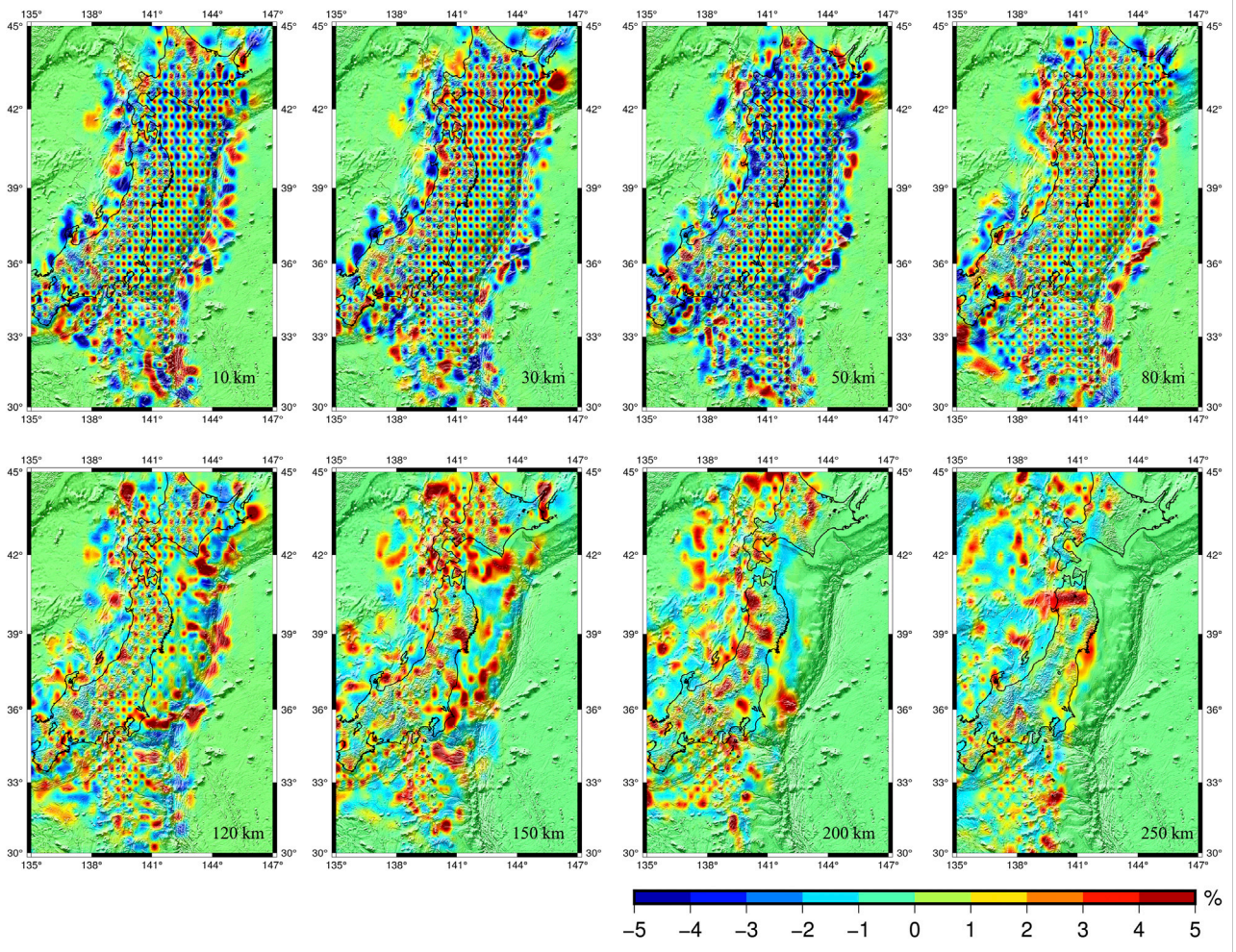


FIGURE 7
The same as Figure 6 but for a checkerboard resolution test for S-wave tomography.

5 Interpretation and discussion

5.1 Velocity structures of subducting slab and the mantle wedge

P- and S-wave velocity images show a similar pattern of velocity variation on horizontal slices (Figures 8, 9) and vertical cross-sections (Figures 10, 11), suggesting that they are reliable features. Oceanic crust subducted into the deep mantle is much denser than the surrounding mantle, the imaging results also confirm this phenomenon. The present results clearly image that the Pacific plate is tilted at high speed below Japan and significant low-V anomalies are visible in the crust and uppermost mantle beneath the active arc volcanoes and in the central portion of the mantle wedge. The subducted Pacific slab is clearly imaged as high-V anomalies, 4%–6% higher than the normal mantle. Based on the analysis of velocity structure imaging results (Zhao et al., 1992; Nakajima et al., 2001; Wang and Zhao, 2005), many scholars inferred the geometry of the upper boundary of the Pacific subduction zone. As a result, some scholars introduced a Pacific subduction plate with a thickness of 85–100 km into the initial model for tomographic studies (Zhao et al., 1992; Zhao et al., 2009; Zhao et al., 2012; Liu and Zhao, 2016). The one-dimensional velocity model used in this paper does not impose geometric constraints on the initial model shape, but the imaging results can clearly reflect the morphological characteristics of the subduction zone, which can also indicate that the imaging results are reliable.

Thermal structure and attenuation imaging can also provide important additional information on slow thermal structure and dynamics (Gung and Romanowicz, 2004). Wang et al (2019) determine a model of P- and S-wave attenuation (*Qp*, *Qs*) tomography of the Japan subduction zone using an improved inversion scheme. Attenuation imaging also reveals strong lateral heterogeneities at each depth beneath the Japan Islands. The high-V

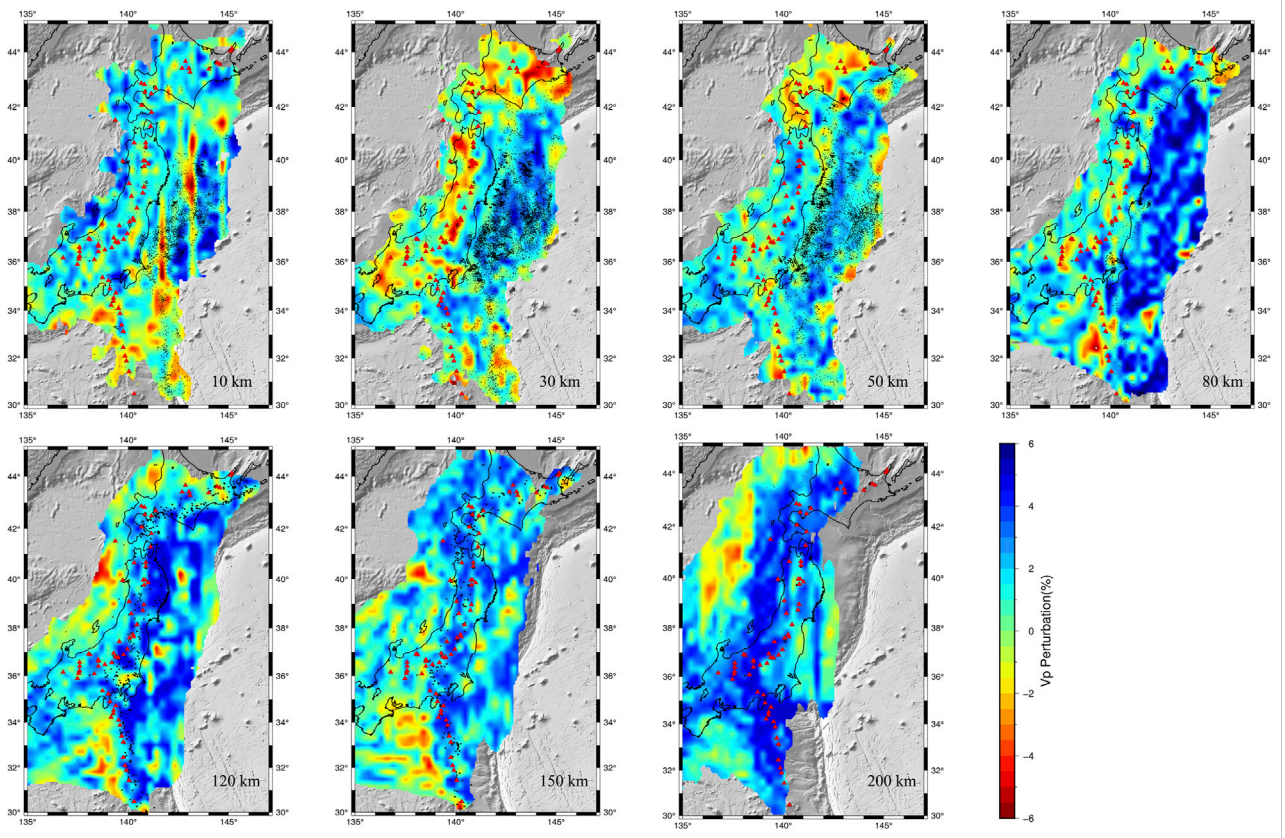


FIGURE 8
Map views of *Vp* structures. Black circles denote the background earthquakes that occurred within a layer of 30 km thickness bound to each slice. The red triangles denote the active arc volcanoes.

anomalies in this paper corresponds to the low-attenuation (high-Q) subducting Pacific slab. Similarly, high-attenuation (low-Q) mantle wedge beneath the volcanic front and back-arc areas corresponds to the low-V in our results. In addition, through some thermal structure studies, it was found that the heat flow near the trench is very low, then increases sharply near the volcanic front, reaches a maximum at the back of the arc, and then tapers off at the back of the arc (Lu et al., 1981; Yamano et al., 1989; Furukawa, 1993; Wang et al., 2022). Thermal structure imaging using two lithological models of the upper mantle (a peridotite assemblage and a pyrolite assemblage) revealed a low-temperature (low-T, ≤ ~900°C) feature in the forearc region and a high-temperature (high-T, ~1,400°C) anomaly in the back-arc region of the volcanic forearc (Wang et al., 2022). The distribution of heat flow values is also consistent with our imaging results: high-T and low-V are under back-arc.

5.2 Slab dehydration and partial melt

One of the most important findings of subduction zone tomography studies is that significant low-V anomalies are visible in the crust and uppermost mantle beneath the active arc volcanoes and in the middle of the mantle wedge. These low-V anomalies may have provided the main source of material for arc magmatism and volcanism. Such features have also been found by using different seismic tomography methods, which are also consistent with some petrological studies (Tatsumi, 1989; Peacock, 1990; Iwamori and Zhao, 2000; Hacker et al., 2003). In this paper, Figure 10 demonstrate the presence of low-V anomalous velocities (white dashed areas) in the crust and mantle wedge beneath the volcanic front, although the extended depths of the low velocity anomalies are different from one another. For example, in the AA′ profile in northeastern Japan, the low-V anomaly extends to ~120 km. The CC′ and DD′ profiles in Honshu Island show that the low-V anomalies extend to ~110 km, while the EE′ and FF′ profiles show that the low-V anomaly extends to ~80 km depth. Figure 11 shows the vertical cross section of the S-wave velocity tomography along the 8 profiles, with the extension of the low-V anomalies generally consistent with Figure 10. Unraveling the source of these low-V anomalies is key to understanding arc magmatism. During the subduction of the Pacific slab, higher temperature, fluid content, and melting

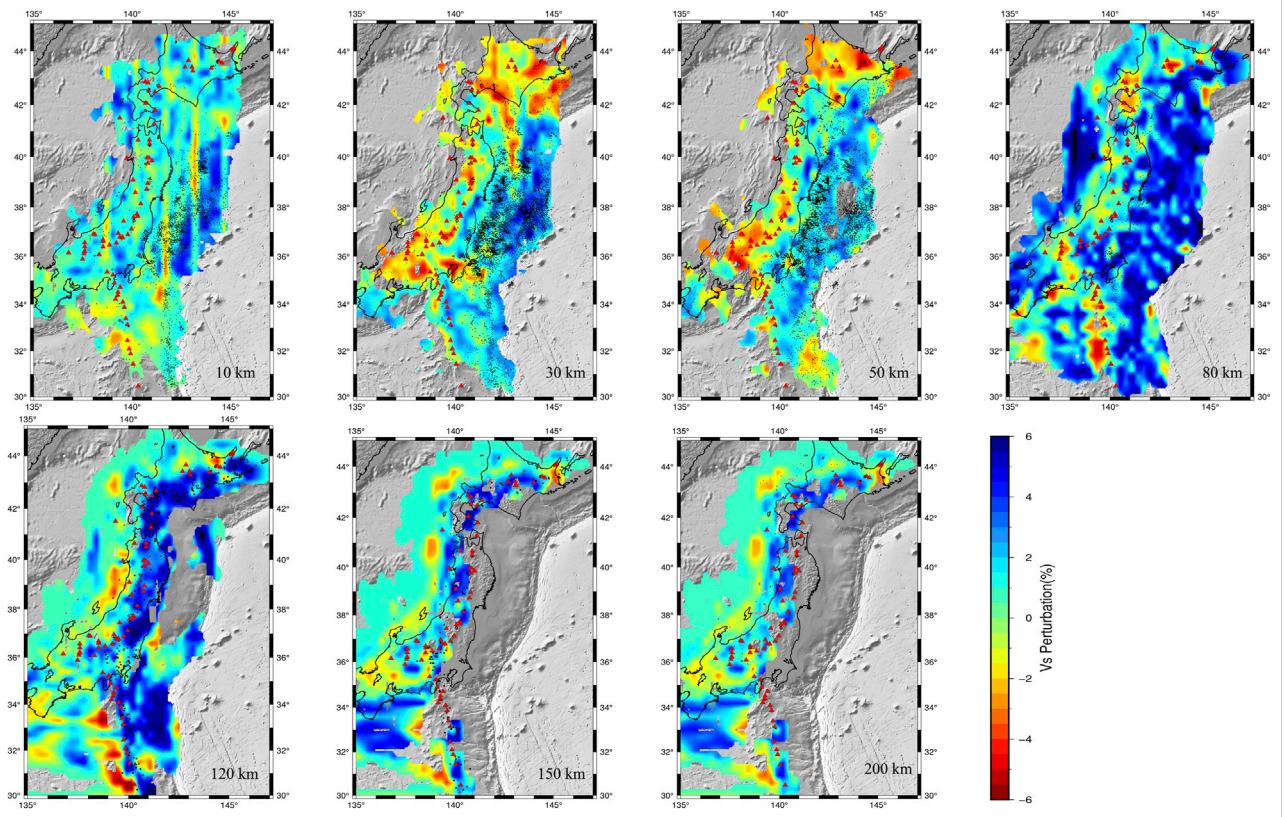


FIGURE 9
Map views of *Vs* structures. Black circles denote the background earthquakes that occurred within a layer of 30 km thickness bound to each slice. The red triangles denote the active arc volcanoes.

fraction can all contribute to anomalous velocity structures (Nakajima et al., 2001). In the subduction zone, the fluid content is considered to be an important factor contributing to the low V in the forearc zone. The black dashed ellipses in Figures 10, 11 show the low-Vp and low-Vs at the shallow subducting slab in the forearc region. At shallow depths, free water is released from oceanic crust, unconsolidated sediments and fluid-filled accretionary complexes after being affected by the high temperature of the surrounding mantle material (Mishra et al., 2003; Wang et al., 2012; Wang et al., 2019; Wang et al., 2022; Wang and Lin, 2022). This may reduce seismic velocity in the forearc region. The hydrated rocks continue to subduct into the deep mantle wedge and experiences a series of progressive geochemical reactions under the influence of high pressure and temperature (Kita et al., 2012; Wang et al., 2022). In this study, at a depth of about 70–150 km, there is a relatively low-V along the upper boundary of the slab (red dashed rectangle, Figures 10, 11). The imaged seismic models infer that the low-Vp and Vs bodies anomalies in the crust and mantle wedge are closely linked to the Pacific slab subduction.

We hypothesize that there are three possible sources of magma for arc magmatism: direct melting of subducting oceanic crust; melting of subducting plate upper mantle peridotite associated with plate dehydration; or both. According to the calculation of peridotite assemblage (Wada et al., 2015), the temperature at a depth of 60–120 km at the upper boundary of the slab is about 1,000–1,200°C. This temperature is sufficient to melt or partially melt the hydrated peridotite of the subducting plate. The low V anomaly in the red dashed rectangle above the plate at depths of 70–150 km shown in Figure 10 may indirectly reflect the state of partial melting of the slab. It should be noted that this low-V anomaly is not continuous above the plate. This spatial feature may indicate that partial melting occurs only locally, or the imaging resolution of this study is not sufficient to fully describe the spatial distribution of molten material. It is generally accepted that the main minerals in the upper mantle (≤400 km depth) are olivine, orthopyroxene, clinopyroxene, and garnet with minor chromite and ilmenite (Ringwood, 1975; Anderson and Bass, 1984; Anderson, 1989; Duffy and Anderson, 1989). However, adding water to a mantle wedge composed of olivine and orthopyroxene may form a variety of hydrous minerals (e.g., anti-olivine, chrysotile, lizardite, talc, and brucite). Therefore, the supply of H_2O from the slab is believed to play an important role in the formation of

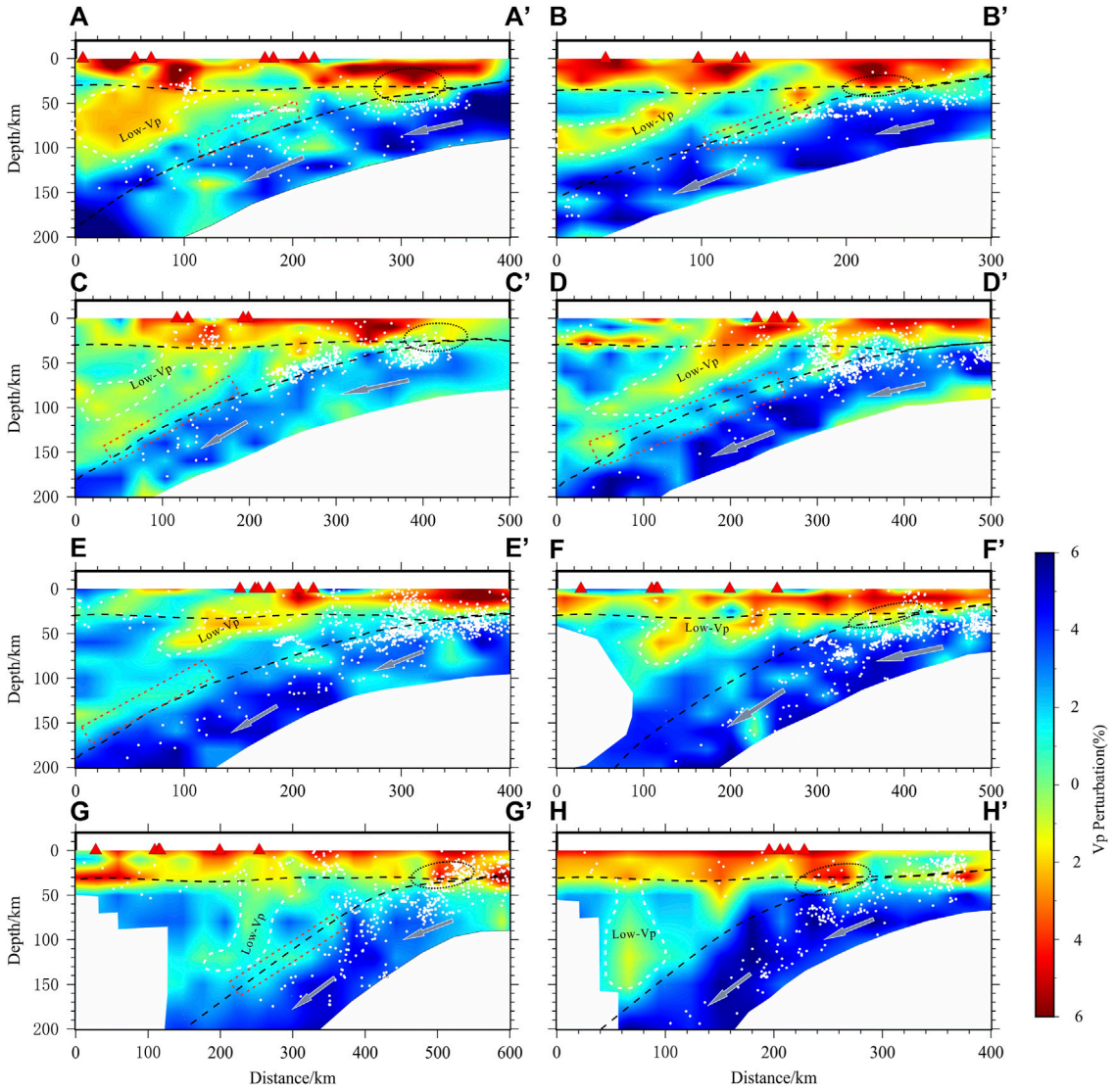


FIGURE 10
Vertical cross-sections of P-wave velocity (*Vp*) tomography along the 8 profiles shown on the Figure 2A. The red and blue colors denote low and high *Vp* perturbations (in %). The scales of *Vp* perturbation are exhibited at the right. Two black dash lines show the discontinuities of the Moho and the upper interface of the subducting Pacific plate along each section, respectively. The red triangles denote the active arc volcanoes. The gray arrow mark indicates the direction of subduction of the Pacific plate. The white dashed area represents the low-velocity anomaly in the mantle wedge. The white dots represent the relocated earthquakes within ~35 km near the profile.

arc magma in the mantle wedge. In the mantle wedge, hydrous fluids are primarily released from extensive metamorphic reactions in the subducted Pacific slab crust. The temperature of the mantle wedge in the subduction zone is greater than 900°C at depths above 60 km (Abers et al., 2017). Upwelling fluids from the subducting plates may have caused partial melting in the overlying mantle wedge due to the high temperatures there, reducing seismic wave velocities (Low-V anomalies in the mantle in Figures 10, 11). In conclusion, the possible magmatic sources of arc magmatism mainly include partial melting of subducting plates at depths of 70–150 km and melting of mantle material with the participation of water fluids.

5.3 Subduction dynamics and arc magmatism

Section 5.2 focuses on the analysis of the main sources of these low-V anomalies, but the dynamical mechanisms of low-V anomalies are still under investigation. In this section, we

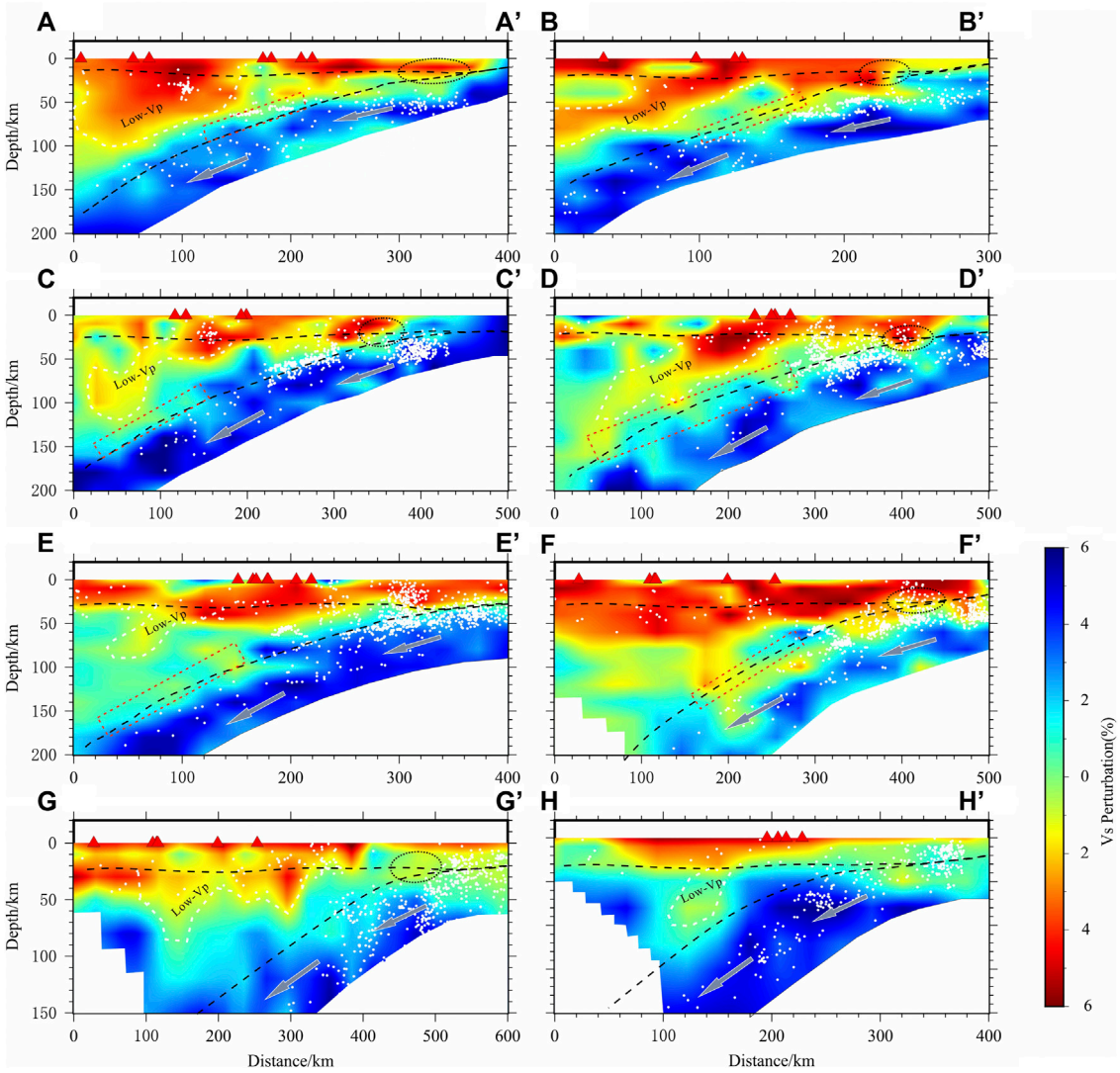


FIGURE 11
The same as Figure 10, but indicates S-wave velocity (*Vs*).

try to analyze subduction dynamics and arc magmatism by combining the previous studies and the results of this paper. According to the research of scholars, the Pacific plate becomes stagnant in the mantle transition zone and eventually collapses into the lower mantle due to the huge gravitational instability generated by the phase transition, which will cause turbulence and thermal instability in the mantle transition zone and the lower mantle. Perhaps it is the thermal instability of the thermal boundary layer that creates the upward thermal buoyancy (Maruyama et al., 2007; Zhao et al., 2012). We represent this buoyancy in the schematic structure model in Figure 12 with three upward white arrows. In addition, many studies have shown that mantle upwelling and downwelling (mantle corner flow, schematic arrows as shown in Figure 12) are prevalent in the mantle above subducting oceanic plates (Martinez and Taylor, 2002; Kelemen et al., 2003; Currie and Hyndman, 2006). As the mantle molten material migrates to the shallow part, the pressure and temperature decrease, and the viscous coupling between the mantle wedge and the subducting plate further promotes the circulation of the mantle to the deep part together with the overlying subducting plate. Although the phenomenon of mantle corner flow has been widely recognized, it is established through indirect observations such as seismic imaging and thermal structure simulation. The mantle corner flow processes on subducting oceanic plates have not been confirmed by direct petrological studies.

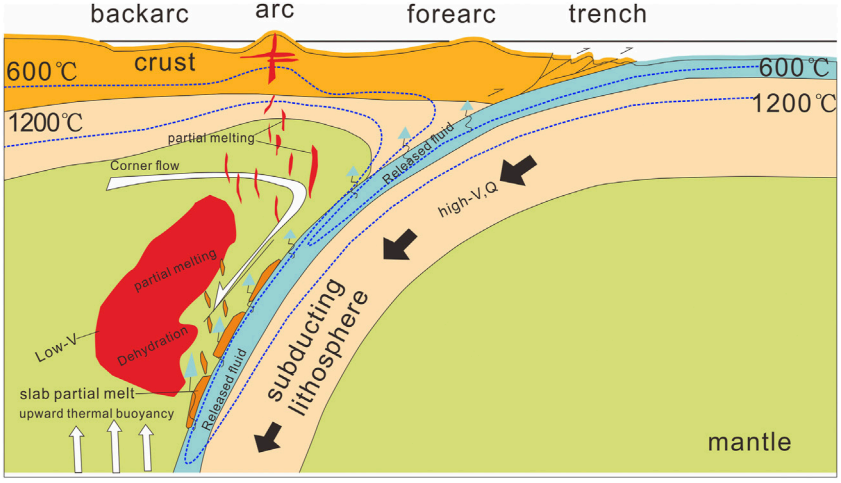


FIGURE 12
Schematic structure model of Japan subduction zone built on the calculated seismic velocity structures. Temperature contours are referenced from (Wada et al., 2015).

Water fluids play an irreplaceable role in subduction dynamics and arc magmatism. During the subduction process of the cold Pacific plate, surface water and sediments are carried into the interior of the Earth, which not only affects the physical and chemical properties of mantle materials (such as density, seismic wave velocity and elasticity, *etc.*), but also significantly changes the melting temperature and rheological properties. Firstly, significant dewatering of the oceanic plate occurs in the forearc region (released fluid as shown in Figure 12), which may reduce the seismic velocity at shallow depths within the forearc region. As subduction proceeds, the pressure and temperature increase and water is further released from the oceanic crust. Then, these released waters enters the mantle wedge, lowering the melting point of the mantle material and undergoing partial melting, forming a low-V anomaly. Moreover, Rayleigh-Taylor instability that can arise during melting, which may propel higher-velocity anomalies ("cold plumes") within the mantle wedge (Gerya and Yuen, 2003; Gorczyk et al., 2006). As the plate continues to subduct, the garnet-peridotite slab may undergo direct partial melting along its upper boundary (as shown in the pink thin layer in Figure 12). The molten material migrates upward into the overlying mantle wedge and merges with fluid-dependent melting, where it forms magma. Low-frequency volcanic earthquakes (LFEs) studies show that many low-frequency micro seismic events occur in and around the low-V zone in the lower crust and top of the upper mantle (Hasegawa et al., 2005; Wang et al., 2019), which may represent the subduction of island arc magma from the mantle wedge to the surface. Therefore, we suggest that fluids associated with plate dehydration, mineral composition and thermal state play a fundamental role in arc magmatism and plate melting in the mantle wedge behind the Japan Trench. The repeated supply of magma from these molten low-V body in the mantle wedge into the overlying arc crust cause uplift and volcano formation.

6 Conclusion

We used advanced double-difference tomography to determine the 3-D velocity structure of the P- and S-waves under Japan Islands from the Japan Trench to the back-arc. We use the initial one-dimensional velocity model without geometric constraints on the subduction plate shape, and the imaging results can clearly reflect the morphological features of the subduction zone and the low-V anomalies in the mantle wedge, which can also illustrate the advanced imaging method and the reliability of the inversion results. The results well reveal the morphological and high-velocity characteristics of the subduction of the Pacific subducting plate and low-V anomalies in the surrounding mantle beneath the Japan Islands. The possible source of the significant low-V anomaly are partial melting of the mantle material and direct melting of the subducting oceanic crust itself, in which fluids released from extensive dehydration of the subducting oceanic crust are presumed to play a key role. These molten low-V bodies in the mantle wedge are upwelling into the overlying arc crust under the action of corner flow, leading to uplift and volcano formation.

Data availability statement

The original contributions presented in the study are included in the article/Supplementary Material, further inquiries can be directed to the corresponding authors.

Author contributions

All authors collected and analyzed the data; ZZ, JZ, and FL participated discussion; ZZ and SW drew the figures; ZZ and JZ wrote the paper with the help of all authors. All authors contributed to writing the manuscript and approved the submitted version.

Funding

This work was jointly supported by International Cooperative Research on Earthquake Predictability of China Earthquake Science Experiment Site (Grant No. 2018YFE0109700), Hebei Key Laboratory of Earthquake Dynamics (Grant No. FZ212204) and Earthquake Science and Technology Spark of the China Earthquake Administration (Grant No. XH20034Y).

Acknowledgments

We are very grateful to Prof. Haijiang Zhang of the University of Science and Technology of China for providing the double-difference tomography program and Dr. Lei Gao for his guidance in using the program. Most of the figures were made by using free software GMT (Wessel et al., 2019).

Conflict of interest

The authors declare that the research was conducted in the absence of any commercial or financial relationships that could be construed as a potential conflict of interest.

Publisher's note

All claims expressed in this article are solely those of the authors and do not necessarily represent those of their affiliated organizations, or those of the publisher, the editors and the reviewers. Any product that may be evaluated in this article, or claim that may be made by its manufacturer, is not guaranteed or endorsed by the publisher.

References

Abdelwahed, M. F., and Zhao, D. (2007). Deep structure of the Japan subduction zone. *Phys. Earth Planet. Inter.* 162, 32–52. doi:10.1016/j.pepi.2007.03.001

Abers, G. A., van Keken, P. E., and Hacker, B. R. (2017). The cold and relatively dry nature of mantle forearcs in subduction zones. *Nat. Geosci.* 10, 333–337. doi:10.1038/ngeo2922

Aki, K., Christoffersson, A., and Husebye, E. S. (1977). Determination of the three-dimensional seismic structure of the lithosphere. *J. Geophys. Res.* 82, 277–296. doi:10.1029/JB082i002p00277

Anderson, D. L. (1989). *Theory of the Earth*. Osney Mead, Oxford: Blackwell Scientific Publications, 1–366.

Anderson, D. L., and Bass, J. D. (1984). Mineralogy and composition of the upper mantle. *Geophys. Res. Lett.* 11, 637–640. doi:10.1029/JB082i002p00277

Bird, P. (2003). An updated digital model of plate boundaries: Updated model of plate boundaries. *Geochem. Geophys. Geosyst.* 4, 1027. doi:10.1029/2001GC000252

Comte, D., Carrizo, D., Roecker, S., Ortega-Culaciati, F., and Peyrat, S. (2016). Three-dimensional elastic wave speeds in the northern Chile subduction zone: Variations in hydration in the supraslab mantle. *Geophys. J. Int.* 207, 1080–1105. doi:10.1093/gji/ggw318

Currie, C. A., and Hyndman, R. D. (2006). The thermal structure of subduction zone back arcs. *J. Geophys. Res.* 111, B08404. doi:10.1029/2005JB004024

DeMets, C., Gordon, R. G., Argus, D. F., and Stein, S. (1994). Effect of recent revisions to the geomagnetic reversal time scale on estimates of current plate motions. *Geophys. Res. Lett.* 21, 2191–2194. doi:10.1029/94GL02118

DeMets, C., Gordon, R. G., and Argus, D. F. (2010). Geologically current plate motions. *Geophys. J. Int.* 181, 1–80. doi:10.1111/j.1365-246X.2009.04491.x

Duffy, T. S., and Anderson, D. L. (1989). Seismic velocities in mantle minerals and the mineralogy of the upper mantle. *J. Geophys. Res.* 94, 1895–1912.

Eberhart-Philips, D. (1986). Three-dimensional velocity structure in northern California Coast Ranges from inversion of local earthquake arrival times. *Bull. Seismol. Soc. Am.* 76, 1025–1052.

Eberhart-Phillips, D., and Michael, A. J. (1993). Three-dimensional velocity structure, seismicity, and fault structure in the Parkfield Region, central California. *J. Geophys. Res.* 98, 15737. doi:10.1029/93JB01029

Furukawa, Y. (1993). Depth of the decoupling plate interface and thermal structure under arcs. *J. Geophys. Res.* 98, 20005–20013. doi:10.1029/93JB02020

Gerya, T. V., and Yuen, D. A. (2003). Rayleigh–Taylor instabilities from hydration and melting propel 'cold plumes' at subduction zones. *Earth Planet. Sci. Lett.* 212, 47–62. doi:10.1016/S0012-821X(03)00265-6

Gorczyk, W., Gerya, T. V., Connolly, J. A. D., Yuen, D. A., and Rudolph, M. (2006). Large-scale rigid-body rotation in the mantle wedge and its implications for seismic tomography: Rotation in the mantle wedge. *Geochem. Geophys. Geosyst.* 7, Q05018. doi:10.1029/2005gc001075

Gung, Y., and Romanowicz, B. (2004). Q tomography of the upper mantle using three-component long-period waveforms. *Geophys. J. Int.* 157, 813–830. doi:10.1111/j.1365-246X.2004.02265.x

Hacker, B. R., Abers, G. A., and Peacock, S. M. (2003). Subduction factory 1. Theoretical mineralogy, densities, seismic wave speeds, and H_2O contents: Subduction zone mineralogy and physical properties. *J. Geophys. Res.* 108, B12029. doi:10.1029/2001JB001127

Hasegawa, A., Nakajima, J., Umino, N., and Miura, S. (2005). Deep structure of the northeastern Japan arc and its implications for crustal deformation and shallow seismic activity. *Tectonophysics* 403, 59–75. doi:10.1016/j.tecto.2005.03.018

Hasegawa, A., Nakajima, J., Uchida, N., Okada, T., Zhao, D., Matsuzawa, T., et al. (2009). Plate subduction, and generation of earthquakes and magmas in Japan as inferred from seismic observations: An overview. *Gondwana Res.* 16, 370–400. doi:10.1016/j.gr.2009.03.007

Heki, K., and Miyazaki, S. (2001). Plate convergence and long-term crustal deformation in central Japan. *Geophys. Res. Lett.* 28, 2313–2316. doi:10.1029/2000GL012537

Honda, S. (1985). Thermal structure beneath Tohoku, northeast Japan. *Tectonophysics* 112, 69–102. doi:10.1016/0040-1951(85)90173-8

Huang, J., and Zhao, D. (2006). High-resolution mantle tomography of China and surrounding regions. *J. Geophys. Res.* 111, B09305. doi:10.1029/2005JB004066

Huang, Z., Zhao, D., and Wang, L. (2011). Seismic heterogeneity and anisotropy of the Honshu arc from the Japan Trench to the Japan Sea: Heterogeneity and anisotropy of Honshu arc. *Geophys. J. Int.* 184, 1428–1444. doi:10.1111/j.1365-246X.2011.04934.x

Humphreys, E., and Clayton, R. W. (1988). Adaptation of back projection tomography to seismic travel time problems. *J. Geophys. Res.* 93, 1073. doi:10.1029/JB093iB02p01073

Iwamori, H., and Zhao, D. (2000). Melting and seismic structure beneath the Northeast Japan Arc. *Geophys. Res. Lett.* 27, 425–428. doi:10.1029/1999GL010917

Kelemen, P. B., Rilling, J. L., Parmentier, E. M., Mehl, L., and Hacker, B. R. (2003). "Thermal structure due to solid-state flow in the mantle wedge beneath arcs," in *Geophysical monograph series*. Editor J. Eiler (Washington, D. C.: American Geophysical Union), 293–311. doi:10.1029/138GM13

Kita, S., Hasegawa, A., Nakajima, J., Okada, T., Matsuzawa, T., and Katsumata, K. (2012). High-resolution seismic velocity structure beneath the hokkaido corner, northern Japan: Arc-arc collision and origins of the 1970 M 6.7 hidaka and 1982 M 7.1 urakawa-oki earthquakes: Seismic velocity structure in hokkaido. *J. Geophys. Res.* 117, B12301. doi:10.1029/2012jb009356

Kubo, A., Fukuyama, E., Kawai, H., and Nonomura, K. (2002). NIED seismic moment tensor catalogue for regional earthquakes around Japan: quality test and application. *Tectonophysics* 356, 23–48. doi:10.1016/S0040-1951(02)00375-X

Lin, G., Thurber, C. H., Zhang, H., Hauksson, E., Shearer, P. M., Waldhauser, F., et al. (2010). A California statewide three-dimensional seismic velocity model from both Absolute and differential times. *Bull. Seismol. Soc. Am.* 100, 225–240. doi:10.1785/0120090028

Liu, X., and Zhao, D. (2016). P and S wave tomography of Japan subduction zone from joint inversions of local and teleseismic travel times and surface-wave data. *Phys. Earth Planet. Inter.* 252, 1–22. doi:10.1016/j.pepi.2016.01.002

Lu, R. S., Pan, J. J., and Lee, T. C. (1981). Heat flow in the southwestern Okinawa trough. *Earth Planet. Sci. Lett.* 55, 299–310. doi:10.1016/0012-821X(81)90109-6

Martinez, F., and Taylor, B. (2002). Mantle wedge control on back-arc crustal accretion. *Nature* 416, 417–420. doi:10.1038/416417a

Maruyama, S., Santosh, M., and Zhao, D. (2007). Superplume, supercontinent, and post-perovskite: Mantle dynamics and anti-plate tectonics on the Core–Mantle Boundary. *Gondwana Res.* 11, 7–37. doi:10.1016/j.gr.2006.06.003

Menzies, M., Xu, Y., Zhang, H., and Fan, W. (2007). Integration of geology, geophysics and geochemistry: A key to understanding the North China craton. *Lithos* 96, 1–21. doi:10.1016/j.lithos.2006.09.008

Mishra, O. P., Zhao, D., Umino, N., and Hasegawa, A. (2003). Tomography of northeast Japan forearc and its implications for interplate seismic coupling: Tomography of Northeast Japan forearc. *Geophys. Res. Lett.* 30, GL017736. doi:10.1029/2003GL017736

Miyazaki, S., and Heki, K. (2001). Crustal velocity field of southwest Japan: Subduction and arc-arc collision. *J. Geophys. Res.* 106, 4305–4326. doi:10.1029/2000JB900312

Nakajima, J., Matsuzawa, T., Hasegawa, A., and Zhao, D. (2001). Seismic imaging of arc magma and fluids under the central part of northeastern Japan. *Tectonophysics* 341, 1–17. doi:10.1016/S0040-1951(01)00181-0

Niu, X., Zhao, D., and Li, J. (2018). Precise relocation of low-frequency earthquakes in Northeast Japan: new insight into Arc magma and fluids. *Geophys. J. Int.* 212, 1183–1200. doi:10.1093/gji/ggx445

Paige, C. C., and Saunders, M. A. (1982). Algorithm 583: LSQR: Sparse linear equations and least squares problems. *ACM Trans. Math. Softw.* 8, 195–209. doi:10.1145/355993.356000

Panayotopoulos, Y., Hirata, N., Sato, H., Kato, A., Imanishi, K., Kuwahara, Y., et al. (2014). Investigating the role of the Itoigawa-Shizuoka tectonic line towards the evolution of the Northern Fossa Magna rift basin. *Tectonophysics* 615–616, 12–26. doi:10.1016/j.tecto.2013.12.014

Peacock, S. A. (1990). Fluid processes in subduction zones. *Science* 248, 329–337. doi:10.1126/science.248.4953.329

Ringwood, A. E. (1975). *Composition and Petrology of the Earth's Mantle*. New York: McGraw-Hill, 618.

Statz-Boyer, P., Thurber, C., Pesicek, J., and Prejean, S. (2009). High precision relocation of earthquakes at Iliamna Volcano, Alaska. *J. Volcanol. Geotherm. Res.* 184, 323–332. doi:10.1016/j.jvolgeores.2009.04.016

Tao, K., Grand, S. P., and Niu, F. (2018). Seismic structure of the upper mantle beneath eastern Asia from full waveform seismic tomography. *Geochem. Geophys. Geosyst.* 19, 2732–2763. doi:10.1029/2018GC007460

Tatsumi, Y. (1989). Migration of fluid phases and Genesis of basalt magmas in subduction zones. *J. Geophys. Res.* 94, 4697–4707. doi:10.1029/JB094iB04p04697

Um, J., and Thurber, C. (1987). A fast algorithm for two-point seismic ray tracing. *Bull. Seismol. Soc. Am.* 77, 972–986. doi:10.1785/BSSA0770030972

van Keken, P. E. (2003). The structure and dynamics of the mantle wedge. *Earth Planet. Sci. Lett.* 215, 323–338. doi:10.1016/S0012-821X(03)00460-6

Wada, I., He, J., Hasegawa, A., and Nakajima, J. (2015). Mantle wedge flow pattern and thermal structure in Northeast Japan: Effects of oblique subduction and 3-D slab geometry. *Earth Planet. Sci. Lett.* 426, 76–88. doi:10.1016/j.epsl.2015.06.021

Waldhauser, F. (2002). Fault structure and mechanics of the Hayward Fault, California, from double-difference earthquake locations. *J. Geophys. Res.* 107, 2054. doi:10.1029/2000JB000084

Wang, Z., and Lin, J. (2022). Role of fluids and seamount subduction in interplate coupling and the mechanism of the 2021 Mw 7.1 Fukushima-Oki earthquake, Japan. *Earth Planet. Sci. Lett.* 584, 117439. doi:10.1016/j.epsl.2022.117439

Wang, Z., and Zhao, D. (2005). Seismic imaging of the entire arc of Tohoku and Hokkaido in Japan using P-wave, S-wave and sP depth-phase data. *Phys. Earth Planet. Inter.* 152, 144–162. doi:10.1016/j.pepi.2005.06.010

Wang, J., and Zhao, D. (2008). P-wave anisotropic tomography beneath Northeast Japan. *Phys. Earth Planet. Inter.* 170, 115–133. doi:10.1016/j.pepi.2008.07.042

Wang, J., and Zhao, D. (2009). P-wave anisotropic tomography of the crust and upper mantle under Hokkaido, Japan. *Tectonophysics* 469, 137–149. doi:10.1016/j.tecto.2009.02.005

Wang, J., and Zhao, D. (2010). Mapping P-wave anisotropy of the Honshu arc from Japan Trench to the back-arc. *J. Asian Earth Sci.* 39, 396–407. doi:10.1016/j.jseaes.2010.04.009

Wang, J., and Zhao, D. (2012). P wave anisotropic tomography of the Nankai subduction zone in Southwest Japan. *Geochem. Geophys. Geosyst.* 13, Q05017. doi:10.1029/2012GC004081

Wang, Z., and Zhao, D. (2019). Updated attenuation tomography of Japan subduction zone. *Geophys. J. Int.* 219, 1679–1697. doi:10.1093/gji/ggz339

Wang, Z., Huang, W., Zhao, D., and Pei, S. (2012). Mapping the tohoku forearc: Implications for the mechanism of the 2011 East Japan earthquake (mw 9.0). *Tectonophysics* 524–525, 147–154. doi:10.1016/j.tecto.2011.12.032

Wang, C., Wu, J., and Yang, T. (2018). Crustal structure beneath the Taiyuan Basin and adjacent areas revealed by double-difference tomography. *Chin. J. Geophys Chin.* 61, 963–974. doi:10.6038/cjg2018L0114

Wang, Z., Fukao, Y., Miyakawa, A., Hasegawa, A., and Takei, Y. (2019). Crustal extension and graben formation by fault slip-Associated pore Opening, kyushu, Japan. *J. Geophys. Res. Solid Earth* 124, 4879–4894. doi:10.1029/2018JB016649

Wang, X., Chen, Q.-F., Niu, F., Wei, S., Ning, J., Li, J., et al. (2020). Distinct slab interfaces imaged within the mantle transition zone. *Nat. Geosci.* 13, 822–827. doi:10.1038/s41561-020-00653-5

Wang, Z., Jin, Z., and Lin, J. (2022). Slab melting and arc magmatism behind the Japan Trench: Evidence from seismic and thermal structure imaging. *Tectonophysics* 833, 229340. doi:10.1016/j.tecto.2022.229340

Wei, W., Xu, J., Zhao, D., and Shi, Y. (2012). East Asia mantle tomography: New insight into plate subduction and intraplate volcanism. *J. Asian Earth Sci.* 60, 88–103. doi:10.1016/j.jseaes.2012.08.001

Wessel, P., Luis, J. F., Uieda, L., Scharroo, R., Wobbe, F., Smith, W. H. F., et al. (2019). The generic mapping tools version 6. *Geochem. Geophys. Geosyst.* 20, 5556–5564. doi:10.1029/2019GC008515

Xin, H., Zhang, H., Kang, M., He, R., Gao, L., and Gao, J. (2019). High-resolution lithospheric velocity structure of continental China by double-difference seismic travel-time tomography. *Seismol. Res. Lett.* 90, 229–241. doi:10.1785/0220180209

Yamano, M., Uyeda, S., Foucher, J.-P., and Sibuet, J.-C. (1989). Heat flow anomaly in the middle Okinawa Trough. *Tectonophysics* 159, 307–318. doi:10.1016/0040-1951(89)90136-4

Yang, F., Kim, S. W., Tsunogae, T., and Zhou, H. (2021). Multiple enrichment of subcontinental lithospheric mantle with Archean to Mesozoic components: Evidence from the Chicheng ultramafic complex, North China Craton. *Gondwana Res.* 94, 201–221. doi:10.1016/j.gr.2021.03.005

Zhang, H., and Thurber, C. (2006). Development and Applications of double-difference seismic tomography. *Pure Appl. Geophys.* 163, 373–403. doi:10.1007/s00024-005-0021-y

Zhang, H., Thurber, C. H., Shelly, D., Ide, S., Beroza, G. C., and Hasegawa, A. (2004). High-resolution subducting-slab structure beneath northern Honshu, Japan, revealed by double-difference tomography. *Geology* 32, 361. doi:10.1130/G20261.2

Zhang, H., Wang, F., Myhill, R., and Guo, H. (2019). Slab morphology and deformation beneath Izu-Bonin. *Nat. Commun.* 10, 1310. doi:10.1038/s41467-019-09279-7

Zhang, G., He, Y., Ai, Y., Jiang, M., Mon, C. T., Hou, G., et al. (2021). Indian continental lithosphere and related volcanism beneath Myanmar: Constraints from local earthquake tomography. *Earth Planet. Sci. Lett.* 567, 116987. doi:10.1016/j.epsl.2021.116987

Zhang, H. (2003). Double-difference tomography: The method and its Application to the Hayward Fault, California. *Bull. Seismol. Soc. Am.* 93, 1875–1889. doi:10.1785/0120020190

Zhao, D., Hasegawa, A., and Horiuchi, S. (1992). Tomographic imaging of *P* and *S* wave velocity structure beneath northeastern Japan. *J. Geophys. Res.* 97, 19909. doi:10.1029/92JB00603

Zhao, D., Hasegawa, A., and Kanamori, H. (1994). Deep structure of Japan subduction zone as derived from local, regional, and teleseismic events. *J. Geophys. Res.* 99, 22313–22329. doi:10.1029/94JB01149

Zhao, D., Mishra, O. P., and Sanda, R. (2002). Influence of fluids and magma on earthquakes: seismological evidence. *Phys. Earth Planet. Inter.* 132, 249–267. doi:10.1016/S0031-9201(02)00082-1

Zhao, D., Wang, Z., Umino, N., and Hasegawa, A. (2007). Tomographic imaging outside a seismic Network: Application to the Northeast Japan Arc. *Bull. Seismol. Soc. Am.* 97, 1121–1132. doi:10.1785/0120050256

Zhao, D., Wang, Z., Umino, N., and Hasegawa, A. (2009). Mapping the mantle wedge and interplate thrust zone of the northeast Japan arc. *Tectonophysics* 467, 89–106. doi:10.1016/j.tecto.2008.12.017

Zhao, D., Yanada, T., Hasegawa, A., Umino, N., and Wei, W. (2012). Imaging the subducting slabs and mantle upwelling under the Japan Islands: Subducting slabs and mantle upwelling. *Geophys. J. Int.* 190, 816–828. doi:10.1111/j.1365-246X.2012.05550.x

Zhao, D., Yamamoto, Y., and Yanada, T. (2013). Global mantle heterogeneity and its influence on teleseismic regional tomography. *Gondwana Res.* 23, 595–616. doi:10.1016/j.gr.2012.08.004

Zhao, D., Kitagawa, H., and Toyokuni, G. (2015). A water wall in the Tohoku forearc causing large crustal earthquakes. *Geophys. J. Int.* 200, 149–172. doi:10.1093/gji/ggu381

Zhao, D. (2004). Global tomographic images of mantle plumes and subducting slabs: insight into deep earth dynamics. *Phys. Earth Planet. Inter.* 146, 3–34. doi:10.1016/j.pepi.2003.07.032

Zhao, D. (2017). Big mantle wedge, anisotropy, slabs and earthquakes beneath the Japan Sea. *Phys. Earth Planet. Inter.* 270, 9–28. doi:10.1016/j.pepi.2017.06.009

Zhao, D. (2021). Seismic imaging of Northwest Pacific and East Asia: New insight into volcanism, seismogenesis and geodynamics. *Earth. Sci. Rev.* 214, 103507. doi:10.1016/j.earscirev.2021.103507

frontiers | Frontiers in Earth Science

TYPE Original Research
PUBLISHED 12 January 2023
DOI 10.3389/feart.2022.966085

Check for updates

OPEN ACCESS

EDITED BY
Gilby Jepson,
University of Arizona, United States

REVIEWED BY
Giovanna Rizzo,
Università degli Studi della Basilicata, Italy
Eirini Poulaki,
University of Texas at Austin, United States

*CORRESPONDENCE
Limei Tang,
tanglm@sio.org.cn

SPECIALTY SECTION
This article was submitted to Geochemistry, a section of the journal Frontiers in Earth Science

RECEIVED 10 June 2022
ACCEPTED 31 October 2022
PUBLISHED 12 January 2023

CITATION
Gao P, Tang L and Chen L (2023), Geochemistry and zircon U–Pb ages of early Ordovician syenites from the Inexpressible Island, Antarctica and tectonic implications.
Front. Earth Sci. 10:966085.
doi: 10.3389/feart.2022.966085

COPYRIGHT
© 2023 Gao, Tang and Chen. This is an open-access article distributed under the terms of the Creative Commons Attribution License (CC BY). The use, distribution or reproduction in other forums is permitted, provided the original author(s) and the copyright owner(s) are credited and that the original publication in this journal is cited, in accordance with accepted academic practice. No use, distribution or reproduction is permitted which does not comply with these terms.

Geochemistry and zircon U–Pb ages of early Ordovician syenites from the Inexpressible Island, Antarctica and tectonic implications

Peng Gao[1,2], Limei Tang[1,2]* and Ling Chen[1,2]

[1]Key Laboratory of Submarine Geosciences, Ministry of Natural Resources, Hangzhou, China, [2]Second Institute of Oceanography, Ministry of Natural Resources, Hangzhou, China

The Ross Orogenic Belt is in the Antarctica Transantarctic Mountains. North Victoria Land Granite Harbour Intrusive complex (GHI) records the tectonic-magmatism evolution of Ross orogeny. Extensively developed post-collisional granites around this margin of early Paleozoic magmatism can provide insights into the growth of continental crust through accretionary orogenesis. We provide geochemical and geochronological data from syenites from Terra Nova Bay, north Victoria Land in order to constrain its tectonic evolution and setting. The syenite belongs to the potassium-alkaline, calc-alkaline series and is characterized by high concentrations of rare Earth elements and large ion lithophile elements (LILE), and low content in high field strength elements (Nb, Ta, P, Ti). The petrographic and geochemical signatures show a possible island-arc granite affinity. LA-ICP-MS zircon U-Pb dating results suggest that the Inexpressible Island syenite was emplaced at ca. 471.8 ± 1.8 Ma and 477.3 ± 1.7 Ma, respectively. Zircon $\varepsilon_{Hf}(t)$ values range from −7.4 to −9.1; average −8.2 and whole-rock ε_{Nd} (t) values range from −8.5 to −10.3, indicating that formed by the partial melting of the lithospheric mantle enriched with subduction slab fluids and subcontinental lithosphere. Whereas, the syenite has a strong positive Eu anomaly and a positive Sr anomaly, suggesting that plagioclase cumulate crystallization occurred in the magma source area. Furthermore, through integration with previous studies, we suggest that syenite is a result of the melting zone of an older previously subduction enriched layer of the subcontinental lithospheric mantle (SCLM). To enable syenite emplacement we suggest a tectonic-magmatic model that invokes alternating phases of extension and contraction in the overriding plate. Finally, we report the youngest age of (post-orogenic) magmatism occurred during extension in the overriding plate ca. 478–471 Ma.

KEYWORDS

U-Pb geochronology, geochemistry, Rose orogeny, syenite, Inexpressible island

Introduction

Accretionary orogenesis is characterized by repeated cycles of subduction–accretion at interoceanic and continental convergent plate margins (Di Vincenzo and Rocchi, 1999; Condie, 2007; Li et al., 2016). The composition of accretionary orogenic belt complexes includes trench-arc-basin systems, seamounts, oceanic crust, and other relic geological records. It is also important for plate (especially micro-continental blocks) collision, assembly, and growth (Li et al., 2016) Repeated subduction–accretion cycles of rock units from continental and oceanic magmatic arcs, supra-subduction zone backarcs, and forearcs loaded with continent-derived materials form magmatic arcs. These magmatic igneous rocks record key information about the evolution of the subduction regimes of orogenic belts, such as subduction-dominating slab rollback and backarc opening, with mantle modifications occurring throughout. The origin of arc magmas involves multiple stages (Cawood et al., 2009; Rocchi et al., 2015), components, and processes, including, 1) the nature of the mantle source, 2) the activity and type of subduction components, and 3) the degree and depth of partial melting (Di Vincenzo and Rocchi, 1999; Rocchi et al., 2015). This variety of materials and processes makes orogenic igneous complexes a rich source of information. The identification of magmatic arcs in ancient accretionary orogens is thus important for understanding the structure and history of orogen genesis.

The Ross Orogen exposed in Victoria Land, Antarctica, is located at the Southern Ocean termination of the Transantarctic Mountains. It represents the along-strike continuation of the southeastern Australia margin prior to the Cretaceous breakup of Gondwana (Cawood, 2005; Cawood and Buchan, 2007; Paulsen et al., 2007; Elliot and Fanning, 2008; Vaughan and Pankhurst, 2008; Goodge, 2020). The Ross Orogen formed in the early Paleozoic within the framework of the convergence of the Paleo-Pacific oceanic plate and the Gondwana continental margin (Goodge, 2020). The Late Proterozoic to Early Paleozoic was characterized by widespread igneous activity in response to convergence along the Cambro-Ordovician margin of Gondwana (Cawood, 2005). In northern Victoria Land, Antarctica, large amounts of felsic to mafic plutonic rocks, known as the Granite Harbour Intrusive complex (GHI) (Gunn and Warren, 1962), were emplaced during the Cambro-Ordovician Ross Orogeny. In the coastal area of Terra Nova Bay, where Inexpressible Island is located, it is referred to as the Terra Nova Intrusive Complex (TeNIC) (Di Vincenzo and Rocchi, 1999), shows variable geochemical characteristics, suggesting the involvement of various distinct source rocks during the melting process (Di Vincenzo and Rocchi, 1999; Rocchi et al., 2015).

In the northern Victoria Land area, most of magma intrusive activity spanned ca. 545–485 Ma (Black and Sheraton, 1990; Tonarini and Rocchi, 1994; Rocchi et al., 1998; Fioretti et al., 2005; Tiepolo and Tribuzio, 2008; Hagen-Peter et al., 2015). Similar series of intrusion rocks in Australia which have the oldest age up to 514 Ma (Weis et al., 2006). In the central Transantarctic Mountains, calc-alkaline magmatism may have initiated as early as 590 Ma, and persisted for over 100 Ma (Goodge et al., 2012). As most of Antarctica is covered by ice and snow, it is difficult to know the age of the oldest magmatism. The age and geochemical patterns of intrusive rocks suggest oblique convergence along a tectonically segmented margin (Encarnación and Grunow, 1996; Rocchi et al., 1998; Goodge, 2002; Stump et al., 2003; Goodge et al., 2004; Goodge et al., 2012). The most recent magmatic processes formed the Vegetation Unit (~475 Ma), Abbott Unit (508 Ma), Irizar granite complex (~490 Ma) which have different source regions and intrusion depths but possess nearly identical rock compositions including granite, syenite, and lamprophyre (Borg et al., 1986; Borsi et al., 1995; Perugini et al., 2005; Chen et al., 2019). Research suggests that the Abbott Unit and Irizar complex was derived from partially melted mantle wedge above the subduction zone mixing with the continental lithospheric mantle, whereas the Vegetation Unit Lamprophyre was derived from partially melted ancient sub-continental lithospheric mantle mixing with crustal material under thinning lithosphere within the orogen (Di Vincenzo and Rocchi, 1999).

In this study, we conducted Sr-Nd isotope on two samples (N=2), major and trace element analysis of the whole rock (N=7), and zircon U-Pb dating as well as Hf isotopes ratios on two samples (N=2, n=40), from the early Ordovician syenite in the Inexpressible Island, northern Victoria Land, to further determine the nature, geochemical characteristics and petrogenesis of magmatism in the extensional environment of the late Ross orogeny.

Geological setting and sample characteristics

Convergence between the Antarctic part of Gondwana and the Paleo-Pacific oceanic lithosphere during the early Paleozoic (Dalziel, 1992) formed the Ross orogenic belt, which deformed and metamorphosed sedimentary rocks and granitic (sensu lato) plutons exposed along the Transantarctic Mountains (Borg and Depaolo, 1994; Stump, 1995) (Figure 1). The Proterozoic history and plate tectonic reconstruction of cratonic Antarctica as part of the Rodinia supercontinent are still a matter of debate (Moores, 1991; Dalziel, 1997; Fitzsimons, 2003; Pisarevsky et al., 2003). Northern Victoria Land lies at the Pacific termination of the Transantarctic Mountains. It is comprised of three different crustal blocks (Bradshaw and Laird, 1983) (Figure 1): 1) the Robertson Bay Terrane, with a Cambrian to early Ordovician thick flysch-type sequence (Kleinschmidt and Tessensohn, 1987; Stump, 1995; Rocchi et al., 1998; Bomparola et al., 2007); 2) the Bowers Terrane, a Cambrian complex of volcanic rocks and

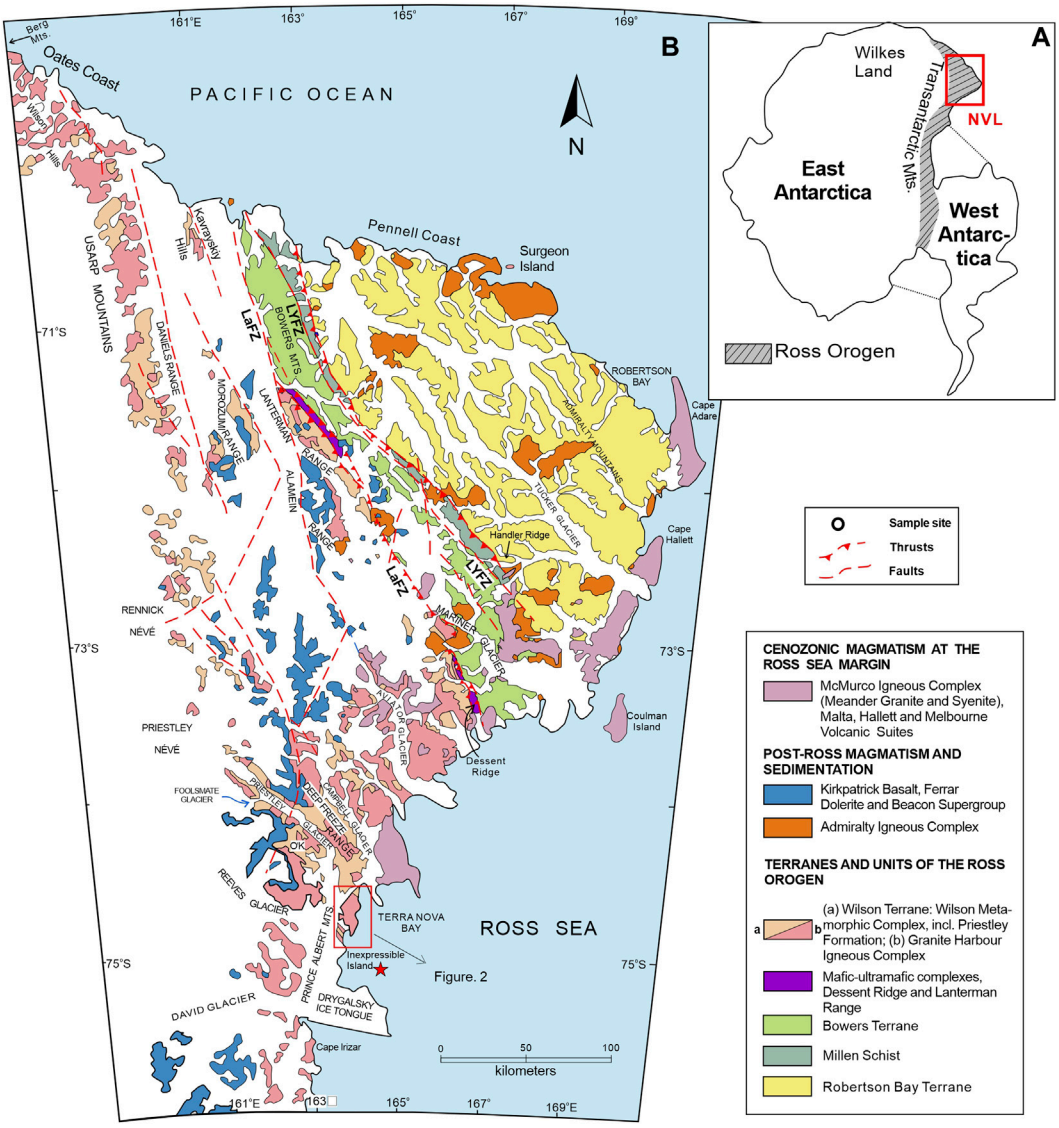


FIGURE 1
(A) The insert shows the location of the Ross Orogen and NVL (Boger, 2011; Rossetti et al., 2011; Fergusson et al., 2007). **(B)** Geological and tectonic sketch map of northern Victoria Land (NVL), Antarctica (modified after Estrada et al., 2016; Läufer et al., 2011; Di Vincenzo and Rocchi, 1999). LaFZ; Lanterman Fault Zone, LYFZ; Leap Year Fault Zone, O'K; O'Kane Canyon.

related sediments (Weaver et al., 1984; Crispini et al., 2007); and 3) the Wilson Terrane (Stump et al., 1983; Rossetti et al., 2006b; Di Vincenzo et al., 2014), a metasedimentary sequence including remnants of a polymetamorphic granulite complex (Castelli et al., 1991; Talarico and Castelli, 1995; Talarico et al., 1995) that experienced low-pressure low-to high-grade metamorphism during the Cambrian-Ordovician Ross Orogeny (Grew and Sandiford, 1984; Palmeri et al., 1994; Palmeri, 1997). An extensive association of mantle-derived calc-alkaline magmas and crustal melts that intruded the Wilson Terrane during the Ross Orogeny are collectively named the GHI (Gunn and Warren, 1962; Borg et al., 1987; Ghezzo et al., 1987; Kleinschmidt and Tessensohn, 1987; Vetter and Tessensohn, 1987; Armienti et al., 1990; Biagini et al., 1990; Stump, 1995; Di Vincenzo and Rocchi, 1999; Rocchi et al., 2004). Recent work (Fedrico et al., 2006; Bracciali et al., 2009; Rocchi et al., 2015, 2011) lead some models of tectonic evolution of the Ross Orogeny in the North Victoria Land (Rocchi et al., 2009; Rocchi et al., 2015). Studies show that the convergent margin of Gondwana land consists of a main continuous subduction zone coupled with local plate and transient subduction zones. These transient subduction zones are related to the continuous ribbons of outboard pieces of stretched forearc regions (Rocchi et al., 2011). The Ross Orogeny in Victoria Land was the result of

TABLE 1 Summary of syenites analyses project and mineral assemblage.

Sample name	Rock description		Location		Sr and Nd isotope ratio analysis	Photomicrographs	Bulk major and trace element analysis	Zircon cathodoluminescence (CL) images	U-Pb dating of zircon	In suit Hf isotope analysis	Mineral assemblage
			Lat (oS)	Long (oE)							
DJS-1	medium-to-coarse-grained with a granitic texture	Gray Bt syenite	−74.9194	163.6975	√	√	—	—	—	—	Q (25%) + Pl (25%) + Mc (20%) + *P*th (10%) + Bt (15%)
DJS-5a		Gray Bt syenite	−74.9194	163.6975	√	√	—	—	—	—	Q (35%) + Pl (15%) + Mc (25%) + *P*th (10%) + Bt (12%)
DJS-6		Gray syenite	−74.9194	163.6975	√	√	√	√	√	√	Q (35%) + Pl (12%) + Mc (25%) + *P*th (15%) + Bt (8%)
DJS-7		Gray Bt syenite	−74.9194	163.6975	√	√	—	—	—	—	Q (35%) + Pl (25%) + Mc (10%) + *P*th (10%) + Bt (15%)
DJS-13		Gray Hbl syenite	−74.9201	163.6943	√	√	√	√	√	√	Q (30%) + Pl (13%) + Mc (13%) + *P*th (25%) + Hbl (6%) + Bt (7%)
DJS-14		Gray Hbl syenite	−74.9201	163.6943	√	√	—	—	—	—	Q (30%) + Pl (17%) + Mc (13%) + *P*th (25%) + Hbl (6%) + Bt (7%)
DJS-15		Gray Hbl syenite	−74.9201	163.6943	√	√	—	—	—	—	Q (30%) + Pl (32%) + Mc (13%) + *P*th (12%) + Hbl (5%) + Bt (3%)

Note: Bt: biotite, Kfs: K-feldspar, Pl: plagioclase, Q: quartz; Mc: Microcline, *P*th: Perthite; Abbreviations of minerals based on Kretz (1983). Items that have been analyzed are indicated by "√", otherwise by "-"

10.3389/feart.2022.966085

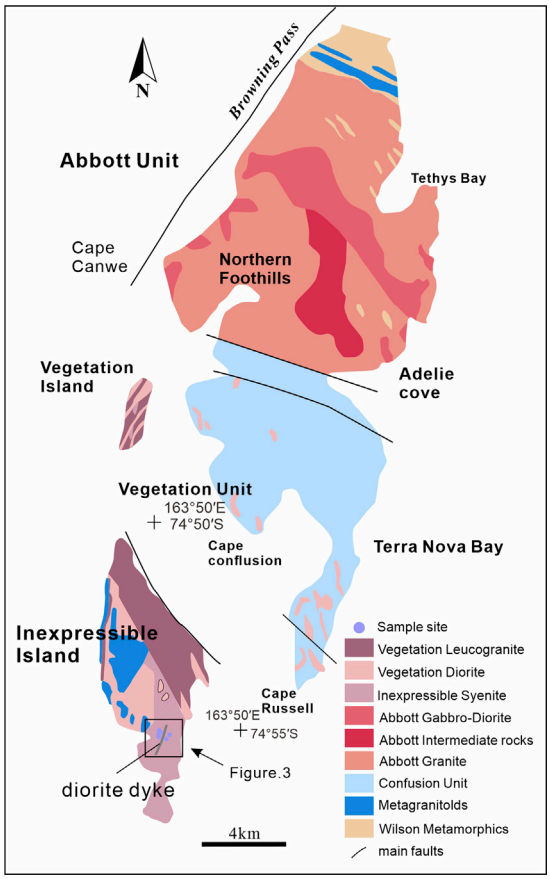


FIGURE 2
Geological and tectonic setting of the Inexpressible Island area showing the sample sites (Chen et al., 2019).

many stages of advancing and retreating subduction zone(s) (Rocchi et al., 2015, 2011). Thus, as an important part of the boundary between the Wilson arc and the forearc ribbon underwent subduction accretion and detachment, there is an abundance of magmatism in the North Victoria Land.

Syenite in the Inexpressible Island, Northern Victoria Land, is a confused and different part of the TeNIC unit, which is important to determining the nature, geochemical characteristics, and petrogenesis of magmatism in the extensional environment of the late Ross orogeny. We analyzed seven syenite samples (DJS-1, DJS-5a, DJS-6, DJS-7, DJS-13, DJS-14, and DJS-15) (see summary in Table 1) from the Inexpressible Island Dingjunshan area (Figure 2). A~ 5 m wide mafic dyke occurs with an approximately N-S trend and extends over 300 m across the syenite bedrock outcrop area (Figure 3A) (Chen et al., 2019). The syenite outcrops are composed of medium-to coarse-grained with gray-white color (Figures 3A–C), and samples were fresh and unweathered. The rock is mesocrystalline granitic structure and massive structure with a mineral assemblage of quartz 30%–35%, plagioclase 17%–25%, micro-plagioclase 10%–25%, Perthite 10%–25% and biotite 12%–15% (Figures 4D–I), and feldspars have experienced sericitization (Figure 4H). Some of syenite contain hornblende, which are associated with biotite, showing light green-brown green polychromatism (Figure 4H). The secondary mineral facies are mainly sericite and chlorite (Figure 4H), magnetite, zircon and apatite. Quartz ranges from euhedral and subhedral, sometimes can see anhedral crystal, and it can be seen that quartz and feldspar intergrow to form graphic texture (Figure 4H). The rock is a quartz syenite with a homogeneous isotropic texture (Figures 4D–I). A total of 7 samples are used in the study area.

Analytical methods

Zircon cathodoluminescence images

The internal structure of zircon can be revealed by the cathodoluminescence (CL) imaging technique. CL image can reflect the difference in the abundances of some trace elements (such as U, Y, Dy, and Tb) (Wu and Zheng, 2004), which can be influenced by temperatures at which the melts crystallized (Rubatto and Gebauer, 2000; Wu and Zheng, 2004; Rubatto and Gubauer, 2007), also the change of structural parameters such as crystallinity or the presence of defect centres can be reflected in CL image (Nasdala et al., 2002). The CL image can be used as a reference for tracing zircon origin. We have carried out CL photography on 40 zircon grains collected from two samples of DJS-6, DJS-13. Zircon CL images using an Analytical Scanning Electron Microscope (JSM-IT300) connected to a Delmic sparc system. The imaging condition was 0.5–30 kV voltage of electric field and 72 μA current of the tungsten filament.

U-Pb dating of zircon by LA-ICP-MS

40 zircon grains were collected using conventional density and magnetic separation techniques and picked out under a binocular microscope from two samples of DJS-6 and DJS-13, which finally have been used to do U-Pb dating. The grains were subsequently mounted in epoxy resin, polished to half their thickness and they were later photographed in transmitted and reflected light. We selected the location of the oscillatory-zoned rim or the location of the uniform color of cathode luminescence. And we avoided choosing cracks or inclusions area in the transmission-reflected image of zircon grains, the specified analysis spots are shown (Figure 5). U–Pb dating of zircon grains by LA-ICP-MS at the Wuhan SampleSolution Analytical Technology Co., Ltd., Wuhan, China. Detailed operating conditions for the laser ablation system and the ICP-MS instrument and data reduction are the same as described by Zong et al. (2017). Laser sampling was performed using a GeolasPro laser ablation system that consists of a COMPexPro 102 ArF excimer laser (wavelength of 193 nm and maximum energy



FIGURE 3
Representative outcrops and photomicrographs of granites from Inexpressible Island, NVL. **(A)** The field contact relationship between diorite and syenite is shown in the figure, which shows diorite dyke. **(B)** Massive syenite occurs in the field. **(C)** Syenite bedrock in the eastern bay region.

of 200 mJ) and a MicroLas optical system. An Agilent 7900 ICP-MS instrument was used to acquire ion-signal intensities. Helium was applied as a carrier gas. Argon was used as the make-up gas and mixed with the carrier gas *via* a T-connector before entering the ICP. A "wire" signal smoothing device is included in this laser ablation system (Hu et al., 2015). The laser beam spot and frequency of the GeolasPro for this analysis were 32 μm and 5 Hz, respectively. Zircon isotope ratios were calibrated by standard sample Plešovice 338.15 ± 1.7 Ma (Sláma et al., 2008), and isotope ratio monitoring standard sample GJ-1,599.0 ± 1.7 Ma (Jackson et al., 2004). All time-resolved analysis data consisted of approximately 20–30 s of blank signal and 50 s of sample signal. Offline processing of the analytical data (including the selection of sample and blank signals, instrument sensitivity drift correction, and U-Pb isotope ratio and age calculation) was undertaken using the software ICPMSDataCal (Liu et al., 2008, 2010). U-Pb age harmonic mapping and age-weighted average calculations of zircon samples were carried out using Isoplot/Ex_ver3 (Ludwig, 2003).

Whole rock major element analysis

We have analyzed the content of major elements in seven syenite samples (DJS-1, DJS-5a, DJS-6, DJS-7, DJS-13, DJS-14, DJS-15) from the Inexpressible Island. Major element analyses of whole rock were conducted on XRF (Primus II, Rigaku, Japan) at the Wuhan Sample solution Analytical Technology Co., Ltd., Wuhan, China. The detailed sample-digesting procedure was as follows: 1) Sample powder (200 mesh) was placed in an oven at 105°C for drying of 12 h; 2) ~1.0gdried sample was accurately weighted and placed in the ceramic crucible and then heated in a muffle furnace at 1000°C for 2 h. After cooling to 400 °C, this sample was placed in the drying vessel and weighed again in order to calculate the loss on ignition (LOI). 3) 0.6 g sample powder was mixed with 6.0 g cosolvent ($Li_2B_4O_7$: $LiBO_2$: LiF = 9: 2:1) and 0.3 g oxidant (NH_4NO_3) in a Pt crucible, which was placed in the furnace at 1,150°C for 14 min. Then, this melting sample was quenched with air for 1 min to produce flat discs on the fire brick for the XRF analyses.

Whole rock trace element analysis

We have analyzed the content of trace and rare Earth elements in seven syenite samples (DJS-1, DJS-5a, DJS-6, DJS-7, DJS-13, DJS-14, DJS-15) from the Inexpressible Island. Whole-rock trace and rare Earth elements were analyzed by ICP-MS (Agilent 7700e). The detailed sample-digesting procedure was as

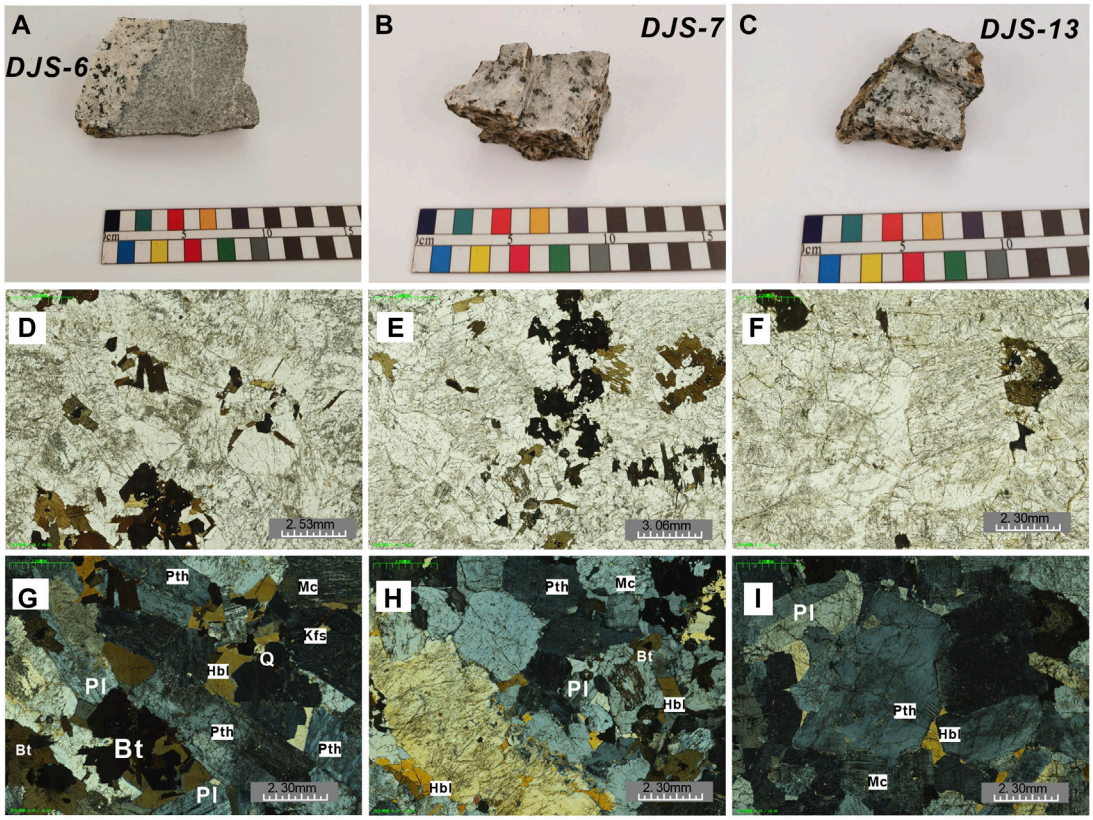


FIGURE 4
Representative photomicrographs of Early Ordovician syenite from Inexpressible Island. **(A)**, **(B)** and **(C)** Photographs of the syenite. **(D)**–**(I)** polarizing microscope and Cross polarized light photomicrograph. Bt: biotite, Kfs: K-feldspar, Pl: plagioclase, Q: quartz; Mc: Microcline, Pth: Perthite.

follows: 1) Sample powder (200 mesh) was placed in an oven at 105°C for drying of 12 h; 2) 50 mg sample powder was accurately weighed and placed in a Teflon bomb; 3) 1 ml HNO_3 and 1 ml HF were slowly added into the Teflon bomb; 4) Teflon bomb was put in a stainless-steel pressure jacket and heated to 190°C in an oven for >24 h; 5) After cooling, the Teflon bomb was opened and placed on a hotplate at 140°C and evaporated to incipient dryness, and then 1 ml HNO_3 was added and evaporated to dryness again; 6) 1 ml of HNO_3, 1 ml of MQ water and 1 ml internal standard solution of 1ppm In were added, and the Teflon bomb was resealed and placed in the oven at 190°C for >12 h; 7) The final solution was transferred to a polyethylene bottle and diluted to 100 g by the addition of 2% HNO_3.

Zircon *in situ* Hf isotope analysis of zircon by LA-MC-ICP-MS

We choose to conduct Hf analysis in a place where the surface is relatively uniform or close to the U-Pb analysis spots, in order to obtain fairly accurate Hf isotope ratios, these analytical spots are as shown (Figure 5). 40 zircon grains collected from two samples of DJS-6 and DJS-13 have been used to do *in situ* Hf dating. Experiments using *in situ* Hf isotope ratio analysis were conducted using MC-ICP-MS in combination with an excimer ArF laser ablation system hosted at Wuhan Sample Solution Analytical Technology Co., Ltd. All data were acquired on zircon in single spot ablation mode at a spot size of 44 μm. The energy density of the laser ablation used in this study was ~8.0 J cm^{-2}. Each measurement consisted of 20 s of acquisition of the background signal followed by 50 s of ablation signal acquisition. The operating conditions for the laser ablation system and the MC-ICP-MS instrument and analytical method were the same as described (Hu et al., 2012). To ensure the reliability of the analysis data, three international zircon standards of 91500 $^{176}Hf/^{177}Hf$= 0.282308, (Zhang and Hu, 2020), and GJ-1 $^{176}Hf/^{177}Hf$= 0.282013, (Zhang and Hu, 2020), were analyzed simultaneously with the samples. GJ-1 was used as the second standards to monitor the quality of the data correction. The external precision (2SD) of 91,500 and GJ-



FIGURE 5
Representative cathodoluminescence images of zircons from the dated samples from Inexpressible Island showing U-Pb ages and the location of the analyzed Hf.

1 was better than 0.000020. The Hf isotopic compositions of 91,500 and GJ-1 have been reported (Zhang and Hu, 2020).

Sr and Nd isotope ratio analysis by LA-ICP-MS

We analyzed the content of Sr and Nd isotope ratios in two syenite samples (DJS-6, DJS-13) from the Inexpressible Island. Sr and Nd isotope analyses were performed on an MC-ICP-MS at the Wuhan Sample Solution Analytical Technology Co. Analyses of the NBS 987standard solution yielded $^{87}Sr/^{86}Sr$ratio of 0.710244 ± 22 (2SD, n=32, Thirlwall M. F, 1991), which is identical within error to their published values (0.710241 ± 12, Thirlwall, 1991). All data reduction for the MC-ICP-MS analysis of the Sr isotope ratios was conducted using Iso-Compass software (Zhang et al., 2020). The USGS reference materials BCR-2 (basalt) and RGM-2 (rhyolite)yielded results of 0.705034 ± 14 (2SD, n=4) and 0.704192 ± 10 (2SD, n=4) for $^{87}Sr/^{86}Sr$, respectively, which is identical within error to their published values (Li et al., 2012). In addition, One JNdi-1standard was measured for every ten samples analyzed in Nd isotopes analysis. Analyses of the JNdi-1standard yielded $^{143}Nd/^{144}Nd$ratio of 0.512118 ± 15 (2SD, n=31), which is identical within error to their published values (0.512115 ± 07, Tanaka et al., 2000).

Results

Zircon U-Pb geochronology

In this study, LA-ICP-MS zircon U-Pb dating analysis was performed on syenite samples DJS-6 and DJS-13 from the TeNIC. The results are shown in (Supplementary Table SA1) and Figure 6. All spots on the oscillatory-zoned rim domains of zircon grains from the samples tightly cluster or are close to the Concordia line, all data Concordia filter better than 95% in error ellipses. The integration time is set to 30–35s according to the

recommended value of the monitoring standard sample. We allow for an age error of better than 1% (See Supplementary Table SA1). Most zircons from the syenite samples of DJS-6 and DJS-13 were dominantly euhedral to subhedral. The CL images display reduced CL contrast between bands which are sometimes broad, also sometimes appear as sector zoning, were generally 100–180 μm and 80–100 μm in size, and had length/width ratios of 1:1–3:1 and 1:1–2:1, respectively (Figure 5). In total, 40 grains were analyzed from sample DJS-6 and DJS-13, yielded Th/U ratios of 0.58–0.78 and 0.46–0.83, respectively (Supplementary Table SA1). The concordia ages of DJS-6 is 471.8 ± 1.8 Ma (2σ, MSWD = 0.87, Probability = 0.35, *n*=20) (Figure 6A), giving a weighted mean $^{206}Pb/^{238}U$ age of 471.8 ± 3.5 Ma (2σ, MSWD = 0.87; *n*=20) (Figure 6B). The concordia ages of DJS-13 is 477.3 ±1.7 Ma (2σ, MSWD = 0.59, Probability = 0.44, *n*=20) (Figure 6C). $^{206}Pb/^{238}U$ age of 477.3 ± 3.4 Ma (2σ, MSWD = 0.59; *n*=20) (Figure 6D).

Whole rock geochemistry

The whole-rock geochemical compositions of the syenite unit are listed in (Supplementary Table SA2). The rocks yielded concentrations of 60.88–62.81 wt% SiO_2 with 10.02–11.72 wt% total alkalis. The K_2O/Na_2O ratios varied from 0.34 to 0.39 (Supplementary Table SA2). The Inexpressible Island high-potassium syenite shows different evolutionary paths (Figures 7A,B). All the samples are plotted in the shoshonite series field on the K_2O vs. SiO_2 diagram (Figure 7C). Our samples contain low MgO (0.36–0.53 wt%), TiO_2 (0.43–0.66 wt%), and P_2O_5 (0.11–0.18 wt%) contents with a relatively high Al_2O_3 (17.46–18.46 wt%), the $Al_2O_3/(CaO + Na_2O + K_2O)$ (A/CNK) in molar proportion values ranging from 0.94 to 1.08, indicating that metaluminous to peraluminous (Figure 7B). Chondrite-normalized rare Earth elements (REE) concentrations of the syenite are shown in (Figure 8A) (Sun and McDonough, 1989). The ΣREE

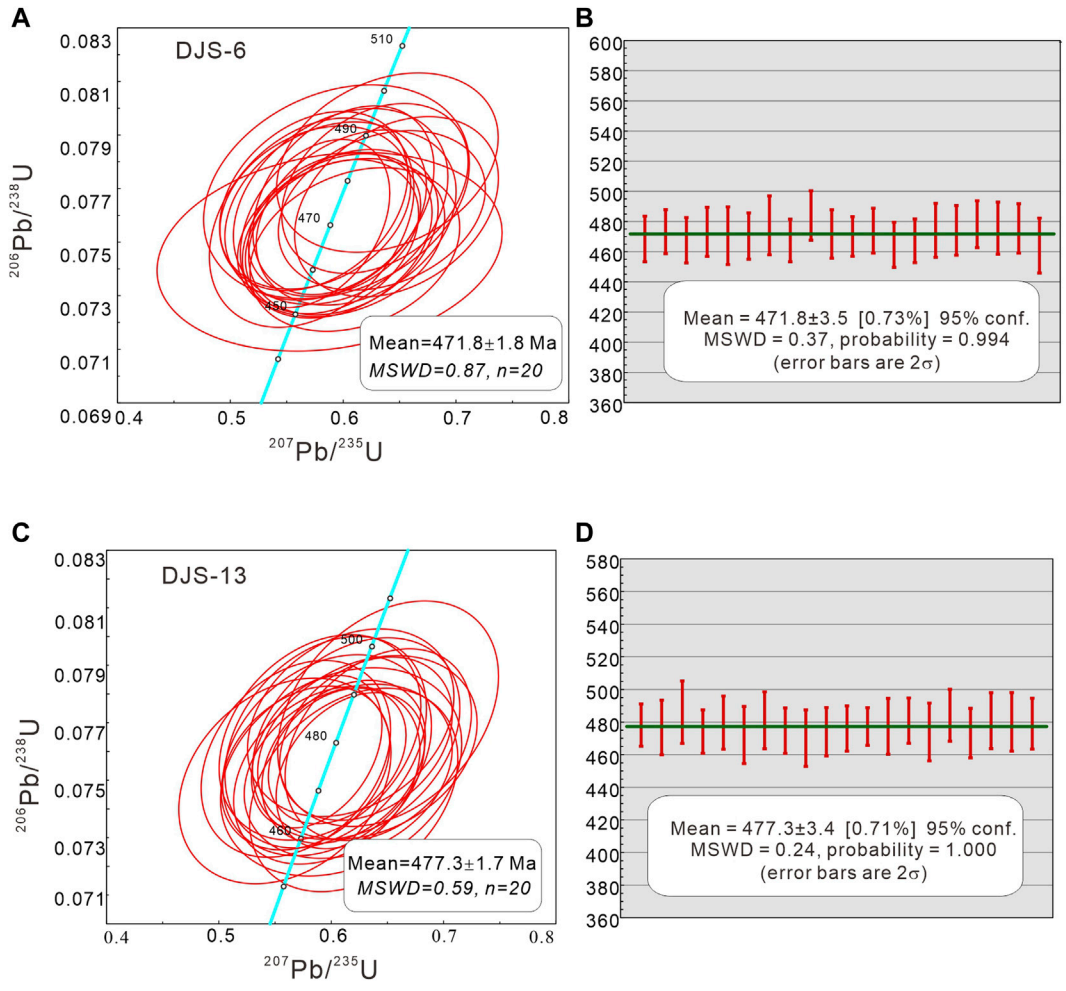


FIGURE 6
Zircon U–Pb concordia diagrams **(A,C)**, weighted mean $^{206}Pb/^{238}U$ ages **(B,D)** of the Inexpressible Island syenites, northern Victoria Land.

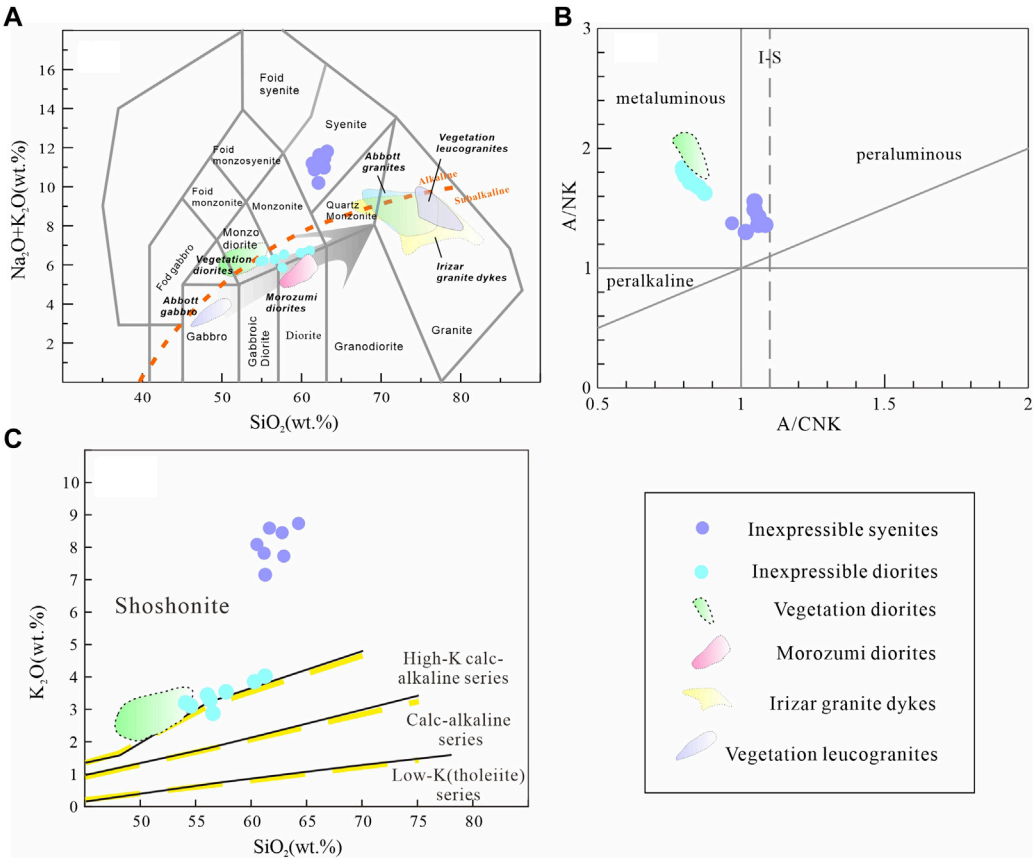


FIGURE 7
(A) Total alkali-silica diagram for the Inexpressible Island syenite (Middlemost, 1994), **(B)** A/NK vs. A/CNK modifications (Maniar and Piccoli, 1989). and **(C)** K_2O vs. SiO_2 diagram (Peccerillo and Taylor, 1976), Inexpressible Island syenite compared to the Inexpressible Island diorite dyke (Chen et al., 2019; Gao et al., 2022), Vegetation Island diorites (Rocchi et al., 2009) and Irizar dyke, and Morozumi diorite samples (Rocchi et al., 2015).

concentrations displayed negative trend than diorites, and strongly enriched Eu anomalies (0.89–5.58) (Supplementary Table SA3). On the primitive mantle-normalized multi element diagram, the syenite showed negative Th (1.60–5.78 ppm), P (4.82–8.31 ppm), and Ti (1.98–3.02 ppm) anomalies and positive Rb (134.8–269.4 ppm), Ba (3,368–5,003 ppm), Pb (14.31–34.89 ppm), K (241.0–289.2 ppm), and Zr (92.6–465.9 ppm) anomalies than the Inexpressible Island diorites (Figure 8B).

Whole-rock Sr-Nd isotopes

Whole-rock Sr-Nd isotope data for the Inexpressible medium- and coarse-grained syenites are listed in Supplementary Table SA4. Whole-rock $(^{87}Sr/^{86}Sr)_i$ and $\varepsilon_{Nd}(t)$ values were calculated as 471.8 Ma for DJS-6 and 477.3 Ma for DJS-13. The Inexpressible syenites had similar $\varepsilon_{Nd}(t)$ values, ranging from −8.5 to −10.3, and a high and narrow range of initial $^{87}Sr/^{86}Sr$ values, ranging from 0.7104 to 0.7128.

Zircon Lu-Hf isotopes

The zircons used for the U-Pb dating were used for the *in situ* or counterpoint zircon Hf isotope analyses (Supplementary Table SA5). The initial $^{176}Hf/^{177}Hf$ ratios for the zircons from the DJS-13 syenite with Early Ordovician ages ranged from 0.282228 to 0.282276. Their $\varepsilon_{Hf}(t)$ ranged from −7.4 to −9.1 (Figure 9). (Supplementary Table SA5). The $\varepsilon_{Hf}(t)$ values for the zircons from the DJS-6 syenite ranged from −7.4 to −9.0.

Discussion

Timing of the magmatism

Previous published chronological studies of the Terra Nova igneous body suggest the extensive Rose Orogeny magmatism, such as, calc-alkaline granites in the eastern Mountaineers Range

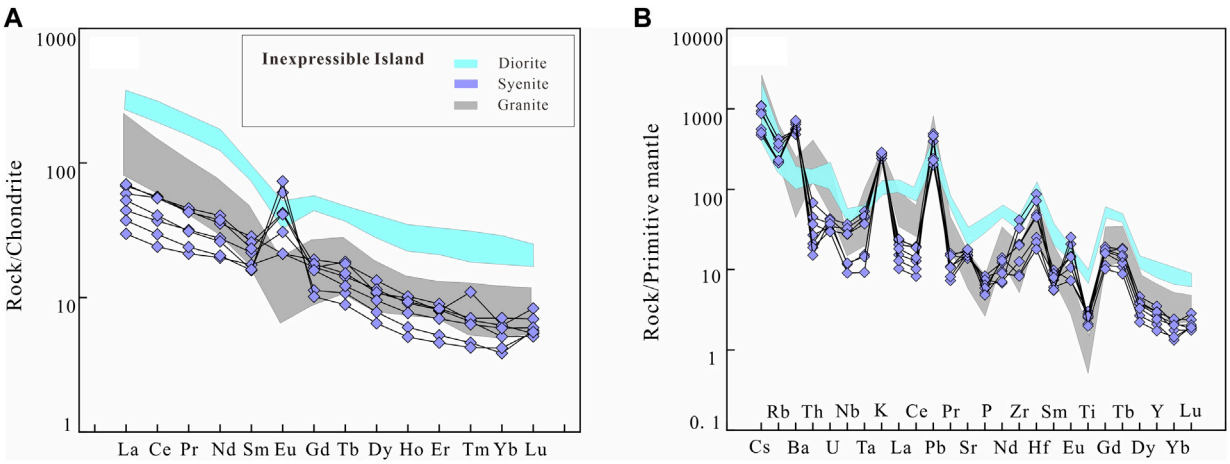


FIGURE 8
Primitive mantle-normalized plots of incompatible elements and chondrite-normalization plots (Sun and McDonough, 1989) of trace elements, trace element data from the diorite and granite are from Gao et al. (2022) and Chen et al. (2019), respectively.

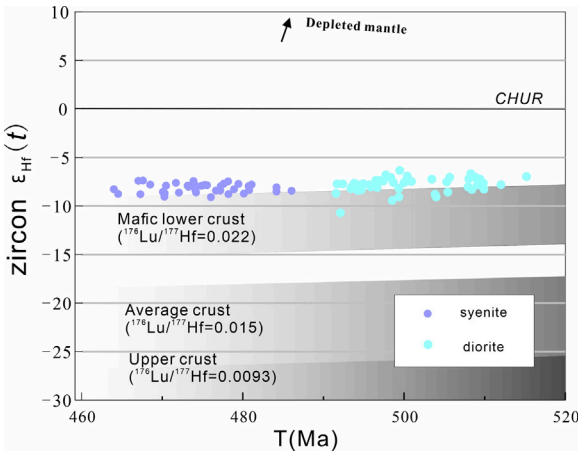


FIGURE 9
Zircon $\varepsilon_{Hf}(t)$ vs. T (Ma) plot of the Inexpressible Island syenite and diorite (Gao et al., 2022).

by Rb-Sr pseudo-isochron dating are 610 Ma ages (Bomparola et al., 2007); The granodiorite of the Wilson terrane zircon shows U-Pb ages of 496.7 ± 6.8 Ma (Rocchi et al., 2015); The U-Pb ages of quartz diorite and tonalite intrusions of the granitic mafic body in the Vegetation Island zircon are ranging from 521 Ma to 487 Ma (Rocchi et al., 2004); Zircon U-Pb age of tonalites from the Inexpressible Island is 482 ± 4.2 Ma (Wang et al., 2014). In this study, zircon U-Pb dating (Supplementary Table SA1) of the medium- and coarse-grain potassic syenite (DJS-6) and the medium-grain potassic syenite (DJS-13) from Inexpressible Island yielded crystallization ages of 471.8 ± 1.8 Ma and 477.3 ± 1.7 Ma, respectively, (Figures 6A,B). These results suggest that the syenites were emplaced in the early Ordovician. Based on the age variation of intrusions, an extensive and long-lasting multi-episode magmatism was active at the Wilson Terrane continental margin (Borg et al., 1986; Borsi et al., 1995; Perugini et al., 2005; Rocchi et al., 2004; Chen et al., 2019; Goodge, 2020; Gao et al., 2022). In addition, it shows slightly different core-mantle relationships in different zircon grains of the same massive syenite rock in CL images. Most grains have gray-dark cores and bright mantles, with high Th/U ratios (Supplementary Table SA1). And some zircon grains display reduced CL contrast between bands in CL images which are sometimes broad, and also sometimes appear as sector zoning, yielding Th/U ratios of 0.46–0.83, with average Th/U >0.5 (Figure 5 and Supplementary Table SA1). Generally,

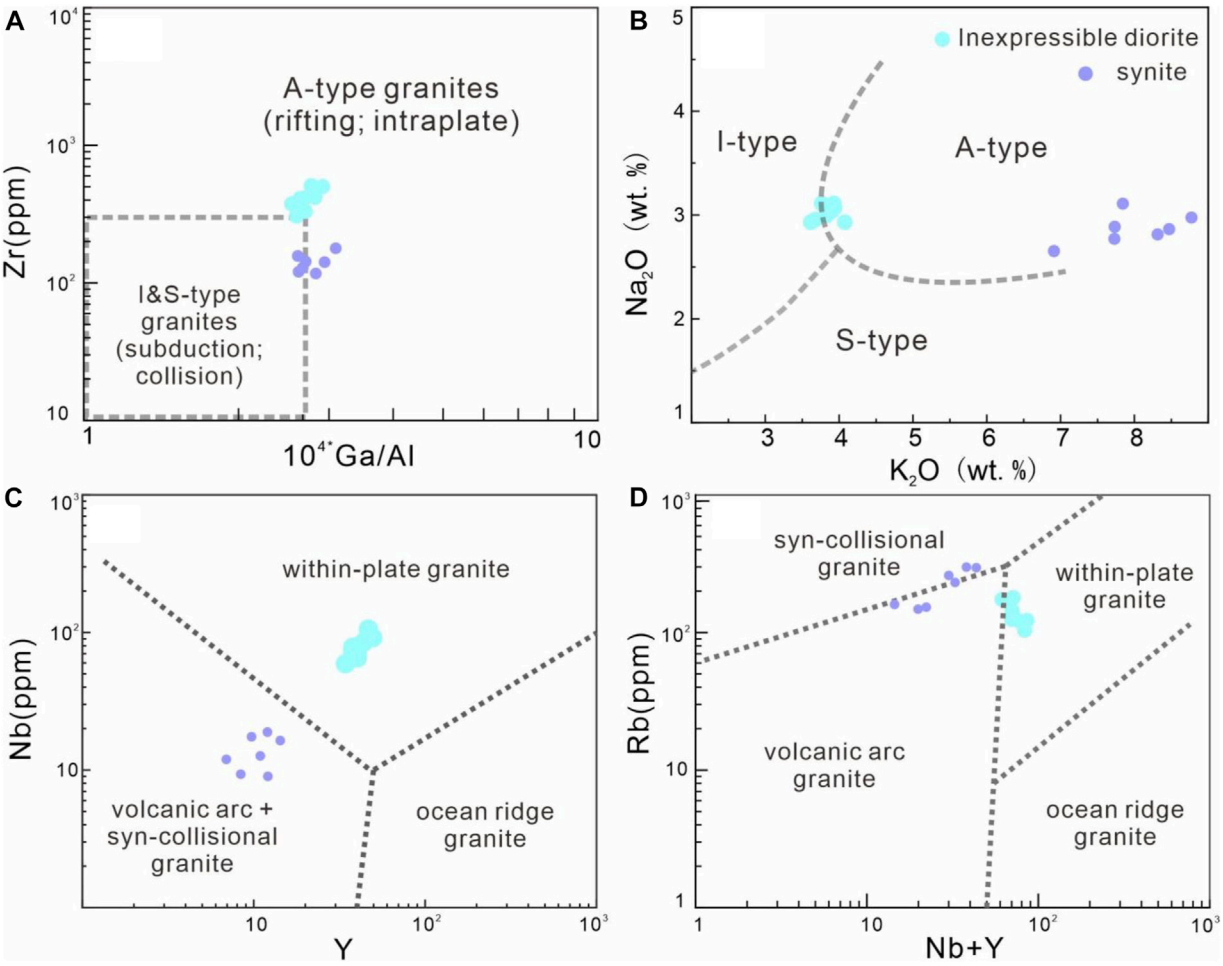


FIGURE 10
Structural environment diagram of the rocks in the Inexpressible Island intrusive. **(A)** 10^4*Ga/Al vs. Zr diagram (Whalen et al., 1987); **(B)** K_2O vs. Na_2O; **(C)** and **(D)** Nb vs. Y and Rb vs. Nb+Y diagrams (Pearce et al., 1984).

the Th/U of magmatic zircon is greater than 0.1 (Hoskin and Schaltegger, 2003). Combined with CL image and Th/U content characteristics, we suggest that zircons of the Inexpressible Island syenites belong to magmatic origin. Bomparola et al. (2007) point out the presence of long-term shallow crustal magmatism in the north Victoria land. They suggest that extensive and long-term extensional processes occurred during the Ross Orogeny as early as 530 Ma, which indicates prolonged thermal anomalous thermal activity beneath this region (Bomparola et al., 2007). We suggest that long-period magmatic events extended to ca. 470 Ma. Further, in the tectonic discrimination diagrams of 10^4Ga/Al vs. Zr, K_2O vs. Na_2O, Y vs. Nb, and Nb+Y vs. Rb (Figures 10A–D), all the syenite samples belong to either A-type granite and syncollisional or volcanic arc granite and represent post-orogenic granitoids (Pearce et al., 1984). A-type granitoids are generally emplaced in an extensional environment: post-collisional or anorogenic (Whalen et al., 1987; Eby, 1992, 1990; Wu et al., 2002; Bonin, 2007). Although, it is possible for the magma geochemistry to vary independently of the tectonic setting (Volkert et al., 2000; Jacobs and Thomas, 2004; Köksal et al., 2004; Whalen et al., 2006). But the Inexpressible Island syenites are associated with magmatic activity in widespread tectonic extension (Rocchi et al., 2004; Bomparola et al., 2007).

Petrogenesis

The mineralogical and chemical composition of the syenites associated with the Inexpressible Island area, comprising of alkaline-feldspar and perthite, coupled with high content of high field strength elements such as Zr, Hf, slightly decrease in their ΣREE content (expect for Eu) (Figures 8A,B), when compared to S-type and I-type granitoid suggest that the granitoid are typically syenite and A-type (e.g., Eby, 1992).

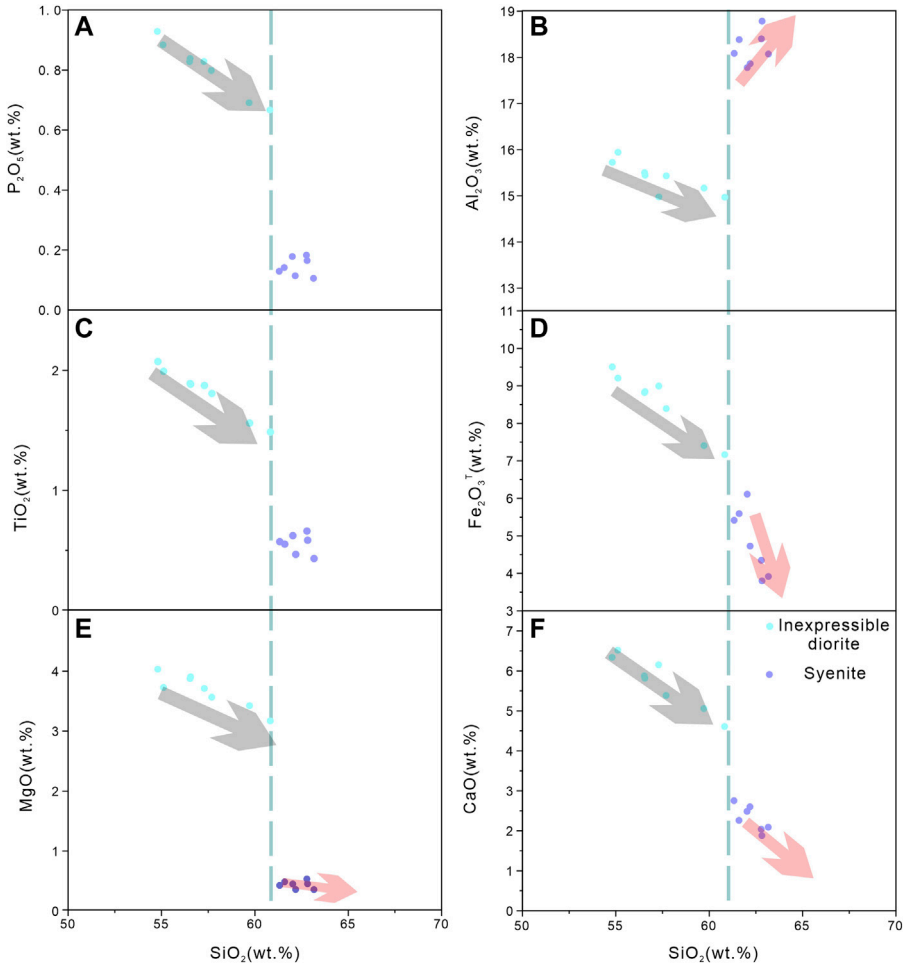


FIGURE 11
Harker diagrams for the medium- and coarse-grained syenites. Diorite data are derived from Gao et al., 2022. The dashed blue line indicates distinct chemical gaps.

Similarly, these syenites are equivalent to TeNIC post-collisional granitoids complex is also have common content of HFSE and LILE, also low content of Ti, P, Nb, Ta, Th, and ΣREE. region monzogranites, diorites, and granites were all in the calc-alkaline series (Rocchi et al., 2009) (Figure 7C). Whole-rock geochemistry from the Inexpressible Island syenite indicates weakly peraluminous to metaluminous with high potassium-alkaline content (Figure 7B). The average K_2O/Na_2O was 2.77, and on a SiO_2 vs. K_2O diagram (Figure 7C), the samples fall in the shoshonite region, indicating a highly potassium-rich source. Among the mafic igneous rocks from the early Paleozoic Ross Orogen of northern Victoria Land, the Morozumi diorite displayed a strong affinity to potassic rocks, such as the Vegetation Island lamprophyres, representing mantle-derived magmas emplaced during the late orogenic to post-collisional stage (Di Vincenzo and Rocchi, 1999; Rocchi et al., 2009). Whole rocks of the Inexpressible Island syenites have a very high total alkali content, which is over than the evolution trend of other TeNIC (Terra Nova intrusive complex) rock masses in the TAS diagram (gray arrow in the figure) (Figure 7A). The Harker diagrams and REE distribution patterns suggest that fractional crystallization played an important role in the differentiation of the syenite rocks. More specifically, the decrease of MgO, $Fe_2O_3^T$ (Figures 11D,E), with SiO_2 indicates the fractional crystallization of clinopyroxene and hornblende. The decrease of $Fe_2O_3^T$ also indicates the fractional crystallization of magnetite. The decrease of CaO and Sr with SiO_2 in the syenites is consistent with cumulus crystal of plagioclase while the decrease of Ba, and the strong positive Eu anomaly, are consistent with cumulus crystal of plagioclase. This is also in accordance with petrographic observations. Elements Nb, Ta and Ti are usually used to differentiate the rocks' formation as well as in tracing contamination of mantle derived *via* crustal assimilation (e.g., Niu and O' Hara, 2009; Wang et al., 2017). This came from the

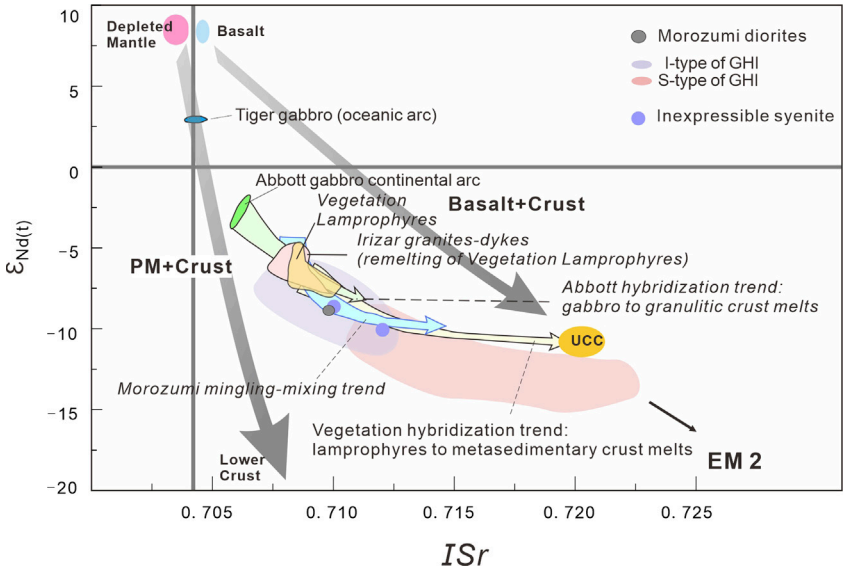


FIGURE 12
$\varepsilon_{Nd}(t)$ vs $(^{87}Sr/^{86}Sr)_i$ plot of the Inexpressible Island intrusive rocks. Also reported for comparison are 1) intrusive complexes emplaced around 490–500 Ma in the Wilson arc; 2) Abbott gabbro and its hybridization from deep-crust melts, Vegetation Island leucogranites and their hybridization from metasedimentary upper-crust melts (Di Vincenzo and Rocchi, 1999; Rocchi et al., 2004); 3) Irizar granites and dykes (Rocchi et al., 2009); 4) intrusive rocks emplaced earlier in the Tiger oceanic arc, that is, the Tiger gabbro (Bracciali et al., 2009); 5) intrusive rocks of the Morozumi mafic-intermediate (Rocchi et al., 2015); and 6) I-type and S-type Granites Harbour Intrusive (Armienti et al., 1990). Modifications (Jahn, et al., 1999; Rocchi et al., 2015). The gray arrow shows a simple mixing-milling trend for source and melts contaminations. The mixing parameters used are referred to. UM denotes upper mantle peridotites, UCC, upper continental crust elemental data (Taylor and McLennan, 1985), MCC-LCC, middle to lower crust data of middle crust (Rudnick and Fountain, 1995).

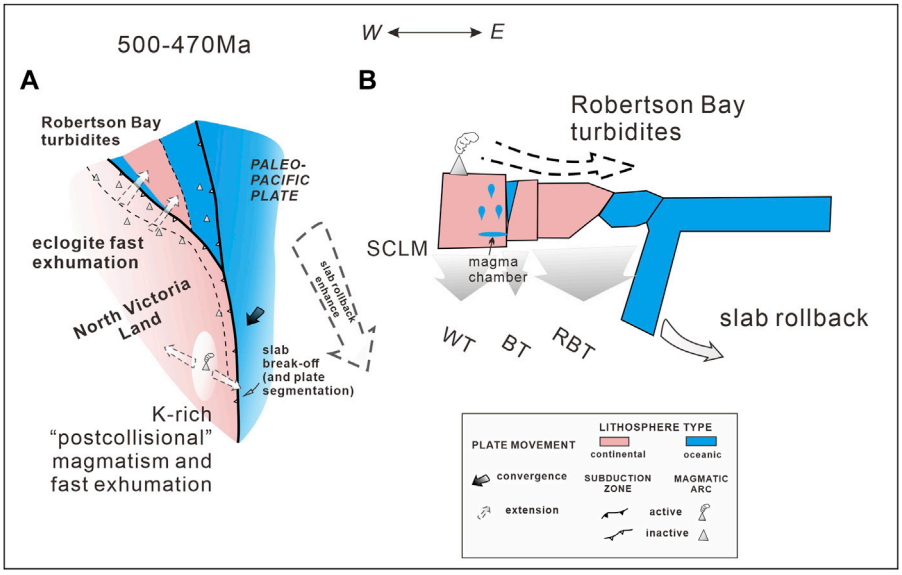


FIGURE 13
Regional tectonic schematic cartoon after **(A)** Late Ross orogenic stage post-collisional potassic magmatism. **(B)** Schematic diagram of subduction zone structure. Modifications after reference (Goodge, 2002; Rocchi et al., 2009; Rocchi et al., 2011).

fact that rocks that formed from melting of crustal material generally showed significant depletion in Nb, Ta, and Ti when compared to rocks that formed from mantle derived magmas (e.g., Niu and O' Hara, 2009'; HaraStanley, 1984; Rudnick and Gao, 2003; Taylor and McLennan, 1985; Taylor, 1977). This suggests a genetic link between the formation of continental crust and subduction related (island arc) magmatism (Taylor, 1977; Taylor and McLennan, 1985). The obviously negative Nb and Ta anomalies in cal-alkaline syenites from the Inexpressible Island is therefore consistent with rocks derived from melting of crustal sources. And also, the geochemical characteristics of the syenites such as their high K_2O and Na_2O and low Y/Nb ratio<2 are commonly considered as derivatives of enriched OIB mantle sources (Eby, 1992, 1990; Bonin, 2007). Otherwise, ratios of some LILE and HFSE such as Th/Ta, Th/Nb, Rb/Nb, Ba/Nb generally reflect the source materials from which igneous rock was derived (e.g., Shellnutt et al., 2009). This is because these trace elements remain largely immobile throughout the course of magmatic differentiation (Shellnutt and Zhou, 2007; Shellnutt et al., 2009; Wang et al., 2017). Typically, mantle derived rocks generally have lower Th/Ta ratio≈2 compared to the upper crust (Th/Ta≈6.9) or lower crust (Th/Ta≈7.9) (Rudnick and Gao, 2003; Shellnutt et al., 2009). The average Th/Ta values obtained from the samples of syenites are approximately 2, the ratio of individual is up to 9.5, which further suggests that the syenites were most likely derived from the mantle. The syenite is characterized by high $(^{87}Sr/^{86}Sr)_i$ values (0.7033–0.7045) and low $\varepsilon_{Nd}(t)$ values (Figure 12 and Supplementary Table SA4), which exhibit evolutionary isotopic characteristics to initial melts simulated by a previous study on TeNIC rocks, indicate syenite of the Inexpressible Island are hybridization from metasedimentary upper-crust and mantle melts (Di Vincenzo and Rocchi, 1999; Rocchi et al., 2015). The $\varepsilon_{Hf}(t)$ values of the oscillatory magmatic zircon rims show a range from −7.4 to −9.1 (Figure 9), suggesting that the occurrence of Mesoproterozoic crust and both reworked ancient crustal (Condie et al., 2005; Wu et al., 2006; Zheng et al., 2007). In addition, trace element geochemical signatures of the syenite show significant enrichment (Sr, Zr and Eu) than granites (Figure 8B), and similar to diorite (Chen et al., 2019), it suggests that the syenite magmas associated with these previous diorites. No coeval mafic-ultramafic rocks have been found in the Inexpressible Island, so as Morozumi diorite and Vegetation lamprophyre, are considered to be enriched by enrich mantle melting (Rocchi et al., 2009; Rocchi et al., 2015). However, compared with the spatially proximal diorite, trace element composition is more depleted (Figure 8A). Considering the significant differences in the evolution of major and trace elements, we believe that the lithospheric mantle beneath the Wilson continental margin is heterogeneous or represents a more complex compositional evolution.

Rocchi et al. (2015) established a genetic link between mafic, diorite, and granite of GHI in the northern Victoria Land *via* a liquid line of decent involving fractional crystallization and/or assimilation fractional crystallization (AFC) of enrich mantle derived magmas. Parabolic trends of the Granite Harbour intrusive samples suggest mixing between old crust with low $\varepsilon_{Nd}(t)$ and high $(^{87}Sr/^{86}Sr)_i$ and a juvenile component with higher $\varepsilon_{Nd}(t)$ and low $(^{87}Sr/^{86}Sr)_i$ (Figure 12). These results are consistent with the interpretation of Rocchi et al. (2009), who suggested that the late-stage diorite with low $\varepsilon_{Nd}(t)$ in northern Victoria Land was sourced from enriched subcontinental lithospheric mantle. In addition, Hagen-Peter et al. (2015) suggest that low Subcontinental lithospheric mantle Hf values may be in response which may be due to metasomatism of subduction materials that occurred during the late Ross orogeny, including fluid metasomatism, subduction of pelagic sediments, and introduction of crust-derived materials by subduction erosion.

The definition of "ultrapotassic rocks" introduced by (Foley et al., 1987) is based on their whole-rock chemistry rather than mineralogy. Commonly, all of these tectonic settings, except for intra-plate settings, are related to subduction zones. Several models have been proposed to explain the origin of ultrapotassic rocks, all of which invoke low degrees of melting of a metasomatized upper mantle. Experimental work has demonstrated that peridotite melts which formed in the presence of CO_2 at pressures ~27 kbar would be carbonatitic, whereas the presence of H_2O or F may enhance the stability of phlogopite (Eggler, 1978; Wendlandt, 1984). These studies suggest that small degrees of partial melting of phlogopite-bearing peridotite at depths below the level of amphibole stability and in the presence of CO_2 produces a high K_2O liquid with high Mg/Ca. All of these metasomatic processes and often associated with either intraplate rifting or subduction (Nelson et al., 1986). Extensive geochemical analysis (N100 samples) and zircon U–Pb geochronology (n = 70) confirm that alkaline and carbonatitic magmatism was partially contemporaneous with the emplacement of large subduction-related igneous complexes in adjacent areas. The SCLM has frequently been invoked as a potential source of alkaline silicate rocks and associated carbonatites in many localities (Bailey, 1987; Serri et al., 1993; Arzamastsev et al., 2001; Downes et al., 2005). The ultra-potassium syenite of the Inexpressible Island has a positive Eu anomaly (From 0.8 to 5.58) and is enriched in Sr (Figures 8A,B), which is indicative of that plagioclase cumulate crystallization occurred in the magma chamber. Experimental petrology shows that phlogopite has higher Rb/Sr and lower Ba/Rb values in the residual phase during partial melting, while hornblende shows the opposite (Furman and Graham, 1999). The Rb/Sr (0.36–0.92; mean 0.61) and Ba/Rb ratios (12.63–35.35; average 23.44) in the syenite samples shown considerable variation (Supplementary Table SA3). We suggest that the variation in Rb/Sr and Ba/Rb ratios reflect the complex genesis of the magma source, which may have been jointly controlled by phlogopite and hornblende.

Tectonic implications

Early Paleozoic convergence between the East Antarctic Craton and the Paleo-Pacific oceanic plate gave rise to southwest-directed

subduction (present-day coordinates) and related continental and oceanic arc magmatism (Weaver et al., 1984; Borg et al., 1986; Kleinschmidt and Tessensohn, 1987; Dalziel, 1997; Rocchi et al., 1998). The ongoing convergence eventually led to the formation of the Ross Orogen (Stump, 1995), as a result of accretion on the Antarctic margin of variable crustal blocks, although this is still a matter of debate (Weaver et al., 1984; Finn et al., 1999; Federico et al., 2006). A synthesis of recent research suggests that the final northern Victoria Land juxtaposition occurred during the Early Paleozoic and was accompanied by extensive post-collisional extensional magmatism (Goodge, 2020; Rocchi et al., 2015; Federico et al., 2009). At this time, the edge of the subduction zone was being obliquely subducted along the Ross orogenic belt toward northern Victoria Land (Janosy and Wilson, 1995) alkaline magmatism is interpreted to be a result of either crust-mantle interactions or a mantle plume in the shallow part of the crust due to intra-plate rifting or post-orogenic extensional tectonics (Wilson et al., 1995; Yang et al., 2012). Lithosphere delamination (Bird, 1979; Liégeois and Black, 1987) convective removal of the lithosphere (Houseman et al., 1981), and slab breakoff (Liégeois and Black, 1987; Davies and Von Blankenburg, 1995) have been proposed to explain magmatism in post-collisional and post-orogenic settings, also are used to make an explanation of the tectonic setting of the Ordovician granitic magmatism in the Wilson terrane (Rocchi et al., 2015; Hagen-Peter and Cottle, 2016), These processes induce an upwelling of the asthenosphere, which in turn, induces melting of the subcontinental mantle lithosphere (Wilson et al., 1995; Yang et al., 2012). Previous studies have shown that the typical post-collisional magmatic assemblages of highly differentiated calc-alkaline and alkaline granites, potassic volcanic rocks, and peralkaline intrusions also represent magmatic activity in a shear zone geotectonic setting, where the orogenic belt was dominated by transcurrent faulting and evolved into a non-orogenic environment (Oyhantcabal et al., 2007). Under continuous extensional tectonic environments, multiple stages intrusive in shallow crust made the closely related field genesis of the Inexpressible Island syenite and diorite dyke, this is consistent with the results of previous studies on TeNIC petrography (Rocchi et al., 2004; Bomparola et al., 2007). If we consider that the Inexpressible syenite has a similar evolutionary relationship to the lamprophyres of the Vegetation Island extension to Inexpressible Island (called a diorite dyke in Inexpressible Island), the gross petrologic, geochemical, and geochronologic differences in the magmatism can be explained by alternating phases of extension and contraction in the overriding plate (Figure 13A). In northernmost northern Victoria Land, multiple continental and oceanic arcs were syn-tectonically active (Figure 13A). Rather, accretion alternated with the detachment of a continental material-laden forearc–backarc from the main margin (Rocchi et al., 2011). During the late Ross Orogeny, horizontal transcurrent convergence caused the collision of transient coupling between convergent plates locked in the subduction process, and the slab lost its horizontal velocity component, sank into the mantle, and rolled back (Rocchi et al., 2009) (Figure 13B). The rise of asthenosphere material that replaced ductile lithosphere exposed previously insulated portions of the mechanical boundary layer of the subcontinental mantle to asthenosphere mantle heating. The melting of the metasomatized thermal boundary layer of the subcontinental lithosphere gave way to the generation of diorite melts and subsequent syenites sources magma (Rocchi et al., 2011; Rocchi et al., 2015) Thus, we suggested that the ultrapotassic syenite may be the partial melting product of potassium-rich SCLM in this tectonic environment. The Inexpressible Island syenite formed from the evolved fraction of these melts (Figure 12). The emplacement of these rocks was probably controlled by some deep-seated fault/shear zones. Extension continued form late Cambrian to the early Ordovician Period. This period facilitated the upwelling of metasomatized SCLM derived sources and the emplacement of mafic rocks such as the Irizar diorite and Vegetation diorite, Inexpressible Island diorites (Figure 7A). The Inexpressible Island syenites probably formed from the same mafic magma through assimilation fractional crystallization (Figure 13).

In summary, we suggest that based on the tectonic and geochemical similarities of the Vegetation Island mafic rocks, Irizar granite dyke, Abbott gabbro, and granite with both late to post-orogenic shoshonites and lamprophyres (Turner, 1996; Turner and Foden, 1996; Di Vincenzo et al., 1997) coupled with field occurrence, age, and extensional emplacement regime suggest that the Inexpressible Island magmatism was linked to local involvement in the melting zone of an older previously enriched layer of the subcontinental lithospheric mantle, which was further metasomatized by a more recent subduction component.

Conclusion

1. The Inexpressible Island syenite samples (DJS-6 and DJS-13) zircon U-Pb ages are 471.8 ± 1.8 Ma (MSWD=0.87, *n*=20) and 477.3 ± 1.7 Ma (MSWD=0.59, n=20), respectively, indicating early Ordovician magmatic intrusive activity.
2. Whole-rock geochemistry shows that the Inexpressible Island syenite is weakly peraluminous metaluminous and ultra-potassium, with typical island-arc magmatic affinity. We interpret the syenite as an Ordovician intrusion associated with regional extensional in Wilson continental margin. The magma source is linked to local involvement in the melting zone of an older previously enriched layer of the subcontinental lithospheric mantle, which was further metasomatized by a more recent subduction component. Otherwise, plagioclase cumulate crystallization reflects the complex genesis of the magma source controlled by phlogopite and hornblende.
3. We support an active continental margin accretion model, which existed on the Antarctic margin of east Gondwana during the

Early Paleozoic, in which multiple plates and ocean arcs were active. Plate tectonic deformation led to slab roll-back or tear of subducted plates, and upwelling asthenosphere mantle activate the subcontinental lithospheric mantle beneath the continental arc, which components be modified by subduction component before, and the derived mantle magma is significantly more evolved, ultimately intrude in the current stratum, formed the Inexpressible Island syenite.

Data Availability Statement

The original contributions presented in the study are included in the article/Supplementary Material, further inquiries can be directed to the corresponding author.

Author contributions

LT contributed to conception and design of the study. PG organized the database. LC performed the statistical analysis. PG wrote the first draft of the manuscript. LT and LC wrote sections of the manuscript. All authors contributed to manuscript revision, read, and approved the submitted version.

Funding

This work was supported by the National Natural Science Foundation of China (No. 41976072), the Fundamental Research Funds for Second Institute of Oceanography, Ministry of Natural Resources (No. QNYC1901) and (No. JG2002).

Acknowledgments

We would like to acknowledge China's 34th Antarctic Scientific Expedition for help with the samples and investigation. Thanks are due to LT and LC for their guidance in the study and writing process. We are grateful to Dr. Eirini Poulaki and Dr. Giovanna Rizzo, and editor Gilby Jepson whose reviews have significantly improved this work.

Conflict of interest

The authors declare that the research was conducted in the absence of any commercial or financial relationships that could be construed as a potential conflict of interest.

Publisher's note

All claims expressed in this article are solely those of the authors and do not necessarily represent those of their affiliated organizations, or those of the publisher, the editors and the reviewers. Any product that may be evaluated in this article, or claim that may be made by its manufacturer, is not guaranteed or endorsed by the publisher.

Supplementary material

The Supplementary Material for this article can be found online at: https://www.frontiersin.org/articles/10.3389/feart.2022.966085/full#supplementary-material

References

Armienti, P., Ghezzo, C., Innocenti, F., Manetti, P., Rocchi, S., and Tonarini, S. (1990). Granite Harbour intrusives from north Victoria land between david and campbell glaciers: New geochronological data. *Zentralblatt für Geol. Paläontologie* 1, 63–74.

Arzamastsev, A. A., Bea, F., Glaznev, V. N., Arzamastseva, L. V., and Montero, P. (2001). Kola alkaline province in the paleozoic: Evaluation ofprimary mantle magma composition and magma generation conditions. *Russ. J. Earth Sci.* 3, 1–32. doi:10.2205/2001es000054

Bailey, D. K. (1987). "Mantle metasomatism—perspective and prospect," in *The alkaline rocks*. Editors J. G. Fitton and B. G. J. Upton (Oxford: Blackwell Scientific), 1–13.

Biagini, R., Cappelli, B., and Di Vincenzo, G. (1990). *P-T estimates of the Mt. Abbott intrusives and enclosed metamorphic "septa" at Terra Nova Bay*. North Victoria land, Antarctica: Vulcanismo potassico. *Ischia*.

Bird, P. (1979). Continental delamination and the Colorado plateau. *J. Geophys. Res.* 84, 7561–7571. doi:10.1029/jb084ib13p07561

Black, L. P., and Sheraton, J. W. (1990). The influence of Precambrian source components on the U-Pb zircon age of a Palaeozoic granite from northern Victoria Land, Antarctica. *Precambrian Res.* 46, 275–293. doi:10.1016/0301-9268(90)90016-J

Blichert-Toft, J., and Albarède, F. (1998). The Lu-Hf isotope geochemistry of chondrites and the evolu-tion of the mantle-crust system. *Earth Planet. Sci. Lett.* 148 (1-2), 349–258. doi:10.1016/s0012-821x(97)00198-2

Boger, S. (2011). Antarctica—Before and after Gondwana. *Gondwana Res.* 19, 335–371. doi:10.1016/j.gr.2010.09.003

Bomparola, R. M., Ghezzo, C., Belousova, E., Griffin, W. L., and O'Reilly, S. Y. (2007). Resetting of the U–Pb zircon system in cambro–ordovician intrusives of the deep freeze range, northern victoria land, Antarctica. *J. Petrology* 48, 327–364. doi:10.1093/petrology/egl064

Bonin, B. (2007). A-type granites and related rocks: Evolution of a concept, problems and prospects. *Lithos* 97 (1/2), 1–29. doi:10.1016/j.lithos.2006.12.007

Borg, S. G., and DePaolo, D. J. (1994). Laurentia, Australia, and Antarctica as a late Proterozoic supercontinent: Constraints from isotopic mapping. *Geology* 22, 307–310. doi:10.1130/0091-7613(1994)022<0307:laaaaa>2.3.co;2

Borg, S. G., Stump, E., Chappell, B. W., McCulloch, M. T., Wyborn, T., Armstrong, R. L., et al. (1987). Granitoids of northern victoria land, Antarctica: Implications of chemical and isotopic variations to regional crustal structure and tectonics. *Am. J. Sci.* 287, 127–169. doi:10.2475/ajs.287.2.127

Borg, S. G., Stump, E., and Holloway, J. R. (1986). Granitoids of northern victoria land, Antarctica: A reconnaissance study of field relations, petrography, and geochemistry. *Geol. Investigations North. Vic. Land* 46, 115–188. doi:10.1029/ar046p0115

Borsi, L., Petrini, R., Talarico, F., and Palmeri, R. (1995). Geochemistry and Sr-Nd isotopes of amphibolite dykes of northern Victoria Land, Antarctica. *Lithos* 35, 245–259. doi:10.1016/0024-4937(95)99070-d

Bracciali, L., Di Vincenzo, G., Rocchi, S., and Ghezzo, C. (2009). The Tiger Gabbro from northern Victoria Land, Antarctica: The roots of an island arc within the early Palaeozoic margin of Gondwana. *J. Geol. Soc. Lond.* 166, 711–724. doi:10.1144/0016-76492008-098

Bradshaw, J. D., and Laird, M. G. (1983). "The pre-Beacon geology of northern Victoria Land," in *Antarctic earth science*. Editor J. B. Jago (Canberra: Australian Academy of Science), 98–101.

Castelli, D., Lombardo, B., Oggiano, G., Rossetti, P., and Talarico, F. (1991). Granulite facies rocks of the Wilson terrane (northern victoria land): Campbell glacier. *Mem. della Soc. Geol. Ital.* 46, 197–203.

Cawood, P. A., and Buchan, C. (2007). Linking accretionary orogenesis with supercontinent assembly. *Earth-Science Rev.* 82 (3-4), 217–256. doi:10.1016/j.earscirev.2007.03.003

Cawood, P. A., Kroner, A., Collins, W. J., Kusky, T. M., Mooney, W. D., and Windley, B. F. (2009). Accretionary orogens through Earth history. *Geol. Soc. Lond. Spec. Publ.* 318, 1–36. doi:10.1144/sp318.1

Cawood, P. A. (2005). Terra australis orogen: Rodinia breakup and development of the pacific and iapetus margins of Gondwana during the neoproterozoic and paleozoic. *Earth-Science Rev.* 69, 249–279. doi:10.1016/j.earscirev.2004.09.001

Chen, H., Wang, W., and Zhao, Y. (2019). Constraints on early paleozoic magmatic processes and tectonic setting of inexpressible island, northern victoria land, Antarctica. *Adv. Polar Sci.* 30 (1), 52–69.

Condie, K. C., Beyer, E., Belousova, E., Griffin, W., and O'Reilly, S. Y. (2005). U–Pb isotopic ages and Hf isotopic composition of single zircons: The search for juvenile precambrian continental crust. *Precambrian Res.* 139, 42–100. doi:10.1016/j.precamres.2005.04.006

Condie, K. C. (2007). "Accretionary orogens in space and time,". Editors R. D. HatcherJr., M. P. Carlson, J. H. McBride, and J. R. Martínez Catalán (Geological Society of America), 200, 145–158.*4D Framew. Cont. Crust* Boulder, CO, United States.

Crispini, L., Di Vincenzo, G., and Palmeri, R. (2007). Petrology and 40Ar–39Ar dating of shear zones in the lanterman range (northern victoria land, Antarctica): Implications for metamorphic and temporal evolution at terrane boundaries. *Mineralogy Petrology* 89, 217–249. doi:10.1007/s00710-006-0164-2

Dalziel, I. W. D. (1992). Antarctica: A tale of two supercontinents? *Annu. Rev. Earth Planet. Sci.* 20, 501–526. doi:10.1146/annurev.ea.20.050192.002441

Dalziel, I. W. D. (1997). Overview: Neoproterozoic-Paleozoic geography and tectonics: Review, hypothesis, environmental speculation. *Geol. Soc. Am. Bull.* 109 (1), 16–42. doi:10.1130/0016-7606(1997)109<0016:onpgat>2.3.co;2

Davies, J. H., and von Blanckenburg, F. (1995). Slab breakoff: A model of lithosphere detachment and its test in the magmatism and deformation of collisional orogens. *Earth Planet. Sci. Lett.* 129, 85–102. doi:10.1016/0012-821x(94)00237-s

Di Vincenzo, G., Grande, A., and Rossetti, F. (2014). Paleozoic siliciclastic rocks from northern Victoria Land (Antarctica): Provenance, timing of deformation, and implications for the Antarctica–Australia connection. *Geol. Soc. Am. Bull.* 126, 1416–1438. doi:10.1130/b31034.1

Di Vincenzo, G., Rocchi, S., Ghezzo, C., and Andriessen, P. A. M. (1997a). "Felsic and mafic magmas in the Terra Nova intrusive complex (northern Victoria Land, Antarctica)," in *The antarctic region: Geological evolution and processes*. Editor C. A. Ricci (Siena: Terra Antartica Publications), 253–260.

Di Vincenzo, G., and Rocchi, S. (1999). Origin and interaction of mafic and felsic magmas in an evolving late orogenic setting: The Early Paleozoic Terra Nova Intrusive Complex, Antarctica. *Contributions Mineralogy Petrology* 137 (1-2), 15–35. doi:10.1007/s004100050579

Downes, H., Balaganskaya, E., Beard, A., Liferovich, R., and Demaiffe, D. (2005). Petrogenetic processes in the ultramafic, alkaline and carbonatitic magmatism in the kola alkaline province: A review. *Lithos* 85, 48–75. doi:10.1016/j.lithos.2005.03.020

Eby, G. N. (1992). Chemical subdivision of the A-type granitoids: Petrogenetic and tectonic implications. *Geol.* 20 (7), 641–644. doi:10.1130/0091-7613(1992)020<0641:csotat>2.3.co;2

Eby, G. N. (1990). The A-type granitoids: A review of their occurrence and chemical characteristics and speculations on their petrogenesis. *Lithos* 26 (1/2), 115–134. doi:10.1016/0024-4937(90)90043-z

Eggler, D. H. (1978). The effect of CO_2 upon partial melting of peridotite in the system Na_2O-CaO-Al_2O_3-MgO-SiO-CO_2 to 34 Kb. with an analysis of melting in a peridotite-H_2O-CO_2 system. *Am. J. Sci.* 278, 305–343. doi:10.2475/ajs.278.3.305

Elliot, D. H., and Fanning, C. M. (2008). Detrital zircons from upper permian and lower triassic victoria group sandstones, shackleton glacier region, Antarctica: Evidence for multiple sources along the Gondwana plate margin. *Gondwana Res.* 13, 259–274. doi:10.1016/j.gr.2007.05.003

Encarnación, J., and Grunow, A. (1996). Changing magmatic and tectonic styles along the paleo-Pacific margin of Gondwana and the onset of early Paleozoic magmatism in Antarctica. *Tectonics* 15, 1325–1341. doi:10.1029/96tc01484

Estrada, S., Läufer, A., Eckelmann, K., Hofmann, M., Gärtner, A., and Linnemann, U. (2016). Continuous neoproterozoic to ordovician sedimentation at the east Gondwana margin - implications from detrital zircons of the ross orogen in northern victoria land, Antarctica. *Gondwana Res.* 37, 426–448. doi:10.1016/j.gr.2015.10.006

Federico, L., Capponi, G., and Crispini, L. (2006). The ross orogeny of the transantarctic mountains: A northern victoria land perspective. *Int. J. Earth Sci.* 95 (5), 759–770. doi:10.1007/s00531-005-0063-5

Federico, L., Crispini, L., Capponi, G., and Bradshaw, J .D. (2009). The Cambrian ross orogeny in northern Victoria Land (Antarctica) and New Zealand: A synthesis. *Gondwana Research* 15 (2), 188–196. doi:10.1016/j.gr.2008.10.004

Fergusson, C. L., Henderson, R. A., Fanning, C. M., and Withnall, I. W. (2007). Detrital zircon ages in neoproterozoic to ordovician siliciclastic rocks, northeastern Australia: Implications for the tectonic history of the east Gondwana continental margin. *J. Geol. Soc. Lond.* 164, 215–225. doi:10.1144/0016-76492005-136

Finn, C., Moore, D., Damaske, D., and Mackey, T. (1999). Aeromagnetic legacy of early Paleozoic subduction along the Pacific margin of Gondwana. *Geol.* 27, 1087–1090. doi:10.1130/0091-7613(1999)027<1087:aloeps>2.3.co;2

Fioretti, A. M., Capponi, G., Black, L. P., Varne, R., and Visona, D. (2005). Surgeon island granite shrimp zircon ages: A clue for the cambrian tectonic setting and evolution of the palaeopacific margin of Gondwana (northern victoria land, Antarctica). *Terra nova.* 17, 242–249. doi:10.1111/j.1365-3121.2005.00606.x

Fitzsimons, I. C. W. (2003). "Proterozoic basement provinces of southern and southwestern Australia, and their correlation with Antarctica," in *Proterozoic east Gondwana: Supercontinent assembly and break-up*. Editor S. Dasgupta (London: Geological Society), 93–130.

Foley, S. F., Venturelli, G., Green, D. H., and Toscani, L. (1987). The ultrapotassic rocks: Characteristics, classification and constraints for petrogenetic models. *Earth. Sci. Rev.* 24, 81–134. doi:10.1016/0012-8252(87)90001-8

Furman, T., and Graham, D. (1999). Erosion of lithospheric mantle beneath the east african rift system: Geochemical evidence from the kivu volcanic province. *Lithos* 24, 237–262. doi:10.1016/s0024-4937(99)00031-6

Gao, P., Tang, L. M., Chen, L., Yuan, T., and YinXia, F. (2022). Geochronology and geochemistry of the dioritic rocks from the Inexpressible Island, Northern Victoria Land, Antarctica and their geological implications. *Acta Petrol. Sin.* 38 (3), 923–941. doi:10.18654/1000-0569/2022.03.19

Ghezzo, C., Baldelli, C., Biagini, L., Carmignani, L., Di Vincenzo, G., Gosso, G., et al. (1987). Granitoids from the david glacier-aviator glacier segment of the transantarctic mountains, north Victoria land, Antarctica. *Mem. della Soc. Geol. Ital.* 33, 143–159.

Goodge, J. W., Fanning, C. M., Norman, M. D., and Bennett, V. C. (2012). Temporal, isotopic and spatial relations of early Paleozoic Gondwana-margin arc magmatism, central Transantarctic Mountains, Antarctica. *J. Petrology* 53, 2027–2065. doi:10.1093/petrology/egs043

Goodge, J. W., and Fanning, C. M. (2002). "Precambrian crustal history of the Nimrod Group, central Transantarctic mountains," in *Proceedings of the 8th international symposium on antarctic earth sciences*. Editors J. A. Gamble, D. A. Skinner, and S. Henrys (Wellington: Royal Society of New Zealand Bulletin), 43–50.

Goodge, J. W. (2020). Geological and tectonic evolution of the Transantarctic Mountains, from ancient craton to recent enigma. *Gondwana Res.* 80, 50–122. doi:10.1016/j.gr.2019.11.001

Goodge, J. W., Williams, I. S., and Myrow, P. (2004). Provenance of Neoproterozoic and lower Paleozoic siliciclastic rocks of the central Ross orogen, Antarctica: Detrital record of rift-passive-and active-margin sedimentation. *Geol. Soc. Am. Bull.* 116, 1253–1279. doi:10.1130/b25347.1

Grew, E. S., and Sandiford, M. (1984). A staurolite-talc assemblage in tourmaline-phlogopite-chlorite schist from northern Victoria Land, Antarctica, and its petrogenetic significance. *Contr. Mineral. Pet.* 87 (4), 337–350. doi:10.1007/bf00381290

Gunn, G. M., and Warren, G. (1962). Geology of victoria land between mawson and mullock glaciers, Antarctica. *N. Z. Geol. Surv. Bull.* 71, 157.

Hagen-Peter, G., and Cottle, J. M. (2016). Synchronous alkaline and subalkaline magmatism during the late neoproterozoic–early paleozoic ross orogeny, Antarctica: Insights into magmatic sources and processes within a continental arc. *Lithos* 262, 677–698. doi:10.1016/j.lithos.2016.07.032

Hagen-Peter, G., Cottle, J. M., Tulloch, A. J., and Cox, S. C. (2015). Mixing between enriched lithospheric mantle and crustal components in a short-lived subduction-related magma system, dry valleys area, Antarctica: Insights from U-Pb geochronology, Hf isotopes, and whole-rock geochemistry. *Lithosphere* 7, 174–188. doi:10.1130/l384.1

HartStanley, R. (1984). A large-scale isotope anomaly in the southern hemisphere mantle. *Nature* 309 (5971), 753–757. doi:10.1038/309753a0

Hoskin, P. W., and Schaltegger, U. (2003). The composition of zircon and igneous and metamorphic petrogenesis. *Rev. Mineral. Geochem.* 53, 27–62. doi:10.2113/0530027

Houseman, G. A., McKenzie, D. P., and Molnar, P. J. (1981). Convective instability of a thickened boundary layer and its relevance for the thermal evolution of continental convergent belts. *J. Geophys. Res.* 86, 6115–6132. doi:10.1029/jb086ib07p06115

Hu, Z. C., Liu, Y. S., Gao, S., Liu, W., Yang, L., Zhang, W., et al. (2012). Improved *in situ* Hf isotope ratio analysis of zircon using newly designed X skimmer cone and Jet sample cone in combination with the addition of nitrogen by laser ablation multiple collector ICP-MS. *J. Anal. At. Spectrom.* 27, 1391–1399. doi:10.1039/c2ja30078h

Jackson, S. E., Pearson, N. J., Griffin, W. L., and Belousova, E. A. (2004). The application of laser ablation-inductively coupled plasma-mass spectrometry to in situ U-Pb zircon geochronology. *Chemical Geology* 211, 47–69. doi:10.1016/j.chemgeo.2004.06.017

Jacobs, J., and Thomas, R. J. (2004). Himalayan-type indenterescape tectonics model for the southern part of the late Neoproterozoic–early Paleozoic East African–Antarctic orogen. *Geol.* 32 (8), 721–724. doi:10.1130/G20516.1

Jahn, B. M., Wu, F., Lo, C. H., and Tsai, C. H. (1999). Crust–mantle interaction induced by deep subduction of the continental crust: Geochemical and Sr–Nd isotopic evidence from post-collisional mafic–ultramafic intrusions of the northern dabie complex, central China. *Chem. Geol.* 157 (1-2), 119–146. doi:10.1016/s0009-2541(98)00197-1

Janosy, R. J., and Wilson, T. J. (1995). "Tectonic setting of the early Paleozoic dike swarm in southern Victoria Land," in *VII international symposium on antarctic earth sciences abstracts*. Editor C. A. Ricci (Siena, Italy: Terra Antartica Publications).

Kleinschmidt, G., and Tessensohn, F. (1987). Early paleozoic westward directed subduction at the pacific continental margin of Antarctica, sixth Gondwana symposium. *Geophys. Monogr.* 105, 89. doi:10.1029/GM040p0089

Köksal, S., Romer, R. L., Göncüoglu, M. C., Romer, R. L., and Toksoy-Köksal, F. (2004). Timing of post-collisional H-type to A-type granitic magmatism: U-Pb titanite ages from the alpine central anatolian granitoids (Turkey). *Int. J. Earth Sci.* 93, 974–989. doi:10.1007/s00531-004-0432-5

Kretz, R. (1983). Symbols for rock-forming minerals. *Am. Mineralogist* 68 (1-2), 277–279.

Läufer, A., Lisker, F., and Phillips, G. (2011). Late ross-orogenic deformation of basement rocks in the northern deep freeze range, victoria land, Antarctica: The lichen hills shear zone. *Polarforschung* 80 (2), 60–70.

Li, C. F., Li, X. H., Li, Q. L., Guo, J. H., and Yang, Y. H. (2012). Rapid and precise determination of sr and nd isotopic ratios in geological samples from the same filament loading by thermal ionization mass spectrometry employing a single-step separation scheme. *Anal. Chim. Acta* 727 (10), 54–60. doi:10.1016/j.aca.2012.03.040

Li, S. Z., Yang, Z., and Zhao, S. J. (2016). Global early paleozoic orogen (II): Subduction accretionary type Orogeny.Journal of jilin university. *Earth Sci. Ed.* (464), 968–1004.

Liégeois, J. P., and Black, R. (1987). "Alkaline magmatism subsequent to collision in the Pan-African belt of the Adrar des Iforas (Mali),". Editors J. G. Fitton and B. J. G. Upton (London: Geological Society Special Publication), 30, 381–401.*Alkaline Igneous Rocks*

Liu, Y. S., Gao, S., Hu, Z. C., Gao, C. G., Zong, K. Q., and Wang, D. B. (2010). Continental and oceanic crust recycling-induced melt-peridotite interactions in the trans-north China orogen: U-Pb dating, Hf isotopes and trace elements in zircons from mantle xenoliths. *J. Petrology* 51 (1–2), 537–571. doi:10.1093/petrology/egp082

Liu, Y. S., Hu, Z. C., Gao, S., Günther, D., Xu, J., Gao, C. G., et al. (2008). *In situ* analysis of major and trace elements of anhydrous minerals by LA-ICP-MS without applying an internal standard. *Chem. Geol.* 257 (1-2), 34–43. doi:10.1016/j.chemgeo.2008.08.004

Ludwig, K. R. (2003). A geochronological toolkit for microsoft excel. *ISOPLOT* 2003, 39.

Maniar, P. D., and Piccoli, P. M. (1989). Tectonic discrimination of granitoids. *Geol. Soc. Am. Bull.* 101 (5), 635–643. doi:10.1130/0016-7606(1989)101<0635:tdog>2.3.co;2

Middlemost, E. A. K. (1994). Naming materials in the magma/igneous rock system. *Earth. Sci. Rev.* 37, 215–224. doi:10.1016/0012-8252(94)90029-9

Moores, E. M. (1991). Southwest U.S. - east Antarctic (SWEAT) connection: A hypothesis. *Geol.* 19, 425–428. doi:10.1130/0091-7613(1991)019<0425:suseas>2.3.co;2

Nasdala, L., Lengauer, C. L., Hanchar, J. M., Kronz, A., Wirth, R., Blanc, P., et al. (2002). Annealing radiation damage and the recovery of cathodoluminescence. *Chem. Geol.* 191 (1-3), 121–140. doi:10.1016/s0009-2541(02)00152-3

Nelson, D. R., Mcculloch, M. T., and Sun, S. S. (1986). The origins of ultrapotassic rocks as inferred from Sr, Nd and Pb isotopes. *Geochimica Cosmochimica Acta* 50 (2), 231–245. doi:10.1016/0016-7037(86)90172-9

Niu, Y. L., and O'Hara, M. J. (2009). MORB mantle hosts the missing Eu (Sr, Nb, Ta and Ti) in the continental crust: New perspectives on crustal growth, crust-mantle differentiation and chemical structure of oceanic upper mantle. *Lithos* 112 (1/2), 1–17. doi:10.1016/j.lithos.2008.12.009

Oyhantcabal, P., Siegesmund, S., Wemmer, K., Frei, R., and Layer, P. (2007). Post-collisional transition from calc-alkaline to alkaline magmatism during transcurrent deformation in the southernmost Dom Feliciano belt (Braziliano–Pan-African, Uruguay). *Lithos* 98, 141–159. doi:10.1016/j.lithos.2007.03.001

Palmeri, R. (1997). P-T paths and migmatite formation: An example from Deep Freeze range, northern Victoria Land, Antarctica. *Lithos* 42, 47–66. doi:10.1016/s0024-4937(97)00036-4

Palmeri, R., Pertusati, P. C., Ricci, C. A., and Talarico, F. (1994). Late proterozoic (?)-early paleozoic evolution of the active pacific margin of Gondwana: Evidence from the southern Wilson terrane (northern victoria land, Antarctica). *Terra Antarct.* 1, 5–9.

Paulsen, T. S., Encarnación, J., Grunow, A. M., Layer, P. W., and Watkeys, M. (2007). New age constraints for a short pulse in Ross orogen deformation triggered by East-West Gondwana suturing. *Gondwana Res.* 12, 417–427. doi:10.1016/j.gr.2007.05.011

Pearce, J. A., Harris, N. B., and Tindle, A. G. (1984). Trace element discrimination diagrams for the tectonic interpretation of granitic rocks. *J. Petrology* 25, 956–983. doi:10.1093/petrology/25.4.956

Peccerillo, A., and Taylor, S. R. (1976). Geochemistry of eocene calc-alkaline volcanic rocks from the kastamonu area, northern Turkey. *Contr. Mineral. Pet.* 58 (1), 63–81. doi:10.1007/bf00384745

Perugini, D., Poli, G., and Rocchi, S. (2005). Development of viscous fingering between mafic and felsic magmas: Evidence from the Terra Nova intrusive complex (Antarctica). *Mineral. Pet.* 83, 151–166. doi:10.1007/s00710-004-0064-2

Pisarevsky, S. A., Wingate, M. D. T., Powell, C. M., Johnson, S., and Evans, D. A. D. (2003). "Models of Rodinia assembly and fragmentation," in *Proterozoic east Gondwana: Supercontinent assembly and break-up*. Editor S. Dasgupta (London: Geological Society), 35–55.

Rocchi, S., Bracciali, L., Di Vincenzo, G., Gemelli, M., and Ghezzo, C. (2011). Arc accretion to the early paleozoic antarctic margin of Gondwana in victoria land. *Gondwana Res.* 19, 594–607. doi:10.1016/j.gr.2010.08.001

Rocchi, S., Di Vincenzo, G., Ghezzo, C., and Nardini, I. (2009). Granite–lamprophyre connection in the latest stages of the early paleozoic ross orogeny (victoria land, Antarctica). *Geol. Soc. Am. Bull.* 121, 801–819. doi:10.1130/b26342.1

Rocchi, S., Di Vincenzo, G., and Ghezzo, C. (2004). The Terra Nova intrusive complex (victoria land, Antarctica), with 1:50, 000 geopetrographic map. *Terra Antarct. Rep.* 10, 51.

Rocchi, S., Tonarini, S., Armienti, P., Innocenti, F., and Manetti, P. (1998). Geochemical and isotopic structure of the early Palaeozoic active margin of Gondwana in northern Victoria Land, Antarctica. *Tectonophysics* 284, 261–281. doi:10.1016/s0040-1951(97)00178-9

Rocchi, S., Vincenzo, G. D., Dini, A., Petrelli, M., and Vezzoni, S. (2015). Time-space focused intrusion of genetically unrelated arc magmas in the early paleozoic ross-delamerian orogen (morozumi range, Antarctica). *Lithos* 232, 84–99. doi:10.1016/j.lithos.2015.06.006

Rossetti, F., Tecce, F., Aldega, L., Brilli, M., and Faccenna, C. (2006b). Deformation and fluid flow during orogeny at the palaeo-pacific active margin of Gondwana: The early palaeozoic Robertson Bay accretionary complex (North Victoria land, Antarctica). *J. Metamorph. Geol.* 24, 33–53. doi:10.1111/j.1525-1314.2005.00620.x

Rossetti, F., Vignaroli, G., Di Vincenzo, G., Gerdes, A., Ghezzo, C., Theye, T., et al. (2011). Long-lived orogenic construction along the paleo-pacific margin of Gondwana (deep freeze range, north Victoria land, Antarctica). *Tectonics* 30. doi:10.1029/2010tc002804

Rubatto, D., and Gebauer, D. (2000). *Use of cathodoluminescence for U-Pb zircon dating by ion microprobe: Some examples from the western cathodoluminescence in geosciences*. Berlin, Heidelberg: Springer, 373–400.

Rubatto, D., and Hermann, J. (2007). Experimental zircon/melt and zircon/garnet trace element partitioning and implications for the geochronology of crustal rocks. *Chem. Geol.* 241 (1-2), 38–61. doi:10.1016/j.chemgeo.2007.01.027

Rudnick, R. L., and Fountain, D. M. (1995). Nature and composition of the continental crust: A lower crustal perspective. *Rev. Geophys.* 33, 267–309. doi:10.1029/95rg01302

Rudnick, R. L., and Gao, S. (2003). Composition of the continental crust. *Treatise Geochem.* 3, 1–64. doi:10.1016/b0-08-043751-6/03016-4

Serri, G., Innocenti, F., and Manetti, P. (1993). Geochemical and petrological evidence of the subduction of delaminated Adriatic continental lithosphere in the Genesis of the Neogene-quaternary magmatism of Central Italy. *Tectonophysics* 223, 117–147. doi:10.1016/0040-1951(93)90161-c

Shellnutt, J. G., Wang, C. Y., Zhou, M. F., and Yang, Y. (2009). Zircon Lu-Hf isotopic compositions of metaluminous and peralkaline A-type granitic plutons of the emeishan large igneous province (SW China): Constraints on the mantle source. *J. Asian Earth Sci.* 35 (1), 45–55. doi:10.1016/j.jseaes.2008.12.003

Shellnutt, J. G., and Zhou, M. F. (2007). Permian peralkaline, peraluminous and metaluminous A-type granites in the panxi district, SW China: Their relationship to the emeishan mantle plume. *Chem. Geol.* 243 (3/4), 286–316. doi:10.1016/j.chemgeo.2007.05.022

Sláma, J., Košler, J., Condon, D. J., Crowley, J. L., Gerdes, A., Hanchar, J. M., et al. (2008). Plešovice zircon-A new natural reference material for U-Pb and Hf isotopic microanalysis. *Chem. Geol.* 249 (1–2), 1–35. doi:10.1016/j.chemgeo.2007.05.022

Steiger, R. H., and Jager, E. (1977). Subcommission on geochronology: Convention on the use of decay constants in geo- and cosmochronology. *Earth Planet. Sci. Lett.* 36 (3), 359–362. doi:10.1016/0012-821X(77)90060-7

Stump, E. (1995). *The Ross orogen of the transantarctic Mountains*. Cambridge University Press, 284.

Stump, E., Gootee, B., and Talarico, F. (2003). *Proceedings of the IX international symposium of antarctic earth sciences*. PotsdamBerlin Heidelberg New York: Springer-Verlag, 181–190.

Stump, E., Laird, M. G., Bradshaw, J. D., Holloway, J. R., Borg, S. G., and Lapham, K. E. (1983). Bowers graben and associated tectonic features cross northern Victoria Land, Antarctica. *Nature* 304, 334–336. doi:10.1038/304334a0

Sun, S. S., and McDonough, W. F. (1989). "Chemical and isotopic systematics of oceanic basalts: Implications for mantle composition and processes," in *Magmatism in the ocean basins*. Editors A. D. Saunders and M. J. Norry (London: Geological Society of London Special Publication), 313–345.

Talarico, F., Borsi, L., and Lombardo, B. (1995). Relict granulites in the ross orogen of northern victoria land (Antarctica), II. Geochemistry and palaeo-tectonic implications. *Precambrian Res.* 75, 157–174. doi:10.1016/0301-9268(95)80004-2

Talarico, F., and Castelli, D. (1995). Relict granulites in the Ross orogen of northern Victoria Land (Antarctica), I. Field occurrence, petrography and metamorphic evolution. *Precambrian Res.* 75, 141–156. doi:10.1016/0301-9268(95)80003-z

Tanaka, T., Togashi, S., Kamioka, H., Amakawa, H., Kagami, H., Hamamoto, T., et al. (2000). Jndi-1: A neodymium isotopic reference in consistency with lajolla neodymium. *Chem. Geol.* 168 (168), 279–281. doi:10.1016/s0009-2541(00)00198-4

Taylor, S. R. (1977). island arc models and the composition of the continental crust. *Union Maurice Ewing Ser.* 1, 325–335.

Taylor, S. R., and McLennan, S. M. (1985). The continental crust: Its composition and evolution. *Blackwell, Geol.* 157 (1–2), 119–146.

Thirlwall, M. F. (1991). Long-term reproducibility of multicollector sr and nd isotope ratio analysis. *Chem. Geol.* 94 (2), 85–104. doi:10.1016/s0009-2541(10)80021-x

Tiepolo, M., and Tribuzio, R. (2008). Petrology and U-Pb zircon geochronology of amphibole-rich cumulates with sanukitic affinity from Husky Ridge (northern Victoria Land, Antarctica): Insights into the role of amphibole in the petrogenesis of subduction-related magmas. *J. Petrology* 49, 937–970. doi:10.1093/petrology/egn012

Tonarini, S., and Rocchi, S. (1994). Geochronology of cambro–ordovician intrusives in northern victoria land: A review. *Terra Antarct.* 1, 46–50.

Turner, S. P., and Foden, J. (1996)., 56. South Australia, 147–169. doi:10.1007/BF01162601Magma mingling in late-Delamerian A-type granites at Mannum, South Australia*Mineralogy Petrology*

Turner, S. P. (1996). Petrogenesis of the late Delamerian gabbroic complex at Black Hill, South Australia: Implications for convective thinning of the lithospheric mantle. *Mineralogy Petrology* 56, 51–89. doi:10.1007/BF01162657

Vaughan, A. P., and Pankhurst, R. J. (2008). Tectonic overview of the west Gondwana margin. *Gondwana Res.* 13 (2), 150–162. doi:10.1016/j.gr.2007.07.004

Vervoort, J. D., and Blichert-Toft, J. (1999). Evolution of the depleted mantle: Hf isotope evidence from juvenile rocks through time. *Geochimica Cosmochimica Acta* 63 (3-4), 533–556. doi:10.1016/s0016-7037(98)00274-9

Vetter, U., and Tessensohn, F. S., (1987). S- and I-type granitoids of North Victoria Land, Antarctica, and their inferred geotectonic setting. *Geol. Rundsch.* 76 (1), 233–243. doi:10.1007/bf01820585

Volkert, R. A., Feigenson, M. D., Patino, L. C., Delaney, J. S., and Ala Drake, A. J. (2000). Sr and Nd isotopic compositions, age and petrogenesis of A-type granitoids of the Vernon Supersuite, New Jersey Highlands, USA. *Lithos* 50, 325–347. doi:10.1016/S0024-4937(99)00065-1

Wang, R. R., Xu, Z. Q., Santosh, M., Liang, F., and Fu, X. (2017). Petrogenesis and tectonic implications of the early paleozoic intermediate and mafic intrusions in the south qinling belt, central China: Constraints from geochemistry, zircon U-Pb geochronology and Hf isotopes. *Tectonophysics* 712/713, 270–288. doi:10.1016/j.tecto.2017.05.021

Wang, W., Hu, J. m., Chen, H., Yu, G. W., Zhao, Y., and Liu, X. C. (2014). La-icp-ms Zircon U-Pb ages of the Inexpressible Island intrusive rocks in north Victoria, Antarctica and their geological implications. *Geol. Bull. China* 33 (12), 9.

Weaver, S. D., Bradshaw, J. D., and Laird, M. G. (1984). Geochemistry of cambrian volcanics of the Bowers supergroup and implications for the early palaeozoic tectonic evolution of northern victoria land, Antarctica. *Earth Planet. Sci. Lett.* 68, 128–140. doi:10.1016/0012-821x(84)90145-6

Weis, D., Kieffer, B., Maerschalk, C., Barling, J., Jong, J. D., Williams, G. A., et al. (2006). High-precision isotopic characterization of usgs reference materials by tims and mc-icp-ms. *Geochem. Geophys. Geosyst.* 7 (8), 139–149. doi:10.1029/2006gc001283

Wendlandt, R. F. (1984). "An experimental and theoretical analysis of partial melting in the system $KAlSiO_4$-CaO-MgO-SiO_2-CO_2 and applications to the Genesis of potassic magmas. carbonatites and kimberlites," in *Kimberlites and related rocks*. Editor J. KRONPROBST, 359–369.

Whalen, J. B., Currie, K. L., and Chappell, B. W. (1987). A-type granites: Geochemical characteristics, discrimination and petrogenesis. *Contrib. Mineral. Pet.* 95 (4), 407–419. doi:10.1007/bf00402202

Whalen, J. B., McNicoll, V. J., van Staal, C. R., Lissenberg, C. J., Longstaffe, F. J., Jenner, G. A., et al. (2006). Spatial, temporal and geochemical characteristics of Silurian collision-zone magmatism, Newfoundland Appalachians: An example of a rapidly evolving magmatic system related to slab break-off. *Lithos* 89, 377–404. doi:10.1016/j.lithos.2005.12.011

Wilson, M., Downes, H., and Cebriá, J. M. (1995). Contrasting fractionation trends in coexisting continental alkaline magma series; cantal, massif central, France. *J. Petrology* 36, 1729–1753.

Wu, F. Y., Sun, D. Y., Li, H. M., Jahn, B. m., and Wilde, S. (2002). A-type granites in northeastern China: Age and geochemical constraints on their petrogenesis. *Chem. Geol.* 187 (1/2), 143–173. doi:10.1016/s0009-2541(02)00018-9

Wu, R. X., Zheng, Y. F., Wu, Y. B., Zhao, Z. F., Zhang, S. B., Liu, X. M., et al. (2006). Reworking of juvenile crust: Element and isotope evidence from neoproterozoic granodiorite in south China. *Precambrian Res.* 146, 179–212. doi:10.1016/j.precamres.2006.01.012

Wu, Y. B., and Zheng, Y. F. (2004). Genesis of zircon and its constraints on interpretation of U-Pb age. *Chin. Sci. Bull.* 49 (15), 1554–1569. doi:10.1360/04wd0130

Yang, J. H., Sun, J. F., Zhang, M., Wu, F. Y., and Wilde, S. A. (2012). Petrogenesis of silica-saturated and silica-undersaturated syenites in the Northern North China Craton related to post-collisional and intraplate extension. *Chem. Geol.* 328, 149–167. doi:10.1016/j.chemgeo.2011.09.011

Zhang, W., Hu, Z. C., and Liu, Y. S. (2020). Iso-compass: New freeware software for isotopic data reduction of LA-MC-ICP-MS. *J. Anal. At. Spectrom.* 35, 1087–1096. doi:10.1039/d0ja00084a

Zhang, W., and Hu, Z. (2020). Estimation of isotopic reference values for pure materials and geological reference materials. *At. Spectrosc.* 41 (3), 93–102. doi:10.46770/as.2020.03.001

Zheng, Y. F., Zhang, S. B., Zhao, Z. F., Wu, Y. B., Li, X. H., Li, Z. X., et al. (2007). Contrasting zircon Hf and O isotopes in the two episodes of neoproterozoic granitoids in south China: Implications for growth and reworking of continental crust. *Lithos* 96, 127–150. doi:10.1016/j.lithos.2006.10.003

Zong, K. Q., Klemd, R., Yuan, Y., He, Z. Y., Guo, J. L., Shi, X. L., et al. (2017). The assembly of Rodinia: The correlation of early Neoproterozoic (ca. 900 Ma) high-grade metamorphism and continental arc formation in the southern Beishan Orogen, southern Central Asian Orogenic Belt (CAOB). *Precambrian Res.* 290, 32–48. doi:10.1016/j.precamres.2016.12.010

frontiers | Frontiers in Earth Science

TYPE Original Research
PUBLISHED 12 January 2023
DOI 10.3389/feart.2022.1017632

Check for updates

OPEN ACCESS

EDITED BY
Fei Xue,
Hohai University, China

REVIEWED BY
Yunjian Li,
Hohai University, China
Chunhui Song,
China University of Mining and Technology, China
Guangwei Zhang,
National Institute of Natural Hazards, China

*CORRESPONDENCE
Fangbin Liu,
liufangbin8908@163.com

†These authors have contributed equally to this work and share first authorship

SPECIALTY SECTION
This article was submitted to Structural Geology and Tectonics, a section of the journal Frontiers in Earth Science

RECEIVED 12 August 2022
ACCEPTED 24 October 2022
PUBLISHED 12 January 2023

CITATION
Liu C, Liu F, Cai Y, Ni R, Xu X, Li G, Hao W and Tian Z (2023), The present-day stress field along the Northwest Pacific Wadati-Benioff zone constrained by focal mechanisms of moderate earthquakes.
Front. Earth Sci. 10:1017632.
doi: 10.3389/feart.2022.1017632

COPYRIGHT
© 2023 Liu, Liu, Cai, Ni, Xu, Li, Hao and Tian. This is an open-access article distributed under the terms of the Creative Commons Attribution License (CC BY). The use, distribution or reproduction in other forums is permitted, provided the original author(s) and the copyright owner(s) are credited and that the original publication in this journal is cited, in accordance with accepted academic practice. No use, distribution or reproduction is permitted which does not comply with these terms.

The present-day stress field along the Northwest Pacific Wadati-Benioff zone constrained by focal mechanisms of moderate earthquakes

Chengyu Liu[1†], Fangbin Liu[2*†], Yin Cai[1], Ran Ni[3], Xiujie Xu[1], Guoyi Li[1], Weiduo Hao[4] and Zhaoyang Tian[5]

[1]Shandong Earthquake Agency, Ji'nan, China, [2]Key Laboratory of Western China's Environmental Systems, Ministry of Education, College of Earth and Environmental Sciences, Lanzhou University, Lanzhou, China, [3]Qilu Normal College, Ji'nan, China, [4]Department of Earth and Atmospheric Sciences, University of Alberta, Edmonton, AB, Canada, [5]Shandong Provincial Key Laboratory of Marine Environmental and Geology Engineering, Ocean University of China, Qingdao, China

The present-day stress field in the northwest Pacific Wadati-Benioff Zone (WBZ) has been investigated on the basis of earthquake focal mechanism catalog covering the period from 2012 to 2021. Our catalog contains 201 focal mechanism solutions (Mw 4.0–5.9) compiled from the F-net network along three profiles (southern Kurile trench, central Japan trench and northern Izu-Bonin trench). According to the spatial variations in the stress regimes, we outlined 12 subvolumes for three profiles. Our results present that the maximum compressive stress is, slab-normal in trench-outer rise regions and nearly strike-normal and sub-horizontal in the depth range 0–70 km. At intermediate depths, a two-planar stress pattern is observed (70–200 km) in southern Kurile and central Japan trench WBZ, with the maximum compressive stress closely parallel to the slab in upper plane and slab-normal in lower plane, respectively. However, the southern Kurile trench WBZ exposes an extension stress regime in 200–300 km depth range. At depths below 300 km, northern Izu-Bonin trench WBZ shows a stress regime of pure compression. We infer the dominant forces may be the slab blending in the shallow trench-outer rise regions, slab pull and ridge push at shallow depths, and the slab resistance provided by the mantle to the penetration of the slab at deep depths. Whereas the two-planar stress pattern may be caused by the unbending of the slab, and the unusual stress state along the junction of the trench WBZ at intermediate depths may be influenced by lateral deformation due to increasing slab's dip.

KEYWORDS

focal mechanisms, Wadati-Benioff zone, stress field, Northwest Pacific plate, F-net

Introduction

Subduction zones are home to the most seismically active faults on Earth (Hayes et al., 2018). The Northwest Pacific subduction zone, located at the eastern edge of the Eurasian continent, is one of the most typical subduction zones in the world (Figure 1A) Schellart et al., 2007; Sandiford et al., 2020). At the Northwest Pacific margin, the Pacific plate is subducting west-northwestward the North American plate from the Kuril and Japan trenches at a rate of ~8.2–9.2 cm/yr, and meanwhile subducting beneath the Philippine Sea plate at ~5.5 cm/yr (Figure 1A) (Seno et al., 1993; DeMets et al., 1994; Schellart et al., 2007; Wei et al., 2015; Gong et al., 2021). As a product of the mutual subduction collision between different plates, numerous earthquakes (Figure 1B) occurred on the subducting Pacific slab and formed a clear Wadati-Benioff Zone (WBZ) that extends down to the mantle transition zone. Besides, the Northwest Pacific subduction zone has a typical "trench-arc-basin" system with magmatic activities and regional metamorphism (Forsyth and Uyedaf, 1975; Schellart et al., 2007; Liu et al., 2017; Yang et al., 2018; Liu et al., 2022). Such complex and intense tectonics has characterized this region with a complicated stress state.

Knowledge of the crustal stress field is a prerequisite for understanding the kinematics and distribution of continental deformation (Konstantinou et al., 2017; Liu et al., 2021). Focal mechanism solutions (FMS) of earthquakes and their spatial distributions play a key role in evaluating tectonic/local stress fields (Townend and Zoback, 2006; Terakawa and Matsu'ura, 2010; Saito et al., 2018; Song et al., 2022). Many scholars have carried out a series of stress field analyses in the Pacific WBZ based on the spatial variation of the stress regimes. The stress

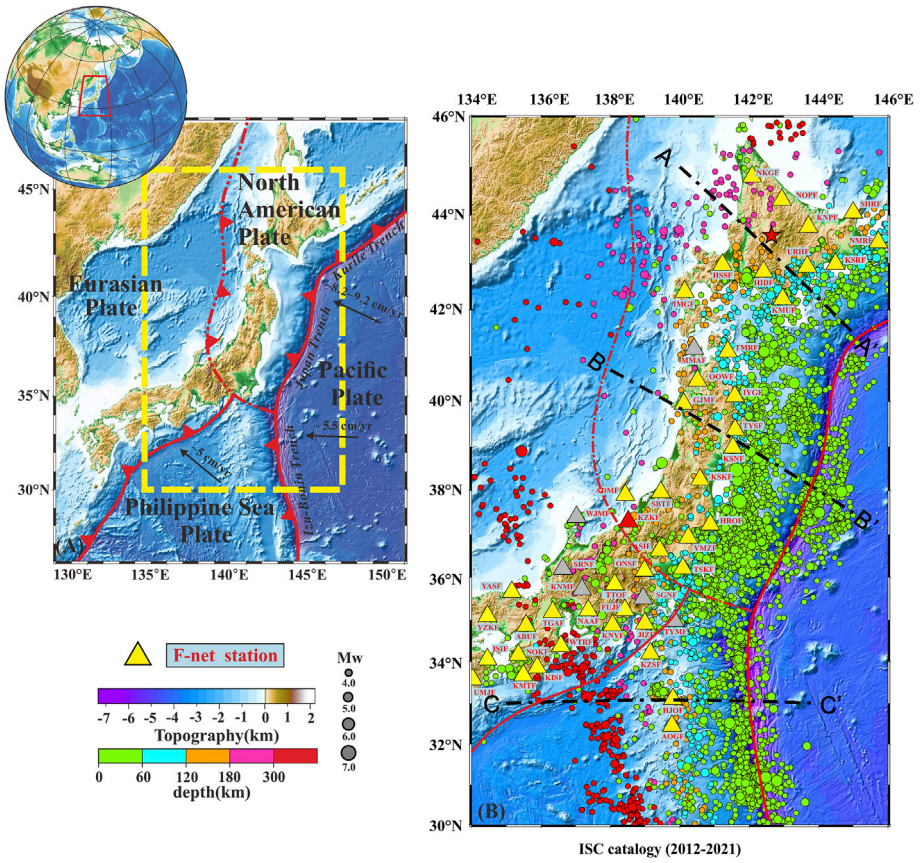


FIGURE 1
(A) Topography of the Northwestern Pacific Ocean; The black arrows show an estimate of the motion (cm/year) of the Pacific Plate relative to the North American Plate and Philippine Sea Plate. The red solid (dash) line and represents the boundary (presumed boundary) of the plates, with red triangles on it indicating the direction of movement of the plates. The names of the three trenches are described in orange italic letters. **(B)** The seismicity with the Mw ≥4.0 of the study area (2012–2021). The seismicity from the ISC catalogue is denoted by the dots. The depth and magnitude of earthquakes are shown by the color bar and sizes of the dots, respectively. The location of the study area is denoted by the yellow box in **(A)**. The black solid lines illustrate the trench-normal profiles (LINE A-A', B-B', and C-C'). The triangles represent the stations of F-NET. The yellow ones represent the stations used for moment tensor inversion in this paper, while the other stations of F-NET are in grey. The red star in the northeast of the figure represents the location of a reverse faulting event as an example of earthquake waveform fitting using the Mttime technology.

models have been proposed in previous studies such as 1) the stress state within the subducting plate varies with the geotectonic position and thrust depth (e.g., Yoshida et al., 2015; Maeda et al., 2020; Gong et al., 2021); 2) the stress pattern in Kurile trench WBZ and Japan trench WBZ with the down-dip compression in the upper plane and down-dip tension in the lower plane at intermediate-depth (e.g., Hasegawa et al., 1979; Kita et al., 2010; Reynard et al., 2010; Florez and Prieto, 2019) and 3) the non-parallel directional stress states to slab subduction in some shallow and deep depth (e.g., Christova, 2015; Li and Chen, et al., 2019). These efforts enriched our recognition of the shape and dynamics processes of subducting plate. The present-day stress field, however, remains highly controversial along the Northwest Pacific WBZ (especially double seismic zone), which may be attributable to the different time periods of data collection, the various FMS datasets, and different evaluation methods used. In addition, it remains enigmatic whether the stress field characteristics are consistent between different trenches (e.g., Kuril, Japan, and Izu-Bonin) within the Northwest Pacific subduction system.

To address the above questions, we accurately inverted the Centroid Moment Tensor of moderate earthquakes (Mw 4.0–5.9) and established a new high-quality dataset of FMS to investigate the stress field along the Northwest Pacific WBZ. Combined with previous geological and geophysical analysis, we aim to provide a more robust comparative analysis of the stress field at the different depths of trench WBZ and tectonic position. Our findings provide new insight into stress states and intrinsic dynamical mechanisms along the WBZ in southern Kuril, central Japan, and northern Izu-Bonin trenches.

Data and method

Dataset

For this study, we used seismic waveform data that have been recorded by the regional broadband stations of F-net (Okada et al., 2004; Kimura et al., 2015; NIED, 2019) in the time span between 2012 and 2021 (Figure 1A). A total of 201 earthquakes with $4.0 \leq Mw < 6.0$ were collected along the southern Kurile arc, the central Japan arc, and the northern Izu-Bonin arc (Figure 3A; Table 1). Accordingly, we eliminated all the earthquakes above Mw 6.0, since large earthquakes can have important effects on the short-term stress field and cause stress field deviation (Huang et al., 2011; Yoshida et al., 2012; Yoshida et al., 2016a, 2016b; Hardebeck and Okada, 2018; Sheng and Meng, 2020). Meanwhile, indicated by the distribution of the epicenters from ISC earthquake catalogue (http://ds.iris.edu), seismic profiles with widths of 60–100 km were firstly selected with Mw greater than 4.0 for a period between 1 January2017 and 31 December 2021. Due to the lack of seismic events at depth range 70–180 km in profile A-A' and profile B-B', we then expanded the geographic width of the profile and extended the time interval (Table 1). In addition, the principles of seismic profile selection are to cover as many intermediate to deep source earthquakes as possible, and we excluded seismic events that were clearly far from the subduction zone based on their epicenter distribution. Afterwards, we inverted the FMS *via* these data and the following method.

Focal mechanism calculation

We utilize the Mttime software to determine FMS of selected earthquakes (Chiang, 2019). Mttime is a procedure developed for time domain inversion of full seismic waveform data to obtain the Centroid Moment Tensor. This technique employs a time-domain, generalized least squares inversion method (Minson and Dreger, 2008), and the details of the procedure are described in previous work (e.g., Dreger,2003; Chiang et al., 2016). The waveforms were firstly instrument corrected to ground displacement, rotated to the great-circle path, decimated to one sample per second and filtered between 0.05 and 0.2 Hz. Then, after constructing the velocity model, synthetic seismograms were generated using the frequency-wavenumber integration method through the "Computer Programs in Seismology" software package proposed by Herrmann (2013). The same filtering and down-sampling parameters are applied to the synthetic seismograms. Finally, the FMS were estimated according to the maximum variance reduction (VR) percentage between the observed waveforms and synthetic data. In the step of generating synthetic seismograms, we adopted a one-dimensional (1-D) velocity structure model (Table 2) derived from NIED (https://www.fnet.bosai.go.jp/faq/) and Kubo et al. (2002). We set searching step to 5–10 km firstly when conduct moment tensor inversion, and then we perform the inversion again around optimal solution of the initial inversion and set searching step to 1 km. The inversion method also allows for small time shifts between the data and synthetic seismograms to compensate for uncertainties in origin time, location, and velocity structure (Pasyanos and Chiang, 2020). The depth with the optimum fit is taken as an estimate for focal depth, and the corresponding source mechanism provides an estimate for the moment tensor. The results are demonstrated in the form of the double couple component with the scalar moment (Mo), FMS depth, strike, dip, and rake.

Stress field inversion

One of the challenges in stress field determination from FMS is the ambiguous choice of a fault plane from the two nodal planes. Compared with previous stress field inversion (Gephart and Forsyth, 1984; Michael, 1984, 1987; Zoback, 1992; Delvaux and Barth, 2010), we used an updated iterative stress inversion

TABLE 1 The information of each profile.

Profile	Start: Finish	Depth			
		0–70 km	70–180 km	180–300 km	300–500 km
A-A'	140°E, 45°N 145°E, 41.5°N	Width: 60 km	Width: 120 km	Width: 60 km	—
		Period: 2017–2021	Period: 2012–2021	Period: 2017–2021	—
B-B'	137°E, 40.8°N 145°E, 37.5°N	Width: 60 km	Width: 200 km	—	—
		Period: 2017–2021	Period: 2012–2021	—	—
C-C'	135°E, 33°N 144°E, 33°N	Width: 100 km	Width: 100 km	Width: 100 km	Width: 100 km
		Period: 2017–2021	Period: 2017–2021	Period: 2017–2021	Period: 2017–2021

TABLE 2 Velocity structure for the used Green Function (Kubo et al., 2002).

Depth (km)	Thichness (km)	V_P (km/s)	V_S (km/s)	RHO (gm/cc)	Q_P	Q_S
0	3.0000	5.50	3.14	2.30	600.00	300.00
3	15.0000	6.00	3.55	2.40	600.00	300.00
18	15.0000	6.70	3.83	2.80	600.00	300.00
33	67.0000	7.80	4.46	3.20	600.00	300.00
100	125.0000	8.00	4.57	3.30	600.00	300.00
225	100.000	8.40	4.80	3.40	600.00	300.00
325	100.000	8.60	4.91	3.50	600.00	300.00
425	—	9.30	5.31	3.70	600.00	300.00

method based on the Mohr-Coulomb failure criterion, for identifying the fault plane based on evaluating the fault instability (Michael, 1984, 1987; Vavryčuk, 2011, 2014). The iterative joint stress inversion can be run using the open STRESSINVERSE code written in Python available at http://www.ig.cas.cz/stress-inverse. Random bootstrap uncertainty assessments using 2,000 re-samplings of the original input are performed to calculate uncertainties with 95% confidence level. The stress inversion allows us to estimate the orientation of the principal stress axes and the shape ratio $R = \frac{(\sigma_2-\sigma_1)}{(\sigma_3-\sigma_1)}, 0 \le R \le 1$, where σ_i are the principal stresses. The value of R estimates the magnitude of the intermediate principal stress (σ_2) relative to the maximum (σ_1) and the minimum (σ_3) principal stresses. When $R = 0$, σ_3 remains relatively stable, σ_1 and σ_2 rotate freely in the plane perpendicular to σ_3, and both are in compression; when $R = 0.5$, the σ_1, σ_2 and σ_3 are relatively stable; When $R = 1$, σ_1 is relatively stable, σ_3 and σ_2 are free to rotate in the plane perpendicular to σ_1, and both are in tension (Guiraud et al., 1989; Wan et al., 2011; Cui et al., 2019). Furthermore, we evaluate the relative homogeneity of the regional stress field by the average misfit angle β between the observed and predicted slip directions of the focal mechanisms (Michael et al., 1990; Michael, 1991; Sheng and Meng, 2020). Michael, (1991) found that this requirement can be satisfied when β is <~35–45°, assuming that the focal mechanism error is on the order of ~10–20°. In this paper, considering the accuracy of FMS, we strictly set the lower limit of β as 35°. When $\beta \le 35°$, we suggest the stress field to be homogenous.

Results

We obtained a total of 201 FMS in our study area, among them, the number of solutions in profiles A-A', B-B', and C-C' are 42, 96, and 63 respectively (Figure 4; Table 3). The depths of all events range from 5 to 450 km (Table 3; Supplementary Table S1). In the waveform inversion, we conducted the inversion quality by the number of stations used, the percentage of double-couple (DC) and VR between the observed waveforms and synthetic data. We excluded the data that the number of stations used for inversion less than 3 and the VR< 0.5. Figure 2 shows an example of earthquake waveform fitting using the Mttime technology. This earthquake event occurred on 20 June 2021 in profile A-A' (Figure 1B). The upper panel shows the waveforms fitting between vertical, radial and tangential components of waves. The robust and reliable results show high VR and DC% value, with the number of stations used for inversion more than 3. The lower panel

TABLE 3 Results of the stress inversion.

Profile	S.V	Depth (km)	E.N	*R*	σ_1		σ_2		σ_3		β
					Azi (°)	Plu (°)	Azi (°)	Plu (°)	Azi (°)	Plu (°)	
A-A'	Ra1	0–65	16	0.55	101	8.2	197.7	39.1	1.2	49.7	35.0
	Ra2	80–200	8	0.60	288.7	38.3	171.5	30.1	55.4	37.2	12.3
	Ra3	65–170	9	0.16	198.1	59.1	96.6	6.8	2.7	29.9	11.9
	Ra4	200–280	9	0.15	177.8	55.1	303.0	21.9	44.2	25.7	25.8
B-B'	Rb0	0–35	14	0.77	345.2	78.9	191.5	10.0	100.6	4.8	23.9
	Rb1	0–70	56	0.72	108.4	29.1	16.9	2.8	281.9	60.7	16.6
	Rb2	70–140	19	0.71	286.9	25.0	194.4	5.4	93.0	64.3	21.3
	Rb3	100–195	9	0.69	351.2	82.1	179.1	7.8	88.9	1.1	23.7
C-C'	Rc0	0–20	5	0.82	7.5	69.8	157.5	17.7	250.6	9.5	3.8
	Rc1	0–70	36	0.71	91.9	1.1	1.6	17.3	185.3	72.7	29.3
	Rc2	70–210	10	0.93	335.6	20.6	235.2	25.8	99.4	56.0	53.8
	Rc3	320–420	15	0.52	289.4	21.6	193.9	13.7	73.9	64.1	19.3

S.V, is the subvolume we divided in each profile; E. N, is the number of events in each profile; R, is the stress ratio; Azi, is the Azimuth; Plu, is the Plunge; β, is the average misfit angle.

shows that the FMS depth is constrained at 160 km, while the magnitude is Mw 5.45. The same procedure is used to obtain FMS for the remaining earthquakes in the three profiles. All FMS we conducted are available in Supplementary Material (Supplementary Table S1). The distribution of the FMS in this study area is projected into Figure 3.

According to the spatial variations in the stress regimes, we divided them into 12 WBZ subvolumes for three profiles (Figure 4; Supplementary Table S1). The principles of classification are as follows.

Firstly, Rb0 and Rc0 were outlined separately since they are located in the region of trench-outer rise, where a subducting oceanic plate begins to flex and descends into the trench (Lefeldt and revemeyer, 2008; Moscoso and Grevemeyer, 2015; Hatakeyama et al., 2017). Secondly, according to Gutenberg & Richter (1954), shallow, intermediate and deep earthquakes have traditionally been defined as those in the approximately 0–70 km, 70–300 km, and above 300 km. Meanwhile, indicated by the distribution of the epicenters (Figure 5), the dips of the WBZ are not the same in different depth intervals. We can clearly see that along profile A-A' (Figure 5A), the dip of the WBZ is about 15°at shallow depths and then turns to steeper approximately 30° at intermediate depths. Figure 5B shows that the dip of the WBZ along profile B-B' is about 30° at shallow depth, while turn to about 60°at intermediate depths. Along profile C-C' (Figure 5C), corresponding to the shallow, intermediate and deep depths, the dips of the WBZ are characterized by a complex change from 30° to 60°–45°. Therefore, Ra1 and Rb1 and Rc1 were defined as the shallow portion of the WBZ with depths between 0 and 70 km. However, the outline of subvolumes at intermediate depths is complex, since the possible existence of a double seismic zone at intermediate depths (e.g., Brudzinski et al., 2007; Hasegawa and Nakajima, 2017; Florez and Prieto, 2019). The outlining of WBZ subvolumes here is carried out manually, based on a detailed analysis of the orientation spatial distribution of the P and T axes of the individual earthquake FMS. Then we outlined 6 subvolumes at intermediate depths namely Ra2, Ra3, Ra4, Rb2, Rb3, Rc2. Finally, Rc3 was outlined as the deep portion (300–500 km) of the WBZ. In order to further analyze the faulting types and distribution of FMS in the study area, we categorized the data using a ternary visualization (Kaverina diagram) of the relative proportion of variations in normal, thrust, and strike-slip faulting components for the respective profiles (Figure 6).

In the trench-outer rise regions (Rb0 and Rc0), the P axes for a depth range of 5–35 km cluster around the slab normal, but the T axes, while lying in the slab plane, show a greater range of directions (Figure 4). The results are consistent with the stress inversions, showing slab normal σ_1 and slab horizontal σ_3 within its 95% confidence ranges (Figure 7; Table 3). Such stress inversions indicate that the slab plane is under a pure extensional stress regime dominated by the normal earthquakes type (Figures 6E,I).

In a shallow portion of the WBZ (Ra1 and Rb1 and Rc1), we can clearly see that the dominant faulting style is characterized by a considerable number of reverse faulting earthquakes (Figures 6A,F,J) which have steeply plunging T and gently plunging P axes.

In addition, the distribution of P and T axes at intermediate depths (70–300 km) are more complex, as well as faulting types. Notably, Double Seismic Zones existed in the shallow portion of intermediate-depth (70–180 km) of profiles A-A' and B-B' (Figures 4A,B). There are distinct interfaces, in which the distribution of P and T axes varies significantly.

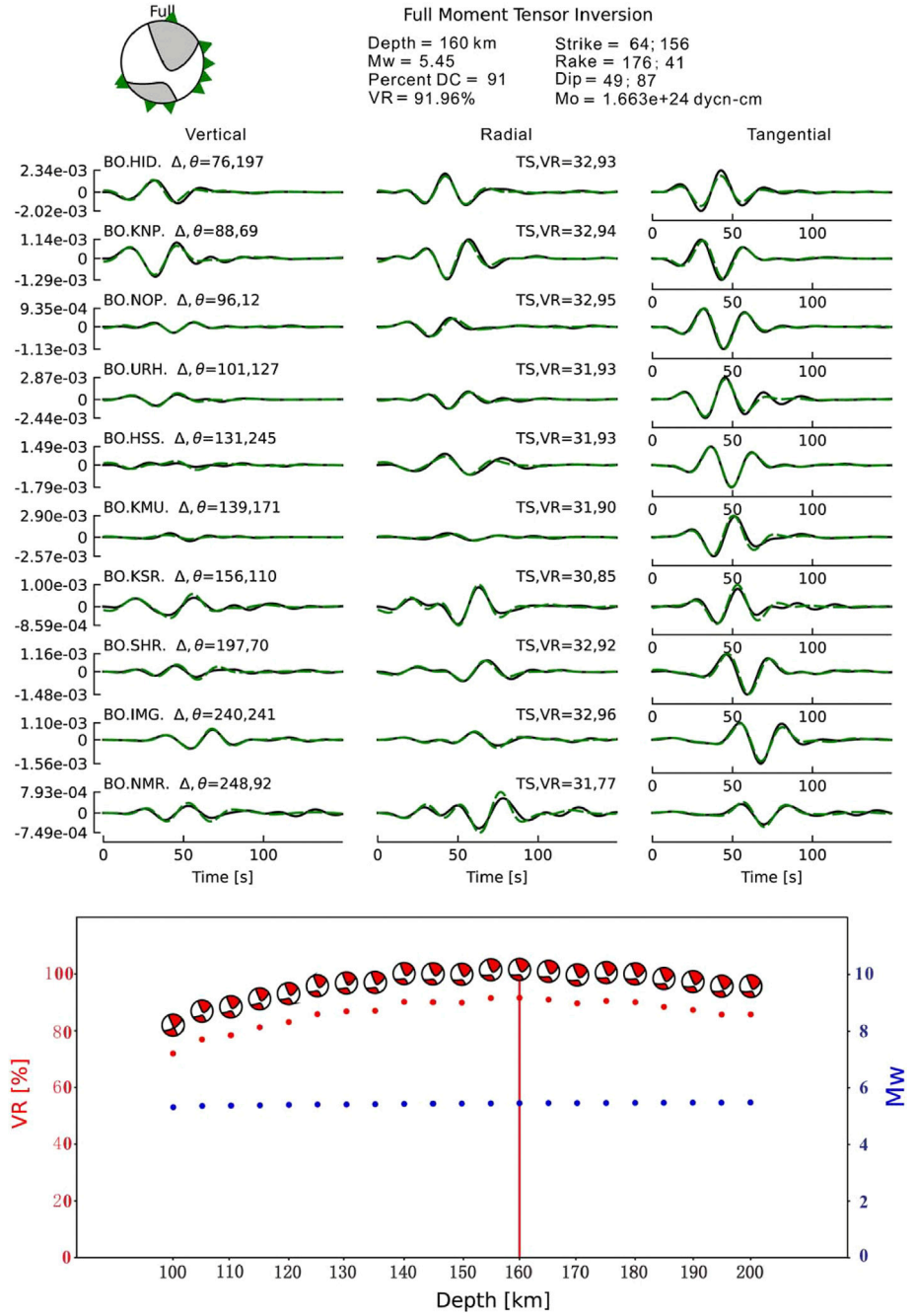


FIGURE 2
A reverse faulting event in the Profile A-A'. The location of this event is indicated by a red star in Figure 1B. Top panel shows the best solution and waveform fits (the black observed and green synthetic waveforms) at selected stations. Green triangles around the beach ball indicate station azimuth, and the numbers below the radial and vertical component seismograms are, from left to right: distance, azimuth, time shift in samples, and station-specific VR. Bottom panel shows the solution, in terms of waveform fits (variance reduction; VR) and Mw, with respect to FMS depth.

Subvolumes in the upper WBZ plane (UP), i.e., above the interfaces, were named Ra2 and Rb2, while lower WBZ plane (LP), i.e., below the interfaces, were named Ra3 and Rb3, respectively. A notable feature of Double Seismic Zones in profile A-A' is that the Ra2 (UP) favors oblique strike-slip with a reverse component faulting, while the dominant faulting style in Ra3 (LP) is normal with a strike-slip component (Figures 6B,C). In profile B-B', the Double Seismic Zone is

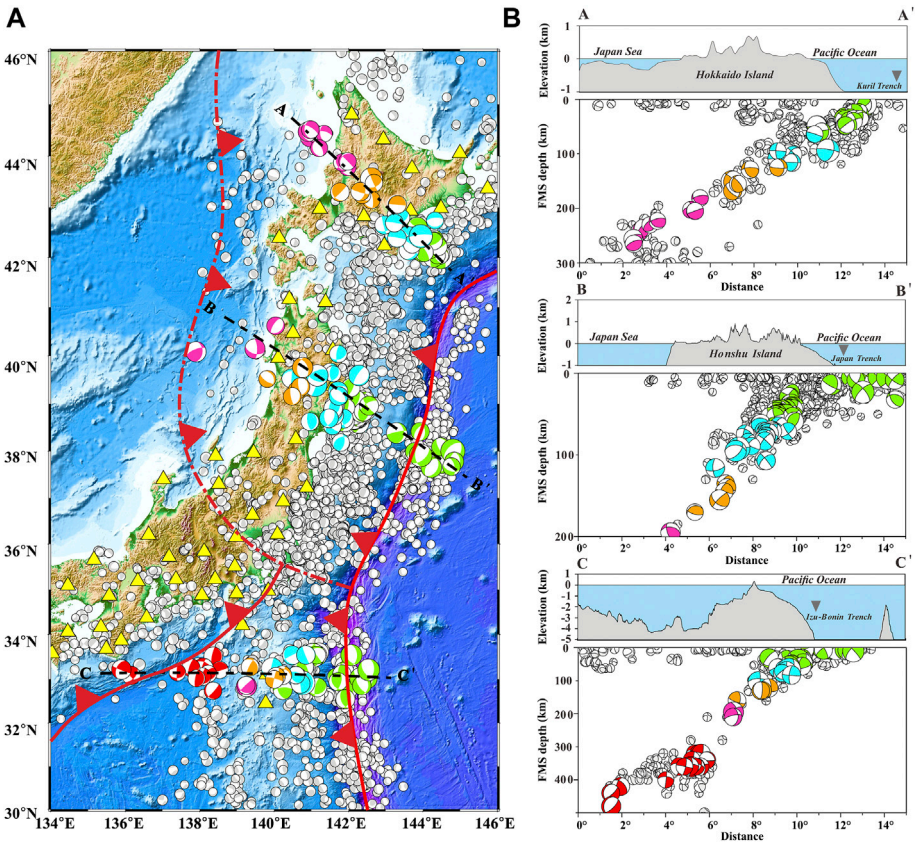


FIGURE 3
Focal mechanism solutions (FMS) in study area with the lower hemisphere projected onto the plane. The red solid (dash) line and represents the boundary (presumed boundary) of the plates, with red triangles on it indicating the direction of movement of the plates. Three tectonic segments (Profile A-A′ and B-B′ and C-C′) are plotted with black dotted lines. The boundaries of the plates are indicated by the red lines and stations are shown in yellow triangles. Beach balls with color-filled compressional quadrants were calculated in this study. The solutions with gray-filled compressional quadrants are from Japan Meteorological Agency (JMA) with time period 2012–2021. Compressional quadrants of all shallow (≤60 km) FMS are green in color. FMS with FMS depth ranges 60–120 km, 120–180 km, 180–300 km are cyan, orange, and pink in color, respectively. Compressional quadrants of all deep (300–500 km) of FMS are red in color. The Mechanisms are magnitude-wise size scaled (the colored beach balls have twice the radius of gray ones). **(B)** Depth-wise distribution of faulting mechanism solutions (the hemisphere behind the vertical plane is projected onto the plane) across the profiles are shown in **(B)**. Corresponding topography, along the same profile lines are plotted above with the sea level below filled with light blue. Labeled inverted grey triangles represent the location of the trench. Topographic data is from Tozer et al. (2019). The color of the FMS compressional quadrants is the same as that in **(A)**.

characterized by reverse faulting with steeply plunging T axes in Rb2 (UP) and normal faulting with steeply plunging P axes in Rb3 (LP) (Figures 6G,H). Ra4 belongs to the deep portion of intermediate depths (200–300 km). This subvolume is dominated by the normal fault with a strike-slip component, in which the T axes cluster within the NE quadrant, and P axes scatter within the SW quadrant (Figures 4A, 6D). At deep depths (300–500 km), Rc3 is dominated by the reverse fault with the P axes clustered in NW quadrant and the T axes scattered in SE quadrant (Figures 4C, 6L).

Discussion

Table 3 lists the number of the input data, and the best-fit stress models obtained for the considered WBZ subvolumes: the directions of σ_1, σ_2, σ_3, the R-value estimate, the average misfit angle β, and depth. Obviously, most WBZ subvolumes can reflect the homogeneous stress field characteristics. However, in Rc2, the value of β exceeds the threshold reflecting the inhomogeneous stress field. Therefore, it is not meaningful to study its stress state. In the following, we analyze and discuss the stress field in four parts.

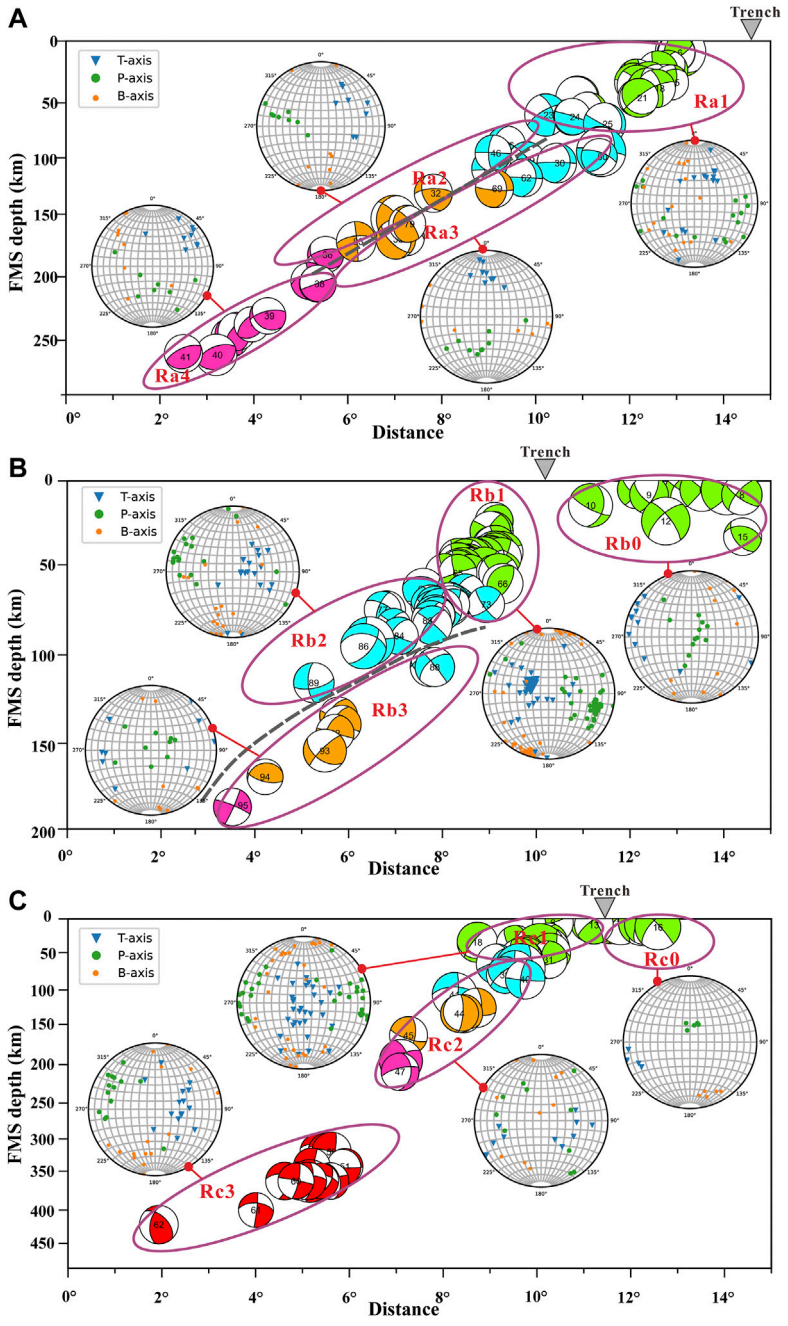


FIGURE 4
The outlining of WBZ subvolumes of homogeneous stress field, based on a detailed analysis of the orientation spatial distribution of the P and T axes in Profile A-A′ **(A)** and B-B′ **(B)** and C-C′ **(C)**, respectively. Stereographic projection of the P (green dots) and T (blue inverted triangles) and B axes (yellow polygons) of the focal mechanisms are plotted next to the subvolumes and linked by a red solid line. Stereographic projection diagrams were produced using an open-source python package named mplstereonet (version 0.6.2). The gray dashed lines in **(A,B)** show the interface of WBZ upper and lower plane. The number in the center of focal mechanisms corresponds to the events number in Supplementary Table S1.

The stress field in trench-outer rise regions

As described in the above section, the Rb0 and Rc0 represent trench-outer rise regions in the Northwest Pacific plate subduction system (Figure 4). We clearly observe that most of FMS are normal-faulting type in these regions (Figures 6E,I). The stress tensors in both subvolumes are almost similar (Figure 7; Table 3), showing the slab-normal σ_1 and sub-horizontal σ_3. The shape ratios (R values) in Rb0 and Rc0 are 0.77 and 0.82, respectively, indicating a stable σ_1.

The above analysis shows that the region of shallow trench-outer rise is most likely under a pure tension regime, which is consistent with the previous studies (Emry and Wiens, 2015; Uchida et al., 2016; Gong et al., 2021). The force driving the normal-faulting in these regions is attributed to slab pull prior to subduction, which causes the elastic lithosphere bending (Hatakeyama et al., 2017; Obana et al., 2019; Contreras-Reyes et al., 2021). The shallow extensional stress regime also explains bending-related normal faults that are widely observed in such regions (e.g., Obana et al., 2019), which may play an important role in promoting water circulation in subduction zones. According to Ranero et al. (2003), a large normal fault event that ruptures the surface may provide a pathway for sea water to penetrate the mantle. The amount of water brought into the mantle is related to the maximum depth of tension fault cut into the lithosphere which is directly linked to the maximum FMS depths (Lefeldt and Grevemeyer, 2008). As a consequence, the hydrated oceanic lithosphere produces a reduction of crustal and upper mantle velocities, supporting serpentinization of the upper mantle (Lefeldt and Grevemeyer, 2008; Moscoso and Grevemeyer, 2015; Hatakeyama et al., 2017).

The stress field in double seismic zones

Double Seismic Zones are ubiquitous features of subduction zones (Brudzinski et al., 2007; Reynard et al., 2010; Florez and Prieto, 2019). Earthquakes within the subducted lithosphere cluster into two distinct layers, that eventually merge at depth (Green II et al., 2010; Hasegawa and Nakajima, 2017; Wei et al., 2017).

In Ra2 (UP), σ_1 is closely parallel to the slab, while σ_3 is NE trending with a gentle plunging (37.2°), i.e., close to in-slab all along the arc. The R value is 0.6, implying a relatively stable σ_1. In Ra3 (LP), the best-fit stress models obtained show close to slab-normal σ_1 with a steeply plunging (59.1°) and close to slab-parallel σ_3 (N2.7°E) with a gentle plunging (29.9°). The R value is 0.16, implying a very stable σ_3. Compared with the stress state in Ra2 and Ra3, the azimuth of σ_1 is rotated counter-clockwise by 90° from NWW (288.7°) in Ra2 to the SSW (198.1°) in Ra3. Our model indicates that the dominant stress regime in Ra2 and Ra3 shifts from general compression to general extension (Guiraud et al., 1989).

In Rb2 (UP), the best-fit stress models show close to slab-parallel σ_1 (286.9°), the σ_3 is close to slab-normal. The intermediate compression σ_2 is almost horizontal trending NE close to in-slab all along the arc. In Rb3 (LP), the best-fit stress models show close to slab normal σ_1 and close to slab-parallel σ_3. The intermediate compressive stress σ_2 is close to in-slab. The R value in Rb2 is 0.71 while in Rb3 is 0.69, both implying relatively

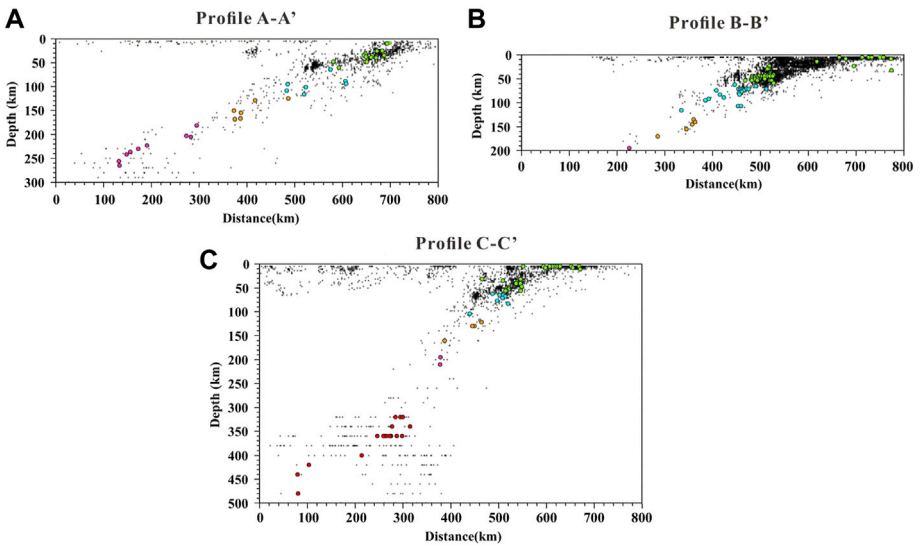


FIGURE 5
The distribution of earthquakes on Profile A-A' **(A)**, B-B' **(B)** and C-C'**(C)**. The seismicity from the Japan Meteorological Agency (JMA) catalogue is denoted by the small black dots for a period from 2012–2021. The larger dots represent the events that we selected for the focal mechanism calculation in this study. The color of these dots indicates the source depth which is consistent with Figure 1B.

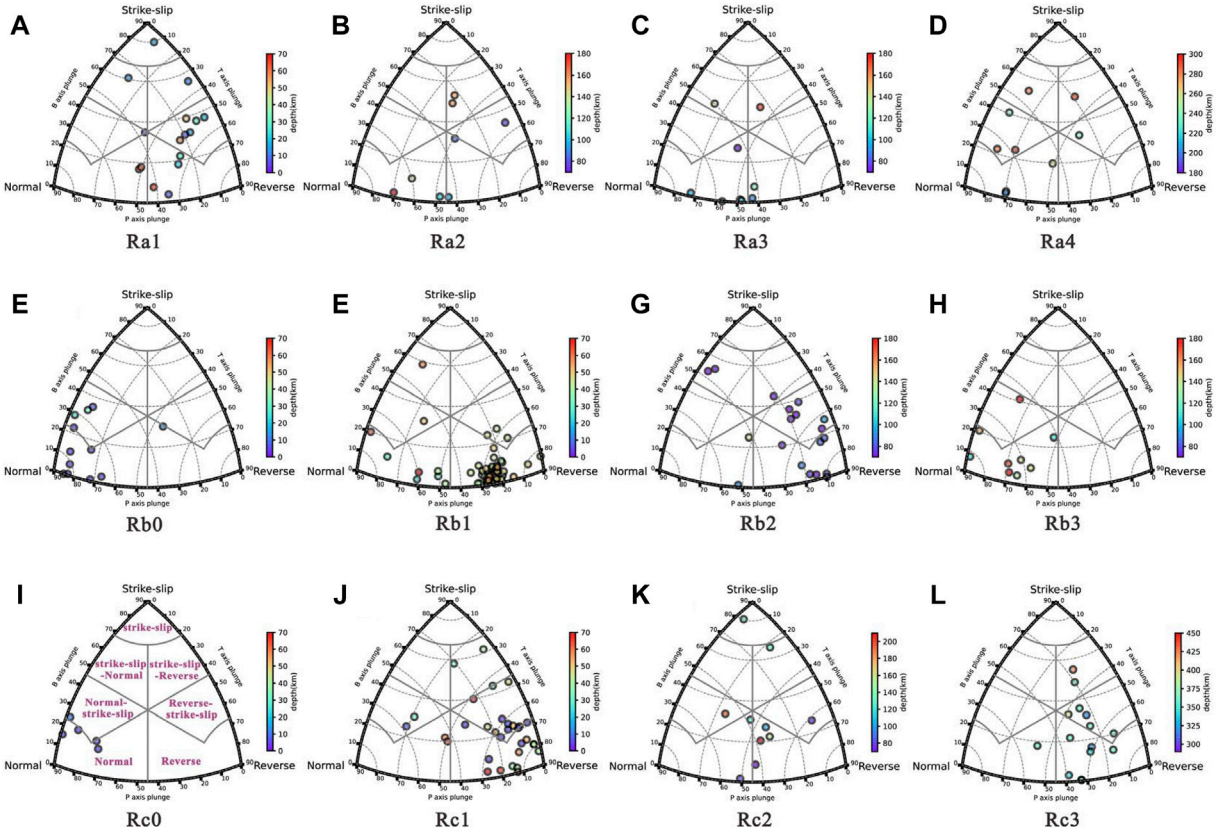


FIGURE 6
(A–L): A ternary diagram representing the distribution of earthquake faulting characteristics at various profiles. Ternary diagrams representing the distribution of earthquake faulting characteristics at various profiles. It is plotted as a function of the orientation of the P, T, and B-axes for the thrust, normal, and strike-slip faulting earthquakes. The ternary classification is based on Frohlich (1992) and visualized using Álvarez-Gómez (2019). The reader may refer the panel I for a general distribution of the faulting regimes in a ternary classification. Events are represented by color filled circles based on depth (scale on the right).

stable σ_1. Our model indicates that the dominant stress regime in Ra2 is pure compression while in Ra3 is pure extension (Guiraud et al., 1989).

Overall, we find that the UP and LP have almost opposite stress states. The stress regime in UP is dominantly down-dip compression type while in LP is dominantly down-dip tension type. The findings are consistent with the typical stress model of Double Seismic Zones, which is described in the previous studies (Hasegawa et al., 1979, 1994; Christova, 2015; Li & Chen, 2019).

In the last century, several mechanisms have been proposed to explain the coexistence of parallel compression and tension of the slabs observed at Double Seismic Zones, including sagging of the plate (Sleep, 1979; Yoshii, 1979), thermoelastic stress (Fujita and Kanamori, 1981; Goto et al., 1985), and unbending of the slab (Engdahl and Scholz, 1977; Kawakatsu, 1986). However, the recent dehydration-related embrittlement of different hydrate minerals in subducted slabs is widely considered as a promising hypothesis for events of Double Seismic Zones (Reynard et al., 2010; Chernak and Hirth, 2011; Proctor and Hirth, 2015; Okazaki and Hirth, 2016). According to Faccenda et al. (2012), the Double Seismic Zones observed in many subduction zones can be explained by the formation of the Double Hydrated Zone during plate dehydration. The redistribution of fluids caused by the unbending of the plate at intermediate depths is responsible for the formation of the Double Hydrated Zone. Reynard et al. (2010) argued that the driving force that keeps slab unbending comes from the mantle flow which sustaining the slab pushes the tip of the slab forward. Our results also support the conclusion of numerical models (Reynard et al., 2010; Faccenda et al., 2012) that down-dip compression is enhanced by mantle flow opposing the dip of the slab, whereas overall downdip extension is favored by mantle flow in the same direction of the slab dip. Thus, we believe that the unbending of the slab is more likely to be the kinetic explanation for the stress state of Double Seismic Zones.

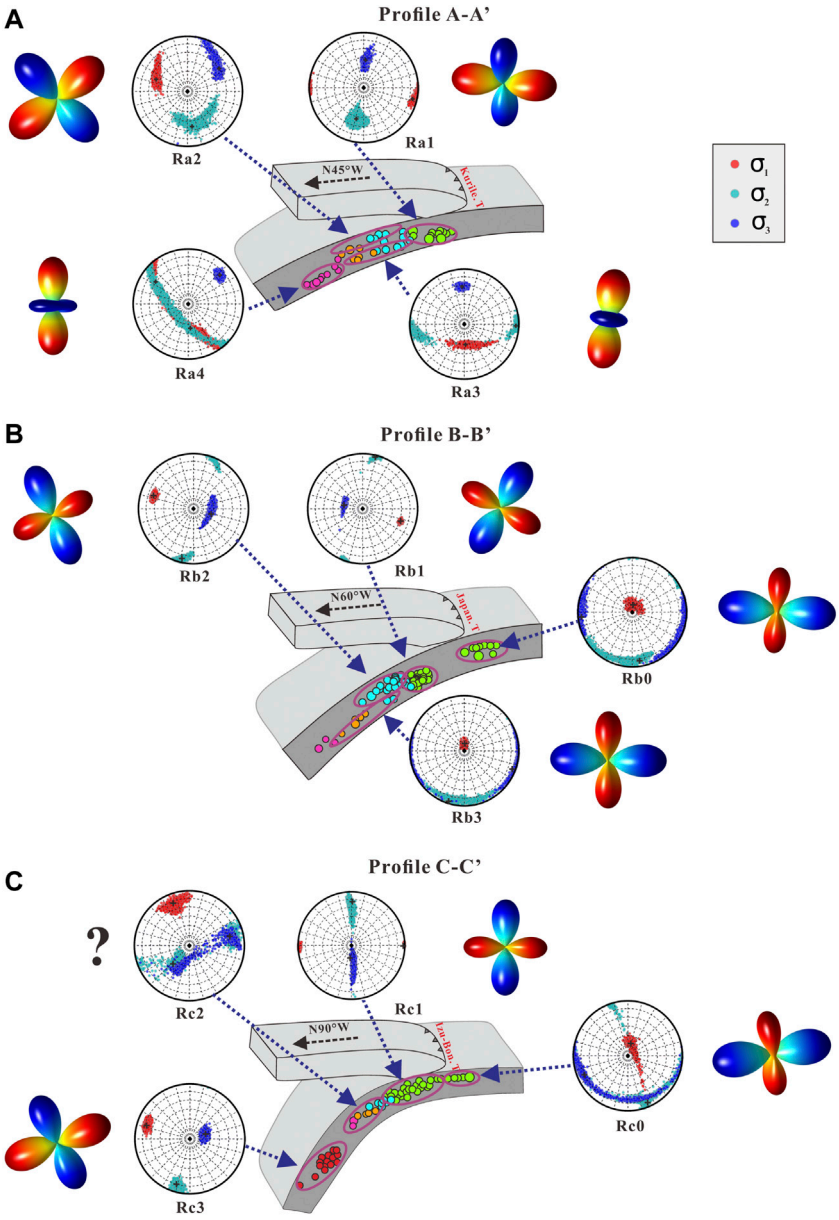


FIGURE 7
Tectonic cross-sections (not in scale) of all the three profiles discussed in this paper (Profile A-A' **(A)**, B-B' **(B)** and C-C'**(C)**). The dashed black arrows represent the orientation of the sections, as well as the direction of plate subduction. The earthquakes we used in this paper is denoted by the dots. The depth of earthquakes is shown by the color bar in Figure 1. Respective region-wise principal stress axes with their 95% confidence limits are plotted on lower hemisphere stereonets, where red: the maximum compressive stress (σ_1), cyan: intermediate principal axis (σ_2) and blue: minimum compressive stress (σ_3). 3D figures of spatial distribution for principal stress regime (Wan et al., 2011) are plotted around the stereographic projection, where the warm color represents the compressional stress state, while cold color corresponds to the tensional stress state.

The stress field in shallow and deep portions of the Wadati-Benioff zone

The Ra1, Rb1, and Rc1 represent the shallow regions of the WBZ in Northwest Pacific plate subduction system. Overall, the reverse faults account for the majority of earthquake types (Figures 6A,F,J). The best-fit stress models show that σ_1 is sub-horizontal and strike-normal, while σ_3 is close to slab-normal, and σ_2 is close to in-slab all along the arc (Figure 7; Table 3). All the *R* values are higher than 0.5 (Ra1: 0.55; Ra2: 0.72; Ra3: 0.71) implying a relatively stable σ_1. A combination of the best-fit stress model and the R values indicates a stress regime of pure compression. Since the parallelism of the stress axes with the plunge of the subducted slab is the primary evidence that the earthquakes occur in the subducted slab in response to

stresses within the plate (Isacks and Molnar, 1971), our results reveal that the present-day stress state of the shallow WBZ is nearly uniform across the three selected profiles. The orientation of the maximum compressive σ_1 have geomorphological expression and points to the axes of the trench, which is interpreted as the relative motion of two converging plates of lithosphere. The dominant forces acting within the shallow WBZ are related to negative buoyancy of the plate and convergence between the plates, consistent with plate pull or ridge push mechanics (Isacks and Molnar, 1971; Christova et al., 2004, 2015; Doglioni et al., 2007).

The Rc3 represents the deep portion of the slab in our study area with the depth of 320–420 km. The reverse faults also account for the majority of earthquake types (Figure 6L) which is similar to the shallow regions of the WBZ. The best-fit stress model and the *R* value (0.52) indicates a stress regime of pure compression with close to slab-parallel σ_1, nearly horizontal σ_2 close to in-slab and close to slab-normal σ_3 with a steeply plunge of 64.1° (Guiraud et al., 1989). Our results are consistent with the hypothesis that predominance of compression below about 300 km in several arcs, i.e., the most striking regularity in the mechanisms of deep earthquakes is the tendency of the compressional axis to parallel the local dip of the seismic zone (Isacks et al., 1968; Stauder and Mualchin, 1976; Christova, 2015). A reasonable interpretation is that there are forces on the lower portions of the slab that resist its motion. The compressive stress inside the slab will be the result of a downward-directed force applied to the upper portions of the slab and the upward-directed resisting force applied to the lower part of the slab. The cause of this resistance might be either an increase in strength in the surrounding mantle or a buoyant effect if the density of the slab were lower than that in the surrounding mantle. Our speculation agrees with the numerical models conducted by Carminati and Petricca (2010). They suggested the mantle flow drives the plate downward suffering resistance offered by the mantle to the penetration of the slab.

The stress field along the junction of the trench Wadati-Benioff zone

The junction of the Kurile and Japan arcs is expressed as a cuspate feature at the trench with a complex lithospheric structure, is known as the Hokkaido corner (Miller et al., 2006). Since the profile A-A' (southern Kurile trench WBZ) is located here, it can be served as a window to understanding the stress characteristics of intermediate-depth earthquakes and investigating deformation of the oceanic lithosphere beneath the arc junction in this paper.

A closer look through the FMS data of Double Seismic Zones in profile A-A', we find that more than half of them have considerate strike-slip component (Figures 6B,C) in contrast to the central Japan trench WBZ (Figures 6G,H), although the best-fit stress models are characterized with down-dip compression or down-dip tension in both the UP and LP (Figure 7A; Table 3). Going forward to the deeper at intermediate-depth, in Ra4, the best-fit stress model shows close to in-slab σ_3 and slab-normal σ_1. The *R* value is 0.15, indicating a general extension stress regime (Guiraud et al., 1989). However, this extensional feature revealed by best-fit stress model is inconsistent with the present-day overall stress field in northeast Japan, which is characterized by a reverse-faulting regime (Zoback, 1992; Kubo et al., 2002; Townend and Zoback, 2006).

The above two unusual stress states imply the additional forces acting at intermediate depths. The lateral deformation at intermediate depths is considered to be the more likely hypothesis (Isacks and Molnar, 1971; DeMets, 1992). Tomography imaging revealed by Miller et al. (2006) shows that a region of low-velocity depth and a distorted, buckled lower slab boundary exists at approximately 50–150 km depth beneath the Hokkaido corner, which are likely to be related to lateral deformation of the subducted Pacific plate at the arc-arc junction. The possible causes of lateral stretching are local hinge folding of the slab plate, which resulting from the increase of the slab's dip, as well as the different subduction rate between the two trench WBZs (Katsumata, 2003). Unfortunately, the lack of enough FMS from that particular segment hurdles us to look for more finer variations in spatial stress.

Conclusion

A new subset of 201 earthquakes with high-quality FMS was inverted to investigate the stress field along the Northwest Pacific WBZ. Combined with previous geological and geophysical studies, our results shed light on new constraints as follows:

(1) The shallow trench-outer rise region is most likely under a pure tension regime. The geodynamic force in the region is attributed to slab pull, which priors to subduction and causes the elastic lithosphere bending.
(2) Double Seismic Zones exist at the intermediate depths of southern Kurile trench and central Japan trench WBZ. The stress regimes in UP are dominantly down-dip compression type while in LP are dominantly down-dip tension type. Slab unbending is more likely to be the kinetic explanation for the coexistence of parallel compression and tension of the slabs.
(3) The present-day stress state in shallow WBZ segment shows pure compression. The dominant geodynamic forces are related to negative buoyancy of the plate and convergence between the plates, which is consistent with plate pull or ridge push mechanics. The deep segment of northern Izu-Bonin trench WBZ shows a stress regime of pure

compression, perhaps casing by the resistance offered by the mantle to the penetration of the slab.

(4) The unusual stress states were found at intermediate depths along the junction of the trench WBZ manifested by a considerable strike-slip component in Double Seismic Zones (70–200 km) and a general extension stress regime at deeper (200–300 km) depths. We suspect that these might be influenced by lateral deformation due to increasing slab's dip.

Data availability statement

The original contributions presented in the study are included in the article/Supplementary material, further inquiries can be directed to the corresponding author.

Author contributions

CL and FL are responsible for the original content and initial manuscript of this work. All authors collected and analyzed the data; CL and FL participated discussion; CL and YC drew the figures; CL and FL wrote the paper with the help of all authors.

Funding

This work was jointly supported by the Earthquake Science and Technology Spark of the China Earthquake Administration (XH20034Y), Information Building and Intelligent Service Team Fund of Shandong Earthquake Agency (ZD202201) and General Research Project of Shandong Earthquake Agency (YB 2005).

Acknowledgments

Most figures in this paper were generated using the Generic Mapping Tool (Wessel et al., 2019).

Conflict of interest

The authors declare that the research was conducted in the absence of any commercial or financial relationships that could be construed as a potential conflict of interest.

Publisher's note

All claims expressed in this article are solely those of the authors and do not necessarily represent those of their affiliated organizations, or those of the publisher, the editors and the reviewers. Any product that may be evaluated in this article, or claim that may be made by its manufacturer, is not guaranteed or endorsed by the publisher.

Supplementary material

The Supplementary Material for this article can be found online at: https://www.frontiersin.org/articles/10.3389/feart.2022.1017632/full#supplementary-material

References

Álvarez-Gómez, J. A. (2019). FMC—earthquake focal mechanisms data management, cluster and classification. *SoftwareX* 9, 299–307. doi:10.1016/j.softx.2019.03.008

Benioff, H., Gutenberg, B., and Richter, C. F. (1954). Progress report, seismological laboratory, California Institute of technology, 1953. *Trans. AGU.* 35 (6), 979–987. doi:10.1029/TR035i006p00979

Brudzinski, M. R., Thurber, C. H., Hacker, B. R., and Engdahl, E. R. (2007). Global prevalence of double benioff zones. *Science* 316, 1472–1474. doi:10.1126/science.1139204

Carminati, E., and Petricca, P. (2010). State of stress in slabs as a function of large-scale plate kinematics. *Geochem. Geophys. Geosyst.* 11 (4). doi:10.1029/2009GC003003

Chernak, L. J., and Hirth, G. (2011). Syndeformational antigorite dehydration produces stable fault slip. *Geology* 39, 847–850. doi:10.1130/G31919.1

Chiang, A., Dreger, D. S., Ford, S. R., Walter, W. R., and Yoo, S. (2016). Moment tensor analysis of very shallow sources. *Bull. Seismol. Soc. Am.* 106, 2436–2449. doi:10.1785/0120150233

Chiang, Andrea, and USDOE National Nuclear Security Administration (2020). Time domain moment tensor inversion in Python. Computer softwareUSDOE National Nuclear Security Administration (NNSA). 11 Feb, 2020, Available At https://www.osti.gov//servlets/purl/1602708. Vers. 0.1. doi:10.11578/dc.20200303.3

Christova, C., Scholz, C. H., and Kao, H. (2004). Stress field in the Vanuatu (New Hebrides) Wadati–Benioff zone inferred by inversion of earthquake focal mechanisms. *J. Geodyn.* 37, 125–137. doi:10.1016/j.jog.2003.11.001

Christova, C. V. (2015). Spatial distribution of the contemporary stress field in the Kurile Wadati-Benioff zone by inversion of earthquake focal mechanisms. *J. Geodyn.* 83, 1–17. doi:10.1016/j.jog.2014.11.001

Contreras-Reyes, E., Cortés-Rivas, V., Manríquez, P., and Maksymowicz, A. (2021). The silent bending of the oceanic Nazca Plate at the Peruvian Trench. *Tectonophysics* 807, 228810. doi:10.1016/j.tecto.2021.228810

Cui, H., Wan, Y., Huang, J., Sheng, S., and Jin, Z. (2019). Inversion for the tectonic stress field and the characteristic of the stress shape factor of the detachment slab in the Pamir-Hindu Kush area. *Chin. J. Geophys.* 62 (5), 1633–1649. (in Chinese). doi:10.6038/cjg2019M0202

Delvaux, D., and Barth, A. (2010). African stress pattern from formal inversion of focal mechanism data. *Tectonophysics* 482, 105–128. doi:10.1016/j.tecto.2009.05.009

DeMets, C., Gordon, R. G., Argus, D. F., and Stein, S. (1994). Effect of recent revisions to the geomagnetic reversal time scale on estimates of current plate motions. *Geophys. Res. Lett.* 21, 2191–2194. doi:10.1029/94GL02118

DeMets, C. (1992). Oblique convergence and deformation along the Kuril and Japan trenches. *J. Geophys. Res.* 97, 17615. doi:10.1029/92JB01306

Doglioni, C., Carminati, E., Cuffaro, M., and Scrocca, D. (2007). Subduction kinematics and dynamic constraints. *Earth. Sci. Rev.* 83, 125–175. doi:10.1016/j.earscirev.2007.04.001

Dreger, D. S. (2003).TDMT_INV: Time domain seismic moment tensor inversion, *Int. Geophys.*, 81. Academic Press, 1627. doi:10.1016/S0074-6142(03)80290-5

Emry, E. L., and Wiens, D. A. (2015). Incoming plate faulting in the Northern and Western Pacific and implications for subduction zone water budgets. *Earth Planet. Sci. Lett.* 414, 176–186. doi:10.1016/j.epsl.2014.12.042

Engdahl, E. R., and Scholz, C. H. (1977). A double Benioff Zone beneath the central Aleutians: An unbending of the lithosphere. *Geophys. Res. Lett.* 4, 473–476. doi:10.1029/GL004i010p00473

Faccenda, M., Gerya, T. V., Mancktelow, N. S., and Moresi, L. (2012). Fluid flow during slab unbending and dehydration: Implications for intermediate-depth seismicity, slab weakening and deep water recycling. *Geochem. Geophys. Geosyst.* 13 (1). doi:10.1029/2011GC003860

Florez, M. A., and Prieto, G. A. (2019). Controlling factors of seismicity and geometry in double seismic zones. *Geophys. Res. Lett.* 46, 4174–4181. doi:10.1029/2018GL081168

Forsyth, D., and Uyedaƒ, S. (1975). On the relative importance of the driving forces of plate motion. *Geophys. J. Int.* 43 (1), 163–200. doi:10.1111/j.1365-246X.1975.tb00631.x

Frohlich, C. (1992). Triangle diagrams: Ternary graphs to display similarity and diversity of earthquake focal mechanisms. *Phys. Earth Planet. Interiors* 75, 193–198. doi:10.1016/0031-9201(92)90130-N

Fujita, K., and Kanamori, H. (1981). Double seismic zones and stresses of intermediate depth earthquakes. *Geophys. J. Int.* 66, 131–156. doi:10.1111/j.1365-246X.1981.tb05950.x

Gephart, J. W., and Forsyth, D. W. (1984). An improved method for determining the regional stress tensor using earthquake focal mechanism data: Application to the San Fernando Earthquake Sequence. *J. Geophys. Res.* 89, 9305–9320. doi:10.1029/JB089iB11p09305

Gong, W., Jiang, X., Xing, J., Xu, C., Zhang, H., An, L., et al. (2021). Heterogeneous outer-rise seismicity within the Izu–Bonin subduction zone and its tectonic implications. *Geol. J.* 56, 4699–4718. doi:10.1002/gj.4206

Goto, K., Hamaguchi, H., and Suzuki, Z. (1985). Earthquake generating stresses in a descending slab. *Tectonophysics* 112, 111–128. doi:10.1016/0040-1951(85)90175-1

Green, H. W., II, Chen, W.-P., and Brudzinski, M. R. (2010). Seismic evidence of negligible water carried below 400-km depth in subducting lithosphere. *Nature* 467, 828–831. doi:10.1038/nature09401

Guiraud, M., Laborde, O., and Philip, H. (1989). Characterization of various types of deformation and their corresponding deviatoric stress tensors using microfault analysis. *Tectonophysics* 170, 289–316. doi:10.1016/0040-1951(89)90277-1

Hardebeck, J. L., and Okada, T. (2018). Temporal stress changes caused by earthquakes: A review. *J. Geophys. Res. Solid Earth* 123, 1350–1365. doi:10.1002/2017JB014617

Hasegawa, A., Horiuchi, S., and Umino, N. (1994). Seismic structure of the northeastern Japan convergent margin: A synthesis. *J. Geophys. Res.* 99, 22295–22311. doi:10.1029/93JB02797

Hasegawa, A., and Nakajima, J. (2017). Seismic imaging of slab metamorphism and Genesis of intermediate-depth intraslab earthquakes. *Prog. Earth Planet. Sci.* 4, 12–31. doi:10.1186/s40645-017-0126-9

Hasegawa, A., Umino, N., Takagi, A., and Suzuki, Z. (1979). Double-planed deep seismic zone and anomalous structure in the upper mantle beneath northeastern Honshu (Japan). *Tectonophysics* 57 (1), 1–6. doi:10.1016/0040-1951(79)90098-2

Hatakeyama, K., Katayama, I., Hirauchi, K., and Michibayashi, K. (2017). Mantle hydration along outer-rise faults inferred from serpentinite permeability. *Sci. Rep.* 7, 13870. doi:10.1038/s41598-017-14309-9

Hayes, G. P., Moore, G. L., Portner, D. E., Hearne, M., Flamme, H., Furtney, M., et al. (2018). Slab2, a comprehensive subduction zone geometry model. *Science* 362, 58–61. doi:10.1126/science.aat4723

Herrmann, R. B. (2013). Computer Programs in Seismology: An evolving Tool for instruction and research. *Seismol. Res. Lett.* 84, 1081–1088. doi:10.1785/0220110096

Huang, Z., Zhao, D., and Wang, L. (2011). Stress field in the 2008 Iwate-Miyagi earthquake (M7.2) area. *Geochem. Geophys. Geosyst.* 12 (6). doi:10.1029/2011GC003626

Isacks, B., and Molnar, P. (1971). Distribution of stresses in the descending lithosphere from a global survey of focal-mechanism solutions of mantle earthquakes. *Rev. Geophys.* 9, 103. doi:10.1029/RG009i001p00103

Isacks, B., Oliver, J., and Sykes, L. R. (1968). Seismology and the new global tectonics. *J. Geophys. Res.* 73, 5855–5899. doi:10.1029/JB073i018p05855

Katsumata, K. (2003). Newly imaged shape of the deep seismic zone within the subducting Pacific plate beneath the Hokkaido corner, Japan-Kurile arc-arc junction. *J. Geophys. Res.* 108, 2565. doi:10.1029/2002JB002175

Kawakatsu, H. (1986). Double seismic zones: Kinematics. *J. Geophys. Res.* 91, 4811. doi:10.1029/JB091iB05p04811

Kimura, T., Murakami, H., and Matsumoto, T. (2015). Systematic monitoring of instrumentation health in high-density broadband seismic networks. *Earth Planets Space* 67 (1), 55–15. doi:10.1186/s40623-015-0226-y

Kita, S., Okada, T., Hasegawa, A., Nakajima, J., and Matsuzawa, T. (2010). Existence of interplane earthquakes and neutral stress boundary between the upper and lower planes of the double seismic zone beneath Tohoku and Hokkaido, northeastern Japan. *Tectonophysics* 496, 68–82. doi:10.1016/j.tecto.2010.10.010

Konstantinou, K. I., Mouslopoulou, V., Liang, W.-T., Heidbach, O., Oncken, O., and Suppe, J. (2017). Present-day crustal stress field in Greece inferred from regional-scale damped inversion of earthquake focal mechanisms. *J. Geophys. Res. Solid Earth* 122, 506–523. doi:10.1002/2016JB013272

Kubo, A., Fukuyama, E., Kawai, H., and Nonomura, K. (2002). NIED seismic moment tensor catalogue for regional earthquakes around Japan: Quality test and application. *Tectonophysics* 356, 23–48. doi:10.1016/S0040-1951(02)00375-X

Lefeldt, M., and Grevemeyer, I. (2008). Centroid depth and mechanism of trench-outer rise earthquakes. *Geophys. J. Int.* 172, 240–251. doi:10.1111/j.1365-246X.2007.03616.x

Li, T., and Chen, Q. (2019). Stress regime inversion in the Northwest Pacific subduction zone, the segment from northern Honshu, Japan to Northeast China. *Chin. J. Geophys.* 62 (2), 520–533. (in Chinese). doi:10.6038/cjg2019M0044

Liu, C., Li, G., and Liu, F. (2022). Early cretaceous-cenozoic exhumation history of luxi terrane and adjacent areas, eastern North China craton. *Geol. J.* 57, 2735–2748. doi:10.1002/gj.4445

Liu, F., Miao, Q., and Qu, J. (2021). Multi-method study on seismogenic structure of rushan earthquake sequence in Shandong province, China. *Izv. Phys. Solid Earth* 57, 965–979. doi:10.1134/S106935132106015X

Liu, X., Zhao, D., Li, S., and Wei, W. (2017). Age of the subducting Pacific slab beneath East Asia and its geodynamic implications. *Earth Planet. Sci. Lett.* 464, 166–174. doi:10.1016/j.epsl.2017.02.024

Maeda, S., Matsuzawa, T., Okada, T., Katao, H., Yoshida, T., Kosuga, M., et al. (2020). Spatiotemporal variations in the stress field in the northeasternmost part of the NE Japan arc: Constraints from microearthquakes. *Earth Planets Space* 72, 117. doi:10.1186/s40623-020-01245-8

Michael, A. J. (1984). Determination of stress from slip data: Faults and folds. *J. Geophys. Res.* 89, 11517–11526. doi:10.1029/JB089iB13p11517

Michael, A. J. (1987). Use of focal mechanisms to determine stress: A control study. *J. Geophys. Res.* 92, 357–368. doi:10.1029/JB092iB01p00357

Michael, A.J., Ellsworth, W.L., and Oppenheimer, D.H. (1990). Coseismic stress changes induced by the 1989 Loma Prieta, California Earthquake. *Res. Lett.* 17, 1441–1444. doi:10.1029/GL017i009p01441

Michael, A.J. (1991). Spatial variations in stress within the 1987 Whittier Narrows, California, aftershock sequence: New techniques and results. *J. Geophys. Res. Solid Earth* 96, 6303–6319. doi:10.1029/91JB00195

Miller, M. S., Kennett, B. L. N., and Gorbatov, A. (2006). Morphology of the distorted subducted Pacific slab beneath the Hokkaido corner, Japan. *Phys. Earth Planet. Interiors* 156, 1–11. doi:10.1016/j.pepi.2006.01.007

Minson, S. E., and Dreger, D. S. (2008). Stable inversions for complete moment tensors. *Geophys. J. Int.* 174, 585–592. doi:10.1111/j.1365-246X.2008.03797.x

Moscoso, E., and Grevemeyer, I. (2015). Bending-related faulting of the incoming oceanic plate and its effect on lithospheric hydration and seismicity: A passive and active seismological study offshore maule, Chile. *J. Geodyn.* 90, 58–70. doi:10.1016/j.jog.2015.06.007

NIED (2019). *NIED F-net*. Tsukuba: National Research Institute for Earth Science and Disaster Resilience. doi:10.17598/nied.0005

Obana, K., Fujie, G., Takahashi, T., Yamamoto, Y., Tonegawa, T., Miura, S., et al. (2019). Seismic velocity structure and its implications for oceanic mantle hydration in the trench–outer rise of the Japan Trench. *Geophys. J. Int.* 217, 1629–1642. doi:10.1093/gji/ggz099

Okada, Y., Kasahara, K., Hori, S., Obara, K., Sekiguchi, S., Fujiwara, H., et al. (2004). Recent progress of seismic observation networks in Japan—hi-net, F-net, K-net and KiK-net. *Earth Planets Space* 56 (8). doi:10.1186/BF03353076

Okazaki, K., and Hirth, G. (2016). Dehydration of lawsonite could directly trigger earthquakes in subducting oceanic crust. *Nature* 530, 81–84. doi:10.1038/nature16501

Pasyanos, M. E., and Chiang, A. (2020). *Report for department of state (DoS) V-fund Project "tying moment tensor solutions to explosive yield" (No. LLNL-TR-*

812313). Livermore, CA (United States): Lawrence Livermore National Lab. (LLNL). doi:10.2172/1638008

Proctor, B., and Hirth, G. (2015). Role of pore fluid pressure on transient strength changes and fabric development during serpentine dehydration at mantle conditions: Implications for subduction-zone seismicity. *Earth Planet. Sci. Lett.* 421, 1–12. doi:10.1016/j.epsl.2015.03.040

Ranero, C. R., Phipps Morgan, J., McIntosh, K., and Reichert, C. (2003). Bending-related faulting and mantle serpentinization at the Middle America trench. *Nature* 425, 367–373. doi:10.1038/nature01961

Reynard, B., Nakajima, J., and Kawakatsu, H. (2010). Earthquakes and plastic deformation of anhydrous slab mantle in double Wadati-Benioff zones. *Geophys. Res. Lett.* 37 (24). doi:10.1029/2010GL045494

Saito, T., Noda, A., Yoshida, K., and Tanaka, S. (2018). Shear strain energy change caused by the interplate coupling along the nankai trough: An integration analysis using stress tensor inversion and slip-deficit inversion. *J. Geophys. Res. Solid Earth* 123, 5975–5986. doi:10.1029/2018JB015839

Sandiford, D., Moresi, L. M., Sandiford, M., Farrington, R., and Yang, T. (2020). The fingerprints of flexure in slab seismicity. *Tectonics* 39 (8). doi:10.1029/2019TC005894

Schellart, W. P., Freeman, J., Stegman, D. R., Moresi, L., and May, D. (2007). Evolution and diversity of subduction zones controlled by slab width. *Nature* 446, 308–311. doi:10.1038/nature05615

Seno, T., Stein, S., and Gripp, A. E. (1993). A model for the motion of the Philippine Sea Plate consistent with NUVEL-1 and geological data. *J. Geophys. Res.* 98 (17), 17941–17948. doi:10.1029/93jb00782

Sheng, S., and Meng, L. (2020). Stress field variation during the 2019 ridgecrest earthquake sequence. *Geophys. Res. Lett.* 47 (15). doi:10.1029/2020GL087722

Sleep, N. H. (1979). The double seismic zone in downgoing slabs and the viscosity of the mesosphere. *J. Geophys. Res.* 84, 4565–4571. doi:10.1029/JB084iB09p04565

Song, C.-H., Lu, C.-P., Zhang, X.-F., Wang, C., Xie, H.-D., Yan, X.-Y., et al. (2022). Moment tensor inversion and stress evolution of coal pillar failure mechanism. *Rock Mech. Rock Eng.* 55, 2371–2383. doi:10.1007/s00603-022-02783-1

Stauder, W., and Mualchin, L. (1976). Fault motion in the larger earthquakes of the Kurile-Kamchatka Arc and of the Kurile-Hokkaido corner. *J. Geophys. Res.* 81, 297–308. doi:10.1029/JB081i002p00297

Terakawa, T., and Matsu'ura, M. (2010). The 3-D tectonic stress fields in and around Japan inverted from centroid moment tensor data of seismic events. *Tectonics* 29 (6). doi:10.1029/2009TC002626

Townend, J., and Zoback, M. D. (2006). Stress, strain, and mountain building in central Japan. *J. Geophys. Res.* 111. doi:10.1029/2005JB003759

Tozer, B., Sandwell, D. T., Smith, W. H., Olson, C., Beale, J. R., and Wessel, P. (2019). Global bathymetry and topography at 15 arc sec: SRTM15+. *Earth Space Sci.* 6 (10), 1847–1864. doi:10.1029/2019EA000658

Uchida, N., Kirby, S. H., Umino, N., Hino, R., and Kazakami, T. (2016). The great 1933 sanriku-oki earthquake: Reappraisal of the main shock and its aftershocks and implications for its tsunami using regional tsunami and seismic data. *Geophys. J. Int.* 206, 1619–1633. doi:10.1093/gji/ggw234

Vavryčuk, V. (2014). Iterative joint inversion for stress and fault orientations from focal mechanisms. *Geophys. J. Int.* 199, 69–77. doi:10.1093/gji/ggu224

Vavryčuk, V. (2011). Principal earthquakes: Theory and observations from the 2008 west bohemia swarm. *Earth Planet. Sci. Lett.* 305, 290–296. doi:10.1016/j.epsl.2011.03.002

Wan, Y., Sheng, S., Xu, R., and Wu, Y. (2011). Effect of stress ratio and friction coefficient on composite P wave radiation patterns. *Chin. J. Geophys. (in Chin.* 54 (4), 994–1001. doi:10.3969/j.issn.0001-5733.2011.04.014

Wei, S. S., Wiens, D. A., van Keken, P. E., and Cai, C. (2017). Slab temperature controls on the Tonga double seismic zone and slab mantle dehydration. *Sci. Adv.* 3 (1), e1601755. doi:10.1126/sciadv.1601755

Wei, W., Zhao, D., Xu, J., Wei, F., and Liu, G. (2015). P and S wave tomography and anisotropy in Northwest Pacific and East Asia: Constraints on stagnant slab and intraplate volcanism. *J. Geophys. Res. Solid Earth* 120 (3), 1642–1666. doi:10.1002/2014JB011254

Wessel, P., Luis, J. F., Uieda, L., Scharroo, R., Wobbe, F., Smith, W. H. F., et al. (2019). The generic mapping tools version 6. *Geochem. Geophys. Geosyst.* 20, 5556–5564. doi:10.1029/2019GC008515

Yang, F., Santosh, M., and Kim, S. W. (2018). Mesozoic magmatism in the eastern North China Craton: Insights on tectonic cycles associated with progressive craton destruction. *Gondwana Res.* 60, 153–178. doi:10.1016/j.gr.2018.04.003

Yoshida, K., Hasegawa, A., and Okada, T. (2015). Spatial variation of stress orientations in NE Japan revealed by dense seismic observations. *Tectonophysics* 647, 63–72. doi:10.1016/j.tecto.2015.02.013

Yoshida, K., Hasegawa, A., and Okada, T. (2016a). Heterogeneous stress field in the source area of the 2003 M6.4 Northern Miyagi Prefecture, NE Japan, earthquake. *Geophys. J. Int.* 206, 408–419. doi:10.1093/gji/ggw160

Yoshida, K., Hasegawa, A., Okada, T., Iinuma, T., Ito, Y., and Asano, Y. (2012). Stress before and after the 2011 great Tohoku-oki earthquake and induced earthquakes in inland areas of eastern Japan. *Geophys. Res. Lett.* 39 (3). doi:10.1029/2011GL049729

Yoshida, K., Hasegawa, A., Saito, T., Asano, Y., Tanaka, S., Sawazaki, K., et al. (2016b). Stress rotations due to the *M* 6.5 foreshock and *M* 7.3 main shock in the 2016 Kumamoto, SW Japan, earthquake sequence. *Geophys. Res. Lett.* 43. doi:10.1002/2016GL070581

Yoshii, T. (1979). A detailed cross-section of the deep seismic zone beneath northeastern Honshu, Japan. *Tectonophysics* 55, 349–360. doi:10.1016/0040-1951(79)90183-5

Zoback, M. L. (1992). First- and second-order patterns of stress in the lithosphere: The world stress map Project. *J. Geophys. Res.* 97, 11703–11728. doi:10.1029/92JB00132

frontiers | Frontiers in Earth Science

TYPE Original Research
PUBLISHED 13 January 2023
DOI 10.3389/feart.2022.1033541

Check for updates

OPEN ACCESS

EDITED BY
Fan Yang,
Lanzhou University, China

REVIEWED BY
Wang Guangzeng,
Ocean University of China, China
Min Liu,
Northwest University, China
Liang Qiu,
China University of Geosciences, China

*CORRESPONDENCE
Chang-Hao Xiao,
xiaochanghao1986@126.com

SPECIALTY SECTION
This article was submitted to Structural Geology and Tectonics, a section of the journal Frontiers in Earth Science

RECEIVED 31 August 2022
ACCEPTED 01 November 2022
PUBLISHED 13 January 2023

CITATION
Hu J-X, Xiao C-H, Wei C-S, Shen Y-K, Chen Z-L, Zhang Y and Zhang D (2023), Polyphase deformation of the Youjiang fold-and-thrust belt during the Mesozoic: Implications for the tectonic transition of the South China block. *Front. Earth Sci.* 10:1033541. doi: 10.3389/feart.2022.1033541

COPYRIGHT
© 2023 Hu, Xiao, Wei, Shen, Chen, Zhang and Zhang. This is an open-access article distributed under the terms of the Creative Commons Attribution License (CC BY). The use, distribution or reproduction in other forums is permitted, provided the original author(s) and the copyright owner(s) are credited and that the original publication in this journal is cited, in accordance with accepted academic practice. No use, distribution or reproduction is permitted which does not comply with these terms.

Polyphase deformation of the Youjiang fold-and-thrust belt during the Mesozoic: Implications for the tectonic transition of the South China block

Jia-Xiu Hu[1,2], Chang-Hao Xiao [2,3]*, Chang-Shan Wei[2,3], Yu-Ke Shen[2,3], Zheng-Le Chen[2,3], Yu Zhang[1,2] and Da Zhang[1]

[1]School of Earth Sciences and Resources, China University of Geosciences (Beijing), Beijing, China, [2]Laboratory of Dynamic Diagenesis and Metallogenesis, Institute of Geomechanics, Chinese Academy of Geological Sciences, Beijing, China, [3]Key Laboratory of Paleomagnetism and Tectonic Reconstruction, Ministry of Natural Resources, Beijing, China

The South China block (SCB) experienced the tectonic transition from the Paleo-Tethys to the Paleo-Pacific tectonic domains during the Mesozoic, but the transition process is hotly debated. The Youjiang fold-and-thrust belt (YFTB), in the interior of the Youjiang Basin in the southwestern SCB, is located in a junction of these two tectonic domains and thus witnessed their tectonic evolution. It also separates the northern thin-skinned structures from the southern thick-skinned structures in the basin. Therefore, the YFTB is an intriguing window into the Mesozoic evolution in the southwestern SCB and the Mesozoic tectonic transition of the SCB. In this study, we conduct structural analysis at the middle of the YFTB and discuss the Mesozoic tectonic transition of the SCB. Four phases of deformation are identified in the YFTB during the Mesozoic. The first phase of deformation (D_1) is characterized by a series of conjugate joints, NW–SE trending thrust faults and folds resulting from NE–SW shortening that was related to the collision between the SCB and Indochina block. The second phase of deformation (D_2) is manifested by the pre-existing NW–SE striking thrust faults transformed to normal faults and the Late Triassic mafic magmatism. Our structural observations, combined with previous geochronological data for mafic dykes, suggest the study area experienced post-orogenic extension in the Late Triassic. The third phase of deformation (D_3), accompanied with the westward subduction of the Paleo-Pacific oceanic plate, is represented by a series of conjugate joints and NE–SW-striking faults formed by NW–SE compression. As a result of the continuous subduction of the Paleo-Pacific plate and its subsequent slab rollback, the fourth phase of deformation (D_4) is featured with normal faults, magmatic-hydrothermal activities, and regional mineralization, which are associated with the nearly E–W extension setting. Our study results indicate that, in the Early Mesozoic, the Youjiang Basin was dominated by the Paleo-Tethys domain and then transitioned to the Paleo-Pacific domain. Together with the magmatic lull between the Triassic and the

Early-Middle Jurassic identified in the SCB, we propose that the tectonic transition process manifested in the YFTB more likely initiated in the Early Jurassic.

KEYWORDS

Paleo-Tethys, Paleo-Pacific, structural analysis, South China block, Youjiang fold-and-thrust belt

Introduction

The South China block (SCB), as an important component of southeastern Asia, is located at a junction impacted by the Paleo-Tethys and Paleo-Pacific tectonic domains (Figure 1A). During the Late Paleozoic-Mesozoic, the SCB experienced both the assembly of the Indochina block and the SCB and the subduction of Paleo-Pacific plate, triggering tectonic transition and extensive tectono-magmatic activities (Zhang et al., 2013, Zhang D.et al., 2021; Xiao et al., 2018, 2022). The Mesozoic tectonic superposition and transition of the SCB have attracted much attention and prompted numerous studies (Li and Li, 2007; Zhang et al., 2012; Li et al., 2014; Shu et al., 2021). However, the tectonic transition process, especially its initiation timing, is still in dispute (Zhou et al., 2006; Li and Li, 2007; Chen et al., 2008; Wang et al., 2013; Xu et al., 2019). One opinion is that, based on the statistics of the granite ages and types in the SCB, the subduction began in the Late Permian through flat-slab subduction (Li and Li, 2007). This perspective seems to be feasible in relation to some further studies both on magmatism and deformation (Li et al., 2012; Meng et al., 2012). Others have argued that the transition occurred in the Mesozoic, varying from the Late Triassic (Jiang et al., 2015; Xu et al., 2019), the Early Jurassic (Sun et al., 2005; Zhou et al., 2006; Xu et al., 2017), the Middle–Late Jurassic (Wang et al., 2013), to the Cretaceous (Chen et al., 2008). One of the reasons for this controversy is the superposition and complexity of the structural deformation of the two tectonic domains. Hence, distinguishing the deformation sequence is important to elucidate the transition process and onset timing of the SCB.

The Youjiang Basin, as a part of the southwestern margin of the SCB, is situated at the intersection of the Cathaysia, Yangtze, and Indochina blocks (Figure 1B). It is a superimposed location affected by Paleo-Tethys and Paleo-Pacific domains and strongly reworked during the Permian to the Triassic (Chen and Zeng, 1990; Zeng et al., 1995). Due to its particular position, knowledge regarding the evolution of the Youjiang Basin is critical to better understand the Mesozoic tectonic regime transition of the SCB. However, the ambiguity of the geodynamic setting of the Youjiang Basin hinders our understanding of its tectonic evolution. The Triassic Youjiang Basin has generally been recognized as a foreland basin connected with the closure of the Paleo-Tethys Ocean and the succeeding collision between the SCB and the Indochina block (Du et al., 2013; Hu et al., 2015; Lehrmann et al., 2015; Qiu et al., 2016), whereas other studies have suggested that it was a back-arc basin in response to the subduction of the Paleo-Tethys (Chen and Zeng, 1990; Zeng et al., 1995) or the Paleo-Pacific plate (Duan et al., 2020; Wang et al., 2020, 2021).

The structural characteristics of the Youjiang Basin are featured by a progressive deformation from thick-skinned hinterland belt to thin-skinned foreland belt due to the Indosinian orogeny, and these two types of deformation were divided by the Nanpanjiang–Youjiang fault. The earlier structures resulting from the Indosinian tectonic event were transformed in the Yanshanian tectonic event, represented by the N- to NE-striking cleavage and the curving of the Indosinian fold axes (Yang et al., 2021). However, Li et al. (2017) identified that the NE-striking structures related to the subduction of the Paleo-Pacific plate overprinted the NW-striking structures in the Long'an area, the junction of the Youjiang and Shiwandashan structural belts, indicating that the subduction of Paleo-Pacific plate preceded and facilitated the closure of the Paleo-Tethys Ocean. The lack of detailed deformation analysis of these two tectonic domains makes the Mesozoic tectonic setting of the Youjiang Basin poorly constrained and limits our understanding of the tectonic transition of the SCB. Therefore, reconstructing the deformation sequence of the YFTB is conducive to comprehensively discerning the Mesozoic tectonic evolution of the basin and constraining the tectonic transition process of the SCB.

In this contribution, we conduct structural analysis on the geometry and kinematics characteristics of different stages of structures, including faults, folds, and conjugate joints in the YFTB. Combined with regional geology and detailed structural mapping, the results are used to recognize the Mesozoic tectonic evolution of the YFTB and, moreover, elucidate the Mesozoic tectonic transition process of the SCB.

Regional geology

Geological setting

The SCB is formed by the amalgamation of the Yangtze and Cathaysia blocks along the Jiangnan Orogenic belt during the early Neoproterozoic (Lin et al., 2008; Wang et al., 2010, 2013; Zhang et al., 2013; Shu et al., 2021). It is adjacent to the Pacific Ocean and linked to the North China block by the Qinling–Dabie Orogenic belt in the north, the Indochina block by the Song Ma

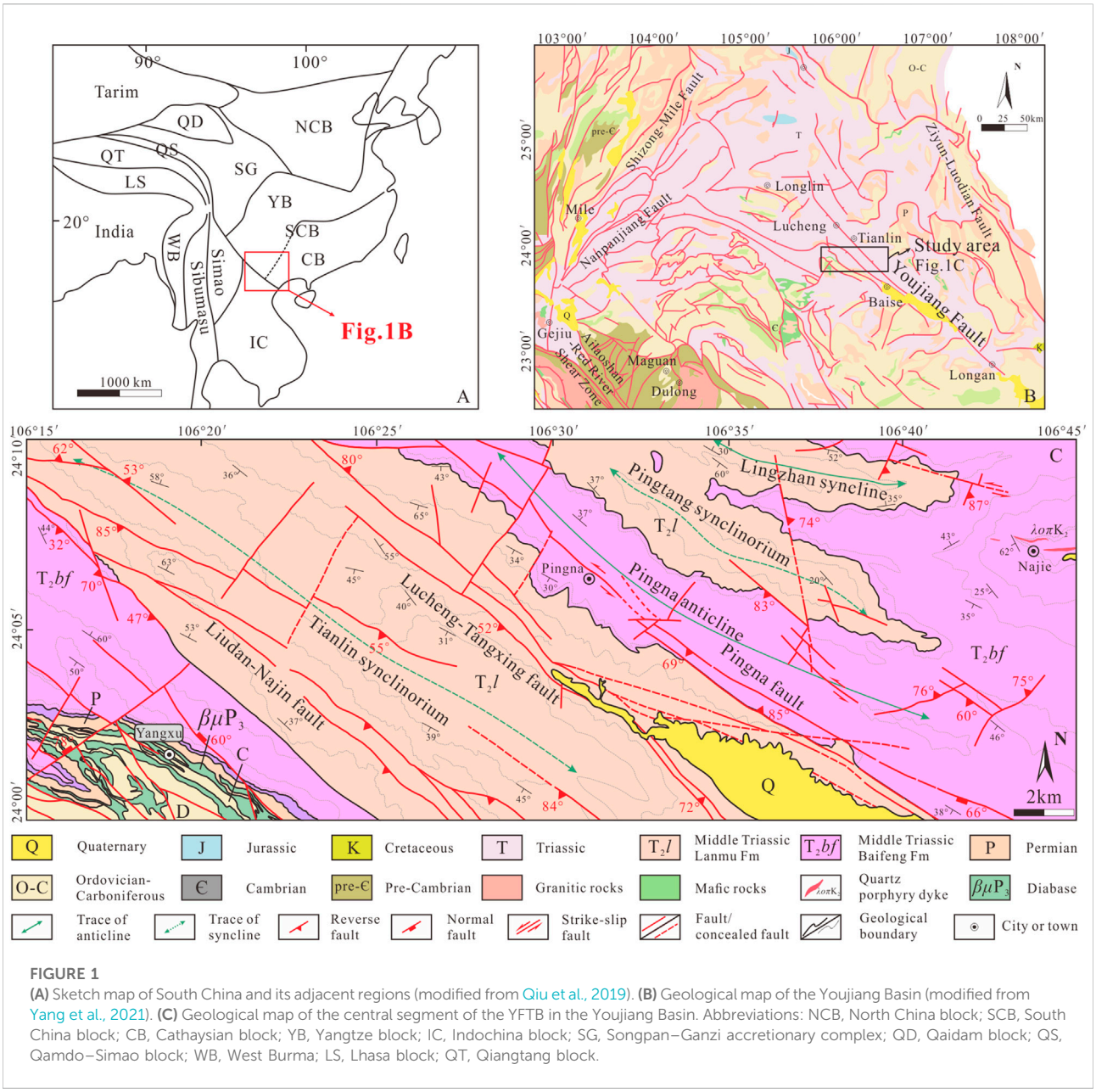


FIGURE 1
(A) Sketch map of South China and its adjacent regions (modified from Qiu et al., 2019). **(B)** Geological map of the Youjiang Basin (modified from Yang et al., 2021). **(C)** Geological map of the central segment of the YFTB in the Youjiang Basin. Abbreviations: NCB, North China block; SCB, South China block; CB, Cathaysian block; YB, Yangtze block; IC, Indochina block; SG, Songpan–Ganzi accretionary complex; QD, Qaidam block; QS, Qamdo–Simao block; WB, West Burma; LS, Lhasa block; QT, Qiangtang block.

suture in the southwest, and the Longmenshan fault zone by the Tibetan Plateau in the west, respectively (Figure 1A). During the Phanerozoic, the SCB was dominated by three tectonic events that are known as the Early Paleozoic intracontinental orogeny between the Yangtze and Cathaysia blocks (the Caledonian tectonic event), the Permian–Triassic continental collision between the SCB and the Indochina block during the Early Triassic (the Indosinian tectonic event) and the Jurassic–Cretaceous Paleo-Pacific plate subduction beneath the SCB (the Yanshanian tectonic event) (Wang et al., 2013; Faure et al., 2014; Xiao et al., 2022; Qiu et al., 2020; Yang et al., 2021).

The Youjiang Basin in the southwestern margin of the SCB is a superimposed location affected by the Tethys tectonic domain, Paleo-Pacific tectonic domain, and Tibetan tectonic domain (Wang et al., 2021). It is a foreland basin bounded by the ShiZong–MiLe fault belt in the northwest, the Ziyun–Luodian fault belt in the northeast, the Ailaoshan–Red River shear zone in the southwest, and the Pingxiang–Nanning fault belt, with the Shiwandashan Basin in the southeast (Figure 1B; Xiao et al., 2018). The basin consists of a pre-Cambrian to Ordovician basement covered by Devonian to Triassic strata (Yang et al., 2020). The major faults are well-developed in NW–NWW-

striking and NE-striking (Chen and Zeng, 1990). They were mostly formed as syn-sedimentary normal faults along the initial rifting of the basin in the Early Devonian (Zeng et al., 1995; Du et al., 2013), and then underwent various movements corresponding to different tectonic events (Wang et al., 2013).

From the Early Devonian to the Early Triassic, the Youjiang Basin was initiated as a rifted basin and gradually developed into a back-arc basin corresponding to the opening of the Ailaoshan Ocean and its subsequent subduction (Zeng et al., 1995). Consequently, the Early Devonian to Early Triassic sedimentation of Youjiang Basin is characterized by the coexistence of deep-water facies, mainly comprising pelite, chert, limestone, and shallow-water facies that primarily include limestone, bioclastic limestone, marlstone, and conglomerates (Du et al., 2013). During the Middle Triassic, accompanied by the closure of the Paleo-Tethys Ocean and the convergence of the Indochina block and SCB along the Song Ma Suture, the Youjiang Basin evolved into a foreland basin, with massive thick Triassic terrigenous turbiditic units consisting of marlstone, mudstone, siltstone, and sandstone (Yang et al., 2020).

Felsic rocks in the Youjiang Basin are mainly exposed along the basin boundary. Minor quartz porphyry dykes and most (ultra-) mafic rocks are revealed in the interior of the basin (Jiang et al., 2019; Qiu et al., 2019; Yang et al., 2020). Previous studies have reported Permian–Early Jurassic mafic rocks with ages of ca. 269–183 Ma and Late Cretaceous mafic and quartz porphyry dykes in northwestern Guangxi and southwestern Guizhou with ages of ca. 100–80 Ma (Chen et al., 2012; Zhu et al., 2017; Xiao et al., 2018; Qiu et al., 2019).

Geology of the Youjiang fold-and-thrust belt (YFTB)

The YFTB is a major fault zone in the interior of the Youjiang Basin, and it begins at Longlin, extending over 360 km through Tianlin and Baise to Nanning. In the northern segment, the YFTB occurs as one main fault, whereas the southern segment is divided into three to five secondary parallel faults from Baise to Nanning, with the whole belt striking NW and steeply dipping to the northeast (Wang et al., 2013). A previous study on the geophysics and structural geology showed that the YFTB, with an overall framework of NE-verging thrusting, produced duplex and imbricate structures in deep and shallow levels respectively. It cut through pre-Cambrian metamorphic basement and Cambrian to Triassic strata and formed a thick-skinned structure. In contrast, the basement on the northeast of the YFTB was not involved in the deformation, indicating a thin-skinned structure (Yang et al., 2021).

The sedimentary rock in the middle of the YFTB is primarily comprised of Devonian, Carboniferous, and Permian and Triassic rocks. The Paleozoic rocks are locally outcropped in the southwest of the study area and primarily comprise carbonate, chert, and mudstone (Figure 1C). The Middle Triassic clastic rocks are the main exposed rocks in the middle of the YFTB and comprise the Middle Triassic Baifeng Formation (T_2bf) and Lanmu Formation (T_2l). The Middle Triassic Baifeng Formation (T_2bf) in the study area includes sandstone, siltstone intercalated with mudstone, and argillaceous siltstone, and the Lanmu Formation (T_2l) is composed of calcareous mudstone, siltstone, and sandstone (Figure 1C). The middle of the YFTB consists of a series of sub-parallel secondary faults, including the Liudan–Najin, Lucheng–Tangxing, and Pingna faults. They strike northwest and dip steeply toward the northeast at high angles of 60°–85° (Figure 1C). A series of folds developed along the fault zone, such as the Tianlin synclinorium, the Pingna anticline, the Pingtang synclinorium, and the Lingzhan syncline. The Tianlin synclinorium is a NW-trending tight fold with a sub-vertical axial plane and a slightly curved hinge, with a core of the Lanmu Formation (T_2l) and limbs of the Baifeng Formation (T_2bf). The Pingna anticline is a secondary fold in the Tianlin synclinorium, cored by the Baifeng Formation (T_2bf) with limbs of the Lanmu Formation (T_2l). It is a NW-trending inclined open fold with southwestern limbs dipping at 25°–50° and northeastern limbs dipping at 60°–80°, and tension joints are well developed in its core. The Pingtang synclinorium is a NWW-trending fold with a curved hinge, a core of the Lanmu Formation (T_2l), and limbs of the Baifeng Formation (T_2bf). The Lingzhan syncline is a NWW-trending fold with steeply-dipping northeastern limbs and moderately-dipping southwestern limbs. It is cored by the Lanmu Formation (T_2l) with limbs of the Baifeng Formation (T_2bf) (Figure 1C). Sporadic magmatic rocks are exposed in the study area, including Early Triassic and Early Jurassic post-orogenic mafic rocks in Badu and Yangxu areas along the Youjiang fault, and Late Cretaceous quartz porphyry dykes in Najie area that formed in the extensional setting (Chen et al., 2012; Zhu et al., 2017; Qiu et al., 2019). A previous study has suggested concealed intrusions in depth based on the regional gravity and magnetic anomalies (Chen et al., 2012).

Methods

The tectonic transition process and evolution can be well archived in the paleo-tectonic stress field in existing structural features and the paleo stress field inversion based on the statistics and analysis of slip vectors is an effective way to determine the paleo-tectonic stress field (Angelier, 1984). The dipping direction and angle of fault planes and the strike and pitch of the striations on fault planes were measured. The sense of movement was determined by mineral steps and syntectonic minerals. The fault-slip vector data were analyzed using FaultKin™ software and listed in Supplementary Table S1 (Allmendinger, 2002).

The conjugate joints were also measured for structural analysis. The orientation of the acute angle bisector between the joints indicates the maximum principal compression stress



FIGURE 2
Field photographs of main structures developed in the D_1 deformation in the YFTB. **(A)** The fold in the siltstone of the Triassic Baifeng Formation at PN2009 indicating a top-to-the-NE movement. **(B)** Asymmetric fold in the siltstone of the Triassic Lanmu Formation at PN2044 indicating a top-to-the-SW movement. **(C)** Asymmetric fold involving the Triassic Lanmu Formation in the Tianlin synclinorium at PN2059 indicating a top-to-the-NE movement. **(D)** Asymmetric fold in the siltstone of the Triassic Baifeng Formation at PN2036 showing a top-to-the-NE movement. **(E)** NE-verging thrusts and fault-related folds involving siltstone of the Triassic Baifeng Formation in the Tianlin synclinorium at PN2007 indicating a top-to-the-NE movement. **(F)** Asymmetric folds involving the siltstone of the Triassic Lanmu Formation in the Tianlin synclinorium at PN2043 demonstrating a NE–SW oriented shortening. **(G)** Asymmetric fold in Triassic siltstone in bedding siltstone of the Triassic Baifeng Formation at PN2032 indicating a top-to-the-NE movement. **(H)** Strike-slip striations on the NWW-striking fault plane indicating a NE–SW compression. **(I)** Sinistral striations and mineral steps in the siltstone of the Triassic Baifeng Formation at PN2057 showing a sinistral strike-slip movement. **(J)** Thrusting striations on the siltstone of the Triassic Baifeng Formation in the Pingna underground tunnel at YM1-11 indicating a NE–SW compression. **(K)** Thrusting striations and mineral steps on the siltstone of the Triassic Baifeng Formation at PN2103 indicating a NE–SW compression. **(L)** Steeply-dipping cleavage (S_1) and structural transposition in the Triassic weakly competent argillaceous siltstones at PN2030 indicating an interlayer shearing.

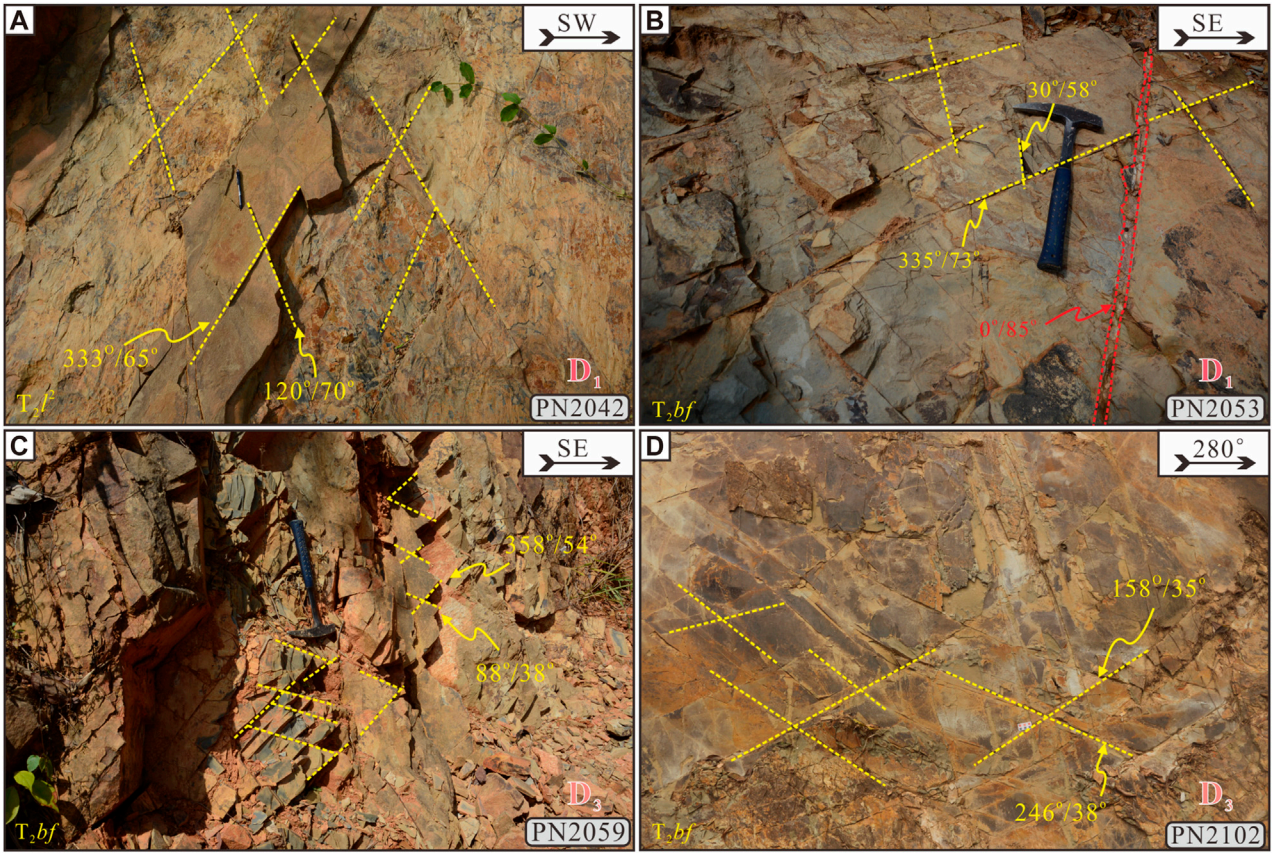


FIGURE 3
Field photographs of conjugate joints developed in the D_1 and D_3 structures in the YFTB. **(A)** Conjugated joints developed in the siltstones of the Triassic Lanmu Formation at PN2042 documenting NE–SW-oriented compression. **(B)** Conjugated joints developed in the siltstones of the Triassic Baifeng Formation at PN2053 indicating NE–SW-oriented compression. **(C)** Conjugated joints developed in the siltstones of the Triassic Baifeng Formation at PN2059 demonstrating NW–SE shortening. **(D)** Conjugated joints developed in the siltstone of the Triassic Lanmu Formation at PN2102 indicating NW–SE compression.

(σ1) (Arlegui and Simón, 2001; Wu et al., 2019). The dipping bedding with conjugate joints was calibrated to horizontal, and the corrected attitudes were then plotted in the rose diagram through Stereonet™ to determine their predominant direction and to infer the maximum principal stress (Allmendinger, 2002). The data of conjugate joints were presented in Supplementary Table S2.

Fault-related folds were also analyzed to determine the sense of thrusting. The overprinting relationships, including the fault plane crosscutting, striation superposition, and limitation between different sets of conjugate joints, were beneficial in deducing the sequence of the paleo-stress field.

Geometry and kinematic analysis

The study area is dominated by NW-trending folds and faults, which are locally crosscut by the NE-trending faults. The kinematic analysis indicates that the study area underwent polyphase tectonic movements. Based on the geometry, kinematic, and dynamic characteristic analysis of deformation conducted in the middle of the YFTB and the superposition and reworking relationships between these structural features, we have identified four phases of deformation with their paleo-stress field during the Mesozoic in the middle of the YFTB.

NE–SW shortening deformation (D_1)

The first phase of deformation (D_1), which established the tectonic framework in the study area, mainly consists of a NE-verging fold-and-thrust system in the Triassic and its underlying strata, such as the Tianlin synclinorium developed in the Tianlin district and the Lucheng–Tangxing fault outcropped around Baise city, as well as some strike-slip

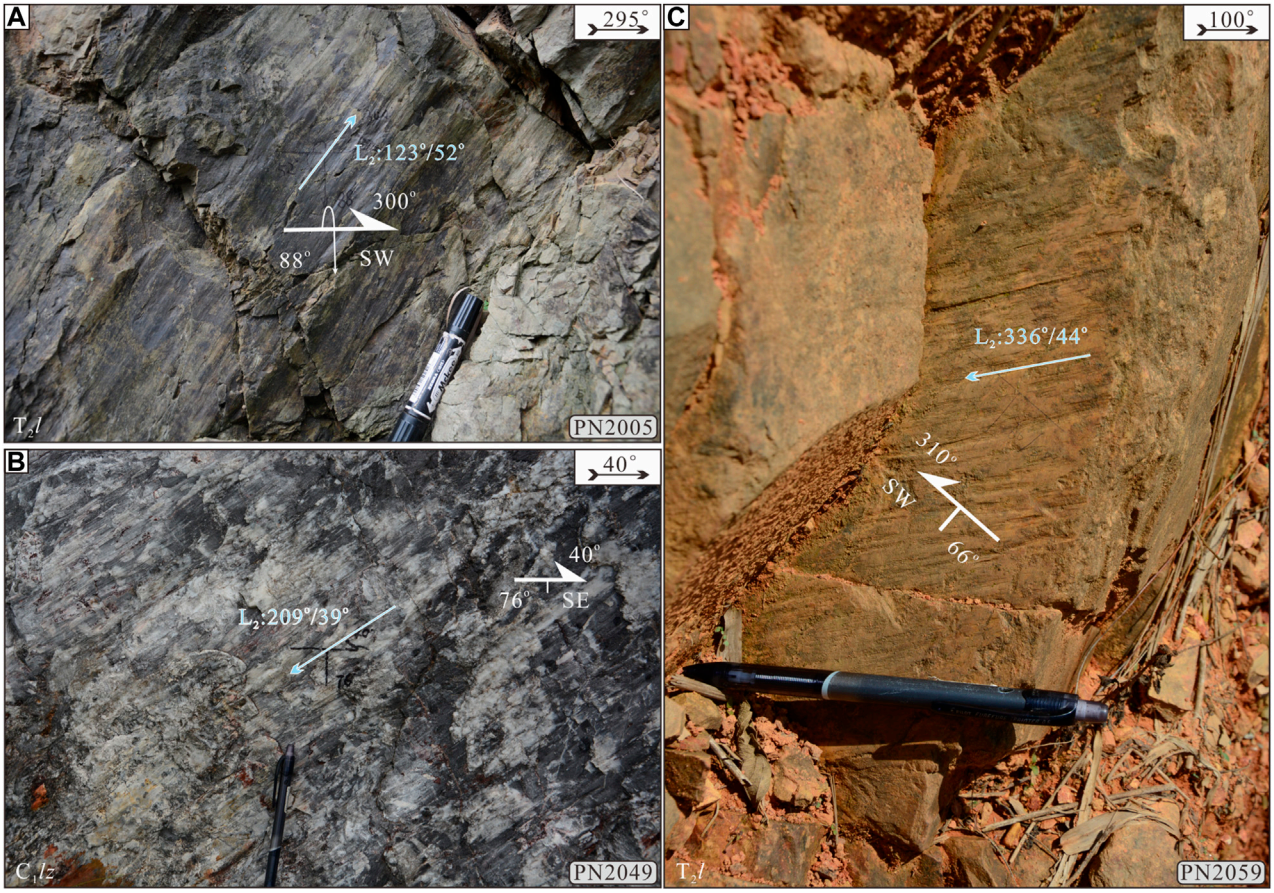


FIGURE 4
Field photographs of main structures developed in the D_2 deformation in the YFTB. **(A)** Sinistral striations and mineral steps on the hanging wall of the NW-striking fault plane in the siltstone of the Triassic Lanmu Formation at PN2005. The striations and mineral steps imply the top-to-the downward shear. **(B)** Striations and calcite mineral steps on the inter-bedding fault plane in the chert of the Carboniferous Luzhai Formation at PN2049 indicating a top-to-downward movement. **(C)** Striations developed on the NW-striking fault plane at PN2059 indicating top-to-downward movement.

faults. Most of these faults dip steeply and bear oblique-slip striations and mineral steps. Inversion results for the slip vectors show principal stress distributions of sub-horizontal σ1, sub-vertical σ2, and sub-horizontal σ3, indicating a NE–SW compression. This NE–SW-oriented compression regime has also been recorded by conjugate sets of NNE-striking dextral and E–W-striking strike-slip faults. The slip vector data from these fault planes demonstrate a NE–SW-oriented compressional regime that features sub-horizontal NE-trending σ1, sub-vertical σ2, and sub-horizontal NW-trending σ3 (Figures 2H–J). Similar kinematic characteristics are also manifested by the nearly dip-slip striations developed on the limb of the NW-trending fold (Figure 2K), with horizontal σ1, sub-horizontal σ2, and vertical σ3 indicating a NE–SW compression.

Furthermore, asymmetric fault-related folds with NW-striking hinges and NE- or SW-dipping axial planes are well developed in the study area, with gently dipping southern limbs and steeply dipping northern limbs, and *vice versa*, indicating a NE–SW trending compression. For example, the southern part of the NWW-trending Youjiang fault was outcropped and cut the Middle Triassic Baifeng Formation siltstone at PN2007 (Figure 2E), producing a series of fault-related folds. The asymmetric fault-related folds indicate a top-to-the-NE thrusting. The geometrical characteristics of other well-developed NW-trending folds also demonstrate a NE–SW-oriented shortening (Figures 2A–D,F,G).

In addition, plenty of conjugate joints developed in both limbs of the Tianlin synclinore in this regime (Figures 3A,B). The acute angle bisector between the joints indicates that they were formed by a NE–SW compression. Moreover, steeply-dipping cleavage (S_1) resulted from the D_1 deformation, which is well developed within the weak competent argillaceous layers in both limbs of the NW-trending folds. It transposes the

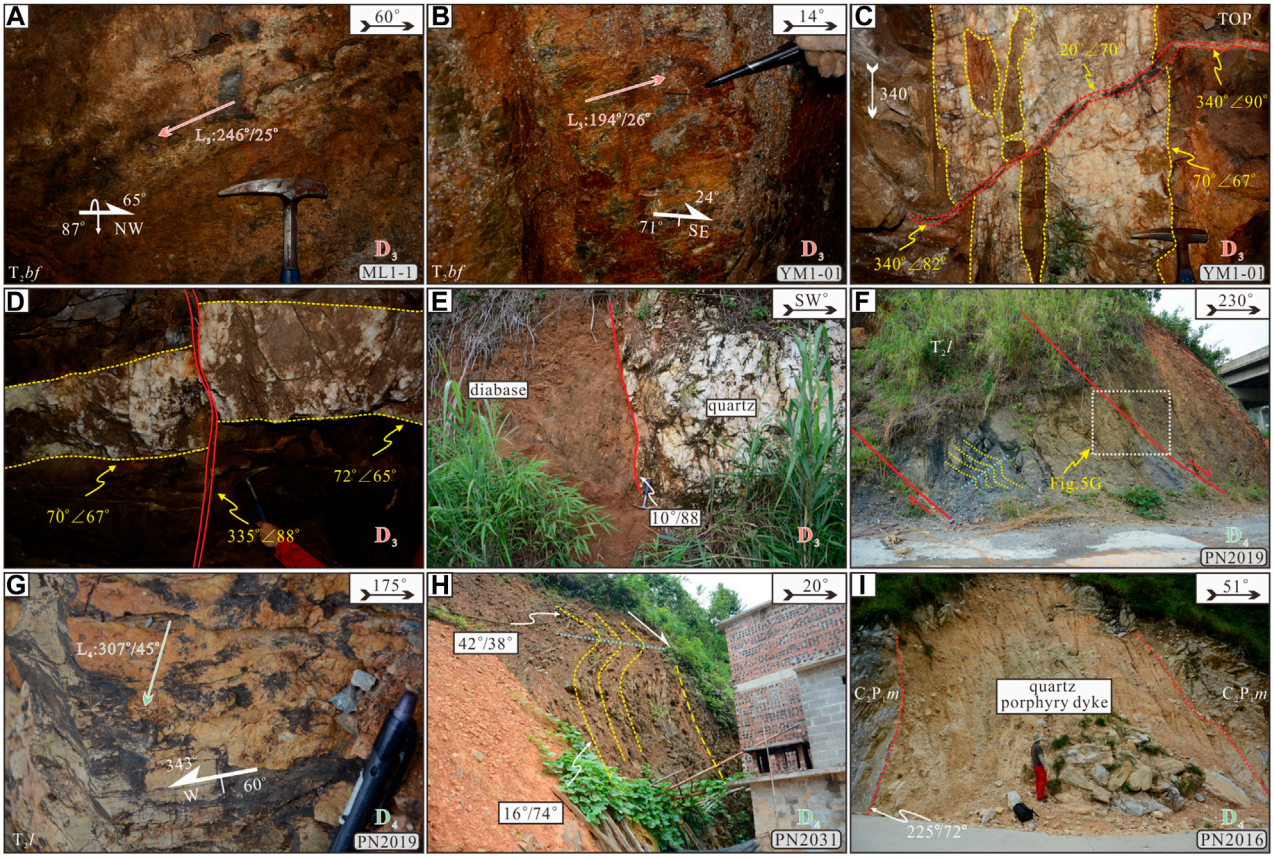


FIGURE 5
Field photographs of main structures and intrusions developed in the D_3 and D_4 structures in the YFTB. **(A)** Oblique striations on the NE-strike-slip fault plane in the siltstones of the Triassic Baifeng Formation at ML1-1 showing a NW–SE-oriented compression. **(B)** Strike-slip striations on the NNE-striking fault plane in the siltstones of the Triassic Baifeng Formation at YM1-01 indicating a NW–SE-oriented compression. **(C)** NW-striking fault crosscut NE-striking fault at YM1-01 in the Pingna underground tunnel. **(D)** NW-striking fault plane crosscut NE-striking fault in the Pingna underground tunnel. **(E)** NNE-striking fault crosscut the diabase that ourcropped in the Yangxu area. **(F)** The NW-striking normal fault and drag folds in the mudstones of the Triassic Lanmu Formation at PN2019 indicating nearly E–W-oriented extension. **(G)** The downward striations in the mudstones of the Triassic Lanmu Formation at PN2019 showing nearly E–W-oriented extension. **(H)** Asymmetric fold in Triassic siltstone at PN2031 implying the nearly E–W extension. **(I)** Quartz porphyry dyke intruded along the NW-striking fault. The fault crosscut the limestone of the Carboniferous Maping Formation at PN2016.

original bedding (S_0) and indicates an interlayer shearing (Figure 2L).

Nearly N–S extension (D_2)

This phase of deformation (D_2) is mostly manifested as the reworking of the pre-existing structures formed in the D_1 deformation, and it includes NW-trending normal faults and inter-bedding fractures developed on the limbs of NW-striking folds (Figure 4A).

Fault-related NE-verging folds developed along the NW-striking Liudan–Najin fault indicate that the NE–SW shortening coincides with the D_1 deformation (Figure 2C). The NW-trending fault is a sinistral fault dipping steeply with nearly dip-slip striations at PN2059, indicating that it was transposed by the D_2 deformation (Figure 4C). The fault slip vector is featured by horizontal σ1, sub-vertical σ2, and horizontal σ3, exhibiting a nearly N–S extension. The inter-bedding fault slip vectors developed on the Carboniferous chert at PN2049 record the same nearly N–S extension regime, with sub-vertical σ1, sub-horizontal σ2, and horizontal σ3 (Figure 4B).

In addition, diabase intrusions observed in the study area can provide constraints regarding the deformation timing (Figure 5E).

NW–SE shortening (D_3)

The third phase of deformation (D_3) is represented by the NE–SW-trending faults that crosscut previous NW–SE-

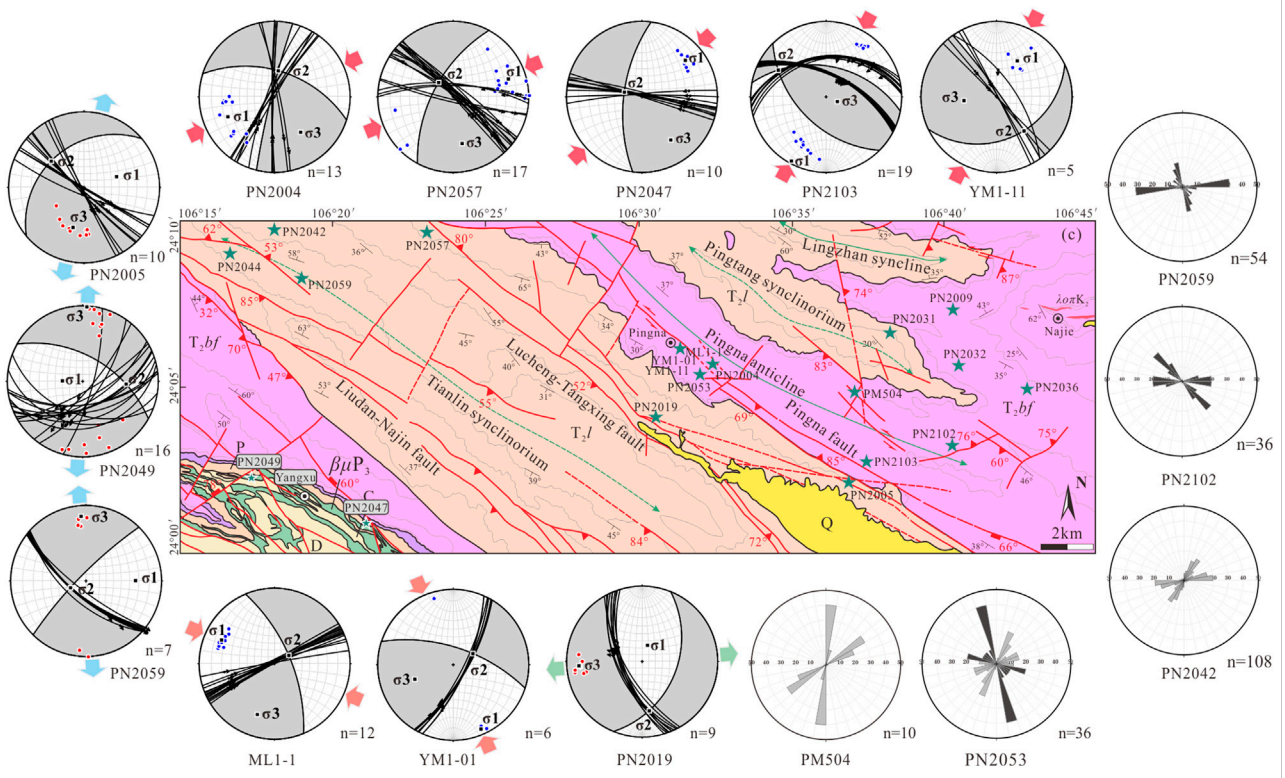


FIGURE 6
Stereographic plots of the main faults and conjugated joints in the study area. The observation points are shown with green pentagrams. The lower-hemisphere stereographic projection of brittle faults documents four phases of deformation and the rose diagram of conjugate documents a NE–SW and NW–SE compression regime.

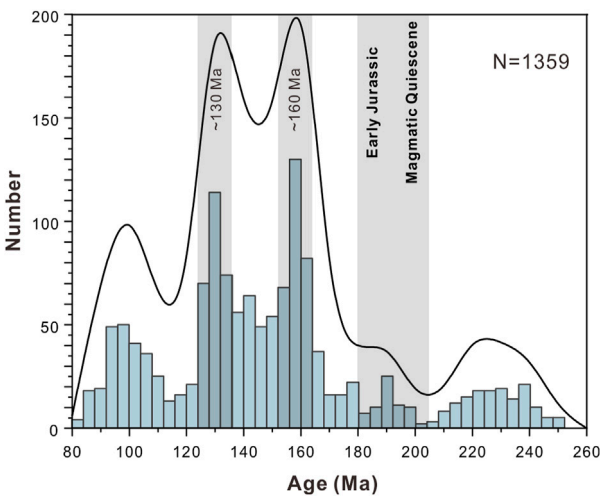


FIGURE 7
Age histogram of Mesozoic igneous rocks in the SCB. Age data are from Li and Li (2007), Gao et al. (2017), Gan et al. (2021), Li et al. (2021), and references therein. An apparent magmatic lull is inferred between the Late Triassic and the Early Jurassic.

striking thrust faults, the diabase, and a series of conjugate joints. A series of NE–SW-striking faults are observed in the underground tunnel of the Pingna deposit and crosscut the NW–SE-trending Pingna fault, indicating that they formed after the D_1 deformation (Figures 5A–D). The faults dip steeply with minor oblique-slip striations. Inversion results for the striations show a NW–SE compression that is characterized by a horizontal σ1, sub-horizontal σ2, and horizontal σ3 (Figures 5A,B, 6). This phase of deformation also crosscut the diabase formed at 249–187 Ma, indicating that it formed after the Early Jurassic (Figure 5E; Qiu et al., 2019).

Another set of conjugate joints was developed on the limbs of the Tianlin synclinorium (Figures 3C,D). The acute angle bisector between the joints indicates they were the product of the NW–SE compression (Figure 6). Regionally, the NE–SW-trending faults crosscut pre-existing NW–SE-striking faults formed in D_1 and the mafic rocks intruded in D_2 deformation.

As mentioned above, the structures formed in D_3 crosscut NW-striking faults formed in D_1 and overprint the structures and diabase formed in D_2, indicating that the NW–SE

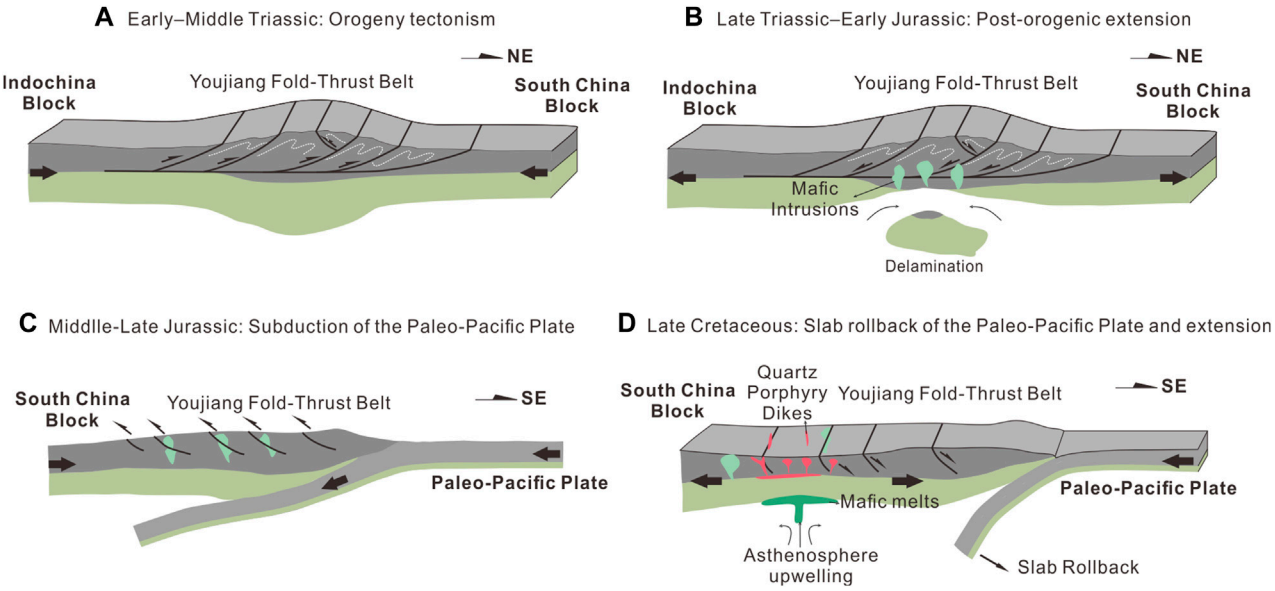


FIGURE 8
Tectonic model for the Mesozoic evolution of YFTB. **(A)** Collision between the Indochina block and SCB results in a series of NE-verging fold-and-thrust faults. **(B)** The delamination and post-collision rework the pre-existing structures and lead to the intrusion of mafic rocks. **(C)** The subduction of the Paleo-Pacific oceanic plate produces the N(N)E-striking faults that crosscut pre-existing structures and mafic rocks. **(D)** The rollback of the Paleo-Pacific plate leads to the back-arc extension setting and felsic dykes' emplacement. Modified from Qiu et al. (2019), Yang et al. (2021), and Zhang X. M. et al. (2021).

compression (D_3) occurred after NE–SW compression (D_1) and the nearly N–S extension and related structures (D_2).

Nearly E–W extension (D_4)

The fourth deformation (D_4) determined in the YFTB is characterized by several normal faults and lead to the Late Cretaceous W–Sn mineralization and quartz porphyry dyke emplacement. The normal faults are steeply dipping and have arrays of steeply dipping striations, with the inversion results documenting an extensional regime that features an E–W orientated σ3 (Figure 6).

The Youjiang fault outcrops in the Lanmu Formation, producing drag folds with gently dipping northeastern limbs, steeply dipping southwestern limbs, and NEE-dipping axial planes at PN2019. The geometrical characteristics of the drag fold indicate a nearly NEE–SWW extension (Figure 5F). The fault plane is steeply dipping with oblique-slip striations (l_4), documenting an extensional regime that features sub-vertical σ1, horizontal σ2, and horizontal σ3 (Figure 5G). Similar asymmetric fold are observed at PN2031 (Figure 5H). The striations (l_4) on the fault plane, together with the geometry characteristics of drag folds, suggest a nearly E–W-orientated extension.

Minor quartz porphyry dykes are exposed in the northeastern part of the study area. They intruded in the limestone of the Carboniferous Maping Formation (C_2P_1m) at PN2016 and in the siltstone of the Triassic Baifeng Formation (T_2bf) with NW-trending in the Najie area (Figure 5I). Previous studies have suggested that they were related to an extensional setting and formed in the Late Cretaceous (Chen et al., 2012; Zhu et al., 2017).

Discussion

Structural evolution of the Youjiang fold-and-thrust belt

The contraction of the Paleo-Tethys Ocean began through subduction in the Early Permian and mostly ended up with a closure in the Triassic (Wang et al., 2020; Feng et al., 2022). It induced the continental collision of the SCB with the Indochina block at Song Ma suture on the southern margin, causing extensive and intense intra-continental deformation in the SCB (Lin et al., 2008; Li S. Z. et al., 2017; Shu et al., 2021). The Indosinian orogeny generated the Late Triassic unconformity and pervasive E–W- and NW–SE-striking structures in the SCB, such as the intra-plate deformation of E–W-trending folds and faults widespread in the SCB (Zhang

et al., 2009), the NW–NWW-oriented thrust-and-fold sheets, and top-to-the-NE shearing reported in the Yunkai massif (Lin, 2008), NW–NWW- and E–W-trending faults and folds recorded in the Youjiang Basin and its adjacent region (Qiu, 2016; Yang et al., 2021), and the NW–SE-trending fold-and-thrust belt and ductile shearing zone outcropping in NE Vietnam (Lepvrier et al., 1997, 2011). The Indosinian orogeny also produced extensive magmatism in the SCB, which is distinguished from the Late Mesozoic magmatism by the quiescence between 205–180 Ma (Figure 7; Zhou et al., 2006). This tectonic event in the YFTB is characterized with prevailing NE- and NW-verging folds and NW-striking thrust faults (Figure 8A). The D_1 deformation, caused by the NE–SW-orientated compression and characterized by NE-verging fold-and-thrust, is consistent with the Indosinian orogeny (Figure 6).

Furthermore, previous research has suggested that the Indosinian magmatism in the SCB can be further divided into two stages (Mao et al., 2014). The early stage is considered as products of the collision between the Indochina block and the SCB with zircon U–Pb isotopic ages from 243 to 233 Ma, whereas the late stage occurred in a post-collisional extension setting with zircon U–Pb ages of 220–206 Ma (Sun et al., 2005; Wang et al., 2007b). In addition, Qiu et al. (2019) reported Early Jurassic mafic rocks linked to the post-orogenic extension in the Badu diabase with an LA–ICP–MS zircon U–Pb isotopic age of 187 Ma in the northwestern part of the study area. This extension may correspond to the D_2 deformation with nearly N–S-orientated extension in the YFTB (Figure 6), leading to the superimposition on pre-existing structures and mafic rocks emplacement (Figure 8B).

After the Indosinian orogeny, the SCB experienced the NW–SE compression due to the subduction of the Paleo-Pacific plate under the SCB (Figure 8C; Mao et al., 2014, 2021; Shu, 2021; Zhang et al., 2021; Shi et al., 2022). It produced a series of NE- to NNE-trending folds and thrust structures and vast intracontinental magmatism and structural belts in the SCB (Wang, 2013; Suo et al., 2019), which superimposed and reworked the Indosinian structures (Zhang, 2009). The same overprinting relationships have also been identified in the Youjiang Basin (Yang et al., 2021). In the YFTB, the D_3 deformation is represented by crosscutting between earlier NW–SE-striking faults and later NE–SW-striking faults. The D_3 NNE–SSW-trending faults also truncated the diabase that formed in D_2. These structural features are consistent with our investigations in the YFTB, indicating a NW–SE compression setting during the Middle Jurassic that resulted from the subduction of the Paleo-Pacific plate (Figure 6).

Along with the continuous subduction of the Paleo-Pacific plate and the subsequent high-angle subduction retreat or rollback, the SCB was dominated by an extensional setting (Figure 8D; Qiu et al., 2022a). It resulted in numerous extensional basins and domes and triggered intense magmatism and mineralization (Li et al., 2014). Coetaneous W–Sn mineralization and magmatism were mainly discovered along the boundary of the Youjiang Basin (Xiao et al., 2022). Minor igneous rocks outcropped in the interior of the basin including quartz porphyry dykes and (ultra-) mafic rocks (Chen, 2012). Chen et al. (2012) reported Ar^{40}–Ar^{39} ages of 96–95 Ma for muscovite from the quartz porphyry dykes. Zhu et al. (2017) determined zircon U–Pb ages for the quartz porphyry dykes of 99–95 Ma. These geochronological results indicated a Late Cretaceous magmatism in the Youjiang Basin and have been interpreted as the products of a lithospheric thinning and crustal extension event. Xiao et al. (2018) also reported LA–ICP–MS zircon U–Pb isotopic ages ranging from 93 to 92 Ma for the quartz porphyry, monzogranite, and biotite granite in the southeastern margin of the Youjiang Basin, inferring that they were linked to the extensional setting caused by the rollback of the Paleo-Pacific plate and the Neo-Tethys ocean slab. In the YFTB, sporadic quartz porphyry dykes intruded along the D_3 NW-trending faults (Figure 5I). The W–Sn ore-related granitoid and quartz porphyry dyke emplacement in the YFTB, together with these geochronological data, suggest that the YFTB experienced a nearly E–W-orientated extension (D_4) in the Late Cretaceous (Figure 6).

Two sets of conjugate joints recorded NW–SE and NE–SW compression. Integrated with regional geology, slickensides, fault-related folds, magmatic rocks, and their overprinting relationships, four phases of deformation in the Mesozoic have been recognized in the YFTB. D_1 and D_2 deformation were related to the Paleo-Tethys tectonic domain, and D_3 and D_4 deformation were associated with the Paleo-Pacific tectonic domain. The paleo-stress field and deformation characteristics in the YFTB demonstrate the Youjiang Basin was in a Paleo-Tethys-dominated setting as a foreland basin and then switched into the Paleo-Pacific domain, and the switch likely occurred between D_2 deformation, marked by the post-orogenic setting, and D_3, corresponding to the subduction of the Paleo-Pacific plate.

Tectonic implications

The Indosinian tectonic event was the most significant tectonic event in the Phanerozoic evolution history of the SCB and has essentially built up the structural architecture of the SCB (Wang et al., 2013; Li et al., 2017). Its occurrence could be constrained by the timing of the collision between the Sibumasu and Indochina blocks during 258–243 Ma (Carter et al., 2001; Lepvrier et al., 2004).

The Permian–Triassic tectono-magmatism in the SCB has been considered to be either associated with 1) the subduction of the Paleo-Tethys Ocean and the collision between the

Indochina and SCB (Jiang et al., 2015; Gao et al., 2017; Qiu et al., 2019) or 2) the subduction of the Paleo-Pacific plate (Li and Li, 2007; Shen et al., 2018). The hypothesis that the subduction of the Paleo-Pacific plate commenced in the Permian is supposed to produce a NW–SE compression, which contradicts the pervasive NW–SE-striking fold-and-thrust formed in D_1 deformation in the Youjiang Basin. In addition, this model cannot explain the absence of the Permian–Triassic subduction-related mafic rocks in the southeastern SCB (Gao et al., 2017). Niu et al. (2014) also noted that it would be theoretically difficult for a flat subduction to occur, especially on such a tremendous scale. Furthermore, Gan et al. (2021) identified apparent variations in geochemistry and rock associations and obvious magmatic quiescence between the Triassic and Early–Middle Jurassic magmatic rocks, implying that the transition commenced in the Early Jurassic. Zhou et al. (2006) recognized a relative quiescence in the SCB during the Early Jurassic (205–180 Ma), which is regarded as the transition timing of the SCB (Li S. Z. et al., 2017). In this study, we collected and summarized published geochronological data of the Mesozoic magmatism in the SCB and plotted them in a histogram. The statistical results indicated that there is an apparent quiescence between the Late Triassic and the Early Jurassic, followed by a magmatic peak at 160 Ma (205–180 Ma, Figure 7). A similar lull also existed in the mineralization in the SCB, which symbolizes the transition that occurred in the Early Jurassic (Zhao et al., 2022).

Li et al. (2017) identified the earlier NW-verging folds were overprinted by the NE-verging folds at the junction of the Youjiang Basin and Shiwandashan Basin, inferring that the subduction of the Paleo-Pacific plate was initiated in the Permian and facilitated the closure of the Paleo-Tethys Ocean. However, this kind of superposition is inconsistent with the deformation developed in the YFTB. On the contrary, Zhang et al. (2009) determined the superimposed relationship between the older nearly E–W-trending fold belt and younger NNE-trending fold in the SCB, proposing a transition from Paleo-Tethys to Paleo-Pacific tectonic domains in the Middle–Late Jurassic, combined with the strata contact and magmatism data.

Furthermore, Shu and Zhou (2002) considered that the Early–Middle Jurassic A-type granites and bimodal volcanic rocks in the Jurassic basin in the Nanling region marked the transition in the southeastern SCB. Li S. Z. et al. (2017) believed that different transitions happened in the SCB, including the Late Triassic in the Xuefengshan region and Early–Middle Jurassic in the Nanling region. In summary, the Early Jurassic was a significant changing period both for magmatism and structural features in the SCB.

The deformation features and overprinting relationships in the YFTB are pervasive in the SCB and the evolution of four phases of deformation in the YFTB witnessed the transition of two tectonic domains. The paleo-stress field and deformation characteristics in the YFTB demonstrate that the Youjiang Basin was in a Paleo-Tethys-dominated setting as a foreland basin in the Triassic. The quiescence of the magmatism and mineralization is compelling evidence to constrain the transition timing, which suggests the SCB likely experienced a transition from the Paleo-Tethys to the Paleo-Pacific tectonic domains in the Early Jurassic (Figure 8C).

Conclusion

1) Our structural analysis and paleo-stress field inversion, together with regional geology, determined the deformation sequence in the YFTB during the Mesozoic. Four phases of deformation are identified, including NE–SW shortening deformation (D_1) in the Permian–Middle Triassic, nearly N–S extension (D_2) in the Late Triassic, NW–SE shortening (D_3) in the Jurassic, and nearly E–W extension (D_4) in the Cretaceous.
2) D_1 and D_2 deformation corresponded to the collision and post-collision stages in the Indosinian orogeny, respectively. D_3 and D_4 deformation were respectively associated with the subduction of the Paleo-Pacific plate and slab-rollback in the Yanshanian tectonic event (Jurassic to Cretaceous).
3) Our study suggests that the tectonic transition of the SCB in response to the subduction of the Paleo-Pacific plate more likely occurred in the Early Jurassic, not the Permian.

Data availability statement

The original contributions presented in the study are included in the article/Supplementary Material; further inquiries can be directed to the corresponding author.

Author contributions

J-XH collected the data for analysis, and compiled the results and wrote the manuscript. J-XH also finished the figures and table. C-HX designed the study, collected the data for analysis, and compiled the results and wrote the manuscript. C-SW, Y-KS, Z-LC, and YZ collected the data for analysis and provided feedback to the manuscript. DZ provided feedback to the manuscript.

Funding

This study was financially supported by the Basic Research Fund of the Chinese Academy of Geological Sciences (Grant: DZLXJK202203) and the China Geological Survey (Grants: DD20190161; DD20221660-3).

Acknowledgments

Richard W. Allmendinger is thanked for sharing the structural software *FaultKin* and *Stereonet*. We sincerely thank the Guest Editor FY, the reviewer LQ, and the other two reviewers for their hard work and constructive comments that have improved the quality of our paper.

Conflict of interest

The authors declare that the research was conducted in the absence of any commercial or financial relationships that could be construed as a potential conflict of interest.

Publisher's note

All claims expressed in this article are solely those of the authors and do not necessarily represent those of their affiliated organizations, or those of the publisher, the editors and the reviewers. Any product that may be evaluated in this article, or claim that may be made by its manufacturer, is not guaranteed or endorsed by the publisher.

Supplementary material

The Supplementary Material for this article can be found online at: https://www.frontiersin.org/articles/10.3389/feart.2022.1033541/full#supplementary-material

References

Allmendinger, R. W. (2002). *Stereonet V. 1.1.6 and FaultKin V. 1.2.2.* Ithaca, New York shareware software: Cornell University, Department of Geological Sciences. geo. cornell.edu/pub/rwa.

Angelier, J. (1984). Tectonic analysis of fault slip data sets. *J. Geophys. Res.* 89, 5835–5848. doi:10.1029/JB089iB07p05835

Arlegui, L., and Simón, J. L. (2001). Geometry and distribution of regional joint sets in a non-homogeneous stress field: Case study in the Ebro basin (Spain). *J. Struct. Geol.* 23, 297–313. doi:10.1016/S0191–8141(00)00097–3

Carter, A., Roques, D., Bristow, C., and Kinny, P. (2001), .Understanding Mesozoic accretion in southeast Asia: Significance of Triassic thermotectonism (Indosinian orogeny) in Vietnam, *Geology*, 29, 2112–2214. doi:10.1130/0091-7613(2001)029<0211

Chen, C. H., Lee, C. Y., and Shinjo, R. (2008). Was there Jurassic paleo-pacific subduction in South China? Constraints from $^{40}Ar/^{39}Ar$ dating, elemental and Sr-Nd-Pb isotopic geochemistry of the Mesozoic basalts. *Lithos* 106, 83–92. doi:10.1016/j.lithos.2008.06.009

Chen, H. D., and Zeng, Y. F. (1990). [Evaluation of effects of dust prevention in the principal tungsten mines in Jiangxi]. *Zhonghua Yu Fang. Yi Xue Za Zhi* 10, 28–30. (in Chinese). doi:10.16108/j.issn1006-7493.2012.01.011

Chen, M. H., Lu, G., and Li, X. H. (2012). Muscovite 40Ar/39Ar dating of the quartz porphyry veins from Northwest Guangxi, China, and its geological significance. *Geol. J. China Univ* 1, 106–116. (in Chinese with English abstract).

Du, Y. S., Huang, H., Yang, J. H., Huang, H. W., Tao, P., Huang, Z. Q., et al. (2013). The basin translation from the late Paleozoic to Triassic of the Youjiang basin and its tectonic signification. *Geol. Rev.* 59, 1–11. (in Chinese). doi:10.16509/j.georeview.2013.01.009

Duan, L., Meng, Q. R., Wu, G. L., Yang, Z., Wang, J. Q., and Zhan, R. R. (2020). Nanpanjiang basin: A window on the tectonic development of South China during Triassic assembly of the southeastern and eastern Asia. *Gondwana Res.* 78, 189–209. doi:10.1016/j.gr.2019.08.009

Faure, M., Lepvrier, C., Nguyen, V., Vu, T., Lin, W., and Chen, Z. (2014). The South China block-Indochina collision: Where, when, and how? *J. Asian Earth Sci.* 79, 260–274. doi:10.1016/j.jseaes.2013.09.022

Feng, H. W., Xu, S. M., Wang, J. D., Zhang, G. L., Zeng, Z. P., and Shu, P. C. (2022). Jurassic provenances and their transition mechanism of the Delingha Sag in the eastern segment of northern margin of the Qaidam Basin, North Tibet. *Geosystems Geoenvironment* 1, 100097. doi:10.1016/j.geogeo.2022.100097

Gan, C. S., Zhang, Y. Z., Wang, Y. J., Qian, X., and Wang, Y. (2021). Reappraisal of the Mesozoic tectonic transition from the Paleo-Tethyan to Paleo-Pacific domains in South China. *Bull. Geol. Soc. Am.* 133, 2582–2590. doi:10.1130/B35755.1

Gao, P., Zheng, Y. F., and Zhao, Z. F. (2017). Triassic granites in South China: A geochemical perspective on their characteristics, petrogenesis, and tectonic significance. *Earth. Sci. Rev.* 173, 266–294. doi:10.1016/j.earscirev.2017.07.016

Hu, L. S., Cawood, P. A., Du, Y. S., Yang, J. H., and Jiao, L. X. (2015). Late Paleozoic to early Mesozoic provenance record of paleo-Pacific subduction beneath South China. *Tectonics* 34, 986–1008. doi:10.1002/2014TC003803

Jiang, W., Yan, Q. R., Deng, L., Zhou, B., Xiang, Z. J., and Xia, W. J. (2019). Early Jurassic mafic intrusions in the southern Youjiang Basin, SW China: Petrogenesis, tectonic and metallogenic implications. *Minerals* 9, 771. doi:10.3390/min9120771

Jiang, Y. H., Wang, G. C., Liu, Z., Ni, C. Y., Qing, L., and Zhang, Q. (2015). Repeated slab advance-retreat of the Palaeo-Pacific plate underneath SE China. *Int. Geol. Rev.* 57, 472–491. doi:10.1080/00206814.2015.1017775

Lehrmann, D., Chaikin, D., Enos, P., Minzoni, M., Payne, J., Yu, Y., et al. (2015). Patterns of basin fill in Triassic turbidites of the Nanpanjiang basin: Implications for regional tectonics and impacts on carbonate-platform evolution. *Basin Res.* 27 (5), 587–612. doi:10.1111/bre.12090

Lepvrier, C., Maluski, H., Van Tich, Vu, Leyreloup, A., Truong Thi, P., and Van Vuong, N. (2004). The early Triassic Indosinian orogeny in Vietnam (Truong Son belt and Kontum Massif): Implications for the geodynamic evolution of Indochina. *Tectonophysics* 393, 87–118. doi:10.1016/j.tecto.2004.07.030

Lepvrier, C., Faure, M., Van, V. N., Vu, T., Van Lin, W., Trong, T. T., et al. (2011). North-directed Triassic nappes in northeastern Vietnam (East Bac Bo). *J. Asian Earth Sci.* 41, 56–68. doi:10.1016/j.jseaes.2011.01.002

Lepvrier, C., Maluski, H., Vuong, N. Van, Roques, D., Axente, V., and Rangin, C. (1997). Indosinian NW-trending shear zones within the Truong Son belt (Vietnam) ^{49}Ar-^{39}Ar Triassic ages and Cretaceous to Cenozoic overprints. *Tectonophysics* 283, 105–127. doi:10.1016/S0040-1951(97)00151-0

Li, C. L., Wang, Z. X., Lü, Q. T., Tan, Y. L., Li, L. L., and Tao, T. (2021). Mesozoic tectonic evolution of the eastern South China block: A review on the synthesis of the regional deformation and magmatism. *Ore Geol. Rev.* 131, 104028. doi:10.1016/j.oregeorev.2021.104028

Li, J. H., Zhang, Y. Q., Dong, S. W., and Johnston, S. T. (2014a). Cretaceous tectonic evolution of South China: A preliminary synthesis. *Earth. Sci. Rev.* 134, 98–136. doi:10.1016/j.earscirev.2014.03.008

Li, J. H., Zhao, G. C., Johnston, S. T., Dong, S. W., Zhang, Y. Q., Xin, Y. J., et al. (2017). Permo-Triassic structural evolution of the Shiwandashan and Youjiang structural belts, South China. *J. Struct. Geol.* 100, 24–44. doi:10.1016/j.jsg.2017.05.004

Li, S. Z., Zang, Y. B., Wang, P. C., Suo, Y. H., Li, X. Y., Liu, X., et al. (2017a). Mesozoic tectonic transition in South China and initiation of Palaeo-Pacific subduction. *Earth Sci. Front.* 24 (4), 213–225. (in Chinese with English abstract). doi:10.13745/j.esf.yx.2017–4–13

Li, Z. X., Li, X. H., Chung, S. L., Lo, C. H., Xu, X. S., and Li, W. X. (2012). Magmatic switch-on and switch-off along the South China continental margin since the Permian: Transition from an Andean-type to a Western Pacific-type plate boundary. *Tectonophysics* 532–535, 271–290. doi:10.1016/j.tecto.2012.02.011

Li, Z. X., and Li, X. H. (2007). formation of the 1300-km-wide intracontinental orogen and postorogenic magmatic province in Mesozoic South China: A flat-slab subduction model. *Geol.* 35, 179–182. doi:10.1130/G23193A.1

Lin, W., Wang, Q. C., and Chen, K. (2008). Phanerozoic tectonics of South China block: New insights from the polyphase deformation in the Yunkai massif. *Tectonics* 27, 1–16. doi:10.1029/2007TC002207

Mao, J. R., Li, Z. L., and Ye, H. M. (2014). Mesozoic tectono-magmatic activities in South China: Retrospect and prospect. *Sci. China Earth Sci.* 57, 2853–2877. doi:10.1007/s11430-014-5006-1

Meng, L. F., Li, Z. X., Chen, H. L., Li, X. H., and Wang, X. C. (2012). Geochronological and geochemical results from Mesozoic basalts in southern South China block support the flat-slab subduction model. *Lithos* 132 (133), 127–140. doi:10.1016/J.LITHOS.2011.11.022

Niu, Y. L. (2014). Geological understanding of plate tectonics: Basic concepts, illustrations, examples and new perspectives. *gtm.* 10, 23–46. doi:10.1127/gtm/2014/0009

Qiu, L., Kong, R. Y., Yan, D. P., Mu, H. X., Sun, W. H., Sun, S. H., et al. (2022a). Paleo–Pacific plate subduction on the eastern Asian margin: Insights from the Jurassic foreland system of the overriding plate. *GSA Bull.* 134, 2305–2320. doi:10.1130/b36118.1

Qiu, L., Yan, D. P., Tang, S. L., Chen, F., Song, Z. D., Gao, T., et al. (2020). Insights into post-orogenic extension and opening of the Palaeo-Tethys Ocean recorded by an Early Devonian core complex in South China. *J. Geodyn.* 135, 101708. doi:10.1016/j.jog.2020.101708

Qiu, L., Yan, D. P., Tang, S. L., Wang, Q., Yang, W. X., Tang, X. L., et al. (2016). Mesozoic geology of southwestern China: Indosinian foreland overthrusting and subsequent deformation. *J. Asian Earth Sci.* 122, 91–105. doi:10.1016/j.jseaes.2016.03.006

Qiu, L., Yang, W. X., Yan, D. P., Wells, M. L., Qiu, J. T., Gao, T., et al. (2019). Geochronology of early Mesozoic diabase units in southwestern China: Metallogenic and tectonic implications. *Geol. Mag.* 156, 1141–1156. doi:10.1017/S0016756818000493

Shen, L. W., Yu, J. H., O'Reilly, S. Y., Griffin, W. L., and Zhou, X. Y. (2018). Subduction-related middle Permian to early Triassic magmatism in Central Hainan Island, South China. *Lithos* 318–319, 158–175. doi:10.1016/j.lithos.2018.08.009

Shi, W., Dong, S. W., and Zhang, Y. Q. (2022). Jurassic contractional deformation in the central–Western North China craton in response to multi-plate convergence in the East Asia. *Geosys. Geoenviron.*, 100099. doi:10.1016/j.geogeo.2022.100099

Shu, L. S., Yao, J. L., Wang, B., Faure, M., Charvet, J., and Chen, Y. (2021). Neoproterozoic plate tectonic process and Phanerozoic geodynamic evolution of the South China block. *Earth. Sci. Rev.* 216, 103596. doi:10.1016/j.earscirev.2021.103596

Shu, L. S., and Zhou, X. M. (2002). Late Mesozoic tectonism of southeast China. *Geol. Rev.* 48 (3), 249–260. (in Chinese with English abstract).

Sun, T., Zhou, X. M., Chen, P. R., Li, H. M., Zhou, H. Y., Wang, Z. C., et al. (2005). Strongly peraluminous granites of Mesozoic in eastern Nanling range, southern China: Petrogenesis and implications for tectonics. *Sci. China Ser. D-Earth. Sci.* 48, 165–174. doi:10.1360/03YD0042

Suo, Y. H., Li, S. Z., Jin, C., Zhang, Y., Zhou, J., Li, X. Y., et al. (2019). Eastward tectonic migration and transition of the Jurassic-Cretaceous Andean-type continental margin along Southeast China. *Earth. Sci. Rev.* 196, 102884. doi:10.1016/j.earscirev.2019.102884

Wang, Q. F., Yang, L., Xu, X. J., Santosh, M., Wang, Y. N., Wang, T. Y., et al. (2020). Multi–stage tectonics and metallogeny associated with phanerozoic evolution of the South China block: A holistic perspective from the Youjiang Basin. *Earth. Sci. Rev.* 211, 103405. doi:10.1016/j.earscirev.2020.103405

Wang, Y. J., Fan, W. M., Sun, M., Liang, X. Q., Zhang, Y. H., and Peng, T. P. (2007). Geochronological, geochemical and geothermal constraints on petrogenesis of the Indosinian peraluminous granites in the South China block: A case study in the Hunan Province. *Lithos* 96, 475–502. doi:10.1016/j.lithos.2006.11.010

Wang, Y. J., Fan, W. M., Zhang, G. W., and Zhang, Y. H. (2013). Phanerozoic tectonics of the South China block: Key observations and controversies. *Gondwana Res.* 23, 1273–1305. doi:10.1016/j.gr.2012.02.019

Wang, Y. N., Wang, Q. F., Deng, J., Xue, S. C., Li, C. S., and Ripley, E. M. (2021). Late Permian-Early Triassic mafic dikes in the southwestern margin of the South China block: Evidence for Paleo-Pacific subduction. *Lithos* 105994, 384–385. doi:10.1016/j.lithos.2021.105994

Wang, Y. J., Zhang, F. F., Fan, W. M., Zhang, G. W., Chen, S. Y., Cawood, P. A., et al. (2010). Tectonic setting of the South China Block in the early Paleozoic: Resolving intracontinental and ocean closure models from detrital zircon U-Pb geochronology. *Tectonics* 29. doi:10.1029/2010TC002750

Wu, Y., Zhang, S., Huang, Z., Wang, F., Li, J., Xiao, C., et al. (2019). Meso-Cenozoic tectonic evolution of the Nandan-Libo area, northwestern Guangxi, China: Evidence from palaeo-tectonic stress fields analyses. *Geotecton. Metallog.* 43, 872–893. doi:10.16539/j.ddgzyckx.2019.05.002

Xiao, C. H., Chen, Z. L., Liu, X. C., Wei, C. S., Wu, Y., Tang, Y. W., et al. (2022). Structural analysis, mineralogy, and cassiterite U–Pb ages of the Wuxu Sb-Zn-polymetallic district, Danchi Fold-and-Thrust belt, South China. *Ore Geol. Rev.* 150, 105150. doi:10.1016/j.oregeorev.2022.105150

Xiao, C. H., Shen, Y. K., Wei, C. S., Su, X. K., Le, X. W., and Zhang, L. (2018). LA–ICP–MS zircon U–Pb dating, Hf isotopic composition and Ce4+/Ce3+ characteristics of the Yanshanian acid magma in the Xidamingshan cluster, southeastern margin of the Youjiang fold belt, Guangxi. *Geoscience* 32 (2), 289–304. (in Chinese with English abstract).

Xu, C. H., Zhang, L., Shi, H. S., Brix, M. R., Huhma, H., Chen, L. H., et al. (2017). Tracing an early Jurassic magmatic arc from South to East China Seas. *Tectonics* 36, 466–492. doi:10.1002/2016TC004446

Xu, X. B., Li, Q. M., Gui, L., Su, Y. P., and Zhang, X. F. (2019). Early Mesozoic tectonic transition of the eastern South China block: Constraints from late Triassic Dashuang complex in Eastern Zhejiang Province. *Int. Geol. Rev.* 61, 997–1015. doi:10.1080/00206814.2018.1490931

Yang, L., Deng, J., Groves, D. I., Wang, Q. F., Zhang, L., Wu, W., et al. (2020). Recognition of two contrasting structural- and mineralogical-gold mineral systems in the Youjiang basin, China-Vietnam: Orogenic gold in the south and Carlin-type in the north. *Geosci. Front.* 11, 1477–1494. doi:10.1016/j.gsf.2020.05.011

Yang, W. X., Yan, D. P., Qiu, L., Wells, M. L., Dong, J. M., Gao, T., et al. (2021). formation and forward propagation of the Indosinian foreland fold-thrust belt and Nanpanjiang foreland basin in SW China. *Tectonics* 40, 1–24. doi:10.1029/2020TC006552

Zeng, Y. F., Liu, W. J., Chen, H. D., Zheng, R. C., Zhang, J. Q., Li, X. Q., et al. (1995). Evolution of sedimentation and tectonics of the Youjiang composite basin, South China. *Acta Geol. Sin.* 69 (2), 113–124. (in Chinese).

Zhang, D., Li, F., He, X. L., Hu, B. J., Zhang, X. M., Bi, M. F., et al. (2021). Mesozoic tectonic deformation and its rock/ore-control mechanism in the important metallogenic belts in South China. *J. Geomech.* 27 (4), 497–506. (in Chinese with English abstract). doi:10.12090/j.issn.1006-6616.2021.27.04.045

Zhang, G. W., Guo, A. L., Wang, Y. J., Li, S. Z., Dong, Y. P., Liu, S. F., et al. (2013). Tectonics of South China continent and its implications. *Sci. China Earth Sci.* 56, 1804–1828. doi:10.1007/s11430-013-4679-1

Zhang, X. M., Zhang, D., Bi, M. F., Wu, G. G., Fan, Z. Z., Que, C. Y., et al. (2021). Genesis and geodynamic setting of the Nanyangtian tungsten deposit, SW China: Constraints from structural deformation, geochronology, and S–O isotope data. *Ore Geol. Rev.* 138, 104354. doi:10.1016/j.oregeorev.2021.104354

Zhang, Y. Q., Dong, S. W., Li, J. H., Cui, J. J., Shi, W., Su, J. B., et al. (2012). The new progress in the study of Mesozoic tectonics of South China. *Acta Geol. Sin.* 33, 257–279. (in Chinese with English abstract).

Zhang, Y. Q., Xu, X. B., Jia, D., and Shu, L. S. (2009). Deformation record of the change from Indosinian collision-related tectonic system to Yanshanian subduction-related tectonic system in South China during the Early Mesozoic. *Earth Sci. Front.* 16 (1), 234–247. (in Chinese with English abstract).

Zhao, Z., Chen, Y. C., Wang, D. H., Li, J. K., Liu, S. B., Chen, Z. Y., et al. (2022). Transformation of Mesozoic dynamic systems and superposition of metallogenic series of W-Sn-Li-Be-Nb-Ta-REE mineral deposits in South China. *Acta Petrol. Sin.* 38 (2), 301–322. (in Chinese with English abstract). doi:10.18654./1000–0569./2022.02.01

Zhou, X. M., Sun, T., Shen, W. Z., Shu, L. S., and Niu, Y. L. (2006). Petrogenesis of Mesozoic granitoids and volcanic rocks in South China: A response to tectonic evolution. *Episodes* 29, 26–33. doi:10.18814/epiiugs/2006/v29i1/004

Zhu, J. J., Hu, R. Z., Richards, J. P., Bi, X. W., Stern, R., and Lu, G. (2017). No genetic link between Late Cretaceous felsic dikes and Carlin–type Au deposits in the Youjiang basin, Southwest China. *Ore Geol. Rev.* 84, 328–337. doi:10.1016/j.oregeorev.2017.01.014

frontiers | Frontiers in Earth Science

TYPE Original Research
PUBLISHED 26 January 2023
DOI 10.3389/feart.2022.1027620

Check for updates

OPEN ACCESS

EDITED BY
Fei Xue,
Hohai University, China

REVIEWED BY
Teng Ding,
Hohai University, China
Hailong Huo,
Chinese Academy of Geological Sciences (CAGS), China

*CORRESPONDENCE
Sen Wang,
wangsen_cug@163.com

SPECIALTY SECTION
This article was submitted to Economic Geology, a section of the journal Frontiers in Earth Science

RECEIVED 25 August 2022
ACCEPTED 07 November 2022
PUBLISHED 26 January 2023

CITATION
Wang S, Cao K, Zhang D, Yi J-J, Hu B-J, Yang J, Cai M-Y, Zhang Y-Y, Yuan Y and Pan T-W (2023), Mineralization age and genesis of the makeng-style iron deposits in the Paleo-Pacific tectonic domain of South China: *In situ* LA-ICPMS garnet U-Pb chronological and geochemical constraints.
Front. Earth Sci. 10:1027620.
doi: 10.3389/feart.2022.1027620

COPYRIGHT
© 2023 Wang, Cao, Zhang, Yi, Hu, Yang, Cai, Zhang, Yuan and Pan. This is an open-access article distributed under the terms of the Creative Commons Attribution License (CC BY). The use, distribution or reproduction in other forums is permitted, provided the original author(s) and the copyright owner(s) are credited and that the original publication in this journal is cited, in accordance with accepted academic practice. No use, distribution or reproduction is permitted which does not comply with these terms.

Mineralization age and genesis of the makeng-style iron deposits in the Paleo-Pacific tectonic domain of South China: *In situ* LA-ICPMS garnet U-Pb chronological and geochemical constraints

Sen Wang[1,2,3]*, Ke Cao[4], Da Zhang[5], Jin-Jun Yi[6], Bo-Jie Hu[5], Jing Yang[1,2,3], Meng-Ying Cai[5], Yao-Yao Zhang[5], Yuan Yuan[5] and Tian-Wang Pan[5]

[1]Institute of Geomechanics, Chinese Academy of Geological Sciences, Beijing, China, [2]Key Laboratory of Paleomagnetism and Tectonic Reconstruction, Ministry of Natural Resources, Beijing, China, [3]Research Center of Polar Geosciences, China Geological Survey, Beijing, China, [4]Beijing Research Institute of Uranium Geology, Beijing, China, [5]China University of Geosciences (Beijing), Beijing, China, [6]Cores and Samples Centre of Natural Resources, China Geological Survey, Sanhe, China

To reveal the genesis of Makeng-style iron polymetallic deposits from SE China in the paleo-Pacific tectonic domain, a new analytical method of LA-ICPMS garnet U-Pb dating and rare Earth element analysis was conducted for the Makeng, Luoyang, Dapai and Pantian deposits. The U-Pb dating results of nine garnet skarn samples from these deposits suggested that the Makeng-style iron polymetallic deposits mainly formed during 137–130 Ma, which is consistent with the zircon U-Pb and molybdenite Re-Os ages. This study provides more direct evidence of the mineralization age and the relationship between mineralization and granite, compared with previous studies on the zircon U-Pb dating for granites in the ore fields. Rare Earth element (REE) analysis results and REE patterns of four representative garnet samples from the Makeng, Luoyang, Dapai and Pantian deposits show that they are similar to typical skarn deposits, but obvious differences in the REE distribution types indicate that the ore-forming process may be distinct due to different mineralizing fluid for these Makeng-style deposits. Our new garnet U-Pb dating and rare Earth element analysis result not only provides new evidence for the mineralization age and genesis of the Makeng-style deposits but is also of great significance to promote the application of U-Pb dating methods to research skarn type deposits.

KEYWORDS

garnet U-Pb dating, ore genesis, makeng-type deposits, mineralization age, southweatern fujian

Introduction

The Southwestern Fujian Iron Polymetallic Metallogenic Belt (SFIPMB) is one of the most important mineralization zones in the Southeast China Block of the paleo-Pacific tectonic domain (Figure 1A), and abundant iron deposits were hosted along this belt, such as the Makeng, Dapai, Pantian, Luoyang, Yangshan, Tangquan, and Zhongjia deposits (Figure 1B). These deposits are typically referred to as "Makeng-style iron deposits" due to their spatial and genetic association with the super large scale Makeng iron polymetallic deposit (Zhang et al., 2018a; Wang et al., 2018a; Wang et al., 2021). These deposits have similar metallogenic characteristics, and ore bodies are usually found between the early Carboniferous siliceous clastic rocks and late Carboniferous - middle Permian limestones with stratiform or stratoid shapes and large sizes. Many studies have been performed on the genesis of Makeng-style iron polymetallic deposits (Han and Ge, 1983; Zhang et al., 2018a; Zhang et al., 2013; Zhang and Zhang, 2014; Zhang and Zuo, 2014; Zhang et al., 2015; Wang et al., 2017a; Yang et al., 2017; Wang et al., 2018a), but controversy remain due to different understanding on the mineralization age. Some scholars held on the idea that the mineralization of the Makeng-style iron deposit was related to Early Cretaceous granites (ca. 135–130 Ma, Zhang et al., 2018a; Zhang et al., 2013; Zhang et al., 2018a). However, other scholars put forward different opinions on the mineralization age according to the relationship between the magnetite orebodies and other wall rocks, and provided chronological evidences of 160–150 Ma (Wang et al., 2010; Yan, 2013; Zhang et al., 2015; Wang et al., 2017a). Especially in the last few years, zircon U-Pb ages of 160–150 Ma for granites from these Makeng-style deposits were reported, such as 154.9 ± 0.9 Ma for Makeng deposit (Yan, 2013), 152.7 ± 1.4 Ma for the Luoyang deposit (Yu, 2017), and 150.2 ± 0.5 Ma for Dapai deposit (Yuan et al., 2020). Together with garnet Sm-Nd ages (157 ± 15 Ma, Zhang et al., 2015), zircon U-Pb ages of granites and basic rocks suggested that the mineralization may occur at 160–150 Ma (Yan, 2013; Zhang et al., 2015; Wang et al., 2017a; Yu, 2017; Yuan et al., 2020). To sum up, there are two main viewpoints on the mineralization age for the Makeng-style deposits due to different research objects and analytical methods they selected. In addition, different understandings on the mineralization age further affects explanations of the ore genesis, and therefore, the controversy on the mineralization age for the Makeng-style

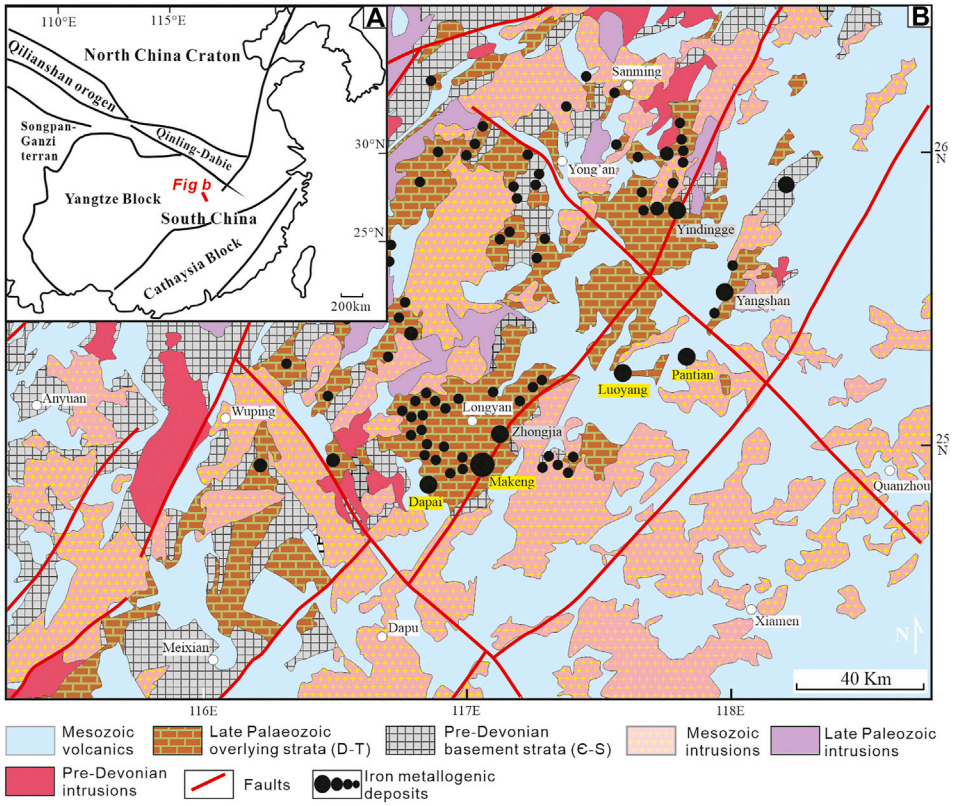


FIGURE 1
Tectonic sketch map showing the location of the study area **(A)** and regional geological map of southwest Fujian and the location of Makeng-style deposits **(B)**.

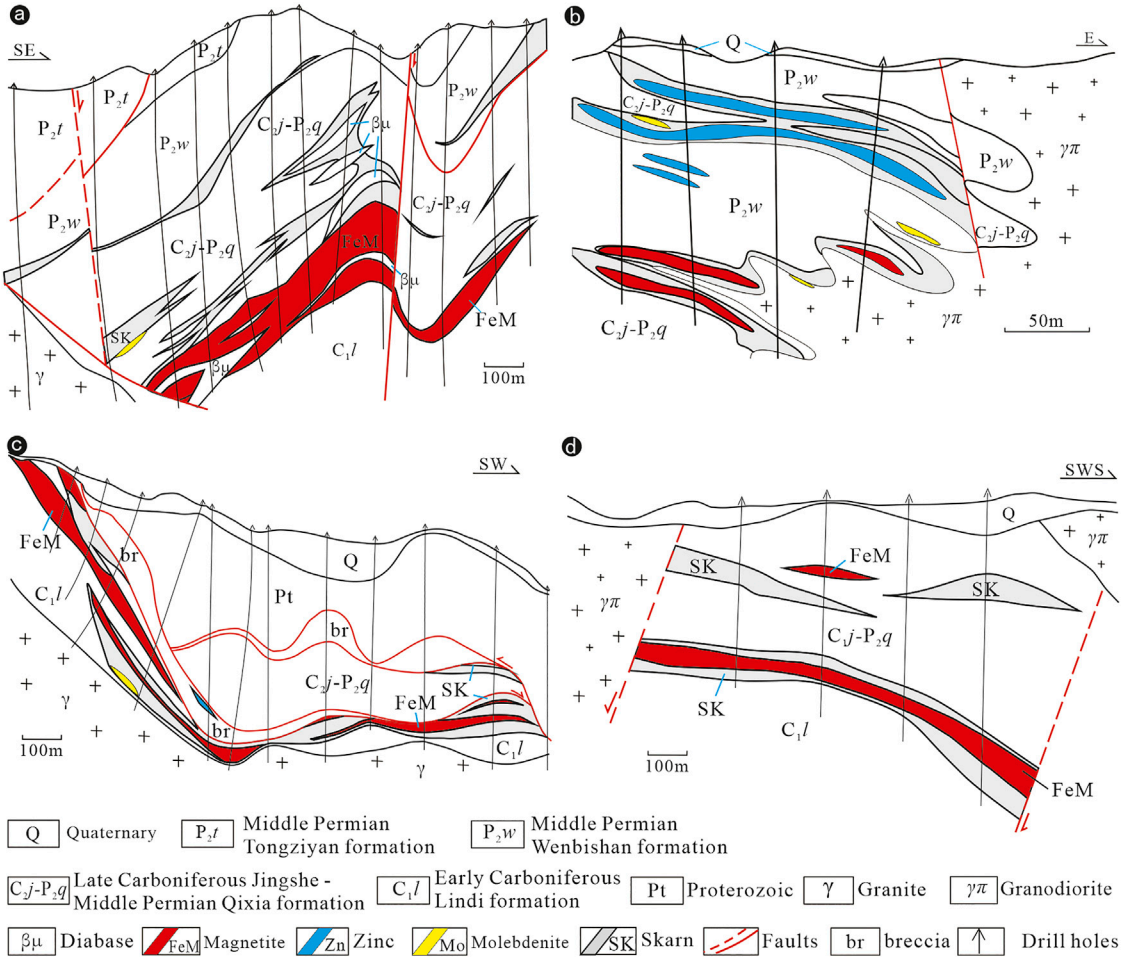


FIGURE 2
Geological Section Maps of the Makeng **(A)**, Dapai **(B)**, Pantian **(C)** and Luoyang **(D)** Fe-polymetallic deposits.

deposits needs to be solved urgently. Garnet-magnetite and diopside-magnetite are the major ore types with massive and banded structures for these Makeng-style deposits. The garnets are mainly andradites and closely associated with the magnetites in space. These garnets usually have good crystal shapes, and they are accompanied by xenomorphic magnetites. At present, it is impossible to carry out direct dating on magnetites, and therefore, the dating research on garnets can provide more direct constrains on the mineralization age due to their close spatial relationship with magnetites. Along with the development of laser ablation inductively coupled plasma-mass spectrometry (LA-ICPMS), *in-situ* garnet U-Pb isotope analysis has been gradually realized (Chen et al., 2016; Deng et al., 2017; Seman et al., 2017; Tang et al., 2021). As a main kind of skarn mineral, garnet has been used in dating research the skarn type deposits and yields accurate U-Pb ages (Deng et al., 2017; Li et al., 2018; Wafforn et al., 2018; Stifeeva et al., 2019; Duan et al., 2020; Tang et al., 2021). In this paper, ore-bearing skarns were selected from the Makeng, Luoyang, Dapai and Pantian deposits to carry out garnet U-Pb dating and rare Earth element analysis research and provide new evidence on the mineralization age and ore genesis for the Makeng-style iron polymetallic deposits. This research not only provides new chronology and geochemical evidence for the generation of the Makeng-style deposits but is also of great significance to promote the application of new U-Pb dating methods to the study of skarn type deposits.

Regional geological setting

The global tectonic pattern underwent some major changes with frequent magmatic-polymetallic mineralization in eastern China during the Yanshanian period. Located in the eastern part of the South China Plate, the southwestern Fujian area has been affected by the subduction of the Pacific Plate since the Mesozoic and Cenozoic, and the metallogenic domains of the circum-

Pacific have occurred with large-scale copper, molybdenum, iron, gold silver, lead and zinc mineralization, such as the Zijinshan copper-gold deposit and Makeng iron deposit.

Located on the western margin of the Paleo-Pacific tectonic domain, the Makeng-style deposits are important iron polymetallic ore deposits in the SE China. These iron polymetallic ores are controlled by regional structures with an obvious NE-trending distribution (Figure 1). Sedimentary rocks distributed in the metallogenic belt are mainly.

The following three types in general: pre-Devonian basement rocks, late Paleozoic-middle Triassic clastic sedimentary and cap carbonate strata, and Mesozoic continental clastic and volcanic rocks (Wang et al., 2017b). Among these rocks, Early Carboniferous siliceous clastic rocks and Late Carboniferous - middle Permian limestones are most closely related to the iron polymetallic ore bodies in space (Figure 2). The iron polymetallic metallogenic belt is a most important part of the Mesozoic tectonic-magmatic zone on the west side of the Pacific plate. Mesozoic acidic and intermediate-acidic magmatic rocks are widely developed in the ore districts of Makeng-style deposits, with U-Pb ages mainly ranging from 135 to 130 and 160 to 150 (Wang et al., 2015). These intrusive rocks are closely related to the magnetite ore bodies in space, but there is a lack of direct evidence for the relationship between them. The iron orebodies mainly occurred in the garnet skarn and obviously controlled by strata, not in the contact zone of the granites. The Makeng-style iron polymetallic deposits are accompanied by Mo-, Pb- and Zn-bearing minerals, and previous studies have demonstrated that the molybdenite formed during 135–130 Ma (Zhang et al., 2018a; Zhang et al., 2012b); however, unlike the magnetites, molybdenites were only found within the granite bodies and in the fracture surface of wall rocks and iron ores. Therefore, there is no direct evidence to suggest that the molybdenite is contemporaneous with magnetite. The Early Cretaceous granites are the major magmatic rocks in the SFIPMB (Figure 2), and they are most likely metallogenic rocks; however, there is no direct evidence to verify that the iron mineralization is related to the Cretaceous granite, especially for the Makeng deposit.

Ore features

As one of the most important super large iron deposits in South China, the Makeng iron polymetallic deposit was taken as an example to display its ore features in this paper. The Makeng iron deposit is characterized by thick and large single orebody with a maximum thickness of >50 m (>200 m in the Makeng deposit), but it shows remarkable variations in different positions due to the control of folds and faults. The main ore bodies formed in the contact zone between the Early Carboniferous clastic rocks (C_1l) and Late Carboniferous-Middle Permian carbonate rocks (C_2j-P_2q) with bedded and para-bedded shapes. Magnetite is the major metal-bearing mineral in these deposits, with some hematite, pyrite, molybdenite and sphalerite. As a kind of later hydrothermal modified mineral, molybdenite is often filled in the fracture surface of wall rocks and iron ores with vein and scattered shapes. Garnet and diopside is the primary gangue minerals and they are closely associated with the iron-rich ores. The garnet associated with magnetite is reddish brown and dark in color, which has typical characteristics of andradite garnet. In addition, vein magnetite is often observed in the mineralized bodies, and they are always accompanied by skarn minerals. The iron ores mainly show semi-euhedral to euhedral medium—coarse granular texture, with a small amount of metasomatic texture. Dense massive structure is the most important ore structure in the Makeng deposit, accounting for more than 70%. Skarn is the most important alteration type in this deposit. Associated with magnetites, the garnet and diopside accounted for a vast majority of the altered minerals. Despite it has large size of iron ore bodies and the wide variety of skarn minerals, there is no obvious zonation of skarn observed in the mine.

Sampling and analytical methods

Sample description

Samples of garnet skarn collected from the Makeng, Luoyang, Dapai and Pantian deposits were selected to carry out LA-ICPMS garnet U-Pb dating in this paper. A total of nine samples were collected from the mine channel and drill holes of the Makeng (102-2-b4, 108-1-b6, ZK7525-b1, and 214-b9), Luoyang (ZK405-b13 and BL23), Dapai (ZK403-b92 and ZK403-b67), and Pantian (PTPD-b1) iron polymetallic ore deposits. These samples were collected from the ore-bearing garnet skarn in different deposits and different orebodies of a same deposit. The garnets were concomitant with magnetites in these selected samples. Magnetite was the main ore mineral with little pyrite, pyrrhotite and chalcopyrite, along with garnet as major gangue mineral. Micrographs of representative samples showed that garnet was formed with good crystal morphology and closely association with magnetite in space (Figure 3). The garnets have euhedral and semi-euhedral granular textures with crystal size ranging from 200 to 500 μm, with typical growth bands developed locally.

Analytical method

These spots with no cracks and inclusions were selected from each thin section of these samples to carry out the experiment. Garnet U-Pb dating and rare element analysis was performed using a GeoLasHD ArF laser ablation (LA) and an Agilent

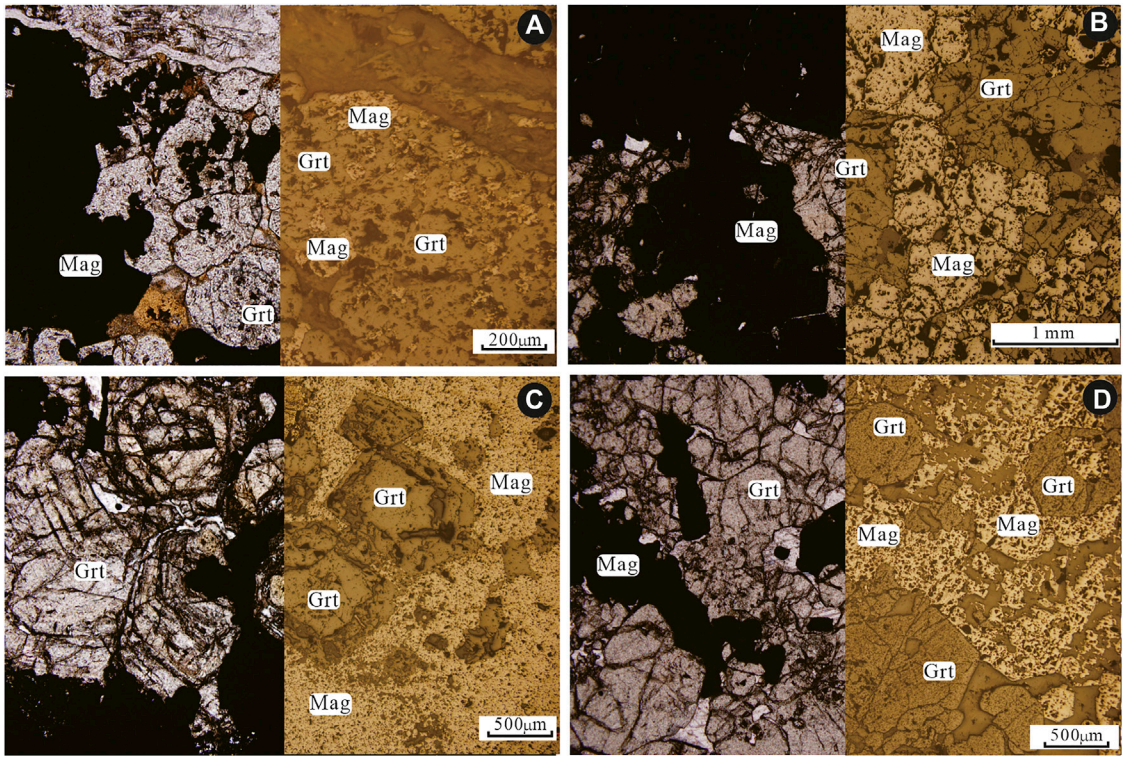


FIGURE 3
Microphotographs showing the accompanying relationship between garnets and Magnetites from Makeng **(A)**, Luoyang **(B)** Dapai **(C)** and Pantian **(D)** deposits. (The left photos are cross-polarized light; the right photos are plane-polarized light). Gr—Garnet; Mag—Magnetite.

TABLE 1 Major parameters for the garnet LA-ICP-MS U-Pb dating method.

La ablation (GeoLasHD 193 nm ArF)	
Energy density	5 mJ/cm^2
Ablation frequency	5 Hz
Sampling time	50 s
Spot beam diameter	90 μm
Carrier gas type	He
Flow rate of carrier gas	0.4 L/min
Inductively Coupled Plasma Mass Spectrometer (Agilent 7900)	
Plasma flow (Ar)	15 L/min
RF power	1550 W
Sample depth	6.0 mm
Nebulizer gas	0.7–0.9 L/min
Analyzed Isotopes	204 Pb, 206 Pb, 207 Pb, 208 Pb, 232Th, and 238U
Integral time	25 ms/isotope

7900 inductively coupled plasma mass spectrometer (ICP-MS) at the Key Laboratory of Paleomagnetism and Tectonic Reconstruction, Ministry of Natural Resources, Beijing, China. A detailed introduction to the instrumental conditions was described in Wang et al. (2022). A spot beam size of 90 μm was used during the analysis, and the garnet Willsboro (Seman et al., 2017) was used as an external standard to test the isotope ratios of the samples. Detailed instrument parameters and analytical methods were listed in Table 1. After the analyses, ICPMSDataCal software (version 10.9) was applied to calculate the $^{207}Pb/^{206}Pb$, $^{206}Pb/^{238}U$, $^{207}Pb/^{235}U$ and $^{208}Pb/^{232}Th$ ratios (Liu et al., 2010). Tera-Wasserburg lower intercept ages were calculated using ISOPLOT 3.0 with quotes at the 1σ and 95% confidence levels (Ludwig, 2003).

The experimental conditions and instrument parameters for *in-situ* rare Earth element analysis were the same as those for U-Pb dating, and it was done at the same time as U-Pb isotope analysis. The synthetic glass samples NIST 610 and NIST 612 were used as external standards to test the rare Earth element contents. ICPMSDataCal software (version 10.9) was applied to calculate the trace element contents (Liu et al., 2010).

TABLE 2 Rare Earth element analytical results (10^{-6}) of garnets from the Makeng-style Fe-polymetallic deposits.

	La	Ce	Pr	Nd	Sm	Eu	Gd	Tb	Dy	Ho	Er	Tm	Yb	Lu	ΣREE	ΣLREE	ΣHREE
ZK7525-b1(Makeng)																	
01	1.0511	6.9195	1.4148	6.5141	1.2001	1.4638	1.2303	0.1731	1.0909	0.1926	0.5554	0.0565	0.3849	0.0424	22.29	18.56	3.73
02	7.7441	16.1248	1.5024	4.5794	0.5664	1.5918	0.4048	0.0399	0.2755	0.0653	0.1418	0.0202	0.1294	0.0102	33.20	32.11	1.09
03	1.9392	10.6070	1.7749	7.3752	0.7531	1.1787	0.3680	0.0388	0.2796	0.0529	0.1255	0.0178	0.1281	0.0127	24.65	23.63	1.02
04	4.3721	21.6796	3.1853	10.9134	0.5770	2.1307	0.0981	0.0088	0.0749	0.0116	0.0398	0.0037	0.0328	0.0030	43.13	42.86	0.27
05	2.3394	13.8120	2.7234	13.5269	2.1568	2.0080	0.7899	0.0888	0.4821	0.0957	0.2481	0.0240	0.1882	0.0250	38.51	36.57	1.94
06	1.9611	12.7000	2.7739	14.3987	2.2763	2.0123	0.7815	0.0654	0.3577	0.0667	0.1652	0.0209	0.1188	0.0170	37.72	36.12	1.59
07	4.3600	10.8181	1.2398	4.0751	0.5735	1.0614	0.2687	0.0273	0.1407	0.0140	0.0468	0.0043	0.0244	0.0020	22.66	22.13	0.53
08	2.2326	10.5603	1.8081	7.4349	0.9926	1.8925	0.7205	0.0914	0.6364	0.1308	0.3517	0.0510	0.3070	0.0392	27.25	24.92	2.33
09	1.4338	12.5633	2.7543	12.2188	1.3476	1.9096	0.8892	0.0915	0.5660	0.0948	0.2554	0.0301	0.2157	0.0265	34.40	32.23	2.17
10	1.5277	12.3138	2.5876	12.0579	1.4400	2.3044	0.9618	0.1098	0.6338	0.1066	0.2912	0.0408	0.2563	0.0321	34.66	32.23	2.43
11	5.8394	24.2897	3.8759	14.1335	1.0092	1.6410	0.6452	0.0667	0.4062	0.0734	0.1796	0.0235	0.1330	0.0164	52.33	50.79	1.54
12	5.5209	30.6717	5.3221	19.3850	1.6243	2.3132	0.9414	0.0868	0.4797	0.0861	0.2385	0.0326	0.1782	0.0256	66.91	64.84	2.07
13	1.4196	10.5001	2.2783	9.9149	1.3746	2.4626	1.0956	0.1468	0.9445	0.2041	0.6027	0.0710	0.4836	0.0624	31.56	27.95	3.61
14	4.5438	25.1296	4.1587	15.5537	1.3910	2.0632	0.9133	0.0936	0.5490	0.1028	0.2785	0.0299	0.2113	0.0299	55.05	52.84	2.21
15	6.5024	32.8156	5.1419	18.0854	1.5075	2.0113	0.8631	0.0930	0.5877	0.1049	0.2540	0.0322	0.2244	0.0369	68.26	66.06	2.20
16	5.6732	26.1321	4.3100	15.9903	1.5073	1.8369	0.8971	0.1022	0.6701	0.1363	0.3596	0.0414	0.2457	0.0287	57.93	55.45	2.48
17	1.6416	12.1852	2.4598	10.4882	1.1855	2.5414	0.7662	0.0834	0.5293	0.0948	0.2766	0.0332	0.2260	0.0285	32.54	30.50	2.04
18	3.2099	14.1695	2.2996	8.3870	0.9917	2.1379	0.7278	0.0968	0.6288	0.1170	0.3305	0.0425	0.2848	0.0342	33.46	31.20	2.26
19	3.7863	15.8384	2.3186	8.0912	0.9939	2.0534	0.7337	0.0961	0.6300	0.1068	0.3005	0.0318	0.2483	0.0284	35.26	33.08	2.18
20	3.7038	9.2883	1.1049	3.5706	0.4840	0.4452	0.6994	0.1002	0.7451	0.1583	0.5056	0.0631	0.4328	0.0609	21.36	18.60	2.77
21	5.1273	24.5835	4.0859	15.2168	1.4227	1.7921	0.8538	0.1063	0.5707	0.1083	0.2771	0.0277	0.2370	0.0283	54.44	52.23	2.21
22	4.6833	24.0051	4.1259	15.8967	1.6407	1.9769	0.9464	0.1001	0.6607	0.1093	0.3323	0.0373	0.2478	0.0359	54.80	52.33	2.47
23	3.7407	11.5888	1.6581	5.9554	0.4976	0.8663	0.3709	0.0573	0.2710	0.0589	0.1474	0.0172	0.1362	0.0170	25.38	24.31	1.08
24	1.9029	7.4841	1.7470	7.1613	0.3856	1.3424	0.1337	0.0148	0.1026	0.0171	0.0549	0.0042	0.0445	0.0062	20.40	20.02	0.38
25	3.8681	12.2527	1.3884	4.1080	0.7592	0.6075	1.1233	0.1721	1.2859	0.2609	0.8491	0.0940	0.6128	0.0955	27.48	22.98	4.49
ZK405-b13(Luoyang)																	
01	1.6318	18.9420	3.6208	12.4251	1.3776	0.6372	1.2234	0.1610	1.1978	0.2327	0.7492	0.0922	0.6246	0.0896	43.00	38.63	4.37
02	2.5307	10.8800	1.8997	7.0440	0.7744	0.3625	0.8221	0.1068	0.8130	0.1650	0.5310	0.0549	0.3660	0.0587	26.41	23.49	2.92
03	1.1500	12.3946	3.2999	18.9805	3.4782	1.7076	2.1913	0.2622	1.6916	0.2997	0.9533	0.1278	0.9230	0.1325	47.59	41.01	6.58
04	2.7416	22.4241	3.4705	12.1399	1.2964	0.7525	1.0840	0.1144	0.7568	0.1699	0.5386	0.0659	0.4678	0.0714	46.09	42.82	3.27
05	3.1893	29.5146	4.6395	16.3949	2.2518	0.9138	1.6419	0.1702	1.2485	0.2539	0.6339	0.0796	0.5522	0.0734	61.56	56.90	4.65
06	2.8131	26.6198	4.0631	14.4076	1.3854	0.8251	0.9553	0.1156	0.8145	0.1630	0.4740	0.0599	0.3744	0.0457	53.12	50.11	3.00

(Continued on following page)

10.3389/feart.2022.1027620

TABLE 2 (*Continued*) Rare Earth element analytical results (10^{-6}) of garnets from the Makeng-style Fe-polymetallic deposits.

	La	Ce	Pr	Nd	Sm	Eu	Gd	Tb	Dy	Ho	Er	Tm	Yb	Lu	ΣREE	ΣLREE	ΣHREE
07	2.6806	23.0889	3.3669	12.3883	1.4310	0.8080	1.0582	0.1205	0.8064	0.1478	0.4494	0.0514	0.3800	0.0429	46.82	43.76	3.06
08	3.6590	31.7782	5.0659	16.9251	2.0380	1.0113	1.5688	0.1805	1.2012	0.2314	0.6359	0.0706	0.4904	0.0686	64.92	60.48	4.45
09	2.9906	27.6522	4.6948	17.1033	2.1231	1.0702	1.6320	0.1873	1.1819	0.2237	0.6390	0.0768	0.4648	0.0765	60.12	55.63	4.48
10	2.2799	16.3760	2.5404	10.2058	1.3589	0.6961	1.1160	0.1321	0.8839	0.1837	0.4992	0.0611	0.3911	0.0530	36.78	33.46	3.32
11	1.9842	18.7467	3.5725	14.4271	1.3018	0.8764	0.9108	0.1001	0.7425	0.1478	0.4394	0.0541	0.3407	0.0393	43.68	40.91	2.77
12	2.0561	17.1829	3.1177	13.4685	1.9524	0.8579	1.1443	0.1463	0.8513	0.1791	0.4934	0.0618	0.4393	0.0529	42.00	38.64	3.37
13	1.3272	15.9018	3.5039	16.7142	2.7288	1.4957	1.7032	0.1811	1.1234	0.2061	0.5119	0.0670	0.5056	0.0730	46.04	41.67	4.37
14	1.9870	23.8286	4.9443	19.0179	1.9027	1.0655	1.2220	0.1386	0.8507	0.1693	0.5032	0.0655	0.4290	0.0570	56.18	52.75	3.44
15	1.6974	12.6234	2.3900	8.6535	0.9495	0.5565	0.8308	0.1084	0.7517	0.1801	0.5176	0.0700	0.4437	0.0540	29.83	26.87	2.96
16	2.3394	20.6711	4.4303	19.8793	2.2919	1.6971	1.6334	0.1996	1.1229	0.2179	0.6130	0.0677	0.6060	0.0704	55.84	51.31	4.53
17	2.5043	20.7491	4.5627	20.9617	2.4509	1.8231	1.6039	0.1881	1.2107	0.2346	0.7125	0.0773	0.6187	0.0758	57.77	53.05	4.72
18	1.6721	15.6917	3.5312	19.2296	2.5949	1.8019	1.5529	0.2048	1.1545	0.2379	0.5918	0.0774	0.5299	0.0784	48.95	44.52	4.43
19	2.2575	19.8059	4.4235	22.9732	2.9503	2.2468	1.7226	0.1830	1.0384	0.1736	0.5458	0.0597	0.4310	0.0560	58.87	54.66	4.21
20	1.0096	8.6143	2.2036	14.2014	2.4888	1.6490	1.4456	0.1484	0.9554	0.1591	0.4616	0.0527	0.4022	0.0524	33.84	30.17	3.68
21	1.5477	14.7754	3.7550	21.1765	3.2197	1.9556	2.2330	0.2134	1.2389	0.2062	0.5344	0.0598	0.3741	0.0538	51.34	46.43	4.91
22	1.0500	9.6963	2.4312	15.3127	2.4693	1.5986	1.5289	0.1463	0.7984	0.1434	0.4291	0.0420	0.3018	0.0427	35.99	32.56	3.43
23	1.5153	12.1859	2.6746	14.2925	2.2667	1.8449	1.3271	0.1256	0.8049	0.1267	0.3598	0.0386	0.2207	0.0339	37.82	34.78	3.04
24	1.5672	13.9509	3.4848	21.1427	3.5179	1.8598	2.4281	0.2796	1.6110	0.2859	0.8612	0.0870	0.6380	0.0858	51.80	45.52	6.28
25	2.3183	20.8837	4.5128	23.1011	3.1123	2.3469	1.9260	0.2016	1.2147	0.2266	0.5537	0.0675	0.4921	0.0554	61.01	56.28	4.74
26	1.7706	15.7116	4.0399	22.4558	3.7175	2.0435	2.3147	0.2569	1.4514	0.2688	0.6309	0.0776	0.5666	0.0853	55.39	49.74	5.65
27	1.5241	13.2116	3.0803	17.2316	2.5783	1.3475	1.8729	0.2164	1.3648	0.2383	0.7241	0.0803	0.6582	0.0703	44.20	38.97	5.23
28	1.9561	16.9369	3.8442	21.6208	3.2557	1.8414	2.1736	0.2408	1.4061	0.2790	0.7740	0.0823	0.6583	0.0887	55.16	49.46	5.70
29	2.0867	18.8196	4.7336	27.6026	3.7510	2.0496	2.4128	0.2489	1.4280	0.2750	0.7249	0.0846	0.5935	0.0716	64.88	59.04	5.84
30	1.0997	9.4070	2.4717	15.2702	2.8361	1.6101	1.7516	0.1890	1.1344	0.1895	0.5303	0.0679	0.4043	0.0571	37.02	32.69	4.32
31	1.3328	10.8895	2.5593	15.1774	2.9426	1.3439	2.2765	0.2557	1.7314	0.3027	0.7544	0.1069	0.6489	0.0803	40.40	34.25	6.16
32	2.2941	22.0588	5.0177	24.9277	3.1857	2.3627	2.4321	0.2846	1.6468	0.3411	0.9765	0.1116	0.8064	0.1139	66.56	59.85	6.71
ZK403-b67(Dapai)																	
01	18.5676	149.7086	24.8918	119.1647	25.5925	5.5164	21.2497	2.9471	17.7748	2.8081	7.4125	0.9392	6.7246	0.9317	404.23	343.44	60.79
02	13.7164	84.8239	13.3404	63.7800	15.9032	3.3963	16.0317	2.5336	16.3790	2.8714	8.2263	1.0606	8.1771	1.1976	251.44	194.96	56.48
03	19.9302	147.1071	26.2998	133.1006	30.3442	6.3753	24.5112	3.3014	20.3203	3.3324	8.7916	1.0685	7.7181	1.0178	433.22	363.16	70.06
04	21.5561	135.3794	19.7195	78.4955	14.2821	2.9630	11.3037	1.6736	10.8462	1.8543	5.3637	0.7171	5.7557	0.9602	310.87	272.40	38.47
05	22.6094	146.9015	19.7643	71.1965	12.8132	2.4104	8.8981	1.2342	7.1507	1.2583	3.2478	0.4676	3.5896	0.6306	302.17	275.70	26.48
06	10.4163	69.4935	12.0579	60.6923	21.8035	5.5561	30.9912	5.7637	41.4288	7.9139	22.8901	3.0051	21.8317	2.8535	316.70	180.02	136.68
07	6.5006	52.9525	10.8622	66.5356	29.9339	6.3153	42.6875	6.7155	43.7278	7.5586	20.9671	2.5982	18.1306	2.2773	317.76	173.10	144.66

(Continued on following page)

10.3389/feart.2022.1027620

TABLE 2 (*Continued*) Rare Earth element analytical results (10^{-6}) of garnets from the Makeng-style Fe-polymetallic deposits.

	La	Ce	Pr	Nd	Sm	Eu	Gd	Tb	Dy	Ho	Er	Tm	Yb	Lu	ΣREE	ΣLREE	ΣHREE
08	8.2492	63.0378	11.0353	55.0853	17.4637	4.7145	20.0108	2.9897	17.4843	2.7007	6.8854	0.8046	5.3306	0.6999	216.49	159.59	56.91
09	8.9883	89.5815	16.2302	65.6549	12.6399	1.8628	14.3808	2.2937	15.0911	2.8584	8.2767	1.0587	8.1866	1.1272	248.23	194.96	53.27
10	8.1247	75.1676	18.5828	120.1977	44.2088	9.4458	55.5477	8.8890	54.0320	8.5230	21.1186	2.5130	16.4826	1.8071	444.64	275.73	168.91
11	4.1680	45.7377	11.1144	70.6844	33.7360	10.2825	38.7804	5.5886	32.3750	5.3092	13.8423	1.6789	11.9645	1.4005	286.66	175.72	110.94
12	14.0696	108.9676	19.4068	90.0510	15.8997	3.5855	11.8507	1.6980	10.4921	1.9101	5.3956	0.7315	5.0559	0.6855	289.80	251.98	37.82
13	14.8768	108.3804	17.0199	74.6314	13.0850	3.7308	9.4994	1.3083	7.8643	1.2949	3.3736	0.4268	3.0908	0.3904	258.97	231.72	27.25
14	11.3556	80.3302	12.5499	54.8846	14.5022	3.3162	17.6682	2.8869	19.4817	3.5216	9.6850	1.2726	8.9936	1.1793	241.63	176.94	64.69
15	15.9084	115.2267	19.6550	85.9887	19.5723	5.2849	22.7809	3.9570	26.9652	4.9329	14.7900	1.9058	13.2983	1.5703	351.84	261.64	90.20
16	8.5553	56.0627	12.9183	72.7570	31.2280	4.1640	44.5373	6.4971	33.9623	4.6973	10.6233	1.1534	7.4609	0.9006	295.52	185.69	109.83
17	19.4520	151.8294	25.7649	109.6677	23.9800	6.4696	25.6234	3.9784	23.7282	3.7748	9.6261	1.1244	7.3011	0.7992	413.12	337.16	75.96
18	16.2071	111.8097	20.3680	96.7396	23.5256	6.5582	22.4537	3.2160	18.7413	2.8578	7.0014	0.7713	5.2475	0.5941	336.09	275.21	60.88
19	23.8900	130.8813	21.1451	111.2794	45.0579	8.9812	60.4282	9.5094	56.6118	9.0306	22.6732	2.6545	18.6269	2.2643	523.03	341.23	181.80
20	12.0831	93.4766	16.6909	73.7938	22.3876	4.0885	22.8136	3.1909	17.1161	2.6214	6.6858	0.8250	5.5461	0.7690	282.09	222.52	59.57
21	18.0946	125.3588	19.9945	90.5357	21.9612	3.6869	16.7259	2.1196	11.7362	1.8704	5.0722	0.6339	4.5003	0.6571	322.95	279.63	43.32
22	14.2638	119.3521	24.7194	130.4673	28.3763	7.3833	23.9593	3.9553	26.6862	5.0473	15.3923	2.0461	15.6476	2.1463	419.44	324.56	94.88
23	27.1295	199.4180	34.6795	171.3148	34.6050	7.4103	20.5384	2.4036	13.6708	2.1496	5.8639	0.7589	5.7670	0.8251	526.53	474.56	51.98
24	9.7301	100.5082	22.1331	130.4838	35.0412	7.5390	34.3516	5.0471	30.9258	4.9991	12.9653	1.5924	11.6520	1.5574	408.53	305.44	103.09
25	9.1961	97.5050	24.9159	156.1901	43.6286	9.2681	44.5966	6.7840	41.5643	7.0233	18.7588	2.3335	17.2282	2.3871	481.38	340.70	140.68
26	9.7282	96.1372	22.6761	138.4134	36.5328	7.2238	28.5554	3.8666	23.1895	3.9320	10.6480	1.3927	10.5211	1.4818	394.30	310.71	83.59
PTPD-b1(Pantian)																	
01	6.3058	45.5843	8.0230	30.7870	5.3362	1.2981	4.9196	0.7883	4.8678	1.0397	3.3214	0.5157	4.1664	0.6003	117.55	97.33	20.22
02	22.3512	133.3816	16.7390	50.9776	8.3350	1.8368	8.7390	1.6002	11.5199	2.5636	8.4628	1.5953	11.1727	1.6390	280.91	233.62	47.29
03	7.4608	99.0428	23.8060	106.4404	22.7510	3.4912	20.8460	3.6718	24.1642	5.2232	15.6804	2.7145	20.4964	3.2533	359.04	262.99	96.05
04	7.4408	102.6949	21.6307	87.4132	19.7832	2.8736	18.5519	3.1569	20.3985	4.8428	14.2465	2.3364	19.3547	2.7915	327.52	241.84	85.68
05	10.4879	135.2963	24.2545	93.3241	18.7525	3.0873	15.7440	2.5207	14.9216	3.0587	8.6533	1.5196	11.4994	1.6790	344.80	285.20	59.60
06	9.8248	127.6298	26.6301	97.1864	16.3760	2.9649	13.0568	2.0624	11.8008	2.5271	7.4594	1.1876	9.8769	1.4278	330.01	280.61	49.40
07	9.3586	120.7242	23.0635	90.8147	20.5674	3.0758	19.2776	3.2766	20.5932	4.6146	13.5263	2.2445	17.2010	2.8073	351.15	267.60	83.54
08	7.9458	98.9252	20.3456	81.1135	19.4790	2.6929	19.9564	3.4173	23.2977	5.2051	15.7355	2.7661	20.8296	3.2826	324.99	230.50	94.49
09	11.1338	134.2343	24.3647	85.1230	16.2063	2.5787	12.3034	1.9986	12.3979	2.7270	7.9586	1.2855	10.1962	1.6371	324.15	273.64	50.50
10	21.8164	146.9816	30.7482	158.0526	13.5590	4.4101	4.9693	0.7740	5.0552	1.1068	3.2651	0.5376	4.3627	0.6637	396.30	375.57	20.73
11	8.4329	100.9965	20.9209	90.3626	21.4806	3.1773	19.8503	3.4544	22.6205	4.9886	13.8999	2.5011	18.6586	2.9563	334.30	245.37	88.93
12	12.3024	79.7952	12.2410	45.8204	9.9223	1.6452	9.7065	1.5795	9.7280	2.0911	6.4566	1.1253	8.2648	1.3012	201.98	161.73	40.25
13	7.4845	46.9549	7.7741	31.3827	5.5891	1.3315	4.9949	0.7266	4.5024	0.9247	2.8264	0.4965	3.7786	0.5386	119.31	100.52	18.79
14	6.4952	87.0313	20.3883	102.1250	27.9114	3.8984	22.5160	3.3706	19.4713	3.8379	10.7546	1.8508	13.3980	1.9994	325.05	247.85	77.20

(Continued on following page)

10.3389/feart.2022.1027620

10.3389/feart.2022.1027620

TABLE 2 (*Continued*) Rare Earth element analytical results (10^{-6}) of garnets from the Makeng-style Fe-polymetallic deposits.

	La	Ce	Pr	Nd	Sm	Eu	Gd	Tb	Dy	Ho	Er	Tm	Yb	Lu	ΣREE	ΣLREE	ΣHREE
15	11.7144	112.7933	21.5060	111.7169	34.5537	4.5668	32.7462	5.6857	35.8346	7.9833	23.0757	3.9930	31.2993	4.7864	442.26	296.85	145.40
16	11.7457	98.3608	16.9213	86.1467	23.4916	3.3077	16.7525	2.7928	15.4025	3.2594	9.1188	1.4689	11.5576	1.6895	302.02	239.97	62.04
17	35.3771	183.1398	17.2836	35.0713	4.3689	0.9204	3.3946	0.5543	4.0902	0.9300	2.9085	0.5259	4.2352	0.6350	293.43	276.16	17.27
18	13.7926	96.3972	18.5461	80.0898	7.3199	2.0818	3.2058	0.4923	3.5562	0.7200	2.2042	0.3436	2.6456	0.4530	231.85	218.23	13.62
19	8.4601	62.9767	10.3445	36.6332	5.1563	1.1925	3.9761	0.6046	3.7850	0.8828	2.5417	0.4390	2.8301	0.4904	140.31	124.76	15.55
20	58.2553	146.1940	11.7743	29.2120	5.8579	0.9499	7.0135	1.6399	12.8074	3.4517	10.9856	2.1551	15.3119	2.2481	307.86	252.24	55.61
21	6.1153	45.5799	8.6548	35.1030	6.7341	1.3370	5.4722	0.9654	6.0196	1.3766	4.2950	0.7112	5.0095	0.7813	128.15	103.52	24.63
22	7.3029	51.6917	8.7893	34.9098	5.9583	1.1541	4.7305	0.7094	4.5991	1.0450	3.0534	0.5169	3.5433	0.4795	128.48	109.81	18.68
23	7.3427	89.8233	19.0443	85.8071	20.6900	2.8808	18.1352	3.0233	18.5837	3.9962	11.5017	1.9785	14.5404	2.2834	299.63	225.59	74.04

Results

Rare earth element analysis results

The rare Earth element analysis results are shown in Table 2. A total of 25 and 32 spots of garnet sample ZK7525-b1 from the Makeng deposit and ZK405-b13 from the Luoyang deposit were selected to carry out rare Earth element analysis, respectively. Both of the two samples had lower REE contents with total REE contents (∑REE) of 22.29–68.26 ppm (average value of 38.22 ppm) and 26.41–66.56 ppm (average value of 48.78 ppm), respectively. They were enrichment in light rare Earth elements with positive Eu anomalies. These samples showed right-sloping features in the chondrite-normalized REE patterns (Figure 4). Representative garnet sample ZK403-b67 and PTPD-b1 from Dapai and Pantian deposits had lower REE contents, with total REE contents (∑REE) of 216.49–526.53 ppm (n = 26, average value = 349.14 ppm) and 117.55.41–396.30 ppm (n = 23, average value = 278.74 ppm), respectively. They showed flat REE distribution curves with weak negative Eu anomalies on the chondrite-normalized REE patterns (Figure 4).

U-Pb dating results

The LA-ICPMS garnet U-Pb analysis results were listed in Table 3. Four ore-bearing garnet samples (102-2-b1, 108-1-b6, ZK7525-b1, and 214-b9) were collected from different orebodies of the Makeng iron polymetallic deposit to analyze the U-Pb isotopic ratios. These spots of each sample showed good linear distribution features in the Tera-Wasserburg diagrams (Figures 5A–D). It yielded lower interception ages of 133.3 ± 2.5 Ma, 130.4 ± 4.6 Ma, 132.6 ± 3.5 Ma and 130.3 ± 8.6 Ma, respectively. A total of 17 and 28 spots were selected for two samples (ZK405-b13 and BL23) from the Luoyang deposit, which exhibited linear features on the Tera-Wasserburg diagram (Figures 5E,F) and yielded lower interception ages of 137.5 ± 3.7 Ma and 136.9 ± 3.0 Ma, respectively. A total of 25 and 30 spots were selected for two samples (ZK403-b92 and ZK403-b67) from the Dapai deposit, and it yielded lower interception ages of 130.9 ± 2.5 Ma and 132.1 ± 2.0 Ma respectively (Figures 5G,H). A total of 26 spots were selected for sample PTPD-b1 collected from the Pantian deposit, yielding a lower interception age of 133.8 ± 3.3 Ma. Although these spots did not show a good linear feature, they were located near the concordant curve (Figure 5I), and therefore the lower interception age can represent the forming time of the garnet.

From a general view, the U-Pb ages of garnet skarn from the Makeng-style deposits are close with relatively concentrated ages ranging from 137 Ma to 130 Ma.

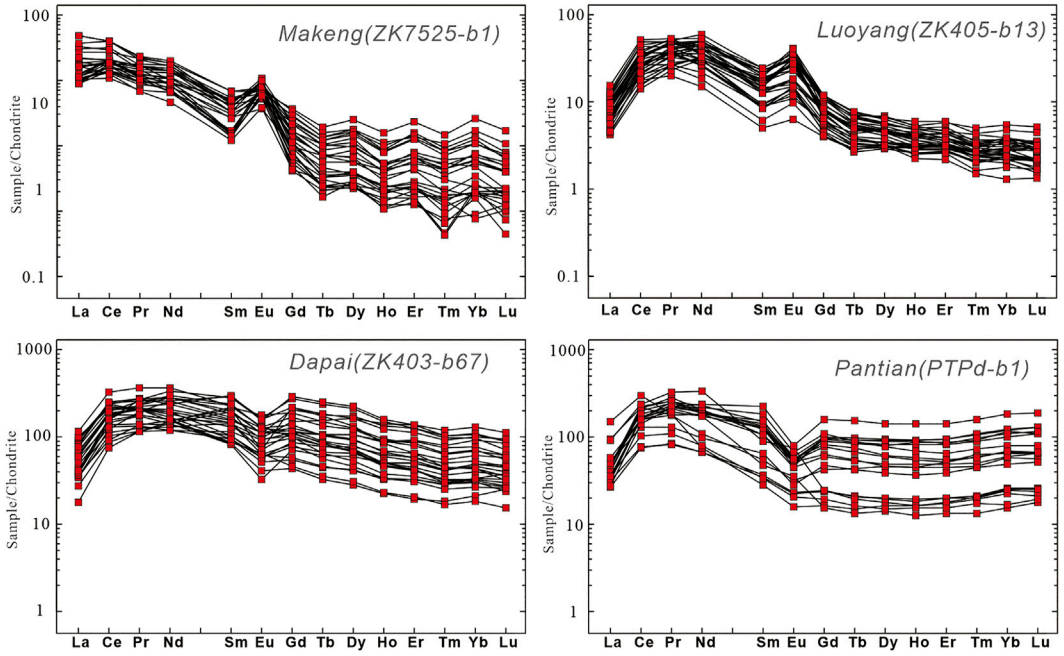


FIGURE 4
Chondrite-normalized REE patterns of garnets from Makeng-style iron deposits.

Discussion

Mineralization age

Dating the mineralization age is an important part in the ore genesis research, and the uncertainty of mineralization age will affect our understanding on the ore genesis. Due to the controversy on the mineralization age, there has been different understanding on the generation of the Makeng-style deposits, such as the sedimentary modified genesis and magmatic-hydrothermal genesis hypothesis (Han and Ge, 1983; Chen et al., 1985; Zhang et al., 2012b; Zhang et al., 2013; Wang et al., 2021). Previous research on the Makeng-style deposits mainly concentrated on zircon U-Pb dating for granites and Re-Os dating for molybdenites in ore districts (Zhang et al., 2018a; Zhang et al., 2012b; Lai et al., 2014; Yuan et al., 2014; Zhang et al., 2015; Zhao et al., 2016; Wang et al., 2018b), but the molybdenites were usually found in the interior of granite bodies and the fracture surface of the iron ores. Thus far, there is still no strongly evidence to prove that the magnetite mineralization is related to the intrusive rocks, or the magnetite are simultaneous with the molybdenites because they are not associated in space.

The ore-bearing garnet skarn rocks were selected to carry out LA-ICPMS garnet U-Pb dating, which can more directly constrain the mineralization age of the Makeng-style deposits because the garnet was always concomitant with the magnetite in space. Four representative ore-bearing garnet samples from different orebodies of the Makeng deposit yielded lower interception ages of 133.3 ± 2.5 and 130.4 ± 4.6 Ma, 132.6 ± 3.5 Ma and 130.0 ± 8.6 Ma, respectively. These garnet U-Pb ages were close to each other and consistent with the zircon U-Pb dating results reported by Zhang et al. (129.6 ± 0.8 and 132.6 ± 1.3 Ma, Zhang et al., 2012b) and Wang et al. (132.0 ± 0.6 Ma and 132.4 ± 0.8, Wang et al., 2015). In addition, the garnet and zircon U-Pb ages are close to the molybdenite Re-Os dating results with model ages ranging from 131.9 ± 1.9 to 133.3 ± 2.3 Ma (Zhang et al., 2012b).

To determine if the ore-forming ages were consistent among different deposits, five representative ore-bearing garnet samples from Luoyang, Dapai and Pantian were selected for U-Pb dating and yielded similar U-Pb ages. Two garnet samples from the Luoyang deposit yielded lower interception ages of 137.5 ± 3.7 Ma and 136.9 ± 3.0 Ma respectively, which are close to the zircon U-Pb ages of 137.2 ± 2.3 Ma (Zhang et al., 2018b) and 131.6 ± 0.6 Ma (Wang et al., 2021), and the molybdenite Re-Os ages of 133.0 ± 1.9 Ma, 133.1 ± 1.9 Ma and 134.0 ± 4.2 Ma (Zhang et al., 2012b). Two samples selected from the Dapai deposit yielded lower interception ages of 130.9 ± 2.5 Ma and 132.1 ± 2.0 Ma respectively, which were consistent with the zircon U-Pb ages of 132.4 ± 0.8 Ma (Yuan et al., 2020) and molybdenite Re-Os age of 133.5 ± 4.1 Ma (Zhao et al., 2016). One sample collected

TABLE 3 LA-ICPMS garnet U-Pb data for skarn rocks from the Makeng-style iron polymetallic deposits.

Spot	U	Th	207Pb/206 Pb		207 Pb/235U		206 Pb/238U		207Pb/206 Pb		207 Pb/235U		206 Pb/238U	
	ppm	ppm	Ratio	1σ	Ratio	1σ	Ratio	1σ	Age (Ma)	1σ	Age (Ma)	1σ	Age (Ma)	1σ
102-2-b4 (Makeng)														
1	0.83	13.83	0.3148	0.0185	1.2978	0.0613	0.0330	0.0006	3546	90	845	27	209	4
2	0.13	0.76	0.7083	0.0440	21.1907	0.9921	0.2433	0.0076	-	-	3147	45	1404	39
3	1.52	67.71	0.1075	0.0053	0.3077	0.0121	0.0226	0.0004	1767	95	272	9	144	3
4	3.41	52.52	0.1149	0.0069	0.3438	0.0180	0.0234	0.0005	1880	108	300	14	149	3
5	0.03	7.50	0.1008	0.0083	0.2880	0.0208	0.0217	0.0005	1640	154	257	16	138	3
6	0.26	8.69	0.0601	0.0050	0.1856	0.0120	0.0218	0.0005	606	180	173	10	139	3
7	0.28	4.93	0.1844	0.0187	0.5900	0.0477	0.0260	0.0012	2694	168	471	30	165	7
8	0.71	68.47	0.0487	0.0027	0.1372	0.0072	0.0211	0.0004	132	126	131	6	134	2
9	0.16	42.26	0.0508	0.0028	0.1498	0.0074	0.0221	0.0003	232	126	142	7	141	2
10	0.11	35.00	0.0587	0.0028	0.1728	0.0074	0.0222	0.0003	567	101	162	6	142	2
11	0.11	13.08	0.0627	0.0045	0.1948	0.0122	0.0223	0.0005	698	152	181	10	142	3
12	0.09	11.95	0.0689	0.0054	0.2076	0.0141	0.0223	0.0005	896	161	192	12	142	3
13	0.05	9.47	0.0806	0.0059	0.2489	0.0177	0.0223	0.0005	1213	144	226	14	142	3
14	0.68	2.99	0.4757	0.0263	2.9812	0.1656	0.0482	0.0015	4168	82	1403	42	303	9
15	0.44	6.59	0.2992	0.0215	1.2300	0.0866	0.0320	0.0010	3466	112	814	39	203	7
16	0.40	4.40	0.2412	0.0164	0.8493	0.0518	0.0276	0.0007	3127	108	624	28	176	5
17	0.05	8.72	0.1261	0.0089	0.3721	0.0239	0.0230	0.0005	2056	125	321	18	147	3
18	0.03	8.76	0.1245	0.0098	0.3594	0.0243	0.0226	0.0006	2022	145	312	18	144	4
19	0.71	32.12	0.1666	0.0120	0.5557	0.0467	0.0245	0.0005	2524	121	449	31	156	3
20	0.57	10.57	0.2652	0.0137	0.9947	0.0438	0.0298	0.0006	3277	81	701	22	189	4
21	0.63	17.98	0.3815	0.0176	1.8904	0.0915	0.0375	0.0009	3838	70	1078	32	237	6
22	0.55	42.38	0.0574	0.0031	0.1523	0.0075	0.0205	0.0003	506	119	144	7	131	2
23	0.23	24.54	0.1075	0.0063	0.2969	0.0163	0.0215	0.0004	1758	103	264	13	137	2
24	0.12	33.56	0.0955	0.0056	0.2599	0.0141	0.0210	0.0004	1537	111	235	11	134	2
25	0.08	10.95	0.3525	0.0190	1.5364	0.0819	0.0336	0.0009	3718	82	945	33	213	6
26	0.44	21.23	0.3571	0.0150	1.5462	0.0592	0.0334	0.0005	3738	69	949	24	212	3
27	0.37	1.83	0.7281	0.0319	17.3629	0.7181	0.1854	0.0048	-	-	2955	40	1096	26
28	0.04	7.97	0.1215	0.0082	0.3390	0.0206	0.0213	0.0004	1977	120	296	16	136	3
29	0.32	21.50	0.2495	0.0128	0.8657	0.0432	0.0265	0.0005	3183	81	633	24	168	3
30	0.46	31.50	0.0839	0.0059	0.2171	0.0133	0.0202	0.0004	1300	137	200	11	129	3
108-1-b6 (Makeng)														
1	0.94	4.56	0.4336	0.0297	2.1821	0.1769	0.0375	0.0013	4031	102	1175	56	237	8
2	1.11	6.77	0.1252	0.0095	0.3786	0.0238	0.0237	0.0006	2032	135	326	18	151	4
3	0.42	2.93	0.4673	0.0319	2.7365	0.1940	0.0450	0.0016	4141	101	1338	53	284	10
4	0.79	2.96	0.6953	0.0417	10.2987	0.5488	0.1155	0.0036	-	-	2462	49	705	21
5	0.40	6.80	0.4961	0.0417	2.8404	0.2343	0.0443	0.0022	4230	125	1366	62	279	14
6	0.19	4.24	0.5021	0.0264	3.4804	0.1802	0.0532	0.0015	4247	78	1523	41	334	9
7	0.25	4.29	0.1102	0.0108	0.3458	0.0244	0.0230	0.0007	1802	180	302	18	147	4
8	0.17	4.50	0.1748	0.0144	0.5955	0.0424	0.0253	0.0007	2603	137	474	27	161	4
9	0.12	3.75	0.4045	0.0231	2.3733	0.1326	0.0447	0.0014	3926	85	1235	40	282	9
10	0.29	3.81	0.0950	0.0145	0.3441	0.0374	0.0209	0.0008	1529	290	300	28	133	5
11	0.17	5.67	0.1250	0.0120	0.4242	0.0356	0.0233	0.0006	2028	172	359	25	148	4
12	0.35	4.24	0.5456	0.0246	6.8869	0.4221	0.0907	0.0039	4369	66	2097	54	559	23

(Continued on following page)

TABLE 3 (*Continued*) LA-ICPMS garnet U-Pb data for skarn rocks from the Makeng-style iron polymetallic deposits.

Spot	U	Th	207Pb/206 Pb		207 Pb/235U		206 Pb/238U		207Pb/206 Pb		207 Pb/235U		206 Pb/238U	
	ppm	ppm	Ratio	1σ	Ratio	1σ	Ratio	1σ	Age (Ma)	1σ	Age (Ma)	1σ	Age (Ma)	1σ
13	0.79	5.45	0.5889	0.0252	8.2782	0.4150	0.1048	0.0041	4481	62	2262	45	642	24
14	2.72	15.09	0.4251	0.0208	2.8987	0.1531	0.0500	0.0014	4400	73	1382	40	314	9
15	2.99	15.07	0.4617	0.0220	3.4461	0.1575	0.0549	0.0014	4123	71	1515	36	345	9
16	0.45	4.62	0.2967	0.0221	1.2369	0.0816	0.0316	0.0011	3453	116	817	37	201	7
17	0.25	5.12	0.3193	0.0244	1.5665	0.1422	0.0350	0.0015	3566	118	957	56	222	9
18	0.66	2.42	0.4373	0.0230	2.6376	0.1306	0.0460	0.0015	4043	79	1311	36	290	10
19	0.71	2.60	0.2372	0.0188	0.8748	0.0616	0.0286	0.0009	3102	132	638	33	182	5
20	0.15	4.14	0.3921	0.0289	2.1059	0.1352	0.0398	0.0013	3879	111	1151	44	252	8
21	0.50	4.72	0.1692	0.0144	0.6018	0.0509	0.0258	0.0008	2550	144	478	32	164	5
22	1.21	5.42	0.1847	0.0173	0.6328	0.0565	0.0240	0.0010	2696	155	498	35	153	6
23	0.21	3.80	0.1364	0.0143	0.4624	0.0386	0.0219	0.0007	2183	183	386	27	140	4
24	0.18	2.32	0.4007	0.0318	1.7772	0.1458	0.0335	0.0015	3912	121	1037	53	212	9
25	0.10	3.32	0.2240	0.0176	0.8708	0.0625	0.0284	0.0009	3010	127	636	34	180	6
26	0.68	3.37	0.5753	0.0323	6.3957	0.3214	0.0845	0.0025	4447	82	2032	44	523	15
27	0.59	3.79	0.4616	0.0286	2.2948	0.1296	0.0389	0.0015	4123	92	1211	40	246	9
ZK7525-b1 (Makeng)														
1	0.23	2.77	0.6239	0.0328	17.5861	0.8487	0.2029	0.0060	4565	76	2967	46	1191	32
2	0.06	2.09	0.3683	0.0347	1.9964	0.1627	0.0428	0.0017	3785	143	1114	55	270	11
3	0.00	1.31	0.5501	0.0575	4.0186	0.3264	0.0587	0.0029	4383	153	1638	66	368	18
4	0.06	1.54	0.5186	0.0303	5.8729	0.3032	0.0828	0.0024	4295	86	1957	45	513	14
5	0.00	3.33	0.6577	0.0340	36.8511	1.7438	0.3926	0.0076	4643	78	3690	47	2135	35
6	0.02	1.82	0.4471	0.0358	3.8427	0.2798	0.0632	0.0024	4076	119	1602	59	395	15
7	0.08	1.84	0.6491	0.0416	29.0486	1.6758	0.3169	0.0112	4622	94	3455	57	1774	55
8	0.03	2.22	0.6366	0.0339	13.8873	0.6181	0.1561	0.0038	4594	77	2742	42	935	21
9	0.10	2.03	0.6200	0.0391	10.9974	0.6007	0.1269	0.0041	4567	92	2523	51	770	24
10	0.09	1.85	0.4462	0.0360	2.6494	0.2005	0.0429	0.0019	4073	120	1314	56	271	12
11	0.04	1.34	0.5422	0.0357	7.1853	0.4034	0.0956	0.0036	4360	97	2135	50	589	21
12	0.31	5.83	0.6663	0.0352	29.7964	1.5244	0.3153	0.0091	4660	78	3480	50	1767	45
13	0.27	4.94	0.5370	0.0295	6.8047	0.4195	0.0898	0.0036	4346	80	2086	55	555	21
14	0.14	5.62	0.5825	0.0296	6.7949	0.3102	0.0845	0.0024	4465	75	2085	40	523	14
15	0.30	9.71	0.5703	0.0391	5.7821	0.3444	0.0761	0.0026	4434	100	1944	52	473	15
16	0.19	4.40	0.4055	0.0491	1.9113	0.1999	0.0378	0.0026	3931	183	1085	70	239	16
17	0.20	8.09	0.4268	0.0334	2.4378	0.1582	0.0433	0.0015	4006	117	1254	47	273	10
18	0.29	10.25	0.5885	0.0378	7.7209	0.4383	0.0949	0.0037	4480	94	2199	51	585	22
19	0.22	7.09	0.6551	0.0265	20.6765	0.7495	0.2237	0.0044	4636	58	3124	35	1301	23
20	0.14	4.67	0.2077	0.0208	0.8576	0.0769	0.0306	0.0013	2888	163	629	42	195	8
21	0.15	4.54	0.6044	0.0312	10.9048	0.5029	0.1306	0.0035	4520	75	2515	43	791	20
22	0.17	4.95	0.5425	0.0314	6.1762	0.3004	0.0835	0.0024	4361	85	2001	43	517	14
23	0.21	4.72	0.6086	0.0332	16.7701	0.7951	0.1999	0.0069	4529	79	2922	45	1175	37
24	0.19	6.78	0.5474	0.0293	6.7716	0.3131	0.0891	0.0026	4376	78	2082	41	550	15
25	0.22	7.63	0.6137	0.0292	13.8224	0.5782	0.1594	0.0039	4543	69	2738	40	954	22
26	0.06	3.33	0.6611	0.0329	26.2616	1.1962	0.2795	0.0070	4650	75	3356	45	1589	35
27	0.07	1.70	0.7000	0.0446	22.2869	1.2207	0.2310	0.0080	-	-	3196	53	1340	42
28	0.26	6.84	0.6050	0.0359	13.4717	0.6859	0.1576	0.0038	4520	86	2713	48	943	21

(Continued on following page)

TABLE 3 (*Continued*) LA-ICPMS garnet U-Pb data for skarn rocks from the Makeng-style iron polymetallic deposits.

Spot	U	Th	207Pb/206 Pb		207 Pb/235U		206 Pb/238U		207Pb/206 Pb		207 Pb/235U		206 Pb/238U	
	ppm	ppm	Ratio	1σ	Ratio	1σ	Ratio	1σ	Age (Ma)	1σ	Age (Ma)	1σ	Age (Ma)	1σ
214-b9 (Makeng)														
1	0.22	1.66	0.6476	0.0337	18.2123	0.8815	0.2034	0.0057	4620	75	3001	47	1194	31
2	1.89	0.43	0.3521	0.0330	2.0037	0.1797	0.0433	0.0017	3716	144	1117	61	273	11
3	0.29	0.35	0.5683	0.0504	4.4714	0.3107	0.0631	0.0027	4429	130	1726	58	394	16
4	4.33	0.85	0.6873	0.0376	39.2219	1.9702	0.4026	0.0080	4705	81	3751	50	2181	37
5	4.32	1.65	0.4728	0.0393	4.0125	0.2934	0.0640	0.0024	4159	124	1637	59	400	15
6	1.92	0.52	0.6628	0.0440	29.2187	1.7465	0.3153	0.0112	4652	99	3461	59	1767	55
7	2.94	1.06	0.6510	0.0359	13.9961	0.6509	0.1554	0.0038	4626	80	2749	44	931	21
8	0.71	0.72	0.7131	0.0420	32.7050	2.2300	0.3199	0.0136	-	-	3572	67	1789	66
9	1.70	1.05	0.6363	0.0402	11.1457	0.6205	0.1265	0.0042	4593	92	2535	52	768	24
10	2.10	0.72	0.4605	0.0397	2.5832	0.2177	0.0407	0.0020	4119	128	1296	62	257	12
11	1.50	0.62	0.5559	0.0366	7.3142	0.4170	0.0956	0.0036	4397	97	2151	51	589	21
12	0.23	0.51	0.6819	0.0362	30.3447	1.5802	0.3158	0.0092	4693	78	3498	51	1769	45
13	4.56	1.92	0.5485	0.0304	6.9331	0.4333	0.0901	0.0036	4377	81	2103	55	556	21
14	3.01	1.50	0.5940	0.0307	6.9263	0.3259	0.0849	0.0024	4494	76	2102	42	525	14
15	1.25	0.59	0.5805	0.0404	5.8967	0.3595	0.0766	0.0026	4460	101	1961	53	476	15
16	1.12	1.38	0.4120	0.0502	1.9501	0.2060	0.0381	0.0026	3954	184	1098	71	241	16
17	2.46	1.47	0.4394	0.0326	2.7387	0.1965	0.0464	0.0017	4050	111	1339	53	292	11
18	1.22	1.26	0.5842	0.0383	7.7194	0.4510	0.0960	0.0037	4469	96	2199	53	591	22
19	0.47	1.07	0.6508	0.0280	20.9695	0.8545	0.2308	0.0057	4626	62	3137	40	1339	30
20	0.80	1.15	0.5746	0.0318	10.2931	0.5042	0.1309	0.0038	4445	81	2461	45	793	22
21	2.19	1.18	0.5316	0.0327	5.8249	0.3025	0.0811	0.0025	4331	91	1950	45	503	15
22	1.42	1.24	0.5243	0.0286	6.5007	0.3129	0.0900	0.0026	4311	80	2046	42	556	15
23	0.61	1.09	0.5913	0.0284	12.9369	0.5678	0.1565	0.0042	4487	70	2675	41	937	23
24	0.55	1.22	0.6290	0.0326	24.6211	1.2098	0.2779	0.0076	4576	75	3293	48	1581	38
25	1.90	1.90	0.6604	0.0410	21.7912	1.1920	0.2405	0.0081	4647	93	3174	53	1389	42
26	0.66	1.99	0.7624	0.0374	64.0261	3.2036	0.5995	0.0225	-	-	4239	50	3028	90
27	0.78	1.43	0.7677	0.0358	54.5306	2.2318	0.5057	0.0144	-	-	4079	41	2638	62
28	0.50	1.80	0.6190	0.0323	10.0960	0.4652	0.1186	0.0037	4553	76	2444	43	723	21
29	1.22	1.75	0.3069	0.0293	1.2068	0.0803	0.0318	0.0012	3505	148	804	37	201	8
30	0.47	1.80	0.6552	0.0334	13.8713	0.6265	0.1508	0.0041	4636	74	2741	43	906	23
31	1.24	1.62	0.6521	0.0363	17.0459	0.8827	0.1855	0.0053	4629	80	2937	50	1097	29
32	0.35	1.26	0.6981	0.0337	26.6159	1.3560	0.2712	0.0088	-	-	3369	50	1547	45
33	0.77	1.62	0.4686	0.0343	3.8031	0.2486	0.0607	0.0020	4145	109	1593	53	380	12
34	0.22	1.58	0.4679	0.0408	2.9109	0.2173	0.0492	0.0021	4144	162	1385	56	310	13
35	0.53	1.57	0.6166	0.0413	9.5925	0.5477	0.1162	0.0038	4548	97	2396	53	708	22
36	0.24	1.31	0.5042	0.0367	3.4483	0.2213	0.0528	0.0019	4253	107	1515	51	331	12
37	0.22	1.16	0.6342	0.0335	8.2359	0.3839	0.0947	0.0025	4589	77	2257	42	584	14
38	0.16	1.02	0.5573	0.0367	5.4621	0.3017	0.0724	0.0024	4400	97	1895	47	450	14
39	1.06	1.35	0.6693	0.0352	12.7570	0.5790	0.1383	0.0038	4666	78	2662	43	835	22
40	0.34	1.43	0.5314	0.0328	4.1324	0.2090	0.0568	0.0017	4331	90	1661	41	356	10
41	0.20	1.25	0.6691	0.0358	12.5708	0.5670	0.1357	0.0036	4666	79	2648	42	820	20
42	0.34	1.95	0.4735	0.0276	4.1350	0.2066	0.0650	0.0023	4161	86	1661	41	406	14
43	0.27	1.43	0.7715	0.0346	44.8081	1.8817	0.4117	0.0092	-	-	3883	42	2223	42
44	0.18	1.14	0.7576	0.0467	35.2102	1.9867	0.3374	0.0108	-	-	3645	56	1874	52

(Continued on following page)

TABLE 3 (*Continued*) LA-ICPMS garnet U-Pb data for skarn rocks from the Makeng-style iron polymetallic deposits.

Spot	U	Th	207Pb/206 Pb		207 Pb/235U		206 Pb/238U		207Pb/206 Pb		207 Pb/235U		206 Pb/238U	
	ppm	ppm	Ratio	1σ	Ratio	1σ	Ratio	1σ	Age (Ma)	1σ	Age (Ma)	1σ	Age (Ma)	1σ
45	0.26	1.86	0.3002	0.0302	1.4530	0.1686	0.0334	0.0017	3471	157	911	70	212	10
46	0.27	1.80	0.4826	0.0435	2.6538	0.1808	0.0442	0.0017	4191	133	1316	50	279	10
47	0.20	1.59	0.3486	0.0343	1.5584	0.1219	0.0360	0.0013	3701	151	954	48	228	8
48	0.15	1.56	0.5385	0.0373	5.4403	0.3266	0.0749	0.0025	4350	102	1891	52	466	15
ZK405-b13(Luoyang)														
1	0.27	5.85	0.0597	0.0079	0.1834	0.0242	0.0229	0.0007	594	289	171	21	146	4
2	0.28	4.71	0.3951	0.0210	2.3081	0.1146	0.0426	0.0010	3891	80	1215	35	269	6
3	0.32	5.55	0.4057	0.0257	2.1981	0.1236	0.0401	0.0011	3931	101	1180	39	254	7
4	0.36	5.10	0.5241	0.0337	3.7563	0.2152	0.0525	0.0017	4310	95	1583	46	330	11
5	0.38	6.29	0.0777	0.0140	0.2065	0.0312	0.0213	0.0008	1139	366	191	26	136	5
6	0.37	5.38	0.0924	0.0113	0.2626	0.0282	0.0219	0.0007	1476	233	237	23	140	4
7	0.33	5.26	0.0885	0.0106	0.2587	0.0252	0.0230	0.0008	1392	232	234	20	147	5
8	0.40	6.92	0.2255	0.0207	0.9103	0.0852	0.0284	0.0010	3020	148	657	45	180	6
9	0.24	3.57	0.6084	0.0361	6.1001	0.4115	0.0694	0.0028	4528	86	1990	59	433	17
10	0.19	5.54	0.0688	0.0109	0.1922	0.0241	0.0220	0.0007	894	330	179	21	140	4
11	0.18	3.60	0.7043	0.0407	19.5640	1.2119	0.1928	0.0081	-	-	3070	60	1137	44
12	0.79	3.57	0.5231	0.0312	4.9819	0.2636	0.0681	0.0019	4308	88	1816	45	424	11
13	0.83	3.15	0.7001	0.0316	28.2689	1.3376	0.2828	0.0080	-	-	3428	46	1606	40
14	0.57	2.92	0.7568	0.0350	97.5009	4.3223	0.8959	0.0161	-	-	4661	45	4124	55
15	0.89	3.49	0.7136	0.0332	78.6587	3.6026	0.7780	0.0267	-	-	4445	46	3710	97
16	0.46	7.95	0.5335	0.0261	4.5184	0.2469	0.0593	0.0018	4337	72	1734	45	371	11
17	0.78	3.63	0.7479	0.0391	74.2827	4.0644	0.7019	0.0219	-	-	4388	55	3428	83
BL23(Luoyang)														
1	0.62	12.40	0.5453	0.0279	5.5355	0.2573	0.0710	0.0014	4369	75	1906	40	442	8
2	0.36	13.14	0.5162	0.0239	4.9035	0.2246	0.0665	0.0018	4288	68	1803	39	415	11
3	0.43	9.52	0.3367	0.0198	2.1276	0.1435	0.0434	0.0015	3648	90	1158	47	274	9
4	0.82	13.56	0.3391	0.0170	2.0941	0.1268	0.0420	0.0014	3659	77	1147	42	266	9
5	0.65	13.34	0.3097	0.0171	1.4384	0.0778	0.0327	0.0011	3519	85	905	32	207	7
6	0.18	70.20	0.0684	0.0039	0.2090	0.0103	0.0215	0.0004	880	114	193	9	137	2
7	1.09	12.71	0.3223	0.0149	1.9169	0.0790	0.0416	0.0008	3581	71	1087	27	263	5
8	0.51	10.92	0.1433	0.0093	0.5080	0.0309	0.0252	0.0006	2333	113	417	21	160	4
9	0.60	12.23	0.0695	0.0051	0.2222	0.0148	0.0228	0.0005	922	152	204	12	145	3
10	0.26	43.49	0.1403	0.0073	0.5099	0.0251	0.0254	0.0005	2231	90	418	17	162	3
11	0.53	16.92	0.4639	0.0237	4.3702	0.1961	0.0661	0.0015	4131	76	1707	37	413	9
12	0.35	8.61	0.5186	0.0272	6.4925	0.3460	0.0877	0.0028	4295	77	2045	47	542	17
13	0.37	9.72	0.5837	0.0308	11.6576	0.5219	0.1405	0.0036	4468	77	2577	42	848	20
14	0.63	11.74	0.4061	0.0210	2.9096	0.1380	0.0503	0.0015	3932	78	1384	36	317	9
15	0.56	10.85	0.5065	0.0216	6.5565	0.2977	0.0907	0.0029	4260	63	2054	40	559	17
16	0.45	11.35	0.5081	0.0223	6.5896	0.3300	0.0900	0.0031	4265	65	2058	44	556	18
17	0.66	12.82	0.5194	0.0244	6.1065	0.2766	0.0819	0.0021	4297	69	1991	40	507	13
18	0.61	114.40	0.2560	0.0125	1.1599	0.0554	0.0314	0.0009	3222	77	782	26	199	6
19	0.29	8.85	0.5275	0.0227	8.0546	0.3646	0.1057	0.0031	4320	64	2237	41	648	18
20	0.68	12.93	0.4070	0.0259	2.7360	0.1714	0.0471	0.0016	3936	96	1338	47	297	10

(Continued on following page)

TABLE 3 (*Continued*) LA-ICPMS garnet U-Pb data for skarn rocks from the Makeng-style iron polymetallic deposits.

Spot	U	Th	207Pb/206 Pb		207 Pb/235U		206 Pb/238U		207Pb/206 Pb		207 Pb/235U		206 Pb/238U	
	ppm	ppm	Ratio	1σ	Ratio	1σ	Ratio	1σ	Age (Ma)	1σ	Age (Ma)	1σ	Age (Ma)	1σ
21	0.19	12.80	0.0739	0.0056	0.2358	0.0162	0.0224	0.0005	1040	153	215	13	143	3
22	0.71	11.29	0.3722	0.0201	2.6009	0.1608	0.0478	0.0014	3800	82	1301	45	301	9
23	0.53	22.85	0.1327	0.0088	0.4906	0.0338	0.0256	0.0006	2200	121	405	23	163	4
24	0.60	58.06	0.0436	0.0038	0.1320	0.0108	0.0213	0.0004	-	-	126	10	136	3
25	0.61	33.12	0.1540	0.0097	0.5692	0.0327	0.0259	0.0005	2391	108	458	21	165	3
26	0.51	10.44	0.3427	0.0223	1.8143	0.1191	0.0368	0.0013	3675	100	1051	43	233	8
27	0.36	24.23	0.1519	0.0094	0.5756	0.0316	0.0261	0.0005	2369	106	462	20	166	3
28	0.36	11.67	0.3005	0.0177	1.8585	0.0963	0.0424	0.0010	3473	91	1066	34	268	6
ZK403-b92 (Dapai)														
1	6.38	15.29	0.1025	0.0090	0.3113	0.0283	0.0211	0.0005	1669	167	275	22	134	3
2	4.38	22.12	0.2908	0.0238	1.6083	0.1707	0.0357	0.0029	3422	128	973	66	226	18
3	5.83	13.23	0.3110	0.0175	1.3736	0.0770	0.0314	0.0007	3526	87	878	33	199	5
4	3.85	20.12	0.1367	0.0120	0.4726	0.0493	0.0232	0.0006	2187	153	393	34	148	4
5	3.18	17.71	0.0904	0.0070	0.2731	0.0206	0.0216	0.0005	1435	148	245	16	138	3
6	3.96	20.51	0.1044	0.0061	0.3192	0.0180	0.0219	0.0004	1706	109	281	14	140	2
7	4.33	16.34	0.0904	0.0070	0.2669	0.0190	0.0216	0.0005	1433	147	240	15	138	3
8	4.12	16.38	0.0736	0.0067	0.2227	0.0189	0.0218	0.0005	1031	185	204	16	139	3
9	3.66	16.24	0.0563	0.0045	0.1634	0.0121	0.0210	0.0004	465	180	154	11	134	3
10	4.98	17.54	0.1258	0.0081	0.4272	0.0263	0.0243	0.0005	2040	113	361	19	155	3
11	3.00	14.73	0.0689	0.0058	0.2020	0.0159	0.0213	0.0005	894	174	187	13	136	3
12	3.22	14.76	0.1645	0.0139	0.5798	0.0443	0.0256	0.0007	2502	143	464	28	163	4
13	6.33	12.27	0.1612	0.0132	0.5127	0.0370	0.0234	0.0006	2469	144	420	25	149	4
14	6.36	13.84	0.1458	0.0156	0.5955	0.0812	0.0249	0.0009	2298	185	474	52	159	5
15	0.35	3.64	0.5805	0.0296	7.0387	0.4870	0.0854	0.0043	4460	74	2116	62	528	26
16	4.34	13.70	0.4408	0.0233	3.1375	0.1442	0.0506	0.0011	4055	79	1442	35	318	6
17	2.49	14.81	0.1592	0.0113	0.5709	0.0442	0.0251	0.0007	2448	121	459	29	160	4
18	3.21	16.66	0.3608	0.0210	1.8279	0.1355	0.0355	0.0016	3753	89	1056	49	225	10
19	4.31	13.58	0.2332	0.0147	0.8684	0.0488	0.0267	0.0007	3076	101	635	27	170	4
20	3.30	16.25	0.1363	0.0117	0.4428	0.0399	0.0225	0.0007	2181	145	372	28	143	4
21	5.50	17.38	0.3170	0.0171	1.5066	0.0928	0.0327	0.0008	3567	83	933	38	208	5
22	9.64	17.23	0.1372	0.0098	0.4618	0.0297	0.0242	0.0007	2192	124	386	21	154	4
23	6.88	14.74	0.3104	0.0189	1.4818	0.0998	0.0336	0.0013	3523	94	923	41	213	8
24	6.39	18.95	0.1673	0.0140	0.6146	0.0555	0.0253	0.0007	2531	141	486	35	161	4
25	3.35	15.73	0.0844	0.0069	0.2761	0.0236	0.0229	0.0005	1303	155	248	19	146	3
ZK403-b67 (Dapai)														
1	1.45	16.94	0.2843	0.0185	1.2824	0.0794	0.0314	0.0008	3387	102	838	35	200	5
2	0.64	10.19	0.5129	0.0301	4.4107	0.3155	0.0578	0.0024	4279	87	1714	59	362	14
3	1.11	22.78	0.0637	0.0049	0.1889	0.0130	0.0216	0.0005	733	163	176	11	138	3
4	0.55	20.79	0.4067	0.0256	2.2012	0.1290	0.0382	0.0014	3934	95	1181	41	242	8
5	0.58	22.85	0.1937	0.0152	0.7254	0.0643	0.0255	0.0007	2774	129	554	38	163	5
6	0.22	9.46	0.0887	0.0096	0.2856	0.0304	0.0226	0.0007	1398	208	255	24	144	4
7	0.69	5.56	0.2481	0.0228	0.9697	0.0753	0.0297	0.0011	3173	145	688	39	189	7
8	0.87	5.69	0.4668	0.0261	3.2118	0.1680	0.0498	0.0015	4140	83	1460	41	313	9

(Continued on following page)

TABLE 3 (*Continued*) LA-ICPMS garnet U-Pb data for skarn rocks from the Makeng-style iron polymetallic deposits.

Spot	U	Th	207Pb/206 Pb		207 Pb/235U		206 Pb/238U		207Pb/206 Pb		207 Pb/235U		206 Pb/238U	
	ppm	ppm	Ratio	1σ	Ratio	1σ	Ratio	1σ	Age (Ma)	1σ	Age (Ma)	1σ	Age (Ma)	1σ
9	0.28	17.44	0.0703	0.0048	0.2084	0.0147	0.0209	0.0004	937	141	192	12	133	3
10	0.69	35.38	0.0585	0.0050	0.1685	0.0133	0.0207	0.0004	546	189	158	12	132	2
11	0.19	21.81	0.0491	0.0039	0.1449	0.0110	0.0211	0.0004	154	178	137	10	135	3
12	0.43	2.01	0.4007	0.0565	1.6943	0.1957	0.0344	0.0020	3912	214	1006	74	218	12
13	0.39	9.19	0.5353	0.0268	5.8320	0.3417	0.0762	0.0027	4342	73	1951	51	473	16
14	0.17	5.53	0.3864	0.0321	2.7138	0.2367	0.0486	0.0018	3857	126	1332	65	306	11
15	0.72	13.30	0.4201	0.0208	2.5875	0.1232	0.0434	0.0012	3982	74	1297	35	274	7
16	0.55	14.94	0.2787	0.0244	1.9319	0.2393	0.0379	0.0021	3367	137	1092	83	240	13
17	0.43	8.10	0.2569	0.0170	1.1437	0.0704	0.0313	0.0008	3228	104	774	33	199	5
18	0.47	17.02	0.2646	0.0210	1.1339	0.0882	0.0304	0.0012	3276	125	770	42	193	7
19	0.17	3.39	0.1314	0.0153	0.4535	0.0571	0.0243	0.0010	2117	206	380	40	155	7
20	0.37	22.48	0.1834	0.0134	0.6469	0.0406	0.0249	0.0007	2684	155	507	25	158	5
21	0.37	17.63	0.0713	0.0056	0.2133	0.0158	0.0217	0.0005	965	163	196	13	139	3
22	0.33	13.69	0.3515	0.0184	1.8779	0.1130	0.0370	0.0011	3714	80	1073	40	234	7
23	0.68	13.20	0.1138	0.0116	0.3765	0.0426	0.0228	0.0006	1861	185	324	31	145	4
24	0.27	10.99	0.1947	0.0179	0.7718	0.0763	0.0278	0.0011	2782	151	581	44	177	7
25	0.42	16.94	0.0663	0.0055	0.1826	0.0138	0.0207	0.0006	817	176	170	12	132	4
26	0.88	16.28	0.3239	0.0171	1.4577	0.0857	0.0317	0.0008	3589	81	913	35	201	5
27	1.28	33.45	0.0634	0.0047	0.1864	0.0133	0.0214	0.0005	720	159	174	11	136	3
28	1.81	8.02	0.0664	0.0073	0.1875	0.0196	0.0206	0.0007	820	231	175	17	131	4
29	1.84	8.65	0.0721	0.0089	0.2076	0.0229	0.0209	0.0007	989	256	192	19	133	4
30	1.23	11.29	0.2108	0.0165	0.8196	0.0653	0.0276	0.0008	2922	128	608	36	175	5
PTPD-b21 (Dapai)														
1	1.45	20.38	0.0946	0.0077	0.2604	0.0214	0.0205	0.0006	1520	149	235	17	131	4
2	1.20	21.97	0.2246	0.0211	0.5433	0.0488	0.0220	0.0010	3014	151	441	32	140	7
3	1.54	28.78	0.2360	0.0260	0.5458	0.0537	0.0210	0.0010	3094	177	442	35	134	6
4	1.52	27.94	0.3648	0.0895	0.5987	0.0503	0.0209	0.0010	3770	381	476	32	133	6
5	1.46	25.93	0.3178	0.0412	0.6831	0.0746	0.0211	0.0011	3561	201	529	45	134	7
6	1.26	21.45	0.1008	0.0081	0.2664	0.0208	0.0202	0.0005	1639	151	240	17	129	3
7	1.60	29.86	0.1231	0.0127	0.3149	0.0226	0.0221	0.0007	2002	185	278	17	141	5
8	2.36	28.23	0.1597	0.0158	0.3664	0.0258	0.0202	0.0007	2454	169	317	19	129	5
9	1.18	21.38	0.1171	0.0119	0.2825	0.0264	0.0207	0.0007	1913	182	253	21	132	4
10	0.02	14.47	0.1363	0.0139	0.3462	0.0281	0.0212	0.0008	2181	179	302	21	135	5
11	0.64	21.70	0.1981	0.0245	0.4882	0.0398	0.0211	0.0009	2810	204	404	27	135	6
12	0.13	11.98	0.2372	0.0310	0.5176	0.0386	0.0221	0.0012	3102	210	424	26	141	8
13	0.18	6.54	0.1037	0.0088	0.2532	0.0190	0.0211	0.0007	1691	157	229	15	134	4
14	0.31	9.91	0.0862	0.0063	0.2416	0.0201	0.0206	0.0006	1343	141	220	16	131	4
15	1.11	15.56	0.0699	0.0070	0.1855	0.0164	0.0208	0.0006	928	207	173	14	133	4
16	1.28	20.38	0.3167	0.0794	0.5793	0.0534	0.0212	0.0011	3554	397	464	34	135	7
17	1.01	17.78	0.1285	0.0115	0.3421	0.0255	0.0214	0.0007	2077	159	299	19	136	4
18	0.31	7.68	0.0598	0.0050	0.1697	0.0137	0.0213	0.0004	594	151	159	12	136	2
19	0.39	13.03	0.0842	0.0089	0.2433	0.0223	0.0225	0.0006	1298	208	221	18	144	4
20	0.31	35.86	0.0738	0.0053	0.2046	0.0148	0.0205	0.0005	1035	145	189	13	131	3
21	0.30	29.39	0.1051	0.0097	0.2875	0.0253	0.0221	0.0006	1717	170	257	20	141	4
22	1.23	21.29	0.2345	0.0258	0.6071	0.0621	0.0225	0.0010	3083	178	482	39	144	6

(Continued on following page)

TABLE 3 (*Continued*) LA-ICPMS garnet U-Pb data for skarn rocks from the Makeng-style iron polymetallic deposits.

Spot	U	Th	207Pb/206 Pb		207 Pb/235U		206 Pb/238U		207Pb/206 Pb		207 Pb/235U		206 Pb/238U	
	ppm	ppm	Ratio	1σ	Ratio	1σ	Ratio	1σ	Age (Ma)	1σ	Age (Ma)	1σ	Age (Ma)	1σ
23	0.41	13.30	0.1225	0.0096	0.3084	0.0246	0.0191	0.0006	1994	140	273	19	122	4
24	0.23	56.34	0.1617	0.0178	0.3962	0.0350	0.0206	0.0007	2473	186	339	25	132	4
25	0.39	9.54	0.1014	0.0099	0.2743	0.0249	0.0204	0.0006	1650	182	246	20	130	4
26	0.40	10.63	0.0882	0.0072	0.2467	0.0192	0.0211	0.0005	1387	162	224	16	135	3

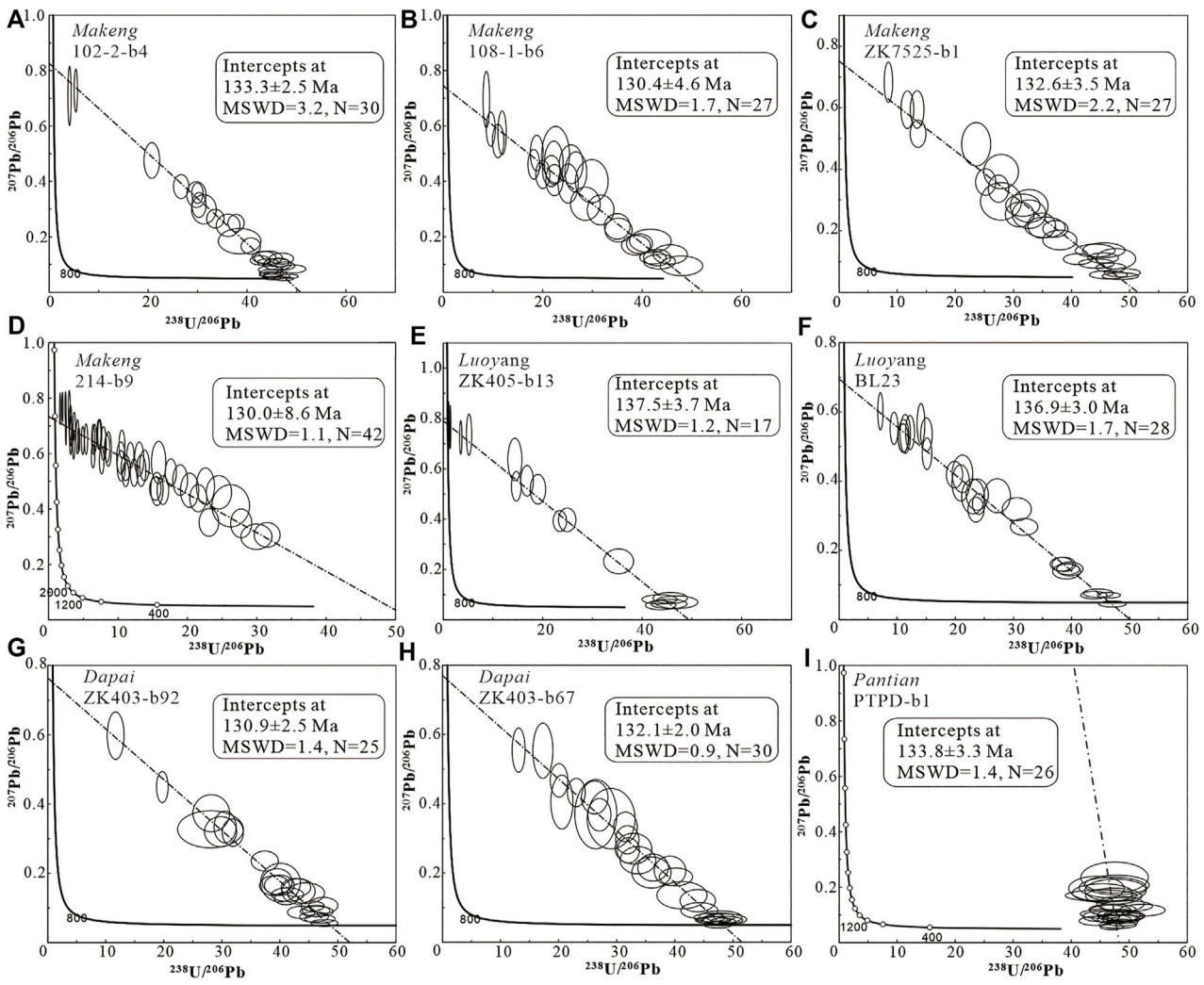


FIGURE 5
Tera-Wasserburg lower interception ages of Garnet from Makeng-style iron deposits. MSWD, mean squared weighted deviation; N, number of the spots.

TABLE 4 Geochronological results of Makeng-style Fe-polymetallic deposits.

Testing objects	Age (Ma)	Sample no.	Methods	Data source
Makeng deposit	132.04 ± 0.61	D3083-b1	Zircon U-Pb	Wang et al. (2015)
	132.43 ± 0.84	D3086-b1		
	130 ± 1	JZ02		Zhang et al. (2013)
	129 ± 1	JZ03		
	136.0 ± 1.7	97LB4-1		
	154.9 ± 0.9	CM218-13		Yan (2013)
	152.7 ± 1.4	MK03		Wang et al. (2017a)
	161.2 ± 4.9	MK420	Garnet Sm-Nd	Wang et al. (2010)
	133.0 ± 0.8	MK24-MK77	Mobdenite Re-Os	Zhang et al. (2012a)
	133.2 ± 2.5	102-2-b4	Garnet U-Pb	This study
	130.4 ± 4.6	108-1-b6		
	132.6 ± 3.5	ZK7525-b1		
	130.0 ± 8.6	214-b9		
Dapai deposit	131.72 ±0.41	ZK3102-b12	Zircon U-Pb	Yuan et al. (2014)
	132.35 ±0.83	ZK403-b21		
	150.23±	DP08-07		Yuan et al. (2020)
	134.8 ± 1.2	ZK302	Mobdenite Re-Os	Yuan et al. (2014)
	130.9 ± 2.5	ZK403-b92	Garnet U-Pb	This study
	132.1 ± 2.0	ZK403-b67		
Luoyang deposit	131.31 ± 0.66	ZK1108-b1	Zircon U-Pb	Wang et al. (2021)
	137.2 ± 2.3	BL130		
	154.1 ± 1.4	ZK1108-b27		Yu. (2017)
	133.0 ± 1.9	BL128	Mobdenite Re-Os	Zhang et al. (2012b)
	137.5 ± 3.7	ZK405-b13	Garnet U-Pb	This study
	136.9 ± 3.0	BL23		
Pantian deposit	131.68 ± 0.48	ZK1204-b1	Zircon U-Pb	Lai et al. (2014)
	133.8 ± 3.3	PTPD-b1	Garnet U-Pb	This study

from the Pantian deposit yielded a lower interception age of 133.8 ± 3.3 Ma, which was close to the zircon U-Pb age of 131.7 ± 0.5 Ma (Lai et al., 2014).

Together with the zircon U-Pb and molybdenite Re-Os dating results mentioned above and our new garnet U-Pb analysis results, we can draw a conclusion that the mineralization age constrained by associated minerals of Makeng-style deposits mainly concentrated around 137 Ma to 130 Ma (Table 4). This research can well resolve the disagreement about the mineralization age of the Makeng-style deposits due to a lack of direct chronological evidence. It shows that the magnetite and molybdenite are nearly simultaneous and consistent with the emplacement age of the Cretaceous granites, which indicates that the magnetite mineralization may be related to the granites.

Ore deposit type

The ore genesis of the Makeng-style Fe polymetallic deposits has been a controversial issue since they were discovered, and different genesis theories exist such as the marine sedimentation and hydrothermal modification, strata-bound skarn alteration, and silica-calcareous-plane mineralization hypotheses (Han and Ge, 1983; Wang et al., 2018a). A major reason for the controversy is the lack of direct chronological constraints. Magnetite ore bodies of the Makeng-style deposits mainly formed on the interface between Lower-Middle Permian carbonates and Late Devonian—Early Carboniferous clastic rocks, which caused the controversial understanding on the relationship between the mineralization and the granites. In addition, zircon U-Pb ages show that emplacement of the granites occurred in two main stages: ca. (160–150) Ma and ca. (135–130) Ma (Yan, 2013; Yu, 2017; Yuan et al., 2020); thus, it yields a

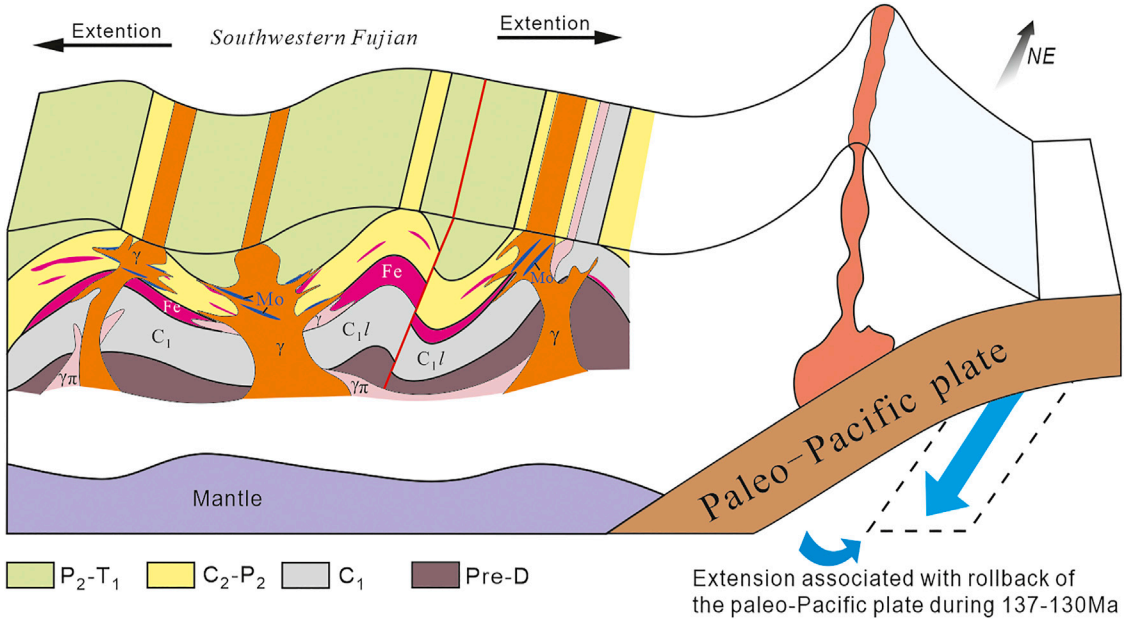


FIGURE 6
Ore-forming model of the Makeng-style deposits in southwestern Fujian.

significant controversy on the genesis due to the lack of more direct evidences and the different interpretation of the mineralization age. In this paper, ore-bearing garnet samples collected from different orebodies and ore deposits were selected to provide new direct chronological constraints on ore genesis, and all the garnet U-Pb dating results for these four deposits were close overall, which indicated that the mineralization of Makeng-style deposits was related to Cretaceous granites (ca. 137–130 Ma).

The rare Earth element analysis results of representative ore-bearing garnet samples showed that the REE contents and chondrite-normalized REE patterns were distinct between different deposits. The total REE contents of garnet samples from the Makeng and Luoyang deposits were relatively low (22.29–68.26 ppm and 26.41–66.56 ppm) with features LREE (light rare Earth element) enrichment and HREE (heavy rare Earth element) depletion and positive Eu anomalies. The rare Earth element distribution features were similar to those of garnet formed by magmatic hydrothermal action, and the REE distribution types were similar to granites with REE decreases in garnet due to the dilutive effect of transudation (Auwera and Andre, 1991; Hong et al., 2012). In addition, the REE distribution features are similar to those of garnets from the Huangganglang Sn-Fe deposit (Wang et al., 2002), Huangshaping W-M-Pb-Zn deposit (Ding et al., 2018a; Ding et al., 2018b) and Mengku Fe deposit (Yang et al., 2007), and they are regarded as typical skarn polymetallic deposits. The REE contents of garnet samples from the Dapai and Pantian deposits were relatively higher than those of the Makeng and Luoyang deposits, with total REE contents (∑REE) of 216.49–526.53 ppm and 117.55.41–396.30 ppm, respectively. It showed flat features of the REE distribution curves on the chondrite-normalized REE patterns with weak negative Eu anomalies, which were different from the Makeng and Luoyang deposit. The reason for this difference may be the distinct compositions of the mineralizing fluid. These mineralized bodies of Dapai and Pantian deposits locate in the contact zone of the granites and have similar hydrothermal components, and therefore it may be a major factor causing their relatively high REE contents and negative Eu anomalies. Unlike the Dapai and Pantian deposits, mineralized bodies of the Makeng and Luoyang deposits mainly locate on the interface between the between Lower-Middle Permian carbonates and Late Devonian—Early Carboniferous clastic rocks. Therefore, it indicates that the ore-forming process may be distinct due to different mineralizing fluid for these deposits.

In summary, garnet U-Pb dating results of different deposits and different ore bodies of the same deposit showed that the ore-forming ages of the Makeng-style iron-polymetallic deposits were relatively close (concentrated among 137–130 Ma) with those of the zircon U-Pb ages of granites, indicating that the formation of magnetite was closely related to Cretaceous granite emplacement. The rare Earth element analysis results REE distribution features showed that these Makeng-style deposits are similar to typical skarn deposits with features of magmatic hydrothermal fluid, but there were some obvious differences between different deposits, indicating that there may be some differences in the mineralizing fluid and ore-forming process between different deposits.

Metallogenic tectonic setting

A large—scale magmatic activity and mineralization event occurred in eastern China during the Yanshanian period; thus, studying the geochemical dynamic background and genesis mechanism of the deposit is of great significance to understand the Mesozoic tectonic transformation in eastern China and guide ore prospecting. Determining the mineralization age is a premise and key to understand the ore genesis and metallogenic mechanism, and therefore, the purpose of this study is to accurately determine the mineralization age and provide a reference for understanding the metallogenic mechanism and tectonic background of the iron-polymetallic deposits in the western margin of the Paleo-Pacific Plate.

Located on the southeastern margin of the Cathaysian Plate, the Makeng-style iron-polymetallic deposits are controversial due to their unique metallogenic geological characteristics, especially the controversy focused on the metallogenic age and metallogenic tectonic setting (Yan, 2013; Wang et al., 2018b; Zhang et al., 2018b). Our garnet U-Pb dating results provide more direct chronological evidence for the relationship between mineralization and Cretaceous granite bodies, and it proves that mineralization occurred at approximately 137–130 Ma rather than at 150 Ma or earlier time. Previous studies showed that the South China continent underwent a tectonic transition in the Early Cretaceous, that is, the transition from a compressional tectonic system dominated by intracontinental orogeny in the middle and late Jurassic to an extensional tectonic system in the early Cretaceous (Dong et al., 2008; Xing et al., 2008; Zhang et al., 2012c; Li et al., 2012). The possible deep dynamic mechanism for this tectonic transition is the rollback of the paleo- Pacific plate with a subduction dip angle of the subducting oceanic crust plate increasing from low-angle subduction to high-angle subduction, the retreat of the trench, and thickening of the crust, which caused the extensional collapse of the thickened continental crust under a relaxed stress environment (Zhang et al., 2012c; Li et al., 2012). In addition, the metallogenic tectonic background could be reflected by research on the diagenetic tectonic environment of the granites which are closely related to mineralization. The whole-rock geochemical results indicate that the granites from the Makeng, Luoyang, Dapai, and Pantian deposits are high-Si, high-K calc-alkaline and metaluminous to weakly peraluminous rocks, with features of highly fractionated I-type granites, which reflected an extensional tectonic setting with features of the transformational tectonic environment (Zhang et al., 2012b; Lai et al., 2014; Wang et al., 2015; Wang et al., 2021). Therefore, we believe that the Makeng-style iron-polymetallic deposits may have been formed in an extensional tectonic environment caused by rollback after the subduction of the paleo-Pacific plate (Figure 6), with features of a transitional tectonic system.

Conclusion

1) The garnet U-Pb dating method was applied to reveal the mineralization age and genesis of Makeng-style deposits, yielding 137–130 Ma ages for nine ore-bearing garnet samples from different deposits and orebodies of the same deposit.
2) The garnet U-Pb dating results (137–130 Ma) are consistent with the zircon U-Pb and molybdenite ages, which provides more direct evidence of the mineralization age for the Makeng-style deposits and indicates that the magnetite was closely related to Cretaceous granite emplacement.
3) Rare Earth element analysis results and REE patterns showed that there were typical skarn deposits, but obvious differences in the REE distribution types between different deposits, indicating that the ore-forming process may be distinct due to different mineralizing fluid for these deposits.
4) The Makeng-style iron-polymetallic deposits may have been formed in an extensional tectonic environment caused by rollback after subduction of the Paleo-Pacific Plate.

Data availability statement

The original contributions presented in the study are included in the article/Supplementary Material, further inquiries can be directed to the corresponding author.

Author contributions

SW: completion of manuscript KC: data treating DZ: writing guidance Others: Field and experimental assistance.

Funding

This work was supported by the Fundamental Research Projects from the Institute of Geomechanics, Chinese Academy of Geological Sciences, National Natural Science Foundation of China (No. 41873063), and projects from the China Geological Survey (No. DD20221644 and 12120113089600).

Acknowledgments

We are indebted to Yueheng Yang senior engineer from the Institute of Geology and Geophysics, Chinese Academy of Sciences,

for his kind assistance in providing standard samples. Great thanks to the reviewers and editors for their helpful comments.

Conflict of interest

The authors declare that the research was conducted in the absence of any commercial or financial relationships that could be construed as a potential conflict of interest.

Publisher's note

All claims expressed in this article are solely those of the authors and do not necessarily represent those of their affiliated organizations, or those of the publisher, the editors and the reviewers. Any product that may be evaluated in this article, or claim that may be made by its manufacturer, is not guaranteed or endorsed by the publisher.

References

Auwera, J. V., and Andre, L. (1991). Trace elements (REE) and isotopes (O, C, Sr) to characterize the metasomatic fluid sources: Evidence from the skarn deposit (Fe, W, Cu) of traversella (ivrea, Italy). *Contr. Mineral. Pet.* 106, 325–339. doi:10.1007/bf00324561

Chen, S. R., Xie, J. H., Xu, C. N., and Guo, W. W. (1985). The origin of makeng iron deposit, fujian. *Geochimica* 4, 350–357. doi:10.19700/j.0379-1726.1985.04.008

Chen, W., Zhang, W. Q., Simonetti, A., and Jian, S. Y. (2016). Mineral chemistry of melanite from calcitic ijolite, the Oka carbonatite complex, Canada: Implications for multi-pulse magma mixing. *J. Earth Sci.* 27, 599–610. doi:10.1007/s12583-016-0715-3

Deng, X. D., Li, J. W., Luo, T., and Wang, H. Q. (2017). Dating magmatic and hydrothermal processes using andradite-rich garnet U–Pb geochronometry. *Contrib. Mineral. Pet.* 172, 71–81. doi:10.1007/s00410-017-1389-2

Ding, T., Ma, D. S., Lu, J. J., and Zhang, R. Q. (2018b). Magnetite as an indicator of mixed sources for W-Mo-Pb-Zn mineralization in the Huangshaping polymetallic deposit, southern Hunan Province, China. *Ore Geol. Rev.* 95, 65–78. doi:10.1016/j.oregeorev.2018.02.019

Ding, T., Ma, D. S., Lu, J. J., and Zhang, R. Q. (2018a). Garnet and scheelite as indicators of multi-stage tungsten mineralization in the Huangshaping deposit, southern Hunan province, China. *Ore Geol. Rev.* 94, 193–211. doi:10.1016/j.oregeorev.2018.01.029

Dong, S. W., Zhang, Y. Q., Long, C. X., Yang, Z. Y., Ji, Q., Wang, T., et al. (2008). Jurassic tectonic revolution in China and new interpretation of the "yanshan movement. *Acta Geol. Sin.* 82, 334–347. doi:10.1111/j.1755-6724.2008.tb00583.x

Duan, Z., Gleeson, S. A., Gao, W. S., Wang, F. Y., and Li, J. W. (2020). Garnet U-Pb dating of the Yinan Au-Cu skarn deposit, Luxi District, North China Craton: Implications for district-wide coeval Au-Cu and Fe skarn mineralization. *Ore Geol. Rev.* 118, 103310–103318. doi:10.1016/j.oregeorev.2020.103310

Han, F., and Ge, C. H. (1983). Geological and geochemical characteristics of the marine volcanic hydrothermal - sedimentary origin of Makeng iron ore deposit in Fujian Province (in Chinese). *Annu. Rep. Chin. Acad. Geol. Sci.* 8, 154–156.

Hong, W., Zhang, Z. H., Jiang, Z. S., Li, F. M., and Liu, X. (2012). Magnetite and garnet trace element characteristics from the Chagangnuoer iron deposit in the Western Tianshan Mountains, Xinjiang, NW China: Constrain for ore Genesis (in Chinese with English abstract). *ActaPetrologica Sin.* 28, 2089–2102.

Lai, S. H., Chen, R. Y., Zhang, D., Di, Y. J., Gong, Y., Yuan, Y., et al. (2014). Petrogeochemical features and zircon LA-ICP-MS U-Pb ages of granite in the Pantian iron ore deposit, Fujian Province and their relationship with mineralization (in Chinese with English abstract). *Acta Petrol. Sin.* 30, 1780–1792.

Li, D. F., Fu, Y., and Sun, X. M. (2018). Onset and duration of Zn-Pb mineralization in the Talate Pb-Zn (-Fe) skarn deposit, NW China: Constraints from spessartine U-Pb dating. *Gondwana Res.* 63, 117–128. doi:10.1016/j.gr.2018.05.013

Li, J. H., Zhang, Y. Q., Dong, S. W., and Li, H. L. (2012). Late mesozoic–early cenozoic deformation history of the yuanma basin, central South China. *Tectonophysics* 570-571, 163–183. doi:10.1016/j.tecto.2012.08.012

Liu, Y. S., Hu, Z. C., Zong, K. Q., Gao, C. G., Chen, H. H., Xu, J., et al. (2010). Reappraisement and refinement of zircon U-Pb isotope and trace element analyses by LA-ICP-MS. *Chin. Sci. Bull.* 55, 1535–1546. doi:10.1007/s11434-010-3052-4

Ludwig, K. R. (2003). *Isoplot 3.00: A geochronological toolkit for microsoft excel*. California, Berkeley: Berkeley Geochronology Center.

Seman, S., Stockli, D. F., and Mclean, N. M. (2017). U-Pb geochronology of grossular-andradite garnet. *Chem. Geol.* 460, 106–116. doi:10.1016/j.chemgeo.2017.04.020

Stifeeva, M., Salnikova, E., Samsonov, A. V., Kotov, A. B., and Gritsenko, Y. D. (2019). Garnet U–Pb age of skarns from dashkesan deposit (lesser caucasus). *Dokl. Earth Sc.* 487, 953–956. doi:10.1134/S1028334X19080178

Tang, Y. W., Gao, J. F., Lan, T. G., Cui, K., Han, J. J., Zhang, X., et al. (2021). *In situ* low-U garnet U-Pb dating by LA-SF-ICP-MS and its application in constraining the origin of Anji skarn system combined with Ar-Ar dating and Pb isotopes. *Ore Geol. Rev.* 130, 103970–104015. doi:10.1016/j.oregeorev.2020.103970

Wafforn, S., Seman, S., Kyle, J. R., Stockli, D., Cloos, M., Sonbait, D., et al. (2018). Andradite garnet U-Pb geochronology of the big Gossan skarn, Ertsberg-Grasberg mining district, Indonesia. *Econ. Geol.* 113, 769–778. doi:10.5382/econgeo.2018.4569

Wang, D. H., Chen, Z. H., Chen, Y. C., and Tan, J. X. (2010). New data of the rock forming and ore-forming chronology for China's important mineral resources areas (in Chinese with English abstract). *Acta Geol. Sin.* 84, 1030–1040.

Wang, L. J., Wang, J. B., Wang, Y. W., and Shimazaki, H. (2002). REE geochemistry of the Huangguangliang skarn Fe-Sn deposit, Inner Mongolia (in Chinese with English abstract). *Acta Petrol. Sin.* 18, 575–584.

Wang, S., Zhang, D., Vatuva, A., Yan, P. C., Ma, S., Feng, H. B., et al. (2015). Zircon U-Pb geochronology, geochemistry and Hf isotope compositions and their implications of the dayang and juzhou granites from longyan area in fujian province(in Chinese with English abstract). *Geochemica* 44, 440–468.

Wang, S., Zhang, D., Wu, G. G., Cao, K., Qu, H. J., Ma, S., et al. (2017a). New geochronologic evidence of diabases and their metallogenic relationship with the Makeng-type iron deposits in Southwest Fujian, SE China. *Acta Geol. Sin. - Engl. Ed.* 91, 2324–2326. doi:10.1111/1755-6724.13473

Wang, S., Zhang, D., Wu, G. G., Vatuva, A., Di, Y. J., Yan, P. C., et al. (2017b). Late Paleozoic to Mesozoic extension in southwestern Fujian Province, South China: Geochemical, geochronological and Hf isotopic constraints from basic-intermediate dykes. *Geosci. Front.* 8, 529–540. doi:10.1016/j.gsf.2016.05.005

Wang, S., Zhang, D., Wu, G. G., Yi, J. J., and Li, X. J. (2018a). Metallogenic structctural plane characteristics and its prospecting importance for makeng type Fe deposits in southwestern fujian province (in Chinese with English abstract). *J. Geomechanics* 24, 199–211. doi:10.12090/j.issn.1006-6616.2018.24.02.021

Wang, S., Zhang, D., Yu, T. D., Wu, G. G., Di, Y. J., Zhang, Y. Y., et al. (2021). Geochronology and S-Pb-O-H isotopic constraints on the generation of the Luoyang Fe deposit in southwest Fujian Province, SE China. *Resour. Geol.* 71, 63–79. doi:10.1111/rge.12247.1111/rge.12247

Wang, S., Zhang, S. H., Zhag, Q. Q., Liang, X., Kong, L. H., Hu, G. H., et al. (2022). *In-situ* zircon U-Pb dating method by LA-ICP-MS and discussions on the effect of different beam spot size on the dating results (in Chinese with English abstract). *J. geomechanics* 28, 642–652. doi:10.12090/j.issn.1006-6616.2021140

WangZhang, S. D., Wu, G. G., Yi, J. J., Li, X. J., Gao, X. Q., Vatuva, A., et al. (2018b). Late mesozoic tectonic evolution of southwestern fujian province, South China: Constraints from magnetic fabric, zircon U-Pb geochronology and structural deformation. *J. Earth Sci.* 29, 391–407. doi:10.1007/s12583-017-0968-5

Xing, G. F., Lu, Q. D., Chen, R., Zhang, Z. Y., Nie, T. C., Li, L. M., et al. (2008). Study on the ending time of late mesozoic tectonic regime transition inSouth China: Comparing to the yanshan area in north China (in Chinese with englis abstract). *Acta Geol. Sin.* 82, 451–463.

Yan, P. C. (2013). *Discussion the genesis of Makeng iron ore-deposit, Fujian Province (in Chinese with English abstract)*. Beijing: China University of Geosciences, 1–84.

Yang, F. Q., Mao, J. W., Xu, L. G., Zhang, Y., and Liu, F. (2007). REE geochemitry of the Mengku iron deposit, Xinjiang, and its indication for iron mineralization (in Chinese with English abstract). *Petrol. Sin.* 23, 2443–2456.

Yang, Y. L., Ni, P., Pan, J. Y., Wang, G. G., and Xu, Y. F. (2017). Constraints on the mineralization processes of the Makeng iron deposit, eastern China: Fluid inclusion, H-O isotope and magnetite trace element analysis. *Ore Geol. Rev.* 88, 791–808. doi:10.1016/j.oregeorev.2016.11.018

Yu, T. D. (2017). *The "Three-in-One" characteristics and metallogenic mechanism of Luoyang iron ore in zhangping city, fujian province (in Chinese with English abstract)*. Beijing: China University of Geosciences, 1–70.

Yuan, Y. (2020). *Petrogenesis of early cretaceous granitoids and Fe-Mo polymetallic mineralization in yongding—dehua area*. Beijing: China University of Geosciences, 1–221.

Yuan, Y., Zhang, D., Feng, H. B., Di, Y. J., Wang, C. M., and Ni, J. H. (2014). The Re-Os isotope geochronology of Dapai iron polymetallic ore deposit in Yongding County, Fujian Province and its genetic significance. *Acta Geol. Sin. - Engl. Ed.* 88, 1025–1026. doi:10.1111/1755-6724.12378_30

Zhang, C. S., Li, L., Zhang, Q. Q., and Wang, J. R. (2012a). LA-ICP-MS zircon U-Pb ages and Hf isotopic compositions of Dayang granite from Longyan, Fujian Province (in Chinese with English abstract). *Geoscience* 26, 433–544.

Zhang, C. S., Mao, J. W., Zhang, C. Q., and Yu, M. (2013). Fluid inclusion characteristics and metallogenic mechanism of Makeng skarn Fe-Mo deposit in Fujian Province (in Chinese with Englis abstract). *Mineral. Deposits* 32, 390–396.

Zhang, D., Wu, G. G., Di, Y. J., Wang, C. M., and Yao, J. M. (2012b). Geochronology of diagenesis and mineralization of the Luoyang iron deposit in Zhangping city, Fujian province and its geological dignificance (in Chinese with English abstract). *Earth Sci.* 37, 1217–1231. doi:10.3799/dqkx.2012.130

Zhang, X. D., Meng, X. H., Chen, Z. X., Wang, J., and Xiu, C. X. (2018a). Comprehensive study of the geological and geophysical characteristics of the metallogenic belt in Southwest Fujian-A case study in the Yongding-Dapai polymetallic ore deposit (in Chinese with English abstract). *Chin. J. Geophys.* 61, 1588–1595. doi:10.6038/cjg2018L0666

Zhang, Y. Q., Dong, S. W., Li, J. H., Cui, J. J., Shi, W., Su, J., et al. (2012c). The new progress in the study of Mesozoic tectonics of South China (in Chinese with English abstract). *Acta Geol. Sin.* 33 (03), 257–279. doi:10.3975/cagsb.2012.03.01

Zhang, Z. J., Cheng, Q. M., Yang, J., and Hu, X. L. (2018b). Characterization and origin of granites from the Luoyang Fe deposit, southwestern fujian province, South China. *J. Geochem. Explor.* 184, 119–135. doi:10.1016/j.gexplo.2017.10.015

Zhang, Z. J., Zuo, R. G., and Cheng, Q. M. (2015). The mineralization age of the makeng Fe deposit, South China: Implications from U-Pb and Sm-Nd geochronology. *Int. J. Earth Sci.* 104, 663–682. doi:10.1007/s00531-014-1096-4

Zhang, Z. J., and Zuo, R. G. (2014). Sr-Nd-Pb isotope systematics of magnetite: Implications for the Genesis of Makeng Fe deposit, southern China. *Ore Geol. Rev.* 57, 53–60. doi:10.1016/j.oregeorev.2013.09.009

Zhang, Z., and Zhang, C. S. (2014). Skarn mineral characteristics and zonation of the Makeng Fe-Mo deposit in Fujian Province. *Acta Petrol. Sin.* 30, 1339–1354.

Zhao, X. L., Yu, S. Y., Yu, M. G., Jiang, Y., and Mao, J. R. (2016). Geological characteristics and metallogenic epochs of the Dapai Fe-Pb-Zn polymetallic deposit in yongding county, fujian province. *Geol. China* 43, 174–187.

frontiers | Frontiers in Earth Science

TYPE Original Research
PUBLISHED 27 January 2023
DOI 10.3389/feart.2023.1048509

Check for updates

OPEN ACCESS

EDITED BY
Liang Zhang,
China University of Geosciences, China

REVIEWED BY
Jilong Han,
China University of Geosciences, China
Qingquan Liu,
Central South University, China
Binghan Chen,
Institute of Mineral Resources, Chinese Academy of Geological Sciences, China

*CORRESPONDENCE
Jun-Jian Li,
tjlijunjian@163.com
Zhi-Cai Dang,
dangzhicai@163.com

SPECIALTY SECTION
This article was submitted to Structural Geology and Tectonics, a section of the journal Frontiers in Earth Science

RECEIVED 19 September 2022
ACCEPTED 17 January 2023
PUBLISHED 27 January 2023

CITATION
Li J-J, Dang Z-C, Fu C, Zhang P-P, Tian J-P and He J-T (2023), Genesis of the Yangjiakuang gold deposit, Jiaodong peninsula, China: Constraints from S-He-Ar-Pb isotopes, and Sm-Nd and U-Pb geochronology.
Front. Earth Sci. 11:1048509.
doi: 10.3389/feart.2023.1048509

COPYRIGHT
© 2023 Li, Dang, Fu, Zhang, Tian and He. This is an open-access article distributed under the terms of the Creative Commons Attribution License (CC BY). The use, distribution or reproduction in other forums is permitted, provided the original author(s) and the copyright owner(s) are credited and that the original publication in this journal is cited, in accordance with accepted academic practice. No use, distribution or reproduction is permitted which does not comply with these terms.

Genesis of the Yangjiakuang gold deposit, Jiaodong peninsula, China: Constraints from S-He-Ar-Pb isotopes, and Sm-Nd and U-Pb geochronology

Jun-Jian Li[1,2]*, Zhi-Cai Dang[1,2]*, Chao Fu[1,2], Peng-Peng Zhang[3], Jie-Peng Tian[4] and Jiang-Tao He[5]

[1]Tianjin Center, China Geological Survey, Tianjin, China, [2]North China Center for Geoscience Innovation, China Geological Survey, Tianjin, China, [3]Institute of Geophysical and Geochemical Exploration, Chinese Academy of Geological Science, Langfang, China, [4]School of Civil Engineering, Shandong Jianzhu University, Jinan, China, [5]Institute of Geological Surveying, Hebei GEO University, Shijiazhuang, China

Located in the Penglai-Qixia-Fushan Gold Belt, the Yangjiakuang gold deposit formed in the marble of the Paleoproterozoic Fenzishan Group is different from the previous altered rock-type gold deposits whose host gold-bearing rocks are Archean gneiss and Mesozoic granite. Two gold orebodies have been explored within the Yangjiakuang gold deposit, and both of them were controlled by the Yangjiakuang syncline. Three ore-forming stages have been recognized, including the pyrite-sericite stage (I), the gold, polymetallic sulfide, and quartz stage (II), and quartz-calcite stage (III). The calcites, which represent the main metallogenic stage (II) at Yangjiakuang gold deposit, yielded a Sm-Nd isochron age of 123.5 ± 8.1 Ma (MSWD = 0.042). Subsequent geologic events were recorded by quartz diorite porphyrite dyke which are dated at 122.75 ± 0.66 Ma (MSWD = 1.5) by zircon LA-ICP-MS U-Pb dating. It is suggested that the gold mineralization took place in the early period of Early Cretaceous. The *in situ* $\delta^{34}S$ values of pyrites from two stages have a narrow range from + 5.65 to + 9.63‰ with an average value of 8.14‰, which indicate that the source of $\delta^{34}S$ is related to the Guojialing granite and the Fenzishan Group. The lead isotopic compositions of pyrites ($^{206}Pb/^{204}Pb$ = 16.615 to 16.832; $^{207}Pb/^{204}Pb$ = 15.275 to 15.403; $^{208}Pb/^{204}Pb$ = 36.829–37.470) show a consistent origin of the lower crust. The measured $^{3}He/^{4}He$ ($^{40}Ar/^{36}Ar$) of hydrothermal fluids in pyrites are 0.641–1.132 Ra (637.5–1162.7), indicating that the ore-forming fluid originating from a mixing of crustal and mantle components. It is suggested that the gold mineralization is associated with extensional tectonic inversion caused by the rollback of the subducting Izanagi Plate during the early Cretaceous, which triggered partial melting of mantle and lower crust, and subsequent magma mixing and exsolution of ore-bearing fluids. These fluids extracted ore-forming materials from the enclosing rocks of the Jiaodong Group, the Fenzishan Group, and the Guojialing granite to form the ore-forming fluids.

KEYWORDS

S-He-Ar-Pb isotopes, Sm-Nd isochron age, LA-ICP-MS zircon U-Pb dating, Yangjiakuang gold deposit, Jiaodong peninsula

1 Introduction

The Jiaodong Peninsula is located in the southeastern North China Craton (NCC) and hosts world-class gold deposits with total proven reserves of more than 5,000 t of gold (Song et al., 2021; Tian et al., 2022). In the Jiaodong Peninsula, three major gold metallogenic belts have been identified, including the Zhaoyuan-Laizhou Gold Belt, the Penglai-Qixia-Fushan Gold Belt, and the Muping-Rushan Gold Belt (Deng et al., 2020a; Wu et al., 2021). Three types of gold deposits have been identified so far, i.e., the auriferous quartz vein type, the altered rock type, and the interstratified breccia type (Mao et al., 2008; Yang et al., 2014a). Based on the evidence from geological, geochronological, geochemical, and isotope geochemical, previous researcher have been proposed various models for the genesis of three types of gold deposits (Yang and Zhou, 2001; Zhai et al., 2004; Li et al., 2006; Mao et al., 2008; Deng et al., 2011; Zhai and Santosh, 2013; Li et al., 2017; Li and Santosh, 2017; Yuan et al., 2019; Xu Y. et al., 2022; Tian et al., 2022). More recently, several gold deposits of altered rock types (e.g., Yangjiakuang, Dujiaya) (Figure 1B) have been identified in the Penglai-Qixia-Fushan Gold Belt (Ding et al., 2015). The host rocks for these deposits are Paleoproterozoic metamorphic rocks, which are different from the previous altered rock type for the gold deposits whose gold-bearing host rocks are Archean gneiss and Mesozoic granite. However, these deposits have not drawn much attention in the past, and whether the gold deposits distributed along the Penglai-Qixia-Fushan Gold Belt belong to a new episodic gold mineralization is poorly understood. A study on the genesis and geochronology of the Yangjiakuang gold deposit can expand our knowledge regarding the metallogenic theory concerning the Jiaodong gold deposit and provide a theoretical basis for the prospecting of the same type of gold deposit in the area. In this study, the isotopic compositions of sulfur, lead and He-Ar isotopes of the fluid inclusions were used to decipher the source of the fluids responsible for the Yangjiakuang gold mineralization. Calcite Sm-Nd isotopic dating and zircon U-Pb dating for post-mineralized quartz diorite porphyritic dyke were also conducted to constrain the metallogenic age for the Yangjiakuang gold deposit.

2 Geological background

2.1 Regional geology

The Jiaodong Peninsula consists of two major terranes, namely, the Jiaobei terrane to the northwest and the Sulu ultrahigh-pressure (UHP) terrane to the southeast. These terranes are split by the Wulian-Yantai Fault (Deng et al., 2006; 2018; Yang et al., 2014b; Song et al., 2015; Li et al., 2021). The Jiaobei terrain can be further divided into the Jiaobei Uplift in the north and the Jiaolai Basin in the south (Figure 1A) (Deng et al., 2015).

The Jiaodong Peninsula is composed primarily of the Precambrian basement and Mesozoic igneous rocks. The former includes the Archean tonalite-throndhjemite-granodiorite (TTG) gneisses with small amounts of the Jiaodong Group comprising metamorphic supracrustal rocks and mafic granulite/amphibolite lenses, the Paleoproterozoic Fenzishan and Jingshan Groups, and the Neoproterozoic Penglai Group that consist of metasedimentary rocks (Tang et al., 2007; Yang et al., 2014b; Hao et al., 2020). Geochronological and geochemical studies have revealed that the TTG gneiss, amphibolite, and granulite have protolith ages of ~2.9 to 2.7 Ga, 2.5 Ga, and 2.4 Ga, respectively (Jahn et al., 2008; Xie et al., 2014; Liu et al., 2015; Xie et al., 2015; Dang et al., 2022). The Jingshan Group which is composed of biotite granulite, garnet-biotite-graphite gneiss, dolomitic marble, diopside amphibolite, marble, and biotite-graphite schist (An, 1990; Li et al., 2018; Liu. Z. K et al., 2021), were metamorphosed at 1.8–1.7 Ga under amphibolite to granulite facies (Zhao and Zhai, 2013). The coeval Fenzishan Group has similar source rocks and lithologic compositions to those of the Jingshan Group, whereas the metamorphic grade is low, ranging from greenschist to lower amphibolite facies (Wang et al., 2009; Tan et al., 2015). Subsequently, the Neoproterozoic Penglai Group, which consists of fluvial-clastic and carbonate rocks, underwent lower greenschist-facies metamorphism to form slate, quartzite, and limestone (Faure et al., 2003; Zhang et al., 2010; Tan et al., 2015; Liu. Z. K et al., 2021). This Precambrian basement is partly overlain by Cretaceous continental sediments and volcanic associations emplaced in the Jiaolai Basin (Liu. Z. K et al., 2021).

During the Mesozoic, extensive magmatism took place and formed a series of granitoids and mafic dykes. These processes can be divided into four magma activities based on detailed U-Pb dating: 1) The late Triassic post-collisional rocks (230–200 Ma, Chen et al., 2003; Yang et al., 2005; Guo et al., 2005; Zhang. L et al., 2020) consisting of quartz syenite, pyroxene syenite, and alkaline gabbro, distributed in the Sulu orogenic belt and represented by Shidao, Ningjinsuo, and Chashan intrusions. 2) The late Jurassic calc-alkaline granites (160–141 Ma, Yang et al., 2012; Ma et al., 2013; Li et al., 2019; Wang et al., 2022), which occur as a large batholith and are composed of biotite monzogranite, monzodiorite, quartz diorite, and granodiorite, such as Linglong, Kunyushan, Queshan and Wendeng plutons. 3) The early stage of the Early Cretaceous high-potassium calc-alkaline granodiorite (132–123 Ma, Wang et al., 2014; Liu et al., 2014; Zhao et al., 2018). They are probable mixed crust-mantle components and are represented by the Sanshandao, Shangzhuang, Beijie, Congjia, and Guojialing intrusions (Dang et al., 2022). 4) The late period of the Early Cretaceous alkaline granites and intermediate basic dykes (118–108 Ma, Qiu et al., 2008; Ding et al., 2013; Zhao et al., 2018; Li et al., 2019; Song et al., 2020), which are composed of diorite, granodiorite, and granite assemblages (Yang et al., 2014a; Ding et al., 2015; Dang et al., 2022).

The dominant structures in the Jiaodong Peninsula are NNE-to NE-trending fault systems (Figure 1B). These faults are characterized by a parallel and uniform distribution. From west to east, they are represented by the Sanshandao, Jiaojia, Zhaoping, Qixia, Muping-Jimo, and Jinniushan faults. These structures control the distribution of the Jiaodong gold deposits, which are divided into three gold belts according to their spatial distribution and traditionally have been grouped into three main types (Figure 1B): the auriferous quartz vein type (Linglong type), the altered rock type (Jiaojia type), and the interstratified breccia type (Pengjiakuang type) (Zhang et al., 2003; Mao et al., 2008; Guo et al., 2013). The Linglong type deposits are represented by deposits at Linglong, Denggezhuang, Dayingezhuang, and Jinqingding, whereas the Jiaojia type deposits are exemplified by deposits at Sanshandao, Jiaojia, Xincheng, Xiadian, and Dayingezhuang. The Pengjiakuang type deposits include those at Pengjiakuang and Dazhuangzi.

In recent years, several gold deposits or outcrops have been discovered in the Penglai-Qixia-Fushan Gold Belt, which are represented by the Yangjiakuang and Dujiaya gold deposits. Although these deposits have a similar fault-controlled nature of

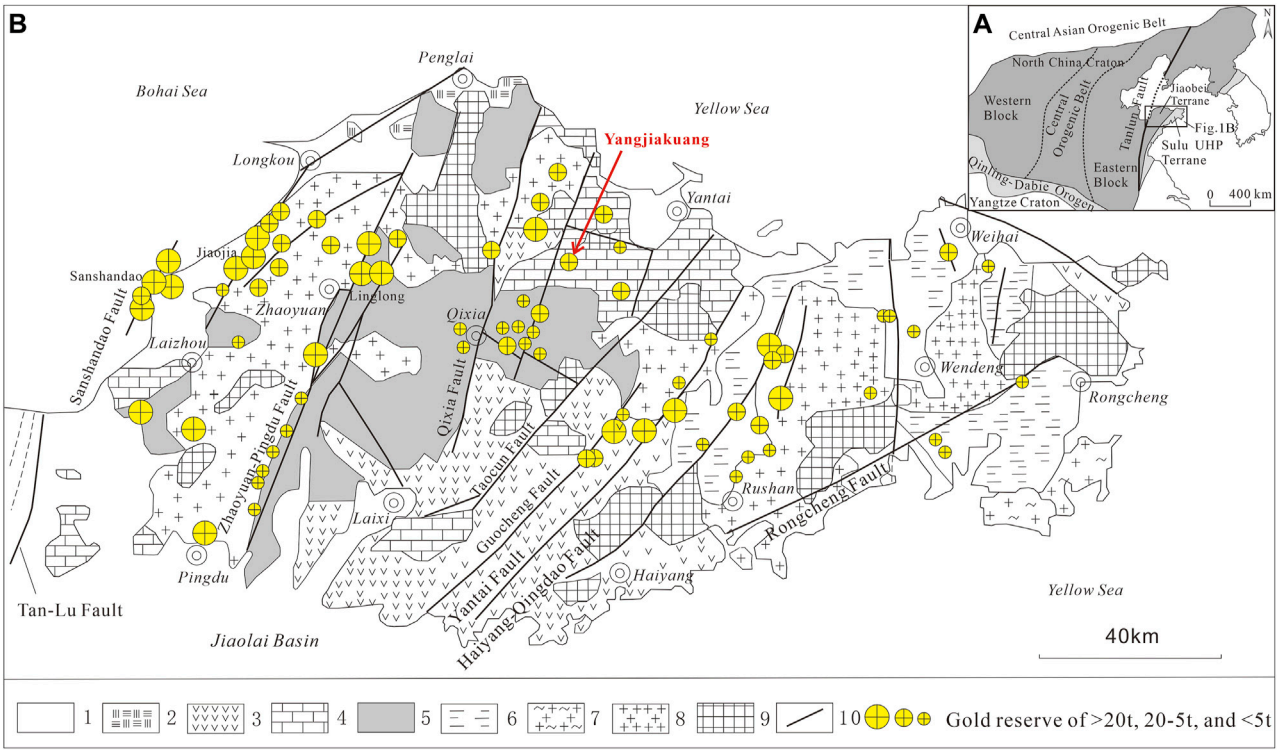


FIGURE 1
Simplified geological map of the Jiaodong Peninsula, showing the distribution of gold deposits, strata, magmatic rocks, and main faults **(B)**. Inset shows tectonic blocks of the North China Craton and the location of the Jiaodong Peninsula **(A)** (simplified from Ding et al., 2015; Li et al., 2020; Dang et al., 2022). 1. Cenozoic sedimentary rocks; 2. Cenozoic basalts; 3. Cretaceous volcanic rocks; 4. Paleoproterozoic Jingshan Group and Fenzishan Group metamorphic rocks; 5. Neoarchean TTG and metamorphic supracrustal rocks; 6. Proterozoic granitic complex rocks; 7. Triassic granites; 8. Jurassic granites; 9. Cretaceous granites; 10. Regional faults.

the mineralization when compared to the traditional three types of Jiaodong deposits, they are characterized by the fact that the gold deposits are hosted in the Paleoproterozoic Fenzishan Group which consist of metamorphic rocks. The detailed geology, mineralization, and alterations are summarized below.

2.2 Deposit geology

The Yangjiakuang gold deposit is located in the Qixia-Penglai-Fushan Gold Belt and belongs to the Jiaobei uplift in the Northeastern margin of the North China Craton (Li et al., 2005; Ding et al., 2015; Song et al., 2015) (Figure 1B). The area mainly exposes thick dolomite marble with biotite granulite, tremolite schist, and tremolite marble in the Paleoproterozoic Zhanggezhuang Formation of the Fenzishan Group, followed by thin-layer calcareous slate, siliceous slate, phyletic slate, and dolomite marble in the Neoproterozoic Baoshankou Formation of the Penglai Group. Mesozoic dykes are developed in the area, including quartz diorite porphyrite, lamprophyre, and pegmatite. All of them are filled with irregular veins and lenticular faults in different directions.

The structure in the area is dominated by a syncline. Mineralization is structurally controlled by the Yangjiakuang syncline in this area. The axis of the syncline, distributed in an EW direction, is located in the west of the Yangjiakuang village (Figure 1). The stratum of the axis consists of the third member of the Zhanggezhuang Formation in the Fenzishan Group, and the two wings consist of the second member, and the first member of the Zhanggezhuang Formation (Figure 2). The strata of the wings present as a reverse sequence. The Western end of the syncline is cut by NNE trending faults, and the eastern end of the syncline dips. The faults are divided into NNE and EW groups. The shape and scale of the Yangjiakuang gold deposit are controlled by the Yangjiakuang syncline. The gold ore body occurs mainly in the marble of the Paleoproterozoic Fenzishan Group, and it is controlled by the interlayer detachment structure and the NE trending fault (Zhang et al., 2004).

Both No. III and No. IV gold orebodies that were explored in the Yangjiakuang deposit are controlled by the Yangjiakuang syncline (Yu et al., 2014). The shape of gold orebody is V-shaped (Figure 2). No. III gold orebody is located in dolomite marble of the third member of Zhanggezhuang Formation near the axis of the structure of Yangjiakuang syncline and has a length of about 950 m and a width of 10–70 m. No. IV gold orebody is hosted in the contact zone between the second and third members of the Zhanggezhuang Formation and has a length of 850 m and a width of 5–16 m (Figure 3), whose proven gold resource is 1.02 t. No. III gold orebody is the largest in the Yangjiakuang deposit and strikes EW, dips to the north at 20–30°, and has a length of 300 m, and a thickness of 4.2–18.0 m. The gold proven resource is 2.58 t. The grade of gold varies from 2.5 to 4.5 g/t, with an average value of 3.79 g/t. The boundary between the orebody and the ore-bearing rock is not clear and shows a gradual

10.3389/feart.2023.1048509

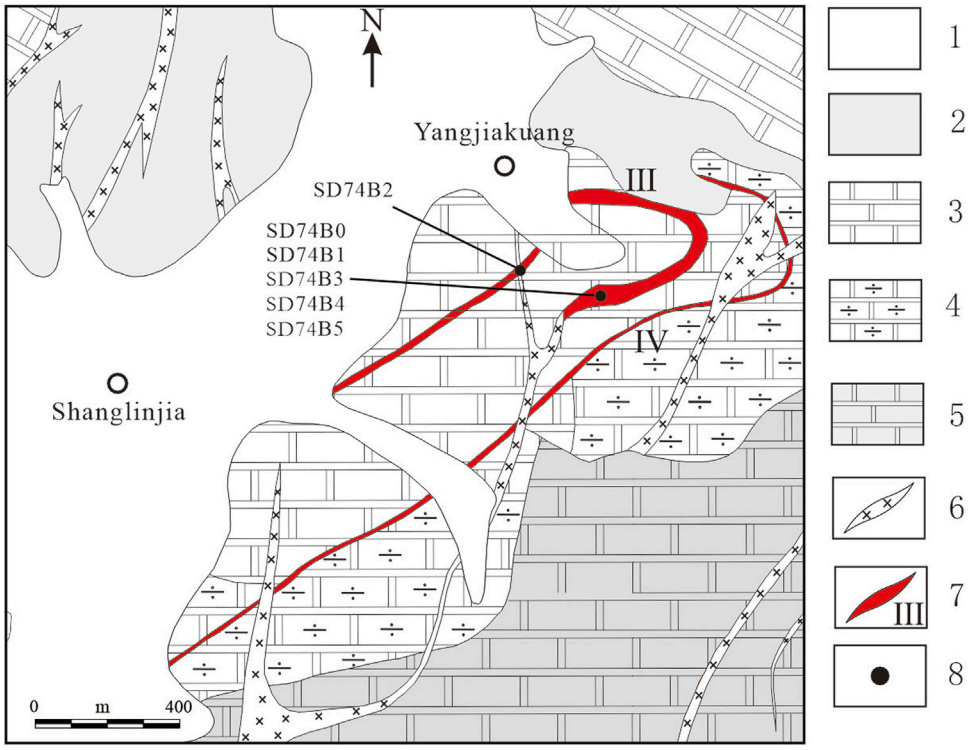


FIGURE 2
Geological sketch map of the Yangjiakuang gold deposit (after Ding, 2014). 1. Quaternary; 2. Slate (Baoshankou Formation); 3. Dolomite marble (Third member of the Zhanggezhuang Formation); 4. Diorite marble (Second member of the Zhanggezhuang Formation); 5. Dolomite marble (First member of the Zhanggezhuang Formation); 6. Quartz diorite porphyrite; 7. Gold orebody; 8. Sample location.

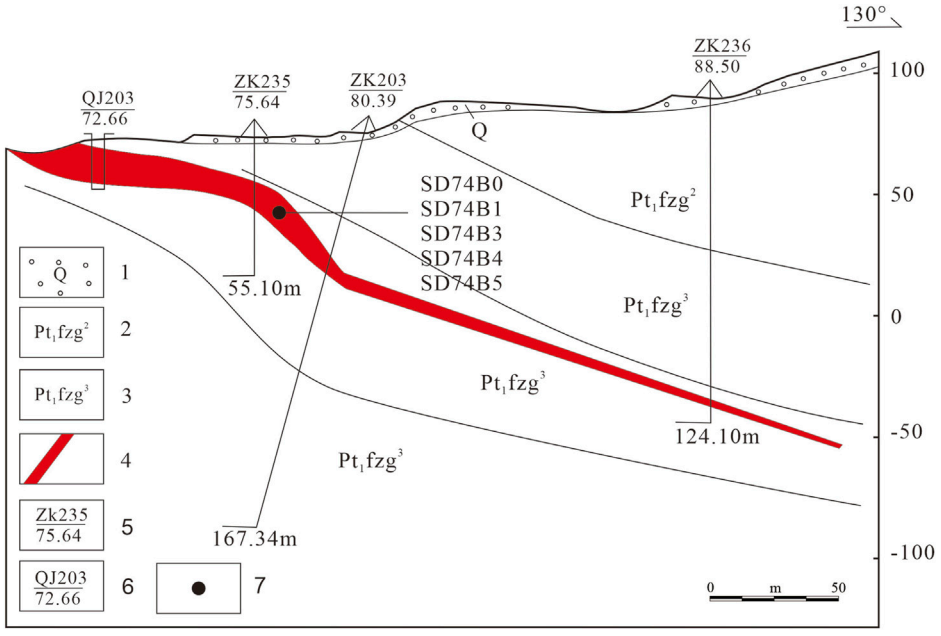


FIGURE 3
Geological profile along No. 252 line of the Yangjiakuang gold deposit, showing the sampling sites in this study (after Yu et al., 2014). 1. Quaternary; 2. Second member of the Zhanggezhuang Formation; 3. Third member of the Zhanggezhuang Formation; 4. Gold vein; 5. Drill hole; 6. Drilling shallow well; 7. Sample location.

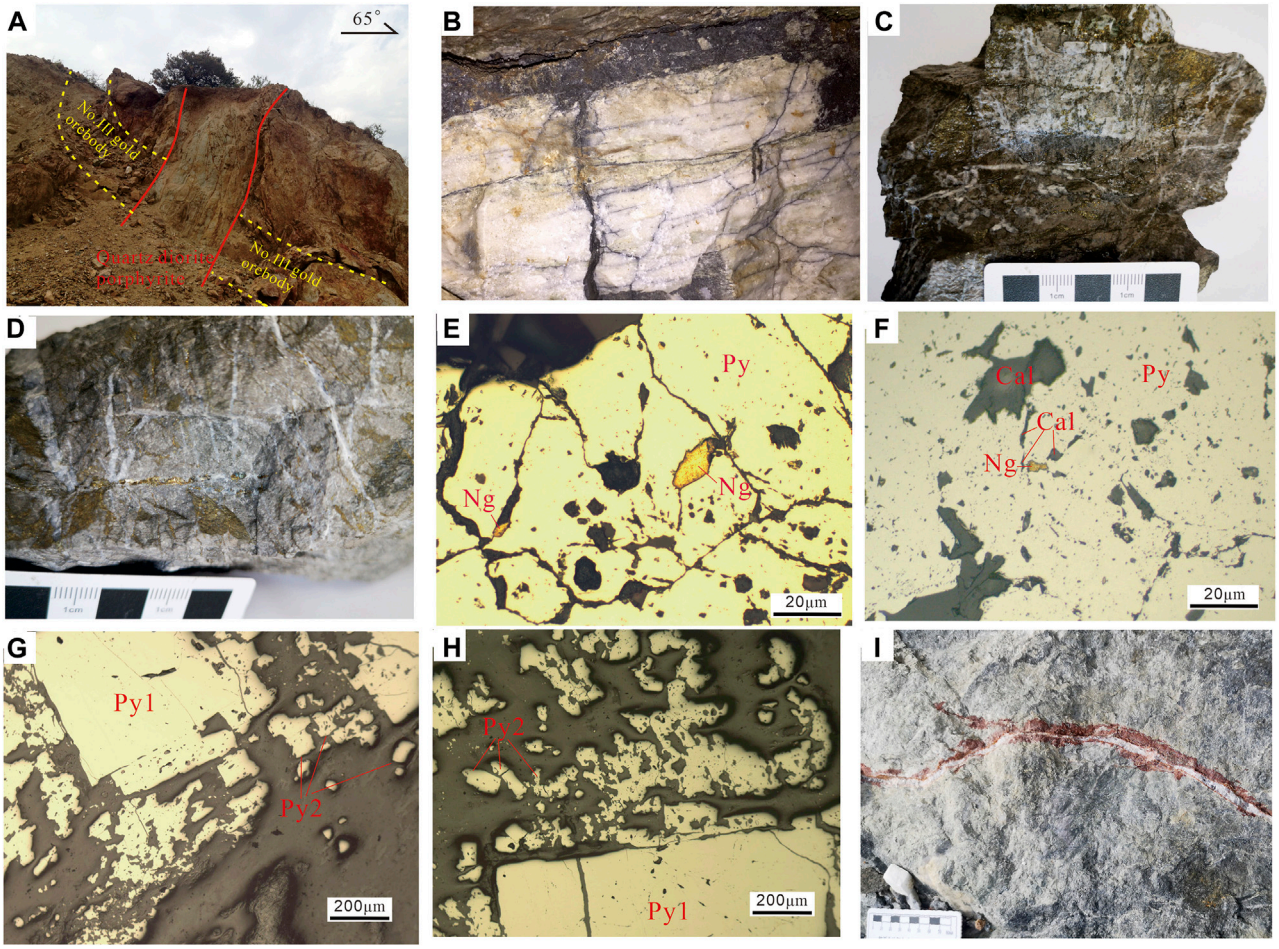


FIGURE 4
Photographs showing mineral assemblages and mineralization stages in the Yangjiakuang gold deposit **(A)** Quartz diorite porphyrite dyke cutting through the gold orebody; **(B)** Disseminated-type ore; **(C,D)** Veinlet-type ore; **(E,F)** Irregular native gold inclusions within Py; **(G,H)** Micrographs of Py1 and Py2; **(I)** Quartz and calcite vein; Mineral abbreviations used are as follows: Py, Pyrite; Cal, Calcite; Ng, Natural gold.

transitional relationship, which is determined solely by the grade of gold. The ore-bearing rock near the orebody is mainly sericite cataclastic marble, followed by granulite, amphibolite, diorite, slate, *etc.* The quartz diorite porphyry dyke located in the west of Yangjiakuang gold deposit cuts through No. III gold orebody (Figure 4A), which should be close to or later than the gold mineralization. The strike is mostly 0°–10° and dips 75° to East, and measure 5–20 m in width and 750 m in length. The quartz diorite porphyrite is gray and featured a massive porphyritic structure. The phenocrysts were composed of plagioclase and quartz, and the substrate was composed of plagioclase, amphibole, biotite, and quartz. The content of plagioclase was 65%, which was an idiomorphic plate with lamellar twins; the hornblende content was 5%–10% with an idiomorphic plate; the quartz content was about 15%, the phenocryst melting corrosion was round, and the matrix was granular in nature; the K-feldspar content was 10%–15%, appearing in the matrix in the form of lath.

Disseminated- and veinlet-type ores can be observed in the Yangjiakuang gold deposit (Figures 4B–D). Ore minerals are dominated by pyrite with lesser amounts of chalcopyrite, sphalerite, arsenopyrite, and magnetite. The main precious metals are natural gold, silver-bearing natural gold and natural silver. The gangue minerals consist of quartz, calcite, and sericite, with subordinate chlorite, epidote, tremolite, graphite, and barite. The main elements in the ore are Au, followed by Ag. Gold occurs mostly as natural gold and silver-bearing natural gold. The microscopic observations show that the visible gold mainly occurs as filling microfractures in pyrite or as inclusions in pyrite and less commonly in calcite (Figures 4E, F). Native gold grains are generally less than 10 μm.

Three hydrothermal stages can be recognized in the Yangjiakuang gold deposit, on the basis of field evidence and microscopic texture, from oldest to youngest they are: the pyrite-sericite stage (I), the gold, polymetallic sulfide, and quartz stage (II), and quartz-calcite Stage (III). Stage I is represented by an assemblage of quartz, sericite and pyrite. The pyrite of this stage is euhedral, with 3–10 μm in size and essentially barren of gold (Figures 4G, H). The quartz is milky white and fine-grained. The sericite is distributed in fine grain orientation. Stage II is characterized by gold-bearing fine pyrite, quartz, and a small amount of chalcopyrite, sphalerite, galena, and calcite. A large amount of gold-bearing pyrites are formed in this stage (Figures 4G, H), which represents the main gold mineralization stage. Stage III is dominated by carbonate minerals (mainly calcite) and quartz (Figure 4I). They

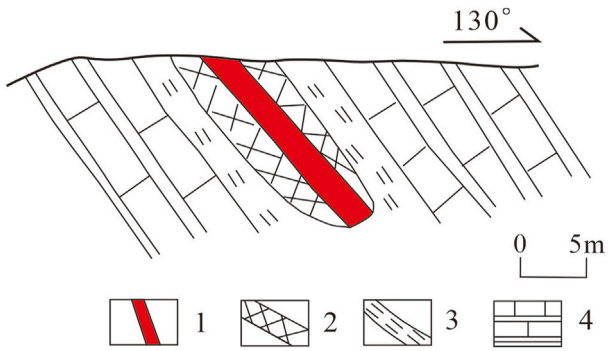


FIGURE 5
Diagram of wall-rock alteration zone for the Yangjiakuang gold deposit. 1. Gold vein; 2. Auriferous pyrite-quartz vein; 3. Sericitization zone; 4. Carbonation zone.

often occur as micro-to macroscopic veinlet-shaped forms. This is the latest mineralization stage.

Hydrothermal alteration is widespread, including sericitization, silicification, pyritization, carbonation, chloritization, and tremolite. The silicification, pyritization, and sericitization are closely related to gold mineralization (Wang et al., 2017). There is a gradual transitional relationship between the gold orebody and the surrounding rocks (Figure 5). The core of the gold orebody is mainly composed of quartz, sericite, and pyrite. The sericite is distributed in a scale-like orientation, quartz is arranged in an allomorphic granular orientation, and pyrite occurs in a veined and disseminated form. The wall rock near the orebody is composed of quartz, sericite, and a small amount of calcite, which developed silicification and sericitization alteration. In the wall rock distant to the orebody, the mineral compositions are mainly protolith, and quartz and calcite veinlets which formed by the late alteration and filled along the fractures.

3 Analytical methods

Except for the quartz diorite porphyry dyke which was mined in the shallow surface, all of the samples were mined underground in tunnels of depth 60 m.

In situ S isotope analyses of five samples from different stage sulfides in thin sections were performed by LA-MC-ICP-MS at the State Key Laboratory of Geological Processes and Mineral Resources, China University of Geosciences (Wuhan). The analytical methods are based on Bendall et al. (2006) and Craddock et al. (2008). A Nu Plasma II MC-ICP-MS equipped with a Resolution-S155 excimer ArF laser ablation system was used for the analyses. The detailed experimental procedures and instrument test parameters were conducted according to Liu et al. (2018), Tian et al. (2020) and Xu Y. W. et al (2022).

He-Ar isotope analyses were performed at the Analytical and Testing Center in the Beijing Institute of Geological Research of Nuclear Industry, Beijing. The Helix SFT™ Split Flight Tube noble gas mass spectrometer was used, which had blank background signals of less than 5×10^{-14} ccSTP, a Faraday cup resolution greater than 400, and an ion multiplier resolution better than 700. The sensitivity of the He and Ar measurements were better than 2×10^{-4} A/Torr and 1×10^{-3}A/Torr, respectively. Four samples corresponding to stage II were measured. The analytical procedures adopted were the same as those described by Wang (2016), Tian et al. (2020) and Xu Y. et al (2022).

Lead isotope analyses were performed by a thermal ionization mass spectrometer (ISOPROBE-T) at the Beijing Institute of Geological Research of Nuclear Industry. The measured Pb isotopic ratio measurements for the international standard NBS 981 are around 0.1‰. The analytical values for the standard NBS 981 were as follows: $^{206}Pb/^{204}Pb = 16.937 \pm 0.002$ (2σ), $^{207}Pb/^{204}Pb = 15.457 \pm 0.002$ (2σ), and $^{208}Pb/^{204}Pb = 272\ 36.611 \pm 0.004$ (2σ) (Tian et al., 2020).

In order to constrain the timing of the main mineralization, eight calcites were collected for Sm-Nd dating. The calcite of the Yangjiakuang gold deposit was milky white and veinlet, coexisting with disseminated pyrite and other gold-bearing minerals. The aforementioned samples were collected and pulverized in the field to 40–60 mesh, and calcite was selected with the aid of a binocular lens, The sample, of purity better than 99%, was rinsed with distilled water, steam dried at low temperature, and then ground to about 200 mesh in the agate mortar prior to testing. Analyses of the Sm-Nd isotopes were carried out at the Isotope Geochronology Laboratory of the Tianjin Center, China Geological Survey. A description of the separation processes including the use of a specific resin are given elsewhere (Liu et al., 2017; Liu et al., 2018; Li et al., 2020), and the isochron age was calculated by the ISOPLOT program.

The U-Pb isotopic dating of zircon by LA-ICP-MS was undertaken in the laboratory of isotopic geochronology of the Tianjin Center, China Geological Survey. First, Zircons were separated from the quartz diorite porphyry dyke (SD74B2) using conventional crushing and sieving followed by standard heavy liquid and magnetic separation before pure separates were obtained by hand-picking under a binocular microscope at the Hebei Institute of Regional Geological and Mineral Resource Survey (Langfang). The separated zircons were then mounted in epoxy and polished to expose grain center for optical microscopy and cathodoluminescence (CL) imaging to identify target areas for U-Pb analyses (Figure 6).

Zircon LA-ICP-MS U-Pb analysis was undertaken in the laboratory of isotopic geochronology of the Tianjin Center, China Geological Survey. This analysis used laser energy and frequency settings of 13–14 J/cm^2 and 9 Hz, respectively, with a spot size of 35 μm. Helium was used as a carrier gas, and each analysis incorporated a background acquisition of ~20 s (gas blank), followed by 40 s of acquisition (ablated sample). GJ-1 was used as the external standard for the zircon age with correction for fractionation in the U-Pb isotope measurement (Jackson et al., 2004). The DataCal program for ICP-MS developed by Liu et al. (2010) and the Isoplot program developed by Ludwig (2003) were used for data processing. The isotopic data for the common lead was corrected by the ^{208}Pb correction method (Andersen, 2002). The Pb, U, and Th contents of the zircon samples were calculated based on using the NIST 610 glass standard as an external standard. Please consult Li et al. (2009) for full information on the instrument operating procedures and conditions.

4 Results

4.1 *In situ* sulfur isotopes

In situ measurements of sulfur isotopes at 18 locations on pyrite were conducted and the results are presented in Table 1. The pyrite

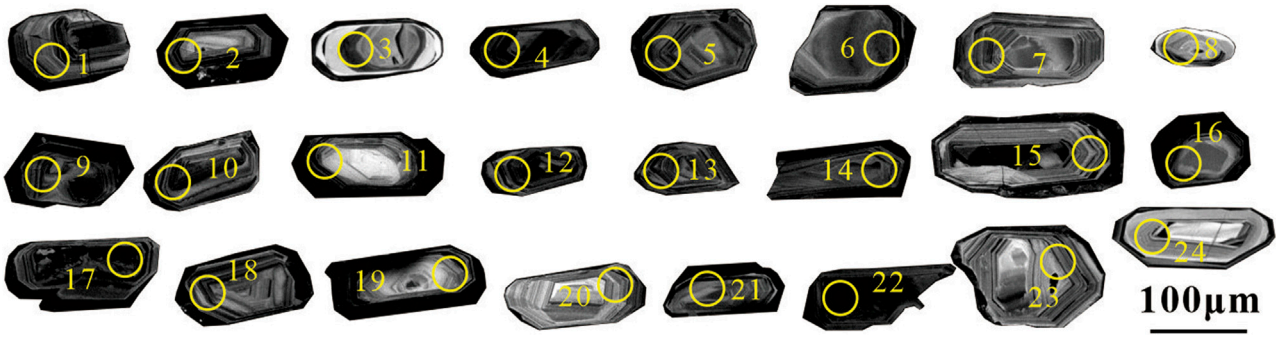


FIGURE 6
CL images and U-Pb data of zircons in diorite porphyrite (SD74B2).

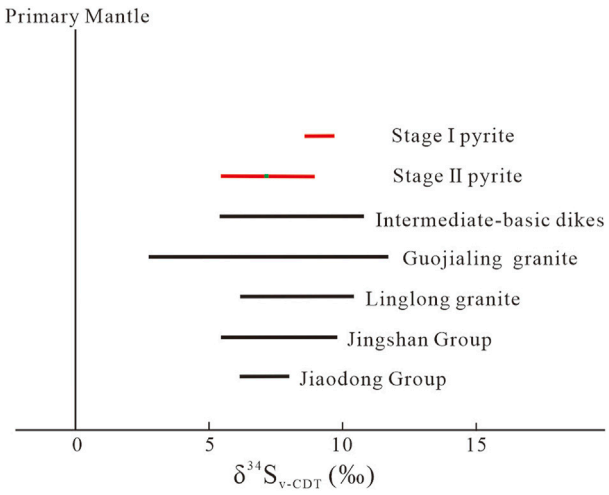


FIGURE 7
Sulfur isotopic compositions of pyrites from the Yangjiakuang gold deposit. The ranges of major geologic units are from Tian et al., 2020; Li et al., 2021; Liu. X. Y et al., 2021.

$\delta^{34}S$ values were distributed in a narrow range of 5.65–9.63‰, with an average value of 8.14‰. Pyrite $\delta^{34}S$ values (n = 6) for Stage I were 8.5–9.6‰ (avg. 9.1‰) and pyrite $\delta^{34}S$ values (n = 12) for stage II were 5.6–8.9‰ (avg. 7.6‰) (Figure 7).

The pyrite $\delta^{34}S$ values for the Yangjiakuang deposit were positive in different hydrothermal stages (9.1‰ for stage I→7.6‰ for stage II), which are similar to those of other Jiaodong gold deposits (e.g., Linglong deposit = 5.6–7.9‰, Guo et al., 2020; Dayingezhuang deposit = 4.8–9.0‰, Yuan et al., 2019; Heilangou deposit = 5.5–7.8‰; Xincheng deposit = 7.2–9.7‰, Majiayao deposit = 6.0–10.7‰, Tian et al., 2020 and Zhaoxian deposit = 6.0–10.7‰, Xu et al., 2022). These results indicate that the source of sulfur for the Yangjiakuang gold deposit was similar to the other neighboring gold deposits.

4.2 Helium-argon isotopes

The Helium and argon isotopic compositions of pyrites from different mineralization stages are shown in Table 2. The ^{3}He values for the fluid inclusions in pyrites ranged from 3.587 to 5.016 × 10^{-13} cm^3 STP/g, with an average value of 4.516 × 10^{-13} cm^3STP/g; the ^{4}He values ranged from 31.61 to 78.63 × 10^{-8} cm^3STP/g, with an average value of 53.95 × 10^{-8} cm^3STP/g. The $^{3}He/^{4}He$ ratios ranged from 0.641 to 1.132 Ra, with an average value of 0.901 Ra (Table 2). In the evolution diagram for the ^{3}He-^{4}He isotopes, the Helium and Argon isotopic values are projected in the crust and mantle transition field (Figure 8). In the diagram of Rc/Ra-$^{40}Ar/^{36}Ar$, the Helium and Argon isotopic values are also projected in the crust and mantle transition field which is near the meteoric water (Figure 9). The results show that the ore-forming fluids represent a mixture of crust and mantle fluids, and litter meteoric water.

4.3 Lead isotopes

The lead isotope ratios for seven pyrites were measured and the results are presented in Table 3. The values for $^{206}Pb/^{204}Pb$, $^{207}Pb/^{204}Pb$, and $^{208}Pb/^{204}Pb$ ranged from 16.615 to 16.832, 15.275 to 15.403, and 36.829 to 37.470, respectively. All the lead isotope values plotted in the field correspond to a lower crustal origin as per the diagram of lead isotope tectonic environments created by Zartman and Doe (1981) (Figure 10).

LC, lower crust; UC, upper crust; OIV, ocean island volcanic; OR, orogenic belts.

The region of Pb isotopes for the Jiaodong sulfide or ore is determined by Liu. Z. K et al., 2021.

4.4 Calcite Sm-Nd age

The Sm-Nd isotopic dating for eight calcites were measured and the results are shown in Table 4.

The mass fractions for Sm and Nd of calcites ranged from 1.23 to 4.73 × 10^{-6} and 5.90 to 17.18 × 10^{-6} with $^{147}Sm/^{144}Nd$ and $^{143}Nd/^{144}Nd$ values ranging from 0.1045 to 0.1664 and 0.511135 to 0.511185, respectively. The $^{147}Sm/^{144}Nd$ and $^{143}Nd/^{144}Nd$ values for calcites exhibited a good linear relationship. An isochronous age of 123.5 ± 8.1 Ma (MSWD = 0.042) and an initial $^{143}Nd/^{144}Nd$ value of 0.5110504 for calcites were obtained (Figure 11). It represents that the Yangjiakuang gold mineralization is the early period of Early Cretaceous.

TABLE 1 LA-MC-ICP-MS *in situ* S isotopic compositions of different hydrothermal stages of pyrites from the Yangjiakuang gold deposit.

Stage	Sample serial number	Mineral	$\delta^{34}S_{CDT}$ (‰)	Source
Stage Ⅰ	SD74B0-1	Pyrite	8.7	This study
	SD74B0-2	Pyrite	9.6	
	SD74B0-3	Pyrite	9.6	
	SD74B0-1	Pyrite	8.5	
	SD74B0-2	Pyrite	9.1	
	SD74B0-3	Pyrite	9.3	
Stage Ⅱ	SD74B1-1	Pyrite	8.6	This study
	SD74B1-2	Pyrite	8.9	
	SD74B1-3	Pyrite	7.1	
	SD74B1-4	Pyrite	5.6	
	SD74B3-1	Pyrite	7.1	
	SD74B3-2	Pyrite	7.8	
	SD74B4-1	Pyrite	7.3	
	SD74B4-2	Pyrite	8.3	
	SD74B4-3	Pyrite	6.5	
	SD74B5-1	Pyrite	8.2	
	SD74B5-2	Pyrite	7.1	
	SD74B5-3	Pyrite	8.5	

TABLE 2 He and Ar isotopic compositions of fluid inclusions in pyrites from the Yangjiakuang gold deposit.

Sample No.	$^{40}Ar/^{36}Ar$	Standard Error	$^{36}Ar/^{38}Ar$	Standard Error	$^{3}He/^{4}He$ (10^{-7})	Standard Error	Content (cm^3STP/g)		
							^{40}Ar (10^{-8})	^{4}He (10^{-8})	^{3}He (10^{-13})
SD74B 1-1	637.5	0.93	5.31	0.04	6.41	0.45	53.71	78.63	5.052
SD74B 1-2	1162.7	1.39	5.29	0.01	7.32	0.89	49.52	60.12	4.411
SD74B 3-1	960.8	1.25	5.36	0.03	11.01	1.07	21.11	45.43	5.016
SD74B4-1	981.5	3.78	5.33	0.05	11.32	1.28	47.59	31.61	3.587

Notes: Rc is the.^{3}He/4He value of samples, Ra is the· ^{3}He/^{4}He of the atmosphere (1.40×10^{-6}). The He isotopes were measured at the Mineral Resources Research Institute, Chinese Academy of Geological Sciences.

TABLE 3 Lead isotopic compositions of pyrites from the Yangjiakuang gold deposit.

Sample No.	Mineral	$^{206}Pb/^{204}Pb$	$^{207}Pb/^{204}Pb$	$^{208}Pb/^{204}Pb$	References
SD74B1-1	Pyrite	16.832	15.403	37.470	This study
SD74B1-2	Pyrite	16.803	15.401	37.352	
SD74B3-1	Pyrite	16.795	15.383	37.298	
SD74B3-3	Pyrite	16.812	15.379	37.295	
SD74B4-2	Pyrite	16.814	15.386	37.320	
SD74B4-3	Pyrite	16.615	15.275	36.829	
SD74B5-1	Pyrite	16.715	15.312	37.128	

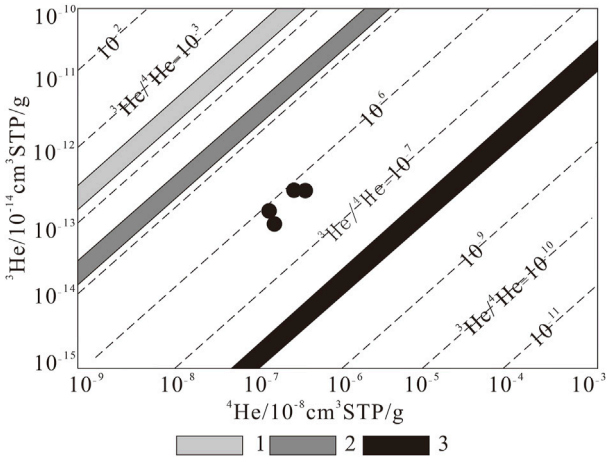


FIGURE 8
Helium isotopic compositions of fluid inclusions in pyrites from the Yangjiakuang gold deposit (after Mamyrin & Tolstikhin, 1984). 1. Initial argon; 2. Mantle argon; 3. Crustal argon.

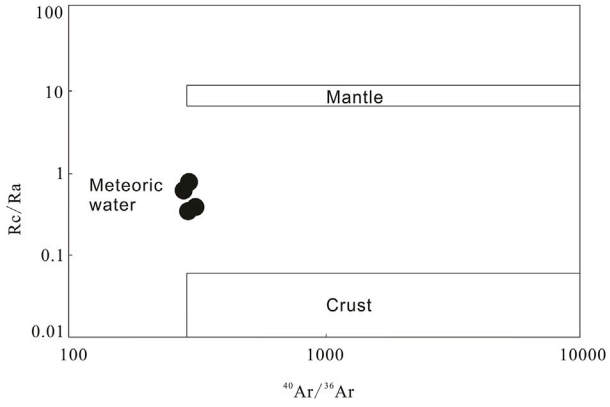


FIGURE 9
Plot of Rc/Ra–^{40}Ar/^{36}Ar ratios of fluid inclusions in pyrites from the Yangjiakuang gold deposit.

4.5 Zircon U-Pb dating

Zircons from the quartz diorite porphyrite dyke (SD74B2) in the Yangjiakuang gold deposit were mostly short columns, with high transparency, euhedral or subhedral, about 60 μm–90 μm in length. The zircons had a typical magmatic concussion zone. Representative CL images are shown in Figure 6. The U content for the zircons ranged from 289 × 10^{-6} ~ 1603 × 10^{-5} and the Th content was from 36 × 10^{-7} ~ 579 × 10^{-6}. The Th/U ratios ranged from 0.12 to 0.73 and the average value was 0.26 (Table 5; Figure 12). The results for the ages of 24 analysis points were relatively concentrated and they could be classified into three groups. The first group was the magmatic zircon age consisting of 21 analysis results. This age was concentrated on the consistent curve on the harmonic map of Figure 11. The range for the ^{206}Pb/^{238}U age was 126–121 Ma, and the weighted average age was 122.75 ± 0.66 Ma (MSWD = 1.5) (Figure 12), which represents the emplacement age of the quartz diorite porphyrite dyke. The second group was the inherited zircon age, which consisted of three analysis results. The ^{206}Pb/^{238}U ages for sample No. 3 and sample No. 8 were 2472 Ma and 2490 Ma, respectively. It is speculated that these ages represent the inherited zircon ages of ancient gneiss in the Jiaodong area. The third group has only one inherited zircon age (sample No. 24), the apparent age being 151 Ma, which may reflect the inherited zircon age of Linglong granite.

5 Discussion

5.1 Mineralization age

Based on various isotopic dating methods (e.g., hydrothermal zircon U-Pb dating, hydrothermal monazite U-Pb dating, mineralization related muscovite Ar-Ar dating), decades of geochronological research on large-scale gold mineralization in the Jiaodong Peninsula indicate an episode of gold mineralization was 130–120 Ma (Luo and Miao, 2002; Zhai et al., 2004; Chen et al., 2005; Fan et al., 2005; Li et al., 2005; Li et al., 2008; Yang et al., 2014b; Zhu et al., 2015; Li and Santosh, 2017; Deng et al., 2020b, 2020c; Zhang. H. Y et al., 2020). Li et al. (2020) proposed that there were two large-scale gold mineralization events, including the early period of Early Cretaceous (126–120 Ma), which formed the Laizhou-Zhaoyuan and Qixia-Penglai-Fushan Gold Belts in the north-west of Jiaodong terrane, and the late period of Early Cretaceous (110–104 Ma), forming the Muping-Rushan Gold Belt in the north-east of the Jiaodong terrane (Li et al., 2020).

Recent studies have shown that strong fractionation between rare Earth elements can occur during the formation of hydrothermal deposits, leading to large changes in Sm and Nd contents in some hydrothermal minerals, reaching values far higher than the normal values of crustal rocks. This discovery lays a foundation for the application of Sm-Nd isotopes in metallogenic chronology (Zhao & Jiang, 2004). Calcium-bearing minerals are always rich in rare Earth elements, making fluorite, calcite, and other calcium-bearing minerals to be the ideal targets for Sm-Nd isotopic dating of hydrothermal deposits (Bell et al., 1989; Jiang et al., 2000; Brugger et al., 2002; Li et al., 2006; Jahn et al., 2008; Peng et al., 2008; Li et al., 2020). The calcite is the main mineral formed during the metallizing stage in the Yangjiakuang and Tudui gold deposits, and contains natural gold in the calcite quartz veinlets (Ding et al., 2015; Zhang, 2018). Therefore, the calcite can represent the age of main gold mineralization. This paper yields calcite Sm-Nd isochron age as 123.5 ± 8.1 Ma, which represents the main gold metallogenic stage (II) at Yangjiakuang gold deposit.

LA-ICP-MS zircon U-Pb dating for quartz diorite porphyrite dyke is 122.75 ± 0.66 Ma, which represents the post-mineralization age. In summary, the mineralization of Yangjiakuang gold deposit is the early period of Early Cretaceous, and it is consistent with the first large-scale gold mineralization in Jiaodong Peninsula.

5.2 Source of the ore-forming materials and fluids

The δ^{34}S values of sulfides from the Yangjiakuang gold deposit vary from 5.65 to 9.63‰, with an average value of 8.14‰. This narrow range of sulfur isotope compositions suggests that the physicochemical

TABLE 4 Sm-Nd isotopic compositions of calcites from the Yangjiakuang gold deposit.

Sample No.	Sm (× 10^{-6})	Nd (× 10^{-6})	$^{147}Sm/^{144}Nd$	$^{143}Nd/^{144}Nd$	2σ
SD74B1-1	3.42	12.70	0.1628	0.511182	0.0009
SD74B1-2	2.56	10.63	0.1456	0.511168	0.0006
SD74B1-3	2.57	11.71	0.1326	0.511157	0.0005
SD74B1-4	1.72	9.97	0.1045	0.511135	0.0007
SD74B1-5	1.23	5.90	0.1264	0.511153	0.001
SD74B1-6	4.73	17.18	0.1664	0.511185	0.0005
SD74B1-7	2.52	13.76	0.1107	0.511140	0.0006
SD74B1-8	3.08	12.18	0.1529	0.511174	0.0009

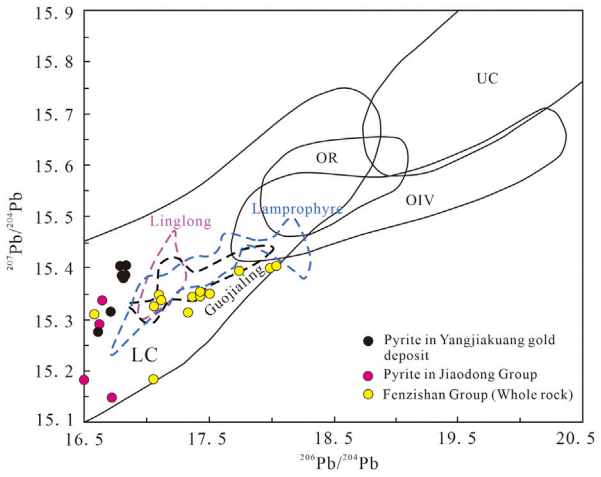


FIGURE 10
$^{206}Pb/^{204}Pb$–$^{207}Pb/^{204}Pb$ diagram of the Yangjiakuang gold deposit (after Zartman & Doe, 1981).

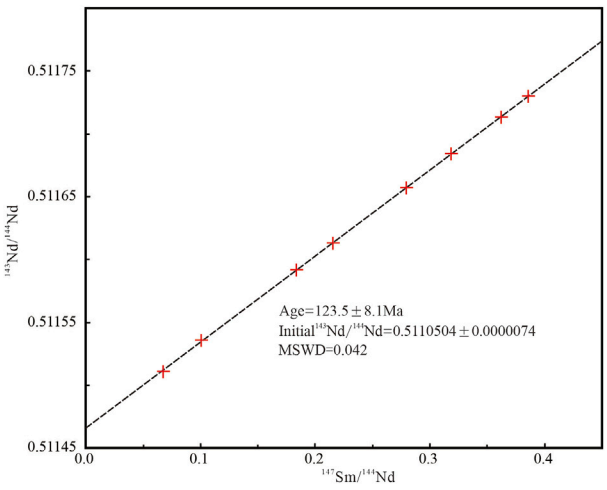


FIGURE 11
Diagram of calcite Sm-Nd isochronous age for the Yangjiakuang gold deposit.

parameters of the mineralizing fluids were relatively constant (Saravanan and Mishra, 2009; Li et al., 2012). In addition, the sulfide assemblage is simple and dominated by pyrite, and thus the $\delta^{34}S$ values of pyrite can be used for tracing the source of ore fluids (Kajiwara and Krouse, 1971; Ohmoto, 1972).

The values of the sulfur isotopes observed are clearly larger than those of magmatic-derived sulfur. Combined with the geologic constraints, at least five sources might account for such sulfur signatures: Precambrian basement, Paleoproterozoic Fenzishan Group, Mesozoic granitoid intrusions, mafic dykes, or multiple sources. Previous studies reported that the sulfur isotopic values of the Fenzishan Group, the Jiaodong Group, the Jurassic-Cretaceous granites, and the Cretaceous dykes were 5.6–12.0‰, 0.0–10.8‰, 2.0–9.9‰, and -3.4–9.9‰, respectively (Figure 7) (Yang et al., 2005; Li et al., 2015; Guo et al., 2017; Deng et al., 2020a). However, the metamorphic devolatization of the Precambrian basement cannot provide sulfur and mineralizing fluids directly, although the Fenzishan Group has similar $\delta^{34}S$ values to the sulfide ores studied (Tan et al., 2015). The apparent time gap (20–40 Ma) between the gold mineralization and the Jurassic granitoids (Linglong granite) (160–150 Ma, Yang et al., 2012; Ma et al., 2013; Li et al., 2019) precludes a hydrothermal link between these two. In addition, the Cretaceous intermediate dyke (118–108 Ma, Qiu et al., 2008; Ding et al., 2013; Zhao et al., 2018; Li et al., 2019; Song et al., 2020), also cannot provide the source of ore-forming sulfur, because of its formation later than that of gold mineralization. The potential candidate for the source of sulfur may be represented by Guojialing granite that intruded intensively in this district. Integrating the values with the aforementioned $\delta^{34}S$ values of the Fenzishan Group, we suggest that there were multi-sources for the sulfur in the ore system *via* magmatic-derived fluids leaching from the Fenzishan Group.

The noble gases have distinct isotopic compositions in the different reservoirs, and the magnitude of the isotopic ratio values can signify the presence of crust and mantle components during the ore-forming processes (Kendrick and Burnard, 2013). Therefore, noble gases can be used as an ideal tracer for the crust and mantle contributions to ore-forming fluids (Turner et al., 1993; Stuart et al., 1995). The $^{3}He/^{4}He$ ratios for the fluid inclusions in pyrite ranged from 0.64 to 1.13 Ra with an average value of 0.90 Ra (Table 2), which is 1–2 orders of magnitude higher than the crustal values (0.01–0.05 Ra, Burnard et al., 1999) but lower than the mantle

TABLE 5 LA-ICP-MS zircon U-Pb data for the quartz diorite porphyrite dyke.

Sample No.	Content (ppm)			Isotopic ratio						Age (Ma)					
	Pb	U	Th/U	$^{206}Pb/^{238}U$	1σ	$^{207}Pb/^{235}U$	1σ	$^{207}Pb/^{206}Pb$	1σ	$^{206}Pb/^{238}U$	1σ	$^{207}Pb/^{235}U$	1σ	$^{207}Pb/^{206}Pb$	1σ
SD74B2-1	12	612	0.31	0.0195	0.0002	0.0485	0.0014	0.0485	0.0014	122	1	122	4	123	68
SD74B2-2	11	562	0.22	0.0199	0.0002	0.0491	0.0016	0.0491	0.0016	125	1	126	4	150	77
SD74B2-3	165	319	0.32	0.4677	0.0048	0.1705	0.0019	0.1705	0.0019	2472	26	2521	33	2560	19
SD74B2-4	16	833	0.24	0.0197	0.0002	0.0485	0.0010	0.0485	0.0010	124	1	124	3	123	48
SD74B2-5	18	983	0.19	0.0191	0.0002	0.0493	0.0018	0.0493	0.0018	120	1	122	5	161	85
SD74B2-6	21	1099	0.28	0.0192	0.0002	0.0505	0.0011	0.0505	0.0011	120	1	125	3	215	53
SD74B2-7	5	289	0.12	0.0199	0.0002	0.0476	0.0026	0.0476	0.0026	125	1	123	7	76	130
SD74B2-8	13	25	0.5	0.4720	0.0107	0.1665	0.0026	0.1665	0.0026	2490	56	2507	69	2521	26
SD74B2-9	20	1072	0.25	0.0192	0.0002	0.0496	0.0010	0.0496	0.0010	121	1	123	3	173	46
SD74B2-10	11	582	0.27	0.0195	0.0002	0.0493	0.0012	0.0493	0.0012	122	1	124	3	160	58
SD74B2-11	18	955	0.17	0.0194	0.0002	0.0495	0.0011	0.0495	0.0011	122	1	124	3	170	52
SD74B2-12	19	1031	0.21	0.0194	0.0002	0.0499	0.0010	0.0499	0.0010	122	1	125	3	190	45
SD74B2-13	14	727	0.21	0.0196	0.0002	0.0489	0.0012	0.0489	0.0012	123	1	124	3	142	57
SD74B2-14	16	829	0.23	0.0198	0.0002	0.0472	0.0010	0.0472	0.0010	124	1	121	3	57	52
SD74B2-15	31	1603	0.25	0.0198	0.0002	0.0481	0.0007	0.0481	0.0007	124	1	123	2	102	35
SD74B2-16	8	417	0.23	0.0197	0.0002	0.0492	0.0021	0.0492	0.0021	124	1	126	6	157	101
SD74B2-17	8	404	0.21	0.0198	0.0002	0.0478	0.0016	0.0478	0.0016	124	1	123	4	90	77
SD74B2-18	21	1119	0.23	0.0193	0.0002	0.0496	0.0009	0.0496	0.0009	121	1	124	2	173	41
SD74B2-19	22	1158	0.21	0.0196	0.0002	0.0486	0.0009	0.0486	0.0009	125	1	123	3	126	45
SD74B2-20	13	689	0.15	0.0199	0.0002	0.0483	0.0013	0.0483	0.0013	125	1	125	4	113	66
SD74B2-21	13	669	0.19	0.0197	0.0002	0.0497	0.0014	0.0497	0.0014	123	1	126	4	1820	67
SD74B2-22	17	930	0.15	0.0198	0.0002	0.0471	0.0009	0.0471	0.0009	124	1	121	3	51	48
SD74B2-23	18	795	0.73	0.0196	0.0002	0.0500	0.0010	0.0500	0.0010	123	1	126	3	192	47
SD74B2-24	10	410	0.29	0.0240	0.0003	0.0493	0.0016	0.0493	0.0016	151	2	151	5	159	76

10.3389/feart.2023.1048509

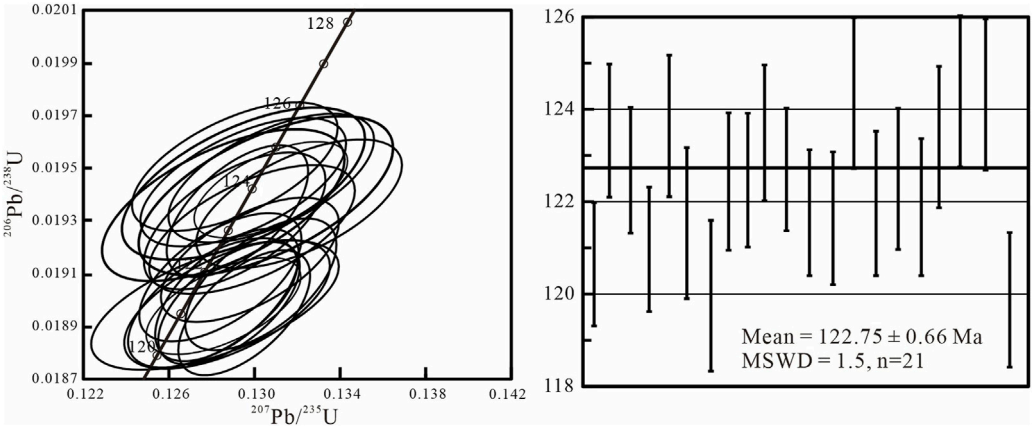


FIGURE 12
Zircon U-Pb Concordia diagram for the quartz diorite porphyrite dyke (SD74B2).

values (6–9 Ra, Stuart et al., 1995), revealing a mixing between the crustal and mantle-derived components in the ore-forming fluids. In the ^{4}He vs. ^{3}He plot, the ^{3}He and ^{4}He isotopic compositions are between the mantle Helium line and the crustal Helium line (Figure 8). In the R/Ra vs. $^{40}Ar/^{36}Ar$ plot (Figure 9), the He and Ar isotopic compositions spread between the mantle field and the crustal field. All these He-Ar isotopic signatures suggest that the ore-forming fluid at Yangjiakuang gold deposit can be regard as a combination of crustal and mantle components.

Lead isotope is a useful indicator for the source of ore-forming materials. The Pb isotopic compositions of pyrites were characterized by a crust-mantle mixing. In the $^{207}Pb/^{204}Pb$ vs. $^{206}Pb/^{204}Pb$ diagram, the pyrites yield a similar lead isotopic compositions and plot in the compositions area of the upper crust (Figure 10). In light of the overlapping field in the Pb isotope diagram (Figure 10), the metamorphic basement of the Jiaodong and Fenzishan Groups, as a member of the lower crust, is suggested as the most likely source of Pb. There is the possibility that the mineralizing fluids selectively leached Pb from the Jiaodong and Fenzishan Groups.

5.3 Geodynamic significance

The age of Yangjiakuang gold mineralization is the early period of Early Cretaceous, which is consistent with the first large-scale gold mineralization in Jiaodong terrane. As it discussed above, the potential candidate for the source of ore-forming materials and fluids may be represented by the Guojialing granites. The S-He-Ar-Pb isotopes suggest that the ore-forming materials of the Yangjiakuang gold deposit may originate from a mixture of crustal and mantle components. The deep crust-mantle derived magma (Guojialing granite) maybe provide the heat sources in the extensional regime for melt and fluid circulation, and then the ore fluid can be separated during the ascent into the upper crust and leached the ore-forming materials from the Fenzishan Group, the Jiaodong Group and the Guojialing granite.

This metallogenic event is widely developed in the Jiaodong gold province. It is suggested that the extensional tectonic inversion event triggering gold mineralization was related to the rollback of the subducting Izanagi plate. Most researchers agree that the Izanagi Plate was subducted beneath northeastern China at ca. 170 Ma (Isozaki, 1997; Maruyama et al., 1997; Zhu et al., 2018). The initial subduction of the plate was rapid and low angle, generating compressive stress in eastern China (Zhang and Zhang., 2007). This low angle subduction meant that the Izanagi Plate was located below northeastern China, thickening and compressing the already thickened orogenic crust formed by earlier continental collisional events, which caused partial melting of the lower crust and lithospheric delamination (Dang et al., 2022). The loss of the lithospheric keel caused the asthenospheric upwelling, lithospheric extension and thinning in the Early Cretaceous. This was associated with the steepening of the angle and the associated rollback of the subducting Izanagi Plate. In an extensional regime, eastern NCC witnessed craton destruction or decratonization (Wu et al., 2005; Yang and Li, 2008; Zhu et al., 2015), regional tectonic inversion and strong crust-mantle interaction (Menzies and Xiu., 1998; Cai et al., 2013), which led to partial melting and dehydration of the lithospheric mantle and the lower crust as the temperature increased (Yang et al., 2003; Tan et al., 2015; Wen et al., 2015; Guo et al., 2020), and form a large-scale high heat flow, extensive crust-mantle mixture magmas. The magma migrated upward to the upper crust, subsequent magma mixing and the exsolved fluids extracted the ore-forming elements from the enclosing rocks to form the ore-forming fluids.

6 Conclusion

(1) The calcites which represent the main gold metallogenic stage (II) yielded a Sm-Nd isochron age of 123.5 ± 8.1 Ma (MSWD = 0.042). Subsequent geologic events were recorded by quartz diorite porphyrite dyke which are dated at 122.75 ± 0.66 Ma (MSWD = 1.5) by zircon LA-ICP-MS U-Pb dating. It is suggested that the Yangjiakuang gold mineralization took place in the early period of Early Cretaceous, which coincided with the first large-scale gold mineralization in the Jiaodong Peninsula.
(2) The S-Pb-He-Ar isotope compositions of pyrites in the Yangjiakuang gold deposit suggest that the ore-forming

materials and fluids are characterized by a mixture of crustal and mantle components.
(3) The gold mineralization is associated with extensional tectonic inversion caused by the rollback of the subducting Izanagi Plate during the early Cretaceous.

Data availability statement

The datasets presented in this study can be found in online repositories. The names of the repository/repositories and accession number(s) can be found in the article/Supplementary Material.

Author contributions

J-JL is the first corresponding author of this article, responsible for comprehensive technical guidance in the research process, comprehensively analyzed the test data and wrote the first draft of the article; Z-CD is the second corresponding author of this article. He participated in field investigation and sample collection, conducted surfer and lead isotope analysis and testing, and participated in the reviewing and finalizing the paper. CF carried out zircon U-Pb dating and participated in the revision of the manuscript. P-PZ, J-PT, and J-TH participated in sample collection and microscopic observation, data processing and isotope dating, and the revision of the manuscript. All authors contributed to the manuscript revision, read, and approved the submitted version.

Funding

The National Key Research and Development Program of China (Grant 2016YFC0600107) and projects from the China Geological Survey (Grants DD20190379-31, DD20221695-30 and 200110200038) support the financial of this work.

Acknowledgments

We thank the National Key Research and Development Program of China (Grant 2016YFC0600107) and projects from the China Geological Survey (Grants DD20190379-31, DD20221695-30 and 200110200038) for financial support for this work. The State Key Laboratory of Geological Processes and Mineral Resources [China University of Geosciences (Wuhan)], and the Beijing Institute of Geological Research of Nuclear Industry and Tianjin Center of China Geological Survey are thanked for supporting the laboratory analyses. We are grateful to Prof. Li Xiu-Zhang, Zhang Pi-Jian and Liao Xiao-Ming for field assistance and to Prof. Zhou Hong-Ying, Geng Jian-Zhen and Liu Wen-Gang for help with Sm-Nd and U-Pb isotopic dating.

Conflict of interest

The authors declare that the research was conducted in the absence of any commercial or financial relationships that could be construed as a potential conflict of interest.

Publisher's note

All claims expressed in this article are solely those of the authors and do not necessarily represent those of their affiliated organizations, or those of the publisher, the editors and the reviewers. Any product that may be evaluated in this article, or claim that may be made by its manufacturer, is not guaranteed or endorsed by the publisher.

References

An, Y. (1990). A new division of the metamorphosed strata in the Jiaodong region and account on the newly delimited Jiaodong Group and Jingshan Group. *Shandong Geol.* 6, 97–103.

Andersen, T. (2002). Correction of common lead in U-Pb analyses that do not report ^{204}Pb. *Chem. Geol.* 1-2 (192), 59–79. doi:10.1016/s0009-2541(02)00195-x

Bell, K., Anglin, C. D., and Franklin, J. M. (1989). Sm-Nd and Rb-Sr isotope systematics of scheelites: Possible implications for the age and Genesis of vein-hosted gold deposits. *Geology* 17, 500–504. doi:10.1130/0091-7613(1989)017<0500:snarsi>2.3.co;2

Bendall, C., Lahaye, Y., Fiebig, J., Weyer, S., and Brey, G. P. (2006). *In situ* sulfur isotope analysis by laser ablation MC-ICPMS. *Appl. Geochem.* 21, 782–787. doi:10.1016/j.apgeochem.2006.02.012

Brugger, J., Maas, R., Lahaye, Y., McRae, C., Ghaderi, M., Costa, S., et al. (2002). Origins of Nd-Sr-Pb isotopic variations in single scheelite grains from Archaean gold deposits, Western Australia. *Chem. Geol.* 182, 203–225. doi:10.1016/s0009-2541(01)00290-x

Burnard, P. G., Hu, R. Z., Turner, G., and Bi, X. W. (1999). Mantle, crustal and atmospheric noble gases in Ailaoshan Gold deposits, Yunnan Province, China. *Geochim. Cosmochim. Acta* 63, 1595–1604. doi:10.1016/s0016-7037(99)00108-8

Cai, Y. C., Fan, H. R., Santosh, M., Liu, X., Hu, F. F., Yang, K. F., et al. (2013). Evolution of the lithospheric mantle beneath the southeastern North China craton: Constraints from mafic dikes in the Jiaobei terrain. *Gondwana Res.* 24, 601–621. doi:10.1016/j.gr.2012.11.013

Chen, J. F., Xie, Z., Li, H. M., Zhang, X. D., Zhou, T. X., Park, Y. S., et al. (2003). U-Pb zircon ages for a collision-related K-rich complex at Shidao in the Sulu ultrahigh pressure terrane, China. *Geochem. J.* 37, 35–46. doi:10.2343/geochemj.37.35

Chen, Y. J., Pirajno, F., and Qi, J. P. (2005). Origin of gold metallogeny and sources of ore-forming fluids, Jiaodong province, eastern China. *Ore Geol. Rev.* 47 (5), 530–549. doi:10.2747/0020-6814.47.5.530

Craddock, P. R., Rouxel, O. J., Ball, L. A., and Bach, W. (2008). Sulfur isotope measurement of sulfate and sulfide by high-resolution MC-ICP-MS. *Chem. Geol.* 253, 102–113. doi:10.1016/j.chemgeo.2008.04.017

Dang, Z. C., Li, J. J., Tian, J. P., He, J. T., Sun, Z. B., Tang, W. L., et al. (2022). Petrogenesis and geodynamic setting of the Late Jurassic Queshan adakitic granite, Jiaodong Peninsula, southeastern North China Craton: Zircon U-Pb geochronological, geochemical, and Lu-Hf isotopic evidence. *Geol. J.* 57 (5), 1891–1911. doi:10.1002/gj.4386

Deng, J., Liu, X. F., Wang, Q. F., and Pan, R. G. (2015). Origin of the jiaodong-type xinli gold deposit, Jiaodong Peninsula, China: Constraints from fluid inclusion and C-D-O-S-Sr isotope compositions. *Ore Geol. Rev.* 65, 674–686. doi:10.1016/j.oregeorev.2014.04.018

Deng, J., Qiu, K. F., Wang, Q. F., Goldfarb, R. J., Yang, L. Q., Zi, J. W., et al. (2020b). *In-situ* dating of hydrothermal monazite and implications on the geodynamic controls of ore formation in the Jiaodong gold province, eastern China. *Econ. Geol.* 115, 671–685. doi:10.5382/econgeo.4711

Deng, J., Wang, C. M., Bagas, L., Santosh, M., and Yao, E. Y. (2018). Crustal architecture and metallogenesis in the south-eastern North China Craton. *Earth-Science Rev.* 182, 251–272. doi:10.1016/j.earscirev.2018.05.001

Deng, J., Wang, Q. F., Santosh, M., Liu, X. F., Liang, Y. Y., Yang, L. Q., et al. (2020a). Remobilization of metasomatized mantle lithosphere: A new model for the Jiaodong gold province, eastern China. *Miner. Deposita* 55, 257–274. doi:10.1007/s00126-019-00925-0

Deng, J., Wang, Q. F., Wan, L., Liu, H., Yang, L. Q., and Zhang, J. (2011). A multifractal analysis of mineralization characteristics of the Dayingezhuang disseminated veinlet gold deposit in the Jiaodong gold province of China. *Ore Geol. Rev.* 40, 54–64. doi:10.1016/j.oregeorev.2011.05.001

Deng, J., Yang, L. Q., Ge, L. S., Wang, Q. F., Zhang, J., Gao, B. F., et al. (2006). Research advances in the Mesozoic tectonic regimes during the forming of Jiaodong ore cluster area. *Propress Nat. Sci.* 16 (8), 777–784. doi:10.1080/10020070612330069

Deng, J., Yang, L. Q., Groves, D. I., Zhang, L., Qiu, K. F., and Wang, Q. F. (2020c). An integrated mineral system model for the gold deposits of the giant Jiaodong province, eastern China. *Earth-Sciences Rev.* 208, 103274. doi:10.1016/j.earscirev.2020.103274

Ding, Z. J. (2014). *Study on metallogenic regularity of mesozoic precious and non-ferrous deposits in Jiaodong Peninsula: [Doctoral dissertation]*. Changchun: Jilin University.

Ding, Z. J., Sun, F. Y., Liu, F. L., Liu, J. H., Liu, D. H., Zhang, P. J., et al. (2013). U-Pb dating of zircons from the Weideshan molybdenum copper polymetallic deposits in Jiaodong Peninsula, China, and its geological significance. *Acta Petrol. Sin.* 29 (2), 607–618. doi:10.3724/SP.J.1008.2010.00937

Ding, Z. J., Sun, F. Y., Liu, F. L., Liu, J. H., Peng, Q. M., Ji, P., et al. (2015). Mesozoic geodynamic evolution and metallogenic series of major metal deposits in Jiaodong Peninsula. *Acta Petrol. Sin.* 31 (10), 3045–3080.

Fan, H. R., Hu, F. F., Yang, J. H., Shen, K., and Zhai, M. G. (2005). Fluid evolution and large-scale gold metallogeny during Mesozoic tectonic transition in the eastern Shandong province. *Acta Petrol. Sin.* 21 (5), 1317–1328.

Faure, M., Lin, W., Moni´ e, P., Le Breton, N., Poussineau, S., Panis, D., et al. (2003). Exhumation tectonics of the ultrahigh-pressure metamorphic rocks in the qinling orogen in east China: New petrological–structural–radiometric insights from the shandong Peninsula. *Tectonics* 22, 1018. doi:10.1029/2002tc001450

Guo, J. H., Chen, F. K., Zhang, X. M., Siebel, W., and Zhai, M. G. (2005). Evolution of syn-to post collisional magmatism from north Sulu UHP belt, eastern China: Zircon U-Pb geochronology. *Acta Petrol. Sin.* 21 (4), 1281–1301. doi:10.3321/j.issn:1000-0569.2005.04.025

Guo, L. N., Deng, J., Yang, L. Q., Wang, Z. L., Wang, S. R., Wei, Y. J., et al. (2020). Gold deposition and resource potential of the Linglong gold deposit, Jiaodong Peninsula: Geochemical comparison of ore fluids. *Ore Geol. Rev.* 120, 103434. doi:10.1016/j.oregeorev.2020.103434

Guo, L. N., Goldfarb, R. J., Wang, Z. L., Li, R. H., Chen, B. H., and Li, J. L. (2017). A comparison of Jiaojia- and Linglong-type gold deposit ore-forming fluids: Do they differ? *Ore Geol. Rev.* 88, 511–533. doi:10.1016/j.oregeorev.2016.12.003

Guo, P., Santosh, M., and Li, S. R. (2013). Geodynamics of gold metallogeny in the shandong province, NE China: An integrated geological, geophysical and geochemical perspective. *Gondwana Res.* 24 (3-4), 1172–1202. doi:10.1016/j.gr.2013.02.004

Hao, G. J., Wang, H. C., Niu, G. H., Kang, J. L., and Hao, S. (2020). Metamorphic geotectonic research and scientific in China. *Geol. Surv. Res.* 43 (2), 89–96.

Isozaki, Y. (1997). Permo-Triassic boundary superanoxia and stratified superocean: Records from lost deep sea. *Science* 276 (5310), 235–238. doi:10.1126/science.276.5310.235

Jackson, S. E., Pearson, N. J., Griffin, W. L., and Belousova, E. A. (2004). The application of laser ablation-inductively coupled plasma-mass spectrometry to *in situ* U-Pb zircon geochronology. *Chem. Geol.* 211 (1-2), 47–69. doi:10.1016/j.chemgeo.2004.06.017

Jahn, B. M., Liu, D. Y., Wan, Y. S., Song, B., and Wu, J. S. (2008). Archean crustal evolution of the Jiaodong Peninsula, China, as revealed by zircon SHRIMP geochronology, elemental and Nd-isotope geochemistry. *Am. J. Sci.* 308, 232–269. doi:10.2475/03.2008.03

Jiang, S. Y., Slack, J. F., and Palmer, M. R. (2000). Sm-Nd dating of the giant Sullivan Pb-Zn-Ag deposit, British Columbia. *Geology* 28, 751–754. doi:10.1130/0091-7613(2000)028<0751:sndotg>2.3.co;2

Kajiwara, Y., and Krouse, H. R. (1971). Sulfur isotope partitioning in metallic sulfide systems. *Can. J. Earth Sci.* 8, 1397–1408. doi:10.1139/e71-129

Kendrick, M. A., and Burnard, P. (2013). "Noble gases and halogens in fluid inclusions: A journey through the earth's crust," in *The noble gases as geochemical tracers* (Germany: Springer).

Li, G. H., Ding, Z. J., Song, M. C., Li, J. J., Li, X. Z., Ji, P., et al. (2017). The liaoshang pyrite–carbonate veined deposit: A new type of gold deposit in Jiaodong Peninsula. *Acta Geosci. Sin.* 38 (3), 423–429. doi:10.3975/cagsb.2017.03.12

Li, H. K., Geng, J. Z., Hao, S., Zhang, Y. Q., and Li, H. M. (2009). Study on the age of zircon U-Pb isotopes by laser ablation multi-receiver plasma mass spectrometer (LA-MC-ICPMS). *Acta Mineral. Sin.* 29 (S1), 600–601. doi:10.16461/j.cnki.1000-4734.2009.s1.014

Li, H., Sun, H. S., Evans, N. J., Li, J. W., Wu, J. H., Jiang, W. C., et al. (2019). Geochemistry and geochronology of zircons from granite-hosted gold mineralization in the Jiaodong Peninsula, North China: Implications for ore Genesis. *Ore Geol. Rev.* 115, 103188–103215. doi:10.1016/j.oregeorev.2019.103188

Li, J. J., Luo, Z. K., Liu, X. Y., Xu, W. D., and Luo, H. (2005). Geodynamic setting for formation of large-superlarge gold deposits and Mesozoic granites in Jiaodong area. *Mineral. Deposits* 24 (4), 361–372.

Li, J. J., Peng, Y., Zhang, T., Song, L. J., Ni, Z. P., Zhou, J. H., et al. (2021). Division of metallogenic units in North China. *North China Geol.* 44 (3), 4–24. doi:10.19948/j.12-1471/P.2021.03.02

Li, J. J., Zhang, P. P., Li, G. H., Liu, W. G., Zhao, Z. L., Li, X. Z., et al. (2020). Formation of the Liaoshang gold deposit, Jiaodong Peninsula, eastern China: Evidence from geochronology and geochemistry. *Geol. J.* 55 (8), 5903–5913. doi:10.1002/gj.3718

Li, J. W., Li, Z. K., Zhou, M. F., Chen, L., Bi, S. J., Deng, X. D., et al. (2012). The EarlyCretaceousYangzhaiyu lode gold deposit, north China craton: A link between craton reactivation and gold veining. *Econ. Geol.* 107, 43–79. doi:10.2113/econgeo.107.1.43

Li, J. W., Vasconcelos, P., Zhou, M. F., Zhao, X. F., and Ma, C. Q. (2006). Geochronology of the Pengjiakuang and rushan gold deposits, eastern Jiaodong gold province, northeastern China: Implications for regional mineralization and geodynamic setting. *Econ. Geol.* 101, 1023–1038. doi:10.2113/gsecongeo.101.5.1023

Li, K., Chen, Y., She, Z., Tang, H., and Chen, W. (2018). Carbon isotope compositions and geochemical characteristics of the Zhangshe graphite deposit of the Jingshan Group. *Jiaobei. Earth Sci. Front.* 25, 19–33. doi:10.13745/j.esf.sf.2018.4.11

Li, Q. L., Chen, F. K., Yang, J. H., and Fan, H. R. (2008). Single grain pyrite Rb-Sr dating of the Linglong gold deposit, eastern China. *Ore Geol. Rev.* 34, 263–270. doi:10.1016/j.oregeorev.2007.10.003

Li, S. R., and Santosh, M. (2017). Geodynamics of heterogeneous gold mineralization in the North China Craton and its relationship to lithospheric destruction. *Gondwana Res.* 50, 267–292. doi:10.1016/j.gr.2017.05.007

Li, Y. J., Li, S. R., Santosh, M., Liu, S. A., Zhang, L., Li, W. T., et al. (2015). Zircon geochronology, geochemistry and stable isotopes of the wang'ershan gold deposit, Jiaodong Peninsula, China. *Asian Earth Sci.* 113, 695–710. doi:10.1016/j.jseaes.2015.03.036

Liu, S. J., Jahn, B. M., Wan, Y. S., Xie, H. Q., Wang, S. J., Xie, S. W., et al. (2015). Neoarchean to Paleoproterozoic high-pressure mafic granulite from the Jiaodong Terrain, North China Craton: Petrology, zircon age determination and geological implications. *Gondwana Res.* 28, 493–508. doi:10.1016/j.gr.2014.07.006

Liu, W. G., Li, G. Z., Liu, H., and Li, H. M. (2018). Micro-fluorite sample digestion technology and high precision thermionic mass spectrometry determination for Sm-Nd isotopes. *Acta Geosci. Sin.* 39 (1), 119–124. doi:10.3975/cagsb.2017.122701

Liu, W. G., Liu, H., Li, G. Z., Zhou, H. Y., Xiao, Z. B., and Li, H. M. (2017). The application of ion exchange resins in Sr-Nd isotopic assay geological samples. *Acta Geol. Sin.* 91 (11), 2584–2592.

Liu, X. Y., Tan, J., He, H. Y., and Gan, J. G. (2021). Origin of the Tudui–Shawang gold deposit, Jiaodong Peninsula, north China Craton: Constraints from fluid inclusion and H-O-He-Ar-S-Pb isotopic compositions. *Ore Geol. Rev.* 133, 104125. doi:10.1016/j.oregeorev.2021.104125

Liu, Y., Deng, J., Wang, Z. L., Zhang, L., Zhang, C., Liu, X. D., et al. (2014). Zircon U-Pb ages, Lu-Hf isotopes and petrogeochemistry of the monzogranites from Xincheng gold deposit, northwestern Jiaodong Peninsula, China. *Acta Petrol.* 30 (9), 2559–2573.

Liu, Y., Gao, S., Hu, Z. C., Gao, C., and Wang, D. (2010). Continental and oceanic crust recycling-induced melt-peridotite interactions in the trans-north China orogen: U-Pb dating, Hf isotopes and trace elements in zircons from mantle xenoliths. *J. Petrology* 51 (1-2), 537–571. doi:10.1093/petrology/egp082

Liu, Z. K., Hollings, P., Mao, X. C., Christopher, J. M., Yang, B., and Lei, T. (2021). Metal remobilization from country rocks into the Jiaodong-type orogenic gold systems, Eastern China: New constraints from scheelite and galena isotope results at the Xiadian and Majiayao gold deposits. *Ore Geol. Rev.* 134, 104126. doi:10.1016/j.oregeorev.2021.104126

Ludwig, K. R. (2003). "User's manual for isoplot/ex version 3.00: A geochronological toolkit for microsoft excel," in *Berkeley geochronology center special publication No.* (Berkeley CA: World Cat).

Luo, Z. K., and Miao, L. C. (2002). *Granite and gold deposits in Zhaolai area, Jiaodong region*. Beijing: Metallurgical Industy Press.

Ma, L., Jiang, S. Y., Dai, B. Z., Jiang, Y. H., Hou, M. L., Pu, W., et al. (2013). Multiple sources for the origin of Late Jurassic Linglong adakitic granite in the Shandong Peninsula, eastern China: Zircon U-Pb geochronological, geochemical and Sr-Nd-Hf isotopic evidence. *Lithos* 162-163, 251–263. doi:10.1016/j.lithos.2013.01.009

Mamyrin, B. A., and Tolstikhin, I. N. (1984). *Helium isotopes in nature*. Amsterdam: Elsevier.

Mao, J. W., Wang, Y. T., Li, H. M., Pirajno, F., Zhang, C. Q., and Wang, R. T. (2008). The relationship of mantle-derived fluids to gold metallogenesis in the Jiaodong Peninsula: Evidence from D-O-C-S isotope systematics. *Ore Geol. Rev.* 33, 361–381. doi:10.1016/j.oregeorev.2007.01.003

Maruyama, S., Isozaki, Y., Kimura, G., and Terabayashi, M. (1997). Paleogeographic maps of the Japanese islands: Plate tectonic synthesis from 750 Ma to the present. *Isl. Arc* 6 (1), 121–142. doi:10.1111/j.1440-1738.1997.tb00043.x

Menzies, M. A., and Xu, Y. G. (1998). "Geodynamics of the North China craton," in *Mantle dynamics and plate interactions in east asia* (United States: American Geophysical Union).

Ohmoto, H. (1972). Systematics of sulfur and carbon isotopes in hydrothermal ore deposits. *Econ. Geol.* 67, 551–578. doi:10.2113/gsecongeo.67.5.551

Peng, J. T., Zhang, D. L., Hu, R. Z., Wu, M. J., and Lin, Y. X. (2008). Sm-Nd and Sr isotope geochemistry of hydrothermal scheelite from the Zhazixi W-Sb deposit, Western Hunan. *Acta Geol. Sin.* 82 (11), 1514–1521.

Qiu, L. G., Ren, F. L., Cao, Z. X., and Zhang, Y. Q. (2008). Late Mesozoic magmatic activities and their constraints on geotectonics of Jiaodong region. *Geotect. Metallogenia* 32 (1), 117–123. doi:10.16539/j.ddgzyckx.2008.01.003

Saravanan, C. S., and Mishra, B. (2009). Uniformity in sulfur isotope composition in the orogenic gold deposits from the Dharwar Craton, southern India. *Min. Deposita* 44, 597–605. doi:10.1007/s00126-009-0241-7

Song, M. C., Li, J., Yu, X. F., Song, Y. X., Ding, Z. J., and Li, S. Y. (2021). Metallogenic characteristics and tectonic setting of the Jiaodong gold deposit, China. *Solid Earth Sci.* 6, 385–405. doi:10.1016/j.sesci.2021.07.002

Song, M. C., Song, Y. X., Li, J., and Li, S. Y. (2015). Metallogenic series of gold and nonferrous metal deposits related tocretaceous granites in eastern Shandong Peninsula. *Geotect. Metallogenia* 39 (5), 828–843. doi:10.16539/j.ddgzyckx.2015.05.007

Song, M. C., Zhou, J. B., Song, Y. X., Wang, B., Li, S. Y., Li, J., et al. (2020). Mesozoic Weideshan granitoid suite and its relationship to large-scale gold mineralization in the Jiaodong Peninsula, China. *Geol. J.* 55, 5703–5724. doi:10.1002/gj.3607

Stuart, F. M., Burnard, P. G., Taylor, R. P., and Turner, G. (1995). Resolving mantle and crustal contributions to ancient hydrothermal fluids: He-Ar isotopes in fluid inclusions from DaeHwa W-Mo mineralisation, South Korea. *Geochim. Cosmochim. Acta* 59, 4663–4673. doi:10.1016/0016-7037(95)00300-2

Tan, J., Wei, J. H., Li, Y. J., Fu, L. B., Li, H. M., Shi, W. J., et al. (2015). Origin and geodynamic significance of fault-hosted massive sulfide gold deposits from the guocheng-liaoshang metallogenic belt, eastern Jiaodong Peninsula: Rb-Sr dating, and H-O-S-Pb isotopic constraints. *Ore Geol. Rev.* 65, 687–700. doi:10.1016/j.oregeorev.2014.06.007

Tang, J., Zheng, Y. F., Wu, Y. B., Gong, B., and Liu, X. M. (2007). Geochronology and geochemistry of metamorphic rocks in the Jiaobei terrane: Constraints on its tectonic affinity in the Sulu orogen. *Precambrian Res.* 152 (1), 48–82. doi:10.1016/j.precamres.2006.09.001

Tian, J. P., Li, J. J., Zhang, P. P., Li, X. Z., Liu, W. G., Tang, W. L., et al. (2020). Formation of the Majiayao gold deposit, Jiaodong Peninsula, eastern China: Constraints from fluid inclusions, H-O-S-Pb isotopes, and pyrite Rb-Sr age. *Geol. J.* 55 (8), 5885–5902. doi:10.1002/gj.3719

Tian, R. C., Li, D. P., Tian, J. P., Yu, X. W., Zhang, W., Zhu, P. G., et al. (2022). Genesis of the Jiudian gold deposit, Jiaodong Peninsula, eastern China: Fluid inclusion and C-H-O-Pb isotope constraints. *Ore Geol. Rev.* 149, 105086. doi:10.1016/j.oregeorev.2022.105086

Turner, G., Burnard, P., Ford, J. L., Gilmour, J. D., Lyon, I. C., and Stuart, F. M. (1993). Tracing fluid sources and interactions. *Phil. Trans. R. Soc. Lond. A* 344, 127–140.

Wang, B., Song, M. C., Zhou, J. B., and Ding, Z. J. (2022). Four stages A-type granitoids in Shandong Province and their implications for tectonic evolution. *North China Geol.* 45 (2), 1–17.

Wang, G. Q. (2016). *Mineralization of the Xincheng gold deposit, northwest Jiaodong Peninsula: Multiple isotope tracer*. Beijing: China University of Geosciences.

Wang, J. N., Qu, H. F., and Sun, Z. W. (2017). Geological charteristics of Yangjiakuang gold deposit and prospecting. *Inn. Mong. Sci. Technol. Econ.* 387 (17), 51–53.

Wang, S. J., Wan, Y. S., Zhang, C. J., Yang, E. X., Song, Z. Y., Wang, L. F., et al. (2009). Forming ages of early precambrian metamorphic strata in shandong province—Proofs of zircon SHRIMP U-Pb dating. *Shandong Land Resour.* 25, 18–24.

Wang, Z. L., Zhao, R. X., Zhang, Q., Lu, H. W., Li, L., and Cheng, W. (2014). Magma mixing for the high Ba-Sr guojialing-type granitoids in northwest Jiaodong Peninsula: Constraints from petrogeochemistry and Sr-Nd isotopes. *Acta Petrol. Sin.* 30 (9), 2595–2608.

Wen, B. J., Fan, H. R., Santosh, M., Hu, F. F., Pirajno, F., and Yang, K. F. (2015). Genesis of two different types of gold mineralization in the Linglong gold field, China: Constrains from geology, fluid inclusions and stable isotope. *Ore Geol. Rev.* 65, 643–658. doi:10.1016/j.oregeorev.2014.03.018

Wu, F. Y., Lin, J. Q., Wilde, S. A., Zhang, X. O., and Yang, J. H. (2005). Nature and significance of the early cretaceous giant igneous event in eastern China. *Earth Planet. Sci. Lett.* 233, 103–119. doi:10.1016/j.epsl.2005.02.019

Wu, J. H., Chen, Y. L., Zheng, C. Y., Li, H., Yong, Z. K., Tang, Y. Y., et al. (2021). Genesis of the Longkou–Tudui gold deposit, Jiaodong Peninsula, eastern China: Constraints from zircon U-Pb dating, fluid inclusion studies and C-H-O-S stable isotopes. *Ore Geol. Rev.* 139, 104449. doi:10.1016/j.oregeorev.2021.104449

Xie, S. W., Wang, S. J., Xie, H. Q., Liu, S. J., Dong, C. Y., Ma, M. Z., et al. (2015). Petrogenesis of ca. 2.7 Ga TTG rocks in the Jiaodong terrane, North China craton and its geological implications. *Acta Petrol. Sin.* 31 (10), 2974–2990.

Xie, S. W., Xie, H. Q., Wang, S. J., Krönera, A., Liu, S. J., Zhou, H. Y., et al. (2014). Ca.2.9 Ga granitoid magmatism in eastern Shandong, North China Craton: Zircon dating, Hf-in-zircon isotopic analysis and whole-rock geochemistry. *Precambrian Res.* 255, 538–562. doi:10.1016/j.precamres.2014.09.006

Xu, Y., Mao, G., Liu, X., An, P., Wang, Y., and Cao, M. (2022a). Genesis of the zhaoxian gold deposit, Jiaodong Peninsula, China: Insights from *in-situ* pyrite geochemistry and S-He-Ar isotopes, and zircon U-Pb geochronology. *Front. Earth Sci.* 10, 886975. doi:10.3389/feart.2022.886975

Xu, Y. W., Mao, G. Z., Liu, X. T., An, P. R., Wang, Y., and Cao, M. P. (2022b). Genesis of the zhaoxian gold deposit, Jiaodong Peninsula, China: Insights from *in-situ* pyrite geochemistry and S-He-Ar isotopes, and zircon U-Pb geochronology. *Front. Earth Sci.* 10. doi:10.3389/feart.2022.886975

Yang, J. H., Chung, S. L., Wilde, S. A., Wu, F. Y., Chu, M. F., Lo, C. H., et al. (2005). Petrogenesis of post-orogenic syenites in the Sulu orogenic belt, east China: Geochronological, geochemical and Nd-Sr isotopic evidence. *Chem. Geol.* 214, 99–125. doi:10.1016/j.chemgeo.2004.08.053

Yang, J. H., Wu, F. Y., and Wilde, S. A. (2003). A review of the geodynamic setting of large-scale late mesozoic gold mineralization in the North China craton: An association with lithospheric thinning. *Ore Geol. Rev.* 23, 125–152. doi:10.1016/s0169-1368(03)00033-7

Yang, J. H., and Zhou, X. H. (2001). Rb-Sr, Sm-Nd, and Pb isotope systematics of pyrite: Implications for the age and Genesis of lode gold deposits. *Geology* 29, 711–714. doi:10.1130/0091-7613(2001)029<0711:rssnap>2.0.co;2

Yang, K. F., Fan, H. R., Santosh, M., Hu, F. F., Wilde, S. A., Lan, T. G., et al. (2012). Reactivation of the Archean lower crust: Implications for zircon geochronology, elemental and Sr–Nd–Hf isotopic geochemistry of late Mesozoic granitoids from northwestern Jiaodong Terrane, the North China Craton. *Lithos* 146, 112–127. doi:10.1016/j.lithos.2012.04.035

Yang, L. Q., Deng, J., Goldfarb, R. J., Zhang, J., Gao, B. F., and Wang, Z. L. (2014b). $^{40}Ar/^{39}Ar$ geochronological constraints on the formation of the Dayingezhuang gold deposit: New implications for timing and duration of hydrothermal activity in the Jiaodong gold province, China. *Gondwana Res.* 25, 1469–1483. doi:10.1016/j.gr.2013.07.001

Yang, L. Q., Deng, J., Wang, Z. L., Zhang, L., Guo, L. N., Song, M. C., et al. (2014a). Mesozoic gold metallogenic system of the Jiaodong gold province, eastern China. *Acta Pet. Sin.* 30, 2447–2467.

Yang, W., and Li, S. (2008). Geochronology and geochemistry of the mesozoic volcanic rocks in western liaoning: Implications for lithospheric thinning of the North China craton. *Lithos* 102, 88–117. doi:10.1016/j.lithos.2007.09.018

Yu, P. X., Xiao, X., Xie, J. M., Zhao, Y. B., Liu, D. S., and Shi, H. J. (2014). Analysis on geological and ore controlling conditions of Yangjiakuang gold deposit in Qixia city of shandong province. *Shandong Land Resour.* 30 (9), 7–9.

Yuan, Z. Z., Li, Z. K., Zhao, X. F., Sun, H. S., Qiu, H. N., and Li, J. W. (2019). New constraints on the Genesis of the giant Dayingezhuang gold (silver) deposit in the Jiaodong district, North China Craton. *Ore Geol. Rev.* 112, 103038. doi:10.1016/j.oregeorev.2019.103038

Zartman, R., and Doe, B. (1981). Plumbotectonics—The model. *Tectonophysics* 75, 135–162. doi:10.1016/0040-1951(81)90213-4

Zhai, M. G., Fan, H. R., Yang, J. H., and Miao, L. C. (2004). Large-scale cluster of gold deposits in east shandong: Anorogenic metallogenesis. *Earth Sci. Front.* 11 (1), 85–98.

Zhai, M. G., and Santosh, M. (2013). Metallogeny of the North China craton: Link with secular changes in the evolving earth. *Gondwana Res.* 24, 275–297. doi:10.1016/j.gr.2013.02.007

Zhang, F. X., Xiao, L., and Qi, Y. L. (2004). Exploration and study of Carlin and Carlin-like type gold deposits: Review and prospect. *Geol. China* 04, 406–412.

Zhang, H. Y., Blenkinsop, T., and Yu, Z. W. (2020). Timing of Triassic tectonic division and postcollisional extension in the eastern part of the Jiaodong Peninsula. *Gondwana Res.* 83, 141–156. doi:10.1016/j.gr.2020.01.018

Zhang, J., Zhao, Z. F., Zheng, Y. F., and Dai, M. (2010). Postcollisional magmatism: Geochemical constraints on the petrogenesis of Mesozoic granitoids in the Sulu orogen, China. *Lithos* 119, 512–536. doi:10.1016/j.lithos.2010.08.005

Zhang, L. C., Liu, T. B., Shen, Y. C., Zeng, Q. D., and Li, G. M. (2003). Structure, isotopes, and $^{40}Ar/^{39}$ Ar dating of the Pengjiakuang gold deposit, Mesozoic Jiaolai basin, eastern China. *Int. Geol. Rev.* 45, 691–711. doi:10.2747/0020-6814.45.8.691

Zhang, L., Weinberg, R. F., Yang, L. Q., Groves, D. I., Sai, S. X., Matchan, E., et al. (2020). Mesozoic orogenic gold mineralization in the Jiaodong Peninsula, China: A focused event at 120 ± 2 Ma during cooling of pregold granite intrusions. *Econ. Geol.* 115, 415–441. doi:10.5382/econgeo.4716

Zhang, P. P. (2018). *Study on the mineralization of gold deposits in the guocheng district, Jiaodong: [Master dissertation]*. Tianjin: Sinosteel Tianjin Geological Academy Co., Ltd.

Zhang, T., and Zhang, Y. Q. (2007). Geochronological sequence of Mesozoic intrusive magmatism in Jiaodong Peninsula and its tectonic constraints. *Geol. J. China Univ.* 13 (2), 323–336.

Zhao, G. C., and Zhai, M. G. (2013). Lithotectonic elements of precambrian basement in the North China craton: Review and tectonic implications. *Gondwana Res.* 23, 1207–1240. doi:10.1016/j.gr.2012.08.016

Zhao, K. D., and Jiang, S. Y. (2004). Direct isotope dating for metallic ore deposits. *Earth Sci. Front.* 11 (2), 425–434.

Zhao, R., Wang, Q. F., Deng, J., Santosh, M., Liu, X. F., and Cheng, H. Y. (2018). Late mesozoic magmatism and sedimentation in the Jiaodong Peninsula: New constraints on lithospheric thinning of the North China craton. *Lithos* 322, 312–324. doi:10.1016/j.lithos.2018.10.020

Zhu, G., Liu, C., Gu, C., Zhang, S., Li, Y., Su, N., et al. (2018). Oceanic plate subduction history in the Western pacific ocean: Constraint from late mesozoic evolution of the tan-Lu fault zone. *Sci. China Earth Sci.* 61 (4), 386–405. doi:10.1007/s11430-017-9136-4

Zhu, R. X., Fan, H. R., Li, J. W., Meng, Q. R., Li, S. R., and Zeng, Q. D. (2015). Decratonic gold deposits. *Sci. China Earth Sci.* 45 (8), 1523–1537. doi:10.1007/s11430-015-5139-x

frontiers | Frontiers in Earth Science

TYPE Original Research
PUBLISHED 30 January 2023
DOI 10.3389/feart.2022.1083608

Check for updates

OPEN ACCESS

EDITED BY
Fei Xue,
Hohai University, China

REVIEWED BY
Sam Uthup,
National Taiwan Normal University, Taiwan
Jian Li,
Shandong University of Technology, China
Chao Zhao,
Chang'an University, China

*CORRESPONDENCE
Leilei Dong,
leileidong@ustb.edu.cn

SPECIALTY SECTION
This article was submitted to Geochemistry, a section of the journal Frontiers in Earth Science

RECEIVED 29 October 2022
ACCEPTED 05 December 2022
PUBLISHED 30 January 2023

CITATION
Dong L, Yang Z, Bai X and Deng C (2023), Generation of the Early Cretaceous granitoid in the Dazeshan region, Jiaodong Peninsula: Implications for the crustal reworking in the North China Craton.
Front. Earth Sci. 10:1083608.
doi: 10.3389/feart.2022.1083608

COPYRIGHT
© 2023 Dong, Yang, Bai and Deng. This is an open-access article distributed under the terms of the Creative Commons Attribution License (CC BY). The use, distribution or reproduction in other forums is permitted, provided the original author(s) and the copyright owner(s) are credited and that the original publication in this journal is cited, in accordance with accepted academic practice. No use, distribution or reproduction is permitted which does not comply with these terms.

Generation of the Early Cretaceous granitoid in the Dazeshan region, Jiaodong Peninsula: Implications for the crustal reworking in the North China Craton

Leilei Dong[1]*, Zhiming Yang[1,2], Xin Bai[1] and Chen Deng[3]

[1]School of Civil and Resource Engineering, University of Science and Technology Beijing, Beijing, China, [2]Institute of Geology, Chinese Academy of Geological Sciences, Beijing, China, [3]Postdoctoral Programme, Guosen Securities, Shenzhen, China

Lower crust-derived granitic rocks provide constraints on the crustal reworking process and consequently give hints on the destruction mechanism of the cratons. The North China Craton (NCC) underwent extensive crustal melting in the Mesozoic. This study investigated granitic intrusions in the Dazeshan region of the Jiaodong Peninsula. Whole-rock major and trace element analyses and zircon U-Pb ages coupled with Hf isotopes were used to reveal the crustal reworking processes. Zircons separated from the quartz porphyry, Linglong granite, rhyolite porphyry, and biotite granite showed weighted mean ^{206}Pb-^{238}U ages of 119.2 ± 1.0 Ma, 140.2 ± 1.0 Ma, 120.6 ± 0.5 Ma, and 119.9 ± 0.7 Ma, respectively. The quartz porphyry, rhyolite porphyry, and biotite granite had high silica contents (SiO_2 = 74–77 wt.%) but low MgO, Co, and Ni concentrations. The calculated $\varepsilon_{Hf}(t)$ values for the rhyolite porphyry and the biotite granite ranged from −18.3 to −20.0 and −17.8 to −20.2, respectively. These geochemical features imply ancient crust sources. The quartz porphyry showed distinct primitive mantle-normalized rare earth element (REE) patterns and was characterized by lower ΣREE content and lack of pronounced negative Eu anomalies. Whole-rock and zircon Dy/Yb ratios showed no correlation with whole-rock Rb/Sr ratios and zircon Hf contents, reflecting limited effects of crystal fractionation. The Ba/La ratios were also high (>150), but the Sr/Y and La/Yb ratios were low (Sr/Y < 50; La/Yb < 15). These features likely indicate that the quartz porphyry was generated by water-fluxed melting without differentiation. The rhyolite porphyry and biotite granite shared many geochemical similarities, denoting a unified source. The high La/Yb (>30) but low Sr/Y (<20) ratios and apparent negative Eu anomalies indicated plagioclase fractionation. Decreased zircon Dy/Yb with increasing Hf concentrations reflected noticeable amphibole fractionation. These two suites had fairly low Ba/La ratios. These data together point toward an identical source: dehydration melting of a relatively thickened crust. These melts experienced crystal fractionation after extraction. We propose that the intrusions were generated by the underplating of water-rich mafic magma, which provided both fluid and heat and finally induced two kinds of melting.

KEYWORDS
Jiaodong, North China Craton, granite, petrogenesis, crustal reworking

1 Introduction

Cratons are generally considered the most stable part of the lithosphere because the great thickness of the continental mantle beneath cratons prevents them from being destroyed by the convective mantle. However, decades of research have greatly improved our understanding and we now know that stable cratons can be destroyed (Gao et al., 2004; Xu et al., 2009; Lee et al., 2011; Wu et al., 2019). The NCC has stabilized following the amalgamation between the western and eastern blocks at about 1.9 Ga (Zhao et al., 2005). However, it was reworked during the Mesozoic and the thick lithosphere underwent extensive thinning, particularly at the eastern part of the NCC (Menzies et al., 2007; Chen et al., 2008; Wu et al., 2019). The destruction of NCC was accompanied by crustal reworking and the development of extensional structures and many metamorphic core complexes (like the Gudaoling and Linglong) and sedimentary basins (Charles et al., 2012; Meng et al., 2019; Wu et al., 2019; Zheng and Gao, 2021). Thus, these processes are used as indicators of decratonization in the NCC.

This thinning process of the lithosphere mantle can be traced at the shallow crustal levels by Jurassic-Cretaceous granitic rocks, as they represent thermal or tectonic disturbances underneath the thick crust (Chappell, 2004; Weinberg and Hasalová, 2015; Gao et al., 2016; Zheng and Gao, 2021). Although extensive studies have been conducted on these magmatic rocks to demonstrate the timing and mechanisms of NCC destruction, some divergences exist regarding the timing and duration of the NCC destruction. The onset of NCC destruction remains elusive because the understanding of "destruction" differs (Xu et al., 2009). The northern and southern margins of the NCC were subducted by the Paleo-Asian Oceanic slab and the South China Block during the Carboniferous-Permian and Late Triassic, respectively (Windley et al., 2010). The resultant magmatism in the northern and southern margins indicated changes in lithospheric structure and thermal structure. Following this logic, the NCC destruction initiated in different craton margins in the Carboniferous and Triassic (Xu et al., 2009). Nevertheless, the destruction of NCC is now broadly recognized to have peaked in the Early Cretaceous (Wu et al., 2005a), as indicated by extensive granitic magmatism associated with mantle-crust interactions.

The mechanism of lithosphere thinning also remains under debate. One school of thought argues that the thinning occurs mechanically by delamination (Gao et al., 2004; Ma et al., 2014), while other researchers believe that the thinning proceeds gradually *via* a thermal-chemical erosion process (Xu et al., 2009; Geng et al., 2019). Hou et al. (2007) inferred that the ~130 Ma Guojialing suite adakitic granitoids were formed by crustal thickening during the descent into the asthenosphere (delamination). Ma et al. (2014) proposed that the lithosphere mantle was rapidly replaced by the fertile asthenosphere mantle at ca. 120 Ma by delamination based on investigations of the mafic dykes in Jiaodong. These results drive the timing of delamination, if it occurred, towards later times. Therefore, the genesis of these Early Cretaceous magmatic rocks is crucial for understanding the crustal evolution of the NCC. However, how these granitic rocks were generated remains undetermined in the NCC (e.g., fluid fluxed or dehydration melting), particularly those magmatic rocks formed at ca. 120 Ma. This impedes our knowledge of decratonization processes. This study investigated the petrogenesis of the granitic rocks that intruded into the Jurassic Linglong granite in the Dazeshan region in Jiaodong Penisular, to reveal the crustal reworking processes.

2 Geological background

The Jiaodong Penisular is an integral part of the NCC, which has Early Archean crustal remnants (Jahn and Zhang, 1984; Liu et al., 1992). The NCC was stabilized through the amalgamation of the eastern and western blocks during a Paleoproterozoic orogenic event along the Trans-North China Orogen (Figure 1) (Zhao, 2001). Both blocks are dominated by Late Archaean tonalitic–trondhjemitic–granodioritic (TTG) gneiss complexes with minor supracrustal rocks with metamorphic ages of ~2.5 Ga (Zhao, 2001). The Jiaodong Penisula is located in the southeastern part of the NCC and was displaced to its current location by the approximately 2,400 km Tanlu fault (Zhu et al., 2009). Three main tectonic units constitute the Jiaodong Peninsula: the Jiaobei terrane, the Sulu orogen, and the Jiaolai basin (Figure 1).

The Jiaobei terrane, an integral part of the NCC, comprises Archean-Paleozoic metamorphic rocks and TTG gneiss (such as biotite gneiss and plagioclase amphibolite). These rock units are mainly located in the Qixia area. The Jurassic Linglong granite, along with the Luanjianhe and Biguo granites, intrudes into the Precambrian rocks and together constitute the composite Linglong pluton (Figure 1). The zircon U-Pb ages of this composite pluton range from 170 to 150 Ma (Yang et al., 2012; Yang et al., 2017). The volumetrically smaller Guojialing, Congjia, Beijie, and Shangzhuang granodiorite were subsequently emplaced during the Early Cretaceous. The zircon U-Pb ages of these plutonic rocks range from 130 to 127 Ma (Yang et al., 2012; Jiang et al., 2016). The Aishan and Nansu porphyry granites, which feature large K-feldspar phenosrysts, are emplaced within the Guojialing granodiorite and the Linglong granite, respectively, and have zircon U-Pb ages of 118–116 Ma (Goss et al., 2010; Li et al., 2012). The Sulu orogen

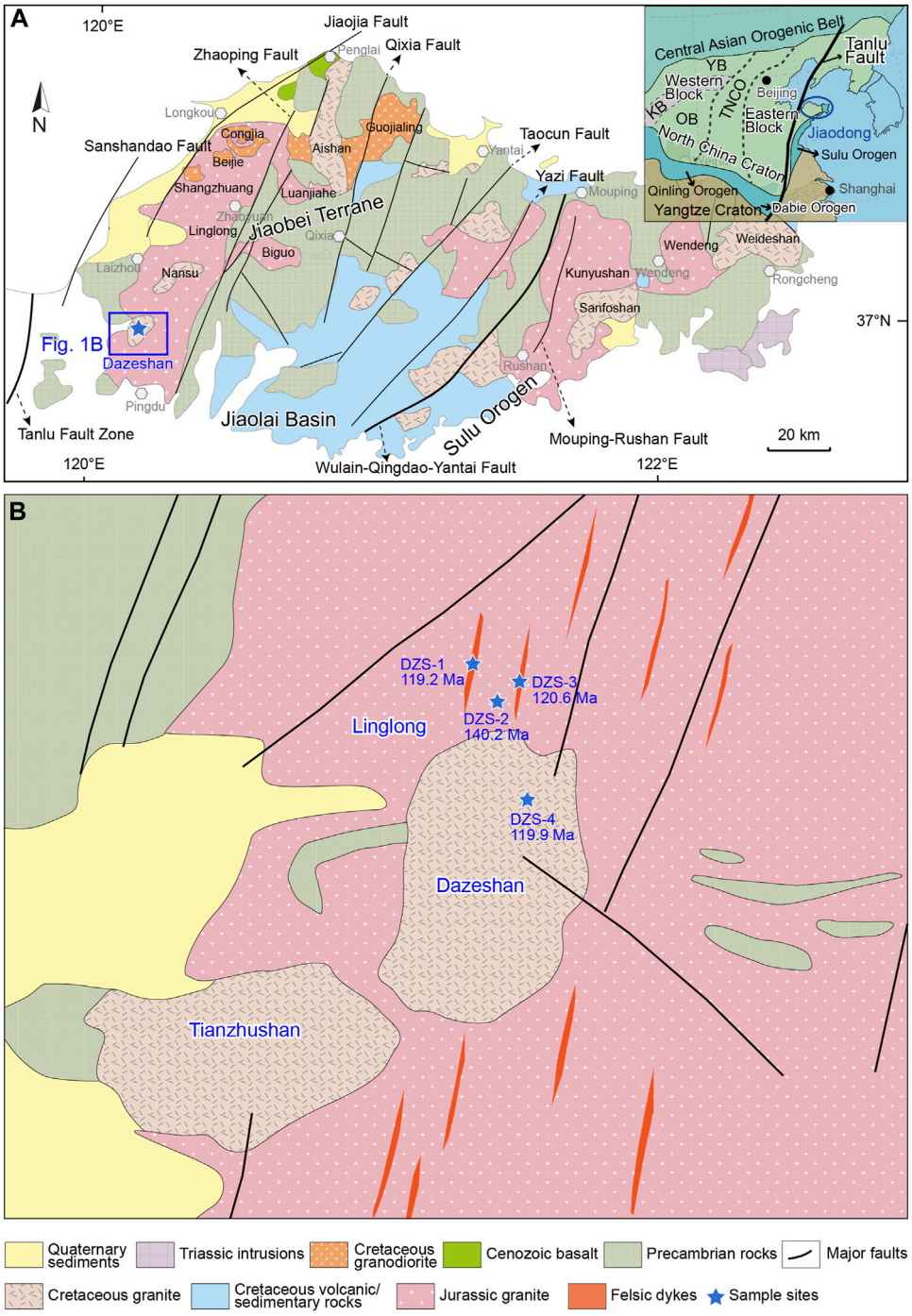


FIGURE 1
(A) Geological map of the Jiaodong Peninsula, showing major structures, lithological units, and study area (Song et al., 2021). **(B)** The U-Pb ages obtained in this study are noted on the map.

is situated to the east of the Wulian-Qingdao-Yantai fault and is considered the suture zone separating the NCC and South China Block (Wu and Zheng, 2013). Many ultrahigh- to high-pressure metamorphic rocks are preserved in the Sulu orogen. Additionally, the Triassic alkaline complex in the Rongcheng area (Shidao) dates to 225–205 Ma and represents magmatism related to mantle upwelling after continent-continent collision (Chen et al., 2003). The Jiaolai basin comprises volcanic and

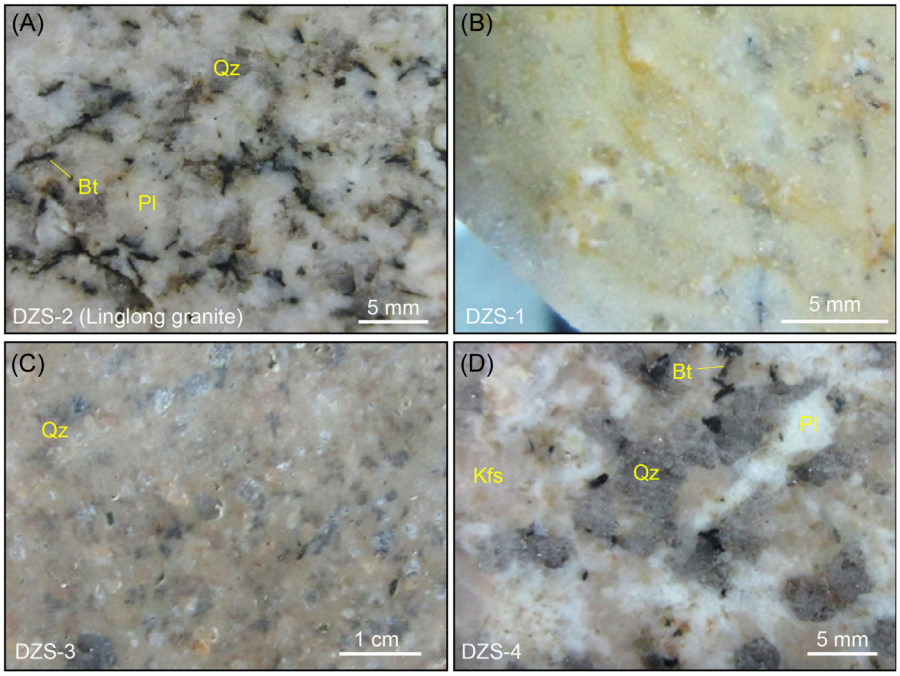


FIGURE 2
(A–D) Photographs of Linglong granite, quartz porphyry, rhyolite porphyry, and Dazeshan biotite granite.

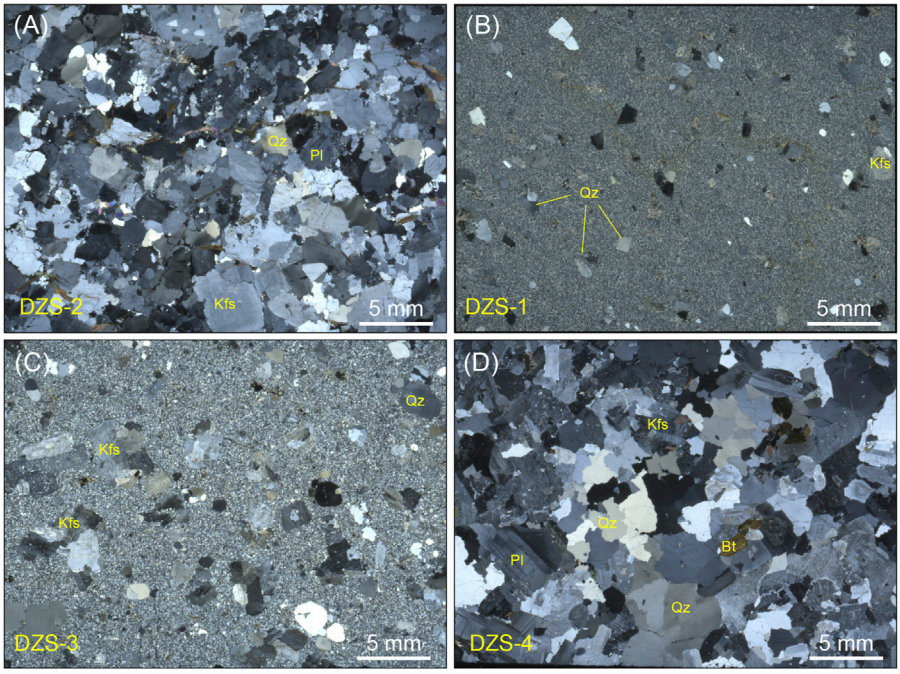


FIGURE 3
Microscopic images of Linglong granite **(A)**, quartz porphyry **(B)**, rhyolite porphyry **(C),** and Dazeshan biotite granite **(D)**. Abbreviations: Kfs = K-feldspar, Pl = plagioclase, Qz = quartz, Bt = biotite. The abbreviations for the minerals are after Whitney and Evans. (2010).

sedimentary sequences deposited in the Early Cretaceous (Zhang et al., 2008). The main volcanic rocks in the Jiaolai basin are Qingshan group basic to felsic rocks, including rhyolite, andesite, dacite, and tuff. Laiyang and Wangshi group sedimentary rocks (sandstone and mudstone) cover the Qingshan group volcanic rocks. Cenozoic basalt, although rarely exposed, is mainly reported in the Penglai area (Figure 1).

3 Samples and analytical methods

The samples investigated in this study were collected in the Dazeshan region at the Jiaobei terrane (Figure 1B). Four types of magmatic rocks were sampled: quartz porphyry (DZS-1), Linglong granite (DZS-2), rhyolite porphyry (DZS-3), and Dazeshan biotite granite (DZS-4) (Figure 2). From field observations, the quartz porphyry, rhyolite porphyry, and Dazeshan biotite granite all intruded the Linglong granite. The Linglong granite is predominantly composed of plagioclase, K-feldspar, quartz, and biotite (Figures 2A, 3A). The sizes of the plagioclase, K-feldspar, and quartz are similar (2–5 mm). The biotite crystals are smaller and appear to be tabular. The samples from the Linglong granite were fresh. The quartz porphyry is a fine-grained grayish felsic rock that contains quartz and minor K-feldspar phenocrysts (Figures 2B, 3B). The volume fraction of the quartz phenocryst is <5%. The matrix contains micron-scale quartz and feldspar crystals. The K-feldspar in both phenocrysts and matrix was subjected to weathering and formed small amounts of sericite. The rhyolite porphyry sample (DZS-3) contained quartz and K-feldspar phenocrysts (Figures 2C, 3C). The phenocrysts were approximately 2–5 mm in diameter. The Dazeshan biotite granite (DZS-4) is a coarse-grained plutonic rock that intruded into the Linglong granite (Figure 1). The Dazeshan biotite granite had the same mineral assemblages as the Linglong granite but with larger crystal sizes.

3.1 Major and trace element analyses

Major element data for whole-rock samples were obtained by X-ray fluorescence (XRF) spectrometry on fused glass discs using a PANalytical AXIOS Minerals instrument at the Institute of Geology and Geophysics, Chinese Academy of Sciences. Glass discs for WD-XRF analyses were prepared by fusing 0.5 g of the standard sample with 5.0 g of lithium tetraborate-metaborate mixture (2:1) using Pt-Au crucibles and moulds on fusion equipment with gas burners. Loss on ignition (LOI) was measured as the weight loss of the samples after 1 h of baking at a constant temperature of 1,000°C in a muffle furnace. The ferrous iron content was determined using the titration method described by Xue et al. (2017). Whole-rock trace element analyses were performed at the National Research Center of Geoanalysis, Chinese Academy of Geological Science by inductively coupled plasma mass spectrometry (ICP-MS) on a TJA PQ-ExCell system. Standards GSR1 and GSR9 were used to monitor the analytical reproducibility. 2σ uncertainties are <5% for elements >10 ppm and <10% for elements <10 ppm.

3.2 Zircon U-Pb dating and trace elements

Zircons were separated using conventional heavy liquid and magnetic separation techniques. They were mounted in epoxy and polished to a surface. Transmitted, reflected light and cathodoluminescence (CL) images were captured to acquire information about the inner structure, surface characteristics, and CL textures of the zircons, respectively. Laser ablation-inductively coupled plasma-mass spectrometry (LA-ICPMS) zircon U-Pb analyses were performed on an Agilent 7900 ICP-MS instrument equipped with a 193 nm laser ablation system at the Institute of Geology, Chinese Academy of Geological Sciences. A laser spot size of 30 μm was used to ionize the samples. The laser was operated at an energy of 2 J/cm^2 and a repetition rate of 5 Hz.

3.3 Zircon Lu-Hf isotopes

In situ zircon Lu-Hf isotopic analyses were performed on a Neptune MC-ICPMS coupled with a 193 nm laser ablation system at the National Research Center for Geoanalysis. An ArF excimer laser ablation system was used for the laser ablation analysis. The analyses used a laser repetition rate of 10 Hz at 100 mJ. A spot size of ca. 40 μm was applied depending on the size of the zircon grains. The ionized samples were carried by Ar gas. The detailed analytical procedures are described in (Wu et al., 2006).

4 Analytical results

4.1 Whole-rock major and trace elements

Eleven sample powders from three intrusions (except for the Linglong granite) were analyzed. The whole-rock geochemical data are presented in Figures 4, 5, 6 and Table 1. Overall, the silica contents of the quartz porphyry, rhyolite porphyry, and Dazeshan biotite granite are high (74–77 wt.%). In the total alkali vs. silica diagram (Figure 4A), these samples plot in the granite field. They belong to the high-K calc-alkaline series in the plot of SiO_2 vs. K_2O diagram (Figure 4B). In the plots of SiO_2 vs. CaO, Al_2O_3, MgO, TFeO, TiO_2, and P_2O_5, the three types of magmatic rocks display distinct major element contents (Figure 5). CaO concentrations in the Dazeshan biotite granite are the highest among the samples, while the quartz porphyry and rhyolite porphyry have CaO contents around 0.4 wt.%. The

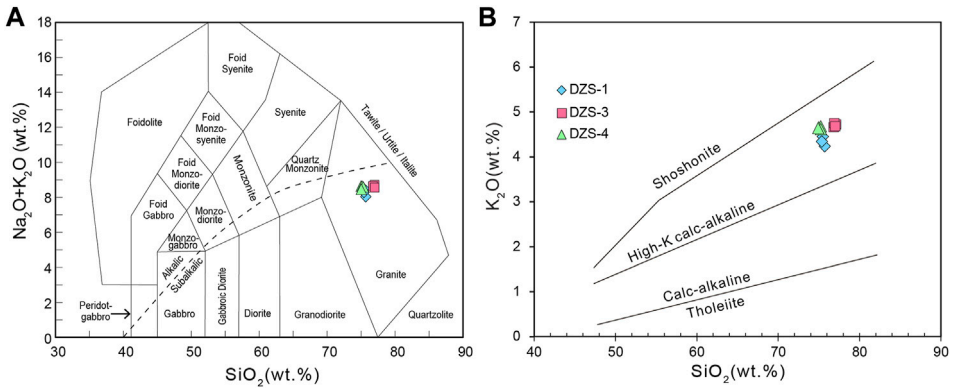


FIGURE 4
Total alkaline vs. SiO_2 **(A)** and SiO_2 vs. K_2O **(B)** diagrams (Peccerillo and Taylor, 1976; Le Bas et al., 1986).

aluminum content for the quartz porphyry is the highest among the three intrusions (14.01–14.34 wt.%), about 1–2 wt.% higher than the other two suites. The Al_2O_3 contents in the Dazeshan biotite granite are in the range of 13.22–13.29 wt.%. The MgO concentrations in the intrusions are low (<0.4 wt.%) and show negative correlations with SiO_2 (Figure 5C). Total FeO contents are lower in the quartz porphyry and rhyolite porphyry (1.11–1.40 wt.% and 1.07–1.12 wt.%, respectively) and higher in the Dazeshan biotite granite (1.63–1.72 wt.%) (Figure 5D). The concentrations of TiO_2 and P_2O_5 are elevated in the Dazeshan biotite granite compared to those in the quartz and rhyolite porphyries (Figures 5E, F).

The whole-rock trace element data are normalized to the primitive mantle (PM) in REE and spider diagrams (Figure 6). In the REE diagram, the three intrusions display different enrichment and/or depletion patterns. The samples from quartz porphyry have low contents of total REE (20.7–27.7 ppm). Additionally, the light rare earth elements (La-Eu; LREE) are not strongly fractionated from the heavy rare earth elements (Gd-Lu; HREE) given the LREE/HREE ratios from 6.8 to 7.6. No apparent negative Eu anomaly is observed in the PM-normalized REE pattern. The calculated Eu/Eu* values range from 0.89 to 0.98 for the quartz porphyry samples (Eu/Eu* represents the europium anomaly calculated as $Eu_N/(Sm_N \times Gd_N)^{0.5}$, the subscript "N" denotes the PM normalized value from McDonough and Sun, 1995). In the spider diagram (Figure 6B), high field strength elements (HFSE) like P and Ti in the quartz porphyry show negative anomalies. However, the large ion lithophile elements (LILE) like Rb and Ba, along with fluid mobile element Pb, are strongly enriched.

The REE patterns for the rhyolite porphyry and Dazeshan biotite granite show contrasting features compared to the quartz porphyry. Generally, these two intrusions have elevated REE concentrations compared to the quartz porphyry and display listric-shaped patterns. Y These two porphyries also show obvious negative Eu anomalies. The Eu/Eu* for the rhyolite porphyry and Dazeshan biotite granite are 0.40–0.48 and 0.52–0.66, respectively. The LREE and HREE are strongly fractionated in these two intrusions. The LREE/HREE ratios are 23.7–26.0 for the rhyolite porphyry and 16.8–26.8 for the Dazeshan biotite granite. However, the Dazeshan biotite granite has higher total REE concentrations than that of the rhyolite porphyry (97.6–150.2 ppm vs. 69.7–96.4 ppm). In the spider diagram, the rhyolite porphyry and Dazeshan biotite granite display overall similar patterns except for Ba and Sr. The rhyolite porphyry shows more depletion of these two elements compared to the Dazeshan biotite granite (Figure 6B). Elements from Th to Pb in Figure 6B are elevated compared to the quartz porphyry.

4.2 Zircon U-Pb ages and trace elements

Four sets of zircon U-Pb ages and trace element data were obtained in this study. The analytical results are presented in Figures 7, 8 and Table 2 and Table 3. The LA-ICPMS zircon data from each rock type are briefly described below.

4.2.1 Quartz porphyry (DZS-1A)

Zircons from this sample are clear by microscopy and contain little mineral inclusions. Additionally, they display oscillatory zoning patterns under CL images. The lengths of these zircons are about 100–200 μm, while the widths are about 40–100 μm. Most of the zircons have a CL brighter grayish core without oscillatory zoning but are overgrown by CL dark rims with oscillatory zonings (Figure 7A). The zircon U-Pb ages in these two different areas are consistent. Twenty-one spot analyses on zircons were conducted. These isotope data cannot construct a well-defined Concordia U-Pb age but give a weighted mean ^{206}Pb-^{238}U age of 119.2 ± 1.0 Ma (Figures 7A, B;

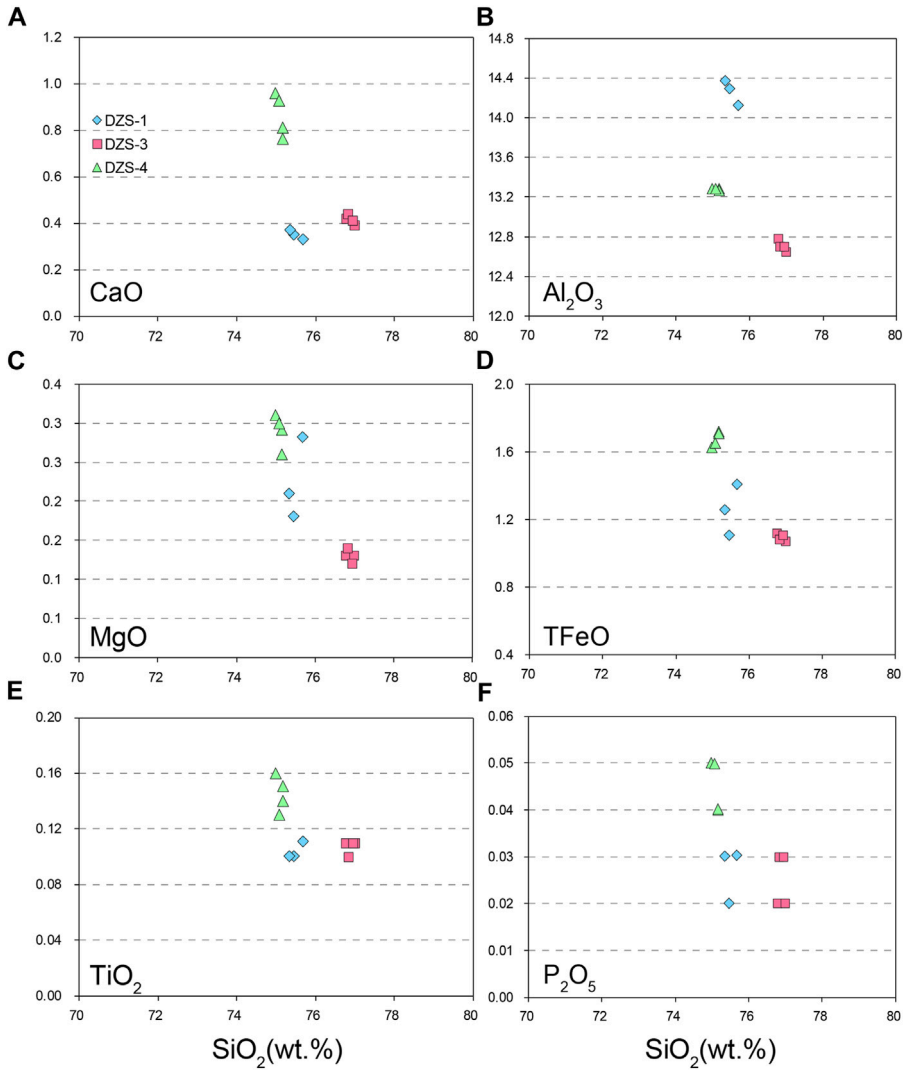


FIGURE 5
(A–F) Harker-type diagrams of whole-rock CaO, Al_2O_3, MgO, total FeO, TiO_2, and P_2O_5 versus SiO_2 contents for the studied intrusions.

MSWD = 3.6, N = 21). The U and Th concentrations in the zircons have wide ranges (201–3,411 ppm and 74–2084 ppm, respectively), whereas the Th/U ratios are relatively restricted between 0.36 and 1.03, with an average value of 0.62 (Table 2).

4.2.2 Linglong granite (DZS-2A)

Twenty-three zircons were analyzed in this sample. Most of these zircons are columnar with lengths of about 100–200 μm, and widths of 50–100 μm (mostly ~50 μm). Mineral inclusions like apatite or rutile are common in these zircons. The zircons have simple CL textures, with or without an oscillatory zoning rim. The cores of the zircons appear to be dark gray. Inherit zircons, however, are frequently observed and featured by bright CL (Figure 7C inset). Six of the twenty-four zircons underwent Pb loss and fall out of the Concordia line, yet they construct two ages intercepting at 139 ± 37 and 1973 ± 48 Ma (MSWD = 4.9, N = 23). The two oldest zircons have ^{207}Pb-^{236}Pb ages of 2078 ± 30 Ma and 1838 ± 86 Ma, respectively. The young group of zircons constructs a weighted mean ^{206}Pb-^{238}Pb age of 140.2 ± 1.0 Ma (Figure 7D, MSWD = 2.4, N = 16). For the younger group zircons, which are considered the crystallization phase from the magma (see later discussion), the U concentrations range from 348 to 3,048 ppm, while the Th content varies between 58 and 1866 ppm (Table 2). The corresponding Th/U ratios are 0.08–1.29, with an average value of 0.47.

4.2.3 Rhyolite porphyry (DZS-3A)

Twenty-four zircons were separated from the rhyolite porphyry sample. Zircon morphology exhibits tiny differences from the quartz porphyry and Linglong granite samples. These

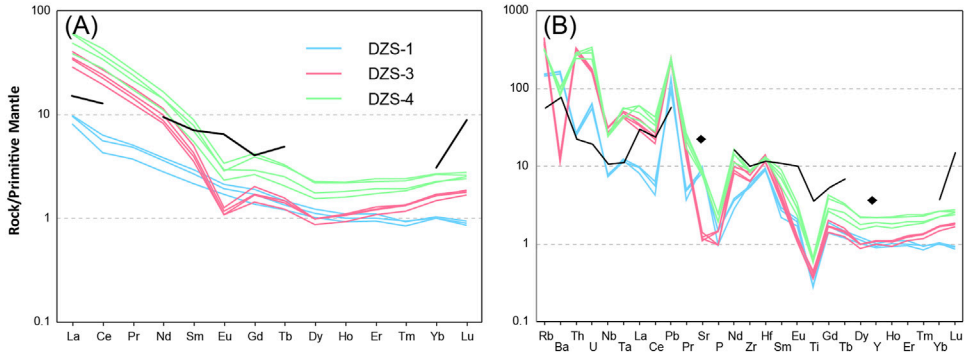


FIGURE 6
Primitive mantle-normalized REE patterns **(A)** and trace element variation diagrams **(B)** for the quartz porphyry, rhyolite porphyry, and Dazeshan biotite granite. The normalization values are from McDonough and Sun (1995). Black line: average granulite terrane/xenolith concentrations in the NCC (Jahn and Zhang, 1984; Liu et al., 2001; Zhai et al., 2001).

grains are equally sized, with length-to-width ratios of around 1.5–2.0. The lengths of most zircons are around 150 μm. Their CL characters vary. Some zircons have a bright core with CL dark/bright oscillatory zoning rims, while others have CL bright oscillatory zoning in the whole grain. Nevertheless, the zircon ages in these different areas are the same. All the zircons construct a Concordia U-Pb age of 120.7 ± 0.5 Ma (Figure 7E; MSWD = 1.7, N = 24 and a weighted mean ^{206}Pb-^{238}Pb age of 120.6 ± 0.5 Ma (Figure 7F; MSWD = 1.5, N = 24). The zircon U and Th concentrations are 179–1,533 ppm and 191–1,037 ppm, respectively. The average U and Th concentrations are 575 ppm and 360 ppm, respectively. The zircon Th/U ratios are 0.42–1.58.

4.2.4 Dazeshan biotite granite (DZS-4A)

Zircons from the biotite granite are characterized by low length-to-width ratios (1–1.5). Most of these zircons are 100–150 μm in size and have CL bright/dark oscillatory zoning occupying the whole zircon grain. Generally, the CL bright zone is rimmed by a CL dark zone with or without oscillatory zoning patterns. The data of the 26 analyzed zircons yielded ages that intercept at 1,364 ± 800 Ma and 118.5 ± 2.0 Ma (Figure 7G, MSWD = 0.81). The weighted mean ^{206}Pb-^{238}Pb age is 119.9 ± 0.7 Ma (Figure 7H, MSWD = 1.9). The zircon U concentrations are 181–3,275 ppm, while the Th concentrations are 148–2,233 ppm. The Th/U ratios in zircons range from 0.47 to 1.46 (Table 2).

Zircon trace element data of the four samples are presented in Figure 8 and Table 3. All zircons feature HREE enrichment but LREE depletion (except for Ce, which displays a strong positive anomaly) in PM-normalized REE patterns (Figures 8A–D). Europium shows a relatively weak negative anomaly in zircons from the quartz porphyry. However, the negative Eu anomalies are strikingly obvious in the other three zircon samples.

4.3 Zircon Lu-Hf isotopes

Zircon Hf isotopes were analyzed in rhyolite porphyry and the Dazeshan biotite granite. The hafnium isotope data are presented in Figure 9 and Table 4. For the rhyolite porphyry, ^{176}Hf/^{177}Hf values are 0.282133–0.282181. The calculated $\varepsilon_{Hf}(t)$ was −18.3 to −20.0. The two stage model ages are 3.2 to 3.4 Ga. Five spot analyses of zircons from the Dazeshan biotite granite give a^{176}Hf/^{177}Hf values between 0.282130 and 0.282195 ($\varepsilon_{Hf}(t)$ = −17.8 to −20.2).

5 Discussion

5.1 Genesis of the ~120 Ma magmatic rocks

Granites are produced predominantly by anatexis of crustal rocks (Brown, 2013; Clemens et al., 2020), although in some cases, the granites are generated by fractional crystallization of mantle-derived melts (Soesoo, 2000; Thompson et al., 2002). For the samples investigated in this study, the SiO_2 contents of the three intrusions (except for the Linglong granite) are very high (74–77 wt. %). Meanwhile, no considerable mafic melts occurred along with these granites (Figure 1), eliminating the possibility of fractional crystallization of mantle-derived melts. The Hf isotope compositions from the zircons also provide information on the sources of the melts well (Figure 9). The ε_{Hf}(t) values are restricted for both the rhyolite porphyry and Dazeshan biotite granite (ca. −18 to −20), comparable to other granitic rocks reported in the Jiaodong Penisula (e.g., Linglong granite and Aishan granodiorite). For example, the Linglong granite was interpreted to be the melting products of the Archean lower crust, with almost no contribution from the mantle (Ma et al.,

TABLE 1 Major (*wt %*) and trace (*ppm*) element concentrations for igneous rocks in the Dazeshan region.

	DZS-1A	DZS-1B	DZS-1E	DZS-3A	DZS-3B	DZS-3D	DZS-3E	DZS-4A	DZS-4B	DZS-4D	DZS-4E
SiO_2	75.23	75.06	75.18	76.83	77.04	76.75	77.02	74.96	75.04	74.89	75.11
$Al2O_3$	14.25	14.01	14.34	12.79	12.65	12.69	12.71	13.28	13.26	13.22	13.29
TFe_2O_3	1.11	1.40	1.26	1.12	1.07	1.08	1.11	1.63	1.72	1.71	1.66
MgO	0.18	0.28	0.21	0.13	0.13	0.14	0.12	0.31	0.26	0.29	0.30
CaO	0.35	0.33	0.37	0.42	0.39	0.44	0.41	0.96	0.81	0.76	0.93
Na_2O	4.01	3.74	3.93	3.97	3.89	3.93	3.88	3.90	3.88	3.92	3.87
K_2O	4.44	4.21	4.35	4.67	4.74	4.72	4.70	4.67	4.64	4.62	4.65
TiO_2	0.10	0.11	0.10	0.11	0.11	0.10	0.11	0.16	0.14	0.15	0.13
P_2O_5	0.02	0.03	0.03	0.02	0.02	0.03	0.03	0.05	0.04	0.04	0.05
MnO	0.01	0.01	0.01	0.01	0.02	0.02	0.01	0.04	0.04	0.03	0.05
LOI	0.67	0.97	0.92	0.33	0.28	0.30	0.29	0.38	0.25	0.34	0.39
Total	100.36	100.14	100.70	100.41	100.35	100.20	100.39	100.34	100.08	99.97	100.43
Mg#	24	28	24	19	16	40	38	40	48	32	34
ppm											
P	88	132	131	87	87	131	131	218	175	175	218
Ti	342	344	334	428	541	460	507	779	695	713	796
Sc	1.68	1.70	1.62	1.57	1.53	1.38	1.29	2.16	2.08	2.39	2.41
V	3.68	3.11	3.99	2.25	2.89	3.36	2.79	6.88	6.41	6.48	7.03
Cr	3.63	7.78	8.75	5.70	17.6	8.57	7.70	6.60	5.58	8.37	7.96
Co	0.36	0.48	0.77	0.57	0.57	0.69	0.67	1.40	1.10	1.21	1.18
Ni	0.36	0.98	2.89	0.83	0.25	1.87	1.62	1.65	1.67	2.25	3.58
Rb	89.9	92.4	87.1	227	264	242	275	191	194	195	189
Sr	194	179	162	23	28	24	22	174	157	153	181
Zr	63.8	58.1	56.7	66.9	87.0	67.9	80.3	90.5	86.8	92.1	90.9
Nb	5.12	4.77	4.84	16.9	20.5	18.1	20.9	16.0	16.6	16.6	16.1
Ba	1,114	1,084	1,014	75.1	88.6	87.6	76.3	660	528	570	682
Y	3.86	4.37	3.97	4.24	4.66	4.74	4.70	8.11	9.36	7.31	9.32
La	5.27	6.32	6.24	18.7	22.9	21.9	26.4	38.6	31.4	25.0	39.1
Ce	7.17	10.6	9.27	32.4	40.5	37.3	45.1	62.8	56.7	46.9	72.3
Pr	0.94	1.29	1.24	3.26	3.99	3.69	4.66	6.10	5.42	4.40	6.81
Nd	3.52	4.77	4.47	10.2	12.3	11.0	14.3	17.9	17.9	13.8	20.9
Sm	0.88	1.19	1.09	1.43	1.73	1.60	2.02	2.81	3.17	2.21	3.63
Eu	0.26	0.33	0.30	0.17	0.18	0.17	0.20	0.45	0.44	0.36	0.52
Gd	0.75	1.03	0.93	0.78	0.92	0.91	1.09	1.58	2.11	1.43	2.30
Tb	0.12	0.15	0.13	0.12	0.15	0.14	0.16	0.25	0.32	0.20	0.33
Dy	0.69	0.83	0.76	0.59	0.67	0.66	0.66	1.19	1.52	1.04	1.48

(Continued on following page)

TABLE 1 (*Continued*) Major (*wt %*) and trace (*ppm*) element concentrations for igneous rocks in the Dazeshan region.

	DZS-1A	DZS-1B	DZS-1E	DZS-3A	DZS-3B	DZS-3D	DZS-3E	DZS-4A	DZS-4B	DZS-4D	DZS-4E
Ho	0.14	0.16	0.15	0.14	0.16	0.16	0.16	0.27	0.33	0.24	0.33
Er	0.42	0.48	0.44	0.48	0.56	0.53	0.54	0.85	1.05	0.76	0.98
Tm	0.06	0.06	0.06	0.08	0.09	0.09	0.09	0.13	0.16	0.13	0.16
Yb	0.44	0.46	0.44	0.65	0.76	0.73	0.73	0.99	1.18	0.98	1.16
Lu	0.06	0.06	0.06	0.11	0.12	0.12	0.13	0.16	0.19	0.17	0.17
Hf	2.67	2.61	2.49	3.20	3.95	3.31	3.83	3.46	3.54	3.73	3.72
Ta	0.44	0.46	0.42	1.56	1.82	1.62	1.87	1.53	2.08	1.67	1.99
Pb	20.2	14.2	14.7	33.7	36.8	33.9	36.9	35.6	36.9	33.9	36.6
Th	1.97	2.10	2.02	23.5	26.7	25.7	25.9	22.2	20.9	23.0	19.5
U	1.11	1.30	1.27	3.27	3.63	3.32	3.45	5.81	6.42	6.88	4.89
Cs	0.81	0.80	0.85	1.76	1.96	1.92	2.14	3.82	5.89	3.79	6.38
Cu	3.28	4.29	6.01	5.72	2.90	5.06	4.71	3.83	3.76	5.39	5.06
Zn	6.28	4.47	5.58	1.37	1.62	1.52	1.98	12.9	13.4	11.6	14.3
Ga	16.3	17.4	17.0	14.3	17.3	15.5	17.7	17.1	17.1	15.2	18.1
Bi	0.05	0.09	0.09	0.03	0.02	0.02	0.03	0.12	0.19	0.11	0.22

2013; Li et al., 2019). The two stage model ages calculated *via* zircon Hf isotope compositions are 3.2–3.4 Ga for the rhyolite porphyry and Dazeshan biotite granite (Table 4), demonstrating their ancient continental crust source. Therefore, these granite rocks are generated by crustal anatexis.

From the perspective of the whole-rock and zircon trace element data, the three intrusions have strikingly different geochemical features (Figures 6, 10). This implies that these intrusions probably experienced distinct melting or differentiation processes. The following section discusses the chemical variations in these magmatic rocks and their magmatic evolution.

5.1.1 Quartz porphyry (DZS-1)

The quartz porphyry is characterized by low LREE content and a lack of negative Eu anomaly in the REE pattern (Figure 6A). The LREE concentrations in the quartz porphyry here are even lower than the average concentrations of the granulite terranes/xenoliths in the NCC, which were regarded as representative of the lower crust fragments (Liu et al., 1999; Zhai et al., 2001; Liu et al., 2004). Partial melting of the granulite rocks would give rise to higher REE content in the melt considering their incompatibility. The discordant REE patterns between the quartz porphyry and granulite terranes/xenoliths differ from what would be expected if the quartz porphyry is the melting product of lower-crust granulite. Magmatic processes like fractionation crystallization or magma mixing could exert a conspicuous influence on the compositions of the melt (DePaolo, 1981; Yang et al., 2004; Cao et al., 2022).

The whole-rock major and trace elements, trace elements ratios (Th/Nb, La/Sm, and Rb/Sr), and $Mg^{\#}$ values vary little among the three samples from the quartz porphyry, indicating that fractionation crystallization of major mineral phases (e.g., amphibole, K-feldspar) probably plays a negligible role in generating such low REE concentrations. This supposition is supported by the fact that Dy/Yb in zircons does not decrease with increasing Hf concentrations (Figure 11A), implying no considerable amphibole fractionation (Davidson et al., 2007). Rather, Dy/Yb increases with Hf enrichment in zircons. This may indicate zircon separation, which reduces the Yb contents of the remnant melt. Eu/Eu^{*} values in zircon are high and are not linearly correlated with Hf concentrations (Figure 11B), eliminating the potential influence of plagioclase fractionation.

The effects of magma mixing, if it occurs, rely on the composition of the mixing end-members. The relatively depleted features of LREE require at least one end-member of REE-depleted melt, most likely the depleted mantle source. However, the low $Mg^{\#}$ numbers (<30), together with low Ni and Co concentrations (<2 ppm) imply that the mantle component is not involved in the magma genesis for the quartz porphyry. Therefore, the quartz porphyry was probably generated by the remelting of the REE-depleted lower crust at around 120 Ma.

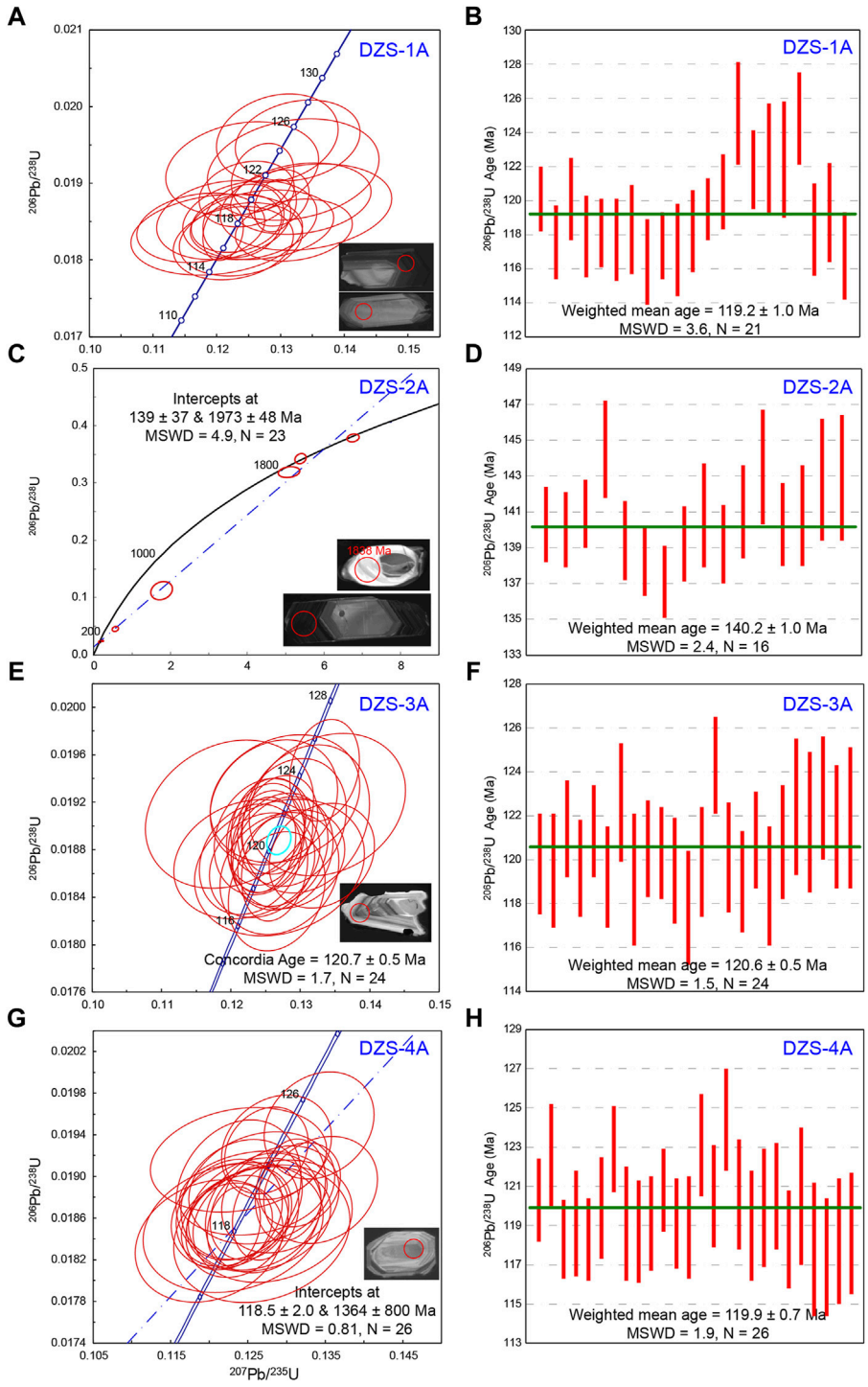


FIGURE 7
Zircon U-Pb concordia and weighted mean $^{238}U/^{206}Pb$ ages of the studied magmatic rocks. The red circles in the zircon grains are analytical spots and are 30 μm in diameter. **(A,B)** Quartz porphyry; **(C,D)** Linglong granite; **(E,F)** rhyolite porphyry; **(G,H)** Dazeshan biotite granite.

5.1.2 Rhyolite porphyry (DZS-3)

The rhyolite porphyry also features extremely low $Mg^{\#}$ values and low Ni and Co concentrations (Figure 10A; Table 1), ruling out the possibility of the involvement of the mantle component. These rocks show obvious Sr, P, and Ti depletion. Moreover, they are characterized by

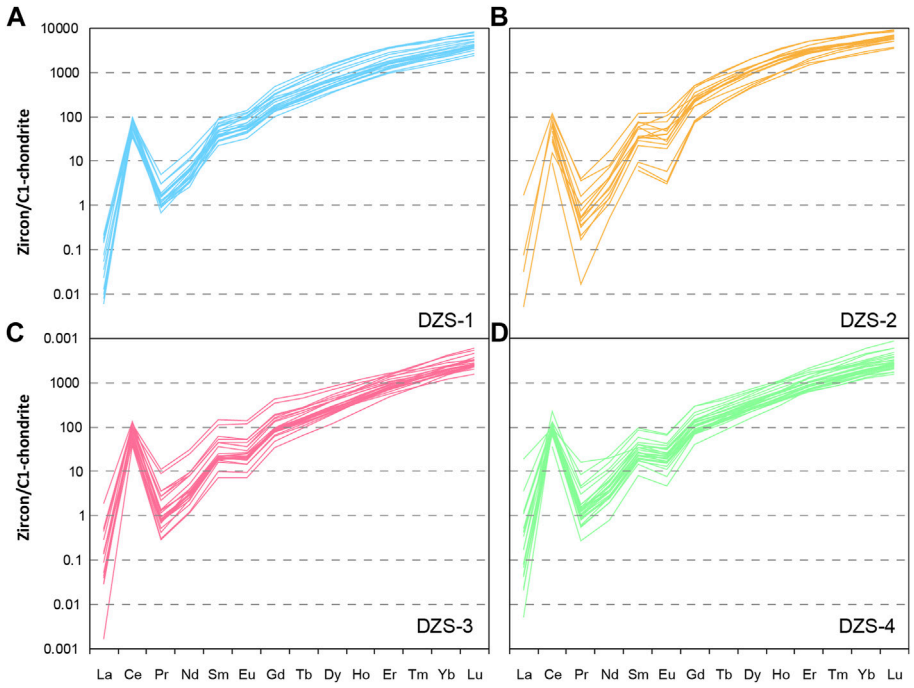


FIGURE 8
Zircon REE concentrations of quartz porphyry, Linglong granite, rhyolite porphyry, and Dazeshan biotite granite, respectively **(A–D)**. The normalization values are from Sun and McDonough (1989).

negative Eu anomalies and listric-shaped REE patterns (Figure 6A). These geochemical features imply that fractionation crystallization plays an important role in generating rhyolite porphyry. As shown in Figure 10B, whole-rock Dy/Yb ratios remain consistent with increasing Rb/Sr ratios, although the Rb/Sr ratios only show slight variation within samples. Zircon trace elements likely reflect more clear trends. The Zircon Dy/Yb ratio decreases from 0.45 to 0.1 when the Hf concentrations in zircon increase from 7,000 to 15,000 ppm (Figure 11A). Eu/Eu* values in zircon also show a decreasing trend with increasing Hf content (Figure 11B). This evidence supports the fractionation crystallization of amphibole and plagioclase. The amphibole incorporates more MREE (e.g., Dy) compared to HREE (e.g., Yb), thus leading to higher Dy/Yb values in the remnant melt (Davidson et al., 2007). Hafnium is an incompatible element during magmatic differentiation and its concentration will increase in the melt with progressive crystallization (Rollinson, 1993), which can be recorded in the co-crystallized zircon. In the current case, Dy/Yb decreases with increasing Hf content in zircon, implying amphibole fractionation. The negative Eu anomaly and decreasing zircon Eu/Eu* trend along with rising Hf concentrations reflect plagioclase fractionation because Eu preferentially partitions into plagioclase and replaces Ca in the lattice site under most geological environments.

Negative zircon Hf isotopes (−18.3 to −20.0) and the Archean two-stage Hf model ages suggest that the rhyolite porphyry is derived from the old crust source, consistent with the ancient nature of the NCC (Liu et al., 1992). Therefore, the rhyolite porphyry was derived from the melting of the ancient lower crust and experienced amphibole and plagioclase fractionation during magmatic evolution.

5.1.3 Dazeshan biotite granite (DZS-4)

The Dazeshan biotite granite shares overall similar geochemical features to those of the rhyolite porphyry in both REE pattern and spider diagram (Figure 6). Zircon trace elements and Hf isotopic compositions were almost identical (Figures 8–9, 11). Therefore, the origin of Dazeshan biotite granite was certainly the same as that of the rhyolite porphyry (crust anatexis with limited mantle contribution). The minor differences in REE and Sr concentrations were likely the result of discrepancies in differentiation processes between these two intrusions. As noted above, the negative Eu anomaly in the PM-normalized REE pattern and low zircon Eu/Eu* values indicated plagioclase fractionation. The listric-shaped REE pattern and decreasing zircon Dy/Yb values with rising Hf concentrations reflect amphibole-dominated fractionation. Therefore, it is reasonable to conclude that the Dazeshan biotite granite is derived from the partial

TABLE 2 LA-ICPMS U-Pb age data for zircons from Dazeshan magmatic rocks.

No.	207 Pb/ 235U	±σ %	206 Pb/ 238U	±σ %	ρ	207Pb/ 206 Pb	±σ %	207Pb/206 Pb age (Ma)	±σ	206 Pb/238U age (Ma)	±σ	207 Pb/235U age (Ma)	±σ	U (ppm)	Th (ppm)	Th/ U
DZS-1A																
1	0.1297	0.0039	0.0188	0.0003	0.1710	0.0494	0.0015	150	65	120.1	1.9	123.5	3.5	1,307	758	0.58
2	0.1321	0.0075	0.0184	0.0003	0.0470	0.0518	0.0030	180	110	117.5	2.1	125.0	6.7	316	211	0.67
3	0.1332	0.0090	0.0188	0.0004	0.0568	0.0514	0.0035	140	130	120.1	2.4	125.7	8.0	230	237	1.03
4	0.1271	0.0092	0.0185	0.0004	0.1030	0.0502	0.0037	110	140	117.9	2.4	120.2	8.3	196	144	0.74
5	0.1231	0.0058	0.0185	0.0003	0.1388	0.0485	0.0024	77	97	118.1	2.0	117.3	5.2	515	358	0.70
6	0.1175	0.0082	0.0184	0.0004	0.0592	0.0461	0.0034	−30	130	117.7	2.4	112.7	7.6	259	209	0.81
7	0.1252	0.0086	0.0185	0.0004	−0.0354	0.0494	0.0036	70	140	118.3	2.6	118.6	7.8	180	91	0.51
8	0.1226	0.0077	0.0182	0.0004	0.1759	0.0482	0.0030	70	120	116.4	2.5	116.6	7.0	267	127	0.47
9	0.1210	0.0026	0.0184	0.0003	0.3541	0.0475	0.0010	75	46	117.3	1.9	115.8	2.4	3,411	2084	0.61
10	0.1200	0.0110	0.0183	0.0004	0.1542	0.0476	0.0044	10	170	117.1	2.7	114.0	10.0	184	115	0.62
11	0.1242	0.0052	0.0185	0.0004	0.3177	0.0487	0.0020	117	86	118.2	2.4	118.6	4.7	1,119	471	0.42
12	0.1292	0.0027	0.0187	0.0003	0.2960	0.0494	0.0011	154	46	119.5	1.8	123.2	2.4	2,601	1,356	0.52
13	0.1247	0.0061	0.0189	0.0004	0.0785	0.0481	0.0025	56	98	120.5	2.2	118.7	5.5	466	211	0.45
14	0.1295	0.0078	0.0196	0.0005	0.1936	0.0481	0.0029	60	120	125.1	3.0	123.7	7.2	270	135	0.50
15	0.1272	0.0040	0.0191	0.0004	0.2233	0.0484	0.0016	97	68	121.8	2.3	121.8	3.7	1,206	862	0.71
16	0.1240	0.0098	0.0192	0.0005	−0.0522	0.0473	0.0039	−30	150	122.5	3.2	117.4	8.8	201	200	0.99
17	0.1320	0.0110	0.0192	0.0005	0.0577	0.0507	0.0047	100	180	122.4	3.4	126.0	11.0	196	118	0.60
18	0.1327	0.0080	0.0196	0.0004	0.2092	0.0491	0.0029	90	110	124.8	2.7	125.5	7.2	262	95	0.36
19	0.1211	0.0086	0.0185	0.0004	0.2171	0.0474	0.0034	10	130	118.3	2.7	114.8	7.7	190	110	0.58
20	0.1340	0.0110	0.0187	0.0005	0.1470	0.0522	0.0042	130	150	119.3	2.9	125.9	9.6	169	74	0.43
21	0.1238	0.0079	0.0183	0.0004	0.1023	0.0486	0.0031	70	130	116.7	2.5	117.5	7.1	258	212	0.82
DZS-2A																
1	0.1492	0.0036	0.0220	0.0003	0.2866	0.0490	0.0011	134	51	141.0	3.2	140.3	2.1	1844	937	0.51

(Continued on following page)

10.3389/feart.2022.1083608

TABLE 2 (*Continued*) LA-ICPMS U-Pb age data for zircons from Dazeshan magmatic rocks.

No.	207 Pb/ 235U	±σ %	206 Pb/ 238U	±σ %	ρ	207Pb/ 206 Pb	±σ %	207Pb/206 Pb age (Ma)	±σ	206 Pb/238U age (Ma)	±σ	207 Pb/235U age (Ma)	±σ	U (ppm)	Th (ppm)	Th/ U
2	0.1460	0.0036	0.0220	0.0003	0.3123	0.0479	0.0012	81	51	138.2	3.2	140.0	2.1	1835	1,188	0.65
3	0.1536	0.0039	0.0221	0.0003	0.2095	0.0503	0.0013	187	55	144.9	3.4	140.9	1.9	1,572	683	0.43
4	0.1536	0.0052	0.0227	0.0004	0.3013	0.0497	0.0017	157	74	144.8	4.6	144.5	2.7	1,467	789	0.54
5	0.1475	0.0028	0.0219	0.0004	0.2327	0.0489	0.0010	135	45	139.6	2.5	139.4	2.2	3,048	1866	0.61
6	0.1455	0.0033	0.0217	0.0003	0.1645	0.0485	0.0012	111	53	137.7	3.0	138.2	1.9	1,530	1,106	0.72
7	0.1465	0.0055	0.0215	0.0003	0.1122	0.0492	0.0018	137	80	138.8	4.9	137.1	2.0	593	188	0.32
8	0.1521	0.0061	0.0218	0.0003	0.0626	0.0508	0.0021	192	85	143.9	5.5	139.2	2.1	632	172	0.27
9	0.1454	0.0097	0.0221	0.0005	-0.0327	0.0478	0.0032	50	130	136.5	8.6	140.8	2.9	217	87	0.40
10	0.1536	0.0050	0.0218	0.0004	0.2430	0.0508	0.0016	209	68	144.8	4.4	139.2	2.2	852	258	0.30
11	0.1573	0.0056	0.0221	0.0004	0.2835	0.0514	0.0018	218	75	147.9	4.9	141.0	2.6	662	202	0.30
12	0.1508	0.0071	0.0225	0.0005	0.3310	0.0485	0.0022	100	93	141.9	6.3	143.5	3.2	453	58	0.13
13	0.1478	0.0043	0.0220	0.0004	0.2735	0.0484	0.0014	104	61	139.7	3.8	140.3	2.3	1,444	1,360	0.94
14	0.1540	0.0057	0.0221	0.0004	0.3470	0.0500	0.0017	167	72	145.0	5.0	140.8	2.8	849	72	0.08
15	0.1463	0.0077	0.0224	0.0005	0.3108	0.0469	0.0024	7	97	137.7	6.8	142.8	3.4	348	450	1.29
16	0.1553	0.0076	0.0224	0.0006	0.2971	0.0500	0.0024	180	100	146.2	6.6	142.9	3.5	876	68	0.08
17	6.7600	0.1300	0.3787	0.0056	0.4781	0.1295	0.0023	2078	30	2080	17.0	2069	26.0	134	85	0.63
18	5.0900	0.2300	0.3190	0.0077	0.2145	0.1181	0.0056	1838	86	1814	38.0	1781	37.0	14	40	2.85
19	5.3900	0.1200	0.3425	0.0072	0.5861	0.1123	0.0021	1826	35	1878	19.0	1900	35.0	164	96	0.59
20	0.1716	0.0078	0.0226	0.0005	0.3789	0.0546	0.0023	345	90	160.2	6.7	143.8	2.8	869	244	0.28
21	1.7700	0.2300	0.1120	0.0130	0.9813	0.1054	0.0034	1,687	63	921.0	78.0	668.0	71.0	349	86	0.25
22	0.2270	0.0170	0.0241	0.0006	0.3051	0.0678	0.0047	710	130	206.0	14.0	153.2	3.5	418	150	0.36
23	0.5630	0.0680	0.0451	0.0035	0.9629	0.0813	0.0036	1,144	89	423.0	38.0	283.0	21.0	480	160	0.33
DZS-3A																
1	0.1331	0.0062	0.0188	0.0004	0.0072	0.0508	0.0025	180	100	126.3	5.6	119.8	2.3	360	187	0.52
2	0.1223	0.0086	0.0187	0.0004	0.0557	0.0472	0.0035	−10	130	116.1	7.7	119.5	2.6	236	224	0.95

(Continued on following page)

10.3389/feart.2022.1083608

TABLE 2 (*Continued*) LA-ICPMS U-Pb age data for zircons from Dazeshan magmatic rocks.

No.	207 Pb/ 235U	±σ %	206 Pb/ 238U	±σ %	ρ	207Pb/ 206 Pb	±σ %	207Pb/206 Pb age (Ma)	±σ	206 Pb/238U age (Ma)	±σ	207 Pb/235U age (Ma)	±σ	U (ppm)	Th (ppm)	Th/ U
3	0.1270	0.0045	0.0190	0.0003	0.2608	0.0480	0.0017	81	73	121.1	4.1	121.4	2.2	885	337	0.38
4	0.1287	0.0063	0.0187	0.0003	0.2528	0.0493	0.0024	121	98	122.3	5.6	119.6	2.2	374	255	0.68
5	0.1254	0.0044	0.0190	0.0003	0.1855	0.0473	0.0016	56	72	119.7	4.0	121.3	2.1	1,101	463	0.42
6	0.1245	0.0062	0.0187	0.0004	0.0921	0.0480	0.0024	60	100	118.5	5.6	119.2	2.3	375	228	0.61
7	0.1262	0.0075	0.0192	0.0004	0.0237	0.0479	0.0030	30	120	119.7	6.8	122.6	2.7	260	237	0.91
8	0.1270	0.0100	0.0187	0.0005	-0.0235	0.0492	0.0040	60	150	120.2	8.9	119.1	3.0	179	283	1.58
9	0.1251	0.0045	0.0189	0.0004	0.2859	0.0479	0.0017	91	72	119.4	4.1	120.5	2.2	998	691	0.69
10	0.1247	0.0038	0.0188	0.0003	0.3156	0.0482	0.0015	89	64	119.1	3.4	120.3	2.1	1,278	1,037	0.81
11	0.1228	0.0060	0.0187	0.0004	0.2471	0.0479	0.0023	68	97	117.1	5.4	119.5	2.4	483	261	0.54
12	0.1266	0.0057	0.0185	0.0004	0.0700	0.0497	0.0025	130	100	121.3	5.0	117.8	2.6	512	241	0.47
13	0.1275	0.0059	0.0188	0.0004	0.1818	0.0499	0.0024	136	98	121.9	5.4	119.9	2.5	435	353	0.81
14	0.1335	0.0041	0.0195	0.0004	0.3119	0.0500	0.0015	170	63	126.9	3.7	124.3	2.2	1,533	921	0.60
15	0.1270	0.0057	0.0188	0.0004	0.1453	0.0497	0.0024	128	96	120.9	5.2	120.1	2.5	492	234	0.48
16	0.1263	0.0039	0.0186	0.0004	0.2897	0.0496	0.0016	153	65	120.6	3.5	119.0	2.3	1,235	523	0.42
17	0.1250	0.0046	0.0189	0.0004	0.1310	0.0484	0.0019	94	78	119.2	4.1	120.9	2.2	799	409	0.51
18	0.1270	0.0070	0.0186	0.0004	0.1238	0.0498	0.0028	130	110	120.7	6.3	118.8	2.7	348	189	0.54
19	0.1247	0.0058	0.0189	0.0004	0.0851	0.0484	0.0024	87	98	119.5	5.4	120.8	2.6	544	290	0.53
20	0.1339	0.0092	0.0192	0.0005	0.0650	0.0517	0.0037	160	140	127.4	8.4	122.4	3.1	211	251	1.19
21	0.1308	0.0075	0.0191	0.0005	0.0510	0.0504	0.0030	150	120	124.1	6.7	121.7	3.2	281	279	0.99
22	0.1278	0.0088	0.0192	0.0004	0.1647	0.0490	0.0034	70	130	120.9	7.9	122.8	2.8	265	191	0.72
23	0.1288	0.0064	0.0190	0.0004	0.1900	0.0496	0.0024	135	99	122.4	5.8	121.5	2.8	442	239	0.54
24	0.1198	0.0099	0.0191	0.0005	0.1635	0.0461	0.0038	−70	150	113.3	8.9	121.9	3.2	185	305	1.65
DZS-4A																
1	0.1257	0.0078	0.0188	0.0003	0.0917	0.0490	0.0031	70	120	119.3	7.0	120.3	2.1	284	203	0.72
2	0.1238	0.0093	0.0192	0.0004	0.1395	0.0472	0.0035	−20	140	117.9	8.4	122.6	2.6	208	235	1.13

(Continued on following page)

10.3389/feart.2022.1083608

TABLE 2 (*Continued*) LA-ICPMS U-Pb age data for zircons from Dazeshan magmatic rocks.

No.	207 Pb/ 235U	±σ %	206 Pb/ 238U	±σ %	ρ	207Pb/ 206 Pb	±σ %	207Pb/206 Pb age (Ma)	±σ	206 Pb/238U age (Ma)	±σ	207 Pb/235U age (Ma)	±σ	U (ppm)	Th (ppm)	Th/ U
3	0.1232	0.0028	0.0185	0.0003	0.4343	0.0484	0.0010	121	47	117.8	2.5	118.3	2.0	3,275	2,233	0.68
4	0.1226	0.0056	0.0187	0.0004	0.1726	0.0485	0.0024	77	96	116.9	5.0	119.1	2.7	403	390	0.97
5	0.1223	0.0048	0.0185	0.0003	0.3027	0.0483	0.0017	99	74	117.3	4.3	118.3	2.1	1,021	539	0.53
6	0.1292	0.0062	0.0188	0.0004	0.1193	0.0497	0.0024	150	99	122.7	5.6	119.9	2.6	540	787	1.46
7	0.1274	0.0044	0.0193	0.0003	0.2315	0.0483	0.0016	94	69	121.5	3.9	122.9	2.2	1,215	715	0.59
8	0.1270	0.0061	0.0187	0.0005	0.1663	0.0496	0.0025	150	100	121.0	5.5	119.1	2.9	707	676	0.96
9	0.1264	0.0076	0.0186	0.0004	0.0393	0.0501	0.0032	110	120	120.0	6.8	118.7	2.6	353	271	0.77
10	0.1273	0.0035	0.0187	0.0004	0.4760	0.0497	0.0012	167	53	121.4	3.1	119.1	2.4	2,703	1,268	0.47
11	0.1317	0.0043	0.0189	0.0003	0.2500	0.0509	0.0017	204	71	125.4	3.9	120.8	2.1	1,351	1,032	0.76
12	0.1254	0.0043	0.0186	0.0004	0.2975	0.0488	0.0016	118	71	119.7	3.9	119.1	2.3	1,159	679	0.59
13	0.1227	0.0062	0.0186	0.0004	0.1707	0.0478	0.0023	80	100	117.0	5.5	118.9	2.6	550	406	0.74
14	0.1287	0.0058	0.0193	0.0004	0.3724	0.0487	0.0020	111	83	122.5	5.2	123.1	2.6	940	790	0.84
15	0.1305	0.0037	0.0189	0.0004	0.4446	0.0500	0.0013	184	57	124.3	3.3	120.5	2.6	1825	1,428	0.78
16	0.1342	0.0058	0.0195	0.0004	0.1741	0.0507	0.0022	186	92	128.7	5.5	124.4	2.6	626	561	0.90
17	0.1268	0.0077	0.0189	0.0004	0.2470	0.0494	0.0030	90	120	121.1	7.1	120.6	2.8	298	230	0.77
18	0.1259	0.0070	0.0186	0.0004	0.1977	0.0496	0.0028	110	110	120.4	6.4	119.0	2.8	315	214	0.68
19	0.1242	0.0064	0.0188	0.0005	0.1944	0.0480	0.0025	90	100	119.0	5.9	119.9	3.0	409	279	0.68
20	0.1344	0.0060	0.0189	0.0004	0.2450	0.0519	0.0023	229	94	128.1	5.5	120.5	2.7	504	377	0.75
21	0.1236	0.0054	0.0185	0.0004	0.1627	0.0485	0.0021	104	90	117.8	4.9	118.3	2.5	568	396	0.70
22	0.1238	0.0066	0.0189	0.0006	0.2921	0.0476	0.0024	70	100	117.9	6.0	120.5	3.5	419	339	0.81
23	0.1268	0.0093	0.0185	0.0005	0.0179	0.0504	0.0039	100	150	119.8	8.4	117.8	3.4	181	148	0.82
24	0.1200	0.0078	0.0184	0.0005	0.0888	0.0480	0.0032	20	130	114.2	7.0	117.4	3.0	254	221	0.87
25	0.1231	0.0095	0.0185	0.0005	0.1911	0.0485	0.0038	20	140	116.5	8.5	118.2	3.2	189	155	0.82
26	0.1282	0.0084	0.0186	0.0005	0.2125	0.0503	0.0033	120	130	121.4	7.5	118.6	3.1	386	435	1.13

10.3389/feart.2022.1083608

TABLE 3 Zircon trace element data for zircons from Dazeshan magmatic rocks.

	Age	P	Ti	Y	Nb	La	Ce	Pr	Nd	Sm	Eu	Gd	Tb	Dy	Ho	Er	Tm	Yb	Lu	Hf
DZS_1A_3	120.1	440	7.6	3,600	15.3	0.005	51.4	0.083	1.66	8.61	5.52	64.3	23.6	304	117	559	115	1,034	200	11,160
DZS_1A_4	117.5	200	5.7	1,648	2.8	0.037	32.7	0.143	2.78	6.49	3.69	35.8	11.8	141	53.1	255	53.1	475	97.1	10,180
DZS_1A_6	120.1	260	8.5	1,680	2.0	0.036	48.4	0.294	4.72	10.1	5.75	49.6	14.6	155	56.1	264	51.6	467	97.2	9,170
DZS_1A_7	117.9	326	5.4	1,519	1.5	0.001	37.0	0.162	2.71	5.48	3.31	31.6	10.1	126	48.1	244	52.2	470	103	8,650
DZS_1A_8	118.1	302	4.5	2040	3.2	0.003	26.1	0.093	1.22	5.37	3.12	35.0	12.4	168	65.9	346	69.4	620	128	10,810
DZS_1A_9	117.7	245	8.9	1700	2.9	0.002	45.9	0.161	3.21	7.31	4.04	41.8	13.1	159	56.7	269	55.0	481	100	9,440
DZS_1A_10	118.3	152	4.6	976	1.0	0.050	20.6	0.164	3.21	5.81	2.95	25.9	7.57	88.6	31.9	151	31.5	284	58.6	9,950
DZS_1A_11	116.4	207	8.9	1,524	2.9	0.041	36.3	0.126	1.98	4.40	2.66	27.9	10.1	127	48.7	246	49.7	450	95.1	9,730
DZS_1A_12	117.3	329	10.2	4,190	35.0	—	58.9	0.093	2.30	13.1	7.83	94.6	33.2	395	140	606	117	934	171	13,710
DZS_1A_14	117.1	230	4.2	1,230	1.3	0.013	24.6	0.180	3.68	6.80	3.43	30.6	9.39	110	39.9	190	42.0	376	79.2	9,970
DZS_1A_15	118.2	301	8.6	3,690	15.2	—	47.2	0.066	1.58	7.13	5.56	63.4	23.8	311	121	576	115	1,005	194	12,110
DZS_1A_16	119.5	312	9.3	3,860	32.5	0.052	52.5	0.096	1.91	10.6	6.77	77.5	28.6	358	129	580	110	924	166	13,360
DZS_1A_18	120.5	217	10.0	2,595	7.3	—	50.1	0.097	1.86	5.69	4.10	47.1	17.3	221	86.3	409	80.5	718	143	10,920
DZS_1A_19	125.1	192	8.8	1,607	3.6	0.042	39.1	0.162	2.97	5.94	2.92	32.1	11.3	140	54.1	256	52.7	489	99.2	9,870
DZS_1A_20	121.8	272	11.3	2,880	16.0	—	61.1	0.109	2.66	9.23	5.86	64.6	21.5	261	96.4	441	86.4	759	143	11,110
DZS_1A_21	122.5	281	10.2	1884	2.5	0.018	59.9	0.288	5.38	9.34	5.05	48.6	14.4	175	65.7	300	61.5	561	117	8,710
DZS_1A_22	122.4	249	5.3	1,310	1.6	0.008	25.4	0.155	3.01	5.09	3.10	28.6	8.76	110	41.1	209	44.5	430	89.2	9,710
DZS_1A_23	124.8	191	7.9	1,362	3.7	0.002	28.3	0.090	1.49	4.03	2.42	26.1	9.34	115	46.6	227	47.4	406	88.4	9,970
DZS_1A_24	118.3	212	10.1	1,294	2.3	—	35.1	0.112	2.09	4.29	2.55	26.6	9.03	112	41.7	201	44.2	394	84.3	9,280
DZS_1A_26	119.3	176	7.2	1,006	1.7	—	24.1	0.098	1.59	3.28	1.87	20.5	6.74	84.4	34.2	165	34.3	312	65.2	9,390
DZS_1A_27	116.7	254	5.1	1829	2.0	0.033	48.8	0.473	7.70	13.0	7.07	56.9	15.6	179	60.5	283	58.2	545	107	10,170
DZS_2A_1	141.0	333	4.6	3,112	42.3	—	36.6	0.02	0.69	5.22	1.73	47.6	18.5	264	104	472	88.1	752	139	14,600
DZS_2A_2	138.2	556	6.0	3,990	37.4	—	41.5	0.05	1.81	8.49	1.57	69.6	25.8	355	131	568	107	843	152	15,900
DZS_2A_3	144.9	347	5.5	3,370	48.7	0.02	41.0	0.05	1.08	5.12	1.73	45.4	19.1	277	107	510	98.7	840	151	14,170
DZS_2A_4	144.8	385	10.3	5,700	36.6	—	47.6	0.07	2.09	10.9	4.43	102	38.0	492	189	825	152	1,233	213	12,450
DZS_2A_5	139.6	627	9.2	5,810	97.1	0.40	72.7	0.34	3.64	11.5	2.72	91.5	36.3	501	185	826	149	1,212	203	14,680

(Continued on following page)

10.3389/feart.2022.1083608

TABLE 3 (*Continued*) Zircon trace element data for zircons from Dazeshan magmatic rocks.

	Age	P	Ti	Y	Nb	La	Ce	Pr	Nd	Sm	Eu	Gd	Tb	Dy	Ho	Er	Tm	Yb	Lu	Hf
DZS_2A_8	137.7	288	7.8	3,121	33.2	—	40.5	0.05	1.86	7.83	2.99	58.9	22.2	278	103	455	85.9	678	125	13,210
DZS_2A_10	138.8	408	3.6	3,410	7.75	—	18.8	0.04	1.16	4.84	2.23	47.5	19.0	272	107	519	102	862	161	12,640
DZS_2A_11	143.9	499	3.7	4,330	14.2	—	22.0	0.03	0.65	5.37	2.23	49.9	22.4	330	137	674	138	1,206	229	12,260
DZS_2A_12	136.5	154	5.5	1772	2.08	0.00	9.22	0.10	1.88	4.94	3.09	35.2	11.8	148	56.1	262	49.7	428	84.9	10,220
DZS_2A_13	144.8	286	6.0	3,570	30.6	—	28.6	0.03	0.88	4.36	1.36	43.3	19.0	278	113	541	105	888	161	13,370
DZS_2A_15	147.9	391	2.9	2,790	12.6	—	16.8	0.02	0.51	3.37	1.10	34.6	15.3	223	90.5	438	87.2	765	143	12,940
DZS_2A_16	141.9	286	0.9	1,483	11.0	—	5.49	0.00	0.23	1.41	0.32	15.7	7.26	110	45.9	240	52.6	482	92.5	18,250
DZS_2A_18	139.7	344	17.9	3,850	33.2	0.01	60.2	0.39	7.90	17.2	6.87	98.3	31.1	349	122	534	97.4	778	138	12,090
DZS_2A_21	145.0	354	–	1,654	27.8	—	5.57	—	—	0.90	0.18	14.3	7.35	115	55.7	289	69.4	641	125	23,950
DZS_2A_22	137.7	253	12.9	2,750	11.7	—	51.5	0.15	3.27	8.91	5.84	54.3	18.7	242	95.1	444	94.1	869	171	9,610
DZS_2A_23	146.2	349	1.3	1831	32.1	—	5.63	—	—	1.11	0.20	15.8	8.52	133	55.7	319	77.0	712	140	23,900
DZS_2A_7	2078	336	5.4	996	5.10	—	17.7	0.06	1.36	2.96	0.36	21.3	7.24	90.3	34.1	161	33.1	289	58.6	10,750
DZS_2A_9	1838	198	6.1	253	0.35	—	4.09	0.03	0.33	0.90	0.09	4.94	1.92	22.0	8.42	39.2	7.98	72.2	14.9	12,150
DZS_2A_25	1826	531	4.9	1,281	8.96	—	11.6	0.02	0.54	1.96	0.38	18.3	7.86	108	44.6	225	47.2	421	81.5	11,970
DZS_2A_14	149.4	200	1.6	934	8.28	—	4.44	0.02	0.28	1.08	0.64	9.93	4.54	68.0	29.9	155	32.4	294	61.5	21,850
DZS_2A_17	160.2	563	4.1	3,850	28.5	1.72	27.1	1.03	6.73	6.62	1.52	47.0	21.3	287	120	584	113	989	175	15,540
DZS_2A_19	921.0	420	4.4	2,140	12.2	2.00	25.7	0.90	5.50	4.24	1.13	29.8	12.4	177	70.5	332	67.4	604	109	13,350
DZS_2A_20	206.0	337	6.0	2,510	5.37	0.06	13.4	0.07	1.08	4.32	2.05	36.7	14.0	198	78.8	396	78.4	735	133	10,230
DZS_2A_24	423.0	277	4.9	2,590	19.3	—	26.6	0.05	1.07	4.70	1.23	38.4	15.6	209	86.5	401	79.9	739	126	13,680
DZS_3A_2	119.8	112	3.9	734	4.05	—	36.7	0.05	0.82	2.35	0.84	13.1	4.20	53.6	21.1	112	26.7	270	60.6	10,810
DZS_3A_3	119.5	69.0	2.9	612	1.66	—	30.4	0.06	1.84	3.30	1.42	16.5	4.73	51.8	19.8	91.9	20.1	197	39.3	11,420
DZS_3A_4	121.4	51.0	1.8	526	3.21	0.00	22.9	0.03	0.52	1.07	0.41	6.89	2.35	29.8	13.1	75.6	20.6	238	57.0	14,130
DZS_3A_5	119.6	138	4.7	926	4.75	0.01	56.3	0.11	1.84	3.71	1.48	19.5	6.05	72.7	28.0	137	30.4	309	67.0	10,640
DZS_3A_6	121.3	167	2.1	848	5.02	—	30.8	0.03	0.57	1.48	0.54	9.69	3.44	46.9	21.5	127	32.6	367	92.0	12,760
DZS_3A_7	119.2	114	3.5	763	4.13	—	45.4	0.07	1.16	3.07	1.05	15.7	5.10	60.4	22.9	118	26.1	265	58.2	10,870
DZS_3A_8	122.6	288	5.1	1,085	2.71	0.02	56.5	0.26	3.76	6.75	2.60	30.9	8.66	96.7	34.0	154	31.3	292	57.1	10,220

(Continued on following page)

10.3389/feart.2022.1083608

TABLE 3 (*Continued*) Zircon trace element data for zircons from Dazeshan magmatic rocks.

	Age	P	Ti	Y	Nb	La	Ce	Pr	Nd	Sm	Eu	Gd	Tb	Dy	Ho	Er	Tm	Yb	Lu	Hf
DZS_3A_9	119.1	236	8.8	1,661	1.64	0.12	56.4	0.84	11.2	16.8	6.57	68.5	16.7	175	55.0	226	44.8	383	75.4	8,410
DZS_3A_10	120.5	123	3.4	1,461	7.41	0.01	59.4	0.13	2.39	5.25	1.64	26.8	7.91	95.7	40.2	209	51.0	513	115	11,960
DZS_3A_11	120.3	189	4.8	1805	10.5	0.45	79.8	0.33	3.68	6.59	2.02	33.2	10.1	130	50.8	252	62.1	618	132	11,160
DZS_3A_12	119.5	165	3.2	759	2.36	0.03	33.6	0.13	1.52	3.20	1.37	15.8	4.91	58.0	22.0	110	26.2	254	58.4	11,520
DZS_3A_13	117.8	132	3.3	683	3.15	0.01	28.7	0.04	1.09	2.60	0.83	12.2	3.92	48.6	20.6	103	25.7	266	63.3	11,890
DZS_3A_14	119.9	191	4.4	1,072	4.11	0.12	65.5	0.22	3.65	6.72	2.03	27.5	8.51	94.0	34.3	165	35.1	322	66.6	11,180
DZS_3A_15	124.3	125	4.2	1,582	17.3	0.03	79.1	0.09	1.36	2.96	1.02	19.0	6.99	96.6	43.0	238	60.8	670	151	12,830
DZS_3A_16	120.1	122	3.5	812	4.50	0.04	38.5	0.08	1.32	2.84	1.08	16.9	5.16	63.5	24.9	125	29.0	285	63.8	11,240
DZS_3A_17	119.0	131	2.0	993	4.34	0.03	26.3	0.07	1.01	3.29	1.18	18.1	5.95	71.1	26.8	146	33.5	361	77.1	13,170
DZS_3A_18	120.9	116	3.2	981	6.78	—	48.3	0.07	1.38	3.00	1.01	17.0	5.51	70.6	28.5	146	36.9	384	83.5	11,970
DZS_3A_19	118.8	131	4.2	808	4.29	—	44.2	0.08	1.18	2.72	1.21	15.8	5.18	65.0	24.8	124	27.1	272	58.2	10,510
DZS_3A_20	120.8	130	2.1	760	2.29	—	23.7	0.07	1.16	3.02	1.17	15.2	4.54	55.2	22.4	119	29.6	316	66.9	13,010
DZS_3A_21	122.4	304	9.3	1,260	3.80	0.07	76.2	0.34	4.39	8.01	2.90	36.6	9.64	115	40.3	189	38.7	360	69.6	8,800
DZS_3A_23	121.7	147	4.3	1,117	2.00	0.01	54.8	0.27	4.40	9.07	2.91	38.9	9.98	107	37.8	172	35.4	305	60.9	10,170
DZS_3A_24	122.8	129	4.5	743	3.72	0.11	54.3	0.12	1.64	3.29	1.28	18.1	5.18	64.7	24.7	116	27.2	252	49.8	9,970
DZS_3A_25	121.5	123	4.1	806	5.08	0.01	46.6	0.08	1.50	2.82	1.16	15.9	5.35	66.1	25.3	131	29.5	308	61.4	10,000
DZS_3A_26	121.9	221	7.4	1822	1.69	0.11	72.6	1.06	14.2	22.1	7.66	84.2	20.2	207	64.1	260	49.9	452	79.9	8,330
DZS_4A_1	120.3	106	2.9	714	3.50	—	41.5	0.06	1.18	2.78	0.88	14.5	4.80	56.4	21.5	113	24.4	238	52.2	11,420
DZS_4A_2	122.6	188	4.0	670	2.54	0.01	45.7	0.10	1.69	3.31	1.13	14.9	5.10	60.4	21.1	104	21.9	210	42.9	10,470
DZS_4A_3	118.3	157	2.6	2,331	22.4	0.30	73.4	0.16	1.70	4.00	0.88	27.7	10.4	139	61.5	353	88.9	966	214	14,730
DZS_4A_4	119.1	132	3.3	1,128	3.83	0.02	54.7	0.17	2.96	5.09	1.90	29.0	8.28	97.2	34.9	167	34.9	329	67.6	10,800
DZS_4A_5	118.3	127	3.2	896	5.67	0.13	42.7	0.14	1.59	3.37	1.11	18.2	5.41	66.9	26.3	137	31.9	312	69.2	11,940
DZS_4A_6	119.9	287	5.9	1819	6.74	0.04	135	0.46	7.45	13.0	3.69	59.4	16.1	182	61.1	274	53.4	491	94.9	9,440
DZS_4A_8	122.9	87.0	3.3	1,232	10.9	0.02	47.7	0.06	0.93	2.50	0.72	15.5	5.84	80.3	33.7	197	47.3	501	108	11,710
DZS_4A_9	119.1	108	2.7	872	5.63	0.04	55.2	0.08	1.27	3.00	0.93	15.8	5.08	66.0	24.7	128	29.4	281	61.3	11,470
DZS_4A_10	118.7	154	3.9	901	4.70	0.00	56.6	0.09	1.71	3.83	1.23	20.7	6.31	74.6	29.3	149	33.1	305	62.9	10,440

(Continued on following page)

10.3389/feart.2022.1083608

TABLE 3 (*Continued*) Zircon trace element data for zircons from Dazeshan magmatic rocks.

	Age	P	Ti	Y	Nb	La	Ce	Pr	Nd	Sm	Eu	Gd	Tb	Dy	Ho	Er	Tm	Yb	Lu	Hf
DZS_4A_11	119.1	270	2.1	1,388	13.2	0.01	62.8	0.05	0.91	2.17	0.43	13.6	5.31	78.2	36.1	216	59.0	683	151	13,610
DZS_4A_13	120.8	174	3.4	1,688	5.69	0.26	54.7	0.29	4.57	6.74	2.19	35.3	11.1	127	49.8	256	55.5	547	117	11,460
DZS_4A_14	119.1	199	2.1	710	5.47	—	22.6	0.03	0.37	1.22	0.26	8.10	2.99	41.2	17.4	113	28.6	316	70.8	12,530
DZS_4A_15	118.9	370	4.3	970	4.01	0.02	55.5	0.13	2.02	3.97	1.17	21.8	6.87	79.5	29.2	145	32.6	320	65.0	10,430
DZS_4A_16	123.1	190	4.8	1,332	7.85	0.01	76.7	0.13	2.71	5.83	1.43	29.3	9.47	109	41.7	203	47.2	431	89.6	10,780
DZS_4A_17	120.5	126	3.7	1999	9.92	0.26	60.2	0.40	5.34	8.70	2.43	42.2	12.4	152	57.5	305	70.6	736	148	12,640
DZS_4A_19	124.4	179	3.5	1,102	4.40	—	44.1	0.13	2.31	5.15	1.34	25.1	7.43	88.9	31.8	162	39.5	388	73.4	11,360
DZS_4A_20	120.6	255	4.5	888	2.60	0.01	44.4	0.14	2.15	4.62	1.32	21.4	6.43	74.9	29.8	134	31.8	265	53.4	10,730
DZS_4A_21	119.0	125	4.0	720	3.81	0.10	39.5	0.10	1.34	2.88	0.88	15.4	4.88	61.2	22.0	111	26.5	250	51.5	11,020
DZS_4A_22	119.9	135	3.8	826	5.12	—	47.6	0.08	1.28	3.24	0.95	16.1	5.27	67.7	25.1	129	29.8	290	58.5	10,500
DZS_4A_23	120.5	110	3.3	737	5.62	0.10	47.9	0.08	1.12	2.62	0.63	13.4	4.39	54.6	21.3	115	27.5	279	55.9	11,630
DZS_4A_24	118.3	145	4.4	1,108	7.26	0.08	60.5	0.10	1.59	3.40	1.09	21.6	6.89	86.6	34.8	173	41.3	413	81.6	10,820
DZS_4A_25	120.5	132	3.6	1,084	3.15	0.01	47.2	0.14	3.44	5.97	1.88	27.7	8.45	97.7	36.0	166	38.2	368	68.0	10,890
DZS_4A_26	117.8	313	4.7	666	2.19	—	44.4	0.12	1.76	3.85	1.09	17.4	5.73	60.8	20.9	102	21.7	208	38.3	9,320
DZS_4A_27	117.4	222	5.9	1,043	4.47	0.02	78.2	0.17	2.74	5.94	1.71	26.7	7.50	91.1	32.6	159	34.9	308	60.3	9,720
DZS_4A_28	118.2	423	4.1	727	2.29	4.60	59.4	1.56	9.00	4.97	1.47	20.6	6.34	63.8	23.5	115	24.5	235	42.5	9,850
DZS_4A_29	118.6	286	4.5	1,586	2.92	0.87	82.4	0.82	10.0	14.5	3.83	59.4	14.8	160	55.7	247	50.7	448	78.8	10,410

10.3389/feart.2022.1083608

TABLE 4 Zircon Hf isotope data for the rhyolite porphyry and Dazeshan biotite granite.

Spot no.	$^{176}Yb/^{177}Hf$	2σ	$^{176}Lu/^{177}Hf$	2σ	$^{176}Hf/^{177}Hf$	2σ	εHf (t)	T_{DM1} (Ma)	T_{DM2} (Ma)	$f_{Lu/Hf}$	Age
DZS-3A-2	0.042275	0.000167	0.001093	0.000005	0.282177	0.000015	−18.5	1,521	3,290	−0.9671	119.8
DZS-3A-4	0.033602	0.000317	0.000916	0.000009	0.282133	0.000013	−20.0	1,575	3,425	−0.9724	121.4
DZS-3A-5	0.031352	0.000349	0.000776	0.000008	0.282175	0.000014	−18.5	1,510	3,292	−0.9766	119.6
DZS-3A-6	0.038969	0.000316	0.001067	0.000007	0.282181	0.000013	−18.3	1,513	3,273	−0.9679	121.3
DZS-3A-9	0.039306	0.000836	0.000937	0.000019	0.282181	0.000015	−18.4	1,508	3,276	−0.9718	119.1
DZS-3A-11	0.040962	0.000431	0.001003	0.000010	0.282140	0.000014	−19.8	1,568	3,404	−0.9698	120.3
DZS-4A-1	0.027038	0.000154	0.000678	0.000005	0.282195	0.000017	−17.8	1,479	3,229	−0.9796	120.3
DZS-4A-6	0.035255	0.000556	0.000911	0.000014	0.282161	0.000015	−19.0	1,536	3,336	−0.9726	122.9
DZS-4A-8	0.038623	0.000698	0.000964	0.000019	0.282130	0.000013	−20.2	1,580	3,436	−0.9710	119.1
DZS-4A-9	0.036108	0.000394	0.000882	0.000011	0.282147	0.000015	−19.6	1,554	3,385	−0.9734	118.7
DZS-4A-10	0.041680	0.000512	0.000988	0.000012	0.282141	0.000013	−19.8	1,566	3,402	−0.9702	119.9

10.3389/feart.2022.1083608

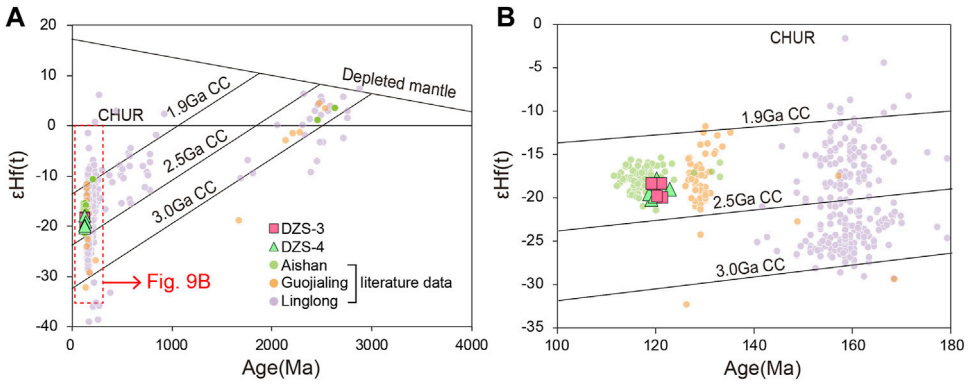


FIGURE 9
Zircon Hf isotopic data from rhyolite porphyry **(A)** and Dazeshan biotite granite **(B)**. Published zircon isotope data are compiled from Yang et al. (2012; 2017), Ma et al. (2013; 2014), and Li et al. (2019).

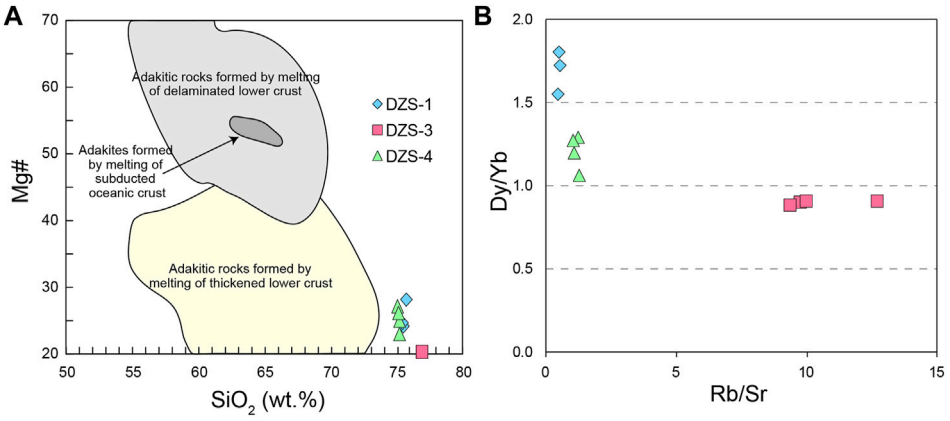


FIGURE 10
$Mg^{\#}$ vs. SiO_2 **(A)** and Dy/Yb vs. Rb/Sr **(B)** diagrams. Adakite fields are adopted from Sen and Dunn (1994), Rapp and Watson (1995), and Rapp et al. (1999) and references therein.

melting of the lower crust with subsequent fractionation crystallization.

5.2 Multiple reworking events of the NCC lower crust

Previous studies have shown that the widely distributed Jurassic Linglong granite in the Jiaodong Penisular has adakite-like geochemical signatures with high Sr/Y and La/Yb ratios, which were considered to be the result of the melting of the thickened lower crust at the garnet stability field (Ma et al., 2013; Yang et al., 2017). The geodynamic model for the crustal thickening is probably related to the subduction of the Paleo-Pacific plate (Wu et al., 2005b; Ma et al., 2013). This left a residue with large portions of garnet in the lower crust, which by inference should be depleted of LILE and LREE due to the prior melt extraction. The crust-mantle interaction was strikingly extensive during the Early Cretaceous (~130 Ma) given the widespread granitic and/or mafic magmatism and extensional deformation-related sedimentary basins (Wu et al., 2005b; Cai et al., 2013; Yang et al., 2018a, b; Meng et al., 2019). Furthermore, the ~130 Ma granitic rocks in Jiaodong (e.g., Guojialing pluton), which also show adakite-like characters, were interpreted to be derived either from the melting of the delaminated eclogitic crust (Hou et al., 2007) or multi-stage magma mixing between Archean lower crust derived felsic magma

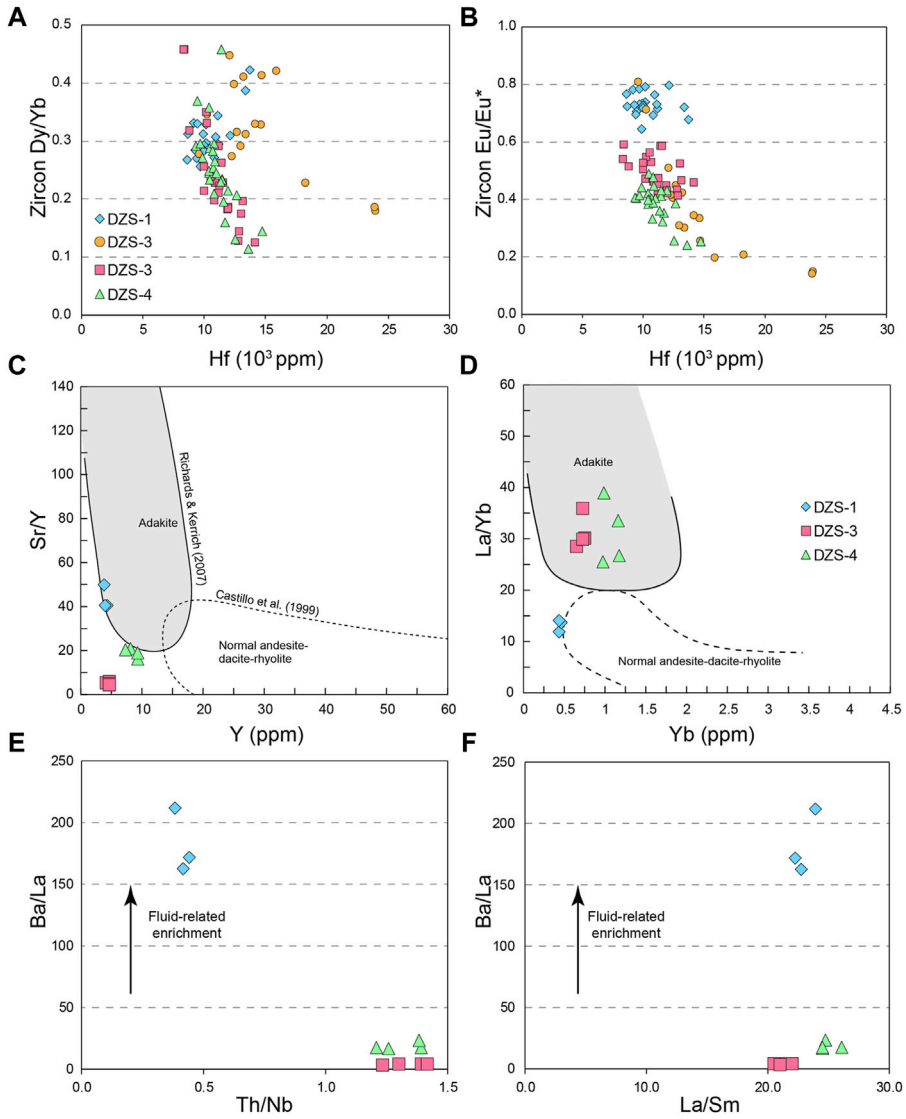


FIGURE 11
Zircon Dy/Yb **(A)** and Eu/Eu* **(B)** vs. Hf contents for the studied magmatic rocks. **(C)** Sy/Y vs. Y plot. The adakite and normal andesite-dacite-rhyolite fields are from Richards and Kerrich (2007) and Castillo et al. (1999), respectively. **(D)** La/Yb vs. Yb plot. Ba/La vs. Th/Nb **(E)** and La/Sm **(F)** plots. See the text for explanation.

and mafic lower crust-derived dioritic magma (Jiang et al., 2016).

The three intrusions are emplaced at around 120 Ma based on the zircon U-Pb ages obtained in the present study (Figure 7). These magmatic rocks were derived from the melting of the ancient lower crust of the NCC, as discussed in the previous section. The strontium concentrations for these samples (<200 ppm) are not as high as those in the Linglong and Guojialing magmatic rocks reported by Yang et al. (2012) (>300 ppm). Consequently, the Sr/Y values of the quartz porphyry, rhyolite porphyry, and the Dazeshan biotite granite are low (Figure 11C), unlike the Jurassic and Early Cretaceous granitoids in Jiaodong. However, the La/Yb ratios are high and plot within the "adakite field" (Figure 11D) (Condie, 2005; Castillo, 2006). This antinomy can be explained by the dominant crystal fractionation of amphibole and plagioclase during the magmatic evolution. As mentioned above, limited crystal fractionation occurred in the parent magma of the quartz porphyry. Therefore, the Sr/Y and La/Yb ratios probably represent its original character in these magmatic rocks. The low Sr/Y and La/Yb ratios (<50 and <15, respectively; Figures 11C, D), imply that little or no garnet remained as a residue phase in the source. Thus, the quartz porphyry may have been derived

from a shallow crustal level rather than a thickened lower crust (>50 km) as in Linglong granite. Fluid flux played an important role in inducing the melting reaction because the Ba/La ratios for these samples are elevated (Figures 11E, F). Barium is a fluid mobile element, while the La is less so (Kessel et al., 2005). Therefore, the subduction-related fluid carried more Ba than La and generated high Ba/La ratios in the resultant magma.

The rhyolite porphyry and Dazeshan biotite granite, however, experienced amphibole + plagioclase fractionation, as evidenced by the geochemical data. Both suites have low Sr/Y but high La/Yb ratios. We propose that the plagioclase fractionation depleted the Sr concentration in the remnant melt but did not affect the La or Yb contents of the magma. Garnet, which retains most of the Y and Yb in the source, should have been stable when the parent magma of the rhyolite porphyry and the Dazeshan biotite granite formed. Under such a scenario, these two suites were probably generated by melting of a thicker crust compared to the quartz porphyry. These two suites were most likely formed by dehydration melting considering the low Ba/La but high Th/Nb and La/Sm ratios in these samples. Thorium is more incompatible than Nb while La is more incompatible than Sm; thus, Th/Nb and La/Sm ratios would be promoted during dehydration melting when no external element is introduced into the system.

Therefore, the melting may have occurred at different crustal levels at around 120 Ma, with distinct triggers. The fluid responsible for the fluxed melting very likely originated from the upwelling mafic magma, which was ultimately sourced from the dehydration of the subducted Paleo-Pacific plate (Windley et al., 2010; Geng et al., 2019). The dehydration melting in the case of rhyolite porphyry and the Dazeshan biotite granite may have been induced by heat loss from the underplated mafic magma. Regardless of fluid fluxed or dehydration melting, this change required a deeper source of heat and fluid. This required water-rich mafic magma, among which lithosphere mantle-derived magma is a possible candidate (Geng et al., 2019).

6 Conclusion

The results of this study reveal that the magmatic rocks in the Dazeshan region have zircon ages of ~120 Ma and were generated by crustal melting; however, they experienced different melting/differentiation processes. The quartz porphyry was formed by fluid-mediated melting without apparent crystal crystallization. The rhyolite porphyry and the Dazeshan biotite granite were produced by dehydration melting and underwent amphibole and plagioclase fractionation, as indicated by whole-rock and zircon trace element data. Our results imply that, in the Early Cretaceous, the lower crust of the NCC was reworked multiple times in different ways. The driving force for the reworking probably invoked the underplating of water-rich mafic magma under an extensional regime (Li et al., 2012), which not only provided fluid to generate the quartz porphyry but also released heat to promote the dehydration melting of the lower crust to form the rhyolite porphyry and biotite granite.

Data availability statement

The original contributions presented in the study are included in the article/Supplementary Material. Further inquiries can be directed to the corresponding author.

Author contributions

LD collected samples, performed whole-rock and zircon geochemical analyses, and wrote the manuscript. XB drew the maps and figures. CD performed the data processing. ZY reviewed and edited the manuscript.

Funding

This study was financially supported by the National Natural Science Foundation of China-Shandong Joint Fund Program (U2006201), the National Key Research and Development Project of China (2016YFC0600305), and Fundamental Research Funds for the Central Universities (FRF-TP-20-042A1).

Acknowledgments

We express our sincere thanks to Li Huawei, Yu Chao, and Zhou Limin for their help with the LA-(MC)-ICPMS zircon U-Pb dating and Hf isotope analyses, and to Zhou Yiwei and Liu Yanhong for their help with the whole-rock major element analyses.

Conflict of interest

CD was employed in the Postdoctoral Programme of the Guosen Securities company.

The remaining authors declare that the research was conducted in the absence of any commercial or financial relationships that could be construed as a potential conflict of interest.

Publisher's note

All claims expressed in this article are solely those of the authors and do not necessarily represent those of their affiliated organizations, or those of the publisher, the editors, and the reviewers. Any product that may be evaluated in this article, or claim that may be made by its manufacturer, is not guaranteed or endorsed by the publisher.

References

Brown, M. (2013). Granite: From Genesis to emplacement. *Geol. Soc. Am. Bull.* 125, 1079–1113. doi:10.1130/b30877.1

Cai, Y. C., Fan, H. R., Santosh, M., Liu, X., Hu, F. F., Yang, K. F., et al. (2013). Evolution of the lithospheric mantle beneath the southeastern North China Craton: Constraints from mafic dikes in the Jiaobei terrain. *Gondwana Res.* 24, 601–621. doi:10.1016/j.gr.2012.11.013

Cao, K., Yang, Z. M., White, N. C., and Hou, Z. Q. (2022). Generation of the giant porphyry Cu-Au deposit by repeated recharge of mafic magmas at Pulang in eastern Tibet. *Econ. Geol.* 117, 57–90. doi:10.5382/econgeo.4860

Castillo, P. R. (2006). An overview of adakite petrogenesis. *Chin. Sci. Bull.* 51, 257–268. doi:10.1007/s11434-006-0257-7

Castillo, P. R., Janney, P. E., and Solidum, R. U. (1999). Petrology and geochemistry of Camiguin Island, southern Philippines: Insights to the source of adakites and other lavas in a complex arc setting. *Contributions mineralogy petrology* 134, 33–51. doi:10.1007/s004100050467

Chappell, B. (2004). Towards a unified model for granite Genesis. *Earth Environ. Sci. Trans. R. Soc. Edinb.* 95, 1–10. doi:10.1017/s0263593300000870

Charles, N., Gumiaux, C., Augier, R., Chen, Y., Faure, M., Lin, W., et al. (2012). Metamorphic core complex dynamics and structural development: Field evidences from the Liaodong Peninsula (China, East Asia). *Tectonophysics* 560-561, 22–50. doi:10.1016/j.tecto.2012.06.019

Chen, J. F., Xie, Z., Zhang, X. D., Zhou, T. X., Park, Y. S., Ahn, K. S., et al. (2003). U-Pb zircon ages for a collision-related K-rich complex at Shidao in the Sulu ultrahigh pressure terrane, China. *Geochem. J.* 37, 35–46. doi:10.2343/geochemj.37.35

Chen, L., Tao, W., Zhao, L., and Zheng, T. (2008). Distinct lateral variation of lithospheric thickness in the Northeastern North China Craton. *Earth Planet. Sci. Lett.* 267, 56–68. doi:10.1016/j.epsl.2007.11.024

Clemens, J. D., Stevens, G., and Bryan, S. E. (2020). Conditions during the formation of granitic magmas by crustal melting-hot or cold; drenched, damp or dry? *Earth-Science Rev.* 200, 102982. doi:10.1016/j.earscirev.2019.102982

Condie, K. C. (2005). TTGs and adakites: Are they both slab melts? *Lithos* 80, 33–44. doi:10.1016/j.lithos.2003.11.001

Davidson, J., Turner, S., Handley, H., Macpherson, C., and Dosseto, A. (2007). Amphibole "sponge" in arc crust? *Geol.* 35, 787–790. doi:10.1130/g23637a.1

DePaolo, D. J. (1981). Trace element and isotopic effects of combined wallrock assimilation and fractional crystallization. *Earth Planet. Sci. Lett.* 53, 189–202. doi:10.1016/0012-821x(81)90153-9

Gao, P., Zheng, Y. F., and Zhao, Z. F. (2016). Experimental melts from crustal rocks: A lithochemical constraint on granite petrogenesis. *Lithos* 266–267, 133–157. doi:10.1016/j.lithos.2016.10.005

Gao, S., Rudnick, R. L., Yuan, H. L., Liu, X. M., Liu, Y. S., Xu, W. L., et al. (2004). Recycling lower continental crust in the North China craton. *Nature* 432, 892–897. doi:10.1038/nature03162

Geng, X., Foley, S. F., Liu, Y., Wang, Z., Hu, Z., and Zhou, L. (2019). Thermal-chemical conditions of the North China Mesozoic lithospheric mantle and implication for the lithospheric thinning of cratons. *Earth Planet. Sci. Lett.* 516, 1–11. doi:10.1016/j.epsl.2019.03.012

Goss, S. C., Wilde, S. A., Wu, F., and Yang, J. (2010). The age, isotopic signature and significance of the youngest mesozoic granitoids in the Jiaodong terrane, Shandong province, north China craton. *Lithos* 120, 309–326. doi:10.1016/j.lithos.2010.08.019

Hou, M. L., Jiang, Y. H., Jiang, S. Y., Ling, H. F., and Zhao, K. D. (2007). Contrasting origins of late mesozoic adakitic granitoids from the northwestern Jiaodong Peninsula, east China: Implications for crustal thickening to delamination. *Geol. Mag.* 144, 619–631. doi:10.1017/s0016756807003494

Jahn, B. M., and Zhang, Z. Q. (1984). Archean granulite gneisses from eastern Hebei province, China: Rare Earth geochemistry and tectonic implications. *Contr. Mineral. Pet.* 85, 224–243. doi:10.1007/bf00378102

Jiang, P., Yang, K. F., Fan, H. R., Liu, X., Cai, Y. C., and Yang, Y. H. (2016). Titanite-scale insights into multi-stage magma mixing in early cretaceous of NW Jiaodong terrane, north China craton. *Lithos* 258–259, 197–214. doi:10.1016/j.lithos.2016.04.028

Kessel, R., Schmidt, M. W., Ulmer, P., and Pettke, T. (2005). Trace element signature of subduction-zone fluids, melts and supercritical liquids at 120–180 km depth. *Nature* 437, 724–727. doi:10.1038/nature03971

Le Bas, M. J., Le Maitre, R. W., Streckeisen, A., and Zanettin, B. (1986). A chemical classification of volcanic rocks based on the total alkali – silica diagram. *J. Petrology* 27, 745–750. doi:10.1093/petrology/27.3.745

Lee, C. T. A., Luffi, P., and Chin, E. J. (2011). Building and destroying continental mantle. *Annu. Rev. Earth Planet. Sci.* 39, 59–90. doi:10.1146/annurev-earth-040610-133505

Li, X. C., Fan, H. R., Santosh, M., Hu, F. F., Yang, K. F., Lan, T. G., et al. (2012). An evolving magma chamber within extending lithosphere: An integrated geochemical, isotopic and zircon U-Pb geochronological study of the Gushan granite, eastern North China Craton. *J. Asian Earth Sci.* 50, 27–43. doi:10.1016/j.jseaes.2012.01.016

Li, X. H., Fan, H. R., Hu, F. F., Hollings, P., Yang, K. F., and Liu, X. (2019). Linking lithospheric thinning and magmatic evolution of late Jurassic to early cretaceous granitoids in the Jiaobei Terrane, southeastern North China Craton. *Lithos* 324–325, 280–296. doi:10.1016/j.lithos.2018.11.022

Liu, D. Y., Nutman, A. P., Compston, W., Wu, J. S., and Shen, Q. H. (1992). Remnants of ≥3800 Ma crust in the Chinese part of the Sino-Korean craton. *Geol.* 20, 339–342. doi:10.1130/0091-7613(1992)020<0339:romcit>2.3.co;2

Liu, Y., Gao, S., and Tingchuan, L. (1999). Geochemistry of granulites in north China craton: Implications for the composition of archean lower crus. *Geology-Geochemistry* 27, 40–46.

Liu, Y., Gao, S., Yuan, H., Zhou, L., Liu, X., Wang, X., et al. (2004). U-Pb zircon ages and Nd, Sr, and Pb isotopes of lower crustal xenoliths from north China craton: Insights on evolution of lower continental crust. *Chem. Geol.* 211, 87–109. doi:10.1016/j.chemgeo.2004.06.023

Liu, Y. S., Gao, S., Jin, S. Y., Hu, S. H., Sun, M., Zhao, Z. B., et al. (2001). Geochemistry of lower crustal xenoliths from neogene hannuoba basalt, north China craton: Implications for petrogenesis and lower crustal composition. *Geochimica Cosmochimica Acta* 65, 2589–2604. doi:10.1016/s0016-7037(01)00609-3

Ma, L., Jiang, S. Y., Dai, B. Z., Jiang, Y. H., Hou, M. L., Pu, W., et al. (2013). Multiple sources for the origin of Late Jurassic Linglong adakitic granite in the Shandong Peninsula, eastern China: Zircon U-Pb geochronological, geochemical and Sr–Nd–Hf isotopic evidence. *Lithos* 162–163, 251–263. doi:10.1016/j.lithos.2013.01.009

Ma, L., Jiang, S. Y., Hofmann, A. W., Dai, B. Z., Hou, M. L., Zhao, K. D., et al. (2014). Lithospheric and asthenospheric sources of lamprophyres in the Jiaodong Peninsula: A consequence of rapid lithospheric thinning beneath the north China craton? *Geochimica Cosmochimica Acta* 124, 250–271. doi:10.1016/j.gca.2013.09.035

McDonough, W. F., and Sun, S. S. (1995). The composition of the Earth. *Chem. Geol.* 120, 223–253. doi:10.1016/0009-2541(94)00140-4

Meng, Q. R., Wu, G. L., Fan, L. G., and Wei, H. H. (2019). Tectonic evolution of early Mesozoic sedimentary basins in the North China block. *Earth-Science Rev.* 190, 416–438. doi:10.1016/j.earscirev.2018.12.003

Menzies, M., Xu, Y., Zhang, H., and Fan, W. (2007). Integration of geology, geophysics and geochemistry: A key to understanding the north China craton. *Lithos* 96, 1–21. doi:10.1016/j.lithos.2006.09.008

Peccerillo, A., and Taylor, S. R. (1976). Geochemistry of eocene calc-alkaline volcanic rocks from the Kastamonu area, Northern Turkey. *Contr. Mineral. Pet.* 58, 63–81. doi:10.1007/bf00384745

Rapp, R. P., and Watson, E. B. (1995). Dehydration melting of metabasalt at 8–32 kbar: Implications for continental growth and crust-mantle recycling. *J. Petrology* 36, 891–931. doi:10.1093/petrology/36.4.891

Rapp, R., Shimizu, N., Norman, M., and Applegate, G. (1999). Reaction between slab-derived melts and peridotite in the mantle wedge: Experimental constraints at 3.8 GPa. *Chem. Geol.* 160, 335–356. doi:10.1016/s0009-2541(99)00106-0

Richards, J. P., and Kerrich, R. (2007). Special paper: Adakite-like rocks: Their diverse origins and questionable role in metallogenesis. *Econ. Geol.* 102, 537–576. doi:10.2113/gsecongeo.102.4.537

Rollinson, H. R. (1993). *Using geochemical data: Evaluation, presentation, interpretation*. Singapore: Longman Singapore Publishers (Pte) Ltd.

Sen, C., and Dunn, T. (1994). Dehydration melting of a basaltic composition amphibolite at 1.5 and 2.0 GPa: Implications for the origin of adakites. *Contr. Mineral. Pet.* 117, 394–409. doi:10.1007/bf00307273

Soesoo, A. (2000). Fractional crystallization of mantle-derived melts as a mechanism for some I-type granite petrogenesis: An example from lachlan fold belt, Australia. *J. Geol. Soc. Lond.* 157, 135–149. doi:10.1144/jgs.157.1.135

Song, M.-C., Li, J., Yu, X.-F., Song, Y.-X., Ding, Z.-J., and Li, S.-Y. (2021). Metallogenic characteristics and tectonic setting of the Jiaodong gold deposit, China. *Solid Earth Sci.* 6 (4), 385–405. doi:10.1016/j.sesci.2021.07.002

Sun, S.-s., and McDonough, W. F. (1989). "Chemical and isotopic systematics of oceanic basalts: Implications for mantle composition and processes," in *Magmatism in the ocean basins*. Editors D. Saunders and M. J. Norry (London: Geological Society), 313–345.

Thompson, A. B., Matile, L., and Ulmer, P. (2002). Some thermal constraints on crustal assimilation during fractionation of hydrous, mantle-derived magmas with examples from central alpine batholiths. *J. Petrology* 43, 403–422. doi:10.1093/petrology/43.3.403

Weinberg, R. F., and Hasalová, P. (2015). Water-fluxed melting of the continental crust: A review. *Lithos* 212–215, 158–188. doi:10.1016/j.lithos.2014.08.021

Whitney, D. L., and Evans, B. W. (2010). Abbreviations for names of rock-forming minerals. *Am. mineralogist* 95, 185–187. doi:10.2138/am.2010.3371

Windley, B. F., Maruyama, S., and Xiao, W. J. (2010). Delamination/thinning of sub-continental lithospheric mantle under Eastern China: The role of water and multiple subduction. *Am. J. Sci.* 310, 1250–1293. doi:10.2475/10.2010.03

Wu, F., Yang, J., Xu, Y., Wilde, S. A., and Walker, R. J. (2019). Destruction of the north China craton in the mesozoic. *Annu. Rev. Earth Planet. Sci.* 47, 173–195. doi:10.1146/annurev-earth-053018-060342

Wu, F. Y., Lin, J.-Q., Wilde, S. A., Zhang, X. O., and Yang, J. H. (2005a). Nature and significance of the Early Cretaceous giant igneous event in eastern China. *Earth Planet. Sci. Lett.* 233, 103–119. doi:10.1016/j.epsl.2005.02.019

Wu, F. Y., Yang, J. H., Wilde, S. A., and Zhang, X. O. (2005b). Geochronology, petrogenesis and tectonic implications of Jurassic granites in the Liaodong Peninsula, NE China. *Chem. Geol.* 221, 127–156. doi:10.1016/j.chemgeo.2005.04.010

Wu, F. Y., Yang, Y. H., Xie, L. W., Yang, J. H., and Ping, X. (2006). Hf isotopic compositions of the standard zircons and baddeleyites used in U–Pb geochronology. *Chem. Geol.* 234, 105–126. doi:10.1016/j.chemgeo.2006.05.003

Wu, Y., and Zheng, Y. (2013). Tectonic evolution of a composite collision orogen: An overview on the Qinling-Tongbai-Hong'an-Dabie-Sulu orogenic belt in central China. *Gondwana Res.* 23, 1402–1428. doi:10.1016/j.gr.2012.09.007

Xu, Y., Li, H., Pang, C., and He, B. (2009). On the timing and duration of the destruction of the North China Craton. *Sci. Bull. (Beijing).* 54, 3379–3396. doi:10.1007/s11434-009-0346-5

Xue, D., Wang, H., Liu, Y., Xie, L., and Shen, P. (2017). An improved procedure for the determination of ferrous iron mass fraction in silicate rocks using a schlenk line-based digestion apparatus to exclude oxygen. *Geostand. Geoanal. Res.* 41, 411–425. doi:10.1111/ggr.12164

Yang, F., Santosh, M., and Kim, S. W. (2018a). Mesozoic magmatism in the eastern North China Craton: Insights on tectonic cycles associated with progressive craton destruction. *Gondwana Res.* 60, 153–178. doi:10.1016/j.gr.2018.04.003

Yang, F., Santosh, M., and Tang, L. (2018b). Extensive crustal melting during craton destruction: Evidence from the Mesozoic magmatic suite of Junan, eastern North China Craton. *J. Asian Earth Sci.* 157, 119–140. doi:10.1016/j.jseaes.2017.07.010

Yang, J., Wu, F., Chung, S., Wilde, S. A., and Chu, M. (2004). Multiple sources for the origin of granites: Geochemical and Nd/Sr isotopic evidence from the gudaoling granite and its mafic enclaves, northeast China. *Geochimica Cosmochimica Acta* 68, 4469–4483. doi:10.1016/j.gca.2004.04.015

Yang, K. F., Fan, H. R., Santosh, M., Hu, F. F., Wilde, S. A., Lan, T. G., et al. (2012). Reactivation of the Archean lower crust: Implications for zircon geochronology, elemental and Sr–Nd–Hf isotopic geochemistry of late Mesozoic granitoids from northwestern Jiaodong Terrane, the North China Craton. *Lithos* 146–147, 112–127. doi:10.1016/j.lithos.2012.04.035

Yang, L. Q., Dilek, Y., Wang, Z. L., Weinberg, R. F., and Liu, Y. (2017). Late Jurassic, high Ba–Sr Linglong granites in the Jiaodong Peninsula, east China: Lower crustal melting products in the eastern north China craton. *Geol. Mag.* 155, 1040–1062. doi:10.1017/s0016756816001230

Zhai, M., Guo, J., and Liu, W. (2001). An exposed cross-section of early Precambrian continental lower crust in North China craton. *Phys. Chem. Earth Part A Solid Earth Geodesy* 26, 781–792. doi:10.1016/s1464-1895(01)00127-2

Zhang, Y., Li, J., Zhang, T., Dong, S., and Yuan, J. (2008). Cretaceous to Paleocene Tectono-Sedimentary Evolution of the Jiaolai basin and the Contiguous Areas of the Shandong Peninsula(North China) and Its Geodynamic Implications. *Acta Geol. Sin.* 82, 1229–1257.

Zhao, G. (2001). Palaeoproterozoic assembly of the North China craton. *Geol. Mag.* 138, S0016756801005040–S0016756801005091. doi:10.1017/s0016756801005040

Zhao, G., Sun, M., Wilde, S. A., and Li, S. (2005). Late Archean to Paleoproterozoic evolution of the North China Craton: key issues revisited. *Precambrian Res.* 136, 177–202. doi:10.1016/j.precamres.2004.10.002

Zheng, Y. F., and Gao, P. (2021). The production of granitic magmas through crustal anatexis at convergent plate boundaries. *Lithos* 402–403, 106232. doi:10.1016/j.lithos.2021.106232

Zhu, G., Liu, G. S., Niu, M. L., Xie, C. L., Wang, Y. S., and Xiang, B. (2009). Syn-collisional transform faulting of the Tan-Lu fault zone, East China. *Int. J. Earth Sci.* 98, 135–155. doi:10.1007/s00531-007-0225-8

frontiers | Frontiers in Earth Science

TYPE Original Research
PUBLISHED 02 February 2023
DOI 10.3389/feart.2023.1121856

Check for updates

OPEN ACCESS

EDITED BY
Fan Yang,
Lanzhou University, China

REVIEWED BY
Leilei Dong,
University of Science and Technology Beijing, China
Xiaoqiang Zhu,
Anhui Normal University, China
Li Tang,
China University of Geosciences, China

*CORRESPONDENCE
Jingguo Du,
dujgcugb@163.com

SPECIALTY SECTION
This article was submitted to Economic Geology, a section of the journal Frontiers in Earth Science

RECEIVED 12 December 2022
ACCEPTED 19 January 2023
PUBLISHED 02 February 2023

CITATION
Lu W, Zhang Y, Du J and Song Z (2023), Melt- and fluid-inclusions studies in the Wunugetushan porphyry Cu–Mo deposit, NE China: Constraints on the separation of Cu and Mo.
Front. Earth Sci. 11:1121856.
doi: 10.3389/feart.2023.1121856

COPYRIGHT
© 2023 Lu, Zhang, Du and Song. This is an open-access article distributed under the terms of the Creative Commons Attribution License (CC BY). The use, distribution or reproduction in other forums is permitted, provided the original author(s) and the copyright owner(s) are credited and that the original publication in this journal is cited, in accordance with accepted academic practice. No use, distribution or reproduction is permitted which does not comply with these terms.

Melt- and fluid-inclusions studies in the Wunugetushan porphyry Cu–Mo deposit, NE China: Constraints on the separation of Cu and Mo

Wei Lu[1], Yuecheng Zhang[2], Jingguo Du[1,2]* and Zhiwei Song[3]

[1]School of Earth Science and Resources, Chang'an University, Xi'an, China, [2]School of Earth Sciences and Resources, China University of Geosciences, Beijing, China, [3]China Gold Inner Mongolia Mining Co Ltd, Manchuria, China

The Wunugetushan large porphyry Cu–Mo deposit in NE China is hosted by Mesozoic quartz monzonite porphyry and has a Mo-rich core and Cu-rich rim in space. In this paper, melt inclusions in porphyry intrusions and fluid inclusions in different-stage quartz veins were studied to explore potential parameters leading to Cu–Mo decoupling. Melt inclusions in porphyry intrusions have rhyolitic compositions of 71.7–85.3 wt.% SiO_2, 1.9–31.3 ppm Cu and 1.7–2.6 ppm Mo. Hydrothermal activity occurred over three stages: 1) Early Mo mineralization at high temperatures (543°C–560°C) and CO_2-rich fluids of intermediate salinity (11.0–17.3 wt.% NaCl equivalent), accompanied by biotitization and minor K-feldspathization; 2) Late Mo mineralization involving high-salinity (up to 77.0 wt.% NaCl equiv.) oxidized fluids at intermediate temperatures (400°C–454°C), with K-feldspathization and minor sericitization; 3) A Cu-mineralization stage with high-salinity (up to 45.6 wt.% NaCl equiv.) and CO_2-barren fluids characterized by temperature peaks at 250°C–300°C and 400°C–450°C, accompanied by sericitization and illitization. Given possible variations in melt Cu/Mo ratios during magmatic activity and redox conditions, pH, fluid composition, and temperature during the hydrothermal-fluid stage led to the separation of Cu and Mo, we found that integrated parameters including increased Cu/Mo ratios in residual melt, variations in the redox state and more acidic environment of hydrothermal fluids determine spatial separation of two metals.

KEYWORDS

melt inclusion, fluid inclusion, Cu and Mo decoupling, wunugetushan, porphyry Cu-Mo deposit

1 Introduction

Porphyry Cu–(Au–Mo) deposits are main suppliers for various metals and account for 75% of global Cu reserves, 50% of Mo reserves, and 20% of Au reserves (Sillitoe, 2010). In general, the metals Cu, Au, Mo, Ag, Pb, and Zn are temporospatially coupled in Cu–Au ± Mo, Cu–Mo, Zn–Pb ± Ag, and Ag–Au deposits (Pak et al., 2004; Sillitoe, 2010). An understanding of the association and separation of these metals is helpful in practical geological prospecting. In porphyry Cu–Mo deposits, Cu orebodies are usually concentrated in shallow outer areas, and Mo orebodies occur at deeper levels in the core (Redmond and Einaudi, 2010; Sillitoe, 2010; Li et al., 2012; Seo et al., 2012; Chang et al., 2018), but mineralization time is not always consistent with their spatial distributions. In the Bingham Canyon (USA; Seo et al., 2012), Hucunnan (eastern China; Cao et al., 2017), and Yulong (Tibet in

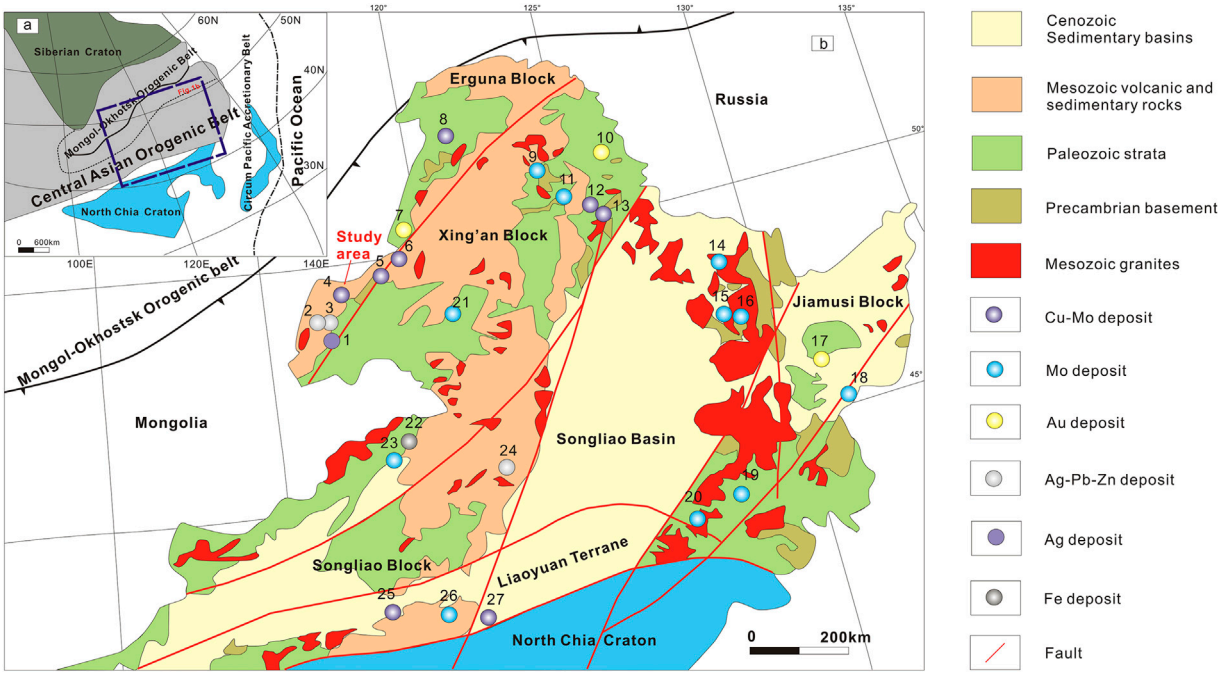


FIGURE 1
(A) Geological map of NE China (after Safonova, 2009), showing **(B)** distribution of Mesozoic igneous rocks and ore deposits (modified from Wu et al., 2014). Names of ore deposits: 1– Erentaolegai Ag deposit; 2–Chaganbulagen Ag–Pb–Zn deposit; 3–Jiawula Ag–Pb–Zn deposit; 4–Wunugetushan Cu–Mo deposit; 5–Babayi Cu–Mo deposit; 6–Badaguan Cu–Mo deposit; 7–Xiaoyinuogaigou Au deposit; 8–Taipingchuan Cu–Mo deposit; 9–Chalukou Mo deposit; 10–Sandaowanzi Au (Sb)deposit; 11—Xinga Mo deposit; 12–Duobaoshan Cu–Mo deposit; 13–Tongshan Cu–Mo deposit; 14–Huojihe Mo deposit; 15–Cuiling Mo deposit; 16– Luming Mo deposit; 17–Laozhashan Au deposit; 18–Jinchanggou Mo deposit; 19–Dashihe Mo deposit; 20–Daheishan Mo deposit; 21– Taipinggou Mo deposit; 22–Chagan'aobao Fe–Zn deposit; 23– Diyanqinamu Mo deposit; 24–Meng'entaolegai Pb–Zn–Ag deposit; 25—Xiaodonggou Mo deposit; 26–Jiguanshan Mo deposit; 27–Kulitu Mo–Cu deposit.

southwestern China; Chang et al., 2018) deposits, molybdenite precipitation postdates chalcopyrite crystallization, whereas in the Bangpu (Tibet in southwestern China; Wang et al., 2015) and Wunugetushan (northeastern China; Li et al., 2012) deposits, Mo mineralization predates Cu mineralization. Numerous progresses have been made to explore possible drivers of Cu–Mo decoupling and mainly include 1) saturation temperatures of molybdenite and chalcopyrite in hydrothermal fluids (Li et al., 2012; Seo et al., 2012; Cao et al., 2017); 2) vapour–brine immiscibility (Cao et al., 2017; Chang et al., 2018); 3) changes in fluid compositions (Seo et al., 2011; Kokh et al., 2017) including H_2, S, Cl, and CO_2 contents; and 4) the degree of magmatic differentiation (Candela and Holland, 1986). Previous studies have focused on changes in physical and chemical conditions during differentiation of metals in melt and the evolution of hydrothermal fluids.

This study intends to explored the causes of Cu–Mo separation during both the magmatic and hydrothermal stages of mineralization, with a focus on melt inclusions in porphyry and fluid inclusions (FIs) in quartz veins in the Wunugetushan porphyry deposit, where Cu and Mo orebodies are typically separated.

2 Geological background

Northeastern (NE) China lies in the southeastern Central Asian Orogenic Belt (CAOB; Safonova, 2009; Xiao and Santosh, 2014), which developed between the Siberian Craton in the north and the North China Craton in the south during the Neoproterozoic–Phanerozoic (Figures 1A,B). The CAOB experienced complex tectonic events and extensive magmatism during the Palaeozoic–Mesozoic, including evolution of the Palaeo-Asian and Mongol–Okhotsk oceans and subduction of the Palaeo-Pacific Plate (Xu et al., 2009; Metelkin et al., 2010; Tan et al., 2013; Xu et al., 2013; Liu et al., 2014). As a consequence, a series of E–W- and NE–NNE-trending faults developed, and massive magmatic–hydrothermal ore deposits formed in NE China (Figure 1B). Most of these deposits are related to the Mesozoic subduction of the Palaeo-Pacific Plate (Metelkin et al., 2010; Wu et al., 2011; Liu et al., 2014), and >20 ore deposits are hosted by Mesozoic magmatic rocks, including the Badaguan porphyry Cu–Mo (Gao et al., 2016), Wunugetushan porphyry Cu–Mo (Qin et al., 1999; Chen et al., 2011), Luming porphyry Mo (Hu et al., 2014), Erentaolegai epithermal Ag (Chen et al., 1997), Jiawula hydrothermal vein-type Pb–Zn–Ag (Zhai et al., 2013) and Chaganbulagen hydrothermal vein-type Ag–Pb–Zn (Pan and Sun, 1990; Wu et al., 2010) deposits. Other ore deposits, such as the Duobaoshan and Tongshan Cu–Mo deposits (Zeng et al., 2014), are related to Palaeozoic magmatic activity.

3 Ore deposit geology

The Wunugetushan porphyry Cu–Mo deposit (Figure 2) has reserves of 1.27 million tonnes (Mt) Cu and 0.42 Mt Mo (Qin et al., 1999). The deposit was first discovered by the Inner Mongolia Geological Survey Bureau in 1960 and has been explored

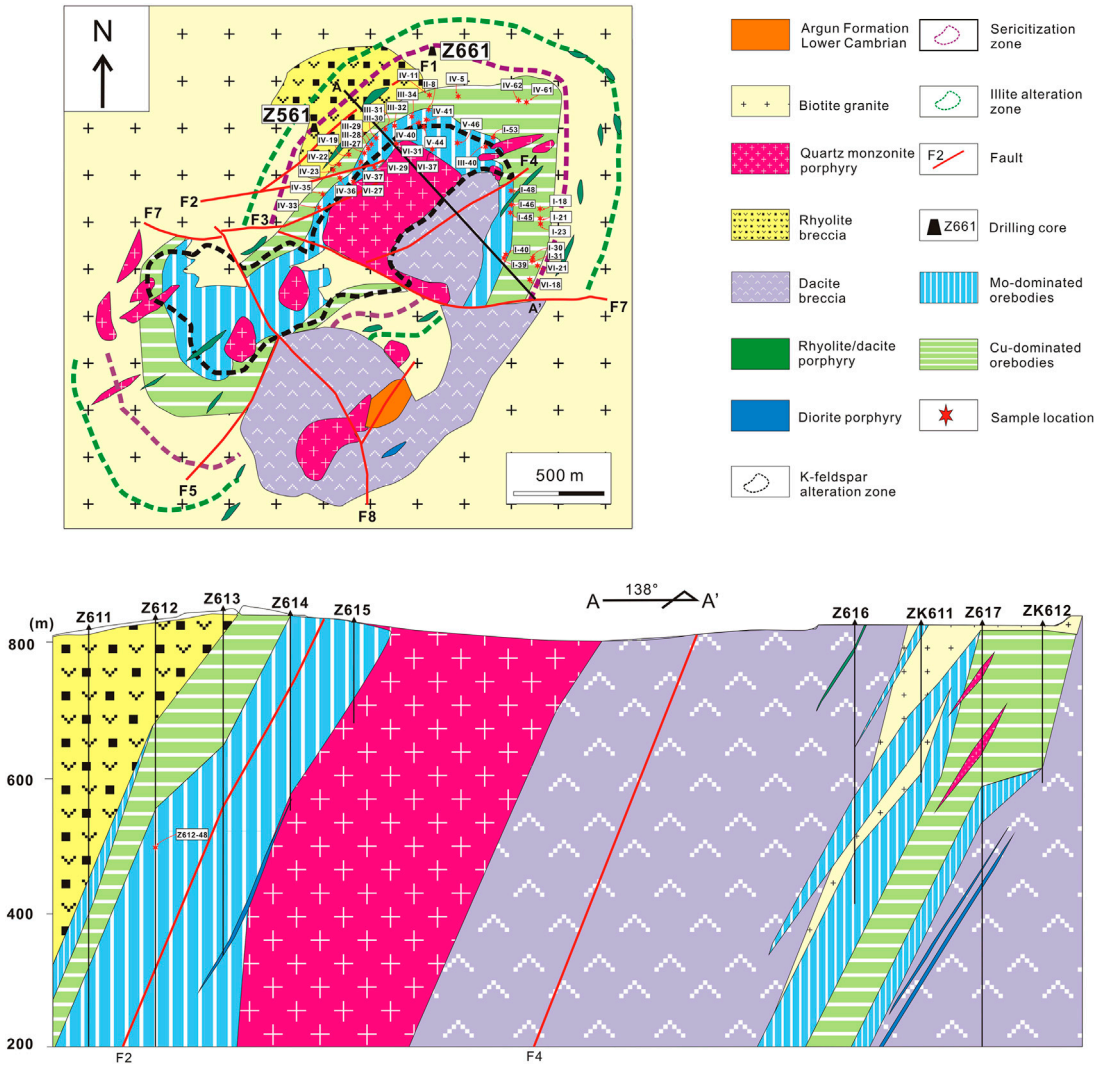


FIGURE 2
Geological map of the Wunugetushan porphyry Cu–Mo deposit geological map (modified from Wang et al. (2015)) including sample locations.

by the Metallurgical and Geological Prospecting Company of Heilongjiang Province and the China National Gold Group Corporation. Exposed strata in the deposit are mainly Quaternary sandstones, mudstones, and conglomerates. Magmatic activity was concentrated in two pulses, as indicated by Late Triassic biotite granite that covers an area of ~110 km^2 and yields a zircon U–Pb crystallization age of 210.0 ± 2.0 Ma (Mi et al., 2014), and Jurassic volcanic–subvolcanic stocks, including quartz monzonite porphyry, rhyolite porphyry, and dacite porphyry (Figure 2). Quartz monzonite porphyry is the main host rock for Cu–Mo mineralization, and it covers an area of ~0.42 km^2 (Figure 3A) and intrudes earlier biotite granite. The crystallization age (180.4 ± 1.4 Ma) of the quartz monzonite porphyry is consistent with the molybdenite ore Re–Os age of 180.5 ± 2.0 Ma (Wang et al., 2015). NE-trending faults and volcanic ring fractures are the major structures in the Wunugetushan mining area, which shape the distribution of Cu–Mo orebodies. Late NW-trending faults and associated rhyolite porphyry dikes (Figures 3B–D) represent post-mineralization events, cutting through or deforming the orebodies.

The mining area includes a typical alteration halo of porphyry Cu deposits comprising quartz–K-feldspar (QK), quartz–sericite (QS), and illite–hydromuscovite (IH) zones from core to rim (Qin et al., 1993; Li et al., 2012). The area of alteration in the northern section of the deposit is 2,500–2,800 m long and 200–350 m wide; and that in the southern section is 2000–2,600 m long and 1,000–1800 m wide. The total area of alteration is ~5 km^2. Mo orebodies are 70–400 m thick and occur mainly in the QK and QS zones; Cu orebodies occur mainly in the QS zone, and are up to 500 m thick in the northern section. Molybdenite-dominated quartz veins are commonly cut by chalcopyrite–pyrite-dominated quartz veins (Figure 3E), indicating earlier Mo mineralization.

Based on crosscutting relationships, alteration of mineral assemblages, and the different mineralization types in quartz veins, the formation of quartz veins is inferred to have involved three main stages (Figure 4): I) quartz + biotite ± molybdenite ± K-feldspar + magnetite (Figures 4A–C); II) quartz + K-feldspar ± sericite + molybdenite (Figures 4B,D); and III) quartz + sericite + chalcopyrite + pyrite (Figures 4E,F). Mo mineralization is associated with Stage I and II, with alteration minerals including mainly biotite + magnetite ± K-feldspar + sericite. Biotite predated K-feldspar

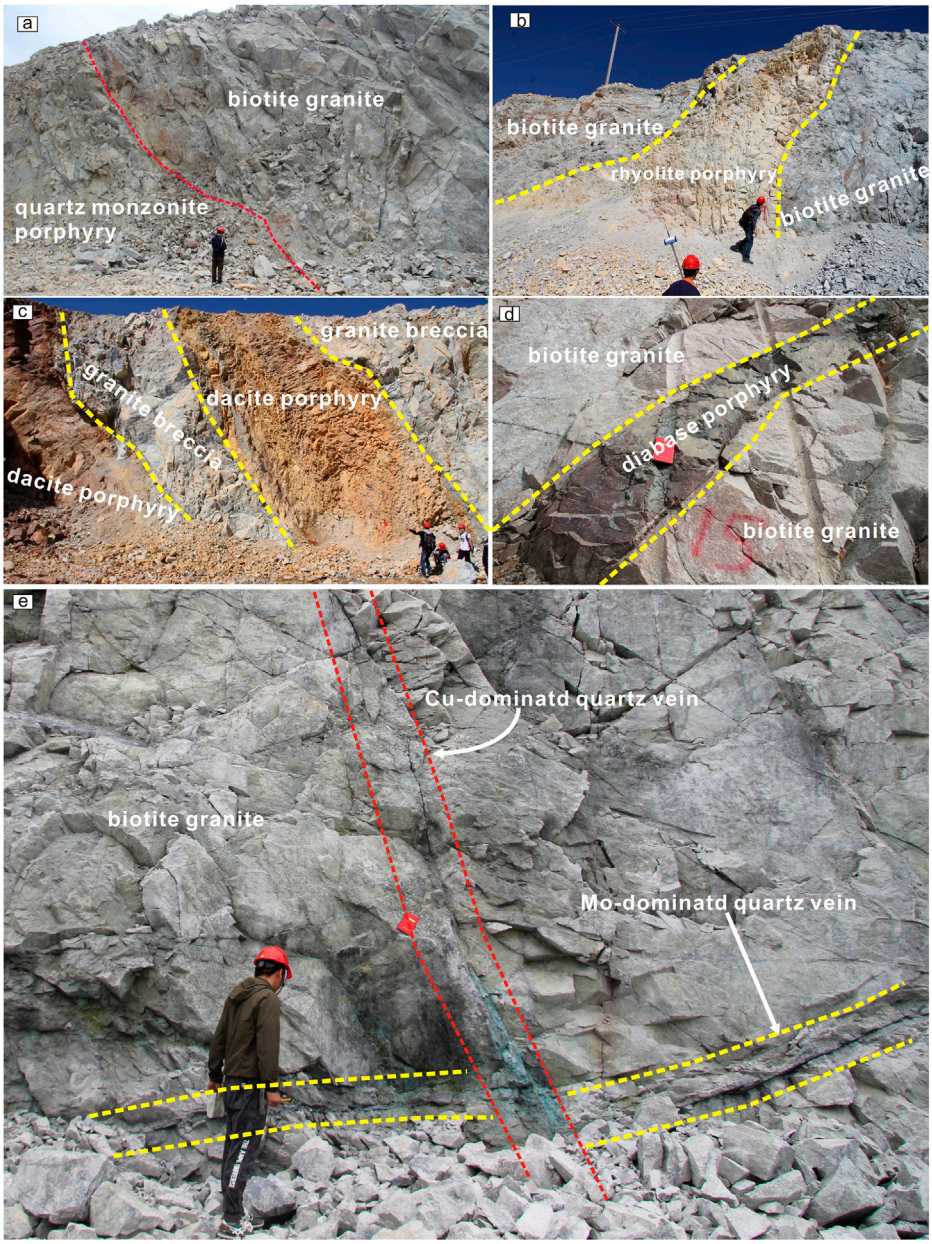


FIGURE 3
Field photographs of magmatic rocks and quartz veins in Wunugetushan porphyry Cu-Mo deposit. **(A)** quartz monzonite porphyry has a contact with biotite granite by fault; late **(B)** rhyolite porphyry, **(C)** dacite porphyry and **(D)** diabase porphyry dikes distribute along the faults or cracks within biotite granite. **(E)** Mo-dominated quartz vein is cut by late Cu-dominated quartz vein.

(biotite ± K-feldspar + quartz veins are cut by K-feldspar + molybdenite + quartz veins; Figure 4B). Stage III was the main period of Cu mineralization, with Cu sulphides (e.g., chalcopyrite and bornite) being precipitated together with pyrite, sericite, and minor illite (Figures 4E,F).

4 Samples and analytical methods

4.1 FI petrography and microthermometry

Representative quartz veins were sampled in the Cu and Mo orebodies (16 and 32 samples, respectively; Figure 2). Up to seven thin sections (70–100 μm thick) from each sample were polished and studied by optical microscopy. Because fluid inclusions may be modified during fracturing to form secondary inclusions, only primary inclusions could represent the physical and chemical conditions of the hydrothermal fluid. Petrographic observations were undertaken at the China University of Geosciences, Beijing, China, using an Olympus BX51 microscope to identify primary FIs. Identification of primary FIs was based on their being isolated and completely enclosed by the quartz host, or growing along quartz growth zones or *c* axes (Figure 5). Only primary inclusions or inclusion assemblages exhibiting consistent phase proportions at room temperature (Figure 5) were selected for further

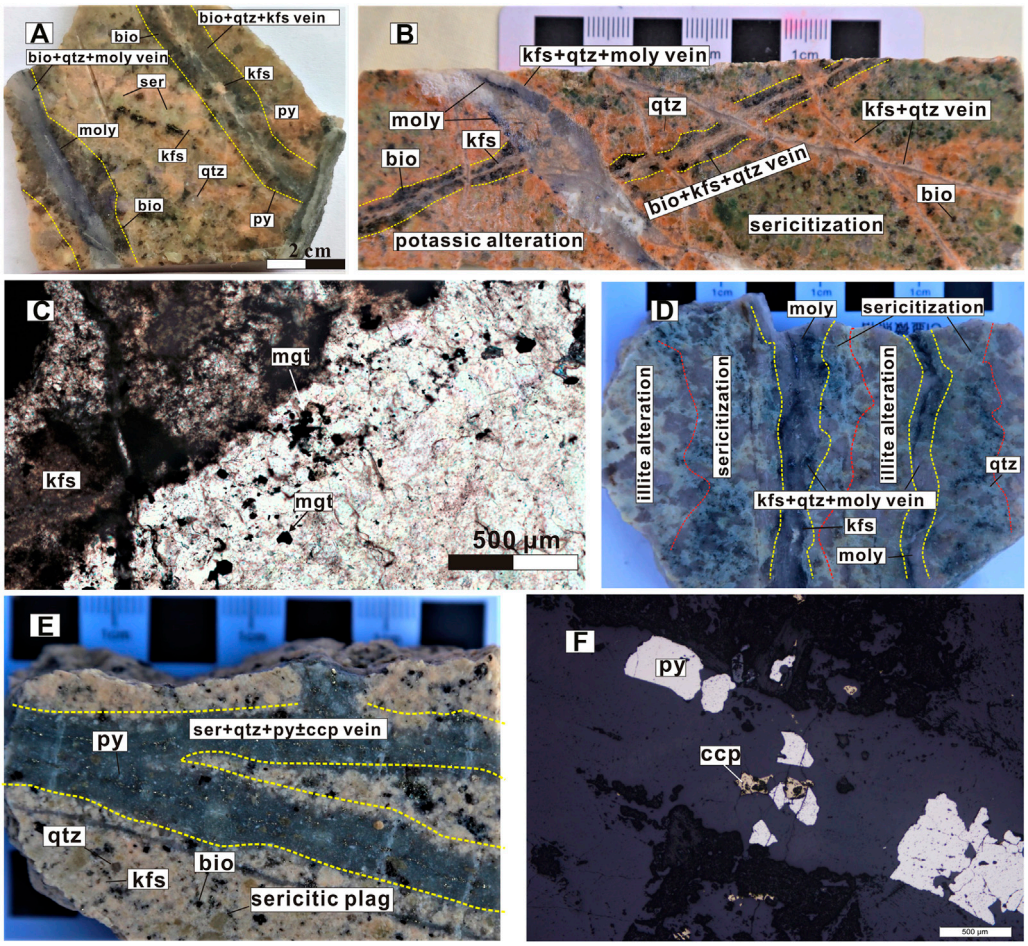


FIGURE 4
Alteration and mineralization hosted in various quartz veins. **(A)** bio + qtz + moly vein, accompanied with biotitization. **(B)** early bio + qtz + kfs± moly vein is cut by kfs + qtz + moly vein, early K-feldspathization alteration is overprinted by sericitization. **(C)** kfs + qtz + moly vein, feldspar is replaced by illite. **(D)** sericite and illite distribute symmetrically on the two sides of kfs + qtz + moly vein. **(E, F)** ser+qtz+py±ccp vein. Abbreviations: kfs–K-feldspar; plag–plagioclase; qtz–quartz; ser–sericite; bio–biotite; py–pyrite; moly–molybdenite; ccp–chalcopyrite.

microthermometric study at the MLR Key Laboratory of Metallogeny and Mineral Assessment, Institute of Mineral Resources, Chinese Academy of Geological Sciences (CAGS), Beijing, China. The analyses employed a Linkham (United Kingdom) THMS600 temperature-control stage with a range of −180°C–580°C (precision ±0.1°C for cooling and ±2°C for heating). Ice melting temperatures were observed at a heating rate of 0.1°C min^{-1}, and homogenization temperatures at 1°C min^{-1}. Salinities (wt.% NaCl equivalent) of aqueous FIs and those containing halite daughter minerals were calculated from ice melting (Bodnar, 1993) and halite dissolution (Sterner et al., 1988) temperatures, respectively.

4.2 Laser Raman microspectroscopy

Laser Raman spectroscopic analysis of FIs employed a LabRAM HR800 (Horiba, Japan) microspectrometer at the Beijing Research Institute of Uranium Geology, Beijing, China. An Ar^+ ion laser with a wavelength of 532 nm and a source power of 25 mW were used, with a spectral resolution of ±1 cm^{-1}.

4.3 LA–ICP–MS analysis of melt inclusions

Laser ablation–inductively coupled plasma–mass spectrometry (LA–ICP–MS) analyses of melt inclusions were undertaken at the State Key Laboratory of Ore Deposit Geochemistry, Institute of Geochemistry, China Academy of Science (CAS), Guiyang, using an Agilent 7900 ICP–MS system coupled to a GeoLasPro 193 nm ArF excimer LA system (Lan et al., 2017a; Lan et al., 2017b). Details of instrumental operating conditions can be found in Lan et al. (2017a), Lan et al. (2017b). The sample chamber was flushed with He gas at 0.5 L min^{-1}. A laser spot of diameter of 30–50 μm was applied with repetition rates of 4–10 Hz and energy densities of 8–10 J cm^{-2}, depending on melt-inclusion size. Inclusions connected to micro-cracks or surrounded by late FI trails were excluded. Only entire, isolated, unexposed melt inclusions being drilled out of the host quartz. Signals associated with excess ablated host were subtracted from sample signals following Halter et al. (2004). Elements were quantified against the US National Institute of Standards and Technology Standard Reference Material (SRM) 610 as an external standard, and the constant Al_2O_3 content (~14 wt.%) of whole-rock quartz monzonite porphyry was used as an internal standard. A typical LA–ICP–MS signal of melt inclusions ablated through host quartz

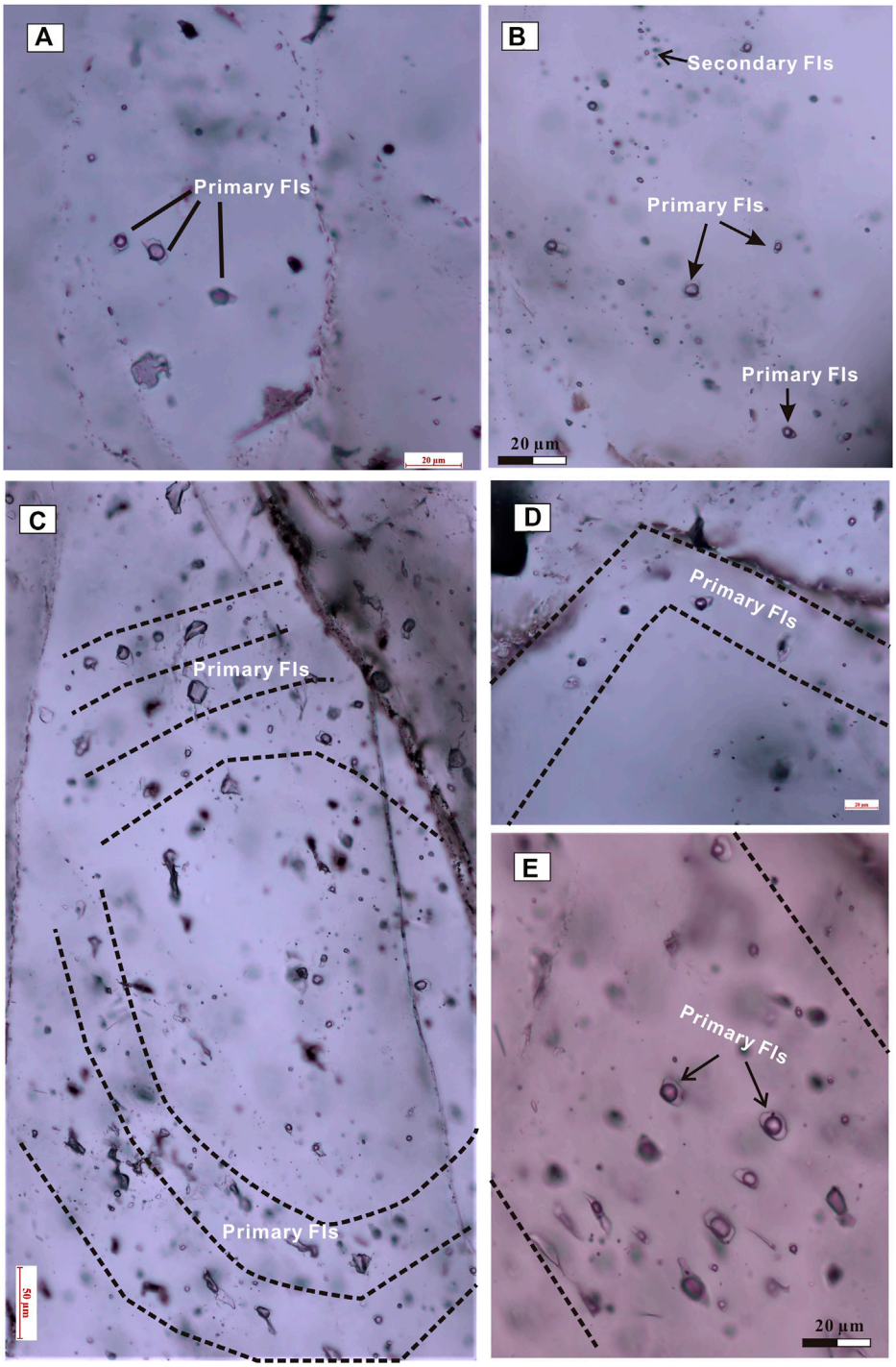


FIGURE 5
The criteria for identifying primary fluid inclusions. **(A, B)** isolated, totally enclosed by quartz; **(C, D)** fluid inclusions growing along the growth zoning of quartz; **(E)** primary fluid inclusion assemblages with the consistent phase ratios.

is provided in Supplementary Figure S1. Melt compositions were finally calculated by subtracting the host until the results fit on whole-rock composition trends (see in Supplementary Figure S2). This approach irreversibly will cause the compositional change that leads to misfits with regard to whole-rock trends (Heinrich et al. 2003). The major elements results from Wunugetushan agree well with trends defined by the whole-rock data (see in Supplementary Figure S2).

5 Results

5.1 Fluid inclusion petrography

FIs are hosted in quartz at Wunugetushan deposit, with four types identified on the basis of phase types and ratios at room temperatures (22.5°C), as follows. 1) C-type FIs contain either pure

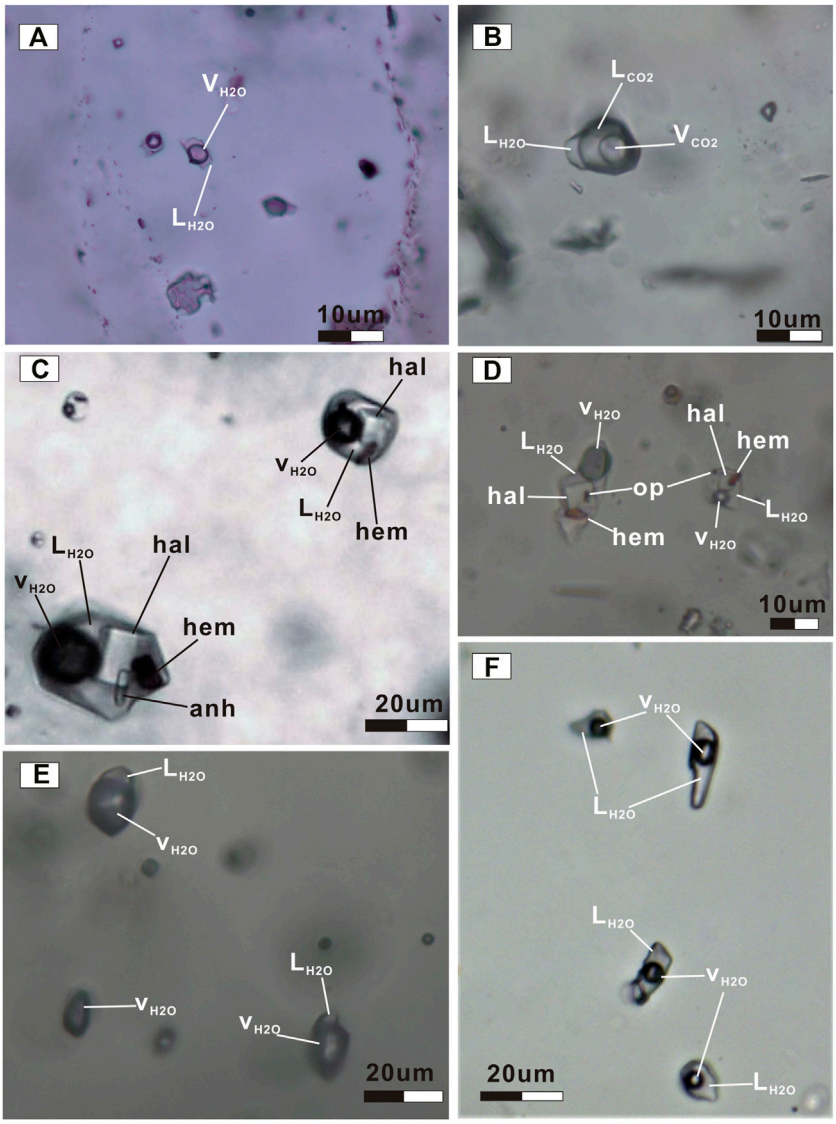


FIGURE 6
Representative fluid inclusion types in Wunugetushan porphyry Cu-Mo deposit. **(A)** C-type inclusions in early Mo mineralization stage and **(B)** late Mo mineralization stage. **(C)** S-type inclusions in late Mo mineralization stage and **(D)** Cu mineralization stage. **(E)** V-type inclusions in early Mo mineralization stage and **(F)** L-type inclusions in Cu mineralization. Abbreviations: L_{H2O}- liquid H_2O, L_{CO2}- liquid CO_2, V_{CO2}- vapor CO_2, V_{H2O}- vapor H_2O, hal-halite, hem-hematite, anh-anhydrite, op-opaque mineral.

CO_2 vapour or an aqueous phase plus one or two carbonic phases (Figures 6A,B). They are generally small (<12 μm diameter) with a subhedral to irregular crystal morphology (Figure 6A). Most are hosted in early molybdenite + K-feldspar + quartz veins. In the two- and three-phase FIs, CO_2-bearing vapour accounts for 10–30 vol.% and 40–60 vol.% of the total inclusion, respectively (Figure 6B). C-type FIs usually homogenize into liquid or occasionally vapour-phase inclusions, while some pure CO_2 vapour inclusions are transformed into two- or three-phase CO_2 inclusions at room temperatures (23°C–25°C). 2) Solid-bearing S-type FIs contain one or more daughter minerals, an aqueous liquid, and a relatively small vapour bubble (Figures 6C,D). They include negative crystal clusters or isolated individuals hosted in late Stage II and III quartz veins. Daughter minerals include hematite, halite, anhydrite, sylvite, and other opaque minerals (Figures 6C,D). During heating, sylvite disappear first, then halite crystals, the bubbles, and finally the anhydrite. Most S-type inclusions homogenize to a liquid phase. 3) Vapour-dominated V-type FIs (Figure 6E) contain 60–100 vol.% vapour and coexist with other types of FIs. They are round or subhedral in shape with diameters of 7–13 μm (Figure 6E), and usually grow together with S-type FIs in quartz growth zones. V-type fluid inclusions are more abundant in early Stage I and II quartz veins than in later veins. 4) Liquid-rich L-type FIs (Figure 6F) contain 10–30 vol.% vapour and >60 vol.% liquid. They are irregular in shape with diameters of 5–15 μm (Figure 6F). L-type FIs occur mainly in Stage III quartz veins, and commonly coexist with V-type FIs and occasionally S- and C-type FIs.

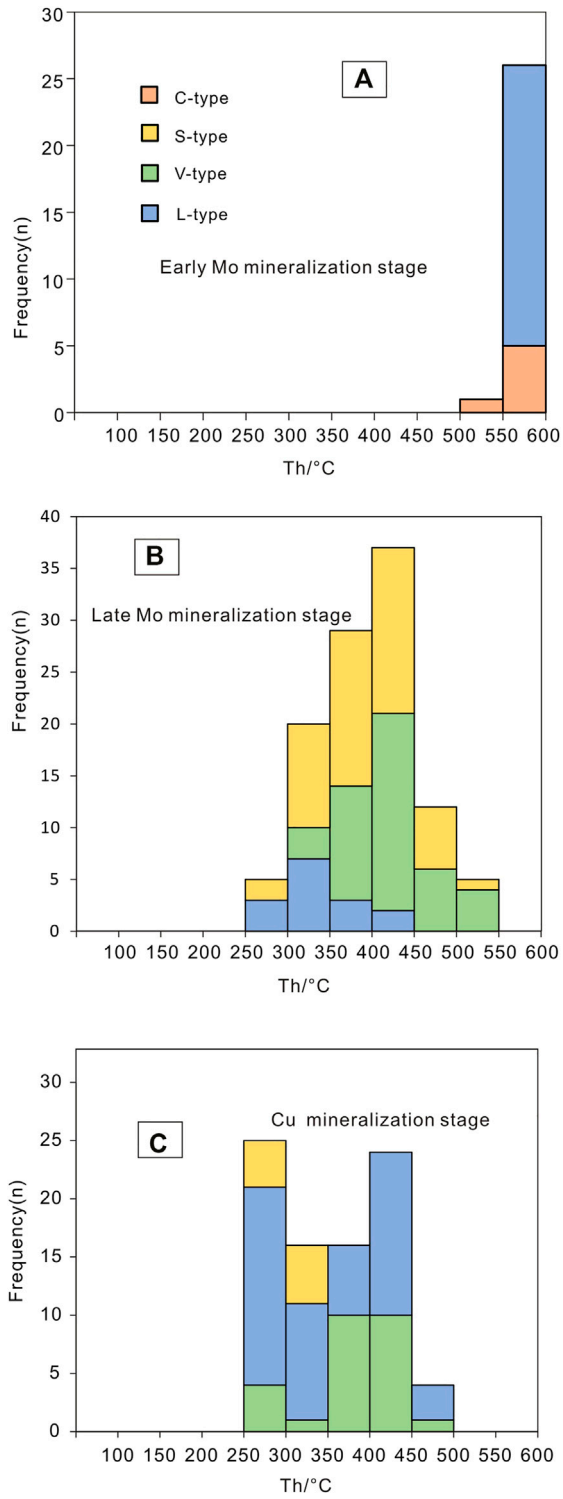


FIGURE 7
Frequency histograms of total homogenization temperatures (Th) for fluid inclusions in different stages. **(A)** early Mo mineralization stage; **(B)** late Mo mineralization stage; **(C)** Cu mineralization stage.

5.2 Microthermometry

Microthermometric data for FIs are summarized in Table S1 and Figure 7. Relationships between different generations of quartz vein and mineralization type indicate that mineralization stages can be further subdivided into Mo mineralization and Cu mineralization stages, with the former including early and late Mo stages based on alteration type.

In the early Mo mineralization stage, FIs are mainly of the C- and V-types, with minor L-type FIs. The C-type FIs yield homogenization temperatures of 543°C–560°C and clathrate-melting temperatures of 4.1°C–6.4°C (two yielded carbonic-phase homogenization temperatures of 21.5°C–25.5°C). L-type FIs have homogenization temperatures of 560°C–570°C (Figure 7A) and ice-melting temperatures of −7.4°C to −13.5°C (corresponding to salinities of 11.0–17.3 wt.% NaCl equiv.). V-type FIs of this stage are usually difficult to observe during heating because of their limited liquid content.

In the late Mo mineralization stage, the abundance of FIs follows the order V-type > S-type > L-type. Homogenization temperatures of FIs are clustered at 340°C–460°C (Figure 7B) with peaks at 400°C and 450°C. V-type FIs have homogenization temperatures of 302°C–512°C, ice-melting temperatures of −6.2°C to −19.7°C, and salinities of 9.5–22.5 wt.% NaCl equiv. During heating, the vapour bubbles disappear before dissolution of the daughter-mineral crystal. This is opposite that of other S-type FIs, possibly due to the fluid system being heterogeneously saturated or oversaturated. Homogenization temperatures of S-type FIs are in the range of 291°C–503°C, with salinities of 42.4–77.0 wt.% NaCl equiv.

In the Cu mineralization stage, FI abundance follows the order: L-type > V-type > S-type. Homogenization temperatures are in the range 230°C–500°C with peaks at 250°C–300°C and 400°C–450°C; the latter is similar to that of FIs of the late Mo mineralization stages (Figure 7C). The L-type FIs have homogenization-temperature peaks at 300°C–350°C and 400°C–450°C, and ice-melting temperatures of −7.1°C to −15.4°C (corresponding to salinities of 11.2–19.0 wt.% NaCl equiv.). V-type FIs have homogenization temperatures of 400°C–450°C and ice-melting temperatures of −7.5°C to −16.9°C, with salinities of 7.2–20.1 wt.% NaCl equiv. Vapour bubbles within S-type FIs disappear earlier than the halite (except for two outliers) during heating. The S-type FIs have homogenization temperatures of 244°C–319°C, daughter-mineral melting temperatures of 244°C–315°C, and salinities of 32.9–45.6 wt.% NaCl equiv.

5.3 Laser Raman microspectroscopy

Laser Raman microspectroscopy results (Figure 8) indicate that CO_2 is detectable only in FIs from early molybdenite-bearing quartz veins (Figures 8A,B). The red-coloured daughter mineral in FIs from Cu- and Mo-dominated quartz veins is hematite (Figure 8C). H_2O is the major liquid phase in all FIs (Figure 8D).

5.4 Melt inclusion composition

Melt inclusions in quartz from the monzonite porphyry are completely crystallized, and those in dacite porphyry are crystallized or partly glassy (Figure 9). Melt inclusions from monzonite porphyry and dacite porphyry have similar major- and trace-element compositions, including 71.7–85.3 wt.% SiO_2, ~14.0 wt.% Al_2O_3, <0.7 wt.% FeO^t, 3.8–6.1 wt.% K_2O, 0.1–0.2 wt.% Na_2O, 0.3–1.0 wt.% CaO, 67–79 ppm Rb, 1.4–2.0 ppm Cs, 1.9–41.5 ppm Cu, and 1.0–2.6 ppm Mo (Table S2).

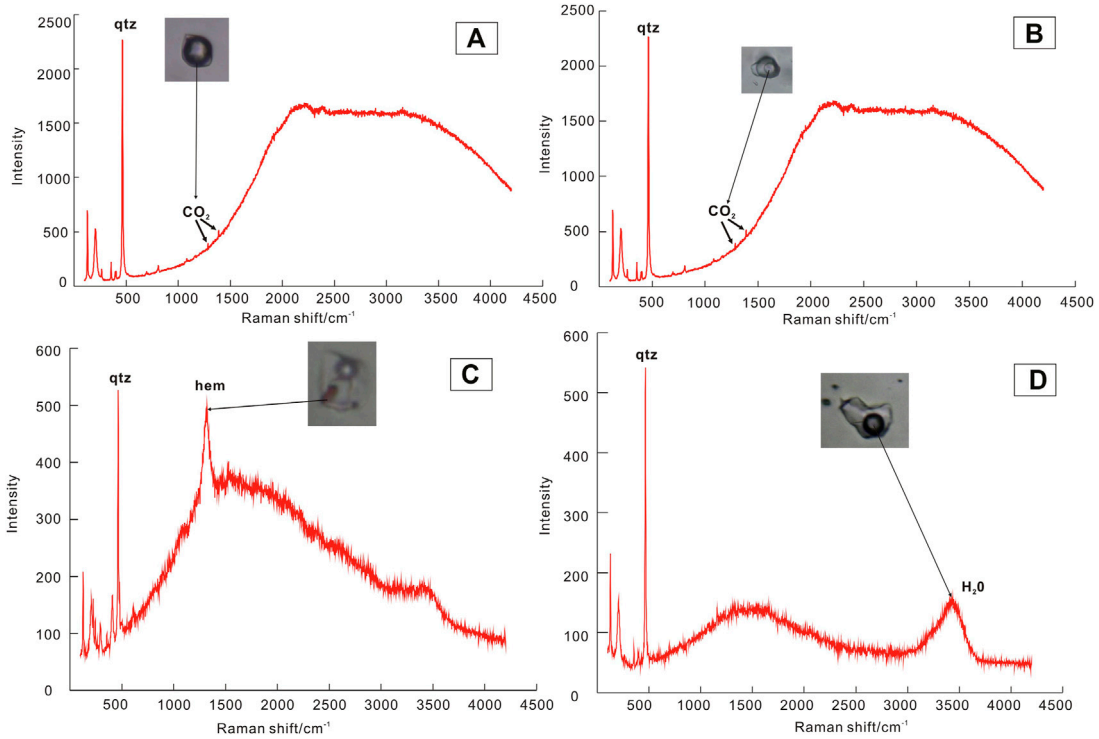


FIGURE 8
Laser Raman spectra of fluid inclusions. **(A, B)** CO_2 in vapor phase of V-type inclusion. **(C)** hematite daughter mineral in S-type inclusion. **(D)** H_2O in vapor phase of L-type inclusion. Abbreviations: hem-hematite, qtz-quartz.

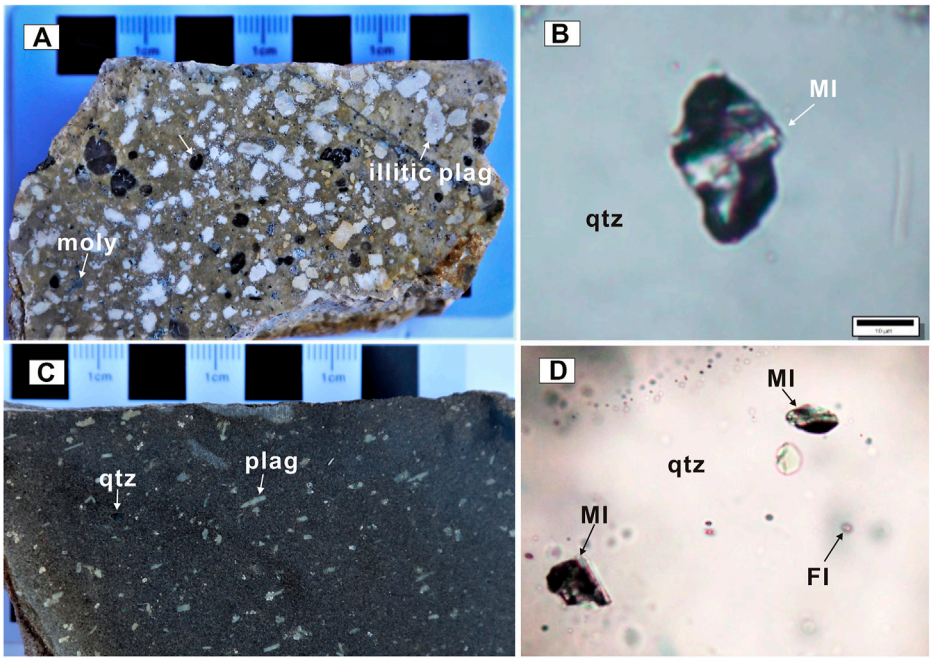


FIGURE 9
Representative hand specimen of quart monzonite porphyry and dacite porphyry and photomicrographs of melt inclusions within them. **(A)** quart monzonite porphyry comprising of plag (45%), qtz (10%), and matrix (45%). **(B)** totally isolated crystalline melt inclusion hosted in quartz of monzonite porphyry. **(C)** dacite porphyry consisting of plag + quartz (10%) and matrix (90%). **(D)** quartz-hosted melt inclusions in dacite porphyry. Abbreviations: qtz-quartz, plag–plagioclase, melt inclusion–MI, fluid inclusion–FI.

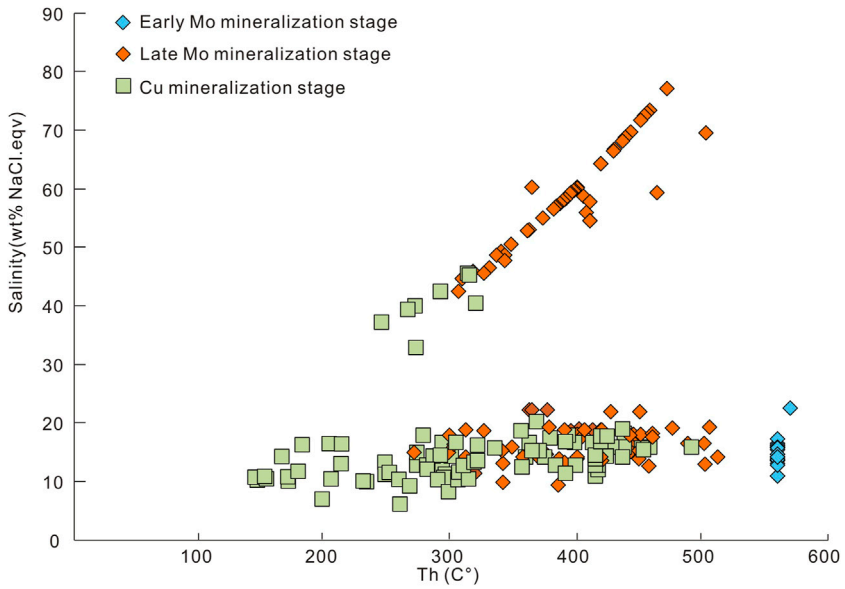


FIGURE 10
Plot of homogenization temperatures (Th) and salinity of individual fluid inclusion in different stages.

6 Discussion

6.1 Fluid evolution in the wunugetushan ore deposit

The physicochemical evolution of magmatic–hydrothermal fluids depends strongly on emplacement depth. Fluids exsolved from deep granitic intrusions under conditions of high temperature and pressure approximate the granite solidus, and lithostatic initial fluids are typically single-phase, of intermediate salinity, and CO_2-rich, as in most porphyry-mineralized systems (Williams-Jones and Heinrich, 2005; Audétat et al., 2008; Kouzmanov and Pokrovski, 2012; Audétat and Li, 2017; Audétat, 2019).

In the early Mo mineralization stage of the Wunugetushan porphyry Cu–Mo deposit, a high-temperature (>550°C), CO_2-rich fluid was first exsolved from the magmatic–hydrothermal system. This fluid evolved near the interior of the porphyry host and was similar to the intermediate-density-type fluid of Audétat. (2019), having a variable and relatively low salinity (4.1–17.3 wt.% NaCl equiv.; Figure 10). During this stage, alteration involved strong alkali metasomatism, as indicated by the abundance of biotite and K-feldspar resulting from interaction between hydrothermal fluid and wall rock. The preservation of magnetite coexisting with biotite indicates the high oxygen fugacity (fO_2) of the primary fluids (Figure 4C). This resulted in limited sulphur activity, and little molybdenite and pyrite were precipitated.

Fluids of the late Mo mineralization stage were highly oxidized, alkali-rich and of high salinity, resulting in the growth of high-fO_2 minerals (anhydrite and hematite), many daughter minerals within FIs, and strong potassic alteration. In contrast to the early mineralization stage, fluids were depleted in CO_2, possibly because of fluid boiling or mixing during local depressurization and the addition of meteoric water into the open hydrothermal system, as indicated by previously published FI δD and $\delta^{18}O$ data (Ye and Wang, 1989; Tan et al., 2013). A high H^+ activity may also promote CO_2 escape through reactions such as $2H^+ + CO_3^{2-} \rightarrow H_2O + CO_2\uparrow$. With the gradual assumption of alkali cations and OH^-, crystallization of anhydrite and hematite, and escape of CO_2, the activity of H^+ in fluids would have increased while fO_2 decreased (Hu et al., 2002; Ulrich et al., 2001; Heinrich, 2005; Seo et al., 2012). Acidic alteration minerals (sericite and illite) and sulphides (mainly molybdenite) would then have precipitated.

In the late Cu mineralization stage, fluids became more acidic with low fO_2, and were CO_2-barren after the crystallization of alkali cations (K^+) and OH-bearing minerals (e.g., biotite and K-feldspar), anhydrite and hematite, and loss of CO_2 (Heinrich, 2005). The low fO_2 and high H^+ activity of fluids led to extensive deposition of acidic alteration minerals (sericite and illite) and sulphides (mainly chalcopyrite). In the Cu mineralization stages, S-type FIs coexisting with V-type FIs in single quartz grains homogenized to a liquid phase, and the latter homogenized to a vapour phase at similar homogenization temperatures, indicating a boiling-fluid system. Fluid mixing is represented by the two temperature peaks (Figure 7C) with the hot magmatic-hydrothermal fluid adding by cold meteoric water.

6.2 Factors controlling the separation of Cu and Mo

Temporospatial decoupling of Cu and Mo has been documented in many porphyry Cu–(Mo–Au) deposits (Sillitoe, 2010 and reference therein) but the causative factors remain elusive. The Cu content of magma is strongly influenced by early sulphide saturation (Audétat et al., 2011). Because of the high partition coefficient for Cu between sulphide and silicate melt (Dsulphide/melt Cu= 250–900; Audétat et al., 2011) and general sulphide saturation in mantle sources or during early crystal fractionation (Lee et al., 2012; Lee and Tang, 2020), the Cu content of the melt will decrease as magma evolves (e.g., Du

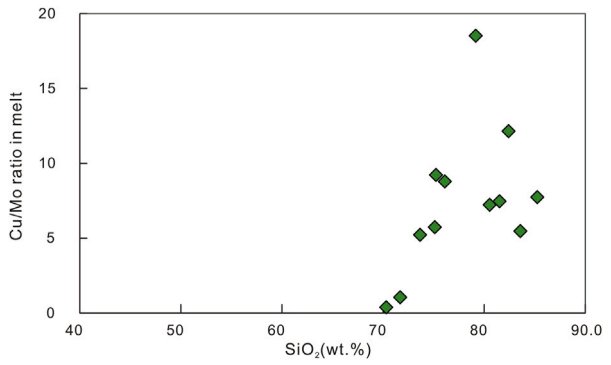


FIGURE 11
Cu/Mo ratios in melt vs. SiO_2 in melt.

and Audétat, 2020). In comparison with the strongly chalcophilic behaviour of Cu, the melt Mo content increases during magma evolution and is less affected by early molybdenite saturation (Audétat et al., 2011) because of the low partition coefficient for Mo between sulphide and silicate melt (Dsulphide/melt Mo= 0.2–10; Audétat et al., 2011). Progressive magma differentiation should therefore lower the Cu/Mo ratio of residual melt in multi-phase porphyry intrusion stocks (Candela and Holland, 1986), and in such a scenario molybdenite-bearing quartz veins are hosted by late porphyry intrusions and molybdenite precipitation generally postdating chalcopyrite crystallization. This is observed in most porphyry Cu–Mo deposits, as in the Bingham Canyon (USA; Seo et al., 2012), Hucunnan (E China; Cao et al., 2017), and Yulong (Tibet in southwestern China; Chang et al., 2018) deposits, where early chalcopyrite precipitation is accompanied with widespread potassic alteration. As a consequence, the contrasting behaviours of Cu and Mo during sulphide saturation will reduce the Cu/Mo ratio in melt, leading to Cu behaving compatibly and Mo incompatibly, with spatial Cu–Mo decoupling. However, early sulphide saturation is limited in relatively basic to intermediate melts with SiO_2 contents of 50–65 wt.%, and as magma evolves to more acidic compositions (SiO_2 content >70 wt.%) the decrease of melt Cu/Mo ratio will be depressed (Audétat et al., 2011) and a high Cu/Mo ratio might be expected due to the high saturation temperature of molybdenite (close to the granite solidus at >550°C; Audétat and Li, 2017) relative to chalcopyrite.

In the Wunugetushan deposit, the effect of early sulphide saturation is weak and Cu–Mo orebodies tend to be simple, featuring a single orebody related to a single acidic intrusion phase. Early sulphide saturation and the possible injection of mafic magma pulses have negligible effects on the Cu and Mo contents of the magma. This inference is supported by the lack of significant Mo or Cu mineralization in late diabase porphyry at Wunugetushan. Melt-inclusion data indicate that causative magmas of the Wunugetushan deposit have a rhyolitic composition (71.7–83.6 wt.% SiO_2), relatively more acidic than other porphyry Cu(–Mo) deposits. The melt Cu/Mo ratio increases with SiO_2 content (Figure 11), possibly due to early molybdenite crystallization at high temperatures of 560°C–570°C (approximating the granite solidus) leading to a decrease in Mo content of the evolved melt. The molybdenite saturation also has been observed in many high-silica rhyolite (75–85 wt.% SiO_2) worldwide (Audétat et al., 2011). Therefore, for a highly acidic intrusive phase, as in the Wunugetushan example, selective precipitation of two metals with contrasting crystallization temperatures could lead to the separation of Cu and Mo.

Molybdenum orebodies in the Wunugetushan deposit are concentrated in the deep interior of the porphyry host, while Cu orebodies occur more towards the exterior, with their spatial distribution being similar to that in many other porphyry Cu–Mo deposits (e.g., the Yulong deposit; Chang et al., 2018). However, the Wunugetushan case differs in the timing of molybdenite and chalcopyrite, with molybdenite precipitating earlier than chalcopyrite, contrary to the situation in other ore deposits. Oxidized fluids generally promote metal transport because the high solubility, but deposition requires a reducing environment, as achieved by the breakdown of oxidized minerals such as anhydrite and magnetite. Chalcopyrite precipitation is promoted by neutral or oxidized fluids, contrasting with molybdenite, which tends to precipitate from more reduced and acidic fluids (Seo et al., 2012). Small changes in the redox state or pH of hydrothermal fluids may thus be responsible for spatial separation of Cu and Mo. In the early molybdenite–quartz veins, molybdenite was first precipitated from alkaline and high-fO_2 fluids, but amounts of molybdenite are small due to the high fO_2 of the initial fluids. Molybdenite precipitation occurred mainly during the late mineralization stage, when oxidizing minerals were consumed and fluids became more acidic and less oxidized. Chalcopyrite precipitation was accompanied by strong acidic alteration (sericitization and illitization) and the formation of more oxidized minerals such as hematite (Figure 5D). Increasing fluid fO_2 and acidity, from the Mo to Cu mineralization stages, thus played a positive role in the spatial separation of the two metals.

Higher CO_2 concentrations in aqueous fluids may reduce the solubility of Mo (Kokh et al., 2017). Decompression during emplacement, condensation of magma bodies and CO_2 escape may thus cause the early precipitation of molybdenite, but variations in CO_2 concentration from the Mo to Cu mineralization stages would merely affect the molybdenite saturation of initial fluids, whether causing the separation of Cu and Mo is not clear. Ascent and decompression of porphyry intrusions would lead to the original single-phase fluids entering brine and vapour phases, which are immiscible in many porphyry Cu systems (Williams-Jones and Heinrich, 2005; Audétat et al., 2008; Kouzmanov and Pokrovski, 2012; Audétat, 2019). Experimental studies have shown that brine inclusions generally host higher Mo concentrations than vapour-rich inclusions (Klemm et al., 2008; Zajacz et al., 2017; Chang et al., 2018), whereas Cu also preferentially be transported by hypersaline brines than vapour-dominated FIs (Lerchbaumer and Audétat, 2012). Both Mo- and Cu-rich brine phases could have condensed from fluids and accumulated deep in the ore deposit due to their high densities. Chang et al. (2018) reported local Cu–Mo decoupling in the Yulong Cu–Mo deposit caused by the sequential deposition of Mo and Cu from a condensed brine phase, but whether vapour/brine immiscibility could be a dominant factor in Cu–Mo separation in an ore-deposit scale is still need explored. In the case of Wunugetushan, vapor-brine immiscibility of FI is not popular and whether such a process affect the Cu/Mo decoupling still need to be explored in the future.

Taken together, the spatial separation of Cu and Mo in the Wunugetushan deposit resulted from the combined effects of multiple factors, including melt Cu/Mo ratios, and the redox state and pH variations of the hydrothermal fluid. It is unclear whether vapor-brine immiscibility predominates in causing Cu–Mo separation, especially on the scale of an ore deposit.

7 Conclusion

Field surveys and melt- and fluid-inclusion studies of the Wunugetushan porphyry Cu–Mo deposit have led to the following conclusions. The Cu and Mo orebodies are hosted by a single monzonite porphyry, with Mo orebodies tending to be concentrated within the porphyry host and Cu orebodies externally. The hydrothermal fluid evolved through three main stages: early and late Mo mineralization and Cu mineralization. Across these stages, fluids changed from initially being of intermediate salinity, CO_2-rich, oxidized, and high temperature, to being of high salinity and CO_2-depleted, and finally to again being of intermediate salinity but highly oxidized. The separation of Cu and Mo was promoted by a combination of factors including increased Cu/Mo ratios in residual melt, and the changing redox state and acidity of ore-forming fluids.

Data availability statement

The datasets presented in this study can be found in online repositories. The names of the repository/repositories and accession number(s) can be found in the article/Supplementary Material.

Author contributions

JD designed the project and collected the samples; WL wrote the first manuscript and studies the melt inclusions; YZ anticipated the field work and fluid inclusion studies; ZS did the field work.

Funding

This study was supported financially by the National Natural Science Foundation of China (No. 42002072), Fundamental Research Funds for the Central Universities (Grant 300102271304), Natural Science Basic Research Program of Shaanxi (Program No. 2023-JC-QN-0336).

Acknowledgments

We also want to thank associate editor Fan Yang and three reviewers for their constructive suggestions.

Conflict of interest

ZS was employed by China Gold Inner Mongolia Mining Co Ltd.

The remaining authors declare that the research was conducted in the absence of any commercial or financial relationships that could be construed as a potential conflict of interest.

The reviewer LT declared a shared affiliation with the author YZ to the handling editor at time of review.

Publisher's note

All claims expressed in this article are solely those of the authors and do not necessarily represent those of their affiliated organizations, or those of the publisher, the editors and the reviewers. Any product that may be evaluated in this article, or claim that may be made by its manufacturer, is not guaranteed or endorsed by the publisher.

Supplementary material

The Supplementary Material for this article can be found online at: https://www.frontiersin.org/articles/10.3389/feart.2023.1121856/full#supplementary-material

References

Audétat, A., Dolejs, D., and Lowenstern, J. B. (2011). Molybdenite saturation in silicic magmas: Occurrence and petrological implications. *J. Pet.* 52, 891–904. doi:10.1093/petrology/egr008

Audétat, A., and Li, W. T. (2017). The Genesis of Climax-type porphyry Mo deposits: Insights from fluid inclusions and melt inclusions. *Ore. Geol. Rev.* 88, 436–460. doi:10.1016/j.oregeorev.2017.05.018

Audétat, A., Pettke, T., Heinrich, C. A., and Bodnar, R. J. (2008). Special paper: The composition of magmatic-hydrothermal fluids in barren and mineralized intrusions. *Econ. Geol.* 103, 877–908. doi:10.2113/gsecongeo.103.5.877

Audétat, A. (2019). The metal content of magmatic-hydrothermal fluids and its relationship to mineralization potential. *Econ. Geol.* 114 (6), 1033–1056. doi:10.5382/econgeo.4673

Bodnar, R. J. (1993). Revised equation and table for determining the freezing point depression of H_2O–NaCl solutions. *Geochim Cosmochim. Acta.* 57, 683–684. doi:10.1016/0016-7037(93)90378-a

Candela, P. A., and Holland, H. D. (1986). A mass transfer model for copper and molybdenum in magmatic hydrothermal systems:the origin of porphyry-type ore deposits. *Econ. Geol.* 81, 1–19. doi:10.2113/gsecongeo.81.1.1

Cao, Y., Zheng, Z. J., Du, Y. L., Gao, F. P., Qin, X. L., Yang, H. M., et al. (2017). Ore geology and fluid inclusions of the Hucunnan deposit, Tongling, Eastern China: Implications for the separation of copper and molybdenum in skarn deposits. *Ore. Geol. Rev.* 81, 925–939. doi:10.1016/j.oregeorev.2016.04.013

Chang, J., Li, J. W., and Audétat, A. (2018). Formation and evolution of multistage magmatic-hydrothermal fluids at the Yulong porphyry Cu-Mo deposit, eastern Tibet: Insights from LA-ICP-MS analysis of fluid inclusions. *Geochim. Cosmochim. Acta.* 232, 181–205. doi:10.1016/j.gca.2018.04.009

Chen, X., Li, H. N., and Duan, G. Z. (1997). Origin of the Erentaolegai granite and its relations with silver deposit, Inner Mongolia. *Min. Resour. Geol.* 11, 91–98.

Chen, Z. G., Zhang, L. C., Wan, B., Wu, H. Y., and Cleven, N. (2011). Geochronology and geochemistry of the Wunugetushan porphyry Cu–Mo deposit in NE China, and their geological significance. *Ore Geol. Rev.* 43, 92–105. doi:10.1016/j.oregeorev.2011.08.007

Du, J. G., and Audétat, A. (2020). Early sulfide saturation is not detrimental to porphyry Cu-Au formation. *Geology* 48, 519–524. doi:10.1130/G47169.17

Gao, B. Y., Zhang, L. C., Jin, X. D., Li, W. J., Chen, Z. G., and Zhu, M. T. (2016). Geochronology and geochemistry of the Badaguan porphyry Cu–Mo deposit in Derbugan metallogenic belt of the NE China, and their geological significances. *Int. J. Earth Sci. Geol. Rundsch)* 105, 507–519. doi:10.1007/s00531-015-1261-4

Halter, W. E., Pettke, T., and Heinrich, C. A. (2004). Laser-ablation ICP-ms analysis of silicate and sulfide melt inclusions in an andesitic complex I:

Analytical approach and data evaluation. *Contrib. Mineral. Pet.* 147, 385–396. doi:10.1007/s00410-004-0562-6

Heinrich, C. A., Pettke, T., Halter, W. E., Aigner-Torres, M., Audétat, A., Gunther, D., et al. (2003). Quantitative multi-element analysis of minerals, fluid and melt inclusions by laser-ablation inductively-coupled-plasma mass-spectrometry. *Geochim. Cosmochim. Acta.* 67, 3473–3497. doi:10.1016/s0016-7037(03)00084-x

Heinrich, C. A. (2005). The physical and chemical evolution of low-salinity magmatic fluids at the porphyry to epithermal transition: A thermodynamic study. *Min. Deposita.* 39, 864–889. doi:10.1007/s00126-004-0461-9

Hu, S. X., Zhao, Y. Y., Sun, J. G., Ling, H. F., Ye, Y., Lu, B., et al. (2002). Fluids and their sources for gold mineralization in the north China platform. *J. Nanjing Univ. Nat. Sci.* 38, 381–391.

Hu, X. L., Ding, Z. J., Yao, S. Z., He, M. C., Shen, J., Zhu, B. P., et al. (2014). Geochronology and Sr–Nd–Hf isotopes of the mesozoic granitoids from the great xing'an and lesser xing'an ranges: Implications for petrogenesis and tectonic evolution in NE China. *Geol. J.* 51, 1–20. doi:10.1002/gj.2576

Klemm, L. M., Pettke, T., and Heinrich, C. A. (2008). Fluid and source magma evolution of the Questa porphyry Mo deposit, New Mexico, USA. *Min. Deposita* 43, 533–552. doi:10.1007/s00126-008-0181-7

Kokh, M. A., Akinfiev, N. N., Pokrovski, G. S., Salvi, S., and Guillaume, D. (2017). The role of carbon dioxide in the transport and fractionation of metals by geological fluids. *Geochim. Cosmochim. Acta.* 197, 433–466. doi:10.1016/j.gca.2016.11.007

Kouzmanov, K., and Pokrovski, G. S. (2012). Hydrothermal controls on metal distribution in porphyry Cu (-Mo-Au) systems. *Soc. Econ. Geol. Special Publ.* 16, 573–618. doi:10.5382/SP.16.22

Lan, T. G., Hu, R. Z., Bi, X. W., Mao, G. J., Wen, B. J., Liu, L., et al. (2017b). Metasomatized asthenospheric mantle contributing to the generation of Cu-Mo deposits within an intracontinental setting: A case study of the ~128 Ma wangjiazhuang Cu-Mo deposit, eastern north China Craton. *J. Asian Earth Sci.* 160, 460–489. doi:10.1016/j.jseaes.2017.07.014

Lan, T. G., Hu, R. Z., Fan, H. R., Bi, X. W., Tang, Y. W., Zhou, L., et al. (2017a). *In-situ* analysis of major and trace elements in fluid inclusion and quartz: LA-ICP-MS method and applications to ore deposits. *Acta Pet. Sin.* 33, 3239–3262 in Chinese with English abstract.

Lee, C.-T., Luffi, P., Chin, E. J., Bouchet, R., Dasgupta, R., Morton, D. M., et al. (2012). Copper systematics in arc magmas and implications for crust–mantle differentiation. *Science* 336 (6077), 64–68. doi:10.1126/science.121731

Lee, C.-T.-A., and Tang, M. (2020). How to make porphyry copper deposits. *Earth Planet. Sci. Lett.* 529, 1–11. doi:10.1016/j.epsl.2019.115868

Lerchbaumer, L., and Audétat, A. (2012). The metal content of silicate melts and aqueous fluidsin subeconomically Mo-mineralized granites: Implications for porphyry Mo genesis. *Econ. Geol.* 108, 987–1013. doi:10.2113/econgeo.108.5.987

Li, N., Chen, Y. J., Ulrich, T., and Lai, Y. (2012). Fluid inclusion study of the Wunugetu Cu–Mo deposit, Inner Mongolia, China. *Min. Deposita* 47, 467–482. doi:10.1007/s00126-011-0384-1

Liu, J., Mao, J. W., Wu, G., Wang, F., Luo, D. F., Hu, Y. Q., et al. (2014). Fluid inclusions and H–O–S–Pb isotope systematics of the Chalukou giant porphyry Mo deposit, Heilongjiang Province, China. *Ore Geol. Rev.* 59, 83–96. doi:10.1016/j.oregeorev.2013.12.006

Metelkin, D. V., Vernikovsky, V. A., Kazansky, A. Y., and Wingate, M. T. D. (2010). Late Mesozoic tectonics of Central Asia based on paleomagnetic evidence. *Gondwana Res.* 18, 400–419. doi:10.1016/j.gr.2009.12.008

Mi, K. F., Liu, Z. J., Li, C. F., Liu, R. B., and Wang, J. P. (2014). U-Pb ages and Hf isotopes of Zircon in biotite granite from Wunugeshan porphyry Cu-Mo deposit. *Geol. J.* 33, 113–114 in Chinese with English abstract.

Pak, S. J., Choi, S. G., and Choi, S. H. (2004). Systematic mineralogy and chemistry of gold-silver vein deposits in the Taebaeksan district, Korea: Distal relatives of a porphyry system. *Mineral. Mag.* 68 (3), 467–487. doi:10.1180/0026461046830199

Pan, L. J., and Sun, E. Y. (1990). Geological characteristics of the Chaganbulagen silver–lead–zinc deposit, Inner Mongolia. *Min. Explor.* 5, 1–9.

Qin, K. Z., Li, H. M., Li, W. S., and Ishihara, S. (1999). Intrusion and mineralization ages of the Wunugetushan porphyry Cu–Mo deposit, Inner Mongolia, Northwestern China. *Geol. Rev.* 45, 181–185.

Qin, K. Z., Wang, Z. T., Wang, L. J., Bao, Y. H., and Li, Y. M. (1993). Studies on hydrothermal convection, alteration superimposition and ore-forming processes of the Wunugetushan porphyry copper molybdenum deposit, Inner Mongolia. *Geol. Explor. Non-Ferrous Metals* 2, 136–143.

Redmond, P. B., and Einaudi, M. T. (2010). The Bingham Canyon porphyry Cu-Mo-Au deposit. I. Sequence of intrusions, vein formation, and sulfide deposition. *Econ. Geol.* 105, 43–68. doi:10.2113/gsecongeo.105.1.43

Safonova, I. Y. (2009). Intraplate magmatism and oceanic plate stratigraphy of the paleo-asian and paleo-pacific oceans from 600 to 140 Ma. *Ore. Geol. Rev.* 35, 137–154. doi:10.1016/j.oregeorev.2008.09.002

Seo, J. H., Guillong, M., Aerts, M., Zajacz, Z., and Heinrich, C. A. (2011). Microanalysis of S, Cl, and Br in fluid inclusions by LA-ICP-MS. *Chem. Geol.* 284, 35–44. doi:10.1016/j.chemgeo.2011.02.003

Seo, J. H., Guillong, M., and Heinrich, C. A. (2012). Separation of molybdenum and copper in porphyry deposits: The roles of sulfur, redox, and pH in ore mineral deposition at Bingham Canyon. *Econ. Geol.* 107, 333–356. doi:10.2113/econgeo.107.2.333

Sillitoe, R. H. (2010). Porphyry copper systems. *Econ. Geol.* 105, 3–41. doi:10.2113/gsecongeo.105.1.3

Sterner, S. M., Hall, D. L., and Bodnar, R. J. (1988). Synthetic fluid inclusions. V. Solubility relations in the system NaCl–KCl–H_2O under vapor–saturated conditions. *Geochim.Cosmochim. Acta* 52, 989–1005. doi:10.1016/0016-7037(88)90254-2

Tan, G., She, H. Q., Yin, J. P., Yang, Y. C., Li, J. W., Xiang, A. P., et al. (2013). Source and evolution of ore-fluid in wunugetushan large Cu-Mo deposit, inner Mongolia: Evidence from fluid inclusions and hydrogen and oxygen isotopic geochemistry. *Glob. Geol.* 32 (3), 463–482 in Chinese with English abstract.

Ulrich, T., Gunther, D., and Heinrich, C. A. (2001). The evolution of a porphyry Cu–Au deposit, based on LA-ICP-MS analysis of fluid inclusions: Bajo de la Alumbrera, Argentina. *Econ. Geol.* 97, 1889–1920. doi:10.2113/gsecongeo.97.8.1889

Wang, L. Q., Tang, J. X., Chen, W. B., Chen, W., Zhang, Z., Lin, X., et al. (2015a). Origin of the ore-forming fluids and metals of the Bangpu porphyry Mo–Cu deposit of tibet, China: Constraints from He–Ar, H–O, S and Pb isotopes. *J. Asian Earth Sci.* 103, 276–287. doi:10.1016/j.jseaes.2014.07.041

Wang, Y. H., Zhao, C. B., Zhang, F. F., Liu, J. J., Wang, J. P., Peng, R. M., et al. (2015b). SIMS zircon U–Pb and molybdenite Re–Os geochronology, Hf isotope, and whole-rock geochemistry of the Wunugetushan porphyry Cu–Mo deposit and granitoids in NE China and their geological significance. *Gondwana Res.* 28, 1228–1245. doi:10.1016/j.gr.2014.10.001

Williams-Jones, A. E., and Heinrich, C. A. (2005). 100th anniversary special paper: Vapor transport of metals and the formation of magmatic-hydrothermal ore deposits. *Econ. Geol.* 100, 1287–1312. doi:10.2113/gsecongeo.100.7.1287

Wu, C., Tian, J., Chang, F., Liu, C., and Liu, W. (2014). Early cretaceous A-type granites and Mo mineralization, aershan area, eastern inner Mongolia, northeast China: Geochemical and isotopic constraints. *Int. Geol. Rev.* 56, 1357–1376. doi:10.1080/00206814.2014.935965

Wu, F. Y., Sun, D. Y., Ge, W. C., Zhang, Y. B., Grant, M. L., Wilde, S. A., et al. (2011). Geochronology of the Phanerozoic granitoids in northeastern China. *J. Asian Earth Sci.* 41, 1–30. doi:10.1016/j.jseaes.2010.11.014

Wu, G., Mei, M., and Gao, F. J. (2010). Ore-forming fluid characteristics and Genesis of silver–lead–zinc deposits in the Manzhouli area, Inner Mongolia, China. *Earth Sci. Front.* 17, 239–255 in Chinese with English abstract.

Xiao, W. J., and Santosh, M. (2014). The Western central asian orogenic belt: A window to accretionary orogenesis and continental growth. *Gondwana. Res.* 25, 1429–1444. doi:10.1016/j.gr.2014.01.008

Xu, W. L., Ji, W. Q., Pei, F. P., Meng, E., Yu, Y., Yang, D. B., et al. (2009). Triassic volcanism in eastern Heilongjiang and Jilin Provinces,NE China: Chronology, geochemistry, and tectonic implications. *J. Asian Earth Sci.* 34, 392–402. doi:10.1016/j.jseaes.2008.07.001

Xu, W. L., Pei, F. P., Wang, F., Meng, E., Ji, W. Q., Yang, D. B., et al. (2013). Spatial–temporal relationships of Mesozoic volcanic rocks in NEChina: Constraints on tectonic overprinting and transformationsbetween multiple tectonic regimes. *J. Asian Earth Sci.* 74, 167–193. doi:10.1016/j.jseaes.2013.04.003

Ye, X., and Wang, L. J. (1989). A study on fluid inclusion and metallogenesis of a porphyry Cu–Mo deposit, Urugetu Hill, Inner Mongolia, China. *Sci. Geol. Sin.* 33, 84–92.

Zajacz, Z., Candela, P. A., and Piccoli, P. M. (2017). The partitioning of Cu, Au and Mo between liquid and vapor at magmatic temperatures and its implications for the Genesis of magmatic-hydrothermal ore deposits. *Geochim. Cosmochim. Acta.* 207, 81–101. doi:10.1016/j.gca.2017.03.015

Zeng, Q. D., Liu, J. M., Chu, S. X., Wang, Y. B., Sun, Y., Duan, X. X., et al. (2014). Re–Os and U–Pb geochronology of the Duobaoshan porphyry Cu–Mo–(Au)deposit, northeast China, and its geological significance. *J. Asian Earth Sci.* 79, 895–909. doi:10.1016/j.jseaes.2013.02.007

Zhai, D. G., Liu, J. J., Wang, J. P., Yao, M. J., Wu, S. H., Fu, C., et al. (2013). Fluid evolution of the Jiawula Ag–Pb–Zn deposit, inner Mongolia: Mineralogical, fluid inclusion, and stable isotopic evidence. *Int. Geol. Rev.* 55, 204–224. doi:10.1080/00206814.2012.692905

frontiers | Frontiers in Earth Science

TYPE Original Research
PUBLISHED 02 February 2023
DOI 10.3389/feart.2023.1085767

Check for updates

OPEN ACCESS

EDITED BY
Fan Yang,
Lanzhou University, China

REVIEWED BY
Fan Huang,
CAGS, China
Xingyuan Li,
Lanzhou University, China
Qian Liu,
Northwest University, China

*CORRESPONDENCE
Da Zhang,
zhangda@cugb.edu.cn

SPECIALTY SECTION
This article was submitted to Geochemistry, a section of the journal Frontiers in Earth Science

RECEIVED 31 October 2022
ACCEPTED 13 January 2023
PUBLISHED 02 February 2023

CITATION
Hu B, Zhang D, Zhang X, Zhang Z, Wang S and Hu J (2023), Identification of Baihesi aluminous A-type granite: Magmatic response to the onset of Cretaceous extension in eastern Jiangnan Massif, South China.
Front. Earth Sci. 11:1085767.
doi: 10.3389/feart.2023.1085767

COPYRIGHT
© 2023 Hu, Zhang, Zhang, Zhang, Wang and Hu. This is an open-access article distributed under the terms of the Creative Commons Attribution License (CC BY). The use, distribution or reproduction in other forums is permitted, provided the original author(s) and the copyright owner(s) are credited and that the original publication in this journal is cited, in accordance with accepted academic practice. No use, distribution or reproduction is permitted which does not comply with these terms.

Identification of Baihesi aluminous A-type granite: Magmatic response to the onset of Cretaceous extension in eastern Jiangnan Massif, South China

Bojie Hu[1], Da Zhang[1]*, Xinming Zhang[1], Zhihui Zhang[2], Sen Wang[3,4,5] and Jiaxiu Hu[1]

[1]School of Earth Sciences and Resources, China University of Geosciences (Beijing), Beijing, China, [2]Development and Research Center, China Geological Survey, Beijing, China, [3]Institute of Geomechanics, Chinese Academy of Geological Sciences, Beijing, China, [4]Key Laboratory of Paleomagnetism and Tectonic Reconstruction, Ministry of Natural Resources, Beijing, China, [5]Research Center of Polar Geosciences, China Geological Survey, Beijing, China

The Cretaceous lithospheric extension in South China is very distinct and expressed by systematic extension-related geological records which are concentrated in the coastal terrane, Shi-Hang Rift, and Jiangnan Massif. The Cretaceous extension in the coastal terrane and Shi-Hang Rift began almost simultaneously during 145–140 Ma, while there is a lack of reliable magmatic indication for tectonic extension in the Jiangnan Massif during 145–140 Ma. This paper reports a newly discovered Baihesi granite with a concordant age of 142.52 ± 0.57 Ma (MSWD = 1.2) on the southeast margin of the eastern Jiangnan Massif with evidence from petrology, geochronology, petrochemistry and Hf isotopes. The Baihesi granite is a monzogranite and classified as a peraluminous, high-K calc-alkaline series. The trace element compositions are characterized by relatively flat rare earth element patterns; strong depletion of Eu; slightly enriched light rare earth elements; enrichment of Cs, Rb, Th, U, and Pb; and depletion of Ba, Sr, P, and Ti. Combined with other petrochemistry characteristics, such as high SiO_2 content, high differentiation index, low Zr/Hf and Nb/Ta ratios, low ratio between light and heavy REEs, low P_2O_5 content, and high zirconium saturation temperature, Baihesi granite is proven to be highly evolved aluminous A-type granite. The $\varepsilon_{Hf}(t)$ values of Baihesi granite range from −5.57 to −2.37, with two-stage model ages (T_{DM2}) ranging from 1,551 to 1,345 Ma, suggesting a similar source to Neoproterozoic arc-related magmatic rocks in the Shuangqiaoshan Group. We argue that Baihesi granite has originated mainly from partial melting of a reworked juvenile crust related to Neoproterozoic arc-related magmatism in the Jiangnan Massif, which was controlled by subduction along the South China active continental margin. Furthermore, we constrain the onset of Cretaceous extension in the eastern Jiangnan Massif to be 145–140 Ma and highlight the Early Cretaceous reactivation of the northeastern Jiangxi Province fault zone and the structural inheritance in intraplate tectonics.

KEYWORDS

Cretaceous lithospheric extension, South China, Baihesi granite, eastern Jiangnan Massif, highly evolved aluminous A-type granite

1 Introduction

The Cretaceous lithospheric extension in South China, even in entire eastern Eurasia, is very remarkable and typical (Chu et al., 2019; Li et al., 2014; Liu et al., 2021). Systematic extension-related geological records, including bimodal volcanic rocks, mafic dikes, A-type granitoids, half-grabens, faulted basins, and low-angle detachment faults, indicate that a long-term extensional regime has dominated the South China Block during the Cretaceous (Chu et al., 2019; Li et al., 2014). As to spatial distribution, these geological records are obviously concentrated in two regions, namely, the coastal terrane (CT) and the intraplate ancient suture zone-related terranes in South China (Figure 1). Many previous studies have been conducted on these records to understand the temporal and spatial evolution of South China during the Cretaceous (e.g., Chu et al., 2019; Ji et al., 2018a, 2018b; Jiang et al., 2015; Li et al., 2013; Lin et al., 2000; Shu et al., 2009; Yu et al., 2006; Zhou and Li, 2000; Zhou et al., 2006). Among these studies, the research of magmatism, which can be used as the "litho-probe" or "window" to help understand the Earth's interior and tectonic evolution, played an important role in constraining the temporal stages and dynamic mechanism of the Cretaceous extension (Mo, 2019).

The Cretaceous magmatism in the CT developed from the earliest Cretaceous to the early Late Cretaceous (140–90 Ma, Zhou et al., 2006), including the felsic volcanic rocks from the eastern Guangdong and Fujian provinces with an early stage of 143–130 Ma (Guo et al., 2012), and the volcanic rocks from the southeastern Zhejiang Province with an early stage of 145–129 Ma or 140–128 Ma (Li et al., 2014; Liu et al., 2012). According to the different output characteristics of the extension-related geological records, the intraplate ancient suture zone-related terranes can be subdivided into the Shi-Hang Rift (SR) and Jiangnan Massif (JM). In the northwestern Zhejiang Province, which is located in the most northeast segment of the SR and closest to the CT, the volcanic activity related to extension began at *ca.*140 Ma (Liu et al., 2014), and A-type granites formed during 136–126 Ma (Wong et al., 2009; Yang et al., 2012). In the Xiangshan region, which is located in the middle segment of the SR and hundreds of kilometers away from the coast, extension-related volcanism and A-type granites occurred between 137 and 135 Ma (Yang et al., 2011). Hence, magmatism related to the Cretaceous extension in the CT and SR began almost simultaneously during 145–140 Ma.

However, in the eastern Jiangnan Massif (EJM), the magmatism related to the Cretaceous extension mainly occurred between 134 Ma

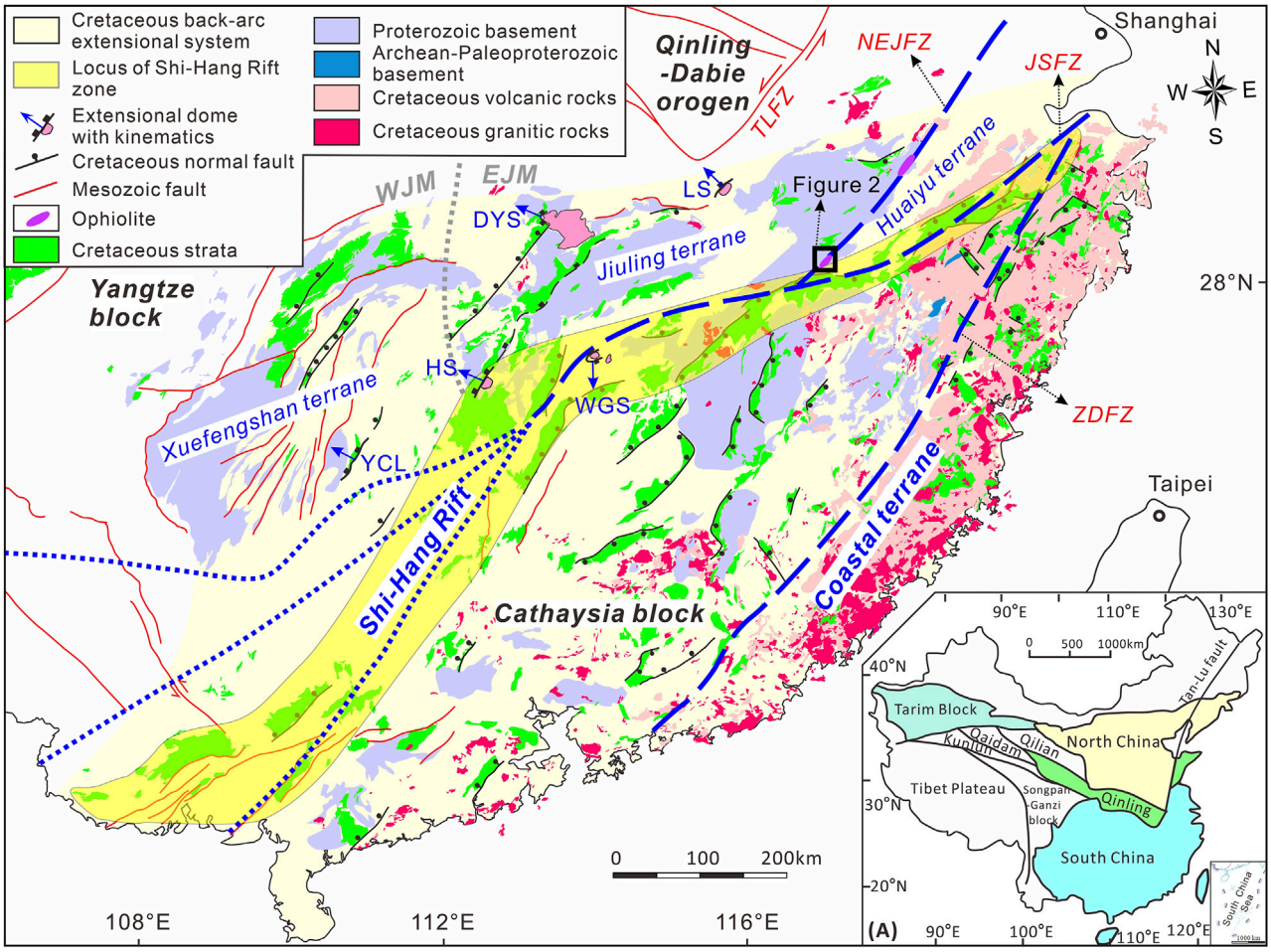


FIGURE 1
Tectonic map and Cretaceous extension-related records of South China (modified from Gilder et al., 1996; Wang et al., 2014; Chu et al., 2019; Li et al., 2022; Wang et al., 2022). Abbreviations for extensional domes and fault zones: WJM, western Jiangnan Massif; EJM, eastern Jiangnan Massif; TLFZ, Tancheng–Lujiang fault zone; NEJFZ, northeastern Jiangxi Province fault zone; JSFZ, Jiangshan–Shaoxing fault zone; ZDFZ, Zhenhe–Dabu fault zone; DYS, Dayunshan dome; HS, Hengshan dome; LS, Lushan dome; WGS, Wugongshan dome; YCL, Yuechengling dome.

TABLE 1 Early Cretaceous granitoids related to lithospheric extension in the EJM.

Location	Lithology	Type of granite	Age (mineral, methods)	Source
Xianglushan	Biotite granite	S	123.81 ± 0.77 Ma (zircon, LA-ICPMS)	Dai et al. (2018)
Dongping	Biotite granite	S	132.9 ± 1.4 Ma (zircon, LA-ICPMS)	Hu et al. (2018)
Pengshan	Granite	I	128 ± 1 Ma (zircon, SHRMP)	Luo et al. (2010)
Maogongdong (Dahutang)	Porphyritic granite		132.5 ± 1.8 Ma (zircon, LA-ICPMS)	Chen et al. (2018)
Yunshan	Topaz-bearing muscovite monzogranite		129.4 ± 0.2 Ma (zircon, LA-ICPMS)	Yang et al. (2021)
	Two-mica monzogranite		130.6 ± 0.2 Ma (zircon, LA-ICPMS)	
	Granophyre		129.7 ± 0.2 Ma (zircon, LA-ICPMS)	
Ehu	Two-mica granites	S	121.7 ± 2.9 Ma (zircon, LA-ICPMS)	Jiang et al. (2011)
	Two-mica monzogranite		132.0 ± 0.6 Ma (zircon, LA-ICPMS)	Qiu and Qiu, (2016)
Zhenzhushan	Granite porphyry	A	133.7 ± 0.2 Ma (zircon, LA-ICPMS)	Yang et al. (2021)

and 121 Ma (Table 1), including Xianglushan (Dai et al., 2018), Dongping (Hu et al., 2018), Penshan (Luo et al., 2010), Yunshan (Yang et al., 2021), Ehu (Jiang et al., 2011; Yang et al., 2021), and Zhenzhushan (Yang et al., 2021). Furthermore, another significant stage of magmatism developed in the EJM mainly during 154–136 Ma (He et al., 2022; Yang et al., 2021; Zhang et al., 2020). It is controversial whether the tectonic setting of 154–136 Ma magmatism in the EJM was lithospheric extension or compression (Huang and Jiang, 2014; Mao et al., 2017; Pan et al., 2018) and has been interpreted as a compression–extension transition (Feng et al., 2018).

It follows that, being different from the coastal zone and the Shi-Hang Zone, the tectonic setting of the EJM in the earliest Cretaceous is not well-constrained. This problem is mainly attributed to the absence of magmatic record, such as bimodal volcanic rocks and A-type granitoids, which could provide explicit evidence for the extensional tectonic setting. The manifestation of extension is attenuated from the coast to the inland regions, which was characterized by less volcanic activity in extensional basins and weaker crust–mantle interaction in magmatism. In this case, A-type granite provides a rare and relatively reliable indicator for recognizing the tectonic extension in the inland region because A-type granites commonly occur in post-orogenic or intraplate extensional tectonic settings (Eby, 1992; Eby and Kochhar, 1990; Whalen et al., 1987).

In this contribution, we report a newly discovered A-type granite with a concordant age of 142.52 ± 0.57 Ma (MSWD = 1.2) on the southeast margin of the EJM, shedding light on the fact that the Cretaceous lithospheric extension has started as early as *ca.* 145-140 Ma in the EJM.

2 Geological setting

The Jiangnan Massif (JM), spanning the central part of the South China Block (SCB) and separating the Yangtze Block in the northwest and the Cathaysia Block in the southeast (Figure 1; Zhao and Cawood, 2012), is an ENE-trending and *ca.* 1,500-km-long tectonic belt consisting of Neoproterozoic undeformed granitoids and low-greenschist facies metamorphosed sedimentary rocks (Wang et al., 2008; Wang et al., 2013; Wang et al., 2014; Yao et al., 2019). Meanwhile, the JM was divided into the Huaiyu terrane (HYT), Jiuling terrane (JLT), and Southeast terrane (ST) from east to west (Figure 1; Wang et al., 2022; Yao et al., 2019). The northeastern Jiangxi Province fault zone (NEJFZ), considered to be the boundary structure between the JLT and HYT, is the most outstanding suture zone for Neoproterozoic Jiangnan orogenesis, in which there is the most systematic evidence including ophiolite, high-pressure metamorphic rock, syn-orogenic granite, and post-orogenic granite (Li et al., 2009; Shu et al., 1994; Wang et al., 2008; Wang et al., 2014; Yao et al., 2012; Ye et al., 2007). The JM originated from the collisional welding of the Yangtze Block and Cathaysia Block during Neoproterozoic (Charvet, 2013; Yao et al., 2019; Zhao and Cawood, 2012) and was strongly modified by intraplate compressional deformation during the Early Paleozoic and Early Mesozoic, so it was also a typical multiphase intraplate orogen (Chu and Lin, 2014; Chu et al., 2015; Li et al., 2016; Shu, 2021).

The Baihesi granite (BHSG), located on the southeastern margin of the JM, is adjacent to the NEJFZ on the southeast. The strata, structures, and magmatic rocks in the study area are controlled by the NNE-trending NEJFZ. The sedimentary strata consist of Neoproterozoic Shuangqiaoshan Group metasedimentary rocks, Carboniferous carbonates, Triassic clastic rocks, Jurassic clastic rocks, and Quaternary sediments. NNE- and NNW-striking faults are developed in the Fuquanshan area where BHSG is located, with dominant NNE-striking. The Fuquanshan anticline is the major fold in the study area. It is cored by Neoproterozoic strata and flanked by Carboniferous to Jurassic strata (Figure 2). Magmatic rocks are widespread in the study area, including the Fuquanshan granitic pluton (FQSG) that intruded in the core of the Fuquanshan anticline and a series of NNE-trending granitic dikes located the southwest of FQSG, namely, BHSG. FQSG intruded in Neoproterozoic metasedimentary rocks and Carboniferous carbonate as a batholith. BHSG intruded along the interlayer structures of the Neoproterozoic metasedimentary rocks with several sub-parallel sheets (Figure 3).

3 Sampling and analytical methods

To ensure the representativeness of the samples, we selected several fresh samples of BHSG from different parts of the outcrop during the

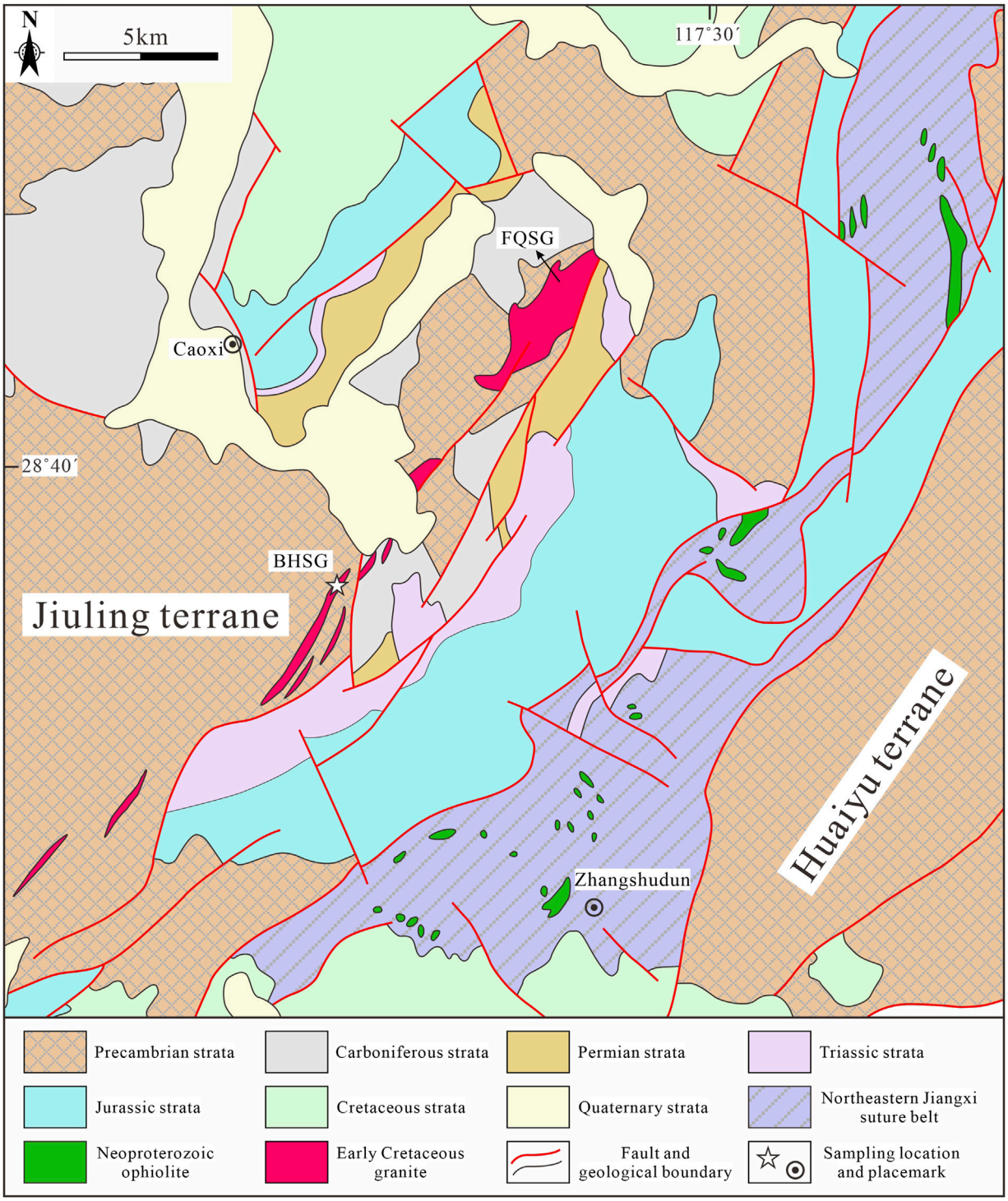


FIGURE 2
Geological map of the Fuquanshan area (modified from Northeastern Jiangxi Geological Party, Bureau of Geology and Mineral Resources of Jiangxi Province).

fieldwork. BHSG shows porphyritic textures with phenocrysts of feldspar and quartz (Figures 4A–C) and is primarily composed of quartz (35%), plagioclase (30%), K-feldspar (30%), and biotite (5%), as well as minor accessory minerals such as zircon (Figures 4A–H). The corrosion of quartz phenocryst is obvious (Figure 4C). The alteration of both types of feldspar is obvious, but the crystalline form and crystal twin can be observed (Figures 4D–G). The sericitization of plagioclase is obvious, and it can be identified according to the polysynthetic twin (Figures 4D, F). The K-feldspar suffered obvious argillation and carbonation, and it can be identified according to the Carlsbad twin (Figures 4E, F). The alteration of biotite is weak (Figure 4H). Five samples of BHSG were analyzed for whole-rock major and trace

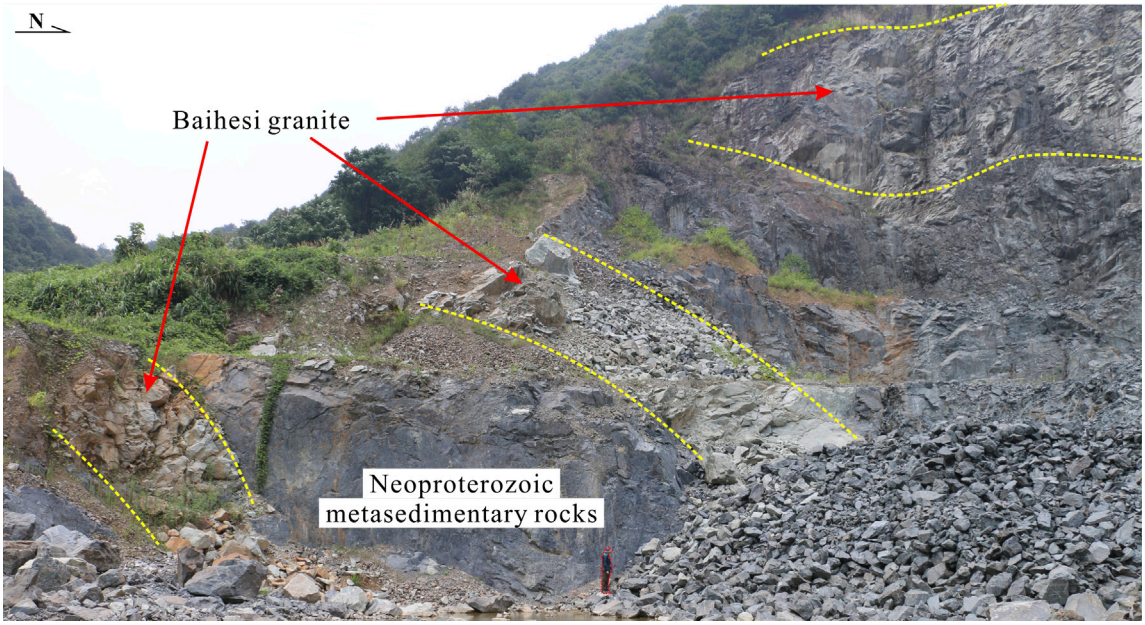


FIGURE 3
Field photo showing the emplacement characteristic of BHSG.

element composition. One of those was analyzed for zircon U–Pb dating, trace element composition, and Hf isotopes.

3.1 U–Pb dating and Hf isotope analysis of zircons

Zircon grains were separated from the samples by conventional heavy liquid and magnetic separation techniques. Transmission and reflected light and cathodoluminescence images (CL) were taken to select optimum laser ablation targets. U–Pb dating and trace element analysis of zircon were performed on an Agilent 7900 ICP-MS instrument using a GeolasPro laser ablation system. Detailed operating conditions for the laser ablation system and the ICP-MS instrument are the same as described by Zong et al. (2017). Zircon GJ-1 and NIST610 were used as an external standard for U–Pb dating and trace element calibration. The concordia age of the GJ-1 sample obtained in this experiment is 601.8 ± 1.3 Ma (MSWD = 0.27), which is consistent with the reference value (TIMS $^{206}Pb/^{238}U$ age = 599.8 ± 4.5 Ma; Jackson et al., 2004). Data processing was performed using ICPMSDataCal software (Liu et al., 2010). IsoplotR (Vermeesch, 2018) was used to calculate the weighted mean age and draw the concordant diagram. After completing the zircon U–Pb isotopic analysis mentioned previously, *in situ* Hf isotopic analysis was performed on the tested zircons. The experiments were performed on a multiple receiver plasma mass spectrometer (MC-ICP-MS). Laser ablation conditions were 10 J/cm^2 of laser energy, 8 Hz of ablation frequency, and 44 μm of spot diameter. Zircon Plesovice was used as the reference standard, yielding an average $^{176}Hf/^{177}Hf$ value of 0.2824780 ± 0.0000034 in this study, which is consistent with the reference value (0.282482 ± 0.000013; Sláma et al., 2008). The aforementioned analyses were performed at the Wuhan Sample Solution Analytical Technology Co., Ltd., Wuhan, China.

3.2 Whole rock major- and trace-element analyses

The whole rock major- and trace-element analyses were performed at the Wuhan Sample Solution Analytical Technology Co., Ltd., Wuhan, China. The sample pretreatment of whole rock major-element analysis was performed by the melting method. A mixture of lithium tetraborate, lithium metaborate, and lithium fluoride, with a mixing ratio of 45:10:5, respectively, was used as a flux. Ammonium nitrate and lithium bromide were used as the oxidant and release agent, respectively. The melting temperature was 1,050°C, and the melting time was 15 min. Whole-rock major element analysis was performed using a Zsx Primus II wavelength dispersive X-ray fluorescence spectrometer (XRF) produced by Rigaku, Japan. The test conditions are 50 kV of voltage and 60 mA of current.

The whole-rock trace-element analysis was conducted on an Agilent 7700e ICP-MS. The detailed digestion procedure is as follows: 1) sample powder (200 mesh) was placed in an oven at 105°C for 12-h drying; 2) 50 mg sample powder was accurately weighed and placed in a Teflon bomb; 3) 1 mL HNO_3 and 1 mL HF were slowly added into the Teflon bomb; 4) the Teflon bomb was put in a stainless steel pressure jacket and heated to 190°C in an oven for more than 24 h; 5) after cooling, the Teflon bomb was opened and placed on a hotplate at 140°C and evaporated to incipient dryness, and then 1 mL HNO_3 was added and evaporated to dryness again; 6) 1 mL of HNO_3, 1 mL of MQ water, and 1 mL internal standard solution of 1 ppm were added, and the Teflon bomb was resealed and placed in the oven at 190°C for more than 12 h; 7) the final solution was transferred to a polyethylene bottle and diluted to 100 g by the addition of 2% HNO_3.

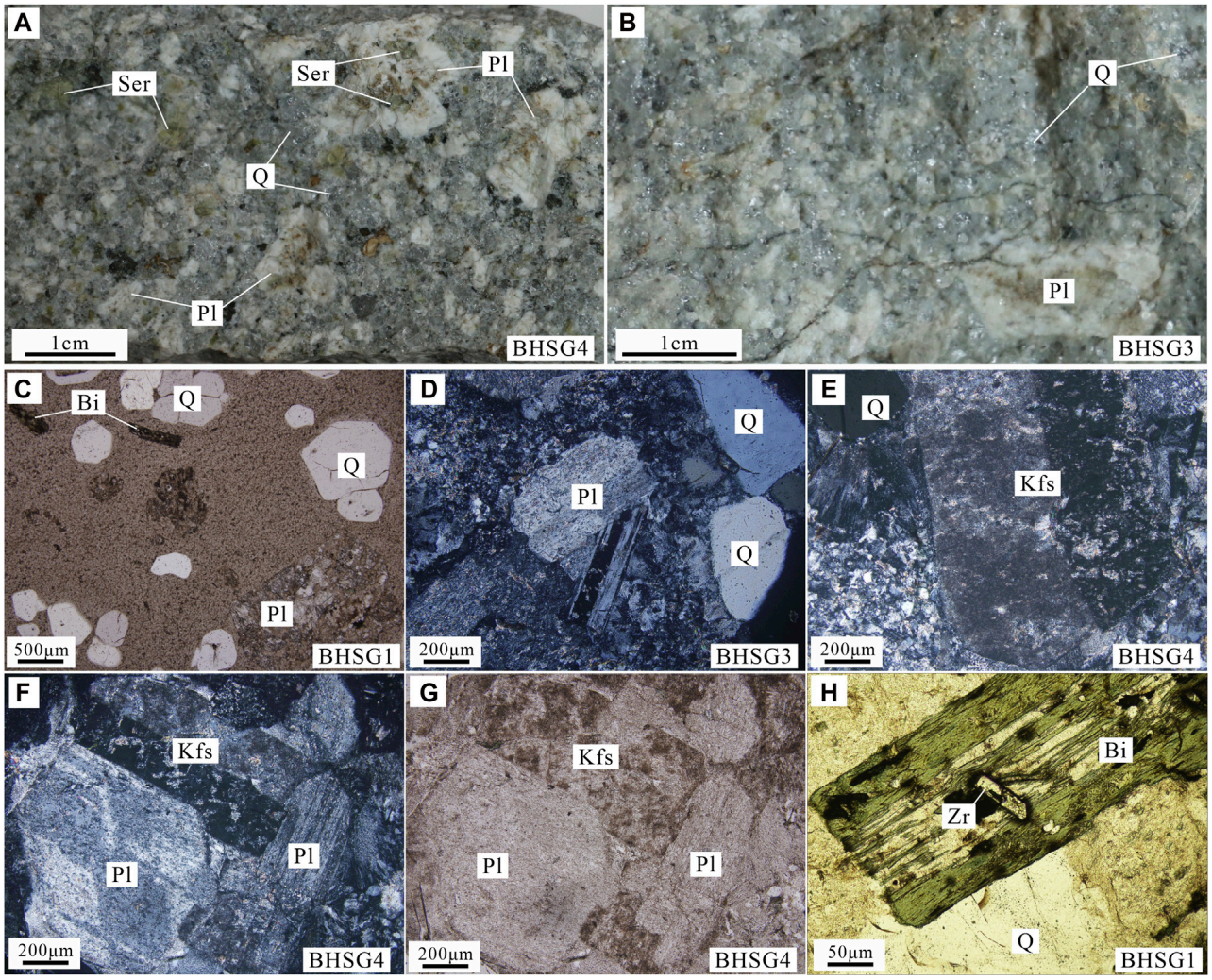


FIGURE 4
Hand specimens **(A,B)** and microscope photographs **(C–H)** of BHSG. Abbreviations: Bi, biotite; Kfs, K-feldspar; Pl, plagioclase; Q, quartz; Ser, sericite; Zr, zircon.

4 Results

4.1 CL image and U–Pb age of zircon

These zircons from BHSG are short or long columnar, oscillatory zoned, and dark in the CL image (Figure 5). The Th/U values of zircons from BHSG vary from 0.26 to 0.82 with an average of 0.42. The BHSG data are mainly on the concordant line, presenting a concordant age of 142.52 ± 0.57 Ma (MSWD = 1.2) with a weighted mean age of 142.52 ± 0.92 Ma (MSWD = 2.6) for BHSG (Figure 5). The specific data and calculated parameters are shown in Table 2 and Table 3.

BHSG zircons have some typical features of magmatic zircons, such as morphology, obvious oscillatory zoning, and a relatively high Th/U ratio. Compared with common magmatic zircon, these zircons show darker colors in CL images and have significantly higher Th and U contents (Hoskin, 2005). Petrographic observation provides evidence that some zircons crystallized simultaneously with phenocrysts (Figure 4H). Combining the similar features of petrography, zircon morphology, obvious oscillatory zoning, high Th/U ratio, and indistinguishable $^{206}Pb/^{238}U$ ages, these zircons are classified as magmatic zircons. Therefore, the obtained zircon U–Pb ages of 142.52 ± 0.57 Ma (MSWD = 1.2) for BHSG can represent the crystallization age of magma.

4.2 Zircon Hf isotopic composition

These zircons from BHSG have calculated $(^{176}Hf/^{177}Hf)_i$ values ranging from 0.282525 to 0.282618 (mean = 0.282573), $\varepsilon_{Hf}(t)$ values ranging from −5.57 to −2.37 (mean = −3.91), and two-stage model ages (T_{DM2}) ranging from 1,551 to 1,345 Ma (mean = 1,444 Ma). The two-stage model ages were calculated using the $^{206}Pb/^{238}U$ age of each zircon. The specific data are shown in Table 4.

4.3 Whole-rock chemistry compositions

The analysis results of major elements, trace elements, and the calculated parameters are shown in Table 5 and Table 6.

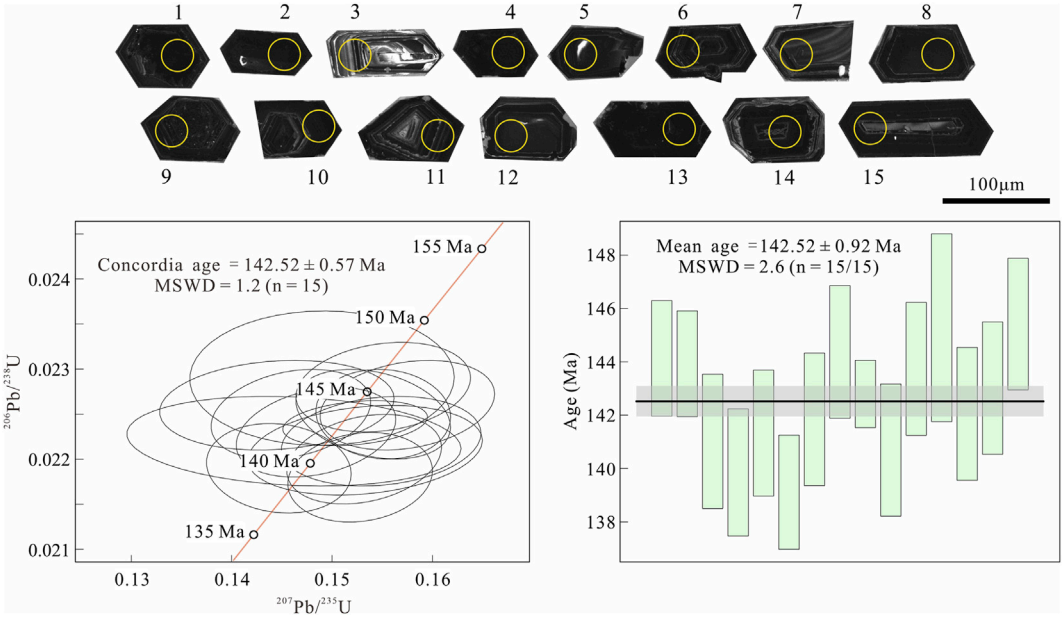


FIGURE 5
Cathodoluminescence images, U–Pb concordant age, and weighted mean age of zircons from BHSG.

TABLE 2 LA-ICPMS U–Pb isotopic ratios and ages of the zircons from BHSG.

	$^{207}Pb/^{206}Pb$	1σ	$^{207}Pb/^{235}U$	1σ	$^{206}Pb/^{238}U$	1σ	$^{207}Pb/^{206}Pb$	1σ	$^{207}Pb/^{235}U$	1σ	$^{206}Pb/^{238}U$	1σ	Concordance (%)
1	0.0499	0.0010	0.1551	0.0027	0.0225	0.0002	190.82	46.29	146.40	2.35	143.22	0.99	97
2	0.0495	0.0012	0.1541	0.0031	0.0225	0.0002	168.60	55.55	145.49	2.76	143.25	1.25	98
3	0.0500	0.0015	0.1533	0.0047	0.0221	0.0002	194.53	70.36	144.86	4.17	140.67	1.29	97
4	0.0504	0.0010	0.1528	0.0029	0.0218	0.0002	216.74	46.29	144.39	2.51	139.20	1.10	96
5	0.0478	0.0023	0.1462	0.0067	0.0222	0.0002	100.09	111.10	138.59	5.94	141.25	1.04	98
6	0.0477	0.0011	0.1447	0.0029	0.0219	0.0002	83.43	83.32	137.22	2.60	139.85	1.02	98
7	0.0504	0.0013	0.1549	0.0040	0.0222	0.0002	213.04	89.80	146.23	3.50	141.75	1.39	96
8	0.0505	0.0011	0.1575	0.0035	0.0226	0.0002	220.44	82.40	148.54	3.08	143.80	1.47	96
9	0.0491	0.0009	0.1523	0.0029	0.0224	0.0001	153.79	44.44	143.93	2.52	142.92	0.92	99
10	0.0504	0.0010	0.1532	0.0031	0.0220	0.0002	213.04	48.14	144.76	2.74	140.19	0.97	96
11	0.0463	0.0015	0.1445	0.0047	0.0226	0.0002	13.06	87.03	137.02	4.17	144.34	1.17	94
12	0.0477	0.0018	0.1490	0.0053	0.0229	0.0003	83.43	88.88	141.03	4.72	146.05	1.66	96
13	0.0480	0.0010	0.1484	0.0032	0.0223	0.0002	98.24	47.22	140.46	2.85	142.29	1.05	98
14	0.0469	0.0010	0.1459	0.0032	0.0225	0.0002	42.69	51.85	138.31	2.80	143.51	1.26	96
15	0.0490	0.0011	0.1551	0.0035	0.0228	0.0002	146.38	51.85	146.40	3.05	145.46	1.06	99

4.3.1 Major- and trace-element composition

The BHSG samples have SiO_2 contents ranging from 76.03 to 77.41 wt%, Al_2O_3 contents ranging from 12.00 to 12.59 wt%, K_2O contents ranging from 3.70 to 4.27 wt%, Na_2O contents ranging from 1.05 to 3.04 wt%, CaO contents ranging from 0.80 to 1.88 wt%, TFe_2O_3 contents ranging from 1.05 to 1.35 wt%, MgO contents ranging from 0.12 to 0.35 wt%, and P_2O_5 contents ranging from 0.008 to 0.017 wt%. Overall, the petrochemical composition of BHSG shows obvious characteristics of high silicon and alkali contents, higher K_2O contents than Na_2O contents, and low CaO and P_2O_5 contents.

TABLE 3 Trace-element composition of the zircons from BHSG.

	La	Ce	Pr	Nd	Sm	Eu	Gd	Tb	Dy	Ho	Er	Tm	Yb	Lu	Hf	Th	U	Th/U
1	0.85	58	0.61	5.7	23.6	0.29	205	97	1,363	554	2,671	586	5,235	945	10,582	12,317	27,201	0.45
2	0.75	33	0.85	6.0	15.1	0.19	122	60	867	355	1749	395	3,684	675	12,019	3,957	14,240	0.28
3	0.12	18	0.14	1.4	4.5	0.12	34	15	204	85	428	98	922	184	11,870	1,259	2,800	0.45
4	2.40	63	1.69	13.8	22.3	0.35	155	70	960	385	1874	411	3,696	692	9,334	10,957	15,421	0.71
5	1.16	56	0.96	7.6	14.1	0.37	82	32	406	153	706	150	1,341	250	9,792	3,220	3,920	0.82
6	0.79	28	0.67	4.5	8.7	0.15	66	31	450	183	910	205	1893	361	12,153	3,359	7,876	0.43
7	17.11	79	9.74	53.7	24.2	0.23	59	21	266	107	509	116	1,097	212	11,378	1,312	3,182	0.41
8	16.04	64	4.94	24.5	17.2	0.21	79	34	448	187	894	201	1880	356	11,189	3,421	6,996	0.49
9	7.01	47	4.59	25.8	22.3	0.24	93	43	578	242	1,190	270	2,615	486	12,875	4,232	11,000	0.38
10	0.09	17	0.11	1.2	4.8	0.10	43	22	319	138	691	159	1,540	299	13,815	1,637	6,041	0.27
11	2.94	26	1.35	9.0	8.5	0.12	47	21	298	126	622	141	1,359	262	13,135	1800	5,622	0.32
12	0.81	25	0.85	8.1	17.5	0.38	78	27	319	112	486	102	912	168	10,101	872	1979	0.44
13	22.69	89	6.75	31.4	19.9	0.17	91	44	634	271	1,363	311	2,981	556	13,594	3,429	13,208	0.26
14	4.23	33	2.64	17.0	15.0	0.21	80	36	501	203	992	221	2067	391	12,632	2,717	8,544	0.32
15	4.44	39	3.20	18.6	17.1	0.22	71	30	392	160	766	170	1,587	301	11,804	1,475	4,802	0.31

TABLE 4 Hf isotope ratios of the zircons from BHSG.

	Age (Ma)	$^{176}Yb/^{177}Hf$	$^{176}Lu/^{177}Hf$	$^{176}Hf/^{177}Hf$	$^{176}Hf/^{177}Hf_i$	$\varepsilon_{Hf}(0)$	$\varepsilon_{Hf}(t)$	TDM (Ma)	TDM2 (Ma)	$f_{Lu/Hf}$
1	144.8	0.088752181	0.003266624	0.282533434	0.2825246	−8.4	−5.6	1,081	1,551	−0.901608
2	143.2	0.14486411	0.005159885	0.282553131	0.2825393	−7.7	−5.1	1,111	1,518	−0.844582
3	140.7	0.078580832	0.002903214	0.282625302	0.2826177	−5.2	−2.4	934	1,345	−0.912554
4	143.5	0.136006445	0.00502482	0.282571554	0.2825581	−7.1	−4.4	1,078	1,476	−0.84865
5	141.3	0.10627651	0.003688358	0.282579275	0.2825695	−6.8	−4.1	1,025	1,452	−0.888905
6	139.9	0.121767181	0.004372213	0.282544319	0.2825329	−8.1	−5.4	1,099	1,535	−0.868307
7	141.8	0.061005395	0.002201254	0.282617852	0.282612	−5.5	−2.5	927	1,357	−0.933697
8	143.8	0.138355074	0.004937153	0.282593812	0.2825806	−6.3	−3.6	1,040	1,426	−0.851291
9	140.2	0.062311217	0.002277112	0.282606438	0.2826005	−5.9	−3.0	946	1,384	−0.931412
10	144.3	0.078730788	0.002849784	0.282606926	0.2825992	−5.8	−2.9	960	1,384	−0.914163
11	146.1	0.045653094	0.001655099	0.282592132	0.2825876	−6.4	−3.3	950	1,409	−0.950148
12	143.5	0.114812582	0.004071666	0.282574459	0.2825635	−7.0	−4.2	1,044	1,464	−0.877359
13	145.5	0.094450328	0.003419791	0.282570639	0.2825613	−7.1	−4.3	1,030	1,468	−0.896994

According to petrographic features (Figure 4), TAS diagram (Figure 6A), and Q′–ANOR normative diagram (Figure 6B), BHSG was classified by monzogranite. The aluminum saturation index (ASI) of BHSG ranges from 1.07 to 1.32, which showed weakly to strongly peraluminous features (Figure 6C). All the BHSG samples belonged to the high-K calc-alkaline series (Figure 6D).

The BHSG samples have total amounts of rare earth elements (REEs) ranging from 190.26×10^{-6} to 251.24×10^{-6}, with an average of 217.54×10^{-6}. The difference between light and heavy REEs is not obvious, and the light REEs are slightly enriched with $(La/Yb)_N$ values ranging from 1.41 to 2.53. The depletion of Eu is obvious, showing relatively flat REE patterns (Figure 7A). In the primitive mantle-normalized diagram of trace elements (Figure 7B), it is shown that some elements such as Cs, Rb, Th, U, and Pb are obviously enriched, and some elements such as Ba, Sr, P, and Ti are obviously negative.

4.3.2 Alteration effect

Alteration can be observed both on hand specimens and under a microscope, which is mainly manifested by sericitization and

TABLE 5 Whole-rock major-element composition of BHSG and standard samples.

Sample	BHSG1	BHSG2	BHSG3	BHSG4	BHSG5	Standard sample	Standard value	Standard sample	Standard value	Standard sample	Standard value
SiO_2	76.03	77.41	76.26	76.40	76.19	72.82	72.83	44.71	44.64	59.60	59.68
TiO_2	0.06	0.08	0.08	0.09	0.09	0.29	0.29	2.39	2.37	0.75	0.77
Al_2O_3	12.29	12.00	12.59	12.12	12.16	13.38	13.40	13.77	13.83	16.64	16.56
TFe_2O_3	1.25	1.27	1.34	1.35	1.05	2.12	2.14	13.54	13.40	6.04	6.06
MnO	0.06	0.03	0.03	0.03	0.03	0.06	0.06	0.17	0.17	0.09	0.09
MgO	0.35	0.20	0.20	0.15	0.12	0.41	0.42	7.73	7.77	2.75	2.81
CaO	1.88	1.04	0.80	0.86	1.25	1.54	1.55	8.87	8.81	4.70	4.72
Na_2O	1.05	2.49	2.66	2.73	3.04	3.08	3.13	3.33	3.38	4.02	4.05
K_2O	3.82	3.70	4.09	4.27	3.76	4.98	5.01	2.28	2.32	3.48	3.50
P_2O_5	0.008	0.015	0.014	0.017	0.014	0.09	0.09	0.94	0.95	0.33	0.34
LOI	2.84	1.60	1.37	1.37	1.61	0.75	0.69	2.03	2.24	1.04	1.04
SUM	99.63	99.84	99.43	99.39	99.30	99.52	99.61	99.75	99.88	99.43	99.63
FeO	0.81	0.87	0.92	0.93	0.69	1.02	1.02	7.53	7.60	3.04	3.08
TFeO	1.13	1.15	1.20	1.22	0.94						
Q	51.96	46.59	43.44	42.44	41.87						
An	3.13	2.09	2.41	1.52	0.87						
Ab	23.34	22.26	24.69	25.75	22.75						
Or	9.19	21.44	22.96	23.59	26.38						
C	9.58	5.17	3.97	4.26	6.25						
Hy	0.89	0.51	0.51	0.39	0.31						
Il	1.24	1.30	1.37	1.38	0.97						
Mt	0.53	0.45	0.47	0.47	0.42						
Ap	0.12	0.15	0.16	0.17	0.17						
Zr	0.02	0.04	0.03	0.04	0.03						
DI	84.36	90.15	90.94	91.64	90.85						
A/NK	2.10	1.48	1.43	1.33	1.34						
A/CNK (ASI)	1.32	1.20	1.23	1.14	1.07						
Na_2O+K_2O	4.87	6.18	6.75	7.00	6.80						

(Continued on following page)

10.3389/feart.2023.1085767

10.3389/feart.2023.1085767

TABLE 5 (*Continued*) Whole-rock major-element composition of BHSG and standard samples.

Sample	BHSG1	BHSG2	BHSG3	BHSG4	BHSG5	Standard sample	Standard value	Standard sample	Standard value	Standard sample	Standard value
K_2O/Na_2O	3.64	1.49	1.54	1.56	1.24						
FeOT/MgO	3.27	5.67	6.05	8.01	7.84						
T_{Zr}	796.62	794.53	805.26	796.96	787.97						

argillation of feldspar phenocrysts (Figures 4D–G). The alteration effect should be evaluated before the geochemistry analysis. Large ion lithophile elements (LILEs) and some major elements, such as calcium (Ca), sodium (Na), potassium (K), rubidium (Rb), barium (Ba), and strontium (Sr), are generally mobile, whereas high field strength elements (HFSEs), rare earth elements (REEs), and some major elements, such as titanium (Ti), aluminum (Al), phosphorus (P), iron (Fe), niobium (Nb), tantalum (Ta), zirconium (Zr), and hafnium (Hf), are relatively immobile during hydrothermal alteration (Smith and Smith, 1976; Maclean, 1990).

The loss on ignition (LOI) is useful as an actual estimate of total volatiles in certain geologic studies and as an indication of volcanic rock alteration resulting from hydration or calcitization of mafic minerals (Lechler and Desilets, 1987). In the diagrams of correlation between mobile elements and LOI (Figure 8), the contents of SiO_2, TiO_2, Al_2O_3, TFeO, K_2O, P_2O_5, Rb, Ba, and Sr exhibit weak or no variation with increasing LOI, suggesting a weak or no alteration effect on these elements. As to the REEs and the other trace elements, although the LOI values of the five samples of BHSG are variable, the chondrite-normalized REE patterns and primitive mantle-normalized multi-element patterns are highly consistent (Figure 7), suggesting a weak or no alteration effect on these elements. Otherwise, the contents of CaO, Na_2O, and MgO changed with increasing LOI (Figures 8E–G), suggesting the sample BHSG1 may be affected. The abnormal Na_2O content may be responsible for the discrete distribution of the sample BHSG1 in the Q′–ANOR normative diagram and A/NK–A/CNK diagram (Figure 6C).

The alteration box plot, combining the Ishikawa alteration index (AI) and the chlorite–carbonate–pyrite index (CCPI), is a powerful means of understanding the relationship between mineralogy, petrogeochemistry, and intensity of alteration (Large et al., 2001). The CCPI vs. AI plot was divided into two parts by the black dotted line in the middle (Figure 9). Hydrothermal alteration produced trends to the upper right, and diagenetic alteration produced trends to the lower left. Meanwhile, a least altered box was defined by AI values ranging from 20 to 65 and CCPI values ranging from 15 to 85 (Large et al., 2001). The contents of major elements of BHSG presented AI values ranging from 47.47 to 58.72 and CCPI values ranging from 13.5 to 23.23, which are mainly plotted within the least altered box and related to the diagenetic trends in the lower left part (Figure 9). According to this plot, slight diagenetic alteration and no hydrothermal alteration may have occurred, which may be related to the replacement of albite by K-feldspar and sericite.

Therefore, the alteration effect on all trace elements, including REEs, is negligible. The CaO, Na_2O, and MgO contents of sample BHSG1 have been affected by diagenetic alteration, whereas the alteration effect on major-element contents of the other samples should be finite.

5 Discussion

5.1 Magmatic differentiation

The BHSG has high SiO_2 content and high differentiation index (Di), indicating a high degree of differentiation. The whole-rock Zr/Hf and Nb/Ta ratios are reliable indicators of the degree of granitic magma differentiation because Zr and Hf, as well as Nb and Ta, are

TABLE 6 Whole-rock trace-element composition of BHSG and standard samples.

Sample	BHSG1	BHSG2	BHSG3	BHSG4	BHSG5	AGV-2	Standard value	BCR-2	Standard value	RGM-2	Standard value
Ba	234.77	257.39	307.41	147.06	353.71	1,122	1,130	668	677	834	810
Rb	248.17	215.90	240.37	223.62	230.68	67.3	66.3	46.2	46.9	150	150
Sr	94.39	74.76	78.91	79.05	103.08	669	661	339	340	111	108
Zr	128.69	137.99	155.09	152.16	146.16	232	230	182	184	229	220
Nb	41.79	36.82	40.76	38.83	38.46	14.4	14.5	12.4	12.6	9.36	9.30
Ni	0.38	0.35	0.37	0.31	0.40	19.1	20.0	12.6	13.0	2.18	5.20
Co	0.44	0.99	1.21	0.86	2.61	16.2	16.0	37.7	37.0	2.07	2.0
Zn	46.98	130.05	185.44	118.26	78.45	87.9	86.0	131	133	31.5	32.0
Cr	0.46	0.54	0.57	0.53	0.56	16.1	16.2	15.3	16.5	3.19	5.90
La	24.55	32.22	30.92	40.24	33.15	38.4	37.9	25.0	24.9	23.2	24.0
Ce	60.90	77.25	70.89	89.68	76.97	70.2	68.6	52.4	52.9	46.5	47.0
Pr	7.45	9.01	8.52	10.84	9.44	8.11	7.84	6.61	6.70	5.29	5.36
Nd	28.54	34.36	33.83	41.11	35.54	30.7	30.5	28.9	28.7	19.5	19.0
Sm	9.08	9.34	9.50	10.98	9.86	5.64	5.49	6.63	6.58	4.00	4.30
Eu	0.20	0.23	0.24	0.28	0.24	1.55	1.54	2.00	1.96	0.61	0.66
Gd	10.67	10.39	10.65	11.85	10.95	4.67	4.52	6.81	6.75	3.64	3.70
Tb	2.34	2.04	2.13	2.33	2.13	0.63	0.64	1.08	1.07	0.62	0.66
Dy	15.25	13.44	14.42	15.09	14.33	3.59	3.47	6.58	6.41	3.85	4.10
Ho	3.40	3.05	3.27	3.32	3.14	0.69	0.65	1.30	1.28	0.78	0.82
Er	11.71	9.86	10.96	10.67	10.33	1.85	1.81	3.71	3.66	2.27	2.35
Tm	1.80	1.55	1.71	1.68	1.66	0.26	0.26	0.53	0.54	0.37	0.37
Yb	12.48	10.50	11.64	11.41	11.41	1.68	1.62	3.44	3.38	2.53	2.60
Lu	1.89	1.61	1.82	1.76	1.71	0.26	0.25	0.52	0.50	0.38	0.40
Y	106.32	92.63	100.88	101.84	100.45	20.4	20.0	36.0	37.0	23.9	23.2
Cs	35.80	11.89	11.08	7.95	11.12	1.10	1.16	1.04	1.10	9.73	9.60
Ta	6.17	5.05	5.61	5.30	5.26	0.88	0.87	0.78	0.78	0.92	0.95
Hf	6.06	5.99	6.80	6.88	6.35	5.27	5.0	4.96	4.90	5.90	6.20
Ga	19.21	19.34	21.52	21.99	18.48	20.9	20.0	22.7	23.0	16.5	16.5
Cu	72.41	101.28	178.43	105.41	309.28	53.0	53.0	20.8	19.7	10.2	9.60
Pb	50.55	143.60	142.51	193.20	74.41	13.4	13.2	10.2	11.0	19.6	19.3
Sn	9.10	6.26	6.10	8.94	7.19	1.99	1.83	2.03	2.03	3.25	3.34
Th	52.67	53.07	55.08	55.69	56.53	6.32	6.10	5.96	5.70	14.7	15.1
U	19.55	17.30	19.30	18.22	19.28	1.93	1.86	1.73	1.69	5.68	5.80
Li	26.99	24.18	22.70	22.14	22.58	10.2	11.0	8.71	9.0	59.1	57.0
Be	15.99	14.35	15.34	12.52	13.52	2.22	2.30	1.96		2.50	2.37
Sc	0.17	0.91	0.91	1.43	0.85	12.5	13.0	33.7	33.0	4.21	4.40
V	3.85	3.04	3.24	2.94	3.47	121	120	416	416	14.1	13.0
Zr/Hf	21.25	23.03	22.81	22.13	23.02						

(Continued on following page)

TABLE 6 (*Continued*) Whole-rock trace-element composition of BHSG and standard samples.

Sample	BHSG1	BHSG2	BHSG3	BHSG4	BHSG5	AGV-2	Standard value	BCR-2	Standard value	RGM-2	Standard value
Nb/Ta	6.78	7.30	7.26	7.33	7.31						
Zr + Nb + Ce +Y	337.70	344.69	367.62	382.51	362.04						
10,000 Ga/Al	2.95	3.04	3.23	3.43	2.87						
ΣREE	190.26	214.83	210.52	251.24	220.85						
ΣLREE	130.73	162.40	153.91	193.13	165.20						
ΣHREE	59.53	52.43	56.61	58.11	55.65						
$(La/Yb)_N$	1.41	2.20	1.90	2.53	2.08						
Eu/Eu*	0.062	0.070	0.074	0.074	0.071						

Eu/Eu* = Eu/SQRT (Sm×Gd); The element values, namely Eu, Sm and Gd, in this formula are chondrite-normalized values.

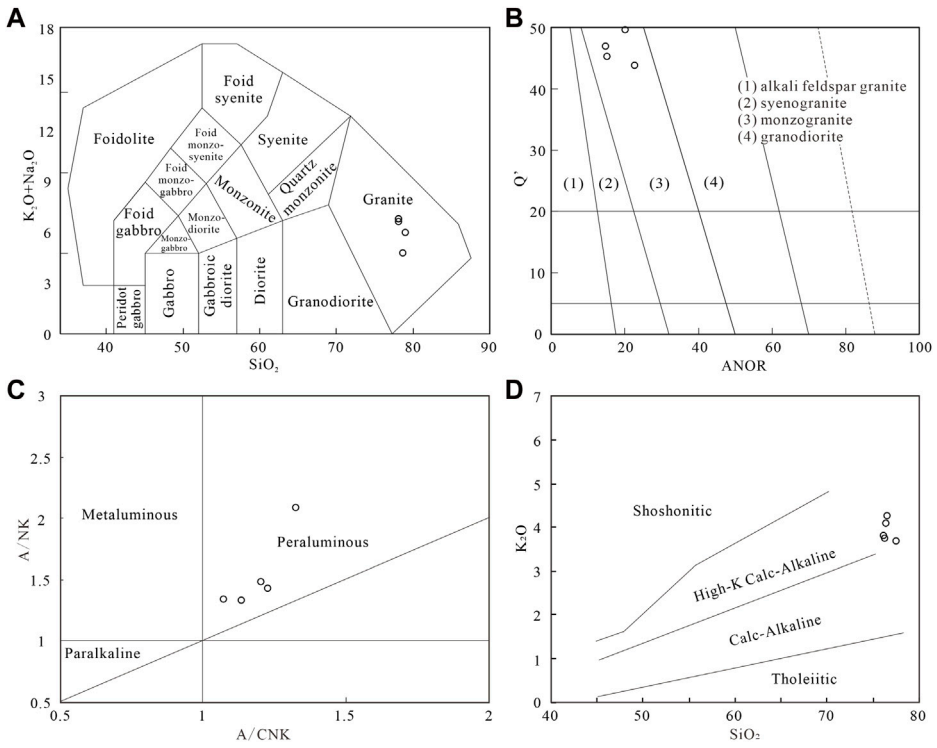


FIGURE 6
TAS diagram [**(A)**; Middlemost, 1994], Q′ versus ANOR diagram [**(B)**; Streckeisen and Le Maitre, 1979], A/NK versus A/CNK diagram [**(C)**; Maniar and Piccoli, 1989], and K_2O versus SiO_2 diagram [**(D)**; Peccerillo and Taylor, 1976] for BHSG.

elements considered to be "geochemical twins" having the same charge and a similar ionic radius (Ballouard et al., 2016). Also, they have similar geochemical properties and should not be fractionated during most geological processes (Goldschmidt, 1937). However, Zr/Hf and Nb/Ta ratios will decrease during fractional crystallization in granites and the interaction with late magmatic fluids in evolved peraluminous granites (Ballouard et al., 2015; Dostal et al., 2015; Wu et al., 2017). The whole-rock Zr/Hf and Nb/Ta ratios of BHSG range from 21.25 to 23.03 and from 6.78 to 7.33. The Zr/Hf ratios are lower than the maximum of the magmatic–hydrothermal transition system (Zr/Hf < 26; Bau, 1996), and Nb/Ta ratios were close to the fingerprint of the magmatic–hydrothermal transition system (Nb/Ta < 5, Ballouard et al., 2016; Figure 10). Moreover, BHSG has other typical characteristics of highly fractionated granites, such as low content of REEs, low ratio between light and heavy REEs, and significant negative Eu anomaly (Figure 7A; Gelman et al., 2014; Miller and Mittlefehldt, 1982; Miller and Mittlefehldt, 1984).

The low total REE contents and the small ratios between light and heavy REEs of BHSG indicate fractional crystallization of REE-rich minerals such as zircon, monazite, epidote, and xenotime. The

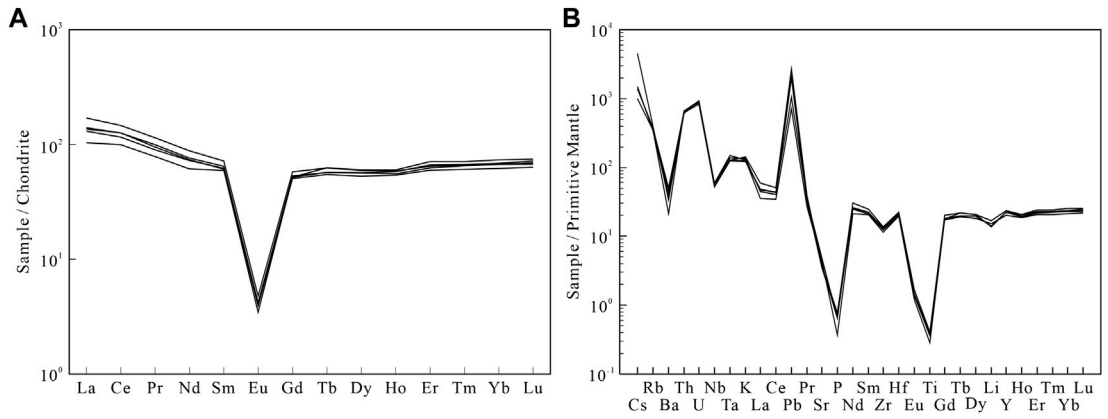


FIGURE 7
Chondrite-normalized REE patterns **(A)** and primitive mantle-normalized multi-element diagrams **(B)** for BHSG and FQSG (the normalization values after Sun and McDonough, 1989).

apparent depletion of Eu, Ba, and Sr reflects the significant fractional crystallization of plagioclase and/or K-feldspar. The apparent depletion of P reflects the significant fractional crystallization of apatite.

5.2 Geochemical affinity to highly evolved aluminous A-type granite

The peraluminous characteristics of BHSG reflects geochemical affinity to S-type, highly evolved I-type, and A-type granitoids (Chappell and White, 1992; Eby, 1992). S-type and I-type granitoids can be distinguished by P_2O_5 content and their relation to SiO_2. The P_2O_5 content increases with crystallization differentiation in S-type granite and decreases with crystallization differentiation in weakly peraluminous I-type granite (Chappell and White, 1992). P_2O_5 abundance is also a reliable criterion for distinguishing A-type and S-type granites (Bonin, 2007). BHSG has an extremely low P_2O_5 content ranging from 0.008 wt.% to 0.017 wt.%, showing affinity to highly evolved peraluminous A-type granite and rejecting the possibility of S-type granite (Supplementary Figure S1) because highly evolved S-type granites have high P_2O_5 contents ranging from 0.4 to 1.6 wt.% (Bonin, 2007).

I- and S-type granites are distinguished by source rocks, while the identification of A-type granite emphasizes its chemical composition. A-type granite was characterized by high SiO_2; high FeO_T/MgO; high total alkali content; high K_2O/Na_2O; high REE (except Eu), Zr, Nb, and Ta abundances; and low CaO, Ba, Sr, and Eu abundances (Collins et al., 1982; Eby, 1992; Eby and Kochhar, 1990; Loiselle and Wones, 1979; Whalen et al., 1987). In terms of major elements, the diagrams related to K_2O, Na_2O, and CaO could not distinguish A-type granite from other granites (Supplementary Figure S2) because the total alkali (K_2O + Na_2O) content and CaO content of different granites in origin are similar when the SiO_2 content is greater than 74 wt.% (Eby and Kochhar, 1990). In terms of trace elements, the discriminant diagrams based on Ga–Zr–Nb–Ce–Y gave a clear distinction of BHSG as A-type granite (Figure 11). Although the data are plotted near the boundary between A-type and the other type granites in Zr-related diagrams (Figure 11), they do not affect the discrimination of A-type granite for BHSG. This can be attributed to the high differentiation of BHSG, which resulted in the crystallization separation of zircons and then the decrease of Zr content in the melt (King et al., 2001). Moreover, the BHSG samples all fell in the WPG ("Within Plate Granite"; Supplementary Figure S3; Pearce et al., 1984) zone, which supported the validity of the diagrams based on Ga–Zr–Nb–Ce–Y (Eby and Kochhar, 1990).

The most essential characteristic of A-type granite is its high temperature. The average crystallization temperature of aluminous A-type granites obtained by a zircon saturation thermometer is usually over 800°C (King et al., 1997). The zirconium saturation thermometer presented a mean temperature of 796°C for BHSG (Watson and Harrison, 1983). High Zr content is the chief criterion for identifying A-type granite, but most felsic A-type granites have lower Zr contents due to removal of zircon during fractionation, which makes the Zr content and further the calculated zircon saturation temperature both lower (King et al., 2001; King et al., 1997). Petrographic observation shows zircon wrapped in biotite phenocryst (Figure 4H), indicating that zircon is a fractionated mineral and zirconium has reached saturation in the early stage of fractional crystallization. BHSG is a highly differentiated granite which has undergone strong fractional crystallization, indicating that zirconium has been further lost after reaching saturation in magma. It means that the actual magma temperature is significantly higher than the calculated zirconium saturation temperature and should be higher than 800°C.

Furthermore, the A-type granitoids can be chemically subdivided into two groups, namely, A_1-subtype granite, which has similar element ratios to oceanic island basalts, and A_2-subtype granite, which has similar element ratios to average crust and island arc basalts (Eby, 1992). BHSG was subdivided into A_2-subtype granite according to the triangle diagram of incompatible elements (Figure 12). Therefore, BHSG is a highly evolved aluminous A-type granite.

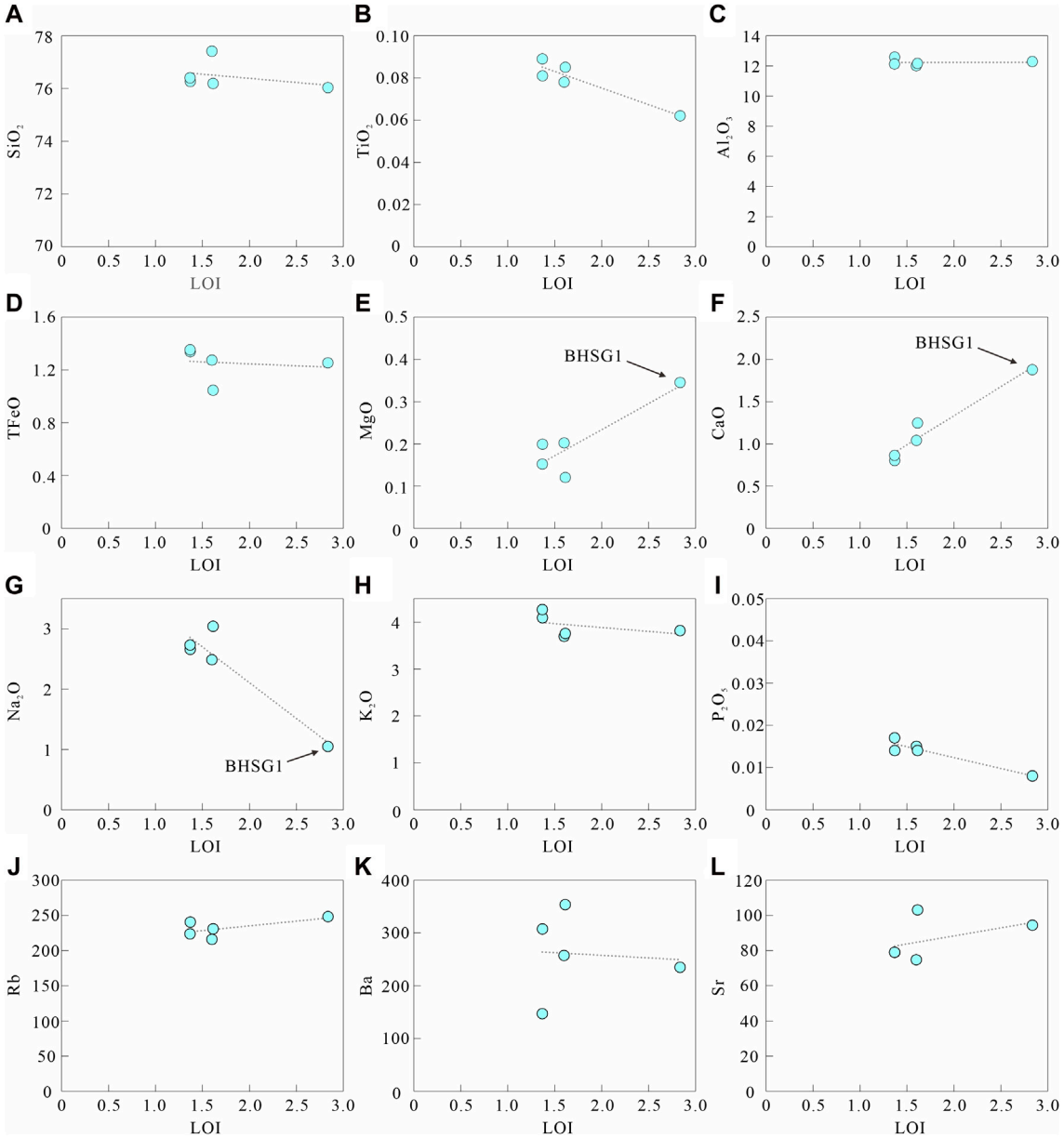


FIGURE 8
LOI versus major elements, Rb, Ba, and Sr plots. The label BHSG1 refers to sample BHSG1 in Table 5.

5.3 Magmatic origin

The $\varepsilon_{Hf}(t)$ values of BHSG and Neoproterozoic arc-related magmatic rocks in the Shuangqiaoshan Group mainly fall near the same crustal evolution line (Figure 13), indicating the similarity of their source. The quartz–keratophyre and tuff are from the base of the Shuangqiaoshan Group and formed in a syn-orogenic back-arc foreland setting at *ca.* 880 Ma. The $\varepsilon_{Hf}(t)$ values of quartz–keratophyre and tuff intersect the depleted mantle curve, reflecting the material contribution of the depleted mantle endmember and Neoproterozoic crustal–mantle interactions during the Neoproterozoic orogeny to these volcanic rocks. The *ca.* 800 Ma gabbro from the Shuangqiaoshan Group had arc-like geochemical features, which was considered to generate from the partial melting of juvenile crustal materials resulting from Neoproterozoic subduction (Wang et al., 2008). The model age of BHSG is basically the same as that of *ca.* 800 Ma gabbro, and there is a large overlap with *ca.* 880 Ma volcanic rocks, suggesting the source of BHSG is similar to that of the *ca.* 800 Ma gabbro and is also related to the juvenile crust formed during Neoproterozoic arc-related magmatism.

The source discriminant diagram indicates that tonalites and metasediments are potential sources of BHSG (Figure 14). Tonalite is a representative component of TTG rock assemblage, which is the main product of crustal growth in the subduction and/or

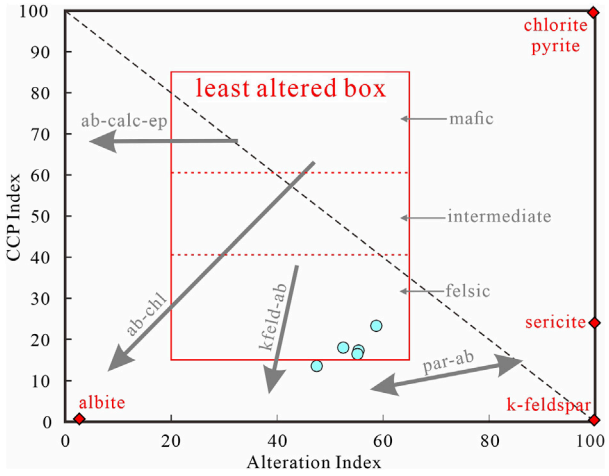


FIGURE 9
Alteration box plot with fields of diagenetic alteration (Large et al., 2001). The arrows show the common trends for diagenetic alteration. Abbreviations: ab-calc-ep, epidote–calcite ± albite trend; ab-chl, albite–chlorite trend; k-feld-ab, early diagenetic trend of K-feldspar replacing albite; par-ab, sericite–albite trend.

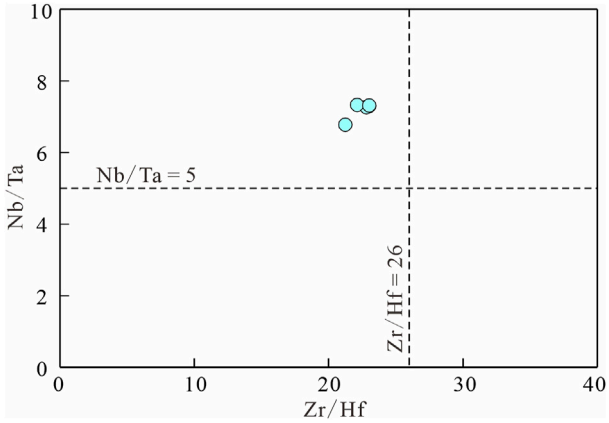


FIGURE 10
Nb/Ta versus Zr/Hf diagram showing the degree of magmatic differentiation.

collision zones (Laurent et al., 2020), and metasediments could originate from the weathering products of TTG. So, the source rocks distinguished are consistent with the preceding interpretation of Hf isotopes and the origin of A_2-type granite, whose source was originally formed by subduction or continent–continent collision (Eby, 1992).

BHSG has high heavy REE content and obvious Eu negative anomaly (Figure 7A), indicating that the magma was derived from an intracrustal source at a relatively shallow depth where plagioclase is stable and garnet is unstable. Therefore, BHSG is thought to have originated mainly from partial melting of a reworked juvenile crust composed of TTGs and its weathered sediments related to Neoproterozoic arc-related magmatism.

5.4 Onset of Early Cretaceous extension in the EJM and structural reactivation of the NEJFZ

Systematic geological records related to the Cretaceous extension in the SCB are concentrated in CT, SR, and JM (Figure 1; Li et al., 2022). The extension in these distribution ranges was expressed by varying combinations and intensities of those geological records. The CT includes the coastal area east of the ZDFZ, where the Cretaceous extension is mainly characterized by the concentrated distribution of volcanic rocks and intrusive rocks and accompanied by extensional basins. Also, the CT is the most important distribution area of Cretaceous magmatism (Zhou and Li, 2000). The Cretaceous extension in SR is mainly characterized by a continuous series of elongated basins, normal faults, volcanic rocks, intrusive rocks, and extensional domes. These normal faults act as basin-bounding structures controlling Cretaceous basins' opening and sedimentary infilling (Li et al., 2022). The Cretaceous extension in the JM is distinctive and characterized by several extensional domes, including Yuechengling (Chu et al., 2019), Hengshan (Li et al., 2013), Wugongshan (Faure et al., 1996; Lou et al., 2005), Dayunshan (Ji et al., 2018a; Ji et al., 2018b), and Lushan (Lin et al., 2000; Wang et al., 2013). Also, extensional basins and intrusive rocks also developed in the JM.

In the CT and SR, the earliest extensional basins can be constrained by the age of volcanic rocks since volcanic rocks are mostly present in the lower part of the sedimentary sequence of the basins. The onset of the Cretaceous extension in the CT and SR can, therefore, be constrained to 145–140 Ma (Figure 15). There may be no significant difference in the onset of the extension in different parts of the CT according the age of volcanic rocks from the southeastern Zhejiang Province and eastern Fujian and Guangdong provinces (Guo et al., 2012; Li et al., 2014; Liu et al., 2012), whereas the onset of the extension in the northeast part of the SR may be earlier than that in the inland according to the age of volcanic rocks from the northwestern Zhejiang Province and Xiangshan Basin (Figure 15; Liu et al., 2014; Yang et al., 2011).

In the JM, the onset of the Cretaceous extension was mainly constrained by the detachment fault with low-temperature thermochronology. In the WJM, the detachment fault in the YCL extensional dome began to move at *ca.* 140 Ma (Chu et al., 2019). In the EJM, the detachment faults in Hengshan, Dayunshan, and Lushan extensional domes began to move at *ca.* 136 Ma (Li et al., 2013), *ca.* 132 (Ji et al., 2018a), and *ca.* 140 Ma (Zhu et al., 2010), respectively. Rare A-type granite formed at *ca.* 134 Ma (Yang et al., 2021). Combined with the newly reported chronological data of BHSG A-type granite, we argue that the Cretaceous lithospheric extension in the EJM has started as early as *ca.* 145–140 Ma, indicating that a lithosphere extensional regime has probably dominated the CT, SR, and JM during 145–140 Ma.

10.3389/feart.2023.1085767

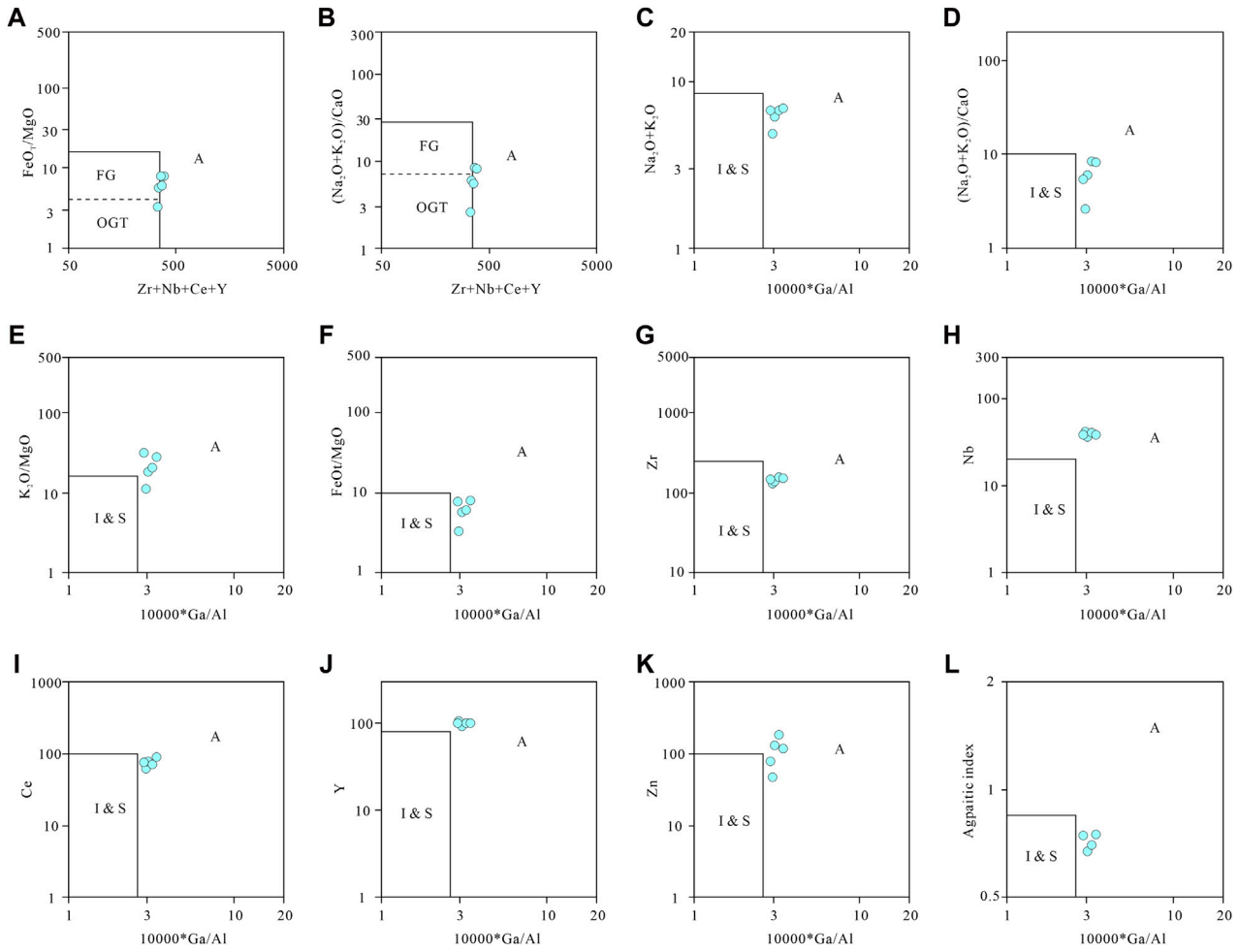


FIGURE 11
Plots to distinguish A-type granites (Whalen et al., 1987). Abbreviations: FG, fractionated felsic granites; OGT, unfractionated M-, I-, and S-type granites. A, A-type granite; I & S, I- and S-type granite.

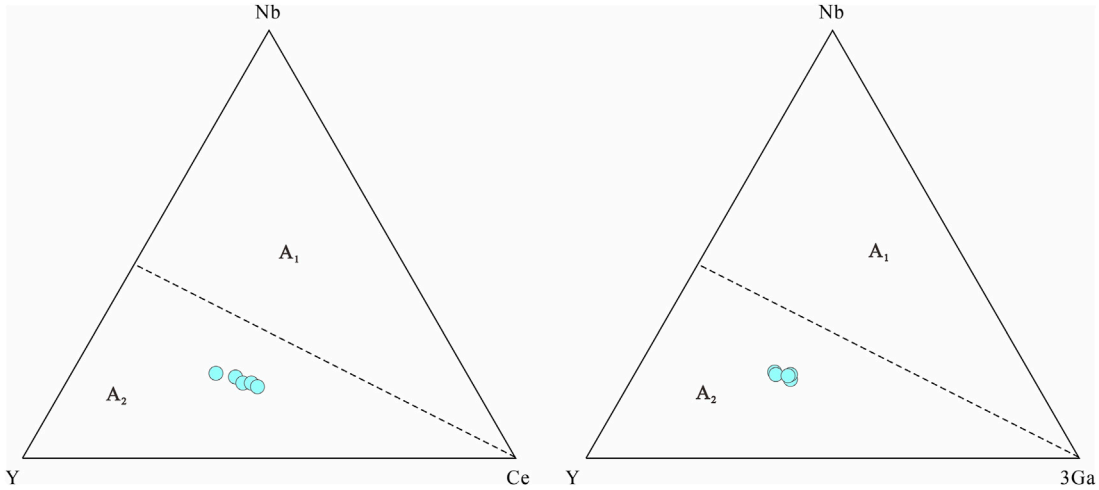


FIGURE 12
Nb–Y–Ce and Nb–Y–3Ga triangle diagrams for distinguishing A_1 and A_2 granites (Eby, 1992).

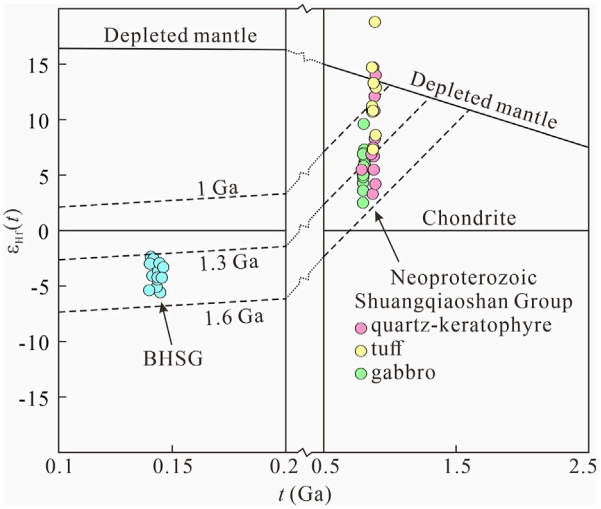


FIGURE 13
$\varepsilon_{Hf}(t)$ versus t diagram of zircons from BHSG. The data of the Shuangqiaoshan Group are from Wang et al., 2008. The crustal evolution lines are after Li et al. (2014).

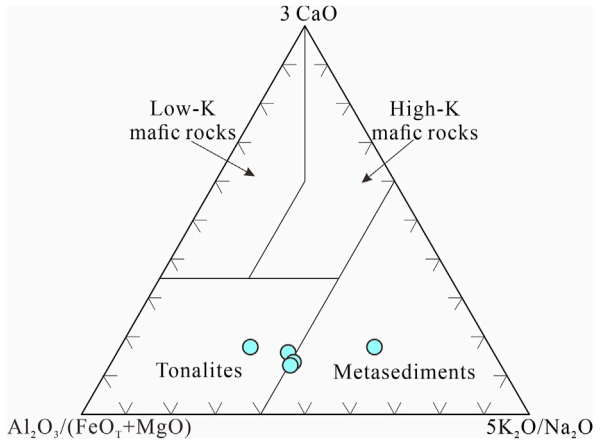


FIGURE 14
$3CaO–Al_2O_3/(FeO_T/MgO)–5K_2O/Na_2O$ triangle diagram for distinguishing the potential sources of granite (Laurent et al., 2020).

The following points are noted: first, the onset of the CT, SR, and JM was almost at the same time, which reflected that these geological units were in a unified tectonic stress field and the source of tectonic stress was controlled by a unified dynamic mechanism. The attenuation of extension-related geological records, especially magmatism, from the coast to the inland indicates that the source of tectonic stress is from the coast, namely, the subduction between eastern Eurasia and the oceanic plate in its east. Second, it does not mean that the entire EJM or JM has been dominated by the lithosphere extensional regime. The spatial distribution of all the extension-related geological records in the SR, the extensional domes in the JM, and BHSG A-type granite consistently exhibit their close correlations with inherited structures. The control of inherited structures over lithosphere extension has been demonstrated in a specific structural deformation study in the JM (Li et al., 2013) and adopted to interpret the petrogenesis and evolution of tectonics in South China (Chu et al., 2019; Pan et al., 2018; Sun et al., 2018; Suo et al., 2019; Wang et al., 2015; Yu et al., 2006; Zhang et al., 2022). Although the tectonic stress field is consistent, the distribution of strain and magmatism is obviously inhomogenous, which shows the dominant control of the inherited structure on the tectono-thermal events in the intraplate area.

A-type granites were thought to form in anorogenic setting at the earliest (Loiselle and Wones, 1979) and were later found to form in a large range of geodynamic contexts (Bonin, 2007), including post-collisional and post-orogenic settings (Sylvester, 1989; Rogers and Greenberg, 1990). According to the original research of Eby (1992), the tectonic setting of A_1-subtype granites was related to hotspots, plumes, or continental rift zones located in anorogenic settings, while the tectonic setting of A_2-subtype granites was related to post-collisional and anorogenic settings.

In the Early Mesozoic, South China was in an intracontinental tectonic setting, and significant intracontinental orogeny took place, including multi-stage compressive tectonic deformation during Indosinian and Yanshanian periods (Li et al., 2016; Chu et al., 2015). Furthermore, a transition from the Tethyan tectonic domain to the Paleo-Pacific tectonic domain in South China has been proven by structural deformation, sedimentary basin, and magmatism studies (Gan et al., 2021; Xu et al., 2019; Zhang et al., 2009). The transition likely occurred during the Early–Middle Jurassic and completed at 165 ± 5 Ma (Gan et al., 2021; Xu et al., 2019). Therefore, the South China Block was dominated by the Paleo-Pacific tectonic domain during the Late Jurassic–Early Cretaceous. Extensive Jurassic–Cretaceous magmatism in southeast China occurred due to subduction of the Paleo-Pacific plate (Li and Li, 2007; Suo et al., 2019; Zhou and Li, 2000; Zhou et al., 2006). Moreover, the oceanward-younging Jurassic–Cretaceous granites and volcanic rocks have been recognized (Zhou and Li, 2000) and were explained by oceanic slab rollback and arc retreat (Li and Li, 2007; Li et al., 2021; Liu et al., 2018). The slab rollback and arc retreat may have provided an extensional tectonic setting for the eastern Jiangnan Massif which was intracontinental and away from the subduction zone. Therefore, we argue that the origin of BHSG is controlled by the reactivation of the NEJFZ triggered by the Early Cretaceous subduction process along the South China active continental margin.

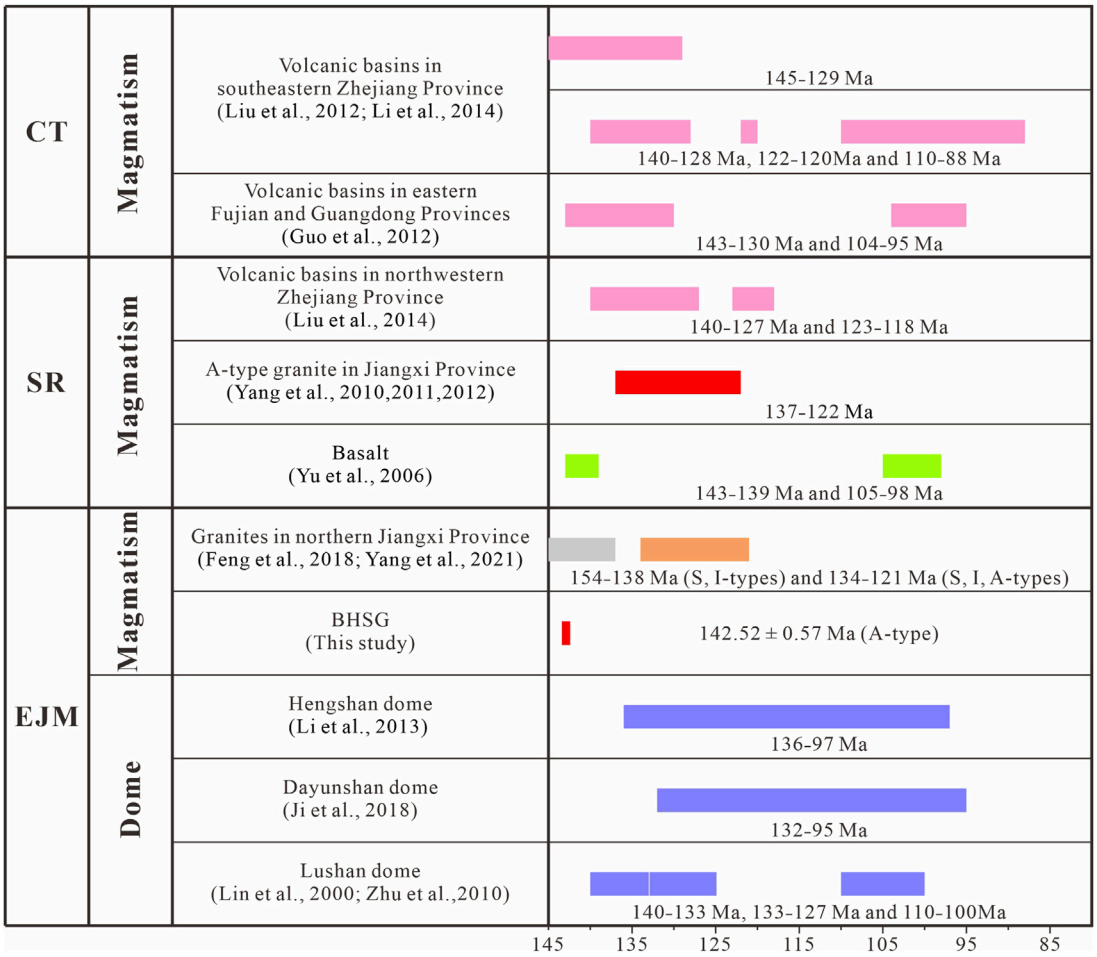


FIGURE 15
Diagram comparing the duration of extension-related geological records in different terranes of the SCB. Abbreviations: CT, coastal terrane, SR, Shi-Hang Rift, EJM, eastern Jiangnan Massif.

6 Conclusion

Baihesi granite is a highly evolved aluminous A-type granite with a concordant age of 142.52 ± 0.57 Ma (MSWD = 1.2), indicating the onset of the Cretaceous extension in the eastern Jiangnan Massif to be *ca.* 145–140 Ma.

The $\varepsilon_{Hf}(t)$ values of Baihesi granite range from −5.57 to −2.37, suggesting Baihesi granite originated mainly from partial melting of a reworked juvenile crust related to Neoproterozoic arc-related magmatism.

The formation of Baihesi granite was controlled by the subduction process along the South China active continental margin.

Data availability statement

The original contributions presented in the study are included in the article/Supplementary Material; further inquiries can be directed to the corresponding author.

Author contributions

Conceptualization, BH and DZ; methodology, BH; software, BH; validation, DZ and BH; formal analysis, BH; investigation, BH, DZ, and XZ; resources, DZ; data curation, BH; writing—original draft preparation, BH and DZ; writing–review and editing, DZ, ZZ, SW, and JH; visualization, BH; supervision, DZ; project administration, DZ; funding acquisition, DZ. All authors have read and agreed to the published version of the manuscript.

Funding

This research was funded by National Natural Science Foundation of China (Number 41772069), and the Geological Survey Achievement Transformation Fund of China University of Geosciences (Beijing).

Acknowledgments

The authors thank the editor and the reviewers for the constructive comments and thank Wuhan Sample Solution Analytical Technology Co., Ltd. for their help in the experimental analysis.

Conflict of interest

The authors declare that the research was conducted in the absence of any commercial or financial relationships that could be construed as a potential conflict of interest.

Publisher's note

All claims expressed in this article are solely those of the authors and do not necessarily represent those of their affiliated organizations, or those of the publisher, the editors, and the reviewers. Any product that may be evaluated in this article, or claim that may be made by its manufacturer, is not guaranteed or endorsed by the publisher.

Supplementary material

The Supplementary Material for this article can be found online at: https://www.frontiersin.org/articles/10.3389/feart.2023.1085767/full#supplementary-material

References

Ballouard, C., Boulvais, P., Poujol, M., Gapais, D., Yamato, P., Tartese, R., et al. (2015). Tectonic record, magmatic history and hydrothermal alteration in the Hercynian Guerande leucogranite, Armorican Massif, France. *Lithos* 220, 1–22. doi:10.1016/j.lithos.2015.01.027

Ballouard, C., Branquet, Y., Tartese, R., Poujol, M., Boulvais, P., and Vigneresse, J. L. (2016). Nb-Ta fractionation in peraluminous granites: A marker of the magmatic-hydrothermal transition. *Geology* 44, 231–234. doi:10.1130/g37475.1

Bau, M. (1996). Controls on the fractionation of isovalent trace elements in magmatic and aqueous systems: Evidence from Y/Ho, Zr/Hf, and lanthanide tetrad effect. *Contributions Mineralogy Petrology* 123, 323–333. doi:10.1007/s004100050159

Bonin, B. (2007). A-type granites and related rocks: Evolution of a concept, problems and prospects. *Lithos* 97, 1–29. doi:10.1016/j.lithos.2006.12.007

Chappell, B. W., and White, A. J. R. (1992). I- and S-type granites in the lachlan fold belt. *Trans. R. Soc. Edinb. Earth Sci.* 83, 1–26. doi:10.1017/s0263593300007720

Charvet, J. (2013). The neoproterozoic–early paleozoic tectonic evolution of the South China block: An overview. *J. Asian Earth Sci.* 74, 198–209. doi:10.1016/j.jseaes.2013.02.015

Chen, W., Chen, B., and Sun, K. (2018). Petrogenesis of the Maogongdong highly differentiated granite in the Dahutang tungsten ore field, Jiangxi Province. *Acta Petrol. Sin.* 34, 1704–1724. (In Chinese with English abstract).

Chu, Y., Lin, W., Faure, M., and Wang, Q. (2015). Early mesozoic intracontinental orogeny: Example of the xuefengshan-jiuling belt. *Acta Petrol. Sin.* 31, 2145–2155. (In Chinese with English abstract).

Chu, Y., Lin, W., Faure, M., Xue, Z., Ji, W., and Feng, Z. (2019). Cretaceous episodic extension in the South China block, east asia: Evidence from the yuechengling massif of central south China. *TECTONICS* 38, 3675–3702. doi:10.1029/2019tc005516

Chu, Y., and Lin, W. (2014). Phanerozoic polyorogenic deformation in southern Jiuling Massif, northern South China block: Constraints from structural analysis and geochronology. *J. Asian Earth Sci.* 86, 117–130. doi:10.1016/j.jseaes.2013.05.019

Collins, W. J., Beams, S. D., White, A. J. R., and Chappell, B. W. (1982). Nature and origin of A-type granites with particular reference to southeastern Australia. *Contributions Mineralogy Petrology* 80, 189–200. doi:10.1007/bf00374895

Dai, P., Mao, J., Wu, S., Xie, G., and Luo, X. (2018). Multiple dating and tectonic setting of the early cretaceous xianglushan W deposit, Jiangxi province, south China. *Ore Geol. Rev.* 95, 1161–1178. doi:10.1016/j.oregeorev.2017.11.017

Dostal, J., Kontak, D. J., Gerel, O., Shellnutt, J. G., and Fayek, M. (2015). Cretaceous ongonites (topaz-bearing albite-rich microleucogranites) from ongon khairkhan, Central Mongolia: Products of extreme magmatic fractionation and pervasive metasomatic fluid: Rock interaction. *Lithos* 236, 173–189. doi:10.1016/j.lithos.2015.08.003

Eby, G. N. (1992). Chemical subdivision of the A-type granitoids:Petrogenetic and tectonic implications. *Geology* 20, 641–644. doi:10.1130/0091-7613(1992)020<0641:csotat>2.3.co;2

Eby, G. N., and Kochhar, N. (1990). Geochemistry and petrogenesis of the Malani igneous suite, north Peninsular India. *J. Geol. Soc. INDIA* 36, 109–130.

Faure, M., Sun, Y., Shu, L., Monie, P., and Charvet, J. (1996). Extensional tectonics within a subduction-type orogen. The case study of the Wugongshan dome (Jiangxi Province, southeastern China). *TECTONOPHYSICS* 263, 77–106. doi:10.1016/s0040-1951(97)81487-4

Feng, C., Wang, H., Xiang, X., and Zhang, M. (2018). Late mesozoic granite-related W-Sn mineralization in the northern Jiangxi region, se China: A review. *J. Geochem. Explor.* 195, 31–48. doi:10.1016/j.gexplo.2018.06.008

Gan, C., Zhang, Y., Wang, Y., Qian, X., and Wang, Y. (2021). Reappraisal of the mesozoic tectonic transition from the paleo-tethyan to paleo-pacific domains in South China. *Geol. Soc. Am. Bull.* 133, 2582–2590. doi:10.1130/b35755.1

Gelman, S. E., Deering, C. D., Bachmann, O., Huber, C., and Gutierrez, F. J. (2014). Identifying the crystal graveyards remaining after large silicic eruptions. *Earth Planet. Sci. Lett.* 403, 299–306. doi:10.1016/j.epsl.2014.07.005

Gilder, S. A., Gill, J., Coe, R. S., Zhao, X. X., Liu, Z. W., Wang, G. X., et al. (1996). Isotopic and paleomagnetic constraints on the Mesozoic tectonic evolution of south China. *J. Geophys. RESEARCH-SOLID EARTH* 101, 16137–16154. doi:10.1029/96jb00662

Goldschmidt, V. M. (1937). The principles of distribution of chemical elements in minerals and rocks: The seventh Hugo Müller Lecture delivered before the Chemical Society on March 17th, 1937. *J. Chem. Soc.*, 655–673. doi:10.1039/JR9370000655

Guo, F., Fan, W., Li, C., Zhao, L., Li, H., and Yang, J. (2012). Multi-stage crust-mantle interaction in SE China: Temporal, thermal and compositional constraints from the Mesozoic felsic volcanic rocks in eastern Guangdong-Fujian provinces. *Lithos* 150, 62–84. doi:10.1016/j.lithos.2011.12.009

He, X., Zhang, D., Di, Y., Wu, G., Hu, B., Huo, H., et al. (2022). Evolution of the magmatic-hydrothermal system and formation of the giant Zhuxi W-Cu deposit in South China. *Geosci. Front.* 13, 101278. doi:10.1016/j.gsf.2021.101278

Hoskin, P. W. O. (2005). Trace-element composition of hydrothermal zircon and the alteration of Hadean zircon from the Jack Hills, Australia. *Geochimica Cosmochimica Acta* 69, 637–648. doi:10.1016/j.gca.2004.07.006

Hu, Z. H., Lou, F. S., Li, Y. M., Li, J. M., Wang, X. G., Chen, J. P., et al. (2018). Geochemistry and petrogenesis of ore-related granite in the dongping tungsten deposit in wuning county, Jiangxi province. *Earth Sci.* 43, 243–263. (In Chinese with English abstract).

Huang, L.-C., and Jiang, S.-Y. (2014). Highly fractionated S-type granites from the giant dahutang tungsten deposit in jiangnan orogen, southeast China: Geochronology, petrogenesis and their relationship with W-mineralization. *Lithos* 202, 207–226. doi:10.1016/j.lithos.2014.05.030

Jackson, S. E., Pearson, N. J., Griffin, W. L., and Belousova, E. A. (2004). The application of laser ablation-inductively coupled plasma-mass spectrometry to *in situ* U-Pb zircon geochronology. *Chem. Geol.* 211, 47–69. doi:10.1016/j.chemgeo.2004.06.017

Ji, W., Chen, Y., Chen, K., Wei, W., Faure, M., and Lin, W. (2018b). Multiple emplacement and exhumation history of the late mesozoic dayunshan-mufushan batholith in southeast China and its tectonic significance: 2. Magnetic fabrics and gravity survey. *J. Geophys. RESEARCH-SOLID EARTH* 123, 711–731. doi:10.1002/2017jb014598

Ji, W., Faure, M., Lin, W., Chen, Y., Chu, Y., and Xue, Z. (2018a). Multiple emplacement and exhumation history of the late mesozoic dayunshan-mufushan batholith in southeast China and its tectonic significance: 1. Structural analysis and geochronological constraints. *J. Geophys. RESEARCH-SOLID EARTH* 123, 689–710. doi:10.1002/2017jb014597

Jiang, Y.-H., Wang, G.-C., Liu, Z., Ni, C.-Y., Qing, L., and Zhang, Q. (2015). Repeated slab advance-retreat of the Palaeo-Pacific plate underneath SE China. *Int. Geol. Rev.* 57, 472–491. doi:10.1080/00206814.2015.1017775

Jiang, Y.-H., Zhao, P., Zhou, Q., Liao, S.-Y., and Jin, G.-D. (2011). Petrogenesis and tectonic implications of Early Cretaceous S- and A-type granites in the northwest of the Gan-Hang rift, SE China. *Lithos* 121, 55–73. doi:10.1016/j.lithos.2010.10.001

King, P. L., Chappell, B. W., Allen, C. M., and White, A. J. R. (2001). Are A-type granites the high-temperature felsic granites? Evidence from fractionated granites of the wangrah suite. *Aust. J. EARTH Sci.* 48, 501–514. doi:10.1046/j.1440-0952.2001.00881.x

King, P. L., White, A. J. R., Chappell, B. W., and Allen, C. M. (1997). Characterization and origin of aluminous A-type granites from the lachlan fold belt, southeastern Australia. *J. Petrology* 38, 371–391. doi:10.1093/petroj/38.3.371

Large, R. R., Gemmell, J. B., Paulick, H., and Huston, D. L. (2001). The alteration box plot: A simple approach to understanding the relationship between alteration mineralogy

and lithogeochemistry associated with volcanic-hosted massive sulfide deposits. *Econ. Geol.* 96, 957–971. doi:10.2113/96.5.957

Laurent, O., Björnsen, J., Wotzlaw, J.-F., Bretscher, S., Pimenta Silva, M., Moyen, J.-F., et al. (2020). Earth's earliest granitoids are crystal-rich magma reservoirs tapped by silicic eruptions. *Nat. Geosci.* 13, 163–169. doi:10.1038/s41561-019-0520-6

Lechler, P. J., and Desilets, M. O. (1987). A review of the use of loss on ignition as a measurement of total volatiles in whole-rock analysis. *Chem. Geol.* 63, 341–344. doi:10.1016/0009-2541(87)90171-9

Li, C., Wang, Z., Lu, Q., Tan, Y., Li, L., Tao, T., et al. (2021). Mesozoic tectonic evolution of the eastern South China Block: A review on the synthesis of the regional deformation and magmatism. *Ore Geol. Rev.*, 131. doi:10.1016/j.oregeorev.2021.104028

Li, C., Wang, Z., Wang, D., Cao, W., Yu, X., Zhou, G., et al. (2014). Crust-mantle interaction triggered by oblique subduction of the Pacific plate: geochronological, geochemical, and Hf isotopic evidence from the Early Cretaceous volcanic rocks of Zhejiang Province, southeast China. *Int. Geol. Rev.*1756, 1732–1753. doi:10.1080/00206814.2014.956347

Li, J., Dong, S., Gao, R., Cawood, P. A., Zhang, Y., Zhao, G., et al. (2022). New insights into phanerozoic tectonics of South China: Part 1, polyphase deformation in the jiuling and lianyunshan domains of the central jiangnan orogen. *Tect. Geophys. Res. Solid Earth* 41121, 3048–3080. doi:10.1002/2015jb012778

Li, J., Dong, S., Zhang, Y., Zhao, G., Johnston, S. T., Cui, J., et al. (2016). New insights into Phanerozoic tectonics of south China: Part 1, polyphase deformation in the Jiuling and Lianyunshan domains of the central Jiangnan Orogen. *J. Geophys. Res. Solid Earth* 121, 3048–3080. doi:10.1002/2015JB012778

Li, J., Zhang, Y., Dong, S., and Johnston, S. T. (2014). Cretaceous tectonic evolution of South China: A preliminary synthesis. *EARTH-SCIENCE Rev.* 134, 98–136. doi:10.1016/j.earscirev.2014.03.008

Li, J., Zhang, Y., Dong, S., Su, J., Li, Y., Cui, J., et al. (2013). The Hengshan low-angle normal fault zone: Structural and geochronological constraints on the Late Mesozoic crustal extension in South China. *TECTONOPHYSICS* 606, 97–115. doi:10.1016/j.tecto.2013.05.013

Li, X.-H., Li, W.-X., Li, Z.-X., Lo, C.-H., Wang, J., Ye, M.-F., et al. (2009). Amalgamation between the Yangtze and Cathaysia blocks in South China: Constraints from SHRIMP U-Pb zircon ages, geochemistry and Nd-Hf isotopes of the shuangxiwu volcanic rocks. *Precambrian Res.* 174, 117–128. doi:10.1016/j.precamres.2009.07.004

Li, X., Long, W., Li, Q., Liu, Y., Zheng, Y., Yang, Y., et al. (2010). Penglai zircon megacrysts: A potential new working reference material for microbeam determination of Hf-O isotopes and U-Pb age. *Geostand. GEOANALYTICAL Res.* 34, 117–134. doi:10.1111/j.1751-908x.2010.00036.x

Li, Z.-X., and Li, X.-H. (2007). formation of the 1300-km-wide intracontinental orogen and postorogenic magmatic province in mesozoic south China: A flat-slab subduction model. *Geology* 35, 179–182. doi:10.1130/g23193a.1

Lin, W., Faure, M., Monie, P., Scharer, U., Zhang, L. S., and Sun, Y. (2000). Tectonics of SE China: New insights from the lushan massif (Jiangxi province). *TECTONICS* 19, 852–871. doi:10.1029/2000tc900009

Liu, J. L., Ni, J. L., Chen, X. Y., Craddock, J. P., Zheng, Y. Y., Ji, L., et al. (2021). Cretaceous Pacific plate movement beneath SE China: Evidence from episodic volcanism and related intrusions. *EARTH-SCIENCE Rev.* 217614, 170–184. doi:10.1016/j.tecto.2013.12.007

Liu, L., Xu, X., and Xia, Y. (2014). Cretaceous Pacific plate movement beneath SE China: Evidence from episodic volcanism and related intrusions. *TECTONOPHYSICS* 614, 170–184. doi:10.1016/j.tecto.2013.12.007

Liu, L., Xu, X., and Zou, H. (2012). Episodic eruptions of the Late Mesozoic volcanic sequences in southeastern Zhejiang, SE China: Petrogenesis and implications for the geodynamics of paleo-Pacific subduction. *Lithos* 154, 166–180. doi:10.1016/j.lithos.2012.07.002

Liu, P., Mao, J., Santosh, M., Bao, Z., Zeng, X., and Jia, L. (2018). Geochronology and petrogenesis of the Early Cretaceous A-type granite from the Feie'Shan W-Sn deposit in the eastern Guangdong Province, SE China: Implications for W-Sn mineralization and geodynamic setting. *Lithos* 300, 330–347. doi:10.1016/j.lithos.2017.12.015

Liu, Y., Gao, S., Hu, Z., Gao, C., Zong, K., and Wang, D. (2010). Continental and oceanic crust recycling-induced melt-peridotite interactions in the trans-north China orogen: U-Pb dating, Hf isotopes and trace elements in zircons from mantle xenoliths. *J. Petrology* 51, 537–571. doi:10.1093/petrology/egp082

Loiselle, M. C., and Wones, D. R. (1979). *Characteristics and origin of anorogenic granites*, 11. San Diego, CA: Geological Society of America Abstracts with Programs, 468.

Lou, F., Shen, W., Wang, D., Shu, L., Wu, F., Zhang, F., et al. (2005). Zircon U-Pb isotopic chronology of the wugongshan dome compound granite in Jiangxi province. *ACTA Geol. SIN.* 79, 636–644. (In Chinese with English abstract).

Luo, L., Jiang, S. Y., Yang, S. Y., and Zhao, K. D. Petrochemistry (2010). Zircon U-Pb dating and Hf isotopic composition of the granitic pluton in the Pengshan Sn-polymetallic orefield, Jiangxi Province. *Acta Petrol. Sin.* 26, 2818–2834. (In Chinese with English abstract).

MacLean, W. H. (1990). Mass change calculations in altered rock series. *Miner. Deposita* 25, 44–49. doi:10.1007/bf03326382

Maniar, P. D., and Piccoli, P. M. (1989). Tectonic discrimination of granitoids. *Geol. Soc. Am. Bull.* 101, 635–643. doi:10.1130/0016-7606(1989)101<0635:tdog>2.3.co;2

Mao, J., Xiong, B., Liu, J., Pirajno, F., Cheng, Y., Ye, H., et al. (2017). Molybdenite Re/Os dating, zircon U-Pb age and geochemistry of granitoids in the Yangchuling porphyry W-Mo deposit (Jiangnan tungsten ore belt), China: Implications for petrogenesis, mineralization and geodynamic setting. *Lithos* 286, 35–52. doi:10.1016/j.lithos.2017.05.023

Middlemost, E. A. K. (1994). Naming materials in the magma/igneous rock system. *EARTH-SCIENCE Rev.* 37, 215–224. doi:10.1016/0012-8252(94)90029-9

Miller, C. F., and Mittlefehldt, D. W. (1982). Depletion of light rare-earth elements in felsic magmas. *Geology* 10, 129–133. doi:10.1130/0091-7613(1982)10<129:dolrei>2.0.co;2

Miller, C. F., and Mittlefehldt, D. W. (1984). Extreme fractionation in felsic magma chambers: A product of liquid-state diffusion or fractional crystallization? *Earth Planet. Sci. Lett.* 68, 151–158. doi:10.1016/0012-821x(84)90147-x

Mo, X. (2019). Magmatism and deep geological process. *Earth Sci.* 44, 1487–1493. (In Chinese with English abstract).

Pan, F.-B., Liu, R., Jin, C., Jia, B.-J., He, X., Gao, Z., et al. (2018). Petrogenesis of early cretaceous granitoids from southwest Zhejiang, NE south China block and its geodynamic implication. *Lithos* 308, 196–212. doi:10.1016/j.lithos.2018.03.011

Pan, X., Hou, Z., Zhao, M., Chen, G., Rao, J., Li, Y., et al. (2018). Geochronology and geochemistry of the granites from the Zhuxi W-Cu ore deposit in South China: Implication for petrogenesis, geodynamical setting and mineralization. *Lithos* 304, 155–179. doi:10.1016/j.lithos.2018.01.014

Pearce, J. A., Harris, N. B. W., and Tindle, A. G. (1984). Trace element discrimination diagrams for the tectonic interpretation of granitic rocks. *J. Petrology* 25, 956–983. doi:10.1093/petrology/25.4.956

Peccerillo, A., and Taylor, S. R. (1976). Geochemistry of eocene calc-alkaline volcanic rocks from the Kastamonu area, Northern Turkey. *Contributions Mineralogy Petrology* 58, 63–81. doi:10.1007/bf00384745

Qiu, J.-T., and Qiu, L. (2016). Geochronology and magma oxygen fugacity of Ehu S-type granitic pluton in Zhe-Gan-Wan region, SE China. *Chem. DER ERDE-GEOCHEMISTRY* 76, 441–448. doi:10.1016/j.chemer.2016.06.004

Rogers, J. J. W., and Greenberg, J. K. (1990). Late-orogenic, post-orogenic, and anorogenic granites: Distinction by major-element and trace-element chemistry and possible origins. *J. Geol.* 98, 291–309. doi:10.1086/629406

Shu, L. (2021). Principal features of intracontinental orogenic belt and discussions on its dynamics. *ACTA Geol. SIN.* 95, 98–106. (In Chinese with English abstract).

Shu, L. S., Zhou, G. Q., Shi, Y. S., and Yin, J. (1994). Study of the high pressure metamorphic blueschist and its late proterozoic age in the eastern jiangnan belt. *Chin. Sci. Bull.* 39, 1200–1204.

Shu, L. S., Zhou, X. M., Deng, P., Wang, B., Jiang, S. Y., Yu, J. H., et al. (2009). Mesozoic tectonic evolution of the Southeast China Block: New insights from basin analysis. *J. Asian Earth Sci.* 34, 376–391. doi:10.1016/j.jseaes.2008.06.004

Sláma, J., Košler, J., Condon, D. J., Crowley, J. L., Gerdes, A., Hanchar, J. M., et al. (2008). Plešovice zircon — a new natural reference material for U–Pb and Hf isotopic microanalysis. *Chem. Geol.* 249, 1–35. doi:10.1016/j.chemgeo.2007.11.005

Smith, R. E., and Smith, S. E. (1976). Comments on the use of Ti, Zr, Y, Sr, K, P and Nb in classification of basaltic magmas. *Earth Planet. Sci. Lett.* 32 (2), 114–120. doi:10.1016/0012-821x(76)90049-2

Streckeisen, A., and Le Maitre, R. W. (1979). A chemical approximation to the modal QAPF classification of the igneous rocks. *Neues Jahrb. fur Mineral. Abh.* 136, 169–206.

Sun, H., Li, J., Zhang, Y., Dong, S., Xin, Y., and Yu, Y. (2018). Early Paleozoic tectonic reactivation of the Shaoxing-Jiangshan fault zone: Structural and geochronological constraints from the Chencai domain, South China. *J. Struct. Geol.* 110, 116–130. doi:10.1016/j.jsg.2018.03.003

Sun, S. s., and McDonough, W. F. (1989). Chemical and isotopic systematics of oceanic basalts: Implications for mantle composition and processes. *Geol. Soc. Lond. Spec. Publ.* 42, 313–345. doi:10.1144/gsl.sp.1989.042.01.19

Suo, Y., Li, S., Jin, C., Zhang, Y., Zhou, J., Li, X., et al. (2019). Eastward tectonic migration and transition of the Jurassic-Cretaceous Andean-type continental margin along Southeast China. *EARTH-SCIENCE Rev.* 196, 102884. doi:10.1016/j.earscirev.2019.102884

Sylvester, P. J. (1989). Post-collisional alkaline granites. *J. Geol.* 97, 261–280. doi:10.1086/629302

Vermeesch, P. IsoplotR. (2018). IsoplotR: A free and open toolbox for geochronology. *Geosci. Front.* 9, 1479–1493. doi:10.1016/j.gsf.2018.04.001

Wang, D., Wang, X.-L., Zhou, J.-C., and Shu, X.-J. (2013). Unraveling the precambrian crustal evolution by neoproterozoic conglomerates, jiangnan orogen: U–Pb and Hf isotopes of detrital zircons. *Precambrian Res.* 233, 223–236. doi:10.1016/j.precamres.2013.05.005

Wang, F., Chen, H., Batt, G. E., Lin, X., Gong, J., Gong, G., et al. (2015). Tectonothermal history of the NE Jiangshan-Shaoxing suture zone: Evidence from 40Ar/39Ar and fission-track thermochronology in the Chencai region. *Precambrian Res.* 264, 192–203. doi:10.1016/j.precamres.2015.04.009

Wang, J.-l., He, B., and Guan, J.-p. (2013). Study on age and mechanism of the metamorphism of the xingzi group in the lushan area, Jiangxi province. *Geotect. Metallogenia* 37, 489–498.

Wang, L.-j., Zhang, K.-x., Lin, S.-f., He, W.-h., and Yin, L.-m. (2022). Origin and age of the shenshan tectonic melange in the jiangshan-shaoxing-pingxiang fault and late early paleozoic juxtaposition of the Yangtze block and the west Cathaysia terrane, south China. *Geol. Soc. Am. Bull.* 134, 113–129. doi:10.1130/b35963.1

Wang, X.-L., Zhao, G., Zhou, J.-C., Liu, Y., and Hu, J. (2008). Geochronology and Hf isotopes of zircon from volcanic rocks of the Shuangqiaoshan Group, South China: Implications for the Neoproterozoic tectonic evolution of the eastern Jiangnan orogen. *Gondwana Res.* 14, 355–367. doi:10.1016/j.gr.2008.03.001

Wang, X.-L., Zhou, J.-C., Griffin, W. L., Zhao, G., Yu, J.-H., Qiu, J.-S., et al. (2014). Geochemical zonation across a Neoproterozoic orogenic belt: Isotopic evidence from granitoids and metasedimentary rocks of the Jiangnan orogen, China. *Precambrian Res.* 242, 154–171. doi:10.1016/j.precamres.2013.12.023

Watson, E. B., and Harrison, T. M. (1983). Zircon saturation revisited: Temperature and composition effects in a variety of crustal magma types. *Earth Planet. Sci. Lett.* 64, 295–304. doi:10.1016/0012-821x(83)90211-x

Whalen, J. B., Currie, K. L., and Chappell, B. W. (1987). A-Type granites: Geochemical characteristics, discrimination and petrogenesis. *Contributions Mineralogy Petrology* 95, 407–419. doi:10.1007/bf00402202

Wong, J., Sun, M., Xing, G. F., Li, X. H., Zhao, G. C., Wong, K., et al. (2009). Geochemical and zircon U-Pb and Hf isotopic study of the Baijuhuajian metaluminous A-type granite: Extension at 125-100 Ma and its tectonic significance for South China. *Lithos* 112, 289–305. doi:10.1016/j.lithos.2009.03.009

Wu, F., Liu, X., Ji, W., Wang, J., and Yang, L. (2017). Highly fractionated granites: Recognition and research. *Sci. China-Earth Sci.* 60, 1201–1219. doi:10.1007/s11430-016-5139-1

Xu, Q., Liu, S., Wang, Z., and Zhang, B. (2019). Provenance of the East Guangdong Basin and Yong'an Basin in southeast China: Response to the Mesozoic tectonic regime transformation. *J. Asian Earth Sci.*, 18. doi:10.1016/j.jseaes.2019.104024

Yang, S.-Y., Jiang, S.-Y., Jiang, Y.-H., Zhao, K.-D., and Fan, H.-H. (2011). Geochemical, zircon U-Pb dating and Sr-Nd-Hf isotopic constraints on the age and petrogenesis of an Early Cretaceous volcanic-intrusive complex at Xiangshan, Southeast China. *MINERALOGY PETROLOGY* 101, 21–48. doi:10.1007/s00710-010-0136-4

Yang, S.-Y., Jiang, S.-Y., Zhao, K.-D., Jiang, Y.-H., Ling, H.-F., and Luo, L. (2012). Geochronology, geochemistry and tectonic significance of two Early Cretaceous A-type granites in the Gan-Hang Belt, Southeast China. *Lithos* 150, 155–170. doi:10.1016/j.lithos.2012.01.028

Yang, Y. S., Pan, X. F., Hou, Z. Q., and Deng, Y. (2021). Redox states and protoliths of late mesozoic granitoids in the eastern jiangnan orogen: Implications for W, Mo, Cu, Sn, and (Au) mineralization. *Ore Geol. Rev.* 134.

Yao, J., Cawood, P. A., Shu, L., and Zhao, G. (2019). Jiangnan orogen, south China: A ~970–820 Ma rodinia margin accretionary belt. *EARTH-SCIENCE Rev.* 196, 102872.

Yao, J., Shu, L., Santosh, M., and Li, J. (2012). Precambrian crustal evolution of the South China Block and its relation to supercontinent history: Constraints from U-Pb ages, Lu-Hf isotopes and REE geochemistry of zircons from sandstones and granodiorite. *Precambrian Res.* 208, 19–48. doi:10.1016/j.precamres.2012.03.009

Ye, M.-F., Li, X.-H., Li, W.-X., Liu, Y., and Li, Z.-X. (2007). SHRIMP zircon U-Pb geochronological and whole-rock geochemical evidence for an early Neoproterozoic Sibaoan magmatic arc along the southeastern margin of the Yangtze Block. *Gondwana Res.* 12, 144–156. doi:10.1016/j.gr.2006.09.001

Yu, X., Wu, G., Zhang, D., Yan, T., Di, Y., and Wang, L. (2006). Cretaceous extension of the ganhang tectonic belt, southeastern China: Constraints from geochemistry of volcanic rocks. *Cretac. Res.* 27, 663–672. doi:10.1016/j.cretres.2006.03.008

Zhang, Y., Xu, X., Jia, D., and Shu, L. (2009). Deformation record of the change from Indosinian collision-related tectonic system to Yanshanian subduction-related tectonic system in South China during the Early Mesozoic. *Earth Sci. Front.* 16, 234–247. (In Chinese with English abstract).

Zhang, Z., Hu, B., Zhang, D., He, X., Zou, J., Tian, X., et al. (2022). *Genesis and significance of late cretaceous granitic magmatism in xianghualing tin-polymetallic orefield, nanling region, South China*. Basel, Switzerland: APPLIED SCIENCES-BASEL, 12. doi:10.3390/app12188984

Zhang, Z., Hu, B., Zhang, D., Xiong, G., Zhu, X., Jia, W., et al. (2020). Zircon U-Pb age, geochemistry and Hf isotope characteristics of Shimensi granite porphyry in northern Jiangxi Province and its constraint on mineralization. *Geol. Bull. China* 39, 1267–1284. (In Chinese with English abstract).

Zhao, G., and Cawood, P. A. (2012). Precambrian geology of China. *Precambrian Res.* 222-223, 13–54. doi:10.1016/j.precamres.2012.09.017

Zhou, X. M., and Li, W. X. (2000). Origin of Late Mesozoic igneous rocks in Southeastern China: Implications for lithosphere subduction and underplating of mafic magmas. *TECTONOPHYSICS* 326, 269–287. doi:10.1016/s0040-1951(00)00120-7

Zhou, X. M., Sun, T., Shen, W. Z., Shu, L. S., and Niu, Y. L. (2006). Petrogenesis of mesozoic granitoids and volcanic rocks in South China: A response to tectonic evolution. *Episodes* 29, 26–33. doi:10.18814/epiiugs/2006/v29i1/004

Zhu, Q., Yang, K., and Wang, Y. (2010). Extensional detachment and magmatism of the lushan metamorphic core complex: Constraints from ~(40)Ar/~(39)Ar and U-Pb geochronology. *Geotect. Metallogenia* 34, 391–401.

Zong, K., Klemd, R., Yuan, Y., He, Z., Guo, J., Shi, X., et al. (2017). The assembly of Rodinia: The correlation of early Neoproterozoic (ca. 900 Ma) high-grade metamorphism and continental arc formation in the southern Beishan Orogen, southern Central Asian Orogenic Belt (CAOB). *Precambrian Res.* 290, 32–48. doi:10.1016/j.precamres.2016.12.010

frontiers | Frontiers in Earth Science

TYPE Original Research
PUBLISHED 07 February 2023
DOI 10.3389/feart.2023.1107833

Check for updates

OPEN ACCESS

EDITED BY
Liang Zhang,
China University of Geosciences, China

REVIEWED BY
Changhong Wang,
China University of Geosciences, China
Zhuang Miao,
China University of Geosciences, China

*CORRESPONDENCE
C. B. Dimalanta,
cbdimalanta@up.edu.ph

SPECIALTY SECTION
This article was submitted to Structural Geology and Tectonics, a section of the journal Frontiers in Earth Science

RECEIVED 25 November 2022
ACCEPTED 25 January 2023
PUBLISHED 07 February 2023

CITATION
Parcutela NE, Austria RS, Dimalanta CB, Valera GTV, Gabo-Ratio JAS, Payot BD, Armada LT, Sangalang KJF, Yumul GP Jr. (2023), Enhanced arc magmatic productivity of the Western Pacific island arcs deduced from gravity-derived arc crustal growth rates.
Front. Earth Sci. 11:1107833.
doi: 10.3389/feart.2023.1107833

COPYRIGHT
© 2023 Parcutela, Austria, Dimalanta, Valera, Gabo-Ratio, Payot, Armada, Sangalang and Yumul. This is an open-access article distributed under the terms of the Creative Commons Attribution License (CC BY). The use, distribution or reproduction in other forums is permitted, provided the original author(s) and the copyright owner(s) are credited and that the original publication in this journal is cited, in accordance with accepted academic practice. No use, distribution or reproduction is permitted which does not comply with these terms.

Enhanced arc magmatic productivity of the Western Pacific island arcs deduced from gravity-derived arc crustal growth rates

N. E. Parcutela[1,2], R. S. Austria[1], C. B. Dimalanta[1]*, G. T. V. Valera[1], J. A. S. Gabo-Ratio[1], B. D. Payot[1], L. T. Armada[1], K. J. F. Sangalang[1] and G. P. Yumul Jr.[3,4]

[1]Rushurgent Working Group, National Institute of Geological Sciences, College of Science, University of the Philippines, Quezon City, Philippines, [2]Energy Development Corporation, Pasig City, Philippines, [3]Cordillera Exploration Co., Inc, Bonifacio Global City, Taguig City, Philippines, [4]School of Environmental Science and Management, University of the Philippines, Laguna, Philippines

Island arcs are postulated as the juvenile components that contribute to the growth of continental crust. Growth rates of arc crusts were previously computed using crustal thicknesses derived from seismic data. Consequently, crustal growth rates of oceanic island arcs are also constrained by the limited seismic data availability. This work presents the first comparison of gravity-derived magmatic growth rates of Western Pacific oceanic island arcs. We used the statistical correlation between Bouguer anomalies and seismic-derived crustal thicknesses to generate an empirical formula. The new empirical formula was utilized to estimate the crustal thicknesses of oceanic island arcs using Bouguer anomalies from the EGM2008 global gravity model. The resulting crustal thicknesses were employed to compute the magmatic growth rates of western Pacific island arcs and the Philippine island arc system. The latest magmatic growth rate estimates show that the magmatic productivity of Western Pacific island arcs, which are directly associated with Pacific Plate subduction, is significantly higher (28–60 km^3/km/m.y). The growth rate of the Pacific island arcs is higher compared to the magmatic growth rate computed for the other oceanic island arcs (12–25 km^3/km/m.y), which are derived from the subduction of other oceanic lithospheres (i.e., the Philippine Sea Plate; Caribbean Sea Plate; and Eurasia-South China Sea slabs). This is attributed to the variation in the ages of the subducting plates. The Pacific Plate, being older, is associated with higher degrees of serpentinization and sediment cover, which introduce more volatiles inducing more robust partial melting of the mantle wedge.

KEYWORDS

oceanic island arc, crustal thickness, magmatic growth rate, Bouguer anomalies, western Pacific, Philippines

1 Introduction

Materials constituting the continents are thought to have possibly originated from the juvenile products generated in active arcs (e.g., Reymer and Schubert, 1984; von Huene and Scholl, 1991; Condie, 1997; Kodaira et al., 2007; Turner and Langmuir, 2015). As such, island arcs can be considered one of the building blocks contributing to the growth of the Earth's continental crust. Moreover, studies on collisions of island arcs with continental crust support

the idea of continental growth through arc-continent collision. This has been documented in Southeast America (e.g., Byrne et al., 1985; Mann et al., 2002; DeMets et al., 2010; Granja Bruña et al., 2014), Timor (e.g., Karig et al., 1987; Nugroho et al., 2009; Harris, 2011), Taiwan (e.g., Huang et al., 1997; Lundberg et al., 1997; Malavieille et al., 2002; Byrne et al., 2011; Hsieh et al., 2020) and the Philippines (e.g., Yumul et al., 2009; Zamoras et al., 2008; Dimalanta et al., 2009; Concepcion et al., 2012; Manalo et al., 2016). Deciphering the processes that control the growth of an arc crust and its structure is, therefore, crucial in understanding crustal processes that actively influence magmatic crustal compositions (e.g., Plank and Langmuir, 1988; Farner and Lee, 2017).

The rate of productivity of arc magmatism is attributed to factors such as the nature of subduction (e.g., rate and angle of subduction) (e.g., Luo and Zhang, 2018); and the degree of hydration in the subduction system (e.g., Rupke et al., 2004; Zellmer et al., 2014). The subducted volatiles can induce flux melting of the mantle wedge and significantly influence the arc magmatic productivity in a trench-arc system. Several studies have shown that the amount of subducted volatiles are somehow related to the age of the subducting plate (e.g., Hay et al., 1998; Olson et al., 2016). These studies demonstrated that older subducting oceanic lithospheres are associated with thicker sediment covers and higher degrees of serpentinization. These conditions promote more volatiles to the subduction system causing a higher degree of flux melting (e.g., Luhr, 1992; Ulmer, 2001; Huang et al., 2006; Zellmer et al., 2014). In addition to subduction zone magmatism, arc crustal growth can also be induced *via* amagmatic contributions primarily from ophiolite emplacement (e.g., Dewey and Windley, 1981; Rait, 2000; Dimalanta and Yumul, 2003; Huang et al., 2015).

In the absence of seismic data, gravity data can be utilized as a reasonable substitute to estimate the thickness of island arcs. Several authors used available seismic data and Bouguer anomalies to generate an empirical formula between the two to compute crustal thickness (e.g., Worzel and Shurbet, 1955; Woollard, 1959; Milsom et al., 1996; Assumpcao et al., 2013). The studies done by Worzel and Shurbet (1955), Woollard (1959), and Assumpcao and others (2013) were all done in continental settings. Milsom and others (1996) also proposed an empirical equation derived using the average physical parameters of a continental crust, e.g., a 30-km thickness for a standard continental crust. Despite this, their equation has been used to estimate the thickness of the crust beneath oceanic island arcs. It is worth noting that crustal thickness studies in island arcs using Bouguer anomalies are not as extensive as crustal thickness estimates in continents. Reliable crustal thickness estimates for arcs are provided by ocean bottom seismometer (OBS) data such as that for the Ryukyu arc (Nishizawa et al., 2017), Izu-Bonin arc system (Suyehiro et al., 1996), and Aleutians arc (Holbrook et al., 1999).

2 Bouguer anomalies as proxies to crustal thickness estimations

One of the earliest crustal thickness models, the CRUST 5.1, was developed by Mooney et al. (1998). The 5° × 5° crustal thickness map of the world was produced using published seismic refraction data and information about the ice and sediment thickness. Subsequent maps and models with greater resolutions were produced by incorporating gravity data to address the need for more local-scale studies involving crustal thickness models. These studies resulted in the CRUST 2.0 model, which is a 2° × 2° crustal thickness map (Bassin et al., 2000), and the CRUST 1.0 model, which is a 1° × 1° crustal thickness map (Laske et al., 2013). While these provide reasonable estimates for the global distribution of crustal thickness, the resolution of these data is unsuitable for local studies such as characterizing the crustal thickness of specific island arcs.

In some island arcs where seismic data are unavailable, passive geophysical methods, such as the gravity method, are a reasonable substitute. The gravity method is significantly cheaper, and the spatial availability of data is also considerably better. The gravity method operates on the principle that the crust-mantle boundary is often marked by a significant change in physical properties, including density (e.g., Maystrenko and Scheck-Wenderoth, 2009; Carbonell et al., 2013). Thus, the depth to the Moho interface is treated as the crustal thickness (Bai et al., 2014). In theory, due to along-arc variations in oceanic island arcs, Bouguer anomalies, through gravity/density inversion, can also be used to produce subsurface models of the oceanic island arcs. For instance, Bouguer anomalies, albeit with additional constraints from seismic data, have been previously applied to produce subsurface models of the Bonin arc (e.g., Kodaira et al., 2011).

Various empirical formulae have been defined showing the relationship between Bouguer anomalies and the thickness of the crust derived from seismic surveys (e.g., Worzel and Shurbet, 1955; Woollard, 1959; Milsom et al., 1996; Assumpcao et al., 2013; Bai et al., 2014). Of these formulae, the one proposed by Milsom and others (1996) has been widely applied to oceanic arc settings (e.g., Dimalanta et al, 2002; Manalo et al., 2015; Parcutela et al., 2020; 2022). Based on experimental modeling, they proposed that a 1-km change in the thickness of a 30-km-thick standard continental crust will be accompanied by a 16-mGal change in the Bouguer anomaly.

This empirical formula is consistent with the observation by Huang and others (2006) regarding the relationship between Bouguer anomalies and depth to Moho in continental settings. While formulas such as these provide good estimates of crustal thickness, their applicability might be limited to the specific geologic setting which the datasets were derived from (Stolk et al., 2013). An empirical formula based on a continental setting might not work well for island arc settings, given the substantial differences between the overall composition of continental and island arc crust. Although the formula proposed by Milsom and others (1996) has been used to estimate the crustal thickness of island arcs (e.g., the Philippines), it should be noted that their formula was not constrained by ocean bottom seismometer (OBS)- or multi-channel seismic (MCS)-derived crustal thicknesses. Hence, there is currently no empirical formula for the relationship between seismic-derived crustal thickness and Bouguer anomalies in oceanic island arcs. This work will estimate the crustal thickness of several oceanic island arcs without seismic data. This, in turn, will be useful in calculating arc crustal growth rates using gravity data.

3 Data and methods

The new empirical formula is based on a linear regression analysis between the seismic-derived crustal thickness of oceanic island arcs with their corresponding Bouguer anomalies.

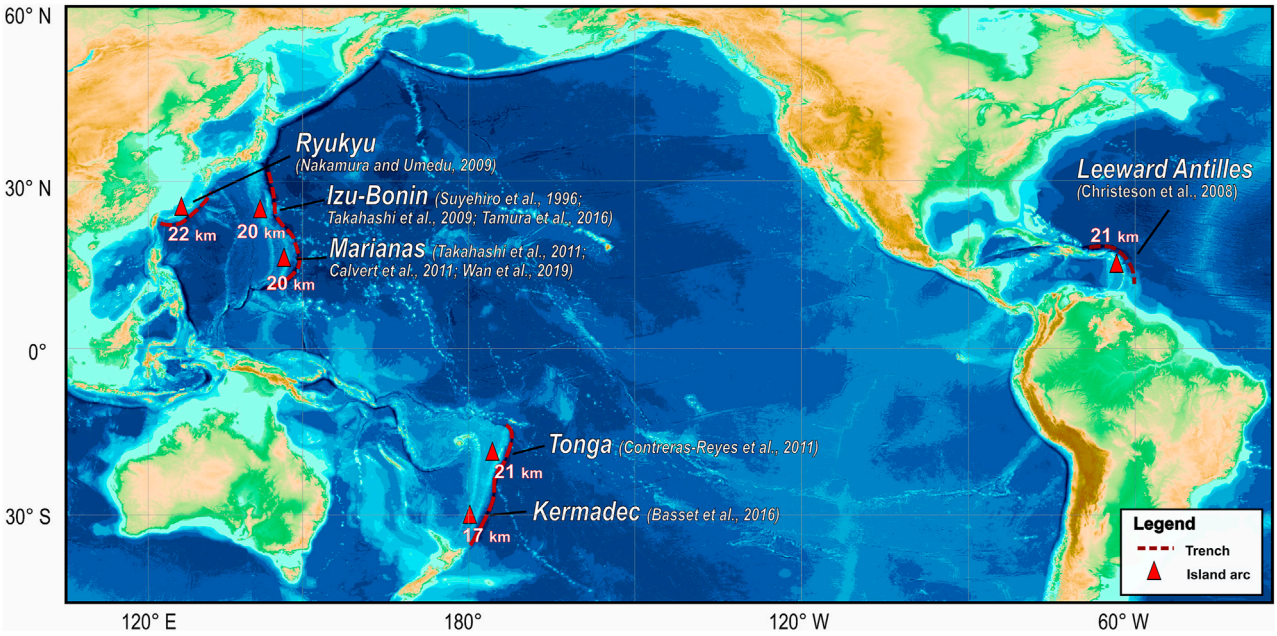


FIGURE 1
Location of the oceanic island arcs used for the regression analysis determining the relationship between crustal thickness and Bouguer anomalies. The numbers shown in the figure represent the average crustal thickness of these oceanic island arcs derived from seismic data. Bathymetric data used in the base map was extracted from GEBCO (2022).

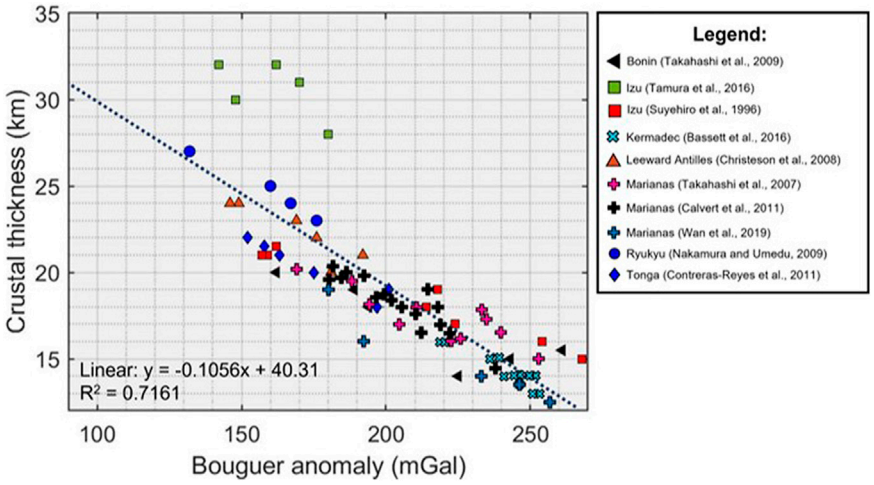


FIGURE 2
Crustal thickness vs. Bouguer anomaly plot for all the arc datasets utilized in this study. A strong negative correlation exists between the two variables as represented by the negative regression curve and a high coefficient of correlation at 0.7161.

3.1 Crustal thickness data of oceanic island arcs

Available crustal thickness data of oceanic island arcs with published crustal thickness sections derived from OBS and MCS surveys were utilized in this study. Transects signifying pure oceanic island arc signatures and only crustal thickness estimates for active modern arcs were selected. These oceanic island arcs are shown in Figure 1.

3.2 Empirical formula for crustal thickness estimations

Crustal thickness sections were digitized and georeferenced to extract the corresponding Bouguer anomalies from the EGM2008 model accurately. Profiles depicting the crustal thickness of modern or active arcs were considered in this study. The Bouguer anomaly and crustal thickness data are presented in a scatter plot generated using Matlab plotting algorithms. The scatter plot consists

of 88 data points (Figure 2). These data were subjected to linear regression analyses where the dependent variable is the crustal thickness, the independent variable is the Bouguer anomaly value, the *y*-intercept is the constant value corresponding to the thickness of a standard oceanic arc crust, and the slope is the rate of gravity signature change per 1-km change in crustal thickness.

A geophysical constraint was further applied to the generated equation. As discussed earlier, the *y*-intercept value and the slope of the line correspond to the standard thickness of oceanic arc crust and the accompanying gravity signature change per 1-km change in crustal thickness, respectively. These values are automatically generated as the best-fit line is produced. However, these can be changed or substituted by other slope and *y*-intercept pairs conforming to the generated line. The average crustal thickness of modern arcs (26 km) (Tetreault and Buiter, 2014) was used as a starting point. Gravity modeling was carried out using the 2D GM-SYS plugin of Oasis Montaj version 9.2 (Sharma, 1997).

3.3 Crustal growth rate computations of oceanic island arcs using gravity-derived crustal thicknesses

The geophysically-constrained empirical formula was applied to the Bouguer anomaly grid of several oceanic island arcs to compute their respective crustal thicknesses. The resulting crustal thicknesses were used to compute the magmatic addition rate of these oceanic island arcs following the methodology introduced by Reymer and Schubert (1984). This method is summarized in the equation below:

$$Growth\,rate = \frac{CT_{-7}\ X\ Area}{CSA\ X\ Age}$$

where: CT_{-7} = arc crustal thickness (7-km-thick oceanic crust already removed), CSA = cross-sectional area of the arc, and age = age of initiation of subduction.

For island arcs that were included in the study of Dimalanta and others (2002), we adopted the values used for the arc area and cross-sectional areas. For the other island arcs, the areas and cross-sectional areas were calculated using ArcMap version 10.6.1. The measured areas were multiplied by the crustal thicknesses obtained by applying the generated empirical formula to the EGM2008-derived Bouguer anomalies. The 7-km average thickness of standard oceanic crust was subtracted from the crustal thickness which yielded the volume of the arc magmatic material. The volume was then divided by the arc length to determine the magmatic contribution per square kilometer. The values were then divided by the age of initiation of subduction to derive the crustal growth rate from magmatic contributions (Reymer and Schubert, 1984).

4 Results and discussion

4.1 Linear regression analyses and gravity modeling

A regression plot was generated with the crustal thickness as the dependent variable and the Bouguer anomaly as the independent variable (Figure 2). The observed relationship was used to determine whether Bouguer anomalies could yield reliable estimates of the crustal thickness of oceanic island arcs. A negatively sloping best-fit line represents the relationship between the two, i.e., a high Bouguer anomaly is associated with a thin crust and *vice versa*. This is expected since the depth or the distance of a dense body from the observation point is a significant factor affecting the Bouguer anomaly (e.g., Weilly, 1961; Chakravarthi et al., 2007). Considering that shorter wavelength gravity signals were removed in a typical oceanic arc setting, the main density contrast occurs between the arc crustal layers and the upper mantle. A thicker arc crust means that the mantle is situated farther from the observation point (i.e., ground) when compared to thinner arc crusts. This would then cause the Bouguer anomalies at a particular observation point to decrease.

The R^2 value of the plot in Figure 2 is 0.7161. This means that crustal thickness only accounts for 71% of the observed variations in the Bouguer anomalies. This is acceptable, considering that several elements within the arc crust can also cause substantial density differences. For example, seismic studies of several oceanic island arcs revealed the presence of a middle crust in oceanic island arcs. These middle arc crustal layers vary in thickness and general composition as deduced from seismic velocities. For instance, the Aleutians arc is inferred to have an andesitic to basaltic middle crust (Fliedner and Klemperer, 1999; Holbrook et al., 1999; Lizarralde et al., 2002; Shillington et al., 2004). On the other hand, the Izu-Bonin arc, represented by green squares plotting way above the regression line, is inferred to have a granitic middle crustal layer (Suyehiro et al., 1996; Takahashi et al., 2007). The presence of this granitic middle crustal layer induced a major change in the expected gravity signatures which caused the points to deviate from the regression line (Figure 1). Furthermore, there are reports associating the observed discrepancies between Bouguer anomaly-derived crustal thicknesses with those derived using seismic data. These were attributed to the effects of deep structures in subduction zone systems (e.g., Zhao et al., 1994; Lo et al., 2018). Since we adopted a constant density contrast representing the crust-mantle interface for the computations of the Bouguer anomalies, the presence of these other bodies at depth might require a revised density contrast for the calculation of the Bouguer anomalies. This might have caused the slight deviation between the Bouguer anomalies and crustal thicknesses relationship in these regions. Despite this being the case, the computed R^2 still indicates that crustal thickness values can be predicted from Bouguer anomalies.

Following the concept used by Milsom and others (1996) for their empirical formula, the intercept of the equation, which in this case is 40.31 km, should represent the standard thickness of an oceanic island crust wherein a 1-km change from this thickness is accompanied by a gravity signature change equivalent to the reciprocal of the slope, which in this case is 9 mGal. However, based on available geologic data, the 40.31-km standard is too thick for oceanic island arcs. Thus, this indicates that the equation herein should be constrained using the average crustal thickness (26 km) reported by Tetreault and Buiter (2014). This will serve as a starting point for plotting the other linear equations that may fit the dataset (Figure 3). Multiple lines with set coefficients from 25 to 30 were plotted in Figure 3. These lines are characterized by their unique slope-intercept value combinations.

Gravity modeling of an arc lithosphere with an average arc density of 2.79 g/cm^3 and an average mantle density of 3.3 g/cm^3 was performed to determine which of these linear equations can satisfy the geophysical constraint. Several iterations of gravity modeling revealed that in a 29-km-thick arc crust, a 1-km change in the

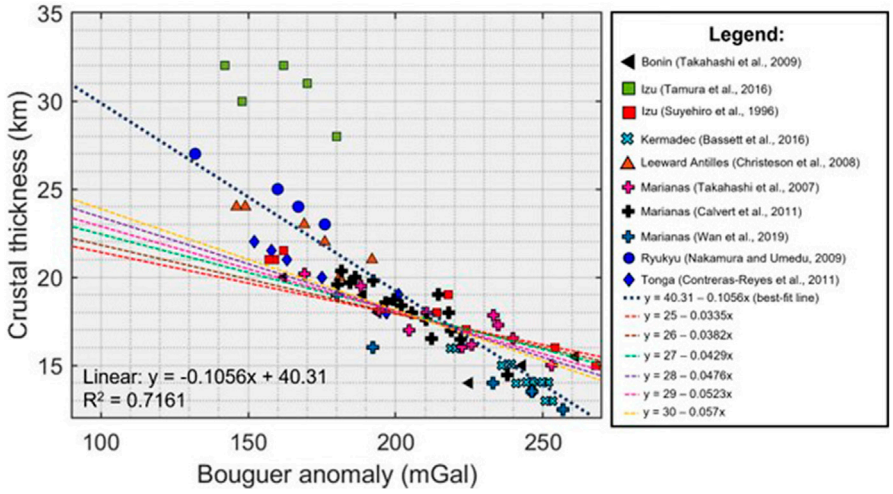


FIGURE 3
Plot showing the other regression curves that fit the dataset. The intercepts of the selected lines were determined following the average arc crustal thickness reported by Tetreault and Buiter (2014).

TABLE 1 New magmatic growth rates computed for oceanic island arcs using Bouguer anomaly-derived crustal thicknesses. Crustal thicknesses were computed following the methodology forwarded by Reymer and Schubert (1984).

Arc	Subducting basin	Bouguer anomaly (mGal)	Crustal thickness (km)	Arc length (km)	Volume (km^3)	Age (m.y.)/ References	Magmatic growth rate (km^3/km/m.y.)
Izu-Bonin (Northern)	Pacific	162	20	285	840,000	49 Taylor (1992)	60
Izu-Bonin (Southern)	Pacific	158	20	290	650,000	49 Taylor (1992)	30
Kermadec	Pacific	220	17	250	54,000	45 Whattam et al. (2008)	28
Tonga	Pacific	152	21	393	392,000	27 Kroenke et al. (1993)	37
Mariana	Pacific	169	20	431	970,000	45 Taylor (1992)	50
Vanuatu	Pacific	98	24	900	25,000	12 Greene et al. (1994)	38
Leeward Antilles	Caribbean	142	21	90	32,500	30 Braszus et al. (2021)	12
South Sandwich	South American	250	15	400	260,000	20 Barker (1995)	27
Ryukyu Arc	Philippine Sea Plate	118	22	800	600,000	30 Hall (2002)	25
East Philippine Arc (Bicol segment)	Philippine Sea Plate	63	26	140	17,000	5 Ozawa et al. (2004)	24
Luzon Arc (Northern Luzon segment)	South China Sea	41	27	320	126,200	22 Bellon and Yumul (2000)	18
Luzon Arc (Bataan segment)	South China Sea	66	25	41	10,300	22 Bellon and Yumul (2000)	11

crustal thickness is accompanied by ~18 mGal change in the total gravity signature. The reciprocal of 18 is 0.056, which should be the slope value for the linear equation that satisfies the results from the geophysical modeling. The closest fit among the available equations is observed with the linear equation where y = 29—0.0523x. This linear equation can be rewritten to conform with the format of the equation of Milsom and others (1996). Based on the results of the statistical analysis and geophysical constraint, the empirical formula proposed to

TABLE 2 Comparison of the volume, age, and magmatic addition rates between Reymer and Schubert (1984), Dimalanta et al. (2002), and this study.

Arc	Volume (km^3/km)	Age (m.y.)	Addition rate (km^3/km/m.y.)
Reymer and Schubert (1984)			
Izu-Bonin	1,250	45	28
Marianas	1,750	45	39
Tonga	1,950	60	33
Vanuatu	1,700	60	28
Dimalanta et al. (2002)			
Izu-Bonin	2,950	49	60
Marianas	2,250	45	50
Tonga	1,500	27	56
Vanuatu	2,365	25	95
This study			
Izu-Bonin	2,947	49	60
Marianas	2,251	45	50
Tonga	997	27	37
Vanuatu	460	38	38

estimate the crustal thickness of oceanic island arcs using Bouguer anomalies is as follows: CT = 29—ΔgB/18, where CT = crustal thickness and ΔgB = Bouguer anomaly. Based on the results of the statistical correlation and gravity modeling, we propose a thickness of 29 km for the oceanic island arc crust, which is thicker than the 26-km crustal thickness obtained by Tetreault and Buiter (2014). Their value was derived by getting the average of the crustal thickness values from 26 island arcs, which include remnant arcs and extinct arcs as well as arcs formed from the subduction of a continental crust.

4.2 New arc magmatic addition rates for the Western Pacific island arcs

Using the crustal thickness estimates computed from regional gravity data, new arc magmatic addition rates of the oceanic island arcs in the western Pacific were computed following the methodology proposed by Reymer and Schubert (1984) (Table 1). Furthermore, since these magmatic addition rates were derived from identical data types and methodologies, a comparison between these rates can be made in a more straightforward manner. As such, the observed differences in the computed arc magmatic addition rates can be used to infer the subduction conditions affecting the magmatic productivity in these island arcs. Table 1 shows the distinction between the arc magmatic growth rates between Pacific island arcs in comparison with other island arcs. The Pacific island arcs (i.e., Bonin, Izu, Kermadec, Mariana, and Vanuatu) recorded higher growth rates (28–60 km^3/km/m.y.) (Table 1). On the other hand, oceanic island arcs caused by the subduction of other younger and smaller plates (i.e., the Philippine Sea Plate, the South China Sea Plate, and the Caribbean Plate) recorded lower arc magmatic addition rates. This is clearly shown in the computed growth rates for the East Philippine Arc, Luzon Arc, Ryukyu Arc, and Leeward Antilles Arc, which range from 11 to 26 km^3/km/m.y. (Table 1).

As mentioned earlier, arc magmatic productivity can be generally influenced by: (1) the nature of subduction, which includes the rate of subduction and angle of subduction, and (2) the amount of sediment in the slab as a function of age. Regarding the rate of subduction, which can be inferred indirectly from the plate velocity, both the Pacific Plate and the Philippine Sea Plate move northwestward. They do not show significant differences in their velocities at approximately 10 cm/year (e.g., Seno et al., 1993). In terms of subducting angles, it seems that older oceanic plates are characterized by steeper slopes as compared with younger subducting slabs. For instance, the subduction of the older Pacific Plate generally shows steeper subduction angles except for some parts subducting further west. Holt et al. (2018) showed through 3-D numerical modeling of seismic data that the Pacific Plate subducting under Japan featured shallow/gentle slab dips. However, the region of the Pacific Plate subducting beneath the Philippine Sea Plate through the IBM trench system is characterized by steep to overturned slab dips (Lallemand, 2016). On one hand, the subduction of younger slabs is generally characterized by gentler slab dips. For instance, the subduction of the South China Sea (SCS) beneath the Manila trench is characterized by gentler slopes, albeit with significant differences from north to south. The northern part of the SCS subducts at a relatively shallower dip of 45° due to the subduction of a buoyant plateau. Further south, the angle of subduction becomes steeper at ~75° (Fan et al., 2016) This is inferred to have been caused by the collision between the Philippine Mobile Belt and Palawan micro-Continental Block (PCB) at the central Philippines (Chen et al., 2015). The Philippine Sea Plate was also reported to be subducting beneath the Ryukyu Arc at a dip of ~75° as identified from the Wadatti-Benioff zone and seismic tomography (e.g., Bijwaard et al., 1998; Widiyantoro et al., 1999; Wang et al., 2008; Wei et al., 2015). The angle of subduction of these island arcs, among other factors related to plate kinematics, is greatly influenced by the age of the subducting slab due to density variations. Previously, it has been established that the angle of subduction affects arc-trench gap (e.g., Cross and Pilger, 1982).

The exact mechanism of how magmatic productivity can also be affected by the dip of subduction remains to be further investigated.

Other factors related to age that can possibly directly affect the magmatic productivity of oceanic island arcs are the sediment thickness and the degree of serpentinization in the subducting slab. The variation of sediment thickness with the age of the subducting oceanic crust might explain this phenomenon. Generally, older oceanic plates are associated with thicker sediment covers and higher degrees of serpentinization as compared to younger subducting plates (e.g., Hay et al., 1988; Olson et al., 2016; Grevemeyer et al., 2018). Sediment cover and a higher degree of serpentinization in the older oceanic crust would contribute to a higher volume of slab-derived fluid during slab dehydration at depth which in turn results in a more robust melting of the mantle wedge. Furthermore, other works have shown that dehydration of the underlying serpentinites during the subduction of a highly serpentinized oceanic crust promotes the melting of the overlying sediments (e.g., Skora and Blundy, 2010). After which, the subducting sediments partial melts will rise and interact with the overlying mantle wedge causing subduction-related magmatism (e.g., Grove et al., 2012; Cruz-Uribe et al., 2018; Forster and Selway, 2021). This higher degree of volatiles introduced to the subduction system as a function of the age of the subducting slab might explain why the computed arc magmatic addition rates for the Pacific island arcs are higher (28–60 km^3/km/m.y). Previous works have shown that the subducting ~132 Ma Pacific slab along its western margin beneath the Izu-Bonin-Mariana trench arc system (Oakley et al., 2008) is marked by significantly thick sediment covers ranging from 0.5 to 2 km (e.g., Abrams et al., 1993). Furthermore, the presence of serpentinite seamounts west of the Izu-Bonin-Mariana trench arc system is postulated to have been caused by old slab devolatilization due to the subduction of the Pacific Plate (Fryer and Hussong, 1981; Fryer and Fryer, 1987; Fryer and Mottl, 1992). Moreover, the chemistry of the vent fluids in the proximity of these serpentinite seamounts is an indication of the presence of a serpentinized mantle beneath the edifice of these volcanoes related to the IBM trench system (Oakley et al., 2008). These are pieces of evidence of the previously forwarded concept that subduction of older oceanic plates is associated with thicker sediment subduction and a higher degree of serpentinization, which in turn caused the higher arc magmatic productivity observed for the Pacific island arcs.

This is compared to the lower magmatic addition rates computed for oceanic island arcs created by the subduction of younger minor plates (11–26 km^3/km/m.y). A similar distinction is also observed between the two volcanic arcs in the Philippine island arc system. The Luzon arc is characterized by a relatively lower growth rate (11–18 km^3/km/m.y.) compared to the East Philippine arc, which has a growth rate of 24 km^3/km/m.y. (Table 1). The Luzon arc and the East Philippine arc are products of the subduction of the South China Sea and the West Philippine Basin, respectively. The South China Sea has a proposed age of 32 Ma (Barckhausen et al., 2014), whereas the West Philippine Basin has a suggested age of 55 Ma (Deschamps and Lallemand, 2002). Moreover, reported sediment covers on the South China Sea Basin subducting beneath the Manila Trench are reported to be ranging from 100 to 1500 m. These values are deduced from seismic velocity profiles converted using a water velocity of 1,480 m/s (Hayes and Lewis, 1985; Armada et al., 2020). While the observed magmatic growth rates showed concurrence with the age of the subducting slabs, this work does not discount the role of other factors which affect the composition, structure, and thickness of different arc crusts, such as crustal anatexis (Izu-Bonin-Marianas Arc—Tatsumi et al., 2008); delamination processes (Kuril Arc—Tsumura et al., 1999); degree of back-arc spreading (Tonga Arc—Zhao et al., 1997), and the level of maturity in crustal evolution (Aleutian Arc—Holbrook et al., 1999). This work presents the latest estimates of the magmatic productivity of oceanic island arcs. Since the method proposed in this study made use of gravity data, we could provide crustal growth rates to more island arcs in comparison with previous works. In this work, the differences in the computed magmatic productivity rates for specific island arcs were attributed to the age of the subducting slab (e.g., older slabs tend to contain thicker sedimentary cover and higher degrees of serpentinization than younger ones). While our results showed concurrence with what is to be expected of the resulting magmatism based on this parameter, future works considering the other factors may improve the values derived from this study.

The values obtained from this study were compared with the results of Reymer and Schubert (1984) and Dimalanta and others (2002). As shown in Table 2, both the estimates from Dimalanta and others (2002) and this study are significantly higher compared to that of Reymer and Schubert (1984). The difference in the computed magmatic addition rates for this study and that of Reymer and Schubert (1984) represents the improvements in how crustal thicknesses are computed over time. Crustal thicknesses used in this study were derived from a more robust dataset and were guided by improved assumptions regarding the nature of oceanic island crusts. The estimates obtained by Dimalanta and others (2002) and this study are nearly identical, even though the former based their estimates on both seismic and gravity data while the latter solely based the estimates on Bouguer anomaly-derived crustal thicknesses. This might be a testament to the robustness of the empirical formula proposed in this study. Furthermore, since this study made use of estimates from gravity data, we were able to provide magmatic addition rates to more island arcs as the computations are no longer limited by seismic data availability.

5 Conclusion

This work presents a new empirical formula that can be employed to estimate crustal thicknesses of oceanic island arcs using Bouguer anomalies. The new empirical formula presented in this study could be applied to areas that have limited seismic data for crustal thickness estimates (e.g., Banda and Sunda Arc). A new set of arc magmatic addition rates computed from Bouguer anomaly-derived crustal thicknesses using this formula was also generated. Oceanic island arcs directly related to the subduction of the relatively older Pacific Plate are observed to record higher magmatic addition rates compared to other oceanic island arcs. This is possibly due to the difference in the amount of volatiles released to the mantle wedge during the subduction of oceanic plates with varying ages. The distinction in the magmatic addition rates between the subduction of older and younger oceanic lithosphere is also observed in the Philippine Island Arc system. This suggests that the magmatic productivity is controlled by the nature/degree of hydration of the subducting slab, which

highlights the complexity of arc magmatism in relation to different subduction conditions.

Data availability statement

Publicly available datasets were analyzed in this study. This data can be found here: Earth Gravitational Model (EGM2008)—https://bgi.obs-mip.fr/data-products/grids-and-models/egm2008-global-model/.

Author contributions

NP, CD, RA, GV, and LA contributed to the conception and design of the study. NP did the statistical analysis and wrote the first draft. KS contributed to the organization of the database. BP, JG-R, and GY provided significant inputs in several sections of the manuscript. All authors contributed to the manuscript revision, read, and approved the submitted version.

Funding

This work was supported by several NIGS research grants awarded to CD.

Acknowledgments

The authors would also like to acknowledge the free access to the EGM2008 model provided by the Bureau Gravimetrique Internationale. Fruitful discussions among the members of the Rushurgent Working Group are acknowledged.

Conflict of interest

NP is employed by the Energy Development Corporation. GY is employed by the Cordillera Exploration Co., Inc.

The remaining authors declare that the research was conducted in the absence of any commercial or financial relationships that could be construed as a potential conflict of interest.

Publisher's note

All claims expressed in this article are solely those of the authors and do not necessarily represent those of their affiliated organizations, or those of the publisher, the editors and the reviewers. Any product that may be evaluated in this article, or claim that may be made by its manufacturer, is not guaranteed or endorsed by the publisher.

References

Abrams, L.J., Larson, R.L., Shipley, T.H., and Lancelot, Y. (1993). Cretaceous volcanic sequences and Jurassic oceanic crust in the East Mariana and Pigafetta basins of the western Pacific. *Geophysical Monograph Series* 77, 77–101.

Armada, L.T., Hsu, S.-K., Dimalanta, C.B., Yumul, G.P., Jr., Doo, W.-B., and Yeh, Y.-C. (2020). Forearc structures and deformation along the Manila Trench. *Journal of Asian Earth Sciences: X* 4, 100036. doi:10.1016/j.jaesx.2020.100036

Assumpcao, M., Bianchi, M., Julia, J., Dias, F., Franca, G., Nascimento, R., Drouet, S., Pavao, C., Albuquerque, D., and Lopes, A. (2013). Crustal thickness map of Brazil: Data compilation and main features. *Journal of South American Earth Sciences* 43, 74–85. doi:10.1016/j.jsames.2012.12.009

Bai, Y., Williams, S., Muller, D., Liu, Z., and Hosseinpour, M. (2014). Mapping crustal thickness using marine gravity data: Methods and uncertainties. *Geophysics* 79 (2), G27–G36. doi:10.1190/geo2013-0270.1

Barckhausen, U., Engels, M., Franke, D., Ladage, S., and Pubellier, M., 2014. Evolution of the South China Sea: Revised ages for breakup and seafloor spreading 58B, 599-611.

Barker, P.F. (1995). "Tectonic framework of the east Scotia Sea," in *Backarc basins: tectonics and magmatism*. Editor B. Taylor (Boston: Springer US), 281–314.

Bassin, C., Laske, G., and Masters, G. (2000). The current limits of resolution for surface wave tomography in North America. *EOS Transactions American Geophysical Union* 81, F897.

Braszus, B., Goes, S., Allen, R., Rietbrock, A., Collier, J., Harmon, N., Henstock, T., Hicks, S., Rychert, C.A., Maunder, B., van Huenn, J., Bie, L., Blundy, J., Cooper, G., Davy, R., Kendall, J.M., Macpherson, C., Wilkinson, J., and Wilson, M. (2021). Subduction history of the Caribbean from upper-mantle seismic imaging and plate reconstruction. *Nature Communications* 12, 4211. doi:10.1038/s41467-021-24413-0

Bellon, H., and Yumul, G.P., Jr. (2000). Mio-Pliocene magmatism in the Baguio Mining District (Luzon, Philippines): age clues to its geodynamic setting. *Comptes Rendus de l'Academie des Sciences, Sciences de la Terre et des Planetes* 331, 295–302. doi:10.1016/s1251-8050(00)01415-4

Bijwaard, H., Spakman, W., and Engdahl, R. (1998). Closing the gap between regional and global travel time tomography. *Journal of Geophysical Research* 103, 30055–30078. doi:10.1029/98jb02467

Byrne, D.B., Suarez, G., and McCann, W.R. (1985). Muertos Trough subduction, microplate tectonics in the northern Caribbean? *Nature* 317, 420–421. doi:10.1038/317420a0

Byrne, T.B., Chan, Y.-C., Rau, R.-J., and Lu, C.-Y. (2011). The Arc-Continent Collision in Taiwan. *Frontiers in Earth Sciences* 4, 213–245.

Carbonell, R., Levander, A., and Kind, R. (2013). The Mohorovicic discontinuity beneath the continental crust: An overview of seismic constraints. *Tectonophysics* 609, 353–376. doi:10.1016/j.tecto.2013.08.037

Chakravarthi, V., Mallesh, K., and Ramamma, B. (2007). Basement depth estimation from gravity anomalies: two 2.5D approaches coupled with the exponential density contrast model. *Journal of Geophysics and Engineering* 14 (2), 303–315. doi:10.1088/1742-2140/aa5832

Chen, P.-F., Olavere, E.A., Wang, C.-W., Bautista, B.C., Solidum, R.U., Jr., and Liang, W-T. (2015). Seismotectonics of Mindoro, Philippines. *Tectonphysics* 640-641, 70–79. doi:10.1016/j.tecto.2014.11.023

Concepcion, R.A.B., Dimalanta, C.B., Yumul, G.P., Jr., Faustino-Eslava, D.V., Queaño, K.L., Tamayo, R.A., Jr., and Imai, A. (2012). Petrography, geochemistry, and tectonics of a rifted fragment of Mainland Asia: evidence from the Lasala Formation, Mindoro Island, Philippines. *International Journal of Earth Sciences* 101, 273–290. doi:10.1007/s00531-011-0643-5

Condie, K. (1997). *Plate Tectonics and Crustal Evolution*. 4th ed. Butterworth/Heinemann, U.K., 282.

Cross, T.A., and Pilger, R.H., Jr. (1982). Controls of subduction geometry, location of magmatic arcs, and tectonics of arc and back-arc regions. *GSA Bulletin* 93 (6), 545–562. doi:10.1130/0016-7606(1982)93<545:cosglo>2.0.co;2

Cruz-Uribe, A.M., Marschall, H.R., Gaetani, G.A., and Le Roux, V. (2018). Generation of alkaline magmas in subduction zones by partial melting of mélange diapirs–An experimental study. *Geology* 46, 343–346. doi:10.1130/g39956.1

DeMets, C., Gordon, R.G., and Argus, D.F. (2010). Geologically current plate motions. *Geophysical Journal International* 181, 1–80. doi:10.1111/j.1365-246x.2009.04491.x

Deschamps, A., and Lallemand, S. (2002). The West Philippine Basin: An Eocene to early Oligocene back arc basin opened between two opposed subduction zones. *Journal of Geophysical Research* 107 (B12), EPM 1-1–EPM 1-24. doi:10.1029/2001jb001706

Dewey, J.F., and Windley, B.F. (1981). *Growth and differentiation of the continental crust*, A301. Philosophical Transactions of the Royal Society of London, 189–206.

Dimalanta, C.B., Taira, A., Yumul, G.P., Jr., Tokuyama, H., and Mochizuki, K. (2002). New rates of western Pacific island arc magmatism from seismic and gravity data. *Earth and Planetary Science Letters* 202, 105–115. doi:10.1016/s0012-821x(02)00761-6

Dimalanta, C.B., and Yumul, G.P., Jr. (2003). Magmatic and amagmatic contributions to crustal growth of an island-arc system: The Philippine example. *International Geology Review* 45, 922–935. doi:10.2747/0020-6814.45.10.922

Dimalanta, C.B., Ramos, E.G.L., Yumul, G.P., Jr., and Bellon, H. (2009). New features from the Romblon Island Group: Key to understanding the arc–continent collision in central Philippines. *Tectonophysics* 479, 120–129. doi:10.1016/j.tecto.2009.02.015

Fan, J., Zhao, D., and Dong, D. (2016). Subduction of a buoyant plateau at the Manila Trench: Tomographic evidence and geodynamic implications. *Geochemistry, Geophysics, Geosystems* 17 (2), 571–586. doi:10.1002/2015gc006201

Farner, F., and Lee, C.-T. (2017). Effects of crustal thickness on magmatic differentiation in subduction zone volcanism: A global study. *Earth and Planetary Science Letters* 470, 96–107. doi:10.1016/j.epsl.2017.04.025

Fliedner, M.M., and Klemperer, S.L. (1999). Structure of an island-arc: Wide-angle seismic studies in the eastern Aleutian Islands, Alaska. *Journal of Geophysical Research* 104, 10667–10694. doi:10.1029/98jb01499

Forster, M.W., and Selway, K. (2021). Melting of subducted sediments reconciles geophysical images of subduction zones. *Nature Communications* 12, 1320. doi:10.1038/s41467-021-21657-8

Fryer, P., and Hussong, D.M. (1981). Seafloor spreading in the Mariana Trough: Results of Leg 60 drill site selection surveys. *Initial Reports of the Deep Sea Drilling Project* 60, 45–55.

Fryer, P., and Fryer, G.J. (1987). Origins of nonvolcanic seamounts in a forearc environment. *Geophysical Monograph Series* 43, 61–69.

Fryer, P., and Mottl, M. (1992). Lithology, mineralogy, and origin of serpentine muds recovered from Conical and Torishima forearc seamounts: Results of Leg 125 drilling. *Proceedings of the Ocean Drilling Prgoram Scientific Results* 125, 343–362.

Granja Bruña, J.L., Carbo-Gorosabel, A., Llanes Estrada, P., Muñoz-Martin, A., ten Brink, U.S., Gomez Ballesteros, M., Druet, M., and Pazos, A. (2014). Morphostructure at the junction between the Beata ridge and the Greater Antilles island arc (offshore Hispaniola southern slope). *Tectonophysics* 618, 138–163. doi:10.1016/j.tecto.2014.02.001

Greene, H.G., Collot, J.Y., Fisher, M.A., and Crawford, A.J. (1994). Neogene tectonic evolution of the New Hebrides island arc: A review incorporating ODP drilling results. *Proceedings of the Ocean Drilling Program, Scientific Results* 134, 19–46.

Grevemeyer, I., Ranero, C.R., and Ivandic, M. (2018). Structure of oceanic crust and serpentinization at subduction trenches. *Geosphere* 14 (2), 395–418. doi:10.1130/ges01537.1

Grove, T.L., Till, C.B., and Krawczynski, M.J. (2012). The role of H2O in subduction zone magmatism. *Annual Reviews in Earth and Planetary Sciences* 40, 413–39. doi:10.1146/annurev-earth-042711-105310

Hall, R. (2002). Cenozoic geological and plate tectonic evolution of SE Asia and the SW Pacific: computer-based reconstructions, model and animations. *Journal of Asian earth sciences* 20 (4), 353–431. doi:10.1016/s1367-9120(01)00069-4

Harris, R. (2011). The nature of the Banda arc-continent collision in the Timor Region. *Geology* 12, 163–211. doi:10.1007/978-3-540-88558-0_7

Hay, W.M., Sloan, J.L., and Wold, C.N. (1988). Mass/Age distribution and composition of sediments on the ocean floor and the global rate of sediment subduction. *Journal of Geophysical Research* 93, 14933–14940. doi:10.1029/jb093ib12p14933

Hayes, D.E., and Lewis, S.D. (1985). Structure and tectonics of the Manila trench system, Western Luzon, Philippines. *Energy* 10 (3-4), 263–279. doi:10.1016/0360-5442(85)90046-5

Holbrook, W.S., Lizarralde, D., McGeary, S., Bangs, N., and Diebold, J. (1999). Structure and composition of the Aleutian island arc and implications for continental crustal growth. *Geology* 27, 31–34. doi:10.1130/0091-7613(1999)027<0031:sacota>2.3.co;2

Holt, A.F., Royden, L.H., Becker, T.W., and Faccenna, C. (2018). Slab interactions in 3-D subduction settings: The Philippine Sea Plate region. *Earth and Planetary Science Letters* 489, 72–83. doi:10.1016/j.epsl.2018.02.024

Huang, C.-Y., Wu, W.-Y., Chang, C.P., Tsao, S., Yuan, P.B., Lin, C.W., and Kuan-Yuan, X. (1997). Tectonic evolution of accretionary prism in the arc-continent collision terrane of Taiwan. *Tectonophysics* 281, 31–51. doi:10.1016/s0040-1951(97)00157-1

Huang, J.-P., Fu, R.-S., Huang, J.-H., and Zheng, Y. (2006). Inversion of gravity and topography data for the crust thickness of China and its adjacent region. *Acta Seismologica Sinica* 19, 264–272. doi:10.1007/s11589-003-0264-6

Huang, H., Zhang, Z.C., Santosh, M., Zhang, D.Y., and Wang, T. (2015). Petrogenesis of the Early Permian volcanic rocks in the Chinese South Tianshan, Implications for crustal growth in the Central Asian Orogenic Belt. *Lithos* 228-229, 23–42. doi:10.1016/j.lithos.2015.04.017

Hsieh, Y.-J., Liu, C.-S., Suppe, J., Bryne, T.B., and Lallemand, S. (2020). The Chimei submarine canyon and fan: A record of Taiwan arc-continent collision on the rapidly deforming overriding plate. *Tectonics* 39 (11), 1–36. doi:10.1029/2020tc006148

Karig, D.E., Barber, A.J., Charlton, T.R., Klemperer, S., and Hussong, D.M. (1987). Nature and distribution of deformation across the Banda Arc-Australian collision zone at Timor. *Bulletin of the Geological Society of America* 98, 18–32. doi:10.1130/0016-7606(1987)98<18:nadoda>2.0.co;2

Kodaira, S., Sato, T., Takahashi, N., Ito, A., Tamura, Y., Tatsumi, Y., and Kaneda, Y. (2007). Seismological evidence for variable growth of crust along the Izu intraoceanic arc. *Journal of Geophysical Research* 112 (B5), B05104–25. doi:10.1029/2006jb004593

Kodaira, S., Fujiwara, T., Noguchi, N., and Takahashi, N. (2011). Structural variation of the Bonin ridge revealed by modeling of seismic and gravity data. *Earth, Planets, and Space* 63, 963–973. doi:10.5047/eps.2011.06.036

Kroenke, L.W., Resig, J.M., and Leckie, R.M. (1993). Hiatus and tephrochronology of the Ontong Java Plateau: Correlation with regional tectono-volcanic events. *Proceedings of the Ocean Drilling Program Scientific Results* 130, 423–445.

Lallemand, S. (2016). Philippine Sea Plate inception, evolution, and consumption with special emphasis on the early stages of Izu-Bonin-Mariana subduction. *Progress in Earth and Planetary Science* 3 (15), 15. doi:10.1186/s40645-016-0085-6

Laske, G., Masters, G., Ma, Z., and Pasyanos, M. (2013). Update on CRUST1.0 - A 1-degree global model of Earth's Crust. *Geophysical Research Abstracts* 15–2658. Abstract EGU2013.

Lizarralde, D., Holbrook, W.S., McGeary, S., Bangs, N.L., and Diebold, J.B. (2002). Crustal structure of a volcanic arc, wide-angle results from the western Alaska Peninsula. *Journal of Geophysical Research* 107, B8 2164.

Lo, Y.-T., Yan, H.-Y., and Chen, C.-R. (2018). Correlation between the Bouguer gravity anomaly and the TAIGER tomography of the Taiwan region. *Terrestrial, Atmospheric and Ocean Sciences* 29, 473–483. doi:10.3319/tao.2018.03.01.01

Luhr, F. (1992). Slab-derived fluids and partial melting in subduction zones: insights from two contrasting Mexican volcanoes (Colima and Ceboruco). *Journal of Volcanology and Geothermal Research* 54, 1–18. doi:10.1016/0377-0273(92)90111-p

Lundberg, N., Reed, D. L., Liu, C. -S., and Lieskes, J.H., Jr. (1997). Forearc basin closure and arc accretion in the submarine suture zone south of Taiwan. *Tectonophysics* 274, 5–23. doi:10.1016/s0040-1951(96)00295-8

Luo, Q., and Zhang, G. (2018). Control of subduction rate on Tonga-Kermadec arc magmatism. *Journal of Oceanology and Limnology* 36, 687–699. doi:10.1007/s00343-018-7026-8

Malavieille, J., Lallemand, S.E., Dominguez, S., and Deschamps, A. (2002). *Arc-continent collision in Taiwan: New marine observations and tectonic evolution*, 358. Geological Society of America Special Paper, 190–213.

Manalo, P.C., Dimalanta, C.B., Faustino-Eslava, D.V., Ramos, N.T., Queaño, K.L., and Yumul, G.P., Jr. (2015). Crustal thickness variation from a continental to an island arc terrane: Clues from the gravity signatures of the Central Philippines. *Journal of Asian Earth Sciences* 104, 205–214. doi:10.1016/j.jseaes.2014.08.031

Manalo, P.C., Dimalanta, C.B., Ramos, N.T., Faustino-Eslava, D.V., Queaño, K.L., and Yumul, G.P., Jr. (2016). Magnetic signatures and curie surface trend across an arc-continent collision zone: An example from Central Philippines. *Surveys in Geophysics* 37, 557–578. doi:10.1007/s10712-016-9357-3

Mann, P., Calais, E., Ruegg, J.-C., DeMets, C., Jansma, P.E., and Mattioli, G. S. (2002). Oblique collision in the north-eastern Caribbean from GPS measurements and geological observations. *Tectonics* 2 (6), 7–26. doi:10.1029/2001tc001304

Maystrenko, Y., and Scheck-Wenderoth, M. (2009). Density contrasts in the upper mantle and lower crust across the continent-ocean transition: constraints from 3-D gravity modelling at the Norwegian margin. *Geophysical Journal International* 179 (1), 536–548. doi:10.1111/j.1365-246x.2009.04273.x

Milsom, J., Hall, R., and Padmawidjaja, T. (1996). Gravity fields in eastern Halmahera and the Bonin Arc: Implications for ophiolite origin and emplacement. *Tectonics* 15, 84–93. doi:10.1029/95tc02353

Mooney, W.D., Laske, G., and Masters, G., 1998. CRUST 5.1: A global crustal model at $5^{\circ} \times 5^{\circ\circ}$. *Journal of Geophysical Research* 103, 727-747, doi:10.1029/97jb02122

Nishizawa, A., Kaneda, K., Oikawa, M., Horiuchi, D., Fujioka, Y., and Okada, C. (2017). Variations in seismic velocity distribution along the Ryukyu (Nansei-Shoto) Trench subduction zone at the northwestern end of the Philippine Sea plate. *Earth, Planets, and Space* 69, 86. doi:10.1186/s40623-017-0674-7

Nugroho, H., Harris, R., Lestariya, A.W., and Maruf, B. (2009). Plate boundary reorganization in the active Banda Arc-continent collision: Insights from new GPS measurements. *Tectonophysics* 479 (1-2), 52–65. doi:10.1016/j.tecto.2009.01.026

Oakley, A.J., Taylor, B., and Moore, G.F. (2008). Pacific Plate subduction beneath the central Mariana and Izu-Bonin fore arcs: New insights from an old margin. *Geochemistry, Geophysics, Geosystems* 9 (6). doi:10.1029/2007gc001820

Olson, P., Reynolds, E., Hinnov, L., and Goswami, A. (2016). Variation of ocean sediment thickness with crustal age. *Geochemistry, Geophysics, Geosystems* 17, 1349–1369. doi:10.1002/2015gc006143

Ozawa, A., Tagami, T., Listanco, E.L., Arpa, C.B., and Sudo, M. (2004). Initiation and propagation of subduction along the Philippine Trench: Evidence from the temporal and spatial distribution of volcanoes. *Journal of Asian Earth Sciences* 23 (1), 105–111. doi:10.1016/s1367-9120(03)00112-3

Parcutela, N.E., Dimalanta, C.B., Armada, L.T., and Yumul, G.P., Jr. (2020). PHILCRUST3.0: New constraints in the crustal growth rate computations for the Philippine arc. *Journal of Asian Earth Sciences* X, 100032. doi:10.1016/j.jaesx.2020.100032

Parcutela, N.E., Austria, R.S.P., Dimalanta, C.B., Armada, L.T., and Yumul, G.P., Jr. (2022). Arc-crustal compression and its effects on the underlying mantle geometry as elucidated from the potential field signatures of the buckled Cretaceous Cebu lithosphere, Philippines. *Tectonophysics* 831, 229341. doi:10.1016/j.tecto.2022.229341

Plank, T., and Langmuir, C.H. (1988). An evaluation of the global variations in the major element chemistry of arc basalts. *Earth and Planetary Science Letters* 90, 349–370. doi:10.1016/0012-821x(88)90135-5

Rait, G.J. (2000). "Continental growth by delamination and obduction of oceanic lithosphere during the birth of a subduction zone," in Canadian Society of Exploration Geophysicists Conference Abstracts, North Island, New Zealand, 4.

Reymer, A., and Schubert, G. (1984). Phanerozoic addition rates to the continental crust and crustal growth. *Tectonics* 3, 63–77. doi:10.1029/tc003i001p00063

Rupke, L.H., Morgan, J.P., Hort, M., and Connolly, J.A.D. (2004). Serpentine and the subduction zone water cycle. *Earth and Planetary Science Letters* 223, 17–34. doi:10.1016/j.epsl.2004.04.018

Seno, T., Stein, S., and Gripp, A. (1993). A model for the motion of the Philippine Sea Plate consistent with NUVEL-1 and geological data. *Journal of Geophysical Research* 98, 17941–17948. doi:10.1029/93jb00782

Sharma, P.V. (1997). *Environmental and Engineering Geophysics*. United Kingdom: Cambridge University Press, 475p.

Shillington, D.J., Avendonk, H.J.A.V., Holbrook, W.S., Kelemen, P.B., and Hornbach, M.J. (2004). Composition and structure of the central Aleutian island arc from arc-parallel wide-angle seismic data. *Geochemistry, Geophysics, and Geosystems* 5. doi:10.1029/2004gc000715

Skora, S., and Blundy, J. (2010). High-pressure hydrous phase relations of radiolarian clay and implications for the involvement of subducted sediment in arc magmatism. *Journal of Petrology* 51, 2211–2243. doi:10.1093/petrology/egq054

Stolk, W., Kaban, M., Beekman, F., Tesauro, M., Mooney, W., and Cloetingh, S. (2013). High resolution regional crustal models from irregularly distributed data: Application to Asia and adjacent areas. *Tectonophysics* 612, 55–68. doi:10.1016/j.tecto.2013.01.022

Suyehiro, K., Takahashi, M., Ariie, Y., Yokie, Y., Hino, R., Shinohara, M., Kanazawa, T., Hirata, N., Tokuyama, H., and Taira, A. (1996). Continental Crust, Crustal Underplating, and Low- **Q** Upper Mantle Beneath an Oceanic Island Arc. *Science* 272, 390–392. doi:10.1126/science.272.5260.390

Takahashi, N., Kodaira, S., Klemperer, S., Tatsumi, S.L., Kaneda, Y., and Suyehiro, K. (2007). Crustal structure and evolution of the Mariana intra-oceanic island arc. *Geology* 35, 203–206. doi:10.1130/g23212a.1

Tatsumi, Y., Shukuno, H., Tani, K., Takahashi, N., Kodaira, S., and Kogiso, T. (2008). Structure and growth of the Izu-Bonin-Mariana arc crust: 2. Role of crust-mantle transformation and the transparent Moho in arc crust evolution. *Journal of Geophysical Research: Solid Earth* 113 (B2), B02203. doi:10.1029/2007jb005121

Taylor, B. (1992). "Rifting and the volcanic-tectonic evolution of the Izu-Bonin-Mariana Arc," in Proceedings of the Ocean Drilling Program, Scienti¢c Results, 627–651.126

Tetreault, J.L., and Buiter, S.J.H. (2014). Future accreted terranes: a compilation of island arcs, oceanic plateaus, submarine ridges, seamounts, and continental fragments. *Solid Earth* 5, 1243–1275. doi:10.5194/se-5-1243-2014

Tsumura, N., Ikawa, H., Ikawa, T., Shinohara, M., Ito, T., Arita, K., Moria, T., et al. (1999). Delamination-wedge structure beneath the Hidaka Collision Zone, Central Hokkaido, Japan inferred from seismic reflection profiling. *Geophysical Research Letters* 26 (8), 1057–1060. doi:10.1029/1999gl900192

Turner, S.J., and Langmuir, C.H. (2015). The global chemical systematics of arc front stratovolcanoes: Evaluating the role of crustal processes. *Earth and Planetary Science Letters* 422, 182–193. doi:10.1016/j.epsl.2015.03.056

Ulmer, P. (2001). Partial melting in the mantle wedge–the role of H_2O in the genesis of mantle-derived "arc related" magmas. *Physics of the Earth and Planetary Interiors* 127, 215–232. doi:10.1016/s0031-9201(01)00229-1

von Huene, R., and Scholl, D.W. (1991). Observations at convergent margins concerning sediment subduction, subduction erosion, and the growth of the continental crust. *Reviews in Geophysics* 29, 279–316.

Whattam, S.A., Malpas, J., Ali, J. R., and Smith, I.E. (2008). New SW Pacific tectonic model: Cyclical intraoceanic magmatic arc construction and near-coeval emplacement along the Australia-Pacific margin in the Cenozoic. *Geochemistry, Geophysics, Geosystems* 9 (3). doi:10.1029/2007gc001710

Wang, Z., Huang, R., Huang, J., and He, Z. (2008). P-wave velocity and gradient images beneath the Okinawa Trough. *Tectonophysics* 455, 1–13. doi:10.1016/j.tecto.2008.03.004

Wei, W., Zhao, D., Xu, J., Wei, F., and Liu, G. (2015). *P*and*S*wave tomography and anisotropy in Northwest Pacific and East Asia: Constraints on stagnant slab and intraplate volcanism. *Journal of Geophysical Research* 120, 1642–1666. doi:10.1002/2014jb011254

Weilly, W.I. (1961). Gravity and crustal thickness in New Zealand. *New Zealand Journal of Geology and Geophysics* 5 (2), 228–233.

Widiyantoro, S., Kennett, B.L.N., and van Der Hilst, R.D. (1999). Seismic tomography with P and S data reveals lateral variations in the rigidity of deep slabs. *Earth and Planetary Science Letters* 173, 91–100. doi:10.1016/s0012-821x(99)00216-2

Woollard, G. (1959). Crustal Structure from gravity and seismic measurements. *Journal of Geophysical Research* 64, 1521–1544. doi:10.1029/jz064i010p01521

Worzel, J., and Shurbet, G. (1955). *Gravity interpretations from standard oceanic and continental crust sections*, 62. Geological Society of America Special Paper, 87–100.

Yumul, G.P., Jr., Dimalanta, C.B., Marquez, E.J., and Queaño, K.L. (2009). Onland signatures of the Palawan microcontinental block and Philippine mobile belt collision and crustal growth process: A review. *Journal of Asian Earth Sciences* 34 (2), 610–623. doi:10.1016/j.jseaes.2008.10.002

Zamoras, L.R., Montes, M.G.A., Queaño, K.L., Marquez, E.J., Dimalanta, C.B., Gabo, J.A.S., and Yumul, G.P., Jr. (2008). Buruanga peninsula and Antique Range: two contrasting terranes in Northwest Panay, Philippines featuring an arc–continent collision zone. *Island Arc* 17, 443–457. doi:10.1111/j.1440-1738.2008.00645.x

Zellmer, G.F., Edmonds, M., and Straub, S.M. (2014). *Volatiles in subduction zone magmatism*, 410. Geological Society of London Special Publications, 1–17.

Zhao, D., Hasegawa, A., and Kanamori, H. (1994). Deep structure of Japan subduction zone as derived from local, regional, and teleseismic events. *Journal of Geophysical Research: Solid Earth* 99 (B11), 22313–22329. doi:10.1029/94jb01149

Zhao, D., Xu, Y., Wiens, D.A., Dorman, L., Hildebrand, J., and Webb, S. (1997). Depth Extent of the Lau Back-Arc Spreading Center and Its Relation to Subduction Processes. *Science* 278, 254–257. doi:10.1126/science.278.5336.254

frontiers | Frontiers in Earth Science

TYPE Review
PUBLISHED 08 March 2023
DOI 10.3389/feart.2023.1047707

Check for updates

OPEN ACCESS

EDITED BY
Fei Xue,
Hohai University, China

REVIEWED BY
Jingcheng Pei,
China University of Geosciences Wuhan, China
Abulimiti Aibai,
Xinjiang Institute of Ecology and Geography (CAS), China
Wen Su,
Institute of Geology and Geophysics (CAS), China

*CORRESPONDENCE
Cun Zhang,
geozhangc@163.com
Fan Yang,
yang_fan1989@126.com

SPECIALTY SECTION
This article was submitted to Structural Geology and Tectonics, a section of the journal Frontiers in Earth Science

RECEIVED 18 September 2022
ACCEPTED 16 February 2023
PUBLISHED 08 March 2023

CITATION
Zhang C, Yang F, Yu X, Liu J, Carranza EJM, Chi J and Zhang P (2023), Spatial-temporal distribution, metallogenic mechanisms and genetic types of nephrite jade deposits in China. *Front. Earth Sci.* 11:1047707. doi: 10.3389/feart.2023.1047707

COPYRIGHT
© 2023 Zhang, Yang, Yu, Liu, Carranza, Chi and Zhang. This is an open-access article distributed under the terms of the Creative Commons Attribution License (CC BY). The use, distribution or reproduction in other forums is permitted, provided the original author(s) and the copyright owner(s) are credited and that the original publication in this journal is cited, in accordance with accepted academic practice. No use, distribution or reproduction is permitted which does not comply with these terms.

Spatial-temporal distribution, metallogenic mechanisms and genetic types of nephrite jade deposits in China

Cun Zhang[1]*, Fan Yang[2]*, Xiaoyan Yu[3], Jinhai Liu[1], Emmanuel John M. Carranza[4], Jie Chi[5] and Peng Zhang[1]

[1]School of Materials Science and Engineering, Qilu University of Technology (Shandong Academy of Sciences), Jinan, China, [2]Key Laboratory of Mineral Resources in Western China (Gansu Province), School of Earth Sciences, Lanzhou University, Lanzhou, China, [3]School of Gemology, China University of Geosciences Beijing, Beijing, China, [4]Department of Geology, University of the Free State, Bloemfontein, South Africa, [5]School of Civil and Resource Engineering, University of Science and Technology Beijing, Beijing, China

The nephrite jade deposits of different tectonic units in China exert significant commercial quality, which have attracted wide attention. However, these deposits have not been systematically summarized to date. Here, we investigate the major nephrite jade deposits in China to decipher their gemological and mineralogical characteristics, spatial-temporal distribution, and mineralization processes as well as to identify their geological settings and gemological properties, *via* integrating published geochronology, major and trace elements as well as H-O isotopes. The compiled data suggest that the major nephrite jade deposits in China can also be generally divided into green jade-type (GJ-type) and white jade-type (WJ-type) which covers different species, but most of them belong to the latter. The GJ-type nephrite deposits predominantly occur in ophiolite/ophiolitic mélange suites or are embedded into ultramafic serpentine jade orebodies. This type of nephrite jade mainly formed through the late auto-metamorphic metasomatism of serpentine or the spontaneous crystallization/precipitation along suture/shear zones that acted as pathways to migrate Ca-rich fluids during orogeny. In contrast, the orebodies of WJ-type nephrite jade are usually hosted at the contact zones between the dolomitic marbles and intermediate-felsic or mafic intrusive rocks, which were produced through metamorphism-metasomatism during post continent-continent collision, such as the Kunlun orogenic belt with about ~1,300 km Hetian nephrite belt, and the eastern nephrite jade deposits along the Pacific Ocean. Our study highlights that the nephrite jade deposits in China originally formed during multiple tectonic stages related to the interactions between hydrothermal fluids and metamorphism under subduction accretion- and collision orogenesis-related settings. In addition, this study also provides insights into the genetic discrimination, mineral exploration, and occurrence characteristics of nephrite jade deposits as well as the evaluation and identification of nephrite jade quality.

KEYWORDS

nephrite jade deposits, spatial-temporal distribution, metallogenic mechanism, genetic type, mineral exploration, China

1 Introduction

The nephrite jade, also termed as tremolite jade or Hetian jade in China, is the unique rock reaching the grade of jade and consists mainly of fibrous amphibole (Yu, 2016; Zhang et al., 2021). The amphibole mostly includes tremolite [$Ca_2Mg_5Si_8O_{22}(OH)_2$] and actinolite to ferro-actinolite [$Ca_2(Mg, Fe^{2+})_5Si_8O_{22}(OH)_2$], which usually formed within complex geological processes or different tectonic settings (Figure 1; Yu, 2016; Zhang et al., 2019; Yu et al., 2021). The nephrite jade is characterized by good color, luster, toughness, and transparency and has been regarded as the main carrier of traditional jade culture in China (Yin et al., 2014; Zhang et al., 2019; Zhang et al., 2021). In addition, the nephrite jade also gets continuous attention by Chinese collectors and has occupied a very important role in jade culture or jewelry market (Figures 2A–F).

World-class nephrite jade deposits characterized by economic values are mostly hosted within more than 20 countries and regions (e.g., China, Russia, Canada, America, Poland, Italy, South Korea, New Zealand, and Australia), where more than 120 primary nephrite jade deposits have been excavated in northern and southern zones at different latitudes (Harlow and Sorensen, 2000; 2005; Adams et al., 2007; Kim, 2007; Adamo and Bocchio, 2013; Gao, 2014; Harlow et al., 2014; Qiu, 2016; Gao et al., 2020; Gil et al., 2020; Yu et al., 2021; Feng et al., 2022). Based on the spatial-temporal distribution of global jade deposits, we identified that significant nephrite jade deposits occur along the oceanic coast, cratonic margin, or inland active orogenic belts. In details, these nephrite jade deposits can be summarized into: 1) green nephrites after serpentinization (S-type); and 2) white nephrites after dolomitization (D-type). The former usually developed within/near the global Phanerozoic ophiolite zones and is more abundant than the latter, which could be evidenced by the west and the middle Alps, central Brazil, California, and Alaska extending greenstone belts (Harlow et al., 2014). However, the occurrences of nephrite jade deposits in China are dominated by D-type nephrite jade deposits (Figure 1; Figures 2G, H; Liu et al., 2011a; b, 2015; Gao et al., 2019; Jiang et al., 2021). This may be attributed to the level of excavation or result from the human environment as most Chinese prefer to white nephrite jade, although the majority of ophiolite suites/belts occur throughout the whole China. The nephrite jade species from different regions in China can be effectively distinguished based on the mineral chemistry *via* $Mg^{2+}/(Mg^{2+}+Fe^{2+})$ ratios (Figure 3). Previous investigations have noticed that the nephrite jade in China exerts higher economic value and has larger reserves, which has attracted extensive attention in terms of gemology, mineralogy, and lithology (Harlow et al., 2014; Zhang et al., 2019; 2021; Yu et al., 2021). However, most of these studies only focused on individual localities, ignoring the evaluation on the spatial-temporal characteristics of nephrite jade deposits in China.

Published studies suggested that the S-type nephrite jade deposits are correlated with the Si-rich metasediments that

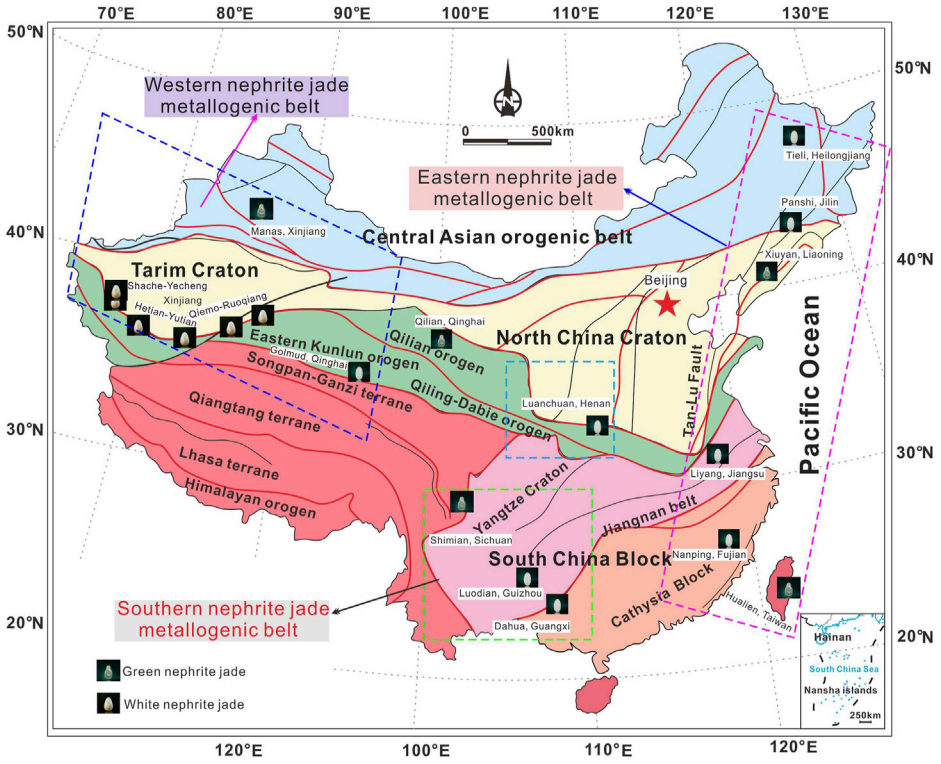


FIGURE 1
Generalized geological and tectonic framework of China, showing different sub-division units (after Qiu et al., 2020; Yu et al., 2021). The major nephrite jade deposits in China are sub-divided into several metallogenic areas, namely, the western nephrite jade metallogenic belt, the eastern nephrite jade metallogenic belt on the west coast of the Pacific Ocean, and the southern nephrite jade metallogenic belt, as well as the central metallogenic belt on the southern margin of North China Craton (NCC), central China, respectively.



FIGURE 2
Representative hand specimen and field photographs. **(A)** The white nephrite jade carving with extremely complex crafts by Yijin Gao (Yu et al., 2021). **(B)** Green nephrite jade from Xiuyan County, Liaoning Province. **(C)** Black placer nephrite jade from the Kalakash River (Black Jade River) shows abundant flaky graphite inclusions. **(D)** White nephrite jade (also named Cuiqing jade) with emerald bands from Qinghai Province. **(E)** Green nephrite jade from Qilian orogenic belts. **(F)** Various colors of nephrite jade from the Gobi Desert. **(G)** D-type nephrite jade deposits showing typical contact between granitoids and dolomitic marble from Yinggelike, Ruoqiang (Jiang et al., 2021). The intrusion of granitoids provided the necessary Si^{4+} and magmatic H_2O, while the old dolomite marble supplied Ca^{2+} and Mg^{2+} during metamorphic-metasomatic processes. **(H)** Nephrite jade open pit from Luchuan, Henan Province. Metagabbro dykes are relatively well developed and emplaced in marbles. And the nephrite ore bodies are generally located in marbles.

interacted with serpentinized mantle peridotite, whereas the D-type nephrite jade deposits are mainly produced by contacting metasomatism between the dolomitic marble and granitic intrusions (Harlow and Sorensen, 2000; 2005; Liu and Yu, 2009; Liu et al., 2011a; 2011b; 2015; Gil et al., 2020; Zhang et al., 2021). These two types of nephrite jade deposits are also widely hosted in China, but which are predominantly related to the serpentine and carbonate bodies, respectively (Liu and Yu, 2009; Yu, 2016; Zhang et al., 2019; Yu et al., 2021; Zhang et al., 2022). However, the formation of nephrite jade deposits is usually controlled by tectonic instability factors that induced the differentials of topographic environments, this further results in the migration and accumulation of source materials, such as Fe, Sr, Si, Ca, Mg, and Cr (Adams et al., 2007; Gil et al., 2020; Zhang et al., 2021; Zhang et al., 2022). Recently, a few studies have correlated the formation environments of S-type nephrite jade with the subduction/obduction–accretionary complex (Yui et al., 2014; Zhang et al., 2021). Based on the investigations of D-type nephrite jade deposit in the Saidikualm, western China, Zhang et al. (2022) identified the formation mechanism of elemental migration variation during nephrite mineralization and also constructed the genetic model of nephrite jade deposits characterized by five mineral assemblage zones. These findings, together with the research outlined by Gao et al. (2019), have theoretically indicated the spatial-temporal variation characteristics of D-type nephrite jade deposits, which also suggested that the formation of nephrite jade deposits was closely correlated with the closure of Proto-Tethys Ocean. Non-etheless, the tectonic evolution for the formation of nephrite jade of these two types of nephrite jade deposits remains unclear, hampering the knowledge of metallogenic mechanisms of nephrite jade deposits.

In this paper, we compiled published studies related to nephrite jade deposits in China, and divided several metallogenic belts of nephrite jade based on their spatial-temporal distributions and variation features, with major aim to provide an overview of detailed characteristics of nephrite jade deposits (Figure 1). In addition, this study also summarizes the gemological properties, geochronological, rare earth elements (REEs), and H-O isotopic features to further probe into the ore genesis of major nephrite jade deposits in China. Further, this study will establish a holistic tectono-metallogenic window in relation to tectonic evolution of the formation of the nephrite jade deposits within subduction/obduction zone or collision orogenic settings.

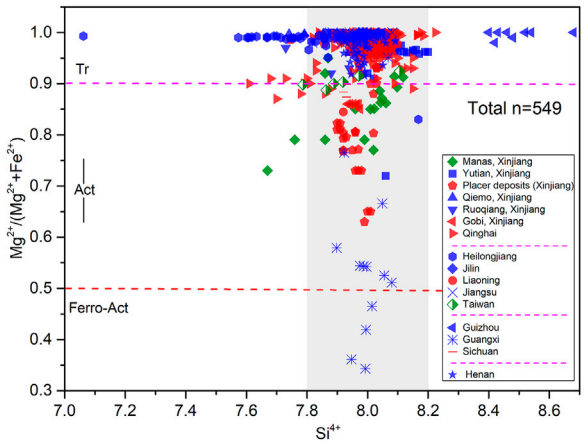


FIGURE 3
The ratios $Mg^{2+}/(Mg^{2+}+Fe^{2+})$ vs. Si^{4+} demonstrate that the nephrite jade is composed of fibrous amphiboles which contain both tremolite and actinolite. The main mineral composition of nephrite jade in China is tremolite, followed by actinolite which is mainly green nephrite and placer nephrite jade, while Ferro-actinolite (black nephrite) is mainly located in Dahua region of Guangxi Province. The contents of Si^{4+} in nephrite are mostly concentrated between 7.8 and 8.2. The contents of Si^{4+} in Luodian nephrite jade are obviously higher than that in other generation areas, while the Tieli nephrite jade from Heilongjiang presents obviously lower content of Si (EMPA Data cited by Liu et al., 2010; 2011; Gao, 2014; Liu et al., 2015; 2016; Yin et al., 2014; Ling et al., 2015; Gao et al., 2019; Bai et al., 2019; Zhong et al., 2019; Zhang et al., 2019; 2021; Jiang et al., 2020; Li et al., 2020; Bai et al., 2020). Tr: tremolite Act: actinolite Ferro-Act: ferro-actinolite.

2 Spatial-temporal distribution of nephrite jade deposits

In China, the S-type nephrite jade deposits are not main jade deposits, which are hosted in Manas, northern slope of Tianshan Mountains of Xinjiang Province (Zhang, 2020). Published studies also suggested that the nephrite jade deposits in China occur predominately in the West Kunlun Orogen along the southern boundary of the Tarim Basin and extend to the northeast of the Altyn Tagh (Figure 1; Liu et al., 2010; 2011; Liu et al., 2015; 2016; Han et al., 2018; Gao et al., 2019; Jiang et al., 2021), which makes up the famous ~1,300 km Hetian nephrite belt and the largest D-type nephrite jade metallogenic belts in the world, although a few D-type nephrite jade deposits formed at different paleo-latitudes within other tectonic units in China. For example, the famous Qinghai nephrite jade deposits distribute along the Hetian nephrite belt extending from southeast to the east of the Kunlun orogenic belt (Lei et al., 2018), but its quality is not as valuable as Xinjiang nephrite jade (Zhang et al., 2019; Zhang et al., 2021). These famous nephrite jade deposits form the western metallogenic belts of nephrite jade in China (Figure 1; Table 1).

In the eastern China, the nephrite jade deposits with different metallogenic scales are distributed along the western Pacific Ocean (Figure 1). Previous studies indicated that these nephrite jade deposits mostly occur in Liaoning (Xiuyan), Jiangsu (Liyang), and Taiwan (Hualien) Province (Figure 1; Table 1; Liao and Zhu, 2005; Zhang et al., 2011; Yin et al., 2014; Yui et al., 2014; Yu, 2016; Zhang et al., 2019; Zhang et al., 2021). With the continuous exploration of nephrite jade deposits, several new nephrite jade deposits have gradually been discovered and are mainly hosted in Heilongjiang (Tieli), Jilin (Panshi), and Fujian (Nanping) Provinces, with small exploration-scales and medium to average jade quality (Table 1; Xu et al., 2014; Gao, 2014; Du, 2015; Ling et al., 2015; Wang et al., 2017; Gao et al., 2019; Bai et al., 2019). Among these, the S-type nephrite jade deposits from Taiwan Province had been confirmed as the youngest nephrite jade deposit on the Earth, which have correlated the metamorphism with the eastward subduction of the South China Sea Plate (Yui et al., 2014). Although these nephrite jade deposits are hosted in the circle-Pacific area as a whole, it is uncertain whether they are related to the subduction of the Pacific plate due to the lack of detailed investigations related to geochronology and tectonic evolution.

In the southern China, the S-type nephrite jade from Shimian County, Sichuan Province shows similar mineralogical characteristics with the Manas S-type nephrite jade (Figure 1; Xu et al., 2015). However, detailed studies on their genesis and tectonic evolution are still lacking at present. Despite the nephrite jade deposits from Guizhou (Luodian) and Guangxi (Dahua) Provinces are all the D-type nephrite jade deposits, their specific genesis and protoliths show quite different characteristics (Figure 1; Yang, 2013; Zhong et al., 2019; Bai et al., 2020). The single metamorphic-hydrothermal metasomatic nephrite jade deposit discovered in Henan (Luanchuan) Province at the southern margin of the North China Craton (Figure 1; Yin, 2006; Ling et al., 2015) can provide significant insights into the tectonic evolution of the North China Craton.

As the valuable jade resources, the nephrite jade deposits can be used as an important proxy to trace geological evolution and non-metallic metallogenic tectonic settings (Zhang et al., 2021). Although the tectonic evolution of these nephrite jade deposits in China are still unclear, based on the spatial-temporal distribution and variation features, we further divided the nephrite jade deposits into four metallogenic belts: 1) the western nephrite jade metallogenic belt, 2) the eastern nephrite jade metallogenic belt along the west coast of the Pacific Ocean, 3) the southern nephrite jade metallogenic belt, and 4) the central nephrite jade metallogenic belt (e.g., Luanchuan nephrite jade deposit at the southern margin of the North China Craton) (Figure 1; Table 1).

3 Genetic types and mineralogy of nephrite jade deposits

The majority of nephrite jade deposits in China are usually correlated with multiple hydrothermal processes (Liu and Yu, 2009). According to the features of ore-forming material sources and fluids differentiation variation, the nephrite jade deposits are divided into the magmatic–hydrothermal metasomatic and metamorphic–hydrothermal metasomatic types. In the following sections, we briefly depict the major characteristics of nephrite jade of each belts. Detailed gemological and mineralogical characteristics of different kinds of nephrite jade were presented in Tables 2, 3.

3.1 Magmatic–hydrothermal metasomatic nephrite jade deposits

All the nephrite jade deposits in the western metallogenic belt are the magmatic–hydrothermal metasomatic type,

TABLE 1 Spatial distributions of major nephrite jade deposits in China.

Provinces		Mineral occurrence	Specific description	Output form	Metallogenic scale prognosis
The western nephrite jade metallogenic belt	Xinjiang	Kunlun Mountain—Altun Mountain ore belts	South of Xinjiang: Shache-Yecheng, Hetian-Yutian, and Qiemo-Ruoqiang metallogenic belts with a total length of ~1,300 km	Primary deposits, primary to secondary/placer deposits, secondary/placer deposits, Gobi nephrite jade	Large scale
		Tianshan Mountain	Northern Xinjiang: the Manas green nephrite jade deposit	Primary deposits, minor secondary or placer deposits	Large scale
	Qinghai	East Kunlun Mountain	Central and western Qinghai: Golmud area	Primary deposits	Large scale
		Qilian orogenic belt	Northeast of Qinghai (including green nephrite jade and serpentine jade)	Primary deposits	Medium to large?
The central nephrite jade metallogenic belt	Henan	Luanchuan County; Tongbai County	West of Henan on the southern margin of the North China Craton	Primary deposits	Medium scale
The eastern nephrite jade metallogenic belt	Heilongjiang	Tieli	Middle of Heilongjiang	Primary deposit	Small scale
	Jilin	Panshi	Central Jilin	Primary deposit	Small scale
	Liaoning	Xiuyan County; Ximu Town	South of Liaoning: Xiyugou (primary jade; placer deposits); Sangpiyu; Ximu jade (placer nephrite jade)	Primary deposits (old jade/primary deposits), Hemo jade (placer type)	Medium to large scale
	Jiangsu	Liyang County	South of Jiangsu (the Meiling jade)	Primary deposit	Medium to small scale
	Fujian	Nanping area	North of Fujian	Primary deposit	Small scale
	Taiwan	Hualien County	East of Taiwan (The Hualien jade)	Primary deposit (green nephrite jade)	Medium scale
The southern nephrite jade metallogenic belt	Sichuan	Western Sichuan region	Shimian County; Wenchuan County	Primary deposits	Medium to small scale
	Guizhou	Luodian County	South of Guizhou (the Luodian jade)	Primary deposit	Medium scale
	Guangxi	Dahua Yao Autonomous County	Central Guangxi	Primary deposit, minor placer or secondary deposit	Medium scale

whereas the majority of nephrite jade deposits in the southern metallogenic belt and few nephrite jade deposits in the eastern metallogenic belt also belong to this genetic type (Figure 2). The nephrite orebodies are controlled by multi-stage fault-fold structures. The hydrothermal fluid were mainly derived from magmatic rocks. It involves the following three sections based on the properties of the intrusion bodies: the ultramafic rock type, the mafic rock type, and the intermediate-felsic rock type (Liu and Yu, 2009).

3.1.1 Ultramafic rock type

The nephrite jade were mainly formed within the ophiolite suites or ophiolite mélange zones, generally featured by green color in its appearance. Their color mainly depends on the content of Fe^{2+} in structure, while Cr^{3+} often plays a marginal role. The protoliths of these deposits can be sourced from a variety of complicated ultramafic complexes, mainly peridotite/serpentinized peridotite and serpentinite with more silicic rocks (Harlow and Sorensen, 2005; Zhang et al., 2021). Representative nephrite jade deposits are mainly discovered in Manas of Xinjiang, Qilian of Qinghai, and Shimian of Sichuan. Details are described below.

3.1.1.1 The Manas green nephrite jade

The jade deposit occurred in the late Paleozoic tectonic belt, which contains carboniferous ophiolite formations with metamorphic peridotite at the bottom, layered gabbro in the middle, and interbedded basalt and siliceous rocks at the top. In details, the orebodies are mainly hosted in Devonian and Carboniferous volcanic rocks and clastic rocks (Tang et al., 2002; Liu and Yu, 2009). The main minerals are featured by tremolite or actinolite with a subordinate association of diopside, chromite, chlorite, serpentine, talc, and sulfide, arsenide of nickel. Published mineral major element data suggested that the main chemical compositions of amphibole in the western section of the nephrite jade deposit are the SiO_2 (59.12–54.89 wt%), MgO (13.50–10.99 wt %), CaO (25.85–20.47 wt%), and FeO (6.25–1.94 wt%; average value: 3.19 wt%). In contrast, the main chemical compositions of SiO_2, MgO, CaO in the eastern section of the deposit vary from 57.97 to 59.23 wt%, 12.48–13.00 wt%, 20.28–21.93 wt%, and 3.57–6.31wt%, respectively. Together, these suggest that the S-type nephrite jade in the western section of this deposit is tremolite, whereas the eastern section of this deposits is actinolite (Tian, 2014; Zhang, 2020). In addition, the H-O isotopic data show that the $\delta^{18}D_{H2O}$ values range from −76.7‰ to −5.8‰; while the $\delta^{18}O_{H2O}$ values range from 9.8‰ to 12.6‰, respectively (Figure 5; Zhang, 2020).

TABLE 2 Overview of the gemological and mineralogical characteristics of nephrite jade deposits in China.

Magmatic-hydrothermal metasomatic nephrite							
Genetic type	Ultramafic rock type			Mafic rock type			References
Locations	Manas, Xinjiang	Shimian, Sichuan	Qilian, Qinghai	Golmud, Qinghai	Luodian, Guizhou	Dahua, Guangxi	
Color	Green, dark green, light green, and yellow jade	Light green, dark green, brown, gray, dark gray, and yellow jade	Green, dark green, and black green jade	White, light greenish white, greenish, green, emerald, and brown jade	White, gray, yellow white, light green, gray green, and brown jade	White, gray, light green, gray green, and black jade	Zhi et al. (2011); Du (2015); Zhang et al. (2021); Bai et al. (2020)
Texture and transparency	Fine texture; microtransparent—opaque	Relatively fine texture; translucent—opaque	Translucent—opaque	Fine texture; microtransparent—translucent	Fine texture; microtransparent—opaque	Fine texture; microtransparent—opaque	Du (2015); Zhang et al. (2021)
Luster	Vitreous—greasy luster	Vitreous luster	Vitreous luster	Weak greasy luster—vitreous luster	Waxy—weak greasy luster	Waxy—weak greasy luster	
Refractive index	1.60-1.61	1.60–1.62	1.60	1.61-1.62, the average: 1.612	1.60–1.62	1.60–1.62	Zhou et al. (2008); Ding (2011); Zhang (2013); Tian (2014); Du (2015); Zhang et al. (2021)
Specific gravity	The average value: 2.97	2.91–3.01	2.95–2.97	2.94–3.06; The average: 2.97	The average value: 2.86-2.87	The average: 2.94	Zhou et al. (2008); Ding (2011); Zhang (2013); Tian (2014); Du (2015); Zhang et al. (2021)
Hardness (Mohs hardness)	6.0–6.5	5.5–6.0	5.5–6.0	The average value: 5.57	6.0–7.0	The average value: 5.70	Ding (2011); Zhang (2013); Du (2015)
Chelsea filter	No change	No change	No change	No change	No change	No change	
Ultraviolet fluorescence	Inertia, related to the content of Fe	Inertia	Inertia	Inertia	Inertia	Inertia	
Spectroscopy characteristics	FTIR: 3,800–3,600 cm^{-1}, 1,200–900 cm^{-1}, 800–600 cm^{-1}, 600–400 cm^{-1}; laser Raman: 3,674 cm^{-1}, 1,060 cm^{-1}, 670 cm^{-1}, 220 cm^{-1}	FTIR: 3,700–3,600 cm^{-1}, 1,100–960 cm^{-1}, 800–600 cm^{-1}, 600–400 cm^{-1}; laser Raman: 1,060 cm^{-1}, 1,030 cm^{-1}, 675 cm^{-1}	FTIR: 1930 cm^{-1}, 1,058 cm^{-1}, 950–920 cm^{-1}, 671 cm^{-1}, 528 cm^{-1}, 505 cm^{-1}, 415 cm^{-1}, 220 cm^{-1}	FTIR: 1,200–900 cm^{-1}, 760–640 cm^{-1}, 550–400 cm^{-1}; laser Raman: 1,056 cm^{-1}, 674 cm^{-1}, 219 cm^{-1}	FTIR: 3,750–3,550 cm^{-1}, 1,200–800 cm^{-1}, 600–400 cm^{-1}	FTIR: 3,700–3,500 cm^{-1}, 1,200–800 cm^{-1}, 800–600 cm^{-1}, 600–400 cm^{-1}; laser Raman: 1,056 cm^{-1}, 674 cm^{-1}, 219 cm^{-1}	Lu et al. (2004); Lu, 2005, 2007, 2008; Yang, et al., 2013, Yang, 2013; Tian (2014); Du (2015); Song et al. (2020); Zhang (2020)
Micro-examination	Fibrous, columnar, acicular, flake and irregular	Tremolite grains extend in a directional fibrous orientation	Tremolite grains present fibrous, columnar, and flaky forms	Tremolite grains show microfibrous, flake and radial forms. The aggregate morphologies include cryptocrystalline aggregates, astatic fiber aggregates, near parallel fiber bundle, and radial fiber cluster	Tremolite grains are mainly fibrous, acicular and scaly	Tremolite grains are mainly acicular, fibrous and columnar	Feng and Zhang (2004)

(Continued on following page)

10.3389/feart.2023.1047707

TABLE 2 (*Continued*) Overview of the gemological and mineralogical characteristics of nephrite jade deposits in China.

Magmatic-hydrothermal metasomatic nephrite							
Genetic type	Ultramafic rock type			Mafic rock type			References
Locations	Manas, Xinjiang	Shimian, Sichuan	Qilian, Qinghai	Golmud, Qinghai	Luodian, Guizhou	Dahua, Guangxi	
Textures	Granulitic crystalloblastic texture, heteroblastic texture, microcrystalline crystalloblastic texture, metasomatism structure	Microfiber crystalloblastic texture, Microscopic porphyritic crystalloblastic texture, with occasionally metasomatism harbour -like structure	Fiber interwoven texture, fiber crystalloblastic texture, metasomatic pseudomorph texture, broom texture, metasomatic rim texture	Felt-like texture, microfiber-cryptocrystalline texture, microflake—cryptocrystalline texture, microflake texture, radial fiber structure, secondary filling texture, metasomatic pseudomorph texture	Felt-like fiber interwoven crystalloblastic texture, fiber interwoven crystalloblastic texture, fiber bundle-crystalloblastic texture, lepidoblastic texture, metasomatic relict texture	Microfiber crystalloblastic Texture, felted fibrous crystalloblastic texture, metasomatic relict texture	Feng and Zhang (2004); Zhou et al. (2008); Qin (2013); Zhang (2013); Du (2015); Yu (2016); Bai et al. (2020)
Structures	Massive	Massive	Massive	Massive and band structure	Massive, flaky, and banded structure	Massive	
Cleavage or fracture	Uneven fracture	Uneven fracture	Uneven fracture	Uneven fracture	Uneven fracture	Uneven fracture	
Major mineral	Tremolite/actinolite	Tremolite/actinolite	Tremolite/actinolite	Tremolite	Tremolite	Tremolite	
Secondary or accessory minerals	Diopside, chromite, chlorite, serpentine, talc, and sulfide, arsenide of nickel	Titanite, chlorite, magnetite, calcite, serpentine, etc.	Actinolite, apatite, chlorite, titanite	Apatite, pyrite, actinite, diopside, titanite, magnetite, chromite (green jade), epidote, dolomite, calcite, quartz, clay minerals, etc. Black jade usually contains graphite, magnetite, and ilmenite	Diopside, albitite, calcite, quartz, moganite, dolomite, apatite, ferromanganese or clay minerals	Diapsite, calcite, chlorite, quartz, apatite, titanite, andradite, talc; stilpnomelane, epidote, diopside, pyrrhotite, and pyrite (black jade)	Lu et al. (2004); Zhou, et al. (2008); Ding (2011); Tang et al. (2002); Qin, Y. (2013); Yang (2013); Zhang (2013); Che (2013); Du (2015); Dong et al. (2014); Zhang (2015); Zhong et al. (2019); Zhang et al. (2021); Lan (2022)

Genetic type	Intermediate-felsic rock type						
Locations	Yutian, Xinjiang	Hetian, Xinjiang	Qiemo, Xinjiang	Ruoqiang, Xinjiang	Gobi nephrite jade, Xinjiang	Liyang, Jiangsu	References
Color	White jade, light greenish white jade, greenish jade, black jade, and brown jade	White jade, greenish jade, black jade, and yellow jade	White jade, light greenish white jade, greenish jade, and brown jade	greenish jade, light greenish white jade, brown jade, and yellow jade	White jade, light greenish white jade, yellowish jade, light brown jade	White jade, light greenish white jade, greenish jade, and green jade	Yu (2016); Wu (2016)

(Continued on following page)

10.3389/feart.2023.1047707

TABLE 2 (*Continued*) Overview of the gemological and mineralogical characteristics of nephrite jade deposits in China.

Genetic type	Intermediate-felsic rock type						
Locations	Yutian, Xinjiang	Hetian, Xinjiang	Qiemo, Xinjiang	Ruoqiang, Xinjiang	Gobi nephrite jade, Xinjiang	Liyang, Jiangsu	References
Texture and transparency	Fine texture; microtransparent—opaque	Fine texture; microtransparent—opaque	Fine texture; microtransparent—opaque	Fine texture; microtransparent—opaque	Fine texture; microtransparent—opaque	Coarse textures; microtransparent—opaque	Yu (2016); Wu (2016)
Luster	Greasy luster	Greasy luster	Vitreousr-greasy luster	Vitreous-greasy luster	Strong greasy luster	Semi-greasy luster	Yu (2016); Wu (2016)
Refractive index	1.60-1.61	1.60-1.61	1.60	1.60–1.62	1.61–1.62	1.60	Li and Cai (2008); Yu (2016); Wu (2016)
Specific gravity	2.95±	The average value: 2.97	2.94–2.98	2.90–3.00	The average value: 2.97; slightly higher than that of primary deposits	The average value: 2.95–2.99	Zhong (1995); Li and Cai (2008); Zhou et al. (2009); Yu (2016); Qiu (2016); Wu (2016); Su et al. (2019)
Hardness (microhardness or Mohs hardness)	The Mohs hardness: 6–6.5	The Mohs hardness: 6.0–6.5	The Mohs hardness: 6.14–6.41, with an average of 6.29	The Mohs hardness: 5.80–6.10	The Mohs hardness: 6.23–6.24	5.5–6.0	Zhong (1995); Yu (2016); Qiu (2016); Wu (2016); Su et al. (2019)
Chelsea filter	No change	No change	No change	No change	No change	No change	
Ultraviolet fluorescence	Inertia	Inertia	Inertia	Inertia	Inertia	Inertia	
Spectroscopy characteristics	FTIR: 1,144–915 cm^{-1}, 758–640 cm^{-1}, 544–460 cm^{-1}	FTIR: 1,100–900 cm^{-1}, 900–600 cm^{-1}, 600–400 cm^{-1}; laser Raman: 3,676 cm^{-1}, 1,060 cm^{-1}, 930 cm^{-1}, 672 cm^{-1}, 395 cm^{-1}, 223 cm^{-1}	FTIR: 1,100–900 cm^{-1}, 800–600 cm^{-1}, 600–400 cm^{-1}; laser Raman: 3,676 cm^{-1}, 677 cm^{-1}, 226 cm^{-1}	FTIR: 3,700–3,600 cm^{-1}, 1,200–900 cm^{-1}, 550–400 cm^{-1}, 800–650 cm^{-1}; Laser Raman: 1,058 cm^{-1}, 675 cm^{-1}, 223 cm^{-1}	FTIR: 1,150–900 cm^{-1}, 760–400 cm^{-1}; laser Raman: 3,672 cm^{-1}, 1,061 cm^{-1}, 225 cm^{-1}	FTIR: 1,100–900 cm^{-1}, 760–400 cm^{-1}, 400–200 cm^{-1}	Zou et al. (2002); Cui and Yang (2002); Yang et al. (2012); Zhang et al. (2012); Chen et al. (2013); Qiu (2016); Wu (2016); Su et al. (2019)
Micro-examination	Tremolite grains are irregular fibrous or columnar, and fibrous tremolite extends semi—directionally, and some areas are intertwined and closely bound together; Some grains show radial or fascicular structures	Tremolite grains are very fine without distinct boundaries, and they are intertwined and closely bound together; Some tremolite grains show radial or fascicular structures	Tremolite grains are irregular fibrous or columnar, and the fibrous tremolite generally extends semi—directionally, and some areas are intertwined and closely bound together	Most of the tremolite grains are fibrous, a few tremolite grains are distributed in fibrous tremolite in columnar or granular forms	Tremolite grains are arranged in felt-like and columnar orientation	Tremolite grains commonly present fibrous, needle-like, columnar, lamellar, radial forms	Liu et al. (2015); Qiu (2016); Wu (2016); Gao et al. (2019)

(Continued on following page)

10.3389/feart.2023.1047707

TABLE 2 (*Continued*) Overview of the gemological and mineralogical characteristics of nephrite jade deposits in China.

Genetic type	Intermediate-felsic rock type						
Locations	Yutian, Xinjiang	Hetian, Xinjiang	Qiemo, Xinjiang	Ruoqiang, Xinjiang	Gobi nephrite jade, Xinjiang	Liyang, Jiangsu	References
Textures	Felt-like fiber interwoven texture, microfiber-cryptocrystalline, microfiber, microflake cryptocrystalline, microflake metamorphosis and radial or broom texture, with occasionally metasomatism residual texture	Felt-like fiber interwoven texture, fiber interwoven—crystalloblastic texture	Felt-like fiber interwoven texture, microacicular—crystalloblastic texture, columnar—crystalloblastic texture, heteroblastic—crystalloblastic textureetc	Felt-like fiber interwoven texture, microfiber-cryptocrystalline crystalloblastic texture, microfiber crystalloblastic texture, broom texture, fiber bundle texture, porphyroblastic texture, metasomatic pseudomorph texture, metasomatism residual texture, secondary filling texture	Felt-like interwoven texture, microfiber crystalloblastic texture	Felt-like structure, radial texture, fiber-columnar texture	Cui and Yang (2002); Liu et al., 2011; Meng, 2014; Liu et al. (2015); Qiu (2016)
Structures	Massive structure with occasionally flake structure	Massive structure	Massive structure	Massive structure	Flake/massive structure	Massive structure	
Cleavage or fracture	Uneven fracture	Uneven fracture	Uneven fracture	Uneven fracture	Uneven fracture	Uneven fracture	
Major mineral	Tremolite (>98%)	Tremolite (>98%)	Tremolite (>98%)	Tremolite	Tremolite/actinolite (green nephrite jade)	Tremolite/actinolite	
Secondary or accessory minerals	Diopside, chlorite, phlogopite, calcite, dolomite, titanite, biotite	Diopside, actinolite, graphite, apatite, allanite, grossularite, zircon, and rutile	Diopside, dolomite, titanite, epidote, magnetite, apatite, limonite, zoisite, chlorite	Pargasite, diopside, epidote, allanite, titanite, andesine, prehnite, calcite	Apatite, titanite, diopside, epidote, chromite (green jade), feldspar, pyrope	Diopside, muscovite, epidote, pyroxene, apatite, magnetite, limonite, clay minerals	Cui and Yang (2002); Zhou et al. (2009); Liu et al., 2010, 2011; Liu et al. (2015); Qiu (2016); Wang (2016); Wu (2016); Gao et al. (2019); Liu et al. (2019)

10.3389/feart.2023.1047707

TABLE 3 Overview of the gemological mineralogical characteristics of nephrite jade deposits in China.

Genetic type	Serpentine rock type	Carbonate rock type		References
Locations	Hualien, Taiwan	Xiuyan, Liaoning	Luanchuan, Henan	
Color	Chartreuse, dark green, bright green, grass green and other green with light yellow and light white jade; Nephrite jade with cat's effect usually show yellow with green, black or brown color	Light greenish white, chartreuse, black green, and dark green jade	White, light greenish white, azury jade	
Texture and transparency	Fine texture; Microtransparent—opaque	Medium - fine texture; Translucent—opaque	Medium—fine texture; Opaque	Ding (2011); Zhang et al. (2019)
Luster	Waxy—greasy luster	Vitreous luster	Waxy luster	Zhang et al. (2019)
Refractive index	1.61–1.63	1.60–1.61	1.60 ± 0.02	Zhang et al. (2019)
Specific gravity	3.02–3.44	2.85–2.96	2.95 ± 0.01	Zhang et al. (2019)
Hardness (microhardness or Mohs hardness)	The Mohs hardness: 5–6	5.90–6.57	—	Zhang et al. (2019)
Chelsea filter	No change	No change	No change	Zhang et al. (2019)
Ultraviolet fluorescence	Inertia related to the content of Fe	Inertia	Inertia	Zhang et al. (2019)
Spectroscopy characteristics	FTIR: 3,700–3,600 cm^{-1}, 1,200–900 cm^{-1}, 600–400 cm^{-1}, 800–600 cm^{-1}; laser Raman: 1,056 cm^{-1}, 671 cm^{-1}, 218 cm^{-1}	FTIR: 1,200–900 cm^{-1}, 600–400 cm^{-1}, 800–600 cm^{-1}; laser Raman: 1,060 cm^{-1}, 1,030 cm^{-1}, 670 cm^{-1}	—	Ding (2011); Li et al. (2011); Ren et al. (2012); Chen, et al. (2013); Zhang et al. (2019)
Micro-examination	Columnar, microfibrous (astatic, parallel, nearly parallel, bunched shapes)	Tremolite grains usually show tabular, columnar, foliaceous and fibrous foem, and generally contain abundant graphite inclusions	Tremolite grains show microfibrous, lamellar forms etc.	Zhang et al. (2019)
Textures	Felt-like crystalloblastic texture, columnar crystalloblastic texture, parallel fiber crystalloblastic texture, metasomatic pseudomorph texture	Felt-like interwoven texture, microfiber crystalloblastic texture, micro-radial (broom) texture, micro leaf-like—crystalloblastic texture	Felt-like fiber interwoven metamorphosis texture, Fiber bundle crystalloblastic texture, radial crystalloblastic texture, porphyritic—crystalloblastic is texture, rotational texture, metasomatic relict texture, etc.	Ding (2011); Li et al. (2011); Ren et al. (2012); Lin (1999); Zhang et al. (2019)
Structures	Massive structure	Massive structure	Massive structure	Tang et al. (2002); Yin (2006); Ling et al. (2008); Ding (2011); Zhang et al. (2019)
Cleavage or fracture	Uneven fracture	Uneven fracture	Uneven fracture	Tang et al. (2002); Ding (2011); Zhang et al. (2019)
Major mineral	Tremolite/actinolite	Tremolite	Tremolite	Tang et al. (2002); Ding (2011); Zhang et al. (2019)
Secondary or accessory minerals	Actinolite, chromite, chromium-bearing essonite, magnetite, titanite, serpentine, chlorite, and graphite	Serpentine, calcite, dolomite, titanite, zoisite, apatite, and graphite	Calcite, titanite, rutile, quartz, serpentine, actinolite, chlorite, pyrite, apatite, magnetite	Tang et al. (2002); Yin (2006); Ding (2011); Li et al. (2011); Liao et al. (2012); Ren et al. (2012); Ling et al. (2015); Zhang et al. (2019)

3.1.1.2 The Qilian green nephrite jade

The jade mainly formed within the North Qilian orogenic belt, but there are still shortage of studies to investigate them (Zhang et al., 2021). A previous investigation suggested that the high-quality S-type nephrite jade in Yushigou region, the Qilian Orogen is predominantly composed of tremolite and actinolite, and underwent the transformation to actinolite with the increasing of Fe and Cr (Zhang et al., 2021). The secondary or accessory minerals consist of apatite, chlorite, and titanite. Usually, the green nephrite jade shows two different colors: deep green and greyish-green, characterized by delicate textures and vitreous luster (Figure 1, Figure 2E). The major element data suggest that the mineral chemical compositions of tremolite are main SiO_2 (55.90–59.04 wt%), MgO (20.36–22.29 wt%), CaO (12.62–13.24 wt%) and FeO (3.47–5.48 wt%) (Zhang et al., 2021).

3.1.1.3 The Shimian green nephrite jade

The jade deposit hosted in Sichuan Province is famous for producing high-quality nephrite with chatoyancy (Xu et al., 2015). The ore-bearing rock masses are mainly serpentinized augite peridotite and peridotite intruding in the middle Proterozoic Ebian Group. Due to uniform directional shear stress during metasomatism, tremolite fibers, needle-like minerals or tubular gas-liquid inclusions were orientated growth, which led to the formation of nephrite jade with the cat's eye effect (Xu et al., 2015). The main minerals of the nephrite jade are characterized by fibrous tremolite or actinolite, together with minor titanite, magnetite, and serpentine, and the major chemical compositions of tremolite are SiO_2 (56.85–57.27 wt%), MgO (21.61–22.99 wt%), CaO (12.29–13.13 wt%), and FeO (up to 5.60 wt%) (Lu, 2005; Ding, 2011; Xu et al., 2015).

3.1.2 Mafic rock type

The nephrite jade orebodies occurred within the contact zones between the dolomitic marbles and mafic intrusive rocks. Most of orebodies are distributed along faults or cracks of dolomitic marble and occur as layers, veins or lenses. Representative nephrite jade deposits are mainly distributed in Sanchakou of Qinghai, Luodian of Guizhou and Dahua of Guangxi. Details are as follows.

3.1.2.1 The Sanchakou nephrite jade

The jade deposit is located in the north of Kunnan fault zone and the south of Kunzhong suture zone, and the nephrite jade of this deposit generally shows characteristics of high hardness, low tremolite content, and high crystallinity (Zhou et al., 2005). The igneous rocks exposed in this ore district are mainly mafic gabbro (Ma, 2013), while the jade ore intrusive body is dioritic porphyrite. The nephrite formation was accompanied by multiple hydrothermal fluids reactions during the mineralization processes.

3.1.2.2 The Luodian nephrite jade

The nephrite jade (also termed as Luodian jade) from Guizhou Province, a new genetic type of jade variety, represents an important part of Chinese nephrite jade (Yang, 2013). The occurrences and mineralization of Luodian jade predominantly occur at contact metamorphic zones, whereas the distribution of it was strictly controlled by anticlinal structure and diabase emplacement (Che, 2013; Zhang, 2013; Zhang, 2015). The Luodian jade consists mainly of white jade, white-green jade, and green jade. The green nephrite jade is caused mainly by trace elements of V and Cr in chemical compositions (Yang, 2013). The main minerals include tremolite as well as minor diopside, calcite, quartz, wollastonite, plagioclase, and talc.

3.1.2.3 The Dahua nephrite jade

The jade deposit (also termed as Dahua jade) located Guangxi occurs in alteration zones of marble overlying diabase, presenting the characteristics of strata-bound ore deposit (Lan, 2022). The major minerals are characterized by fibrous tremolite with a subordinate association of diapsite, calcite, chlorite, quartz, apatite, titanite, and andradite, and talc (Du, 2015; Lan, 2022). Recent published mineral major element data suggested that the main chemical compositions of tremolite in the nephrite jade are the SiO_2 (the average value 59.31 wt%), MgO (the average value 23.63 wt%), CaO (the average value 12.99 wt%) (Lan, 2022). However, the black nephrite jade with high quality consists mainly of actinolite or ferro-actinolite, together with minor stilpnomelane, andradite, patite, epidote, quartz, diopside, pyrrhotite, and pyrite, with a $Mg/(Mg^{2+} + Fe^{2+})$ ratio of 0.765–0.343 (Figure 3; Zhong et al., 2019).

3.1.3 Intermediate-felsic rock type

The primary orebodies of these nephrite jade deposits generally occur at the contact zones between the dolomitic marbles and intermediate-felsic rocks (generally granitoids). The lithologies of these deposit are mainly composed of a suite of calcium–magnesian marbles. Most of orebodies are also distributed along faults or cracks of dolomitic marble and occur as veins or lenses. About 20 nephrite jade deposits are discovered in the Kunlun Mountain, and they are concentrated in several regions: Shache-Yecheng belt, Hetian-Yutian belt, and Qiemo-Ruoqiang belt (Liu et al., 2010; 2011; Liu et al., 2015; 2016; Han et al., 2018; Gao et al., 2019; Jiang et al., 2021). In the following sections, we also briefly introduce the major features of representative nephrite jade of each belts in the order described above.

3.1.3.1 The placer/secondary nephrite jade

The jade deposits are mainly distributed in two tributaries of the Yurungkash River (White Jade River) and Kalakash River (Black Jade River) in Hetian County (Liu et al., 2011; 2016). This kind of nephrite jade was transported by glacial melt-water, and deposited into river (or bed) from the primary deposits in the Kunlun Mountains (Liu et al., 2016). In this mining area, the black nephrite jade can be divided into two types: 1) jade dominated by tremolite and actinolite; and 2) jade with tremolite and graphite (Figure 2C). The nephrite jade generally shows low ΣREE contents, and whole-rock chondrite standardized data display that this nephrite jade has strong negative Eu anomalies, moderate light-REEs enrichments, and flat heavy-REE enrichments (Liu et al., 2011; 2016) (Figure 4A). Moreover, H-O stable isotopes of the nephrite jade ($\delta^{18}D_{H2O}$: −86.1‰–−5.8‰; $\delta^{18}O_{H2O}$: 1.5‰–8.4‰) indicated that the nephrite jade formation is related to carbonate bodies (Liu et al., 2016), but not to serpentinite. SHRIMP zircon U–Pb dating for black nephrite jade yielded $^{206}Pb/^{238}U$ mean ages of 440.7 ± 4.4 Ma, 397.1 ± 3.5, and 389 ± 4 Ma, and of 377.8 ± 6.2 Ma for white-green nephrite jade (Liu et al., 2016) (Figure 6).

3.1.3.2 The Alamas nephrite jade

The jade deposit located in Yutian region was characterized by strong tectonic movement and extensive thrust faults in late Hercynian period. The main minerals are featured by tremolite with a subordinate association of diopside, chlorite, calcite, titanite, and phlogopite. The jade deposit is mainly hosted the contents of tremolite are MgO, CaO and SiO_2, ranging from 18.89 to 26.55 wt%, 10.20–12.67 wt%, and 53.25–58.58 wt% (Liu et al., 2010), respectively. The Alamas nephrite jade also has pronounced Eu negative anomalies (δEu = 0.08–0.17), characterized by depleted in LREEs and flat HREEs in the chondrite-normalized patterns (Liu et al., 2015) (Figure 4A). Nephrites have $\delta^{18}O_{H2O}$ and $\delta^{18}D_{H2O}$ isotope compositions in the range from 3.4‰ to 6.1‰ and −73.0‰ to −61.3‰, respectively (Figure 5). Zircon U–Pb geochronology of granodiorite reveals the age of magmatic zircons was at 418.5 ±

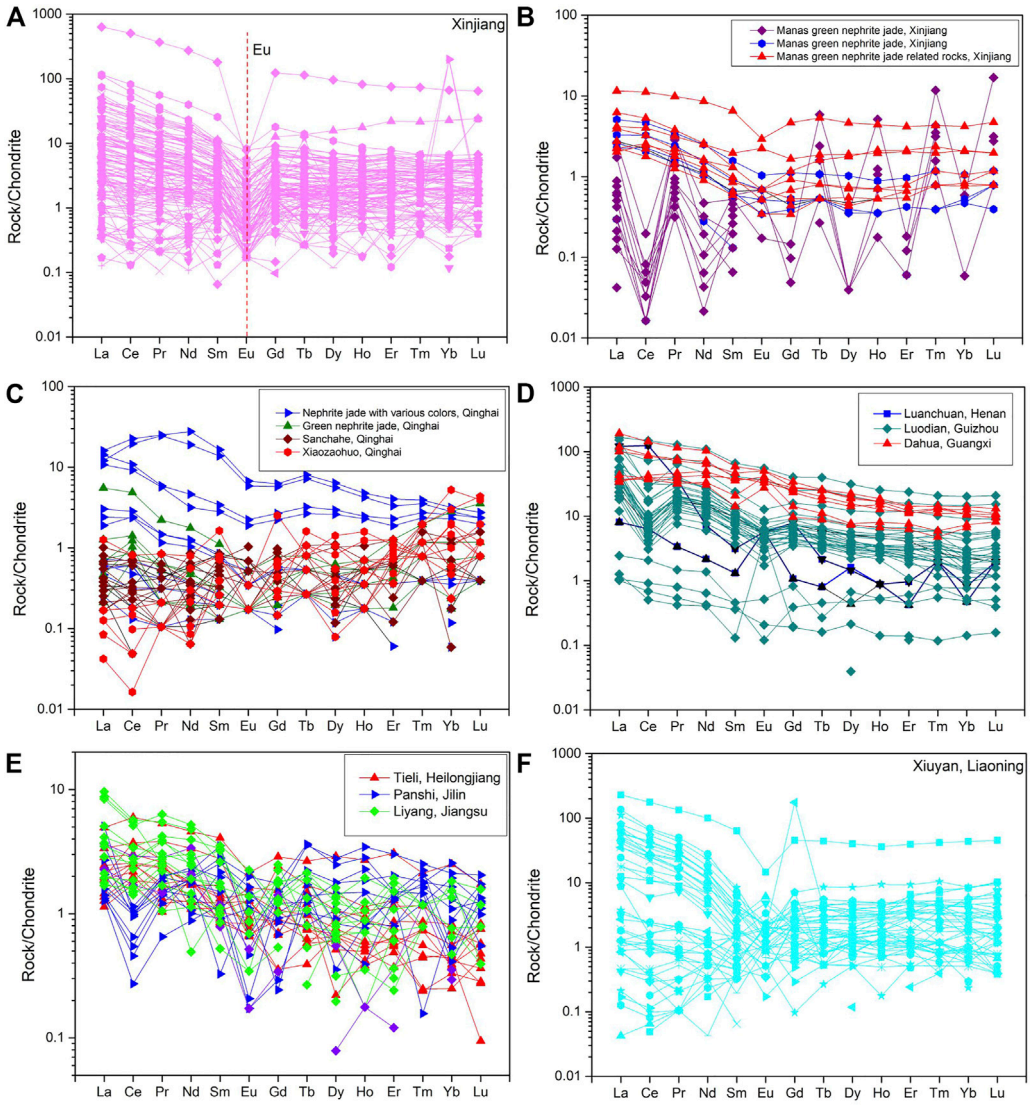


FIGURE 4
The Chondrite-normalized REE patterns of nephrite jade from Xinjiang **(A,B)**, Qinghai **(C)**, Henan **(D)**, Guizhou **(D)**, Guangxi **(D)**, Heilongjiang **(E)**, Jilin **(E)**, Jiangsu **(E)**, as well as Liaoning **(F)**, respectively. The chondrite-normalized values are from McDonough and Sun (1995). Nephrite jade in different regions shows obviously disparate variation of REEs, indicating the distinction of the regularity of ore formation process (Data cited by Ling et al., 2008; Li et al., 2011; Zhi et al., 2011; Yang, 2013; Gao, 2014; Zhang, 2015; Liu et al., 2015; 2016; Yin et al., 2014; Ling et al., 2015; Yu, 2016; Li, 2016; Liu et al., 2019; Gao et al., 2019; Bai et al., 2019; Jiang et al., 2020; Bai et al., 2020).

2.8 Ma, constraining the upper limit age of nephrite jade formation (Liu et al., 2010; 2015) (Figure 6).

3.1.3.3 The Tashsaii nephrite jade

The deposit in the southwest of the Altyn Tagh Fault are mainly hosted in the Qiemo County (Gao et al., 2019). Currently, it is the largest nephrite jade deposit in the Xinjiang Province, including Jinshan, Tiantai, and 8th mine open pits (Gao et al., 2019). Wu (2016) proposed that the dolomite marble was generally characterized by white tremolitization, yellow-green serpentinization, and pink zoisitization. The main minerals are featured by tremolite with a subordinate association of diopside, dolomite, titanite, epidote, magnetite, apatite, limonite, zoisite, chlorite. The predominant mineral of the Tashsaii nephrite jade is tremolite, and its mineral chemical compositions show MgO contents of 23.46–26.01 wt%, CaO contents of 10.87–14.06 wt%, and SiO_2 contents of 57.23–59.50 wt% (Wu, 2016; Gao et al., 2019). The Tashsaii nephrite jade displays enrichment in LREEs and depletion in HREEs (Figure 4A). Zircon U–Pb dating of zoisite-quartz altered rocks constrains that the nephrite jade from this region was formed at 433 ± 10 Ma (Gao et al., 2019) (Figure 6).

3.1.3.4 The Yinggelike and Fuguoling nephrite jade

The jade deposits in the mining area are mainly distributed in Ruoqiang region, among which the Yinggelike nephrite jade generally presents yellow color. The main minerals of nephrite jade are featured by tremolite with a subordinate association of Pargasite, diopside, epidote, allanite, titanite, andesine, prehnite, and calcite (Jiang et al., 2020). Their mineral chemistry compositions of SiO_2, MgO and CaO vary from 56.96 to 59.74 wt%, 21.05–24.07 wt

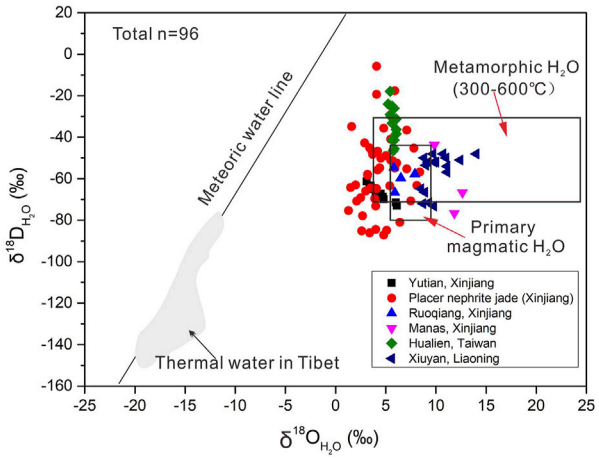


FIGURE 5
δD_{H2O} and $\delta^{18}O_{H2O}$ data for ore-forming fluids of representative nephrites from different regions. The diagram is from Taylor (1997), showing the evolution of hydrothermal fluids (Liu et al., 2011; 2016). The Magmatic water, metamorphic water, together with minor meteoric water were involved to participate in the formation process and evolution of nephrite jade in China (Data cited by Liu et al., 2011; 2015; 2016; Zheng et al., 2019; Jiang, 2020; Zhang, 2020; Gao et al., 2020).

%, and 12.77–13.89 wt%, respectively. The contents of Fe^{3+} and Fe^{2+} are the main factors to control the color of nephrite jade. The REEs distribution patterns and H-O stable isotopic of the Yinggelike nephrite jade ($\delta^{18}D_{H2O}$: −66.7‰ to −54.6‰; $\delta^{18}O_{H2O}$: 5.8‰–7.9‰) indicate a genetic link with dolomite marble (Figure 4A, Figure 6). In contrast, the contents of SiO_2, MgO and CaO in the Fuguoling nephrite jade show variation range of 56.01–58.96 wt%, 21.43–24.14 wt%, and 12.07–14.02 wt%, respectively. Zircon U–Pb dating of granite constrains the upper limit age of tremolite crystallization at 471 ± 16 Ma (Figure 6; Jiang, 2020).

3.1.3.5 The Gobi nephrite jade

The jade is widely hosted in the Qiemo-Ruoqiang County, characterized by certain edges and corners, as well as with strong greasy luster (Fang, 2018). The main minerals of the Gobi nephrite jade is tremolite, and its main mineral chemical compositions of SiO_2, MgO, and CaO range from 56.7 to 58.9 wt%, 23.6–24.8 wt%, and 12.16–15.0 wt% (Liu et al., 2019; Su et al., 2019), respectively. The secondary or accessory minerals consist of apatite, titanite, diopside, epidote, feldspar, and pyrope. In terms of the REEs distribution patterns, the Gobi nephrite has obvious Eu negative anomalies, similar with primary nephrite jade (Figure 4A). Liu et al. (2019) studied trace elements, and REEs of the Gobi nephrite jade from Ruoqiang–Qiemo areas, and concluded that the nephrite jade is correlated with magnesium skarn type (Figure 5). Moreover, SHRIMP zircon U–Pb dating of the nephrite jade yielded $^{206}Pb/^{238}U$ mean ages of ca. 400 Ma, which constrain the formation of the Gobi nephrite jade. Other zircon U-Pb ages of 2,460–1,450 Ma, 785 Ma, and 60–40 Ma may represent new zircon growth, magmatic hydrothermal events, and protolithic sedimentary ages (Liu et al., 2019) (Figure 6), respectively.

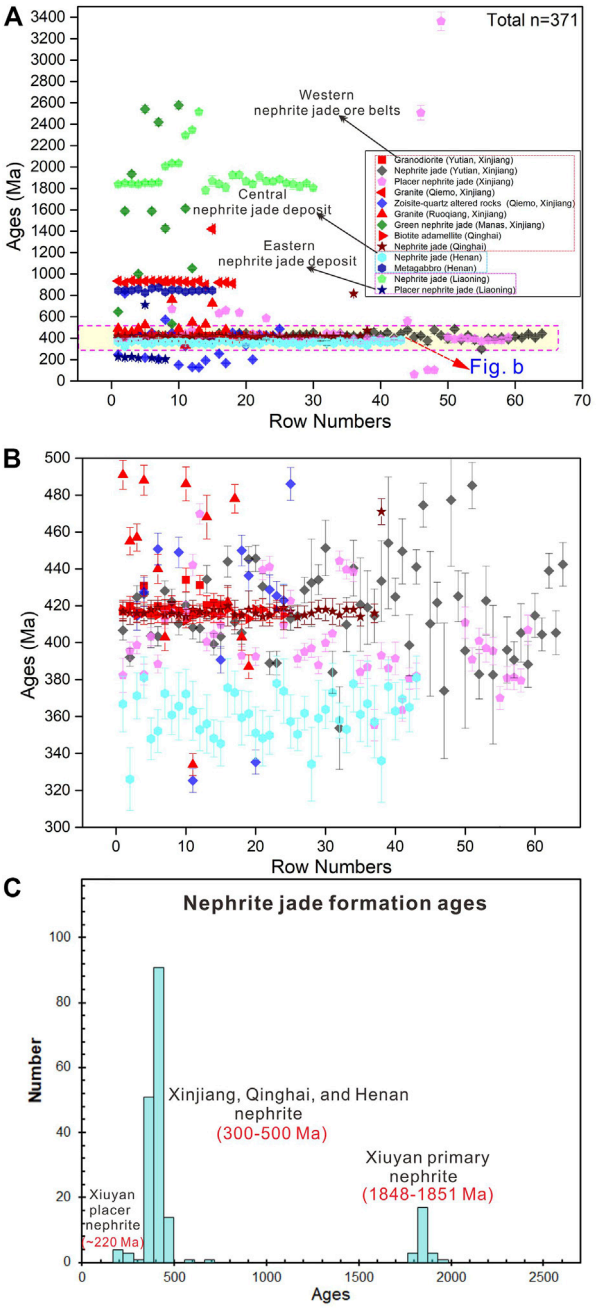


FIGURE 6
Geochronological data of nephrite jade in China. **(A)** Combined with the wide distribution of ages, it can be seen that chronological studies on nephrite jade are mainly concentrated in the Xinjiang regions, with geochronological investigations in other regions being more lacking and information in the southern region being in a state of absence. Overall, the formation ages from different provenances reveal the multi-period characteristics of nephrite jade mineralization in China. **(B)** The ages of nephrite deposit resources in China are mostly constrained at ~500–300 Ma. **(C)** Age data histogram of nephrite jade in China (Data cited by Liu et al., 2010; 2011; 2015; Ling et al., 2015; Liu et al., 2016; Lei et al., 2018; Gao et al., 2019; Zheng et al., 2019; Zou et al., 2021; Jiang et al., 2020). Due to the lack of effective dating data for nephrite jade deposits in the eastern and southern metallogenic belts, it is very limited to infer tectonic evolution mechanisms.

3.1.3.6 The Qinghai nephrite jade

In Qinghai Province, the jade mostly shows weak greasy-glass luster, semi-transparent-slightly transparent, and the overall transparency is higher than that nephrite jade from Xinjiang Province. The majority of jades in Qinghai Province are characterized by typical "waterline," and their economic value is far lower than that nephrite jade in Xinjiang Province (Figure 2D). The major nephrite jade deposits are hosted in Dazaohuo and Xiaozaohuo areas, Golmud City.

The main mineral of the Xiaozaohuo nephrite jade is tremolite (99%), with minor titanite and zircon (~1%). Almost all nephrite jade ores occur as vein, and a few nephrite jade ores even grew as pectinate, which indicates hydrothermal inputs (Lei et al., 2018). Published studies summarized that the Proto-Tethyan orogen in the east Kunlun region probably initiated in the early Cambrian, the subduction of its oceanic crust happened during the early Cambrian to early Silurian (515–438 Ma). Subsequently, the continental crust subduction and collision developed during the early to middle Silurian (436–425 Ma), and the post-collision was constrained in the late Silurian to the early Devonian (423–403 Ma) (Lei et al., 2018). Zircon U–Pb dating of the biotite adamellite indicates that the formation age of the Xiaozaohuo nephrite deposit was constrained at 416.4 ± 1.5 Ma, indicating tectonic correlation with post–collisional orogen of Proto-Tethyan Ocean in the eastern Kunlun region (Figure 6).

3.1.3.7 The Meiling nephrite jade

The jade (also termed as Meiling jade) deposit occurred in Liyang region, Jiangsu Province (Figure 1; Zhong, 1995; Cui and Yang, 2002; Li and Cai, 2008). The main mineral of the Meiling jade is tremolite, which also contains minor diopside, muscovite, epidote, apatite, magnetite, limonite, and clay minerals. The Meiling jade shows characteristics of low tremolite content, good orientation of tremolite fiber, and high crystallinity (Zhou et al., 2009).

3.2 Metamorphic-hydrothermal metasomatic nephrite jade deposits

These deposits were predominately discovered in the eastern nephrite jade metallogenic belt and the southern margin of North China Craton. Base on the characteristics of hydrothermal fluids and protoliths, the genetic type could be involved following two sections: serpentinite type and carbonate type (Liu and Yu, 2009). Most of orebodies which appears in veined and irregular shapes, controlled by multi-stage fault-fold structures.

3.2.1 The serpentinite type

The jade deposit is mainly hosted in the Fengtian and Wanrong areas of Hualien County, Taiwan Province, and the orebodies were embedded into ultramafic serpentinites (Lin, 1999; Ren et al., 2012). The nephrite jade orebodies were formed at the contact zones between the Paleozoic-Mesozoic Dananao schist and serpentinite. The lithologies of the exposed strata comprise mainly black pelitic schist, with minor green schists and mafic-ultramafic igneous rocks (Yui et al., 2014). The major minerals are characterized by fibrous tremolite with a subordinate association of actinolite, chromite, Cr-bearing garnet, magnetite, titanite, serpentine, chlorite, and graphite (Ren et al., 2012; Yui et al., 2014). The H-O stable isotopic data show that the $\delta^{18}D_{H2O}$ values range from −46.5‰ to −17.9‰, while the $\delta^{18}O_{H2O}$ values range from 5.2‰ to 6.0‰, respectively (Figure 5; Zhang, 2020). This type of nephrite jade deposits also have similar characteristics with the S-type nephrite jade deposits that generated in the ophiolite suites/belts.

3.2.2 The carbonate type

The nephrite jade orebodies usually occurred within the magnesium carbonate bodies and the hydrothermal fluid were mainly derived from the surrounding rocks where metamorphism occurs. Representative nephrite jade deposits are mainly distributed in Xiuyan of Liaoning, Luanchuan of Henan. Details are as follows.

3.2.2.1 The Xiuyan nephrite jade

These orebodies were developed in the structural fracture zones of tremolite dolomitic marble within the Dashiqiao Formation (Proterozoic Liaohe Group), Xiuyan County, Liaoning Province (Xu et al., 2000; Duan and Wang, 2002; Wang et al., 2002; Liu, 2013). The nephrite jade deposits generally underwent four stages: 1) dolomite deposition stage, 2) dolomite regional metamorphism stage, 3) hydrothermal metasomatism stage, and 4) weathering (Duan and Wang, 2002). The main mineral of nephrite jade is tremolite, characterized by SiO_2 contents more than 60%. The MgO and CaO contents are slightly lower, and the secondary or accessory minerals consist of calcite, dolomite, titanite, zoisite, apatite, chromite, and graphite (Jiang, 2014; Wu et al., 2014; Zhang et al., 2019). Moreover, the Xiuyan nephrite jade shows depletion in LREEs (Duan and Wang, 2002; Zhang et al., 2019). The similar REEs distribution patterns and H-O stable isotopes ($\delta^{18}D_{H2O}$: −73.3‰–−48.0‰; $\delta^{18}O_{H2O}$: 8.5‰–12.4‰) suggest that the Xiuyan nephrite jade deposit has close genetic correlation with dolomite marble.

3.2.2.2 The Luanchuan nephrite jade

The jade orebodies were developed in the conjugate areas of NE–and NW–trending faults (Yin, 2006; Ling et al., 2015). Most of the nephrite jade are hosted within serpentine jade or marble bodies, followed by altered gabbro veins or small compressive belts. White nephrite jade and dark green serpentine jade alternately occur as layers or veins, indicating typical epigenetic deposits (Figure 2H). The Luanchuan nephrite jade is characterized by tremolite with a subordinate association of dolomitic marble, serpentine, magnetite, and titanite. (Yin, 2006; Wang, 2013). Moreover, the nephrite jade has pronounced positive Eu anomalies, enriched light REE, and flat heavy REE (Yin, 2006; Ling et al., 2008) (Figure 4D). SIMS U–Pb dating of symbiosis titanite yielded lower intercept ages of 361 ± 4 Ma, constraining the formation timing of this jade deposit (Figure 6).

4 Formation mechanisms of nephrite jade deposits

4.1 Nephrite jade classification

Through the summarization the characteristics of nephrite jade in different regions of China, we can recognize that the two types of nephrites were formed in different tectonic geodynamic settings. The green nephrite jade was formed by the metasomatism of

serpentinite protolith (mainly antigorite) or by direct precipitation during orogeny (Zhang et al., 2021). Nephrite jade commonly presents green color, which is attributed to distinct contents of trace elements such as Fe^{2+}, Cr^{3+} (Yu et al., 2021; Zhang et al., 2021). In contrast, the nephrite jade after dolomitization is generally formed through skarn-type metasomatism between intermediate-felsic granitic rocks (granodiorites) and dolomite marbles (mainly from Xinjiang, China), suggesting a post-collision geodynamic setting (Gao et al., 2019; Zhang et al., 2022). High-quality nephrite jade presents white color, generally depending on constituent minerals or Fe trace elements. Accordingly, the distributions of nephrite jade deposits in China are predominantly related to serpentinites (S-type) and carbonate rocks (D-type), or being re-defined as green jade-type (GJ-type) and white jade-type (WJ-type), respectively.

4.2 Metallogenic mechanisms of GJ-type nephrite jade

As summarized above, the GJ-type nephrite deposits are hosted mainly in the north of Kunlun Mountains, the North Qilian orogenic belt, the west margin uplift zone of Yangtze Craton, and the South China Sea plate.

The GJ-type nephrite jade generated in Manas, Qilian, as well as Shimian, are quite similar in terms of tectonic settings and metallogenic processes (Figure 1). Previous investigations suggested that the formation of the Manas GJ-type nephrite jade deposit was related to ultramafic rocks and may have been formed by regional metamorphism of ultramafic magmatic rocks (Yang et al., 2012; Tian, 2014), or it was possibly transformed by serpentine to GJ-type nephrite through metasomatism, as shown in formula (Eqs 4-1-1, 4-1-2; Jiang et al., 2021).

$$3\,(Mg, Fe)_2SiO_4\ (Olivine) + 4H_2O + SiO_2 \rightarrow 2\,(Mg, Fe)_3Si_2O_5\,(OH)_4\ (Serpentine) \quad (4-1-1)$$

$$5\,(Mg, Fe)_3Si_2O_5\,(OH)_4\ (Serpentine) + 14SiO_2aq + 6CaO \rightarrow 3Ca_2\,(Mg, Fe)_5Si_8O_{22}\,(OH)_4\ (Tremolite - Actinolite) + 7H_2O \quad (4-1-2)$$

Zhang (2020) indicated that the Manas nephrite jade deposit originated in the ophiolitic mélange belt and was closely related to supra-subduction zone (SSZ) ophiolite (mantle wedge type ophiolite), suggesting that it was formed in a late subduction or post–subduction environment (Figures 7A, B). Moreover, the formation of tremolite may be linked to metamorphic diopside in two possible transformation modes (Zhang, 2020): 1) metasomatism; or 2) dissolution and precipitation. The presence of fluids may have led to the replacement of pre-existing diopside, which in turn may have facilitated the formation of tremolite. The detailed reaction formula is:

$$2CaMgSi_2O_6\ (Diopside) + 3MgOaq + 4SiO_2aq + H_2Ol = Ca_2Mg_5\,[Si_4O_{11}]_2\,(OH)_2\ (Tremolite/Actinolite) \quad (4-1-3)$$

However, the source or timing of introduction of Ca-rich fluids related to ultramafic rock type is a major concern that need to be addressed (Zhang et al., 2021). The Ca in the Manas nephrite jade deposit may have been derived from the surrounding mafic rocks (Zhang, 2020). The H-O stable isotope data suggest that the ore-forming fluids during the formation processes of green nephrite jade was derived from metamorphic water, implying the role of metamorphism (Zhang, 2020) (Figure 5). Zircon U–Pb dating data suggest the GJ-type nephrite jade is characterized by multi-stage metallogenic characteristics, and the formation ages should be no later than the Carboniferous ophiolite (Zhang, 2020) (Figure 6). Recently, we firstly investigated high-quality GJ-type nephrite (tremolite) jade from the Yushigou ophiolite suite, Qilian orogeny, NW China, which provides insight into the tectonic processes associated with the formation of jade within subduction zone settings (Yu et al., 2021; Zhang et al., 2021). Zircon U–Pb dating of nephrite jade samples in Yushigou region shows the weighted average age of 227.9 ± 5.3 Ma, representing multiple fluid-rock interaction events within suprasubduction zone at mantle and the formation age of nephrite jade. Thus, we propose that the developed faults during North Qilian Orogeniss might have acted as a pathway for the transfer of Ca- or COH-rich fluids in mantle-derived magma and fluid-rock interactions in the convergent margin setting and further facilitated the crystallization of tremolite or actinolite (Zhang, 2019; Yu et al., 2021; Zhang et al., 2021) (Figures 7A–C).

However, the formation processes of the Hualien nephrite jade were characterized by late subduction of the South China Sea plate (Yui et al., 2014). Based on the Barros type metamorphic superposition associated with arc-continent collision, the metamorphic and metasomatic temperature data supported that the fluid-rock interaction may have occurred, which further suggest the formation of the Hualien nephrite jade was constrained in the Mesozoic or earlier subduction-accretion complexes (Yui et al., 2014). The O-H isotopic data suggested that the fluids during the formation of this nephrite jade was derived from metamorphic water (Figure 5). In addition, Yui et al. (2014) obtained the formation age of 3.3 ± 1.7 Ma through NanoSIMS in–situ zircon U–Pb dating on edge of zircons, indicating that the Hualien nephrite jade is the youngest nephrite jade exposed on the Earth surface. Moreover, according to the graphite Raman micro-thermometer, the formation temperatures of the Hualien nephrite jade may be constrained in the range of 410°C–430°C and infer that the Hualien nephrite jade possibly formed in a relatively low P/T environment (Ren et al., 2012; Yui et al., 2014). Although the nephrite ore bodies are discovered at contact zones with serpentinite and greenschist-facies (carbonaceous material -) quartz-mica schist (Liu and Yu, 2009; Li et al., 2011; Yui et al., 2014), it exhibits profound similarities to the GJ-type nephrite jade deposits mentioned above in terms of geotectonics.

Based on the research findings about the GJ-type nephrite jade deposits in Manas, Qilian, and Hualien, we argue that the following doubts could be addressed. 1) The ultramafic nephrite jade usually occurs in/near ophiolite or ophiolite mélange zones, which are formed in different environments. Serpentinization that occurred in a subduction slab and in an overlying mantle wedge obviously has different tectonic significance (Martin et al., 2020; Zhang et al., 2021). Therefore, the detailed metallogenic environments of the green nephrite jade still needs to be clarified further. 2) The Ca sources may have been derived from the natural fluid system released by subducted slabs and then migrated to higher levels

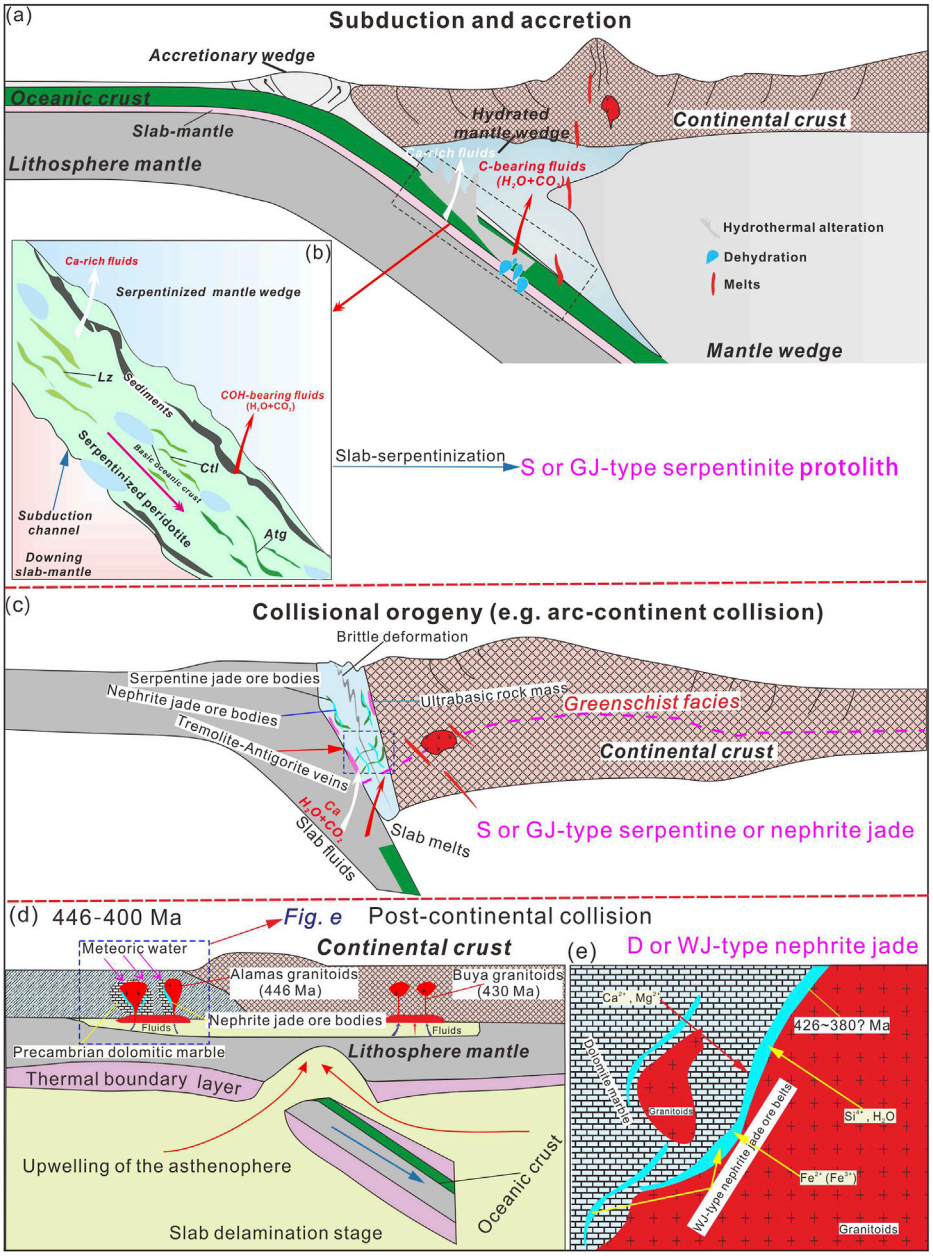


FIGURE 7
(A) Tectonic evolution of jade in initial subduction processes, during which only S or GJ-type primitive serpentinite was formed through the influx of slab derived fluids carrying Ca and CO_2 in the subduction zone (after Zhang et al., 2021). **(B)** Two serpentinization processes in the subducting slabs and overlying mantle wedge are envisaged, accompanied by the release of Ca and C-H-O fluids (Zhang et al., 2021). **(C)** Tectonic setting of jade in collision process, during which S or GJ-type nephrite jade was formed through the late auto-metamorphic metasomatism of serpentine or spontaneous crystallization/precipitation along suture/shear zones being Ca-rich fluids during orogeny at terrane or convergent margin settings in a cooling fore-arc environment (Cluzel et al., 2020; Zhang et al., 2021). **(D)** Post-collisional extension, coupled with limited asthenospheric upwelling, occurred at ~446 Ma (after Zhang et al., 2016). The evolution was accompanied by D-type or WJ-type nephrite jade formation through metamorphic metasomatism triggered by late orogenesis. **(E)** The formation mechanism pattern of D-type or WJ-type nephrite jade ore belts or veins, formed by direct contact between granitoids and marbles. Note that this model also applies to nephrite jade deposits associated with mafic rock types. These two sketches are not to scale. Abbreviations: Lz, Lizardite, Chl, Chrysotile, Atg, Antigorite.

through fluid channels or pathways (Zhang et al., 2021) (Figures 7B, C). 3) Single zircon U–Pb dating data may hardly constrain the metallogenic age of green nephrite jade, but when combined with the characteristics of zircon trace elements, it may provide useful suggestion about its formation and evolution (Zhang et al., 2021). The U–Pb age dating of symbiosis apatite or titanite may serve as reliable constraint for the formation age of green nephrite jade deposits considering their closure temperatures. 4) Research on nephrite mineralization mechanism in the Shimian area is almost non-existent, and so it is urgent to solve ore genesis and carry out

comparative investigations with other appraisal areas. Therefore, although previous researchers have carried out lots of investigations on GJ-type nephrite jade deposits in China (e.g., Yui et al., 2014; Zhang, 2020; Zhang et al., 2021), several issues remain regarding to their ore genesis, occurrence settings, and formation ages, which need to be addressed in further work.

4.3 Metallogenic mechanisms for WJ-type nephrite jade

In the western Hetian Nephrite Belt, representative primary (e.g., Alamas, Tashsaii, and Yinggelike) and secondary nephrite deposits (White Jade River and Black Jade River) in the Xinjiang Province, show high degree of consistency in terms of REEs distribution patterns, H-O isotopes, and information ages, implying similar metallogenic mechanisms (Figures 4–6). Specially, the H-O isotope data of the nephrite jade indicate that the water during nephrite jade formation was derived from metamorphic and magmatic water, as well as minor meteoric water (Figure 5). Whereas the primary nephrite jade deposits are divided into two stages, with the first stage of prograde metasomatism and the second stage of early retrograde alteration (Liu et al., 2011; 2015; 2016; Gao et al., 2019; Jiang et al., 2021). Previous investigations of petrological observations and mineral compositions revealed that WJ-type nephrite jade in Xinjiang underwent two metasomatism-metamorphism processes (Liu et al., 2011; 2015; 2016): 1) dolomite marble → tremolite; or 2) dolomite marble → diopside → tremolite. The principal formation models of primary deposits can be interpreted by the following equilibrium formulas (Eqs 4-2-1–4-2-3), which are consistent with the genetic model (Eq. 4-2-4) proposed by Harlow and Sorensen (2005):

$$5CaMg(CO_3)_2\ (\text{Dolomitic marble}) + 8SiO_2aq + H_2O \rightarrow Ca_2Mg_5[Si_4O_{11}]_2(OH)_2\ (\text{Tremolite}) + 3CaCO_3\ (\text{Calcite}) + 7CO_2aq \quad (4-2-1)$$

$$CaMg(CO_3)_2\ (\text{Dolomitic marble}) + 2SiO_2aq \rightarrow CaMg(Si_2O_6)\ (\text{Diopside}) + 2CO_2aq \quad (4-2-2)$$

$$5CaMg(Si_2O_6)\ (\text{Diopside}) + H_2O \rightarrow Ca_2Mg_5[Si_4O_{11}]_2(OH)_2\ (\text{Tremolite}) + 3Ca^{2+} + 6SiO_2 \quad (4-2-3)$$

$$5Ca(Mg,Fe)(CO_3)_2\ (\text{Dolomitic marble}) + 8SiO_2aq + H_2O \rightarrow Ca_2(Mg,Fe)_5[Si_4O_{11}]_2(OH)_2\ (\text{Tremolite}-\text{Actinolite}) + 3CaCO_3\ (\text{Calcite}) + 7CO_2aq \quad (4-2-4)$$

$$7CaMg(CO_3)_2\ (\text{Dolomitic marble}) + 3Fe^{2+} + 16SiO_2aq + 2H_2O \rightarrow 2Ca_2(Mg,Fe)_5[Si_4O_{11}]_2(OH)_2\ (\text{Tremolite}) + 3Ca^{2+} + 14CO_2aq \quad (4-2-5)$$

Actually, the reaction (Eq. 4-2-4) is applicable to the formation process of green to black jade because it can account for the provenance of Fe sources. However, the green to black WJ-type nephrite jade in China was attributed to a metasomatized dolomite origin due to their low Ni and Cr contents, and is enriched in Fe and Mn as well (Douglas, 1996), suggesting that those components existed either in the protolith of this jade or in the composition of post-magmatic or metasomatizing fluids (Douglas, 1996; 2003; Harlow and Sorensen, 2005). Therefore, the equation (Eq. 4-2-5) proposed by Gao et al. (2019) should be taken into account for the metallogenic process of the WJ-type nephrite in China. Recently, Zhang et al. (2022) proposed that the Fe absorption of epidote-altered diopsidite had a positive impact on the formation of high-quality nephrite jade, which providing new implications for the formation and evolution of the Saidikulam nephrite deposit. In contrast, more complicated formation processes were revealed by placer/secondary nephrite jade deposits, as demonstrated by Liu et al. (2011, 2016), with the presence of abundant mineral associations and metasomatic textures, and therefore, the formation reactions should be the integrated by the comprehensive equations (Eqs 4-2-2, 4-2-3) and (Eqs 4-2-6, 4-2-7):

$$CaMg(CO_3)_2\ (\text{Dolomitic marble}) + 2SiO_2aq \rightarrow Ca_2FeAl_2(SiO_4)(Si_2O_7)O(OH)_2\ (\text{Epidote}) + 2CO_2aq \quad (4-2-6)$$

$$Ca_2FeAl_2(SiO_4)(Si_2O_7)O(OH)_2\ (\text{Epidote}) \rightarrow Ca_2Mg_5[Si_4O_{11}]_2\ (\text{Tremolite}) \quad (4-2-7)$$

The nephrite jade deposits in Qinghai area of the Eastern Kunlun Orogen are commonly attributed to magmatic–hydrothermal deposits (Lei et al., 2018) except for several nephrite deposits combined with distinct igneous intrusive rocks (e.g., Sanchakou), whose formation processes can also be represented by reactions of Eqs 4-2-1–4-2-3.

In the eastern nephrite jade metallogenic belt, nephrite jade deposits (except Liyang, Jiangsu Province) are broadly distributed along the Jiao-Liao-Ji belt, the only generally accepted Paleoproterozoic orogenic belt in the Sino-Korean craton in the western Pacific Ocean (Xu and Liu, 2019; Zhang et al., 2019). The Tieli and Panshi nephrite jade deposits in Heilongjiang and Jilin Provinces, respectively, show similar formation mechanisms although their REEs distribution patterns show distinct characteristics (Figure 4E), which also suggest that the ore-forming fluids had multiple sources with differing characteristics and mineralization occurred as a multi-stage superposition process (Gao et al., 2019; Bai et al., 2020). Previous investigations proposed that the two-stage geological processes for the formation of the Tieli and Panshi nephrite ore bodies included an earlier contact metasomatism and a subsequent tremolitization and diopsidization of dolomitic marble during intrusion of intermediate-felsic intrusive rocks (granitoids) and magmatic hydrothermal metasomatism (Gao et al., 2019; Bai et al., 2020). Recently, Xu and Bai (2022) argued that the subduction of the Pacific Plate may have supplied source materials and power for magmatism and mineralization in the Tieli nephrite deposit based on the $^{87}Sr/^{86}Sr$ isotopic signatures in apatite, which links the subduction-related metasomatism-metamorphism and mineralization events in the circle-Pacific area. The Liyang nephrite (Meiling jade) orebody occurs in the external contact zones where Yanshanian (Jurassic-Cretaceous) Miaoxi granite and Paleozoic Permian Qixia Formation magnesium carbonate facies are discovered (Zhong, 1995; Cui and

Yang, 2002; Li and Cai, 2008), and its formation processes has higher similarity to that of the Tieli and Panshi nephrite deposits. However, significant controversy has arisen regarding to the specific metallogenic model of the Sangpiyu nephrite jade in Xiuyan, Liaoning Province. Wu et al. (2014) suggested that the Sangpiyu nephrite jade deposit was metamorphic–hydrothermal carbonate type based on ^{30}Si stable isotope and REEs distribution patterns that are consistent with the REEs distribution models of the Xinjiang nephrite jade (Figures 4A, F). However, Zhang et al. (2019) argued that the actual hydrothermal fluid metasomatism contained minor Ca during formation of the Sangpiyu nephrite jade. The dolomite was metasomatized by Si-rich hydrothermal fluids to form serpentine, if the contents of Ca are slightly higher, it would be replaced by Si-rich hydrothermal fluids to form tremolite (Zhang et al., 2019). The relevant reactions are (Eq. 4-2-1) and (Eq. 4-2-8):

$$6CaMg[CO_3]_2\ (\text{Dolomitic marble}) + 4SiO_2aq + 4H_2O \rightarrow Mg_6[Si_4O_{10}](OH)_8\ (\text{Serpentine}) + 6CaCO_3\ (\text{Calcite}) + 6CO_2aq \quad (4-2-8)$$

Moreover, Zhang et al. (2019) constrained the formation temperature of graphite inclusions in different types of Sangpiyu nephrite jade samples using graphite Raman microthermometer. This indicates that the graphite inclusions were formed either in high temperature metamorphic facies or low temperature metamorphic facies (Zhang and Yu, 2018; Zhang et al., 2019). The SIMS zircon and titanite U-Pb geochronological data were acquired with ^{207}Pb/^{206}Pb ages of 1924.8 ± 8.3 Ma and 1848 ± 17 Ma (Zou et al., 2021) (Figure 6), respectively, which imply that the Sangpiyu nephrite jade was formed in the dolomite during the period of Paleoproterozoic regional metamorphism along the Jiao–Liao–Ji Belt ca. 2.2–1.9 Ga (Zhang et al., 2019). Notably, Zheng et al. (2019) proposed that the placer nephrite jade (D-type) from Xiuyan region was formed after 220.8 ± 7.6 Ma based on SRIMP zircon U–Pb analysis (Figure 6), which was not derived from primary deposit. Considering the widespread distribution of Mesozoic granites in this area, the relationship between the formation of the Xiuyan nephrite jade and the tectonic settings needs to be further investigated.

In the southern nephrite jade metallogenic belt, the mineralization processes of the Luodian jade and the Dahua jade are related to the contact metamorphism between mafic rocks (diabase) and carbonate rocks (limestone or dolomitic limestone), but they differ significantly in the distribution patterns of REEs, which indicate differences in geological evolution (Figure 4D). The REEs data indicate that the Luodian jade is homologous with diabase and limestone, but its REE patterns are closer to those of limestone, suggesting interactions between the limestone and gas-liquid fluid during the mineralization (Figure 4D). Based on the calculation of ^{18}O fractionation equation between the tremolite and ore-forming fluids, the Luodian jade is classified as a medium-low temperature hydrothermal deposit (Yang, 2013). Accordingly, we argue that the Luodian jade was not produced by contact metasomatism of a single diabase intrusion, but the interactions between the diabase and carbonate. In addition, it was also attested that the bidirectional replenishment model of calcium and magnesium from mafic magma promoted the formation of the Luodian jade (Yang, 2013). For example, the common δEu and δCe exhibit significant negative anomalies in the Luodian jade, indicating that mineralization formed under a relatively reduced environment. However, the significant differences of REEs in the Dahua nephrite jade show multiple sources and the multi-stage superposition of mineralization by ore-forming fluids (Figure 4D; Yin, 2006; Ling et al., 2015). Previous investigation revealed that the mean value of ^{87}Sr/^{86}Sr of the Dahua jade is 0.7071, which is between limestone and diabase, further indicating that close linkages in the sources of ore-forming materials (Lan, 2022). Despite their formation ages and tectonic evolution are not well constrained, their formation processes could be characterized by reactions of Eqs 4-2-1–4-2-3.

4.4 Tectonic implications and prospecting potential of nephrite jade

From the perspective of geotectonic contexts, the formation of GJ-type and WJ-type nephrite deposits was being closely linked to subduction- collision- orogeny processes (Figure 7). Previous investigation indicates that the ophiolites are fragments of on-land oceanic, back-arc, and arc lithosphere, representing arc-continent collisions, or appearing to be isolated bodies that have ramped up upon (obducted onto) continental margins (Harlow and Sorensen, 2005). The tectonic environment for GJ-type is thought to have occurred under this context. Serpentinization during initial subduction provided the necessary serpentinite protolith for the formation of GJ-type nephrite jade in later period, and the evolutionary processes were accompanied by the migration of Ca and the variation of δ^{57}Fe isotopes (Figures 7A, B; Gil, et al., 2020; Zhang et al., 2021). The GJ-type nephrite jade deposits were then formed in the stage of metamorphic metasomatism processes of serpentine induced by the arc-continental collision in response to multiple fluid–rock interactions in mantle of suprasubduction zones (Figure 7C; Yui et al., 2014; Yang et al., 2017; Zhang et al., 2021). In contrast, previous investigations proved that the WJ-type nephrite jade deposits were mostly formed during post continent–continent collision, such as the Kunlun orogenic belt containing ~1,300 km nephrite jade metallogenic belt (Zhang et al., 2016; Lei et al., 2018; Gao et al., 2019) (Figure 1; Figures 7D, E). While the WJ-type nephrite jade deposits near the Pacific orogenic belt may be closely coupled with metamorphism–metasomatism triggered by the subduction of the western Pacific plate.

As the major nephrite jade deposits in China, the geotectonic background of the complex ophiolite suite/ophiolitic mélange belt or the ultramafic serpentine body represents the main prospecting destination for green nephrite jade. The GJ-type nephrite jade associated with ophiolite suites/belts or ultramafic serpentinites in China is presumably even more significant, which should necessitate enhanced investigations and excavation in the future. Further, the contact zones between intermediate-felsic/mafic intrusive rocks and carbonate bodies or sides of carbonate bodies may offer prospecting directions for white nephrite jade or white-green nephrite jade, which mainly depend on the sources of the hydrothermal fluids.

5 Concluding remarks

The integrated geological settings, gemological and mineralogical properties, geochronology, REEs, as well as H-O isotopes data from nephrite jade deposits in China allow us to draw the following preliminary conclusions:

1. The major nephrite jade deposits in China are divided into the western nephrite jade metallogenic belt, the eastern nephrite jade metallogenic belt on the west coast of the Pacific Ocean, the southern nephrite jade metallogenic belt, and the central nephrite jade metallogenic belt at the southern margin of North China Craton. The genetic types of nephrite jade are also defined as GJ-type and WJ-type.
2. The GJ-type nephrite deposits were formed through the late auto-metamorphic metasomatism of serpentine or spontaneous crystallization along suture/shear zones during late orogeny. The WJ-type nephrite jade ore bodies are generally hosted in the contact zones of dolomitic marbles and intermediate-felsic rocks or mafic rocks, which was formed through metamorphism-metasomatism processes during post continent-continent collision.
3. The formation of nephrite jade in China has been linked to the actions of hydrothermal fluids dominantly caused by metamorphic and magmatic sources, characterized by multi-stage metallogenic events.

Author contributions

Conceptualization, CZ, FY, XY, and EC; Methodology, CZ, JC, and PZ; Writing—original draft preparation, all authors; Writing—review and editing, CZ, FY, and EC; Supervision, CZ and FY; Funding acquisition, FY and CZ. All authors have read and agreed to the submitted version of the manuscript.

Funding

This research was jointly supported by the National Natural Science Foundation of China (Grant No. 42202077), the Natural Science Foundation of Gansu Province (Grant No. 22JR5RA440), the Fundamental Research Funds for the Central Universities (Grant No. LZUJBKY-2022-42), the talent research start-up fund of Qilu University of Technology (Shandong Academy of Sciences), and the Guiding Special Funds of "Double First-Class (First-Class University and First-Class Disciplines)" (Grant No. 561119201) of Lanzhou University, China.

Acknowledgments

We are grateful to Ms. Min Zhang (the first author's wife), Dr. Zhengyu Long (China University of Geosciences, Beijing), Ms. Shiyu Ma (Hebei GEO University), and Mr. Lu Niu, Ms. Yanan Bi and Mr. Mingzhe Chen from Qilu University of Technology for their help during data summary and collection. The Mr. Yu Wu (Gemological Inspection Institute of Zhongjian, Xinjiang) is appreciated for his generous sharing of precious placer nephrite jade samples. In addition, we also thank Prof. Jianjun Li (NGDTC) for identifying Luanchuan nephrite jade through FTIR and Dr. Ying Jiang (Jinling Institute of Technology) for providing field investigation figures related to D-type nephrite jade deposits.

Conflict of interest

The authors declare that the research was conducted in the absence of any commercial or financial relationships that could be construed as a potential conflict of interest.

Publisher's note

All claims expressed in this article are solely those of the authors and do not necessarily represent those of their affiliated organizations, or those of the publisher, the editors and the reviewers. Any product that may be evaluated in this article, or claim that may be made by its manufacturer, is not guaranteed or endorsed by the publisher.

References

Adamo, I., and Bocchio, R. (2013). Nephrite jade from val malenco, Italy: Review and update. *Gems Gemology* 49 (2), 98–106. doi:10.5741/gems.49.2.98

Adams, C. J., Beck, R. J., and Campbell, H. J. (2007). Characterisation and origin of New Zealand nephrite jade using its strontium isotopic signature. *Lithos* 97 (3), 307–322. doi:10.1016/j.lithos.2007.01.001

Bai, F., Du, J. M., Li, J.-J., and Jiang, B. H. (2020). Mineralogy, geochemistry, and petrogenesis of green nephrite from Dahua, Guangxi, Southern China. *Ore Geol. Rev.* 118, 103362. doi:10.1016/j.oregeorev.2020.103362

Bai, F., Li, G. M., Lei, J. L., and Sun, J. X. (2019). Mineralogy, geochemistry, and petrogenesis of nephrite from Panshi, Jilin, northeast China. *Ore Geol. Rev.* 115, 103171. doi:10.1016/j.oregeorev.2019.103171

Che, Y. D. (2013). *Gemology and Mineralogy study on Luodian nephrite. Master thesis.* Beijing, China: China University of Geosciences. (in Chinese with English Abstract).

Chen, Q. L., Bao, D. Q., and Yin, Z. W. (2013). Study on XRD and infrared spectroscopy of nephrites from Xinjiang and xiuyan. *Liaoning. Spectrosc. Spectr. Analysis* 33 (11), 3142–3146. (in Chinese with English Abstract).

Cluzel, D., Boulvais, P., Iseppi, M., Lahondère, D., LesimpleetMaurizot, S., Paquette, J. L., et al. (2020). Slab-derived origin of tremolite–antigorite veins in a supra-subduction ophiolite: The peridotite nappe (New Caledonia) as a case study. *Int. J. Earth Sci.* 109, 171–196. doi:10.1007/s00531-019-01796-6

Cui, W. Y., and Yang, F. X. (2002). Study on Hetian jade (tremolite jade). *Acta Petrologica Mineralogica* 21 (1), 26–23. (in Chinese with English Abstract).

Ding, Y. (2011). Brief discussion on comparison and market prospect of Longxi nephrite and nephrite cat's-eye in Sichuan Province. *J. Graduate Sun Yat-sen Univ. Nat. Sci. Med.* 32 (02), 79–84. (in Chinese with English Abstract).

Dong, J. W., Wang, Y. Q., Qiu, C. J., Wang, J. W., and Huang, Y. X. (2014). Mineralogy characteristics of Guizhou nephrite. *J. East China Univ. Sci. Technol. Nat. Sci. Ed.* 4 (60), 713–717. (in Chinese with English Abstract).

Douglas, J. G. (2003). "Exploring issues of geological source for jade worked by ancient Chinese cultures with the aid of X-ray fluorescence," in *Scientific study in the field of Asian art*. Editor P. Jett (London, UK: Archetype Publications Ltd.), 192–199.

Douglas, J. G. (1996). The study of Chinese archaic jades using non-destructive X-ray fluorescence spectroscopy. *Acta Geol. Taiwanica* 32, 43–54.

Du, J. M. (2015). *The study on gemological and mineralogical characteristics of nephrite in Dahua, Guangxi. Master thesis*. Beijing, China: China University of Geosciences. (in Chinese with English Abstract).

Duan, T. Y., and Wang, S. L. (2002). Study on stable isotopes of Xiuyan nephrite (tremolite). *Acta Petrologica Mineralogica* 21 (1), 115–119. (in Chinese with English Abstract).

Fang, T. (2018). Characteristics and cause of formation of Gobi nephrite from southern Xinjiang. *J. Gems Gemmology* 20 (05), 27–38. (in Chinese with English Abstract).

Feng, X. Y., and Zhang, B. L. (2004). Study on compositions and texture characteristics of nephrite from Qinghai province. *J. Gems Gemmology* 6 (4), 7–9.

Feng, Y. H., He, X. M., and Jing, Y. T. (2022). A new model for the formation of nephrite deposits: A case study of the chuncheon nephrite deposit, South Korea. *Lithos* 141, 104655. doi:10.1016/j.oregeorev.2021.104655

Gao, K., Fang, T., Lu, T. J., Lan, Y., Zhang, Y., Wang, Y. Y., et al. (2020). Hydrogen and oxygen stable isotope ratios of dolomite-related nephrite: Relevance for its geographic origin and geological significance. *Gems Gemmology* 56 (2), 266–280. doi:10.5741/gems.56.2.266

Gao, K., Shi, G. H., Wang, M. L., Xie, G., Wang, J., Zhang, X. C., et al.(2019). The tashisayi nephrite deposit from south Altyn Tagh, Xinjiang, northwest China. *Geosci. Front.* 10 (4), 1597–1612. doi:10.1016/j.gsf.2018.10.008

Gao, S. J. (2014). *Master thesis*. Beijing, China: China University of Geosciences. (in Chinese with English Abstract).The study on gemological and mineralogical characteristics and Genesis of nephrite in Tieli Heilongjiang

Gil, G., Bagiński, B., Gunia, P., Madej, S., Sachanbiński, M., Jokubauskas, P., et al. (2020). Comparative Fe and Sr isotope study of nephrite deposits hosted in dolomitic marbles and serpentinites from the Sudetes, SW Poland: Implications for Fe-As-Au-bearing skarn formation and post-obduction evolution of the oceanic lithosphere. *Ore Geol. Rev.* 118, 103335. doi:10.1016/j.oregeorev.2020.103335

Han, D., Liu, X. F., Liu, Y., Zhang, Y., Zheng, F., Maituohuti, A., et al. (2018). Genesis of dolomite-related nephrite from Hetian and color-forming factors of typical nephrite in Hetian, Xinjiang. *Acta Petrologica Mineralogica* 37 (6), 1011–1026. (in Chinese with English Abstract).

Harlow, G. E., and Sorensen, S. S. (2005). Jade (nephrite and jadeitite) and serpentinite: Metasomatic connections. *Int. Geol. Rev.* 47 (2), 113–146. doi:10.2747/0020-6814.47.2.113

Harlow, G. E., and Sorensen, S. S. (2000). *31st international geologic congress*. Rio de JaneiroAbstracts: Congress Program, 72. Brazil, August 6-17, 2000.Jade: Occurrence and metasomatic origin [abs

Harlow, G. E., Sorensen, S. S., Sisson, V. B., and Shi, G. (2014). "Chapter 10: The Geology of jade deposits," in *The Geology of gem deposits. Short course handbook series 44*. Editor Lee A. Groat 2nd Edition (Quebec: Mineralogical Association of Canada), 305–374.

Jiang, B. H., Bai, F., and Zhao, J. K. (2021). Mineralogical and geochemical characteristics of green nephrite from Kutcho, northern British Columbia, Canada. *lithos* 399-389, 106030. doi:10.1016/j.lithos.2021.106030

Jiang, T. L. (2014). *The study on gemological and mineralogical characteristics of nephrite in Sangpiyu, liaoning province. Master thesis*. Beijing, China: China University of Geosciences. (in Chinese with English Abstract).

Jiang, Y., Shi, G. H., Xu, L. G., and li, X. L. (2020). Mineralogy and geochemistry of nephrite jade from Yinggelike deposit, Altyn Tagh (Xinjiang, NW China). *Minerals* 10 (5), 418. doi:10.3390/min10050418

Jiang, Y. (2020). *Study on petro-mineral features and genetic mechanism of Ruoqiang nephrite, Xinjiang province. PhD thesis*. Beijing, China: China University of Geosciences. (in Chinese with English Abstract).

Kim, W. S. (2007). Addressing disparities in access to oral health care in Canada. *Can. Gemmol.* 4 (28), 119–124. doi:10.53581/jopv.2022.4.1.119

Lan, Y. (2022). *Geochemical characteristics and genesis of tremolite jade in Dahua, Guangxi. Master thesis*. Gunagxi: Guilin University of Technology. (in Chinese with English Abstract).

Lei, C., Yang, M. X., and Zhong, Z. Q. (2018). Zircon U–Pb ages and Hf isotopes of the Xiaozaohuo nephrite, eastern Kunlun orogenic belt: Constraints on its ore-forming age. *Geotect. Metallogenia* 42 (1), 108–125. (in Chinese with English Abstract).

Li, H. J., and Cai, Y. T. (2008). Study on characteristics of nephrite from Liyang, Jiangsu province. *J. Gems Gemmology* (03), 16–19. (in Chinese with English Abstract).

Li, J. (2016). *PhD thesis*. China: China University of Geosciences Wuhan. (in Chinese with English Abstract).Mineralogical and gemological characteristics of typical nephrites in China for the origin identification on Liangzhu ancient jades

Li, X., Zhang, C., Behrens, H., and Holtz, F. (2020). Calculating amphibole formula from electron microprobe analysis data using a machine learning method based on principal components regression. *Lithos* 362-363, 105469. doi:10.1016/j.lithos.2020.105469

Li, Y. Z., Liao, G. L., and Zhi, Y. X. (2011). Microstructure and vibration spectrum study of Nephrite from Taiwan. *Acta Petrologica Mineralogica*, 73–77. (in Chinese with English Abstract).

Liao, G. L., Zhou, Z. Y., and Liao, Z. T. (2012). XRD and IR spectra study on green nephrite from taiwan. *J. Gems Gemmology* 14 (04), 23–29. (in Chinese with English Abstract).

Liao, R. Q., and Zhu, Q. W. (2005). Chemical composition analyses of nephrite from all Chinese locations in China. *J. Gems Gemmology* 1 (07), 25–30. (in Chinese with English abstract).

Lin, S. S. (1999). Varieties and characteristics of nephrite (amphibole jade) from taiwan province. *J. Gems Gemmology* (03), 18–20. (in Chinese with English Abstract).

Ling, X. X., Schmädicke, E., Qiu, L.-L., Gose, J., Wu, R. H., Wang, S. Q., et al. (2015). Age determination of nephrite by *in-situ* SIMS U–Pb dating syngenetic titanite: A case study of the nephrite deposit from luanchuan, henan, China. *Lithos* 220-223, 289–299. doi:10.1016/j.lithos.2015.02.019

Ling, X. X., Wu, R. H., Bai, F., Yin, J. N., and Li, W.-W. (2008). A study of tremolite jade from Luanchuan, Henan Province. *Acta Petrologica Mineralogica* 27 (2), 157–163. (in Chinese with English Abstract).

Liu, F., and Yu, X. Y. (2009). Types of deposits and mineralogical characteristics of nephrite in China. *Mineral Resour. Geol.* 23 (04), 375–380. (in Chinese with English abstract).

Liu, X. F., Jia, Y. H., and Liu, Y. (2019). Geochemical characteristics and genetic types of Gobi nephrite in ruoqiang-qiemo, Xinjiang. *Rock Mineral Analysis* 38 (03), 316–325. (in Chinese with English Abstract).

Liu, Y., Deng, J., Shi, G. H., Lu, T. J., He, H. Y., Ng, Y. N., et al. (2010). Chemical zone of nephrite in Alamas, Xinjiang, China. *Resour. Geol.* 60 (3), 249–259. doi:10.1111/j.1751-3928.2010.00135.x

Liu, Y., Deng, J., Shi, G. H., Sun, X., and Yang, L. (2011a). Geochemistry and petrogenesis of placer nephrite from hetian, Xinjiang, northwest China. *Ore Geol. Rev.* 41 (01), 122–132. doi:10.1016/j.oregeorev.2011.07.004

Liu, Y., Deng, J., Shi, G. H., Yu, T. F., Zhang, G., Abuduwayiti, M., et al. (2011b). Geochemistry and petrology of nephrite from Alamas, Xinjiang, NW China. *J. Asian Earth Sci.* 42 (03), 440–451. doi:10.1016/j.jseaes.2011.05.012

Liu, Y. F. (2013). *Metallogenic regularity and prospecting indicator of the jade deposit in the Xiuyan area, liaoning province*. Master thesis. Jilin: Jilin University. (in Chinese with English Abstract).

Liu, Y., He, M. Y., Maituohuti, A., and Shi, G. H. (2011). Genesis of the nephrite from Alamas in hetian, Xinjiang. *Acta Petrologica Mineralogica* 30, 39–46. (in Chinese with English Abstract).

Liu, Y., Zhang, R. Q., Abuduwayiti, M., Wang, C., Zhang, S. P., Shen, C. H., et al. (2016). SHRIMP U–Pb zircon ages, mineral compositions and geochemistry of placer nephrite in the Yurungkash and Karakash River deposits, West Kunlun, Xinjiang, northwest China: Implication for a Magnesium Skarn. *Ore Geol. Rev.* 72, 699–727. doi:10.1016/j.oregeorev.2015.08.023

Liu, Y., Zhang, R., Zhang, Z., Shi, G. H., Zhang, Q., Anuduwayiti, M., et al. (2015). Mineral inclusions and SHRIMP U–Pb dating of zircons from the Alamas nephrite and granodiorite: Implications for the Genesis of a magnesian skarn deposit. *Lithos* 212–215, 128–144. doi:10.1016/j.lithos.2014.11.002

Lu, B. Q., Qi, L. J., Xia, Y. B., and Zhou, K. C. (2004). Mineralogy of nephrite (tremolite) cat's eye from Sichuan Province. *Acta Petrologica Mineralogica* (03), 268–272. (in Chinese with English Abstract).

Lu, B. Q., Qi, L. J., and Xia, Y. B. (2007). Raman spectra of nephrite cat's eye and the relationship between Raman spectra and the cat's eye colors. *J. Chin. Ceram. Soc.* (11), 1492–1494. (in Chinese with English Abstract).

Lu, B. Q., Qi, L. J., and Xia, Y. B. (2008). Study on the vibration spectra of nephrite cat's eye from Sichuan Province. *Shanghai Geol.* (03), 57–60. (in Chinese with English Abstract).

Lu, B. Q. (2005). *The gemological mineralogy and spectroscopy nephrite cat's eye sichuan, sichuan province, southwest China*. PhD thesis. Shanghai: Shanghai University. (in Chinese with English Abstract).

Ma, D. R. (2013). *Characteristics and metallogenic law of the Sanchakou jade ore in Golmud, Qinghai. Master thesis*. Beijing: China University of Geosciences. (in Chinese with English abstract).

Martin, C., Flores, K. E., Vitale-Brovaroned, A., Angiboustf, S., and Harlow, G. E. (2020). Deep mantle serpentinization in subduction zones: Insight from *in situ* B isotopes in slab and mantle wedge serpentinites. *Chem. Geol.* 545, 119637. doi:10.1016/j.chemgeo.2020.119637

McDonough, W. F., and Sun, S. S. (1995). The composition of the Earth. *Chem. Geol.* 120 (3), 223–253. doi:10.1016/0009-2541(94)00140-4

Meng, Y. (2014). *The causes and genesis study of nephrite in Alamas Yutian Xinjiang China*. Master thesis. Beijing, China: China University of Geosciences. (in Chinese with English Abstract).

Qin, Y. (2013). *Study on gemological Characteristics and mineral components of Qinghai black Nephrite*. Master thesis. Beijing, China: China University of Geosciences. (in Chinese with English Abstract).

Qiu, K. F., Goldfarb, R. J., Deng, J., Yu, H. C., Gou, Z. Y., Ding, Z. J., et al. (2020). Gold deposits of the jiaodong peninsula, eastern China. *Seg. Spec. Publ.* 23, 753–773.

Qiu, L. (2016). *Gemological study of nephrite gravel*. Master thesis. Beijing, China: China University of Geosciences. (in Chinese with English Abstract).

Ren, S. M., Zhang, L. J., and Zhang, J. (2012). Mineral composition, microstructure characteristics and generation of taiwan nephrite. *J. Guilin Univ. Technol.* 32 (1), 36–42. (in Chinese with English Abstract).

Song, H. L., Tan, H. L., and Zu, E. D. (2020). Spectral characteristics of Qinghai nephrite with different colors. *Bull. Chin. Ceram. Soc.* 39 (01), 242–246. (in Chinese with English Abstract).

Su, Y., Yang, M. X., Wang, Y. Y., Chang, Y. Y., and Li, Y. (2019). Gemological characteristics of Gobi nephrite from southern Xinjiang, China. *J. Gems Gemmology* 21 (04), 1–10. (in Chinese with English Abstract).

Tang, Y. L., Liu, D. Q., and Zhou, R. H. (2002). Geological characteristics of Manasi green jade in Xinjiang. *Acta Petrologica Mineralogica* 21 (1), 22–25. (in Chinese with English Abstract).

Taylor, H. P., Jr. (1997). "Oxygen and hydrogen isotope relationships in hydrothermal mineral deposits," in *Geochemistry of hydrothermal ore deposits*. Editor H. L. Barnes 3rd ed. (New York: Wiley-Interscience), 229–302.

Tian, S. (2014). *Gemological characteristics and mineral typomorphic characteristics of green Xinjiang manasi nephrite*. Master thesis. Hebei: Shijiazhuang University of Economics. (in Chinese with English Abstract).

Wang, B. Y., Chen, H., and Zhang, Y. (2017). *Mineralogical and gemological characteristics of green nephrite from linwu, hunan province, China*. International Gem and Jewelry Academic Conference. (in Chinese with English Abstract).

Wang, F. (2016). *Black nephrite's characteristics and preliminary study of graphite's influence on its quality. Master thesis*. Xinjiang: Xinjiang University. (in Chinese with English Abstract).

Wang, S. B. (2013). Study on mineralogy and metallogenic temperature of luanchuan nephrite in henan province zhao. *Public Sci. Technol.* 15 (12), 82–84. (in Chinese with English Abstract).

Wang, S. Q., Duan, T. Y., and Zheng, Z. Z. (2002). Mineralogical and petrological characteristics of Xiuyan nephrite and its minerogenetic model. *Acta Petrologica Mineralogica* 21 (1), 79–90. (in Chinese with English Abstract).

Wu, L. J. (2016). *Study on gemological and mineralogical characteristics and genesis of nephrite in Tiantai, Qiemo, Xinjiang. Master thesis*. Beijing, China: China University of Geosciences. (in Chinese with English Abstract).

Wu, Z. Y., Wang, S. Q., and Ling, X. X. (2014). Characteristics and origin of nephrite from Sangpiyu, xiuyan country, liaoning province. *Acta Petrologica Mineralogica* 33 (2), 15–24. (in Chinese with English Abstract).

Xu, H. P., Feng, A. P., Wang, S. Q., Zhu, W. J., and Deng, W. (2000). The origin of Liaoning Xiuyan nephrite placer resources and their protection. *Resour. Sci.* 22 (2), 24–29. (in Chinese with English Abstract).

Xu, H. S., and Bai, F. (2022). Origin of the subduction-related Tieli nephrite deposit in Northeast China: Constraints from halogens, trace elements, and Sr isotopes in apatite group minerals. *Ore Geol. Rev.* 142, 104702. doi:10.1016/j.oregeorev.2022.104702

Xu, L. G., Yu, X. J., and Wang, S. Q. (2014). The gemological characteristics and origin of Donggang Village tremolite jade in Dahua,Guangxi. *Acta Petrologica Mineralogica* (1), 55–60. (in Chinese with English Abstract).

Xu, W., and Liu, F. L. (2019). Geochronological and geochemical insights into the tectonic evolution of the paleoproterozoic jiao-liao-ji belt, Sino-Korean craton. *Earth-Science Rev.* 193, 162–198. doi:10.1016/j.earscirev.2019.04.019

Xu, Y. X., Lu, B. Q., and Qi, L. J. (2015). A petromineralogical and SEM microstructural analysis of nephrite in Sichuan Province. *Shanghai Land and Resour.* 36 (03), 87–89. (in Chinese with English Abstract).

Yang, F., Santosh, M., Tsunogae, T., Tang, L., and Teng, X. M. (2017). Multiple magmatism in an evolving suprasubduction zone mantle wedge: The case of the composite mafic–ultramafic complex of Gaositai, North China Craton. *Lithos* 284-285, 525–544. doi:10.1016/j.lithos.2017.05.004

Yang, J., Zhang, Y. F., Qiu, Z. L., Jia, D. L., and Zheng, X. Y. (2021). Geochemistry and petrogenesis of greenstone belt type serpentine jade from taishan, shandong. *Geotect. Metallogenia* 45 (05), 1044–1059. (in Chinese with English abstract).

Yang, L., Lin, J. H., Wang, L., Wang, B., and Du, Y. (2013). IR spectrum characteristics and significance of luodian jade from Guizhou. *Spectrosc. Spectr. Analysis* 33 (8), 2087–2091. (in Chinese with English Abstract).

Yang, L. (2013). *Study on petro-mineral features and genetic mechanism of luodian jade, Guizhou province. PhD thesis*. Sichuan: Chengdu University of Technology. (in Chinese with English Abstract).

Yang, X. D., Shi, G. H., and Liu, Y. (2012). Vibrational spectra of black species of hetian nephrite (tremolite jade) and its color genesis. *Spectrosc. Spectr. Analysis* 32 (3), 681–685. (in Chinese with English Abstract).

Yin, J. N. (2006). *Petrology and deposit research on nephrite and serpentine of luan chuan, henan province abstract. Master thesis*. Beijing, China: China University of Geosciences. (in Chinese with English Abstract).

Yin, Z., Jiang, C., Santosh, M., Chen, Y. M., Bao, Y., and Chen, Q. L. (2014). Nephrite jade from Guangxi province, China. *Gems Gemology* 50 (3), 228–235. doi:10.5741/gems.50.3.228

Yu, H. Y. (2016). *Coloring and metallogenic mechanisms of different colors in Qinghai nephrite. PhD thesis*. Jiangsu: Nanjing University.

Yu, X. Y. (2016). *Colored gemmology*. 2nd Edition. BeijingBeijing, China: Geology Press, 236–244. (in Chinese).

Yu, X. Y., Long, Z. Y., Zhang, Y., Qi, L. J., Zhang, C., Xie, Z. R., et al. (2021). Overview of gemstone resources in China. *Crystals* 11 (10), 1189. doi:10.3390/cryst11101189

Yui, T. F., Usuki, T., Chen, C. Y., Ishida, A., Sano, Y., Suga, K., et al. (2014). Dating thin zircon rims by NanoSIMS: The fengtien nephrite (taiwan) is the youngest jade on earth. *Int. Geol. Rev.* 56 (16), 1932–1944. doi:10.1080/00206814.2014.972994

Zhang, C., Yu, X. Y., and Jiang, T. L. (2019). Mineral association and graphite inclusions in nephrite jade from Liaoning, northeast China: Implications for metamorphic conditions and ore Genesis. *Geosci. Front.* 10 (2), 425–437. doi:10.1016/j.gsf.2018.02.009

Zhang, C., and Yu, X. Y. (2018). Spectral characteristic and origin identification of tremolite jade from Sangpiyu, liaoning province. *J. Gems Gemmology* 20 (S1), 41–53. (in Chinese with English Abstract).

Zhang, C., Yu, X. Y., Yang, F., Santosh, M., and Huo, D. (2021). Petrology and geochronology of the Yushigou nephrite jade from the North Qilian Orogen, NW China: Implications for subduction related processes. *Lithos* 380-381, 105894. doi:10.1016/j.lithos.2020.105894

Zhang, H. Q. (2019). *Gemology, mineralogy and trace element study on green nephrite from Qinghai province*. Master thesis. Beijing: China University of Geosciences. (in Chinese with English abstract).

Zhang, L. Q. (2013)., 20. Beijing, China: China University of Geosciences, 41–53. (in Chinese with English Abstract).The study on the characteristics of composition, structure and spectroscopy of the nephrite from Luodian*Guizhou Prov. Master thesis*S1

Zhang, Q. C., Liu, Y., Huang, H., Wu, Z. H., and Zhou, Q. (2016). Petrogenesis and tectonic implications of the high-K Alamas calc-alkaline granitoids at the northwestern margin of the Tibetan Plateau: Geochemical and Sr–Nd–Hf–O isotope constraints. *J. Asian Earth Sci.* 127, 137–151. doi:10.1016/j.jseaes.2016.05.026

Zhang, X. C., Shi, G. H., Zhang, X. M., and Gao, K. (2022). formation of the nephrite deposit with five mineral assemblage zones in the central western Kunlun Mountains, China. *J. Petrology* 63, egac117. doi:10.1093/petrology/egac117

Zhang, X. M. (2020). *Mineralogy and genesis of green nephrite in the western section of Manas region, Xinjiang. PhD thesis*. Beijing, China: China University of Geosciences. (in Chinese with English Abstract).

Zhang, Y. D. (2015). *Study on geologic-geochemical property and metallogenic regularity of nephritic ore in luodian county, Guizhou province*. Guizhou: Guizhou University. (in Chinese with English Abstract).

Zhang, Y. W., Liu, Y., Liu, T., and Muhetaer, Z. (2012). Vibrational spectra of hetian nephrite of Xinjiang. *Spectrosc. Spectr. Analysis* 32 (2), 398–401. (in Chinese with English Abstract).

Zhang, Z. W., Gan, F. X., and Cheng, H. S. (2011). PIXE analysis of nephrite minerals from different deposits. *Nucl. Instrum. Methods Phys. Res. B Beam Interact. Mater. Atoms* 269 (4), 460–465. doi:10.1016/j.nimb.2010.12.038

Zheng, F., Liu, Y., and Zhang, H. Q. (2019). The petrogeochemistry and zircon U–Pb age of nephrite placer deposit in xiuyan. *Liaoning, Rock Mineral Analysis* 38 (04), 438–448. (in Chinese with English Abstract).

Zhi, Y. X., Liao, G. L., Chen, Q., Li, Y. Z., and Zhou, Z. Y. (2011). Gemmological and mineralogical characteristics of nephrite from luodian, Guizhou province. *J. Gems Gemmology* 13 (4), 7–13. (in Chinese with English Abstract).

Zhong, H. B. (1995). The discovery of meiling jade in south Liyang,Jiangsu. *Geol. Jiangsu* 19 (3), 176–178. (in Chinese with English Abstract).

Zhong, Q., Liao, Z. T., Qi, L. J., and Zhou, Z. Y. (2019). Black nephrite jade from Guangxi, southern China. *Gems Gemology* 55 (2), 198–215. doi:10.5741/gems.55.2.198

Zhou, Z. Y., Chen, Y., Liao, Z. T., and Y, Y. (2009). A petrological and mineralogical study of Liyang nephrite. *Rock Mineral Analysis* 28 (05), 490–494. (in Chinese with English Abstract).

Zhou, Z. Y., Liao, Z. T., Chen, Y., Li, Y. J., and Ma, T.-T. (2008). Petrological and mineralogical characteristics of Qinghai nephrite. *Rock Mineral Analysis* (01), 17–20. (in Chinese with English Abstract).

Zhou, Z. Y., Liao, Z. T., Ma, T. T., and Yuan, Y. (2005). Study on ore-forming type and genetic mechanism of Sanchakou nephrite deposit in Qinghai province. *J. Tongji Univ. Nat. Sci.* (09), 1191–1194+1200. (in Chinese with English Abstract).

Zou, T. R., Guo, L. H., Li, W. H., and Duan, Y. R. (2002). A study on Raman spectra of Hetian jade, Manasi green jade and Xiuyan old jade. *Acta Petrolocgica Mineralogica* (S1), 72–78. (in Chinese with English Abstract).

Zou, Y., Li, P., Wu, Z. Y., Kang, M. L., and Wang, S. Q. (2021). A study of the mineralization age of nephrite from Sangpiyu, xiuyan count, liaoning province. *Acta Petrologica Mineralogica* 40 (4), 825–834. (in Chinese with English abstract).

frontiers | Frontiers in Earth Science

TYPE Original Research
PUBLISHED 05 April 2023
DOI 10.3389/feart.2023.1124860

Check for updates

OPEN ACCESS

EDITED BY
Fei Xue,
Hohai University, China

REVIEWED BY
Jingyi Wang,
China University of Geosciences, China
Xinkai Hu,
Ministry of Natural Resources, China
Xiaofang He,
China University of Mining and Technology, Beijing, China

*CORRESPONDENCE
Yingjie Li,
liyingjie820@126.com

SPECIALTY SECTION
This article was submitted to Structural Geology and Tectonics, a section of the journal Frontiers in Earth Science

RECEIVED 15 December 2022
ACCEPTED 20 March 2023
PUBLISHED 05 April 2023

CITATION
Wang S, Li Y, Jin S, Dong P, Zhang X, Zhao D, Kong X and Liu P (2023), Petrogenesis and tectonic implications of the Late Jurassic A-type granite in central Inner Mongolia, North China. *Front. Earth Sci.* 11:1124860. doi: 10.3389/feart.2023.1124860

COPYRIGHT
© 2023 Wang, Li, Jin, Dong, Zhang, Zhao, Kong and Liu. This is an open-access article distributed under the terms of the Creative Commons Attribution License (CC BY). The use, distribution or reproduction in other forums is permitted, provided the original author(s) and the copyright owner(s) are credited and that the original publication in this journal is cited, in accordance with accepted academic practice. No use, distribution or reproduction is permitted which does not comply with these terms.

Petrogenesis and tectonic implications of the Late Jurassic A-type granite in central Inner Mongolia, North China

Shuai Wang[1], Yingjie Li[2,3]*, Song Jin[4], Peipei Dong[2], Xiawei Zhang[1], Dongfang Zhao[2,4], Xingrui Kong[2] and Pengyu Liu[5]

[1]School of Earth Sciences and Resources, China University of Geosciences, Beijing, China, [2]College of Earth Sciences, Hebei GEO University, Shijiazhuang, China, [3]Hebei Key Laboratory of Strategic Critical Mineral Resources, Hebei GEO University, Shijiazhuang, China, [4]Geological Institute of China Chemical Geology and Mine Bureau, Beijing, China, [5]School of Science, China University of Geosciences, Beijing, China

Lying along the south of Mongol–Okhotsk Suture Belt (MOSB) in Horqin Right Middle Banner of Inner Mongolia, the Chuhuertu granite is exposed in the Duerji tectonic melange. Based on systematic field geological characteristics, petrology, geochemistry, and zircon U-Pb chronology, we determined the petrogenesis of pluton and the tectonic setting, and provide evidence for the dominant factors of granite magmatism of the study area. LA-ICP-MS zircon U-Pb dating showed an age of 155.6 ± 1.6 Ma, indicating that the formation age of the Chuhuertu granite is Late Jurassic. The granite is geochemically characterized by high SiO_2 (73.04–76.01 wt.%) and alkali (Na_2O + K_2O = 7.81–9.50 wt.%) but low CaO (0.20–0.98 wt.%) and MgO (0.10–0.22 wt.%). The granite has obvious negative Eu anomaly (Eu = 0.30–0.75), relative enrichment of Rb, Th, U, K, and Ga, depletion of Ba, Sr, P, and Ti, as well as high 10000Ga/Al (2.52–2.90), and TFeO/MgO (5.76–14.90). The differentiation index (DI) of the samples is 92.05–96.36. The petrological, mineralogical, and geochemical characteristics of the granite show the characteristics of highly differentiated A-type granite. In accordance with the region, Mesozoic A-type granites have positive correlation $\varepsilon_{Nd}(t)$ values, which suggest that the granite may have formed through partial melting of intermediate basic crust in neoaccretion under low pressure and high temperature, and subsequent crystallization differentiation. Therefore, Chuhuertu granite is the product of extension of the closure of the Mongol–Okhotsk Ocean (MOO), and, together with other A-type granites distributed in mid-eastern Inner Mongolia, indicates extensive middle and lower crust extension in the Late Jurassic.

KEYWORDS

A-type granite, late Jurassic, post orogenic extension, Mongol–Okhotsk Ocean, Inner Mongolia

1 Introduction

The southeastern Central Asian Orogenic Belt (CAOB), which is distributed throughout central Inner Mongolia in North China, is a key area for understanding the tectonic evolution of the CAOB, the world's largest Phanerozoic accretionary orogen between the Siberian Craton (SC) to the north and the Tarim and North China Craton (NCC) to the

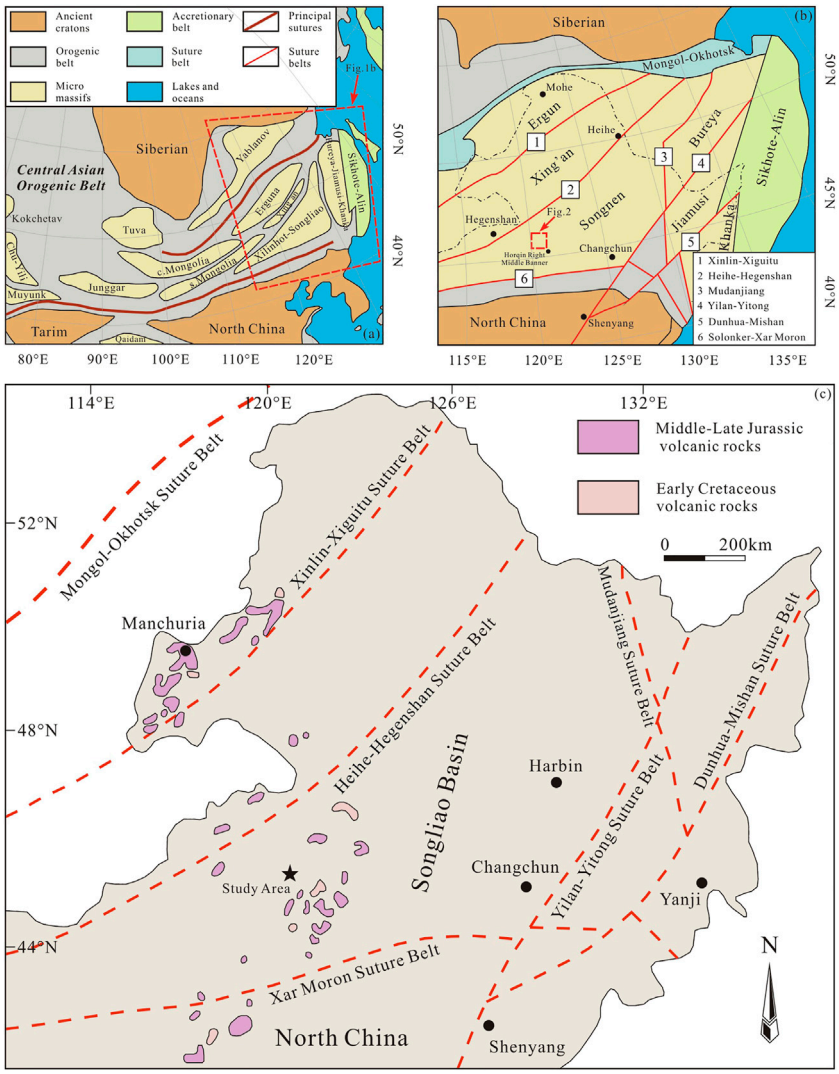


FIGURE 1
(A) Tectonic framework of the North China–Mongolia segment of the Central Asian Orogenic Belt (adapted from Liu et al., 2017). **(B)** Simplified geological map of NE China showing the main tectonic subdivisions (adapted from Zhou et al., 2015a). **(C)** Distribution map (adapted from Xu et al., 2013) of Middle-Late Jurassic and Early Cretaceous volcanic rocks in NE China.

south (Figure 1A) (Xiao et al., 2003; Windley et al., 2007). It is characterized by a series of island arcs, forearc and back-arc basins, ophiolitic belts, and microcontinental fragments with ages ranging from the Neoproterozoic to the Mesozoic (Jahn et al., 2000; Zhang et al., 2009a; Zhang et al., 2014; Li et al., 2018; Cheng et al., 2014; Cheng et al., 2020; Li et al., 2020; Liu et al., 2021). Before the Early Mesozoic, the southeastern CAOB was strongly influenced by the Paleo-Asian Ocean (PAO) tectonic regime (Nozaka and Liu, 2002; Liu et al., 2005; Miao et al., 2008; Jian et al., 2010; Safonova et al., 2017). There are two main viewpoints on the final closure time of the PAO. One viewpoint is based on the chronology and geochemistry of ophiolites and Carboniferous–Permian intrusive rocks. It is believed that the PAO continued to subduct from the Ordovician to the Permian, until the closure during the Late Permian–Early Triassic (Xiao et al., 2003; Jian et al., 2010; Li et al., 2018; Li et al., 2020). The other viewpoint is based on the study of orogenic belt structure, tectonic deformation, stratigraphic unconformity, and post orogenic A-type granite, and suggests that the PAO was closed before the Late Devonian–Early Carboniferous (Xu et al., 2014; Shao et al., 2015). During the Jurassic, with the final closure of the PAO, the southeastern CAOB was already in the tectonic environment of the Paleo-Pacific Ocean (PPO) and MOO tectonic regimes (Meng et al., 2011; Xu et al., 2013; Wang et al., 2015; Wu et al., 2017; Gao et al., 2021; Jiang et al., 2021). Thus, it is considered an ideal region in which to study the PAO tectonic regime and the superposition of MOO and PPO tectonic regimes during the Late Jurassic period.

The multi-plate convergence in NE China has resulted in a widespread occurrence of voluminous Late Mesozoic granitic–magmatic rocks, making it one of the world's largest granitic provinces (Wu et al., 2011; Xu et al., 2013). However, researchers have yet to clarify the trigger system of Late

Mesozoic granitic magmatism, especially for Late Jurassic granitic magmatism.

According to some researchers, the Late Jurassic granitic magmatism in NE China has been connected to flat-slab subduction of the PPO plate (Zhang et al., 2010; Ji et al., 2019). Several additional studies hypothesized that the MOO slab retreat and oceanic ridge subduction (Deng et al., 2019), as well as orogenic collapse following the closure of the MOO, were responsible for the Late Jurassic granitic magmatism in NE China (Xue et al., 2015; Li et al., 2018). These Late Jurassic granitic magmatic rocks in NE China are mainly located in the Ergun-Xing'an Massifs, southwestern Songnen Massif, and at the northern margin of NCC. The perspectives described previously are almost entirely based on the Jurassic tectonic magmatism in the Ergun, southwestern Songnen, and the northern Xing'an Massifs. However, the southeastern CAOB west of the Greater Xing'an Range has received little attention (Gillespie et al., 2017). As a result, additional research on the Late Jurassic igneous rocks in the southeastern CAOB is required to constrain its Jurassic tectonic setting.

In general, granitic rock types with various origins have a remarkable correlation with the tectonic environment (Pearce, 1996). Hence granitoids may provide important information regarding the coeval tectonic setting. A Late Jurassic granite was identified during our investigation in the southeastern CAOB and classed as an A-type granite. These findings, combined with the existing geochronology and geochemistry results for Jurassic-Early Cretaceous magmatic rocks in the southeastern CAOB (Zorin, 1999; Parfenov et al., 2001; Wang et al., 2006; Xu et al., 2013; Jiang et al., 2021), provide petrological, geochemical, and chronological evidence for determining the dominant factors controlling the Late Jurassic granite magmatism in the region.

2 Geological setting

The southeastern CAOB is bordered by the Pacific tectonic system to the east, the northern margin of NCC to the south, and the southern margin of SC to the north (Figure 1A), and formed by collision and suture of several microcontinental fragments (Liu et al., 2017). From north to south, it is divided into Ergun Massif, Xing'an Massif, Songnen Massif, and Bureya–Jiamusi–Khanka Massif by Xinlin–Xiguitu Suture Belt, Heihe–Hegenshan Suture Belt, and Mudanjiang Suture Belt (Figure 1B).

The southeastern CAOB is characterized by large-scale Phanerozoic magmatism (Wu et al., 2002; Wu et al., 2011). The Paleozoic magmatism in the southeastern CAOB is considered the result of southward subduction of the PAO plate (Zhang et al., 2009b). The Late Triassic tectonomagmatic events may have been related to the slab retreat of the subducting MOO (Meng et al., 2020). During the Jurassic and Cretaceous, the southeastern CAOB experienced overprinting effects from the Paleo-Pacific tectonic regime in the east (Wu et al., 2002; Wu et al., 2011; Zhu and Xu, 2019) and the Mongol–Okhotsk tectonic regime in the north (Wang et al., 2015; Wang et al., 2017).

The subduction of the Paleo-Pacific plate beneath the Northeast Asian continental margin has been differentially considered to have occurred at the Early Permian, the Triassic, or the Jurassic (Wang et al., 2017). Recently, growing evidence indicates that the subduction of the Paleo-Pacific plate started no later than the Early Jurassic (Xu et al., 2013; Zhang et al., 2018; Ji et al., 2019; Gao et al., 2021). Furthermore, the previous study suggested that low-angle flat slab subduction of the Paleo-Pacific plate beneath the eastern Eurasia continent occurred during the Jurassic, and then, the subducting slab experienced a slab rollback during the Early Cretaceous (Ji et al., 2019). On the other hand, although the timing of the opening of the MOO remains controversial, its subduction history has been constrained to the period from the Devonian to the Jurassic (Donskaya et al., 2013). The MOO closed in a scissor-like pattern and finally formed the MOSB, which was related to the collision between the SC in the north and the Central Mongolian Massif in the south, from west to east (Donskaya et al., 2013). Thus, many researchers suggested that the western part of the MOO closed earlier, i.e., in the Early-Middle Jurassic (Parfenov et al., 2001; Zhang et al., 2020), whereas the eastern part closed later, i.e., in the Late Jurassic–Early Cretaceous (Donskaya et al., 2013).

Jurassic–Cretaceous granitoids developed mainly in NE China, but have been reported, albeit rarely, in southeastern Inner Mongolia. Furthermore, through zircon U-Pb dating of 370 samples from granites widely developed in NE China, and combining those data with 63 ages obtained by other researchers, Wu et al. (2011) concluded that Jurassic granites developed mainly in the east and Cretaceous granites in the west. Jurassic granitoids in the east portion of NE China were likely related to the subduction of the Pacific plate, whereas the contemporaneous granitoids in the Erguna Massif in the northwest might be related to the subduction and subsequent closure of the MOO (Wu et al., 2011).

The newly discovered granite described here is located in the Chuhuertu farm area, ~40 km to the northwest of the Horqin Right Middle Banner. The Chuhuertu granite is exposed in the southwest of the Duerji tectonic melange. The pluton is distributed as a small stock in the ENE-WSW, of about 3.5 km length and 1 km width, with an exposed area of about 3.5 km^2. The southeast intrudes Late Triassic syenogranite, the northwest is intruded by Early Cretaceous monzonitic granite, and the pluton is partially intruded by Early Cretaceous granite-porphyry and covered by Quaternary rocks. The main rock type is syenogranite, the middle is medium-grained syenogranite, and the edge is transited to fine-grained, without obvious mylonitization (Figure 2). The Duerji tectonic melange is composed of "matrix" and "blocks." The "matrix" is mainly a set of marine clastic rocks with strong deformation and weak metamorphism, composed of tectonic schist, metasandstone, and phyllite, and some of them have the characteristics of flysch sedimentary formation, formed in the tectonic environment of an active continental margin. On the other hand, the "blocks" rock type is pyroxene amphibolite, amphibolite, basalt, diabase, and diorite, and has no significant deformation. The marine clastic rocks are strongly deformed. Due to strong compression, crumple developed and local fractures are sandwiched between magmatic rocks as fault gouges. The surface outcrops are mainly magmatic rocks, which are wrapped in marine clastic rocks as irregular blocks. Different magmatic rocks are also in fault contact, and the edges are developed with different degrees of schistosity. Simultaneous schistosity or mylonitic foliation is developed at the contact segment of rock faults (Jin, 2020).

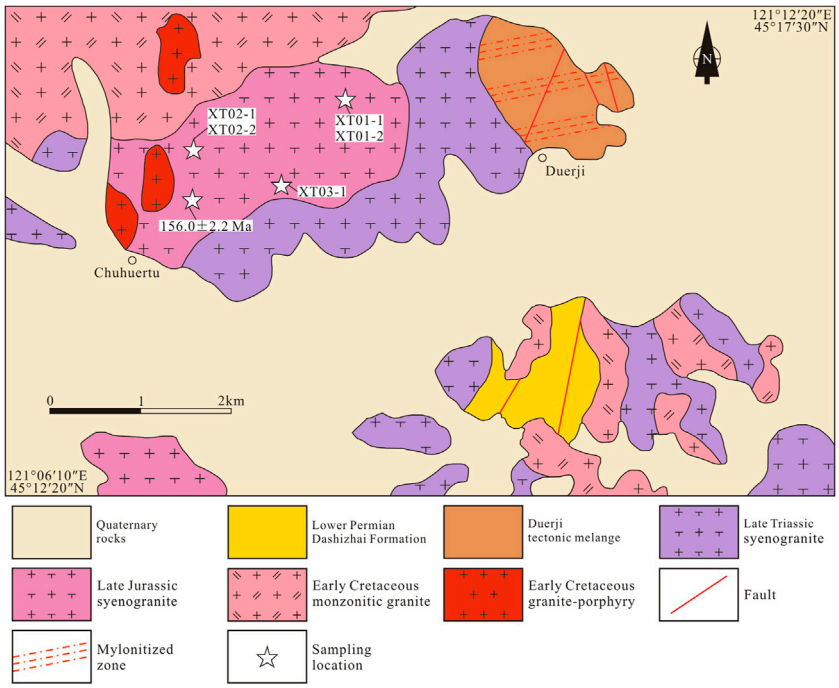


FIGURE 2
Simplified geological map of the Chuhuertu region in Horqin Right Middle Banner, Inner Mongolia.

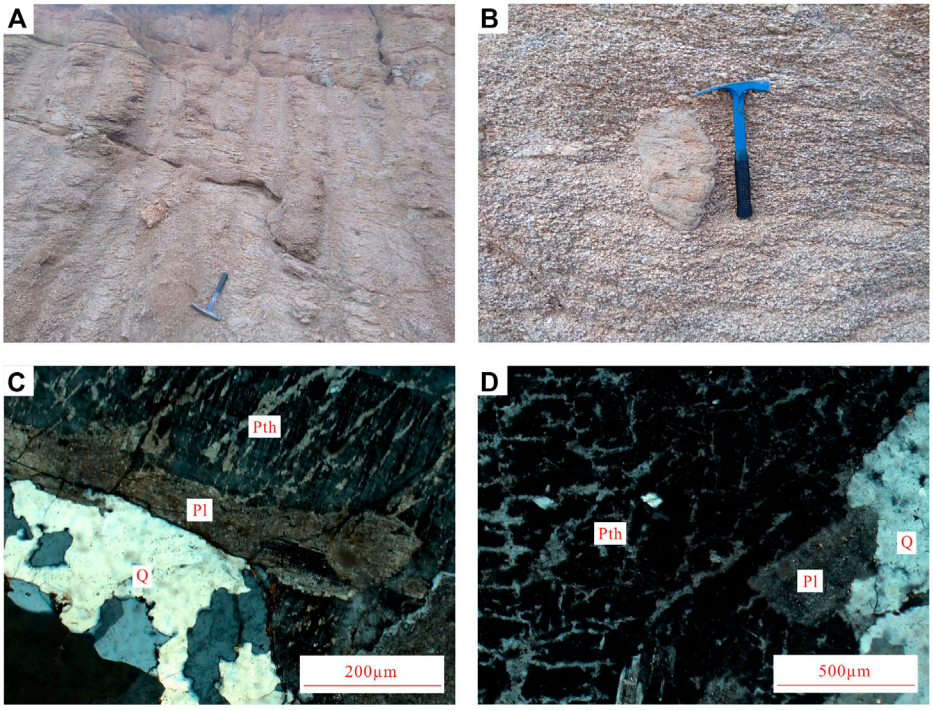


FIGURE 3
Macrofeatures and photomicrographs of the granite in Chuhuertu. **(A)** Macrofeatures; **(B)** field occurrence; **(C,D)** micrographs of the granite. Pl, plagioclase; Pth, perthite; Q, quartz.

10.3389/feart.2023.1124860

TABLE 1 Major and trace element data from Chuhuertu granite.

Sample	XT01-1	XT01-2	XT02-1	XT02-2	XT03-1	A-type granite worldwide	A-type granite in China
Major element (wt%)[a]							
SiO_2	74.30	74.89	75.28	76.01	73.04	73.81	73.55
TiO_2	0.17	0.19	0.18	0.11	0.15	0.26	0.23
Al_2O_3	13.02	13.01	12.50	12.15	13.85	12.40	12.81
FeO^{Tb}	1.66	1.21	1.46	1.49	1.36	2.70	2.46
MnO	0.04	0.06	0.06	0.04	0.05	0.060	0.090
MgO	0.20	0.21	0.22	0.10	0.15	0.20	0.27
CaO	0.54	0.98	0.31	0.20	0.35	0.75	0.82
Na_2O	3.42	3.56	3.99	3.58	4.69	4.07	3.76
K_2O	4.73	4.25	5.44	5.11	4.81	4.65	4.69
P_2O_5	0.06	0.06	0.03	0.03	0.03	0.040	0.070
Total[c]	99.10	99.08	100.38	99.67	99.09		
LOI	0.87	0.63	0.82	0.78	0.55		
$K_2O + Na_2O$	8.15	7.81	9.43	8.69	9.50		
A/CNK	1.11	1.06	0.96	1.03	1.02		
A/NK	1.21	1.24	1.00	1.06	1.07		
TFeO/MgO	8.30	5.76	6.64	14.90	9.07		
DI	93.19	92.05	96.69	96.36	95.70		
Trace element (ppm)							
Rb	201	163	215	210	158	169	269.69
Zr	144	125	111	122	198	528	333.77
Hf	5.72	5.36	4.06	5.78	7.53		
Ta	1.39	1.20	0.82	0.75	1.30		
Sr	118	242	69.3	59.1	179	48	57.54
Sample	XT01-1	XT01-2	XT02-1	XT02-2	XT03-1	A-type granite worldwide	A-type granite in China
Ba	359	432	453	269	528	352	235.96
Nb	10.0	7.67	8.05	5.95	8.71	37	34.93
Ga	18.4	19.9	16.7	18.7	19.5	24.6	18.54
Th	26.3	18.0	27.9	21.3	27.8	23	
U	4.45	2.20	2.42	1.65	3.61	5.00	
La	32.6	30.1	15.8	30.8	28.4		
Ce	69.8	39.8	57.0	64.5	58.3		
Pr	7.91	7.30	4.45	7.00	6.4		
Nd	29.4	27.6	16.3	26.3	24.4		
Sm	5.80	4.50	3.36	4.80	4.40		
Eu	0.65	0.90	0.75	0.40	0.60		
Gd	4.52	3.50	2.75	4.10	4.00		
Tb	0.81	0.50	0.48	0.70	0.70		

(Continued on following page)

TABLE 1 (*Continued*) Major and trace element data from Chuhuertu granite.

Sample	XT01-1	XT01-2	XT02-1	XT02-2	XT03-1	A-type granite worldwide	A-type granite in China
Dy	4.99	2.70	3.13	4.00	4.20		
Ho	1.01	0.50	0.62	0.80	0.90		
Er	2.92	1.60	1.79	2.40	2.50		
Tm	0.48	0.30	0.33	0.40	0.40		
Yb	3.30	2.10	2.26	2.90	2.80		
Lu	0.54	0.40	0.33	0.40	0.50		
Y	28.6	15.5	17.8	21.9	24.3	75	54.03
Total REE	164.73	121.76	109.35	149.55	138.38		
LREE	146.16	110.18	97.66	133.83	122.49		
HREE	18.57	11.58	11.69	15.72	15.89		
LREE/HREE	7.87	9.51	8.35	8.51	7.71		
$(La/Yb)_N$	7.09	10.14	5.01	7.57	7.17		
δEu	0.39	0.68	0.75	0.30	0.43		
10,000*Ga/Al	2.67	2.88	2.52	2.90	2.66	3.75	
T_{Zr} (°C)	787	771	750	767	803		

[a]All oxide contents of the samples have been recalculated to 100% on a volatile-free basis.
[b]FeO^T as total FeO.
[c]Total before normalization.
Data sources: A-type granite worldwide and in China (Wu et al., 2007).

3 Samples and analytical methods

3.1 Samples

The Chuhuertu granite is generally grayish white to pink in color, with medium-fine-grained hypidiomorphic granular structure and stripe structure, and massive texture (Figures 3A, B). This rock contains mainly alkali feldspar (55–60 vol.%), quartz (−20 vol.%), plagioclase (10–15 vol.%), biotite (−5 vol.%), and accessory magnetite. Mineral particle size is generally 0.2–5 mm. The alkaline feldspar is in the form of hypidiomorphic–xenomorphic plate-type, mainly composed of orthoclase, perthite, and microcline feldspar, with a particle size of 0.2–5 mm. Among them, perthite is primarily in the form of fine veins and branches arranged in the same direction (Figure 3D). The plagioclase is mainly andesine and oligoclase, in the form of euhedral-hypidiomorphic plate-type, with polysynthetic twin, occasionally with ring structure, and a particle size of 0.2–4 mm. Quartz is found as fill between plagioclase and alkali feldspar, with xenomorphic granular texture, a particle size of 0.2–5 mm, cracks, and wavy extinction. Biotite is distributed in a scale-blade shape with a diameter of 0.2–2 mm (Figures 3C, D).

In order to study the geochemical and chronological characteristics of the Chuhuertu granite, five geochemical samples were collected (Table 1), along with one (Table 2) zircon U-Pb sample, from different parts of the pluton on the basis of detailed field geological observations. The weathering degree of the samples was low, and free from oxidation, pollution, and obvious alteration. See Figure 2 for the sampling locations.

3.2 Analytical methods

The whole-rock geochemical analyses were undertaken at the Central Laboratory of China Chemical Geology and Mine Bureau, Beijing, China. The zircon selection and target making were completed by the Beijing Kehui Testing Technology Co., Ltd., Beijing, China, and zircon U-Pb isotopic analyses were undertaken at the Beijing SHRIMP Center.

A Zsx Primus II wavelength dispersive X-ray fluorescence spectrometer (XRF) produced by RIGAKU, Japan, was used for the analysis of major elements in the whole rock; the X-ray tube was a 4.0 Kw end window Rh target. All major element analysis lines were kα, and the standard curve used the national standard material: the rock standard sample GBW07101-14. The relative standard deviation (RSD) was less than 2%.

Trace-element analyses of whole-rock were conducted on an Agilent 7700e ICP-MS. The detailed sample-digesting procedure was as follows: 1) Sample powder (200 mesh) was placed in an oven at 105°C for drying for 12 h; 2) an amount of 50 mg of sample powder was accurately weighed and placed in a Teflon bomb; 3) a measure of 1 mL of HNO_3 and 1 mL of HF were slowly added into the Teflon bomb; 4) the Teflon bomb was enclosed in a stainless steel pressure jacket and heated to 190°C in an oven for >24 h; 5) after cooling, the Teflon bomb was opened and placed on a hotplate at 140°C and evaporated to incipient dryness, and then, 1 mL HNO_3 was added and evaporated to dryness again; 6) a measure of 1 mL of HNO_3, 1 mL of MQ water, and 1 mL of internal standard solution at 1 ppm were added, and the Teflon bomb was resealed and placed in the oven at 190°C for >12 h; 7) the final solution was transferred to a

TABLE 2 LA-ICP-MS zircon U-Pb isotopic analysis of the Chuhuertu granite.

Spot no.	Element (ppm)		Th/U	Isotopic ratios						Apparent age (Ma)					
	Th	U		$^{206}Pb/^{238}U$	1σ	$^{207}Pb/^{235}U$	1σ	$^{207}Pb/^{206}Pb$	1σ	$^{206}Pb/^{238}U$	1σ	$^{207}Pb/^{235}U$	1σ	$^{207}Pb/^{206}Pb$	1σ
TW04 Chuhuertu granite															
01	195	470	0.42	0.0238	0.0003	0.1628	0.0050	0.0496	0.0014	152	2	153	4	176	65
02	200	486	0.41	0.0243	0.0004	0.1648	0.0050	0.0492	0.0014	155	2	155	4	167	73
03	106	228	0.46	0.0247	0.0005	0.1695	0.0083	0.0497	0.0022	157	3	159	7	183	104
04	111	218	0.51	0.0248	0.0003	0.1798	0.0082	0.0529	0.0025	158	2	168	7	324	109
05	395	682	0.58	0.0247	0.0002	0.1726	0.0046	0.0507	0.0014	157	2	162	4	228	68
06	100	247	0.41	0.0248	0.0004	0.1756	0.0083	0.0513	0.0024	158	2	164	7	254	110
07	415	882	0.47	0.0243	0.0002	0.1812	0.0047	0.0540	0.0013	155	1	169	4	372	56
08	92	152	0.60	0.0242	0.0007	0.1807	0.0125	0.0543	0.0037	154	5	169	11	383	156
09	130	299	0.44	0.0248	0.0003	0.1630	0.0083	0.0482	0.0027	158	2	153	7	109	130
10	418	882	0.47	0.0244	0.0003	0.1791	0.0063	0.0533	0.0018	155	2	167	5	343	78

10.3389/feart.2023.1124860

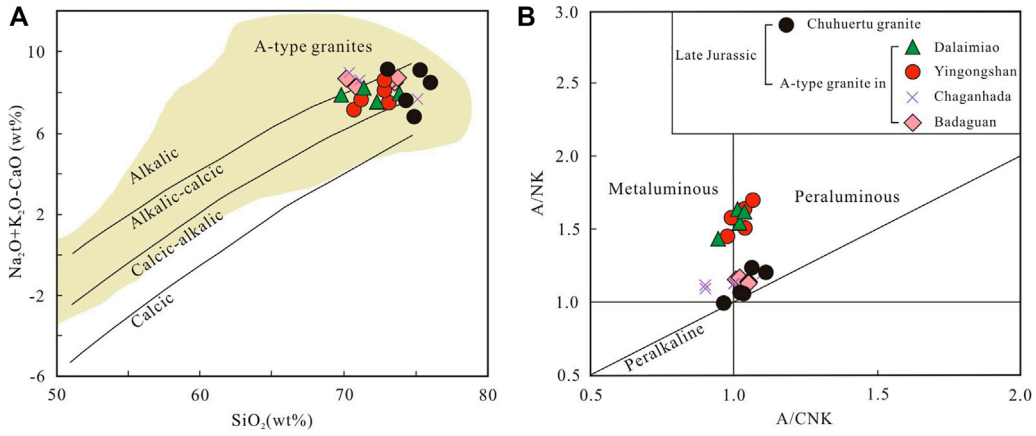


FIGURE 4
(A) SiO_2 versus Na_2O + K_2O—CaO diagram (adapted from Frost and Frost, 2008) and **(B)** A/CNK versus A/NK diagram (adapted from Maniar and Piccoli, 1989) for the granite in Chuhuertu. Data sources: A-type granite in Dalaimiao (Xue et al., 2015), Yingongshan (Gao et al., 2021), Chaganhada (Gao et al., 2022), and Badaguan (Tang et al., 2015).

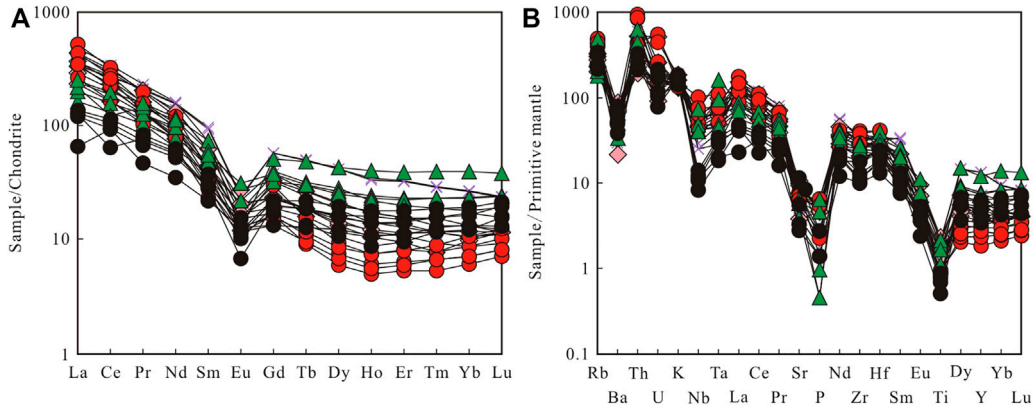


FIGURE 5
(A) Chondrite-normalized REE diagram and **(B)** primitive-mantle-normalized trace element diagram for the granite in Chuhuertu. The normalizing values are from Sun and McDonough (1989). Symbols are the same as in Figure 4.

polyethylene bottle and diluted to 100 g *via* the addition of 2% HNO_3.

The zircon U-Pb dating method used was LA-ICP-MS *in-situ* U-Pb isotope dating, and the test instrumentation included a NWR193 laser ablation system and Jena PQMS inductively coupled plasma mass spectrometry. The depth of laser denuded zircons was 20–40 μm. The diameter of the denudation beam spot was 35 μm. The international standard zircon 91,500 was used as the external zircon age standard for isotopic fractionation correction, and the element content was corrected with the standard sample NIST SRM610 as the external standard and ^{29}Si as the internal standard. The test results were processed and mapped using ICPMSDataCal software (Liu et al., 2008), and the ^{208}Pb correction method was used to correct the common lead (Anderson, 2002).

4 Analytical results

4.1 Major and trace element geochemistry

The Chuhuertu granite has LOI content ranging from 0.55 to 0.87 wt.% (Table 1), consistent with petrographic evidence for partial alteration. In addition, the elements Li, Rb, Cs, K, U, and P may be readily mobilized in rocks during hydrothermal alteration (Hart et al., 1999; Bach et al., 2001). Consequently, in the following descriptions and discussion, the major element contents were normalized to 100 wt.% on an anhydrous basis, considering all Fe as FeO; we preferentially used elements that are relatively insensitive to alteration, such as SiO_2, Al_2O_3, TiO_2, MgO, Fe_2O_3, high-field-strength elements (HFSE), rare-earth elements (REE), Th, and Ba.

Chemical data for five whole-rock samples of the Chuhuertu granite are presented in Table 1. The samples showed high SiO_2

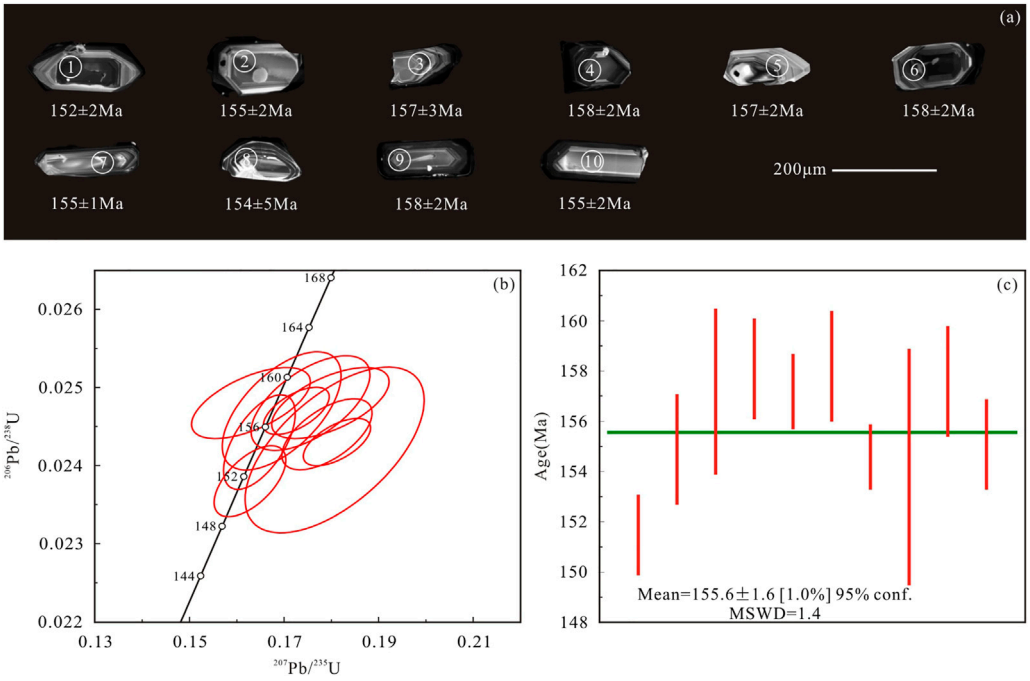


FIGURE 6
(A) Representative cathodoluminescence (CL) images, **(B)** concordia curves, and **(C)** weighted mean age of LA-ICP-MS U-Pb data for the granite in Chuhuertu.

(73.04–76.01 wt.%) and K_2O (4.25–5.44 wt.%) content. At the same time, the samples had high Na_2O (3.42–4.69 wt.%) content, and the high total K_2O + Na_2O content (7.81–9.50 wt.%) suggested material rich in alkali. The SiO_2 versus Na_2O + K_2O – CaO diagram (Figure 4A) indicates samples with calcic-alkali to alkali features. The samples had low CaO (0.20–0.98 wt.%), MgO (0.10–0.22 wt.%), P_2O_5 (0.03–0.06 wt.%), and TiO_2 (0.11–0.19 wt.%) content. The Al_2O_3 content of samples was high, at 12.86–13.45 wt.%. In the A/CNK versus A/NK diagram (Figure 4B), samples fall into quasi-aluminous and peraluminous areas, with A/CNK values (molar $Al_2O_3/(CaO + Na_2O + K_2O)$ = 0.96–1.11) and A/NK values (molar $Al_2O_3/(Na_2O + K_2O)$ = 1.00–1.24) showing weakly peraluminous characteristics.

The total amount of rare earth elements (ΣREE) found in the samples was in the range of 109.35–164.73 ppm, with an average of 136.75 ppm (Table 1). The normalized REE distribution diagram of chondrites indicates "Seagull type" (Figure 5A), with obvious negative Eu anomaly, and δEu of 0.30–0.75, with an average value of 0.51. The REE curve for the samples has a generally gentle right dip, the light REE (LREE) appears slightly enriched, and the heavy REE (HREE) curve is relatively flat. The negative Eu of the samples is abnormally significant, suggesting that the pluton may be affected by the fractional crystallization of plagioclase or related to residual plagioclase in the source area (Eby, 1992). In terms of trace elements, the samples were enriched in Rb, Th, U, K, and Ga, and depleted in Ba, Sr, P, and Ti (Figure 5B), showing the unique component characteristics of A-type granite (Eby, 1992).

4.2 Zircon U-Pb ages

The representative zircon U-Pb data are listed in Table 2. Most zircon grains separated from the granite sample TW04 showed similar crystal shapes and subhedral to euhedral morphologies, with no evidence of resorption or inherited cores. The zircon grains were transparent, colorless, and showed oscillatory zoning, consistent with a magmatic origin (Figure 6A). All zircon grains had high Th/U ratios (0.41–0.60); Table 2), supporting a magmatic origin (Hoskin and Schaltegger, 2003). Ten analyses of zircons from sample TW04 yielded concordant zircon $^{206}Pb/^{238}U$ ages, ranging from 152 ± 2 to 158 ± 2 Ma. These data yielded a weighted-mean age of 155.6 ± 1.6 Ma (MSWD = 1.4) (Figures 6B, C), interpreted as the crystallization age of the Chuhuertu granite.

5 Discussion

5.1 Petrogenesis of the Chuhuertu granite

The Chuhuertu granite was characterized by high concentrations of SiO_2 and K_2O + Na_2O, but low CaO, MgO, P_2O_5, and TiO_2, with obvious negative Eu anomaly. The trace elements Rb, Th, K, Ta, and Hf were relatively enriched, while the elements Ba, Sr, P, and Ti were relatively depleted, and all had high (Na_2O + K_2O)/CaO (15.08–21.39) and TFeO/MgO (29.16–57.82) values. At the same time, the Chuhuertu granite had high Ga (16.70–19.86 ppm) values, and its 10000Ga/Al value was 2.52–2.90. Except for sample XT02-1, the samples had greater

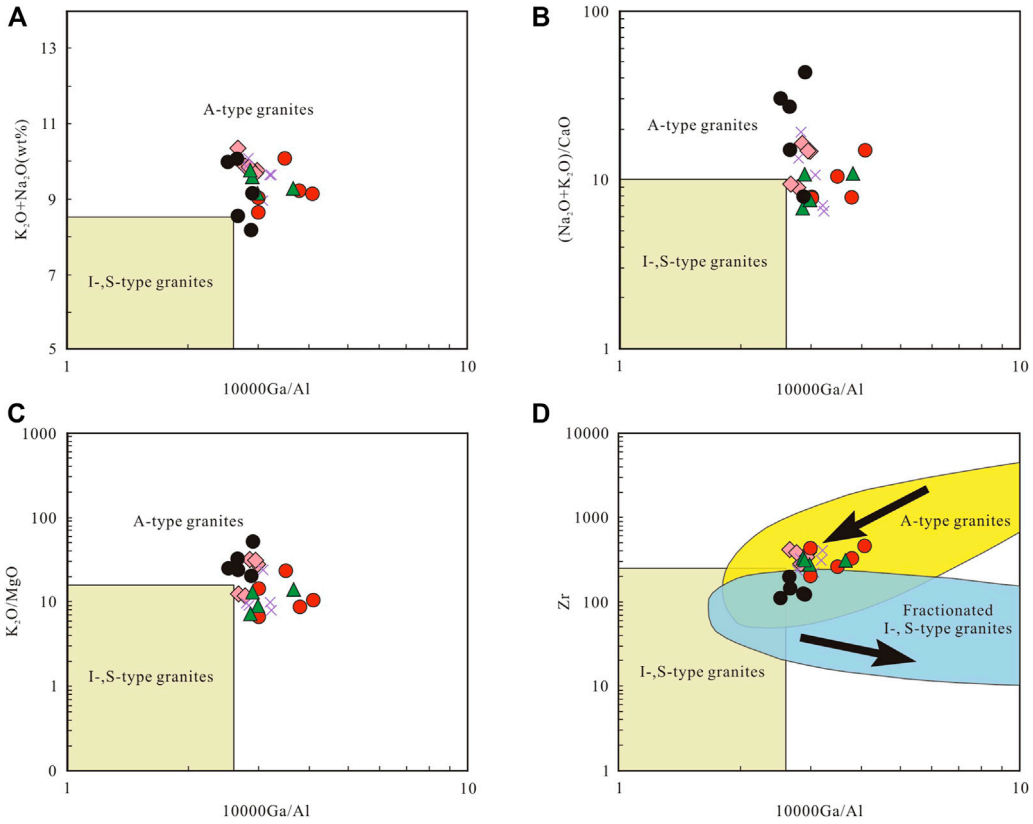


FIGURE 7
10000Ga/Al versus $K_2O + Na_2O$ **(A)**, $(N_2O + ka_2O)/CaO$ **(B)**, K_2O/MgO **(C)**, and TFeO/MgO **(D)** diagram (adapted from Whalen et al., 1987; Wu et al., 2017) for the granite in Chuhuertu. Symbols are the same as in Figure 4.

than the lower limit of 2.6 for A-type granite. In the four widely used 10000Ga/Al versus $K_2O + Na_2O$, $(N_2O + ka_2O)/CaO$, K_2O/MgO, and Zr granite discrimination diagrams (Figure 7), except for sample XT02-1 in Figure 7D, the samples fall into the A-type granite area. The aforementioned geochemical characteristics show that the Chuhuertu granite has the characteristics of A-type granite. However, the DI of the samples was found to be 92.05–96.36, and some samples plot in the fractional granite field (Figure 7D), which may be a result of crystallization fractionation. Crystallization fractionation could easily modify the geochemical composition of granite, and most of the highly fractionated granites have pseudo A-type features. Therefore, it remains unclear whether crystallization fractionation has taken place in Chuhuertu granite.

It is not a straightforward task to distinguish the highly fractionated from A-type granites, especially aluminous A-type granites. Whalen et al. (1987) found that A-type granites are low in Al but high in Ga and Zr concentrations, and then proposed that 10000Ga/Al = 2.6 and Zr = 250 ppm might indicate boundaries between A-type and other types of granites (A-type granite has 10000Ga/Al ratio > 2.6 and Zr > 250 ppm). However, quite a few highly fractionated granites also have a high 10000Ga/Al ratio similar to A-type granites (Perez-Soba and Villaseca, 2010; Breiter et al., 2013). Likewise, A-type granite, if intensively fractionated, is geochemically overlapping with highly fractionated granite (King et al., 2001). To address this problem, we adopted the classification method proposed by Wu et al. (2017). First, A-type granite is characterized by its high temperature of magma. However, the crystallization temperature of magma tends to decrease in the process of magmatic differentiation. Second, fractional crystallization will shift rock type from A-type to highly fractionated granite, as shown in Figure 7D. On the contrary, the fractionation of I- or S-type granites by crystal differentiation would increase their 10000Ga/Al ratios, and thus, another kind of evolutionary trend is observed (Figure 7D). Therefore, A-type granite can be effectively distinguished from highly fractionated I- or S-type granites, although the former occasionally shows an intensive magmatic differentiation. The data from samples from the Chuhuertu granite clearly showed an A-type granite differentiation trend (Figure 7D), indicating its A-type affinity. In addition, highly fractionated granitic magma is easily contaminated by country rocks due to its relatively prolonged crystallization time (Wu et al., 2017). During the early stage, the surrounding rocks are continuously assimilated by the magma, but the fractional crystallization leads to the surrounding rock being rarely observed in this granite. However, as the temperature of the magma gradually decreases with differentiation, the residual melt is not able to digest the surrounding rocks as assimilation proceeds. At the same time, the residual melt is low in capacity for movement, resulting in abundant xenocrysts of the surrounding rocks in the final solidified granite. Although the Chuhuertu granite has

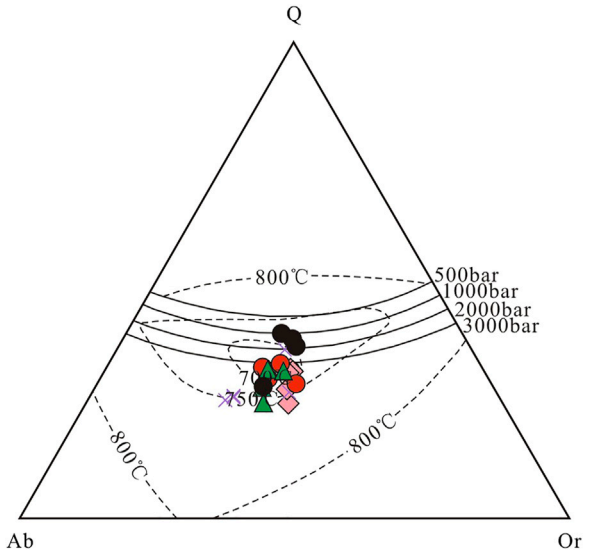


FIGURE 8
Q-Ab-Or-H_2O diagram (adapted from Chen et al., 2005) for the granite in Chuhuertu. Symbols are the same as in Figure 4.

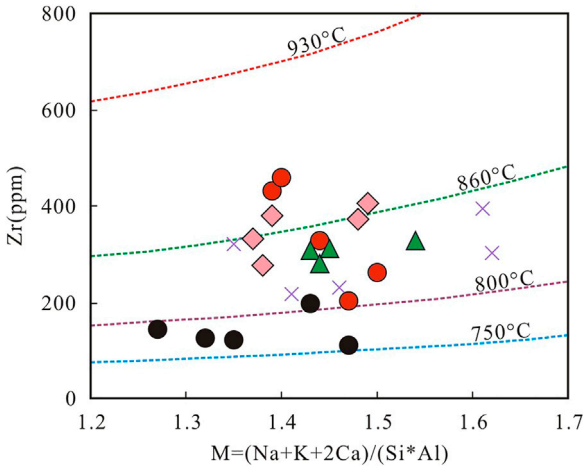


FIGURE 9
M values versus Zr content diagram (adapted from Gao et al., 2021) for the granite in Chuhuertu. Symbols are the same as in Figure 4.

undergone crystallization differentiation, there are few xenocrysts in the pluton. Therefore, the Chuhuertu granite may have been in the early stage of contamination when it crystallized. At the same time, in the A/CNK versus A/NK diagram (Figure 4B), the samples fall into quasi-aluminous and peraluminous areas, with A/CNK values (0.96–1.11) and A/NK values (1.00–1.24), indicating that the A-type granite should be weakly peraluminous, which is consistent with the geochemical characteristics of A-type granite in the eastern segment of CAOB (Liu et al., 2005; Zhou et al., 2010; Zhang et al., 2012; Shi et al., 2014; Xue et al., 2015).

A-type granites can be formed in a variety of petrogenetic processes, which can be summarized into the following three types: mixing of crust-derived acidic magma and mantle-derived basic magma (Griffin et al., 2002; Barbarin, 2005); low degree partial melting or crystallization differentiation of mantle-derived basaltic magma (Turner et al., 1992; Lee and Bachmann, 2014); and partial melting of crust-derived materials (Chappell and White, 2001; Sisson et al., 2005). The Chuhuertu granite has high SiO_2 content and narrow range. There are no contemporaneous mafic rocks or mafic enclaves, and Chuhuertu granite does not have the characteristics of crystallization fractionation of mantle-derived alkaline basaltic magma and mixing of mantle-derived magma and crust-derived magma formed by deep melting. The lower REE content and right-dipping REE diagram (Figure 5A) of the Chuhuertu granite indicate that there is no residual garnet in the source area. The strong depletion of Sr and Ba indicates that the residual phase in the source area contains feldspar, and the strong depletion of Sr and Eu (Figure 5B) reveals that the plagioclase in the source area is the main residual phase, reflecting that the source area is a shallow low pressure area (<10 kbar) without garnet residue and enriched plagioclase (Rapp and Watson, 1995), which should be the petrogenesis of partial high-temperature melting of intermediate basic crust in neoaccretion under low pressure and subsequent crystallization differentiation. These characteristics of Chuhuertu granite reveal that the area is in an extensional environment, similar to the petrogenesis of the A-type granite in the eastern segment of CAOB in mid-eastern Inner Mongolia (Zhang et al., 2012).

As for the high temperature anomaly required by the low pressure and high temperature melting of the shallow intermediate basic crust in neoaccretion, more and more scholars believe that it is related to the post orogenic mantle-derived basaltic magma underplating caused by the upwelling of mantle materials in the asthenosphere induced by the previous subducted slab breaking-off and gravity collapse (Jahn et al., 2000; Bonin, 2007; Wu et al., 2007; Zhang et al., 2012; Xue et al., 2015). In mid-eastern Inner Mongolia, Mesozoic aluminous A-type granites generally have a positive $\varepsilon_{Nd}(t)$ value, which suggests that the underplating of mantle-derived magma related to slab break-off in the post-orogenic stage plays an important role in the formation of Mesozoic aluminum A-type granitic magma in mid-eastern Inner Mongolia (Jahn et al., 2000; Chen et al., 2008; Zhou et al., 2010; Shi et al., 2014; Xue et al., 2015). In terms of petrography, perthite (Figures 3C, D) is found locally in the samples and inherited zircon is not found in S-type granite. This reveals that the melt was high-temperature and water poor, and that the early magmatic crystallization occurred under high-temperature conditions. These characteristics also reflect the petrogenesis of partial high-temperature melting of the intermediate basic crust in neoaccretion under low pressure and its subsequent differentiation.

5.2 Temperature and pressure conditions of the magmatic source

It is generally believed that A-type granite is formed under high temperature and low pressure, which generally occurs in the shallow middle and upper crust (Clemens et al., 1986). Therefore, the calculation of temperature and pressure conditions for the formation of Chuhuertu pluton indicates A-type granite from the

side. At the same time, the temperature and pressure conditions of magma formation can be used to speculate on the depth of its magmatic source, thus providing constraints for the origin and evolution mechanism of magma.

5.2.1 Q-Ab-Or-H_2O equilibrium pressure calculation

Based on many petrological experimental data, predecessors summarized the equilibrium phase diagram of quartz (Q), albite (Ab), orthoclase (Or), and H_2O, which can be used to calculate temperature and pressure during magma formation (Whitney and Stormer, 1985; Holland and Blundy, 1994; Rajesh, 2000; Liu et al., 2003; Chen et al., 2005).

Q, Ab, and Or are CIPW standard mineral content. It can be seen from the Q-Ab-Or-H_2O equilibrium phase diagram (Figure 8) of the granite that the formation pressure is about 0.1–0.3 Gpa, equivalent to the depth of 4–11 km, indicating shallow crust. However, the formation temperature is about 700°C–750°C, which is slightly lower than the average level of A-type granite (800°C–900°C). These results may be due to the disaggregation of fluid, which reduces the near solidus temperature of A-type granite, while the temperature value of the Q-Ab-Or-H_2O equilibrium phase diagram is the eutectic temperature (Liu et al., 2003). In addition, this may be caused by crystallization fractionation of Chuhuertu granite (Wu et al., 2017).

5.2.2 Zircon saturation thermometry

Compared with water-rich and low-temperature I- and S-type granites, A-type granites are generally considered to have been formed by relatively anhydrous and high-temperature magmas (Loiselle and Wones, 1979; Bonin, 2007). Zircon saturation thermometry (T_{Zr}) can provide a simple and robust means of estimating magma temperatures (Watson, 1979). Because zircon crystallizes early in acid magma, the zircon saturation temperature can be approximately regarded as the temperature of magma formation. This paper adopts the simulation formula of T_{Zr} (°C) = 12,900/[2.95 + 0.85M + lnD_{zr} (zircon/melt)]-273 zircon solubility-saturation temperature obtained by Watson (1979). Here, D is the distribution coefficient. Assuming that the whole rock Si + Al + Fe + Mg + Ca + Na + K + p = 1 (atomic fraction), the whole rock petrochemical parameter M = (2Ca + Na + K)/(Si × Al). When the whole-rock zircon minerals Zr and Hf are not corrected, Zr = 497,626 × 10^{-6} in pure zircon. At the same time, the Zr contents of the whole rock are approximately used to represent the Zr contents in the melt. The calculated sample formation temperature is basically concentrated between 750°C and 803°C (Figure 9), which is close to, but slightly lower than, the average temperature of A-type granite formation. It is also understood that the crystallization fractionation of the Chuhuertu granite reduces its crystallization temperature (Wu et al., 2017).

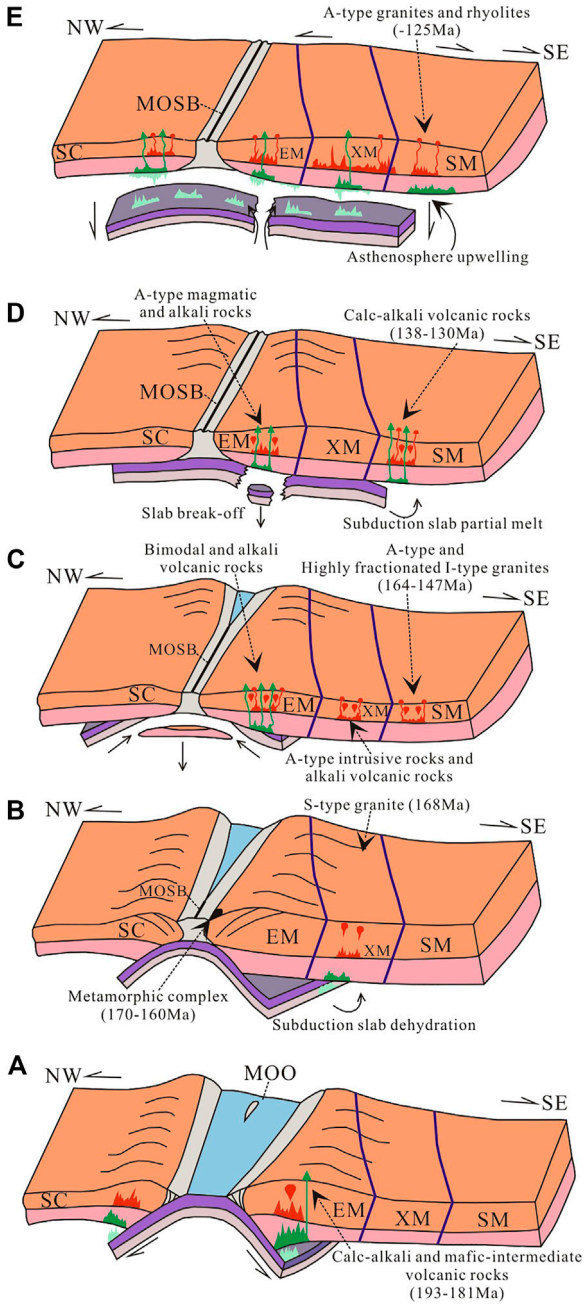


FIGURE 10
Schematic diagram (adapted from Zhang et al., 2020) showing a petrogenetic model for Late Mesozoic magmatic rocks in the southern Great Xing'an Range. SC, Siberian Craton; EM, Erguna Massif; XM, Xing'an Massif; SM, Songliao Massif; MOO, Mongol-Okhotsk Ocean; MOSB, Mongol-Okhotsk Suture Belt.

5.3 Tectonic implications of the granite in Chuhuertu: Under the control of the Mongol–Okhotsk or the Paleo-Pacific tectonic regime?

For a long time, the driving mechanism of the evolution of the Northeast Asian continent has been generally manifested in the subduction of the Paleo-Pacific plate and the closure of MOO (Meng et al., 2011; Xu et al., 2013; Wang et al., 2015; Wu et al., 2017).

Recently, Ji et al. (2019) reported a Late Jurassic oceanic crust-derived low-K adakitic lava in the Hailar Basin and linked it to the flat-slab subduction of the Paleo-Pacific plate. The low-K adakitic lava was considered to represent the final pulse of slab-melt-related volcanism, which also suggests that the Hailar Basin might be the farthest position ever reached by the subducting Paleo-Pacific plate

(Ji et al., 2019). When the flat-slab of the Paleo-Pacific plate subducted under the Hailar–Tamtsag Basin and the Greater Xing'an Range region with thick lithosphere, the increased subduction depth of the slab led to the eclogitization of the originally light oceanic crust, which increased the density of the subducted slab and returned it to negative buoyancy (Antonijevic et al., 2015). It was suggested that the flat-slab of the subducted slab was also unstable and decoupled from the overlying mantle wedge, which led to the rollback accompanied by the gravitational subsidence of the subducted slab (Antonijevic et al., 2015). The appearance of Late Jurassic A-type granites in the Hailar–Tamtsag Basin and the Greater Xing'an Range (Yang et al., 2014; Jiang et al., 2021) also suggests that the upwelling of asthenosphere mantle material caused by the slab rollback of the Paleo-Pacific plate in the Late Jurassic-Early Cretaceous provided some high-temperature conditions required for the formation of A-type granite magmas in the region (Ji et al., 2019).

In addition, many scholars believe that the destruction of NCC is related to the subduction of the Paleo-Pacific plate (Wu et al., 2005; Zhang et al., 2014; Zhu and Xu, 2019; Gao et al., 2021), and its remote effects caused large-scale Early Cretaceous massive magmatism and craton destruction of NCC, resulting in large-scale extension of the middle and lower crust (Zhang et al., 2009b; Zhang et al., 2014; Zhu and Xu, 2019; Gao et al., 2021). The lithospheric reconstruction of NCC by the Middle-Late Jurassic Paleo-Pacific plate was mainly limited to the eastern part of North China and the eastern part of Western Liaoning. A study of the lithofacies paleogeography showed that the Jurassic strata in the eastern part of NCC are obviously lost, which indicates that the area was in a tectonic setting of uplift in the Jurassic (Zhu and Xu, 2019), which was manifested by crustal thickening caused by subduction and compression, and formed a NE trending low-temperature and water-rich granite belt between the Jurassic granite in the eastern part of North China and the Zhangguangcai Ridge in NE China, which is parallel to the Paleo-Pacific subduction belt at the edge of Eurasia (Wu et al., 2005). The Chuhuertu granite is located in the Mesozoic magmatic active belt of the Greater Xing'an Range in the southeastern CAOB, and its emplacement age is Late Jurassic (ca. 156 Ma). Through petrology, mineralogy, and geochemistry, it is classified as A-type granite (water poor and formed under low pressure and high temperature). It is obvious that the Chuhuertu granite is unlikely to be the product of the subduction of the Paleo-Pacific plate in terms of space, time, and rock type.

The study area is located in southeastern Inner Mongolia-North Hebei. There are many Late Jurassic–Early Cretaceous volcanic eruption basins in the region. The crater is obviously distributed in the NE. The volcanic eruption basins are mainly depression type, and a large number of collapse calderas are developed inside. The long axis directions of the basins and the calderas are basically the same, both of which are in the NE, indicating that they are mainly controlled by large extension faults in the NE (Meng et al., 2011; Xu et al., 2013; Jiang et al., 2021). The direction is consistent with that of MOSB. At the same time, the volcanic rocks in the Late Jurassic and Early Cretaceous have similar distribution ranges, which are only distributed west of the Songnen Basin-North Hebei line (Figure 1C) (Wang et al., 2006; Zhang et al., 2008; Meng et al., 2011; Xu et al., 2011; Xu et al., 2013), and show more extensive features exposed to the west. These characteristics indicate that the Late Jurassic–Early Cretaceous volcanic rocks in the study area are remotely affected by the Mongol–Okhotsk tectonic system on the northwest side.

Chuhuertu A-type syenogranite is located in southeastern Inner Mongolia-North Hebei, and its emplacement age is Late Jurassic (ca. 156 Ma). Combined with a series of Late Jurassic A-type granites (Chen et al., 2008; Xie et al., 2012; Xue et al., 2015; Zhu et al., 2020) determined successively in the southeastern CAOB and NCC in recent years, the middle and lower crust in this area have been shown to have generally been in an extensional flow state in the Late Jurassic. In addition, alkaline-subalkaline volcanic rocks and rhyolites were widely exposed in the Greater Xing'an Range and the North Hebei-Western Liaoning during the Late Jurassic and Early Cretaceous (Meng et al., 2011; Li, 2012; Peng et al., 2012; Wang et al., 2013). The alkaline volcanic rock associations of the two periods of volcanic rocks indicate the regional extensional environment, which correspond to the extensional environment after A and B phases of Yanshan movement, respectively, suggesting that the two periods of magmatic events are related to the evolution of the Mongol–Okhotsk tectonic system (Zheng et al., 2000). Therefore, based on spatial fit and temporal correlation, Late Jurassic magmatism in the southeastern CAOB was mainly controlled by the Mongol–Okhotsk tectonic regime. During the Early Jurassic, the southern subduction of the Mongol-Okhotsk oceanic plate resulted in the formation of calc-alkali and mafic-intermediate volcanic rocks in the Ergun region (Figure 10A) (Xu et al., 2013). During the Middle Jurassic, the closure of the western MOO was completed, and a continental collision resulted in crustal thickening. The partial melting of the thickened crust formed S-type granite on the Xing'an Massif (Figure 10B) (Li et al., 2018a). During the Late Jurassic, with the "scissors" closure of the MOO from west to east, the subduction zone retreated in the NE trending, resulting in the subsequent rollback of the subduction slab, causing the collapse and delamination of the thickened crust, triggering the asthenospheric mantle upwelling, leading to the extension of the continental lithosphere (Tang et al., 2015; Zhang et al., 2018). The Chuhuertu A-type syenogranite in the study area is the product of the orogenic extension setting after the closure of MOO, and its emplacement under a certain extension event (Figure 10C). In the early Early Cretaceous, the rapid closure of the eastern MOO provided high-speed subduction, pushing the slab forward and causing flat-slab subduction of the oceanic plate. As the subduction slab continued to advance southward and the mantle wedge retreated, a set of basic to intermediate-acidic arc volcanic rocks were formed by partial melting of the mantle wedge in the Greater Xing'an Range (Figure 10D) (Meng et al., 2011; Xu et al., 2013). In the late Early Cretaceous, after the ocean closed, the convergence power of the subduction slab disappeared, and the subduction oceanic crust gradually collapsed from south to north due to the influence of gravitational potential energy, resulting in crustal thinning, mantle upwelling, and partial melting of crustal

materials. A-type granite and rhyolite were formed in the Bahrain Left Banner-Zarut Banner in the southern segment of the Greater Xing'an Range (Figure 10E) (Zhang et al., 2020).

6 Conclusions

(1) Chuhuertu granite is exposed in the northwest of the Duerji tectonic melange in Horqin Right Middle Banner. The zircon U-Pb age of LA-ICP-MS is 155.6 ± 1.6 Ma, revealing that its emplacement age is Late Jurassic.
(2) The geochemical characteristics of Chuhuertu granite are high SiO_2 and alkali; low CaO and MgO; A/CNK = 0.96–1.11; A/NK = 1.00–1.24; obvious negative Eu anomaly; enrichment of Rb, Th, U, K, and Ga elements; relative loss of Ba, Sr, P, and Ti elements; and high values of 10000Ga/Al, TFeO/MgO, and DI. The geochemical characteristics indicate that it is highly differentiated A-type granite.
(3) Under conditions of low pressure and high temperature, the partial melting of basic–intermediate crust in neoaccretion and subsequent crystallization differentiation may represent the petrogenesis of Chuhuertu granite, while superimposing the influence of the Paleo-Pacific plate rollback. Chuhuertu granite is the product of extension of the closure of MOO and, together with other A-type granites distributed in mid-eastern Inner Mongolia, it indicates extensive middle and lower crust extension in the Late Jurassic.

Data availability statement

The original contributions presented in the study are included in the article/Supplementary Material, further inquiries can be directed to the corresponding author.

Author contributions

Conceptualization, YL; data curation, DZ and XK; formal analysis, PD and PL; investigation, SJ and XZ; writing—original draft, SW. All authors have read and agreed to the published version of the manuscript.

Funding

This research was funded by the National Natural Science Foundation of China (41972061), the China Geological Survey (1212011120711 and DD20160048-14), and the Science and Technology Innovation Team Program of Hebei GEO University (KJCXTD-2021-07).

Conflict of interest

The authors declare that the research was conducted in the absence of any commercial or financial relationships that could be construed as a potential conflict of interest.

The reviewer JW declared a shared affiliation with the authors SW, XZ, PL to the handling editor at time of review.

Publisher's note

All claims expressed in this article are solely those of the authors and do not necessarily represent those of their affiliated organizations, or those of the publisher, the editors, and the reviewers. Any product that may be evaluated in this article, or claim that may be made by its manufacturer, is not guaranteed or endorsed by the publisher.

References

Anderson, T. (2002). Correction of common lead U-Pb analyses that do not report ^{204}Pb. *Chem. Geol.* 192 (1-2), 59–79. doi:10.1016/S0009-2541(02)00195-X

Antonijevic, S. K., Wagner, L. S., Kumar, A., Beck, S. L., Long, M. D., Zandt, G., et al. (2015). The role of ridges in the formation and longevity of flat slabs. *Nature* 524, 212–215. doi:10.1038/nature14648

Bach, W., Alt, J. C., Niu, Y. L., Humphris, S. E., Erzinger, J., and Dick, H. J. (2001). The geochemical consequences of late-stage low-grade alteration of lower ocean crust at the SW Indian Ridge: Results from ODP Hole 735B (Leg 176). *Geochimica Cosmochimica Acta* 65 (19), 3267–3287. doi:10.1016/s0016-7037(01)00677-9

Barbarin, B. (2005). Mafic magmatic enclaves and mafic rocks associated with some granitoids of the central sierra Nevada batholith, California: Nature, origin, and relations with the hosts. *Lithos* 80 (1-4), 155–177. doi:10.1016/j.lithos.2004.05.010

Bonin, B. (2007). A-type granites and related rocks: Evolution of a concept, problems and prospects. *Lithos* 97 (1-2), 1–29. doi:10.1016/j.lithos.2006.12.007

Breiter, K., Gardenová, N., Kanický, V., and Vaculovič, T. (2013). Gallium and germanium geochemistry during magmatic fractionation and post-magmatic alteration in different types of granitoids: A case study from the bohemian Massif (Czech republic). *Geol. Carpath.* 64, 171–180. doi:10.2478/geoca-2013-0018

Chappell, B. W., and White, A. J. R. (2001). Two contrasting granite types: 25 years later. *Aust. J. Earth Sci.* 48 (4), 489–499. doi:10.1046/j.1440-0952.2001.00882.x

Chen, H. W., Luo, Z. H., and Mo, X. X. (2005). Underplating mechanism of Triassic granite of magma mixing origin in the East Kunlun orogenic belt. *Geol. China* 32 (3), 386–395.

Chen, Z. G., Zhang, L. C., Wu, H. Y., Wan, B., and Zeng, O. D. (2008). Geochemistry study and tectonic background of A style host granite in Nianzigou molybdenum deposit in Xilamulun mollybdenum mhetallogenic belt, Inner Mongolia. *Acta Petrol. Sin.* 24 (4), 879–889.

Cheng, Y. H., Duan, L. F., Wang, S. Y., Li, Y., Teng, X. J., and Zhang, T. F. (2020). Termination of the hegenshan orogen in the xing'an-Mongolian orogenic belt, north China: Geochemical and zircon U-Pb geochronological constraints from early permian mafic dykes. *Geol. J.* 55, 845–861. doi:10.1002/gj.3463

Cheng, Y. H., Teng, X. J., Li, Y. F., Li, M., and Zhang, T. F. (2014). Early permian east-ujimqin mafic-ultramafic and granitic rocks from the xing'an-Mongolian orogenic belt, north China: Origin, chronology, and tectonic implications. *J. Asian Earth Sci.* 96 (15), 361–373. doi:10.1016/j.jseaes.2014.09.027

Clemens, J. D., Holloway, J. R., and White, J. A. R. (1986). Origin of an A-type granite; experimental constraints. *Am. Mineralogist* 71 (3), 317–324.

Deng, C. Z., Sun, D. Y., Han, J. S., Chen, H. Y., Li, G. H., Xiao, B., et al. (2019). Late-stage southwards subduction of the Mongol-Okhotsk oceanic slab and implications for porphyry Cu-Mo mineralization: Constraints from igneous rocks associated with the Fukeshan deposit, NE China. *Lithos* 326-327, 341–357. doi:10.1016/j.lithos.2018.12.030

Donskaya, T. V., Gladkochub, D. P., Mazukabzov, A. M., and Ivanov, A. V. (2013). Late Paleozoic-Mesozoic subduction related magmatism at the southern margin of the Siberian continent and the 150-million-year history of the Mongol-Okhotsk Ocean. *J. Asian Earth Sci.* 62, 79–97. doi:10.1016/j.jseaes.2012.07.023

Eby, G. N. (1992). Chemical subdivision of the A-type granitoids: Petrogenetic and tectonic implications. *Geology* 20 (7), 641. doi:10.1130/0091-7613(1992)020<0641:csotat>2.3.co;2

Frost, B. R., and Frost, C. D. (2008). A geochemical classification for feldspathic igneous rocks. *J. Petrology* 49 (11), 1955–1969. doi:10.1093/petrology/egn054

Gao, S., Chen, W. F., Hu, J., Xie, G. A., and Ling, H. F. (2022). A Late Jurassic A-type granitic-magmatic belt in the westernmost Northeast China and its tectonic implications. *Tectonophysics* 834, 229339. doi:10.1016/j.tecto.2022.229339

Gao, S., Chen, W. F., Ling, H. F., Sun, L. Q., Ren, Q., Xie, G. A., et al. (2021). A latest jurassic A-type granite in the middle of inner Mongolia: Petrogenesis and tectonic implications. *Lithos* 394-395, 106167. doi:10.1016/j.lithos.2021.106167

Gillespie, J., Glorie, S., Xiao, W. J., Zhang, Z. Y., Collins, A. S., Evans, N., et al. (2017). Mesozoic reactivation of the beishan, southern central asian orogenic belt: Insights from low-temperature thermochronology. *Gondwana Res.* 43, 107–122. doi:10.1016/j.gr.2015.10.004

Griffin, W. L., Wang, X., Jackson, S. E., Pearson, N. J., O'Reilly, S. Y., Xu, X. S., et al. (2002). Zircon chemistry and magma mixing, SE China: *In-situ* analysis of Hf isotopes, tonglu and pingtan igneous complexes. *Lithos* 61 (3-4), 237–269. doi:10.1016/s0024-4937(02)00082-8

Hart, S. R., Blusztajn, J., Dick, H. J., Meyer, P. S., and Muehlenbachs, K. (1999). The fingerprint of seawater circulation in a 500-meter section of ocean crust gabbros. *Geochimica Cosmochimica Acta* 63 (23), 4059–4080. doi:10.1016/s0016-7037(99)00309-9

Holland, T., and Blundy, J. (1994). Non-ideal interactions in calcic amphiboles and their bearing on amphibole-plagioclase thermometry. *Contributions Mineralogy Petrology* 116, 433–447. doi:10.1007/bf00310910

Hoskin, P. W., and Schaltegger, U. (2003). The composition of zircon and igneous and metamorphic petrogenesis. *Rev. Mineralogy Geochem.* 53 (1), 27–62. doi:10.2113/0530027

Jahn, B. M., Griffin, W. L., and Windley, B. F. (2000). Continental growth in the phanerozoic: Evidence from central asia. *Tectonophysics* 328, 1–227. doi:10.1016/s0040-1951(00)00174-8

Ji, Z., Meng, Q. A., Wan, C. B., Zhu, D. F., Ge, W. C., Zhang, Y. L., et al. (2019). Geodynamic evolution of flat-slab subduction of Paleo-Pacific plate: Constraints from jurassic adakitic lavas in the Hailar Basin, NE China. *Tectonics* 38 (12), 4301–4319. doi:10.1029/2019tc005687

Jian, P., Liu, D. Y., Kroner, A., Windley, B. F., Shi, Y. R., Zhang, W., et al. (2010). Evolution of a permian intraoceanic arc-trench system in the solonker suture zone, central asian orogenic belt, China and Mongolia. *Lithos* 118 (1), 169–190. doi:10.1016/j.lithos.2010.04.014

Jiang, X. J., Peng, Y. B., Dong, X. J., Li, H. M., and Tu, Y. (2021). The remote role of Mongolia-okhotsk ocean: Evidences from the origin of rhyolite porphyry in yangpangou area, the southeast of inner Mongolia. *Earth Sci.* 46 (9), 3057–3073. doi:10.3799/dqkx.2020.335

Jin, S. (2020). Study of material composition and tectonic properties of the Duerji tectonic melange, Inner Mongolia. *Acta Geol. Sin.* 94 (8), 2227–2242. doi:10.19762/j.cnki.dizhixuebao.2020062

King, P. L., Chappell, B. W., Allen, C. M., and White, A. J. R. (2001). Are A-type granites the high-temperature felsic granites? Evidence from fractionated granites of the wangrah suite. *Aust. J. Earth Sci.* 48, 501–514. doi:10.1046/j.1440-0952.2001.00881.x

Lee, C. T. A., and Bachmann, O. (2014). How important is the role of crystal fractionation in making intermediate magmas? Insights from Zr and P systematic. *Earth Planet. Sci. Lett.* 393, 266–274. doi:10.1016/j.epsl.2014.02.044

Li, W. P. (2012). Magma evolution of the late jurassic volcanic rocks and its Genesis of the langi formation, beipiao area, Western liaoning province. *Earth Sci.* 37 (1), 47–56. doi:10.3799/dqkx.2012.005

Li, Y. J., Wang, G. H., Santosh, M., Wang, J. F., Dong, P. P., and Li, H. Y. (2020). Subduction initiation of the SE Paleo-Asian Ocean: Evidence from a well preserved intra-oceanic forearc ophiolite fragment in central Inner Mongolia, North China. *Earth Planet. Sci. Lett.* 535, 116087. doi:10.1016/j.epsl.2020.116087

Li, Y. J., Wang, G. H., Santosh, M., Wang, J. F., Dong, P. P., and Li, H. Y. (2018b). Supra-subduction zone ophiolites from inner Mongolia, north China: Implications for the tectonic history of the southeastern central asian orogenic belt. *Gondwana Res.* 59, 126–143. doi:10.1016/j.gr.2018.02.018

Li, Y., Xu, W. L., Tang, J., Pei, F. P., Wang, F., and Sun, C. Y. (2018a). Geochronology and geochemistry of Mesozoic intrusive rocks in the Xing'an Massif of NE China: Implications for the evolution and spatial extent of the Mongol-Okhotsk tectonic regime. *Lithos* 304-307, 57–73. doi:10.1016/j.lithos.2018.02.001

Liu, C. S., Chen, X. M., Chen, P. R., Wang, R. C., and Hu, H. (2003). Subdivision, discrimination criteria and Genesis for A type rock suites. *Geol. J. China Univ.* 9 (4), 573–591. doi:10.16108/j.issn1006-7493.2003.04.011

Liu, H. D., Cheng, Y. H., Santosh, M., Teng, X. M., Zhang, X. W., and Teng, X. J. (2021). Magmatism associated with lithospheric thinning, mantle upwelling, and extensional tectonics: Evidence from Carboniferous-Permian dyke swarms and granitoids from Inner Mongolia, Central Asian Orogenic Belt. *Lithos* 386-387, 106004. doi:10.1016/j.lithos.2021.106004

Liu, W., Siebel, W., Li, X. J., and Pan, X. F. (2005). Petrogenesis of the Linxi granitoids, northern Inner Mongolia of China: Constraints on basaltic underplating. *Chem. Geol.* 219 (1-4), 5–35. doi:10.1016/j.chemgeo.2005.01.013

Liu, Y. J., Li, W. M., Feng, Z. Q., Wen, Q. B., Neubauer, F., and Liang, C. Y. (2017). A review of the paleozoic tectonics in the eastern part of central asian orogenic belt. *Gondwana Res.* 43, 123–148. doi:10.1016/j.gr.2016.03.013

Liu, Y. S., Hu, Z. C., Gao, S., Günther, D., Xu, J., Gao, C. G., et al. (2008). *In situ* analysis of major and trace elements of anhydrous minerals by LA-ICP-MS without applying an internal standard. *Chem. Geol.* 257 (1), 34–43. doi:10.1016/j.chemgeo.2008.08.004

Loiselle, M. C., and Wones, D. R. (1979). Characteristics and origin of anorogenic granites. *Geol. soc. am. abstr. Progr* 11, 468.

Maniar, P. D., and Piccoli, P. M. (1989). Tectonic discrimination of granitoids. *Geol. Soc. Am. Bull.* 101, 635–643. doi:10.1130/0016-7606(1989)101<0635:tdog>2.3.co;2

Meng, E., Xu, W. L., Yang, D. B., Qiu, K. F., Li, C. H., and Zhu, H. T. (2011). Zircon U-Pb chronology, geochemistry of Mesozoic volcanic rocks from the Lingquan Basin in Manzhouli area, and its tectonic implications. *Acta Petrol. Sin.* 27 (4), 1209–1226.

Meng, Q. R., Wu, G. L., Fan, L. G., Wei, H. H., and Wang, E. (2020). Late Triassic uplift, magmatism and extension of the northern North China block: Mantle signatures in the surface. *Earth Planet. Sci. Lett.* 547, 116451. doi:10.1016/j.epsl.2020.116451

Miao, L. C., Fan, W. M., Liu, D. Y., Shi, Y. R., and Guo, F. (2008). Geochronology and geochemistry of the Hegenshan ophiolitic complex: Implications for late-stage tectonic evolution of the Inner Mongolia-Daxinganling Orogenic Belt, China. *J. Asian Earth Sci.* 32 (5-6), 348–370. doi:10.1016/j.jseaes.2007.11.005

Nozaka, T., and Liu, Y. (2002). Petrology of the Hegenshan ophiolite and its implication for the tectonic evolution of northern China. *Earth Planet. Sci. Lett.* 202 (1), 89–104. doi:10.1016/s0012-821x(02)00774-4

Parfenov, L. M., Popeko, L. I., and Tomurtogoo, O. (2001). Problems of tectonics of the mongol-okhotsk orogenic belt. *Geol. Pac. Ocean* 16 (5), 797–830.

Pearce, J. A. (1996). Sources and settings of granitic rocks. *Episodes* 19, 120–125. doi:10.18814/epiiugs/1996/v19i4/005

Peng, Y. D., Huang, F., Xing, D. H., and Lv, A. C. (2012). Geochemical characteristics and tectonic setting for volcanic rocks of Zhangjiakou Formation in the Chaoyang area,'Western Liaoning. *J. Northeast. Univ. Nat. Sci.* 33 (9), 1331–1335. doi:10.1007/s11783-011-0280-z

Pérez-Soba, C., and Villaseca, C. (2010). Petrogenesis of highly fractionated I-type peraluminous granites: La pedriza pluton (Spanish central system). *Geol. Acta* 8, 131–149. doi:10.1344/105.000001527

Rajesh, H. M. (2000). Characterization and origin of a compositionally zoned aluminous A-type granite from South India. *Geol. Mag.* 137, 291–318. doi:10.1017/s001675680000399x

Rapp, R. P., and Watson, E. B. (1995). Dehydration melting of metabasalt at 8-32kbar: Implications for continental growth and crust-mantle recycling. *J. Petrology* 36 (4), 891–931. doi:10.1093/petrology/36.4.891

Safonova, I., Kotlyarov, A., Krivonogov, S., and Xiao, W. J. (2017). Intra-oceanic arcs of the Paleo-Asian ocean. *Gondwana Res.* 50 (3), 167–194. doi:10.1016/j.gr.2017.04.005

Shao, J. A., Tian, W., Tang, K. D., and Wang, Y. (2015). Petrogenesis and tectonic settings of the late carboniferous high M basalts of inner Mongolia. *Earth Sci. Front.* 22 (5), 171–181. doi:10.13745/j.esf.2015.05.014

Shi, Y. R., Liu, C., Deng, J. F., and Jian, P. (2014). Geochronological frame of granitoids from Central Inner Mongolia and its tectonomagmatic evolution. *Acta Petrol. Sin.* 30 (11), 3155–3171.

Sisson, T. W., Ratajeski, K., Hankins, W. B., and Glazner, A. F. (2005). Voluminous granitic magmas from common basaltic sources. *Contributions Mineralogy Petrology* 148 (6), 635–661. doi:10.1007/s00410-004-0632-9

Sun, S. S., and McDonough, W. F. (1989). Chemical and isotopic systematics of oceanic basalts: Implications for mantle composition and processes. *Geol. Soc. Lond. Special Publ.* 42, 313–340.

Tang, J., Xu, W. L., Wang, F., Zhao, S., and Li, Y. (2015). Geochronology, geochemistry, and deformation history of Late Jurassic-Early Cretaceous intrusive rocks in the Erguna Massif, NE China: Constraints on the late Mesozoic tectonic evolution of the Mongol-Okhotsk orogenic belt. *Tectonophysics* 658, 91–110. doi:10.1016/j.tecto.2015.07.012

Turner, S. P., Foden, J. D., and Morrison, R. S. (1992). Derivation of some A-type magmas by fractionation of basaltic magma: An example from the padthaway ridge, south Australia. *Lithos* 28 (2), 151–179. doi:10.1016/0024-4937(92)90029-x

Wang, F., Zhou, X. H., Zhang, L. C., Ying, J. F., Zhang, Y. T., Wu, F. Y., et al. (2006). Late mesozoic volcanism in the Great xing'an range (NE China): Timing and implications for the dynamic setting of NE asia. *Earth Planet. Sci. Lett.* 251 (1-2), 179–198. doi:10.1016/j.epsl.2006.09.007

Wang, J. G., He, Z. H., and Xu, W. L. (2013). Petrogenesis of riebeckite rhyolites in the southern Da Hinggan Mts: Geohronological and geochemical evidence. *Acta Petrol. Sin.* 29 (3), 853–863.

Wang, T., Guo, L., Zhang, L., Yang, Q. D., Zhang, J. J., Tong, Y., et al. (2015). Timing and evolution of jurassic-cretaceous granitoid magmatisms in the mongol-okhotsk belt and adjacent areas, NE asia: Implications for transition from contractional crustal thickening to extensional thinning and geodynamic settings. *J. Asian Earth Sci.* 97 (1), 365–392. doi:10.1016/j.jseaes.2014.10.005

Wang, T., Tong, Y., Zhang, L., Li, S., Huang, H., Zhang, J. J., et al. (2017). Phanerozoic granitoids in the central and eastern parts of Central Asia and their tectonic significance. *J. Asian Earth Sci.* 145, 368–392. doi:10.1016/j.jseaes.2017.06.029

Watson, E. B. (1979). Zircon saturation in felsic liquids: Experimental results and applications to trace element geochemistry. *Contributions Mineralogy Petrology* 70 (4), 407–419. doi:10.1007/bf00371047

Whalen, J. B., Currie, K. L., and Chappell, B. W. (1987). A-Type granites: Geochemical characteristics, discrimination and petrogenesis. *Contributions Mineralogy Petrology* 95 (4), 407–419. doi:10.1007/bf00402202

Whitney, J. A., and Stormer, J. C. (1985). Mineralogy, petrology, and magmatic conditions from the fish canyon tuff, central san juan volcanic field, Colorado. *J. Petrology* 26, 726–762. doi:10.1093/petrology/26.3.726

Windley, B. F., Alexeiev, D., Xiao, W. J., Kroner, A., and Badarch, G. (2007). Tectonic models for accretion of the central asian orogenic belt. *J. Geol. Soc.* 164 (1), 31–47. doi:10.1144/0016-76492006-022

Wu, F. Y., Liu, X. C., Ji, W. Q., Wang, J. M., and Yang, L. (2017). Highly fractionated granites: Recognition and research. *Sci. China Earth Sci.* 7, 1201–1219. doi:10.1007/s11430-016-5139-1

Wu, F. Y., Sun, D. Y., Ge, W. C., Zhang, Y. B., Grant, M. L., Wilde, S. A., et al. (2011). Geochronology of the Phanerozoic granitoids in northeastern China. *J. Asian Earth Sci.* 41 (1), 1–30. doi:10.1016/j.jseaes.2010.11.014

Wu, F. Y., Sun, D. Y., Li, H., Jahn, B. M., and Wilde, S. A. (2002). A-type granites in northeastern China: Age and geochemical constraints on their petrogenesis. *Chem. Geol.* 187 (1-2), 143–173. doi:10.1016/s0009-2541(02)00018-9

Wu, F. Y., Yang, J. H., Wilde, S. A., and Zhang, X. O. (2005). Geochronology, petrogenesis and tectonic implications of Jurassic granites in the Liaodong Peninsula, NE China. *Chem. Geol.* 221 (1), 127–156. doi:10.1016/j.chemgeo.2005.04.010

Wu, S. P., Wang, M. Y., and Qi, K. J. (2007). Present situation of researches on A-type granites: A revie. *Acta Petrologica Mineralogica* 26 (1), 57–66. doi:10.3969/j.issn.1009-2374.2007.08.079

Xiao, W. J., Windley, B. F., Hao, J. J., and Zhai, M. G. (2003). Accretion leading to collision and the Permian Solonker suture, Inner Mongolia, China: Termination of the central Asian orogenic belt. *Tectonics* 22 (6), 1069. doi:10.1029/2002tc001484

Xie, H. J., Wu, G., Zhu, M. T., Liu, J., and Zhang, L. C. (2012). Geochronology and geochemistry of the Daolanghuduge A-type granite in Inner Mongolia, and its geological significance. *Acta Petrol. Sin.* 28 (2), 483–494.

Xu, B., Zhao, P., Bao, Q. Z., Zhou, Y. H., Wang, Y. Y., and Luo, Z. W. (2014). Preliminary study on the pre-Mesozoic tectonic unit division of the Xing-Meng Orogenic Belt (XMOB). *Acta Petrol. Sin.* 30 (7), 1841–1857.

Xu, M. J., Xu, W. L., Meng, E., and Wang, F. (2011). LA-ICP-MS zircon U-Pb chronology and geochemistry of Mesozoic volcanic rocks from the Shanghulin-Xiangyang Basin in Ergun area, northeastern Inner Mongolia. *Geol. Bull. China* 30 (9), 1321–1338. doi:10.3969/j.issn.1671-2552.2011.09.001

Xu, W. L., Wang, F., Pei, F. P., Meng, E., Tang, J., Xu, M. J., et al. (2013). Mesozoic tectonic regimes and regional ore-forming background in NE China: Constraints from spatial and temporal variations of Mesozoic volcanic rock associations. *Acta Petrol. Sin.* 29 (2), 339–353.

Xue, F. H., Zhang, X. H., Deng, J. X., and Yuan, L. L. (2015). Late Jurassic A-type granite from the Dalai region of central Inner Mongolia: Geochemistry, petrogenesis and tectonic implication. *Acta Petrol. Sin.* 31 (6), 1774–1788.

Yang, Q. D., Guo, L., Wang, T., Zeng, T., Zhang, L., Tong, Y., et al. (2014). Geochronology, origin, sources and tectonic settings of Late Mesozoic two-stage granites in the Ganzhuermiao region, central and southern Da Hinggan Range, NE China. *Acta Petrol. Sin.* 30 (7), 1961–1981.

Zhang, C., Quan, J. Y., Zhang, Y. J., Liu, Z. H., Li, W., Wang, Y., et al. (2020). Late Mesozoic tectonic evolution of the southern Great Xing'an Range, NE China: Evidence from whole-rock geochemistry, and zircon U-Pb ages and Hf isotopes from volcanic rocks. *Lithos* 362-363, 105409. doi:10.1016/j.lithos.2020.105409

Zhang, J. H., Gao, S., Ge, W. C., Wu, F. Y., Yang, J. H., Wilde, S. A., et al. (2010). Geochronology of the mesozoic volcanic rocks in the Great xing'an range, northeastern China: Implications for subduction-induced delamination. *Chem. Geol.* 276, 144–165. doi:10.1016/j.chemgeo.2010.05.013

Zhang, J. H., Ge, W. C., Wu, F. Y., Wilde, S. A., Yang, J. H., and Liu, X. M. (2008). Large-scale early cretaceous volcanic events in the northern Great xing'an range, northeastern China. *Lithos* 102 (1-2), 138–157. doi:10.1016/j.lithos.2007.08.011

Zhang, Q., Ran, H., and Li, C. D. (2012). A-type granite: What is the essence? *Acta Petrologica Mineralogica* 31 (4), 621–626.

Zhang, S. H., Zhao, Y., Davis, G. A., Ye, H., and Wu, F. (2014). Temporal and spatial variations of mesozoic magmatism and deformation in the North China craton: Implications for lithospheric thinning and decratonization. *Earth Sci. Rev.* 131, 49–87. doi:10.1016/j.earscirev.2013.12.004

Zhang, S. H., Zhao, Y., Liu, X. C., Liu, D. Y., Chen, F. K., Xie, L. W., et al. (2009a). Late paleozoic to early mesozoic mafic–ultramafic complexes from the northern North China block: Constraints on the composition and evolution of the lithospheric mantle. *Lithos* 110 (1-4), 229–246. doi:10.1016/j.lithos.2009.01.008

Zhang, S. H., Zhao, Y., Song, B., Hu, J. M., Liu, S. W., Yang, Y. H., et al. (2009b). Contrasting late carboniferous and late permian–middle triassic intrusive suites from the northern margin of the North China craton: Geochronology, petrogenesis, and tectonic implications. *Geol. Soc. Am. Bull.* 121 (1-2), 181–200. doi:10.1130/b26157.1

Zhang, Y. T., Sun, F. Y., Wang, S., and Wei, X. (2018). Geochronology and geochemistry of late jurassic to early cretaceous granitoids in the northern Great xing'an range, NE China: Petrogenesis and implications for late mesozoic tectonic evolution. *Lithos* 312-313, 171–185. doi:10.1016/j.lithos.2018.05.006

Zheng, Y. D., Davis, G. A., Wang, C., Darby, B. J., and Zhang, C. H. (2000). Major mesozoic tectonic events in the yanshan belt and the plate tectonic setting. *Acta Geol. Sin.* 19 (4), 289–302. doi:10.3321/j.issn:0001-5717.2000.04.001

Zhou, J. B., Han, J., Zhao, G. C., Zhang, X. Z., Cao, J. L., Wang, B., et al. (2015a). The emplacement time of the Hegenshan ophiolite: Constraints from the unconformably overlying Paleozoic strata. *Tectonophysics* 662, 398–415. doi:10.1016/j.tecto.2015.03.008

Zhou, Z. H., Lv, L. S., Yang, Y. J., and Li, T. (2010). Petrogenesis of the early cretaceous A-type granite in the huanggang Sn-Fe deposit, inner Mongolia: Constraints from zircon U-Pb dating and geochemistry. *Acta Petrol. Sin.* 26 (12), 3521–3537.

Zhu, H. T., Wu, J. H., Tang, D. W., Guo, H. F., Yang, D. G., Wang, L. Y., et al. (2020). Geochemistry of late jurassic biotite granite in the hongshanzi area, hexigten banner, inner Mongolia, and its geological implications. *Acta Geol. Sin.* 66 (3), 765–785. doi:10.16509/j.georeview.2020.03.017

Zhu, R., and Xu, Y. (2019). The subduction of the west Pacifific plate and the destruction of the North China Craton. *Sci. China Earth Sci.* 9, 1340–1350. doi:10.1007/s11430-018-9356-y

Zorin, Y. A. (1999). Geodynamics of the Western part of the Mongolia-okhotsk collisional belt, trans-baikal region (Russia) and Mongolia. *Tectonophysics* 306 (1), 33–56. doi:10.1016/s0040-1951(99)00042-6

frontiers | Frontiers in Earth Science

TYPE Original Research
PUBLISHED 16 June 2023
DOI 10.3389/feart.2023.1084673

Check for updates

OPEN ACCESS

EDITED BY
Fan Yang,
Lanzhou University, China

REVIEWED BY
Jian Li,
Shandong University of Technology, China
Leilei Dong,
University of Science and Technology Beijing, China
Yong Wang,
Chengdu University of Technology, China

*CORRESPONDENCE
Haiqin Wang,
haiqinw@163.com

RECEIVED 30 October 2022
ACCEPTED 24 May 2023
PUBLISHED 16 June 2023

CITATION
Tian R, Wang H, Tian J, Shan W, Wang X, Chi N, Ma X, Chu Z, Li S and Lv Q (2023), Preliminary investigation of the eruption time of kimberlite in the Late Devonian in Mengyin, Shandong.
Front. Earth Sci. 11:1084673.
doi: 10.3389/feart.2023.1084673

COPYRIGHT
© 2023 Tian, Wang, Tian, Shan, Wang, Chi, Ma, Chu, Li and Lv. This is an open-access article distributed under the terms of the Creative Commons Attribution License (CC BY). The use, distribution or reproduction in other forums is permitted, provided the original author(s) and the copyright owner(s) are credited and that the original publication in this journal is cited, in accordance with accepted academic practice. No use, distribution or reproduction is permitted which does not comply with these terms.

Preliminary investigation of the eruption time of kimberlite in the Late Devonian in Mengyin, Shandong

Ruicong Tian[1], Haiqin Wang[2]*, Jingxiang Tian[2], Wei Shan[2], Xiufeng Wang[2], Naijie Chi[2], Xiaodong Ma[2], Zhiyuan Chu[3], Shenghu Li[2] and Qing Lv[3]

[1]School of Geography and Tourism, Qilu Normal University, Jinan, China, [2]Ministry of Natural Resources Key Laboratory of Gold Mineralization Processes and Resources Utilization, Shandong Key Laboratory of Metallogenic Processes and Resource Utilization of Metallic Minerals, Shandong Institute of Geological Sciences, Jinan, China, [3]The 7th Institute of Geology and Mineral Exploration of Shandong Province, Linyi, Shandong, China

Kimberlite in the Mengyin area serves as an excellent medium for studying the characteristics and evolutionary processes of the Paleozoic mantle. In order to determine the age of the primary calcite within the kimberlite, *in situ* carbonate U–Pb dating was conducted in the Mengyin area. The results indicate that the primary calcite in the kimberlite originated approximately 383 ± 18 Ma (MSWD = 6.6). This age constraint suggests that the eruption of the kimberlite took place during this period, leading to the thermal alteration of limestone xenoliths, ultimately forming marble. Consequently, it can be inferred that lithospheric thinning occurred no later than the Late Devonian period. Fluid inclusions found within the marble provide further insights into its formation. The recorded formation temperature of the marble ranges from 243°C to 370°C, with a salinity range of 2.57%–14.77% (NaCl). The pressure estimates fall within the range of 3.22–20.70 MPa, indicating a depth mainly between 900 and 1,000 m. Based on these findings, it can be inferred that the overall denudation depth in the west Shandong area, since the Late Devonian, is estimated to be approximately 900–1,000 m. Furthermore, the overall crustal rise rate is estimated to be approximately 3 m/Ma.

KEYWORDS

kimberlite, diamond, fluid inclusions, carbonate dating, plate subduction, Mengyin region

1 Introduction

Kimberlite, classified as alkaline mafic ultrabasic rocks, represents the deepest form of magma found in nature. It originates from the upper mantle, at depths ranging from 150 to 300 km, under high temperature and pressure (Heaman et al., 2003; Giuliani et al., 2016). Due to its unique origin, kimberlite carries valuable geological information, making it a vital channel for studying mantle compositions. Sheng (2004) characterized the metallogenic conditions of diamond deposits as follows: a thick upper mantle with low heat flow and high depletion beneath ancient cratons, which provides a favorable environment for the formation of kimberlite magma and the upward migration of diamonds. In addition, deep faults in the supercrustal region act as channels for the ascent of kimberlite. Lu et al. (1995) discovered that the crystallization processes of diamonds in the mantle exhibit a

prolonged time interval characterized by distinct stages. They further suggested that the magmatic activities of diamond-bearing kimberlite in eastern China were linked to the late Middle Ordovician continental uplift in the North China platform. According to Boyd et al. (1986), diamonds crystallize at the base of the lithosphere, with temperature and pressure being the primary controlling factors. Haggerty (1986) proposed that, in addition to temperature and pressure, oxygen fugacity also plays a significant role in diamond formation. During the extraction of mafic magma from the upper mantle, H_2O and CO_2 escape, resulting in a lithosphere that is not only compositionally depleted but also in a low oxidation state compared to the asthenosphere. Consequently, the interface between these two regions becomes the most favorable zone for diamond growth.

Kimberlite, which contains primary diamond ore deposits, was initially discovered in the Mengyin area of Shandong Province in 1965 (Liu, 2002; Wang et al., 2013; Wang and Wang, 2014; Wang et al., 2015). Since then, it has garnered significant attention, and numerous studies have extensively investigated its petrology, chronology, geochemistry, and its role in the evolution of the continental crust (Zhang, 2006; Zhang et al., 2007; Lu, 2010). Determining the precise formation age of the kimberlite in the Mengyin area has been a subject of debate. In the early 1980s, researchers from The 7th Institute of Geology and Mineral Exploration of Shandong Province discovered that the kimberlite vein intersected the diabase vein in the crystalline basement, with an isotopic age of 113 million years (Ma) at that time. Combining this with the 77–88 Ma obtained through K–Ar dating of the entire kimberlite, it was initially considered to be a product of the Cretaceous period in the Mesozoic era. In the following years, further investigations provided additional insights into the formation age of the kimberlite in the Mengyin area. Ion probe U–Pb analysis of perovskite yielded an age of 457 ± 7 Ma (Lu et al., 1995). This finding led to the proposal that the formation of diamonds occurred during the Paleozoic era, specifically in the Ordovician period, rather than in the Mesozoic era. Subsequent studies generated more Paleozoic age data, primarily concentrated in the range of 455–481 Ma, with the majority of model ages pointing toward the Ordovician period. Accurately constraining the formation age of the kimberlite remains a challenge in geochronological investigations. This is primarily due to the presence of extensive heterologous breccias within the kimberlite and the potential influence of late-stage alteration. These factors contribute to the complexities and uncertainties encountered when determining the precise age of the kimberlite formation.

The isotopic model age of perovskite in the Mengyin kimberlite was determined through U–Pb analysis, yielding a constraint of 465 ± 8 Ma (Song et al., 2009). Similarly, Yang et al. (2009) employed the U–Pb method to measure the isotopic model age of perovskite in the Mengyin kimberlite, resulting in a constraint of 470 ± 4 Ma. Phlogopite megacrysts collected from the Shengli No. 1 kimberlite pipe in the Changmazhuang rock belt were subjected to ^{39}Ar–^{40}Ar dating, yielding a plateau age of 466.3 ± 3 Ma and an isochron age of 464.9 ± 2.7 Ma. These ages align closely with the plateau age of 463.9 ± 0.9 Ma and isochron age of 463.9 ± 6.3 Ma obtained from phlogopite megacrysts in the No. 50 kimberlite pipe in Fuxian, Liaoning Province (Yang et al., 2009). Zhang et al. (2007) proposed that both Mengyin and Fuxian kimberlites were intruded at 465 Ma.

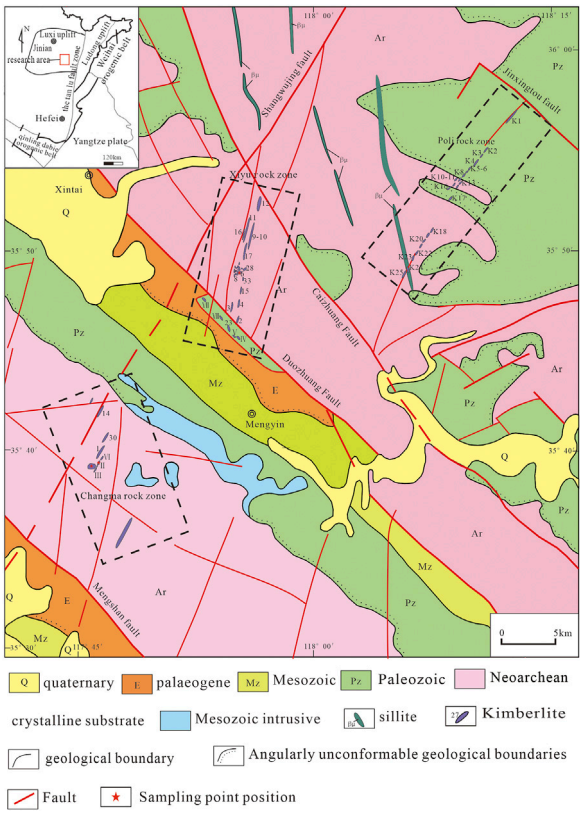


FIGURE 1
Geological map of kimberlite distribution in the Mengyin area (Lv and Ge, 2016). 1: Quaternary; 2: Paleogene; 3: Mesozoic; 4: Paleozoic; 5: Neoarchean crystalline substrate; 6: Mesozoic intrusive; 7: sillite; 8: kimberlite; 9: geological boundary; 10: angularly unconformable geological boundaries; 11: fault.

In a comprehensive study conducted by Li et al. (2016), multi-method tests were conducted on kimberlites taken from the Mengyin and Fuxian areas. Single-grain mica Rb–Sr isochron analysis and perovskite and baddeleyite ion probe U–Pb methods were utilized. The results indicated that the kimberlites in both areas were contemporaneous and formed 480 ± 3 Ma. By analyzing the results from different institutions, minerals, and analytical methods, Li et al. (2016) concluded that the intrusion ages of the kimberlite in the Mengyin area were likely constrained to the range of 450–460 Ma.

Kimberlite magma, originating from depths of approximately 200 km in the mantle, represents the deepest form of magma found in nature. It contains a wealth of deep geological information (Zhou et al., 2007) and serves as a crucial window for investigating the Earth's interior. Among the various components found within kimberlite, the xenoliths derived from the mantle are the most abundant. These xenoliths primarily consist of garnet peridotite, spinel peridotite, and dunite, as well as various types of pyroxene, eclogites, and metasomatic rocks (Lu et al., 1998; Lu, 2008). The age of kimberlite intrusion can be inferred from the thermal alteration of limestone breccias often found in brecciated kimberlite. These breccias undergo thermal alteration by the kimberlite magma, resulting in the formation of marble. In this study, we investigate

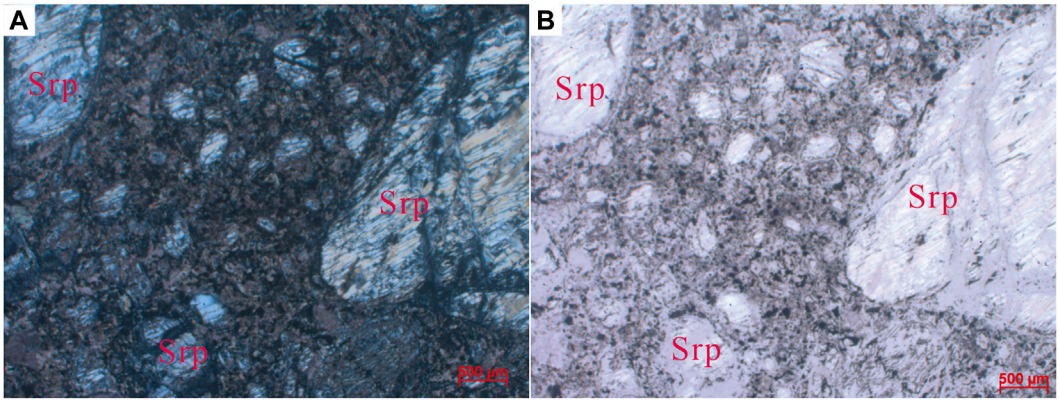


FIGURE 2
Photomicrographs of carbonatized-serpentinized kimberlite from Changmazhuang. **(A)** cross-polarized light photo; **(B)** plane-polarized photo. Srp-serpentine.

the pressure–temperature (P/T) conditions and the timing of the final consolidation of kimberlite at lower temperatures. This is achieved through the examination of fluid inclusions and U–Pb isotopic ages in calcite obtained from the kimberlite matrix and xenolithic marble, respectively.

2 Geological background

The kimberlite belt investigated in this study is situated in the eastern part of the North China Craton within the central Shandong uplift. It is bordered by the east Shandong uplift and the Sulu ultra-high pressure (UHP) metamorphic belt to the east, the Cenozoic Bohai Bay Basin to the north, and the Cenozoic Jining depression to the west. The geological composition of the area primarily comprises a Neoarchean crystalline basement consisting of metamorphic intrusive rocks, Paleozoic marine sedimentary cover, and Meso-Cenozoic continental basin sedimentary strata. Additionally, there are minor occurrences of Mesozoic diorite intrusive rock masses (Song et al., 2020). The Shangwujing fault, NW Mengshan fault, Xintai–Duozhuang fault, and Tongyedian–Sunzu fault are the major fault structures in the region (Figure 1).

The kimberlite belts in the Mengyin area are distributed across the Changmazhuang, Xiyu, and Poli regions (Figure 1). The overall orientation of these three kimberlite belts is approximately 55°, with a combined length of approximately 55 km and a width of 15 km. Each individual belt has a length of 12–15 km, gradually curving northeastward from south to north, resulting in a "broom" shape in their planar morphology as they scatter toward the north. The Changma rock belt is located in the southern region and consists of concentrated pipe distributions. The Xiyu rock belt is primarily controlled by two NNE-trending tectonic fracture zones, exhibiting a significant number of distributed pipes, with a predominant concentration around Xiyu. The Poli rock belt, situated in the northeastern area, displays a parallel intermittent distribution of single veins. The orientation of the individual veins within the rock belt remains consistent with each other. The diamond content in these three rock belts gradually decreases from south to north (Luo et al., 1999; Wang et al., 2015; Zhao, 2019), with the Poli kimberlite belt showing little or no presence of diamonds. Each vein is composed of numerous small veinlets arranged in a plume-like pattern, ranging in length from a few hundred meters to approximately 1,500 m. The individual veinlets within the veins generally exhibit a monomeric orientation of 20°–30°, tending toward the southwest or northwest with a steep dip.

The Changmazhuang rock belt is situated in the southern part of the Mengyin kimberlite area and comprises a total of two rock pipes and 113 single veins. The dense distribution of single veins allows for their subdivision into eight vein groups. The rock belt stretches over a length of 14 km and has a width of approximately 2.5 km (Zhang, 2006; Wang et al., 2013; Chen et al., 2018; Yang et al., 2018; Chu, 2019). The predominant lithologies within the Changmazhuang rock belt are porphyritic kimberlite, accompanied by carbonated-serpentinized kimberlite. These rocks exhibit a porphyritic texture as well as a massive structure. The mineral composition of the rocks is largely composed of olivine, garnet, phlogopite, calcite, opaque minerals, and other minerals (Figure 2).

The Xiyu rock belt is situated in the central part of the Mengyin kimberlite area and encompasses a total of 10 rock pipes and 11 groups of veins, consisting of 151 single veins. It stretches over a length of 15 km and has a width ranging from 0.5 km to 1 km (Chu, 2019). The overall strike of the rock belt is approximately 15°. The surrounding rocks in the area mainly consist of Neoarchean monzonitic granitic gneisses and early Paleozoic Cambrian–Ordovician sedimentary covers. The highest level of kimberlite intrusion is observed in the Wuyangshan Formation of the Middle Ordovician Majiagou Group. The major lithologies within the veins of the Xiyu rock belt predominantly exhibit phlogopite porphyritic kimberlite. At the northern end of the veins, there is a strong presence of limonitization and silicification. The veins oriented in the northwest direction display carbonated porphyritic kimberlite and fine porphyritic microporphyritic kimberlite (porphyrite) containing limestone or granitic breccia. The rock pipes within the belt are primarily composed of porphyritic kimberlite, followed by kimberlite breccia, porphyritic pyrope-kimberlite, fine-grained kimberlite, carbonated kimberlite, and porphyritic rock ball-bearing kimberlite, among others (Figure 3).

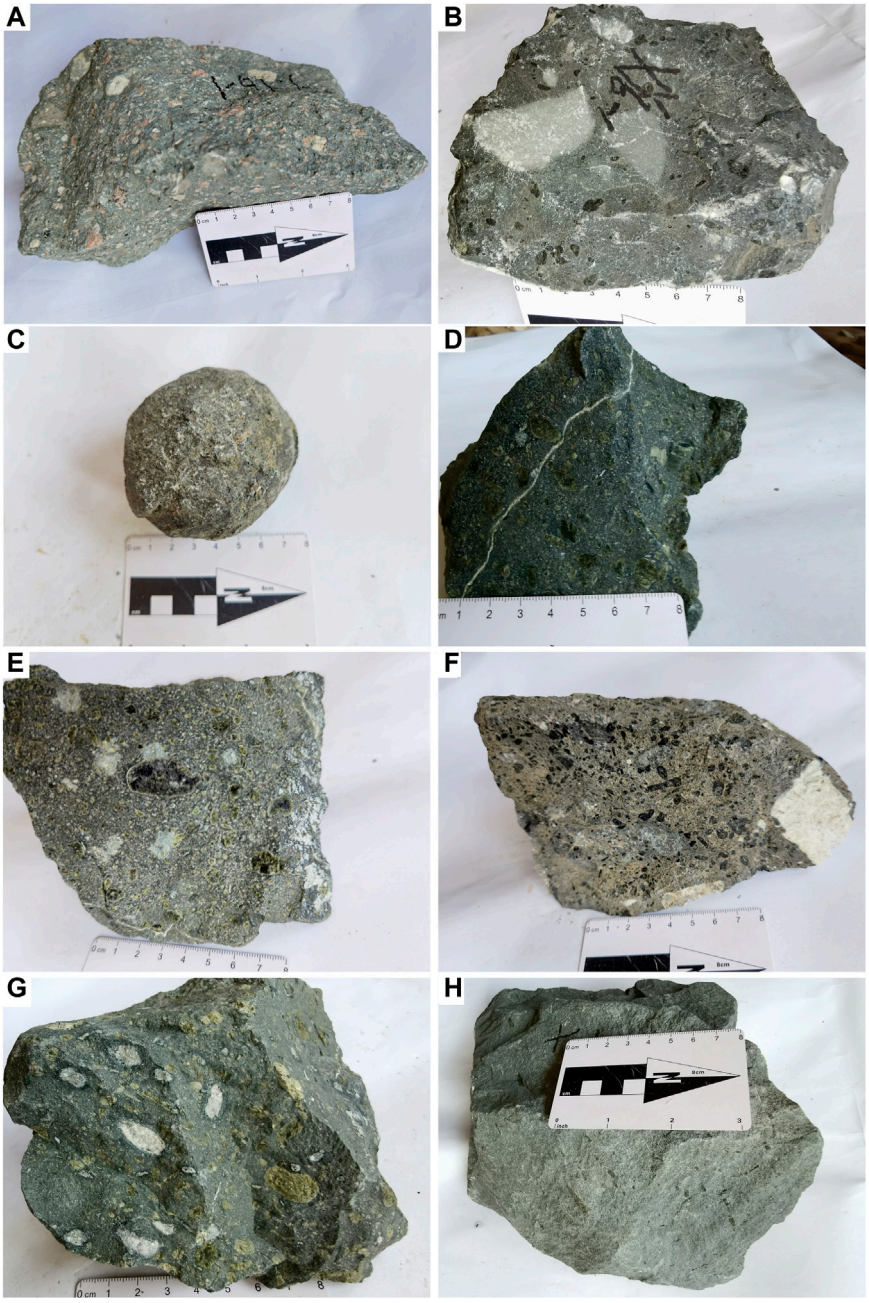


FIGURE 3
Various types of kimberlite from Xiyu. **(A)** Granitic kimberlite breccia. **(B)** Marbled kimberlite. **(C)** Kimberlite rock ball. **(D, E)** Porphyritic kimberlite containing pyrope. Porphyritic kimberlite containing pyrope. **(F, G)** Porphyritic kimberlite. Porphyritic kimberlite. **(H)** Fine-grained kimberlite.

The Poli rock belt is situated in the northern part of the Mengyin kimberlite area, with a general strike ranging from 35° to 40°. It comprises a total of 25 veins, with four groups consisting of 2–8 veins each (Chu, 2019). The prevailing lithology within the belt is finely porphyritic, microgranular phlogopite-bearing kimberlite, with the northern section, which is generated in the sedimentary cover, exhibiting a stronger degree of carbonation (Jin et al., 1999). The surrounding rocks invaded by the veins primarily consist of Neoarchean monzonitic granitic gneisses and Cambrian–Ordovician sedimentary covers (Du et al., 2019).

In terms of the diamond grade, the Changmazhuang rock belt generally exhibits a high grade and the Xiyu rock belt shows a medium grade, while the Poli rock belt presents a lower grade. This indicates a gradual decrease in diamond grade from south to north in the spatial–temporal distribution. In the first two rock belts, the mineralization of the rock pipes is generally higher than that of the veins, and it gradually depletes toward the deeper part. Based on the classification of magmatic stage minerals, hydrothermal alteration minerals, and xenolith minerals, the mineral assemblages of kimberlite in the Mengyin area can be divided into primary minerals, altered metasomatic minerals, and xenoliths (Table 1).

TABLE 1 Mineral assemblages of kimberlite in the Mengyin region.

Primary mineral (magmatic stage mineral)	Altered metasomatic mineral (minerals of hydrothermal alteration)	Xenolith mineral	
		Deep source	Generally surrounding rock
Olivine, phlogopite, pyrope, chrome spinel, diamond, chrome (green) diopside, picroilmenite, ilmenite, apatite, perovskite, yimengite, mathiasite, moissanite, graphite	Serpentine, bornite, calcite, sphalerite, talc, galena, chlorite, pyrite, titanite, millerite, hydromuscovite, magnetite, vermiculite, diopside, perovskite, covellite, leucoxene, malachite, hematite, chalcopyrite, limonite, pyrolusite, barite, andradite, grossular, uvarovite, phlogopite	Olivine, phlogopite, pyrope, chromitehrome (green) diopside, picroilmenite, diamond orthopyroxene, graphite	Pyrope–almandine, pyrope, tourmaline, hornblende, biotite, zircon, hematite, imonite, magnetite, rutile, anatase, quartz, feldspar, apatite

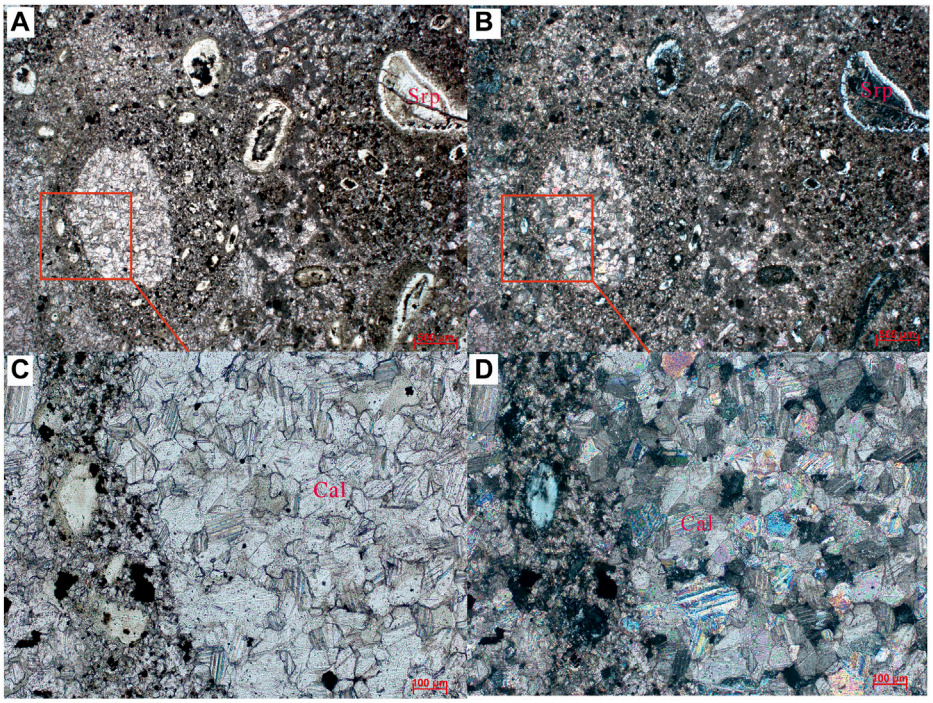


FIGURE 4
Characteristics of marble inclusions in kimberlite. **(A)** Plane-polarized light; **(B)** perpendicular polarized light; **(C)** partial of plane-polarized light; **(D)** partial of perpendicular polarized light. Srp, serpentine; Cal, calcite.

3 Sampling and analytical methods

3.1 Sampling

The samples were primarily collected from the rocks of the Changmazhuang, Xiyu, and Poli kimberlite belts in the Mengyin area, with a particular emphasis on the kimberlite-containing marble xenoliths in the Xiyu rock belt.

3.2 Analytical methods

In this study, several analytical procedures were conducted, including petrographic study using thin rock sections for identification, measurement of fluid inclusion temperatures, and U–Pb dating of carbonates.

The petrographic study and fluid inclusion temperature measurement were carried out at the Key Laboratory of Gold Mineralization Processes and Resource Utilization, affiliated with the Ministry of Land and Resources, and the Key Laboratory of Metallogenic Geological Process and Resources Utilization in Shandong Province. The fluid inclusions' homogenization and freezing temperatures were determined using a Linkam THMS600 hot and cold platform, manufactured in the United Kingdom, with temperature intervals ranging from −196°C to +600°C.

For carbonate U–Pb isotope age dating, calcite samples were collected from marble inclusions and kimberlite matrix in the Xiyu kimberlite. The marble was formed through the thermal alteration of limestone surrounding the kimberlite (Figure 4), providing information on the timing of the kimberlite diagenesis. *In situ* U–Pb dating was conducted using a laser-ablation microprobe at

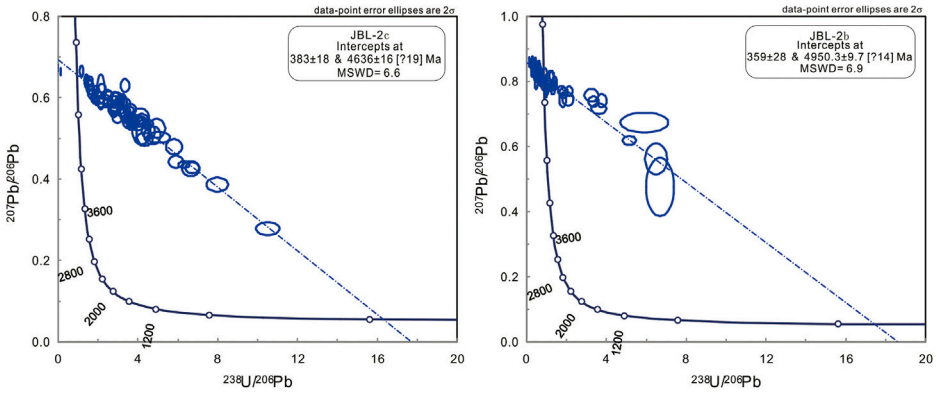


FIGURE 5
U–Pb concordia plot of carbonate in Xiyu kimberlite. JBL-2b, marble inclusions; JBL-2C, matrix calcite.

the Radioisotope Laboratory, University of Queensland. The sample was prepared as a 2.5-cm-diameter target and placed in a Laurin Technic cuvette. The ASI RESOlution SE laser-ablation system was coupled with a Thermo iCAP-RQ four-stage rod ICP-MS for ion scanning of ^{206}Pb, ^{207}Pb, ^{208}Pb, ^{238}U, and ^{232}Th. The laser-ablation frequency was set at 10 Hz, with a density of 3 J/cm^2, resulting in a laser ablation pit diameter of approximately 100 μm.

Sample processing involved the use of the international standard NIST-614 for isotope fractionation and offset correction of instrument sensitivity. U–Pb age correction was performed using calcite standards AHX-1D (203.3 ± 2.3 Ma), WC01-A (252.9 ± 1.8 Ma), and PTKD-2A (151.3 ± 6.0 Ma). The lower intercept ages were calculated using the Excel-loaded term Tera–Wasserburg of Isoplot (Paton et al., 2011) to obtain the U–Pb age of calcite (Yang et al., 2021).

3.3 Results

3.3.1 Results of carbonate U–Pb dating

The marble xenoliths can be observed as white masses within the kimberlite (Figure 4). In sample area b, the marble exhibits an average U content of 0.327×10^{-6} and a Pb content of 1.158×10^{-6} in calcite. On the other hand, the calcite in the matrix of area c shows an average U content of 4.618×10^{-6} and a Pb content of 4.468×10^{-6}. The Tera–Wasserburg diagram reveals a significant number of data points clustering around the upper intercept. Despite this, the resulting lower intercept ages of 359 ± 28 Ma (MSWD=6.9) and 383 ± 18 Ma (MSWD=6.6) remain reliable (Figure 5). The higher U and Pb contents in area c suggest less error and greater reliability in the data, which can be interpreted as the ages of primary calcite in the marble and kimberlite, respectively. Therefore, the formation time of the kimberlite can be constrained to 383 ± 18 Ma, while the marbleization process occurred slightly later, approximately 359 ± 28 Ma.

3.3.2 Petrographic characteristics and microthermometry of fluid inclusions

The Mengyin area showcases a diverse range of kimberlite types, including carbonated kimberlite, which contains a significant amount of recrystallized calcite and primary calcite particles. Within the calcite, both single-phase and two-phase fluid inclusions of varying sizes and quantities are present. For our current investigation, we collected fresh samples of carbonated kimberlite from the Mengyin area. These samples were prepared as double-polished microtonalite sheets, allowing for microscopic observation and subsequent microthermometry analysis.

3.3.2.1 Petrographic characteristics of fluid inclusions

Fluid inclusions within carbonated kimberlites are relatively scarce and not well-developed. Microscopic observation reveals the presence of three types of inclusions: single-phase liquid inclusions (type Ia, Figure 6A), single-phase gas inclusions (type Ib, Figure 6B), and water–gas–liquid two-phase inclusions (type II, Figures 6C–L). Among these types, the water–gas–liquid two-phase inclusions are more abundant than the single-phase inclusions. The inclusions can be found isolated, scattered, or clustered within calcite particles (Figures 6C–L). The individual inclusions are generally small, with most ranging from 2–8 μm, although some may exceed 10 μm in size (Figures 6C–F). In terms of shape, the inclusions typically exhibit a negative crystal shape of calcite (Figure 6G), columnar shape (Figures 6F, H), spherical shape (Figures 6D, I, J), oval shape (Figures 6K, L), and irregular shape (Figures 6C, E). The gas–liquid ratio of the majority of the two-phase inclusions is approximately 20%, while some bubbles within the two-phase inclusions with smaller gas–liquid ratios exhibit constant movement. Individual inclusions with larger gas–liquid ratios account for approximately 40% (Figures 6F, J).

3.3.2.2 Microthermometry of fluid inclusions

Given that the size of the single-phase inclusions was found to be smaller than 2 μm, only the microthermometry analysis of the aqueous two-phase inclusions was performed in this temperature measurement experiment.

During the analysis, the gas–liquid two-phase inclusions were homogenized into the liquid phase, and the homogenization temperature ranged from 243°C to 370°C. The freezing point temperature, which corresponds to the final melting temperature of water ice, varied between −10.8 and −1.5°C.

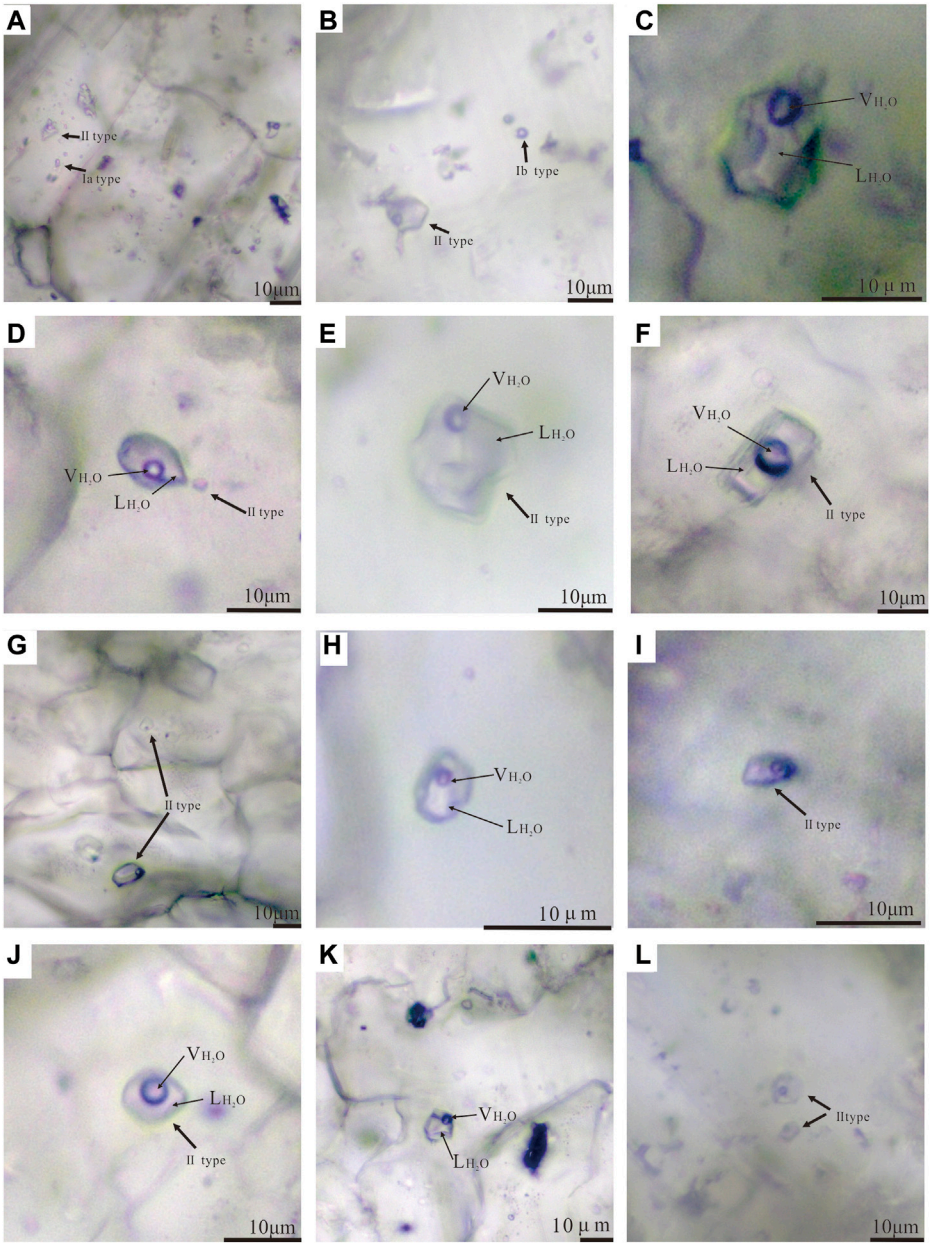


FIGURE 6
Photomicrographs showing representative examples of calcite-hosted fluid inclusions within the Mengyin kimberlites. **(A, B)** Ia Type and II Type fluid inclusions. **(C–F)** fluid inclusions exceed 10 μm in size. **(G)** inclusions exhibit a negative crystal shape of calcite. **(F, H)** columnar shape fluid inclusions. **(D, I ,J)** spherical shape fluid inclusions. **(K, L)** oval shape fluid inclusions. **(C, E)** irregular shape fluid inclusions. **(F, J)** Type II inclusions containing ~40% vapor phase. Abbreviations: V, vapor; L, liquid.

3.3.2.3 Physical and chemical parameters of the fluid inclusions

Based on the temperature measurement results of fluid inclusions, the complete homogenization temperature (Th-$_{TOT}$, ˚C) and freezing point (Tm-ice, ˚C) of fluid inclusions can be derived directly.

The salinity of gas–liquid two-phase inclusions was estimated using the salinity equation proposed by Potter et al. (1978), which utilizes the freezing point temperature (Tm-ice, ˚C), which is given as follows:

$S = 0.00 + 1.78 \times Ti\text{-}0.0442 \times Ti^2 + 0.000557 \times Ti^3$ (where Ti represents freezing point temperature).

When the salinity S is between 1% and 30%, the density of the brine solution in the inclusions can be obtained using formulas proposed by Haas (1970) and Bodnar (1983): $\rho = A + B \times t + C \times t^2$.

Here, ρ—brine solution density (g/cm^3), t—homogenization temperature (˚C), and A, B, C—a function of salinity.

Here, $A = 0.993531 + 8.72147 \times 10^{-3} \times S - 2.43975 \times 10^{-5} \times S^2$,
$B = 7.11652 \times 10^{-5} - 5.2208 \times 10^{-5} \times S + 1.26656 \times 10^{-6} \times S^2$,
$C = -3.4997 \times 10^{-6} + 2.12124 \times 10^{-7} \times S - 4.52318 \times 10^{-9} \times S^2$,

TABLE 2 Microthermometry and physicochemical parameters of calcite mineral inclusions.

Sample no.	Inclusion type	Homogenization temperature (°C)	Freezing point temperature (°C)	Salinity (wt %NaCl)	Density (g/cm^3)	Pressure P(Mp)	Depth (m)
1	Gas–liquid two-phase (saline) inclusions	260	−8.5	12.28	0.89	4.30	962.34
2		256	−10.8	14.77	0.92	3.93	1014.15
3		243	−8.7	12.51	0.91	3.22	905.51
4		247	−9.7	13.62	0.92	3.42	949.54
5		270	−8.5	12.28	0.88	5.04	999.36
6		370	−8.3	12.05	0.74	19.13	1360.14
7		283	−3.2	5.26	0.79	6.50	796.87
8		370	−1.5	2.57	0.59	20.70	883.84

where Th—homogenization temperature (°C) and s—salinity (%).

Pressure and depth estimation follows the empirical equation by Shao (1988):

$T0 = 374 + 9.20 \times N$, $P0 = 219 + 26.20 \times N$, $P1 = P0 \times T1/T0$, and $H1 = P1/(300 \times 10^5)$. In the aforementioned formulas, T0 is the initial temperature (°C), P0 is the initial pressure value (10^5 Pa), T1 is the actual metallogenic temperature (°C), P1 is the metallogenic pressure value (10^5 Pa), H1 is the metallogenic depth (km), and N presents salinity of ore-forming fluid (NaCl%).

According to the aforementioned equations, the NaCl salinity of the fluid inclusions ranges from 2.57 to 14.77 wt% (NaCl equivalent). The density (ρ) of the inclusions varies from 0.59 to 0.92 g/cm^3. The pressure of inclusions varies between 3.22 and 20.70 megapascals (MPa). The estimated formation depth ranges from 796.87 m to 1,360.14 m, with the majority falling between 900 m and 1,000 m (Table 2).

4 Discussion

4.1 Formation age of kimberlite

The determination of the formation age of kimberlite primarily relies on the age of its characteristic minerals such as perovskite, phlogopite, baddeleyite, pyrope, and whole kimberlite. Various methods are used, including U–Pb analysis, Sm–Nd analysis, Ar–Ar isochron analysis, and K–Ar analysis (Table 3; Figure 7). The perovskite U–Pb system has closure temperatures of approximately 875°C–900°C, which are relatively high compared to other kimberlite minerals (Wu et al., 2010). As perovskite is less affected by late alteration and weathering (Paton et al., 2007; Yang et al., 2009), its recorded magma crystallization age is generally considered more reliable. Perovskite is believed to have originated from a single source and crystallized directly from the kimberlitic magma, reducing the complexity of interpreting mineral sources and ages (Heaman et al., 2019). Therefore, many researchers (Yang et al., 2009; Li et al., 2010; Sun et al., 2014; Sun et al., 2018) argue that perovskite U—Pb dating is the preferred method for dating kimberlites due to its statistical performance and widespread acceptance.

The intrusive age of diamond-bearing kimberlites (porphyrites) is estimated to be approximately 455 Ma but remains controversial. Wang et al. (2014) suggested that kimberlite emplacement in the area occurred during the Permian of the Paleozoic era (250–300 Ma), based on multiple constraints, including the age of emplacement strata, denudative sedimentary strata, paleomagnetism, joint structure, and isotopic dating. Chu et al. (2019) conducted LA-ICP-MS zircon U–Pb dating on diabase veins invaded by kimberlite and obtained a minimum age of 117–121 Ma, suggesting late Mesozoic Yanshanian kimberlite intrusion. Further comprehensive investigations are needed to resolve these controversies.

The Mengyin kimberlite magma is characterized by multiple intrusions (Hu, 1985), with three main intrusions identified in the Changmazhuang rock belt and five in the Xiyu rock belt. The second intrusion in the Xiyu rock belt is predominantly composed of massive limestone brecciated kimberlite. While ascending, kimberlite magma is rarely known to cause thermal effects, such as contact metamorphism, on the surrounding rocks of the breccia pipe zone or xenoliths, so kimberlite is generally considered a "cold" rock (Sun and Sun, 2021). However, the kimberlite in the Mengyin area contains a significant amount of surrounding rock xenoliths, where most of the early Paleozoic limestone has been thermally altered to marble after being trapped. No large-scale magmatic thermal events have been recorded in the area after the emplacement of kimberlite. Therefore, the age of the marble in this kimberlite can represent the final formation time of the kimberlite cooling epoch.

The U–Pb dating results indicate that the calcite found in the kimberlite matrix has an age of 383 ± 18 Ma, while the calcite in the marble has an age of 359 ± 28 Ma. The high U and P contents in the calcite from the matrix suggest a different origin compared to the marble, indicating a deep-seated source for the kimberlite. The ages of the kimberlite represent the time when it solidified, while the ages of the marble indicate the period when it was formed through thermal alteration, which is slightly later than the kimberlite matrix.

Various dating methods were used to analyze and test the kimberlite in the area, resulting in a significant amount of isotopic dating data ranging from 77 Ma to 765 Ma (Table 2). Field observations reveal that the kimberlite intruded into the Ordovician strata. No kimberlite breccia was found in the Badou

TABLE 3 List of ages of kimberlites in the Mengyin region.

Rock belt	Name of the rock mass	Lithology	Measured minerals	Analysis method	Dating(Ma)	Reference
Changma rock belt	Shengli No. 1	Pyrope coarse-grained kimberlite	Whole rock	K–Ar	634	Yang et al. (2015)
Changma rock belt	Shengli No. 1	Pyrope coarse-grained kimberlite	Whole rock	K–Ar	716	Yang et al., 2015; Lv et al., 2016
Changma rock belt	Shengli No. 1	Pyrope coarse-grained kimberlite	Phlogopite	Rb–Sr	494	Yang et al. (2015)
Changma rock belt	Shengli No. 1	Kimberlite	Phlogopite	Rb–Sr	484	Yang et al. (2015)
Changma rock belt	Shengli No. 1	Kimberlite	Phlogopite	Rb–Sr	474	Yang et al. (2015)
Changma rock belt	Shengli No. 1	Kimberlite	Perovskite	U–Pb SHIMP	457	Lu et al. (1995)
Changma rock belt	Shengli No. 1	Kimberlite	Perovskite	U–Th–Pb	480	Li (2016)
Changma rock belt	Shengli No. 1	Kimberlite	Phlogopite	Rb–Sr	485	Wang et al. (1997)
Changma rock belt	Shengli No. 1	Kimberlite	Whole rock	Rb–Sr isochron	616	Wang et al. (1997)
Changma rock belt	Shengli No. 1	Kimberlite	Whole rock + serpentine	Rb–Sr isochron	605	Wang et al. (1997)
Changma rock belt	Shengli No. 1	Kimberlite	Whole rock + matrix phlogopite	Rb–Sr isochron	560	Wang et al. (1997)
Changma rock belt	Shengli No. 1	Kimberlite	Whole rock + megacryst phlogopite	Rb–Sr isochron	573	Wang et al. (1997)
Changma rock belt	Shengli No. 1	Kimberlite	Whole rock +garnet	Rb–Sr isochron	651	Wang et al. (1997)
Changma rock belt	Shengli No. 1	Kimberlite	Pyrope	Rb–Sr isochron	633	Lv et al. (2016)
Changma rock belt	Shengli No. 1	Globular kimberlite	Whole rock	Rb–Sr isochron	644	Lu et al. (1995)
Changma rock belt	Shengli No. 1	Kimberlite	Phlogopite megacryst	Rb–Sr isochron	499	Lu et al. (1995)
Changma rock belt	Shengli No. 1	Fine-grained kimberlite	Whole rock	Rb–Sr isochron	765	Lu et al. (1995)
Changma rock belt	Shengli No. 1	Mantle-derived inclusions	Pyrope	Sm–Nd	550	Lv et al. (2016)
Changma rock belt	Hongqi No. 1	Kimberlite	Pyrope	Sm–Nd	625	Lv et al. (2016)
Changma rock belt	Hongqi No. 1	Fine-grained kimberlite	Whole rock	Sm–Nd	567	Lv et al. (2016)
Changma rock belt	Hongqi No. 1	Pyrope coarse-grained kimberlite	Phlogopite	K–Ar	554	Yang et al. (2015)
Changma rock belt	Hongqi No. 1	Pyrope coarse-grained kimberlite	Phlogopite	K–Ar	530	Yang et al. (2015)
Changma rock belt	Hongqi No. 1	Pyrope coarse-grained kimberlite	Phlogopite	K–Ar	476	Yang et al. (2015)
Changma rock belt	Hongqi No. 1	Pyrope coarse-grained kimberlite	Phlogopite	K–Ar	455	Yang et al. (2015)
Changma rock belt	Hongqi No. 1	Fine-grained kimberlite	Whole rock	Sm–Nd	702	Lv et al. (2016)

(Continued on following page)

TABLE 3 (*Continued*) List of ages of kimberlites in the Mengyin region.

Rock belt	Name of the rock mass	Lithology	Measured minerals	Analysis method	Dating(Ma)	Reference
Changma rock belt	Hongqi No. 2	Fine-grained kimberlite	Whole rock	Sm–Nd	486	Lv et al. (2016)
Changma rock belt	Hongqi No. 3	Porphyritic kimberlite	Whole rock	Sm–Nd	455	Lv et al. (2018)
Changma rock belt	Hongqi No. 4	Porphyritic kimberlite	Whole rock	Sm–Nd	375	Lv et al. (2016)
Changma rock belt	Shengli No. 1	Kimberlite	Perovskite	U–Pb	457	Lv et al. (2016)
Changma rock belt	Shengli No. 1	Kimberlite	Pyrope	Sm–Nd	633	Lv et al. (2016)
Changma rock belt	Shengli No. 1	Mantle-derived inclusions	Pyrope	Sm–Nd	550	Lv et al. (2016)
Changma rock belt	Shengli No. 1	Kimberlite	Phlogopite	Ar–Ar isochron	466.3	Zhang et al. (2007)
Changma rock belt	Shengli No. 1	Kimberlite	Phlogopite	Ar–Ar isochron	464.9	Zhang et al. (2007)
Changma rock belt	Hongqi No. 1	Kimberlite	Pyrope	Sm–Nd	625	Lv et al. (2016)
Xiyu rock belt	Hongqi No. 6	Phlogopite coarse-grained kimberlite	Whole rock	K–Ar	81	Yang et al. (2015)
Xiyu rock belt	Hongqi No. 6	Phlogopite coarse-grained kimberlite	Whole rock	K–Ar	88	Yang et al. (2015)
Xiyu rock belt	Hongqi No. 6	Phlogopite coarse-grained kimberlite	Whole rock	K–Ar	77	Yang et al. (2015)
Xiyu rock belt	Hongqi No. 6	Phlogopite coarse-grained kimberlite	Brown mica	K–Ar	484.6	Lv et al. (2016)
Xiyu rock belt	Hongqi No. 2	Kimberlite	Pyrope	Sm–Nd	461	Lv et al. (2016)
Xiyu rock belt	Hongqi No. 6	Porphyritic kimberlite	Whole rock	Sm–Nd	619	Zhu and Mao (1991)
Xiyu rock belt	Hongqi No. 6	Kimberlite	Whole rock	Sm–Nd	375	Lv et al. (2016)
Xiyu rock belt	Hongqi No. 2	Kimberlite	Pyrope	Sm–Nd	461	Lv et al. (2016)
Poli rock belt		Phlogopite-bearing kimberlite	Whole rock	K–Ar	371.8	Lv et al. (2016)
Poli rock belt		Phlogopite-bearing coarse-grained kimberlite	Whole rock	K–Ar	233.8	Chu et al. (2019)
Poli rock belt		Phlogopite-bearing coarse-grained kimberlite	Whole rock	K–Ar	379	Chu et al. (2019)
Poli rock belt		Kimberlite	Whole rock	Sm–Nd	479	Chu et al. (2019)
Xiyu rock belt		Kimberlite	Marble	U–Pb	332	This study
Xiyu rock belt		Kimberlite	Calcite	U–Pb	366	This study
Changma rock belt	Shengli No. 1	Kimberlite	Perovskite	U–Pb	470	Yang et al. (2009)

Formation, which is the uppermost stratum of the Ordovician, indicating that the kimberlite formed after the diagenesis of the Ordovician strata. The ages of the Ordovician Majiagou Group range from 485.4 ± 1.9 Ma to 453.0 ± 0.7 Ma (Du et al., 2019; Fan et al., 2021). Therefore, the formation age of the kimberlite should be later than 485.4 ± 1.9 Ma, after eliminating ages before 485 Ma. The remaining ages can be roughly divided into three intervals: 484.6–455 Ma, 379–332 Ma, and 233–77 Ma. In the region, the Silurian and Devonian strata are absent, and no contact relationship between the kimberlite and the strata above the Majiagou Formation (Carboniferous–Permian) has been found (Song et al., 2020). Additionally, only four whole-rock K–Ar ages exist within the interval of 233–77 Ma, which are mixed ages with low credibility. Furthermore, there is limited geological evidence to

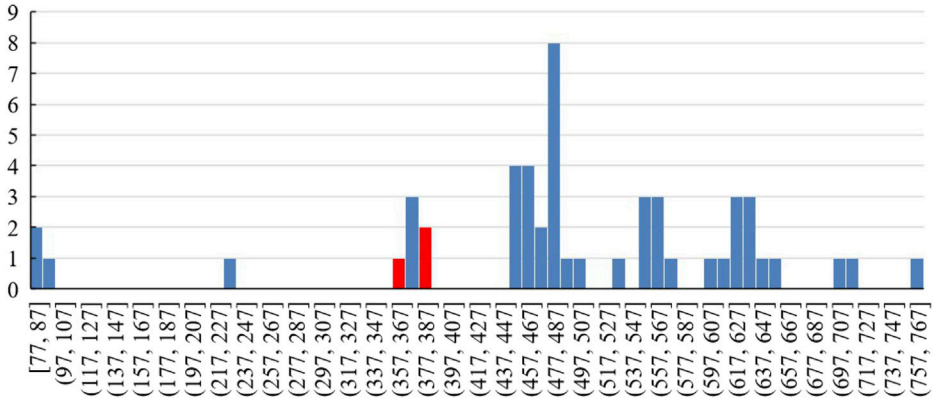


FIGURE 7
Age histograms of kimberlite in the Mengyin region.

support the formation of kimberlite during this stage, making it unlikely that the kimberlite formed at 233 Ma and beyond. Therefore, it is proposed that there were two episodes of kimberlite eruption, with the first one occurring approximately 455 Ma in the Late Ordovician and the second one ending approximately 366 Ma.

In summary, one stage of kimberlite cooling took place during the Late Devonian period (383 ± 18 Ma). Considering previous research findings, the Mengyin area witnessed two periods of kimberlite eruption: one during the Late Ordovician in the Paleozoic and another in the Late Devonian. Subsequently, the partial limestone xenoliths within the kimberlite underwent thermal metamorphism, resulting in the formation of marble, which occurred until approximately 359 ± 28 Ma. The thinning of the lithosphere in this region is believed to have occurred after the Devonian period.

Yin et al. (2005) extensively investigated the temperature, pressure, and depth conditions during diamond formation. They conducted analyses using techniques such as CL (cathode luminescence), FTIR (Fourier transform infrared reflection), and laser Raman on diamond samples from the Shengli No.1 rock pipe in Mengyin, Shandong Province. The findings indicated that most diamonds exhibited uniform CL colors, except for some samples that showed flat growth color bands under CL. This suggests that the diamond growth process was continuous and not subjected to significant dissolution or melting. By analyzing the Raman shift of olivine inclusions within the diamonds, the pressure in the source areas was estimated to be 4.6 GPa, 5 GPa, and 5.5 GPa, with corresponding formation depths for the Mengyin diamonds of 152 km, 165 km, and 181 km. These depths are close to the bottom of the lithosphere, indicating that the lithosphere's thickness during diamond formation was between 150 and 180 km. In contrast, the temperature, pressure, and depth conditions during the kimberlite eruption have not been extensively studied. In the present investigation, a comprehensive study of fluid inclusions in calcite from the kimberlite matrix and xenolithic marble was conducted to determine the temperature, pressure, and consolidation depth during a later kimberlite eruption. The analysis revealed that the temperature during the late eruption ranged from 243°C to 370°C, with a salinity ranging 2.57%–14.77% (NaCl) and pressure ranging 3.22–20.70 MPa. The formation depth was mainly estimated to be between 900 and 1,000 m, indicating that the denudation depth from the time of formation (Late Devonian) to the present is approximately 900–1,000 m. Furthermore, the denudation rate, or the rate of upward movement, from the Late Devonian to the present was estimated to be 3 m/Ma.

5 Conclusion

1) The U–Pb dating results of calcite from the Xiyu kimberlite matrix in the Mengyin area yielded an age of 383 ± 18 Ma (MSWD = 6.6), with average U and Pb contents of 4.618×10^{-6} and 4.468×10^{-6}, respectively. These age data are reliable and indicate the occurrence of a kimberlite eruption in the Mengyin area during the Late Devonian period. The *in situ* U–Pb dating age of calcite from the xenolithic marble in the kimberlite was determined to be 359 ± 28 Ma (MSWD = 6.9), with average U and Pb contents of 0.327×10^{-6} and 1.158×10^{-6}, respectively. Although the U and Pb contents are relatively low and the data quality is somewhat poor, the age value remains credible, representing the thermal alteration of kimberlite limestone xenoliths to form marble at the end of the Late Devonian.
2) It is likely that two periods of kimberlite eruption occurred in the Mengyin area, namely, during the Late Ordovician and the Late Devonian, possibly extending until the end of the Late Devonian. This suggests that the thinning of the lithosphere first took place after the Late Devonian period.
3) The analysis of fluid inclusions in calcite from the kimberlite xenolithic marble reveals important information about temperature, salinity, pressure, and formation depth. The temperature range is estimated to be between 243°C and 370°C, with salinity ranging 2.57%–14.77% (NaCl) and pressure ranging 3.22–20.70 MPa. The main formation depth is determined to be approximately 900–1,000 m, and the total denudation depth from the Late Devonian to the present is also estimated to be 900–1,000 m. Additionally, the overall rate of crustal ascent is calculated to be 3 m/Ma(Cohen et al., 2013, Du et al., 2020, Wang, 2016, Zhang et al., 2011).

Data availability statement

The original contributions presented in the study are included in the article/Supplementary Material; further inquiries can be directed to the corresponding author.

Author contributions

Conceptualization, RT, HW, and JT; Methodology, RT, HW, JT, and WS; Writing—original draft preparation, all authors; Writing—review and editing, RT, HW, and JT; Supervision, RT and HW; Funding acquisition, HW and WS. All authors have read and agreed to the submitted version of the manuscript.

Funding

This research was jointly supported by the General Project of Natural Science Foundation of Shandong Province (ZR2020MD030 and ZR2021MD052), the Science and Technology Innovation Cultivation Program of Shandong Academy of Geological Sciences (PYJH202102), and the Youth Fund from Natural Science Foundation of Shandong Province (ZR2020QD029).

Conflict of interest

The authors declare that the research was conducted in the absence of any commercial or financial relationships that could be construed as a potential conflict of interest.

Publisher's note

All claims expressed in this article are solely those of the authors and do not necessarily represent those of their affiliated organizations, or those of the publisher, the editors, and the reviewers. Any product that may be evaluated in this article, or claim that may be made by its manufacturer, is not guaranteed or endorsed by the publisher.

References

Bodnar, R. J. (1983). A method of calculating fluid inclusion volumes based on vapor bubble diameters and P-V-T-X properties of inclusion fluids. *Fluids Econ. Geol.* 78, 535–542. doi:10.2113/gsecongeo.78.3.535

Boyd, F. R., and Gurney, J. J. (1986). Diamonds and the african lithosphere. *Science* 232 (4749), 472–477. doi:10.1126/science.232.4749.472

Cai, Y. C., Fan, H. R., Hu, F. F., Yang, K. F., Lan, T. G., Yu, H., et al. (2011). Ore-forming fluids stable isotope and mineralizing age of the Hu bazhuang gold deposit Jiaodong Peninsula of eastern China. *Acta Petrol. Sin.* 27 (5), 1341–1351.

Chen, Y. M., Yang, Z. J., Huang, S. S., Lei, X. Y., Li, X. X., and Zeng, X. (2018). Microfabrics of perovskites in the menyin kimberlites and their geological implications. *Bull. Mineralogy, Petrology Geochem.* 37 (4), 1–10.

Chu, Z. Y., Wang, W. D., Lv, Q., Kang, C. X., and Wang, S. X. (2019). The formation age of the kimberlite zone in Poli area of Mengyin, Shandong Province: Zircon U-Pb dating data of diabase. *Geol. Bull. China* 38 (1), 44–50.

Cohen, K. M., Finney, S. C., Gibbard, P. L., and Fan, J.-X. (2013). The ICS international chronostratigraphic chart. *Episodes* 36, 199–204. doi:10.18814/epiiugs/2013/v36i3/002

Du, S. X., Liu, F. C., Chen, J., Gao, L. M., Song, X. S., Chen, C., et al. (2019). The cretaceous- paleocene biostratigraphy and boundary in the pingyi basin, Shandong province. *Acta Geol. Sin.* 93 (8), 1831–1848.

Du, Z. Z., Cheng, Z. Z., Yao, X. F., et al. (2020). 40Ar-39Ar age of altered potash feldspar of xiejiagou gold deposit in jiaodong and its geological significance. *J. Jilin Univ. (Earth Sci. Ed.* 50 (5), 1570–1581.

Giuliani, A., Phillips, D., Kamenetsky, V. S., and Goemann, K. (2016). Constraints on kimberlite ascent mechanisms revealed by phlogopite compositions in kimberlites and mantle xenoliths. *Lithos* 240-243, 189–201. doi:10.1016/j.lithos.2015.11.013

Haas, J. L. (1970). An equation for the density of vapor-saturated NaCl-H2O solutions from 75 degrees to 325 degrees C. *Am. J. Sci.* 269 (5), 489–493. doi:10.2475/ajs.269.5.489

Haggerty, S. E. (1986). Diamond Genesis in a multiply-constrained model. *Nature* 320 (6057), 34–38. doi:10.1038/320034a0

Heaman, L. M., Kjarsgaard, B. A., and Creaser, R. A. (2003). The timing of kimberlite magmatism in North America: Implications for global kimberlite Genesis and diamond exploration. *Lithos* 71 (2), 153–184. doi:10.1016/j.lithos.2003.07.005

Heaman, L. M., Phillips, D., and Pearson, G. (2019). Dating kimberlites: Methods and emplacement patterns through time. *Elements* 15 (6), 399–404. doi:10.2138/gselements.15.6.399

Hu, S. Y. (1985). The forming temperatures and pressures for the Mengyin kimberlites. *Geology of Shandong* 1 (1), 79–84. (in Chinese with English Abstract).

Jin, Z. K., Liu, Z. R., and Shi, Z. R. (1999). Types of fault structures and their formation mechanisms in the Western Shandong Province. *J. Univ. Petroleum, China* 23 (5), 1–5.

Li, Q. L., Li, X. H., Liu, Y., Wu, F. Y., Yang, J. H., and Mitchell, R. H. (2010). Precise U-Pb and Th-Pb age determination of kimberlitic perovskites by secondary ion mass spectrometry. *Chem. Geol.* 269 (3-4), 396–405. doi:10.1016/j.chemgeo.2009.10.014

Liu, J. T. (2002). Study on primary diamond ore-forming future in Shandong province. *Geol. Shandong* 18 (3-4), 100–104.

Lu, F. X. (2008). Kimberlite and diamond. *Chin. J. Nat.* 30 (2), 63–66.

Lu, F. X. (2010). Multiple-geological events of ancient lithospheric mantle beneath North China craton: As inferred from peridotite xenoliths in kimberlite. *Acta Petrol. Sin.* 26 (11), 3177–3188.

Lu, F. X., Zhao, L., Deng, J. F., and Zheng, J. P. (1995). The discussion on the ages of kimberlitic magma activity in north China platform. *Acta Pet. Sin.* 11 (4), 365–374.

Lu, F. X., Zheng, J. P., and Chen, M. H. (1998). Discussion on formation condition of diamonds. *Earth Sci. Front.* 5 (3), 125–131.

Luo, S. X., Ren, X. R., and Zhu, Y. (1999). *Diamond geology of Shandong*. Jinan, China: Shandong Science and Technology Publishing House, 1–131.

Lv, Q., and Ge, Y. J. (2016). Study on age dating methods and age dating samples of kimberlite. *Shandong Land Resour.* 32 (10), 12–15.

Paton, C., Hellstrom, J., Paul, B., Woodhead, J., and Hergt, J. (2011). Iolite: Freeware for the visualisation and processing of mass spectrometric data. *J. Anal. Atomic Spectrom.* 26 (12), 2508–2518. doi:10.1039/c1ja10172b

Paton, C., Hergt, J. M., Phillips, D., Woodhead, J. D., and Shee, S. R. (2007). New insights into the Genesis of Indian kimberlites from the Dharwar Craton via *in situ* Sr isotope analysis of groundmass perovskite. *Geology* 35 (11), 1011–1014. doi:10.1130/g24040a.1

Potter, W., Clynne, M. A., and Brown, L. (1978). Freezing point depression of aqueous sodium chloride solutions. *Econ. Geol.* 73 (2), 284–285. doi:10.2113/gsecongeo.73.2.284

Sheng, X. Y. (2004). Diamond prospecting deserved in persistence: Viewpoints for the anomaly of diamond in East Guizhou 21 (4), 234–239. (in Chinese with English Abstract).

Shao, J. L. (1988). *Mineralogy of gold ore prospecting*. Beijing, China: China University of Geosciences Press, 1–158.

Song, M. C., Xu, J. X., and Wang, P. C. (2009). *Tectonic framework and tectonic evolution of the shandona Province*. Shandong, China: Geology Press, 114.

Song, M. C., Yu, X. S., Song, Y. X., Xiao, B. J., Zhou, D. S., Gao, C. S., et al. (2020). Types, sources, and regional crust-mantle evolution background of diamonds in the Western Shandong Province. *Acta Geol. Sin.* 94 (9), 2606–2625.

Sun, J., Liu, C. Z., Tappe, S., Kostrovitsky, S. I., Wu, F. Y., Yakovlev, D., et al. (2014). Repeated kimberlite magmatism beneath Yakutia and its relationship to Siberian flood volcanism: Insights from *in situ* U-Pb and Sr-Nd perovskite isotope analysis. *Earth Planet. Sci. Lett.* 404, 283–295. doi:10.1016/j.epsl.2014.07.039

Sun, J., Tappe, S., Kostrovitsky, S. I., Liu, C. Z., Skuzovatov, S. Y., and Wu, F. Y. (2018). Mantle sources of kimberlites through time: A U-Pb and Lu-Hf isotope study of zircon megacrysts from the siberian diamond fields. *Chem. Geol.* 479, 228–240. doi:10.1016/j.chemgeo.2018.01.013

Sun, J. X., and Sun, J. (2022). Review of kimberlite dating methods. *Bull. Mineralogy Petrology Geochem.* 41 (1), 175–196.

Wang, X. F. (2016). Orsovocoan tectonic-paleogegraphy in South China and chrono and biostratigraphic divison and correlation. *Earth Sci. Front.* 26 (6), 253–267.

Wang, Y., Ling, W. L., and Lu, F. X. (1997). *Geol. Sci. Technol. Inf.* 16 (3), 9–12.

Wang, Z. B., Cao, H. C., Li, D. P., Bian, Q., Wang, Q. J., and Yang, B. (2015). Mineralization and prospecting significance of kimberlite deposit in fangshan area of Shandong province. *Shandong Land Resour.* 31 (5), 1–6.

Wang, Z. B., Lv, Q., Ge, Y. J., Wang, Q. J., and Peng, J. (2013). Diversity of culturable root-associated/endophytic bacteria and their chitinolytic and aflatoxin inhibition activity of peanut plant in China. *Shandong Land Resour.* 29 (10-11), 1–10. doi:10.1007/s11274-012-1135-x

Wang, Z. B., and Wang, Q. J. (2014). Analysis on regional geological background and metallogenic predication of diamond mineralization in eastern margin of north China plate. *Shandong Land Resour.* 30 (10), 8–14+20.

Wu, F. Y., Yang, Y. H., Mitchell, R. H., Li, Q. L., Yang, J. H., and Zhang, Y. B. (2010). *In situ* U-Pb age determination and Nd isotopic analysis of perovskites from kimberlites in southern Africa and Somerset Island, Canada. *Lithos* 115 (1-4), 205–222. doi:10.1016/j.lithos.2009.12.010

Yang, B., Ma, X. X., Tang, L. L., Lu, W. Q., and Sun, X. Z. (2015). Discussion on forming age of primary diamond ore in Mengyin area of Shandong province. *Shandong Land Resour.* 31 (4), 19–21.

Yang, P., Wu, G., Nuriel, P., Nguyen, A. D., Chen, Y., Yang, S., et al. (2021). *In situ* LA-ICPMS UPb dating and geochemical characterization of fault-zone calcite in the central Tarim Basin, northwest China: Implications for fluid circulation and fault reactivation. *Chem. Geol.* 568, 120125–125. doi:10.1016/j.chemgeo.2021.120125

Yang, Y. H., Wu, F. Y., SimonWildeLiu, A. X. M., Zhang, Y. B., Xie, L. W., Yang, J. H., et al. (2009). *In situ* perovskite Sr–Nd isotopic constraints on the petrogenesis of the Ordovician Mengyin kimberlites in the North China Craton. *Chem. Geol.* 264, 24–42. doi:10.1016/j.chemgeo.2009.02.011

Yang, Z. J., Huang, S. S., Chen, Y. M., Lei, X. Y., Li, X. X., and Zeng, X. (2018). Characteristics and their geological significances of spinel minerals of kimberlite in Mengyin, Shandong province. *Bull. Mineralogy, Petrology Geochem.* 37 (2), 168–179+371.

Yin, Z. W., Lu, F. X., Chen, M. H., and Xu, H. Y. (2005). Ages and environments of formation of diamonds in Mengyin county, Shandong province. *Earth Sci. Front.* 12 (4), 614–621.

Zhang, H. F., and Yang, Y. H. (2007). Emplacement age and Sr-Nd-Hf isotopic characteristics of the diamondiferous Kimberlite from the eastern North China Craton. *Acta Petrol. Sin.* 23 (2), 285–294.

Zhang, P. Q. (2006) Origin of kimberlitic pipes in Shandong Province. PhD thesis. Beijing, China: China University of Geosciences, 24–29.

Zhang, Z. Q., Liu, S. C., Du, S. X., Shan, W., Cheng, G. S., and Zhang, S. K. (2011). Determination opinions on stratigraphic division and correlation in Shandong province. *Shandong Land Resour.* 27 (09), 1–9.

Zhao, X. F. (2019). A study of diamond indicative minerals in the depth and periphery of Xiyu, Mengyin County, Shandong Province: Metallogenic properties of kimberlite predicted by diamond indicating minerals. *Geol. Bull. China* 38 (1), 121–131.

Zhou, Q., Wu, F. Y., Chu, Z. Y., Yang, Y. H., Sun, D. Y., and Ge, W. C. (2007). Sr-Nd-Hf-Os isotopic charaeterizaitons of the Jiaohe Peridotite xenoilhts in Jilin Province and constraints on the lithosPheric mantle age in northeasetrn China. *Aeate Petrol. Sin.* 23 (6), 1269–1280.

Zhu, Y., and Mao, Z. H. (1991). Preliminary investigation on geochemical property of kimberlite isotope in Shandong. *Geol. Sci. Technol. Inf.* 10 (S1), 77–84.

Frontiers in Earth Science

Investigates the processes operating within the major spheres of our planet

Advances our understanding across the earth sciences, providing a theoretical background for better use of our planet's resources and equipping us to face major environmental challenges.

Discover the latest Research Topics

See more →



Frontiers

Avenue du Tribunal-Fédéral 34
1005 Lausanne, Switzerland
frontiersin.org

Contact us

+41 (0)21 510 17 00
frontiersin.org/about/contact